Number 7 Volume 25 1961

BULLETIN

of the

ACADEMY OF SCIENCES OF THE USSR

— PHYSICAL SERIES —

(Izvestiya Akademii Nauk SSSR)
(Seriya fizicheskaya)

Reproduction rights reserved
by
Columbia Technical Translations
5 Vermont Avenue
White Plains, New York

Single Issues
$20

Annual Subscription
$215

Lithographed in U.S.A. by
EDWARDS BROTHERS, INC.
Ann Arbor, Michigan

Transactions

of the

Eleventh Annual Conference on Nuclear Spectroscopy

(Riga, 25 January - 3 February, 1961)

(Continued from Vol.25, No.2)

NEW RESULTS IN THE THEORY OF NONAXIAL NUCLEI

- A.S.Davydov

Introduction

At the present time it is still impossible to perform exact theoretical calculations of the energy levels of heavy and intermediate nuclei consisting of relatively large numbers of nucleons. It thus becomes necessary to simplify the problem by making use of some nuclear model. On the one hand, this model must be simple enough to be handled by modern quantum mechanical techniques, and, on the other hand, it must be capable of describing a rather large amount of experimental data with the minimum possible number of empirical parameters.

In even-even nuclei the low-lying (<2 Mev) states are collective in nature and can be treated as excitations related to changes in shape and orientation of the nucleus. The characteristics of these collective excitations depend strongly on the shape of the nucleus in its ground state.

In the case of nuclei in the vicinity of the double magic numbers the ground state is spherical. The collective excitations of such nuclei involve the production of phonons of frequency ω and angular momentum 2. The theory of such excitations has been discussed by Bohr and Mottelson. Except for the degeneracy in the z-component of the angular momentum, single-phonon excitations of energy $\hbar\omega$ and angular momentum 2 give rise to a nondegenerate state. Two-phonon excitations with energy $2\hbar\omega$ are triply degenerate (I = 0, 2, 4); three-phonon excitations are quintuply degenerate (I = 0, 2, 3, 4, 6), etc.

Such a simple scheme is not observed for any even-even magic-number nucleus (or any nucleus close to it). Many nuclei with magic neutron or proton numbers (O^{16}, Ge^{72}, Zr^{90}), whose equilibrium shape is about as spherical as is possible, have first excited states with spin zero. In the case of Ge^{70}, Ce^{140} and Ca^{42} the spin-zero level lies very close to the first excited state with spin 2. In many other even-even nuclei (Cd^{114}, Pd^{110} and others) the first excited state has spin 2, and the next excited states with spins 2, 4 and sometimes 0 form a close group. Attempts have been made to identify these levels with the triplets expected from oscillation theory. In order to explain the splitting of these levels, the theory was made more complicated by introducing interaction between the surface oscillations and single-particle states (Scharff-Goldhaber, Weneser and others). Nevertheless, these theories did not explain the experimental data. The interaction of some of the nucleons with the surface must inevitably lead to a nonspherical equilibrium shape. For nuclei such as Cd and Pd the deviation from sphericity cannot be small, since their surfaces are highly deformable, as is seen from the large amplitudes of the zero-point β-oscillations. Thus, for instance, according to D.Stelson, for a typical nucleus of this type such as Pd^{110}, the value of $\sqrt{\overline{\beta^2}}$ is 0.27. It then becomes necessary even in the zeroth approximation to take account of the lack of spherical symmetry of the nucleus.

If the equilibrium shape is not spherical, then in addition to surface oscillations one must consider rotations, i.e., changes of orientation in space. If one approximates the nucleus by an ellipsoid, the shape of the nucleus for given volume will be determined by only two parameters, namely, β ($0 \leqslant \beta$) and γ($0 \leqslant \gamma \leqslant \pi/3$). To these two parameters one may add the Euler angles θ_1, θ_2 and θ_3, thus obtaining five dynamic variables which characterize the collective motion in the simplest model of even-even nuclei.

The present communication is a review of the theoretical work in which collective excitations of even-even nuclei have been treated in various approximations.

Section 1 is a brief resume of the adiabatic theory of rotational levels, in which the internal parameters β and γ are considered fixed. Section 2 outlines the theory of rotational-vibrational excitations for fixed γ. Section 3 presents the results of a general theoretical study of quadrupole excitations, which treats variation of all five dynamic variables.

1. Adiabatic Theory of Rotational States

The adiabatic theory deals only with those excited states which have to do with rotational motion of the nucleus without internal excitations, i.e., with fixed β and γ.

Until recently it was thought that all nonspherical nuclei are ellipsoids of rotation, in other words, that the equilibrium shape corresponds to the fixed value $\gamma = 0$ or 60°. If this is so, only rotation about an axis perpendicular to the axial symmetry axis is possible, and the rotational energy of an even-even nucleus will be given by the simple expression

$$E_I = AI(I+1), \text{ where } I = 0, 2, 4, \ldots$$

Then the energies of the excited states should satisfy the simple interval rule:

$$E_2 : E_4 : E_6 : E_8 : \ldots = 1 : \frac{10}{3} : 7 : 12 : \ldots$$

The belief in axial symmetry of all nonspherical nuclei was so axiomatic that fulfillment of the above energy ratio rule was taken as the criterion for the existence of a rotational spectrum in even-even nuclei. Excited states forming exceptions to the rule were identified as internal excitations, and nuclei with such spectra were considered spherical.

A recent analysis of the so-called proofs of axial symmetry has shown that they are not really convincing. Usually the authors of such proofs have in their very statement of the problem postulated that the nucleus is axially symmetric. It has been shown by several authors[1-6] that deviations from spherical symmetry are evinced in many nuclei.

If one allows that the equilibrium shape may not be axially symmetric, then even in the adiabatic approximation the rotational spectrum becomes quite complicated. The rotational states of such nuclei and the probabilities for electromagnetic transitions between them have been studied by the present author with some others[7,8] up to levels with spin 8. Recently a Canadian group[9] has extended these calculations to levels with I = 20. It has been shown that to each nuclear spin there correspond, in general, several energy levels $\frac{\hbar^2}{4B\beta_0^2}\varepsilon_\tau(I)$ with different indices τ. The relative positions of these levels and the probabilities for E2 transitions between them depend only on the single parameter γ, and the value of this parameter can be determined from the ratio of the two excited states with spin 2. Several investigators[10-13] have compared the results of this theory with experiment. All of them note that the adiabatic theory of nonaxial nuclei is able to explain satisfactorily some of the experimental data. Thus, for instance, Grigor'ev and Avotina[10] state, "...this theory correctly describes some of the effects occurring in these nuclei. Undoubtedly the theory of nonaxial nuclei is a step forward in the development of nuclear model concepts."

2. Interaction of Rotation with β-Oscillations

The adiabatic theory of rotational states of nonaxial nuclei is a considerable idealization of reality. The rotation of a nucleus is intimately related to changes in its internal state. If one considers only collective excitations, as was mentioned above, the internal excitations are specified by the dynamic variables β and γ. Our group[14-15] has investigated collective excitations without separating them into rotational and β-vibrational, though still holding the parameter fixed. In this case the ratios of the energies of the higher excited states to the energy of the first excited state are specified by two parameters, the nonaxiality parameter γ and the nonadiabaticity parameter μ. The latter is given by $(\hbar\omega/c\beta_0^2)^{1/2}$. Consequently, μ is proportional to the ratio of the mean square amplitude of the zero-point surface oscillations to the mean square equilibrium value of the parameter β_0.

For rough evaluation one may write approximately $\mu \approx \left(\frac{E_1(2)}{E_\beta(0)}\right)^{1/2}$ (for $\mu < 0.3$), where $E_1(2)$ is the energy of the first excited state with spin two, and $E_\beta(0)$ is the energy of the first β-vibrational state with spin 0.

If one sets μ = 0, one obtains the adiabatic approximation. For $\mu < 1/3$, the energies of states with spin I are given by

$$E_{\tau n}(I) = n\hbar\omega + \frac{\hbar^2\varepsilon_\tau(I)}{4B\beta_0^2}\left[1 + 3\mu^2\left(n + {}^1/_2\right)\right] - \mu^4\frac{\hbar^2}{4B\beta_0^2}\left[\varepsilon_\tau(I)\right]^2, \qquad (2.1)$$

where $\frac{\hbar^2\varepsilon_\tau(I)}{4B\beta_0^2}$ is the energy corresponding to index τ of the rotational state with spin I calculated in the adiabatic approximation.

In the adiabatic approximation (μ = 0) the excited state energy is obtained by adding the energies of surface oscillations and the rotation. For $\mu \neq 0$, there appear correction terms allowing for the interaction of the oscillations with the rotation.

For $\mu > 1/3$ the spin I collective excitation energies are given by the more complicated formula

$$\frac{E_{\tau\nu}(I)}{\hbar\omega} = \left(\nu + \frac{1}{2}\right)\sqrt{1 + \frac{3}{2}(\mu/p)^4\varepsilon_\tau(I)} + {}^1/_4\left(\frac{\mu}{p}\right)^2\varepsilon_\tau(I) + \frac{(p-1)^2}{2\mu^2}, \qquad (2.2)$$

where p is a solution of $2p^3(p-1) = \mu^4\varepsilon_\tau(I)$ and ν, in general not an integer, is a root of the equation

$$[2\Gamma(-\nu)]^{-1}\sum_{l=0}^{\infty}\frac{(-1)^l}{l!}\Gamma\left(\frac{l-\nu}{2}\right)\left(-\frac{2p}{\mu}\right)^l = 0. \qquad (2.3)$$

To every root of this equation there corresponds a rotational-vibrational band of states based on the state with spin 0. For $\mu < 1/3$ the roots of (2.3) are quite close to integers $\nu \approx n$, $n = 0, 1, \ldots$. In this case Eq.(2.2) becomes (2.1), and the collective excitations can be separated approximately into vibrational and rotational. For $\mu > 1/3$, the nucleus is quite "soft". Then its rotation is intimately connected with variations in its internal state, and the collective vibrations cannot be separated as above.

According to (2.2), the collective-state energies are given by two parameters, namely, μ and γ, and these can be determined uniquely if the energies of any three excited states are known. When the values of these two parameters are known, one can calculate the energies and spins of the other levels and the probabilities for electromagnetic transitions between them. A comparison of the theoretical calculations with experiment will be found in Ref.15.

As an illustration we give below the values obtained for μ and γ by fitting the experimental data for some specific nuclei:

Nucleus	γ, degrees	μ
Cd^{114}	23	0.54
Gd^{154}	12	0.36
Er^{166}	12	0.19
Os^{188}	19	0.25
Hg^{198}	21	0.54

In Ref.15 Davydov & Chaban also give a plot showing the variation in the energy of states with spin 6, 4 and 0 as functions of β and γ. Mallmann and his coworkers at the Argonne National Laboratory in the U.S.A. used a computer to calculate the energy levels according to (2.2) for many values of I. The resulting tables, kindly sent us by Mallmann, make it possible to compare experiment and theory much more thoroughly.

3. General Case of Quadrupole Excitation of Even-Even Nuclei

More recently our group[16,17] studied general collective excitations, treating all five parameters β, γ, θ_1, θ_2 and θ_3 as dynamic variables. It was found that the characteristics of these collective excitations in even-even nuclei depend on the ground-state shape of the nucleus; hence we shall consider the cases of spherical and nonspherical nuclei separately.

Spherical Nuclei ($\beta_0 = 0$)

Ordinarily collective excitations of spherical nuclei are dealt with in terms of phonon excited states with total spin 2 (in units of $\hbar$ and z-component $\nu = 0, \pm1, \pm2$. For this treatment one uses five dynamical variables b_ν, each of which satisfies the same oscillation equation with frequency ω.

For a more thorough comparison of the spherical case with the nonspherical one, it is convenient to use β and γ and the Euler angles as the five dynamic variables. Then the potential energy depends only on β, and for small deviations from the equilibrium position it is of the form

$$V(\beta) = \frac{C}{2}\beta^2, \quad C = \omega^2 B.$$

Jankovic[18] and the present author[16] investigated the wave functions as functions of β, γ and the θ_i. It is found[16] that the energy of spin-zero states in spherical nuclei is given by

$$E_{n\lambda}(0) = \hbar\omega\,(2n + 3\lambda), \text{ where } n, \lambda = 0, 1, 2, \ldots \tag{3.1}$$

The wave functions corresponding to this energy are

$$|\,0n\lambda\rangle = N_{n\lambda}\,(Z)^{1+3/2\lambda}\exp(-Z/2)\,F(-n, 3\lambda + {}^5/_2, Z)\,P_\lambda(\cos 3\gamma), \tag{3.2}$$

where the $P_\lambda(x)$ are Legendre polynomials, $F(-n, \alpha, z)$ is the confluent hypergeometric function, the $N_{n\lambda}$ are normalizing constants, and $Z \equiv \beta^2/\beta_{00}^2$, $\beta_{00}^2 \equiv \hbar/\sqrt{BC}$.

For $\lambda = 0$ the wave function depends only on β. Therefore the excited states with $n = 1, 2, \ldots$, may be called β-oscillations. The first excited state of this

kind has energy $E_\beta(0) = 2\hbar\omega$.

The excited states with $n = 0$, $\lambda \neq 0$ will be called γ-oscillations. The first excited state of this kind has energy $E_\gamma(0) = 3\hbar\omega$. It is possible for E0-transitions to take place between spin-zero energy levels.

The matrix element for such an E0-transition between two states is given by

$$\rho = \langle f | \mathfrak{M}(E0) | i \rangle, \tag{3.3}$$

where

$$\mathfrak{M}(E0) = \frac{3Z}{4\pi}\left(\frac{4\pi}{5} + \beta^2 + \frac{5\sqrt{5}}{21\sqrt{\pi}}\beta^3 \cos 3\gamma\right). \tag{3.4}$$

It has been shown[17] that the matrix elements for E0 transitions to the ground state from first excited β and γ states are

$$|\rho(0_\beta \to 0)| = \frac{3Z}{4\pi}\sqrt{\frac{5}{2}}\beta_0^2, \quad \text{with transition energy } 2\hbar\omega;$$

$$|\rho(0_\gamma \to 0)| = \frac{75Z}{8\pi^{3/2}\sqrt{42}}\beta_{00}^3, \quad \text{with transition energy } 3\hbar\omega.$$

Thus β and γ excited states with zero spin differ in their properties.

The matrix element for an E0 transition between the first two spin-2 excited states has also been calculated. It is

$$|\rho(22 \to 21)| = \frac{15\sqrt{5}}{8\pi^{3/2}\sqrt{14}} Z\beta_{00}^3.$$

Nonspherical Nuclei ($\beta_0 \neq 0$); $\gamma_0 = 0$

If there are some nucleons outside the filled shells or a few nucleons lacking to complete the last shell, the potential energy of the nucleus will depend on γ as well as on β. It can be shown that for small deviations from the equilibrium position at the potential energy minimum, the potential may be written in the form

$$V(\beta\gamma) = \frac{C}{2}\beta^2 + \beta\chi(\cos 3\gamma) \approx A + \frac{C}{2}(\beta - \beta_0)^2 + \frac{\beta_0^2 C_\gamma}{2}(\gamma - \gamma_0)^2. \tag{3.5}$$

Nonspherical nuclei (those with $\beta_0 \neq 0$) always have a definite sign of electric quadrupole moment (+ or -). This fact is an experimental indication that the potential energy contains a term depending on γ.

With the potential given by (3.5), the Schrödinger equation for the stationary state wave function $\Psi(\beta\gamma\theta_i) = \frac{1}{\beta^2} f(\beta)\Phi(\gamma, \theta_i)$, can be written in the form of the two equations

$$\left\{-\frac{1}{\sin 3\gamma}\frac{\partial}{\partial\gamma}\left(\sin 3\gamma \frac{\partial}{\partial\gamma}\right) + \frac{1}{4}\sum_{l=1}^{3}\frac{\hat{I}_l^2}{\sin^2\left(\gamma - \frac{2\pi l}{3}\right)} + D(\gamma - \gamma_0)^2 - \Lambda\right\} \times \Phi(\gamma_i\theta_i) = 0; \tag{3.6}$$

$$\left\{-\frac{\hbar^2}{2B}\cdot\frac{d^2}{d\beta^2} + \frac{C}{2}(\beta - \beta_0)^2 + \frac{\hbar^2(\Lambda + 2)}{2B\beta^2} - E\right\} f(\beta) = 0, \tag{3.7}$$

where

$$D = \frac{BC_\gamma\beta_0^4}{\hbar^2}, \quad C_\gamma = \omega_\gamma^2 B.$$

These equations have been treated elsewhere by the present author.[16] In spin-zero states Φ is independent of the Euler angles (pure γ-oscillations). For this case the ground state wave function is given by

$$\Phi(\gamma) = N \exp\left\{-\frac{\gamma^2}{4\Gamma^2}\right\}, \tag{3.8}$$

$$\Gamma^2 = \frac{1}{2\sqrt{D}} = \mu^2 \frac{\omega}{2\omega_\gamma}, \quad \omega_\gamma = \frac{\hbar}{2B\beta_0^2\Gamma^2}. \tag{3.9}$$

Noting that the volume element in γ-space is $\sin 3\gamma d\gamma$, we find from (3.8) that the most probable value of γ is given by $\gamma_m = \Gamma$. Thus even when the potential energy minimum corresponds to an axially symmetric nucleus, the most probable nuclear shape is not one with axial symmetry. We recall that in the ground state of a hydrogen-like atom the most probable separation between the electron and the nucleus is equal to the radius of the first Bohr orbit, while the potential energy minimum occurs at $r = 0$.

It has also been shown[17] that if one sets the parameter used in the adiabatic theory of nonaxial nuclei[7,8] to its most probable value $\gamma_m = \Gamma$ for the ground state, one can explain the ratios of the excited level energies and the probabilities for electromagnetic transitions between these states with satisfactory accuracy for nuclei in which $\gamma_m < 15°$. Thus it becomes clear that the phenomenological value of γ used in several cases[7,8,15] for nuclei with $\gamma < 15°$ can be interpreted as the most probable value γ_m in the ground state.

It has been shown[16] that for $\gamma_0 = 0$ and $\mu \approx 0$, the excitation energy for states with spin 3 is given by

$$E_{n\lambda}(3) = n\hbar\omega + 2\hbar\omega_\gamma(\lambda + {}^1/_2) + \frac{3\hbar^2}{2B\beta_0^2}.$$

Inserting the value of ω_γ from (3.9), we find that for $n = \lambda = 0$ the energy of the first excited state with spin 3 is given by

$$E_{00}(3) = \frac{\hbar^2}{2\Gamma^2 B\beta_0^2} + \frac{3\hbar^2}{2B\beta_0^2}.$$

On the other hand, according to the adiabatic theory of rotational states,[7] the energy of the level with spin 3 is

$$E_{ad}(3) = \frac{18\hbar^2}{4B\beta_0^2\sin^2(3\gamma_m)} \approx \frac{\hbar^2}{2\gamma_m^2 B\beta_0^2} + \frac{3\hbar^2}{2B\beta_0^2}, \quad \gamma_m < 15°.$$

When $\gamma_m < 15°$, it turns out that K (the projection of I on the nuclear symmetry axis) is a relatively good quantum number. In this approximation[16] the energy of the excited state with total spin I and projection thereof K is given by

$$E_{n\lambda}(IK) = n\hbar\omega + \hbar\omega_\gamma(2\lambda + K/2) + \frac{\hbar^2[I(I+1) - {}^3/_4K^2]}{6B\beta_0^2}.$$

Inserting ω_γ from (3.9), we find that for $n = \lambda = 0$

$$E_{00}(IK) = \frac{\hbar^2 K}{4B\Gamma^2\beta_0^2} + \frac{\hbar^2[I(I+1) - {}^3/_4K^2]}{6B\beta_0^2}. \tag{3.10}$$

At the same time, the adiabatic theory of rotational states, for instance, gives the following expressions for the spin 2 levels (with $\gamma_m < 15°$):

$$E_1(2) = \frac{9\hbar^2}{4B\beta_0^2} \frac{1 - \sqrt{1 - {}^8/_9\sin^2(3\gamma_m)}}{\sin^2(3\gamma_m)} \approx \frac{\hbar^2}{B\beta_0^2}; \tag{3.11}$$

$$E_2(2) = \frac{9\hbar^2}{4B\beta_0^2} \frac{1 + \sqrt{1 - {}^8/_9\sin^2(3\gamma_m)}}{\sin^2(3\gamma_m)} \approx \frac{\hbar^2}{2B\beta_0^2\gamma_m^2} + \frac{\hbar^2}{2B\beta_0^2}. \tag{3.12}$$

As may be expected, these equations agree with (3.10) for $\Gamma = \gamma_m$, when I = 2, K = 0, and when I = 2, K = 2, respectively. In particular, it follows from (3.11) and (3.12) that the approximate formula for evaluating γ_m is

$$\frac{E_2(2)}{E_1(2)} = {}^1/_2\left(1 + \frac{1}{\gamma_m^2}\right) \approx \frac{1}{2\gamma_m^2}.$$

Further, using (3.9), we can obtain from (3.11) and (3.12) the approximate equation

$$2E_2(2) - E_1(2) = 2\hbar\omega_\gamma \approx E_\gamma(0). \tag{3.13}$$

Since $E_\gamma(0) = 2\hbar\omega_\gamma$ when $\gamma_0 = 0$, we may also use (3.9) to deduce the formula

$$\Gamma^2 = \mu^2 \frac{E_\beta(0)}{E_\gamma(0)}, \tag{3.14}$$

which makes it possible to calculate $\gamma_m = \Gamma$ from the ratio of the two spin-zero levels, and vice versa. An approximate determination of the $E_\beta(0)/E_\gamma(0)$ can be obtained by using the values of μ and γ found[15] by comparing the experimental values of the spin-2 and spin-4 levels with their theoretical values. For instance, in this way one obtains $\mu = 0.25$ and $\gamma = 19^\circ$ for Os^{188}. Setting $\gamma = \Gamma$ and inserting these values into (3.14), we arrive at

$$[E_\beta(0)/E_\gamma(0)]_{\text{theo}} = \left(\frac{0.324}{0.25}\right)^2 \approx 1.68,$$

which is in good agreement with the experimental value of 1.63 for the spin-zero levels at 1765 and 1086 kev, as obtained by King and Johns.[19] We have identified[15] the higher of these levels with β-oscillations. Therefore the other must be associated with γ-oscillations. This interpretation is substantiated by the approximate agreement with Eq. (3.13). In Os^{188} the energy levels are $E_1(2) = 155$ kev and $E_2(2) = 633$ kev, so that Eq. (3.13) gives 1111 kev, which is not very different from $E_\gamma(0) = 1086.2$ kev.

Wilson and Pool[20] observed two spin-zero levels with energies 1462 and 2168 kev in Er^{166}. The energy of the first excited level with spin 2 in this nucleus is 80.7 kev. Setting at $E_\beta(0) = 2168$ kev and using the formula $\mu \approx \sqrt{\frac{E_1(2)}{E_\beta(0)}}$, we obtain $\mu \approx 0.19$. According to a previous paper[15], the effective value of γ in this nucleus is $\gamma_m = 12.4^\circ$. Using (3.14), we arrive at

$$\left[\frac{E_\beta(0)}{E_\gamma(0)}\right]_{\text{theo}} \approx \left(\frac{0.215}{0.19}\right)^2 \approx 1.26,$$

which is in satisfactory agreement with the experimental value 1.48. Equation (3.13) is approximately satisfied also for Er^{166}: we have $E_2(2) = 788$ kev, so that $2E_2(2) - E_1(r) = 1495$ kev, which is close to the experimental value $E_\gamma(0) = 1462$ kev.

In nonspherical nuclei with $\gamma_0 = 0$ and small values of μ ($< 1/3$), the energy of a spin-zero state is given by

$$E_{n\lambda}(0) = n\hbar\omega + 2\lambda\hbar\omega_\gamma.$$

The normalized wave functions for these states were given in Ref. 17. Using these functions, one can obtain the matrix element for the E0-transition from the first β-vibrational level to the ground state (the transition energy is $E_\beta(0) = \hbar\omega$):

$$\rho(0_\beta \to 0) = \frac{3\sqrt{2}Z}{4\pi}\mu\beta_0^2.$$

The corresponding transition (with energy $E_\gamma = 2\hbar\omega_\gamma$) from the first γ level to the ground state is much less probable, since its matrix element is

$$\rho(0_\gamma \to 0) = \frac{45\sqrt{5}}{28\pi^{3/2}} Z \frac{E_\beta(0)}{E_\gamma(0)} \mu^2 \beta_0^3.$$

The matrix element for the E0-transition between the first β level of zero spin and the corresponding γ level is

$$\rho(0_\beta \to 0_\gamma) = \frac{135\sqrt{5}}{28\sqrt{2}\pi^{3/2}} Z \frac{E_\beta(0)}{E_\gamma(0)} \mu^3 \beta_0^3.$$

As has been shown,[16] when one is studying states with total angular momentum $I \neq 0$, one must bear in mind that K is not a good quantum number. This question has been discussed in some detail by Belyak & Zaikin[21]. For instance, the wave functions of the first two spin-2 excited states are of the form[17]

$$\Psi_1(2) = \psi_{20} + \frac{4\sqrt{2}}{3}\Gamma^3\psi_{22},$$

$$\Psi_2(2) = \psi_{22} - \frac{4\sqrt{2}}{3}\Gamma^3(\psi_{20} + \psi_{20}^1), \qquad (3.15)$$

where

$$\psi_{IK}(\beta\gamma\theta_i) = |IK\rangle \frac{\left(\frac{\gamma^2}{2\Gamma^2}\right)^{K/2} \exp\left\{-\frac{1}{2}\left[\frac{\gamma^2}{2\Gamma^2} + \left(\frac{\beta-\beta_0}{\mu\beta_0}\right)^2\right]\right\}}{\{\sqrt{\pi}\,\mu\beta_0 (K/2)!\}^{1/2}\Gamma};$$

$$|IK\rangle = \left[\frac{2I+1}{16\pi^2(1+\delta_{K0})}\right]^{1/2}\{D^I_{MK} + (-1)^I D^I_{M,-K}\};$$

$$\psi_{20}^1 = |20\rangle \frac{\left(1-\frac{\gamma^2}{2\Gamma^2}\right)}{(\sqrt{\pi}\mu\beta_0)^{1/2}\Gamma} \exp\left\{-\frac{1}{2}\left[\frac{\gamma^2}{2\Gamma^2} + \frac{(\beta-\beta_0)^2}{\mu^2\beta_0^2}\right]\right\}.$$

By using the wave functions of (3.15), one can calculate the matrix element for the E0-transition between the two states with spin 2. One obtains

$$|\rho(22 \to 21)| = \frac{30\sqrt{10}}{7\pi^{3/2}} Z\beta_0^3\Gamma^5.$$

It can also be shown[17] that the probabilities for E2-transitions to the two spin-2 levels from both the ground state and the first β state are in approximately the same ratio:

$$\frac{B(E2;\ 0 \to 22)}{B(E2;\ 0 \to 21)} \approx \frac{B(E2;\ 0_\beta \to 22)}{B(E2;\ 0_\beta \to 21)} \approx 2\Gamma^2. \qquad (3.16)$$

This same ratio for the first γ states is quite different:

$$\frac{B(E2;\ 0_\gamma \to 22)}{B(E2;\ 0_\gamma \to 21)} \approx \frac{2}{\Gamma^2}.$$

Nonspherical Nuclei ($\beta_0 \neq 0$); $\gamma_0 \neq 0$

If the potential energy minimum of the nonspherical nucleus corresponds to $\gamma_0 > 15°$ the wave function of the zero-point γ-oscillations in the nuclear ground state is of the form[16]

$$\Phi(\gamma) = \frac{N \exp\left\{-\left(\frac{\gamma - \gamma_0}{2\Gamma}\right)^2\right\}}{\sqrt{\sin 3\gamma}}.$$

In this case the most probable value of γ is γ_0, i.e., $\gamma_m = \gamma_0$.

The excited state energies for such nuclei have been calculated.[16] The energy of a state with spin I is given by

$$E = \hbar\omega\left\{(\nu + {}^1/_2)\sqrt{1 + 3(\Lambda + 2)(\mu/p)^4} + {}^1/_2(\Lambda + 2)(\mu/p)^2 + \frac{(p-1)^2}{2\mu^3}\right\}, \qquad (3.17)$$

where

$$\Lambda = \frac{\varepsilon_\tau(I)}{2} + \frac{2\lambda + 1}{2\Gamma^2} - \frac{9}{4}\left(1 + \frac{1}{\sin^2 3\gamma_0}\right).$$

Here p is a root of the equation

$$p^3(p - 1) = (\Lambda + 2)\mu^4,$$

and ν is a root of an equation of the form of (2.3).

When $\mu < 1/3$, one finds that $\nu = n$ and $p = 1 + (\Lambda + 2)\mu^4$; therefore using (3.9) with (3.17), we find the excited state energies to be

$$\Delta E = n\hbar\omega + \lambda\hbar\omega_\gamma + \frac{\hbar^2\varepsilon_\tau(I)}{4B\beta_0^2} - \mu^4 S. \qquad (3.18)$$

Thus for small values of μ, the collective excitation energy is the sum of the energies of the β- and γ-oscillations and the rotation. The last term in (3.18) characterizes the interaction between these three kinds of excitation. When $n = \lambda = 0$, the expression for S, the correction term in (3.18), is given by

$$S \approx \frac{\hbar^2\varepsilon_\tau(I)}{8B\beta_0^2}[\varepsilon_\tau(I) + 2/\Gamma^2].$$

According to (3.18), the energy of the spin-zero first excited γ-oscillation state will be

$$E_\gamma(0) \approx \hbar\omega_\gamma = \frac{\hbar^2}{2B\beta_0^2\Gamma^2}.$$

Equation (3.13) need no longer be fulfilled. In other words, $E_\gamma(0)$ does not depend strongly on $E_2(2)$ and $E_1(2)$. It is likely that one may succeed in using this fact to answer the question of which nuclei have $\gamma_0 \neq 0$.

Conclusions

As has been pointed out above, the theory of quadrupole collective excitations in even-even nuclei can be used to explain many experimental facts. This theory has been developed, however, only for small oscillations about the equilibrium position for $\gamma_0 = 0$ and for $\gamma_0 > 15^\circ$. Still uninvestigated is the $0 < \gamma_0 < 15^\circ$ case. There has as yet been no quantitative treatment of the negative parity collective excitations observed in even-even nuclei. There is no quantitative theory of collective excitations in odd and odd-odd nuclei. There does not exist at present a theory which will give the values of the collective parameters from information about individual particle states within the nucleus; in particular, one is not yet able to calculate the potential energy of the nuclear surface as a function of γ and β. The success in explaining the moments of inertia of nuclei leads one to

hope that these problems will be solved in the future through development of theory based on methods taking into account nucleon pairing, leading to superfluidity of nuclear matter.

Moscow State University

References

1. B.T.Geilikman, Zhur.eksp.i teor.fiz., 35, 989 (1958). (Trans.Soviet Physics - JETP.)
2. D.A.Zaikin, Ibid., 35, 529 (1958). (Trans.Ibid.)
3. A.S.Davydov & G.F.Filippov, Ibid., 36, 1497 (1959). (Trans.Ibid.)
4. G.F.Filippov. Ibid., 38, 1316 (1960). (Trans.Ibid.)
5. D.V.Volkov & E.V.Inopin, Ibid., 38, 1765 (1960). (Trans.Ibid.)
6. T.D.Newton, Canad.J.Phys., 37, 944 (1959).
7. A.S.Davydov & G.F.Filippov, Zhur.eksp.i teor.fiz., 35, 440 (1958). (Trans. Soviet Physics - JETP.)
8. A.S.Davydov & V.S.Rostovskii, Ibid., 36, 1788 (1959). (Trans.Ibid.)
9. R.B.Moore & W.White, Canad.J.Phys., 38, 1149 (1960).
10. E.P.Grigor'ev & M.P.Avotina, Izv.AN SSSR, Ser.fiz., 24, 324 (1960). (Trans. Bulletin, 24, 311.)
11. D.M.Van Patter, Nucl.Phys., 14, 42 (1959/60).
12. C.A.Mallmann & A.K.Kerman, Ibid., 16, 105 (1960).
13. W.R.Kane, G.T.Emergy, G.Scharff-Goldhaber & M.McKeown, Phys.Rev., 119, 1953 (1960).
14. A.A.Chaban, Zhur.eksp.i teor.fiz., 38, 1630 (1960). (Trans.Soviet Physics - JETP.)
15. A.S.Davydov & A.A.Chaban, Nucl.Phys., 29, 209 (1960).
16. A.S.Davydov, Vestnik, Moscow State Univ., Phys.Ser., 1, 56 (1961).
17. A.S.Davydov, V.S.Rostovskii & A.A.Chaban, Ibid., 3, 67 (1961).
18. Z.Jankovic, Nuovo Cimento, 14, 1174 (1959).
19. W.J.King & M.W.Johns, Canad.J.Phys., 37, 755 (1959).
20. R.G.Wilson & M.I.Pool, Phys.Rev., 119, 262 (1960).
21. V.I.Belyak & D.A.Zaikin, Izv.AN SSSR, Ser.fiz., 25, 1163 (1961). (Trans. Bulletin, 25, No.9.)

CALCULATION OF THE PROBABILITY OF THE AUGER EFFECT

- M.A.Listengarten

1. The probability of the Auger effect has been calculated by many investigators[1-7] in the non-relativistic approximation. Comparison of the results of these calculations with the experimental data[8-10] showed that the relative intensities of the K - LL Auger lines obtained in this approximation disagree with the experimental results. This disagreement is of the order of 30-50% for medium values of the atomic number Z and reaches a factor of 3-4 in the case of elements with large Z ($Z \geqslant 80$). It might be supposed that this disagreement is due to neglect of relativistic effects. However, the relativistic calculations of Massey & Burhop[11] did not lead to any better agreement with experiment as regards the relative intensities of the K - LL group Auger lines. In view of this, we undertook new calculations for the K - LL group Auger line intensities in the relativistic approximation. Using the general formulas of quantum electrodynamics[12], we have obtained more accurate (in comparison with Ref.11) relativistic expressions for the probability of Auger transitions and have carried out numerical evaluations of these probabilities for Z = 81; in the calculations the effect of screening was taken into account by means of the Thomas-Fermi-Dirac statistical model of the atom.

The recent work of Asaad[13] also contains relativistic calculations for Z = 80. In this work screening is taken into account through the use of the non-relativistic self-consistent Hartree field. Below, our results and those given in Refs. 4, 11 and 13 are compared with each other and with the experimental data.

2. Our calculations of the Auger effect probability are based on the relativistic quantum theory of the retarded interaction of two charges. The transition occurs as a result of interaction of the electrons, which is regarded as a perturbation. The transition probability is given by the invariant theory of excitations, which was systematically developed by Akhiezer & Berestetskii[12]. The theory of the Auger effect is in many ways analogous to the theory of internal conversion. One of the differences is that, in the case of the Auger effect, one must allow for indistinguishability of the electrons participating in the process.

The Auger effect is a second-order process. In the initial state no photons are present and the two electrons are in individual states A and B. In the case under consideration, these electrons will be two L electrons described by the wave functions $\psi_A \equiv \psi_{L_a}(\mathrm{r})$ and $\psi_B \equiv \psi_{L_b}(\mathrm{r})$ in the static field of the nucleus and the other atomic electrons ($a, b = 1, 2, 3$ for the L_{I}, L_{II} and L_{III} shells, respectively). In the final state of the system, the electrons occupy two new individual states C and D, and again there are no photons present. The final state of the electron, which has occupied the vacancy in the K shell, is described by the wave function $\psi_D \equiv \psi_K(\mathrm{r})$. The state of the other electron, which has left the atom, lies in the continuum and is described by the wave function $\psi_C \equiv \psi_\infty(\mathrm{r})$.

The matrix element of the energy perturbation which determines the transition probability is[12]

$$U_{i\to f} = U_{AB;\,CD} - U_{AB;\,DC}\,. \qquad (1)$$

The second term, preceded by the minus sign in (1), is obtained from the first by exchange. The graphical representation of the second-order scattering matrix element ${}^{e}S^{(2)}_{i\to f}$ also includes two diagrams: a direct one and an exchange one. The presence of the second term in (1) is a consequence of the antisymmetry of the two-electron wave function. Following Akhiezer & Berestetskii[12], we write the matrix element $U_{AB;\,CD}$ in the form

$$U_{AB;\,CD} \equiv U_{ab} = e^2 \iint \psi^*_{\infty}(\mathbf{r}_1)\,\psi^*_K(\mathbf{r}_2)\,\frac{1-\vec{\alpha}_1\cdot\vec{\alpha}_2}{|\mathbf{r}_1-\mathbf{r}_2|}\,e^{ik_b|\mathbf{r}_1-\mathbf{r}_2|}\,\psi_{L_a}(\mathbf{r}_1)\times\psi_{L_b}(\mathbf{r}_2)\,(d\mathbf{r}_1)\,(d\mathbf{r}_2); \qquad (2)$$

here the ψ with the indices K, L_a, L_b and ∞ are time independent parts of the four-component wave functions of the electron in the states mentioned above; $k_b = E_{L_b} - E_K$, where E is the energy of the electron. The vector Dirac matrix operators $\vec{\alpha}_1$ and $\vec{\alpha}_2$ operate on the wave functions of the electron with coordinates $\mathbf{r}_1$ and $\mathbf{r}_2$, respectively. In Eq.(2), and in most of the numerical calculations, we have used relativistic units $\left(\hbar = m = c = 1;\ e^2 = \frac{1}{137}\right)$. The exchange matrix element $U_{AB;\,DC}$ is distinguished from $U_{AB;\,CD}$ by interchange of the final states CD or initial states AB of the electrons (interchange of a and b).

For large Z a system consisting of six L electrons (or two vacancies formed as a result of the Auger effect) is described with adequate accuracy by the quantum numbers of relativistic single-electron states in a central field. In this approximation (jj-coupling) the K - LL group of Auger electrons is split into six lines: $K - L_aL_b$ $(a, b = 1, 2, 3)$. Each of the six transition probabilities w_{ab} is given by

$$w_{ab} = 2\pi \sum_{\mu_{L_a},\,\mu_{L_b},\,\varkappa_\infty} |U_{ab} - U_{ba}|^2\,\delta(E_{L_a} + E_{L_b} - E_K - E_\infty). \qquad (3)$$

The quantum number $\varkappa = (l - j)(2j + 1)$, where l is the orbital angular momentum and j the total angular momentum of the electron; μ_{L_a} and μ_{L_b} are the Z-components of the total angular momentum of the electrons in the L shell; δ is the delta-function; $\varkappa_\infty$ is the value of $\varkappa$ in the continuum state. Summation and averaging over the two states of the K electron gives the factor 1.

3. To integrate over the angles ϑ_1, φ_1 and ϑ_2, φ_2 in Eqs.(2) and (3) we use the expansions[12,14]

$$\frac{1}{|\mathbf{r}_1-\mathbf{r}_2|}\,e^{ik|\mathbf{r}_1-\mathbf{r}_2|} = 4\pi ik \sum_{LM} \Phi_L(r_1, r_2)\,Y_{LM}(\vartheta_1, \varphi_1)\,Y^*_{LM}(\vartheta_2, \varphi_2); \qquad (4)$$

$$\frac{\vec{\alpha}\,\vec{\alpha}_2}{|\mathbf{r}_1-\mathbf{r}_2|}\,e^{ik|\mathbf{r}_1-\mathbf{r}_2|} = 4\pi ik \sum_{LM\lambda} \Phi_{L+\lambda}(r_1, r_2)\,(\vec{\alpha}_1\mathbf{Y}^{(\lambda)}_{LM}(\vartheta_1,\varphi_1))\,(\vec{\alpha}_2\mathbf{Y}^{(\lambda)*}_{LM}(\vartheta_2, \varphi_2)); \qquad (5)$$

$Y_{LM}(\vartheta,\varphi)$ is a spherical harmonic; $\mathbf{Y}^{(\lambda)}_{LM}(\vartheta, \varphi)$ is a spherical vector with components (see Refs.12,14)

$$[\mathbf{Y}^{(\lambda)}_{LM}(\vartheta, \varphi)]^\nu = -\,C^{LM}_{L+\lambda,\,\mu-\nu;\,1\nu}\,Y_{L+\lambda;\,M-\nu}(\vartheta, \varphi); \qquad (6)$$

$C^{lm}_{l_1m_1;\,l_2m_2}$ are the Clebsch-Gordan coefficients;

$$\Phi_L(r_1, r_2) = \begin{cases} h_L(kr_1)\,j_L(kr_2) & \text{for } r_1 > r_2, \\ j_L(kr_1)\,h_L(kr_2) & \text{for } r_2 > r_1; \end{cases} \qquad (7)$$

$j_L(kr)$ and $h_L(kr)$ are spherical Bessel and Hankel functions (see, for example, Schiff[15]).

The relativistic wave functions of an electron in a central field have the form[12,14]:

$$\Psi_{\varkappa;\,\mu}(\mathbf{r}) = \begin{pmatrix} -iF_\varkappa(r)\,\hat{Y}^{(-\tau)}_{j\mu}(\vartheta, \varphi) \\ G_\varkappa(r)\,\hat{Y}^{(\tau)}_{j\mu}(\vartheta, \varphi) \end{pmatrix}; \qquad (8)$$

$\hat{Y}^{(\tau)}_{j\mu}$ is a spherical spinor with components[12,14]:

$$[\hat{Y}^{(\tau)}_{j\mu}]_\sigma = (-1)^{\sigma-1/2} C^{j\mu}_{j+\tau;\,\mu+\sigma;\,1/2,\,-\sigma}\, Y_{j+\tau,\,\mu+\sigma}(\vartheta, \varphi), \qquad \tau = l - j = \pm 1/2, \quad \sigma = \pm 1/2 \tag{9}$$

$F_\varkappa(r)$ and $G_\varkappa(r)$ are radial wave functions and are given by the solution of the set of differential equations

$$\frac{dG_\varkappa}{dr} = -\frac{\varkappa+1}{r} G_\varkappa + (E - eV(r) + 1) F_\varkappa,$$
$$\frac{dF_\varkappa}{dr} = \frac{\varkappa-1}{r} F_\varkappa - (E - eV(r) - 1) G_\varkappa; \tag{10}$$

E is the total electron energy, including the rest energy mc^2; $eV(r)$ is the potential energy of the electron in the field of the nucleus and the other atomic electrons. Inserting (4)-(9) into (2) and (3) and performing the angle integrations of the product of the three spherical functions over their angles ϑ_1, φ_1 and the three spherical functions over their angles ϑ_2, φ_2, we obtained expressions for the probabilities w_{ab} expressed in terms of the sum of the radial double integrals with numerical factors.* The integrals are of the form

$$I^{(n)}_{ab} = k \int_0^\infty \left\{ R_\varkappa(r) R_{L_a}(r) h_n(kr) \int_0^r j_n(kr') R_K(r') R_{L_b}(r') r'^2 dr' + \right.$$
$$\left. + R_K(r) R_{L_b}(r) h_n(kr) \int_0^r j_n(kr') R_\varkappa(r') R_{L_a}(r') r'^2 dr' \right\} r^2 dr, \tag{11}$$

where $R(r)$ are the radial wave functions (F and G); here, $\varkappa = \varkappa_\infty$ and $k = k_b$; the indices a, b, n and $\varkappa$ take on the values $a = 1, 2, 3$; $b = 1, 2, 3$; $n = 0, 1, 2$; $\varkappa_\infty = \pm 1, \pm 2, \pm 3$. To find the six probabilities w_{ab} for a given value of Z it is necessary to calculate 158 integrals of the form (11) with different combinations of the wave functions F and G and different sets of the indices a, b, n and $\varkappa_\infty$.

4. The electron wave functions of L electrons must be calculated in the field of an atom lacking one K electron. For the continuum electron, the wave function must be calculated in the field of an atom lacking two L electrons.

The region of the atom which is relevant to the Auger effect is at the same time the region where the statistical model is most applicable. Accordingly, the Thomas-Fermi-Dirac statistical model of the atom (the Thomas-Fermi model taking into account exchange) can be used to allow for screening in the calculations. In the Thomas-Fermi-Dirac atom, the potential $V(r)$ in Eq.(10) will be

$$eV = -\frac{e^2 Z}{r} \chi(r) - e^2 \gamma(r) + \frac{e^4}{2\pi^2}, \tag{12}$$

where $\chi(r)$ is the Thomas-Fermi-Dirac function (to find its numerical values in our case, we interpolated in the tables of Metropolis & Reitz[16] and Thomas[17] for Z = 81); $e^2\gamma(r)$ is the potential of the missing electrons. It is permissible to ignore the small correction $e^4/2\pi^2$ in view of the estimated accuracy (2-3%) of the calculations. The correction $e^2\gamma(r)$ is also much smaller than the leading term $\frac{e^2 Z}{r}\chi(r)$ in the region of the K and L shells and was taken into account only in

---

*On correction of a trivial misprint in Ref.13, the formulas of Assad coincide with those with which we began our calculations in 1957.

calculating the continuum wave functions. For the discrete spectrum wave function, the correction $e^2\gamma(r)$ was not taken into account, and for the bound states we took the radial wave functions that were used by Sliv & Band[18] in calculating internal conversion coefficients. The continuum wave functions were calculated by numerical integration of the set (10). The solution was in the form of a series[19] starting with $r = 0$. The continuum wave functions were normalized by the requirement

$$\int_0^\infty [F(r, E)\,F(r, E') + G(r, E)\,G(r, E')]\,r^2 dr = \delta(E - E') \qquad (13)$$

by a method analogous to that used by Sliv & Band[18]. That is to say: for sufficiently large $r\,(r=\tilde{r}\approx 40\text{-}50$ rel.units), when $eV(\tilde{r}) \ll E \approx 1$, the functions $F(\tilde{r})$ and $G(\tilde{r})$ were expressed as a linear combination of $j_\varkappa(p\tilde{r})$ and $n_\varkappa(p\tilde{r})$ ($n_\varkappa(p\tilde{r})$ is the spherical Neumann[15] function), and $p = \sqrt{E^2 - 1}$). This gives two equations for finding the coefficients A and B for $j_\varkappa(p\tilde{r})$ and $n_\varkappa(p\tilde{r})$. The normalization factor N is given by

$$N = \sqrt{\frac{p(E^2+1)}{\pi(A^2+B^2)}}\,. \qquad (14)$$

The energy E of the electron in the continuum was determined on the basis of experimental values. Since there are no measurements for Z = 81, we used the values of Bergström & Hill[20] for ΔZ (ΔZ = 0.54, 0.55 and 0.76 for L_I, L_{II} and L_{III} shells, respectively) and the tabulated K and L shell electron binding energies for Z = 81. In the work of Asaad[7], expressions are given for the Auger electron energy in the intermediate coupling approximation; however, absolute energy values obtained by using these expressions are no better than the values found by means of the empirical parameter ΔZ (see Ref.10).

5. The integration in Eq.(11) was carried out numerically on an M-20 computer. Each of the integrals in (11) is complex. For $n = 0$, the real parts of the integrals $\mathrm{Re}\,(I)$ proved to be of the same order of magnitude as the imaginary parts $\mathrm{Im}(I)$. For $n = 1$ and 2, $\mathrm{Re}\,(I) \ll \mathrm{Im}\,(I)$. After addition of all the integrals of the form (11) that enter into each of the $|U_{ab} - U_{ba}|^2$ terms in (3), we found that $[\Sigma\,\mathrm{Re}\,(I)]^2/[\Sigma\,\mathrm{Im}(I)]^2 \lesssim 1\%$.

6. The results of our calculations are presented in Tables 1 and 2. For convenience of comparison with the results of Massey & Burhop[11] and Asaad[13] the transition probabilities are expressed in atomic units. Also shown in Tables 1 and 2 are the results of calculations in the non-relativistic approximation for Z ≈ 80.

In Table 3 the calculated intensities of the K-LL lines are compared with the results of recent measurements. From the results of the calculations it follows that the total probability for K - LL transitions, computed with the aid of relativistic wave functions, is more than double the corresponding non-relativistic value. The greatest increase is that of the probability for K - L_1L_1 and K - L_1L_2 Auger transitions. Although the probability of an Auger transition involving only p-electrons is virtually unchanged as a result of taking into account relativistic effects, the comparative importance of K - L_2L_2, K - L_2L_3 and K - L_3L_3 transitions is significantly reduced. This fully agrees with the experimental results. Comparing our data and the results of Asaad[13] with experiment (see Table 2 in Ref. 10) we see that the experimental (K - L_1L_2)/(K - L_1L_1) and (K - L_1L_3)/(K - L_1L_1) ratios are somewhat closer to the results of our calculations, whereas the other three ratios are closer to the values of Asaad. On the other hand, although the (K - L_1L_2)/(K - L_1L_1)/(L - L_1L_1) and (K - L_1L_3)/(K - L_1L_1) ratios as measured by Nall, Baird & Haynes[23] are closer to the values of Asaad, their (K - L_2L_3)/(K - L_1L_1) ratio is closer to our data. The theoretical (K - L_2L_2)/(K - L_1L_1) ratio

Table 1

Transition probabilities for the K - LL Auger electrons per 10^3 atomic time units, calculated on the basis of different assumptions

Line	Nonrelativistic calculations		Calc. in relativistic approximation		
	Z = 79 T-F Ref. 4	Z = 80 H Ref. 13	Z=79 HF Ref. 11	Z=80 H Rf. 13	Z = 81 T-F-D our calc.
$K-L_1L_1$	2,02	2,04	1,74	9,01	10,12
$K-L_1L_{2+3}$	7,10	7,16	18,73	20,32	26,36
$K-L_{2+3}L_{2+3}$	19,25	17,58	—	19,86	19,41
$\Sigma K-LL$	28,37	26,78	—	49,19	55,89

Note: The transition probability per second can be found by multiplying the figures in the table by $4.134 \cdot 10^{13}$. The width in electronvolts can be obtained from the tabulated figures by multiplying by $27.2 \cdot 10^{-3}$.

Symbols indicating the method used to take screening into account: HF - hydrogen-like functions with replacement of Z by Z - σ, where σ is the Slater screening constant; T-F or T-F-D - Thomas-Fermi or Thomas-Fermi-Dirac statistical potential; H - Hartree self-consistent field. The same designations are used in Tables 2 and 3.

Table 2

Comparison of the transition probabilities to different states of the continuum ($\varkappa = \varkappa_\infty$) per 10^3 atomic time units, calculated on the basis of different assumptions

Line	Final state	Z = 79 HF Ref. 11	Z = 80 H Ref. 13	Z = 81 T-F-D our calc.	Line	Final state	Z = 79 HF Ref. 11	Z = 80 H Ref. 13	Z = 81 T-F-D our calc.
$K-L_1L_1$	$\varkappa=-1$	1,74	9,01	10,12	$K-L_2L_2$	$\varkappa=-1$	—	0,78	0,56
$K-L_1L_2$	$\varkappa=-2$	0,62	0,05	0,39	$K-L_2L_3$	$\varkappa=-3$	—	7,25	6,72
	$\varkappa=+1$	8,90	12,91	16,79		$\varkappa=-1$	—	0,24	0,29
	$\Sigma K-L_1L_2$	9,52	12,96	17,18		$\varkappa=+2$	—	5,69	6,26
$K-L_1L_3$	$\varkappa=+3$	—	0,04	0,04		$\Sigma K-L_2L_3$	—	13,18	13,27
	$\varkappa=+1$	0,10	0,14	0,17	$K-L_3L_3$	$\varkappa=-3$	—	4,20	4,20
	$\varkappa=-2$	9,11	7,19	8,97		$\varkappa=-1$	—	0,90	0,75
	$\Sigma K-L_1L_3$	9,21	7,37	9,18		$\varkappa=+2$	—	0,80	0,63
						$\Sigma K-L_3L_3$	—	5,90	5,58

is in any case <0.1. Experimental measurement of this ratio is difficult owing to the fact that the K - L_2L_2 line is the weakest line of the K - LL group. It will be evident from Table 3 that different authors report strongly divergent values for the relative intensity of this line.

7. Using the experimental [(K - LX) + (K - XY)] /(K - LL) ratio (Ref.10 and the data of Table 1), we find that the width of the Auger K level for a Z = 81 atom is Γ_a = 2.52 ev. The radiation width Γ_x for Z = 81 can be found by increasing Asaad's[13] Z = 80 value for the $K \to L_{II}, L_{III}$ transition probability (1713 atomic units) by $(81/80)^4$ and recalling that for x-ray transitions [K—(MNO)] /(K—L) = = 1.29 (Ref.24). This gives Γ_x = 63.2 ev. Consequently, the K fluorescence yield $\omega_K = \Gamma_x/(\Gamma_x + \Gamma_a) = 0.962$. The average experimental value for Z = 81 is $\omega_K = 0.955 \pm$ ± 0.005 (Ref.24).

Table 3

Comparison of the calculated and experimental relative intensities of K - LL Auger lines for heavy elements

Line	Theory				Experiment				
	nonrel. approx.	relative approximation							
	Z = 79 H Ref. 13	Z = 79 HF (Ref. 11)	Z = 80 H (Ref. 13)	Z = 81 F-D our data	Z = 75 Ref. 21 1960	Z = 78 Ref. 22 1959	Z = 80 Ref. 10*	Z = 80 Ref. 23 1960	Z = 94 Ref. 22 1959
$K-L_1L_1$	1,00	1,0	1,00	1,00	1,0	1,0	1,0	1,00	1,00
$K-L_1L_2$	1,18	5,5	1,44	1,70	1,4	1,4 ± 0,25	1,6	1,32 ± 0,10	1,86 ± 0,10
$K-L_1L_3$	2,33	5,3	0,82	0,91	1,1	0,9 ± 0,2	0,9	0,85 ± 0,06	0,65 ± 0,08
$K-L_2L_2$	0,25	—	0,09	0,06	0,10 ± 0,05	0,2 ± 0,1	0,15	0,40 ± 0,03	0,11 ± 0,04
$K-L_2L_3$	5,34	—	1,46	1,31	2,0	1,4 ± 0,25	1,5	1,28 ± 0,08	1,11 ± 0,07
$K-L_3L_3$	3,03	—	0,66	0,55	0,95	0,8 ± 0,2	0,7	0,76 ± 0,05	0,40 ± 0,05

*Average values from several experimental investigations prior to 1960.

8. In order to compare the predictions of theory with the experimental results for $Z > 90$, we must have accurate calculations in this region as well. In addition, we also need precise calculations for $Z \approx 60$, so that in this Z region we may distinguish relativistic effects from those having to do with the intermediate coupling approximation, which may be noticeable in this region. We are undertaking such calculations.

The present investigation was proposed by L.A.Sliv and partially carried out in the Physical-Technical Institute. The computer programing and numerical integration were performed by O.K.Daugavet and E.F.Ozerova, to whom the author is deeply indebted. The author would also like to thank B.S.Dzhelepov for his interest in the work.

Scientific Research Physical Institute,
Leningrad State University

References

1. G.Wentzel, Z.Phys., 43, 524 (1927).
2. L.Pincerle, Nuovo Cimento, 12, 81 (1935).
3. E.H.S.Burhop, Proc.Roy.Soc.A, 148, 272 (1935).
4. E.Ramberg & F.Richtmyer, Phys.Rev., 51, 913 (1937).
5. R.Rubinstein & J.Snyder, Ibid., 97, 1653 (1955); 99, 189 (1955).
6. V.Mokhov & M.Urin, Zhur.eksp.i teor.fiz., 30, 209 (1956).
7. W.N.Asaad & E.H.S.Burhop, Proc.Phys.Soc., 71, 369 (1958).
8. E.H.S.Burhop, Auger Effect and Other Radiationless Transitions. Cambridge, 1952.
9. I.Bergström, in Beta- and Gamma-Ray Spectroscopy, edited by Kai Siegbahn, N.Y., 1955.
10. M.A.Listengarten, Izv.AN SSSR, Ser.fiz., 24, 1041 (1960). (Trans.Bulletin, 24, 1050.)
11. H.Massey & E.H.S.Burhop, Proc.Roy.Soc.A, 153, 661 (1936).
12. A.I.Akhiezer & V.B.Berestetskii, Kvantovaya elektrodinamika (Quantum Electrodynamics), Ch.VII, M., 1953.
13. W.N.Asaad, Proc.Roy.Soc., 249, 555 (1959).

14. V.B.Berestetskii, A.Z.Dolginov & K.A.Ter-Martirosyan, Zhur.eksp.i teor. iz., 20, 527 (1950).
15. L.I.Schiff, Quantum Mechanics, N.Y., 1955.
16. M.Metropolis & J.Reitz, J.Chem.Phys., 19, 555 (1951).
17. L.Thomas, J.Chem.Phys., 22, 1758 (1954).
18. L.A.Sliv & I.M.Band, Tablitsy koeffitsientov vnutrennei conversii γ-luchei, h.I.K-obolochka (Tables of internal conversion coefficients, Part I - K shell; art II - L shell. M., 1956/8; I.M.Band, V.N.Guman & G.A.Sogomonova, Tablitsy adial'nykh funktsii i faz elektronov (Tables of electron radial functions and hases), M.-L., 1959.
19. L.A.Sliv & B.A.Volchek, Tablitsy kulonovskikh faz i amplitud, (Tables of oulomb phases and amplitudes), M.-L., 1956.
20. I Bergström & R.Hill, Arkiv fys., 8, 21 (1954).
21. J.O.Newton, Phys.Rev., 117, 1529 (1960).
22. G.T.Evan, J.S.Geiger, R.L.Graham & D.R.McKenzie, Canad.J.Phys., 37, 174 (1959).
23. J.C.Nall, Q.L.Baird & S.K.Haynes, Phys.Rev., 118, 1278 (1960).
24. A.Wapstra, G.Nijgh & R.van Lieshout, Nuclear Spectroscopy Tables. Amsterdam, 1959.

INVESTIGATION OF THE DECAY SCHEME OF Gd^{147}

- A.A.Sorokin & K.P.Mitrofanov

Introduction

The decay of neutron-deficient Gd^{147} (T = 35 hr) has been studied by a number of investigators.

Bashilov's group[1,2] used a Ketron type spectrometer with a resolution of 0.5% to investigate photoelectrons and conversion electrons from the gadolinium fraction of neutron-deficient rare earth isotopes obtained by spallation of tantalum. On the basis of the decay period there were identified a number of γ-transitions following decay of Gd^{147} to Eu^{147}, and there were determined the conversion coefficients and multipole orders of some of these transitions. Dzhelepov et al[3] used a twin β-spectrometer to investigate e-e coincidences and established that the 229 and 396 kev γ-rays are in cascade. The results of Shirley, Smith & Rasmussen[4] are generally in agreement with the data of Refs.1-3.

On the basis of the data available at that time there was proposed in Ref.1 the tentative decay scheme for Gd^{147} shown in Fig.1. The existence of the 229 and 625 kev levels in Eu^{147} was reliably established. The other levels were introduced on the basis of energy and intensity balance considerations, and their locations can be justified only by recourse to other methods, in particular, to the method of coincidences.

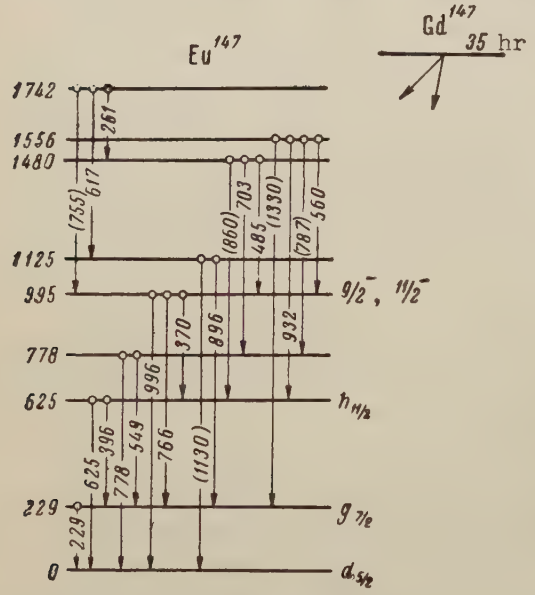

Fig.1. Level diagram of Eu^{147}, proposed in Ref.1.

Finally, Berlovich et al[5] showed that the 625 kev state is metastable. The lifetime of this state, measured by the method of delayed coincidences, proved to be $(7.2 \pm 0.3) \cdot 10^{-7}$ sec.

In the present work we investigated the decay of Gd^{147} by means of a coincidence scintillation spectrometer and a BML type two-lens magnetic β-spectrometer. The Gd^{147} was present in the gadolinium fraction of the neutron-deficient rare earth isotope obtained by proton bombardment of tantalum. The measurements were usually started some 10-20 hours after the end of bombardment.

Conversion Electron Spectrum

The section of the conversion electron spectrum in the range above 1 Mev, obtained on the BML spectrometer, is shown in Fig.2. In addition to the conversion lines of the 1070, 1130 and 1330 kev transitions, observed by the Bashilov group[1], there are discernible lines corresponding to transitions of 1580, 1675 and 1810 kev energy. Their intensity fell off with a period close to 35 hours, which justifies attributing them to Gd^{147}. In view of the rise of the counting rate above the background in the 1400 to 1500 kev region, it may be inferred that there are weak transitions in this region. In the region of lower energies, in addition to the transitions reported in Ref.1, we detected a transition of 310 kev energy, which was mentioned by Shirley et al[4]. In other respects, our data are in good agreement with the results of Ref.1 (allowing for the poorer resolution of our spectrometer).

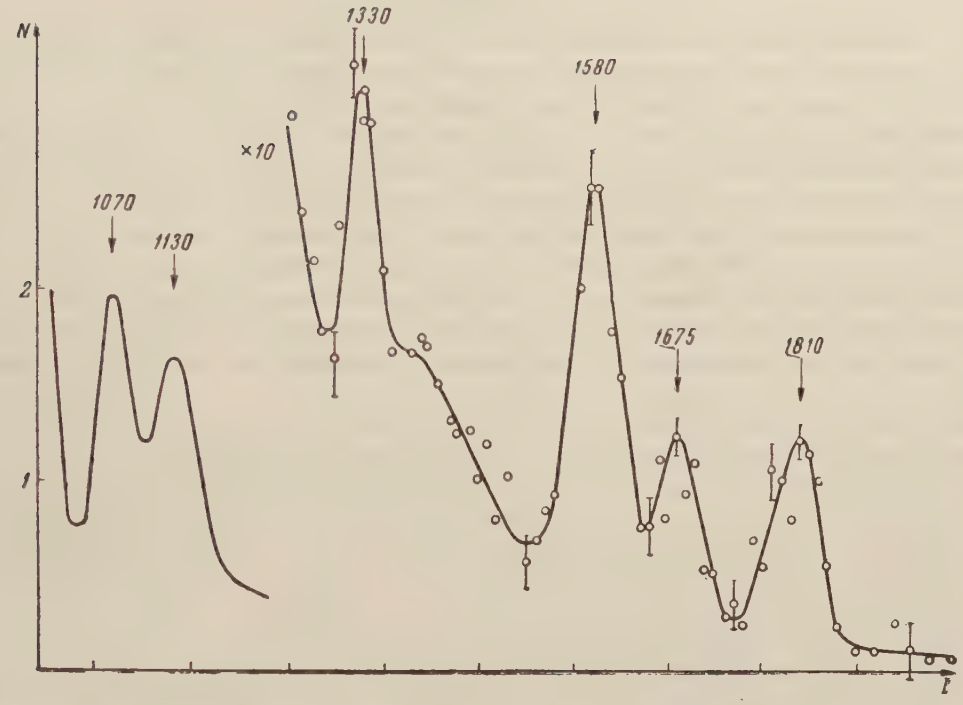

Fig.2. Conversion electron spectrum in the >1 Mev region. The horizontal scale is laid off in values of the current in the spectrometer coil in arbitrary units. The figures at the peaks indicate the γ-ray energies in kev.

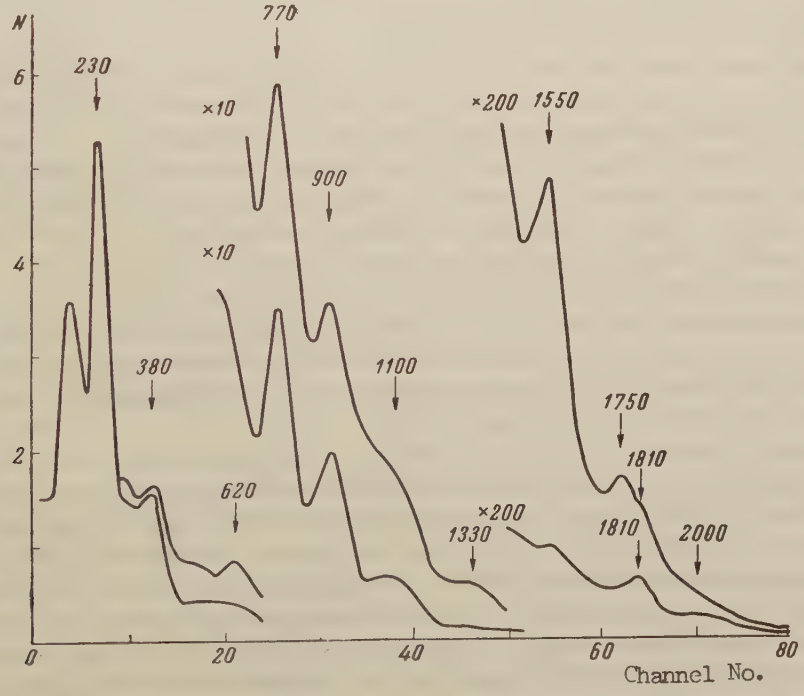

Fig.3. Gamma-ray spectrum of the Gd fraction. Lower curves - spectrum obtained with a source-to-crystal distance of 6 cm. Upper curves - "sum" spectrum.

Gamma-Spectrum

The γ-ray spectrum was measured on a scintillation spectrometer with a 4 x 4 cm NaI(Tl) crystal (half-width of the Cs^{137} 660 kev line ~10%). As follows from the results of Bashilov et al[1], the γ-spectrum of Gd^{147} is very complicated, and many of the observed lines may actually be the result of superposition of several close lines. In addition, in the investigated activities there were present long-lived Gd and Eu isotopes, also emitting a complicated γ-spectrum. Nevertheless, from such measurements one can derive some information on the relative intensities of a number of γ-transitions, particularly in the high energy regions ($\gtrsim$900 kev). In recording the γ-spectrum shown in Fig.3 there were detected γ-rays of up to ~2.3 Mev energy (lower curves). The data on the γ-radiations from Gd^{147} obtained from analysis of the recorded γ-spectrum are summarized in the accompanying table.

Energies and intensities of the Gd^{147} γ-rays, and the K conversion coefficients of some of the transitions

E_γ, keV	I_γ	I_{e_K} [1,2]	α_K	Multipole order	E_γ, keV	I_γ	I_{e_K} [1, 2]	α_K	Multipole order
230	100	100	0,16*	$M1$*	890	14	0,29		
370	23*	6,8	0,051*	$M1$*	930	37	0,86	$3{,}7\cdot10^{-3}$	$M1$, $E2$
395	48*	45	0,15	$M2$*	1070	14	0,05	$5{,}3\cdot10^{-4}$	$E1$
480	(5,5)	0,77	(0,02)	($M1$)	1130	15	0,06	$6\cdot10^{-4}$	$E1$
540	} ~45				1330	2,2	0,006	$3{,}8\cdot10^{-4}$	$E1$
560					1470**	$\leqslant$0,05			
625					1580	~1,3			
705**	~6				1675	~0,7			
770	40				1810	1,4			

*See Refs.1 & 2.

**Transitions brought out by graphic resolution of the γ-spectrum.

The uncertainty in determining the relative intensities of the γ-transitions is appreciable (~30%), owing to the noted complexity of the spectrum and the contributions from longer lived isotopes. It must be noted, however, that the contributions from longer lived impurities during the first 2-3 days after bombardment is relatively small inasmuch as the closest period is appreciable, namely, 10 days (Gd^{149}).

In the spectrum shown in Fig.3 there were observed γ-rays in the ~2 Mev region belonging to neutron-deficient impurities with longer lives than Gd^{147}. The peak located to the left of the 230 kev line is presumably due to 115 and 150 kev γ-rays from long-lived Gd^{146} and Gd^{149}.

The upper curves in Fig.3 represent the spectrum obtained under the following conditions: the source was clamped between the crystals of the two counters which were connected to a linear summing circuit. The amplification factors of the two photomultipliers were equalized, and the pulses from the summing circuit were fed into a 100-channel analyzer. This arrangement resulted in increase in the intensity of the peaks corresponding to the energy sum of the cascade γ-rays. The "singles" and "sum" spectra in Fig.3 have been matched to the 230 kev peak. In this case there resulted increase in the intensity of the 620, 1100, 1330, 1550 and 1750 kev peaks. The increase in the height of the 1550 kev peak is particularly appreciable. On the other hand, the heights of the 770 and 900 kev peaks did not increase. The increase in the counting rate in the corresponding channels

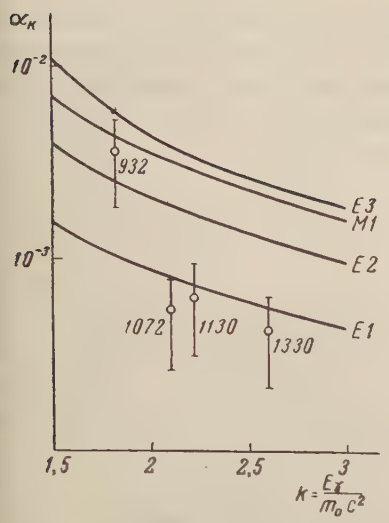

Fig.4. Comparison of the experimental and theoretical[6] values of α_K for the 932, 1070, 1130 and 1330 kev transitions.

is explained by the contribution from harder γ-rays. It is interesting to note that the enumerated energies (except 1330 kev) are close to the Eu^{147} level energies inferred in Ref.1. The results of the "sum" spectrum measurements were taken into account in further investigation of the γ-γ coincidence spectra.

Using our data on the relative intensities of the 229, 932, 1070, 1130 and 1330 kev γ-rays and the data of Ref.1 on the relative intensities of the conversion electron lines, we evaluated the K-shell conversion coefficients. The results of comparison of our experimental values of α_K with the theoretical values[6] for E1, M1, E2 and E3 transitions are shown in Fig.4. Despite the great uncertainty in determining the coefficients (~60%), it may be concluded that the 1070, 1130 and 1330 kev transitions are in all probability type E1. The value of α_K for the 932 kev transition lies between the theoretical values for M1 and E2, but if one takes into account the possible uncertainty one cannot fully exclude E3 either. However, in view of the fact that K/L = 7.1 ± 0.5 (Ref.1) it may be asserted that this transition is M1, E2 or a mixture thereof, but not E3.

Gamma-Gamma Coincidences

In investigating the coincidence spectra we utilized the fact[5] that the 625 kev state in Eu^{147} is an isomeric one with an appreciable lifetime. Hence one can distinguish between "prompt" cascades and cascades going through the isomeric level. To this end one must measure the "prompt" coincidences with a sufficiently short resolving time of the coincidence circuit τ_{cc} and the "delayed" coincidences with a delay $\tau_{cc} < \tau_d \approx \tau_{is}$, where τ_{is} is the lifetime of the isomeric state (in this case $\tau_{is} \approx 1$ microsec). In our experiments the "prompt" coincidences were measured with $\tau_{cc} = 7 \cdot 10^{-8}$ sec, and the "delayed" coincidences with $\tau_{cc} = 2 \cdot 10^{-7}$ sec.

The spectra of "prompt" and "delayed" coincidences with the 230 kev γ-rays are shown in Figs.5 and 6. In the "prompt" coincidence spectrum there are evident peaks due to γ-rays of 310, 390, 540, 760, 890, 1130, 1330 and 1580 kev energy. In the "delayed" coincidence spectrum there are observed peaks at 370, 560 and 930 kev (there were also obtained indications of weak γ-rays in the 0.6-0.75 kev region). In neither case is there any indication of coincidences with the hard 1070, 1675 and 1810 kev γ-rays.

The existence of a number of other cascades was established in measurements by the summing or "adding upon coincidence" technique described by Hoogenboom[7] and used by us in an earlier investigation[8]. In the present experiment the sum analyzer gate was set at 1560 kev. As was noted above, at this energy there appears an intense "sum" peak. Moreover, it could be assumed that at this energy setting the contribution from cascades with a larger energy sum would be small and would not distort the results. The results of these measurements are shown in Fig.7. It will be evident that there appear peaks at 230, 480, 630, 770, 930, 1070 and 1330 kev, which can be interpreted as evidence of 230-1330, 480-1070, 630-930 and 770-770 kev cascades. The existence of the first of these was established in the measurements of the "prompt" coincidences with the 230 kev γ-rays. One could ex-

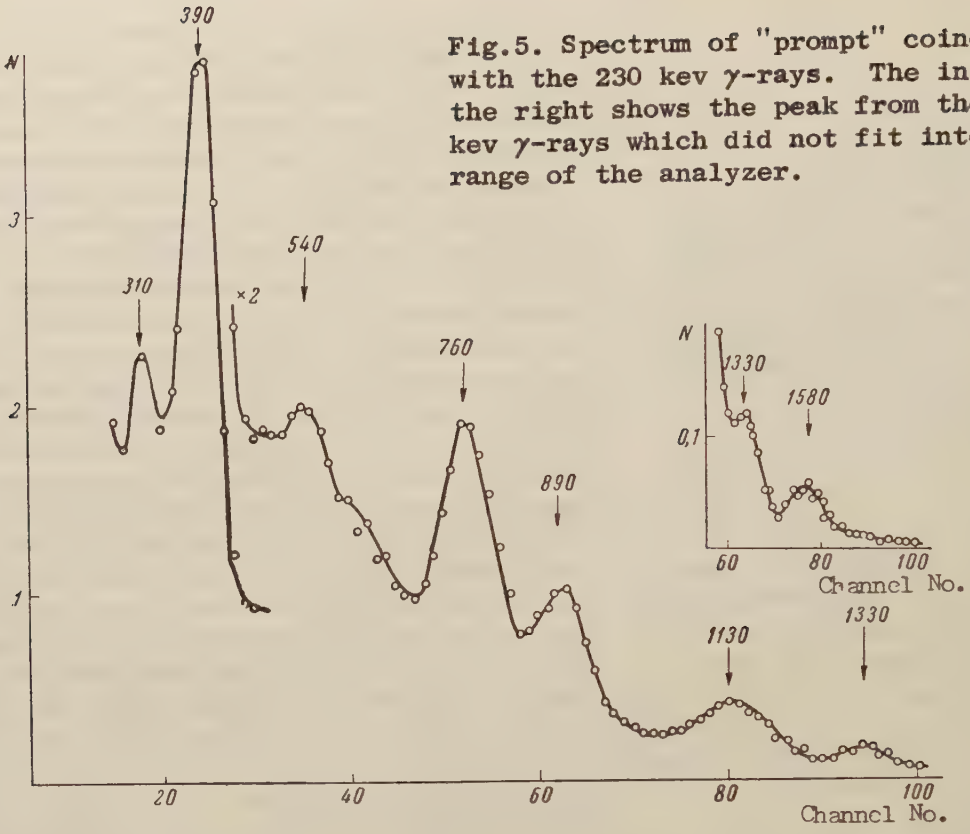

Fig.5. Spectrum of "prompt" coincidences with the 230 kev γ-rays. The insert at the right shows the peak from the 1580 kev γ-rays which did not fit into the range of the analyzer.

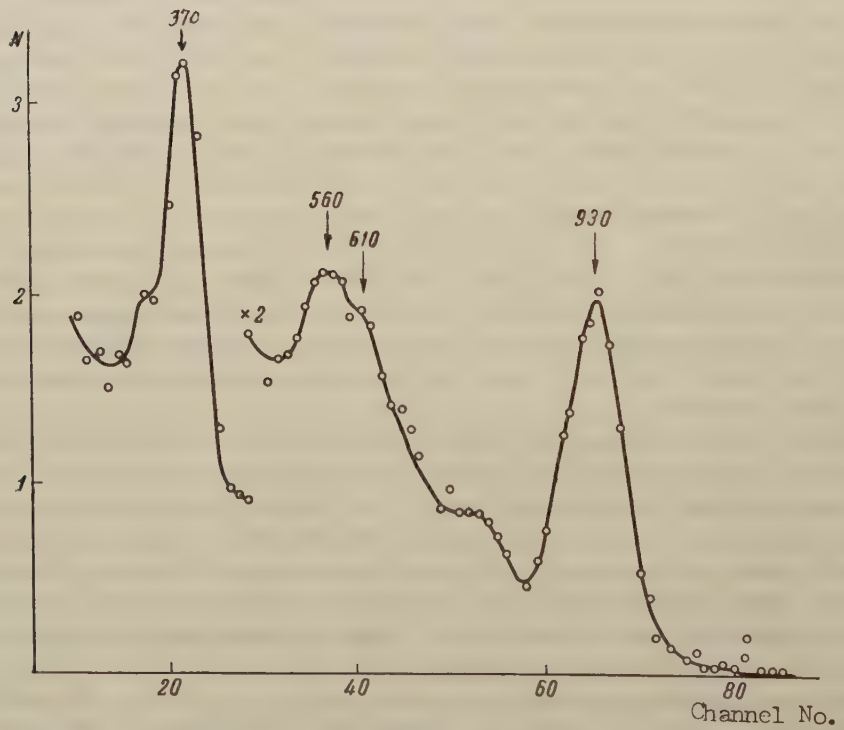

Fig.6. Spectrum of "delayed" coincidences with the 230 kev γ-rays.

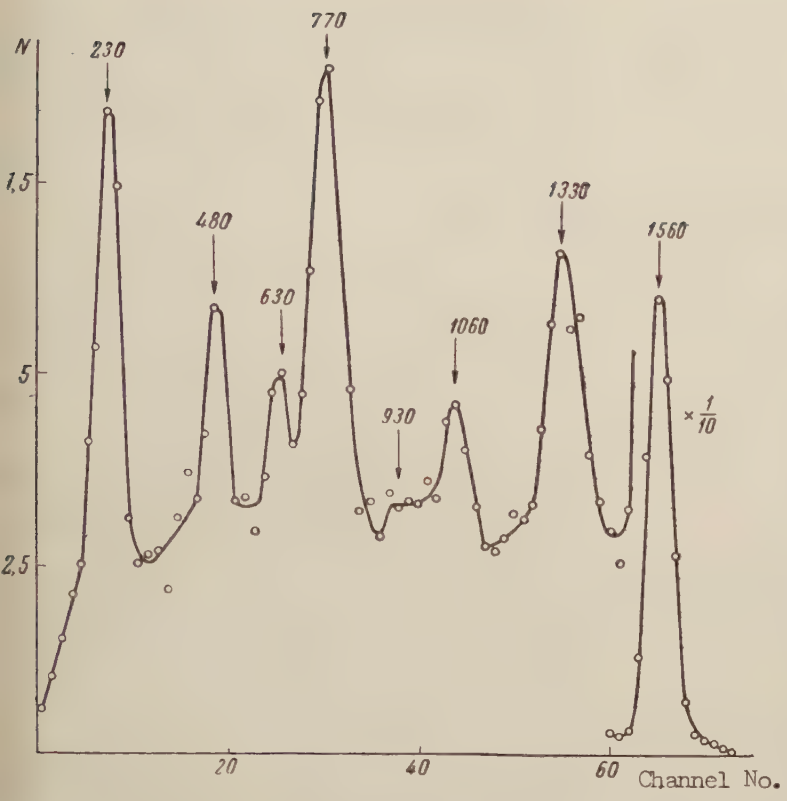

Fig.7. Spectrum of "summed" coincidences for E_{sum} = 1560 kev.

pect the appearance of the 630-930 kev cascade in view of the fact that the 930 kev transition is evinced in the spectrum of "delayed" coincidences and, consequently, feeds the 625 kev level. The low intensity of this cascade is explained by the fact that the intensity of the cross-over 625 kev transition is low compared with that of the 395-229 kev cascade transitions (~0.1 according to Ref.1). The existence of the 480-1070 and 770-770 kev cascades was substantiated by conventional coincidence measurements.

We also carried out measurements of the lifetime of the isomeric 625 kev state by the method of delayed coincidences and obtained a value of $(8.0 \pm \pm 0.6) \cdot 10^{-7}$ sec, which agrees within the limits of the experimental error with the lifetime found by Berlovich et al[5].

Decay Scheme of Gd^{147}

In constructing the decay scheme for Gd^{147} we used the results of our measurements and the data of Refs.1 & 2 (hereinafter we use the transition energy values given in Refs.1 & 2). The proposed scheme is shown in Fig.8.

Also, in constructing the decay scheme we assumed that no levels with energies greater than 1810 kev are excited in Eu^{147}, for in measuring the "sum" spectrum (Fig.3) it was shown that the counts in the energy region >1810 kev are connected with impurities with a period greater than that of Gd^{147}.

Earlier[1] it was shown - and our data wholly substantiates this - that the first excited state in Eu^{147} is located at 229 kev. The existence of the 625 kev state is also substantiated by the intense "prompt" 229-395 kev cascade. Inasmuch as the 370 and 932 kev transitions are observed in the spectrum of "delayed" coincidences, it may be assumed that they feed the 625 kev level and depart, respectively, from levels at 995 and 1560 kev (we chose the value 1560 rather than 1557 kev, inasmuch as in this case one can reconcile the energies of the components of the other cascades departing from this level). From the 995 kev level there apparently departs a 995 kev cross-over transition to the ground state and a 766 kev transition to the first excited level. This transition is evinced as the 760 kev peak in the "prompt" coincidence spectrum.

From the 1560 kev level, according to the "summed" coincidence measurements, there depart the 1330-229, 1072-485, and 932-625 kev cascades and the cascade of two γ-rays with energies close to 770 kev. It may be assumed that these are the 778 and 787 kev γ-rays listed in Ref.1. The presence of a 549 kev transition which, apparently, is in "prompt" coincidence with the 229 kev transition, gives reason to infer that this cascade goes through the 778 kev level. The relative location of the 1072 and 485 kev transitions will be considered below.

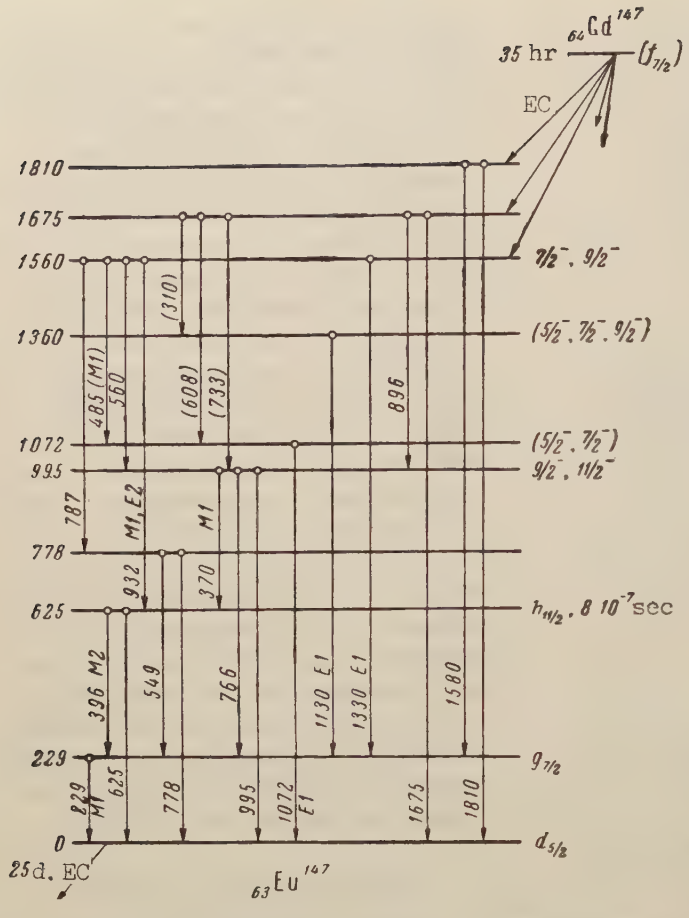

Fig.8. Eu^{147} level diagram proposed on the basis of our experimental results and the data of Refs.1 & 2.

The existence of coincidences between the 229 and 1130 kev γ-rays gives reason to introduce a level at 1360 kev. The absence of coincidences between the 229 kev γ-rays and the 1675 and 1810 kev γ-rays indicates that there must be levels with these energies. The existence of the 1810 kev level is also substantiated by the observed 229-1580 kev coincidences. The 890 kev peak in the spectrum of "prompt" coincidences with the 230 kev gammas is apparently due to γ-rays of 896 kev energy (mentioned in Ref.1). There are two possibilities for explaining this cascade: 1) one can introduce a level at 1125 kev, from which there occurs only the 896 kev transition, or 2) one can assume that this transition departs from the 1675 kev level, feeding the 778 kev level, and that the coincidences are detected due to a 896-549-229 kev cascade. If the spectrum shown in Fig.5 is resolved, the intensities of the 890 and 540 kev peaks prove to be approximately equal, which is not in conflict with this assumption (in general, the 896 kev transition is, apparently, more intense than the 549 kev transition, but the 778 kev level is de-excited mainly by a cross-over transition to the ground state and the intensity balance is not disturbed). In order to choose between these possibilities one must have more accurate values for the γ-ray intensities. In favor of the second possibility is the consideration that in choosing it there is no need to introduce an additional level into the decay scheme. In order to determine whether the intermediate level in the 1072-485 kev cascade is located at 485 or 1072 kev, one must bear in mind the following facts: 1) the 1560 kev level, as will be shown below, has odd parity, while the parity of the ground state is even[1], 2) the multipole order of the 1072 kev transition is E1, 3) the 485 kev transition, according to Ref.1, is a dipole one (E or M). Inasmuch as the 1072-485 kev cascade connects levels of different parity, while the 1072 kev transition does not involve change of parity, the 485 kev transition should not involve a parity change and must therefore be an M1 rather than an E1 type transition. Then if one takes the theoretical value of α_K one can, using the data of Ref.1, calculate the intensity of the 485 kev transition: $I_{\gamma 485} = 5.5$ (taking $I_{\gamma 229} = 100$). This value is some 2-3 times lower than the intensity of the 1070 kev transition. Hence to maintain the balance of intensities it must be assumed that the intermediate level is located at 1072 kev.

The levels introduced above allow of explaining most of the observed γ-transitions and the results of our γ-γ coincidence measurements. Some of the low intensity transitions observed in the work of Ref.1 cannot be fitted into the pro-

posed scheme; to accomodate them one must introduce additional levels. Their population, apparently, is not large, and consequently, they are not evinced in the coincidence measurements. Our data do not conflict with the existence of the 1480 and 1742 kev levels inferred in Ref.1. Inclusion of these levels in the decay scheme allows of explaining almost all the observed γ-transitions except for the very weak 696 and 909 kev transitions.

Spin and Parity Assignments

We now turn to discussion of the spin and parity assignments for the levels. In Ref.1 it was hypothesized, in agreement with experiment, that the ground state and the 229 and 625 kev levels are single-particle states with configurations $d_{5/2}$, $g_{7/2}$ and $h_{11/2}$, respectively. The assignment made for the 995 kev level was 9/2- or 11/2-.

The multipole order (E1) of the 1072, 1130 and 1330 kev transitions requires that the parity of the 1072, 1360 and 1560 kev levels be odd. The possible spin values lie in the range from 3/2 to 7/2 for the 1072 kev level and from 5/2 to 9/2 for the 1360 and 1560 kev levels.

The multipole order of the 932 kev transition from the 1560 kev level to the 625 kev ($h_{11/2}$) level is M1 or E2. Hence the possible spin assignments for the 1560 kev level are 7/2 and 9/2. Inasmuch as the 485 kev transition to the 1072 kev level is a dipole one, one must reject the value 3/2 from among the possible spin assignments for the 1072 kev level.

It follows from the balance of γ-transition intensities that most ($\sim$50%) of the E-captures go to the 1560 kev level and that the intensity of the EC transitions to the 625 kev level is very low. If one takes the value of 2300 kev for the disintegration energy of Gd^{147} to Eu^{147} (the value given by Levy's formula[9]), the log ft values for the EC decays to the 1560 and 625 kev levels prove to be $\sim$5.9 and $\geq$8, respectively. It may be assumed that the first transition is allowed, and that the second is more than first forbidden. The ground state of the spherical Gd^{147} nucleus (N = 83) according to the single-particle model, may be $f_{7/2}$ or $h_{9/2}$. Inasmuch as the transition to the 625 kev level is forbidden, the former configuration is more likely. The allowed character of the EC transition to the 1560 kev level is not in conflict with the above assignment for it.

Calculations of log ft for the EC decays going to other states yield values in the range from 6.5 to 7.5, which precludes drawing any definite inferences regarding the degree of their forbiddenness. The available experimental data are still inadequate for making assignments for the other levels of Eu^{147} and choosing between the possible spins of the nucleus in the 995, 1072, 1360 and 1560 kev states.

As will be evident from the above, the results of the present work largely substantiate the decay scheme proposed in the work of Anton'eva, Bashilov et al[1]. The refinements made herein pertain mainly to high-lying and relatively weakly populated levels. Some of the results, as was noted above, allow of two possible interpretations. There are a number of other facts which it is impossible to explain on the basis of general considerations. For example, if one takes into account the absence of cross-over transitions from the 1360 and 1560 kev levels to the ground state, one can restrict the spin assignments for these levels to 9/2, inasmuch as otherwise there could occur E1 transitions to the ground state. But if we consider the 1072 kev level, we find that for both possible assignments - 5/2 and 7/2 - an E1 transition to the 229 kev level should be allowed. No such transition (843 kev) has been observed. Thus we are dealing either with some exceptional type of forbiddenness (and then our arguments relative to the 1360 and

1560 kev levels become invalid) or the actual level diagram differs somewhat from the proposed one. The availability of more precise γ-transition intensity values would help obviate most of the difficulties.

We desire our express our thanks to the personnel of the Joint Institute for Nuclear Research synchrocyclotron for irradiating the target and I.A.Yutlandov and V.A.Khalkin for the chemical separation of the gadolinium fraction. We are also grateful to V.S.Shpinel' for his interest in the work and helpful discussions.

Scientific-Research Institute of Nuclear Physics,
Moscow State University

References

1. N.M.Anton'eva, A.A.Bashilov, B.S.Dzhelepov & B.K.Preobrazhenskii, Izv.AN SSSR, Ser.fiz., 22, 906 (1958). (Trans.Bulletin, 22, 899.)

2. V.K.Adamchuk, A.A.Bashilov & B.K.Preobrazhenskii, Ibid., 22, 919 (1958). (Trans.Bulletin, 22, 911.)

3. B.S.Dzhelepov, B.K.Preobrazhenskii & V.A.Sergienko, Ibid., 23, 219 (1959). (Trans.Bulletin, 23, 211.)

4. V.Shirley, W.Smith & J.Rasmussen, Nucl.Phys., 4, 395 (1957).

5. E.E.Berlovich, V.N.Klement'ev, L.V.Krasnov, M.K.Nikitin & I.Yursik, Doklady AN SSSR, 133, 789, (1960). (Trans.Soviet Physics - Doklady.)

6. L.A.Sliv & I.M.Band, Tablitsy koeffitsientov vnutrennei konversii γ-izlucheniya (Tables of internal conversion coefficients), M.-L., 1956.

7. A.M.Hoogenboom, Nucl.Instr., 3, 57 (1958).

8. A.Bedesku, K.P.Mitrofanov, A.A.Sorokin & V.S.Shpinel', Izv.AN SSSR, Ser. fiz., 23, 1434 (1959). (Trans.Bulletin, 23, 1424.)

9. B.S.Dzhelepov & G.F.Dranitsyna, Sistematika energii β-raspada (β-decay energy systematics), M.-L., 1960.

INVESTIGATION OF THE DECAY SCHEME OF Gd^{149}

- A.A.Sorokin & K.P.Mitrofanov

Introduction

Decay of Gd^{149} has been investigated by two groups.[1-3] It was established that Gd^{149} converts by electron capture to Eu^{149} with a period of 10 days. According to the data of Anton'eva et al[2], there occur in Eu^{149} γ-transitions with energies of 149.8 (M1), 272, 298 (M1 + E2), 346 (M2), 461, 497 (E3), 517 (M1, E2 or M1 + E2), 535 (M1, E2 or M1 + E2) and 940 kev. Anton'eva et al also evaluated the relative total transition intensities and obtained

$$I_{150}:I_{272}:I_{298}:I_{346}:I_{497}:I_{517}:I_{535} = 1:\sim 0.05:0.4:0.4:0.02:\sim 0.05:\sim 0.05.$$

In the work of Shirley, Smith & Rasmussen[1], in addition to the above transitions, there were observed several other γ-transitions, the attribution of which to Gd^{149} is doubtful. In the studies of Shirley et al[1] and Dzhelepov et al[3] there were observed coincidences between the 149.8 and 346 kev transitions; in the latter investigation there were also recorded coincidences between the 149.8 and 272 kev transitions.

The existence of excited states in Eu^{149} with energies of 149.8 and 496 kev may be regarded as reliably established. For determination of the energies of the other excited states in Eu^{149}, however, more detailed investigation of the γ-γ coincidence spectra is necessary.

Delayed coincidence measurements carried out by Berlovich et al[4] showed that the 496 kev state is a metastable one with a lifetime of $(2.5 \pm 0.1)\cdot 10^{-6}$ sec.

In the source used in the present work, as in the sources employed in Refs.1 & 2, Gd^{149} was present in the gadolinium fraction of the rare earth isotopes formed by the spallation reaction on tantalum. The measurements were carried out on a coincidence γ-spectrometer coupled to a 100-channel AI-100 type[5] pulse height analyzer. In addition, in order to check some of the cascades we carried out measurements of e-γ coincidences on a coincidence set-up consisting of a two-lens magnetic β-spectrometer and a scintillation γ-spectrometer[5]. The measurements were started 10 days after bombardment of the tantalum target, i.e., after virtually complete decay of short-lived Gd^{147} (T = 35 hours).

Measurements and Results

The γ-spectrum of the gadolinium fraction recorded 10 hours after bombardment is shown in Fig.1. In interpreting the experimental data it was necessary to bear in mind that in the source, in addition to Gd^{149}, there were present Gd^{146} (T = 45 days), Gd^{151} (T = 120 days), Gd^{153} (T = 230 days) and the daughter isotopes Eu^{146} (T = 5 days; in equilibrium with Gd^{146}), Eu^{147} (T = 25 days; daughter of Gd^{147}) and Eu^{149} (T $\approx$ 100 days). As measurements carried out several months after bombardment showed, Gd^{151}, Gd^{153} and Eu^{149} make a relatively minor contribution (<10% compared to Gd^{146} and Eu^{146}) to the radiation detected by the scintillation spectrometer. The spectra and decay schemes of Eu^{147}, Gd^{146} and Eu^{146} are relatively simple and well known[2,6,7]. The γ-radiation contribution from these isotopes can be taken into account by appropriate control measurements. For purposes of comparison, in Fig.1 we also show the spectrum of the Gd fraction recorded 5 months after bombardment (dashed line). From the presented data it may be concluded that the 150, 300 and 345 kev γ-rays belong mainly to Gd^{149} (i.e., are associated with 149.8, 298 and 346 kev transitions in Eu^{149}).

As in our investigation[8] of Gd^{147}, we used the isomeric level for identifying the γ-transitions feeding this level.

Fig.2 shows the spectrum of "delayed" coincidences with the 150 kev γ-rays. There is evinced a strong peak at 300 kev and a weak peak at 470 ± 20 kev. Obviously, the 300 kev peak is due to the 298 kev transition; the 470 kev peak to the 461 kev transition. The intensity of the 470 kev γ-rays in this spectrum amounts to ~20% relative to the intensity of the 300 kev γ-rays.

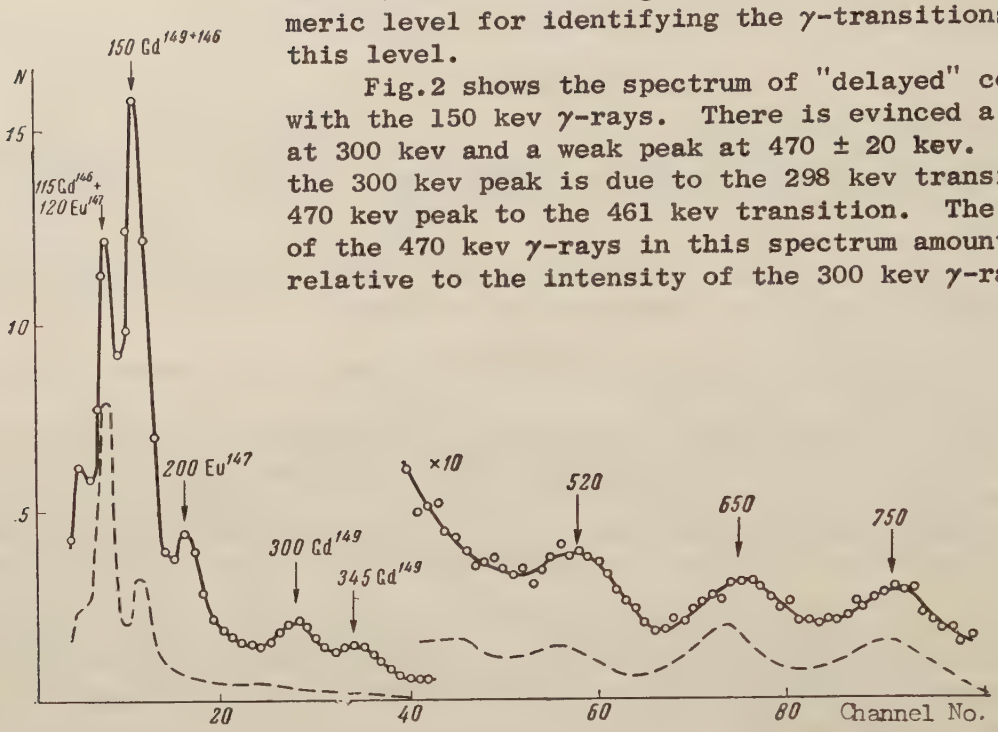

Fig.1. Gamma-ray spectra of the gadolinium fraction measured 10 days (solid line) and 5 months (dashed line) after bombardment of the Ta target.

The "prompt" coincidence spectra with the 150 kev γ-rays, measured under different conditions, are shown in Figs.3 & 4. In Fig.3 there is evident a pronounced peak at 345 kev and a weak peak at 270 kev. We carried out graphical resolution of this spectrum and found that the intensity of the 270 kev γ-rays amounts to 13.4% the intensity of the 345 kev γ-rays in coincidence with the 150 kev γ-rays. In the spectrum of Fig.4, obtained with lower amplification, in addition to the above mentioned peaks, there are evident peaks at 520, 640, 790 and 930 kev. These measurements were repeated by the method of e-γ coincidences. In

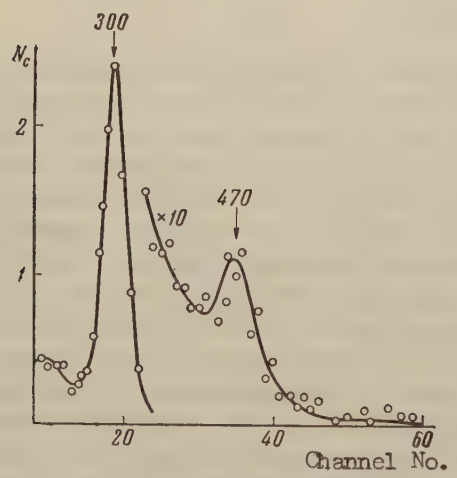

Fig.2. Spectrum of "delayed" coincidences with the 150 kev γ-rays.

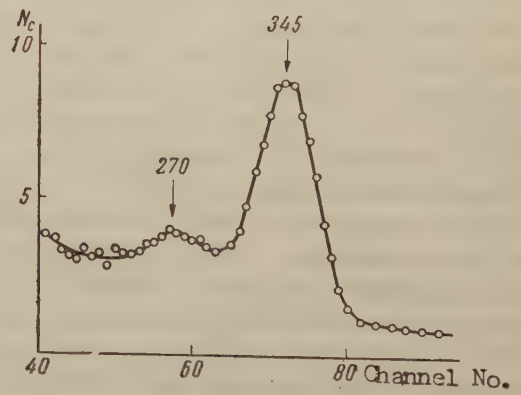

Fig.3. Spectrum of "prompt" coincidences with the 150 kev γ-rays.

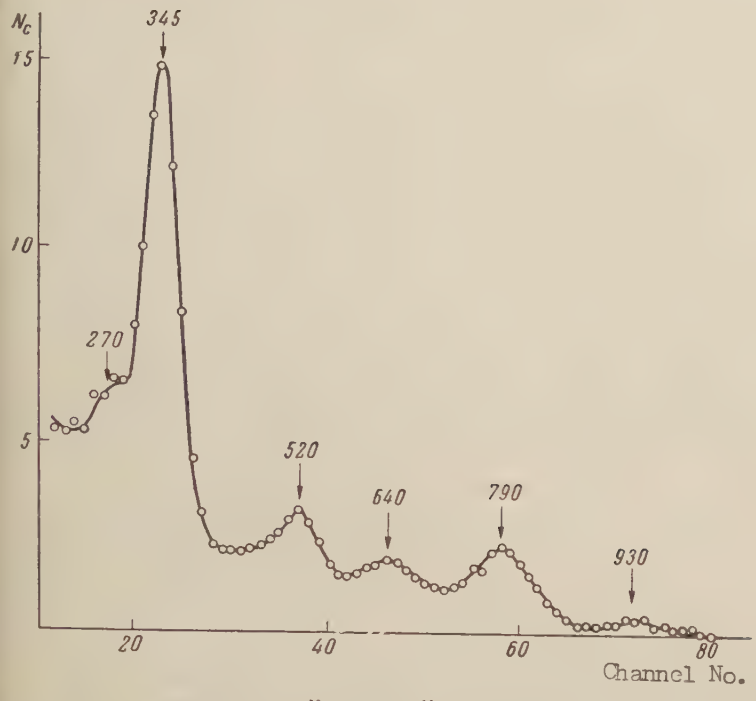

Fig.4. Spectrum of "prompt" coincidences with the 150 kev γ-rays with a lower amplification in the analyzer channel than in the case of Fig.3.

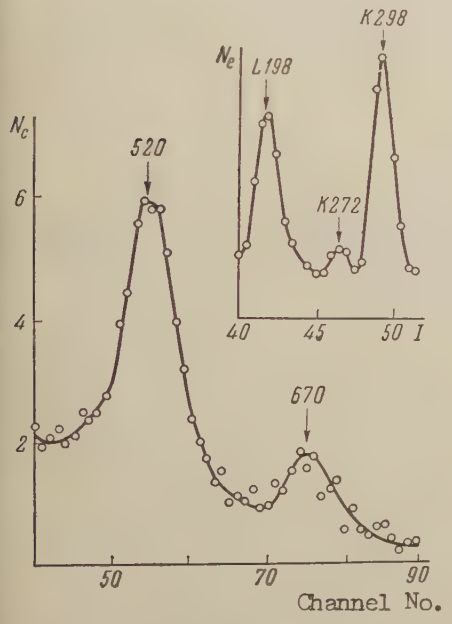

Fig.5. Spectrum of coincidences with the K conversion electrons of the 272 kev transition. Insert - section of the conversion electron spectrum.

this case the β-spectrometer was set on the K or L conversion line of the 150 kev γ-rays. The higher resolution (~3 %) of the β-spectrometer makes possible better discrimination of the 121 and 198 kev γ-rays from Eu^{147} and elimination of the contribution from the 121—676 and 198—600 kev cascades as well as the 630—740 kev cascade in Eu^{146}. In this case the 640 and 930 kev peaks disappeared from the spectrum. Thus it may be assumed that only the following γ-transitions are in coincidence with the 149.8 kev γ-transition: 272, 346, 517 (and, possibly, 535), and 790 kev.

Using the e-γ coincidence set-up, we also measured the spectrum of coincidences with the K conversion electrons of the 272 kev transition (Fig.5). There is evinced in this spectrum a pronounced peak at 520 kev and a weak peak in the region of 670 kev; this last remained in evidence even after making corrections for possible interfering cascades and chance coincidences. We also carried out inverse measurements on the γ-γ coincidence spectrometer, i.e., recorded coincidences with the gate of the single channel analyzer in the control channel set at 670 kev. In this case, in addition to the expected peak at 120 kev (due to Eu^{147}), there was observed a peak at 270 kev. Inasmuch as according to the data in the literature there is no such cascade in Eu^{147}, Gd^{146} or Eu^{146}, we feel safe in attributing the 272—670 kev cascade to Eu^{149}.

Measurements of the lifetime of the 496 kev isomeric state yielded a value of $(3.3 \pm 0.4) \cdot 10^{-6}$ sec, which is in fairly good agreement with the data of Berlovich et al[4].

Decay Scheme of Gd^{149}

The decay scheme for Gd^{149} proposed on the basis of our data and the results of earlier investigations is shown in Fig.6. The levels at 150 and 496 kev, as noted above, were identified earlier and were clearly evinced in our measurements. From the results of the "delayed" coinci-

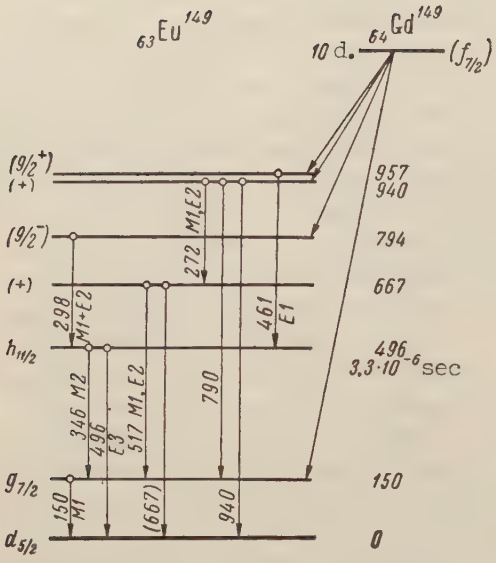

Fig.6. Decay scheme for Gd^{149}.

dence measurements it follows that the 298 kev transition feeds the isomeric 496 kev level and hence departs from a level at 794 kev.

The fact that there occur coincidences between the 150 and 790 kev γ-rays gave reason to introduce a level at 940 kev. Gamma-rays of this energy are observed in the spectrum of Gd^{149}. Apparently, this is a cross-over transition to the ground state.

The 461 kev transition must feed either the 496 kev or the 794 kev level. In the proposed decay scheme we show the more probable variant in view of energy considerations, i.e., we have located this transition above the 496 kev level.

In the work of Refs.2 & 3 it was assumed that the 272 kev transition feeds the 150 kev level and, accordingly, departs from a level at 422 kev. In this variant, between the 422 kev level, on the one hand, and the 940 and 957 kev levels, on the other hand, there can be inserted γ-transitions of 517 and 535 kev energy. Careful measurements after calibration of the spectrometer by means of annihilation radiation showed, however, that the 150 kev γ-rays yield coincidences only with the 517 kev transition, rather than with 517 + 535 kev.

Moreover, in this variant (i.e., on the assumption that there is a level at 422 kev) it is difficult to explain the presence of the 272—670 kev cascade. Accordingly, in constructing the decay scheme we assumed that there is a level of 667 kev energy fed by the 272 kev transition and depopulated by 517 and 667 kev transitions. Evaluation of the relative intensities of these transitions in the spectrum of Fig.5 yields $I_{667}:I_{517} \approx 0.3$.

Spin and Parity Assignments

It was shown by Anton'ev et al[2] that the experimental data can be satisfactorily explained if the ground state and the 150 and 490 kev levels are identified as single-particle levels with configurations $d_{5/2}$, $g_{7/2}$ and $h_{11/2}$, respectively. Further, inasmuch as the 298 kev transition is M1 + E2 (Ref.2), the 794 kev level must have spin and parity 9/2- or 11/2-.

The most populated states in Eu^{149}, after the 150 kev level, are the states with energies of 496 and 794 kev. The intensities of the 298 and 346 kev transitions are equal to within ~10%. This means that the 496 kev level is populated mainly by the 298 kev transitions, while β-decay to this level is, apparently, strongly forbidden, compared with decay to the 794 kev level. Consequently, of the two possible single-particle model assignments for the ground state of Gd^{149} - $f_{7/2}$ or $h_{11/2}$ - one must reject the latter, inasmuch as otherwise β-decay to the 496 kev level would be allowed ($\Delta I = 1$, no). If the ground state of Gd^{149} is $f_{7/2}$ then the only possible assignment for the 794 kev level is 9/2-.

Using the data of Ref.2 on the conversion electron spectrum of Gd^{149} and the relative intensities of the 461 and 272 kev γ-transitions obtained in the present investigation (Figs.2 & 3), we evaluated the K-shell conversion coefficients for these transitions. We assume that these transitions are located in the decay scheme as shown in Fig.6. We obtained the following values: $\alpha_{K461} \approx 3.5 \cdot 10^{-3}$ and

$\alpha_{K272} \approx 10^{-1}$ (uncertainty ~40%). It follows from comparison with the theoretical conversion coefficient values given by Sliv & Band[9] that the multipole order of the 461 kev transition is E1 and that of the 272 kev transition is M1 or E2. In view of the large value of the K/L ratio it may be inferred that the multipole order of the 272 kev transition is M1 or M1 + E2.

It follows from these results that the assignment for the 957 kev level may be 9/2+, 11/2+ or 13/2+, and that the 667 and 940 kev levels must have even parity. If the ground state of Gd^{149} is $f_{7/2}$ as inferred above, the only possible assignment for the 957 kev level is 9/2+, and the spin of the 940 kev level must lie in the range from 5/2 to 9/2; otherwise these levels would not be excited with any appreciable intensity.

We desire to express our gratitude to the personnel of the Joint Institute for Nuclear Research synchrocyclotron for bombardment of the tantalum target and to I.A.Yutlandov and V.A.Khalkin for the chemical separation. We are also grateful to N.V.Forafontov for assistance in carrying out the e-γ coincidence measurements and to V.S.Shpinel' for his interest in the work and valuable discussions.

Scientific Research Institute of Nuclear Physics,
Moscow State University

References

1. V.Shirley, W.Smith & J.Rasmussen, Nucl.Phys., 4, 395 (1957).

2. N.M.Anton'eva, A.A.Bashilov, B.S.Dzhelepov & B.K.Preobrazhenskii, Izv. AN SSSR, Ser.fiz., 22, 895 (1958) (Trans.Bulletin, 22, 889); V.K.Adamchuk, A.A. Bashilov & B.K.Preobrazhenskii, Ibid., 22, 919 (1958)(Trans.Bulletin, 22, 911).

3. B.S.Dzhelepov, B.K.Preobrazhenskii & V.A.Sergienko, Ibid., 23, 219 (1959). (Trans.Bulletin, 23, 211.)

4. E.E.Berlovich, V.N.Klement'ev, L.V.Krasnov, M.K.Nikitin & I.Yursik, Doklady AN SSSR, 133, 789 (1960). (Trans.Soviet Physics - Doklady.)

5. A.Bedesku, O.M.Kalinkina, K.P.Mitrofanov, A.A.Sorokin, N.V.Forafontov & V. S.Shpinel', Zhur.eksp.i teor.fiz., 40, 91 (1961). (Trans.Soviet Physics - JETP.)

6. N.M.Anton'eva, A.A.Bashilov, B.S.Dzhelepov & B.K.Preobrazhenskii, Ibid., 36, 28 (1959). (Trans.Ibid.)

7. Yu.A.Aleksandrov, Yu.A.Nemilov, M.K.Nikitin & Sh.Piskorzh, Izv.AN SSSR, Ser.fiz., 24, 1099 (1960). (Trans.Bulletin, 24, 1105.)

8. A.A.Sorokin, K.P.Mitrofanov, Present issue of the Bulletin, p.810.

9. L.A.Sliv & I.M.Band, Tablitsy koeffitsientov vnutrennei konversii na K-obolchke (Tables of internal conversion coefficients. Part I, K-shell), M.-L., 1956.

INVESTIGATION OF NEUTRON-DEFICIENT Tb ISOTOPES

- A.T.Strigachev, L.S.Novikov, A.A.Sorokin, V.A. Khalkin, N.V.Tsvetkova & V.S.Shpinel'

In the present work we investigated the spectra of neutron-deficient Tb isotopes on a Danysz type spectrograph and a transverse magnetic field β-spectrometer (BPP). In addition, we studied γ-γ coincidences on a scintillation spectrometer in order to identify γ-cascades in the decays.[1]

1. Source

The investigated activity was the terbium fraction of the rare earths formed in a tantalum target bombarded for ~2 hours with 660 Mev protons in the Joint Institute for Nuclear Research synchrocyclotron. Radiochemical separation of the rare earths was started immediately after bombardment.

The sources were prepared by burning out the lactate in which the fraction was dissolved, solution of the residue in 5% acetic acid and evaporation of the drops on an aluminum foil 5 μ thick.

2. Investigation of the conversion Electron Spectra on the Danysz Type Spectrometer

These measurements were carried out on the 180° focusing, constant magnetic field Danysz type spectrometer of the Joint Institute for Nuclear Research. The radius of this spectrometer can be varied in the range from 6.5 cm to 22.5 cm. With a source measuring 0.2-0.3 mm x 10-15 mm the instrument yields a resolution of 0.3% for the 8 cm radius setting and 0.2% for the 20 cm setting. The conversion electron spectra were recorded on thick emulsion type R plates (emulsion thickness 50 μ, plate dimensions 16 x 344 mm) supplied by the Moscow Technical Photoplate Plant.

The exposure of the first plate was started approximately 4-5 hours after the end of bombardment of the Ta target; the exposure time was about 24 hours. Subsequent plates were exposed for periods of 2 to 3 days. There were recorded conversion electrons with energies up to 650 kev. The plates with strong blackening at the locations of the intense conversion lines were photometered on an MF-2 microdensitometer.

For determining the conversion electron energies the spectrometer was calibrated beforehand with reference to the well known F, G, H, I and J lines of active Th deposit.

The results of the measurements on the Danysz spectrometer are shown in Fig. 1. The indicated line energies comprise an uncertainty of 0.2%.

The conversion lines corresponding to 165.1 and 351.9 kev γ-transitions appeared in the first plate, but were not discernible in the second plate, exposure of which started some 24 hours later. According to the data of Toth & Rasmussen[2], these γ-transitions pertain to the decay of Tb^{149} with a period of 4.1 hours. The same thing applies to the 137.32 kev conversion line which is associated with a 187.6 kev transition.

All the observed γ-transitions that pertain to the decay of Tb^{153}, Tb^{154} and Tb^{155} and the γ-transitions with energies of 108.3, 180.1, 192.1, 251.3 and 287.3 kev, which are evinced in the decay of Tb^{151}, were identified by Michelich et al[3].

In investigating a terbium fraction obtained in the same manner as our fraction, Anton'eva et al[4] observed a number of other γ-transitions with a period of 18 hours. Anton'eva et al attributed these transitions to decay of an activity

Table 1

Conversion electron lines appearing in the spectrum of the terbium fraction

E_{e^-}, kev	Line	$E_{\gamma av}$ kev	E_γ, kev	Assignment
115,05 157,21 163,42	*K* *L* *M*	165,1	170 [2]	Tb^{149}
137,32	*K*	187,6		Tb^{149}
301,33 344,43	*K* *L*	351,9	350 [2]	Tb^{149}
58,44 99,94 100,38 101,03 107,01	*K* L_1 L_2 L_3 *M*	108,3	108,3 [3]	Tb^{151}
130,32 171,91 178,29	*K* *L* *M*	180,1	180,3 [3]	Tb^{151}
142,05 183,24	*K* *L*	192,1	192,2 [3]	Tb^{151}
201,22 243,38 249,73	*K* *L* *M*	251,3	252,1 [3]	Tb^{151}
237,06 278,53 286,56	*K* *L* *M*	287,3	287,6 [3]	Tb^{151}
365,26	*K*	415,5	416 [4]	
375,79	*K*	426,0	426 [4]	
392,30	*K*	442,5	442 [4]	Tb^{151}
428,10	*K*	478,3	477 [4]	Tb^{151}
536,50	*K*	586,7	589 [4]	Tb^{151}
220,46 261,86	*K* *L*	270,4	265 [5]	Tb^{152}
293,55 336,40	*K* *L*	344,0	344,1 [5]	Tb^{152}
381,28	*K*	431,5	431 [4]	Tb^{152}
564,44 606,72	*K* *L*	614,7	616 [4]	Tb^{152}
33,71 34,28 34,98 40,54	L_1 L_2 L_3 *M*	42,1	41,5 [3]	Tb^{153}
60,14 101,86 108,41	*K* *L* *M*	110,0	109,8 [3]	Tb^{153}
124,57	*K*	174,8	174,4 [3]	Tb^{153}
145,05	*K*	195,3	195,2 [3]	Tb^{153}
162,17 204,20	*K* *L*	212,2	212,2 [3]	Tb^{153}
199,50	*K*	249,7	249,8 [3]	Tb^{153}
73,47 115,50 121,75	*K* *L* *M*	123,4	123,2 [3]	Tb^{154}
197,22	*K*	247,5	248,1 [3]	Tb^{154}
297,61	*K*	347,8	347,0 [3]	Tb^{154}
36,92 79,41	*K* *L*	87,2	86,7 [3]	Tb^{155}
55,49	*K*	105,7	105,4 [3]	Tb^{155}
113,39	*K*	163,6	163,5 [3]	Tb^{155}
110,65* 133,21*	? ?			

*Line not identified.

Note: The numbers in brackets are References.

Table 2

Comparison of the conversion electron spectra of the dysprosium and terbium fractions

Dy						Tb			
E_{e^-}, keV	Line	E_γ, keV	Assignment	Intensity (visual eval.) Plate 1	Plate 2	E_{e^-}, keV	Line	E_γ, keV	Assignment
128,30	K?	178,5	Tb^{152}?	Weak	–	130,32*	K	180,1	Tb^{151}
129,81	K	180,0	Tb^{155}	Medium	Strong				
171,89	L	180,0	Tb^{155}	–	Weak	171,91	L	180,1	Tb^{151}
220,14	K	270,3	Tb^{152}	Medium	Very weak	220,46	K	270,7	Tb^{152}
293,25	K	343,8	Tb^{152}	Strong	Medium	293,55	K	344,0	Tb^{152}
336,26	L	343,8	Tb^{152}	Medium	Weak	336,40	L	344,0	Tb^{152}
380,89	K	431,2	Tb^{152}	Weak	–	381,28	K	431,5	Tb^{152}
564,60	K	614,8	Tb^{152}	Medium	Very weak	564,44	K	614,7	Tb^{152}

* Very strong line.

consisting of a mixture of Tb^{151} and Tb^{154}; at that time nothing was known regarding Tb^{152}.

In order to identify some of the conversion lines in the terbium fraction spectrum, we investigated the conversion electron spectrum, in the 100 to 650 kev range, of the dysprosium fraction from the Ta spallation products. In this spectrum there should be present, in addition to the lines of Dy, lines that correspond to the decay of its daughter isotopes: Tb^{152} (Ref.5), Tb^{153} and Tb^{155} with half-lives ot 18.5 hours, 62 hours and 5.5 days. Lines associated with the decay of Tb^{151} should not be evinced inasmuch as Dy^{151} has a half-life measured in minutes; hence even prior to separation of the rare earths virtually all the Dy^{151} present should convert to Tb^{151}. Lines associated with the decay of Tb^{154} also should not be evinced in this spectrum inasmuch as Dy^{154} transforms by α-decay to Gd^{150}.

The results of comparison of the conversion electron spectra of the dysprosium and terbium fractions are shown in Table 2.

Two consecutive plates were exposed, each for about 24 hours, with the Dy source in the spectrograph. Rough visual evaluations of the intensities of these conversion lines are given in Table 2.

It is evident from an examination of the table that the 270.4, 344.0, 431.5 and 614.7 kev γ-transitions observed in the spectrum of the terbium fraction must be assigned to the decay of Tb^{152}. This isotope is also apparently responsible for the γ-transition of 178.5 kev energy, which gives rise to the weak conversion line at 128.30 kev. Toth et al[5], as a result of measurements carried out with a scintillation spectrometer and permanent magnet electron spectrographs assigned the observed 180, 265 and 344.1 kev γ-transitions to the decay of Tb^{152}.

The γ-transitions with energies of 442.5, 478.3 and 586.7 kev must be attributed to the decay of Tb^{151} (see Section 5 below).

3. Investigation of the Conversion Electron Spectra on the Transverse Magnetic Field β-Spectrometer

More detailed investigations of the conversion electron spectrum of the terbium fraction were carried out in the transverse magnetic field $\pi\sqrt{2}$ double-focusing

β-spectrometer with a mean radius r_0 = 22.5 cm. The instrument resolution with a 1 x 30 mm source is 0.3%. The electrons were detected by means of gas filled Geiger counters with a 100 v plateau (5% slope).

In view of the fact that the principal aim of the present study was to investigate Tb isotopes with periods of 17-20 hours and less, only 150 to 250 kev sections of the conversion spectrum could be investigated with one source. In all we carried out five series of measurements with five different sources.

In the first series of measurements we investigated the spectrum in the 90 to 230 kev range, in the second series, we covered the 210 to 440 kev range, in the third series, the 390 to 650 kev range; the fourth series of measurements was carried out for the purpose of obtaining more accurate energy values for some of the conversion electron lines and for investigating the lines the intensity of which fell off with a period of 3-5 hours. All four series of measurements were carried out with sources separated from a tantalum target bombarded for 1.5-2 hours in the synchrocyclotron. In the spectra obtained with these sources the lines associated with 5-day Tb^{155} and 5-day Tb^{156} were considerably weaker than the conversion lines of the lighter isotopes. The fifth series of measurements was carried out with a source extracted from a tantalum target bombarded in the synchrocyclotron for 12 hours. In this case the radiochemical separation of the rare earth elements was performed 15 hours after bombardment. Measurement of the spectrum started 12 hours after the radiochemical separation. In view of the longer proton bombardment time in the case of this source, there appeared in the conversion spectrum a large number of lines belonging to 63-hour Tb^{153}, 5-day Tb^{155} and 5-day Tb^{156}. In the fifth series of measurements we reinvestigated the conversion electron spectrum in the energy range from 130 to 650 kev and searched the 650 to 1500 kev region. Each section of the spectrum in all five series of measurements was recorded 3-4 times for the purpose of determining the decay periods.

The results of our measurements on the transverse magnetic field β-spectrometer are given in Tables 3, 4 & 5. The instrument was calibrated in energy with reference to the 192.2, 252.1 and 287.6 kev lines on the assumption that the energies for these lines given by Michelich et al[3] are accurate. The γ-transition energies are given as the average values deduced from the energies of the K, L and M lines. In cases where there are given the average values for the energies of the L and M lines, for obtaining the corresponding γ-transition energy we added 7.86 and 1.51 kev, respectively. In a number of cases when owing to superposition of a number of lines the energy of the corresponding γ-transition differed appreciably from the value obtained from the other conversion lines of the given transition, this energy value was not taken into account in determining E_γ (such conversion lines are identified by an asterisk).

The γ-transition periods listed in Table 3 are average values for the periods obtained in measuring the decay of the corresponding K, L and M lines. The uncertainty in determining the decay periods of the conversion lines is ± 1 hour. The conversion lines associated with the decay of Tb^{153}, Tb^{154} and Tb^{155} were investigated only in the fifth series of measurements. The decrease in intensity of these lines was not measured with adequate accuracy and hence the corresponding periods are not given in Table 3. The relative intensities of the conversion lines were evaluated by measuring the areas under these lines in the spectrograms. In view of the fact that the measurements were carried out with five different sources, the relative intensities were reduced to one series of measurements. In Table 3 we also give the intensities of the conversion electrons and the intensity ratios of the K and L lines of the listed γ-transitions, taken as the average values based on all the measurement series.

Table 3

Lines in the conversion electron spectrum of the terbium fraction recorded on the transverse magnetic field β-spectrometer

E_{e^-}, keV	Line	E_γ, keV	$E_{\gamma av}$, keV	$T_{1/2}$, hr	$T_{1/2\,av}$ hr	Relat. intensity	K/L	Assignment
114,5	K	164,7						
155,8	L_1	164,2	164,4	4	4	120		Tb^{149}
156,8	L_2+L_3	164,5						
162,8	M	164,3	164,4	~4				
136,6	K	186,9	186,9	4,5	4,5	40		Tb^{149}
302,6	K	352,8	352,8	~4	4	25		Tb^{149}
588,1	L	638,3	638,6	4	4	19	3,7	Tb^{150}
630,9	K	638,8		4		5,2		
129,4	K_1	179,6		17				
170,7	L_1	179,2	179,7	17	17			Tb^{151}
171,9	L_2+L_3	179,6						
178,8	M	180,3						
141,4 ●	K	191,7	191,5	19	19	110	4,4	Tb^{151}
183,4	L	191,3		19		25		
201,8	K	292,0		19		245		
243,8	L	251,7	251,9	~20	19	45	5,5	Tb^{151}
250,4	M	251,9		~20				
237,4	K	287,6	287,6	~19	19	195	6,8	Tb^{151}
279,6	L	287,5				27,5		
345,1*	K	395,3	395,6	~19	19			Tb^{151}
387,9	L	395,8						
394,6	K	444,9	444,8	17,5	18	27	7,9	Tb^{151}
436,8	L	444,6		18,5		3,4		
430,4	K	480,7	480,7	19	19	21	7,0	Tb^{151}
472,8	L	480,7				~3		
537,6	K	587,8		18		25	4,0	
579,8	L	587,7	587,8	19	19	6,2		Tb^{151}
586,3	M	587,8		20				
716,3	K	766,5	766,5	17				Tb^{151}
221,0	K	271,3		17,5		46		
263,6	L_1	272,0						
264,3	L_2	272,3	271,9	17	17,5	28	1,6	Tb^{152}
265,7	L_3	273,0						
269,4	M	271,0				17,5		
294,8	K	345,0		17,5		160		
336,6	L	344,5	344,8	17	17	65	2,5	Tb^{152}
345,1*	M	346,6		16,5		—		
362,2	K	412,5	412,7	17	17	6,8	3,4	Tb^{152}
404,9	L	412,8		16,5		2,0		

●Includes the L 149.0 line of Tb^{155}.

Table 3 continued

E_{e^-}, keV	Line	E_γ, keV	$E_{\gamma av}$ keV	$T_{1/2}$, hr	$T_{1/2}$ av hr	Relat. intensity	K/L	Assignment
383,1 425,4	K L	433,3 433,3	433,3	18 17,7	18	38 6,7	5,7	Tb^{152}
566,7 608,9 615,5	K L M	616,9 616,8 617,0	616,9	17 17 17,5	17	83 10	8,3	Tb^{152}
655,3 697,3	K L	705,5 709,2	705,4	17	17			Tb^{152}
728,9 770,5	K L	778,1 778,4	778,3	19	19			Tb^{152}
999,5 1041,3	K L	1049,7 1049,2	1049,5	17	17			Tb^{152}
198,3	K	248,5	248,5					Tb^{154}
367,3 409,7	K L	417,5 417,6	417,5	19	19	4,0 0,6	6,7	
378,2 419,2*	K L	482,5 427,1	428,5	19,5	19	20 5,3	3,8	

Table 4

Unidentified lines and transitions in the spectrum of the terbium fraction

E_{e^-}, keV	Line	E_γ, keV	$E_{\gamma av}$ keV	$T_{1/2}$, hr
681,9	K	732,2	732,2	~20
856,3 896,6	K L	906,5 904,5	~905,5	19
922,7	K?	972,9	972,9	~20
1062,2	K?	1112,5	1112,5	~20

Identification (mass assignment) of the conversion lines of the terbium fraction is greatly hampered by the fact that there are a number of neutron-deficient Tb isotopes with close periods: Tb^{149} (4.1 hours) and Tb^{150} (3.1 hours); Tb^{151} (20 hours), Tb^{152} (18.5 hours), and Tb^{154} (17.5 hours); Tb^{155} (5 days) and Tb^{156} (5 days). Identification is further complicated by the fact that that a number of the isotopes have γ-transitions with close energies; for example: E_γ = 108.3 kev - Tb^{151} and 109.8 kev - Tb^{153}; 180.3 kev - Tb^{151}, 180 kev - Tb^{152} and 180.4 kev - Tb^{155}; 252.1 kev - Tb^{151}, 249.8 kev - Tb^{153} and 248.1 kev - Tb^{154} (Refs.3 and 5).

In making the isotopic assignments we took into account the data of Refs.2, 3 & 5, based on studies of separated isotopes, as well as the results of our γ-γ coincidence measurements (see Section 4).

Moreover, in considering the decay schemes of Tb^{149}, Tb^{151} and Tb^{152} we attributed a number of γ-transitions to one or another of these isotopes on the basis of consistency with the decay scheme. Thus, on the basis of energy balance considerations we assigned the 444.8, 480.7 and 587.6 kev transitions to the decay of Tb^{151} and the 433.3 and 616.9 kev transitions to the decay of Tb^{152}.

The transitions we were unable to identify are listed in Table 4; the intensity of all of these fell off with a period of ~20 hours.

In Table 5 we list the γ-transitions associated with the decay of Tb^{153}, Tb^{155} and Tb^{156}, which were identified in the work of Michelich, Harmatz & Handley[3].

Table 5

Lines and transitions identified in the work of Michelich, Harmatz & Handley[3]

E_{e^-}, keV	Line	E_γ, keV	$E_{\gamma av}$ keV	Assignment
144,5 186,5	*K* *L*	194,7 194,4	194,6	Tb^{153}
161,7 204,0 210,3	*K* *L* *M*	212,0 211,9 211,8	211,9	Tb^{153}
199,1 242,3 247,5	*K* *L* *M*	249,3 250,2 249,0	249,5	Tb^{153}
141,4 146,9	*L* *M*	149,3 148,4	148,9	Tb^{155}
152,7	*L*	160,6	160,6	Tb^{155}
154,7	*L*	162,6	162,6	Tb^{155}
132,8	*K*	183,1	183,1	Tb^{155}
189,5	*K*	239,7	239,7	Tb^{155}
212,3 254,6 260,4	*K* *L* *M*	262,5 262,5 261,9	262,5	Tb^{155}
290,5 333,3	*K* *L*	340,7 341,1	340,9	Tb^{155}
318,1 360,2	*K* *L*	368,3 368,0	368,2	Tb^{155}
148,7 190,8	*K* *L*	198,9 198,7	198,8	Tb^{156}
306,0	*K*	356,2	356,2	Tb^{156} ?
415,8	*L*	423,7	423,7	Tb^{156} ?

The following conversion lines were observed in the terbium fraction spectrum but were not identified: 143.7, 165.7, 180.6, 225.8, 247.5, 312.6, 459.4 and 477.8 kev.

4. Investigation of γ-γ Coincidences

In view of the great complexity of the γ-spectrum of the terbium fraction it would seem well night impossible to arrive at a reliable interpretation of the results of investigation of γ-γ coincidences by means of scintillation spectrometers. As will be evident from what follows, however, we were actually able to draw a number of inferences on the basis of the γ-γ coincidence measurements. These measurements were carried out on a twin scintillation spectrometer; the coincidence spectra were recorded by means of a 100-channel pulse height analyzer (type AI-100). In the scanning channel we used a 30 mm diameter, 14 mm thick NaI(Tl) crystal which yielded a half-width of 12% for the Hg^{203} 279 kev line. The NaI(Tl) crystal in the control (fixed) channel was characterized by somewhat poorer resolution. The coincidence measurements were started 8 hours after bombardment.

Owing to the complexity of the coincidence spectra, we were forced to carry out a number of different control measurements. For example, we repeated the measurements of coincidences with the 110 kev γ-rays with a 0.5 mm lead absorber in front of the crystal in the control channel in order to allow for the coincidences due to the Compton distribution from the higher energy photons.

A. Coincidences with 640 kev gammas

In the singles γ-spectrum there was observed a 640 kev line, the intensity of which fell off rapidly with time. Presumably the isotope responsible for this line is either 4 hour Tb^{149} (Ref.2) or 3.1 hour Tb^{150} (Ref. 6). The gate of the single channel analyzer in the control channel was set on this line and the coincidence spectrum investigated in the range to 700 kev. These measurements were repeated after a lapse of 3.5 hours. In this case it was found that the intensity of the entire spectrum, with the exception of a line at 510 kev, changed very little (~10%). The intensity of the 510 kev line decreased by a factor of 2. From this it may be inferred that the 640 kev transition is in coincidence with the 510 kev transition. Inasmuch as the 510 kev transition was not observed in the electron spectra, it may

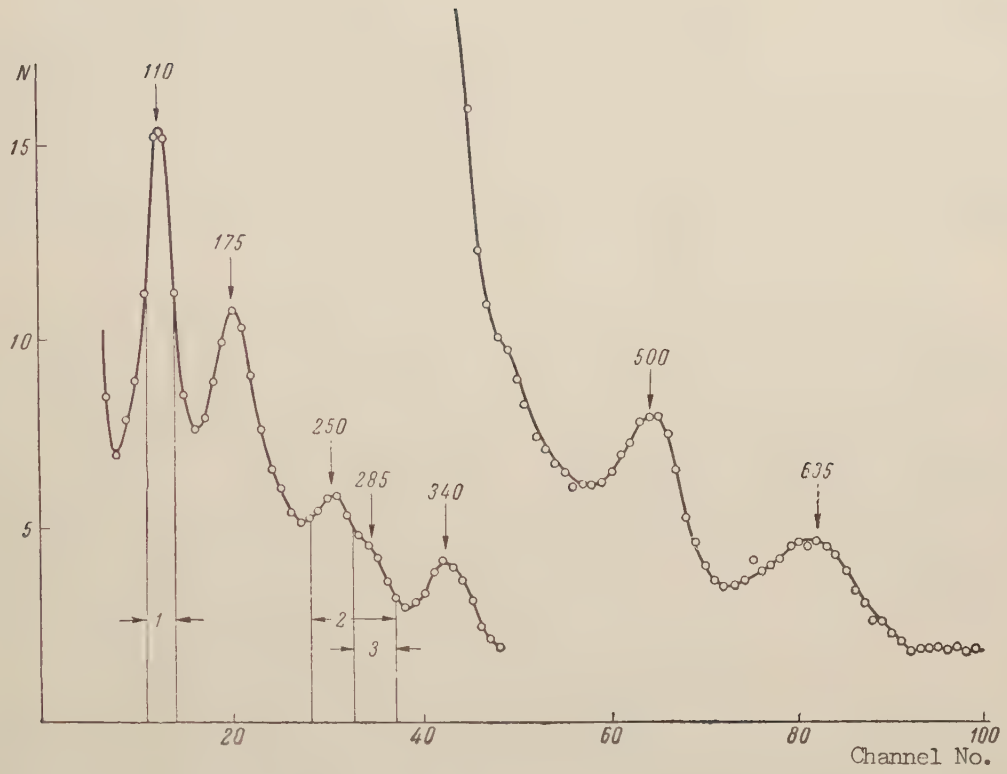

Fig.1. Gamma spectrum of the terbium fraction measured 8 hours after bombardment. 1, 2 & 3 - sections of the spectrum on which the gate of the fixed channel was set in measuring coincidences (Figs.2-4).

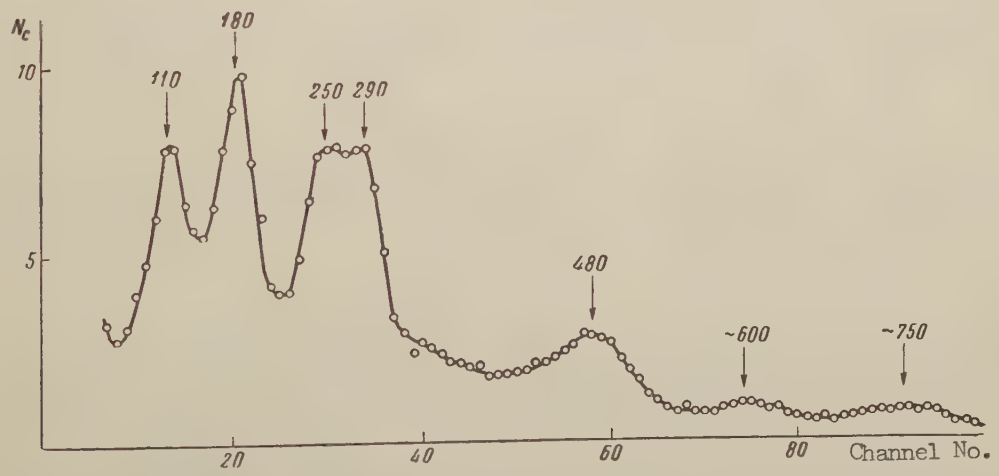

Fig.2. Spectrum of γ-rays in coincidence with the 110 kev γ-rays.

be concluded that this line is due to annihilation radiation.

B. Coincidences with 110 kev gammas

The 110 kev γ-line is the most intense line in the singles spectrum (Fig.1). According to the data in the literature, the transitions that may be responsible

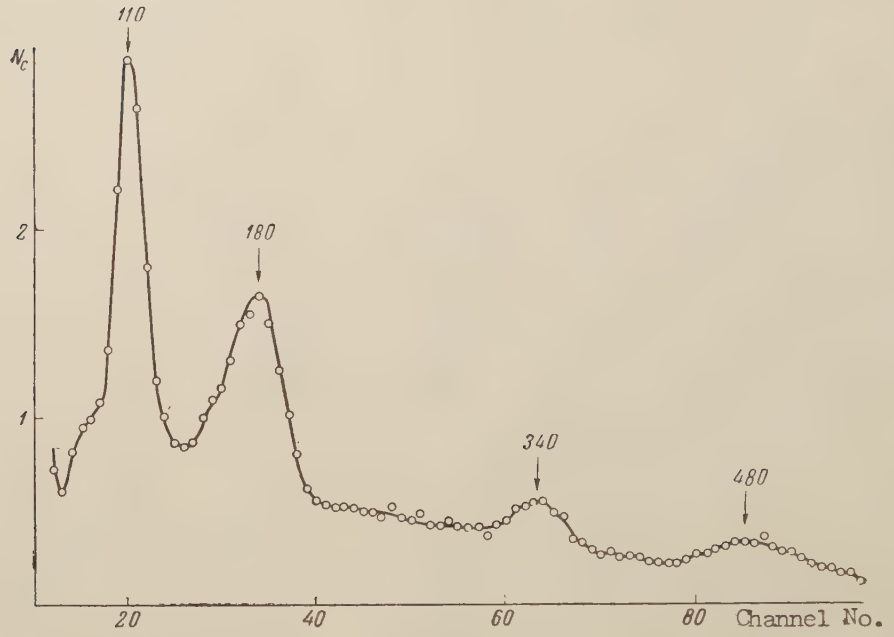

Fig.3. Spectrum of γ-rays in coincidence with the γ-rays in the 240 to 300 kev range.

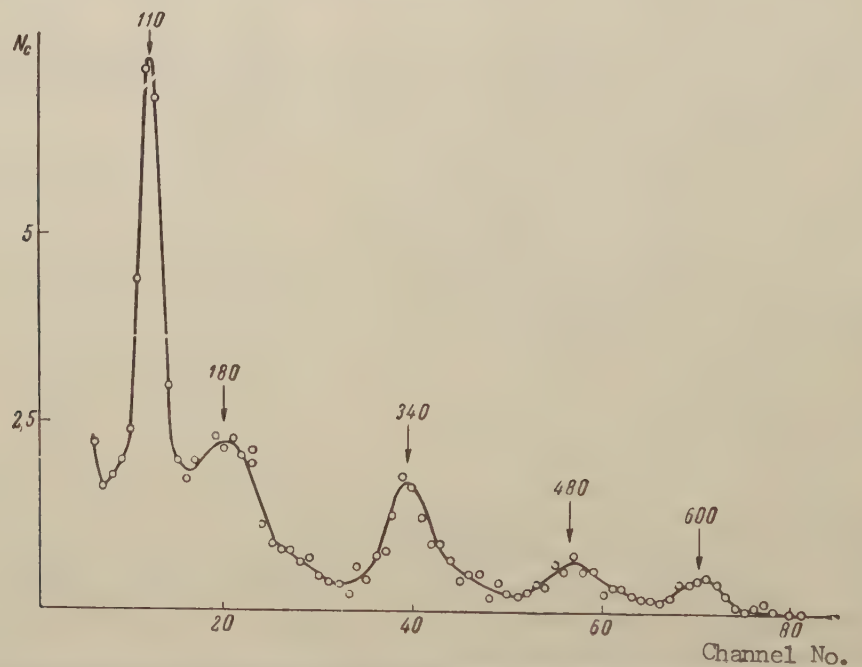

Fig.4. Spectrum of γ-rays in coincidence with the 290 kev γ-rays.

for this line include the 108.3 kev transition of Tb^{151}, the 110.0 kev transition of Tb^{153} and the 105.7 kev transition of Tb^{155} (see Table 1). According to the conversion electron spectrum, the intensity of the 110.0 kev line amounts to ~10% the intensity of the 108.3 kev line, while the intensity of the 105.7 kev line is negligibly low. It may be assumed that approximately the same relative intensities

obtain in the γ-spectrum and that, consequently, the principal contribution to the 110 kev peak is from the 108.3 kev transition of Tb^{151}. In the coincidence spectrum (Fig.2) there were observed peaks at 180, 250, 290 and 480 kev. There were also detected coincidences of low intensity in the 600 to 750 kev region. The intensity of the coincidences decayed with time with a period of ~20 hours. This also indicates that the observed coincidences are associated with the decay of Tb^{151} (20 hours) rather than Tb^{153} (2.3 days). Thus it may be assumed that the listed peaks are connected with 180.1, 251.3, 287.3 and 478.3 kev transitions in Gd^{151}, which are in cascade with the 108.3 kev transition.

C. Coincidences with 250 and 290 kev gammas

At first we measured coincidences with the γ-rays in the 240 to 300 kev interval. In this spectrum there were observed peaks at 110, 180, 345 and 480 kev (Fig.3). No coincidences with γ-rays in the 250 to 290 kev region were observed, which indicates that the 251.3 and 287.3 kev γ-transitions are not in cascade. Then the analyzer gate in the control channel was narrowed to 270-300 kev. As a result the intensity of the 180 kev peak in the coincidence spectrum was diminished. It may be concluded from this that the 180 kev peak observed with the wide gate was due to a 180.1—251.3 kev cascade. The other peaks in the spectrum (110, 345, 480 and 600 kev) remained virtually unaltered (Fig.4).

D. Coincidences with 345 kev gammas

With the fixed channel gate set at 345 kev there were evinced peaks at 180 and 270 kev. No coincidences with the 110 kev γ-rays were detected. The peak at 345 kev is due mainly to the 344.0 kev transition excited in the decay of 18.5-hour Tb^{152}. There are no transitions of close energy in the decay of Tb^{151}; while Tb^{154} has a 347.0 kev transition, the amount of this isotope present in our terbium fraction was very small.

According to Toth et al[5], transitions of 180 and 265 kev energy are excited in the decay of Tb^{152}. These transitions, according to our measurements, are in cascade with the 344.0 kev transition in Gd^{152}.

5. Discussion

We shall discuss the results described above in order of increasing mass number. Except as otherwise noted the γ-transition energies are taken from Table 1.

A = 149

In investigating the conversion electron spectrum there were detected two γ-transitions with energies of 165.1 and 351.9 kev which are characterized by a decay period of 4 hours; these according to Toth & Rasmussen[2], pertain to the decay of Tb^{149}. In addition, there was observed a conversion line at 137.3 kev, the intensity of which fell off with the same period. If it is assumed that this is a K line, the energy of the corresponding transition is 187.5 kev. The sum of 165.1 and 187.5 kev is close to 351.9 kev. Hence it may be inferred that the 187.5 kev transition also belongs to Tb^{149}, and together with the 165.1 kev transition forms a cascade parallel to the 351.9 kev transition.

A = 150

The 638.6 kev transition, detected in investigating the conversion electron spectrum (Table 3), according to the γ-γ coincidence data, yields coincidences with annihilation radiation and, apparently, no coincidences with any other γ-transitions. Inasmuch as according to Toth et al[6] the 640 kev γ-rays belong to Tb^{150}, it may be inferred that the 638.6 kev transition departs from the first excited level of Gd^{150}, which is populated by positron decay of Tb^{150}.

A = 151

Although we did not make quantitative measurements of the γ-ray intensities in the spectrum of Tb^{151}, it may be asserted that the most intense transition in Gd^{151} is the 108.3 kev transition to the ground state of Gd^{151}.

The results of our γ-γ coincidences show that the 251.3 and 287.3 kev γ-transitions yield coincidences with the 108.3 kev γ-transition; there are no coincidences between the 251.3 and 287.3 kev transitions. The intensity of the 180 kev γ-rays in coincidence with the 108.3 kev γ-rays is lower than the total intensity of the 251.3 and 287.3 kev γ-rays. Hence we infer that the 251.3 and 287.3 kev transitions feed the 108.3 kev level, and accordingly depart from levels at 359.6 and 395.6 kev, respectively. In the conversion electron spectrum there were observed the K and L conversion lines associated with a 395.6 kev transition; the intensity of these fell off with a period of ~19 hours. This enabled us to assign this transition to the decay of Tb^{151} and identify it as a cross-over transition to the ground state. It cannot be said with certainty whether the peak at 180 kev in the coincidence spectra (Figs.2 & 3) is due to the 180.1 kev or to the 192.1 kev transition (or both), inasmuch as the uncertainty in determining the energy amounts to approximately ±5 kev. In our opinion, however, it is more probable that this peak is due to the 180.1 kev transition departing from a level at 575.7 kev to the 395.6 kev level.

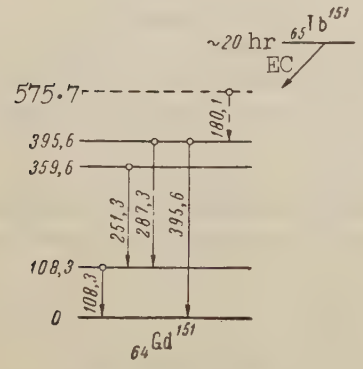

Fig.5. Proposed level diagram for Gd^{151}.

The appearance of the peak at 480 kev in the coincidence spectra reproduced in Figs.2 & 3 gives reason to infer that the 478.3 kev transition inferred from the conversion electron spectra also belongs to the decay of Tb^{151}.

A tentative diagram of the low-lying levels of Gd^{151} excited in the decay of Tb^{151} is shown in Fig.5. The location of higher levels must await further investigation; from the diagram shown in Fig.5, however, it may be concluded that in all probability the Gd^{151} nucleus is still spherical rather than deformed, whereas the level diagram for Gd^{153} is characteristic of a strongly deformed nucleus.

A = 152

In the conversion electron spectrum we observed lines corresponding to γ-transitions with energies 270.4, 344.0, 412.7, 614.7 and 778.3 kev, all characterized by a decay period of ~20 hours. Transitions of like energies in Gd^{152} are excited in the decay of Eu^{152} and Eu^{152m} (Refs.7 & 8). Thus it may be assumed that these transitions are excited in the decay of Tb^{152} and are located in the level diagram as shown in Fig.6. In addition, we inferred the existence

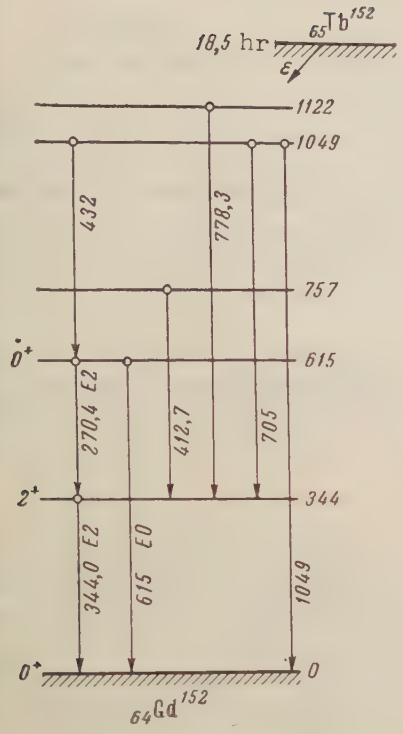

Fig.6. Proposed level diagram for Gd^{152}.

of a level at 1049 kev in Gd^{152}. The introduction of this level makes it possible to accomodate the 431.5, 705 and 1049 kev transitions, which are evinced in the conversion electron spectrum but which have not hitherto been identified.

After completion of the major part of this investigation we received the journal containing the work of Toth, Nielsen & Skielbreid[9], devoted to investigation of the decay of Tb^{152}. These authors established that in Gd^{152}, in addition to the levels known from the decay of the Eu^{152} isomers, there are levels with energies of 929 and 1047 kev. The 929 kev level was introduced on the basis of coincidences observed between the 585 and 344 kev γ-rays and between the conversion electrons of the E0 615 kev transition and the 344 kev γ-rays.

In our γ-γ coincidence measurements the 600 kev peak was clearly evinced when the analyzer gate was set at 110 and 290 kev, but was much weaker when the gate was set at 345 kev. The fact that the 585 kev transition in Gd^{152} is not in cascade with the 271 kev transition led us to attribute the 586.7 kev γ-transition evinced in the conversion electron spectrum to the decay of Tb^{151} rather than to the decay of Tb^{152}. It is possible, of course, that γ-transitions of approximately this energy occur in the decay of both these isotopes.

A > 152

In the conversion electron spectra there were also observed intense γ-transitions excited in the decay of Tb^{153}, Tb^{154} and Tb^{155} (see Tables 3 & 5). However, no new data on the decay of these isotopes were obtained in the present investigation.

As will be evident from Table 4 and the above discussion, in the course of the investigation there were detected several unidentified conversion lines, the intensity of which fell with a period of ~19 hours. These are probably associated with the decay of Tb^{151}, Tb^{152} or Tb^{154}. Qualitative analysis of the experimental results indicates that Tb^{154} was present in the investigated terbium fraction in an appreciably smaller amount than Tb^{151} and Tb^{152}. Hence it may be hypothesized that these transitions occur in the decay of Tb^{151} and Tb^{152} and that the decay schemes of these isotopes are considerably more complicated than those shown in Figs.5 and 6.

We desire to express our deep gratitude to the laboratory personnel of the Joint Institute for Nuclear Research for radiochemical separation of the terbium fraction and to I.A.Yutlandov and K.Ya.Gromov for assistance in carrying out the study.

Scientific-Research Institute of Nuclear Physics,
Moscow State University &
Joint Institute for Nuclear Research

References

1. A.T.Strigachev, L.S.Novikov, A.A.Sorokin, V.A.Khalkin & V.S.Shpinel', Trudy III Coveshchaniya po yadernoi spektroskopii, OIYaI (Transactions of the Third Conference on Nuclear Spectroscopy), Dubna, June, 1960.

2. K.S.Toth & J.O.Rasmussen, J.Inorg. and Nucl.Chem., 10, No.3/4, 198 (1959).

3. J.W.Michelich, B.Harmatz & T.H.Handley, Phys.Rev., 108, 989 (1957).

4. N.M. Anton'eva, A.A.Bashilov, B.S.Dzhelepov & B.K.Preobrazhenskii, Doklady AN SSSR, 119, 241 (1958). (Trans.Soviet Physics - Doklady.)

5. K.S.Toth, K.T.Faler & J.O.Rasmussen, Phys.Rev., 115, 158 (1959).

6. K.S.Toth, S.Bjornholm, M.Jorgensen, O.B.Nielsen & O.Skielbreid, Phys.Rev., 116, 118 (1959).

7. J.M.Cork, M.K.Brice, R.G.Helmer & D.E.Sarason, Phys.Rev., 107, 1621 (1957).

8. I.Markbund, O.Nathan & O.B.Nielsen, Nucl.Phys., 15, 199 (1960).

9. K.S.Toth, O.B.Nielsen & O.Skielbreid, Nucl.Phys., 19, 389 (1960).

POSITRON SPECTRA OF NEUTRON-DEFICIENT TERBIUM AND NEODYMIUM ISOTOPES

- N.A.Bonch-Osmolovskaya, B.S.Dzhelepov, O.E.Kraft & Chou Yüeh-wa

The neutron-deficient Tb and Nd isotopes for the present study were obtained by the spallation of tantalum bombarded with 660 Mev protons in the Joint Institute for Nuclear Research synchrocyclotron. The bombardment periods were 15, 30, 45 min and 2 hours. The respective fractions were separated chromatographically. The eluate drops were deposited on 5 μ thick 15 x 2 mm aluminum foils. The measurements, which were started 3-4 hours after bombardment and 15-30 min after separation, were carried out on the triple focusing β-spectrometer described in Ref.1.

Terbium Fraction

Several positron spectra were observed in the activity of the terbium fraction.

1. T = (18 ± 2) hours

The end-point energies of the components of this spectrum, as evaluated from the Kurie plots, proved to be 2800 ± 100, 1800 ± 150 and ~750 kev. There have been a number of descriptions of this spectrum in the literature[2-4]. Our values for the decay period and the end-point energies are in good agreement with the data of other authors. The mass number assignment for this spectrum may be regarded as reliable[4-6]: it belongs to Tb^{152}.

2. T = (3.1 ± 0.4) hours

In addition to the 18-hour spectrum, we observed an intense β^+-spectrum which fell off with a period of 3.1 ± 0.4 hours (Fig.1) (the initial counting rate at the peak was ~7000 coinc/min).

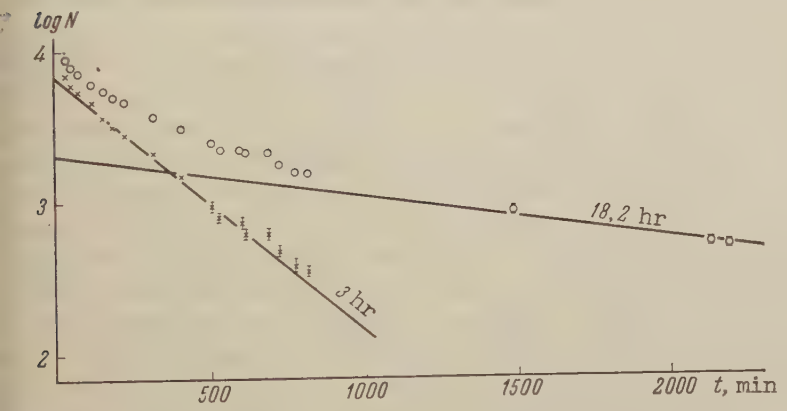

Fig.1. Decay in intensity of the 715 kev terbium β^+-spectra. Open circle points - experimental data; crosses - results of subtraction of the line for T = 18.2 hours.

Analysis of the spectrum by means of the Kurie plot showed that it consists of three components (Fig.2) with end-point energies 3600 ± 100, 2800 ± 150 and 1500 ± 100 kev and relative intensities 1:(0.52 ± 0.10): :(0.54 ± 0.10), as evaluated for the Fermi components.

There have been a number of references in the literature to a terbium fraction with a period of 3-4 hours. Rasmussen, Thompson & Ghiorso[7] observed a terbium activity with T = 4.1 hours in sources obtained by bombarding Gd with 32 to 200 Mev protons and Eu with 60 Mev α-particles. This activity was attributed to Tb^{149} on the basis of mass spectroscopic data. These authors note that they did not detect any positrons.

Rollier & Rasmussen[2] report that in measurements of the terbium fraction obtained by α-particle bombardment of Eu they observed an α-activity falling off with a period of 4 hours. No positrons were observed.

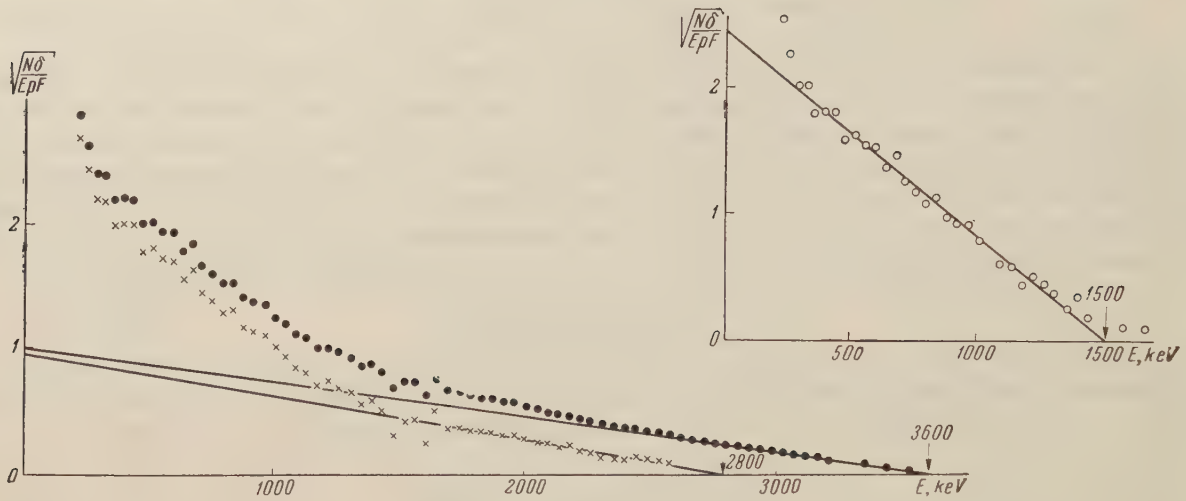

Fig.2. Kurie plot for the Tb^{150} β^+-spectrum (3.1 ± 0.4 hours). Solid points - experimental data; crosses and open circles - results of resolution into components

In a more recent study Toth & Rasmussen[8] used a multiple channel analyzer to investigate the γ-radiation from 4 hour terbium obtained by the $Pr(C^{12},xn)$ reaction (E_C = 65 Mev). They observed a number of γ-lines, but detected no noticeable annihilation peak.

Zhelev et al[9], in investigating a terbium fraction on the triple focusing β-spectrometer at Leningrad State University, observed a hard β^+-spectrum with T = = (3.5 ± 0.1 hours). Inasmuch as their measurements were started 20 hours after bombardment, the β^+-spectrum with T = 3.5 hours was appreciably weaker than the β^+-spectrum with T = 18 hours, so that these authors could investigate only the high energy part of the spectrum, where there is no contribution from the 18-hour component. The end-point energy of the β^+-spectrum was determined as 3720 ± 60 kev According to the tables of Cameron & Levy[10], the Tb^{149} - Cd^{149} mass difference is 3000 kev on the average, whereas on the basis of the disintegration energy measurements it appeared to be $\geqslant$4700 kev. In view of this great divergence, Zhelev et al infer that this spectrum belongs to Tb^{150} or Tb^{148}, the decay energies of which, according to the empirical formulas[10], should be 3700 and 5000 kev, respectively.

Recently there appeared the work of Toth et al[11] in which the authors report on the discovery of a new terbium isotope: Tb^{150}. These authors bombarded a natural mixture of Gd isotopes with 60 Mev protons. The new isotope was isolated by a mass separator from the chemically purified terbium fraction. They give the half-life as 2.1 ± 0.2 hr. At the same time there was observed the activity of 4.1-hour Tb^{149}. The authors investigated the γ-spectra of Tb^{149} and Tb^{150}, and observed annihilation peaks in both spectra; in the case of Tb^{150} the annihilation peak was more pronounced. It must be noted that the mass separation of the fraction was not complete in this case, in contrast to the separation carried out for measuring the periods.

The fact that positrons were not detected in the measurements of Refs.2, 7 and 8, indicates that the β^+-spectrum of Tb^{149} is of low intensity. Judging from its decay period (3.1 ± 0.4 hr), the terbium isotope responsible for the β^+-spectrum observed by us is probably Tb^{150} rather than Tb^{149}. If there were present in the measured β^+-spectrum an appreciable number of positrons from Tb^{149}, we should have observed an increase in the period for measurements in the soft part

of the spectrum. This was not the case. In all the measurements the period had the same value within the limits of the experimental error in all the energy intervals.

3. T = (66 ± 10) min

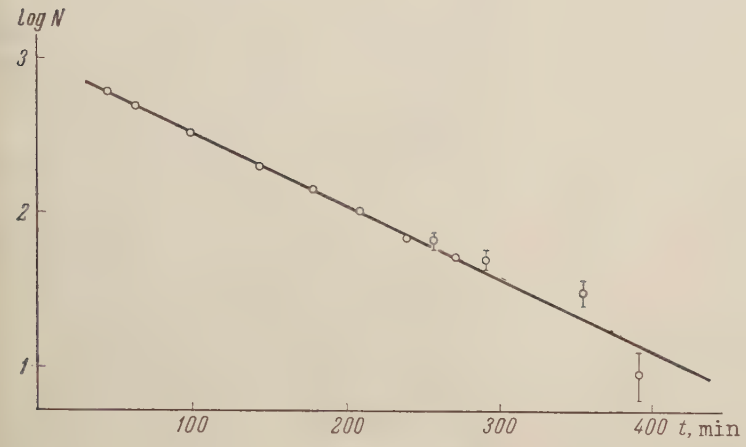

Fig.3. Decrease in intensity of the β^+-spectrum of Tb^{148} (T = 66 min) at 3610 kev.

In the highest energy part of the terbium fraction spectrum in all the experiments we observed an activity with T = (66 ± ± 10 min) (Fig 3). This spectrum is less intense than the β^+-spectrum with T = 3.1 ± 0.4 hr, and hence we could not separate it entirely from the integral spectrum by subtracting the Tb^{150} and Tb^{152} positrons. We were able to separate with reasonable accuracy only the hardest component of the β^+-spectrum, the end-point energy of which proved to be 4600 ± 100 kev (Fig.4). As will be evident from Fig.4, there is reason to infer that there may also be present a second component with end-point energy 2600 ± 200 kev.

Toth & Rasmussen[8] recently reported the discovery of a new terbium isotope, Tb^{148}, with a period of 70 min. They observed a weak annihilation peak. The Tb^{148} - Gd^{148} mass difference according to the empirical mass formulas is 5042 kev (Cameron) or 4956 kev (Riddel-Levy), which is close to our value of ⩾5600 kev. Hence we feel safe in assigning the observed spectrum with T = 66 ± 10 min to Tb^{148}.

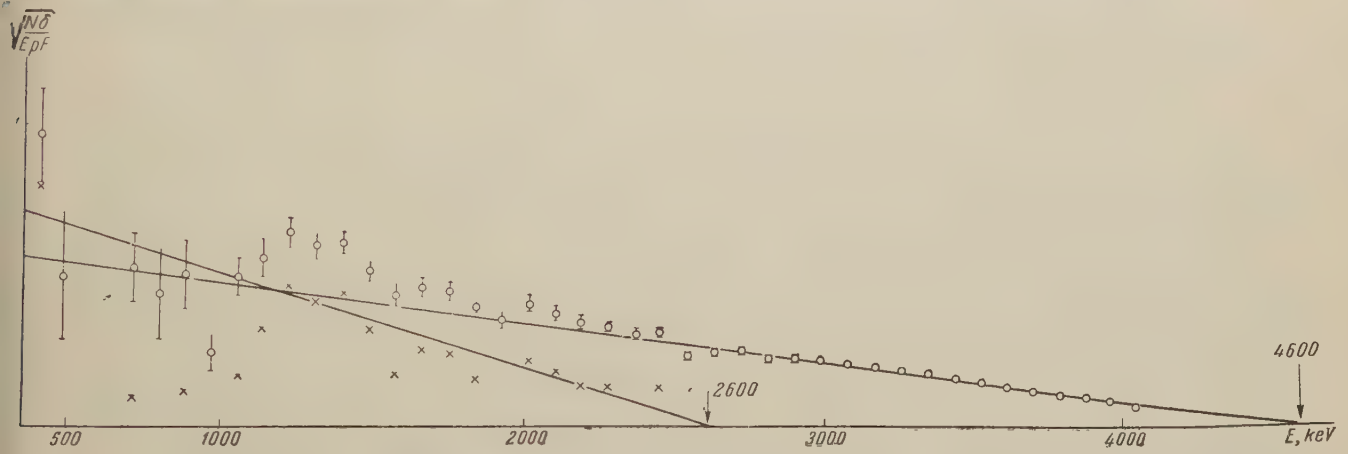

Fig.4. Kurie plot for the β^+-spectrum of Tb^{148} with T = 66 ± 10 min. The crosses give the result of subtracting the hard component of the β-spectrum.

Neodymium Fraction

In investigating the positron spectrum of the neodymium fraction we first detected the known β-spectrum of the chain

$$Nd^{140} \xrightarrow[e]{3.3\ d} Pr^{140} \xrightarrow[e,\beta^+]{3.5\ min} Ce^{140}.$$

The end-point energy of this spectrum as determined from the Kurie plot is 2285 ± ± 100 kev. This value agrees with the data of other authors[12-14]. This β^+-spectrum is rectilinear from the end-point to ~350 kev.

In addition to the β^+-spectrum of the above decay chain, we also observed an intense β^+-spectrum of appreciably higher energy than the β^+-spectrum of Pr^{140}.

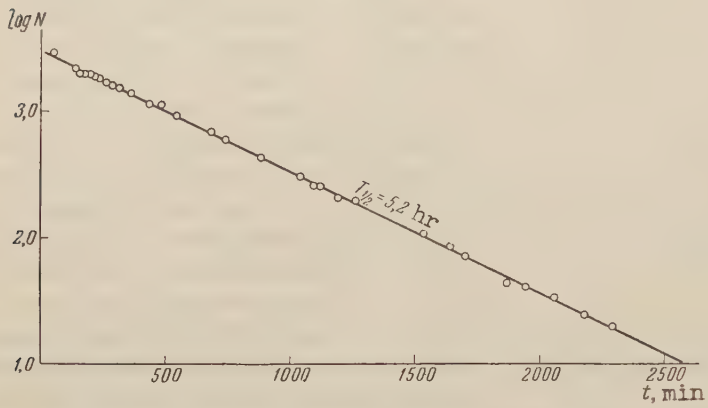

Fig.5. Decay curve of neodymium for E_{β^+} = 2721 kev.

The decay curve obtained for the sections outside the range of the Pr^{140} β^+-spectrum (for a positron energy of 2720 kev - Fig.5) yielded T = 5.2 ± 0.2 hrs.

Observation of the decay in different parts of the spectrum (at E_{β^+} = 402, 558, 971, 1397 and 1836 kev) also showed that in addition to Nd^{140} ± ± Pr^{140}, there was present in the source an activity decaying with a period of 5.2 ± 0.2 hrs.

The β^+-spectrum proved to be complex. It will be evident from the Kurie plot shown in Fig.6, that it comprises three components with end-point energies 3300 ± 100, 1000 ± 100 and 460 ± 60 kev, with relative intensities 1:(0.084 ± 0.005):(0.024 ± ± 0.001). The 460 kev component is very weak and we have only a few points in the Kurie plot for determining it; hence its existence may be regarded as questionable.

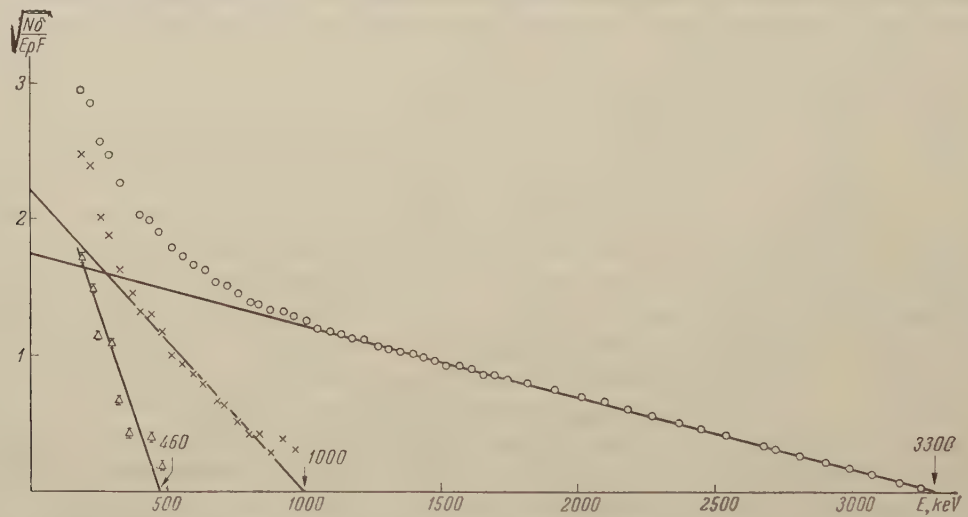

Fig.6. Kurie plot for Nd^{139}. Crosses and trangles - results of resolution into components.

Some years ago Stover[15] reported the existence of the decay chain:

$$Nd^{139} \xrightarrow[e,\beta^+]{5.5\ hr} Pr^{139} \xrightarrow[e,\beta^+]{4.5\ hr} Ce^{139}.$$

According to our earlier measurements and the data of other authors[15,16], the end-point energy of the positron spectrum of Pr^{139} is 1000 kev. If it is assumed that the second component of the β^+-spectrum with end-point energy 1000 kev observed by us for Nd^{139} belongs entirely to Pr^{139}, we should have observed an increase in the intensity ratio $S_{\beta^+ 1000}/S_{\beta^+ 3300}$ during the first 7 hours after separation. Measurements carried out 3 and 8 hours after separation of the source showed, however, that the $S_{\beta^+ 1000}/S_{\beta^+ 3300}$ ratio remains constant within the limits of the experimental error. Hence the number of Pr^{139} positrons in the observed β^+-spectrum is apparently very small and, consequently, one can attribute the component with 1000 kev end-point energy to Nd^{139}.

In addition to measurements of the positron spectra, we also investigated the conversion electron spectrum of the neodymium fraction. There were observed the conversion lines associated with two transitions: E_γ = 694 and E_γ = 1442 kev; the intensities of the lines fell off with T = 5.2 ± 0.3 hr and T = 5.6 ± 0.5 hr, respectively.

Assuming that the observed conversion lines and β^+-spectrum belong to Nd^{139}, we evaluated the relative intensities of the β^+-spectrum and of the conversion lines on the basis of the areas under the peaks and obtained $e^-/\beta^+ = 1.14 \cdot 10^{-3}$ for E_γ = 692 kev and $e^-/\beta^+ = 2.3 \cdot 10^{-4}$ for E_γ = 1442 kev.

References

1. O.E.Kraft & B.S.Dzhelepov, Izv.AN SSSR, Ser.fiz., 20, 318 (1956). (Trans. Bulletin, 20, 293.)
2. Rollier & J.O.Rasmussen, Rend.Acad.nahl.Lindcei, 14, 526 (1953).
3. N.M.Anton'eva & A.A.Bashilov, Doklady AN SSSR, 119, No.2, 241 (1956). (Trans.Doklady.)
4. K.S.Toth, K.T.Faler & J.O.Rasmussen, Phys.Rev., 115, 158 (1959).
5. A.N.Bonch-Osmolovskaya, B.S.Dzhelepov & O.E.Kraft, Izv.AN SSSR, Ser.fiz., 24, 283 (1960). (Trans.Bulletin, 24, 270.)
6. A.S.Basina, K.Ya.Gromov & B.S.Dzhelepov, Materialy X Soveshchaniya po yadernoi spektroskopii (Transactions of the 10th Conference on Nuclear Spectroscopy), M., 1960.
7. J.O.Rasmussen, S.G.Thompson & A.Ghiorso, Phys.Rev., 89, 33 (1953).
8. K.S.Toth & J.O.Rasmussen, Inorg.Nucl.Chem., 10, 198 (1959).
9. Zh.T.Zhelev, A.V.Kudryavtseva & B.S.Dzhelepov, Materialy X Soveshchaniya po yadernoi spektroskopii (Transactions of the 10th Conference on Nuclear Spectroscopy). M., 1960.
10. A.G.W.Cameron, A Revised Semi-Empirical Atomic Masses Formula, CRP 690, Chalk River, 1957; J.Riddel, A Table of Levy's Empirical Masses Formula, CRP 654, Chalk River, 1957.
11. K.S.Toth, S.Bjørnholm, M.Jørgensen, O.B.Nielsen & O.Skilbreid, Phys.Rev., 116, 118 (1959).
12. G.Wilkinson & H.G.Hicks, Ibid., 75, 1687 (1949).
13. C.I.Browne, J.O.Rasmussen, J.P.Surls & D.F.Martin, Ibid., 85, 146 (1952).
14. B.S.Dzhelepov, I.S.Uchevatkin & S.A.Shestopalova, Materialy II Coveshchaniya po neitronodefitsitnym izotopam (Transactions of the 2nd Conference on Neutron-Deficient Isotopes), Dubna, 1959.
15. Betsy J.Stover, Phys.Rev., 81, 8 (1951).
16. T.H.Handley & E.L.Olson, Phys.Rev., 96, 1003 (1954).

INVESTIGATION OF COULOMB EXCITATION OF NUCLEAR LEVELS BY MEANS OF MULTIPLY CHARGED IONS

- D.S.Andreev, V.D.Vasil'ev, G.M.Gusinskii, K.I.Erokhina & I.Kh.Lemberg

The possibilities, advantages and experimental difficulties in utilizing multiply charged ions as the bombarding particles in investigating Coulomb excitation of nuclear levels have been discussed in detail in Refs.1 and 2. The principal advantage is that the γ-ray background from the target is appreciably lower than when one uses α-particles or protons.

A significant development in our work in 1960 in the Physical-Technical Institute was extension of the energy range of the accelerated ions up to 53 Mev ($N^{14;5+}$), on the one hand, and down to 12 ($N^{14;3+}$) and 16 Mev ($Ne^{20;4+}$), on the other hand. As a result it proved feasible to excite high lying ($\Delta E \geqslant 1$ Mev) levels in Mg^{25}, Mg^{26}, Ca^{44}, Co^{59}, In^{115}, Sb, Ba^{138}, and Ce^{140}, as well as levels in such light nuclei as Li^{7} and B^{10}.

The Coulomb excitation of the nuclear levels was investigated by means of cyclotron beams of $Ne^{20;4+}$ ions with energies from 16 to 26 Mev, $N^{14;3+}$ ions with energies from 12 to 22 Mev, $N^{14;4+}$ ions with an energy of 36 Mev and $N^{14;5+}$ ions with an energy of 53 Mev. The Coulomb excitation cross sections were determined from the yield of γ-radiation emitted in de-excitation of the excited levels. The equipment and measurement procedure were similar to those employed earlier[1,2].

In order to enhance the accuracy of the results we used the method of "reference levels" developed earlier[1,3]. In using this procedure, before measuring the excitation cross section for the studied level, one measures the cross section for a reference level for which the reduced excitation probability $(B(E2)\uparrow$ is well known; the reference level should be in a nucleus with a close value of Z and have an energy of the same order as that of the studied level. The discrepancy between the measured and known excitation probability for the reference level is then used to correct the experimental reduced probability for the studied level

In the present work we used the following reference levels:

in investigating Li and B - the 0.44 Mev level in Na^{23} $(B(E2)\uparrow = 0.11\cdot10^{-48}$ e^2 cm^4 - Ref.4);

in investigating Co - the 1.19 Mev level in Ni^{62} $(B(E2)\uparrow = 0.085\cdot10^{-48}$ e^2 cm^4 - Ref.1);

in investigating Mg, Ca and Se - the 0.56 Mev level in Se^{76} $(B(E2)\uparrow = 0.42\cdot10^{-48}$ e^2 cm^4 - Ref.1);

in investigating In, Sb and Ce - the 1.15 Mev level in Sn^{122} $(B(E2)\uparrow = 0.26\cdot10^{-48}$ e^2 cm^4 - Ref.5);

in investigating even Sn isotopes and Ba^{138} - the 1.60 Mev level in Ce^{140} ($\tau = 1.1\cdot10^{-13}$ sec - Ref.6);

in investigating Sn^{117} - the 0.16 Mev level in Ti^{47} $B(E2)\uparrow = 0.040\cdot10^{-48}$ e^2 cm^4 - Ref.7).

The accuracy in determining the reduced probabilities, except as otherwise noted, is estimated to be 15-20%.

The results of our measurements are summarized in Tables 1 and 2. Here ΔE is the level energy; $B(E2)\uparrow$ is the reduced excitation probability; τ is the lifetime of the level; F is the ratio of the experimental $B(E2)\uparrow$ to the reduced probability calculated on the basis of the single particle model ($B(E2)\uparrow_{sp}$) (in the calculations it was assumed that the nuclear radius $R_0 = 1.2\cdot10^{-13}$ $A^{1/3}$ cm); I_0 and I_f are the spins of the nucleus in the ground state and excited state, respectively; $\tau(E2)$ is the partial lifetime of the level with respect to electric quadrupole de-excitation to the ground state. In the even-even nuclei there were excited the first spin 2^+ levels.

Table 1

Coulomb excitation of levels in even-even nuclei

Isotope	ΔE, MeV	$\frac{B(E2)\uparrow}{e^2}\cdot 10^{48}$, см^4	τ, 10^{-13} sec	F	Isotope	ΔE, MeV	$\frac{B(E2)\uparrow}{e^2}\cdot 10^{48}$, см^4	τ, 10^{-13} sec	F
Mg^{26}	1,83	0,035	5,7	15	Sn^{120}	1,18	0,26	7,0	15
Ca^{44}	1,16	0,035	55	7,5	Sn^{122}	1,15	0,26	7,9	14
Se^{74}	0,635	0,44	90	47	Sn^{124}	1,13	0,22	10	12
Sn^{112}	1,26	0,33	4,0	20	Ba^{138}	1,43	0,38	1,8	18
Sn^{114}	1,30	0,25	4,4	15	Ce^{140}	1,60	0,27	1,4	12
Sn^{116}	1,29	0,29	3,9	17	Ce^{142}	0,65	0,41	86	19
Sn^{118}	1,22	0,24	6,2	14					

Table 2

Coulomb excitation of levels in odd-A nuclei and odd-odd B^{10}

Isotope	ΔE, MeV	$\frac{B(E2)\uparrow}{e^2}\cdot 10^{48}$, см^4	I_i	I_f	$\tau(E2)$, sec
Li^7	0,48	0,00050	$^3/_2^-$	$^1/_2^-$	$3,5\cdot 10^{-9}$
B^{10}	0,72	0,00017	3^+	1^+	$1,1\cdot 10^{-9}$ *
Mg^{25}	1,61	0,011	$^5/_2^+$	$^7/_2^+$	$9,0\cdot 10^{-13}$
Mg^{25}	0,98	0,00036	$^5/_2^+$	$^3/_2^+$	$1,7\cdot 10^{-10}$
Mg^{25}	0,58	0,000060	$^5/_2^+$	$^1/_2^+$	$6,9\cdot 10^{-9}$*
Co^{59}	1,10	0,010	$^7/_2^-$	$^5/_2^-$	$3,7\cdot 10^{-12}$
Co^{59}	1,19	0,028	$^7/_2^-$	$^3/_2^-$—$^{11}/_2^-$	$(6—19)\cdot 10^{-13}$
Co^{59}	1,43	0,013	$^7/_2^-$	$^3/_2^-$—$^{11}/_2^-$	$(5—15)\cdot 10^{-13}$
In^{115}	1,15	0,090	$^9/_2^+$	$^5/_2^+$—$^{13}/_2^+$	$(2,7—6,3)\cdot 10^{-13}$
Sn^{117}	0,16	0,00074	$^1/_2^+$	$^3/_2^+$	$2,1\cdot 10^{-6}$
$Sb^{(121)}$	1,05	0,18	$^5/_2^+$	$^1/_2^+$—$^9/_2^+$	$(1,2—6,0)\cdot 10^{-13}$
$Sb^{(123)}$	1,05	0,24	$^7/_2^+$	$^3/_2^+$—$^{11}/_2^+$	$(1,4—4,0)\cdot 10^{-13}$
$Sb^{(121)}$	1,12	0,038	$^5/_2^+$	$^1/_2^+$—$^9/_2^+$	$(4—20)\cdot 10^{-13}$
$Sb^{(123)}$	1,12	0,050	$^7/_2^+$	$^3/_2^+$—$^{11}/_2^+$	$(5—28)\cdot 10^{-13}$

*Total lifetime of the state (τ).

A. Even-Even Nuclei

Mg^{26}

Of interest in the case of Mg^{26} is excitation of the level at 1.83 Mev, known from investigations[8] of β^+-decay of Al^{26} amd experiments[9] on inelastic neutron scattering. Knowledge of the excitation probability for this level makes it possible to elucidate the dependence of $B(E2)$ for even-even magnesium isotopes on the number of neutrons in the nucleus (the value of $B(E2)$ for the 1.37 Mev level in Mg^{24} was determined in the work of Ref.1). Investigation of Coulomb excitation of the 1.83 Mev level in Mg^{26} was hampered by the fact that the abundance of Mg^{26} in the natural mixture of isotopes is only 11%, while a target of magnesium oxide enriched in Mg^{26} to 93% could not be used because under bombardment with nitrogen ions there appeared an intense 1.78 Mev γ-line as a result of the N + O reaction.[10] In working with other ions (for example, $Ne^{22;4+}$) the γ-background owing to presence of oxygen in the target proved to be so strong that it was impossible to measure the yield of 1.83 Mev γ-rays from Mg^{26} with adequate accuracy (the difficulty is aggravated by the fact that in using a magnesium oxide rather than a magnesium metal target the yield of the investigated γ-rays is reduced by a factor of 2). In the present experiments, in order to facilitate observation of Coulomb excitation of the 1.83 Mev level, there was prepared a target of metallic magnesium, separated from magnesium oxide enriched in Mg^{26}. To this end the mag-

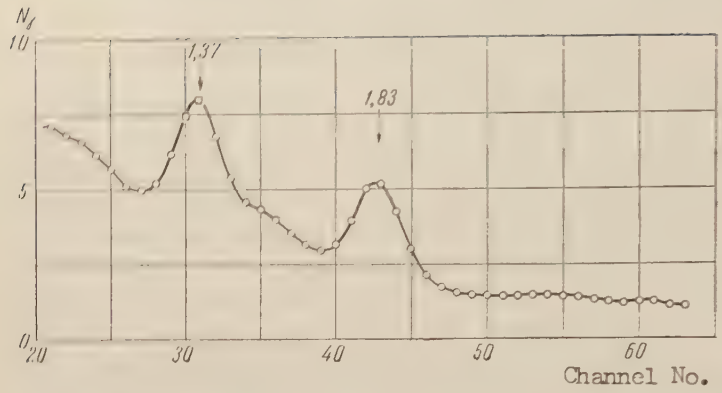

Fig.1. Experimental γ-ray spectrum obtained in Coulomb excitation of Mg^{26} with triply charged N^{14} ions with E = 18.0 Mev. The figures at the peaks indicate the γ-ray energies in Mev.

nesium oxide was heated in a special reactor in mixture with silicon; the reduced magnesium was evaporated and condensed on a cooled nickel backing.* A similar procedure was used in preparing a target of natural magnesium and a Mg^{25} enriched target.

The magnesium targets were bombarded with 16.8 and 18 Mev $N^{14;3+}$ and 25.8 Mev $Ne^{20;4+}$ ions. The γ-ray spectrum obtained in the experiments with the $N^{14;3+}$ ions of 18 Mev energy is shown in Fig.1. The 1.37 Mev line appears as the result of Coulomb excitation of Mg^{24}, which was present in the target in the amount of 5.6%. In addition, this line also appears as the result of the N + C reaction. The 1.83 Mev line corresponds to the excited level of this energy in Mg^{26}. However, some contribution to this γ-line is made by the 1.78 Mev γ-rays appearing as a result of reaction of the nitrogen ions with the oxygen, a minor amount of which was present in the target. To evaluate this contribution, we bombarded targets of natural magnesium and Mg^{25} with the same ions. In the resultant spectra there was evident a ~1.8 Mev line due both to Coulomb excitation of the 1.83 Mev level in Mg^{26} present in the natural magnesium and Mg^{25} targets in the amounts of 11% and 6%, respectively, and to the N + O nuclear reaction. Evaluation of the contribution of the 1.78 Mev gammas from the N + O reaction to the yield of the 1.83 Mev γ-rays emitted in excitation of Mg^{26} was carried out by comparing the yields of ~1.8 Mev γ-rays detected in bombarding the Mg^{26} target and in bombarding natural magnesium and Mg^{25} (taking into account the Mg^{26} content in the three targets) on the assumption that the yield of the 1.78 Mev γ-rays from all three targets was the same.

It must be noted that the γ-ray yield from the N + O reaction determined in this manner on the basis of measurements with the Mg^{25} target and two natural magnesium specimens are in good agreement. This gives reason to infer that the number of 1.78 Mev γ-rays in the experiments with Mg^{26} was correctly evaluated inasmuch as all the targets (Mg^{26}, Mg^{25} and Mg_{nat}) were prepared under identical conditions. In the experiments with 18 Mev $N^{14;3+}$ ions the number of 1.78 Mev γ-rays from the N + O reaction amounts to ~25% of the total number of ~1.8 Mev γ-rays detected in bombarding the Mg^{26} target; in the experiments with 16.8 Mev $N^{14;3+}$ ions the relative number of 1.78 Mev γ-rays amounts to only ~10%.

In bombardment of Mg^{26} with the $Ne^{20;4+}$ ions there were observed in the spectra two γ-lines: 1.63 Mev (self-excitation of Ne^{20}) and 1.83 Mev (excitation of Mg^{26}). These lines had to be resolved in order to determine the yield of 1.83 Mev γ-rays.

We estimate the error in determining $B(E2)\uparrow$ for the 1.83 Mev level in Mg^{26} as 25%.

---

*We take this opportunity to thank V.S.Rylov who developed the procedure for preparing metallic magnesium films from small amounts of magnesium oxide.

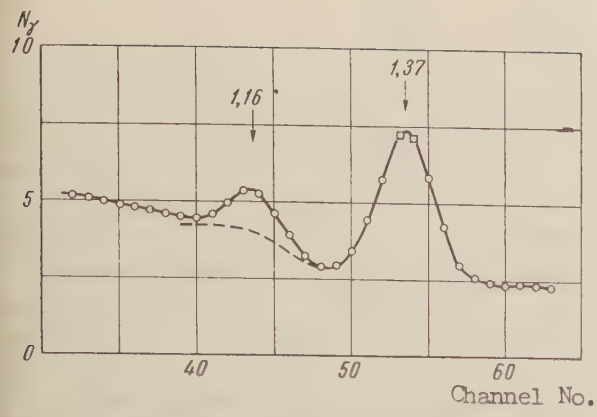

Fig.2. Experimental γ-ray spectrum emitted in Coulomb excitation of Ca^{44} ($Ca^{44}Cl_2$ target with triply charged 16.8 Mev N^{14} ions).

Ca^{44}

Coulomb excitation of the 1.16 Mev level in Ca^{44}, the existence of which is known from studies of β-decay[11] and inelastic neutron scattering[9], was investigated by means of 16.8 and 21.5 Mev $N^{14;3+}$ and 26 Mev $Ne^{20;4+}$ ions. The natural abundance of Ca^{44} is 2%. We had available a quantity of calcium carbonate enriched to 94% Ca^{44}. Use of this as a target, however, led to the appearance of intense γ-radiation owing to nuclear reactions with the oxygen and carbon impurities present. Hence the $Ca^{44}CO_3$ was converted to $Ca^{44}Cl_2$. In view of the hygroscopicity of calcium chloride, before being mounted in the Faraday cup, the target was heated for some time at 300°C.

Fig.2 shows the γ-spectrum obtained in bombardment of the $Ca^{44}Cl_2$ target with 16.8 Mev $N^{14;3+}$ ions. The dashed line in the figure shows the shape of the Compton distribution from the 1.37 Mev line, that resulted from reaction of the nitrogen ions with the carbon impurities present in the target. The shape of the 1.37 Mev line was recorded in a separate experiment involving bombardment of natural $CaCl_2$.

Se^{74}

The 0.635 Mev level in Se^{74} was discovered in investigating β-decay of As^{74} (Ref.12). The lifetime of this state has been measured by Metzger[13] by the nuclear resonance fluorescence method ($\tau \approx 6 \cdot 10^{-12}$ sec) and by Temmer & Heydenburg[14] in investigating Coulomb excitation by α-particles ($\tau = 1.9 \cdot 10^{-11}$ sec). In view of this great difference between the lifetime values, we undertook an investigation of Coulomb excitation of Se^{74} using 18 Mev $N^{14;3+}$ ions. The target was prepared of metallic selenium powder enriched to 41% Se^{74} (the Se content in natural selenium is 0.87%). The other even-even selenium isotopes were present in the target in the following amounts: 8% Se^{76}, 13% Se^{78}, 27% Se^{80}, and 6% Se^{82}.

In bombarding the target with 18 Mev $N^{14;3+}$ ions there was obtained a broad γ-peak comprising contributions of the γ-rays from all four selenium isotopes. In order to determine $B(E2)\uparrow$ for the 0.635 Mev level in Se^{74}, we measured the area of this integral γ-peak and subtracted from it the areas of peaks due to Se^{76}, Se^{78}, Se^{80} and Se^{82} evaluated from the known values of $B(E2)\uparrow$ (Ref.1). It should be noted that the values of $B(E2)\uparrow$ for Se^{76}, Se^{78} and Se^{80} reported by us in Ref.1 are in good agreement with the data of Temmer & Heydenburg[14]. Temmer & Heydenburg did not measure the reduced excitation probability for Se^{82} so that we cannot compare our results for this isotope with the data of other investigators, but there is no reason to assume that our value for Se^{82} is less precise than for the other Se isotopes. Moreover, our target contained only 6% Se^{82} so that any inaccuracy in determining $B(E2)\uparrow$ for Se^{82} could have little effect on our result for Se^{74}.

Our value for the lifetime of the 0.635 Mev state of Se^{74} is approximately half that given by Temmer & Heydenburg[14] and 1.5 times higher than that reported by Metzger[13].

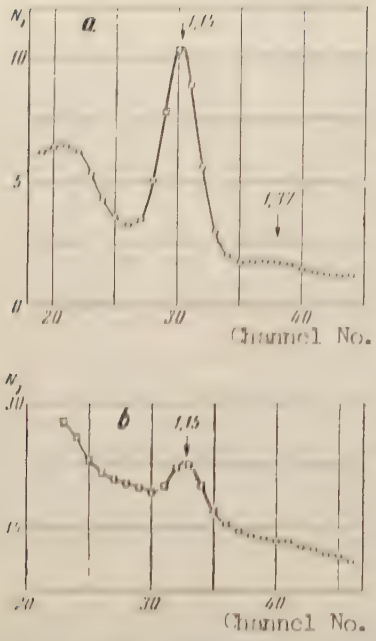

Fig.3. Experimental γ-ray spectrum recorded in Coulomb excitation of Sn^{122}: a - 52.5 Mev $N^{14;5+}$ ions, b - 13.1 Mev α-particles.

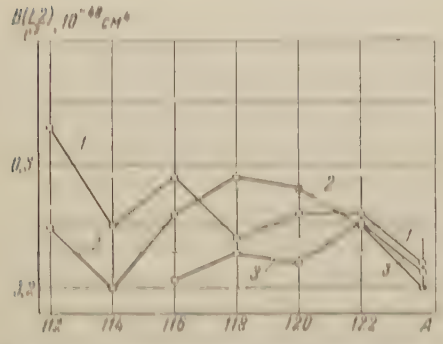

Fig.4. Comparison of the experimental and theoretical values of the reduced transition probability $B(E2)$ for the first levels of even tin isotopes: 1 - results of the present study, 2 - results of the theoretical calculations (Ref.16), 3 - results of Stelson & McGowan[5].

Sn

We first investigated[15] Coulomb excitation of the even isotopes of tin in 1957 using α-particles with energies to 14.5 Mev. Recently, Kisslinger & Sorensen[16] and Marumori[17] calculated the values of $B(E2)\uparrow$ for a number of even-even nuclei, including all the even isotopes of Sn, on the basis of the theory of S.T.Belyaev, taking into account pair correlation. It is of interest to compare the theoretical values of $B(E2)\uparrow$ with the experimental ones.

In view of the fact that our early results[15] differ from the results of Stelson & McGowan[5] (in some cases the divergence exceeds 50%), we undertook a new investigation of excitation of the even isotopes of tin using the new heavy ion procedure. Most of the experiments were carried out with quintuply charged 52.5 Mev N^{14} ions. The results of investigation of Coulomb excitation of Sn^{122} under these conditions are shown in Fig.3. For comparison we give the results obtained in bombarding Sn^{122} with α-particles. The improvement in the effect-to-background ratio realized in employing heavy ions will be evident from a comparison of Figs.3 a and b.

The results obtained in the present investigation are shown in Fig.4 together with the data of Stelson & McGowan[5] and the results of theoretical computations of $B(E2)\uparrow$ by Kisslinger & Sorensen[16]. It may be noted that the mass number variation of the $B(E2)\uparrow$ values obtained in our experiments agrees in general with the variation of $B(E2)\uparrow$ calculated by Kisslinger & Sorensen. The greatest divergence between the theoretical values and our experimental reduced probabilities obtains for Sn^{112} and amounts to about 30%. An error of this magnitude can be explained by the low content of Sn^{112} in the target (52%) and the presence in it of other even Sn isotopes.

Ba^{138}

The most abundant barium isotope has a closed neutron shell. It is known from studies of β^+-decay of La^{138} (Ref.18) that the energy of the first level in Ba^{138} is 1.43 Mev.

Investigation of Coulomb excitation of Ba^{138} involves a number of difficulties. For excitation of high-lying levels in such a heavy nucleus one must use ions of high energy, but with increase of the bombarding ion energy there occurs an appreciable increase in the γ-background from nuclear reactions of the ions with light elements inevitably present in the form of impurities. For this reason it is preferable to use metal-

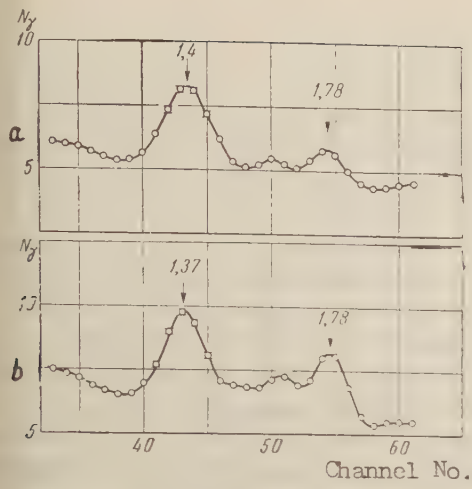

Fig.5. Experimental γ-ray spectrum recorded in bombarding a target of natural Ba (a) and a target of PbO (b) with quintuply charged 52.5 Mev N^{14} ions.

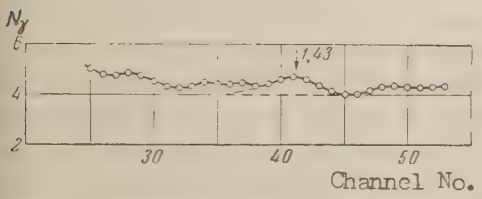

Fig.6. Experimental γ-ray spectrum recorded in bombarding a target of natural barium with 15.1 Mev α-particles.

lic barium rather than some barium compound as the target. It is known that barium readily combines with oxygen and nitrogen. Hence we prepared our metallic barium target in a dry container in an atmosphere of pure argon; this was inserted into the Faraday cup which was then coupled by means of a vacuum lock to the vacuum system through which the beam was extracted from the cyclotron.

Nevertheless, a small amount of oxygen was still present in the target, so that in the γ-spectrum recorded in bombarding the target with quintuply charged 52.5 Mev nitrogen ions there was observed the 1.78 Mev γ-line resulting from the N + O reaction. The same reaction at high bombarding ion energies also gives rise to 1.37 Mev γ-rays (Ref.10), which, being close in energy to the 1.43 Mev γ-rays emitted incident to de-excitation of the first level in Ba^{138}, hinder investigation.

Gamma-rays of 1.37 Mev energy also appear as a result of the N + C reaction, which occurs owing to the presence of a carbon film on the target[10]. However, it was shown in experiments with 52.5 Mev $N^{14;5+}$ ions that the yield of 1.37 Mev gammas at this ion energy is negligibly small (Fig.3,a).

Comparison of the spectra recorded in bombarding targets of natural barium and lead oxide (Fig. 5) shows that some oxygen impurity was present in the barium target. We determined the yield of 1.43 Mev gammas in the following manner: from the ratio of the yield of the 1.37 and 1.78 Mev γ-rays from the PbO target and the measured yield of 1.78 Mev γ-rays from the Ba target, we calculated the yield of 1.37 Mev γ-rays from the Ba target, which was then subtracted from the integral yield of 1.43 and 1.37 Mev γ-rays. It was found that the fraction of 1.43 Mev γ-rays amounts to about 50% of the total yield. This evaluation is not particularly accurate, for experiments have shown that the yields of 1.37 and 1.78 Mev γ-rays from thick and thin oxygen targets may differ appreciably.

We also investigated Coulomb excitation of barium using 15.1 Mev α-particles as the projectiles. In this case there are no parasitic lines associated with nuclear reactions and interfering with determination of the yield of 1.43 Mev γ-rays. Unfortunately, the area of the 1.43 Mev γ-peak is determined in this case with relatively low accuracy inasmuch as in the spectra obtained with α-particles the effect to background ratio is approximately three times smaller than in using nitrogen ions and equals ~1:9 (Fig.6).

The value of $B(E2)\uparrow$ for the 1.43 Mev level in Ba^{138} determined from the α-particle experiment is in good agreement with the results of measurements with nitrogen ions, but in view of the low accuracy involved in the α-particle measurements we have not used this value.

We estimate the uncertainty in determining $B(E2)\uparrow$ for the 1.43 Mev level in Ba^{138} on the basis of the nitrogen ion experiments as 30%. In order to obtain more accurate results for Ba^{138}, we are planning to carry out experiments with metallic barium targets virtually free of oxygen.

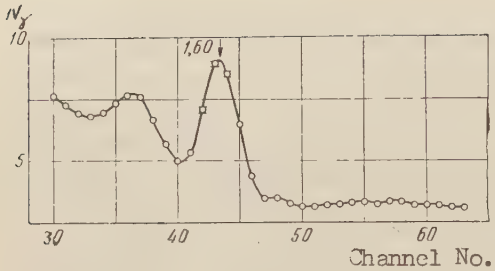

Fig.7. Experimental γ-ray spectrum recorded in Coulomb excitation of Ce^{140} with quintuply charged 52.5 Mev N^{14} ions.

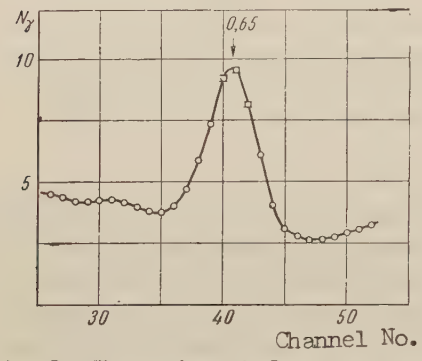

Fig.8. Experimental γ-ray spectrum emitted in Coulomb excitation of Ce^{142} with quintuply charged 52.5 Mev N^{14} ions.

Ce^{140}

Ce^{140} is the most abundant cerium isotope; like Ba^{138} this nucleus has a closed neutron shell. Coulomb excitation of the 1.60 Mev level in Ce^{140} was investigated by means of 52.5 Mev $N^{14;5+}$ ions (Fig.7) and 15.1 Mev α-particles. By way of target we used metallic cerium, and before inserting it in the Faraday cup we usually took appropriate measures to eliminate the cerium oxide film that forms during storage.

The lifetime of the 1.60 Mev level in Ce^{140} was measured by the nuclear resonance fluorescence method by Ofer & Schwarzschild[6] and Dzelepov & Dolgoborolova[19]. Our value for the lifetime agrees within the limits of the experimental error with the value of τ given by Ofer & Schwarzschild and is 32 times lower than the value given by Dzhelepov & Dolgoborolova.

Ce^{142}

It is known from studies[20] of β-decay of La^{142} that Ce^{142} has a level at 0.63 Mev. The natural abundance of Ce^{142} is 11%. Nevertheless it proved feasible to investigate Coulomb excitation of the first level of Ce^{142} using a natural cerium target: the energy of this level is relatively low and the yield of γ-rays emitted in de-excitation of this level proved to be appreciable (Fig.8). We used 52.5 Mev $N^{14;5+}$ ions and 15.1 Mev α-particles for bombarding the target. According to our data the energy of the first level is 0.650 ± 0.007 Mev.

B. Odd A Nuclei and Odd-odd B^{10}

A number of difficulties are commonly encountered in calculating the lifetimes of the excited states of odd-A nuclei. To determine the lifetime one must know $B(E2)\downarrow$, while experiment gives $B(E2)\uparrow$, which is not sufficient if, as is often the case, the spin of the excited level is not known. In such cases one can only give the bounds for $\tau(E2)$ (on the assumption that I_f does not differ from I_0 by more than two $\hbar$ units). The total lifetime τ can be determined only when the intensity ratio of E2 and M1 transitions from the excited state to the ground state is known.

If several levels are excited in the nucleus, then in determining $B(E2)\uparrow$ one must take into account the possibility that in de-excitation of the higher-lying levels there may occur cascade transitions via some of the excited lower-lying levels.

Li^7

The energy of the first excited level in Li^7 is known from the work of Day[9] and Davis[21]. This level lies at 0.48 Mev and has spin and parity 1/2-; the spin of the ground state is 3/2-.

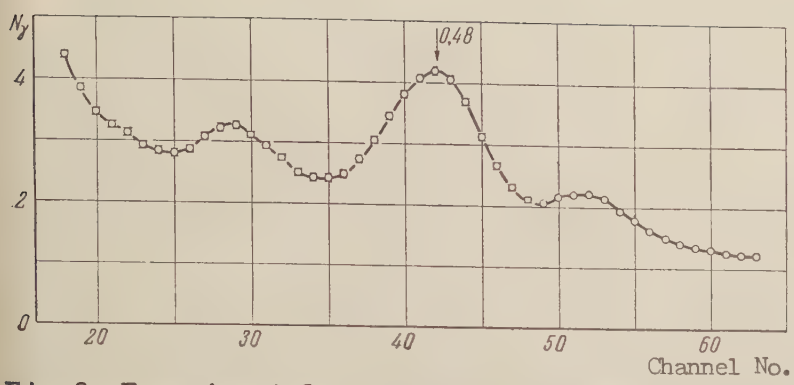

Fig.9. Experimental γ-ray spectrum recorded in Coulomb excitation of Li^7 with quadruply charged 16.0 Mev Ne^{20} ions.

In our experiments on Coulomb excitation of Li^7 we used quadruply charged 16 Mev Ne^{20} ions. The use of such heavy ions reduced the γ-background to such an extent that it proved feasible to measure the yield of 0.48 Mev γ-rays (Fig.9). The target was metallic lithium; in order to prevent oxidation the target was prepared in a dry container in an atmosphere of argon and bombarded in this protected state.

The ground and excited state spins differ by 1; consequently, in de-excitation of the 0.48 Mev level there may occur E2 and M1 type transitions. From the measured value of $B(E2)\uparrow$ one can calculate $\tau(E2)$, the partial lifetime of the 0.48 Mev state for electric quadrupole transitions. By comparison of $\tau(E2)$ and the total lifetime τ measured by Swann et al[22] and Beckman & Sandström[23] one can determine δ^2, the ratio of the abundances of E2 and M1 transitions from the 0.48 Mev level in Li^7. If one takes $\tau = 1.12 \cdot 10^{-13}$ sec (this is the value obtained by Swann et al[22] by the nuclear resonance fluorescence method), we find $\delta^2 = 3.1 \cdot 10^{-5}$. It may be noted that investigation of Coulomb excitation in this case allows of determining this very small value of δ^2 with relatively good accuracy (within ~30%).

Leamer[24] in investigating internal conversion in Li^7 found that the number of E2 transitions lies in the range from 0 to 45% of the total number of transitions from the 0.48 Mev level, which yields a wide range of values for δ^2, namely, from 0 to 0.8.

In a number of cases the anisotropy of the angular distribution of γ-rays proves very sensitive to the value of δ^2; however, the sensitivity of this method for determining δ^2 in the given case is appreciably lower.

Possibly in bombardment of lithium with 16 Mev Ne ions (16 Mev = 0.62 the energy of the barrier) there occurs not only Coulomb excitation of the 0.48 Mev level but also excitation as a result of inelastic scattering of the neon ions. If this process does occur, experiment will yield an overestimate for the reduced excitation probability for the 0.48 Mev level in Li^7.

However, as will be shown below, in investigating the 0.72 Mev level in B^{10} by means of 18 Mev Ne^{20} ions there was obtained a value of τ in good agreement with the results of other investigators. The ratio of the collision energy to the energy of the Coulomb barrier in this case equalled 0.57.

In 1960 (after completion of our measurements) there was published the work of Stelson & McGowan[4], in which they give the results of investigation of excitation of Li^7 using Ne^{20} ions of lower energy (up to 11 Mev, which amounts to 0.4 the energy of the Coulomb barrier). It may be noted that our results for Li^7 agree within the limits of the experimental error with the data of Stelson & Mc Gowan. Thus the contribution to the excitation yield owing to the process of formation of the compound nucleus with increase of the bombarding particle energy up to 0.6 E_{bar} is still small.

B^{10}

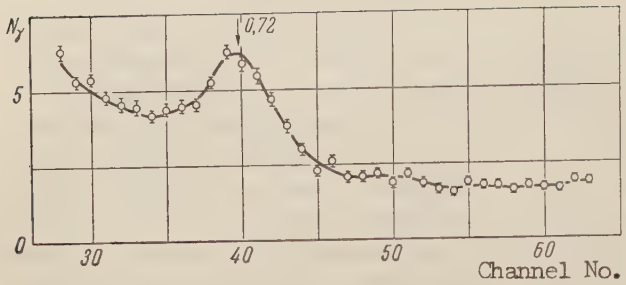

Fig.10. Experimental γ-ray spectrum recorded in Coulomb excitation of B^{10} with quadruply charged 18.0 Mev Ne^{20} ions.

The existence of a 0.72 Mev level in B^{10} is known from investigations[25] of β^+-decay of C^{10}, studies[9] of inelastic neutron scattering, and other experiments. The spin assignment for this level is 1+ (Sherr & Gerhart[25]); the assignment for the ground state is 3+ (Ting & Williams[26]).

As far as we know Coulomb excitation of B^{10} was observed for the first time in the present experiments. The target of compressed boron powder enriched to 83% B^{10} (the natural abundance of B^{10} is 19%) was bombarded with quadruply charged 18 Mev Ne^{20} ions (E_O/E_{bar} = 0.57). The experimental γ-spectrum is shown in Fig.10, where there is clearly evinced the 0.72 Mev line associated with Coulomb excitation of B^{10}.

In this case $\Delta I = 2$ and the transition from the 0.72 Mev state to the ground state must be pure E2. Hence the total lifetime τ can be determined from the measured value of $B(E2)\uparrow$. Our value of $1.1 \cdot 10^{-9}$ sec is in good agreement with the results of measurements of τ by other methods[27-29].

Mg^{25}

The level diagram of Mg^{25} has been investigated by a number of authors. According to Gove & Litherland[30], the energies and spins of the first excited levels of Mg^{25} are 0.58 (1/2+), 0.98 (3/2+), 1.61 (7/2+) and 1.96 Mev (5/2+). The ground state spin is 5/2+.

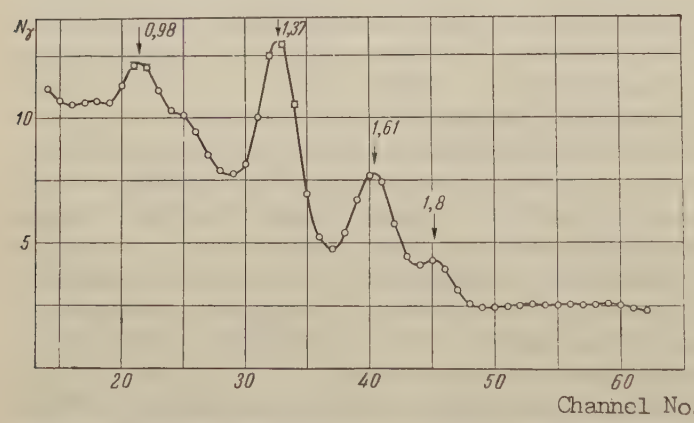

Fig.11. Experimental γ-ray spectrum recorded in Coulomb excitation of Mg^{25} with triply charged 18.0 Mev N^{14} ions.

For Coulomb excitation of Mg^{25} we used triply charged nitrogen ions with energies of 12.2, 16.8, 18 and 21.5 Mev. The metallic target enriched to 89% Mg was prepared by reduction of appropriately enriched magnesium oxide.

In the spectrum reproduced in Fig.11 one can see γ-peaks at 0.98 and 1.61 Mev, corresponding to excitation of levels of these energies in Mg^{25}. The 1.37 and 1.8 Mev γ-lines appear as a result of Coulomb excitation of corresponding levels in Mg^{24} and Mg^{26}, which were present in the target in amounts of 5 and 6%, respectively, and as a result of the N + C and N + O reactions.[10] In the spectra obtained in bombarding Mg^{25} with nitrogen ions there were also observed 0.58 and 0.40 Mev γ-lines, corresponding to excitation of the 0.58 Mev level in Mg^{25} and the cascade transition from the 0.98 Mev level via the 0.58 Mev level, and 0.35 Mev γ-rays from the N + C nuclear reaction[10].

We did not observe a line corresponding to excitation of the 1.96 Mev level. We evaluated the maximum possible intensity of the 1.96 Mev γ-rays; on the basis of this evaluation and taking into account the fact that only about 30% of the transitions from the 1.96 Mev level go to the ground state (Ref.31), we calculated the upper bound for $B(E2)\uparrow$ and obtained $0.006 \cdot 10^{-48}$ e^2 cm^4.

It follows from the results of Gove et al[31] that the relative number of cascade transitions from the 1.61 Mev level does not exceed 5% of the total number of transitions departing from this level. Hence the value of the reduced probability $B(E2)\uparrow$ for this level was determined directly from the yield of 1.61 Mev γ-rays.

For determining the number of excitations of the 0.98 Mev level it was necessary to measure the yields of the 0.98 and 0.40 Mev γ-rays. The ratio K of the number of cascade transitions via the 0.58 Mev level to the number of cross-over transitions to the ground state has been determined in a number of investigations. However, the values of this ratio given by different authors differ appreciably: for example, according to Maeder & Stähelin[32] K = 0.39, while according to Gove et al[31], K = 0.95. From our experiments we obtained K = 0.54; it must be admitted, however, that this value was determined with a large uncertainty, inasmuch as measurement of the yield of 0.40 Mev γ-rays was hampered by the presence of the 0.35 Mev γ-rays from the N + C reaction. The yield of 0.35 Mev γ-rays was evaluated from experiments with Mg^{26} and natural magnesium, in the same way as we evaluated the yield of 1.78 Mev γ-rays from the N + O reaction in investigating Mg^{26} (see above). Experiments with 12.2 Mev $N^{14;3+}$ ions, in which the 0.35 Mev γ-line from the N + C reaction virtually disappears, also did not enable us to determine the value of K inasmuch as the 0.40 Mev line appears in excitation of the relatively high-lying 0.98 Mev level, and reduction of the bombarding particle energy to 12.2 Mev leads to sharp decrease in the yield of 0.40 Mev γ-rays.

The values of $B(E2)\uparrow$ and $\tau(E2)$ for the 0.98 Mev level listed in Table 2, were calculated on the basis of the value of K obtained in the work of Gove et al[31].

Measurement of the yield of 0.58 Mev γ-rays is hindered by two circumstances. First, in the spectra obtained in bombarding the target with nitrogen ions there is present the 0.59 Mev γ-line resulting from the N + C reaction[10]. The yield of 0.59 Mev γ-rays was evaluated from experiments with Mg^{26} and natural magnesium (in the same way as the yield of 1.78 Mev γ-rays in investigating Mg^{26} - see above). Second, part of the 0.58 Mev γ-rays appears as a result of the cascade transition from the 0.98 Mev level; this part of the 0.58 Mev γ-rays can be evaluated from the yield of 0.40 Mev γ-rays or from the yield of the 0.98 Mev γ-rays and the assumed value of K.

With a view to reducing the relative magnitude of these corrections one should carry out measurements using ions of the lowest possible energy. In the spectra obtained in the experiments with 12.2 Mev $N^{14;3+}$ ions (Fig.12) the 0.59 Mev background line is virtually absent (this is evident from the spectra obtained

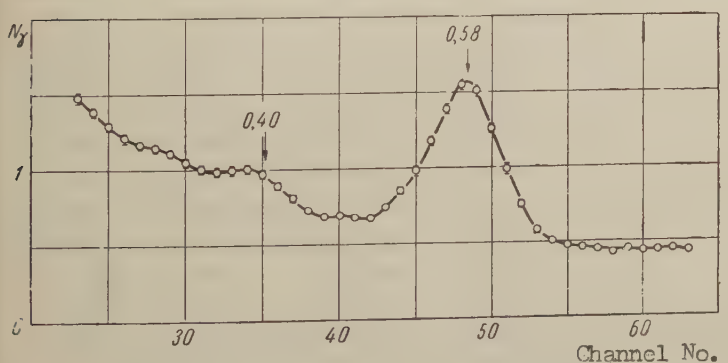

←Fig.12. Experimental γ-ray spectrum recorded in Coulomb excitation of Mg^{25} with triply charged 12.2 Mev N^{14} ions.

with Mg^{26} and Mg_{nat}). The number of excitations of the 0.98 Mev level is also sharply reduced with decrease of the ion energy, and the number of 0.58 Mev γ-rays emitted as a result of the cascade transition from the 0.98 Mev level in working with 12.2 Mev $N^{14;3+}$ ions amounts to only 20% of the total yield of 0.58 Mev γ-rays (whereas in the experiment with 18 Mev $N^{14;3+}$ ions this fraction amounts to more than 50% of the total yield of 0.58 Mev gammas).

Thus the use of 12.2 Mev $N^{14;3+}$ ions enabled us to reduce the error in determining $B(E2)\uparrow$ for the 0.58 Mev level, connected with introduction of correction for the 0.59 Mev background γ-rays from the N + C reaction and the cascade transition from the 0.98 Mev level. According to our estimate, the error in the experimental value of $B(E2)\uparrow$ for the 0.58 Mev level is 20-25%.

The spin of the 0.58 Mev level differs from the ground state spin of Mg^{25} by two units, so that one can determine the total lifetime τ of this level from the measured value of $B(E2)\uparrow$.

Recently Metzger et al[33], who used the method of nuclear resonance fluorescence, reported obtaining $\tau = 2.2 \cdot 10^{-14}$ sec for the 1.61 Mev level in Mg^{25}. Using this value and the value of $\tau(E2)$ based on our measurements, we evaluated the intensity ratio of the E2 and M1 type transitions from this level and obtained $\delta^2 = 2.5\%$.

The values of the reduced probability for excitation of the 0.98 and 0.58 Mev levels are smaller by a factor of 6 and 36, respectively, than the values of $B(E2)\uparrow_{sp}$ calculated on the basis of the single-particle model; on the other hand, the value of $B(E2)\uparrow$ for the 1.61 Mev level exceeds $B(E2)\uparrow_{sp}$ by a factor of 5. This is evidence in favor of the collective character of the 1.61 Mev level (it must be noted that the Mg^{25} nucleus has an odd neutron so that the single proton evaluation of $B(E2)\uparrow_{sp}$ for it is probably an overestimate).

Co^{59}

According to the data of Mazari et al[34], obtained in investigating inelastic proton scattering, the energies of the first excited levels of Co^{59} are 1.097 (5/2-), 1.189, 1.289 (3/2-) and 1.432 Mev. The assignment for the ground state is 7/2-.

In our experiments on Coulomb excitation of Co^{59} we used plates of metallic cobalt and bombarded them with quadruply charged 36 Mev nitrogen ions. In the spectrum there were observed peaks with energies of 1.1, 1.19 and 1.43 Mev, associated with excitation of the corresponding levels in Co^{59}.

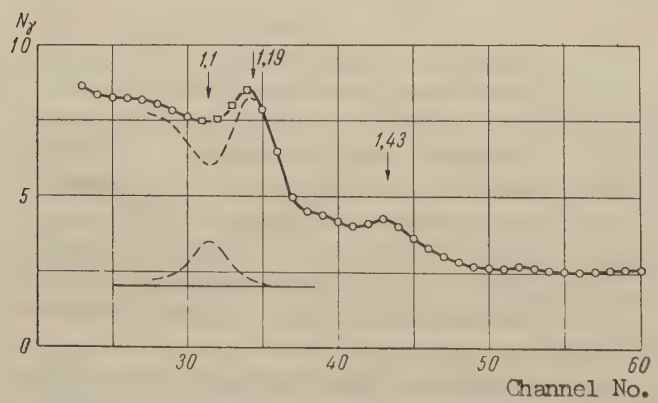

Fig.13. Experimental γ-ray spectrum recorded in Coulomb excitation of Co with quadruply charged 36.0 Mev N^{14} ions.

As was shown in experiments[10] with separated Ni isotopes the 1.37 Mev γ-background line does not appear in the spectrum in bombarding light elements with 36 Mev nitrogen ions.

The dashed line in Fig.13 shows the results of subtraction from the γ-spectrum of the peak due to the 1.19 Mev γ-rays. In view of the uncertainty in resolving the 1.1 and 1.19 Mev lines the error in determining $B(E2)\uparrow$ for the 1.1 Mev level is estimated to be 50%; that in determining the reduced probability for excitation of the 1.19 Mev level - 30%.

The values of $B(E2)\uparrow$ for the levels in Co^{59} were determined from the yields of the corresponding γ-rays; it was assumed that there are no cascade transitions in this nucleus. The spins of the 1.19 and 1.43 Mev levels are not known; hence on the basis of the measured values of $B(E2)\uparrow$ we could calculate only the upper and lower bounds of $\tau(E2)$ for these levels, i.e., the possible range of partial lifetimes with respect to electric quadrupole transitions.

Our results agree within the limits of the experimental error with the data of Adams et al[35] who studied Coulomb excitation of Co^{59} by means of oxygen ions.

On the basis of our data one can evaluate only the lower bound for the lifetime of the 1.29 Mev level: $1\cdot10^{-12}$ sec. According to the data of Berlovich[36] $\tau < 1\cdot10^{-10}$ sec.

In^{115}

In investigations of inelastic scattering of protons[37] and neutrons[38,39] it was established that In^{115} has levels at 1.08, 1.15 and 1.29 Mev. According to Varma & Mandeville[40], this nucleus also has a 0.935 Mev level with spin 7/2+; the ground state spin is 9/2+.

Fig.14. Experimental γ-ray spectrum recorded in Coulomb excitation of In^{115} with quintuply charged 52.5 Mev N^{14} ions.

In our investigation of Coulomb excitation of In^{115} we bombarded an indium foil target with 52.5 Mev $N^{14;5+}$ ions. The resultant spectrum (Fig.15) comprises a 1.15 Mev line corresponding to excitation of the 1.15 Mev level in In^{115} and a broad peak which is probably due to surposition of the 1.29 Mev line (excitation of the corresponding level in In^{115}) and the 1.37 Mev line from the N + C reaction. The fact that the 1.15 Mev γ-line is of normal width indicates the absence of γ-rays of 1.08 Mev energy. Consequently, it may be concluded that the 1.08 Mev level is either not excited at all or only weakly.

In Table 2 we indicate the possible range of values of $\tau(E2)$ for the 1.15 Mev level in In^{115}. The value of $B(E2)\uparrow$ was calculated from the yield of 1.15 Mev γ-rays on the assumption that there are no cascade transitions departing from this level. On the basis of the experimental spectrum we made an approximate evaluation of the reduced probability for excitation of the 0.935 Mev level; our tentative figure is $\sim0.01\cdot10^{-48}$ e^2 cm^4.

Sn^{117}

Earlier[2] we investigated Coulomb excitation of the 0.16 Mev level in this isotope using quadruply charged 36 Mev nitrogen ions. It must be noted that at this ion energy there are excited with a noticeable yield the higher-lying levels of Sn^{117} (1.03 and 0.865 Mev - Ref.15), in the de-excitation of which there may be emitted cascade γ-rays with E_γ = 0.16 Mev.

In the present experiments in investigating Coulomb excitation of the 0.16 Mev level in Sn^{117} we used ions of lower energy: 18.5 Mev $N^{14;3+}$ and 26.5 Mev $Ne^{20;4+}$.

The value of $B(E2)\uparrow$ for the 0.16 Mev level was calculated on the assumption that there are no cascade transitions from the higher-lying 0.865 and 1.03 Mev levels in Sn^{117} and no other transitions of lower energy. Comparison of the partial lifetime $\tau(E2)$ calculated from our experimental results and the total lifetime

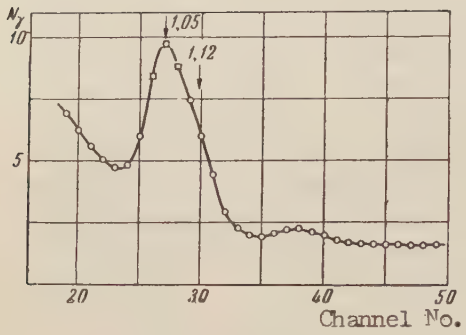

Fig.15. Experimental γ-ray spectrum recorded in Coulomb excitation of Sb with quintuply charged 52.2 Mev N^{14} ions.

$\tau = 5.7 \cdot 10^{-10}$ sec, as measured by Metzger[41], enabled us to determine the intensity ratio of E2 and M1 transitions from the 0.16 Mev level to the ground state of Sn^{117}; we obtained $\delta^2 = 0.03\%$.

Our value for $B(E2)\uparrow$ for the first level in Sn^{117} must be regarded as an upper bound. We plan further experiments using ions of lower energies to determine the precise value of the reduced excitation probability for this level.

Sb

In the spectra obtained in bombarding metallic antimony targets with quadruply charged 36 Mev nitrogen ions, quintuply charged 52.5 Mev nitrogen ions (Fig.15) and 15.1 Mev α-particles (Fig.16) there was evinced a γ-line that undoubtedly represents the superposition of γ-lines of 1.05 and 1.12 Mev energy. Gamma-lines with energies of 1.04 and 1.11 Mev were also observed by Newton & Stephens[42] in bombarding antimony targets with oxygen ions. The fact that these two lines consistently appear in bombardment of antimony targets with different particles indicates that they are due to Coulomb excitation of nuclear levels.

Unfortunately, the separated Sb isotopes available to use contained appreciable amounts of oxygen. Because of this the γ-background from reactions of the nitrogen ions and α-particles with the oxygen was so strong that we were unable to determine in which isotope (Sb^{121} or Sb^{123}) the above mentioned levels are excited. Hence the values of $B(E2)\uparrow$ and $\tau(E2)$ given in Table 2 were calculated twice: for Sb^{121} and for Sb^{123}.

In the calculations it was assumed that there does occur excitation of levels with energies of 1.05 and 1.12 Mev. This assumption is justified by the fact that the values of $B(E2)\uparrow$ obtained in the experiments with 36 and 52.5 Mev nitrogen ions and with α-particles are in good agreement. Nevertheless, we feel that the existence of these levels is in need of further substantiation (this applies particularly to the 1.12 Mev level inasmuch as the accuracy of the results for it does not exceed 50%).

In calculating the reduced probability values we did not take into account the possibility of cascade transitions via lower lying levels.

Conclusions

Extension of the useful energy range of cyclotron accelerated multiply charged ions made it possible to investigate Coulomb excitation of a number of nuclear levels.

Using 16 to 18 Mev neon ions we investigated levels in such light elements is Li and B. We also succeeded in exciting high-lying levels in the following light and medium elements: Mg^{25}, Mg^{26}, Ca^{44}, Co^{59}, In^{115} and Sb.

Increase of the energy of nitrogen ions to 52.5 Mev made it possible to excite levels with energies of 1.4-1.6 Mev in heavier nuclei, namely, Ba^{138} and Ce^{140}.

Investigation of the levels of even-even isotopes is of interest from the standpoint of supplementing the energy level systematics for even-even nuclei and subsequent comparison of the experimental results with calculations based on theory.

In the present experiments there were excited for the first time the lowest spin 2+ levels in Mg^{26}, Ca^{44}, Se^{74}, Ba^{138}, Ce^{140} and Ce^{142}. For the 1.83 Mev level in Mg^{26} we obtained $B(E2)\uparrow = 0.035 \cdot 10^{-48}$ e^2 cm^4. For the 1.37 Mev level in Mg^{24} in the same series of experiments with 16.8 and 18 Mev nitrogen ions and with the same reference level that was used in investigating Mg^{26} (the 0.56 Mev level in Se^{76}) we obtained $B(E2)\uparrow = 0.040 \cdot 10^{-48}$ e^2 cm^4, which is a refinement over the reduced probability value deduced in our earlier investigation[1].

The value of $B(E2)\uparrow$ for Se^{74} proved to be close to the reduced probability for Se^{76} obtained in our earlier work[1], despite the fact that the energies of the first levels of Se^{74} and Se^{76} differ appreciably: the respective values are 0.635 and 0.560 Mev.

For the 1.60 Mev level in Ce^{140}, which has a closed neutron shell, we obtained $B(E2)\uparrow = 0.27 \cdot 10^{-48}$ e^2 cm^4, a value 1.5 times higher than the reduced excitation probability for the 0.65 Mev level of the neighboring even nucleus Ce^{142}.

Recently Kisslinger & Sorensen[16] carried out theoretical calculations of the reduced excitation probability for the first levels in nuclei with a closed shell. Our data on Ba^{138}, Ce^{140} and the even isotopes of Sn together with our earlier results for Ni isotopes and Cr^{52} provide the basis for comparison of the experimental values with the theoretical results. Comparison showed that there is in general good agreement between the experimental and theoretical data (Table 3).

Table 3

Comparison of the experimental and theoretical[16] values of $B(E2)$ for some nuclei

Nucleus	$B(E2)_{theo}$, $10^{-48} e^2$ cm^4	$B(E2)_{exp}$, $10^{-48} e^2$ cm^4
Cr^{52}	0,16	0,062
Ni^{58}	0,02	0,080
Ni^{60}	0,046	0,11
Ni^{62}	0,071	0,085
Ni^{64}	0,064	0,087
Sn^{112}	0,25	0,33
Sn^{114}	0,20	0,25
Sn^{116}	0,26	0,29
Sn^{118}	0,29	0,24
Sn^{120}	0,28	0,26
Sn^{122}	0,25	0,26
Sn^{124}	0,20	0,22
Ba^{138}	0,51	0,38
Ce^{140}	0,73	0,27

We determined the values of the total lifetime τ of the investigated levels in the even-even nuclei and also of the 0.72 Mev level in B^{10} and the 0.58 Mev level in Mg^{25}. For the other levels in odd-A isotopes we give the values of $\tau(E2)$, the partial lifetime as regards electric dipole de-excitation (or, where the values of the excited state spin are not known, we give the upper and lower bounds for the partial lifetime).

We indicate the possible spin assignments for the 1.19 and 1.43 Mev levels in Co^{59}, the 1.15 Mev level in In^{115}, and the 1.05 and 1.12 Mev levels in Sb. These values were determined on the basis of the fact that in the case of Coulomb excitation (E2 transitions) the spin I_f of the excited level can differ from the ground state spin I_0 by not more than two units.

The values of the total lifetime τ for the 0.48 Mev level in Li^7, the 1.61 Mev level in Mg^{25} and the 0.16 Mev level in Sn^{117} are known from other studies. Using these values and the measured $\tau(E2)$, we calculated the values of δ^2, the relative intensity of E2 and M1 transitions in de-excitation of the given levels.

The values of F (the ratio of the experimental $B(E2)\uparrow$ to the reduced probability calculated on the basis of the single particle model) for the levels in even-even nuclei, the 0.48 Mev level in Li^7, the 1.61 Mev level in Mg^{25} and the investigated levels in Co^{59}, In^{115} and Sb indicate that the enumerated levels are probably collective in character.

References

1. D.S.Andreev, A.P.Grinberg, K.I.Erokhina & I.Kh.Lemberg, Nuclear Phys., 19, 400 (1960).
2. D.G.Alkhazov, A.P.Grinberg, G.M.Gusinskii, K.I.Erokhina & I.Kh.Lemberg, Zhur.eksp.i teor.fiz., 37, 1530 (1959). (Trans.Soviet Physics - JETP.)
3. D.S.Andreev, A.P.Grinberg, K.I.Erokhina & I.Kh.Lemberg, Izv.AN SSSR, Ser.fiz., 25, 70 (1961). (Trans.Bulletin, 25, 70.)
4. P.H.Stelson & F.K.McGowan, Nuclear Phys., 16, 92 (1960).
5. P.H.Stelson & F.K.McGowan, Phys.Rev., 110, 489 (1958).
6. S.Ofer & A.Schwarzschild, Phys.Rev., 116, 725 (1959).
7. N.Heydenburg & G.Temmer, Phys.Rev., 96, 426 (1954).
8. R.Johnson & R.Moffat, Bull.Amer.Phys.Soc., 2, 230 (1957).
9. R.B.Day, Phys.Rev., 102, 767 (1956).
10. D.G.Alkhazov, A.P.Grinberg, G.M.Gusinskii & I.Kh.Lemberg, Izv.AN SSSR, Ser.fiz., 23, 1465 (1959). (Trans.Bulletin, 23, 1451.)
11. J.Blue & E.Bleuler, Phys.Rev., 100, 1324 (1955); Phys.Rev., 99, 659 (1955)
12. S.Johansson, J.Cauchois & K.Siegbahn, Phys.Rev., 82, 275 (1951).
13. F.Metzger, J.Franklin Inst., 260, 239 (1955).
14. G.M.Temmer & N.P.Heydenburg, Phys.Rev., 100, 961 (1955).
15. D.G.Alkhazov, D.S.Andreev, K.I.Erokhina & I.Kh.Lemberg, Zhur.eksp.i teor. fiz., 33, 1347 (1957). (Trans.Soviet Physics - JETP.)
16. L.S.Kisslinger & R.A.Sorensen, Kgl.Danske Videnskab.Selskab, Mat.-fys. Medd., 32, No.9 (1960).
17. T.Marumori, Progr.Theoret.Phys., 24, 331 (1960).
18. W.Turchinetz & R.Pringle, Phys.Rev., 103, 1000 (1956).
19. B.S.Dzhelepov & M.A.Dolgoborolova, Izv.AN SSSR, Ser.fiz., 24, 304 (1960). (Trans.Bulletin, 24, 292.)
20. A.Bosch, Physika, 19, 374 (1953).
21. R.Davis,Jr., Phys.Rev., 86, 976 (1952).
22. C.P.Swann, V.K.Rasmussen & F.R.Metzger, Phys.Rev., 114, 862 (1959).
23. O.Beckman & R.Sandström, Nuclear Phys., 5, 595 (1958).
24. R.D.Leamer, Phys.Rev., 114, 1590 (1959).
25. R.Sherr & J.Gerhart, Phys.Rev., 91, 909 (1953).
26. I.Ting & D.Williams, Phys.Rev., 89, 595 (1953).
27. S.D.Bloom, C.M.Turner & D.H.Wilkinson, Phys.Rev., 105, 232 (1957).
28. R.E.Holland, F.J.Lynch & S.S.Hanna, Phys.Rev., 112, 903 (1958).
29. M.Birk, G.Goldring & Y.Wolfson, Phys.Rev., 116, 730 (1959).
30. H.E.Gove & A.E.Litherland, Phys.Rev., 107, 1458 (1957).
31. H.Gove, A.Litherland, E.Paul & G.Bartholomew, Bull.Amer.Phys.Soc.,1,29(195
32. D.Maeder & P.Stähelin, Helv.Phys.Acta, 28, 193 (1955).
33. F.R.Metzger, C.P.Swann & V.K.Rasmussen, Bull.Amer.Phys.Soc.,5,247 (1960).
34. M.Mazari, A.Sperduto & W.Buechner, Phys.Rev., 107, 365 (1957).
35. B.M.Adams, D.Eccleshall & M.J.L.Yates, Proceedings of the Second Conference on Reactions between Complex Nuclei, p.95, Gatlinburg,Tenn. May, 2-4, 1960.
36. E.Berlovich, Izv.AN SSSR, Ser.fiz.,19,343 (1955).(Trans.Bulletin 19, 305.)
37. R.D.Sharp & W.W.Buechner, Phys.Rev., 1112, 897 (1958).
38. V.E.Scherrer, B.A.Allison & W.R.Faust, Phys.Rev., 96, 386 (1954).
39. R.B.Day, Bull.Amer.Phys.Soc., 2, 1, 56 (1956).
40. J.Varma & C.Mandeville, Phys.Rev., 97, 977 (1955).
41. F.R.Metzger, J.Franklin Inst., 270, 138 (1960).
42. J.O.Newton & F.S.Stephens, Proceedings of the Conference on Reactions between Complex Nuclei, p.368, Gatlinburg, Tenn., May, 5-7, 1958.

BETA- AND GAMMA-SPECTRA OF RADIOACTIVE Sb^{113} AND Sb^{115} AND A NEW Sn^{113} ISOMER

- I.P.Selinov, V.L.Chikhladze, D.E.Khulelidze & N.A.Vartanov

1. The β-spectrometer

In 1955, V.V.Kunits, V.L.Chikhladze and N.A.Vartanov constructed a solenoidal type β-spectrometer with two thin, iron-free magnetic lenses. The basic parameters of this instrument are the following: source to detector distance 1000 mm, inside lens diameter 430 mm, outside diameter 900 mm, thickness 100 mm. The spectrometer has provision for displacing the coils in different directions and an auxiliary vacuum chamber to permit interchange of sources without disturbing the vacuum in the main chamber. By longitudinal displacement of the lenses, variation of the opening in the iris diaphragm and change of the aperture in front of the counter the resolution of the instrument can be varied from 1.4 to 3.2% with corresponding change in the transmission factor from 0.5 to 1.4% (for a 5 mm diameter Cs^{137} source). The lens current can be varied from 10 ma to 20 amp; the current is regulated to within $\sim 10^{-2}$%. The instrument is capable of focusing electrons of up to 3.5 Mev energy.

In 1959, V.L.Chikhladze and D.E.Khulelidze made a number of improvements in the design of this instrument. An iris diaphragm with provision for varying the opening from 1 to 40 mm was installed between the source and detector. The optimum transmission to resolution ratio is obtained with the maximum distance (560 mm) between the lenses. Use of a special limiting aperture made it possible to increase the opening of the iris diaphragm to 40 mm. In this case the relative line half-width for a 5 mm diameter source is ~2%; the acceptance angle is ~2.5% of 4π.

An electron gun and moveable fluorescent screen were used for investigating the electron trajectories. On the basis of the test data there was designed a spiral diaphragm for separating electrons from positrons. The separation coefficient is 10^3.

2. Preparation of the antimony sources

The radioactive antimony isotopes, Sb^{113} and Sb^{115}, were obtained by cyclotron bombardment of tin foils with ~11 Mev deuterons.[1] The foils were prepared of tin specimens enriched to 52.3% Sn^{112} or 57.2% Sn^{114} using electromagnetic separation. The radioactive antimony isotopes were obtained by the $Sn^{112}(d,n)Sn^{113}$ and $Sn^{114}(d,n)Sn^{115}$ reactions.

The chemical separation of the antimony and preparation of the sources were carried out by Yu.A.Bliodze and V.K.Kovyrzin under the supervision of E.E.Baroni. The 10-20 mg deuteron-bombarded foil was dissolved in 2 ml hot HCl in the presence of a platinum catalyzer. After solution of the tin, there were added 2 ml water and a drop of carrier - $SbCl_3$ solution (1 mg Sb per 1 ml HCl).

A strip of copper foil, etched in HNO_3 and coated on one side with varnish, was immersed in the solution. Upon heating of the solution to 60°C the antimony was electrochemically deposited on the exposed copper foil surface. The time required for chemical separation was 10-12 min. The copper foil with the antimony coating was cemented to an aluminum support and mounted in the β-spectrometer.

3. Sb^{115} spectrum

As will be evident from Fig.1, the positron spectrum of Sb^{115} is simple. The Fermi-Kurie plot is a straight line. The experimental points rise above this line

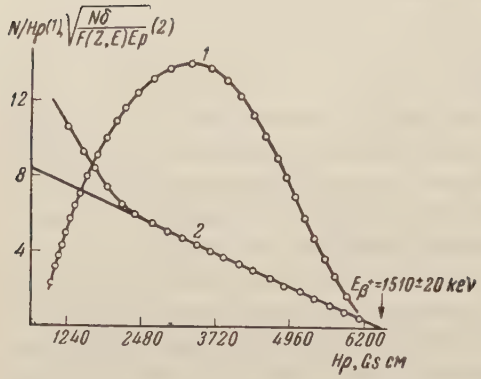

Fig.1. Positron spectrum of Sb^{115} (1) and the Fermi-Kurie plot (2).

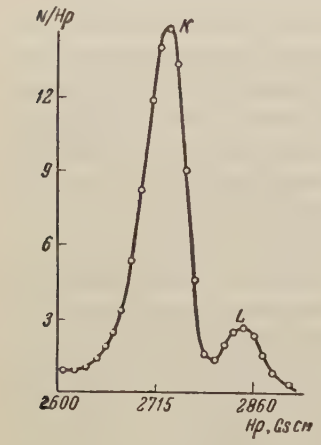

Fig.2. K and L conversion lines of the 499 kev γ-transition in Sb^{115}.

in the low energy region (below ~400 kev); this can be explained by the appreciable back scattering from the copper foil. The end-point energy of the spectrum is 1510 ± 20 kev.

The conversion electron spectrum of Sb^{115} was investigated in the energy range from 25 to 600 kev. There were observed two electron lines with energies of 471 and 495 kev (Fig.2). They were identified as the K and L conversion lines of a 499 ± 2 kev γ-transition. $Ne_K/N_{\beta+} = 0.0183$. No other conversion lines (<1%) were observed.

In investigations[2-4] of Coulomb excitation of indium there was observed a γ-line with E_γ = = 500-512 kev. A transition of this energy does not fit into the level scheme of In^{115}. Hence, Davis et al[4] hypothesized that it pertains to tin isotopes formed by the reactions: $In^{115}(p,n)Sn^{115}$ or $In^{115}(p,\gamma)Sn^{116}$. It follows from our results that the 500 kev γ-line belongs to Sn^{115}. The γ-spectrum of Sb^{115} was investigated on a scintillation spectrometer. There was observed intense x-radiation from tin, indicating abundant K capture with a period of 32 min; the 499 kev γ-line could not be resolved against the strong background of annihilation radiation. A number of very weak γ-lines were detected in the energy range from 1000 to 2500 kev; their total intensity amounts to less than 10% the intensity of the annihilation radiation. We were not able to measure experimentally the intensity ratio of the x-radiation to the annihilation radiation. According to calculations[5,6] for antimony isotopes (Z = 51) and $E_{\beta+}$ = 1500 kev, the ratio

$$\frac{W_K + W_L}{W_{\beta+}} \approx 1.87.$$

We calculated the K shell conversion coefficient using this ratio and our value for $Ne_K/N_{\beta+}$ and obtained

$$\alpha_K = 0.0064 \pm 0.0007.$$

It will be evident from Table 1 that this value of α_K corresponds to M1 or E2 transitions, but is closer to M1. The K/L ratio is 6.5 ± 1 (according to Fig.3), which is also consistent with these multipole orders.

Table 1

Theoretical values of α_K and K/L for the 499 kev transition in Sn^{115} (Ref.7)

ΔI	E1	E2	E3	M1	M2	M3
α_K	0,00198	0,00596	0,0160	0,00655	0,0209	0,0595
K/L	8,75	8,35	6,55	7,85	7,45	7,1

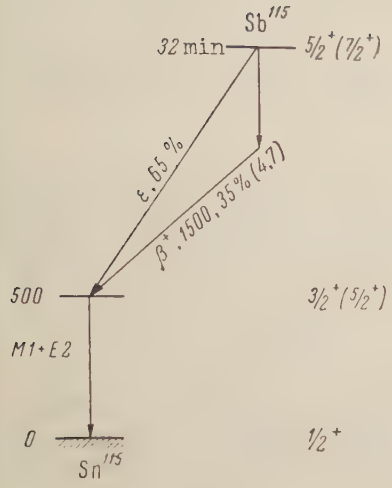

Fig.3. Decay scheme for Sb^{115}.

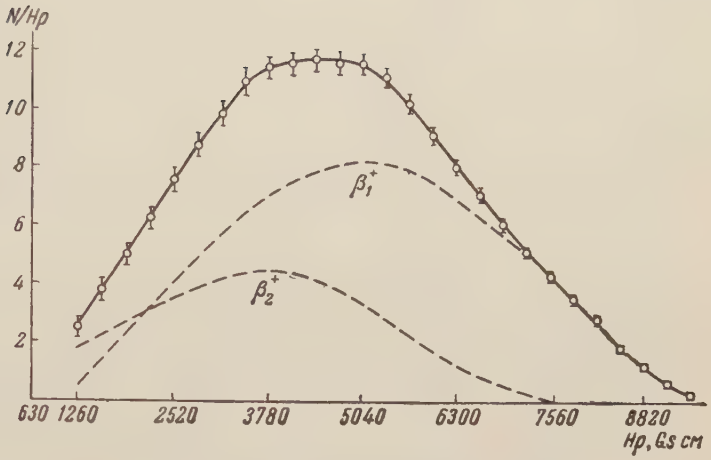

Fig.4. Positron spectrum of Sb^{113}.

In view of the rectilinearity of the Fermi-Kurie plot and the fact that log ƒt equals 4.7 it follows that this β^+-transition is allowed. Proctor[8] and Mack[9] report that the measured value of the Sn^{115} ground state spin is 1/2. On the basis of these data one can propose the decay scheme for Sb^{115} shown in Fig.3. According to this scheme, the Sb^{115} - Sn^{115} mass difference is 3050 kev, which is in good agreement with the theoretical value of 3300 kev calculated by Cameron[10].

4. Sb^{113} spectrum

The positron spectrum of Sb^{113} consists of two components with end-point energies 2420 ± 20 and 1800 ± 40 kev (Figs.4 & 5). $W_{\beta_1^+}/W_{\beta_2^+} = 2.4 \pm 0.3$. Analysis of the Fermi-Kurie plot (Fig.5) shows that both components correspond to allowed decays. In calculating the log ƒt values we took into account the theoretical values[5,6,11] for the probability ratios of β^+-transitions and electron capture for the given E_{β^+} and Z = 51. Accordingly, we find the following percentages for the disintegrations of Sb^{113}: to the lower level of Sn^{113}, β_1^+ transitions 45%, electron capture, 19%; to the higher level β_2^+ transitions 18%, electron capture, 18%. The log ƒt values calculated on the basis of these data are 4.88 and 4.73 for the β_1^+ and β_2^+ transitions, respectively.

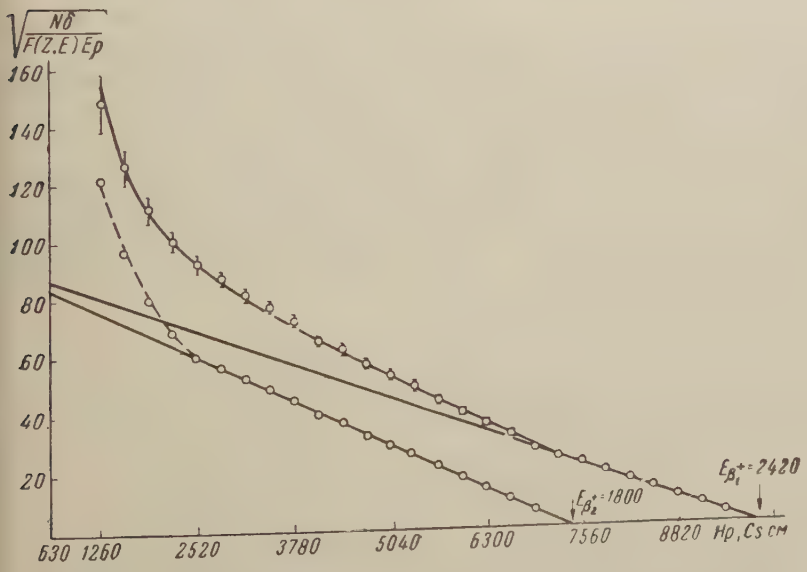

Fig.5. Fermi-Kurie plot for the β^+-spectrum of Sb^{113}.

The γ-spectrum of Sb^{113} recorded on a scintillation spectrometer is shown in Fig.6.

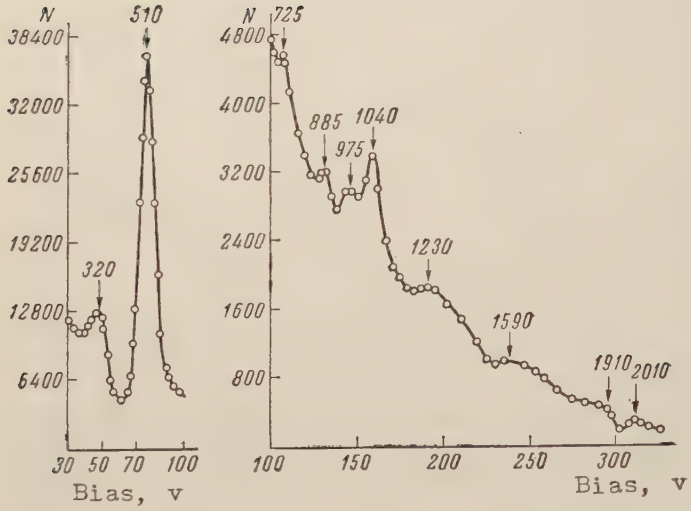

Fig.6. γ-Spectrum of Sb^{113}.

Fig.7. K, L and M conversion electron lines of the Sn^{113m} 79 kev γ-transition.

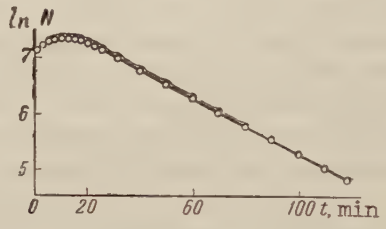

Fig.8. Variation with time of the intensity of the K and L conversion electrons associated with the Sn^{113m} 79 kev γ-transition.

Analysis of the spectrum shows that there are present γ-lines with the following energies, corresponding to the period of Sb^{113} (7 min): 320, 725, 885, 975, 1040 and 1230 kev. The most intense are the 320 and 1040 kev γ-lines.

In addition, our preliminary data indicate that there may be present weak γ-lines with energies ~1590, 1910 and 2010 kev.

5. Sn^{113m}

In investigating the conversion electron spectrum of Sb^{113} on the β-spectrometer there were detected electrons with energies of 49.6, 75.3 and 77.9 kev (Fig.7). They were identified as the K, L and M conversion electrons of a 79.3 ± 0.5 kev transition. It will be evident from Fig.8 that the intensity of the K and L electron lines (the M line is very weak) increases with a period $T_{1/2}$ = 7-8 min and then decreases with $T_{1/2}$ = = 21 ± 1 min. The experimental value for the K/L ratio is 1.7 ± 0.1. The theoretical values of K/L for Z = 50 and E_γ = 80 kev for different multipole orders are listed in Table 2.

From a comparison of the theoretical values with the experimental K/L ratio it will be evident that the multipole order of this transition is a mixture of either E3 (20%) + M2 (80%) or E4 + M3. We believe that the former assignment is more probable, inasmuch as all odd tin isotopes have an excited level with 11/2-, and since the other levels in this region are usually even, the isomeric transition should involve change in parity. Similar data were recorded for Sn^{113m} obtained by the $Cd^{110}(\alpha,n)Sn^{113m}$ reaction.

Table 2

Theoretical values of the K/L ratio for different multipole orders for Z = 50 and E_γ = 80 kev (Ref.7)

ΔI	E1	E2	E3	E4	E5	M1	M2	M3	M4	M5
K/L	7,4	2,33	0,47	0,125	0,04	7,8	4,8	2,07	0,86	0,36

Thus the results of our experiments show that in the decay of Sb^{113}, in addition to 118 day Sn^{113}, there forms the new isomer Sn^{113m} with T = 21 min.

We desire to express our gratitude to B.S.Dzhelepov and L.K.Peker for valuable discussions, to Yu.V.Golovko and I.M.Lapushkin for assistance in the work and to E.N.Khaprov and his volleagues for bombardment of the target.

References

1. P.P.Selinov, Yu.A.Grits, D.E.Khulelidze, E.A.Baroni, Yu.A.Bliodze, A.G. Demin & Yu.P.Kushakevich, Atomnaya energiya, 5, 660 (1959). (Trans.Soviet Jour. of Atomic Energy.)

2. G.M.Temmer & N.P.Heydenburg, Phys.Rev., 93, 351 (1954).

3. H.Mark, C.McClelland & C.Goodman, Ibid., 98, 1245 (1955).

4. R.H.Davis, A.S.Divatia, D.A.Lind & R.D.Moffat, Ibid., 103, 1801 (1956).

5. B.S.Dzhelepov & L.N.Zyryanova, Vliyanie elektricheskogo polya atoma na beta-raspad (Influence of the atomic field of the atom on β-decay), p.103, M., 1956.

6. I.M.Band, L.N.Zyryanova & Tsin Chen-Zhui, Izv.AN SSSR, Ser.fiz., 20, 1387 (1956). (Trans.Bulletin, 20, 1269.)

7. L.A.Sliv & I.M.Band, Tablitsy koeffitsientov vnutrennei konversii γ-luchei, (Tables of internal conversion coefficients). Part I, K shell; Part II, L shell, M.-L., 1956/8.

8. W.Proctor, Phys.Rev., 79, 35 (1950).

9. J.Mack, Revs.Mod.Phys., 22, 64 (1950).

10. A.G.W.Cameron, A Revised Semi-Empirical Atomic Masses Formula, CRP 690, Chalk River, 1957.

11. I.M.Band, L.N.Zyryanova & Yu.P.Suslov, Izv.AN SSSR, Ser.fiz., 22, 952 (1958). (Trans.Bulletin, 22, 943.)

INVESTIGATION OF THE LEVELS OF P^{31} BY MEANS OF THE $Si^{30}(p,\gamma)P^{31}$ REACTION

- A.K.Val'ter, S.P.Tsytko, Yu.P.Antuf'ev, E.G.Kopanets & A.N.L'vov

Radiative proton capture by Si^{30} (Q = 7.292 Mev) was investigated earlier by members of our group.[1-4] In the work of Ref.4, in which thin Si^{30} targets were bombarded with monoenergetic protons in the energy range from 0.4 to 1.0 Mev there were observed 10 resonances and the corresponding levels in P^{31}.

The $Si^{30}(p,\gamma)P^{31}$ reaction in this low proton energy range has been investigated by Broude et al[5] and a number of other authors; the results of these investigations are collected in the review of Endt & Braams[6].

However, there has been only one investigation of this reaction at proton energies above 1 Mev: Paul et al[7] bombarded their silicon targets with protons having energies from 1.7 to 2.3 Mev.

The purpose of the present investigation was to study the $Si^{30}(p,\gamma)P^{31}$ reaction in the proton energy range from 1 to 2.7 Mev.

Procedure and equipment

The monoenergetic protons were obtained by means of the 4 Mev Physical-Technical Institute (Ukrainian SSR Ac. of Sci.) electrostatic generator, which is described in Ref.8. The proton energies were measured by an electrostatic analyzer to within ±0.05%. The thin isotopic targets were prepared by Guseva[9]; the thicknesses of the Si^{30} targets were from 2 to 5 kev for 1 Mev protons.

The γ-ray yield was determined by means of a CsI(Tl) crystal 3 cm in diameter and 2 cm thick, coupled to an FEU-3 photomultiplier. The proton beam charge at the target was measured by a current integrator. The sensitivity of the current integrator was checked regularly and was found to remain constant to within 1% throughout the period of the experiments.

The γ-ray spectra were investigated by means of a scintillation γ-spectrometer, which could be operated as a single-crystal instrument or as a two-crystal coincidence spectrometer. In the spectrometer there were employed NaI(Tl) crystals 4 cm in diameter and 4 cm thick, and also crystals 7 cm in diameter and 6 cm thick. The crystals were coupled to FEU-43 photomultipliers. The spectrometer was operated in conjunction with a 100-channel (type AI-100) pulse height analyzer. The equipment will be described in greater detail in another paper.

The angular distributions of the gammas were determined from spectra measured at different angles. To this end the spectrometer crystals could be rotated about the center of the target; the instrument error associated with inaccuracy in setting the target to crystal distance did not exceed 2-3%. In investigating the γ-ray spectra and angular distributions, the γ-ray yield was monitored by the CsI(Tl) crystal, which was set at a fixed angle $\theta = 90^{\circ}$.

Measurements of the relative γ-ray yield

The results of measurements of the relative γ-ray yield of the Si^{30} target as a function of the proton energy are given in Fig.1 (the background due to γ-rays from the tantalum backing has been subtracted from the reproduced curves). The energies and relative intensities of the resonances are listed in Table 1. The resonance energies have been corrected for the energy loss in the half thickness of the target.

The well defined and not overlapping resonances at proton energies 1096, 1205, 1326, 1393, 1402, 1482 and 1516 kev were investigated in greater detail. For these energies we measured the γ-ray spectra and angular distributions; the

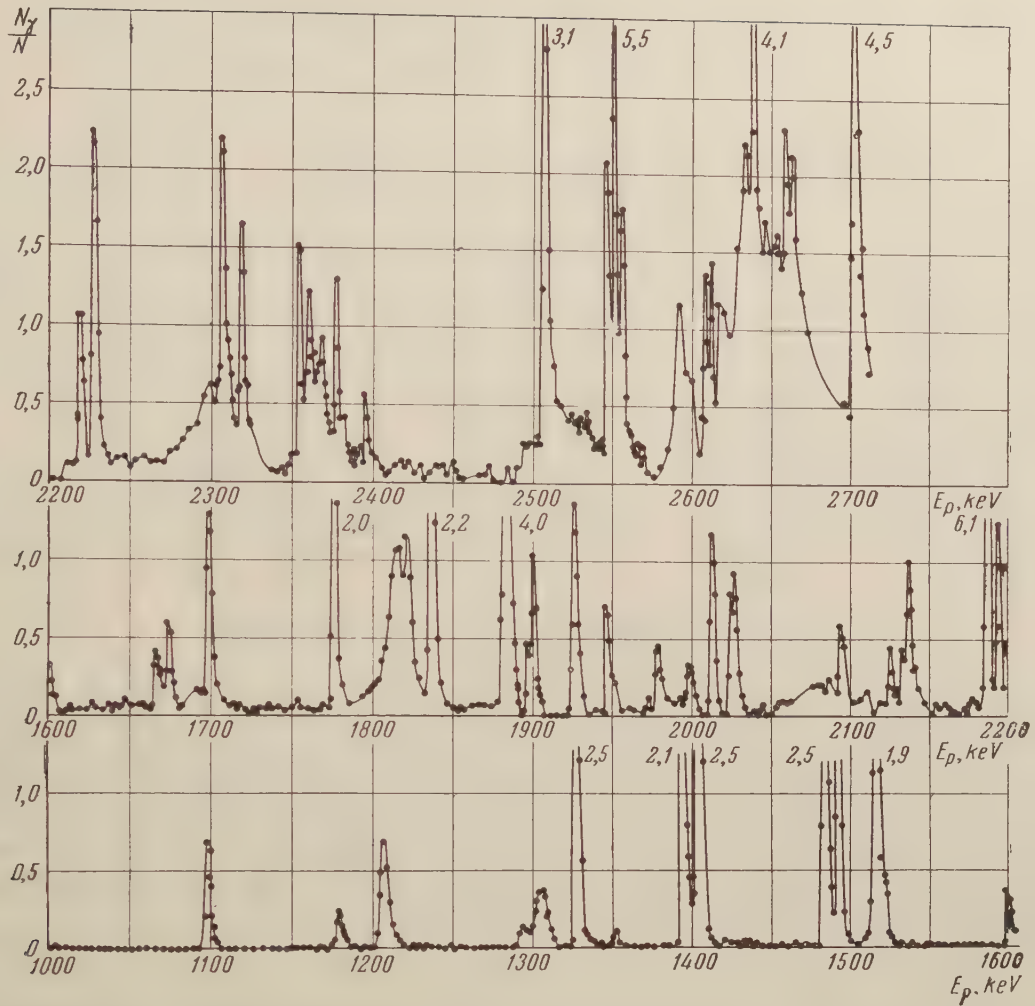

Fig.1. Variation of the γ-ray yield from the $Si^{30}(p,\gamma)P^{31}$ reaction with the proton energy (background due to γ-rays from the tantalum backing subtracted). N_γ/N is the ratio of the number of γ-rays counted by the detector to the number of counts of the current integrator.

excitation energy of the resonance levels in P^{31} was determined by means of the formula

$$W = Q + \frac{30}{31} E_p.$$

Results of investigation of the γ-ray spectra and angular distribution

Investigation of the spectra by the single crystal γ-spectrometer was carried out for four values of the angle θ between the direction of the incident protons and the direction to the crystal: 0, 30, 60 and 90°; in a few cases we carried out additional measurements for $\theta = 45°$.

The measurements of the coincidence spectra by the two-crystal spectrometer were carried out with two geometries. In one geometry the crystal was located at angles $\theta = 90$ and 270°; in the other geometry the angles $\theta = 0$ and 90°. The angular distributions were measured for only the most intense γ-lines.

Table 1

Energies and relative intensities of the resonances observed in proton bombardment of Si^{30}

№	E_p, keV	Relative intensity	№	E_p, keV	Relative intensity	№	E_p, keV	Relative intensity	№	E_p, keV	Relative intensity
1	1096	0,7	14	1672	0,6	28	2093	0,5	41	2506	3,1
2	1178	0,2	15	1697	1,3	29	2125	0,4	42	2545	2,0
3	1205	0,7	16	1774	2,0	30	2136	1,0	43	2550	5,5
4	1292	0,1	17	1811	1,1	31	2187	6,0	44	2554	1,5
5	1302	0,3	18	1820	1,1	32	2193	1,2	45	2590	1,1
6	1326	2,5	19	1835	2,2	33	2217	1,0	46	2610	1,3
7	1393	2,1	20	1881	4,0	34	2225	2,2	47	2615	1,0
8	1402	2,5	21	1898	1,0	35	2305	1,9	48	2620	0,7
9	1482	2,5	22	1925	1,4	36	2317	1,5	49	2630	1,1
10	1491	1,7	23	1945	0,7	37	2355	1,3	50	2635	2,6
11	1516	1,9	24	1987	0,4	38	2362	1,0	51	2660	1,1
12	1599	0,3	25	1997	0,3	39	2378	1,1	52	2665	1,0
13	1665	0,4	26	2011	1,2	40	2394	0,5	53	2701	4,0
			27	2024	0,9						

E_p = 1096 kev resonance and 8.352 Mev level

The γ-ray spectra corresponding to this resonance are reproduced in Fig.2. The observed γ-rays and corresponding transitions in P^{31} are listed in Table 2.

This resonance was one of the weakest and hence it was particularly important in investigating it to take into account the γ-ray background from the tantalum backing, which in the given case was commensurate with the effect. The background from the backing was measured at E_p = 1085 kev, where the yield from the target was minimal ("pedestal" of the resonance peak). The results of these measurements are given in Fig.2, a & b (lower points).

The angular distributions were investigated only for the more intense γ-rays: 7.08 and 1.26 Mev.

The results of these measurements are given in Fig.2,a & b. The experimental angular distribution of the 7.08 Mev γ-rays after reduction of the experimental data by the method of least squares was of the form

$$W_{exp}(\theta) \approx 1 - (0.50 \pm 0.10) \cos^2 \theta.$$

Comparing it with all the possible theoretical angular distributions calculated for dipole and quadrupole γ-transitions to a 3/2 level, we find that the most probable in the present case is the 5/2→3/2 dipole transition, for which the angular distribution predicted by theory is $W(\theta) = 1 - 0.50 \cos^2 \theta$; consequently the assignment for the 8.352 Mev level is 5/2.

The experimental angular distribution of the 1.26 Mev γ-rays was of the form

$$W_{exp}(\theta) \approx 1 - (0.50 \pm 0.10) \cos^2 \theta.$$

This angular distribution is in good agreement with the theoretical distribution calculated for the cascade transition

$$^5/_2\,(L = 1) \rightarrow {}^3/_2\,(L = 1) \rightarrow {}^1/_2$$

for which $W(\theta) = 1 - 0.50 \cos^2 \theta$.

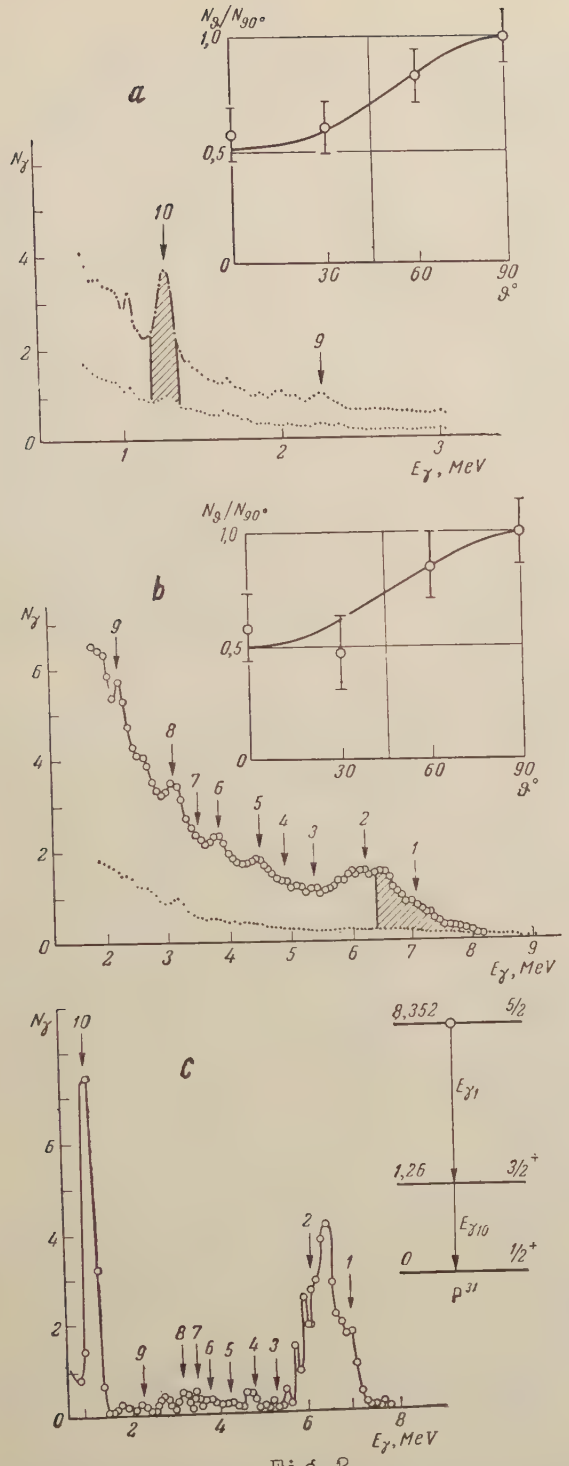

Fig. 2

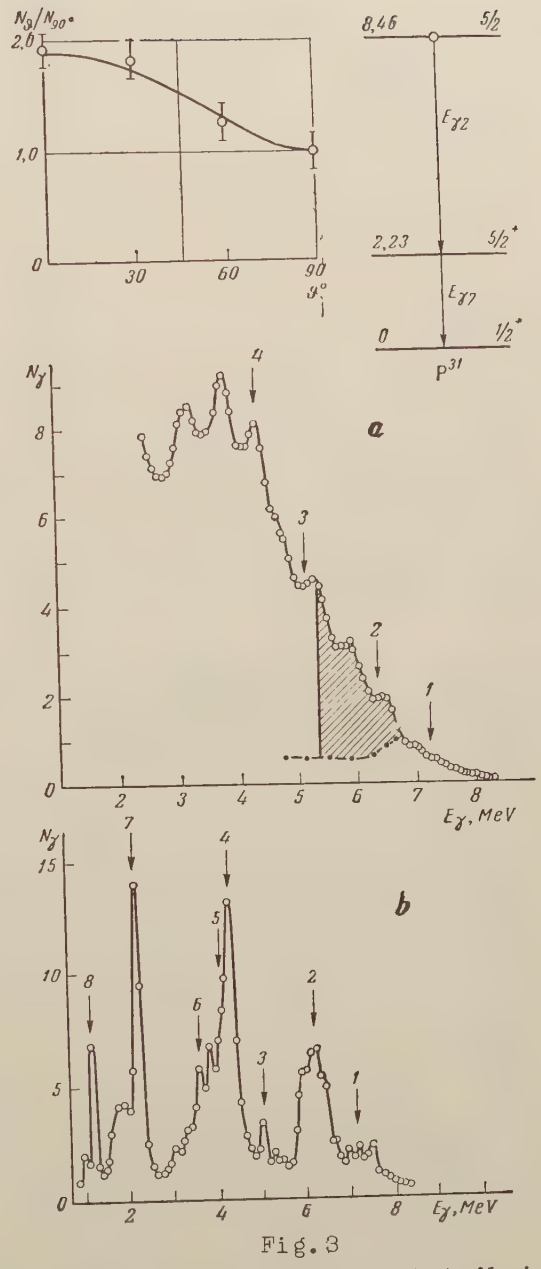

Fig. 3

Fig.2. E_p = 1096 kev resonance: a - soft γ-spectrum and angular distribution of 1.26 Mev γ-rays (lower points - background); b - hard part of the γ-spectrum and angular distribution of the 7.08 Mev γ-rays (lower points - background); c - coincidence spectrum for cascade γ-transitions obtained on the two-crystal summing spectrometer; sum channel set on the energy of the cross-over transition to the ground state.

Fig.3. E_p = 1205 kev resonance: a - hard part of γ-spectrum and angular distribution of the 6.23 Mev γ-rays; b - coincidence spectrum for the cascade γ-transitions (sum channel set on the cross-over transition energy).

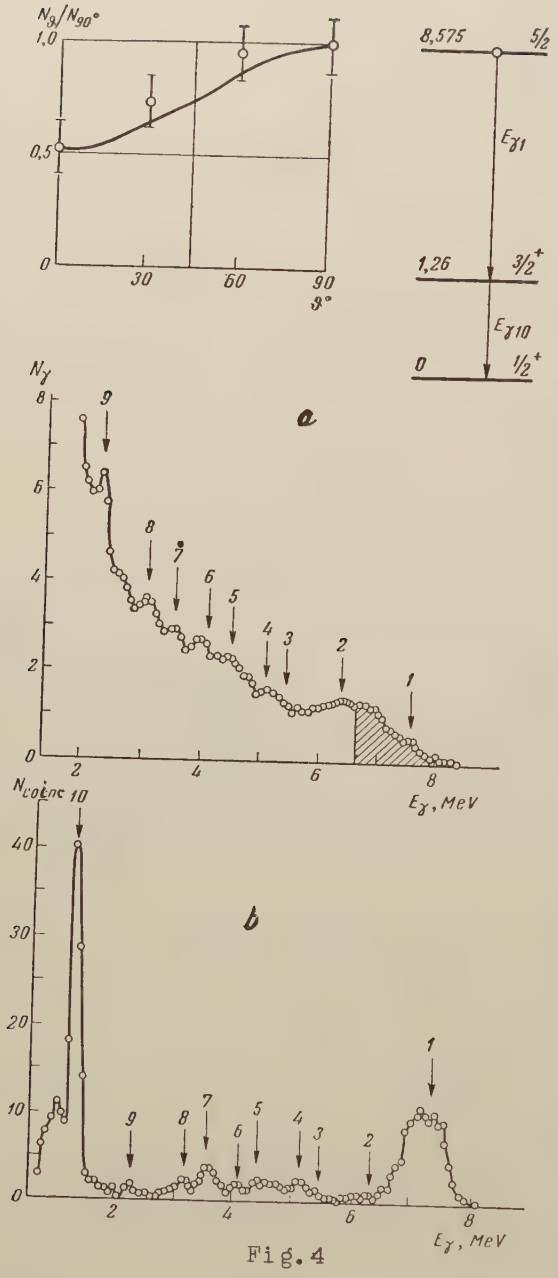

Fig.4

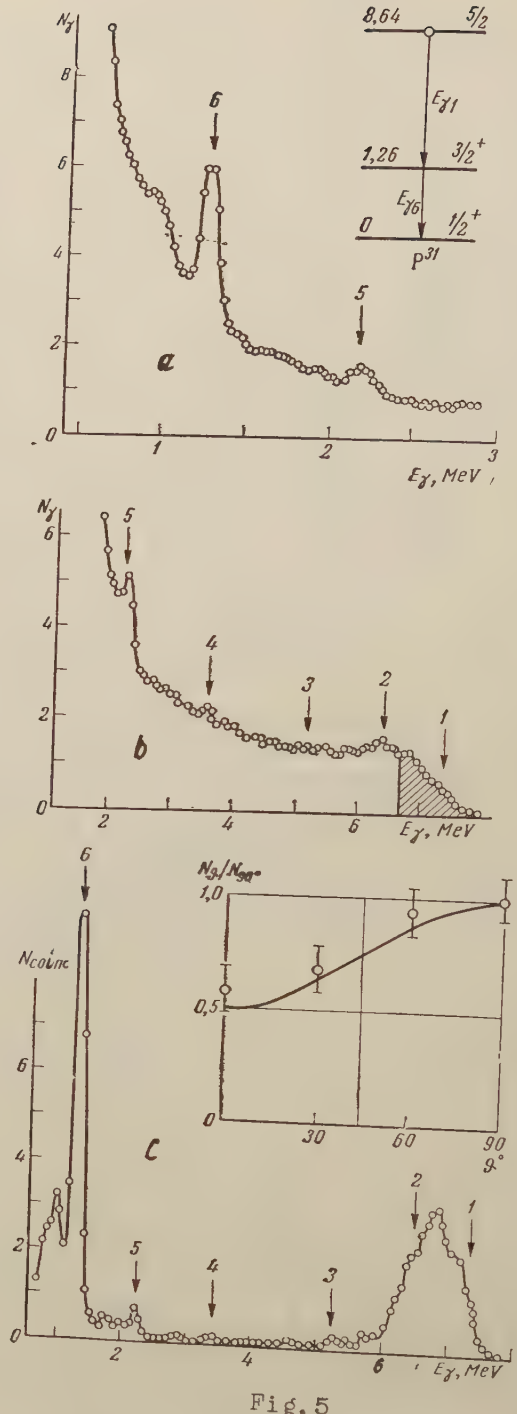

Fig.5

Fig.4. E_p = 1326 kev resonance: a - hard part of γ-spectrum and angular distribution of the 7.31 Mev γ-ray; b - coincidence spectrum for the cascade transition (sum channel set on the cross-over transition energy).

Fig.5. E_p = 1393 kev resonance: a - soft part of γ-spectrum; b - hard part of γ-spectrum; c - coincidence spectrum and angular distribution of the 7.38 Mev γ-rays (sum channel set on the cross-over transition energy).

Table 2

γ-rays associated with the 1096 kev resonance

γ-ray energy	γ-transition, MeV		Relative intensity,%
	Initial level	Final level	
7,08±0,10	8,352	1,26	80
6,12±0,10	8,352	2,23	5
5,22±0,10	8,352	3,13	7
4,84±0,10	8,352	3,51	3
3,92±0,10	8,352	4,43	5
4,43±0,10	4,43	0	5
3,51±0,10	3,51	0	3
3,13±0,10	3,13	0	7
2,23±0,06	2,23	0	5
1,26±0,06	1,26	0	80

*The relative intensities are referred to the total intensity of all the γ-transitions from this resonance level.

Table 3

γ-rays associated with the 1205 kev resonance

γ-ray energy	γ-transition, MeV		Relative intensity,%
	Initial level	Final level	
7,19±0,10	8,46	1,26	16
6,23±0,10	8,46	3,23	40
3,45±0,10	8,46	5,01	4
4,27±0,10	8,46	4,19	40
5,01±0,10	5,01	0	4
4,19±0,10	4,19	0	40
2,23±0,10	2,23	0	40
1,26±0,10	1,26	0	16

Table 4

γ-rays associated with the 1326 kev resonance

γ-ray energy	γ-transition, MeV		Relative intensity,%
	Initial level	Final level	
7,31±0,10	8,575	1,26	74
6,44±0,10	8,575	2,23	4
5,44±0,10	8,575	3,13	6
5,06±0,10	8,575	3,51	10
4,38±0,10	8,575	4,19	6
4,19±0,10	4,19	0	6
3,51±0,10	3,51	0	10
3,13±0,10	3,13	0	6
2,23±0,06	2,23	0	4
1,26±0,06	1,26	0	74

Thus the results of the angular distribution measurements are consistent with the assignment of 5/2 for the 8.352 Mev resonance level in P^{31}.

E_p = 1205 resonance and the 8.46 Mev level

The γ-ray spectra for the 1205 kev resonance are given in Fig.3. The corresponding data are summarized in Table 3.

The experimental angular distribution of the 6.23 Mev γ-rays was of the form

$$W_{exp}(\theta) \approx 1 + (0.90 \pm 0.10) \cos^2 \theta.$$

Inasmuch as these γ-rays correspond to a γ-transition from the 8.46 Mev resonance level to a level at 2.23 Mev (spin 5/2+ - Ref.10), comparing the experimental angular distribution with all the possible theoretical distributions for dipole and quadrupole γ-transition to a level with spin 5/2, we find that the best agreement is obtained for a dipole 5/2→5/2 transition.

Hence the spin of the 8.46 Mev resonance level should be 5/2.

E_p = 1326 kev resonance the the 8.575 Mev level

The γ-ray spectra for this resonance are shown in Fig.4; the corresponding data are given in Table 4.

The angular distribution of the harder γ-rays corresponding to the transition from the 8.575 Mev level to the level of 1.26 Mev (3/2+) is shown in Fig.4,b. After treatment of the experimental results by the method of least squares, the experimental distribution is of the form

$$W_{exp}(\theta) \approx 1 - (0.45 \pm 0.10) \cos^2 \theta.$$

The theoretical distribution and best agreement with this experimental distribution is that for a dipole 5/2→3/2 transition for which $W(\theta) = 1 - 0.50 \cos^2 \theta$. Thus the assignment for the 8.575 Mev level should be 5/2.

E_p = 1393 kev and the 8.64 Mev level

The γ-ray spectra associated with the 1393 kev resonance are shown in Fig.5. The γ-rays observed in the spectra and the corresponding γ-transitions are listed in Table 5.

Table 5

γ-rays associated with the 1393 kev resonance

γ-ray energy	γ-transition, MeV		Relative intensity, %
	Initial level	Final level	
7,38±0,10	8,64	1,26	86
6,41±0,10	8,64	2,23	10
5,13±0,10	8,64	3,51	4
3,51±0,10	3,51	0	4
2,23±0,10	2,23	0	10
1,26±0,06	1,26	0	86

Table 6

γ-rays associated with the 1402 kev resonance

γ-ray energy	γ-transition, MeV		Relative intensity, %
	Initial level	Final level	
7,38±0,10	8,647	1,26	80
6,41±0,10	8,647	2,23	4
5,51±0,10	8,647	3,13	16
3,13±0,10	3,13	0	16
2,23±0,10	2,23	0	4
1,26±0,10	1,26	0	80

Table 7

γ-rays associated with the 1482 kev resonance

γ-ray energy	γ-transition, MeV		Relative intensity, %
	Initial level	Final level	
8,725±0,05	8,725	0	90
7,46±0,10	8,725	1,26	4
6,49±0,10	8,725	2,23	2
5,59±0,10	8,725	3,13	2
5,21±0,15	8,725	3,51	1
4,53±0,10	8,725	4,19	1
4,19±0,10	4,19	0	1
3,51±0,10	3,51	0	1
3,13±0,10	3,13	0	2
2,23±0,04	2,23	0	2
1,26±0,04	1,26	0	4

The experimental angular distribution for the 7.38 Mev γ-rays is shown in Fig.5,c; it is of the form

$$W_{exp}(\theta) \approx 1 - (0.45 \pm 0.10) \cos^2 \theta.$$

This, as in the preceding case, is in best agreement with the theoretical distribution $W(\theta) = 1 - 0.50 \cos^2 \theta$ given by theory for a $5/2 \rightarrow 3/2$ dipole transition. Thus the spin of the 8.64 Mev resonance level should also be 5/2.

E_p = 1402 kev resonance and the 8.647 Mev level

The γ-ray spectra associated with the 1402 kev resonance are shown in Fig.6. The γ-lines observed in the spectra are listed in Table 6. The angular distribution measured for the 7.38 Mev γ-rays is shown in Fig.6,c; it is of the form

$$W_{exp}(\theta) \approx 1 + (0.77 \pm 0.08) \cos^2 \theta.$$

This experimental distribution is in good agreement with the angular distribution $W(\theta) = 1 + 0.75 \cos^2 \theta$ given by theory for a dipole $3/2 \rightarrow 3/2$ transition. All other possible theoretical distributions for dipole and quadrupole γ-transitions to a 3/2 level are either isotropic or comprise a term with $\cos^4 \theta$.

Thus the assignment for the 8.647 Mev level in P^{31} should be 3/2.

E_p = 1482 kev resonance and the 8.725 Mev level

The γ-ray spectra associated with this resonance are shown in Fig.7. This is the only resonance in the spectrum of which there are observed γ-rays corresponding to a cross-over transition to the ground state (8.725 Mev line). The observed γ-rays and corresponding transitions are listed in Table 7.

The angular distribution obtained for the 8.725 Mev γ-rays is shown in Fig.7,b. After the usual treatment by the method of least squares it was of the form

$$W_{exp}(\theta) \approx 1 - (0.52 \pm 0.05) \cos^2 \theta.$$

Comparing it with all the possible theoretical angular distributions calculated for dipole and quadrupole transitions to a level with spin 1/2, we find that the best agreement obtains for the distribution $W(\theta) = 1 - 0.60 \cos^2 \theta$ predicted by theory for a dipole $3/2 \rightarrow 1/2$ transition. Thus the assignment for the 8.725 Mev level is 3/2.

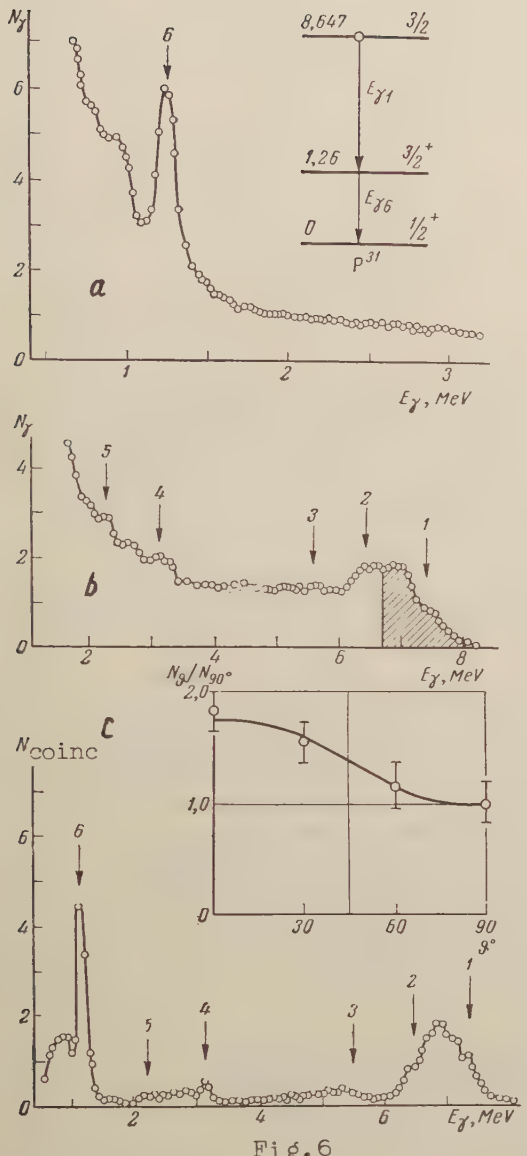

Fig.6

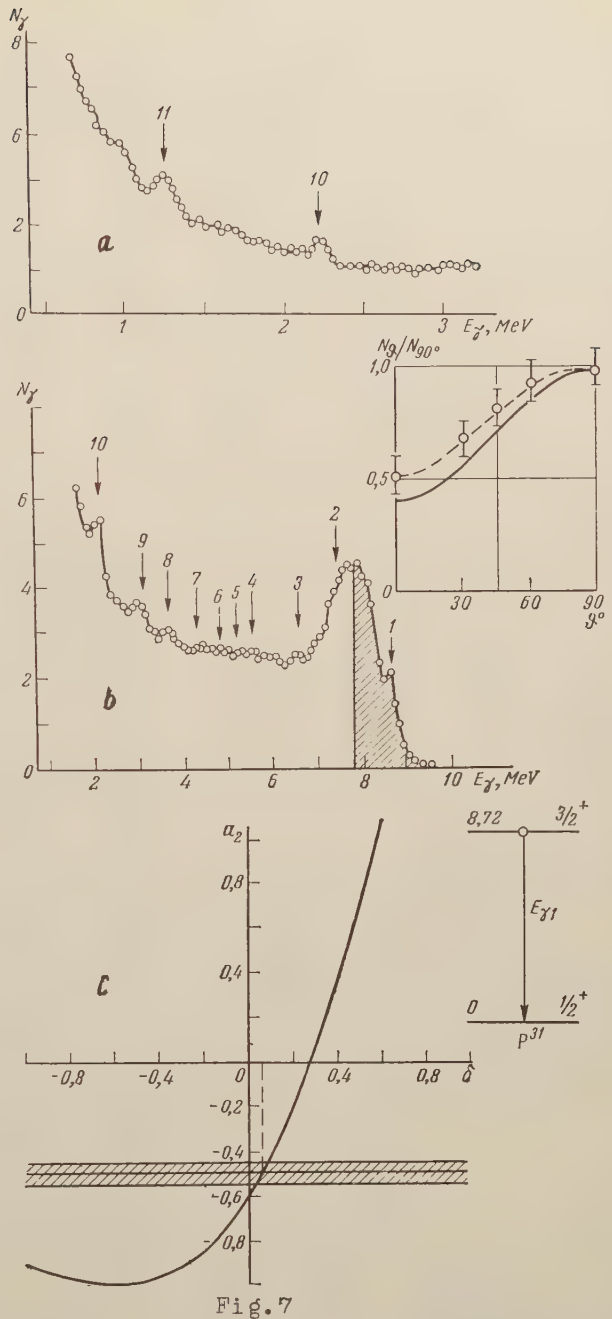

Fig.7

Fig.6. E_p = 1402 kev resonance: a - soft part of the γ-spectrum; b - hard part of the γ-spectrum; c - coincidence spectrum and angular distribution of the 7.38 Mev γ-rays (sum channel set on the cross-over transition energy).

Fig.7. E_p = 1482 kev resonance: a - soft part of the γ-spectrum; b - hard part of the γ-spectrum and angular distribution of the 8.72 Mev γ-rays; c - variation of the coefficient a_2 in the angular distribution for a mixed γ-transition (dipole plus quadrupole radiation) with the mixture coefficient δ. The experimental value of a_2 is -0.52 ± 0.05.

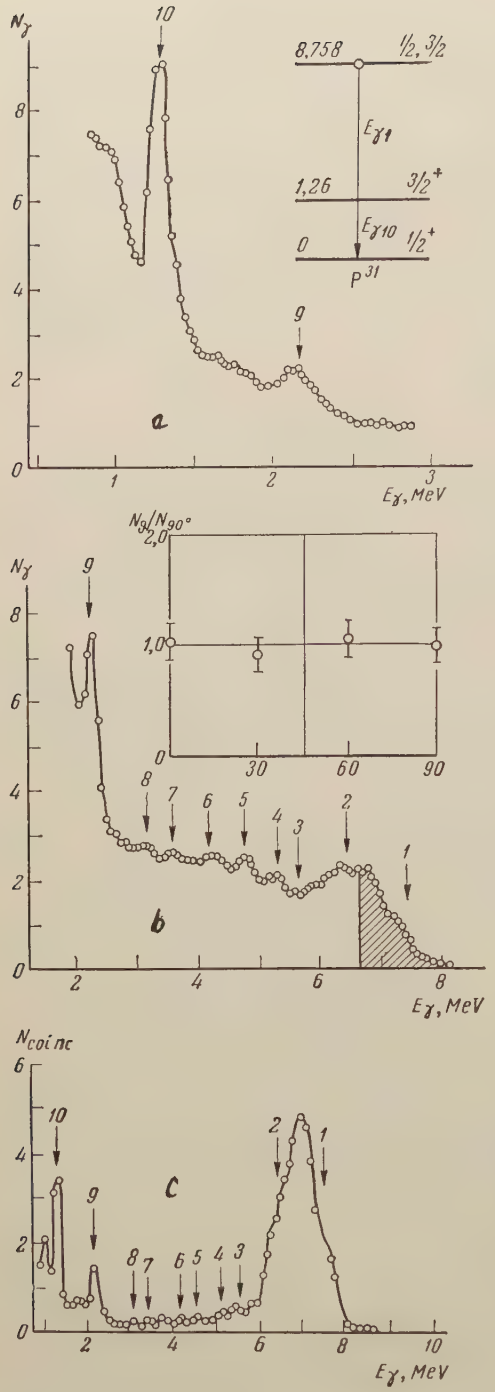

Fig.8. E_p = 1516 kev resonance: a - soft part of the γ-spectrum; b - hard part of the γ-spectrum and angular distribution of the 7.50 Mev γ-rays; c - coincidence spectrum for the cascade γ-transitions (sum channel set on the cross-over transition energy).

Table 8

γ-rays associated with the 1516 kev resonance

γ-ray energy	γ-transition, MeV		Relative intensity, %
	Initial level	Final level	
7,50±0,10	8,758	1,26	70
6,53±0,10	8,758	2,23	16
5,53±0,10	8,758	3,13	4
5,25±0,10	8,758	3,51	4
4,57±0,10	8,758	4,19	6
4,19±0,10	4,19	0	6
3,51±0,10	3,51	0	4
3,13±0,10	3,13	0	4
2,23±0,04	2,23	0	16
1,26±0,04	1,26	0	70

The fact that there is an appreciable divergence (greater than the experimental uncertainty) between the experimental value of the coefficient a_2 (-0.52) and its theoretical value (-0.60) may be interpreted as the result of a small admixture of quadrupole radiation.

Assuming that the radiation is M1 + E2 and taking into account the fact that the ground state of P^{31} has even parity and that in M1 and E2 transitions parity does not change, it may be concluded that the 8.725 Mev resonance level must have spin and parity 3/2+. It is of interest to determine the mixture coefficient δ equal to the ratio of the E2 and M1 radiations. This can be done if one knows the experimental value of the coefficient a_2 and the dependence of δ on the coefficients in the angular γ-ray distribution for mixed transitions. This dependence and the experimental value of the coefficient a_2 are given in Fig.7,c. It will be evident from Fig.7 that the value of δ agreeing with experiment equals 0.06 (accordingly, $\delta^2 = 0.0036$); consequently, the admixture of E2 to the principal M1 radiation amounts to about 0.4%.

E_p = 1516 kev resonance and the 8.758 Mev level

The γ-ray spectrum associated with this resonance is shown in Fig.8; the corresponding γ-rays and transitions are listed in Table 8.

The highest energy and most intense γ-line in the spectrum is the 7.50 Mev line. The angular distribution for these γ-rays is shown in Fig.8,b. It is isotropic. Inasmuch as the 7.50 Mev γ-rays correspond to a transition from a resonance level (8.758 Mev) to the 1.26 Mev level, the spin and parity of which are known to be 3/2+,

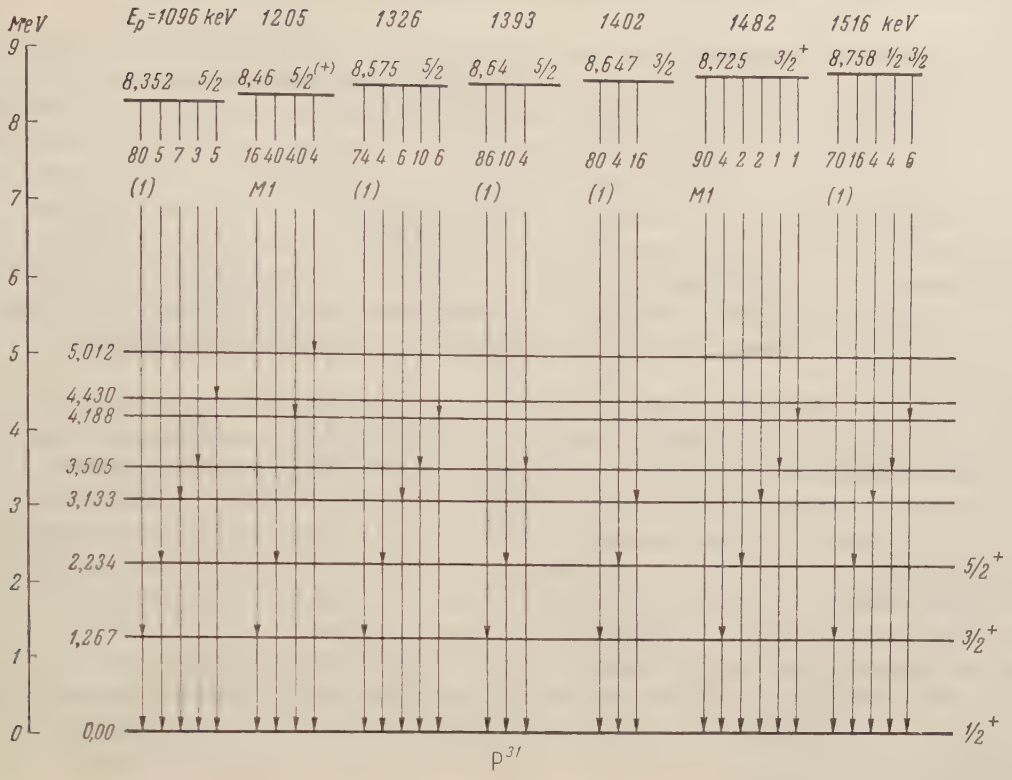

Fig.9. Diagram of γ-transitions between the levels in P^{31}, observed in the γ-ray spectra for the seven investigated resonance levels. The figures under the resonance levels indicate the estimated transition intensities.

the experimental angular distribution must be compared with all the possible theoretical distributions for dipole and quadrupole transitions to a level with spin 3/2. An isotropic distribution in this case is predicted by theory for 3 types of transitions: 1) dipole 1/2→3/2, 2) quadrupole 1/2→3/2, and 3) quadrupole 3/2→3/2. Consequently, the spin of the 8.758 Mev resonance may be either 1/2 or 3/2.

Transition Diagram and Discussion of the Results

On the basis of the experimental results we propose the γ-transition diagram shown in Fig.9, where there are indicated only the P^{31} levels that were observed in the present work. The energies of the low lying levels are given in accord with the most accurate available data[11], the spins and parities were taken from Refs.7 & 10.

We evaluated the relative intensities of the branched transitions on the basis of the measurements of the areas under the γ-line peaks, mainly in the coincidence spectra. The error in the intensity evaluations amounts to about 20% in most cases; only for the weakest γ-lines may the uncertainty be as great as 50%.

As the results of our angular distribution measurements showed, all the γ-transitions to the first excited level and ground state of P^{31} are dipole transitions. In these cases there was not detected any noticeable admixture of quadrupole radiation, except for the transition from the 8.725 Mev resonance level to the ground state which appears to be mixed M1 + E2 (0.4%). Hence it was feasible

to make a definite spin and parity assignment only for the 8.725 Mev resonance level: 3/2+.

One can, however, indicate the most probable parities for the other two resonance levels. Thus, for instance, one can attribute odd parity to the 8.647 Mev resonance level (3/2); then the transition from this resonance level to the 1.26 Mev (3/2+) level must be E1 and the transition to the ground state of P^{31} M2; this may not be observed owing to its low probability compared with the probability for E1 radiation, which is not in conflict with experiment. If one accepts even parity for the 8.647 Mev level, the transition to the 1.26 Mev (3/2+) level would be M1 and the transition to the ground state of P^{31} would be E2. The last would then be noticeable in the spectrum, while in actual fact an 8.647 Mev line was not observed in the spectrum. Consequently, the most probable assignment for the 8.647 Mev level is 3/2-.

One can assign only positive parity to the 8.46 Mev (5/2) resonance level. Then the most intense transition to the 2.23 Mev (5/2+) level should be of the M1 type, and the transitions to the 1.26 Mev (3/2+) level and the ground state of P^{31} (1/2+) should be E2 and M1, which is not in conflict with experiment. If the parity assignment for this resonance level were odd, the above mentioned transitions would be E1, M2 and E3, respectively. But such transitions as M2 cannot compete with E1 transitions and be observed with comparable intensities. Hence the logical spin and parity assignment for the 8.46 Mev level is 5/2+.

We desire to express our deep gratitude to M.I.Guseva for preparation of the isotopic targets and the staff of the electrostatic accelerator, headed by A.A. Tsygikalo & Yu.A.Kharchenko, for insuring operation of the accelerator.

Physical-Technical Institute,
Academy of Sciences of the Ukrainian SSR

References

1. S.P.Tsytko & Yu.P.Antuf'ev, Zhur.eksp.i teor.fiz., 20, 1171 (1956). (Trans. Soviet Physics - JETP.)

2. S.P.Tsytko & Yu.P.Antuf'ev, Trudy sessii Akademii nauk USSR po mirnomu ispol'zovaniyu atomnoi energii (Proceedings of the Session of the Ukrainian SSR Acad.of Sci. on the Peaceful Uses of Atomic Energy), p.70, Kiev, 1958.

3. P.M.Tutakin, S.P.Tsytko, A.N.L'vov, A.K.Val'ter & V.Yu.Gonchar, Atomnaya energiya, 10, 336 (1957). (Trans.Soviet Jour.of Atomic Energy.)

4. Yu.P.Antuf'ev, A.K.Val'ter, V.Yu.Gonchar, E.G.Kopanets, A.N.L'vov, P.M. Tutakin & S.P.Tsytko, In "Yadernye reaktsii pri malykh i srednikh energiyakh" (Nuclear reactions at low and medium energies), p.294, M., 1958.

5. C.Broude, L.L.Green, I.C.Willmott & I.I.Singh, Physica (A),22,1139 (1956).

6. P.M.Endt & C.M.Braams, Revs.Mod.Phys., 29, 683 (1957).

7. E.B.Paul, G.A.Bartolomew, H.E.Gove & A.E.Litherland, Bull.Amer.Phys.Soc., Ser.II, 1, 39 (1956).

8. A.K.Val'ter & A.A.Tsygikalo, PTE (Instruments & Experimental Techniques), No.4, 3 (1957).

9. M.I.Guseva, Ibid., No.5, 112 (1957).

10. L.Simens, Nucl.Phys., 10, 215 (1959).

11. P.M.Endt & C.H.Paris, Phys.Rev., 106, 764 (1957).

TOTAL IONIZATION PRODUCED BY ALPHA-PARTICLES IN GAS MIXTURES

- G.E.Kocharov

The limiting resolution of an ionization α-spectrometer is determined by fluctuation in the number of ion pairs produced by an α-particle in the working gas. The fluctuation in the number of ion pairs is given by

$$\frac{\sqrt{\Delta N^2}}{N} = \sqrt{\frac{F}{N}}, \qquad (1)$$

where $N = E/U$ is the number of ion pairs produced by an α-particle, E is the α-particle energy, U is the mean energy necessary for production of one ion pair, and F is a parameter dependent on the type of gas.

Table 1

Comparison of the mean ion pair production energy with the ionization potential of different gases

Gas	Ionization potential, ev	Mean pair production energy, kev	Energy of first excited level, ev
Helium	24.6	46.0	19.7
Neon	21.6	27.8	16.6
Argon	15.7	26.4	11.5
Krypton	13.9	24.1	9.9
Xenon	12.1	21.4	8.3

It will be evident from the experimental data listed in Table 1 that the mean pair production energy generally exceeds the ionization potential. This is due to the fact that the α-particle expends part of its energy on excitation of the gas atoms. It is obvious, therefore, that to increase the number of ion pairs produced one must utilize the atomic excitation energy for ionization.

If one adds an impurity to the parent gas and the ionization energy of the impurity is less than the excitation energy of the atoms of the parent gas, one can obtain an additional number of ion pairs by the reaction

$$A^* + A_1 = A + A_1^+ + e^-,$$

where A is an atom of the parent gas, and A_1 is an impurity atom (molecule).

The maximum increase in ionization is realized when the ionization energy for the impurity is less than the energy of the first excited state of the parent gas atoms (Table 1).

In experiments carried out by the writer in collaboration with Kirshin[1] it was found that the addition to argon of small amounts of benzene and toluene results in 15 and 10%, respectively, increase in ionization. Melton et al[2] observed an increase of 29% in ionization as a result of addition of 0.5% acetylene to argon.

Hence use of a mixture of gases, leading to increase in the number of ion pairs produced, allows of increasing the energy resolution of an ionization chamber[3-5]. It is known that the pulses appearing on the high voltage electrode and on the grid of the ionization chamber are utilized both for determining the angular distribution function and for "electric" collimation. The shape of the grid and high voltage electrode pulses depends on the size of the α-particle tracks. Hence it is important to make sure that secondary processes (ionization due to second order collisions) do not lead to substantial distortion of the tracks. Otherwise the accuracy of angular distribution measurements is reduced. In connection with this it is necessary to determine the time for secondary processes. This in turn, allows of determining the distortion of the α-particle tracks.

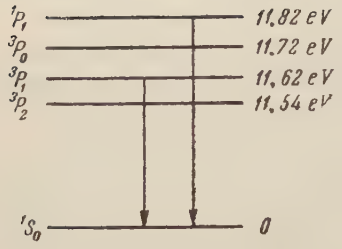

Low lying levels of argon.

For elucidation of the above let us consider the specific case of argon. In the diagram of the low lying levels of argon, shown in the accompanying figure, the levels P_2^3 and P_0^3 are metastable, while the levels P_1^3 and P_1^1 are resonance levels. Inasmuch as de-excitation of higher lying levels occurs mainly by cascade transitions via lower levels[6], we need consider only the low lying levels. The possible modes of de-excitation of these levels are the following:

1. In a collision with a normal atom the excited atom may decay to the ground state by emission of radiation. The probability for this effect is proportional to the gas pressure, and the mean time for the process is $T = 1/Kp$.

2. As a result of a three-body collision there forms an excited argon molecule by the reaction

$$A^* + A + A = A_2^* + A.$$

The mean time for this process is $T_2 = 1/Bp^2$. The excited argon molecule decays to the ground state within a time $T_M = 3.5$ microsec[7], emitting radiation of energy ~10 ev.

3. The excited atom, encountering an impurity atom (molecule), decays to the ground state. In this case the de-excitation or quenching may occur by one of the following reactions[8]:

$$A^* + A_1 \rightarrow A + A_1^* \pm \Delta E; \quad (2a)$$
$$A^* + A_1 \rightarrow A + A_1^{+*} + e^- \pm \Delta E; \quad (2b)$$
$$A^* + A_1B_1 \rightarrow A + A_1 + B_1 \pm \Delta E; \quad (2c)$$
$$A^* + A_1B_1 \rightarrow AA_1 + B_1 \pm \Delta E; \quad (2d)$$

here A^* is the excited argon atom, A_1 is an impurity atom, and A_1B_1 is an impurity molecule.

It follows from the kinetic theory of gases that the lifetime with regard to such processes is $T_3 = 1/N\sigma v$, where N is the impurity concentration, v is the mean relative velocity of the interacting particles, and $\sigma = \Sigma\sigma_i$ is the total cross section for interaction resulting in de-excitation, i.e., the sum of the cross sections for all the reactions.

4. De-excitation occurs by emission of radiation. For the metastable levels (P_2^3 and P_0^3) the mean lifetime is of the order of 10^{-3} sec. The resonance radiation emitted by the atom in de-excitation of the P_1^3 and P_1^1 levels is with high probability absorbed by another atom, i.e., there usually occurs energy transfer. According to Holstein[9], the duration of this process lies in the range from 10^{-5} to 10^{-4} sec.

It can be shown that the time for realization of processes (2) under the usual conditions of operation of an ionization α-spectrometer is less than 10^{-7} sec (Table 2). Hence de-excitation by emission of radiation can be disregarded.

In addition to the above mentioned modes, de-excitation may occur in other ways. For example, in a collision of two excited atoms, one of them may be ionized. However, the probability for this process in the range of low concentrations of excited atoms is very small. An excited atom may diffuse to the wall and interacting with it decay to the ground state. This process is significant only at low pressures (a few mm Hg) and in small chambers.

Table 2

Cross sections for some atomic reactions

Impurity	Ionization potential, ev	Total cross section σ, 10^{-15} cm^2	Ionization cross section σ, 10^{-15} cm^2	Increase in ionization, %	De-excitation time, 10^{-8} sec
1	2	3	4	5	6
Benzene	9.6	22	4	21	0.4
Acetone	10.1	18	1	8	3
Ethylene	10.6	3	0.3	10	2
Propane	11.2	2	0.2	12	1
Acetylene	11.4	6	1.8	29	2
Ethyl alcohol	11.5	6	1	15	1

The mean lifetime of an excited atom can be determined from the expression

$$1/T = Kp + Bp^2 + N\sigma v.$$

According to the data of Futch & Grant[10], even at pressures as low as 70 mm Hg $Bp^2 \gg Kp$. Inasmuch as the working pressure in an ionization spectrometer is usually substantially greater, the first term on the right in the above equation can be dropped, and we can write

$$1/T = Bp^2 + N\sigma v. \qquad (3)$$

Above it was noted that an excited molecule decays by emission of radiation within an average time of 3.5 microsec. This radiation can ionize the impurity.

Thus increase in ionization can be realized either by means of reaction (2b) or at the expense of the energy of the excited molecules. According to the data of Bertolini et al[11], the pulse rise time on the collecting electrode of an ionization chamber upon introduction of an impurity gas decreases and becomes less than 0.5 microsec. This shows that the contribution from excited molecules to the increase in ionization is small.

It follows from Eq.(3) that with increase in the impurity concentration the total number of ion pairs must increase. According to the data of different authors[2,11,12], the total number of ion pairs increases with increase of the impurity concentration up to a maximum at a certain concentration N_m. With further increase in the impurity concentration the number of ion pairs does not change. At very high impurity concentrations, however, the number of ion pairs decreases owing to the effect of δ-electrons.[13] The fact that the total number of ion pairs remains constant within a certain concentration range gives reason to assume, as was done by Jesse & Sadauskis[12] for the case of He, that all the excited gas atoms decay to the ground state by the reactions (2,a-d).

Obviously, for 50% increase in the number of ion pairs there obtains equality of the probabilities for the two processes, i.e.,

$$Bp^2 = N_{1/2}\sigma v. \qquad (4)$$

Having determined experimentally the impurity concentration $N_{1/2}$ for 50% increase in ionization, one can find the cross section σ. (Obviously, the cross

section can be determined not only from increase of the ionization at the concentration $N_{1/2}$, but for any other impurity concentration.)

The cross sections determined for some reactions are listed in Table 2. In column 4 we give the values of σ for ionization (reaction (2b)). In evaluating this cross section it was assumed that 40% of the α-particle energy is expended on excitation. In column 6 we list the values of the mean time for de-excitation owing to collisions with impurity atoms. This time was calculated for a pressure of 1 atm and an impurity concentration corresponding to the maximum increase in ionization.

On the basis of the diffusion coefficient for argon atoms[10] one can determine the distance travelled by an excited atom during its lifetime. At a pressure of 760 mm Hg an excited argon atom travels a distance less than 1 μ during its lifetime of 10^{-8} sec. This result indicates that there occurs virtually no broadening of the particle track. Moreover, it may be assumed with good approximation that the primary electrons and ions are "stationary" during this de-excitation period.

Thus the addition of impurities to argon or other noble gas filling the chamber leads to increase in the number of ion pairs produced without impairing the operating parameters of the chamber.

I desire to express my gratitude to A.P.Komar for valuable comment.

Physical-Technical Institute,
Academy of Sciences of the USSR

References

1. G.F.Kirshin, Thesis, Leningrad Polytechnic Institute, 1957.
2. C.E.Melton, G.S.Hurst & T.E.Bortner, Phys.Rev., 96, 643 (1954).
3. G.E.Kocharov, Thesis, Physical-Technical Institute, USSR Ac.of Sci., 1956.
4. G.E.Kocharov, Dissertation, Radium Institute, USSR Ac.of Sci., 1960.
5. G.E.Kocharov & G.A.Korolev, Izv.AN SSSR, Ser.fiz., 25, 237 (1961). (Trans. Bulletin, 25, 227.)
6. V.O.Herrman, Ann.Phys., 25, 143 (1935).
7. L.Colli, Phys.Rev., 95, 892 (1954).
8. H.S.W.Massey & E.H.S.Burhop, Electronic and Ionic Impact Phenomena, Oxford, 1952.
9. T.Holstein, Phys.Rev., 72, 1212 (1947); 83, 1159 (1951).
10. A.H.Futch & F.A.Grant, Ibid., 104, 356 (1956).
11. G.Bertolini, M.Bettoni & A.Bisi, Nuovo Cimento, 11, 458 (1954).
12. W.P.Jesse & J.Sadauskis, Phys.Rev., 102, 389 (1956).
13. W.Haeberli, P.Huber & E.Baldinger, Helv.phys.acta, 26, 145 (1953).

CONCERNING THE OPERATION OF PROPORTIONAL COUNTERS

- G.A.Korolev & G.E.Kocharov

Introduction

According to the present understanding of the operating mechanism of proportional counters, the addition of a polyatomic impurity to the noble gas results in a decrease of the gas multiplication factor A and in increase of the threshold voltage.[1,2] As a result, the slope of the multiplication versus filament voltage curve is reduced and the operation of the counter becomes more stable.

However, the theory of operation of proportional counters[1,2] does not take into account the additional ionization owing to second order collisions in the presence of an easily-ionized impurity. Hence the addition of such an impurity may result in increase of A.

A detailed investigation of the properties of argon + methane mixtures showed that when small quantities (<6%) of methane are added the gas multiplication factor does not fall off, but on the contrary, increases. In order to detect small changes in A it is necessary to have a counter with good energy resolution. The energy resolution of a proportional counter depends on its geometry and operating conditions. Thus, before discussing our experimental results, it is necessary to examine the operating characteristics of proportional counters.

Description of the proportional counter and its operating characteristics

The proportional counter in question was designed for detecting conversion electrons for coincidence counting with α-particles registered in an ionization chamber.[3,4] The cathode is a truncated brass cylinder, 10 cm in diameter and 20 cm long. The counter base has a circular opening 2 cm in diameter to receive the film source. The anode is a 50 micron diameter platinum wire. The design provides an effective 2π geometry for large sources. To keep the particle range within the counter, the specified operating pressure is 1.3-1.5 atm.

In investigating the operation of the counter we used a U^{234} source (4.768 Mev α-particles), while to check the resolution we employed a natural mixture of uranium isotopes.

Equipment

In studying the α-particle spectra the pulses from the proportional counter were fed, via a preamplifier, an amplifier and a limiter, to a 28-channel pulse height analyzer. The gas multiplication factor was measured by varying the gain of the main amplifier.

In the "ionization chamber regime" the pulse is determined mainly by the electrons. In the case of gas multiplication positive ions begin to play a more important role. Calculations show that for the particular geometry selected, using argon as the working gas in the counter, the pulse rises to half of its maximum height in ~30 microsec. In order to obtain a regular gas multiplication curve it was necessary to provide a sufficiently large time constant in the differentiating circuit (400 microsec).

Energy resolution

The limiting half-width of the line is determined by fluctuation of the primary ionization and the gas multiplication factor A. For $A \gg 1$ the line half-width does not depend on the multiplication factor up to a certain critical value A_{cr};

its dependence on the primary ionization is given by the relation

$$\frac{\Delta E}{E} \approx \frac{2.36}{\sqrt{m_0}},$$

where m_0 is the number of ion pairs produced by a particle. The value of A_{cr} is characterized by[5]

$$EA_{cr} \approx 10^8 \text{ ev.}$$

It is evident that this relation imposes a limitation on the possibility of utilizing large values of gas multiplication for high-energy particles. For gas multiplication factors greater than A_{cr}, the pulse height begins to be affected by space charge. This effect is more pronounced for particles emitted perpendicular to the filament as well as for high gas pressures. The line half-width obtained in practice is always greater than the theoretical half-width, and the discrepancy increases with the particle energy. This is due to the fact that for higher particle energies the relative contribution from the statistical pulse scatter decreases. The main contributions to the half-width stem from factors having to do with imperfections in the design or operation of the counter.

Below we shall consider the most important factors responsible for pulse scatter.

1. Instability of the filament voltage. Since the gas multiplication factor varies exponentially with voltage, the voltage must be closely regulated (stability $\leqslant 10^{-4}$).

2. Nonuniformity and eccentricity of the filament. Variations in filament diameter can contribute up to 1% to the line half-width. Thorough cleansing of the filament is recommended. Tests have shown that eccentricity does not play a significant role.

3. End effects. The weakening of the field at a distance of the order of the radius from the end of the counter causes the appearance of a low-energy tail. This effect can be minimized by using a large length-to-diameter ratio and by providing shielding electrodes to correct the field inhomogeneity.

4. Attachment to electronegative impurities. In this case the pulse height will depend on the spatial location of the particle trajectory. This effect can be eliminated by purifying the gas.

5. Noise. The contribution to the line half-width from noise in proportional counters is usually negligible. Noise is most detrimental in detecting low-energy particles. However, by choosing a sufficiently high gas multiplication factor it is always feasible to obtain a good signal-to-noise ratio (at least 100 to 1).

Other factors such as, for instance, instability of the amplifier and analyzer, changes in gas pressure, large source thickness, etc. are generally minor, and made a significant contribution to the line half-width only in exceptional cases.

For 4.5 Mev α-particles in the case of an argon-filled counter the relative line half-width due only to fluctuations in ionization and gas multiplication amounts to about 0.55%. In our tests with a gas multiplication factor of 5, the half-widths of the α-lines of U^{238} and U^{234} equalled 1.7 and 1.9%, respectively (Fig.1). The counter was filled with spectroscopically pure argon at a pressure of 1.3 atm. The high voltage source was a VS-10 unit (stability 0.001%).

Apparently, end effects contribute greatly to the line half-width. In addition, some pulse scatter is caused by space charge. Owing to these two factors the half-width of the U^{234} line is somewhat greater than that of the U^{238} line. It was also found that the half-width increases with increase of the multiplication factor. This is explained by increase in the effect due to space charge.

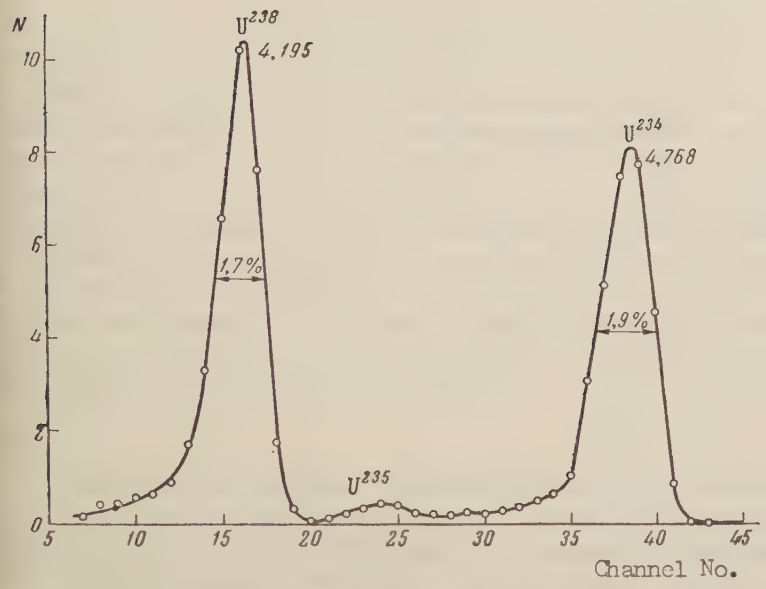

Fig.1. Alpha-particle spectrum obtained for a natural mixture of uranium isotopes. Gas multiplication factor 5; gas pressure 1.3 atm.

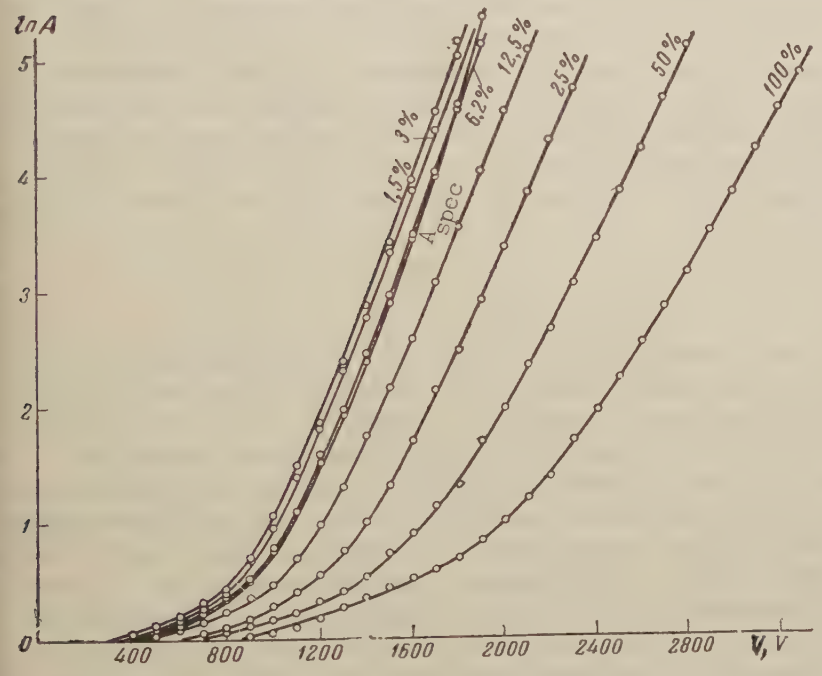

Fig.2. Gas multiplication factor versus filament voltage for different mixtures of argon and methane (CH_4 content indicated in percent at the curves). A_{spec} = spectroscopically pure argon.

Gas multiplication curves

Fig.2 shows the gas multiplication curves for different mixtures of argon and methane. All the curves were recorded at the same pressure: 1.3 atm. It will be noted that for small amounts of methane the multiplication factor of the mixture is greater than for pure argon.

Operation of proportional counter filled with a mixture of gases

The theory of the operation of proportional counters was developed by Rose & Korff[6]. These authors deduced an expression for the multiplication factor on the basis of the following assumptions.

1. The photon mechanism is absent, i.e., the contribution of UV photons to the formation of secondary electrons is negligible.

2. Secondary electron emission by positive ions at the cathode can be neglected.

3. Fluctuations in ionization and electron attachment to electronegative impurities are insignificant.

Analyzing these assumptions, Rose & Korff came to the conclusion that their theory is valid for monatomic gases in the range of multiplication factors up to 100 and for polyatomic gases for factors up to 10^4.

Below we shall show that the theory of Rose & Korff is not valid for gas mixtures wherein electrons can be produced by secondary collisions. It is known that the gas multiplication factor is determined by the number of ionizing collisions undergone by the electron in moving to the filament:

$$A = e \int_{r_0}^{r_a} \alpha dr,$$

where r_0 is the filament radius, r_a the radius where the avalanche begins, and α is the number of ion pairs produced by the electron per unit path length. The value of α, the first Townsend coefficient, depends on the nature of the gas, the gas pressure and the field strength.

If there are N atoms or molecules per unit volume, $\alpha = N\sigma$, where σ is the ionization cross section. Experimental data[2] show that up to an electron energy of 50 ev is a linear function of the energy, i.e., $\sigma = a\varepsilon$, where ε is the mean electron energy above the ionization potential. The value of a is known for many gases[2]. Thus the gas multiplication factor is equal to

$$A = e^{aN \int_{r_0}^{r_a} \varepsilon(r)\, dr} \qquad (1)$$

It follows from Eq.(1) that the multiplication factor depends on the gas pressure (through N), on the nature of the gas (through a), and on the geometry and operating conditions of the counter (through r_0, r_a and ε).

By way of illustration let us consider a mixture of A and CH_4. The coefficients a for argon and methane are 1.81 and 1.24, respectively. Hence for the mixture a will be smaller than for pure argon. It is known that the addition of a polyatomic gas to a monatomic gas results in decrease of the mean electron energy, other conditions being equal. With a decrease in the mean energy, r_a also decreases. Thus, according to Eq.(1), in a mixture of argon and methane the gas multiplication factor must be smaller than in pure argon. True, for high concentrations of methane some reduction of the factor is observed (Fig.2). However, for amounts of methane under 6% the opposite effect obtains. This anomaly may stem from the fact that in the work of Rose & Korff only ionization by electrons was taken into account. Actually the addition of an easily ionizable gas leads to additional ionization due to secondary collisions between excited atoms of the parent gas and the impurity atoms:

$$A^* + A_1 \rightarrow A + A_1^+ + e^- \pm \Delta E, \qquad (2)$$

where A^* is the excited atom of the parent gas, A_1 is an atom or molecule of the impurity, and ΔE is the change in the kinetic energy of the colliding particles.

Argon has more than a hundred excited levels with energies above the ionization potential of methane. Thus in collisions between excited argon atoms and methane atoms the latter may be ionized. A ~2% increase in ionization was observed in a grid ionization chamber upon addition of methane to the parent argon. This is explained by the fact that some of the argon atoms, excited by the α-particles, encounter impurity atoms and ionize them. The increase in ionization due to the primary excited atoms* leads to increase in the pulse height in the ionization regime of the chamber, and, of course, cannot increase the gas multiplication factor. In the vicinity of the filament ($r \leqslant r_a$) the electrons not only ionize the gas atoms, but excite them as well. Moreover, there exists a certain region $r_a \leqslant r \leqslant r_e$ wherein there occurs only excitation. Evaluations show that the main contribution to the increase in the gas multiplication factor is made by those atoms which are excited in the $r_a \leqslant r \leqslant r_e$ region.

---

*By primary excited atoms we mean atoms which are excited by the initial charged particles, in this case the α-particles.

In collisions of excited argon atoms with impurity molecules, in addition to reaction (2), there may occur other de-excitation processes. Consideration of this matter[8] shows that in the case of mixtures of argon and a polyatomic impurity reaction (2) has a high probability and that the lifetime of the excited atom with respect to ionization of the impurity is 10^{-7}-10^{-8} sec. Increase of the multiplication factor by introduction of an impurity gas is possible in all cases when the ionization potential of the impurity is less than the excitation energy of the parent gas atoms.

We desire to express our gratitude to A.P.Komar for his interest in the investigation and stimulating discussions.

Physical-Technical Institute,
Academy of Sciences of the USSR

References

1. V.Veksler, L.Groshev & B.Isaev, Ionizatsionnye metody issledovaniya izluchenii (Ionization methods for studying radiation), M., 1949.
2. S.A.Korff, Electron and Nuclear Counters, N.Y., 1945.
3. A.P.Komar, G.A.Korolev & G.E.Kocharov, Izv.AN SSSR, Ser.fiz., 22, 824 (1958). (Trans.Bulletin, 22, 818.)
4. G.E.Kocharov & G.A.Korolev, Ibid., 25, 237 (1961) (Trans.Bulletin, 26, 227.)
5. V.Pontecorvo, Helv.phys.acta, 23, III, 97 (1949).
6. M.E.Rose & S.A.Korff, Phys.Rev., 59, 850 (1941).
7. G.E.Kocharov, A.P.Komar & G.A.Korolev, Zhur.eksp.i teor.fiz., 36, 68 (1959). (Trans.Soviet Physics - JETP.)
8. G.E.Kocharov, Present issue of the Bulletin, p.873.

ATOMIC MASSES OF TIN AND ANTIMONY ISOTOPES

- R.A.Demirkhanov, T.I.Gutkin, O.A.Samadashvili & I.K.Karpenko

The masses of tin 116, 117 and 120 were measured for the first time in 1950 on a double focusing mass spectrograph by Duckworth & Preston[1]. However, owing to the low resolution of the mass spectrograph (~7000) and the procedure of step comparison of masses of Sn^{116} and Sn^{120} with the secondary standards H^1 and C^{12} there resulted appreciable errors in the values obtained by these authors.

Table 1

Mass doublet differences and isotope masses

Doublet	ΔM, 10^{-3} aMU	Mass of light component, aMU
$C_9^{12}H_8 - Sn^{116}$	160,970±0,050	115,938590±50
$C_9^{12}H_9 - Sn^{117}$	167,535±0,040	116,940170±40
$C_9^{12}H_{10} - Sn^{118}$	176,855±0,045	117,938990±50
$C_9^{12}H_{11} - Sn^{119}$	182,980±0,040	118,941010±40
$C_9^{12}H_{12} - Sn^{120}$	191,880±0,045	119,940250±50
$C_7^{12}H_5O_2 - Sb^{121}$	125,340±0,040	120,942140±40
$C_7^{12}H_6O_2 - Sn^{122}$	133,640±0,040	121,941900±40
$C_9^{12}H_{15} - Sb^{123}$	213,500±0,050	122,943060±50
$C_9^{12}H_{16} - Sn^{124}$	220,240±0,070	123,944460±70

Table 2

Mass defects
(10^{-4} aMU; all negative)

Isotope	Calc. from Table 1	Halsted[2]	Duckworth[1]	Duckworth[5]	Wapstra[6]
Sn^{116}	614,1±0,5	607,3±1,3	614,8±7,0	611,5±3,0	610,3±5,0
Sn^{117}	598,3±0,4	594,8±1,0	579,2±4,7	598,2±3,0	598,0±5,0
Sn^{118}	610,1±0,5	602,2±1,6	—	607,2±2,5	607,0±5,0
Sn^{119}	589,9±0,4	587,8±1,2	—	590,3±2,0	590,0±5,0
Sn^{120}	597,5±0,5	594,1±1,4	598,8±7,2	596,7±1,4	599,4±5,0
Sb^{121}	578,6±0,4	574,0±2,0	—	577,2±2,0	580,0±5,0
Sn^{122}	580,1±0,4	575,1±1,5	—	576,8±2,5	579,0±5,0
Sb^{123}	569,4±0,5	550,0±2,0	—	566,4±2,5	569,0±5,0
Sn^{124}	555,4±0,7	551,0±1,1	—	551,2±3,0	554,6±5,0

Halsted[2] avoided step comparison and measured the masses of all tin isotopes, except for the scarce Sn^{112} and Sn^{114}, on a double focusing mass spectrograph with a better resolution than that of Duckworth & Preston.

To the best of our knowledge there have been hitherto no mass spectroscopic measurements of the masses of antimony isotopes.

In the present report we give the results of new mass measurements for tin and antimony isotopes, which are of interest for determining nuclear binding energies in the region of the magic number Z = 50. The measurements were carried out by the doublet method on a double focusing mass spectrograph.[3] For enhanced accuracy the mass determinations were carried out with reference to doublets in which their singly charged ions were compared directly with the heavy molecules containing H^1, C^{12} and O^{16}. For obtaining the doublets there were used in the canal-ray type ion source pairs of the substances: $Sn(CH_3)_4$, $SbCl_3$, C_9H_{12} and $C_7H_6O_2$. Typical doublet spectrograms are reproduced in the accompanying figure.

Table 3

Comparison of the mass differences (in aMU) calculated on the basis of Table 1 and from the data on nuclear reactions and radioactive decay

Mass difference	from Table 1	Halsted[2]	Wapstra[6]	Duckworth[5]	Nuclear reactions	Type	Q, MeV [] = Ref.
Sn^{117}—Sn^{116}	1+0,00158±6	1+0,00120±15	1+0,00123±70	1+0,00133±36	—	—	—
Sn^{118}—Sn^{117}	1—0,00118±6	1—0,00074±18	1—0,00090±70	1—0,00090±40	1—0,00108±22	Sn^{117} (dp) Sn^{118}	7,14±0,20 [7]
					1—0,00079±22	Sn^{118} (γn) Sn^{117}	—9,10±0,20 [7]
Sn^{119}—Sn^{118}	1+0,00202±6	1+0,00143±20	1+0,00170±70	1+0,00169±32	1+0,00190±22	Sn^{119} (γn) Sn^{118}	—6,60±0,20 [7[
					1+0,00199±16	Sn^{119} (γn) Sn^{118}	—6,51±0,15 [7]
Sn^{120}—Sn^{119}	1—0,00076±6	1—0,00060±18	1—0,00094±70	1—0,00064±24	—	—	—
Sb^{121}—Sn^{120}	1+0,00189±6	—	1+0,00194±70	1+0,00195±24	1+0,00193±38	Sb^{121} (γn) Sb^{120}	—9,25±0,20 [7]
						Sn^{120} (pn) Sb^{120}	—3,47±0,30 [7]
					1+0,00198±21	Sb^{121} (γn) Sb^{120}	—9,25±0,20 [7]
						Sb^{120} (β^+) Sn^{120}	2,72±0,02 [8]
					1+0,00197±8	Sn^{120} (dp) Sn^{121}	3,92±0,07 [9]
						Sn^{121} (β^-) Sb^{121}	0,383±0,005 [8]
Sn^{122}—Sb^{121}	1—0,00015±6	—	1—0,00010±70	1+0,00004±32	1—0,00048±33	Sn^{121} (dp) Sn^{122}	6,20±0,30 [7]
						Sn^{121} (β^-) Sb^{121}	0,383±0,005 [8]
					1+0,00019±21	Sb^{121} (dp) Sb^{122}	4,41±0,20 [7]
						Sb^{122} (β^+) Sn^{122}	1,55±0,05 [10]
					1+0,00002±7	Sb^{121} $(n\gamma)$ Sb^{122}	6,80±0,04 [7]
						Sb^{122} (β^+) Sn^{122}	1,55±0,05 [10]
Sn^{122}—Sn^{120}	2+0,00174±6	2+0,00190±20	2+0,00204±70	2+0,00199±28	2+0,00231±33	Sn^{121} (dp) Sn^{122}	6,20±0,30 [9]
						Sn^{120} (dp) Sn^{121}	3,92±0,07 [7]
Sb^{123}—Sn^{122}	1+0,00107±6	—	1+0,00100±70	1+0,00104±35	1+0,00113±21	Sb^{122} (dp) Sb^{123}	6,64±0,20 [9]
						Sb^{122} (β^+) Sn^{122}	1,55±0,05 [10]
Sb^{123}—Sb^{121}	2+0,00092±6	—	2+0,00110±70	2+0,00108±32	2+0,00132±30	Sb^{121} (dp) Sb^{122}	4,41±0,20 [7]
						Sb^{122} (dp) Sb^{123}	6,64±0,20 [9]
					2+0,00114±22	Sb^{121} $(n\gamma)$ Sb^{122}	6,80±0,04 [7]
						Sb^{123} (dp) Sb^{123}	6,64±0,20 [9]
Sn^{124}—Sb^{123}	1+0,00140±6	—	1+0,00144±70	1+0,00152±40	2+0,00139±16	Sn^{124} (γn) Sn^{123}	—8,50±0,15 [7]
						Sn^{123} (β^-) Sb^{123}	1,42±0,01 [8]

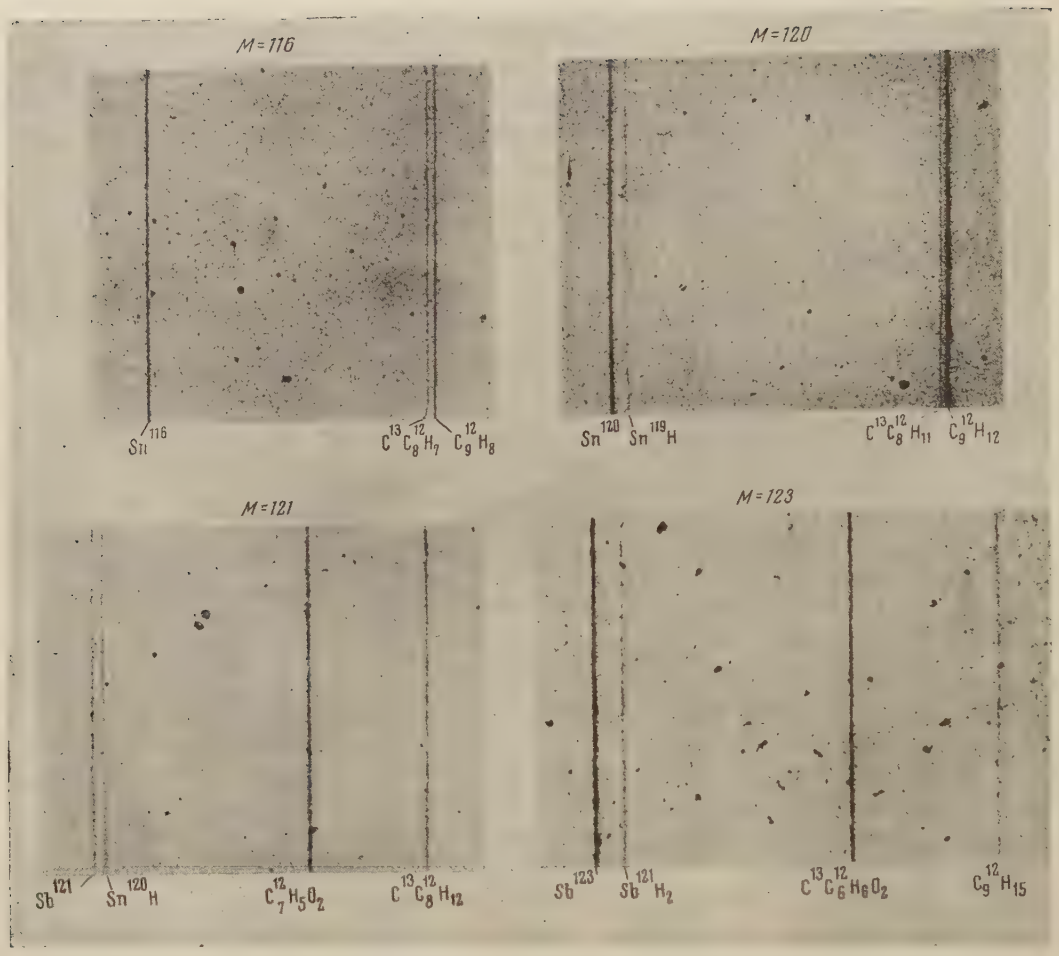

Typical mass doublets. 150 X.

In Table 1 we list the values of the doublet mass difference ΔM and the calculated atomic masses of the isotopes. The doublet mass differences were calculated by the procedure described by Mattauch & Waldman[4] using three dispersed lines. For calculating the masses of the tin and antimony isotopes there were used the values H^1 = 1.0081423 ± 6 and C^{12} & 12.0038247 ± 27, measured on the same set-up. The high resolution of our mass spectrograph (~100 000 — 120 000) enabled us to resolve doublets of the type

$$C^{12}_m H^1_n O^{16}_k - C^{13} C^{12}_{m-1} H^1_{n-1} O^{16}_k$$

at all measured mass numbers and to avoid thereby superposition of the line associated with C^{13}. Comparable resolution for heavy masses has not hitherto been attained in other similar mass spectrographs, which is why many other authors were forced to introduce corrections for the presence of the unresolved C^{13} component[2].

To check for the absence of systematic errors there were measured three control doublets at the mass numbers 121, 122 and 123 with known mass differences, namely,

$$C^{13}C^{12}_8 H_{12} - C^{12}_7 H_5 O_2 = (68.35 \pm 0.05) \cdot 10^{-3} \text{ aMU}$$
$$C^{12}_9 H_{14} - C^{12}_7 H_6 O_2 = (72.73 \pm 0.04) \cdot 10^{-3} \text{ aMU}$$

$$C_9^{12}H_{15} - C^{13}C_6^{12}H_6O_2 = (77.31 \pm 0.05) \cdot 10^{-3} \text{ aMU}.$$

The values obtained indicate that our mass spectrometer was properly adjusted.

In Table 2 we list the mass defects for the tin and antimony isotopes calculated on the basis of the data of Table 1. For comparison we also give the mass defect values obtained by other authors. In most cases our values agree within the limits of the experimental error with the data of other authors, except for the mass spectroscopic measurements of Halsted[2], which lie consistently below ours.

From the values of Table 1 one can also calculate the mass differences between neighboring tin and antimony isotopes and then compare them with the differences calculated on the basis of nuclear reaction Q values and data obtained in investigating radioactive decays. These mass differences are listed in Table 3, from which it will be seen that in most cases there is satisfactory agreement.

We desire to express our gratitude to E.E.Baroni, T.N.Lebsadze and V.M. Shoniya for making available the organic and metal-organic compounds and to V.F. Moskovskii and G.A.Dorokhova for assistance in the work.

References

1. H.E.Duckworth & R.S.Preston, Phys.Rev., 79, 402 (1950); Ibid., 82, 468 (1951).
2. R.E.Halsted, Ibid., 88, 666 (1952).
3. V.Shyuttse, R.A.Demirkhanov, T.I.Gutkin, O.A.Samadashvili & I.K.Karpenko, PTE, No.4, 92 (1960). (Trans.Instruments & Experimental Techniques.)
4. J.Mattauch & L.Waldman, Z.Naturforsch., 8a, 293 (1953).
5. H.E.Duckworth, Progress in Nucl.Phys., 6, 138 (1957).
6. A.Wapstra, Physica, 21, 385 (1955).
7. D.Van-Patter & W.Whaling, Revs.Mod.Phys., 26, 402 (1954).
8. J.A.Harvey, Phys.Rev., 81, 353 (1951).
9. R.King, Revs.Mod.Phys., 26, 373 (1954).
10. L.Lidofsky, Revs.Mod.Phys., 29, 773 (1957).

ALPHA-DECAY TO ELECTRON CAPTURE RATIOS FOR Po^{200}, Po^{201} AND Po^{203}

- B.N.Belyaev, A.V.Kalyamin & A.N.Murin

The present work was concerned with determination of the ratios between the probabilities of decay with emission of an α-particle and by electron capture for polonium 200, 201 and 203 formed as a result of bombardment of Bi^{209} with high energy protons. Direct measurement of the fraction of α-decays and E-captures for these Po isotopes is difficult owing to the presence of a large number of different Po isotopes with complex decay modes.

One can, however, indirectly determine the number of nuclei undergoing α-decay and E-capture by comparing the activities of the investigated isotopes with the corresponding activity of an isotope for which the α-decay—E-capture ratio is known. As our reference isotope we chose Po^{206} for which

$$\frac{\alpha}{E + \alpha} = 5 \pm 1\%.$$

The investigated polonium isotopes were obtained by bombarding Bi with high energy protons in the synchrocyclotron of the Joint Institute for Nuclear Research for a period of 10 to 20 min. The targets were prepared of bismuth oxide, compressed into pellets. The α-activity measurements were performed by means of an ionization chamber with a 31-channel pulse height analyzer, and were started 40-50 min after the end of proton bombardment. We recorded the α-particle spectra and measured the intensity of the α-lines of the investigated Po isotope at different instants.

Then by extrapolation of the α-decay curve we determined for each Po isotope the intensity of its α-particle group, corresponding to the time of end of proton bombardment. These intensities were compared with the intensity of the α-line of the reference isotope Po^{206}. The Po isotopes were identified from the α-particle energies and the decay periods. The chamber geometry and operating conditions were such that the half-width of the peak corresponding to the 5.108 Mev Po^{208} α-particles was 28-32 kev.

In the experiments we used mechanical collimators (diameter 9-10 mm, thickness 150-200 μ, cells 120-150 μ), which provided for adequate resolution of the peaks corresponding to α-groups of close energies. Owing to the appreciable background due to conversion electrons, in investigating the α-particles from short-lived Po isotopes the resolution was somewhat impaired and the line half-width in the case of different targets varied in the range from 35 to 40 kev. By way of illustration two of the α-spectra are reproduced in Figs.1 and 2.

The Po isotope sources for the alpha-chamber were prepared by electrochemical deposition of the polonium from 2n HCl onto polished silver disks.

The fraction of Po nuclei undergoing E-capture was determined by the method of chemical separation of the daughter products (Bi, Pb and Tl) forming in the following decay chains:

$$Po^{206} \xrightarrow[9.5\ days]{E} Bi^{206} \xrightarrow[6.3\ days]{E} Pb^{206}$$

$$Po^{205} \xrightarrow[1.8\ hr]{E} Bi^{205} \xrightarrow[14.5\ days]{E} Pb^{205}$$

$$Po^{203} \xrightarrow[44\ min]{E} Bi^{203} \xrightarrow[12\ hr]{E} Pb^{203} \xrightarrow[52\ hr]{E} Tl^{203}$$

$$Po^{201} \xrightarrow[17.5\ min]{E} Bi^{201} \xrightarrow[1.8\ hr]{E} Pb^{201} \xrightarrow[8.4\ hr]{E} Tl^{201} \xrightarrow[72\ hr]{E} Hg^{201}$$

$$Po^{200} \xrightarrow[10\ min]{E} Bi^{200} \xrightarrow[35\ min]{E} Pb^{200} \xrightarrow[12.6\ hr]{E} Tl^{200} \xrightarrow[25.6\ hr]{E} Hg^{200}.$$

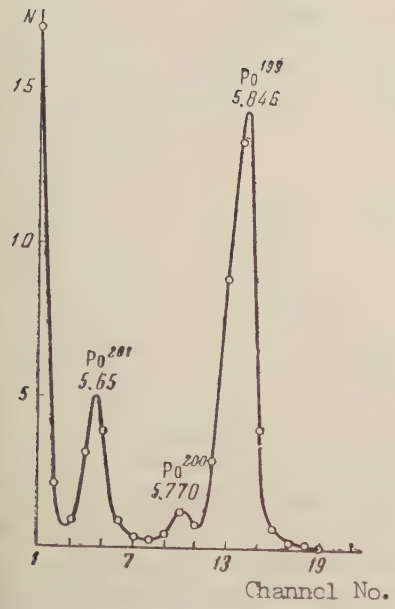

Fig.1. Alpha-spectrum of Po isotopes. The energies at the peaks are in Mev. Interpolation of the curves between the points close to the peaks was carried out taking into account the experimentally determined line half-width in the given energy region (35-40 kev).

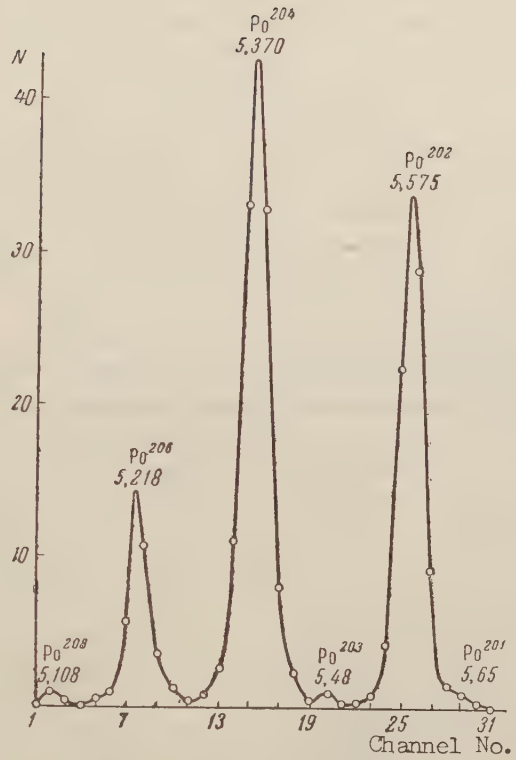

Fig.2. Alpha-spectrum of Po isotopes.

The yields of daughter nuclei undergoing E-capture were determined by means of a 4π scintillation counter.[1]

In order to minimize the errors connected with losses incident to chemical separation and with the appreciable difference between the decay periods, an internal reference was chosen in each fraction. Thus the yield of Po^{200} and Po^{201} nuclei was determined relative to the yield of Po^{203} nuclei; the yield of Po^{203} nuclei was determined relative to the yield of Po^{205}; the yield of Po^{205} nuclei was determined relative to the yield of Po^{206}. This enabled us in the final analysis to refer the number of Po^{200}, Po^{201} and Po^{203} nuclei undergoing electron capture to the total number of Po^{206} nuclei.

The radiated target was dissolved in 6n HCl; the Po was extracted with an organic mixture of 20% tributyl phosphate plus 80% dibutyl alcohol and re-extracted in concentrated nitric acid for purification from the main mass of radioactive products. The polonium was then separated from the HNO_3 solution diluted to 2n by electrochemical deposition for 2-3 min onto a silver plate. The elapsed time from the end of bombardment to deposition on the silver plate was 30-40 min. After some 9-10 hours the daughter products were washed off the silver plate with 1n HNO_3. The Bi and Pb were separated from this solution in an ion exchange column filled with KU-2 resin in the N form[2].

Then for the Bi fraction we determined the ratio of the number of Po^{203} nuclei (from the build-up and decay of Pb^{203}) to the yield of Po^{205} (from the decay of Bi^{205}). For the Pb fraction we determined the ratios of the numbers of Po^{200} and Po^{201} nuclei (from the number of Pb^{200} and Pb^{201} nuclei) to the yield of Po^{203} (from the decay of Pb^{203}).

The numbers of Pb^{200} and Pb^{201} nuclei were determined by repeated separation of the daughter isotopes Tl^{200} and Tl^{201} by the method of distributive chromatography. In the process we determined the period of Pb^{200} and Pb^{201}: 12.6 hours and 8.4 hours, respectively. In calculating the numbers of Pb^{200} and Pb^{201} nuclei formed from Po^{200} and Po^{201} we took into account α-decay of $Po^{204}(\alpha/(E + \alpha) \approx 1\%)$

and of Po^{205} ($\alpha/(E + \alpha) \approx 0.074\%$).

In the Bi fraction, built up from the polonium over a period of 2-4 days, we determined the ratio of the number of Po^{205} nuclei (from the decay of Bi^{205}) to the yield of Po^{206} (from the decay of Bi^{206}).

As a result there were obtained the following ratios for the investigated polonium isotopes:

A	$\frac{\alpha}{E + \alpha}$
200	0.80 ± 0.23%
201	0.79 ± 0.31%
203	~0.02%

For Po^{203} we could only make a rough evaluation of the fraction of α-decay, inasmuch as accurate measurements were hampered by the low intensity of the α-particles. The error is given as the standard deviation for a number of experiments; it includes the error in determining $\alpha/(E + \alpha)$ for Po^{206}. If this last is disregarded, the ratios for Po^{200} and Po^{201} become 0.80 ± 0.17% and 0.79 ± 0.26%, respectively.

The new more accurate half-life values are the following:

Isotope	T
Po^{199}	11.2 ± 0.3 min
Po^{201}	17.5 ± 1.5 min
Po^{202}	44.5 ± 1.5 min
Po^{204}	3.54 ± 0.25 hr
Po^{206}	9.5 ± 0.8 days
Pb^{200}	12.6 ± 1.4 hr

Our periods for Po^{202} and Pb^{200} differ somewhat from the periods given in the standard tables[3,4]. Our period for Po^{202} is in better agreement with the more recent data of Atterling & Forsling[5]. By way of illustration the α-decay curve for Po^{202} is reproduced in Fig.3.

The results of measurement of the $\alpha/(E + \alpha)$ ratios for Po^{200}, Po^{201} and Po^{203} enabled us to determine the partial α-decay periods for these isotopes. Using these data we calculated the square of the normalized α-particle wave function at a distance of $9.3 \cdot 10^{-13}$ cm from the center of the nucleus and the reduced superficial probability δ_0^2 which is related with the decay constant by the expression

$$\lambda = \delta_0^2 \frac{P}{\hbar}.$$

We determined the quantum mechanical barrier penetrability P assuming a square-well potential with infinitely steep walls. To this end we used the methods of calculation of the irregular Coulomb function and its logarithmic derivative employed in the work of Fröberg[6].

Inasmuch as the actual angular momentum of the α-particles is not known, in the calculations we assumed that L = 0. If at some time in the future L is determined experimentally, there will be no difficulty in making the appropriate correction to δ_0^2, connected with decrease of P owing to the centrifugal barrier (the appropriate penetrability reduction coefficients have been tabulated by Perlman & Rasmussen[7]).

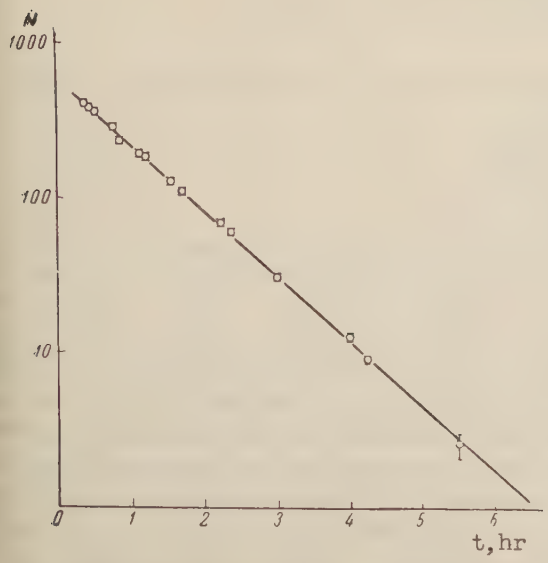

Fig.3. Decay curve for determining the period of Po^{202} (T = 44.5 min).

The values of δ_0^2 for Po^{200}, Po^{201} and Po^{203} and revised values (based on the present more accurate measurements of the periods, α-particle energies and the values of the ratio $\alpha/(E+\alpha)$) for Po^{202}, Po^{204} and Po^{206} are listed in the accompanying table.

Detailed discussion of these results from the standpoint of the theory of α-decay of polonium and astatine[8] isotopes will be published elsewhere.

We desire to express our gratitude to I.A.Yutlandov for his encouragement in the work, B.Dalkhsuren for carrying out a number of measurements, G.M.Gorodinskii for assistance in adjusting the alpha-chamber and the staff of the Joint Institute for Nuclear Research synchrocyclotron for carrying out the irradiations.

"V.G.Khlopin" Radium Institute,
Academy of Sciences of the USSR

Values of δ_0^2 for different Po isotopes

α-emitter	Total α-decay energy, MeV	T_α, sec	Superficial probability	δ_0^2
Po^{200}	5,922	$0,824 \cdot 10^5$	0,00082	0,0154
Po^{201}	5,820	$1,33 \cdot 10^5$	0,0015	0,027
Po^{202}	5,721	$1,335 \cdot 10^5$	0,0040	0,078
Po^{203}	5,62	$1,41 \cdot 10^7$	0,00013	0,0024
Po^{204}	5,511	$1,26 \cdot 10^6$	0,0056	0,107
Po^{206}	5,355	$1,55 \cdot 10^7$	0,0028	0,055

References

1. V.I.Baranovskii & G.M.Gorodinskii, Izv.AN SSSR, Ser.fiz., 24, 313 (1959). (Trans.Bulletin, 24, 301.)

2. B.I.Preobrazhenskii & Yu.P. Saikov, Radiokhimiya, 2, 68 (1960). (Trans.Radiokhimya.)

3. D.Stominger, J.M.Hollander & G.T.Seaborg, Table of Isotopes, Revs.Mod.Phys., 30, 585 (1958).

4. B.S.Dzhelepov & L.K.Peker, Skhemy raspada radioaktivnykh yader (Decay schemes of radioactive nuclei). M.-L., 1958.

5. H.Atterling & W.Forsling, Arkiv.fys., 15, No.1, 89 (1959).

6. C.E.Fröberg, Revs.Mod.Phys., 27, 399 (1955).

7. I.Perlman & J.O.Rasmussen, Alpha Radioactivity, Springer-Verlag (Johnson, N.Y.), 1957.

8. H.J.Mang, Phys.Rev., 119, 1069 (1960).

REDUCED DERIVATIVE WIDTH δ_L^2 FOR POLONIUM ISOTOPES

- B.N.Belyaev, A.V.Kalyamin & A.N.Murin

The probability of α-decay is commonly characterized by the reduced derivative width, introduced by Thomas[1] and defined by

$$\delta_L^2 = \frac{\lambda}{P/h} \sim \sqrt{\frac{A+4}{AQ_{\text{eff}}}} \frac{G_L^2}{RT_{1/2\alpha}} \left(\frac{d\lg G_L}{d\lg r}\right)^2_{r=R},$$

where λ is the α-decay constant, P is the penetrability of the Coulomb barrier, Q_{eff} is the total α-decay energy, R is the nuclear radius ($9.3\cdot10^{-13}$ cm), $T_{1/2\alpha}$ is the partial period for α-decay, and $G_L^2(R)$ and $\left(\frac{d\lg G_L}{d\lg r}\right)^2$ are, respectively, the squares of the irregular Coulomb function and its logarithmic derivative.

The reduced derivative width characterizes the α-transition probability in the absence of a Coulomb barrier and is directly related with the α-particle wave function on the nuclear surface (it equals the "α-width" in the absence of a potential barrier multiplied by 2π). The reduced width can be calculated if one knows from experiment the value of the ratio $\alpha/(\alpha + E)$ and, hence, the partial period with respect to α-decay. Polonium isotopes with $N \leqslant 126$ have a low α-decay probability compared with polonium isotopes with $N > 126$. The sharp decrease in δ_L^2 in going through this shell was formerly explained[2] on the basis of the independent particle model: first, by weak overlapping of the radial proton and neutron functions for nuclei with $N \leqslant 126$, and, second, by decrease of the effective nuclear radius close to closed shells.

According to the recent work of Mang[3], who considers the theory of α-decay of At and Po isotopes (using the independent particle model) the abrupt change in δ_L^2 for nuclei in the vicinity of Pb^{208}, i.e., in going from N = 126 to N = 128, can be explained solely by shell effects without recourse to the hypothesis of change in nuclear radius.

Using the formulas for δ_L^2 proposed by Mang, we calculated the reduced width for Po^{200} and Po^{203} on the assumption of the following shell-model configurations for the ground state of the parent and daughter nuclei with respect to the double magic nucleus Pb^{208} in the ground state:

Shell model configurations for Po isotopes

Nucleus	Proton configuration	Neutron configuration
Po^{200}	$(1h_{9/2}^2)_0$	$(p_{1/2}^{-2})_0 (f_{5/2}^{-6})_0 (p_{1/2}^{-2})_0$
Po^{203}	$(1h_{9/2}^2)_0$	$(p_{1/2}^{-2})_0 (f_{5/2}^{-3})_{5/2} (p_{3/2}^{-2})_0$
Pb^{196}	Closed shell	$(p_{1/2}^{-2})_0 (f_{5/2}^{-6})_0 (p_{3/2}^{-2})_0 (h_{9/2}^{-2})_0$
Pb^{199}	Closed shell	$(p_{1/2}^{-2})_0 (f_{5/2}^{-5})_{5/2} (p_{3/2}^{-2})_0$

Using our experimental data[4] one can compare the experimental A dependence of δ_L^2 with that calculated by means of Mang's formulas (Figs.1 & 2). Our calculations were carried out for a square potential well with infinitely steep sides. Use of the optical model potential in the case of α-decay of Po isotopes changes mainly the absolute values of δ_L^2, but does not affect the general character of the curve. The ratio of the ordinates of the square-well potential and optical

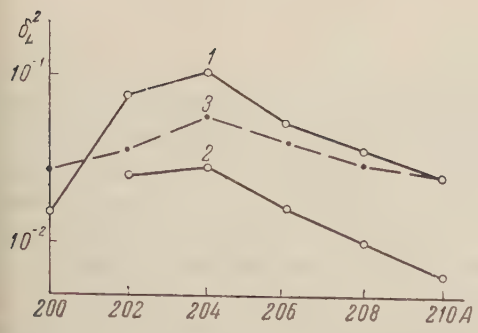

Fig.1. A-dependence of δ_L^2 for even-even Po nuclei: 1 - curve based on the experimental data on the assumption of a potential with infinitely steep walls, 2 - based on experimental data on the assumption of the optical model potential, 3 - calculated according to Mang's theory for a potential with infinitely steep walls.

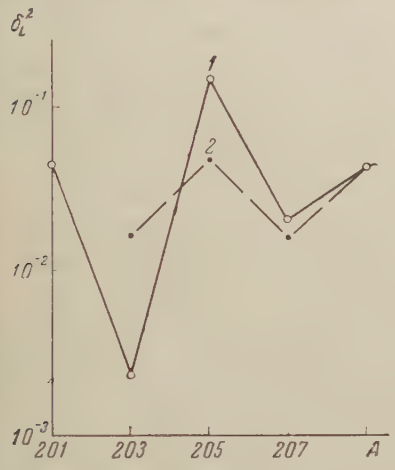

Fig.2. A-dependence of δ_L^2 for even-odd Po nuclei: 1 - curve based on the experimental data on the assumption of a potential with infinitely steep walls, 2 - calculated according to Mang's theory for a potential with infinitely steep walls.

potential curves (curves 1 and 2 in Fig.1) is approximately four over the entire range.

For determining the necessary constants the theoretical expression for the reduced derivative width for one of the isotopes was equated to the reduced width determined directly from experiment. In the case of the even-even polonium nuclei the "normalization" isotope was Po^{210}, while for the even-odd nuclei we used Po^{209} (Figs. 1 & 2). For Po^{202}, Po^{204}, Po^{205}, Po^{206}, Po^{207} and Po^{209} we also determined the values of δ_L^2 from the experimental and theoretical data on the assumption of a potential well with infinitely steep walls, in order to be able to compare these values with those calculated on the basis of our experimental data for Po^{200} and Po^{203}.

The calculated values of δ_L^2 are given in the accompanying table.

Values of δ_L^2 for Po isotopes

A	δ_L^2	Assumed angular momentum L of α-particle
200	0,015	0
201	0,046	2
202	0,078	0
203	0,0024	0
204	0,11	0
205	0,15	0
206	0,055	0
207	0,021	0
208 *	0,039	0
209	0,046	2
210 *	0,027	0

*Based on the data given in Ref.2.

These values of δ_L^2 were obtained using our experimental data[4] for the ratios $\alpha/(\alpha + E)$ and the ratios given in Refs.6 & 7.

As will be evident from Figs.1 and 2, the form of the A-dependence of δ_L^2 given by experiment is in quantitative agreement with the dependence calculated on the basis of Mang's theory.

Owing to the lack of experimental data on the spins of the parent and daughter nuclei in this region, it is difficult to say to what extent the assumed ground state configurations correspond to reality. It is possible that configuration mixing will play an increasingly greater role as one goes away from the filled shell, and that this rough shell model approximation will not truly characterize the quantitative variation of δ_L^2 with A. We also note that the α-transitions may be associated not with the ground state but with excited states.

"V.G.Khlopin" Radium Institute,
Academy of Sciences of the USSR

References

1. R.G.Thomas, Progr.Theoret.Phys., 12, 253 (1954).
2. I.Perlman & J.O.Rasmussen, Alpha Radioactivity, Springer-Verlag (Johnson, N.Y.), 1957.
3. H.J.Mang, Phys.Rev., 119, 1069 (1960).
4. B.N.Belyaev, A.V.Kalyamin & A.N.Murin, Present issue of the Bulletin, p.886.
5. J.O.Rasmussen, Phys.Rev., 113, 1593 (1959).
6. D.Strominger, J.M.Hollander & G.T.Seaborg, Revs.Mod.Phys., 30, 585 (1958).
7. B.S.Dzhelepov & L.K.Peker, Skhemy raspada radioaktivnykh yader (Decay schemes of radioactive nuclei), M.-L., 1958.

CALCULATION OF THE YIELD CROSS SECTIONS FOR SPALLATION REACTIONS

- V.I.Baranovskii & A.N.Murin

Since 1947 there have been numerous investigations of the process of spallation of complex nuclei under the action of high energy (>100 Mev) particles. At present the mechanism of this process is fairly well understood and some of the general regularities involved are known. It is commonly accepted that the first, fast stage of the reaction is a nuclear cascade process in which the bombarding particle p knocks out several nucleons from the target nucleus ${}_zX^A$ and transfers to it part of its energy; the second, slow stage consists of evaporation of the elementary particles from the excited residual nucleus. As a result there forms a large number of product nuclei by the general scheme:

$$ {}_zX^A + p \rightarrow {}_{z'}X^{A'} + \nu_1 p + \nu_2 n + \nu_3 d + \nu_4 T^3 + \nu_5 He^3 + \nu_6 He^4 + \text{heavier fragments.} $$

In a number of cases it is desirable to predict the yield cross sections for the different isotopes formed in the reaction. Thus, in radiochemical investigation of the reaction there cannot be directly determined the formation cross sections for stable and very long-lived and short-lived isotopes; knowledge of these cross sections is essential for determination of a number of parameters as, for example, the total cross section for inelastic interaction of fast particles with nuclei. Moreover, the possibility of predicting the yields of different nuclides is important in connection with searches for new isotopes, in nuclear spectroscopy studies, etc. In particular, in planning experimental investigation of the properties of some specific isotope one can, if the necessary information is available, choose appropriate targets and bombarding particle energies to insure a maximum yield. Information of this type can also be helpful in making mass number assignments for newly discovered isotopes (obviously, in conjunction with other data).

At present, Monte Carlo calculations[1,2] cannot be effectively used in view of technical and other difficulties. Calculations by the Monte Carlo method require a great deal of time even when electronic computers are employed. Moreover, in view of input considerations the statistics are so poor that there result significant errors in the calculated yield cross sections. Even more important is the lack of precise and reliable data on the distribution of energy levels in excited nuclei. Nevertheless, in the course of radiochemical investigations there have been established certain semi-empirical regularities governing the formation cross sections of spallation reaction products. Rudstam[3,4], reviewing and generalizing the data of radiochemical investigations of the interaction of fast particles with elements of medium atomic weight (A = 50 to 70) showed that the isotope yield cross sections can be described by the formula

$$ \sigma(A, Z) = e^{pA - Q - R(Z - SA)^2}, \qquad (1) $$

where A and Z are the mass and atomic numbers of the formed isotope, and p, Q, R and S are parameters, the meaning of which will be made clear below. As will be evident from Eq.(1), the total cross section for the formation of isobars with a given mass number, which will hereinafter denoted by $\sigma(A)$, can be obtained by integrating the right-hand part over Z from -∞ to + ∞:

$$ \sigma(A) = \int_{-\infty}^{\infty} e^{pA - Q - R(Z - SA)^2} dZ = \sqrt{\pi / R}\, e^{pA - Q}. \qquad (2) $$

It will be evident that $\sigma(A)$ falls off exponentially with increase of A; the parameter p is the slope of the straight line characterizing the A dependence of

$\ln \sigma(A)$:

$$p = \frac{d \ln \sigma(A)}{dA} .$$

Q here is a normalizing factor which defines the absolute values of the reaction yield cross sections.

It follows from the above formula that among the isotopes with given A the one with the largest formation cross section is the isotope for which $Z = SA$ and that this cross section equals $\sqrt{R/\pi}\,\sigma(A)$. The decrease in the yield of isobars to both sides of the maximum falls off in accord with the Gaussian distribution law. Thus S determines the most probable Z/A ratio for the reaction products of spallation and R gives the width of the Gaussian distribution.

Rudstam calculated the values of the parameters p, Q, R and S for a number of spallation reactions.[3,4] He showed that log p varies linearly with the logarithm of the bombarding particle energy. Where the parameters R and S are concerned, Rudstam was unable to establish any regularities as regards their variation as a function of such factors as the mass of the target nucleus, the particle energy, etc. This is explained by the narrow range of mass numbers for which Rudstam was able to make calculations. At that time there were no data for heavier nuclei. Nevertheless, such analysis can yield information on how the yield distribution parameters vary depending on the properties of the target nucleus and the energy of the bombarding particles.

At present there has become available some information regarding spallation reactions on heavy nuclei, although the available data are restricted to a relatively small number of nuclei. This is explained by the fact that in splitting of heavy nuclei attention has been concentrated on the fission reaction. In view of the form in which the data are presented it is often difficult to carry out quantitative analyses by the method of Rudstam. In some of the investigations the bombarded elements were not monoisotopic (Hf - Ref.5; Ag - Ref.6); in other studies, there were determined primarily the cumulative yields of radioactive chains, giving only the mass number dependence of $\sigma(A)$ (Bi - Ref.7). Moreover, in some of the studies the uncertainties in the measured reaction yields are appreciable (Hf - Ref.5; Cs - Ref.8; La - Ref.7). Nevertheless, the available data enabled us to undertake an attempt to establish the regularities characterizing the distribution in yields of isotopes forming in the spallation reaction on all the elements in the periodic table. We considered only those cases when monoisotopic elements were subjected to bombardment with fast protons, inasmuch as this is the variant that has been studied most extensively and is most susceptible to theoretical analysis. We note also that all the Monte Carlo calculations have been carried out for the case of bombardment of nuclei with protons.

Moreover, we did not consider data for nuclei in which fission predominates over spallation (thorium, uranium and heavier nuclei).

Calculation Procedure

The method of calculation employed by Rudstam is based on the assumption that the experimentally determined yield of a given isotope may be regarded as the independent yield of this isotope, i.e., that the cross sections for the formation of its parent isotopes are negligibly small. It follows, however, from analysis of the data[9,10] on the isotope yields obtained in proton bombardment of tantalum and bismuth that in going to heavier nuclei this assumption no longer holds. Hence the method of calculation used by Rudstam becomes less applicable and requires appropriate modification.

Equation (1) describes the distribution of individual yields of the reaction products of spallation:

$$\sigma(A, Z)_{\text{ind}} = e^{pA-Q-R(Z-SA)^2};$$

it follows from this formula that $\sigma(A, Z)_{\text{cum}}$, the cumulative or total cross section for the formation of a group of genetically related isotopes the last of which has atomic number Z, can be presented in the form of a sum:

$$\sigma(A, Z)_{\text{cum}} = e^{pA-Q} \sum_{Z'=Z}^{\infty} e^{-R(Z'-SA)^2},$$

of, replacing summation by integration:

$$\sigma(A, Z)_{\text{cum}} = e^{-pA-Q} \int_{Z-1/2}^{\infty} e^{-R(Z'-SA)^2} dZ', \quad \sigma(A) = e^{pA-Q} \int_{-\infty}^{\infty} e^{-R(Z'-SA)^2} dZ.$$

The integration limit must be $Z - 1/2$, rather than Z inasmuch as in this case the distribution is continuous rather than discrete. The individual cross section for the formation of each isotope is characterized by the area under the integration curve; for each isotope there corresponds on the Z axis a section with boundaries at the points $Z + 1/2$ and $Z - 1/2$, which gives the limits of integration. We note that in integrating we so to say "follow" K capture and β^+-decay, going from large to small Z.

Further we can write

$$\frac{\sigma(A, Z)_{\text{cum}}}{\sigma(A)} = \frac{\int_{Z-1/2}^{\infty} e^{-R(Z'-SA)^2} dZ'}{\int_{-\infty}^{\infty} e^{-R(Z-SA)^2} dZ} = \frac{\frac{1}{\sqrt{R}} \int_{(Z-SA-1/2)\sqrt{R}}^{\infty} e^{-t^2} dt}{\frac{1}{\sqrt{R}} \int_{-\infty}^{\infty} e^{-t^2} dt} =$$

$$= \frac{\int_0^{\infty} e^{-t^2} dt - \int_0^{\sqrt{R}(Z-SA-1/2)} e^{-t^2} dt}{2\int_0^{\infty} e^{-t^2} dt} = 0.5 - \frac{1}{\sqrt{\pi}} \int_0^{\sqrt{R}(Z-SA-1/2)} e^{-t^2} dt =$$

$$= 0.5 - \Phi(\sqrt{R}(Z - SA - 1/2)), \tag{3}$$

where $\Phi(a) = \frac{1}{\sqrt{\pi}} \int_0^a e^{-t^2} dt$ is a tabulated function (see, for example, Ref.11).

It follows from the above that

$$\sigma(A, Z)_{\text{cum}} = \sigma(A)\,[0{,}5 - \Phi(\sqrt{R}(Z - SA - 1/2))]; \tag{4}$$

$$\sigma(A, Z)_{\text{ind}} = \sigma(A)\,[\Phi(\sqrt{R}(Z - SA + 1/2)) - \Phi(\sqrt{R}(Z - SA - 1/2))]. \tag{5}$$

If we plot the curve $\sigma(A, Z)_{\text{rel}} = \frac{\sigma(A, Z)_{\text{cum}}}{\sigma(A)} = f(Z - SA)$, then provided the parameter S is correctly chosen all the points should fall on a smooth curve of the form 0.5 - $\Phi(a)$. The shape (slope) of the curve will be determined by the parameter R.

According to Eq.(1), ln $\sigma(A)$ is a linear function of A. Actually, however, as the plot shown in Fig.1 (based on the data for tantalum) shows for mass numbers close to the mass number of the target nucleus $\sigma(A)$ changes little with A and the curve forms a shoulder, a circumstance not taken into account by Eq.(1).

According to Rudstam (see Eqs.(1) and (2)),

$$\sigma(A, Z) = \sigma(A)\sqrt{R/\pi}\, e^{-R(Z-SA)^2}. \qquad (6)$$

As can readily be shown, Eqs.(5) and (6) are equivalent only for $\sqrt{R} \ll 1$, which, as we shall show below, is not true in general. Hence in using Eqs.(4) and (5) it is expedient to introduce a new parameter R' instead of R.

The relation between R and R' can be deduced as follows. We set $Z = SA$; then according to (6)

$$\sigma(A, Z)_{max} = \sigma(A)\sqrt{R/\pi},$$

while according to (5)

$$\sigma(A, Z)_{max} = \sigma(A)\,[\Phi(1/2\sqrt{R'}) - \Phi(-1/2\sqrt{R'})] = \sigma(A)\cdot 2\Phi(1/2\sqrt{R'});$$

whence

$$2\Phi(1/2\sqrt{R'}) = \sqrt{R/\pi}$$

and

$$R = 4\pi\,[\Phi(1/2\sqrt{R'})]^2.$$

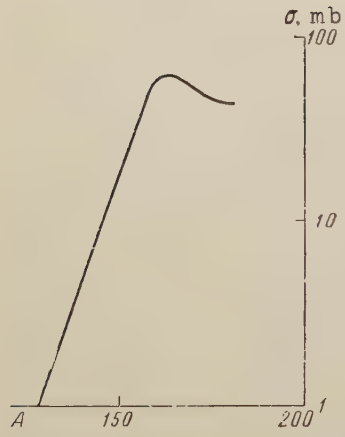

Fig.1. Variation of the total yield of isobars with their mass number. The curve is based on the data obtained in investigating the interaction of 680 Mev protons with tantalum[10].

In accord with the above observations, in the present work, the experimental data were processed as follows:

1. The first step consisted in plotting $\sigma(A)$ as a function of the mass number of the reaction product. As a rule, it proved feasible to find several mass numbers for which it was possible to determine the sum of the isobar yields on the basis of the available experimental data. A smooth curve was then drawn through the points. In doing so we took into account the above mentioned "shoulder" in the $\sigma(A)$ vs A curve and the fact that in the remaining mass number region the variation of $\ln \sigma(A)$ is linear.

2. For each isotope for which the formation cross section is known there was calculated $\sigma(A, Z)_{rel} = \frac{\sigma(A,Z)}{\sigma(A)}$. The values of $\sigma(A)$ were taken from the curve plotted as described in Paragraph 1.

3. We chose a value for the parameter S. To this end there were analyzed the yields of isotopes with the same mass number, which enabled us to determine in the first approximation the atomic number Z of the isotope the yield of which in the given isobaric chain is maximum and, thereby, the value of S.

4. Following Eq.(5), we plotted the $\sigma(A, Z)_{rel} = f(Z - SA)$ curve. If the parameter S was correctly chosen, all the points fell on one smooth curve, as noted above. In this case there corresponded to the $Z - SA = 0$ point the value $\sigma_{rel} = 0.5$ (Fig.2). If the parameter S is not correctly chosen the points do not fall on a single curve but are scattered to a greater or lesser extent and the $\sigma_{rel} = 0.5$ point is shifted to the right or left relative to $Z - SA = 0$. This effect is noticeable even for very small (~0.5%) errors in evaluating S, which provides a means for closer approximation of this parameter.

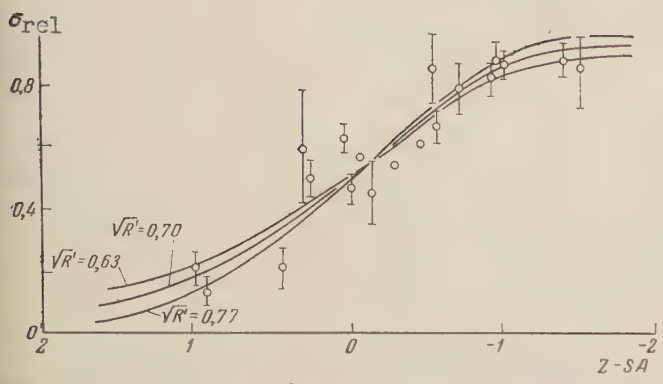

Fig.2. $\sigma_{rel} = f(Z - SA)$ curves plotted on the basis of the experimental data of Ref.10 ($S = 0.426$).

If the $\sigma(A) = f(A)$ curve is not correctly drawn, the plot constructed on the basis of the experimental data proves to be elongated or flattened as compared with the curve calculated according to Eq.(4), which is also readily noticeable and allows of introducing the necessary corrections.

5. On the basis of the new corrected value of S and the new $\sigma(A)$ curve we repeated the construction described in Paragraph 4; the process was repeated until all the points satisfactorily fell on one line (or, at least, until further approximations yielded no improvement).

6. The shape of the resultant curve enabled us to calculate R'. This can be done if one carries out the calculations by means of Eqs.(4) or (5) separately for each experimentally determined formation cross section, treating R' as an unknown.

7. We then used the formula

$$p = \frac{\Delta \ln \sigma(A)}{\Delta A}$$

to calculate the parameter p. The requisite data were taken from the curve plotted as described in Paragraph 1 above.

8. In a number of cases we had recourse to certain simplifying measures, but since they applied only in particular cases they will not be described here.

As will be evident from an examination of Eqs.(4) and (5) the quantity actually employed in the calculations is $\sqrt{R'}$, hence this is the parameter we will refer to hereinafter.

Results

Using the procedure described in the preceding section, we analyzed and processed the experimental data of a number of authors and determined the values of parameters p, S and $\sqrt{R'}$ for several spallation reactions. The results are shown in Table 1. The data of radiochemical investigations of the spallation reaction on Al and Bi are inadequate for complete analysis. Hence for these nuclei we give only approximate values of the parameters p, S and $\sqrt{R'}$.

It was found that for some of the bombarded nuclei the value of the parameter S does not remain the same in the entire investigated mass number interval. In such cases there are two mass number regions inside each of which the parameter remains constant: in one of these, where the shape of the $\sigma(A)$ curve differs from the exponential (the region of the "shoulder"), the value of the parameter S (in the table we designate it as S') is smaller than in the other region comprising all the other mass numbers.

This indicates that in the range of relatively low excitation energies (100 to 200 Mev) there may form relatively fewer neutron-deficient nuclei than at higher energies. It is not impossible that for isobars nearest the initial nucleus the parameter S is a function of A. Lack of adequate data, however, makes it impossible to check this at present.

Table 1

Values of the parameters p, S and $\sqrt{R'}$ for some spallation reactions

Target nucleus	E_p, MeV	Our data							Data of other authors					Source of exp. data
		p	S	S'	$\sqrt{R'}$	R	e^{ξ}	n*	p	S	R	e^{ξ}	Ref.	
$_{13}Al^{27}$	700	—	0,474±0,005		2,5±0,5	2,7±0,7	—	~3	—	—	—	—	—	[13]
$_{23}V^{51}$	187	0,335±0,005	0,468±0,002	0,465±0,002	1,62±0,07	1,75±0,10	1,43	~5	0,377±0,014	0,466	1,80±0,11	1,46	[3]	[14]
	60	0,77±0,03		—	1,65±0,2	1,8±0,3	—	⩽2	—	—	—	—	—	
	100	0,49±0,01		—	1,1±0,3	1,0±0,4	—	⩽2	—	—	—	—	—	[15]
	175	0,325±0,04		—	1,2±0,5	1,13±0,70	—	⩽2	—	—	—	—	—	
	240	0,3±0,05		—	0,85±0,5	0,65±0,60	—	?	—	—	—	—	—	
$_{26}Fe^{56}$	340	0,28±0,01	0,472±0,004		1,4±0,2	1,46±0,3	1,3	~8	0,253±0,018	0,472	1,37±0,11	1,59	[3]	[16]
	430	—	0,472	—	1,45	1,5	—	—	—	—	—	—	—	[17]
	680	—	0,472	—	1,46	1,54	—	—	—	—	—	—	—	[18]
$_{27}Co^{59}$	370	0,24±0,05	0,470±0,002		1,40±0,4	1,46±0,3	1,8	?	0,232±0,024	0,468	1,28±0,17	2,06	[3]	[19]
$_{29}Cu^{63}$	680	0,155±0,010	0,471±0,002		1,41	1,37	1,5	~7	0,15	0,467	1,9	1,65	[20]	[7, 20]
$_{29}Cu^{65}$	680	0,155±0,010	0,464±0,002		1,36	1,34	1,67	~9	0,15	0,467	1,4	1,65	[20]	[7, 20]
$_{39}Y^{89}$	240	0,30±0,02	0,460±0,002	0,445±0,004	1,13±0,15	1,05±0,20	1,6	6—7	—	—	—	—	—	[21]
$_{73}Ta^{181}$	680	0,139±0,020	0,426±0,002	0,424±0,001	0,7±0,07	0,45±0,05	1,25	20	—	—	—	—	—	[10]
	5700	—	—	—	—	—	—	—	—	$S=f(A)\sqrt{R'}=0,75$		—	[22]	—
$_{83}Bi^{209}$	680	0,11	0,418±0,003		0,65±0,20	0,38	—	—	—	—	—	—	—	[7, 9]
	340	—						~20	—					

* n is the width (in mass units) of the "shoulder" in the σ(A) vs A curve.

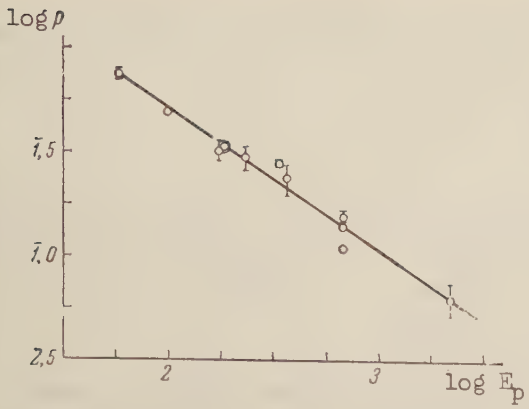

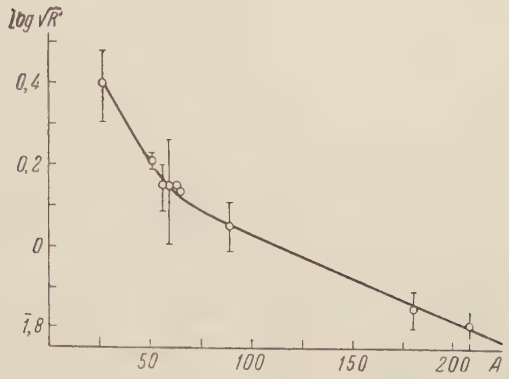

Fig.3. Variation of log p with the logarithm of the bombarding proton energy. The point for 2.2 Bev was taken from Ref.3.

Fig.4. Variation of $\sqrt{R'}$ as a function of A of the target nucleus.

It was established in the work of Grover[22]* that at a bombarding proton energy of 5.7 Bev the parameter S is a function of the mass number for all A from 32 to 153.

This regularity is, apparently, characteristic of a new mechanism, namely, fragmentation, prevailing at such high energies. For the spallation reaction S remains constant (at least in the mass number region where $\sigma(A)$ varies according to the e^{pA-Q} law). This means that S does not depend on the excitation energy of the initial nucleus and, consequently, on the bombarding particle energy. (This will be evident from examination of Table 1.)

For comparison in Table 1 we give the results of analogous calculations performed by other authors. Following Rudstam, we characterize the deviation of the calculated cross section from the experimental value by the quantity e^{ε}, where ε is the root mean square relative deviation. From a comparison of the values of e^{ε} in Table 1 it will be evident that by means of our parameters one can predict the yield cross sections for the products of spallation reactions with an accuracy superior (or at least equal) to that attained by other methods.

Unfortunately, lack of space does not allow of citing detailed data illustrating the good agreement of the results of our calculations with experimental data.

The curves of Figs.3, 4 & 5 show how $p, \sqrt{R'}$ and S vary as a function of the bombarding particle energy, the mass number and the ratio Z_0/A_0 for the target nucleus, respectively. Fig.3 substantiates the fact, established by Rudstam, that log p is a linear function of the logarithm of the proton energy.

It will be evident from Fig.4 that with increase in the mass number of the initial nucleus the parameter $\sqrt{R'}$ first falls off rapidly and then more slowly (exponentially). We were unable to find data that would indicate clearly whether $\sqrt{R'}$ varies with the incident particle energy. Apparently, however, $\sqrt{R'}$ does not depend on the energy; this is supported by the fact that all the points in Fig.4 fit on one smooth curve, although the experiments on which the data are based were carried out at different proton energies.

As for the parameter S, first, we note again that it remains constant in a wide range of excitation energies (except, possibly, in the region of very low energies). Second, Fig.5 makes it possible to substantiate quantitatively our earlier inference regarding the grouping of the products of the spallation reac-

---

*The computation procedure employed by Grover is similar to ours; we received his thesis after completion of all our calculations.

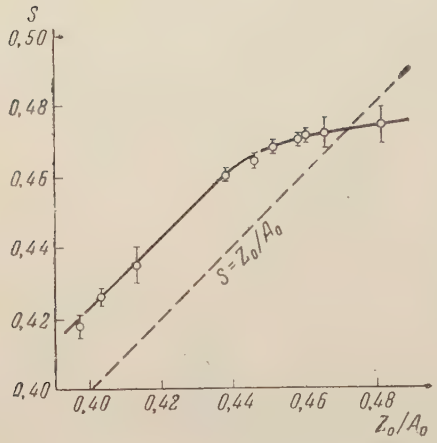

Fig.5. Variation of S with Z_0/A_0.

tion along the line of nuclear stability for light and medium nuclei and of shift of the maximum isobar yields into the neutron-deficient region for heavy nuclei.

All nuclei may be divided into three groups:

1. Light nuclei ($A < 40$) for which the yield maximum does actually occur at the line of nuclear stability, possibly with a minor tendency to shift to the side of neutron-deficient isotopes.

2. Heavy nuclei ($A > 90$) for which $U = S - Z_0/A_0$ (Z_0/A_0 is the charge to mass ratio of the target nucleus) remains constant and equal to 0.023. This shows that the relative shift of the line of maximum yields into the neutron-deficient region relative to the initial nucleus is constant. The absolute value of the shift increases in proportion to the atomic weight of the bombarded element.

3. Intermediate nuclei (A = 40 to 90; $Z_0/A_0 = 0.44$-0.47) for which there is observed a gradual transition from preferential formation of neutron-deficient isotopes ro predominant formation of stable nuclei.

The data presented above can be used for predicting the yield cross sections for isotopes formed as a result of fast proton bombardment of any given element. We suggest the following procedure. First one should plot the total isobar yields as a function of the mass number; in doing so, one must bear in mind the presence of the shoulder in the high A part of the curve (Fig.1). For determining the width of the shoulder one can use some of the results of Monte Carlo calculations (for example, Refs.1, 9 and 21) as well as some of the data presented in Table 1. The value of the parameter p (Fig.3) will determine the slope of the remaining (main) part of the curve (which is a straight line in semilogarithmic coordinates) Absolute values of the yields can be determined if it is assumed that the total reaction cross section is equal to the geometric cross section of the initial nucleus or to the cross section calculated by the Monte Carlo method[1]. We do not recommend using for this purpose the parameter Q, inasmuch as it is introduced on the basis of experimental data and thus brings in errors involved in determining the absolute cross sections. These errors can be very appreciable (up to 50%).

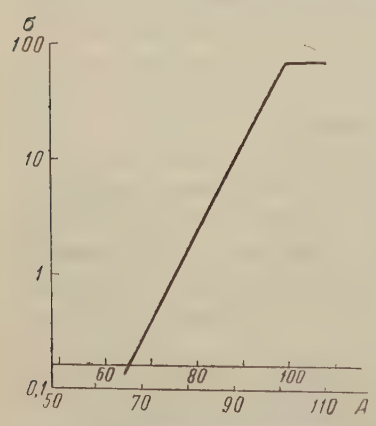

Fig.6. Curve used in calculating the yields of spallation products in bombardment of silver. Ag^{109}.

Knowing the total cross sections for the formation of the isobaric chains and taking the values of $\sqrt{R'}$ and S from the curves of Figs.4 and 5, one can easily by means of Eqs.(4) and (5) calculate the yields of interest.

In order to check the described procedure we calculated the yields of isotopes forming as a result of bombardment of silver with 480 Mev protons. We assume that the width of the horizontal shoulder in the total yield curve equals 9 mass units and that $p = 0.178$ (this curve is shown in Fig.6). The total cross section for

---

The top horizontal scale is for Ag^{107}; the lower for

Table 2

Yields of isotopes from spallation of silver with 480 Mev protons

Isotope	σ_{exp} mb	σ_{calc} mb	$\frac{\sigma_{calc}}{\sigma_{exp}}$	Isotope	σ_{exp} mb	σ_{calc} mb	$\frac{\sigma_{calc}}{\sigma_{exp}}$
Pd^{100}	12,7	40	3,3	Br^{77}	0,73	0,92	1,25
Ru^{97}	15,7	37	2,4	Br^{76}	0,65	0,48	0,75
Ru^{95}	5,7	14,9	2,4	Br^{75}	0,59	0,33	0,56
Mo^{99}	0,054	0,008	0,15	Se^{72}	0,11	0,105	1
Mo^{90}	3	4,2	1,4	As^{74}	0,045	0,192	4
Zr^{89}	7,8	8,8	1,14	As^{72}	0,14	0,23	1,65
Zr^{88}	8,9	7,1	0,8	As^{71}	0,073	0,182	2,5
Zr^{86}	1,78	2,55	1,4	Ge^{71}	0,19	0,16	0,85
Y^{88}	0,46	1,3	2,8	Ge^{69}	0,062	0,14	2,3
Sr^{82}	1,78	1,46	0,82	Ge^{68}	0,054	0,067	0,8
Rb^{84}	0,35	0,45	1,3				

inelastic interaction was taken equal to 1 barn, in accord with the data of Ref.1. The values of $\sqrt{R'}$ and S were taken from Figs.4 and 5: $S = 0.453$ and $\sqrt{R'} = 1.02$ for Ag^{109} and $S = 4.61$ and $\sqrt{R'} = 1.04$ for Ag^{107}. The calculations were carried out separately for Ag^{109} and Ag^{107}, after which the partial yields were added, taking into account the content of stable isotopes in natural silver. The results are presented in Table 2, where for comparison we also give the experimental data of Kurchatov et al[6]. The yield of isotopes with $A < 68$ was not calculated inasmuch as they may form by fast proton fission. The root mean square deviation of the calculated data from the experimental is about 120%. This result, we submit, is satisfactory, particularly if one allows for the fact that the experimental results contain an appreciable error. Thus, for example, the total interaction cross section as determined by Kurchatov et al equals 430 millibarns (about one third the geometric cross section); this value is obviously questionable, and indicates that substantial errors were involved in determining the absolute isotope yield cross sections.

Obviously, the above described procedure can be greatly simplified if one is interested only in determining the relative yields of isotopes with a given mass number or of isotopes of one and the same element (such relative values are important in searches for new isotopes, in certain nuclear spectroscopy studies, etc.).

The results obtained can also facilitate processing of the data of radiochemical investigations of the spallation reaction, particularly in cases when the bombarded target is not monoisotopic. Analagous calculations may also prove useful in comparing the results of radiochemical studies and of experiments with thick emulsion photographic plates.

All such interpolational calculations are based on the assumption that the isotope yields do not depend on the individual properties of the isotopes. Hence they cannot be used for predicting yield cross sections for isotopes with closed nucleon shells.

In conclusion, we want to emphasize the fact that all the arguments and analyses in the present report are based on the assumption that the distribution of yields from the spallation reaction is described by Eq.(1). Introduction of equations such as (4) and (5) serves merely to facilitate calculation; these formulas were deduced on the basis of the available experimental data and, strictly speaking, have no theoretical meaning. It would be desirable to obtain a theoretically justified formula in which the various parameters (possibly there may be more such parameters than were considered in the present discussion) would be present in explicit form as functions of the properties of the target nucleus and bombarding

particles. It may turn out that each parameter is a function not of one but of several variables. Possibly the actual distribution of yields is not symmetrical relative to the maximum yield isotope; if this is the case this fact should also be taken into account in the "ideal" formula.

The complexity of the problem is obvious. Hence for the present one must use an approximate description and have recourse to the simplified procedures described in the present paper.

We desire to express our deep gratitude to B.S.Dzhelepov for his interest in the work.

"V.G.Khlopin" Radium Institute,
Academy of Sciences of the USSR

References

1. N.Metropolis, R.Bivins, S.Storm, A.Turkevich, J.M.Miller & G.Friedlander, Phys.Rev., 110, 185, 204 (1954).
2. I.Dostrovsky, P.Rabinowitz & R.Bivins, Ibid., 111, 1659 (1958).
3. S.G.Rudstam, Phil.Mag., 46, 344 (1955).
4. S.G.Rudstam, Spallation of Medium Weight Elements. Univ. of Uppsala, Sweden, 1956.
5. A.K.Lavrukhina & A.A.Pozdnyakov, Atomnaya energiya, 7, 382 (1959). (Trans. Soviet Journal of Atomic Energy.)
6. B.V.Kurchatov, V.N.Mekhedov, M.N.Borisova, M.Ya.Kuznetsova, L.N.Kurchatova & L.V.Chistyakov, Sessiya AN SSSR, po mirnomu ispol'zovaniyu atomnoi energii (Session of the USSR Ac.of Sci. on the Peaceful Uses of Atomic Energy, OKhI Meeting) p.178, 1955.
7. A.N.Murin, B.K.Preobrazhenskii, I.A.Yutlandov & M.A.Yakimov, Ibid., p.160, 1955.
8. R.W.Fink & E.O.Wiig, Phys.Rev., 94, 1357 (1954); Ibid., 96, 185 (1954).
9. E.T.Hunter & J.M.Miller, Ibid., 115, 1053 (1959).
10. V.I.Baranovskii, A.N.Murin & B.K.Preobrazhenskii, Materialy III Soveshchaniya po neitronodefitsitnym izotopam (Transactions of the 3rd Conference on Neutron-Deficient Isotopes), Dubna, June, 1960.
11. B.Segal & K.Semendyaev, Pyatiznachnye matematicheskie tablitsy (Five-figure mathematical tables), M., 1950.
12. N.T.Porile & N.Sugarman, Phys.Rev., 107, 1422 (1957).
13. G.Friedlander, J.Hudis & R.L.Wolfgang, Ibid., 99, 263 (1955).
14. S.G.Rudstam, Phil.Mag., 44, 1131 (1953).
15. C.G.Heininger & E.O.Wiig, Phys.Rev., 101, 1074 (1956).
16. S.G.Rudstam, P.C.Stevenson & R.L.Folger, Ibid., 87, 358 (1952).
17. O.A.Schaeffer & J.Zähringer, Z.Naturforsch., 13a, 346 (1958).
18. E.K.Gerling & L.K.Levskii, Radiokhimiya, 3, 97 (1961). (Trans.Radiokhimiya.
19. E.Belmont & J.M.Miller, Phys.Rev., 95, 1554 (1954).
20. I.A.Yutlandov, Dissertation, Leningrad State University, 1956.
21. A.A.Caretto,Jr. & E.O.Wiig, Phys.Rev., 103, 236 (1956).
22. J.R.Grover, Reaction of Ta with 5.7 Bev protons, UCRL - 3932 (1957).

EMISSION, ABSORPTION AND REABSORPTION OF GAMMA-RAYS BY IMPURITY NUCLEI IN SOLID SOLUTIONS

- I.P.Dzyub and A.F.Lubchenko

Introduction

Studies of resonant emission and absorption of γ-rays by nuclei in a solid have shown that the emission and absorption spectra each contain a sharp line which is both unshifted (the photon energy is equal to the transition energy) and of practically the natural width. The interpretation of the experimental data (Mössbauer[1] and Visscher[2]) is based on Lamb's theory.[3]

Recently the Mössbauer effect has been used to measure the shift in nuclear energy levels due both to Zeeman and quadrupole splitting, as well as to general relativistic effects.[4] Since these effects have to do with energy shifts of the order of 10^{-7} ev, it is important to take into account all possible details in the interaction between the radiating (or absorbing) nucleus and the crystal lattice, including changes in the lattice frequency and electron-shell energies as a function of the state of the impurity atom.

In the present work we use the adiabatic approximation to calculate the emission and absorption probabilities of photons by radioactive impurity nuclei, including in our calculation the changes in the frequencies of the normal lattice vibration modes. We assume that impurity atoms are incorporated in the solid solute, so that the solution no longer possesses translational symmetry. It should be noted that the theory of the Mössbauer effect, as developed in Refs.1, 2 & 5, is valid only for the case of translational symmetry. Further, we assume that the impurity concentration is small, so that the interaction between the impurity atoms can be neglected. We then calculate the probabilities for emission, absorption and reabsorption of photons for both high and low rates of heat release, we find the position of the Mössbauer line as a function of temperature, and discuss the line width.

1. Energy States of the Solution

The solute + impurity atoms + radiation field system is described by the Hamiltonian

$$H(\rho) + H(r) + V(\rho, r) + H(R) + U(\rho, r, R) + H_f + H' \equiv H_0 + H_f + H'.$$

Here $H(\rho)$ is the Hamiltonian for the internal state of the impurity nuclei, $H(r)$ is the impurity-atom electron Hamiltonian, $V(\rho, r)$ is the interaction energy of the impurity nuclei and electrons, $H(R)$ is the solute Hamiltonian (including the kinetic energy of the impurity atoms), $U(\rho, r, R)$ is the interaction energy of the impurity atoms and the solute, H_f is the radiation Hamiltonian, and H' is the radiation-solute interaction Hamiltonian. The stationary states of the solutions satisfy the equation

$$H_0\Psi(\rho, r, R) = (E - E_f)\Psi(\rho, r, R), \qquad (1)$$

where E_f is the radiation field energy. We shall attempt to solve (1) in the form

$$\Psi(\rho, r, R) = \Phi_m^i(\rho)\,\chi(r, R),$$

where $\Phi_m^i(\rho)$ is the wave function of all the impurity nuclei for an excited state characterized by the quantum number m and localized on the i-th nucleus. Then $\chi(r, R)$ is given by the equation

$$[H(r) + H(R) + W_m^i(r, R)]\,\chi(r, R) = \varepsilon\chi(r, R). \tag{2}$$

Here $W_m^i = \langle\Phi_m^i \mid V + U \mid \Phi_m^i\rangle$, and $\varepsilon = E - E_m - E_f$.

We shall solve Eq. (2) in the adiabatic approximation. To do this we assume that the electrons form a subsystem which changes so rapidly that it is able to reach equilibrium in any nuclear configuration, even if this nuclear configuration is not one of equilibrium. Then separating out the nuclear kinetic energy operator in the Hamiltonian of (2), we rewrite the equation in the form

$$(T_R + H_m^i(r, R))\,\chi(r, R) = \varepsilon\chi(r, R). \tag{3}$$

Here the index m on H indicates that the electron state depends on the state of the nuclei. For fixed R the electrons satisfy the equation

$$H_m^i(r, R)\,\psi_{mn}^i(r, R) = \varepsilon_{mn}^i\psi_{mn}^i(r, R).$$

Knowing ψ_{mn}, we seek the solution of (3) in the form

$$\chi(r, R) = \sum_l F_l(R)\,\psi_l(r, R); \quad l = (m, n).$$

Then F_l satisfies the equation

$$[T_R + U_l^i(R)]\,F_l(R) = \varepsilon F_l(R), \tag{4}$$

where $U_l^i(R) = \varepsilon_l^i(R) + \langle\psi_l^i \mid T_R \mid \psi_l^i\rangle$.

This Hamiltonian can be diagonalized by considering small vibrations of the nuclei about their equilibrium positions and expanding the U_l^i in power series of the displacements from the equilibrium position $u_{\alpha j}$. Then

$$u_{\alpha j} = \sum_{s=1}^{3N} q_{\alpha s}^j \left(\frac{\hbar}{2\omega_s M_j}\right)^{1/2} (b_s + b_s^+), \quad \begin{matrix} j = 1 \ldots N, \\ \alpha = 1, 2, 3, \end{matrix}$$

where N is the number of atoms in the solution, s is the index for the normal vibration of the solution (since we are dealing with a case which does not possess translational symmetry, the vibration cannot be assigned a definite momentum), the $q_{\alpha s}^j$ satisfy a set of homogeneous equations obtained by transforming from Cartesian coordinates to normal coordinates[7] and normalized according to

$$\sum_{\alpha j} q_{\alpha s}^j q_{\alpha s'}^j = \delta_{ss'};$$

and b_s^+ and b_s are creation and annihilation operators for the s-th vibration of the solution.

Neglecting changes in the nuclear equilibrium positions due to changes in the state of the impurity atom, we rewrite (4) in the form

$$\sum_s \hbar\omega_s^l\,(b_s^+ b_s + 1/2)\,F_l = [\varepsilon - U_l^i(R_0)]\,F_l. \tag{5}$$

Here the ω_s^l are the frequencies of the normal vibrations of the system for the l-th state of the nucleus and electrons of the impurity atom (we neglect the dependence of the ω_s^l on i, that is, on the position of the impurity atom in the solution).

Equation (5) has the solution

$$\varepsilon = U_l^i(R_0) + \sum_s \hbar\omega_s^l (n_s + 1/2), \quad F_l = |n_s\rangle; \tag{6}$$

and the wave function $|n_s\rangle$ is determined by the occupation numbers n_s.

Thus the wave functions of the solution + radiation field system and the energy eigenvalues may be written in the form

$$\begin{aligned} \Phi_{l\{n_s\}\{N_\sigma\}} &= C(\ldots N_\sigma \ldots)\, \Phi_m^i(\rho)\, \psi_l(r, R)\, |n_s\rangle, \\ E_{l\{n_s\}\{N_\sigma\}} &= E_m + E_f + U_l^i(R_0) + \sum_s \hbar\omega_s^l (n_s + 1/2), \end{aligned} \tag{7}$$

where $C(\ldots N_\sigma \ldots)$ is the radiation field wave function.

2. Absorption and Emission of γ-Rays by Nuclei

When one knows the wave function of the solution, it is simple to calculate the probability for emission and absorption of γ-rays by impurity nuclei. To be specific let us consider the transition $l_1\{n_s\}\{0\} \to l_0\{n_s'\}\{1_\sigma\}$, in which the j-th nucleus goes over from state m_1 to state m_0 emitting a γ-ray of energy E. Assuming that the matrix elements for the $l_1 \to l_i$ $(i \neq 0)$ transitions are smaller than those for the $l_1 \to l_0$ transition, we arrive at the following expression[6] for the γ-ray emission probability

$$w_l^j = \overline{\sum_{\{n_s'\}}} \frac{\langle l_0\{n_s'\}\{1_\sigma\}|H'|l_1\{n_s\}\{0\}\rangle}{[E - E_0^j + E_{l_0}(n_s') - E_{l_1}(n_s)]^2 + \Gamma^2/4}. \tag{8}$$

Here the bar over the summation sign indicates averaging over initial states of the solution, and

$$\begin{aligned} E_0^j &= E_{m_1} - E_{m_0} + U_{l_1}^j - U_{l_0}^j, \\ E_{l_0}(n_s') &= \sum_s \hbar\omega_s^{l_0}(n_s' + 1/2), \\ E_{l_1}(n_s) &= \sum_s \hbar\omega_s^{l_1}(n_s + 1/2). \end{aligned}$$

Bearing in mind that

$$\langle l_0\{n_s'\}\{1_\sigma\}|H'|l_1\{n_s\}\{0\}\rangle = L\left\langle n_s' \middle| \exp\left\{-i\frac{(\mathbf{p}\mathbf{u}_j)}{\hbar}\right\} \middle| n_s \right\rangle,$$

where L is a nuclear matrix element and p is the momentum of the emitted photon, (8) may be rewritten in the form

$$\begin{aligned} w_l^j = \frac{1}{2\pi}|L|^2 [\mathrm{Sp}\, e^{-H_0^{l_1}/\theta}]^{-1} \int_{-\infty}^{\infty} d\rho \int_{-\infty}^{\infty} d\mu \frac{e^{-i\mu\rho}}{[E - E_0^j - \rho]^2 + \Gamma^2/4} \times \\ \times \mathrm{Sp}\left[e^{-H_0^{l_1}/\theta} e^{i\mu H_0^{l_1}} \exp\left\{i\frac{(\mathbf{p}\mathbf{u}_j)}{\hbar}\right\} e^{-i\mu H_0^{l_0}} \exp\left\{-i\frac{(\mathbf{p}\mathbf{u}_j)}{\hbar}\right\} \right], \end{aligned} \tag{9}$$

where

$$H_0^{l_1} = \sum_s \hbar\omega_s^{l_1}(b_s^+ b_s + 1/2), \qquad H_0^{l_0} = \sum_s \hbar\omega_s^{l_0}(b_s^+ b_s + 1/2).$$

The expression

$$\mathrm{Sp}\left[e^{-H_0^{l_1/\theta}} e^{i\mu H_0^{l_0}} \exp\left\{i\frac{(\mathbf{p}\mathbf{u}_j)}{\hbar}\right\} e^{-i\mu H_0^{l_0}} \exp\left\{-i\frac{(\mathbf{p}\mathbf{u}_j)}{\hbar}\right\}\right] \Big/ \mathrm{Sp}\left[e^{-H_0^{l_1/\theta}}\right]$$

can be calculated exactly; one then finds that the emission probability is given by the formula

$$w_l^j = |L|^2 W_l^j = |L|^2 \frac{2}{\Gamma} R_e \int_0^\infty d\mu e^{-i\mu(E-E_0^j)-\mu\Gamma/2} F(\mu), \tag{10}$$

where

$$F(\mu) = \prod_s \frac{1-e^{-\hbar\omega_s^{l_1/\theta}}}{1-e^{-\hbar\omega_s^{l_1/\theta}+i\mu\hbar\left(\omega_s^{l_1}-\omega_s^{l_0}\right)}} \exp\left\{|\varkappa_{sl_1}^j|^2\left(1-e^{i\mu\hbar\omega_s^{l_1}}\right) - |\varkappa_{sl_1}^j|^2 \left|e^{i\mu\hbar\omega_s^{l_1}}-1\right|^2 \frac{1}{1-e^{-\hbar\omega_s^{l_1/\theta}+i\mu\hbar\left(\omega_s^{l_1}-\omega_s^{l_0}\right)}}\right\},$$

$$\varkappa_{sl_1}^j = i\left(\frac{1}{2M_j\hbar\omega_s^{l_1}}\right)^{1/2} \sum_{\alpha=1}^{3} p_\alpha q_{\alpha s}^j,$$

$$R_e = \sum_s |\varkappa_{sl_1}^j|^2 \hbar\omega_s^{l_1}.$$

Let us write the integral in (10) in the form of a sum of two integrals whose limits are $[0, \mu_0]$ and $[\mu_0, \infty]$, where μ_0 is obtained from the condition $\mu_0\omega_{s\,\max} < 1$.[8,9] Then it is easily shown that under the condition*

$$\sum_s |\varkappa_{sl_1}^j|^2 \operatorname{cth}\frac{\hbar\omega_s^{l_1}}{2\theta}\left(\frac{\omega_s^{l_1}}{\omega_{s\,\max}}\right)^2 > 1, \tag{11}$$

$$\frac{2}{\Gamma} R_e \int_0^{\mu_0} d\mu e^{-i\mu(E-E_0^j)-\mu\Gamma/2} F(\mu) = \frac{4}{\Gamma^2}\left[1 + \frac{C_e\alpha_e^3}{8B_e^6} + \frac{D_e\alpha_e^4}{16B_e^8} + \cdots\right]\psi(x, \eta). \tag{12}$$

Here

$$B_e^2 = \frac{1}{2!}\sum_s |\varkappa_{sl_1}^j|^2 \operatorname{cth}\frac{\hbar\omega_s^{l_1}}{2\theta}\cdot(\hbar\omega_s^{l_1})^2,$$

$$C_e = \frac{1}{3!}\sum_s |\varkappa_{sl_1}^j|^2 (\hbar\omega_s^{l_1})^3,$$

$$D_e = \frac{1}{4!}\sum_i |\varkappa_{sl_1}^j|^2 \operatorname{cth}\frac{\hbar\omega_s^{l_1}}{2\theta}\cdot(\hbar\omega_s^{l_1})^4,$$

$$\alpha_e = E_0^j + \sum_s \hbar(\omega_s^{l_1} - \omega_s^{l_0})\,\bar{n}_s - E - R_e,$$

$$\bar{n}_s = \left[\exp\left\{\frac{\hbar\omega_s^{l_1}}{\theta}\right\} - 1\right]^{-1},$$

$$x = \frac{2\alpha_e}{\Gamma};\quad \eta = \frac{4B_e}{\Gamma},$$

and $\psi(x, \eta) = \int_0^\infty dy \cos xy e^{-y-y^2\eta^2/4}$ is the function giving the shape of the emission spectrum from a free nucleus, including the Doppler effect.[10]

---

*We shall call (11) the condition of high heat release.

In the same way it can be shown that under the condition

$$\sum_s |\varkappa^j_{sl_1}|^2 \operatorname{cth}\frac{\hbar\omega_s^{l_1}}{2\theta}\cdot\frac{\Gamma}{\hbar\omega_{s\max}}\ll 1,\quad \hbar\omega_s^{l_1}\gg\Gamma; \tag{13}$$

$$\frac{2}{\Gamma}R_e\int_{\mu_*}^{\infty}d\mu e^{-i\mu(E-E_0^j)-\mu\Gamma/2}F(\mu)=\frac{\exp\left\{-\sum_s|\varkappa^j_{sl_1}|^2\operatorname{cth}\frac{\hbar\omega_s^{l_1}}{2\theta}\right\}}{\left(E-E_0^j-\sum_s\hbar(\omega_s^{l_1}-\omega_s^{l_0})\bar n_s\right)^2+\Gamma^2/4}. \tag{14}$$

For low heat release, when condition (11) is not fulfilled, the emission spectrum is of different shape. The emission curve can be written in the form

$$W_l^j(E)=\exp\left\{-\sum_s|\varkappa^j_{sl_1}|^2\operatorname{cth}\frac{\hbar\omega_s^{l_1}}{2\theta}\right\}\times\sum_{\ldots\tau_s\ldots\tau'\ldots}\prod_s\frac{a_s^{\tau_s}d_s^{\tau'_s}}{\tau_s!\,\tau'_s!}\frac{1}{\left[E-\widetilde E_0^j-\sum_s\hbar\omega_s^{l_0}(\tau'_s-\tau_s)\right]^2+\Gamma^2/4}, \tag{15}$$

where

$$\widetilde E_0^j=E_0^j+\sum_s\hbar(\omega_s^{l_1}-\omega_s^{l_0})\bar n_s;\quad a_s=\bar n_s|\varkappa^j_{sl_1}|^2,\quad d_s=(\bar n_s+1)|\varkappa^j_{sl_1}|^2.$$

The Mössbauer line is obtained from (15) by writing $\tau_s=\tau'_s$. It can be shown that the intensity of the Mössbauer line in this case, as in the case of high heat release, depends only on the factor

$$\exp\left\{-\sum_s|\varkappa^j_{sl_1}|^2\operatorname{cth}\frac{\hbar\omega_s^{l_1}}{2\theta}\right\}.$$

In exactly the same way one can calculate the shape of the γ-ray absorption curve. This will be given in the cases of high and low rates of heat release, respectively, by equations (12), (14), and (15) in which one makes the replacements $l_1\rightleftarrows l_0$ and $a_e\to a_a=E-\widetilde E_0^j-R_a$.

The measured absorption (or emission) spectrum of impurity nuclei can be written

$$W_{e(a)}(E)=\sum_{j=1}^{N_q}W^j_{e(a)}(E), \tag{16}$$

where N_q is the number of impurity atoms in the solution.

The expressions obtained above can be used to arrive at the following conclusions concerning the γ-ray emission and absorption spectra of nuclei in solid solutions.

1. At high temperatures, when condition (11) is fulfilled, the absorption and emission curves are Gaussian curves; on their wings appears a line of almost Lorentzian shape (the Mössbauer line). In the energy scale the Mössbauer line lies above the peak of the phonon part of the emission spectrum and below the peak of the phonon part of the absorption spectrum. The phonon parts (Gaussian curves) have half-widths given by $\Delta=2B_i\sqrt{\ln 2}$ $(i=e,a)$. With decrease in temperature, the phonon part of the spectrum becomes asymmetric; the emission curve drops more rapidly on the high energy side than on the low energy side (and vice versa for the absorption curve).

2. The intensity of the Mössbauer line increases sharply with decreasing temperature. For temperatures at which $\hbar\omega_{s\max}<\theta$, the increase is exponential. The position of the Mössbauer line also depends on temperature; the temperature shift is given by

$$\alpha=\sum_s(\omega_s^{l_1}-\omega_s^{l_0})\bar n_s.$$

At high temperatures the shift is proportional to the temperature. The magnitude of α can be evaluated only qualitatively. If ω' is the frequency of the electron transition in the impurity, and $\Delta\omega_s$ is the corresponding change in the frequency of the solution as a function of the state of the impurity atom, one has $\alpha \approx \frac{\omega''}{\omega'} \sum_s \bar{n}_s \Delta\omega_s$, where ω'' is the separation between the electron levels for two different states of the nucleus. To order of magnitude, ω'' is about equal to the hyperfine splitting of the electron levels (from 0.1 to 1 cm^{-1}); for impurities in molecular crystals, $\sum_s \bar{n}_s \Delta\omega_s$ varies between 0.1 and 10 cm^{-1} deg^{-1} T (Ref.11), so that $\alpha \approx$ (10^{-4} to 10^{-7} sec^{-1} deg^{-1}) T, which is of the same order of magnitude as the correction for the Doppler effect.[12]

3. It follows from (13) and (14) that the occurrence of a Mössbauer line in the spectrum shows that it is the high-frequency vibrations which play the principal role in the interaction between the nuclear transition and the normal vibrations of the solution. The role of these high frequencies in the Mössbauer effect has been mentioned by Lipkin[5]; in our work it becomes a criterion.

4. If condition (11) is not fulfilled (low rate of heat release), the absorption and emission curves are sums of Lorentzian curves with half-widths $\Gamma/2$, as follows from (15). Then due to superposition and possibly also to broadening, the phonon part of the emission (and absorption) spectrum will be a wide band with a series of intense peaks. The Mössbauer line is located at the edge of this band and is of very high intensity.

5. If the impurity atoms occupy different positions in the solution, so that U_l^j depends on j, that is, on the position of the atom in the solution, the shape of the Mössbauer line, as follows from (16), will be given by

$$\sum_j \frac{1}{(E - E_0^j)^2 + \Gamma^2/4} ;$$

this means that the half-width of the Mössbauer line will be not $\Gamma/2$, but somewhat greater if $E_0^j - E_0^{j'} \leqslant \Gamma/2$. For instance, if there are two equally probable positions for the atom in the lattice, and if $E_0^{j_1} - E_0^{j_2} = \Gamma/2$, the effective width of the Mössbauer line will be 1.4 Γ.

A calculation similar to that for the emission probability can be used to obtain the radiation width Γ_r of the excited level ($\Gamma = \Gamma_r (1 + \alpha)$, where α is the internal conversion coefficient). It is found that Γ_r is virtually temperature independent.

3. Reabsorption of γ-Rays

In the usual Mössbauer experiments, one measures the γ-ray absorption in an absorber containing atoms of the same kind as the emitter. The apparatus is designed to provide for movement of the emitter and/or absorber with some relative velocity v. It is then of interest to establish the dependence of the reabsorption on the thickness of the absorber and on v.[13] The quantity measured in the experiment is the ratio

$$\delta(v, x_a) = \frac{P(v_\infty) - P(v)}{P(v_\infty)}, \qquad (17)$$

where $P(v)$ is the number of pulses registered by a counter behind the absorber, and v_∞ is the relative velocity at which the emission and absorption curves have

essentially no overlap. Now

$$P(v) = C\int_0^\infty dEW_e(\eta E)\quad e^{-\sigma_a(E)n_a x_a},$$

where C is a constant, n_a is the number of atoms per cubic centimeter of the absorber (we are assuming that the absorber consists only of atoms absorbing the γ-rays at resonance), x_a is the absorber thickness, $\eta = 1 \pm v/c$ $(v \ll c)$, $\sigma_a(E) = \Gamma^2/4\sigma_0 W_a(E)$ is the absorption cross section, and σ_0 is the resonance absorption cross section; then it follows that

$$\delta(v, x_a) = 1 - \frac{\Gamma'}{2\pi}\int_0^\infty dEW_e(\eta E)\ e^{-\sigma_a(E)n_a x_a}, \tag{18}$$

where Γ' is the effective width of the Mössbauer emission line. We note that $\Gamma' > \Gamma$ both as a result of the finite thickness of the emitter[4] and because of the possible broadening of the Mössbauer line discussed in the previous section.

When $\sigma_0 f_a n_a x_a \ll 1$ and $v/cE_0 \sim \Gamma$, Eq. (18) becomes

$$\frac{1}{n_a x_a}\delta(v,\ x_a) = \sigma_0 f_e f_a \beta \frac{\xi^2(1+1/\beta) + (\beta^2-1)(1-1/\beta)}{(\beta^2-1+\xi^2)^2 + 4\xi^2} + C_1, \tag{19}$$

where

$$\xi = \frac{v}{c}\cdot\frac{2E_0}{\Gamma};\quad \beta = \Gamma'/\Gamma;$$

f_e and f_a are the intensities of the Mössbauer lines of the emitter and absorber, respectively, and C_1 is the contribution of the phonon part of the spectrum which, for the values of v of interest, is practically independent of v.

For large absorber thicknesses $(\sigma_0 f_a n_a x_a > 1)$ the height of the reabsorption peak depends on the thickness of the absorber according to

$$\delta(0, x_a) = f_e\left[1 - \frac{2\beta}{\beta^2+1}e^{-\zeta}X(\zeta)\right], \tag{20}$$

where

$$\zeta = \frac{1}{2}\sigma_0 f_a n_a x_a;\quad X(\zeta) = \frac{\beta^2+1}{\pi}\int_0^\pi d\vartheta \frac{\exp\{-\zeta\cos\vartheta\}}{1+\beta^2+(\beta^2-1)\cos\vartheta}.$$

To tabulate $X(\zeta)$ one may make use of the equation

$$\frac{\beta^2-1}{\beta^2+1}X'(\zeta) = X(\zeta) - I_0(\zeta),$$

where $I_0(\zeta)$ is the zeroth order Bessel function of an imaginary argument. In particular, when $\beta = 1$, Eq. (20) becomes the same as the formula given by Craig et al[14].

Physics Institute,
Academy of Sciences of the Ukrainian SSR

References

1. R.L.Mössbauer, Z.Phys., 151, 124 (1958); Z.Naturforsch, 14a, 211 (1959).
2. W.M.Visscher, Ann.Phys., 9, 195 (1960).
3. W.E.Lamb, Phys.Rev., 55, 190 (1939).
4. E.Cotton, J.phys.et radium, 21, 23 (1960).
5. H.L.Lipkin, Ann.Phys., 9, 333 (1960).
6. V.Weisskopf & E.Wigner, Z.Physik, 63, 54; Ibid., 65, 18 (1930).

7. Ya.I.Frenkel', Kurs teoreticheskoi mekhaniki (Course of theoretical mechanics), M., 1940.
8. A.S.Davydov, Zhur.eksp.i teor.fiz., 24, 198 (1953).
9. A.F.Lubchenko, Ukr.fiz.zhur. (Ukrainian Phys.Jour.), 1, 265, 281 (1956).
10. M.Born, Optik, Berlin, 1933 (Reprint Edwards Bros., Ann Arbor, 1944.)
11. M.T.Shpak, Ukr.fiz.zhur., 2, 347 (1957); L.G.Pikulik & A.N.Sevchenko, Izv. AN SSSR, Ser.fiz., 24, 729 (1960). (Trans.Bulletin, 24, 732.)
12. R.V.Pound & G.A.Rebka, Phys.Rev.Letters, 4, 274 (1960).
13. R.L.Mössbauer, R.Pound & F.L.Shapiro, Usp.fiz.nauk, 72, 657 (1960).
14. P.P.Craig, J.G.Dash, A.D.McGuire, D.Nagle & R.R.Reiswig, Phys.Rev. Letters, 3, 221 (1959).

RESONANCE SCATTERING OF GAMMA-RAYS BY NUCLEI IN A SOLID

- I.P.Dzyub & A.F.Lubchenko

Introduction

A number of experiments have recently been performed on recoilless Rayleigh and resonance scattering of γ-rays by nuclei in solids.[1,2] These experiments show that at low temperatures (for instance, at 90°K for tin) both resonance and Rayleigh scattering may take place but that resonance scattering predominates.[2] Thus, for investigation of solids one can make use not only of resonance emission and absorption (the Mössbauer effect[3]), but also of resonance and Rayleigh scattering. It is interesting to note[4] that the difference between the diffraction patterns for Rayleigh and resonance scattering can be used to verify Weisskopf's theory of coherence of incident and resonance-scattered photons.

The present paper discusses the characteristics of resonance scattering. We determine the angular distribution of the scattered γ-rays, the excitation spectrum, and the spectrum of the scattered γ-rays. We point out the possibility of determining the normal frequencies of the scatterer both from the scattered γ-ray spectrum and from the intensity of the Mössbauer line, which we shall show exists at other than the Bragg angle. In determining the probability for resonance scattering we consider the general case in which a unit cell of the scatterer contains several resonance-scattering nuclei. We sum over intermediate and final states of the lattice and average over initial states without making any approximations.

1. Probability of Resonance Scattering by Nuclei

Consider a crystal scatterer containing m atoms per unit cell. We characterize the state of the scatterer and radiation field by the set of quantum numbers

$$l\{n_s\}\{N_\sigma\},$$

where l represents the nuclear quantum numbers, and n_s and N_σ are the occupation numbers of the phonon and photon fields, respectively (the index s denotes both the wave vector f of the lattice vibrations and the index i of the vibration mode).

Further, we assume that the l_1 excited state of the nucleus is far from the other excited states, so that the contribution of virtual transitions to the other levels can be neglected compared to the contribution of the transitions to the l_1 level. Then the resonance scattering process may be treated as the sequence of transitions

$$l_0\{n_s^0\}\{N_{\sigma'}\} \to l_1\{n_s\}\{N_{\sigma'}-1\} \to l_0\{n_s'\}\{N_{\sigma'}-1,\ N_{\sigma''}+1\}, \tag{1}$$

where l_0 represents the quantum numbers of the nuclear ground state. For conciseness we shall denote the states in (1) by 0, 1 and 0', respectively, and the corresponding probability amplitudes by b_0, b_1 and $b_{0'}$. It is then a simple matter to write the equations for their time dependence.[5] These equations are

$$i\hbar\dot{b}_0 = \sum_{\{n_s\}\sigma'} b_1 \langle 0|H'|1\rangle e^{\frac{it}{\hbar}(E_0-E_1)}; \tag{2a}$$

$$i\hbar\dot{b}_1 = b_0\langle 1|H'|0\rangle e^{\frac{it}{\hbar}(E_1-E_0)} + \sum_{\{n_s'\}\sigma''} b_{0'}\langle 1|H'|0'\rangle e^{\frac{it}{\hbar}(E_1-E_{0'})}; \tag{2b}$$

$$i\hbar\dot{b}_{0'} = \sum_{\{n_s\}} b_1 \langle 0' \mid H' \mid 1\rangle e^{\frac{it}{\hbar}(E_{0'}-E_1)}; \tag{2c}$$

where H' is the photon-nucleus interaction Hamiltonian, E_0, E_1 and $E_{0'}$ are the initial, intermediate, and final state energies, $\langle 0 \mid H' \mid 1\rangle = N_\sigma^{1/2} L_{l_0 l_1} \langle n_s^0 \mid \exp\{-i\vec{\varkappa}_{\sigma'}\mathbf{R}_n\} \mid n_s\rangle$ is the matrix element of H' between the initial and intermediate states, $\vec{\varkappa}_{\sigma'}$ is the photon wave vector, and $\mathbf{R}_n$ is the coordinate of the n-th nucleus doing the scattering.

We wish to obtain a solution to (2) in the form

$$\begin{aligned} b_0(t) &= \exp\{-\Gamma t/2\hbar\}, \\ b_1(t) &= C(n_s)\left[\exp\left\{-\Gamma t/2\hbar + \frac{it}{\hbar}(E_1 - E_0)\right\} - \exp\{-\gamma t/2\hbar\}\right], \end{aligned} \tag{3}$$

with the initial conditions $b_0(0) = 1$ and all other probability amplitudes zero. Inserting (3) into (2c), we obtain

$$b_{0'}(t) = \sum_{\{n_s\}} \langle 0' \mid H' \mid 1\rangle C(n_s)\left\{\frac{1 - e^{\frac{it}{\hbar}(i\Gamma/2 + E_{0'} - E_0)}}{E_{0'} - E_0 + i\Gamma/2} - \frac{1 - e^{\frac{it}{\hbar}(i\gamma/2 + E_{0'} - E_1)}}{E_{0'} - E_1 + i\gamma/2}\right\}. \tag{4}$$

Proceeding, we insert (3) and (4) into (2b) and make use of the fact that

$$\lim_{t\to\infty} \frac{e^{[\gamma/2 + i(E_1 - E_{0'})]\frac{t}{\hbar}} - 1}{E_{0'} - E_1 + i\gamma/2} = -i\pi\delta(E_{0'} - E_1);$$

we then obtain*

$$\gamma = \frac{2\pi}{\hbar}(N_{\sigma''} + 1)\,\overline{|L_{l_1 l_0}|^2}\,\rho(E), \tag{5}$$

$$C(n_s) = \frac{\langle 1 \mid H' \mid 0\rangle}{E_{0'} - E_1 + i\frac{\gamma - \Gamma}{2}}, \tag{6}$$

where E is the transition energy for the free nucleus, $\rho(E) = \frac{E^2}{(2\pi c)^3\hbar^2}$, and the bar on $|L_{l_1 l_0}|^2$ denotes the integral of the matrix element $|L_{l_1 l_0}|^2$ over the solid angle and the sum over the possible polarizations of the scattered photons.

Finally, inserting (6) and (3) into (2a), we find the level width of the ground state to be given by

$$\Gamma = \frac{2\pi}{c\hbar^2\omega_{\sigma'}}\,\overline{|L_{l_1 l_0}|^2}\,I(\omega_{\sigma'}),$$

where the bar now denotes the same as above, but for the incident photons, and $I(\omega_{\sigma'})$ is the incident beam intensity.

To obtain the probability amplitude for scattering from the entire scatterer, (4) must be summed over all the nuclei. One then obtains

$$\tilde{b}_{0'} = \sum_{nj}\sum_{\{n_s\}} \frac{\langle 0' \mid H' \mid 1\rangle \langle 1 \mid H' \mid 0\rangle}{(E_{0'} - E_0 + i\Gamma/2)(E_{0'} + E_1 + i\gamma/2)},$$

---

*Equation (5) gives the radiation width of the level. If one wants to include the possibility of internal conversion, one must replace γ by $\gamma(1+\alpha)$ (where α is the internal conversion coefficient).

where n is the number of the unit cell, and j is the number of the atom in the cell. Denoting the Gibbs distribution function for the phonons by $w(n_s^0)$, one can write the expression for the total probability W of scattering in the form

$$W = \sum_{\{n_s^0\}\{n_s'\}} w(n_s^0) |\widetilde{b}_0|^2. \tag{7}$$

This equation can be written in integral form without making any assumptions as to the magnitude of $\vec{\varkappa}_{\sigma'}\mathbf{u}_{nj}$.[6,7] (Here $\mathbf{u}_{nj}$ is the displacement of the j-th atom of the n-th cell from its equilibrium position $\mathbf{R}_{nj}^0$.) To do this, we make use of the relations

$$E_{0'} - E_0 = \varepsilon_0 + \sum_s \hbar\omega_s n_s' - \sum_s \hbar\omega_s n_s^0,$$

$$E_{0'} - E_1 = \varepsilon_1 + \sum_s \hbar\omega_s n_s' - \sum_s \hbar\omega_s n_s, \quad w(n_s^0) = \frac{1}{Z}\langle n_s^0 | e^{-\beta H} | n_s^0\rangle,$$

where $\varepsilon_0 = \hbar(\omega_{\sigma''} - \omega_{\sigma'})$, $\varepsilon_1 = -E + \hbar\omega_{\sigma''}$, $H = \sum_s H_s = \sum_s \hbar\omega_s(b_s^+ b_s + {}^1/_2) -$

is the vibrational Hamiltonian of the nuclei of the scatterer, $\beta = \frac{1}{kT}$ and Z is the statistical sum. Then the expression for the scattering probability can be written

$$W = \frac{M}{2\pi Z}\sum_{nn'} e^{i\vec{\varkappa}\Delta\mathbf{R}^0}\int_{-\infty}^{\infty} d\mu \int_{-\infty}^{\infty} dx \frac{e^{i\mu x}}{(\varepsilon_0 + x)^2 + \Gamma^2/4} \times \int_0^{\infty} dt \int_0^{\infty} dt'\, e^{i(t'-t)\varepsilon_1 - \frac{\gamma}{2}(t'+t)} \quad A(t', t, \mu).$$

Here

$$A(t', t, \mu) = \prod_s Sp\{e^{-\beta H_s + i\mu H_s} e^{-i\vec{\varkappa}_{\sigma'}\mathbf{u}_{n'}^s} e^{itH_s} e^{i\vec{\varkappa}_{\sigma''}\mathbf{u}_{n'}^s} e^{-i\mu H_s} e^{i(t'-t)H_s} \times e^{-i\vec{\varkappa}_{\sigma''}\mathbf{u}_n^s} e^{-it'H_s} e^{i\vec{\varkappa}_{\sigma'}\mathbf{u}_n^s}\},$$

$$M = (N_{\sigma''} + 1) N_{\sigma'} |L_{l_1 l_0}|^2 |L'_{l_1 l_0}|^2, \quad \vec{\varkappa} = \vec{\varkappa}_{\sigma''} - \vec{\varkappa}_{\sigma'}, \quad \Delta\mathbf{R}^0 = \mathbf{R}_{n'}^0 - \mathbf{R}_n^0,$$

where for brevity we have used n to denote both the number of the cell and the j number of the atom in the cell. We now use the fact that

$$\vec{\varkappa}_\sigma \mathbf{u}_n^s = P_{\sigma j}^s b_s e^{i\mathbf{f}\mathbf{R}_n^0} + P_{\sigma j}^{*s} b_s^+ e^{i\mathbf{f}\mathbf{R}_n^0},$$

where $P_{\sigma j}^s = \frac{(\mathbf{p}_\sigma \mathbf{v}_j(s))}{(2M_j N\hbar\omega_j)^{1/2}}$, M_j is the mass of the scattering nucleus, $\mathbf{p}_\sigma$ is the momentum of the photon of frequency ω_σ, and $\mathbf{v}_j(s)$ is the displacement of the j-th atom in the $n = 0$ cell.[8] Then grouping terms containing H_s in the trace, making use of the relation $Z^{-1}Sp\{e^{-\beta H} e^{\eta_s b_s} e^{\eta_s^* b_s^+}\} = \exp\{|\eta_s|^2(n_s+1)\}$ and applying Weyl's identity,[9] we arrive at

$$W = \frac{M}{2\pi}\sum_{nn'jj'} e^{i\vec{\varkappa}\Delta\mathbf{R}^0 - G_j - G_{j'}} \int_{-\infty}^{\infty} d\mu \int_{-\infty}^{\infty} dx \frac{e^{i\mu x}}{(\varepsilon_0 + x)^2 + \Gamma^2/4} \times$$

$$\times \int_0^{\infty} dt \int_0^{\infty} dt' \exp\left\{i\varepsilon_1 t' - \frac{\gamma}{2}t' + K_j(t') + \sum_s \bar{n}_s d_s\right\} \exp\left\{-i\varepsilon_1 t - \frac{\gamma}{2}t + \right.$$

$$\left. + K_{j'}(t) + \sum_s (\bar{n}_s + 1)\, d_s\right\}. \tag{8}$$

Here

$$G_j = \sum_s (\bar{n}_s + 1/2)\,(|P^s_{\sigma' j}|^2 + |P^s_{\sigma'' j}|^2),$$

$$K_j(t') = \sum_s P^s_{\sigma' j} P^s_{\sigma'' j}\,\{(\bar{n}_s + 1)\,e^{-i\hbar\omega_s t'} + \bar{n}_s e^{i\hbar\omega_s t'}\},$$

$$d_s = e^{i\mathbf{f}\Delta\mathbf{R}^0 + i\hbar\omega_s \mu}\,(P^s_{\sigma' j} - P^s_{\sigma'' j} e^{-i\hbar\omega_s t'})\,(P^s_{\sigma' j'} - P^s_{\sigma'' j'} e^{i\hbar\omega_s t});$$

$\mathbf{f}$ is the wave vector of the lattice vibration, $\bar{n}_s = (e^{\frac{\hbar\omega_s}{kT}} - 1)^{-1}$ and $K_{j'}(t)$ is obtained from $K_j(t')$ by replacing t' by $-t$ and j by j'.

2. Singularities in Resonance Scattering of Photons by Nuclei

Equation (8) gives the probability for resonance scattering of γ-rays by nuclei in a solid as a function of the incident and scattered radiation and the scattering angle. It is obtained, as has already been mentioned, without assuming that $\vec{\varkappa}_{\sigma'}\mathbf{u}_{nj}$ is small, and therefore is exact in this respect. To go further using (8), however, is in general impossible. Therefore, we shall find the shape of the scattered γ-ray spectrum (as a function of $\omega_{\sigma'}$ or $\omega_{\sigma''}$) and the angular dependence of the scattering for the case $\vec{\varkappa}_{\sigma'}\mathbf{u}_{nj} < 1$; for $\vec{\varkappa}_{\sigma'}\mathbf{u}_{nj} \gtrsim 1$, as will be seen from what follows, Eq.(8) can be used only to arrive at some conclusions concerning the occurrence of the Mössbauer line and its width. To calculate the entire spectrum together with its phonon part is not possible.

The $\vec{\varkappa}_{\sigma'}\mathbf{u}_{nj} < 1$ case corresponds to "soft" γ-rays (of the order of some tenths of a kev) and small displacements $\mathbf{u}_{nj}$. We can therefore expand $\exp\left\{\sum_s \bar{n}_s d_s\right\}$ in a power series in d_s and keep only the first terms. Then by simple calculations we obtain an expression of the form

$$W = W_1 + W_2, \tag{9}$$

for the probability of scattering, in which the first term describes elastic scattering ($\omega_{\sigma'} = \omega_{\sigma''}$), while the second describes inelastic scattering (accompanied by the production or annihilation of a single phonon). In the case of a low rate of heat release[10] the functions W_1 and W_2 can be written

$$W_1 = \frac{M}{\varepsilon_0^2 + \Gamma^2/4}\left|\sum_n e^{\vec{\varkappa}\mathbf{R}^0_n}\right|^2 \left|\sum_{j=1}^m e^{i\vec{\varkappa}\mathbf{r}_j - G_j} F_j(\varepsilon_1)\right|^2,$$

$$W_2 = M\sum_s \left|\sum_n e^{i(\vec{\varkappa}-\mathbf{f})\mathbf{R}^0_n}\right|^2 \left\{\frac{\bar{n}_s}{(\varepsilon_0 - \hbar\omega_s)^2 + \Gamma^2/4}\left|\sum_{j=1}^m e^{i(\vec{\varkappa}-\mathbf{f})r_j - G_j} N_j^-(\varepsilon_1)\right|^2 + \right.$$
$$\left. + \frac{\bar{n}_s + 1}{(\varepsilon_0 + \hbar\omega_s)^2 + \Gamma^2/4}\left|\sum_{j=1}^m e^{i(\vec{\varkappa}-\mathbf{f})\mathbf{r}_j - G_j} N_j^+(\varepsilon_1)\right|^2\right\},$$

where $N_j^-(\varepsilon_1) = P^s_{\sigma' j} F_j(\varepsilon_1) - P^s_{\sigma'' j} F_j(\varepsilon_1 - \hbar\omega_s)$; $N_j^+(\varepsilon_1)$ is obtained from $N_j^-(\varepsilon_1)$ by replacing $-\omega_s$ in F_j by $+\omega_s$; $b_{sj} = (\bar{n}_s + 1)\,P^s_{\sigma' j} P^s_{\sigma'' j}$; $C_{sj} = \bar{n}_s P^s_{\sigma' j} P^s_{\sigma'' j}$; $\mathbf{r}_j$ is the radius vector of the nucleus in the cell; $\mathbf{H}$ is the reciprocal lattice vector;

$$F_j(\varepsilon_1) = \sum_{\substack{\dots\tau_s\dots \\ \dots\tau'_s\dots}} \prod_s \frac{b_{sj}^{\tau_s} c_{sj}^{\tau'_s}}{\tau_s!\,\tau'_s!} \frac{\gamma/2 + i\left[\varepsilon_1 + \sum_s \hbar\omega_s(\tau'_s - \tau_s)\right]_i}{\left[\varepsilon_1 + \sum_s \hbar\omega_s(\tau'_s - \tau_s)\right]^2 + \gamma^2/4}.$$

To obtain the shape of the excitation spectrum, one must sum (9) over the frequencies of the scattered γ-rays and average over the nuclear orientations relative to the incident beam. Then summing the expression so obtained over all values of f ($s = i, \mathrm{f}$) one obtains

$$\widetilde{W}_1 = \frac{\dot{\gamma}}{\Gamma} NN_{\sigma'} |L'_{l_1 l_0}|^2 \left| \sum_{j=1}^{m} e^{i\vec{\varkappa}\mathbf{r}_j - G_j} F_j(\widetilde{\varepsilon}_1) \right|^2 \delta\left(\frac{\omega_{\sigma'}}{c}(\mathbf{t}'' - \mathbf{t}') - \mathbf{H}\right); \tag{10a}$$

$$\widetilde{W}_2 = \frac{\gamma}{\Gamma} NN_{\sigma'} |L'_{l_1 l_0}|^2 \sum_{i=1}^{3m} \left\{ \overline{n}(\mathbf{f}_i) \left| \sum_{j=1}^{m} e^{i(\vec{\varkappa} - \mathbf{f}_i)\mathbf{r}_j - G_j} D_j^+(\widetilde{\varepsilon}_i) \right|^2 + \right.$$

$$\left. + (\overline{n}(\mathbf{f}'_i) + 1) \left| \sum_{j=1}^{m} e^{i(\vec{\varkappa} - \mathbf{f}'_i)\mathbf{r}_j - G_j} D_j^-(\widetilde{\varepsilon}_1) \right|^2 \right\}. \tag{10b}$$

Here

$\widetilde{\varepsilon}_1 = -E + \hbar\omega_{\sigma'}$; $D_j^+(\widetilde{\varepsilon}_1) = P_{\sigma' j} F_j(\widetilde{\varepsilon}_1 + \hbar\omega(f_i)) - P''_{\sigma'' j} F_j(\widetilde{\varepsilon}_1)$; $D_j^-(\widetilde{\varepsilon}_1) = P_{\sigma' j} F_j(\widetilde{\varepsilon}_1 - \hbar\omega(f'_i)) - P''_{\sigma'' j} F_j(\widetilde{\varepsilon}_1)$;

$P'_{\sigma'' j}$ and $P''_{\sigma'' j}$ are obtained from $P^i_{\sigma'' j}$ by replacing $\omega_{\sigma''}$ by $\omega_{\sigma'} + \omega(f_i)$ and $\omega_{\sigma'} - \omega(f'_i)$, respectively, and N is the number of unit cells in the scattering crystal. The vectors $\mathbf{f}_i$ and $\mathbf{f}'_i$, in (10b) satisfy the equations

$$\begin{aligned} \frac{\omega_{\sigma'}}{c}(\mathbf{t}'' - \mathbf{t}') + \frac{\omega_i(\mathbf{f}_i)}{c}\mathbf{t}'' - \mathbf{f}_i = \mathbf{H}, \\ \frac{\omega_{\sigma'}}{c}(\mathbf{t}'' - \mathbf{t}') - \frac{\omega_i(\mathbf{f}'_i)}{c}\mathbf{t}'' - \mathbf{f}'_i = \mathbf{H}, \end{aligned} \tag{11}$$

where $\mathbf{t}'$ and $\mathbf{t}''$ are unit vectors in the directions of the incident and scattered beams.

From (10a) and (10b) it follows that for given fixed $\mathbf{t}'$ and $\mathbf{t}''$ the excitation spectrum consists of a phonon part in the form of a band with a series of sharp peaks and some Mössbauer lines with half width $\gamma/2$. One of these lines is of frequency $E/\hbar$ (we will call it the fundamental line). The other lines are shifted relative to it by an amount $\omega_i(\mathbf{f}_i)$, so that their positions in the spectrum are given by

$$\hbar\omega_{\sigma'} = E \pm \hbar\omega_i(\mathbf{f}_i),$$

where $\mathbf{f}_i$ is obtained from (11). The fundamental Mössbauer line will be the most intense; its intensity is maximum at the Bragg angle.

The number of Mössbauer lines in the excitation spectrum depends on the number of solutions of (11) with $i = 1, 2, \dots, 3m$ and with $\omega_{\sigma'}$ lying within the spectrum of the emitter. In particular, at the Bragg angle, given by

$$\frac{E}{\hbar c}(\mathbf{t}'' - \mathbf{t}') = \mathbf{H},$$

we have

$$\mathbf{f}_i = \pm\frac{\omega_i(\mathbf{f}_i)}{c}\mathbf{t}''.$$

It is easy to see that for the acoustical mode this equation is satisfied only if $\mathbf{f}_i = 0$, $\omega_i = 0$; for the optical mode the equation is satisfied only for

small $|\mathbf{f}|$, and therefore at the Bragg angle the excitation spectrum has, in addition to the fundamental Mössbauer line, lines corresponding to the limiting optical frequencies.

We note that the conclusions we have obtained concerning the shape of the excitation spectrum depend strongly on the incident and scattered beam being ideally collimated. Any dispersion in $\mathbf{t}'$ and $\mathbf{t}''$ leads to diffusion of the Mössbauer lines corresponding to $\mathbf{f}_i \neq 0$.

If one is able to find experimentally the position of the Mössbauer line with frequency $\omega_{\sigma'} = \frac{E}{\hbar} \pm \omega_i$, this same experimental data can be used to establish the vibration spectrum of the scatterer. For this case, finding $\mathbf{f}_i$ corresponding to ω_i reduces to an elementary construction: the vector $\frac{E}{\hbar c}\mathbf{t}'$ is drawn from an arbitrary site of the reciprocal lattice (it is directed at a lattice site); the vector $\frac{E}{\hbar c}\mathbf{t}''$ is drawn from the tail of this vector, and their heads are connected, obtaining $\frac{E}{\hbar c}(\mathbf{t}'' - \mathbf{t}')$.

If we know experimentally the distance from the fundamental Mössbauer line to the i-th such line, we construct the vector $\frac{E \pm \hbar\omega_i}{\hbar c}(\mathbf{t}'' - \mathbf{t}')$ and through its head draw a line parallel to $\mathbf{t}''$. By marking off the vector $\pm \frac{\omega_i}{c}\mathbf{t}''$ on this line and connecting its head to the nearest reciprocal lattice site, we obtain the vector $\mathbf{f}$ corresponding to ω_i. The set of ω_i and $\mathbf{f}_i$ corresponding to them for different $\mathbf{t}''$ can then be used to find ω_i as a function of $\mathbf{f}$.

In order to obtain the scattered γ-ray spectrum (as a function of $\omega_{\sigma''}$) Eq. (9) must be summed over $\omega_{\sigma'}$ and averaged over all nuclear orientations relative to the incident photons. Then summing the expressions so obtained over $\mathbf{f}$, one obtains

$$U = N\,(N_{\sigma''} + 1)\,\overline{|L_{l_1 l_0}|^2}\,(U_1 + U_2),$$

where

$$U_1 = \Big|\sum_{j=1}^{m} e^{i\vec{\varkappa}\mathbf{r}_j - G_j}\,F_j(\varepsilon_1)\Big|^2 \delta\left(\frac{\omega_{\sigma''}}{c}(\mathbf{t}'' - \mathbf{t}') - \mathbf{H}\right) \tag{12a}$$

$$U_2 = \sum_{i=1}^{3m}\left\{\overline{n}(\mathbf{f}_i)\Big|\sum_{j=1}^{m} e^{i(\vec{\varkappa}-\mathbf{f}_i)\mathbf{r}_j - G_j}\widetilde{N}_j^{-}(\varepsilon_1)\Big|^2 + (\overline{n}(\mathbf{f}_i') + 1)\sum_{j=1}^{m} e^{i(\vec{\varkappa}-\mathbf{f}_i')\mathbf{r}_j - G_j}\widetilde{N}_j^{+}(\varepsilon_1)\Big|^2\right., \tag{12b}$$

$$\widetilde{N}_j^{-}(\varepsilon_1) = P'_{\sigma' j}F_j(\varepsilon_1) - P_{\sigma'' j}F_j(\varepsilon_1 - \hbar\omega_i),$$
$$\widetilde{N}_j^{+}(\varepsilon_1) = P''_{\sigma' j}F_j(\varepsilon_1) - P_{\sigma'' j}F_j(\varepsilon_1 + \hbar\omega_i),$$

$P'_{\sigma' j}$ and $P''_{\sigma' j}$ are obtained from $P^{s}_{\sigma' j}$ by replacing $\omega_{\sigma'}$ by $\omega_{\sigma'} - \omega_i$ and $\omega_{\sigma'} + \omega_i$, respectively, δ is the Kronecker delta, and N is the number of unit cells in the scatterer. The vectors $\mathbf{f}_i$ and $\mathbf{f}_i'$ in (12b) satisfy the equations

$$\frac{\omega_{\sigma''}}{c}(\mathbf{t}'' - \mathbf{t}') + \frac{\omega_i(\mathbf{f}_i)}{c}\mathbf{t}' - \mathbf{f}_i = \mathbf{H},$$
$$\frac{\omega_{\sigma''}}{c}(\mathbf{t}'' - \mathbf{t}') - \frac{\omega_i(\mathbf{f}_i')}{c}\mathbf{t}' - \mathbf{f}_i' = \mathbf{H},$$

where t' and t'' are unit vectors in the incident and scattered directions, and H is the reciprocal lattice vector.

As a result of (12), the structure of the scattered γ-ray spectrum (as a function of $\omega_{\sigma''}$) is similar to that of the excitation spectrum, and therefore the results obtained previously for the excitation spectrum will hold for the scattered photon spectrum.

We note also that in both cases the intensities of the lines corresponding to inelastic scattering (Eqs.(10b) and (12b)) increase with increasing temperature.

If the position of the Mössbauer lines with frequencies $\omega_{\sigma''} = \frac{E}{\hbar} \pm \omega_i$, can be established experimentally in the scattered photon spectrum, then similarly as above ω_i can be obtained as a function of f. All constructions in the reciprocal lattice space are performed as in the case of the excitation spectrum, except that $\pm \frac{\omega_i}{c} t''$ is replaced by $\pm \frac{\omega_i}{c} t'$.

We note that the f-dependence of ω_i can also be obtained from the intensity of the fundamental Mössbauer line in a way similar to the x-ray method,[11] with the advantage that the intensity of the Mössbauer line can be found quite accurately.

It is impossible to express the scattering probability (8) analytically when $\vec{\varkappa}_{\sigma'} u_{nj} \gtrsim 1$. From (8) one can obtain only qualitative information on the shape of the excitation and scattered photon spectra. For this purpose we use residue theory to integrate over x in (8), and then choose $\alpha = \mu_0, t_0, t_0'$ so that $\alpha \omega_{s\,max} < 1$ (where $\omega_{s\,max}$ is the maximum normal frequency of the scattering crystal). Each of the integrals in the expression obtained is written as a sum of two integrals with the limits $[0, \alpha]$ and $[\alpha, \infty]$. Then the triple integral with limits $[0, \infty]$ is written as a sum of eight integrals. Four of them, in which one integrates over μ with the limits $[\alpha, \infty]$, are easily evaluated. Both in the excitation spectrum and in the scattered photon spectrum, for observation at the Bragg angle ϑ_B, they lead to a sum of the Mössbauer line and the phonon part of the spectrum, which is represented by a Gaussian curve. The Mössbauer line is located on the side of the Gaussian curve at an energy lower than the maximum of the phonon part in the excitation spectrum and higher than the maximum of the phonon part in the scattered γ-ray spectrum.

The other four integrals, whose limits are $[0, \alpha]$ cannot be written analytically. It can be shown only that they are relatively smooth functions of $\omega_{\sigma'}$ or $\omega_{\sigma''}$ and that the amount of scattering corresponding to these terms will not vanish at angles other than the Bragg angle.

It follows from this that for $\vec{\varkappa}_{\sigma'} u_{nj} \gtrsim 1$ the spectrum will consist of a phonon part, and that at the Bragg angle it will contain a Mössbauer line whose intensity will decrease as $\vec{\varkappa}_{\sigma'} u_{nj}$ increases.

We desire to express our gratitude to N.N.Bogolyubov for valuable discussions and interest in the work.

Physics Institute,
Academy of Sciences of the Ukrainian SSR

References

1. C.Tzara & R.Barloutaud, Phys.Rev.Letters, 4, 405 (1960).
2. R.Barloutaud, J.-L.Picou & C.Tzara, Compt.rend., 250, 2705 (1960).
3. R.L.Mössbauer, Z.Phys., 151, 124 (1958); Z.Naturforsch.a, 14, 211 (1959).
4. A.Kastler, Compt.rend., 250, 509 (1960).
5. W.Heitler, The Quantum Theory of Radiation, Oxford, 1954.
6. W.E.Lamb, Phys.Rev., 55, 190 (1939).
7. W.M.Visscher, Ann.Phys., 9, 194 (1960).
8. R.E.Peierls, Quantum Theory of Solids, Oxford, 1955.
9. L.S.Kothari & K.S.Singwi, Solid State Physics, 8, 118 (1959).
10. I.P.Dzyub & L.F.Lubchenko, Doklady AN SSSR, 136, 66 (1961). (Trans.Soviet Physics - Doklady.)
11. C.B.Walker, Phys.Rev., 103, 547 (1956).

Bulletin of the Academy of Sciences of the USSR - Physical Series
Vol.25, No.7 - July 1961

Transactions of the Eleventh Annual Conference on Nuclear Spectroscopy
(Continued from Vol. 25, No.2)

TABLE OF CONTENTS

	Page Orig.	Trans.
New results in the theory of nonaxial nuclei - A.S.Davydov	782	793
Calculation of the probability of the Auger effect - M.A.Listengarten	792	803
Investigation of the decay scheme of Gd^{147} - A.A.Sorokin & K.P. Mitrofanov	799	810
Investigation of the decay scheme of Gd^{149} - A.A.Sorokin & K.P. Mitrofanov	808	819
Investigation of neutron-deficient Tb isotopes - A.T.Strigachev, L.S. Novikov, A.A.Sorokin, V.A.Khalkin, N.V.Tsvetkova & V.S.Shpinel'	813	824
Positron spectra of neutron-deficient terbium and neodymium isotopes - N.A.Bonch-Osmolovskaya, B.S.Dzhelepov, O.E.Kraft & Chou Yüeh-wa	826	837
Investigation of Coulomb excitation of nuclear levels by means of multiply charged ions - D.S.Andreev, V.D.Vasil'ev, G.M.Gusinskii, K.I.Erokina & I.Kh.Lemberg	832	842
Beta- and gamma-spectra of radioactive Sb^{113} and Sb^{115} and a new Sn^{113} isomer - I.P.Selinov, V.L.Chikhladze, D.E.Khulelidze & N.A.Vartanov	848	857
Investigation of the levels of P^{31} by means of the $Si^{30}(p,\gamma)P^{31}$ reaction - A.K.Val'ter, S.P.Tsytko, Yu.P.Antuf'ev, E.G.Kopanets & A.N.L'vov	854	862
Total ionization produced by alpha-particles in gas mixtures - G.E.Kocharov	862	873
Concerning the operation of proportional counters - G.A.Korolev & G.E.Kocharov	866	877
Atomic masses of tin and antimony isotopes - R.A.Demirkhanov, T.I.Gutkin, O.A.Samadashvili & I.K.Karpenko	871	882
Alpha-decay to electron capture ratios for Po^{200}, Po^{201} and Po^{203} - B.N.Belyaev, A.V.Kalyamin & A.N.Murin	874	886
Reduced derivative width δ_L^2 for polonium isotopes - B.N.Belyaev, A.V. Kalyamin & A.N.Murin	879	890
Calculation of yield cross sections for spallation reactions - V.I.Baranovskii & A.N.Murin	882	893
Emission, absorption and reabsorption of gamma-rays by impurity nuclei in solid solutions - I.P.Dzyub & A.F.Lubchenko	893	903
Resonance scattering of gamma-rays by nuclei in a solid - I.P. Dzyub & A.F.Lubchenko	901	911

Translated in 1962 by
Columbia Technical Translations
5 Vermont Ave., White Plains, N.Y.

Transactions

of the

Fifth Conference on X-Ray Spectroscopy

(Khar'kov, 30 January - 4 February 1961.)

USE OF X-RAY BREMSSTRAHLUNG FOR INVESTIGATION OF ABSORPTION SPECTRA IN THE ULTRASOFT REGION

- A.P.Lukirskii

In an earlier paper[1] we described the possibility of utilizing x-ray bremsstrahlung for investigating absorption spectra in the ultrasoft region. Thus, if one feeds high power into an x-ray tube, which is possible only by applying a high voltage of the order of several kilovolts to the tube, and filters out the short wavelength radiation, one can investigate the absorption spectrum by means of an efficient detector such as a Geiger counter. In our earlier work[1] we obtained effective filtration of the short wavelength radiation by utilizing the effect of "complete external reflection". In the same study we carried out a detailed investigation of diffraction gratings and showed that the lightly ruled glass gratings with 600 lines per mm prepared by the GOI (State Optical Institute) at a grazing angle of incidence of 5° 30' concentrate virtually all the radiation softer than 60 Å in the first order. By means of a combination of such a grating with a reflecting filter, mounted at an appropriate angle, one can obtain a bremsstrahlung spectrum virtually free of higher orders.

The present work was concerned with investigation of the absorption spectrum of beryllium. In this work we used a spectrometer equipped with a focusing reflecting filter[2]. The filter was prepared of glass and mounted at an angle of 9° 36'. The source was a tungsten anode operated at 6 kv (I = 150 ma).

Owing to relatively poor thermal contact between the tungsten plate and the copper base of the anode, the tungsten plate heated to about 2000°C. By virtue of this heating the surface of the anode remained clean over a prolonged period, which insured stability in time of the bremsstrahlung. The bremsstrahlung of the hot anode was measured repeatedly and we obtained excellent agreement as regards intensity (within 1-2%) over the entire region of the spectrum.

The absorber was located in front of the entrance slit of the spectrometer. The distance between the anode and the entrance slit was 150 mm; this appreciable separation protected the specimen from the destructive effects of radiation. The beryllium absorber was prepared by vacuum evaporation. With a view to eliminating the "effect of the backing", we made attempts to prepare absorbers without a backing. To this end the beryllium was evaporated onto a polished slab of rock salt coated beforehand with a celluloid film. The film with the beryllium coating was separated from the salt by immersion in water and was then dissolved in amyl acetate. The specimens prepared in this manner exhibited the metallic luster characteristic of beryllium, were extremely brittle and virtually free of cracks and pin-holes.

For experimental investigation of the absorption spectrum we chose the specimen exhibiting the most contrasty spectrum. After selection of the specimen, we recorded without interruption the absorption spectrum and then the bremsstrahlung spectrum without the absorber. Inasmuch as the bremsstrahlung spectrum without the absorber had a high intensity and overloaded the Geiger counter, in recording the bremsstrahlung spectrum we disadjusted the anode, thereby equalizing the intensities with the absorber and without the absorber. The two spectra were recorded at a number of different counting rates.

The bremsstrahlung spectra with and without an absorber recorded in one of the series of measurements are reproduced in Fig.1. There are clearly evident the $W(N_V—N_{VII})$ emission line and a number of maxima and minima, which either represent the spectrum of glass, arising as a result of absorption of the radiation at surface roughnesses or splinters of glass dust on the diffraction grating and reflector, or are the result of the influence of fluctuation of the absorption

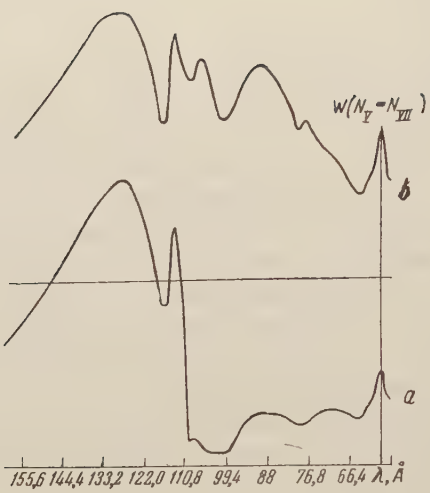

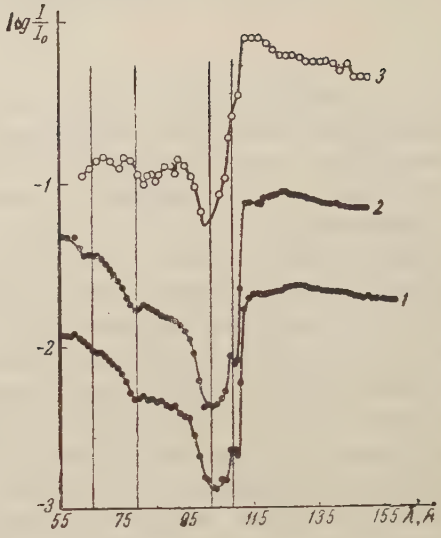

Fig.1. Bremsstrahlung spectrum of the tungsten anode with the beryllium absorber (a) and without the absorber (b).

Fig.2. Variation of log (I/I_O) with the wavelength. The log (I/I_O) values for each of the curves are laid off from an arbitrary datum.

coefficient on the "total external reflection" curve of the reflector and grating. This interpretation is plausible inasmuch as the structure of the bremsstrahlung spectrum is located to the short wavelength side of the absorption edge of silicon. The recorded curves were corrected for the "counting loss" of the counter, the dead time of which was determined by the method of two sources (Co^{60}) and found to be $2.9 \cdot 10^{-4}$ sec. On the basis of the experimental data we calculated the values of log (I/I_O), where I is the transmitted intensity and I_O is the incident intensity. Inasmuch as the thickness of the specimen was not known, the change in I_O as a result of disadjustment of the anode was not significant.

Fig.2 shows the log (I/I_O) vs wavelength curves obtained at different counting rates (curve 1 - maximum counting rate 880 pulses/sec; curve 2 - 380 pulses/sec; maximum counting rate for the bremsstrahlung spectrum without the absorber 290 pulses/sec) and the analogous curve 3 obtained by Johnston & Tomboulian[3]. The spectra were obtained with a diffraction grating having 600 lines per mm and a radius of curvature of 1 meter. The width of both the entrance and exit slits was 50 μ, i.e., the resolved wavelength interval was approximately 1 Å.

Discussion

Comparison of curves 1 and 2 in Fig.2, obtained at different counting rates, shows that they are virtually identical. In comparing our curves, however, with curve 3 there is evident a substantial difference in the short wavelength region: our curves 1 and 2 are appreciably smoother and have only three absorption peaks located at 65, 78.5 and 101.5 Å, assuming that the last peak should not be attributed to the "effect of the backing". The absorption edges coincide; however, in our curves the absorption edge is sharper and has an additional shoulder or hump, not evident in curve 3. There is also a substantial difference between the slopes of the curves on the short wavelength side of the absorption edge. Below

we list the data on the positions of the absorption peaks obtained in the work of Johnston & Tomboulian[3] and in the present study:

Distance of the absorption peaks (in ev) from the absorption edge

Johnston & Tomboulian	Our data	Johnston & Tomboulian	Our data
13.4	10	43.1	
25.9		56.9	
35.8	37	85	79

The divergence between the results of Johnston & Tomboulian and ourselves should be attributed either to inadequate resolution of the spectrograph used by Johnston & Tomboulian or to the small number of lines in the line spectrum of the condensed spark discharge used by Johnston & Tomboulian as the source. The difference between the slopes of the short wavelength sections of the curves can probably be explained by superposition of higher orders or errors in calibrating the photographic plates in the work of Johnston & Tomboulian (in calibrating the photographic plates[4] it was assumed that the photographic effect is independent of the wavelength and the response of the emulsion is "flat" in energy, which is probably not true).

Physics Faculty,
Leningrad State University

References

1. A.P.Lukirskii & Yu.A.Omel'chenko, Optika i spektroskopiya, 8, 563 (1960). (Trans.Optics & Spectroscopy.)

2. A.P.Lukirskii, Present issue of the Bulletin (next article).

3. R.W.Johnson & D.H.Tomboulian, Phys.Rev., 94, 1585 (1954).

4. D.H.Tomboulian, "The experimental methods of soft x-ray spectroscopy and the valence band of the light elements," in Handbuch der Physik, Vol.30, p.246 (Springer, Berlin 1957). (Cited in Russian translation in "Rentgenovskie luchi" (X-Rays), edited by M.A.Blokhin, M.1960).

SPECTROMETER FOR ULTRASOFT X-RADIATION WITH COMBINED DETECTION BY MEANS OF SECONDARY ELECTRON MULTIPLIERS AND A GEIGER COUNTER

- A.P.Lukirskii

Introduction

Geiger counters and secondary emission multipliers (SEM) are the most efficient detectors of ultrasoft x-radiation; in addition, they allow of carrying out accurate relative intensity measurements. It must be noted, however, that the efficiency of SEM depends on the properties of the photocathode. The photoelectron yield of photocathodes, as we showed earlier[1-3], depends substantially on the material of the photocathode, the angle of incidence of the radiation and the wavelength; the last dependence undergoes sharp changes at the wavelengths of the absorption discontinuities of the photocathode material.

The through type Geiger counter is a very reliable and efficient detector. It has been shown that the efficiency in the region of ultrasoft x-radiation is determined entirely by the transmission of the counter window. It is feasible to prepare windows with high transmission even in the ~200 Å region. In preparing such windows, it is essential to check the transmission experimentally inasmuch as evaluation of the thickness of films of the order of a few hundred angstroms is necessarily only approximate; moreover, there is a scarcity of accurate data on the variation of the absorption with frequency in the region of ultrasoft x-radiation. For practical solution of the problem of choosing a suitable radiation detector, in this report we propose a spectrometer design, which incorporates both an SEM and a Geiger counter with provision for interchange of the detectors at any time during operation of the spectrometer by means of an external control.

The interference of higher orders of reflection, particularly in investigating absorption spectra, gives rise to serious difficulties in experimental studies In Ref.4 we described a method of filtering out higher orders of reflection based on utilization of the effect of "complete external reflection". A shortcoming of the filter described in Ref.4 is the fact that it was located close to the anode which led to the appearance of a deposit on the filter in the process of operation and, consequently, a reduction of its reflecting power. Arbitrary increase of the separation between the tube anode and the filter is not expedient inasmuch as it leads to loss in intensity.

In the spectrometer described below the filtering element is a spherical glas mirror, which simultaneously reflects and focuses the radiation. Because it focuses the radiation, the mirror can be mounted at a greater distance from the anode and entrance slit, thereby minimizing the build-up of contaminating deposits and insuring a clean surface for a prolonged period. Locating the anode at an appreciable distance from the slit also makes it possible to mount the absorber (specimen in investigating absorption spectra) immediately in front of the entrance sli which is important in investigating absorption spectra (for example, see Ref.5). We note also that use of a focusing reflector makes it possible to use a sharp focus x-ray tube.

Design of the Spectrometer

The spectrometer is diagramed in Fig.1. The position of the receiving slit 1 on the focusing (Rowland) circle is set by the heavy lever 2. The axis of the lever is positioned by means of a spherical bearing on bracket 3, which is rigidl attached to the flat base 4 of the spectrometer. The end of the lever rests on two caster bearings 11 that roll on the base. The lever is actuated by the screw

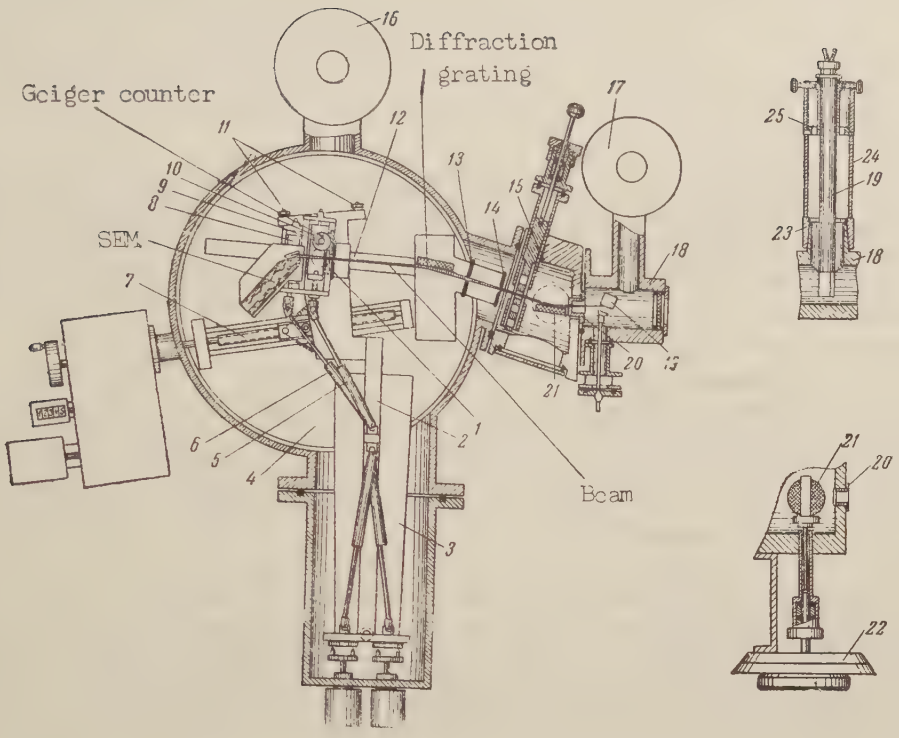

Fig.1. Diagram of the spectrometer.

7, mounted on the chord of the focusing circle (the lever is moved by a nut on the feed screw, moving in a swallow-tail guide mounted on the base). The end of the feed screw is brought out through a vacuum lock and sylphon and is coupled by a cylindrical gear train with the turn counter and the reduction gear of the motor. The counter allows of reading displacements in divisions of 10 μ over the circumference of the focusing circle.

The receiving slit and table carrying the detectors 9 is coupled with the lever by means of two thrust bearings, and can be rotated about the center of the grating by means of rod 12. There are two swallow-tail guides on the table: 10 - for bringing the counter out of the beam and 8 - for adjusting the SEM. The control screws moving these units in the respective swallow-tail guides are connected to two manipulators 5 and 6, which are brought out through appropriate seals. One of the manipulators can be connected for adjusting the angular position of the receiving slit to align it with the beam.

The entrance slit 14 and aperture 13 define the width of the illuminated section of the diffraction grating; the grating is mounted on an adjustable stage, which has provision for adjusting the relative positions of the slit, aperture and grating and the position of the entire assembly relative to the axis of the main lever. All the slits and the aperture have provision for regulating their width. The focusing reflector 21 is mounted in front of the entrance slit; this spherical mirror is mounted on an adjustable stage connected with the axis of the angle gage 22, which allows of setting the angle of the mirror to within 1'. Inasmuch as the mirror focuses only when the source and image are located on the focal circle of the mirror, a number of interchangeable mirrors with different radii of curvature is used for setting different angles of reflection with the same distance between the mirror and the entrance slit and between the mirror and

the anode. The x-ray tube is mounted in front of the mirror; the tube housing 18 is made of stainless steel. The anode 19 is a water cooled copper rod with a four-sided tip. The anode is connected with housing by the insulator 24 and the tapered joint 23; the latter provides for turning any one of the four faces of the anode to the working position. The anode rod is attached to the insulator through membrane 25, which allows of adjusting its position during operation of the spectrometer.

In front of the slit is the manipulator for introducing the absorber 15 into the beam without disturbing the vacuum. The appreciable separation between the absorber and the anode safeguards the absorber from disintegration by intense radiation. Between the tube and the reflector there is the separating slit 20 which helps maintain the pressure differential in separate pumping of the volume of the spectrometer and x-ray tube. The area of this slit is 10 mm^2.

The apparatus is evacuated by two TsVL-100 diffusion pumps 16 and 17. One pump evacuates the volume of the spectrometer; the other the x-ray tube. Each vacuum line has an oil deflector and trap. In addition, there is a trap in the spectrometer and another one in the x-ray tube. This vacuum system allows of obtaining a vacuum of $1 \cdot 10^{-5}$ mm Hg in the spectrometer and $(1-2) \cdot 10^{-6}$ mm Hg in the x-ray tube by direct pumping.

The diffraction grating is mounted at a grazing angle of 5° 30' relative to the beam; this lightly ruled glass grating was prepared in the State Optical Institute and has 600 lines per mm and a radius of curvature of 1 meter. The distance between the receiving slit and the reflector is 75 mm; this is also the distance between the reflector and the anode. The effective range of the spectrometer (with the 600 lines per mm grating) is 40 to 450 Å.

Radiation detectors and recording system

The spectrometer employs a secondary electron multiplier (SEM) and a Geiger counter.

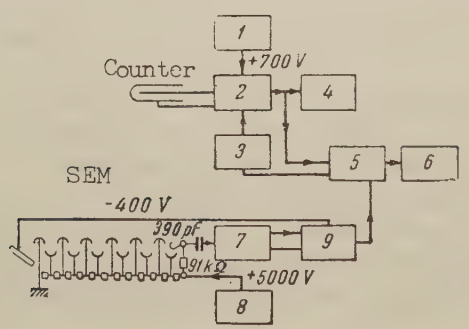

Fig.2. Block diagram of the detecting-recording system: 1) high voltage supply for the Geiger counter, 2) power supply and phase inverter, 3) supply regulator, 4) PS-64 scaler circuit, 5) counting rate meter, 6) electronic PS-1 recorder, 7) cathode follower, 8) high voltage regulator (2500 to 6000 v), 9) "Floks" unit.

The SEM was prepared in the State Optical Institute and has dynodes of beryllium bronze. The standard curved cathode was replaced by a flat photocathode mounted separately from the SEM: flat photocathodes allow of more accurate judgment of the efficiency of the detector owing to the strong dependence of the photoelectron yield on the angle of incidence.[3] The SEM is supplied from a stabilized high voltage source. The first dynode is grounded and a negative potential is applied to the photocathode. This supply system significantly reduces the background of the SEM.

The signal from the SEM is picked up by a cathode follower and fed to a PS-10 000 "Floks" unit. The negative voltage of the "Floks" unit is used for supplying the photocathode. The signal for the counting rate meter and the automatic PS-1 recorder (for installation of which a minor modification of the "Floks" circuit is necessary) is taken off the cathode follower, located in the

"Floks" after the "resolving time" stage. The counting rate meter is based on a system consisting of an integrating capacitor and a vacuum tube voltmeter with negative feedback.[6] This system allows of counting at rates of up to 10^5 pulses/ /sec with an accuracy of ~1%.

The design of the through Geiger counter and the recording system has been described earlier.[7] We note only that in the given instrument the signal from the external stage of the recording circuit of the counter is also applied to the counting rate meter and the automatic recorder. The cathode follower of the SEM and the external counter stage (quenching circuit and phase inverter) are located in the vacuum in the immediate proximity of the detectors. A block diagram of the detecting-recording circuit is shown in Fig.2.

X-ray tube supply

The x-ray tube is supplied from a high voltage sbatilizer and an anode current regulator. The anode current regulator has a circuit similar to that of the stabilizer in the URS-50-I unit. The high voltage regulator is of the same type as in the earlier described x-ray monochromator.[7]

Adjustment of the spectrometer

The initial adjustment of the spectrometer comprised two stages: a) positioning the slits and grating on the focusing circle as set by the lever (2 in Fig.1), and b) checking the parallelism of the slits and grating and the perpendicularity of these units relative to the plane of the focusing circle. The first stage was carried out simply by measuring the distance between the axis of rotation of the lever and the slits and grating. The second stage was carried out by autocollimation: by aligning the image of a point located on the axis of the lever at a certain height with the point itself. The image is reflected either from the center of the diffraction grating or from a plane-parallel plate of glass clamped between the jaws of the slit at a certain height. Obviously, in the process of autocollimation of the grating its angular orientation is also set.

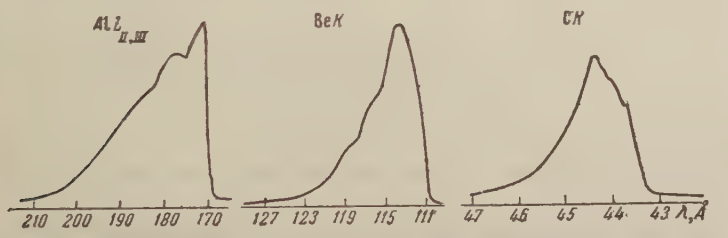

Fig.3. Emission lines obtained without the reflector (automatic recording).

The adjustment of the spectrometer was checked by comparing the Mo_ξ lines in the first and second orders. With a slit width of 5 μ there were obtained experimental line half-widths in the first and second orders equal to 0.75 and 1.25 Å, respectively, which on the assumption that the lines have the classical dispersion shape, yields an instrument error of 0.25 Å. The calculated $\Delta\lambda_{min}$ for 5 μ wide slits is 0.093 Å. Consequently, the inaccuracy in adjustment led to an error of 0.15 Å.

To illustrate the operation of the instrument we show in Fig.3 the familiar emission lines: Be K in the 1st, Al $L_{II,III}$ in the 1st, and C K in the 6th order. These lines were recorded using the Geiger counter as the detector and without the filtering reflector. The Be and Al lines were obtained using metallic powders rubbed into the anode. Obviously, the metals heated up to some extent, hence the short wavelength sides of the lines are somewhat smeared out (temperature broadening of the Fermi edge). In the trace of the Al line there is evident superposition of the fourth order reflection from carbon. These lines were all recorded with slit widths of 10 μ.

Operation of the reflecting filter

The filtering action of the reflector was tested by observing emission lines as well as bremsstrahlung spectra. Fig.4 shows two curves characterizing the Al $L_{II,III}$ emission band recorded under the same conditions with and without the reflector. The reflector had a radius of curvature of 449 cm and was mounted at an angle of 9° 36'. It will be evident from an examination of the curve obtained with the reflector that in this case there is no superposition of the fourth order carbon line. Investigation of the carbon line in the first order showed that it is approximately 20 times weaker than the Al $L_{II,III}$ line. Fig.5 gives the bremsstrahlung spectrum of tungsten recorded with and without the reflector.

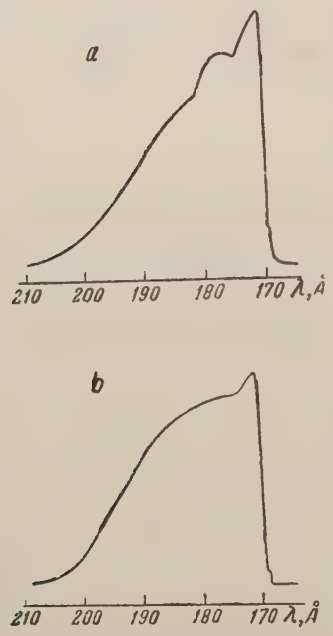

Fig.4

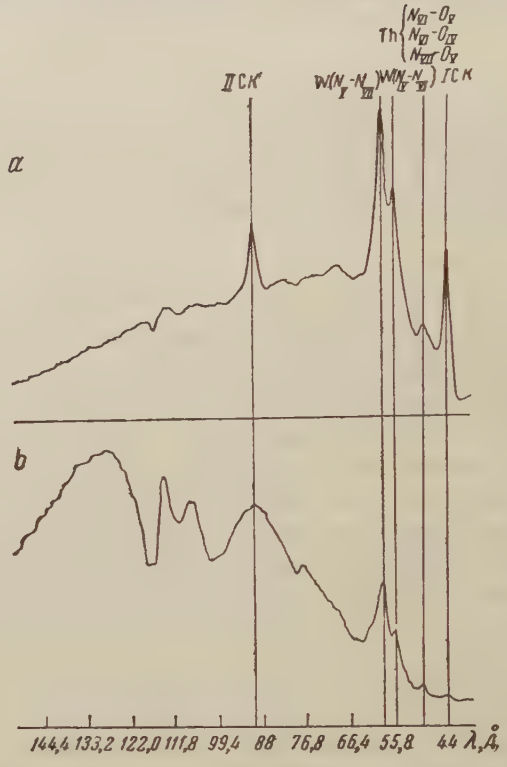

Fig.5

Fig.4. Al $L_{II,III}$ emission band recorded without a reflector (a) and with a reflector (b).

Fig.5. Bremsstrahlung spectrum of tungsten recorded without a reflector (a) and with a reflector (b). The intensity scales are arbitrary. Emission lines are clearly discernible in the curves; in addition, in curve b there are evident sharp maxima and minima. The possible origin of these maxima and minima is discussed in Ref.8.

By means of the diffraction grating employed in the instrument, which concentrates virtually all the radiation of wavelengths > 60 A in the first order, one can obtain the bremsstrahlung spectrum in the $\lambda > 60$ A region free of superposition of higher orders.

Efficiency of the Geiger counter

According to earlier tests[7], for a Geiger counter filled with argon to a pressure above 30 mm Hg the detecting efficiency as regards radiation softer

than 113 Å is determined entirely by the transmission of the counter window. The transmission of the counter window was determined with reference to the characteristic Be K, Al K and Li K lines with the aid of the SEM. The following data were obtained:

λ, Å	Efficiency
113.6	0.65
173.5	0.35
232	0.19

References

1. A.P.Lukirskii, M.A.Rumsh & L.A.Smirnov, Optika i spektroskopiya, 9, 511 (1960). (Trans.Optics & Spectroscopy).
2. A.P.Lukirskii, M.A.Rumsh & I.A.Karpovich, Ibid., 9, 653 (1960). (Trans. Ibid.)
3. M.A.Rumsh, A.P.Lukirskii & V.N.Shchemelev, Doklady AN SSSR, 135, 55 (1960). (Trans.Doklady.)
4. A.P.Lukirskii & O.A.Omel'chenko, Optika i spektroskopiya, 8, 563 (1960). (Trans.Optics & Spectroscopy.)
5. L.G.Parratt, J.O.Porteus, H.W.Schnopper & T.Watanabe, Rev.Sci.Instr., 30, 344 (1959).
6. E.Cooke-Jarrborugh, Proc.Inst.Electr.Eng., 98, II, No.62, 91 (1951).
7. A.P.Lukirskii, M.A.Rumsh & L.A.Smirnov, Optika i spektroskopiya, 9, 505 (1960). (Trans.Optics & Spectroscopy.)
8. A.P.Lukirskii, Present issue of the Bulletin,(preceding article).

MICROFOCUS X-RAY SPECTROGRAPH

- I.B.Borovskii, S.A.Ditsman & V.G.Bogdanov

Development of the method of x-ray spectroscopic chemical analysis of microvolumes has resulted in the design and construction of a number of different microanalysis units[1] including some scanning microanalyzers[2]. In an earlier report[3], we proposed using the method of microfocus spectroscopy for investigating the fine structure of emission x-ray spectra.

Where local x-ray spectrochemical analysis is concerned no particularly rigorous requirements are imposed on the instrument as regards resolution: a resolution of 2 X (for the $K\alpha_1$-$K\alpha_2$ doublet) is generally adequate. On the other hand, for investigating fine structure, the basic requirement is high resolution of the instrument and precise indication of the wavelength of the investigated line, i.e., an accurate wavelength scale.

In the present report we describe the design of a new microfocus x-ray spectrograph intended for investigation of the fine structure of x-ray emission spectra. This instrument can, of course, be also used for analytic purposes.

The spectrograph employs a Kapitsa-Johann mounting with a bent quartz crystal (R = 500 mm). The instrument provides an operating range of Bragg angles from 25 to 60°, using reflection from the $(13\bar{4}0)$, $(10\bar{1}0)$ and $(10\bar{1}1)$ planes to cover the wavelength range from 1 to 7 Å.

To facilitate investigation of the shape of emission lines, the design of the instrument provides for smooth variation of the angle of reflection in a narrow range of Bragg angles (0.5-1°). The minimum change in angle is 5-6" and is read on the displacement indicator. This angular displacement of the crystal corresponds to a $\sim 10^{-2}$ X change in wavelength. With the optimum size of the working surface of the crystal this change agrees in order of magnitude with the monochromaticity of the reflected radiations.[4] The radiation detector and slit are located on the Rowland circle.

The kinematic system of spectrograph operates on the same principle as the systems employed in the instruments developed by Ohlin[5] and Brogren[6]. Change in the conditions of reflection in these instruments is realized by linear displacement of the crystal with simultaneous rotation thereof through an appropriate angle.

Use of the linear displacement kinematic system allowed of simplifying the design of the instrument as a whole as well as of certain of its components. Thus for example, angular indication of the position of the crystal is replaced by indication of its linear displacement. This design also does away with the need for a wide exit window in the x-ray tube. This simplifies the vacuum connections and seals and reduces the total amount of scattered radiation, which enhances the sensitivity of the instrument.

In this type of spectrograph the beam always emerges from the specimen in the same direction. This provides the same conditions for emergence of the radiation in the entire working wavelength range.

The design of the instruments of Ohlin[5], Brogren[6] and Sandström[7] have the shortcoming that they do not assure synchronous displacement of the radiation source, crystal and detector in a wide range of angles. Recently, one of us (see Ref.8) developed a spectrograph for investigating the fine structure of x-ray spectra in which there was also utilized the principle of the Ohlin instrument. In this instrument, however, there was realized automatic coupling between the displacement of the crystal and radiation detector in a wide range of angles. However, the design of this instrument, like that of the other instruments mentioned above, was predicated on work with a wide focus radiation source and thus precluded the use of microsources mounted on the Rowland circle.

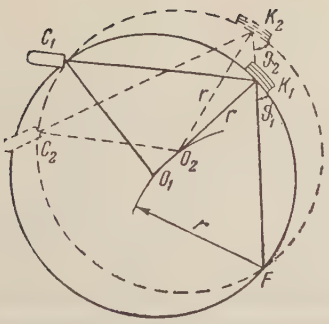

Fig.1

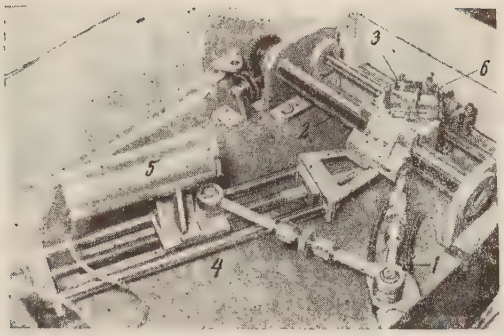

Fig.2

Fig.1. Diagram of the microfocus spectrograph.
Fig.2. Top view of the spectrograph: 1 - curved guide, 2 - crystal carriage guides, 3 - analyzer crystal, 4 - radiation detector carriage guides, 5 - radiation detector, 6 - crystal displacement indicator.

The kinematic system of the present instrument is diagramed in Fig.1. The microfocus source is mounted on the Rowland circle. If the crystal is in position K_1 (angle θ_1) the reflected beam enters the slit of the detector ($FK_1 = K_1C_1$). In this case the center of the Rowland circle is at point O_1. With displacement of the crystal to position K_2 (angle θ_2) to maintain focusing the Rowland circle must be displaced so that its center will occupy position O_2. Now the radiation reflected from the crystal will enter the detector slit if $FK_2 = K_2C_2$ and C_2 lies on the Rowland circle.

The mechanical system of the spectrograph insures fulfillment of these conditions in the following manner. The crystal and counter guides (FK and KC) are equipped with two screws with the same pitch, and these are rotated simultaneously. With displacement of the crystal from K_1 to K_2 there is automatically maintained equality of the chords FK_2 and K_2C_2. At the same time the center of the Rowland circle, which is the end of the rigid arm OK ($O_1K_1 = O_2K_2 = R/2$) is displaced to the point O_2, sliding along the curved guide (1 in Fig.2), the radius of curvature of which is equal to that of the Rowland circle. The arm OK is perpendicular to the surface of the crystal which provides for rotation of it relative to the angle of incidence of the radiation. The arm OC ($O_1C_1 = O_2C_2 = R/2$) maintains the detector slit on the Rowland circle, as the circle is displaced relative to the radiation source F. The instrument design has provision for adjustment of the system to compensate for minor variations in the radius of curvature of the crystal: the lengths of the arms OC and OK and the distance FO can be varied within the range of 5 mm.

The displacement of the crystal is realized by means of an electric motor or manually. Rough indication of the position (angle) of the crystal is read to within 0.2 mm on the indicator scale. In investigating fine structure the position of the crystal is given by the fine displacement indicator to within 0.01 mm. In this type of instrument the wave dispersion is constant in the entire range of working angles.[9] In the given case in using a quartz crystal with reflection from the $(13\bar{4}0)$ planes, the dispersion equals 4.7 X/mm. Displacement of the crystal by 0.01 mm corresponds to a $\sim 10^{-2}$ X change in reflected wavelength. Since the line width in x-ray spectra is of the order of one or more X, the wavelength indicating arrangement insures the precision of displacement necessary for investigating line shapes.

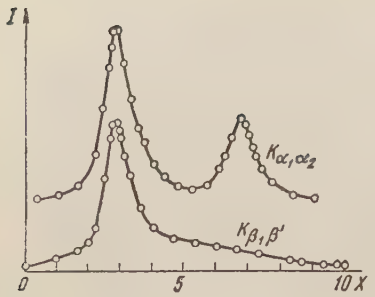

Fig.3. $K\alpha_1$-$K\alpha_2$ and $K\beta_1$-$K\beta'$ lines of Fe recorded on the spectrograph.

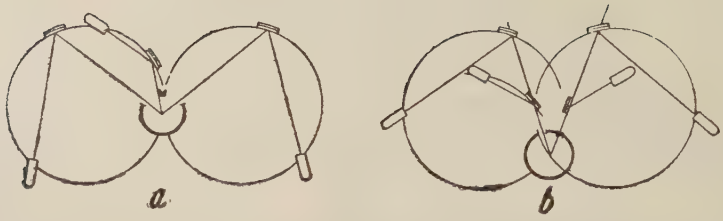

Fig.4. Diagrams of two-channel instruments: a - with displacement of the crystal along the circumference of a circle, b - with linear displacement of the crystal.

A photograph of the spectrograph is reproduced in Fig.2. The other components of the microfocus instrument (electron-optical system, supply units and vacuum system) are similar to those employed in the RSASh-2 spectrograph.

Investigation of the shape of emission lines is carried out by displacement of the crystal in 0.02-0.03 mm steps with reference to the displacement indicator and simultaneous detection of the reflected radiation. Fig.3 shows the results of investigating the shapes of the $K\alpha_1$-$K\alpha_2$ and $K\beta_1$-$K\beta'$ lines of Fe with reflection in the first order from the $(10\bar{1}1)$ planes of the quartz analyzer crystal. The parameters of the recorded lines are in good agreement with the results obtained by means of other x-ray spectrographs.

As was noted above, the present spectrograph design can be used in microanalyzers. In this case there is no need for precise indication of the position of the crystal so that the requirements as regards accuracy in this respect may be relaxed. The developed spectrograph system makes it possible to simplify the design of a two-channel microfocus instrument. The usual system with circular displacements is diagramed in Fig.4,a; in this case the overall range of angles of emergence of the radiation from the specimen chamber and microfocus tube is large. This greatly complicates the design and arrangement of the instrument components. Use of the system with linear displacement of the crystals allows of reducing the angle between channels, using smaller exit windows and simplifying the design of the instruments in a number of respects (Fig.4,b).

"A.A.Baikov" Institute of Metallurgy,
Academy of Sciences of the USSR

References

1. R.Castaing, Laboratoires, 7, No.17, 7 (1957); I.B.Borovskii & N.P.I'lin, Zavodsk, laboratoriya (Industrial laboratory), No.10, 1234 (1957).
2. P.Duncumb, Brit.J.Appl.Phys., 11, 169 (1960).
3. I.B.Borovskii & S.A.Ditsman, Doklady AN SSSR, 124, 1042 (1959). (Trans. Soviet Physics Doklady.)
4. S.A.Ditsman, Izv.AN SSSR, Ser.fiz., 24, 376 (1960). (Trans.Bulletin, 24, 390.)
5. P.Ohlin, Dissertation, Uppsala, 1941.
6. G.Brogren, Nova acta Regiae soc.scient.Uppsala, IV, 14, No.4, 1 (1949).
7. A.E.Sandström, Arkiv.fys., 4, H.6, N 36, 517 (1952).
8. V.A.Batyrev & V.G.Bogdanov, Present issue of the Bulletin, p.
9. M.A.Blokhin, Metody rentgeno-spektral'nykh issledovanii (Methods of x-ray spectroscopic investigation), M., 1959.

INVESTIGATION OF THE REGION OF A MICROFOCUS SOURCE IN AN X-RAY MICROANALYZER

- S.A.Ditsman

The development of microfocus x-ray instruments for spectrochemical analysis in microvolumes has raised a number of problems involving the optics of microanalyzers. Among these are proper choice of the method of focusing the radiation on the working surface of the crystal with a view to obtaining the optimum parameters of the microanalyzer, evaluation of the transmission, sensitivity and resolution of the x-ray spectrograph, the distinctive features of reflection of the x-radiation from a microfocus source from bent and plane crystals of different types (quartz, mica, lithium fluoride, organic crystals), etc.

In an earlier paper[1] we discussed some of the distinctive features of reflection of x-rays from a bent crystal in the case of a microfocus source. In the present contribution we consider the region located near the Rowland circle of a bent crystal in the immediate proximity of the microsource.

The particular interest in this region is due primarily to the development of scanning x-ray spectroscopic microanalyzers[2]. The principal purpose of instruments of this type is to obtain a picture of the distribution of a given element over the surface of the specimen, which may measure up to 150 by 150 microns. In order to obtain an undistorted picture of the distribution of the investigated element, it is essential that the conditions of reflection of the radiation from the crystal remain constant (or change very little) with displacement of the electron probe. Whether these conditions are satisfied depends on the choice of the x-ray-optical system of the microanalyzer; they can, for instance, be readily satisfied if one uses a plane crystal as analyzer. In this case displacement of the source relative to the specimen virtually does not change the conditions of reflection from the crystal. However, enhancement of the quality of the image obtained by means of a scanning microanalyzer requires increase of the effective transmission and improvement of the resolution of the spectrograph. These requirements can usually be satisfied by using a bent crystal. This, however, demands special investigation of the variation in the conditions of reflection of the radiation from the crystal with displacement of the microsource. Fundamental in such investigations is determination of the variation in the intensity of the radiation reflected from the crystal as a function of displacement of the microsource in the vicinity of the Rowland circle. In designing the x-ray-optical section of scanning microanalyzers it is essential to know the extent and location of the region wherein the variation in intensity is insignificant.

Investigation of the region within which the investigated radiation will be reflected from the crystal with displacement of the microsource (hereinafter we shall refer to this region as the "microsource region") is also essential from the standpoint of evaluating the accuracy of adjustment of microanalyzers. For obtaining the maximum transmission factor it is also important to know the parameters of the section of the microsource region, corresponding to the maximum intensity of the reflected radiation. Below we shall consider the geometric theory of the microsource region and the results of experimental investigation thereof in the specific case of a spectrograph with a Kapitsa-Johann mounting.

Geometric theory of the microsource region

For the sake of simplicity we shall first investigate the microsource region in the case of a monochromatic point source and an ideal crystal (reflection curve of infinitesimal width), and shall then extend the results to the case of a nonmonochromatic source and an actual crystal. The existence of the microsource re-

gion is due to the persistence of conditions of reflection of the radiation from the crystal with displacement of the source from the Rowland circle of the crystal in the vicinity of point P (Fig.1). The boundaries of the microsource region correspond to displacements of the source to locations for which the conditions of reflection of the radiation from the crystal no longer obtain.

In the work of Ref.1 we investigated the conditions of reflection for a ray originating at point P, lying on the circle of radius $R/2$ and incident on an arbitrary point L (coordinates h, l) on the surface of the crystal curved to a cylinder of radius R. Usually in x-ray spectrographs $l, h \ll R$. We then have the following expression for the glancing angle at the point L on the surface of the crystal:

$$\sin \vartheta_x = \sin \vartheta + \frac{l^2}{2R^2} \operatorname{ctg} \vartheta \cos \vartheta - \frac{h^2}{2R^2 \sin \vartheta}, \qquad (1)$$

where ϑ is the glancing angle of the ray PO at the central point of the crystal. Let us determine the glancing angle ϑ'_x of the ray at the point L upon displacement of the microsource from point P to point F. For small displacements of the microsource, we obtain from general geometric considerations

$$\sin \vartheta'_x = \sin \vartheta_x - \frac{1}{R} (\operatorname{ctg} \vartheta \cdot dx + dy), \qquad (2)$$

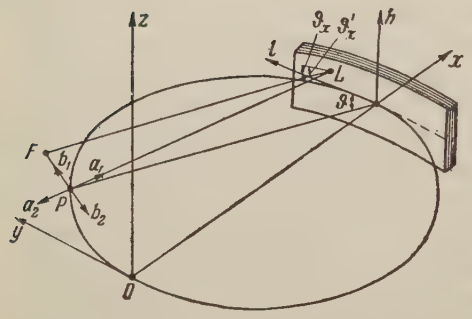

Fig.1. Diagram used for derivation of the equations describing the conditions of reflection of the radiation from a bent crystal with displacement of the microsource from point P.

where dx and dy are the components of the displacement of the microsource. It follows from the last expression that in general displacement of the source leads to change in the conditions of reflection of the ray at the given point on the crystal, i.e., to change in the reflection pattern on the surface of the crystal. Let us find the microsource displacement for which the conditions of reflection do not change significantly. To this end, setting $\vartheta'_x = \vartheta_x$ in (2), we obtain

$$dx = \operatorname{tg} \vartheta dy. \qquad (3)$$

This gives us the displacement of the source for which the reflection pattern on the surface of the crystal does not change.

Let us consider the change in the conditions of reflection of the radiation for the displacements of the source indicated in Fig.1. Determining the components of the displacement for each case from the diagram and introducing them into (2), we obtain

$$\sin \vartheta'_x = \sin \vartheta_x \pm a_{1,2} \frac{l}{R^2 \sin \vartheta}, \qquad (4)$$

$$\sin \vartheta'_x = \sin \vartheta_x \pm \frac{b_{2,1}}{R \sin \vartheta}. \qquad (5)$$

Invoking (1) and setting $\vartheta'_x = \vartheta$, we obtain the equations for the locus of the points of equal glancing angles on the surface of the crystal for the given displacements of the microsource:

$$h^2 = l^2 \cos^2 \vartheta \pm 2a_{1,2} l,$$

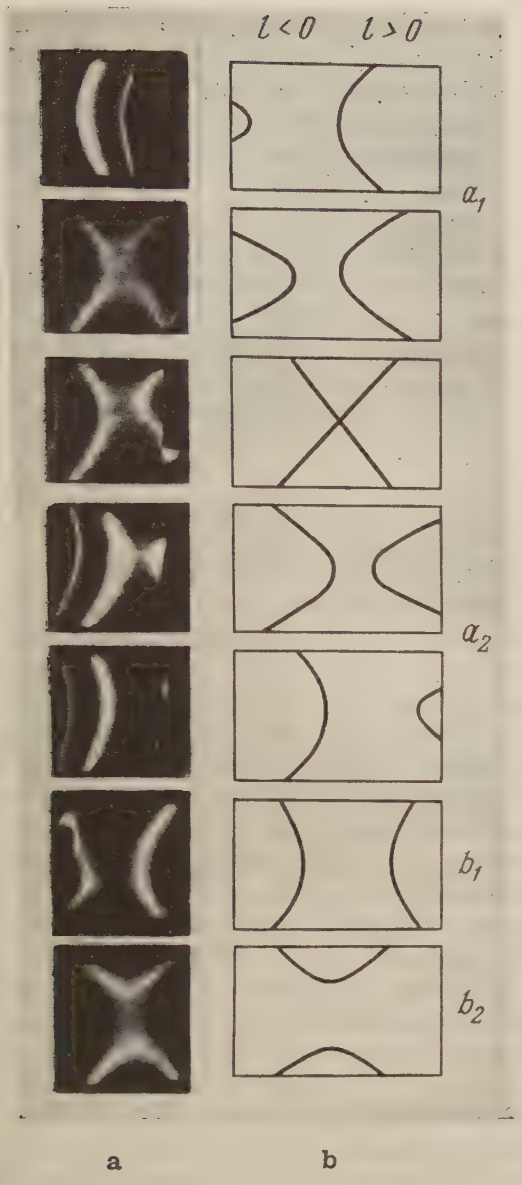

Fig.2. Reflection patterns corresponding to displacements of the microsource, obtained experimentally for Fe $K\alpha_{1,2}$ radiation (a) and from theory (b).

$$h^2 = l^2\cos^2\vartheta \pm 2b_{2,1}R.$$

The first expression characterizes the dependence of the conditions of reflection from the semiplane of the crystal ($l>0$ and $l<0$). The locus of the points for these cases, corresponding to the reflection pattern on the surface of the crystal, is shown in Fig.2,b. It follows from the results that in the case of a type displacements there are always present points near the center of the crystal where there are fulfilled the conditions for reflection of the radiation. The size of the microsource region in this direction is not limited by the dimensions of the crystal. However, in case of displacements of type b the locus of the points shifts outside the boundaries of the working surface of the crystal, thus limiting the size of the microsource region. Let us evaluate the size of region b_1. Now we take into account the nonmonochromaticity of the source and the finite width of the reflection curve of an actual crystal. Using in (5) instead (1), the analogous expression but for the case of a nonmonochromatic source[1], we obtain

$$\sin\vartheta'_x = \sin\vartheta \pm \left(\frac{\Delta\lambda}{\lambda}\operatorname{tg}\vartheta + \frac{r}{R\sin\vartheta} + \frac{\delta}{2}\right) - \frac{b_1}{R\sin\vartheta},$$

whence

$$b_1 = \frac{h^2}{2R} - \frac{l^2}{2R}\cos^2\vartheta \pm \left(\frac{\Delta\lambda}{\lambda}\operatorname{tg}\vartheta + \frac{r}{R\sin\vartheta} + \frac{\delta}{2}\right)R\sin\vartheta.$$

Evaluation of this quantity for $\lambda \approx 2\cdot10^3$ X, $\Delta\lambda \approx 2$ X, $r \approx 10$ μ, $R = 5\cdot10^2$mm, $\delta \approx 10''$ and $\vartheta \approx 20^\circ$ for a crystal with the dimensions $h =$ = 7.5 mm and l = 7.5 mm yields a value of about 100 μ; evaluation of b_2 leads to an analogous result. Thus the full width of the microsource region amounts to ~200 μ, or in the case of a small working surface ($h = l = 0$) to about 100 μ. In the last case the width of the microsource region is determined primarily by the nonmonochromaticity of the investigated line.

One can get a clearer idea of the microsource region by investigating the intensity of the radiation reflected from the crystal as a function of the position of the microsource. It is convenient to present the results of such investigation in the form of a three dimensional figure, where the XOY plane represents the plane of the Rowland circle and the ordinate Z at each point corresponds to the intensity of the reflected radiation with the microsource located at the given point. The maximum intensity of the reflected radiation corresponds to a cruciform reflection pattern on the surface of the crystal (in particular, when the microsource is located at point P), and any change leads to decrease in the intensity of the reflected radiation. On the basis of the above relationship one can form an approximate idea of the cross sections of the three dimensional figure.

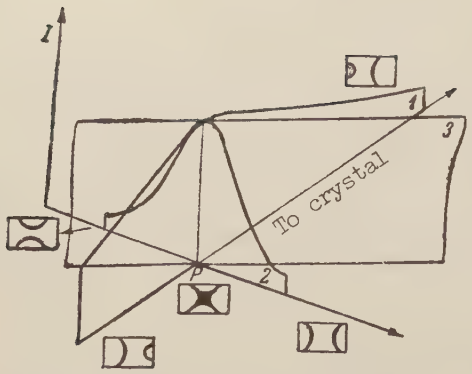

Fig.3. Cross sections of the microsource region and appearance of the corresponding reflection patterns.

Three such cross sections and the corresponding patterns of reflection from the crystal are shown in Fig.3. Cross section 1 is made in the direction a, cross section 2 - in the direction b, and cross section 3 - in the direction given by conditions (3). Cross sections 1 and 2 have a maximum at point P, while cross section 3 is invariant and gives the extent of the microsource region in this direction.

In the above investigation we did not take into account the finite thickness of the reflecting layer on the surface of the crystal; taking this into account can only lead to increase in the size of the microsource region for hard radiation.

Experimental investigation of the microsource region

For experimental investigation of the microsource region we used the equipment described in Ref.3. The electron probe was displaced over the specimen by means of a dc voltage applied to two pairs of deflecting plates, incorporated into the microfocus tube specifically for this purpose. This arrangement made it possible to deflect the electron probe in different directions and set it on any desired spot. The displacements of the probe were also observed visually by means of a microscope.

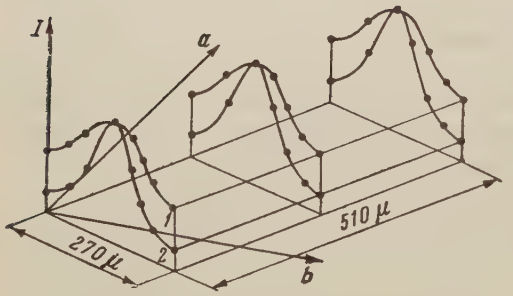

Fig.4. Microsource regions for crystals with working surfaces of different size: 1 - 15 x 15 mm, 2 - 1 x 1 mm.

In our experiments we used Fe $K\alpha_1$ radiation in the second order of reflection from the $(10\bar{1}0)$ planes of a quartz crystal. The radius of curvature of the crystal was 500 mm; the diameter of the microsource about 10 μ.

The results of the experimental investigation of the pattern of reflection from the crystal with displacement of the source in direction a are shown in Fig. 2,a. The maximum displacement equalled 6 mm. These results are in good agreement with the results of theoretical determination of the reflection pattern (Fig.2,b).

Fig.4 shows the shape of the microsource region for different working surfaces of the crystal: 1) $2h = 2l$ = 15 mm and 2) $2h = 2l$ = 1 mm. It will be evident that the size and shape of the microsource region depend on the dimensions of the working surface of the crystal. Thus the width of the region corresponding to half the maximum intensity of the reflected radiation is ~270 μ in the first case, and 130 μ in the second case; this is in agreement with the above evaluation of the size of the microsource region for the case of a small working surface. The microsource region extends over the entire investigated section of the specimen (0.5 x 0.3 mm) and has a clearly pronounced maximum.

Fig.5 shows two sections of the microsource region located at a distance of 2 mm from the point P. It follows from this result that the microsource region has an appreciable size and extends more than 4 mm in the direction given by condition (3).

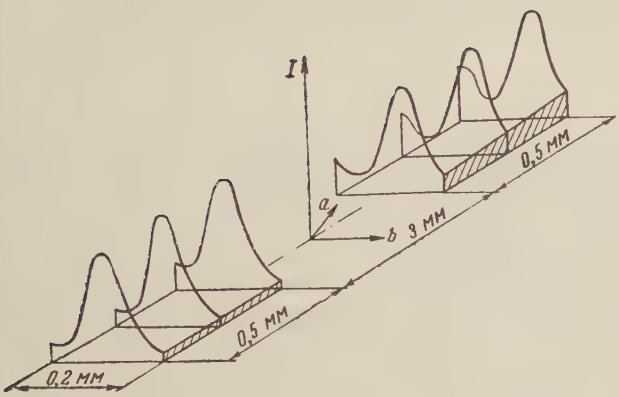

Fig.5. Sections of microsource region.

Of particular interest is determination of the size of the section of the microsource region corresponding to maximum intensity of the radiation reflected from the crystal. Evaluations show that the region of maximum intensity of the reflected radiation for a crystal with dimensions $2h = 2l =$ = 15 mm is less than 20 μ in extent, i.e., is very small compared with the overall size of the microsource region. This section, however, extends at least 0.5 mm in the direction given by the condition (3).

Conclusions

Our experimental and theoretical investigations of the conditions of reflection of radiation from a crystal bent by the method of Kapitsa-Johann showed that with displacement of the microsource from the Rowland circle within the boundaries of a certain region there is obtained acceptable reflection of the radiation. This region has a clearly pronounced section corresponding to maximum intensity of the reflected radiation; under our experimental conditions the dimensions of this maximum intensity section were approximately 20 x 500 μ.

Use of a bent quartz crystal in the x-ray spectrograph of a scanning microanalyzer under the conditions described in the present work is difficult owing to the extremum character of the microsource region. Increase of the region of maximum intensity is feasible by using a larger working surface, but this leads to decrease of the resolution and sensitivity of the instrument.

Evaluation of the accuracy of adjustment of conventional microanalyzers for the purpose of obtaining the maximum intensity of the radiation reflected from the crystal (maximum transmission) shows that the tolerance in matching the radius of curvature of the crystal and the kinematic system of the instrument should not exceed 1 millimeter.

It is not expedient to attempt to investigate the size of the microsource region on the basis of the geometric theory of reflection of radiation from crystals for the cases of focusing of the radiation by the method of DuMond and Johansson. The dimensions and shape of the microsource region, as was shown above, are determined by the character of reflection of the radiation from the crystal. This for the DuMond method of focusing depends on the quality of bending of the crystal and can be taken into account only for ideal curvature of the crystal to a cylindrical surface. This, however, is not realized in practice. Hence in such cases, instead of theoretical analysis, it is expedient to carry out experimental determination of the microsource region.

I desire to express my gratitude to I.B.Borovskii for his interest in the work and helpful discussions.

"A.A.Baikov" Institute of Metallurgy,
Academy of Sciences of the USSR

References

1. S.A.Ditsman, Izv.AN SSSR, Ser.fiz.,24,376 (1960). (Trans.Bulletin, 24, 390.)
2. T.Mulvey, J.Sci.Instr., 36, 150 (1959).
3. S.A.Ditsman, Trudy (Proceedings), Inst.of Metallurgy, No.6, 89 (1960).

ON THE POSSIBILITY OF QUANTITATIVE ANALYSIS BY MEANS OF X-RAY SPECTRA WITHOUT THE USE OF STANDARDS

- N.P. Il'in

The introduction of ionization methods for recording line intensities in x-ray spectra has greatly enhanced the sensitivity and accuracy of quantitative x-ray spectroscopic analysis. There remains, however, one important source of error namely, that involved in calculating the concentration on the basis of the measured line intensities. The complex nature of the variation in the line intensity with conditions of excitation and the composition of the anode material precludes direct evaluation of the concentration from the line intensity; hence in quantitative analyses, the accuracy of determination is determined mainly by the reliability of the external standards and the calibrating procedure employed[1].

In x-ray spectroscopic microanalysis, when it is required to investigate the distribution of all the different elements present in the microstructure of a specimen, the difficulties of the method of external standards increase greatly, inasmuch as it is necessary to provide a large number of standards with a high degree of homogeneity. Preparation of such standards is not easy even for two component systems and for multiple component systems becomes almost impossible.

The correction procedure proposed by Castaing[2] and based on recording the spectrum at different angles of emission of the radiation from the anode does simplify the "standardization" but is complicated and laborious.

The purposes of the present work were to elucidate general regularities governing the variation in intensity of the x-ray lines as a function of the specimen composition and to find a simple correction function that could be calculated on the basis of a few empirical parameters and generally available tabular data.

A typical case of variation of the analytic line intensity as a function of the composition for some standard alloys is illustrated in Fig.1, where the horizontal scale is laid off in concentrations (percent by weight) and the vertical scale in relative intensities of the $K\alpha_1$ line of the element referred to the line intensity for the pure element. Analysis and generalization of the available experimental material for a number of systems led us to the following inferences.

1. Most experimental points lie below the straight line given by $I_{c_i}/I_{e_i} = C_i$, and the deviation from the straight line is the greater the higher the absorption coefficient of the other component for the wavelength of the analytic line.

2. The points for elements that are selectively excited by the radiation from the second component lie consistently above the line.

3. An appreciable difference between the components as regards atomic numbers and densities (for example, Au-Cu and Mo-Be alloys) has less effect than selective absorption and excitation.

Hence the correction function must take into account self-absorption μ of the radiation in the specimen-anode and fluorescence excitation δ_{fl}. One must also take into account the smaller correction A for the variation in depth of penetration of the electrons depending on the anode material.

Hence in general form one can write

$$I_{c_i}/I_{e_i} = C_i f(\mu, A, \delta_{fl}). \qquad (1)$$

Correction for absorption in the specimen

To start, let us consider a two-component system, for example, Ni-Fe, in which the correction for absorption of the radiation in the specimen predominates.

In analysis of a 50% Ni + 50% Fe alloy with reference to the Ni $K\alpha_1$ line there was obtained the intensity ratio $B_{Ni} = I_c/I_{Ni} = 0.34$. Hence the correction function for this alloy $f_1(\mu) = \frac{I_c / I_{Ni}}{C_{Ni}} = \frac{0.34}{0.50} = 0.68$.

It may reasonably be assumed that the function $f_1(\mu)$, taking into account the absorption of the radiation in the specimen, must be exponential ($e^{-\mu x}$), and, taking into account the absorption in the alloy and in the pure element, will be of the form $f_1(\mu) \approx e^{-(\mu_c x_c - \mu_e x_e)}$, where μ_e is the linear absorption coefficient of the Ni $K\alpha_1$ radiation in Ni, and μ_c is the absorption coefficient of Ni $K\alpha_1$ radiation in the alloy. For an alloy of known composition, invoking the law of additivity, we can write

$$\mu_c = \sum_{i=1}^{n} C_i \mu_i,$$

where μ_i can be found directly or by extrapolation from absorption tables for pure elements (for example, Jönsson's tables).

In rigorous calculation of the absorption in the material of the anode one must take into account the absorption in the entire emitting volume of the focal spot, wherein for each point there will be a specific thickness Δx of the absorbing layer. Hence to obtain the total absorption one must integrate over the entire emitting volume, taking into account the variation in electron energy loss with depth and in the case of a microfocus tube with the distance from the center of the beam. It is virtually impossible to carry out such a calculation, particularly taking into account the variation in the material of the specimen-anode.

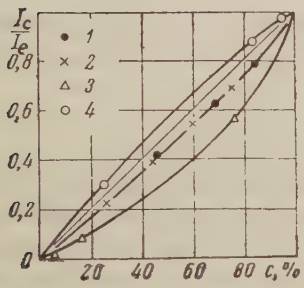

Fig.1

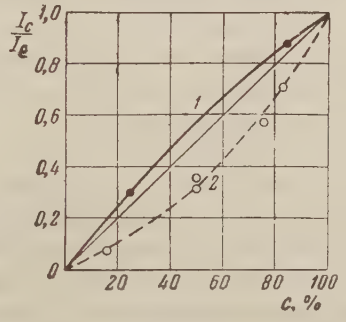

Fig.2

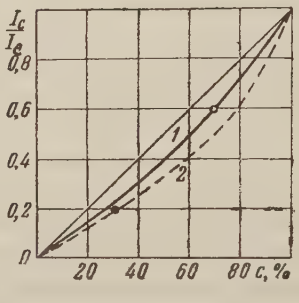

Fig.3

Fig.1. Calibration curves: I_c/I_e versus concentration C. (I_c = line intensity in alloy; I_e = intensity for the pure element.) Experimental points: 1) Mo $K\alpha_1$ line, Mo-Be system; 2) Au $L\alpha_1$ line, Au-Cu system; 3) Ni $K\alpha_1$ line, Ni-Fe system; 4) Fe $K\alpha_1$ line, Ni-Fe system.

Fig.2. Calibration curves for the Ni-Zn system: 1) Ni $K\alpha_1$, 2) Zn $K\alpha_1$.

Fig.3. Calibration curves for the Fe-W system: 1) W $L\alpha_1$, 2) Fe $K\alpha_1$.

Hence we used a different approach: we introduced an "effective" thickness of the absorbing layer $x = d_{ef}$, chosen so that the function $e^{-\mu d_{ef}}$ would give the total attenuation of the analytic line in the working volume of the specimen-anode. As a working hypothesis, we assumed that the effective thickness is inversely proportional to the density of the absorber: $d_{ef} = \text{const}/\rho$. This assumption is upheld by the fact that d_{ef} is related with the total thickness of the emitting layer of the anode, which, according to Widdington's law, for a given accelerating potential is determined by the density of the material. Then $d_1\rho_1 = d_0\rho_0$ or for the case in

question $d_c = d_{Ni}\frac{\rho_{Ni}}{\rho_c}$, where ρ_c is given by the formula $\rho_c = \left(\sum_{i=1}^{n}\frac{C_i}{\rho_i}\right)^{-1}$, which yields good agreement with the experimental data listed in physics handbooks.

On the basis of the above assumptions one can write the following expression for the correction function:

$$f_1(\mu) = e^{-\left[(\mu_{Ni}C_{Ni}+\mu_{Fe}C_{Fe})\left(\frac{C_{Ni}}{\rho_{Ni}}+\frac{C_{Fe}}{\rho_{Fe}}\right)\cdot\rho_{Ni}d_{Ni}-\mu_{Ni}d_{Ni}\right]} = 0.34; \quad (2)$$

whence using the tabular data we can find the argument of the exponential function and obtain $d_{Ni} = 3\cdot10^{-4}$ cm.

Calculations of $B_{Ni} = I_c / I_{Ni}$ for other alloys in the Ni-Fe system by means of the formula

$$I_c / I_{Ni} = C_{Ni}e^{-(\mu_c d_c - \mu_{Ni}d_{Ni})} \quad (3)$$

using $d_{Ni} = 3\cdot10^{-4}$ cm yielded good agreement with experiment. The lowest curve in Fig.1 was calculated by means of Eq.(3).

The parameter $d_{Ni} = 3\cdot10^{-4}$ cm for the function $f_1(\mu)$ was determined experimentally for the given accelerating potential and fixed angles of incidence of the electrons and emergence of the radiation. This parameter takes into account the interaction of electrons of energy E_0 with the matter of the anode, characterized by the density ρ. Hence the relation $d_0\rho_0 = d_i\rho_i$ is valid for any elements and alloys under the same analytic conditions; consequently, one can dispense with the necessity of determining d_i experimentally with reference to some standard alloy, and the correction function for any system of elements can be calculated by using the appropriate tabular data and the parameter $d_0 = d_{Ni} = 3\cdot10^{-4}$ cm in the same way as was done above for the Ni-Fe system. The validity of this procedure for calculating the absorption is illustrated in Figs.1, 2 and 3, which give the calculated $I_c / I_e = C_i f_i(\mu, \rho)$ curves and the experimental points for Ni $K\alpha_1$ (Ni-Fe system), Zn $K\alpha_1$ (Zn-Ni system) and W $L\alpha_1$ (W-Fe system).

Correction for fluorescence

For evaluating the correction for fluorescent excitation of the atoms of the analytic element by the radiation from another element we again turn to the Fe-Ni system in which there is known to be selective excitation of the Fe atoms by the K series radiation of Ni, inasmuch as the Ni lines are located on the short wavelength side of the K absorption edge of Fe.

Using a standard 83% Fe + 17% Ni alloy, we determined $B_{Fe} = I_c / I_{Fe}$ and obtained 0.87. The 4% difference obtained for the iron concentration can be attributed wholly to the effect of excitation of fluorescence: $f_2(\delta_{fl}) = \Delta C_{Fe} = 4\%$. Obviously, the fluorescence contribution for this alloy depends on the number of excited Fe atoms and the number of exciting Ni atoms, i.e.,

$$\delta_{fl} = \beta_{Ni-Fe}a_{Fe}a_{Ni}, \quad (4)$$

where a_{Fe} and a_{Ni} are the atomic concentrations of Fe and Ni, respectively, and β_{Ni-Fe} is the fluorescence coefficient, which should be constant for the given system. Calculation by means of Eq.(4) for the given alloy gives $\beta_{Ni-Fe} = 2.7\cdot10^{-3}$.

The validity of Eq.(4) on the assumption that $\beta = \text{const}$ for the given system can be checked with reference to the data for other alloys in this system. As will be evident from Fig.1, the experimental points fit the calculated curve for Fe.

Let us see what parameters may affect the coefficient β_{Ni-Fe}, which characterizes the probability for emission of a Fe $K\alpha_1$ photon under excitation by the K series radiation of Ni. The coefficient will depend on 1) the number of Ni photons absorbed by the iron atoms, which is characterized by the mass absorption coefficient $\tau^{Fe}_{NiK_\alpha}$, 2) the intensity of the Ni radiation and 3) the fluorescence yield of iron W_{Fe}. The values of $\tau^{Fe}_{NiK_\alpha}$ and W_{Fe} have been tabulated. In evaluating the intensity of the exciting radiation we assume that the main contribution is from the characteristic spectrum, so that we can use tabular data for the relative line intensities.

Hence one can calculate the fluorescence coefficient for any system of elements A—B, using $\beta_{Ni-Fe} = \beta_0 = 2.7 \cdot 10^{-3}$ as the only empirical parameter:

$$\beta_{A-B} = \beta_{Ni-Fe} \frac{\tau_B}{\tau_{Ni}} \cdot \frac{I_A}{I_{Ni}} \cdot \frac{W_B}{W_{Fe}}. \qquad (5)$$

The absolute increment in the intensity of the analytic line of element owing to fluorescence (in atomic percent) is given by

$$\delta^B_{fl} = \beta_{A-B} a_A a_B. \qquad (6)$$

Calculations, using Eqs.(5) and (6), of I_c/I_e for a number of different alloy systems with selective excitation of one of the components yielded good agreement with experiment. By way of illustration in Figs.2 and 3 we reproduce the calculated curves for the Ni-Zn and Fe-W systems in which there is observed strong selective absorption (Zn $K\alpha_1$ and W $L\alpha_1$ radiation) and selective excitation (Ni $K\alpha_1$ and Fe $K\alpha_1$).

In all we investigated 28 alloys in eleven different two-component systems and obtained 47 experimental points. Of these, 39 points (about 85%) fall on the calculated calibration curves (deviation $\leqslant 5\%$).

Conclusions

Proceeding from general physical laws governing the interaction of electrons and characteristic x-radiation with matter, we have deduced formulas for allowing for the variation of the analytic line intensity with the anode material. Using tabular data and the empirical parameters d_0 (effective thickness of the absorbing layer) and β_0 (fluorescence coefficient) one can plot calibration curves (relative line intensity vs concentration) for any element in any two-component system.

The laws of additivity for μ_c and ρ_c, used in deriving our formulas, should make it possible to extend the deductions to multiple-component systems and deduce correction equations for such systems.

"A.A.Baikov" Institute of Metallurgy,
Academy of Sciences of the USSR

References

1. M.A.Blokhin, Metody rentgeno-spektralynykh issledovanii (Methods of x-ray spectroscopic investigation), M., 1959.

2. R.Castaing & Descamps, J.phys.et radium, 16, 304 (1955).

VACUUM X-RAY SPECTROMETER WITH IONIZATION RECORDING

- V.A.Batyrev and V.G.Bogdanov

Investigators of x-ray fine structure have already devoted a great deal of effort to developing spectrometers with ionization recording. One of the main components of such spectrometers is the kinematic system: the mechanical linkages by means of which the various components of the spectrometer are adjusted and aligned. Investigation of x-ray fine structure requires an alignment mechanism which permits accurate measurement of the reflection angle to within a few seconds of arc. It is difficult to attain the requisite accuracy with the common type bent crystal spectrometer,[1] because one must keep track of both the angle of the crystal and the displacement of the counter along the Rowland circle. The accuracy can be enhanced by holding the position of the crystal fixed, while measuring the angle of reflection from the crystal relative to the position of the counter on the Rowland circle. With this arrangement a change of angle always requires resetting all parts of the alignment mechanism to the specified angle of incidence of the x-rays onto the crystal. Consequently, a simple alignment mechanism cannot be used when it is desired to cover a wide range of angles.

To avoid these inadequacies we designed an instrument with a kinematic scheme based on the principle of linear displacement.[2,3] The main features of this mechanism were proposed by I.B.Borovskii in 1953. The instrument was designed and built in the Metallurgical Institute of the Academy of Sciences of the USSR.

The principal features of the mechanism are shown in Fig.1. The crystal and the counter slit are mounted on carriages which are moved in opposite directions along the line AA' by right and left-hand threaded screws. The crystal holder is firmly fastened to a stage which rotates about an axis passing through the center of the crystal. The stage in turn is rigidly attached to the arm OK, which is normal to the line tangent to the center of the crystal. The arm OK, which is the radius of the Rowland circle, terminates with the ball bearing B (Fig.2). Thus, the axis of the ball bearing passes through the center of the Rowland circle. The arm OK is held firmly against the bar EF by a coil spring. Thus the counter slit and the crystal are displaced along a chord of the Rowland circle, always remaining on the circumference thereof. In turning, the arm OK rotates the crystal. The apparatus was designed to work in an angular range from 20° to 70°.

The chief advantage of this arrangement is that the counter is always located on the line AA' and, consequently, with the crystal stationary, the counter always records the intensity of the same wave length. Hence, the accuracy of

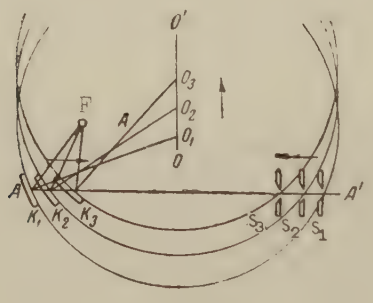

Fig.1

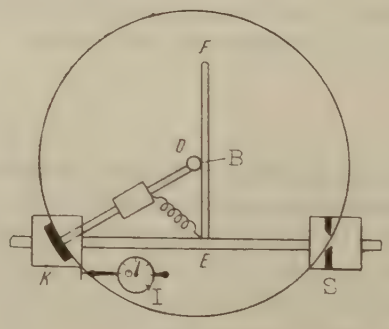

Fig.2

measurement depends only on the precision with which the angle of rotation of the crystal is determined relative to the line AA'. This rotation is measured in terms of the displacement of the crystal along the chord. In our case linear dispersion is a constant of the apparatus. The linear dispersion is given by

$$\frac{\Delta\lambda}{\Delta l} = \frac{4d_n}{nR},$$

where d_n is the lattice constant of the crystal, n is the order of reflection and R is the radius of curvature of the crystal (l is measured along the chord of the Rowland circle). In investigating fine structure, the crystal displacement is determined by means of the micrometric indicator I.

The x-ray tube and the part of the instrument mechanism that moves the crystal are housed in a rectangular vacuum chamber. The chamber has a cylindrical sleeve to accomodate the rod E and the arm OK. A sylphon bellows connects the vacuum chamber with the counter slit. The range of reflection angles from 20° to 70° is covered by using assemblies of three and of five sylphons. The vacuum chamber and the x-ray tube are evacuated simultaneously.

With the above arrangement, the position of the focal spot relative to the line AA' is important. As will be evident from Fig.1, the focal spot must be located in a certain region within the Rowland circle. This region extends about 10 mm in the direction parallel to AA'. Thus if a 10 mm wide x-ray focus is located at this point, the Bragg condition for the angle of incidence of the x-rays onto the crystal will be fulfilled over the working range of angles. However, given the usual limited working surface of a crystal, use of such a broad focal spot would lead to a significant decrease in intensity, because in such cases only part of the focal spot is effectively reflected.

In order to avoid this intensity loss, our apparatus is designed so that the focal spot can be shifted parallel to AA'. To this end, the anode and cathode of the x-ray tube are arranged so that their mutually perpendicular axes are located in the plane of the Rowland circle (Fig.3). The electron beam from the cathode is parallel to AA'. Adjustment of the focusing cap FC sets the desired width of focal spot on the anode. The anode of the x-ray tube can be displaced along its own axis.by means of an externally controlled nut without disturbing the vacuum. Moving the anode changes the position of the focal spot (1 and 2 in Fig.3). By virtue of the fact that in our design the anode is grounded, the focal spot can be adjusted during operation. The tube has a 70 mm wide window, which insures unobstructed exit for the x-rays in the full range of working angles.

The instrument employs a monitor, which permits using an unregulated power supply. The monitor counter is mounted on the wall of the rectangular vacuum chamber. For normal operation, radiation of the same wave length must enter both the main counter and the monitor counter. Therefore a second crystal holder with a plane crystal (Fig.4) is set on the stage of the main crystal, in order to reflect the radiation to the monitor counter. This second crystal has the same lattice constant as the main one. The monitor crystal is displaced somewhat relative to the axis of the main crystal, so to satisfy the Bragg condition it is rotated the appropriate small angle relative to the arm OK. Since accuracy of the order of 1° is adequate for the monitor crystal arrangement, the position of the monitor counter can be held fixed over all angles in the operating range.

A photograph of the spectrometer is reproduced in Fig.5.

The described spectrometer has the following advantages over other extant instruments: 1) it provides for more accurate wavelength measurements; 2) it is characterized by simplicity of adjustment, which consists of determining the radius of curvature of the crystal and setting the appropriate length of the arm

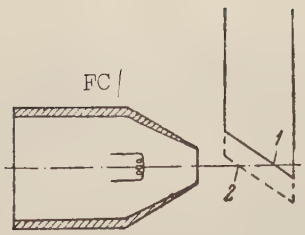

Fig.3

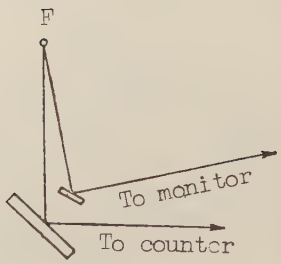

Fig.4

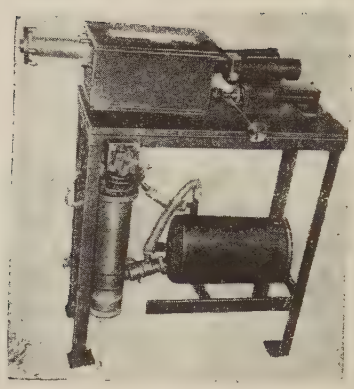

Fig.5

OK; 3) it can be operated with an unregulated power supply; 4) its overall dimensions are minimal.

We desire to express our gratitude to I.B.Borovskii for his valuable advice and help in the accomplishment of the work.

References

1. M.A.Blokhin, Zavodskaya laboratoriya, 16, 941 (1950).
2. P.Ohlin, Dissertation, Uppsala, Sweden (1941).
3. G.Brogren, Nova acta Reg.Soc.Sci.Uppsala, IV, 14, No.4 (1949).

CONSTANT VACUUM X-RAY TUBE FOR A LONG WAVELENGTH X-RAY SPECTROMETER

- K.I.Narbutt, E.M.Fridman & G.M.Nikolaenko

A few years ago we developed a powerful sealed x-ray tube for spectrum analysis[1]; this tube is now being manufactured under the following designations: 5BKhV-1, 5BKhV-2Cu, 5BKhV-2Mo or 5BKhV-2Cr (depending on the target material). These tubes were successfully used in a short wavelength x-ray spectrometers, for fluorescence analysis[2], and in measuring absorption spectra. Introduction of these tubes greatly simplified short wave x-ray spectrometers as compared with previous designs, which used demountable x-ray tubes, and, what is particularly important, made x-ray spectrometers far more reliable in operation.

However, it was still necessary to use demountable x-ray tubes for investigating long wavelength x-ray spectra, including the spectra of many elements commonly determined by x-ray spectroscopic analysis: the rare earths, scandium, titanium, vanadium and others. Moreover, the vacuum part of the demountable tube is usually connected to the evacuated part of the spectrometer. Pumping such a system gives rise to certain difficulties in the course of spectrum analysis. Yet, in the study of the absorption of 3.5 Å x-rays a vacuum of the order of 10^{-2} mm Hg is sufficient in the body of the spectrometer (i.e., a forevacuum), while high vacuum is necessary only in the x-ray tube. This situation has attracted attention for some time, and many researchers have realized a so-called "divided vacuum" even in the Johann mount spectrograph, unsuitable though it is for this purpose, and thereby considerably increased the efficiency of the instrument. However, this type of long wavelength spectrometer still requires a high vacuum pump, and the problem of maintaining high vacuum in the x-ray tube still persists. Hence we felt it would be desirable to obviate the high vacuum problem by using a special constant vacuum x-ray tube. Such a tube is described in the present report.

In designing the tube we tried to meet the following basic requirements:

a) the x-ray tube design must provide for a vacuum-tight seal where the tube envelope enters the evacuated housing of the long wavelength x-ray spectrometer;

b) the tube window must efficiently pass soft x-rays;

c) since the tube is to be used in a Johann mount, the focus of the tube must have the smallest dimensions possible for the rated tube power;

d) the electric parameters of the tube should be 50 kv with a current of up to 100 ma. A section diagram of the long wavelength spectrometer x-ray tube is shown in Fig.1. A steel flange 2 is screwed onto the heavy turned copper base 1. This flange plus the rubber gasket 3 provide a vacuum-tight connection between the x-ray tube and the evacuated housing 4 of the spectrometer, when the window part of the tube is introduced into the spectrometer. There is a threaded hole in the base of the tube for attaching the shielding oil jacket 5. The glass cylinder 7 is sealed to the base by means of the kovar ring 6.

Thorough cooling of the anode and tube base is assured by water circulating through channels drilled and milled in the base of the tube. The cooling water hoses are connected to the nipples 8 screwed into the tube base. As may be seen, the tube has an end window. This window is formed by the beryllium disk 9, the thickness of which does not exceed 0.3 mm in the central area. The anode 10, which is soldered into the base, can be prepared with different specula: copper, tungsten, molybdenum or chromium. The cathode 11 is a cylinder with a tantalum focusing cap 12, which encloses the spiral filament. The cylinder by means of a steel bushing is mounted on the cross-shaped glass stem 13. To protect the anode from tungsten contaminants from the cathode, the spiral cathode is made of thoriated tungsten carbide. Radiation shielding is provided by the lead jacket 14

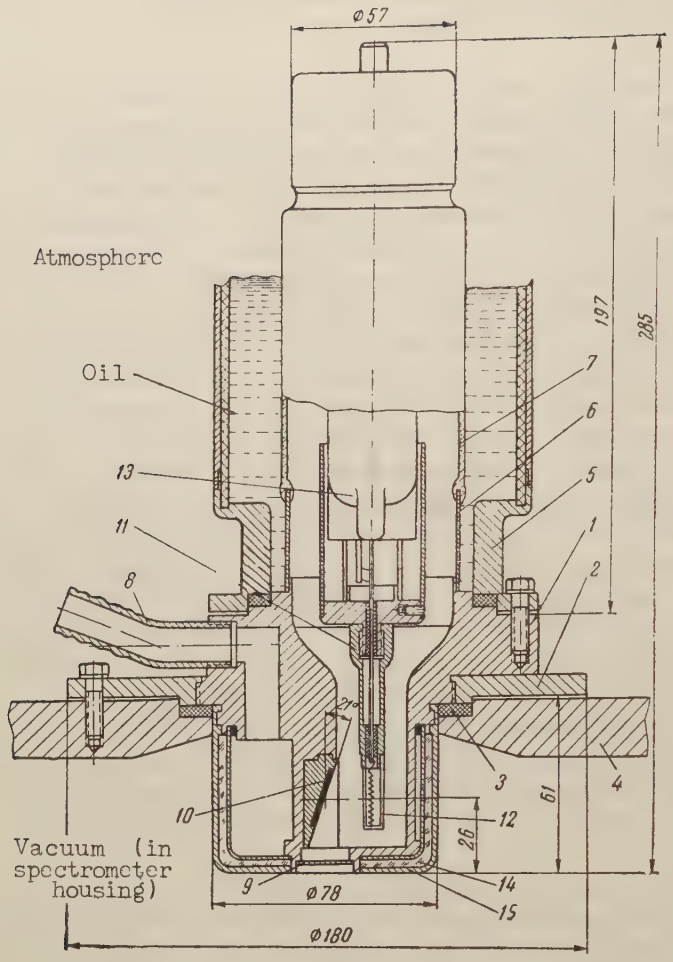

Fig.1. Diagram of the long wavelength x-ray tube.

attached to the base by means of the brass sleeve 15. The cathode neck is mounted on a carbolite base with brass pins.

A general view of the tube is shown in Fig.2. Fig.3 shows the new x-ray tube, designated BKhV5, in its shielding and ready for operation. High voltage is supplied by a high-voltage cable connected through the oil-filled shield. The anode section and the tube base are grounded. Testing of sample tubes has shown that this tube has a 6 x 6 mm focal spot and is reliable under prolonged operation at a power of 5 kva and anode voltage of up to 50 kv.

Tests have shown that the new x-ray tube permits efficient excitation of the L-series fluorescence spectra of the rare earths. Comparative measurements of the efficiency of excitation of the L series x-ray spectrum of lanthanum (the II La $L\alpha_1$ line) were made using the DRUS-3 long wavelength x-ray spectrometer, produced by the Rostov University instrument shop, and a new spectrometer designed by one of us and equipped with our new tube. These tests showed that the new long wavelength x-ray tube has at least tripled the efficiency for excitation of the L emission spectrum of lanthanum. Hence, its use can greatly enhance the sensitivity of x-ray analysis for the rare earths.

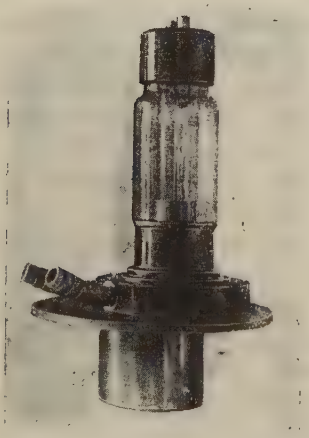

Fig.2. General view of the x-ray tube with the shielding removed.

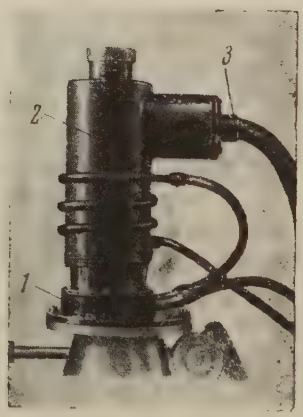

Fig.3. The x-ray tube in its shielding as mounted in the spectrometer: 1) flange of the BKhV5 x-ray tube, 2) oil-filled shield, 3) high voltage cable connector.

References

1. K.I.Narbutt & E. M.Fridman, Izv.AN SSSR, Ser.fiz., 20,136 (1956). (Trans.Bulletin,20,123.)

2. K.I.Narbutt & I.D. Bespalova, Zavodskaya laboratoriya (Industrial Laboratory), 24, 617 (1958).

REFLECTION OF HARD X-RADIATION BY BENT CRYSTALS

- S.A.Ditsman

Bent crystals are commonly employed in x-ray spectrographs and similar instruments for the purpose of increasing the transmission. This, however, leads to distortion of the spectrum (diffraction and geometric distortions), which is particularly undesirable in investigating fine structure of x-ray spectra. Methods of allowing for instrumental distortion have been extensively studied in recent years.[1]

In the present report we consider some of the distinctive features of reflection of hard x-radiation by a bent crystal, features which are connected with the depth of penetration of the radiation into the crystal and which lead to distortion of the spectrum shape. We first consider the distortion in the case of a Kapitsa-Johann mounting with a microfocus source, and then extend the inferences to the case of a wide focus source. We also consider some of the features of focusing of the radiation by the method of DuMond, used in inverted form (Cauchois' method) for investigating hard x-radiation.

Kapitsa-Johann Mounting

In an earlier contribution[2] we investigated reflection on x-radiation by a crystal bent by the method of Kapitsa-Johann for the case of a microfocus source located on the Rowland circle. This investigation was carried out for an infinitely thin crystal, which corresponds to reflection of long wavelength x-radiation essentially from the surface of the crystal, i.e., neglecting penetration of the radiation into the depth of the crystal. The results of experimental investigation of reflection of ~2 Å radiation proved to be in good agreement with the deductions from the geometric theory of reflection of radiation from bent crystals.

Now let us consider the distinctive features of reflection of hard x-radiation from a bent crystal when the crystal cannot be considered infinitely thin. In this case one must take into account the conditions of reflection in the volume of the crystal. For simplicity we shall consider the source to be a point source and the radiation to be monochromatic. The general character of the inferences regarding the conditions of reflection will not be changed in going to nonmonochromatic radiation and a source of finite size.

We assume that the basic condition for reflection is fulfilled for the central point of the crystal (the radiation is incident at the Bragg angle ϑ). Then the glancing angle ϑ_x of the beam at an arbitrary point L on the surface of the crystal will be given by the equality[1]

$$\sin\vartheta_x = \sin\vartheta + \frac{l^2}{2R^2}\operatorname{ctg}\vartheta\cos\vartheta - \frac{h^2}{2R^2\sin\vartheta}, \qquad (1)$$

where h, l are the coordinates of the point L, R is the radius of curvature of the crystal and as usual $h, l \ll R$.

Let us determine the glancing angle ϑ'_x at the point L' in the plane of the crystal located at a depth dR from the surface of the crystal. The change in the glancing angle of the beam PL' relative to the analogous angle for the beam PL (P is the location of the point source) can be found from general geometric considerations and is described by

$$d\vartheta = \frac{dR}{R}\operatorname{ctg}\vartheta. \qquad (2)$$

The glancing angle of the beam at an arbitrary point of the given internal plane will then be given by

$$\sin \vartheta'_x = \sin \vartheta_x + \frac{dR}{R} \operatorname{ctg} \vartheta. \qquad (3)$$

Invoking (1) and setting $\vartheta'_x = \vartheta$ in (3), we obtain the locus of the points of equal glancing angles in the reflecting plane under consideration:

$$h = (l^2 \cos^2 \vartheta + 2R \cos \vartheta \, dR)^{1/2}.$$

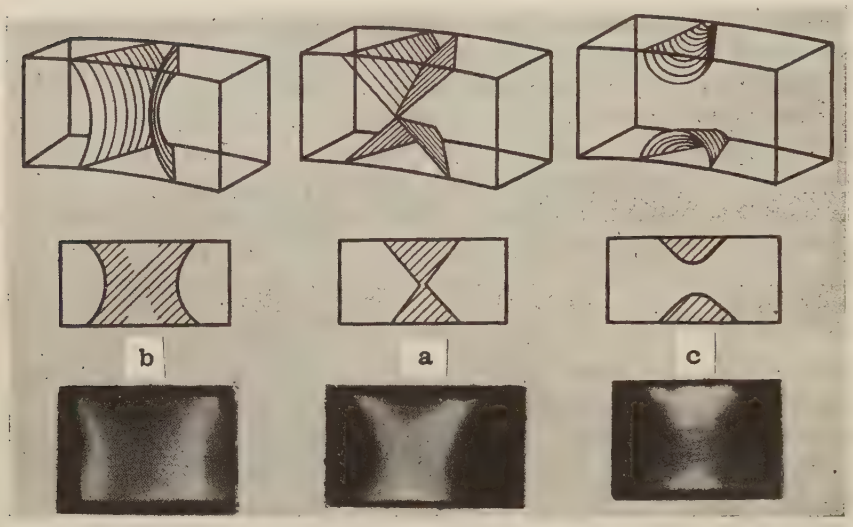

Fig.1. Patterns of reflection of hard radiation from a crystal deduced on the basis of the geometric theory and obtained experimentally for Se $K\alpha_1$ radiation.

Inasmuch as dR ranges from zero to a certain maximum value corresponding to the depth of penetration of the radiation into the crystal, we can distinguish the surfaces in the crystal that reflect the hard radiation. The appearance of these surfaces, their change for different positions of the crystal relative to the microsource and the appearance of the reflection pattern are shown in Fig.1.

Fig.1,a corresponds to the location of the crystal on the Rowland circle, such that the condition for reflection of the radiation is fulfilled for the central point of the crystal; Figs.1,b and c correspond to displacement of the crystal to the short wavelength and long wavelength sides, respectively.

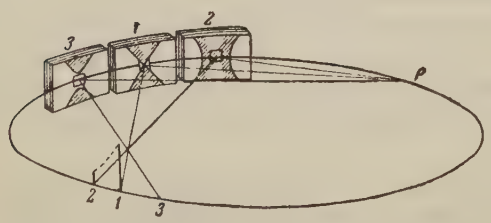

Fig.2. Diagram for investigating reflection of monochromatic radiation in a microfocus spectrograph. P - microfocus source.

To check these deductions we carried out an experimental investigation of the reflection of Se $K\alpha_1$ (λ = 1102.48 X) radiation from the (13$\bar{4}$0) planes of a quartz crystal bent to a radius of 500 mm. The diameter of the microsource was about 10 μ. The results of this investigation are also shown in Fig.1 (photographs) and show good agreement with the reflection patterns predicted by the geometric theory.

These characteristics of reflection of hard radiation must necessarily lead to distortion of the line shape in investigating x-ray spectra on a spectrograph with focusing of the radiation by the Kapitsa-Johann method.

Let us consider the process of reflection of monochromatic radiation in a microfocus x-ray spectrograph (Fig.2). Position 1 of the crystal corresponds to the condition of reflection of the investigated radiation from a small section in the vicinity of the central point of the crystal. The radiation reflected from the crystal enters the detector located at point 1 on the Rowland circle. The intensity of this radiation is shown schematically in the figure. With the crys-

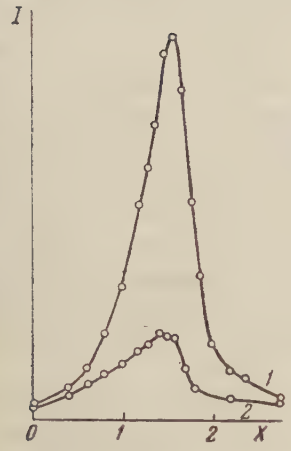

Fig.3. Se $K\alpha_1$ line recorded on a microfocus spectrograph: 1 - $2l$ = = 1.5 mm, symmetry index 0.5; 2 - $2l$ = 0.3 mm, symmetry index 0.35.

tal in position 2 there will also be observed reflection of the radiation from deeper lying layers of the crystal, but with lower intensity. This radiation will be incident at point 2 on the Rowland circle. With the crystal in position 3 there will be no effective reflection of the radiation. Thus monochromatic radiation, for which there should be only one position of the crystal relative to the source and only one point on the Rowland circle for the detector, is actually reflected in an angular interval of crystal displacements, and the reflected radiation forms an image of the line in a certain region of the Rowland circle. This leads to the appearance of short wavelength asymmetry of the investigated line (broadening of the line to the short wavelength side).

The results of investigation of the shape of the Se $K\alpha_1$ line under the above described experimental conditions in a microfocus x-ray spectrograph are shown in Fig.3. It will be seen that the lines are asymmetrical and that the extent of the asymmetry depends on the size of the working surface of the crystal. The index of asymmetry is 0.5 for a working surface of length 1.5 mm, and 0.35 for a working surface of length 0.3 mm (the height of the crystal in both cases was 4 mm). The small size of the surface of the crystal precluded aberration effects, which may also lead to asymmetry of the line to the short wavelength side.

Analogous effects should be observed in the case of a wide-focus radiation source. The results of investigation of the Se and Ge $K\alpha_{1,2}$ lines (1.2 Å) under the same experimental conditions but in a conventional wide focus spectrograph with photographic recording showed that the index of asymmetry of the Se $K\alpha_{1,2}$ line is 0.7 with $2l$ = 2 mm and 0.5 with $2l$ = 1 mm, while the index of asymmetry for the Ge $K\alpha_{1,2}$ line is 0.6 with $2l$ = 2 mm. The Cu $K\alpha_{1,2}$ line proved to be symmetrical with a working surface length of 0.5 mm.

These results show that when a Kapitsa-Johann mounting is used for investigating the fine structure of x-ray spectra in the $\leqslant$1.5 Å region, the structure may be distorted. The magnitude of the distortion will depend both on the wavelength of the radiation and on the size of the working surface of the crystal.

DuMond Mounting

Let us consider some of the features of focusing of x-radiation by the DuMond method in the case of a microsource.

In wide focus x-ray spectroscopy this method in reverse form is known as the method of Cauchois and is widely used for investigating hard radiation.

On the basis of general geometric considerations, one can deduce the expression for the glancing angle of a ray emerging from a microsource on the Rowland circle and incident at an arbitrary point on the surface of the crystal. The expression, which is analogous to Eq.(1) for a Kapitsa-Johann mounting, is

$$\sin\vartheta_x = \sin\vartheta\left(1 - \frac{l^2}{2R^2} - \frac{h^2}{2R^2\cos^2\vartheta}\right), \qquad (4)$$

where ϑ is the glancing angle at the central point of the crystal. Again setting $\vartheta_x = \vartheta$, we find that reflection of monochromatic radiation will occur only from

the central point of the crystal. Cauchois showed that in the case of ideal curvature of the crystal to a cylindrical surface and purely elastic deformation of the crystal the conditions of reflection of the radiation obtaining for its surface should persist unchanged throughout its thickness. Actually, however, experimental studies of the reflection patterns have shown that the observed reflection patterns do not agree with those predicted by theory for a crystal with idea curvature. The appearance of the reflection pattern depends on the quality of th bending of the crystal in the crystal holder. In particular, a typical distortio in the case of a crystal bent in a four-knife-edge holder is twisting. This distortion always occurs owing to the fact that in practice it is impossible to make all four knife-edges strictly parallel. The character of the distortion in the case of a crystal bent in a crystal holder with ground surfaces is even more comples, inasmuch as it depends on chance factors.[3]

In the DuMond mounting insignificant deformations of the crystal lead to coordinal change in the conditions of reflection as compared with the conditions fo ideally curved crystal.

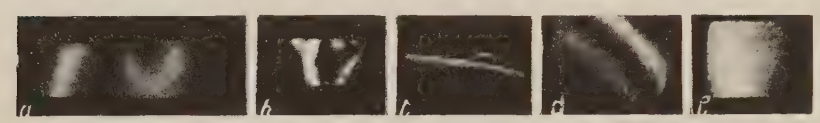

Fig.4. Reflection patterns of Cu $K\alpha_{1,2}$ radiation for a DuMond mounting: a & b - crystal bent in a crystal holder with ground surfaces; c,d & e - in a crystal holder with four knife-edges adjusted to produce different degrees of torsion.

Fig.4 shows the patterns obtained for reflection of Cu $K\alpha_{1,2}$ radiation from the $(10\bar{1}0)$ planes of a quartz crystal bent to a radius of 300 mm. The photographs were made in the spectrograph described in Ref.4. Photographs 4, a & b were recorded using a crystal holder with grou surfaces. Photographs 4,c,d & e were obtained with different degrees of torsion of the crystal in a special crystal holder with four knife-edges. Photograph 4,c was obtained for a crystal with a noticeable degree of torsion; photograph 4,d fo a crystal with almost unnoticeable torsion and photograph 4,e for a crystal adjusted to the best possible degree. It will be seen that in no case was there ob tained a reflection pattern corresponding to that for an ideally bent crystal.

Conclusions

Investigation of the reflection of radiation in the $\lesssim$1.5 Å range in the case of a Kapitsa-Johann mounting showed that the depth of penetration of the radiatio into the crystal has a substantial effect on the results of spectroscopic studies In particular, it leads to distortion of the line shape, consisting mainly of short wavelength asymmetry.

Investigation of reflection of hard x-radiation in a DuMond mounting with a microfocus source showed that the conditions of reflection depend greatly on the quality of bending of the crystal. This greatly complicates determination of the influence of the depth of penetration of the radiation into the crystal on the line shape. One may also expect strong dependence of the conditions of reflectio on the quality of bending of the crystal in the case of focusing by the method of Johansson, which requires ideal grinding of the holder and curvature of the crystal precisely to a cylindrical surface.

On the whole, the Kapitsa-Johann method of focusing is probably the least sensitive to small distortions in adjustment of the crystal.

I desire to thank I.B.Borovskii for valuable suggestions and helpful discussions.

"A.A.Baikov" Institute of Metallurgy,
Academy of Sciences of the USSR

References

1. M.A.Blokhin, Metody rentgeno-spektral'nykh issledovanii (Methods of x-ray spectroscopic investigation), M., 1959.

2. S.A.Ditsman,Izv.AN SSSR, Ser.fiz., 24, 376 (1960). (Trans.Bulletin, 24, 390.)

3. E.E.Vainshtein, K.I.Narbutt & A.B.Gil'barg, Trudy (Proceedings), Institute of Crystallography, USSR Ac.of Sci., 6, 207 (1951).

4. N.P.Il'in, Trudy (Proceedings), Institute of Metallurgy, No.6, 97 (1960).

REGARDING THE RESOLUTION OF JOHANN MOUNTING SINGLE-CRYSTAL SPECTROGRAPHS

- N.D.Borisov & V.V.Nemoshkalenko

The principal factors determining the possibilities of experimental investigation of the fine structure of x-ray spectra with a view to elucidating the electronic structure of metals and alloys are high resolution of the instrument and a reliable procedure for allowing for distortion of the line shape. Whereas a great deal of attention has been given to the latter factor[1-17], the importance of the former has frequently been glossed over. In fact there are cases when this factor is entirely ignored despite the fact that in focusing spectrographs the experimental line width is determined not only by the intrinsic width but by a number of other factors such as the geometric conditions of focusing, defects in the analyzer crystal, the depth of penetration of the radiation into the crystal, etc.

Line broadenings connected with geometric conditions include $B_1 = \frac{O^2}{16r} \operatorname{ctg} \varphi$, the line broadening connected with inaccuracy of focusing of the rays at the point of observation, $B_2 = \frac{l^2}{4r} \operatorname{ctg} \varphi$, the broadening connected with vertical divergence of the beam, and $B_3 = \alpha \operatorname{ctg} \varphi$, line broadening due to oblique incidence of the beam on the photographic film.

It can be shown that for a Johann type spectrograph with a focal circle of radius r = 250 mm, a working section of the crystal O = 14 mm, height of the crystal $2l$ = 6 mm and thickness of the emulsion layer α = 0.0125 mm, the values of the above quantities for a Bragg angle $\varphi = 61.7^{\circ}$ are B_1 = 0.00216 mm, B_2 = 0.00485 mm and B_3 = 0.00675 mm. For the purpose of reducing the broadening of the spectrum lines connected with vertical divergence of the beam and oblique incidence of the rays on the photographic film, in investigations concerned with the fine structure of x-ray bands the height of crystals is generally limited to 4-6 mm and the spectrum is recorded at large angles of incidence (up to 90°).

Taking these factors into account leads to enhancement of the resolution of x-ray spectrographs. On the other hand, the recent tendency to increase the transmission factor of spectrographs with bent crystals by increasing the size of the working area of the crystal leads to impairment of the resolution and hence is not acceptable from the standpoint of the needs of experimenters interested in investigation of fine structure.

Below we give the calculated values of the resolution $\lambda/\Delta\lambda_{min}$ of a Johann mount spectrograph as a function of the extent O of the working section of the crystal (in the calculations it was assumed that r = 250 mm, B_2 = 0.00485, B_3 = = 0.00674 mm and $\varphi = 61.7^{\circ}$):

O,mm	1,0	2,0	3,0	4,0	5,0	10,0	20,0	30,0	40,0
$\lambda/\Delta\lambda_{min}$	79 018	76 385	72 364	67 397	61 933	36 960	14 145	7 633	4 297

The importance of using small crystals for enhancing the resolution of instruments used in investigating fine structure has been demonstrated in Refs.19, 20, & 21. Taking account of this factor, i.e., using crystals with a small working area, does allow of enhancing the resolution of Johann type spectrographs.

The resolution of single crystal spectrographs, which are now predominantly used in Soviet laboratories for investigating the fine structure of x-ray spectra does not exceed 5000 to 10 000, which, as follows from the data in the accompanying table, is greatly inferior to the resolution obtainable with two-crystal

Line	Reflecting planes of quartz crystal	$\lambda/\Delta\lambda_{min}$	Author
TiK_{α_1}	$(11\bar{2}0)$	36 572	Parratt
FeK_{α_1}	$(11\bar{2}0)$	48 301	Brogren
MoK_{α_1}	$(11\bar{2}0)$ $(11\bar{2}0)$	24 407 26 216	Parratt Brogren
CuK_{α_1}	$(11\bar{2}0)$ $(20\bar{2}3)$ $(22\bar{4}0)$	38 435 153 740 153 740	Brogren Brogren Brogren

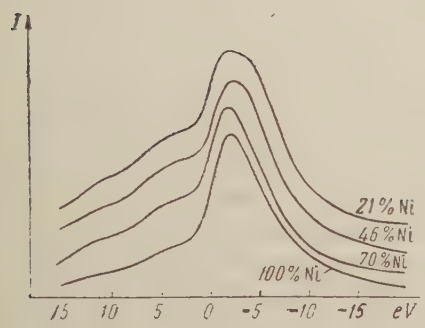

Fig.1

spectrometers. The tendency to increase the luminosity of single crystal spectrometers leads to loss of detail of the fine structure and overoptimistic evaluation of the possibilities of allowing for distortion of the line shape.

Fig.1 shows the shape of the Ni K_{β_5} band obtained under conditions of inadequate resolution of the instrument[22]; Fig.2 shows the shape of the same band recorded by us under conditions of optimum linear dispersion. The presence of the two satellites on the short wavelength side of the Ni K_{β_5} band in the first case cannot be established even with the aid of the most refined techniques for allowing for distortion of the spectrum shape.

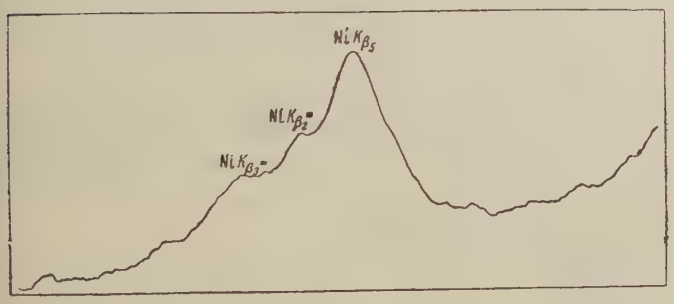

Fig.2

To illustrate the significance of proper choice of the experimental conditions for investigation of the fine structure of the Cr K_{β_5} emission band on a single crystal Johann mounting spectrograph[23] and determination of the resolution of the instrument we can cite the following initial data and results of calculations.

On the basis of the fact that the resolution of spectrographs is proportional to tan φ, where φ is the Bragg angle, we arrive at the choice of a quartz crystal with reflection from the $(13\bar{4}0)$ planes as the analyzer. In this case the linear dispersion in the region of reflection of the Cr K_{β_5} band ($\varphi = 61.7^{\circ}$) is 2.23 X/mm or 6.61 ev/mm.

In photometry of the experimental spectrograms it proved feasible to measure the width of the Cr K_{β_5} band with an accuracy of ±0.01 mm, which corresponds to a resolution of the order of 93 000:

$$R_{\lambda} = \frac{\lambda_{CrK_{\beta_5}}}{\Delta\lambda_{min}} = \frac{2066.53}{0.0223} \approx 93\,000.$$

Experimental selection of the size of the working section of the crystal was

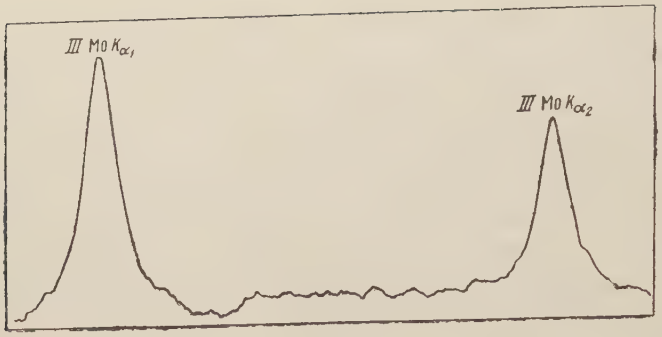

Fig.3

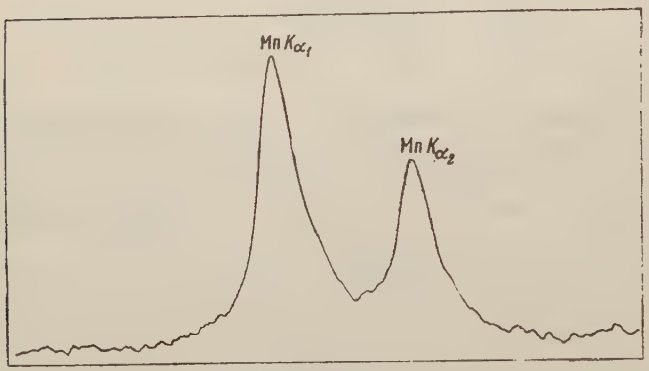

Fig.4

carried out with reference to standard spectrum lines of known widths. In view of mosaicity of the crystal, imperfections of the crystal lattice and the requirements of adjustment, as well as the necessity of providing a reasonably short exposure time, the size of the working section of the crystal was taken equal to 4 mm. The radius of curvature of the crystal after adjustment proved to be 488.99 mm.

The resolution of the spectrograph was determined by comparison of the widths of the Mo $K_{\alpha_{1_{III}}}$ and Mn $K_{\alpha_{1_I}}$ lines with the data obtained on two-crystal spectrometers. We took into account the circumstance that the Mo K_{α_1} line recorded on a two-crystal spectrometer allows of determining the true line width w_T by means of the formula[24] $w_T = w_0 - w_c$, where w_0 is the width of the line in the (1 + 1) position and w_c is the line width in the (1 - 1) position. In the case of the Mn K_{α_1} line, owing to its asymmetry, the determination of the true line width can only be made in the first approximation. For the same reason and in the same approximation by way of reference line one can also use the K_α lines of other elements of the iron group.

In the given case in investigating the structure of the Cr K_{β_5} band we deemed it feasible to use as the reference lines both the Mo $K_{\alpha_{1_{III}}}$ line and the Mn $K_{\alpha_{1_I}}$ line and to compare the results with each other. The data obtained are given below.

1. Evaluation of the resolution with reference to the Mo $K_{\alpha_{1_{III}}}$ line. Fig.3 shows the trace of the Mo $K_{\alpha_{1_{III}}}$ line recorded on an MF-4 microdensitometer (magnification 20 to 1). The index of asymmetry of this line is 1.0; its width is 0.29 X. According to the data of Brogren[24], the true width of the Mo K_{α_1} line is 0.24 X. Hence in this case the resolution of the instrument is

$$R_\lambda = \frac{\lambda}{\Delta\lambda_{min}} = \frac{3 \times 707{,}831}{0{,}05} = 42\,470.$$

2. Calculation of the resolution with reference to the Mn $K_{\alpha_{1_I}}$ line. The microphotometric trace of this line recorded under the same conditions is shown in Fig.4. Here the index of asymmetry is 1.5, and the line width is 2.61 ev. According to the data of Brogren[24], the width of the Mn K_{α_1} is 2.46 ev. Hence in this case the resolution of the instrument is

$$R_\lambda = \frac{\lambda}{\Delta\lambda_{min}} = \frac{2097{,}51}{0{,}053} = 39\,576.$$

All the above observations apply equally to Cauchois type spectrographs.

Accordingly, we recommend that all reports on investigations of the fine structure of x-ray spectra should include experimental data on the resolution of the instrument employed.

Institute of Metal Physics,
Academy of Sciences of the Ukrainian SSR

References

1. R.C.Spenser, Phys.Rev., 38, 618 (1931).
2. P.H.Cittert, Z.Phys., 69, 298 (1931).
3. H.C.Burger & P.H.Cittert, Ibid., 79, 722 (1932).
4. L.S.Ornstein & W.R.Wuk, Ibid., 78, 734 (1932).
5. L.P.Smith, Phys.Rev., 46, 343 (1934).
6. P.P.Shorygin, Zhur.tekh.fiz., 15, 1072 (1941).
7. E.E.Vainshtein, Uspekhi khimii, 15, No.3, 269 (1946).
8. V.M.Chulanovskii & A.V.Timofeva, Izv.AN SSSR, Ser.fiz., 11, 376 (1947).
9. M.M.Sushchinskii, Zhur.eksp.i teor.fiz., 25, 87 (1953).
10. I.V.Peisakhson, Izv.AN SSSR, Ser.fiz., 18, 680 (1954). (Trans.Bulletin, 18, 363.)
11. I.V.Peisakhson, Vestnik, Leningrad State University, No.5, 129 (1955).
12. A.R.Stokes, Proc.Phys.Soc., 61, 382 (1948).
13. R.N.Bracewell, Astr.J.Phys., 8, 61 (1955).
14. M.A.Blokhin, Doklady AN SSSR, 107, 33 (1956). (Trans.Doklady.)
15. M.A.Blokhin, Ibid., 107, 229 (1956). (Trans.Ibid.)
16. M.A.Blokhin, Izv.AN SSSR, Ser.fiz., 20, 142 (1957). (Trans.Bulletin, 20, 127.)
17. I.Ya.Nikiforov, Ibid., 21, 1362 (1957). (Trans.Bulletin, 21, 1351.)
18. G.Brogren, Arkiv fys., 8, 391 (1954).
19. J.J.Bäckobsky, Phys., 9, 471 (1938).
20. D.B.Gogoberidze, Zhur.eksp.i teor.fiz., 10, 96 (1940).
21. N.D.Borisov, Trudy (Proceedings), Inst.of Ferrous Metallurgy, Pub.Ukrainian SSR Ac.of Sci., 6, 110 (1953).
22. H.Friedmann & W.Beeman, Phys.Rev., 58, 400 (1940).
23. N.D.Borisov & Ya.M.Fogel', Zhur.tekh.fiz., 7, 164 (1937); Inventor's Certificate No.45,749. 31, I, 1936.
24. G.Brogren, Arkiv.fys., 8, 391 (1954).
25. M.A.Blokhin & V.P.Sachenko, Izv.AN SSSR, Ser.fiz., 21, 1343 (1957). (Trans.Bulletin, 21, 1333.)

EXPERIMENTAL INVESTIGATION AND CALCULATION OF THE L ABSORPTION SPECTRA OF NOBLE GASES

- R.L.Barinskii

In earlier contributions[1,2] the writer in collaboration with Nadzhakov developed a method for calculating the K absorption spectra of atoms bound in compounds in different states of aggregation. Use of this method enabled us to determine the effective charge and radius of the bound atoms and thus arrive at a characterization of the chemical bonds involved.

However, use of the K absorption spectra for investigating the type of chemical bonds in molecules is feasible only for elements with $Z \leqslant 30$-35. Where the atoms of heavier elements are concerned there arise serious experimental difficulties connected with marked increase in the width of the K state and deterioration of the dispersion in the corresponding (high energy) region of the spectrum. Hence for investigating the type of bonds in compounds consisting of relatively heavy atoms it is more expedient to use the L absorption spectra. Most convenient of these are the L_{III} spectra inasmuch as the L_{III} absorption discontinuity is greater and the width of the L_{III} state is smaller than in the case of the L_I and L_{II} spectra. Hence the L_{III} spectrum can be obtained more easily and is characterized by a more distinct fine structure.

In contrast to the K spectra, the L_{III} absorption spectra of atoms appear incident to transition of electrons from an initial p symmetry orbit; hence the symmetry of the final states will be s and d. The method proposed in Refs.1 & 2 can be applied to calculation of the L_{III} absorption spectra of atoms of non-transition elements in molecules of gases and crystalline complexes. In the hydrogen-like approximation (exciton absorption mechanism) all the formulas used for calculation of the K spectra[2] retain their validity except the expression for the ratio of the intensities of the first absorption line and the continuous absorption. In the case of L_{III} spectra this formula must be replaced by formulas for the probability of transition of an L_{III} electron to s and d orbits. The derivation of these formulas is analogous to the derivation of the K spectrum formula in Ref.1. The derivation is based on the use of hydrogen-like functions: $2p$ functions for the initial state and nd and ns functions for the final state. The final expressions are of the form

$$\frac{\tau_n^d}{\tau_\infty^d} = \frac{4\eta^2}{\pi\Gamma_d} \cdot \frac{(n_d^2-1)(n_d^2-4)}{n_d^7}, \qquad (1)$$

$$\frac{\tau_n^s}{\tau_\infty^s} = \frac{4\eta^2}{\pi\Gamma_s} \cdot \frac{1}{n_s^2}, \qquad (2)$$

where τ_n^d and τ_n^s are the absorption coefficients associated with transition of an L_{III} electron to orbits of nd and ns symmetry, respectively, τ_∞^d and τ_∞^s are the coefficients of absorption associated with transition to the continuum, η is the effective charge of the absorbing atom, Γ is the width of the absorption lines and true edge and n_d and n_s are the effective principal quantum numbers for the d and s orbits.

It will be evident from Eq.(1) that the value of the effective quantum number n_d cannot be smaller than 2. It follows that for the same values of η and Γ as in the K spectrum, the ratio of the height of the first absorption line to the height of the true edge and the extent of the Rydberg series in the L_{III} spectrum will be smaller than in the K spectrum. This means that the structure of the L_{III} absorption spectrum will be less clearly defined than the structure of the K spectrum.

Equations (1) and (2) do not allow of determining the ratio of the transition probabilities for an L_{III} electron to the d and s states. Inasmuch as in

the L_{III} absorption spectrum there are present states of both types of symmetry, knowledge of this ratio is in general necessary for calculating the L_{III} absorption curve. The magnitude of the ratio $\tau_\infty^d / \tau_\infty^s$ can be calculated by means of hydrogen-like functions following the procedure described in Ref.1. There is obtained the equation

$$\frac{\tau_\infty^d}{\tau_\infty^s} \approx 30\left(\frac{\eta}{Z}\right)^5, \qquad (3)$$

where Z is the atomic number of the absorbing atom. It will be evident from Eq. (3) that the probability for transition to d orbits is higher than the probability for transition to s orbits. With increase of Z this difference decreases; however, the degree of Z here is apparently too great, as is usually the case in calculations employing hydrogen-like functions. In any case, for not excessively large Z, absorption with transition to a d state is characterized by an appreciably higher probability, i.e., the L_{III} absorption spectrum reflects mainly the structure of the d levels.

In order to check the applicability of the above-mentioned method of calculating the L_{III} absorption spectra it is most expedient to use the L_{III} spectra of the noble gases. The absorption spectra of argon, krypton and xenon have been investigated by Prins[3] and Brogen[4]. Prins' results, however, were obtained on an instrument with inadequate resolution, employing a recording method of questionable accuracy. Hence, we investigated the L_{III} absorption spectra of krypton and xenon anew.

The spectra were recorded photographically on a Johann type spectrograph with a quartz crystal bent to a radius of 500 mm. The potential on the x-ray tube did not exceed twice the excitation potential of the respective gases. The current through the tube was 50 ma. Both the anode and the tube filament were of tungsten. The gases were admitted to the spectrograph tank at a pressure of 2 mm Hg in the case of krypton and 4 mm Hg in the case of xenon. The x-ray tube window was isolated from the spectrograph tank by a beryllium foil 70 μ thick or a "lavsan" film 5 μ thick. The spectra were recorded on positive motion

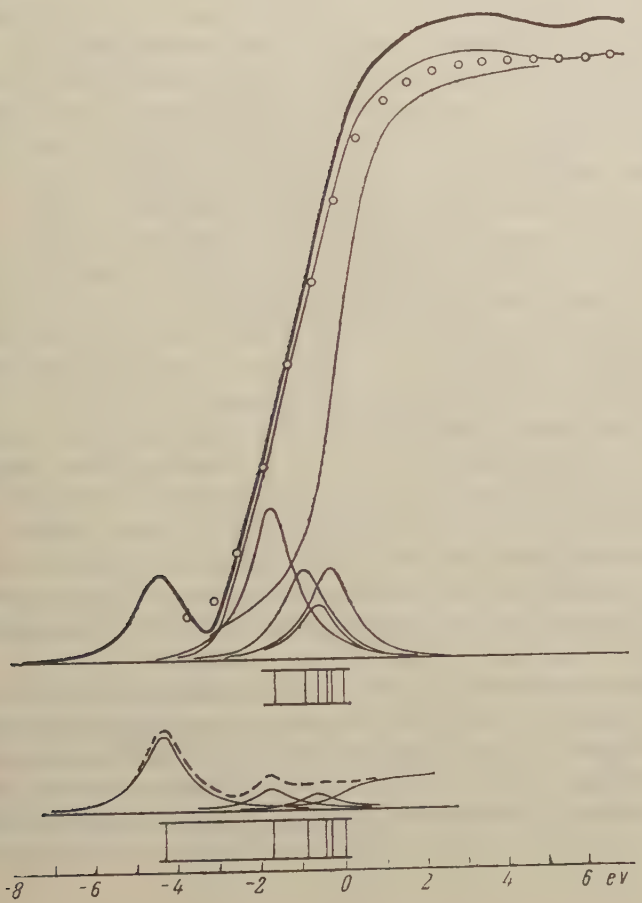

Fig.1. L_{III} absorption spectrum of argon. Heavy solid lines - experimental curve; light solid line - result of subtraction of the s series from the experimental curve; the light lines also indicate the true edge and the absorption lines; dashed lines - sum of the s series; the circle points give the results of synthesis of the d series; the vertical lines indicate the locations of the lines and true edge.

picture film in the first order for krypton and in the third order for xenon. The exposure time varied from 3 to 6 hours.

The spectrograms were scanned (visually) on an MF-4 microphotometer with subsequent averaging of the results of individual series of measurements. The error in evaluating densities did not exceed 2% relative to the height of the spectrum. The dispersion in recording the krypton spectrum was 8.59 X/mm (1.96 ev/mm), and in recording the xenon spectrum 2.24 X/mm (4.12 ev/mm).

The L_{III} absorption spectrum of argon taken from the work of Prins[3] is reproduced in Fig.1. The horizontal scale is laid off in electron volts; the ordinates are proportional to the absorption coefficient. The results of our investigation of the L_{III} absorption spectra of krypton and xenon are given in the upper halves of Figs.2 & 3 (solid heavy lines).

The L_{III} absorption spectra of all three noble gases were calculated in the same way; hence here we shall only describe the calculations for argon. The first absorption line in this spectrum corresponds to the $L_{III}-4s$ transition, inasmuch as in the process of L_{III} absorption the argon atom may be assimilated to the calcium atom in which the lowest lying level is the $4s$ level. The value of the effective quantum number for the ns state of calcium is known from the optical spectrum: $n_s = 1.77$. Knowing the values of Γ_4^s and τ_4^s from the x-ray spectrum (Fig.1) and assuming $\eta = 1$, one can find τ_∞^s for the ns series of argon by means of Eq.(2). Then one can calculate and plot the entire absorption line series and the true edge using the Rydberg formula for the location (wavelength) of the successive lines, the dispersion formula for their states and the arc tangent formula for the shape of the true edge (see Ref.2). The ratio of the heights of the successive lines is found by means of (2). The results of such calculations and plotting are shown in the lower half of Fig.1.

Then, if from the experimental L_{III} absorption curve for argon one subtracts the sum of the ns line series and true edge (dashed line in the upper half of Fig.1), there is obtained a remainder (light solid line in upper half of Fig.1) which is due to transition of L_{III} electrons to d orbits. It is found that the absorption coefficient ratio $\tau_\infty^d/\tau_\infty^s \approx 17$, which agrees in order of magnitude with the results of theoretical calculations (Eq.(3)).

The main part of the absorption curve associated with transition of L_{III} electrons to nd atomic orbits can be calculated if we know τ_∞^d from the x-ray spectrum, $n_d = 2.85$ from the optical spectrum of calcium and set $\Gamma_{nd} = \Gamma_{ns}$ and $\eta = 1$. Then by means of Eq.(1) one can find τ_3^d and then synthesize the entire "d curve", using the same formulas as for plotting the "s curve". The ratio of the height of successive absorption lines is now given by Eq.(1). The results of such synthesis are shown in the upper half of Fig.1 by the circle points.

As noted above, we used the same procedure for calculating the L_{III} absorption spectra of krypton and xenon. Where L_{III} absorption is concerned the atoms of krypton and xenon may be assimilated to rubidium and cesium atoms, respectively; accordingly, the requisite data were taken from the optical spectra of Rb and Cs. These data are listed in the accompanying table together with the results of calculations of the L_{III} spectra (also see Figs.2 & 3).

Parameter	Argon	Krypton	Xenon
n_d	2,85	2,77	2,55
n_s	1,77	1,805	1,87
Γ, ev	1,2	1,2	2,6
η	1	1	1
$\tau_\infty^d/\tau_\infty^s$	17	9	5

The character of the fine structure of the L_{III} absorption spectra of the investigated noble gases substantiate the general regularities following from Eqs.(1) and (3). The fine structure is less clearly pronounced in the L_{III} spectra than in the K spectra, which is particularly clearly

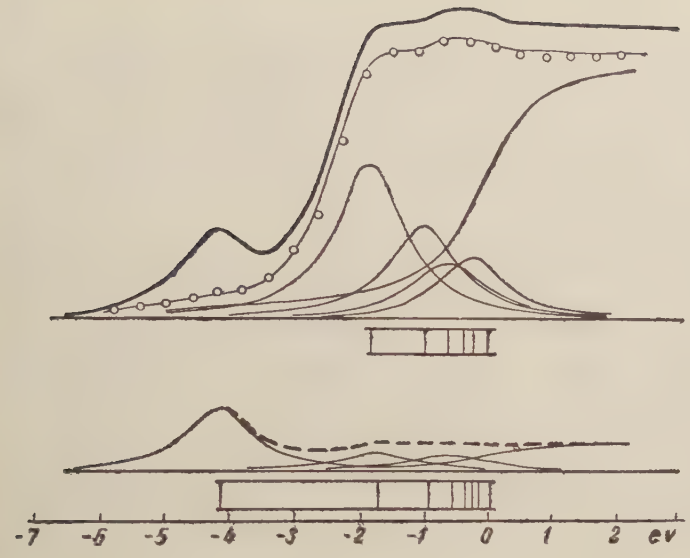

Fig.2. L_{III} absorption spectrum of krypton. Designations same as in Fig.1.

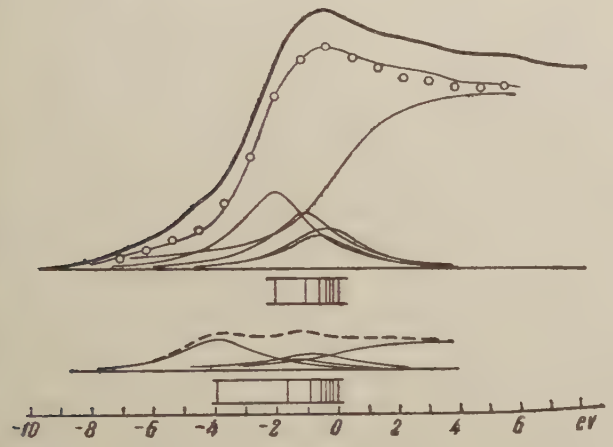

Fig.3. L_{III} absorption spectrum of xenon. Designations same as in Fig.1.

evident from comparison of the respective spectra of argon reproduced in Fig.1 of the present article and in Ref.1. Moreover, the ratio $\tau_\infty^d/\tau_\infty^s$ in the L_{III} spectra of the noble gases decreases from ~17 for argon to ~9 for krypton and to ~5 for xenon, i.e., is inversely proportional to Z. However, the ratio τ_n^d/τ_∞^d calculated by means of Eq.(1) does not agree with the experimental data for krypton and xenon. In order to obtain agreement with experiment one must increase this ratio by a factor of 2 for krypton and 3 for xenon. This means that the right-hand part of (1) must be multiplied by Z/k, where $k \approx 20$; this was done in calculating the spectra of krypton and xenon. In order to justify and explain this, further refinement of the theory is necessary.

The widths of the absorption lines in the L_{III} spectra of krypton and xenon (without taking into account apparatus distortion) are 1.2 and 2.6 ev, respectively. The widths of the L_{III} levels of krypton and xenon, according to the data of Parratt[5], are 1.1 and 2.8 ev (the last figure was obtained by interpolation). If Parratt's value for krypton is correct, the apparatus broadening in the 7 Å region in our case is 10%. However, the smaller experimental value for the width of the xenon line (as compared to Parratt's figure) indicates that Parratt's data are overestimates.

Application to the L_{III} spectra of the transition elements

The above results of investigation and calculation of the fine structure of the L_{III} absorption spectra of the noble gases can be utilized for explaining the specific features observed in the L_{III} absorption spectra of transition atoms bound in chemical compounds. The presence in these absorption spectra of bright lines or bands (as are evident, for example, in the L_{III} spectrum of osmium in $Os(NH_3)_6Br_3$ reproduced in Fig.4) is commonly explained by asserting that the L_{III} electron undergoes a transition to a narrow d level with a high density of states (see, for example, Blokhin[7]). This explanation, however, is incorrect, as will be evident from the following argument.

Let us write the x-ray absorption coefficient for the L_{III} shell in the form

$$\tau(E) \sim N(E)\, P(E), \tag{4}$$

where $N(E)$ is the density of unoccupied d states as a function of the energy, $P(E)$ is the probability for transition of a knocked out L_{III} electron to a d atomic orbit, and E is the energy of the d state. Then the presence of the energy spectrum of a narrow atomic level with a high density of states means that the function $N(E)$ has a sharp maximum with a relatively narrow width. It is, of course, assumed that the probability $P(E)$ is characterized by a more or less uniform distribution over the entire energy range in question. Yet it is known from experimental data (see, for example, Fig.4) that the width of the first absorption line in the L_{III} spectra of the transition elements as a rule is not less than 3 ev (greater, for example, than in the L_{III} spectra of the noble gases), i.e., the energy interval occupied by the d states of the atom is appreciable. The number of unoccupied d states is either the same for all the successive absorption lines and the continuous spectrum or is less for the first line owing to gradual filling of the first d orbit in the series of transition elements. For qualitative evaluation of the intensity of the absorption lines we compare the absorption coefficient within the limits of the line with the absorption coefficient in the region of the continuous spectrum.

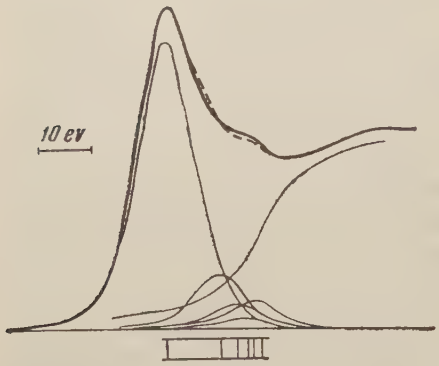

Fig.4. L_{III} absorption spectrum of osmium in $Os(NH_3)_6Br_3$.

On the other hand, in deriving the expression for the line and continuous spectrum absorption coefficients (see Ref.1) the number of states is taken into account by summing the probabilities for transitions to all the nd and εd states. If part of the d states for the first d orbit of the transition element is occupied by its own electrons, the absorption coefficient within the range of the first line will be smaller than follows from Eq.(1), and the ratio of the coefficients of the line and continuous absorption will be smaller than for the L_{III} spectra of nontransition elements. This inference is in obvious conflict with experiment.

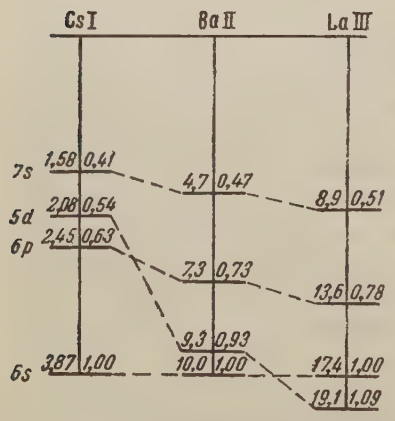

Fig.5. Diagram illustrating the relative strength of the binding of different electrons for Cs I, Ba II and La III.

Thus neither small width of the d level in transition elements nor a large number of d states can explain the presence of bright absorption bands in the L_{III} spectra of the transition elements. The reason for this effect must be sought in the strong (quadratic) dependence of the absorption coefficient for the L_{III}—nd transition on the effective charge of the atom within the given nd orbit, i.e., in the final analysis on the transition probability $P(E)$.

Let us consider from this standpoint the osmium atom (configuration outside the filled shells $5d^6 6s^2$ and use Slater's method for rough evaluation of its charge. We write the effective charge in the region of the $5d$ orbit of osmium, acting on an electron knocked out of the L_{III} shell, in the form

$$\eta_{5d} = \eta_{6d} + \sigma = \eta'_{6d} + 1 + \sigma, \qquad (5)$$

where η'_{6d} is the effective charge due to redistribution of the valence electrons of osmium as a result of formation of the chemical bond (the sign of η'_{6d} may be either plus or minus), and σ is the excess charge in the region of the $5d$ orbit, containing only six $5d$ electrons. The only positive charge arises, as usual, owing to the presence of a hole in the L_{III} shell of osmium. In the neutral atom $\eta'_{6d} = 0$ and $\sigma = 8 - (6 \times 0.35) = 5.9$. Then $\eta_{5d} = 6.9$, as a result of which the intensity of the absorption line associated with the L_{III}—$5d$ transition increases (as compared with the intensity of the line associated with the L_{III}—$6d$ transition) by a factor of approximately 50.

This rough evaluation can be checked by more accurate calculations, since the L_{III} absorption spectrum of osmium in a chemical complex was calculated in the work of Ref.6. The precise value of η'_{6d} (arrived at using Eq.(1)) proves to be 1.5, and the ratio $\tau_{exp}/\tau_{theo} = 3$. The deviation of this ratio from unity is indicative of the effect of screening in the $5d$ shell of osmium (the method of calculating this ratio is given in Ref.6). Taking into account the fact that the number of unoccupied states in the $5d$ shell of osmium $N_{5d} = 4$ (instead of 10), we have

$$\frac{\tau_{exp}}{\tau_{theo}} = \frac{\eta_{5d}^2}{\eta_{6d}^2} \cdot \frac{N_{5d}}{10} = \frac{(\eta_{6d} + \sigma)^2}{\eta_{6d}^2} \cdot \frac{N_{5d}}{10}. \qquad (6)$$

Whence we find $\sigma = 4.3$, i.e., is of the same order of magnitude as the value obtained by Slater's method. The somewhat smaller value of σ calculated from the x-ray spectrum is obviously explained by the fact that Slater's method does not take into account the effect of screening by the outer electrons.

The noted strong increase of the absorption coefficient for the L_{III}—nd transition in the transition elements is accompanied by a sharp decrease in the energy of this transition. Fig.5 illustrates the process of gradual binding of the $5d$ orbit in the isoelectronic series Cs I, Ba II and La III, according to the data derived from optical spectra.[8] The figures at the right of the verticals give the relative strength of the binding (referred to the binding energy of the $6s$ electron); the figures to the left of the verticals give the absolute binding energy in electron volts. It will be evident from the diagram that whereas the variation in the relative strength of the binding of the $7s$ and $6p$ electrons is gradual, there is a rapid increase in the binding strength of the $5d$ electron and a rapid reduction of the energy of the corresponding level. This explains why the intense bands in the L_{III} absorption spectra of the transition elements, associated with transition of an L_{III} electron to nd atomic orbits, are located in the region of longer wavelengths (cf.Figs.1-3 for the noble gases).

I desire to express my sincere gratitude to Yu.A.Lavrent'ev for assistance in carrying out the experimental measurements.

Institute of Rare Elements,
Academy of Sciences of the USSR

References

1. E.G.Nadzhakov & R.L.Barinskii, Doklady AN SSSR, 129, 1279 (1959). (Trans. Doklady.)

2. R.L.Barinskii & E.G.Nadzhakov, Izv.AN SSSR, Ser.fiz., 24, 407 (1960). (Trans.Bulletin, 24, 419.)

3. J.Prins, Nature, 133, 795 (1934).
4. G.Brogren, Nova acta Regiae soc.scient.upsaliensis, 14, No.4 (1949).
5. L.G.Parratt, Revs.Mod.Phys., 31, N 3, 616 (1959).
6. E.G.Nadzhakov & R.L.Barinskii, Izv.AN SSSR, Ser.fiz., 24, 415 (1960). (Trans.Bulletin, 24, 425.)
7. M.A.Blokhin, Fizika rentgenovskikh luchei (Physics of X-Rays), M.-L., 1953
8. M.A.El'yashevich, Spektry redkikh zemel' (Rare Earth Spectra), M.-L., 1953

REGARDING THE ASYMMETRY OF THE $K\alpha_1$ AND $K\alpha_2$ LINES OF ATOMS OF THE IRON GROUP

- L.K. Izraileva

It is a faimilar fact that the $K\alpha_1$ and $K\alpha_2$ lines of elements of the iron group are asymmetrical in the x-ray spectra of the metals and some compounds. Vainshtein[1] suggested that the asymmetry of these lines is due to splitting of the final L_{III} and L_{II} levels into sublevels owing to exchange interaction of the $2p$ electrons with the electrons of the unfilled $3d$ shell and different probabilities for transitions from these sublevels to the K level. However, Vainshtein carried out his calculations not for the x-ray L_{III} and L_{II} levels but for a closed 2_t shell; accordingly, to explain the different transition probabilities from the sublevels it was necessary to introduce additional assumptions.

It is possible to obtain splitting of the L_{II} and L_{III} levels into sublevels in atoms of the iron group and the transition probabilities from the sublevels to the K level by applying the general theory of atomic energy levels[2] to the x-ray levels. In view of the fact that the energy of an atom depends on the magnitude of the total angular momentum J, the x-ray levels of atoms with unfilled outer shells $n'l', n''l'', \ldots$ can split into sublevels with different values of the total angular momentum of the ionized atom:

$$\mathbf{J} = \sum_{n'l'} \mathbf{J}_{n'l'} + \mathbf{J}_{nl},$$

where $\mathbf{J}_{n'l'}$ is the total angular momentum of the outer unfilled shell, and $\mathbf{J}_{nl}$ is the momentum of the ionized shell nl. The separation between sublevels is determined by the electrostatic and magnetic interactions of the electrons in the ionized and outer unfilled shells. Inasmuch as the x-ray levels have a finite width, the fine structure of the x-ray levels of atoms with unfilled outer shells may or may not be evinced in the x-ray spectra, depending on the magnitude of the splitting. One can distinguish between two limiting types of fine structure of the x-ray levels:

Type I. In the case of LS coupling between the ionized and outer unfilled shells the sublevels of the x-ray level are approximately characterised by the values of the total spin S of the ionized level and the total orbital momentum L of the atom. Sublevels of this type have been considered by Horak[3].

Type II. If the ionization occurs in an inner shell in which the coupling approaches the jj type and the interaction of the electrons of the ionized and outer unfilled shells only weakly perturb the jj coupling, each x-ray level with a given j can split into sublevels with different J.

In a radiative transition between x-ray levels of an atom with an unfilled shell there appears an x-ray multiplet. The transition probability between sublevels must, in general, depend on J. If there is fulfilled the condition $E_J - E_{J'} < \Delta E_J$ (E_J is the energy of the J sublevel and ΔE_J is its width), the components of the multiplet may merge into a line of complex shape. It must be noted that in this case there is violated the condition of quasistationarity for the sublevels[4] and thus the concept of sublevels becomes approximate or nebulous.

In the present work, on the basis of these general considerations, we consider the fine structure of the L_{II} and L_{III} of atoms of the iron groups*.

The separation between the L_{II} and L_{III} levels varies from 5 ev in Sc (Z = 21) to 20 ev in Cu (Z = 29)[5] and, as will be evident from our evaluation of the splitting of the L_{II} level, the fine structure of the L_{II} and L_{III} levels in this group corresponds to Type II.

---

*It is assumed that in the $2p$ shell of Fe group atoms there obtains jj type coupling.

On the assumption that the $3d$ electrons are in the lowest lying level $(L, S, J)_{3d}$ given by the empirical rules[4], the L_{II} level $(j = 1/2)$ of atoms of the iron group consists of two sublevels with atomic angular momenta $J = J_{3d} + 1/2$ and $J' = J_{3d} - 1/2$; the L_{III} level $(j = 3/2)$ consists of four sublevels with possible total angular momenta $J = J_{3d} + 3/2$, $J_{3d} + 1/2, J_{3d} - 1/2$ and $J_{3d} - 3/2$ (the individual sublevels may, in general, merge). Using this model we calculated, in the first approximation of perturbation theory, the splitting of the L_{II} level due only to electrostatic interaction of the $2p$ and $3d$ electrons. Similar calculations can be carried out for the L_{III} level. The zeroth approximation wave functions characterized by $2pj = 1/2$, $m_j = \pm 1/2, 3d\ (L, S, J)_{3d} \times M_{3d}$ (M_{3d} is the projection of the total angular momentum J_{3d} of the $3d$ shell) are of the form

$$\Psi\,[2pj = 1/2 m_j;\ 3d\,(L, S, J)_{3d}\, M_{3d}] = \\ = \frac{1}{\sqrt{n+1}} \sum_{i=1}^{n+1} (-1)^{n+1-i} \hat{P}^i_{n+1} \Psi^{M_{3d}}_{(L,S,J)_{3d}}(1, \ldots, n) \cdot \varphi^{m_j}_{2pj=1/2}(n+1); \qquad (1)$$

where n is the number of electrons in the $3d$ shell of the given atom, $\hat{P}^i_{n+1}$ is the exchange operator for the i-th and $n+1$-th electrons. The function $\Psi^{M_{3d}}_{(L,S,J)_{3d}}(1, \ldots, n)$ was determined by the methods of Gray & Wills[6] and Condon & Shortley[2]; $\varphi^{M_j}_{2pj=1/2}(n+1)$ was determined by the method of Condon & Shortley[2].

Inasmuch as the matrix of the electrostatic interaction operator $V = \sum_{i>k=1}^{n+1} \frac{l^2}{r_{ik}}$ is diagonal with respect to J and M_J of the atom and does not depend on M_J for a given J,[2] for finding $\Delta E_{L_{II}}$, the separation between the L_{II} sublevels with $J_{3d} + 1/2$ and $J_{3d} - 1/2$, we used the diagonal sum rule[7]. The resultant expression can readily be brought to the form

$$\Delta E_{L_{II}} = AG^1 + BG^3, \qquad (2)$$

where G^1 and G^3 are the radial exchange integrals for the $2p$ and $3d$ electrons[7], and A and B are coefficients that depend on the angular parts of the exchange integrals.

Using Eq.(2) we found the splitting of the L_{II} level of Mn^{2+} into sublevels with $J = 3$ and $J' = 2$. The $2p$ single electron functions for Mn^{2+} were determined by interpolation of the data of Hartree[8], and the $3d$ functions were taken from the data of Hartree[8]. The splitting $\Delta E_{L_{II}}$ for Mn^{2+} calculated according to these functions equals 1.5 ev. On the other hand, evaluation using the approximate functions of Slater[10] yielded a value of 0.07 ev. As will be evident from the accompanying figure, this divergence is due to the appreciable difference between the r dependence of the $3d$ electron wave functions of Hartree and Slater inside the atom (the $2p$ wave functions are close). Consequently, one should not use the Slater function for such calculations. It will be evident that the magnitude of the splitting is very sensitive to changes in the single-electron wave functions.

The relative probability for transitions from the $J_{3d} + 1/2$ and $J_{3d} - 1/2$ sublevels of the L_{II} level to the K level was calculated by means of the corresponding sublevel wave functions and the sum rule[2]. The transition probability ratio is equal to the ratio of the statistical weights:

$$\frac{2J_{3d} + 2}{2J_{3d}} = 1 + \frac{1}{J_{3d}}. \qquad (3)$$

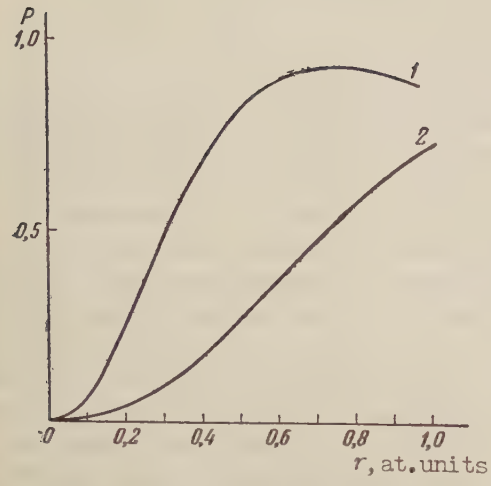

Normalized $3d$ wave functions: 1) according to Hartree, 2) according to Slater.

If one neglects splitting of the K level, this ratio equals the ratio of the integral intensities of the two components of the $K\alpha_2$ line (frequency factor ~1). For Mn^{2+} the ratio equals 7/5.

On the basis of the evaluation of the splitting of the L_{II} level of Mn^{2+} using Hartree functions one can assert that the splitting of the L_{II} and L_{III} levels in atoms of the iron group is of the order of magnitude of up to 1 ev. The width of the $K\alpha_1$ and $K\alpha_2$ lines is of the same order; this means that the fine structure of the L_{II} and L_{III} levels with different integral intensities of the $K\alpha_2$ and $K\alpha_1$ line components may be responsible for asymmetry of these lines in spectra of atoms of the iron group. However, inasmuch as the separation between the different J_{3d} levels of one term of the $3d$ shell $(L, S)_{3d}$ is of the order of 0.01 ev (Ref.9), it is essential to carry out more accurate calculations taking into account all the levels of the lowest term of the $3d$ shell. In Mn one level of the lowest term has $L=0$ and $S=J=2^1/_2$; hence Eq.(2) is valid for Mn. Calculations for the L_{II} level of Fe (configuration $3d^64s^2$) taking into account the three levels with $J_{3d} = 4,3,2$ of the lowest term with $L = 2$ and $S = 2$, showed that the separation between the L_{II} sublevels depends not only on the $2p - 3d$ exchange integrals G^1 and G^3, but also on the $2p - 3d$ Coulomb integrals F^2.[7]

Further refinement of the calculations can be realized if one takes into account the states of the other $3d$ terms. For comparison of the results of calculations with experiment it will be necessary to consider the question of the width of each of the sublevels of the L_{II} and L_{III} levels, inasmuch as there is no a priori reason for considering them to be equal.

I desire to express my gratitude to V.P.Sachenko, I.Ya.Nikiforov & E.N.Rumanov for discussion of the results and to L.A.Shiyanov for assistance in the calculations.

Institute of Physics,
Siberian Section of the
Academy of Sciences of the USSR

References

1. E.E.Vainshtein, Doklady AN SSSR, 40, 116 (1943).
2. E.U.Condon & G.H.Shortley, The Theory of Atomic Spectra, Cambridge, 1944 & 1951.
3. Z.Horak, Czechoslovak.physics journal, N 5 (1960).
4. L.Landau & E.Lifshits, Kvantovaya mekhanika (Quantum mechanics), M.,1948.
5. M.A.Blokhin, Fizika rentgenovskikh luchei (Physics of x-rays), M., 1957.
6. Gray, Wills, Phys.Rev., 38, 248 (1931).
7. J.Slater, Phys.Rev., 34, 1293 (1929).
8. D.R.Hartree, Calculation of Atomic Structures.
9. C.E.Moore, Atomic Energy Levels, II, Nat.Bur.Stand.Circ., 1949.
10. J.C.Slater, Phys.Rev., 36, 57 (1930).

THEORY OF THE FINE STRUCTURE OF X-RAY ABSORPTION SPECTRA

- A.I.Kozlenkov

1. Physical Basis of the Theory of Short-Range Order

The experimentally observed fluctuations of the fine structure in the x-ray absorption spectra of atoms in metals and alloys are explained by two different physical models. Kronig[1] assumes that the fluctuations in absorption are due to fluctuations in the density of states $N(E)$ above the Fermi level. Nonmonotonic variation of N as a function of E follows from band theory. According to band theory, the electron ejected in the process of absorption is described by a Bloch wave. The effect of the lattice field on the electron is regarded as a small perturbation.

The ejected electron moves freely within the crystal so that its behavior in the lattice is determined by all the atoms of the solid collectively. Consequently, the fine structure is a property of all the atoms of the crystal and not the sum of the individual properties of a particular group of atoms. In this sense the Kronig theory is a long-range order theory.

In contrast, Kostarev[2] and recently Shiraiwa, Ishimura & Sawada[3] have attributed the primary role to the nearest neighbors of the absorbing atom. Shiraiwa et al[3] maintain that the ejected electron is better described by a wave packet than by an unlimited plane or Bloch wave. The factor $e^{-\alpha r}$ is introduced into the final state wave function ψ_f, where α is the attenuation coefficient of the electron wave and r is the distance from the nucleus of the absorbing atom. These authors attribute attenuation to inelastic collisions of the electron with the atoms of the crystal.

Another possible limitation on the free path of the ejected electron is its interaction with lattice electrons. These interactions result in losses due to collisions and losses due to excitation of plasma oscillations.[4,5]

Experiments confirm the theories of Kostarev[2] and Shiraiwa et al[3], while the Kronig theory is unable to explain most results.[2,6] Kostarev carefully considered the experimental data in conflict with the long-range order theory, and showed that in fact the only experimentally verified prediction of this theory is the $\Delta E \sim 1/\alpha^2$ law for cubic lattices.

Let us now analyze and investigate the existing theories of fine structure, predicated on the assumption that only nearest neighbors influence the act of absorption. To begin with, we note that these theories attribute absorption fluctuations to changes in the transition probability $P(E)$ or $P(k)$ as a consequence of scattering of the wave of the ejected electron by the nearest neighbor atoms. The density of states $N(E)$ is assumed to be at least a monotonic function of E or k. In particular Shiraiwa et al[3] assume $N(E) \sim E^{1/2}$ as in the case of free electrons. Thus the absorption coefficient $\tau(E) \sim E^{1/2} P(E)$.

Hitherto existing short-range order theories have not been compared with respect to their underlying physical assumptions or as regards the methods of calculating $\tau(E)$ and the final formulas. The difference between Kostarev's[2] formula for $\tau(E)$ and that of Shiraiwa et al[3] has not been explained. Kostarev[2] and Petersen[7] have both treated the field of the nearest neighbor atoms as weak compared with the kinetic energy of the electrons and have used the semiclassical approximation to determine asymptotic scattering phase shifts. This procedure restricts the applicability of the theory to the region of high energies. Near the main absorption edge the theory disagrees with experiment, but it is not know whether the disagreement is due to the approximations used in the calculations or to basic inadequacies in the theory itself.

One should note that to date the theory has been tested for only a few metals. Kostarev calculated the peaks and valleys in the fine structure of copper and α-iron; Shiraiwa et al[3] calculated the absorption curves for copper, iron, and nickel; Hayasi[8] determined the positions of the peaks in the spectrum of lithium. No attempt has been made to calculate the fine structure either of metals with complicated lattice structures or of alloys. Finally, it is still not clear why for metals with the same structure there is approximately fulfilled the law

$$\frac{\Delta E_i}{\Delta E_j} = \frac{a_j^2}{a_i^2}$$

(ΔE_i and ΔE_j are the energy spacings of similar extrema in the spectra of the two metals, and a_i and a_j are the lattice constants of the metals). This relation is easily obtained from the Kronig theory and until now has been regarded as a significant substantiation of the theory.

It is difficult to apply these theories to a more extensive group of metals, either because of the complexity of the phase shift calculations using a Hartree field to approximate the field of the absorbing atom[2] or because it is necessary to introduce parameters that are hard to evaluate.[3] In this paper we shall consider all these problems from a single point of view.

The relative absorption coefficient is proportional to the ratio

$$S = \frac{P(k)}{P_1(k)} = \frac{\sum_{x,y,z} \left| \int \psi_0 x_i \psi_f d\tau \right|^2}{\sum_{x,y,z} \left| \int \psi_0 x_i \psi_{f_1} d\tau \right|^2}, \qquad (1)$$

where ψ_0 is the initial state function (the $1s$ function in the case of K absorption), and ψ_f and ψ_{f_1} are the final state functions of the electron in the lattice of the metal (or molecule) and in the isolated atom, respectively. The $P(k)$ and $P_1(k)$ are the probabilities for transition of an electron from the ψ_0 state to the ψ_f or ψ_{f_1} state. A significant point is that the function ψ_0 is strongly localized in a small region around the nucleus of the absorbing atom. Consequently, the integrations in (1) are taken only over this small volume. In this small region the functions ψ_f and ψ_{f_1} are in fact different only as regards their amplitudes A and A_1, and Eq. (1) becomes $S = |A/A_1|^2$. Thus, the calculation of S reduces to determination of the ratio of the squares of the amplitudes of the wave functions ψ_f and ψ_{f_1} at the zero point.

What is the physical reason for the difference between the amplitudes A and A_1? Let us compare the two systems schematized in Fig.1. Fig.1a shows the absorbing atom in the center of the two nearest atomic layers at distances r_1 and r_2 - the first and second coordination spheres. Fig.1b represents a free atom. Inasmuch as the functions ψ_f and ψ_{f1} pertain to the energy continuum ($E > 0$), the problem of determining them is equivalent to solving the problem of electron scattering from two such scatterers. The nature of the scattering is different in the two cases shown in Fig.1. In contrast to the free atom case, in the system of Fig. 1a there will also occur scattering from the atoms of the spheres r_1 and r_2, giving rise to interference effects at some points in the system. Actually, however, the interference effect is significant only in the small region wherein the initial state function ψ_0 is concentrated. Obviously, the zero point amplitudes in Figs.1a and 1b can be

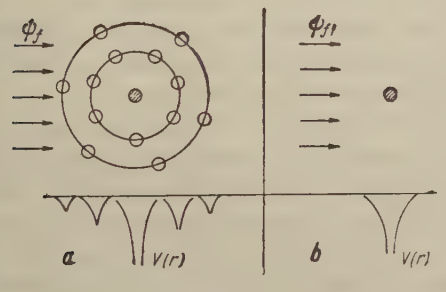

Fig.1

compared only if it is assumed that the amplitudes of the functions are equal at infinity, i.e., in the region where the distortion of the electron wave function by the other atoms of the scattering system is negligible. In other words, both problems are normalized in terms of the same constant particle flux far from the scattering centers. In the immediate neighborhood of the system and particularly near the central atom there is a redistribution of flux associated primarily with interference of the waves scattered by the neighboring atoms. This phenomenon explains the difference between amplitudes A and A_1 at the center.

From simple physical considerations it is clear that the amplitude A will depend on the distances r_1, r_2, etc. and on the electron wave length, i.e., on the wave vector k. In fact, A is determined by the phase shift $2kr_1$ of the primary wave relative to the wave scattered from the atoms of the first coordination sphere. The effect of the further spheres is weaker. The dependence of A on $2kr_1$ will have a maximum or minimum at the zero point. This accounts for the fluctuation of the absorption coefficient $\tau(k)$.

It should be noted that it is meaningful to speak of a phase shift having the value $2kr_1$ at the center of a system only in the case of plane waves being scattered from a point object. In reality the force fields of the atoms of the system distort the wave and change its phase in the region of the effective field. If the radius a of the sphere within which the field acts is substantially less than r_1, then we should expect the "interference" phase shift $2kr_1$ and the "atomic" phase shift $2\eta_1$, where $\eta_1(k)$ is the asymptotic phase due to scattering by the field of the individual atoms, to appear additively in the expression for $\tau(k)$. However, additivity of the phase shifts $2kr_1$ and $2\eta_1$ can be expected only for strongly screened, short-range fields. A long-range potential, such as the Coulomb potential, changes the phase of a wave even at large distances from the nucleus, making the dependence of phase on k more complicated. Electrons interact with metal ions by virtue of a short-range potential rather than by a Coulomb potential, because the nuclear field is screened by the atomic electrons and the field of the ejected electron is screened by the conduction electrons.[5]

It follows that the theories of Kostarev[2] and Shiraiwa et al[3] give correct expressions for τ for metals and alloys, but not for ionic crystals. If the screened Coulomb potential field in metals is approximated by

$$V(r) = \frac{Ze}{r} e^{-\frac{r}{a}},$$

then the smaller the screening constant a, the better Kostarev's expression for $\tau(k)$ agrees with experiment.

The next step in the construction of the theory is the so-called spherical approximation of the field of the atoms surrounding the absorbing atom. The field of the atoms of the first spherical layer of radius r_1 and the fields of succeeding layers have been averaged for molecules by Hayasi[8] and for metals by Kostarev[2]. Averaging is usually regarded as a formal step to make possible separation of variables in the Schrödinger equation and reduction of the problem to radial symmetry. However, examination of the theories[2,3] shows that the spherical approximation is actually a representation of a concrete physical fact: each absorption results in ejection of an electron into the lattice with a specific vector k, while experiment gives the average effect of absorption over the entire crystal and, consequently, an average for the directions of emission of electrons of given energy. Of course, rigorous calculation would involve solution of the Schrödinger equation without first averaging the field over the spheres. For precise determination of ψ_f one should put the probabilities in integral form, calculate the absorption coefficient $\tau(k)$ and then average this over all the directions of k for different

absorption events for electrons of given energy. Unfortunately, this method is mathematically impractical because separation of variables is impossible. Like Kostarev[2] and Petersen,[7] we shall use the spherical approximation where ψ_f is now the solution to the problem of scattering from a radially symmetric field, representing the field $V_0(r)$ of the absorbing atom and the system of concentric layers $V_j(r)$ (j is the layer number). To effect a separation of variables in the Schrödinger equation the wave function is expanded in a series of eigenfunctions $R_l(r) \cdot Y_l(\vartheta, \varphi)$. If the initial state function is S-symmetric (K or L_I absorption), then only the term $l = 1$ is retained in the expansion of ψ_f. Accordingly, only the term $\frac{l(l+1)}{r^2} = \frac{2}{r^2}$ is taken in the radial equation and the solution is just the asymptotic phase with $l = 1$.

All the above considerations pertain to short-range order theory as a whole, regardless of whether the final solution is reached by approximate or exact methods. However, all present short-range order theories are based on the following approximations:

1) The average field $V_j(r)$ of the surrounding atoms is assumed small compared to the electron kinetic energy and to the field of the central absorbing atom[2];

2. The quasiclassical Wentzel-Kramers-Brillouin (WKB) method is used to calculate the scattering phases.

In the first approximation the averaged field of the surrounding atoms is regarded as a small perturbation. This approximation gives, significantly better results than the Born approximation (in which all the potential energy is considered small compared to the kinetic energy of the electron). Consequently, the field of the absorbing atom is considered to contribute only the "atomic" phase shift $2\eta_1 = f(k)$ and the field of the neighboring atoms is simply the cause of the "interference" phase shift $2kr_s$. In Section III we substantiate this approximation and determine the energy region in which it is valid. In general, this approximation restricts applicability of the theory to rather high energies. However, for copper it is adequate beginning with the region 20-40 ev from the main edge.

It is correct to use the WKB approximation to determine the form of the phase shift $\eta_1(k)$ only where the field of the absorbing atom changes slowly over a distance equal to the DeBroglie wavelength. Near the main edge the DeBroglie wavelength is of the order of 4 to 2 Å and the interatomic distance r_1 is 2.5 to 3 Å, so that in this region $\lambda_e \sim r_1$ and the potential in the lattice varies sharply within this distance; the WKB approximation is unsuitable for the phase calculations. This fact apparently explains the discrepancy between experiment and Kostarev's theory in the primary absorption region near the edge.

The formula deduced by Kostarev[2] and Petersen[7] for the absorption coefficient is valid for both metals and molecules. It is of the form

$$\tau(k) = \left[1 - \frac{2m}{\hbar^2 k}\sum_s^{\infty} N_s \sqrt{I_s'^2 + I_s''^2}\sin\left(2kr_s + 2\eta_1 + \operatorname{arctg}\frac{I_s'}{I_s''}\right)\right]^{-1}; \qquad (2)$$

$$I_s' = \int_{-\infty}^{+\infty} \overline{V_s(x)}\sin 2kx\,dx;\quad I_s'' = \int_{-\infty}^{+\infty} \overline{V_s(x)}\cos 2kx\,dx;\quad \overline{V_s(x)} < 0.$$

The sum is taken over the coordination spheres; s is the number of the sphere, r_s is its radius, and N_s is the number of atoms in the sphere. The variable of integration x in the two integrals is $r - r_s$, where r is measured from the center of the absorbing atom. To simplify Eq. (2) we note, first, that both Petersen and Kostarev obtained a field $\overline{V_s(x)}$, averaged over the sphere, which was not symmetric about $x = 0$. This asymmetry is more a mathematical consequence of the method of

averaging than reflection of some actual physical peculiarity of the field of the atoms near the absorbing atom. It is easy to show that the quantity $\operatorname{arctg} I_s'/I_s''$ (Kostarev,[2] Petersen[7]) is quite small even for small k corresponding to the main edge, and is even smaller in the short wavelength region. Furthermore, if we assume that $\overline{V_s(x)}$ is an even function, then $I_s = 0$ and $\operatorname{arctg} I_s'/I_s'' = 0$. Making these assumptions, instead of (2), we obtain

$$\tau(k) = \left[1 - \frac{2m}{\hbar^2 k}\sum_s^{\infty} I_s'' N_s \sin(2kr_s + 2\eta_1)\right]^{-1}. \tag{3}$$

If the fluctuations in absorption are small compared to the mean level of absorption $\tau(k) = 1$, we can write approximately

$$\tau(k) \approx 1 + \tilde{\tau}(k) = 1 + \frac{2m}{\hbar^2 k}\sum_s^{\infty} N_s I_s'' \sin(2kr_s + 2\eta_1); \quad I_s'' < 0; \tag{4}$$

where $\tilde{\tau}(k)$ is the variable part of the function $\tau(k)$. In Section III it will be shown that the quantity $\frac{2m}{\hbar^2 k} N_s I_s''$ is a slowly varying function of k, decreasing as k increases and as the layer index s increases. In fact all the principal peaks of the fine structure are given by the first term in the sum. This fact implies that the positions of the principal peaks are determined by the condition

$$\sin(2kr_1 + 2\eta_1) = -1, \text{ or } \quad 2kr_1 + 2\eta_1 = \frac{3\pi}{2} + 2m\pi. \tag{5}$$

This condition is valid regardless of whether the absorption fluctuations are small or large. Neglecting the contribution of distant spheres to the sum, we obtain

$$\tilde{\tau}(k) \sim B(k) \sin(2kr_1 + 2\eta_1), \tag{6}$$

where $B(k)$ is a monotonic and slowly varying function of k. Equation (6) has a clear physical meaning. The phase shifts $2kr_1$ and $2\eta_1(k)$ enter into the argument additively, which is a consequence of the smallness of the screening constant a compared to r_1. On the other hand, in the formula the field of the absorbing atom contributes only the "atomic" phase $\eta_1(k)$, while the field of the concentric layers of atoms adds only the interference term $2kr_1$. This fact is a consequence of treating the averaged field of the surrounding atoms as a small perturbation. Within its range the field averaged over the sphere changes the phase of the wave only slightly compared to the phase in the absence of the field.

Equation (6) may be readily compared with the expressions derived by Shiraiwa et al[3]. In (6) it is assumed that the final state wave function of the electron is the sum of the primary wave and the waves scattered by the neighboring atoms:

$$\psi_f = e^{i(\mathbf{k},\mathbf{r})} + \sum_j q_j e^{i(\mathbf{k}_{j,0}\,\mathbf{r})};$$

where k_{j0} is a wave vector pointing from atom j toward the absorbing atom. The sum is taken over all the atoms surrounding the absorbing atom. The scattering amplitudes q_j are calculated for the neighboring atoms in the Born approximation with the fields of these atoms being represented by a square well of depth V_0 and radius a. The function ψ_f appears in the integral for the transition probability. The density of states $N(k)$ is assumed proportional to k.

The probability integral is averaged over all directions of electron ejection

from the absorbing atom. The resulting expression for the absorption coefficient, obtained when disregarding all secondary-scattered waves, is of the form

$$\tau(k) = \frac{2mV_0a^3}{\hbar^2}\left[\frac{\cos 2ka}{(2ka)^2} - \frac{\sin 2ka}{(2ka)^3}\right]\sum_s \frac{N_s}{r_s^2}\sin 2kr_s e^{-\alpha r_s}. \qquad (7)$$

It is obvious that the theory of Shiraiwa et al,[3] by assuming a plane primary wave, does not take into consideration the field of the absorbing atom or the phase shift $2\eta_1(k)$ associated with it. In this case theoretical calculation of the change of phase brought about by the field of the neighboring atoms is superfluous, for we know that the averaged field of the surrounding atoms introduces a smaller phase shift than does the field of the central atom. Therefore, if this theory[3] can claim some sort of agreement with experiment, it is only in the sense that, like the other theories, it takes into account interference of the scattered waves, i.e., the phase shifts $2kr_s$. Shiraiwa et al[3] assume that $a \ll r_1$. Therefore the factor in (6) which depends on $2ka$ slowly modulates the leading term $\sum_s \frac{N_s}{r_s^2}\sin 2kr_s$. Calculations show that the shape of the Co, Ni, Cu, Zn and Fe absorption curves is given quite accurately by

$$\tau(k) \sim \sum_s \frac{N_s}{r_s^2}\sin 2kr_s. \qquad (8)$$

The factor $e^{-\alpha r_s}$ is omitted from Eq.(8); according to Shiraiwa et al[3] this factor allows for attenuation of the electron wave as it moves away from the absorbing atom. Actually, while for the first few spheres this factor is negligible, it becomes important in the far short wavelength region. Since the authors give no reasonable method of specifying this quantity, we prefer to treat $e^{-\alpha r_s}$ as a constant, rather than as a parameter to be chosen to fit theory to experiment.

We shall use the simple formula (8) to calculate the absorption curves of Cu, Zn, Ni, Co and Fe. Comparison of (8) with the previously obtained expression (6) shows that if the phase $2\eta_1$ is neglected the formulas agree, not because of the smallness of $2\eta_1$, since in reality the field of the absorbing atom is not weak, but because of the particular form of the k dependence of η_1. Kostarev's calculations[3] for copper and iron show that the phases, calculated semi-classically, behave as shown in Fig.2. From 50 to 200 ev the average value of the phases is $\eta_1 = 3\pi/2$. As k increases, the phase decreases slowly and monotonically, intersecting the line $\eta_1 = 3\pi/2$. Inserting $\eta_1 = 3\pi/2$ into (5), we find that for the metals from Fe to Zn the condition for peaks is

$$2kr_1 = \pi/2 + 2m\pi \quad (m = 1, 2, 3\ldots).$$

The absorption coefficient is given by Eq.(8).

The atomic field of other metals differs from that of copper or iron, and the phase η_1 has a different mean value in the energy region which corresponds to the Kronig structure. The mean value of η_1 may be determined by considering the behavior of the phases calculated for a self-consistent Hartree field for various atoms, e.g., He, O, A, Cl, Fe, Cu, Kr, Hg, etc.[9] The behavior of the phases exhibits general regularities for potentials which fall off faster than $1/r$, in particular for a square well or screened Coulomb field:

1) as $k \to 0$, $\eta_l \to s\pi$, where s is the number of levels in the potential well with angular momentum l;

2) as $k \to \infty$, $\eta_l \to 0$ for fairly large k.

From consideration of the phase curves of the above mentioned atoms it follows that for $k \to 0$: $\eta_1 \to 0$ for He, $\eta_1 \to \pi$ for Cl, $\eta_1 \to 2\pi$ for Kr, etc.

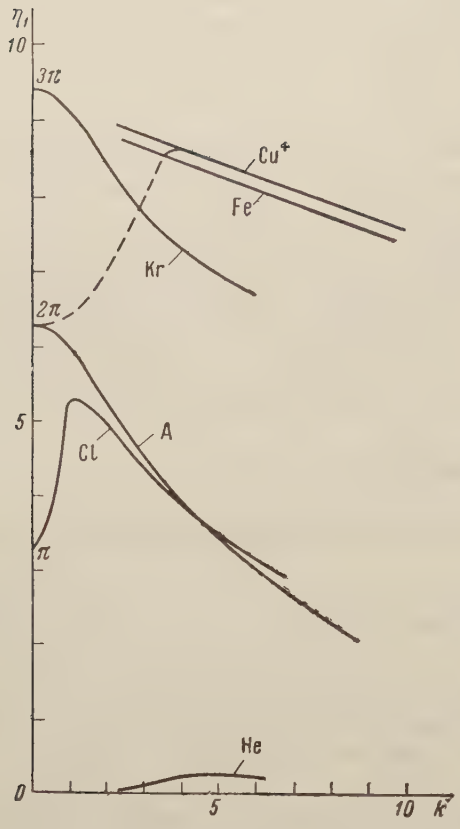

Fig.2. Scattering phase η_1 calculated for a Hartree field.

One can qualitatively establish the k dependence of η_1 for elements with intermediate atomic numbers. In particular, one would expect that for Ca the phase would be close to π on the average (in the energy region from the Fermi surface up to 150 ev); the average value of η_1 for Al is $\pi/2$, for Be $\pi/4$, etc. It is impossible to use Eq.(8) to determine the positions of the principal fine-structure peaks for these elements; the more general expressions (4) and (5) should be used.

The k dependence of the phase for different atoms will be considered in more detail in Section III.

II. Calculation of the Fine Structure of Some Metals

We have shown above that the absorption coefficient for metals is given by Eq.(2), which, subject to the specified approximations can be written as

$$\tau(k) \approx -\sum_s \frac{N_s}{r_s^2} \sin(2kr_s + 2\eta_1). \qquad (9)$$

For V, Fe, Cr, Co, Ni, Cu and Zn the phase $\eta_1(k)$, beginning 15 to 30 ev above the Fermi level, approaches $3\pi/2$, while for Al it is close to $\pi/2$. Then, inserting the mean value $2\eta_1 = 3\pi$ or π into (9), we obtain

$$\tau(k) \approx \sum_s \frac{N_s}{r_s^2} \sin 2kr_s. \qquad (10)$$

The absorption curves for Fe, Co, Ni, Cu, Zn, Cr, V, Ti and Al, which crystallize in a body-centered cubic, face-centered cubic or hexagonal lattice, were calculated by means of Eq.(10). Furthermore, the fine structure of Be and Ca was calculated assuming (see Section 1) that for Be, η_1 averages close to $\pi/4$ and for Ca close to 2π. The positions of the principal absorption peaks are determined for Be from the expression $2kr_1 \approx (2m+1)\pi (m = 0, 1, 2...)$, and for Ca from $2kr_1 = -\pi/2 + 2m\pi$ $(m = 1, 2, 3...)$. The results of the Be and Ca calculations are given in Fig.3.

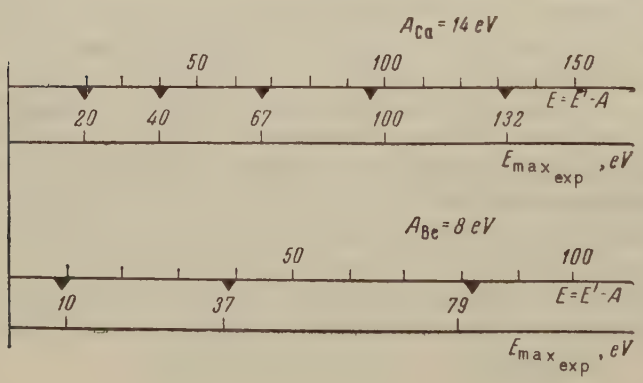

←Fig.3. Positions of the fine structure peaks for Ca and Be.

Figs.4-8 show the absorption curves calculated by means of Eq.(10) for a number of metals and the corresponding experimental curves. Comparative curves for different numbers of spheres in the sum are given in Figs.5,6 and 8. Since all the calculated curves are plotted in terms of k, while experiments give the peaks

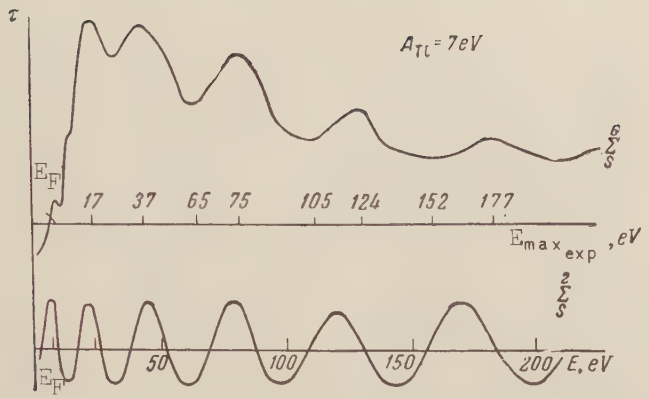

Fig.4. Theoretical absorption curves for Ti calculated for two and six spheres.

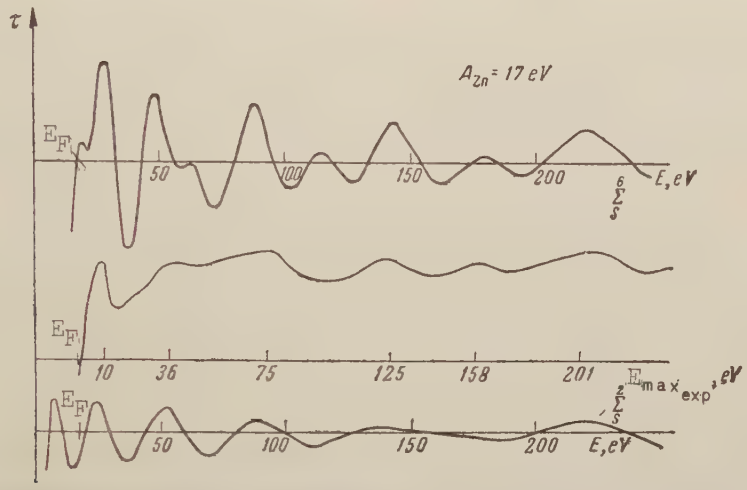

Fig.5. Theoretical and experimental absorption curves for Zn.

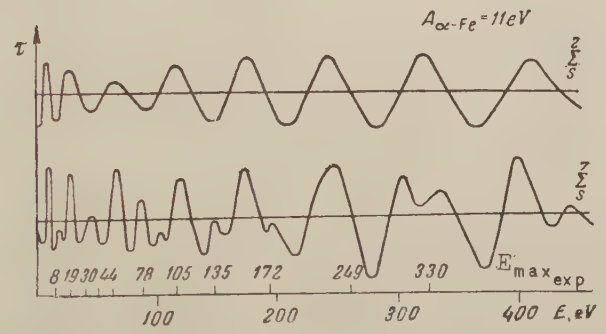

Fig.6. Theoretical absorption curves for Fe, calculated for two and seven spheres.

and valleys in the energy scale, is necessary to know how to convert from k to E. This conversion is accomplished by the formula

$$E = \frac{\hbar^2 k^2}{2m} - A; \qquad (11)$$

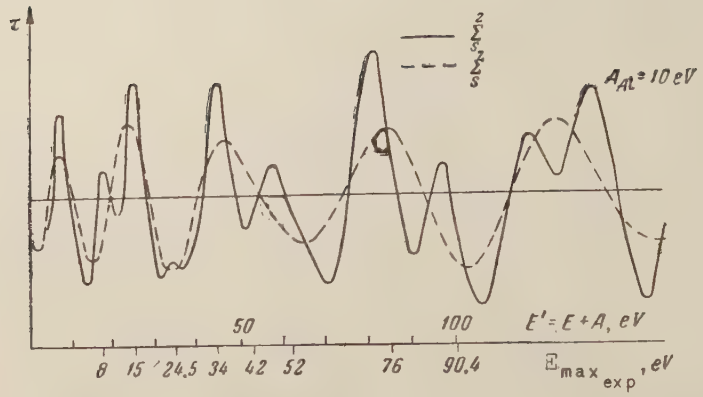

Fig.7. Theoretical absorption curves for Al, calculated for two and seven spheres.

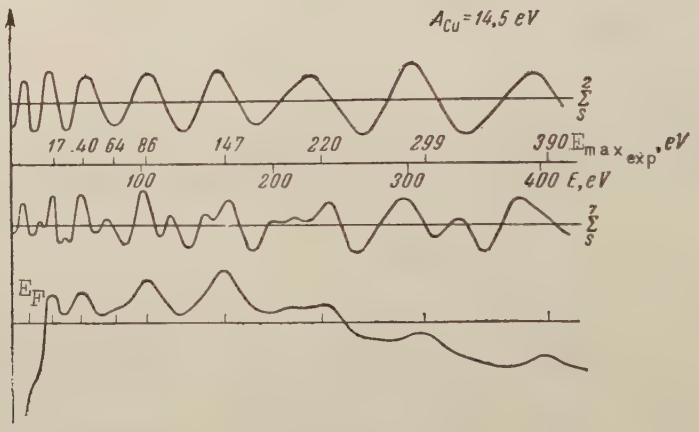

Fig.8. Theoretical absorption curves for Cu, calculated for two and seven spheres.

here E is reckoned from the Fermi level, A is a constant for the particular metal, but is approximately given by $A = V_0 - \varphi$, where V_0 is the mean potential of the electron in the lattice and φ is the work function. The constant A characterizes the kinetic energy datum, which lies below Fermi level. The constant can be found by fitting the experimental curve to the curve plotted by means of Eq.(10). The experimental curve is plotted in terms of energy measured from the Fermi level; accordingly the energy scale $E' = E + A = \frac{\hbar^2 k^2}{2m}$ of the theoretical curve is shifted by the amount A relative to the experimental scale. The curves are fitted by obtaining the best coincidence of peaks. In the far short wavelength region and in the interval 10 to 50 ev, some discrepancy between the two curves is possible because here the phase deviates from the mean value assumed for the given metal. The values of A found in this way agree well with the approximation $V_0 - \varphi$. In particular, for Cu, Fe, Zn and Al the values of A are respectively 15, 11, 17 and 10 ev. On the other hand, a number of authors have evaluated V_0 for these metals and obtained 19, 16, 21 and 12.4 ev, respectively.

The work function φ is 4.7 ev for Cu, 4.8 ev for Fe, 4.2 ev for Zn and 3.0 ev for Al. Consequently, A equals 15, 11, 17 and 9.5 ev for these metals, which is in good agreement with the values found from the absorption curves. Equation (11) gives the correct values of E_{max} corresponding to the values of k_{max} determined from (2), (10) or (9).

Examination of the curves in Figs.3-8 leads to the following conclusions.

1) In the theories of Kostarev[2] and Shiraiwa et al[3] all the principal peaks of the fine structure are explained by scattering from the first sphere. Consideration of further spheres, i.e., inclusion of further terms in the sum of (2), hardly changes the positions of the principal peaks in the primary region of absorption, but it intensifies them and leads to the appearance of additional, weaker maxima of hyperfine structure. In particular Figs.5,6 and 8 show that the 30, 78 and 135 ev peaks of α-Fe, the 77 and 130 ev peaks of Cr, the 64 ev peak of Cu, the 159 ev Zn peak, etc. are not present in curves calculated for the first and second spheres, but they do appear in curves where the sum comprises from three to seven terms. Furthermore, inclusion of scattering from the second and higher order spheres can change the relative intensity of the principal peaks. The zinc lattice provides a particularly good example, for in it, owing to the anomalous c/a ratio, the radii r_1 and r_2 differ greatly. Fig.5 presents curves plotted for two spheres and for one sphere. The second sphere sine curve $\frac{N_2}{r_2^2}\sin 2kr_2$ substantially changes the amplitudes and positions of the peaks plotted for the first sphere. Experiment is in good agreement with the theoretical curve constructed for two spheres, but not with the curve for the first sphere alone. Consideration of further spheres has practically no effect except for small changes in the primary region near the main edge; the positions of the principal peaks remain unchanged.

2) In the far short wavelength region the curve constructed for a large number of spheres exhibits splitting of the principal peaks, which is not observed experimentally (Fig.8). In fact, here agreement with experiment is best when only the first sphere is used in the calculation. This effect is explained by a decrease in the amplitude of scattering from the more remote spheres, owing to the fact that the average field of the distant layers is significantly weaker than the fields of the first spheres. The amplitude of scattering from any layer decreases as k or the electron energy increases, because the barrier penetrability of the electrons increases. Therefore the peaks due to the outer spheres are observed experimentally in the primary part of the absorption curve, while in the far short wavelength region, scattering from all spheres becomes less, so that the scattering amplitude for the outer spheres diminishes to below the sensitivity threshold of the experiment. One can improve agreement with experiment by introducing the factor $e^{-\alpha r_s}$, as done by Shiraiwa et al[3]. However, this procedure is of uncertain value in so approximate a theory. Section III presents a more rigorous calculation of the scattering amplitude as a function of r_s and k.

3) The experimental peaks in the far short wavelength region are systematically shifted to the short wavelength side relative to the peaks calculated by Eq. (10). As previously mentioned, this is a consequence of the monotonic decrease of the phase $\eta_1(k)$ as with increase of k, so that the phase departs noticeably from its average value for large k.

4) Equation (10) agrees with experiment for the initial intense fine structure peak, usually called the "A maximum". For example, the energy of the A peak of copper is 15-17 ev. The expression $2kr_1 = \pi/2 + 2m\pi$ gives 17 ev for $m = 2$, while Kostarev's theory gives 9 ev.

The error in Kostarev's theory[2] is probably due to the semi-classical calculation of the phase η_1, a method which is not appropriate for small k. If the phase for Cu or Fe in the primary region is assumed to diminish to π, then it is clear that the simple expression (10) will agree better with experiment than will the more exact formulas deduced by Kostarev[2] and Shiraiwa et al[3].

Let us now show how to derive the familiar inverse square law $\frac{\Delta E_i}{\Delta E_j} = \frac{a_j^2}{a_i^2}$ of Kronig's theory from Eq.(10), where ΔE_i and ΔE_j are the energy separations of analogous fine structure extrema of two metals with the same structure (face-centered or body-centered cubic) with lattice constants a_i and a_j. The condition for peaks and valleys is

$$\frac{d\tau}{dk} = \sum_s \frac{2N_s}{r_s^2} \cos 2kr_s = 0. \tag{12}$$

For a metal with lattice constant a_i, we have

$$\sum_s \frac{N_s a_i}{r_s} \cos\left(2ka_i \frac{r_s}{a_i}\right) = 0,$$

and for a metal with constant a_j,

$$\sum_s \frac{N_s a_j}{r_s} \cos\left(2ka_j \cdot \frac{r_s}{a_j}\right) = 0.$$

The ratios $\frac{N_s a_i}{r_s} = c_{si}$ and $\frac{N_s a_j}{r_s} = c_{sj}$, $\frac{r_s}{a_i} = b_{si}$ and $\frac{r_s}{a_j} = b_{sj}$ are the same for metals (such as Cu and Ca) with the same structure. Thus

$$\sum_s c_s \cos\,(2ka_i b_s) = 0 \quad \text{and} \quad \sum_s c_s \cos\,(2ka_j b_s) = 0.$$

Let k_{0i} be a solution of the first of these equations. Multiply k_{0i} by $\frac{a_i}{a_j}$. Then $k_{1j} = k_{0i} \cdot \frac{a_i}{a_j}$ satisfies the second equation because it transforms the second equation into the first. Therefore

$$\frac{k_{\max i}}{k_{\max j}} = \frac{k_{0i}}{k_{1j}} \cdot \frac{a_j}{a_i}. \tag{13}$$

Because

$$\frac{\hbar^2 k_{0i}^2}{2m} = E_{0i} + A_i \quad \text{and} \quad \frac{\hbar^2 k_{1j}^2}{2m} = E_{1j} + A_j,$$

then $\frac{E_{0i} + A_i}{E_{1j} + A_j} = \frac{a_j^2}{a_i^2}$; here E_{0i} and E_{1j} are the energies of the peaks figured from the Fermi level. For the two other analogous peaks E'_{0i} and E'_{1j} we have

$$\frac{\hbar^2 k'^2_{0i}}{2m} = E_i + A_i \quad \text{and} \quad \frac{\hbar^2 k'^2_{1j}}{2m} = E'_{1j} + A_j. \tag{14}$$

Eliminating the constants A_i and A_j from Eqs.(14) and (13), we have

$$\frac{\Delta E_i}{\Delta E_j} = \frac{E'_{0i} - E_{0i}}{E'_{1j} - E_{1j}} = \frac{a_j^2}{a_i^2}. \tag{15}$$

Thus, the $\Delta E \sim 1/a^2$ law is obtained from short-range order theory and is, therefore, not a confirmation of the Kronig theory. However, the law is not exact in short-range order theory because we used the average value of the phase η_1 in the initial expression (10).

The theory developed above seems primarily an explanation of the x-ray absorption fine structure of metals. Yet, the mathematical formalism of the theory

was originally worked out[7] for such molecules as $GeCl_4$ and $AsCl_4$.

Even without undertaking specific calculations, we can make several generalizations about the nature of the fine structure in the absorption spectra of molecules:

1) Interference phenomena should occur in molecules as well, since in the case of absorption by atoms of Ge or As there occurs scattering from the Cl atoms.

2) The first coordination number is 4 and is two or three times smaller than for metals. This means that the spherical approximation of the average field is less exact than for metals.

3) The nature of the field differs from that for ions in metals; moreover, there is no screening by conduction electrons. Determination of the scattering phase $\eta_l(k)$ from x-ray spectra data provides information about the field of the central atom of the molecule, e.g., Ge. The behavior of the phase is generally different from that for a metal.

The theory developed here (including Eq.(10)) is also applicable to alloys. In general, one must consider the different scattering powers of the constituent atoms of the alloy. However, if the effect of the second sphere is weak, simple calculation treating the atoms of the alloy as identical leads to the correct positions of the peaks, but not to correct relative intensities. Comparison of the absorption curves of the two kinds of ions in a two-component alloy reveals that the difference is chiefly a consequence of dissimilarities between the phases η_1 of the two ions.

A qualitative explanation of the temperature dependence of fine structure is quite easy. The radius r_s ceases to be fixed and becomes statistically distributed around some average value. The statistical variation of the interatomic distances leads to a variation in phase. Obviously, the shorter the electron wavelength, the greater the mismatch in phase for a particular maximum at a given temperature, i.e., for a given root mean square deviation of the atom from its equilibrium position. Consequently, as experiment confirms, the fine structure begins to "melt" (fade) on the short wavelength side.

III. Relation Between the Fine Structure and the Parameters of the Potential of the Absorbing Atom

In this section we derive an exact expression for the absorption coefficient $\tau(k)$ without the approximations used by Kronig[1], Kostarev[2], Shiraiwa et al[3] and Petersen[7]; furthermore, we use a simpler approximation for the fields of the absorbing atom and the concentric layers. An analytic expression for the phase $\eta_l(k)$ can not be obtained by using complicated fields such as the Hartree field or the Thomas-Fermi potential. The phase in such cases must be calculated by complicated numerical methods.[9] As a first step in the calculation of η_l and $\tau(k)$, we approximate the field of the individual atom in a metal by a square well of radius a and depth V_0. The phases η_l for such a field can be calculated by a familiar formula[9] for all values of k. On the other hand, the square well potential is a special case of a potential falling off faster than $1/r$. The phase $\eta_l(k)$ behaves qualitatively in the same way as for other short-range fields, such as the screened Coulomb field.

For large k the phases η_l tend monotonically to zero, and for small k they tend to $s\pi$, where s is the number of levels in the field $V(r)$ with angular momentum $M_l^2 = \hbar^2 l(l+1)$.

It is also known that the results of scattering from a square-well potential with parameters V_0 and a resemble those of scattering from a screened Coulomb potential $V(r) = \frac{Ze^2}{r} e^{-r/a}$, if we make a the same in both cases and set $V_0 \approx \frac{Ze^2}{a}$.

The results are most similar for high energy electrons.

The interaction of the electron with the field of the atom in the metal is not a Coulomb interaction, but rather a screened Coulomb interaction, and the square-well parameter a roughly characterizes the extend of the screening. One would expect that approximating the field of the atom by a square well and properly selecting V_0 and a would be useful quantitatively as well as qualitatively.

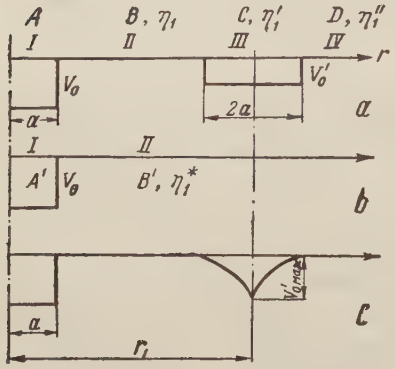

Fig.9

Let us consider a system of an absorbing atom at the center $(r = 0)$ and surrounding atoms at a distance r_1 (Fig.9a); here V_0 and a are parameters of the field of the absorbing atom, and V_0' is the field of the N_1 nearest neighbor atoms, averaged over the sphere of radius r_1. Fig.9b characterizes the case of an isolated atom. Since the problem has central symmetry, we can separate the variables in the Schrödinger equation. To find the relative absorption coefficient $\tau(k)$, we must determine the ratio of the squares of the amplitudes A and A' of the wave functions ψ_f and ψ_{f_1}, describing, respectively, an electron ejected from an atom in a metal and an electron ejected from a free atom. The amplitudes in regions I, II, III and IV of Fig.9a are denoted by A, B, C and D, respectively. The scattering phases in regions II, III and IV are η_l, η_l' and η_l''. In Fig.9b the amplitudes in regions I and II are A' and B', and the phase in region II is η_l^*. For K or L_I absorption, $l = 1$. The ratio A/A' is determined by using the condition $B' = D$, i.e., equality of the amplitudes of the wave functions at infinity.

The radial equation for a function $G(r) = rR(r)$ is

$$\frac{d^2G}{dr^2} + \left[k_i^2 - \frac{l(l+1)}{r^2}\right]G = 0, \qquad (16)$$

where in region I $k_i = k' = \sqrt{k_0'^2 + k^2}$, $k_0^2 = \frac{2mV_0}{\hbar^2}$, in regions II and IV $k_i = k$, and in region III $k_i = k_1' = \sqrt{k_0'^2 + k^2}$, $k_0'^2 = \frac{2mV_0'}{\hbar^2}$.

The general solution is a linear combination of Bessel functions of the type $J_{l+1/2}(kr)$ and $J_{-l-1/2}(kr)$. In region I we can take only functions of the form $J_{l+1/2}(kr)$ because only they are finite for $r = 0$.

For the case of Fig.9a (an atom in a metal), the solution $G(r)$ has the following form in the various regions

$$\text{I. } Ar^{1/2}J_{l+1/2}(k'r).$$

$$\text{II. } B\left(\frac{\pi k}{2}\right)^{1/2}r^{1/2}\left[\cos\eta_1 J_{l+1/2}(kr) + (-1)^l \sin\eta_1 J_{-l-1/2}(kr)\right].$$

$$\text{III. } C\left(\frac{\pi k_1'}{2}\right)^{1/2}r^{1/2}\left[\cos\eta_1' J_{l+1/2}(k_1'r) + (-1)^l \sin\eta_1' J_{-l-1/2}(k_1'r)\right].$$

$$\text{IV. } D\left(\frac{\pi k}{2}\right)^{1/2}r^{1/2}\left[\cos\eta_1'' J_{l+1/2}(kr) + (-1)^l \sin\eta_1'' J_{-l-1/2}(kr)\right].$$

For Fig.9b (the free atom) the solution in regions I and II is

$$\text{I. } A'r^{1/2}J_{l+1/2}(k'r).$$

$$\text{II. } B'\left(\frac{\pi k}{2}\right)^{1/2}r^{1/2}\left[\cos\eta_1^* J_{l+1/2}(kr) + (-1)^l \sin\eta_1^* J_{-l-1/2}(kr)\right].$$

The phases η_1, η_1', η_1'' and η_1^* are determined from the condition of equality of the logarithmic derivatives at the points $r = a$, $r = r_1 - a = b$ and $r = 2a + b = r_1 + a$. It is easily shown that $\eta_1 = \eta_1^*$.

By equating the wave functions at the joining points and using the condition $B' = D$, we can express D in terms of A in problem 9a, and B' in terms of A in problem 9b, and thus obtain the ratio $|A/A'|^2$, i.e., find the absorption coefficient $\tau(k, a, V_0, r_1)$.

Let us consider the case of K or L_I absorption; we set $l = 1$ in all the formulas.

Using the expressions for Bessel functions

$$J_{3/2}(kr) = \sqrt{\frac{2}{\pi kr}}\left(\frac{\sin kr}{kr} - \cos kr\right) \tag{17}$$

and

$$J_{-3/2}(kr) = \sqrt{\frac{2}{\pi kr}}\left(-\frac{\cos kr}{kr} - \sin kr\right) \tag{18}$$

and the joining condition for the logarithmic derivatives we obtain

$$\operatorname{tg}\eta_1 = -\frac{C_1}{D_1} = -\frac{\left(\frac{ka}{k'a} - \frac{k'a}{ka}\right)\operatorname{tg} ka \operatorname{tg} k'a + k'a \operatorname{tg} k'a - ka \operatorname{tg} ka}{\left(\frac{ka}{k'a} - \frac{k'a}{ka}\right)\operatorname{tg} k'a - ka - k'a \operatorname{tg} k'a \operatorname{tg} ka}; \tag{19}$$

$$\operatorname{tg}\eta_1' = \frac{T_1(k_1', b) - R_1(k_1', b)\, S(k, b, \eta_1)}{T_2(k_1', b) + R_2(k_1', b)\, S(k, b, \eta_1)}; \tag{20}$$

$$\operatorname{tg}\eta_1'' = \frac{T_1(k, b+2a) - R_1(k, b+2a)\, S(k_1', b+2a, \eta_1')}{T_2(k, b+2a) + R_2(k, b+2a)\, S(k_1', b+2a, \eta_1')}; \tag{21}$$

$$S(k, b, \eta_1) = \frac{T_1(k, b) - T_2(k, b)\operatorname{tg}\eta_1}{R_1(k, b) + R_2(k, b)\operatorname{tg}\eta_1}.$$

The functions T_1, T_2, R_1 and R_2, appearing in Eqs.(20) and (21), have the form:

$$T_1(k, b) = k \sin kb + \frac{\cos kb}{b} - \frac{\sin kb}{kb^2}, \tag{22}$$

$$T_2(k, b) = -k \cos kb + \frac{\sin kb}{b} + \frac{\cos kb}{kb^2}, \tag{23}$$

$$R_1(k, b) = -\cos kb + \frac{\sin kb}{kb}, \tag{24}$$

$$R_2(k, b) = \sin kb + \frac{\cos kb}{kb}. \tag{25}$$

Thus the absorption coefficient is

$$\tau(k) = \left|\frac{A}{A'}\right|^2 = \left[\frac{\cos\eta_1' \cdot R_1(k_1', b) + \sin\eta_1' \cdot R_2(k_1', b)}{\cos\eta_1 \cdot R_1(k, b) + \sin\eta_1 \cdot R_2(k, b)}\right]^2 \times \left[\frac{\cos\eta_1'' \cdot R_1(k, 2a+b) + \sin\eta_1'' \cdot R_2(k, 2a+b)}{\cos\eta_1' \cdot R_1(k_1', 2a+b) + \sin\eta_1' \cdot R_2(k_1', 2a+b)}\right]^2. \tag{26}$$

From the phase equations (19)-(21) we obtain an expression for the absorption coefficient that is exact because none of the approximations of Kostarev[2], Shiraiwa et al[3] or Petersen[7] were used in its derivation. In principle, the equation can also be used to calculate $\tau(k)$ in the region of the main absorption edge, if we assume that the fine structure at the main edge is determined by the integral $I(k) = \sum_{x,y,z} \left|\int \psi_0 x \psi_f d\tau\right|^2$.

Calculation of the average field V_0'

In the same way as in the work of Petersen[7] and Kostarev[2], the field of N_1 atoms at a distance r_1 from the absorbing atom is replaced by a field averaged over a sphere of radius r_1, namely, $\overline{V_1(r)} = \sum_{j=1} \overline{V_j(r)} = N_1 \overline{V_j(r)}$. If the field of each atom of the first layer is approximated by a square-well potential with the same parameters a and V_0, we obtain for the absorbing atom

$$\overline{V_1(r)} = -\frac{V_0 N_1}{4 r_1 r}\left[a^2 - (r_1 - r)^2\right] \tag{27}$$

for $r_1 - a \leqslant r \leqslant r_1 + a$. For $r = r_1$

$$\overline{V_1(r_1)} = V_{0\max}' = -\frac{N_1 V_0}{4}\left(\frac{a}{r_1}\right)^2, \tag{28}$$

and for $r = r_1 - a$ and $r = r_1 + a$

$$\overline{V_1(r)} = 0.$$

The averaged field has the form shown in Fig. 9b. For simplicity we average it with respect to r between the limits $r_1 - a < r < r_1 + a$, i.e., we introduce a concentric square well of width $2a$ and depth V_0'. This averaging does not in practice change the position of the fine structure extrema, since the positions of the extrema are determined by the quantity $2kr_1$ and the phase $\eta_1(k)$, and these depend only on the parameters of the field of the absorbing atom. We note that the field V_0 is in a sense an average field acting on the electron in a region of radius a, so the V_0', not $V_{0\max}'$, should be compared with V_0.

Averaging over r gives

$$V_0' = \overline{\overline{V_1(r)}} = \frac{N_1 \int_{r_1-a}^{r_1+a} V(x)\, 4\pi x^2 dx}{\int_{r_1-a}^{r_1+a} 4\pi x^2 dx} = -\frac{N_1 V_0}{24}\left(\frac{a}{r_1}\right)^2 \frac{1}{\left(1 + \frac{a^2}{3r_1^2}\right)}. \tag{29}$$

Since $a^2 \ll 3r_1^2$,

$$\left|\frac{V_0'}{V_0}\right| \approx \frac{N_1}{24}\left(\frac{a}{r_1}\right)^2.$$

The coordination number N_1 is 8 or 12, and the constant a in metals at least is no larger than $r_1/2$ (the radius of the atom). In this limiting case, we have for Cu ($r_1 \approx 2.6$ Å) $V_0'/V_0 = 1/8$. Actually this ratio is probably much smaller because $a \ll r_1$.

Equation (29) will be used to evaluate the magnitude of the fluctuations of $\tau(k)$.

Transition to large k

First approximation. Let

$$\frac{1}{kb} = \frac{1}{k(r_1 - a)} \approx \frac{1}{kr_1} \ll 1.$$

For Cu $r_1 \approx 2.6$ Å and for the A maximum (17 ev) $k \approx 2.7 Å^{-1}$, i.e., $1/kr_1 \approx 1/7$. In the short wavelength region the quantity $1/kr_1$ is even smaller, but near the Fermi level and at the main edge where $k = 1$ to 1.5 $Å^{-1}$, $1/kr_1 \approx 1/3$ to 1/5 and the approximation is not valid. Neglecting terms with $1/kb$ in equations (22)-(25), we obtain

$$T_1(k, b) \approx k \sin kb, \quad T_2(k, b) \approx -k \cos kb;$$

$$R_1(k, b) \approx -\cos kb, \quad R_2(k, b) \approx \sin kb.$$

Inserting these functions into (2), (21) and (26), we obtain after obvious manipulations

$$\tau(k) = \frac{(1+A^2)(1+B^2)}{\left(\frac{k_1'}{k}A + B\right)^2 + \left(1 - AB\frac{k}{k_1'}\right)^2}, \tag{30}$$

where

$$A = \operatorname{tg} 2k_1'a, \quad B = \operatorname{tg}[kr_1 - ka + \eta_1(ka)],$$
$$k_1' = \sqrt{k_0'^2 + k^2}, \qquad k_0'^2 = \frac{2mV_0'}{\hbar^2}.$$

Two important results follow from this equation.

1) As $k \to \infty$, $k_1' \to k$ and $\tau(k) \to 1$. This means that the fluctuations in $\tau(k)$ decrease in amplitude as k increases, and they vanish in the limit of the far shortwave region. For $k_1' = k$, $\tau(k) = 1$. The physical cause of the extinction of the fluctuations is the increase in transparency of the potential layer V_0' as the energy of the ejected electron increases. The amplitude of the wave scattered from the layer diminishes as k increases, and, consequently, the fluctuations of the absorption coefficient decrease. This effect occurs even without taking into account thermal vibrations of the atoms.

2) The smaller the quantity k_0', the faster the extinction of the fluctuations. Because

$$k_0'^2 = \frac{2mV_0'}{\hbar^2} = \frac{N_1 V_0}{24}\left(\frac{a}{r_1}\right)^2 \frac{2m}{\hbar^2},$$

and the quantity N/r^2 diminishes for the outer spheres, the absorption peaks due to the remote spheres fade faster with increasing k than the principal peaks due to the first sphere. In agreement with this explanation only the peaks due to the first sphere are experimentally observed in the far short wavelength region, while hypderfine structure (peaks due to the remoter spheres) is observed in the primary region.

Second approximation. Let $\frac{1}{kb} \ll 1$ and $k_0'^2 \ll k^2$. This second condition is equivalent to $E_{\text{kin}} \gg V_0'$. Introducing the small parameter $\Delta = \frac{1}{2} \cdot \frac{k_0'^2}{k^2}$ and substituting $k_1' = k(1 + \Delta)$ in Eq.(30), we obtain, to first order in Δ, the simpler expression

$$\tau(k) \approx \frac{1}{1 + \frac{4AB + 2A^2(1-B^2)}{(1+A^2)(1+B^2)} \cdot \Delta} = \frac{1}{1 + \frac{k_0'^2}{k^2} \sin 2k_1' a \sin(2kr_1 + 2\eta_1)}. \tag{31}$$

If we set $I_s' = 0$ in the Petersen-Kostarev formula (2), approximate $\overline{V_s(x)}$ by a square well with parameters V_0' and a, and include only the first coordination sphere in the sum, this formula reduces to Eq.(31). Consequently, Kostarev's theory corresponds to the approximation $\frac{1}{kr_1} \ll 1$ and $E_{\text{kin}} \gg V_0'$.

We note that in this approximation $\sin 2k_1'a \approx \sin 2ka$. Because $a \ll r_1$, the factor $\sin 2k_1'a$ slowly modulates the leading term $\sin(2kr_1 + 2\eta_1)$ and the quantity $\frac{k_0'^2}{k^2} \sin 2k_1'a$ should be identified as the fluctuation amplitude. If we assume $a =$ = 0.1 to 0.3 Å for Cu, we find that the strongest fluctuations in absorption will be observed in the 70 to 150 ev region, where $\sin 2ka$ has a maximum. And, in fact it has been established experimentally that the most intense peaks in the copper spectrum are the 147 and 80 ev peaks. Similarly, in the spectrum of iron the highest peak is located at 105 ev. Thus the general shape of the absorption curv is determined by the parameter a of the field of the absorbing atom.

The general attenuation of the fluctuations is characterized by the quantity

$$\frac{k_0'^2}{k^2} = \frac{V_0'}{E_{\text{kin}}} = \frac{V_0}{E_{\text{kin}}} \cdot \frac{a^2 N_s}{24 r_s^2}.$$

Calculation of the phase $\eta_1(k)$

The phase $\eta_1(k)$ depends only on the parameters of the field of the absorbing atom and is found by means of Eq.(19). The results of our calculations are shown in Fig.10. The phase is a function of ka and depends on the parameter $k_0a =$ $= \frac{\sqrt{2mV_0}}{\hbar^2} \cdot a$. In the limit as $k \to \infty$, $\eta_1 \to 0$. As $k \to 0$, $\eta_1(ka) \to s\pi$, where s is the number of levels in the well with angular momentum $l = 1$. If $k_0a < \pi$, then $s = 0$; if $\pi \leqslant k_0a < 2\pi$, then $s = 1$; if $2\pi \leqslant k_0a < 3\pi$, then $s = 2$, etc. The previously mentioned similarity of scattering from a square well and from a screened Coulomb potential gives reason to assert that k_0a is proportional to $\sqrt{Za}$, where Z is the atomic number. Allis and Morse[10] showed that the partial scattering cross sections for slow electrons are quasi-periodic with respect to the quantity $\beta = \sqrt{\frac{Z}{2}}$ where a_0 is the Bohr radius and r_0 is the limiting radius of the atom (approximately the Slater radius). Because the partial cross sections are determined by the values of $\sin^2 \eta_l$, the quasi-periodicity of the cross sections is a consequence of the quasi-periodic variation of the phases η_l.

That such behavior of the phases with variation of $\sqrt{Za}$ and $\sqrt{Zr_0}$ is a gene characteristic of all screened fields and potential wells will be evident from F 10. The character of the phase curves for square wells is similar to that of th phase curves calculated for Hartree and Thomas-Fermi fields. The phases for A a Kr are in best agreement with the curves for a well with a parameter k_0a only slightly larger than 2π and 3π, respectively. The dependence of the phase on k more complicated for other atoms or ions, but we assume that the behavior of the phase is similar to that indicated by the curves in Fig.10.

Fig.2 gives a series of curves of $\eta_1(k)$ calculated by different authors, assuming Hartree fields, for various atoms and ions. The semi-classically determi phases[2] for $_{29}$Cu and $_{26}$Fe increase almost linearly as k decreases. However, the WKB method is invalid in the region of small k, and it is to be expected that th phases for Cu and Fe will tend to π for small k, similarly to the curves for a we with k_0a between 9.3 and 9.42. This conjectured behavior of the phase for coppe is indicated by the dashed line. Kostarev's[2] error in determining the position of the 17 ev peak ($k = 2.7$ Å^{-1}) for copper is connected mainly with the semi-class cal method of phase calculation, and disappears if for $k < 4$Å^{-1} the phase actuall decreases and approaches the value $\eta_1 = \pi$.

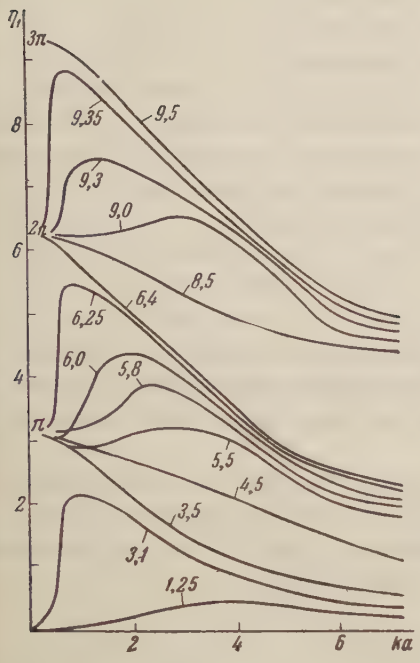

Fig.10. Scattering phase η_l for different potential wells. The numbers at the curves give the value of the parameter $k_0 a$.

For $_{20}$Ca it is reasonable to assume that in the energy region up to 150 ev the phase remains close to π; for $_{13}$Al the phase behavior is similar to that of Cu, but as $k \to 0$, $\eta_1 \to 0$. For beryllium we can assume that as $k \to 0$, $\eta_1 \to 0$; the same is true for helium, while as k increases, the phase increases to $\pi/4$ or $\pi/2$ and remains close to this average value, slowly decreasing as k increases.

Discussion of the Results

We have established that the positions of absorption fine structure extrema are determined by the radii of the coordination spheres of the atoms surrounding the absorbing atom in a metal or alloy and by the potential of the absorbing atom itself.

The amplitude of the absorption fluctuations is determined mainly by the ratio N_1/r_1^2 and the ratio of the field V_0' of the neighboring atoms, averaged over the sphere, to the kinetic energy of the ejected electron. Thus, through investigation of fine structure we are able to determine in principle the significant characteristics of the field of the absorbing atom such as the depth V_0 of the potential well and the screening constant a. The quantity directly associated with the field parameters V_0 and a is the scattering phase $\eta_l(k)$. It must be found from experimental data. The attainable accuracy in determining the phase variation depends on the number of reliable, experimentally determined extrema in the absorption curve. Thus the main edge and the Kronig structure should be surveyed at low temperatures, when the greatest number of extrema are evinced.

The theory proposed in this paper uses a very simple approximation for the potential. To clarify the relation between the absorption curve parameters and a and Z one can solve the problem for potentials of the type used by Allis and Morse[10], the screened Coulomb field and other short-range fields. Phase calculations for more complicated fields such as the self-consistent Hartree field or the Thomas-Fermi potential require numerical methods. The WKB method may be used in the short wavelength region and the variational method in the initial absorption region. The results should be compared with those of phase calculations for simple fields. Clearly, any improvement in the accuracy of determination of $\eta_l(k)$ should be attributable to more precise specification of the field of the absorbing atom. The average field of the surrounding atomic layers can be taken, as before, in the form shown in Fig.9a, since this field does not affect the phase $\eta_l(k)$.

A comparative study of the L_I, L_{II} and L_{III} absorption curves is of interest, since here experiment can yield additional information about the behavior of the phases $\eta_0(k)$ and $\eta_2(k)$. Simultaneous knowledge of the phases $\eta_1(k)$, $\eta_0(k)$ and $\eta_2(k)$ will allow of more accurate determination of the field parameters.

Equations (26), (30) and (31) are also approximately applicable to the calculation of the fine structure in the absorption spectra of alloys.

The positions of the absorption peaks for alloys, as for metals, are determined chiefly by the coordination radii r_s. Therefore one can make approximate

calculations neglecting the difference between the constituent atoms. This difference manifests itself only in the magnitude of the field V_0', i.e., in the comparative intensities of the peaks associated with the different spheres.

For ionic lattices one can give a qualitative explanation of the behavior of the absorption coefficient. If we suppose that this field is of longer range, i.e., that a and V_0' are larger than for the field of an atom in a metal, Eq. (31) indicates that for ionic lattices the extent of the structure is smaller because $\sin 2ka$ goes through zero for smaller k, while the amplitude of the fluctuations in the primary region is greater because the field V_0' is larger.

Conclusions

1. The nature of absorption fine structure in metals and alloys is determine primarily by the parameters N_s and r_s of the nearest coordination sphere atoms an of the field of the absorbing atom. The field of the neighboring atoms determine the intensity of the fluctuations in absorption.

2. Consideration of existing theories indicates that these theories employ two basic approximations: a) weak average field of the atoms near the absorber, and b) short-range interaction of the ejected electron with the field of the atom

3. We have shown that the absorption is given by the equation

$$\tau(k) \sim \left[1 - A(k) \sum \frac{N_s}{r_s^2} \sin(2kr_s + 2\eta_1) \right]^{-1}$$

or by the simpler approximate formula

$$\tau(k) \sim - \sum_s \frac{N_s}{r_s^2} \sin(2kr_s + 2\eta_1),$$

which is applicable to metals, alloys and molecules. This formula was used for calculations for a series of metals with cubic and hexagonal structure. The best agreement with experiment is obtained if the computation k scale is converted to the experimental scale by means of the formula

$$E = \frac{\hbar^2 k^2}{2m} - A,$$

where A is found by fitting the experimental data to the theoretical curve. The constant A is a physical attribute of the material, and its value has been determined for a number of metals.

4. We suggest that the theories of Kostarev[2] and Shiraiwa et al[3] disagree with experiment in the region near the absorption edge because of the use of the semi-classical method for calculating the scattering phases and because of the use of perturbation theory.

5. The first intense peak, the "A maximum" of the fine structure, is interpreted analogously to the shorter wavelength maxima.

6) We have shown that the $\Delta E \sim 1/a^2$ law can be obtained from general short-range order theory.

I desire to thank I.B.Borovskii and V.V.Shmidt for their valuable discussion and comments and T.Kupriyanova for her help with the calculations.

"A.A.Baikov" Institute of Metallurgy,
Academy of Sciences of the USSR

References

1. R.Kronig, Z.Phys., 70, 317 (1931); 75, 191 (1932).
2. A.I.Kostarev, Dissertation, 1952; Zhur.eksp.i teor.fiz., 9, 267 (1939); 16, 739 (1946); 19, 413 (1949); 21, 917 (1951); 22, 628 (1952).
3. T.Shiraiwa, T.Ishimura & M.Sawada, J.Phys.Soc.Japan, 13, 847 (1958).
4. R.Ferrel, Phys.Rev., 101, 554 (1956).
5. D.Pines & D.Bohm, Phys.Rev., 85, 338 (1952); Ibid, 92, 609 (1953); D. Pines, Ibid., 92, 626 (1953).
6. M.Sawada, K.Tsutsumi & A.Hayase, J.Phys.Soc.Japan, 12, 628 (1957).
7. H.Petersen, Z.Phys., 98, 569 (1936).
8. T.Hayasi, Sci.Reports Tohoku Univ., 34, 185 (1951).
9. N.F.Mott & H.S.W.Massey, Theory of Atomic Collisions, Oxford, 1933.
10. H.Allis & P.Morse, Z.Phys., 70, 567 (1931).

CONTRIBUTION TO THE THEORY OF THE TEMPERATURE DEPENDENCE OF THE FINE STRUCTURE OF X-RAY ABSORPTION SPECTRA

- V.V.Shmidt

It is known that when the absorber is heated the contrast of the short wavelength structure decreases, the structure "melts".

A theoretical explanation of this phenomenon is given in the works of Kostarev[1]. He proposed the following explanation of the fine structure of x-ray absorption spectra. The atom from which an electron is ejected in the absorption process is surrounded by neighboring atoms. These nearest neighbors give rise to a potential barrier for the ejected electron. In the region of positive energies (continuum) the solution of the Schrödinger equation with such a potential yields eigenfunctions, the amplitudes of which are non-monotonic functions of the electron energy. This non-monotony is the direct reason for appearance of fine structure in the short wavelength absorption spectrum. Thus, Kostarev's theory of fine structure is a short-range order theory.

According to Kostarev, heating of the absorber causes "smearing out" of the potential barrier and, therefore, by increasing its penetrability, reduces the contrast of the structure. The deductions from this theory are in satisfactory qualitative agreement with experiment.

The ideas presented by Kozlenkov[2] provided the basis for a new approach to the temperature dependence of the fine structure and led to results in a good quantitative agreement with experiment.

Formulation of the Problem

According to short-range order theories[2,3], the appearance of fine structure on the short wavelength side of the absorption edge is the result of interference of electron waves originating at the center of the absorbing atom and scattered by its nearest neighbors.

If all the atoms are in their equilibrium positions, the variable part of the K absorption coefficient in the region more than 15-20 ev to the high energy side of the absorption edge can be described by the formula[2]

$$\mu_0 = \sum_s N_s A_s \sin(2Kr_s + 2\eta_1), \tag{1}$$

where N_s is the number of atoms in the s-th coordination sphere, A_s is the amplitude at the point of the central atom of the wave scattered by an atom of the s-th coordination sphere, K is the wave number of the electron ejected from the central atom, r_s is the radius of the s-th coordination sphere and η_1 is the phase of the scattered wave.

Now, let the atoms be in thermal motion. The characteristic time for an electron (the flight time over a distance of the order of magnitude of the radius of the first coordination sphere) is 10^{-3}-10^{-4} times shorter than the period of the thermal vibrations of the atoms. This means that an electron "senses" the given instantaneous distribution of the atoms and is scattered by it.

We denote the instantaneous displacement of the central atom by $\mathbf{x}_0(t)$ and the displacement of the i-th atom of the s-th sphere by $\mathbf{x}_{is}(t)$. The distance r_{is} between the displaced central atom and the is atom is

$$r_{is} = r_s + (\mathbf{e}_{is}, \mathbf{x}_{is} - \mathbf{x}_0), \tag{2}$$

where $\mathbf{e}_{is}$ is a unit vector directed from the equilibrium position of the central

atom to the equilibrium position of the is atom. Equation (2) was deduced on the assumption that x_{is} and $x_0 \ll r_s$, i.e., the usual assumption that the thermal vibrations are small.

Then, inserting (2) into (1), we obtain the following expression for the instantaneous value of the variable part of the absorption coefficient:

$$\mu(t) = \sum_{si} A_s \left[\sin B_s \cos\left(2K\mathbf{e}_{is}, \mathbf{x}_{is} - \mathbf{x}_0\right) + \cos B_s \sin\left(2K\mathbf{e}_{is}, \mathbf{x}_{is} - \mathbf{x}_0\right)\right], \tag{3}$$

where $B_s = 2Kr_s + 2\eta_1$.

Thus, essentially, the problem reduces to averaging $\mu(t)$ in time.

Calculation of the Time Average of $\mu(t)$

Let us expand the displacements x_{is} and x_0 into normal waves:

$$\left.\begin{aligned} \mathbf{x}_{is}(t) &= \sum_{\vec{\varkappa} j} \mathbf{a}_{\vec{\varkappa} j} \cos\left(\omega_{\vec{\varkappa} j} t - \vec{\varkappa}\mathbf{r}^0_{is} + \delta_{\vec{\varkappa} j}\right), \\ \mathbf{x}_0(t) &= \sum_{\vec{\varkappa} j} \mathbf{a}_{\vec{\varkappa} j} \cos\left(\omega_{\vec{\varkappa} j} t + \delta_{\vec{\varkappa} j}\right); \end{aligned}\right\} \tag{4}$$

here $\mathbf{r}^0_{is} = \mathbf{e}_{is} r_s$. The origin of the coordinate system is located at the equilibrium position of the central atom; the $j = 1,2,3$ are indices indicating one longitudinal (1) and two transverse (2 and 3) waves.

Let us consider the first term in (3):

$$\cos\left(2K\mathbf{e}_{is}, \mathbf{x}_{is} - \mathbf{x}_0\right) = \cos\left\{2K\mathbf{e}_{is}, \sum_{\vec{\varkappa} j} \mathbf{a}_{\vec{\varkappa} j} \left[\cos\left(\omega_{\vec{\varkappa} j} t - \vec{\varkappa}\mathbf{r}^0_{ts} + \delta_{\vec{\varkappa} j}\right) - \cos\left(\omega_{\vec{\varkappa} j} t + \delta_{\vec{\varkappa} j}\right)\right\}. \tag{5}$$

Using the formula for the difference of cosines, Eq.(5) can be reduced to

$$\cos\left(2K\mathbf{e}_{is}, \mathbf{x}_{is} - \mathbf{x}_0\right) = \cos\left(\sum_{\vec{\varkappa} j} y \sin\varphi\right). \tag{6}$$

Here we have introduced the following notation

$$y = 2Kr_s \left(\mathbf{a}_{\vec{\varkappa} j} \mathbf{e}_{is}\right)\left(\vec{\varkappa}\mathbf{e}_{is}\right), \tag{7}$$

$$\varphi = \omega_{\vec{\varkappa} j} t - \vec{\varkappa}\mathbf{r}^0_{is}/2 + \delta_{\vec{\varkappa} j}. \tag{8}$$

In addition, in deducing Eq.(6) it was assumed that the behavior of the system is in accord with Debye's theory of thermal vibrations. Therefore only long waves are considered, i.e., $\varkappa r^0_{is} \ll 1$.

The instantaneous value of the variable part of the absorption coefficient can now be written in the form:

$$\begin{aligned} \mu(t) = \sum_{si} A_s \Bigg\{ &\sin B_s \frac{1}{2}\left[\exp\left(i\sum_{\vec{\varkappa} j} y \sin\varphi\right) + \exp\left(-i\sum_{\vec{\varkappa} j} y \sin\varphi\right)\right] + \\ &+ \cos B_s \frac{1}{2i}\left[\exp\left(i\sum_{\vec{\varkappa} j} y \sin\varphi\right) - \exp\left(-i\sum_{\vec{\varkappa} j} y \sin\varphi\right)\right]\Bigg\}. \end{aligned} \tag{9}$$

The problem is to find the time average of (9), (i.e., the average over φ). Let us examine the first term

$$\exp\left(i\sum_{\vec{\varkappa} j} y \sin\varphi\right) = \prod_{\vec{\varkappa} j} e^{iy\sin\varphi} \tag{10}$$

The phases $\delta_{\vec{\varkappa}j}$ of the normal waves which enter the expression for φ are entirely independent. Therefore, the average of the product should equal the product of the averages of the cofactors. Hence the problem reduces to finding the average of

$$\langle e^{iy \sin \varphi} \rangle = \frac{1}{2\pi} \int_{-\pi}^{\pi} e^{iy \sin \varphi} d\varphi = J_0(y), \tag{11}$$

where J_0 is a Bessel function.

Thus, the time average of (10) is

$$\left\langle \exp\left(i \sum_{\vec{\varkappa}j} y \sin \varphi\right) \right\rangle = \prod_{\vec{\varkappa}j} J_0(y). \tag{12}$$

Let us evaluate y, using (7). For the far short wavelength features of the fine structure $2K \approx 12\text{Å}^{-1}$, $\varkappa r_s \approx 0.1$ (the condition that we consider only the long waves of the lattice vibrations), and the amplitude $a_{\vec{\varkappa}j}$ cannot exceed the root mean square displacement of the atoms of the lattice which, for high temperatures, is of the order of 0.3 Å. Therefore, $y \approx 0.5$. This enables us to use the power series expansion of the Bessel function:

$$J_0(y) = 1 - y^2/4 + y^4/64 - \ldots \tag{13}$$

This series is closely approximated by the function $\exp(-y^2/4)$; therefore (12) becomes:

$$\left\langle \exp\left(i \sum_{\vec{\varkappa}j} y \sin \varphi\right) \right\rangle = \exp\left[-\sum_{\vec{\varkappa}j} K^2 r_s^2 (\mathbf{e}_{is} \mathbf{a}_{\vec{\varkappa}j})^2 (\mathbf{e}_{is}\vec{\varkappa})^2\right]. \tag{14}$$

Since $J_0(y)$ is an even function of y, we obtain the following equality:

$$\left\langle \exp\left(i \sum_{\vec{\varkappa}j} y \sin \varphi\right) \right\rangle = \left\langle \exp\left(-i \sum_{\vec{\varkappa}j} y \sin \varphi\right) \right\rangle. \tag{15}$$

This means that as a result of averaging, the second term in (9) vanishes and the mean value of the variable part of the absorption coefficient becomes

$$\bar{\mu} = \sum_{si} A_s \sin B_s \exp\left[-\sum_{\vec{\varkappa}j} K^2 r_s^2 (\mathbf{e}_{is} \mathbf{a}_{\vec{\varkappa}j})^2 (\mathbf{e}_{is}\vec{\varkappa})^3\right]. \tag{16}$$

Determination of the Temperature Dependence of the Variable Part of the Absorption Coefficient

Replacing in (16) summation over $\vec{\varkappa}$ by integration in $\varkappa$-space, we obtain

$$\sum_{\vec{\varkappa}j} (\mathbf{e}_{is} \mathbf{a}_{\vec{\varkappa}j})^2 (\mathbf{e}_{is}\vec{\varkappa})^2 = \frac{V}{(2\pi)^3} \sum_{j=1}^{3} \int (\mathbf{e}_{is} \mathbf{a}_{\vec{\varkappa}j})^2 (\mathbf{e}_{is}\vec{\varkappa})^2 d^3\varkappa, \tag{17}$$

where V is the volume of the body. Taking the direction of $\mathbf{e}_{is}$ as the direction of the $\varkappa_z$ axis and transforming to spherical coordinates, we obtain

$$d^3\varkappa = 2\pi\varkappa^2 \sin\vartheta \, d\vartheta \, d\varkappa,$$

where ϑ is the angle between the vectors $\mathbf{e}_{is}$ and $\vec{\varkappa}$.

Separating out from (17) the term which corresponds to the longitudinal waves $(\mathbf{a}_{\vec{\varkappa}1} \parallel \vec{\varkappa})$, and integrating over ϑ, we obtain

$$I_1 = \frac{2}{5}\frac{V}{(2\pi)^2}\int_0^{\varkappa_m} a_{\varkappa 1}^2 \varkappa^4 d\varkappa. \tag{18}$$

The amplitude of a normal wave is expressed in terms of its energy by the formula[4]

$$a_{\vec{\varkappa}j}^2 = \frac{2}{mN}\cdot\frac{E_{\vec{\varkappa}j}}{\omega_{\vec{\varkappa}j}^2}, \tag{19}$$

where m is the mass of an atom, N is the number of atoms in the solid and $E_{\vec{\varkappa}j}$ is the energy of the normal wave, given by

$$E_{\vec{\varkappa}j} = \left(n_{\vec{\varkappa}j} + \frac{1}{2}\right)\hbar\omega_{\vec{\varkappa}j}. \tag{20}$$

Here $n_{\vec{\varkappa}j}$ is the number of phonons in the state $(\vec{\varkappa}j)$, which is determined by the Bose-Einstein distribution

$$n_{\vec{\varkappa}j} = (e^{\hbar\omega_{\vec{\varkappa}j}/kT} - 1)^{-1}. \tag{21}$$

Using (19), (20) and (21), we integrate (18) and obtain

$$I_1 = \frac{1}{5}\cdot\frac{V}{(2\pi)^2}\frac{k^4\theta^4}{\hbar^3 mNv^5}\left[F\,(T/\theta) + \frac{1}{2}\right],$$

$$F\,(T/\theta) = (e^{\theta/T} - 1)^{-2} + \frac{1}{3}\cdot\frac{T}{\theta}f_D\,(T/\theta), \tag{22}$$

$$f_D\,(T/\theta) = 3\left(\frac{T}{\theta}\right)^3\int_0^{\theta/T}\frac{e^x x^4}{(e^x - 1)^2}\,dx.$$

Here $\theta = \hbar\omega_m$ is the Debye temperature, v is the propagation velocity of elastic waves, f_D is Debye's specific heat function, a plot of which will be found in Ref. 5. Eq.(18) was integrated on the assumption, as in Debye's theory, of a linear dispersion law, i.e., $\omega_{\vec{\varkappa}j} = v\varkappa$. The calculations were carried out on the assumption that the velocities of the longitudinal waves v_1 and of the transverse waves v_2 are equal to the average propagation velocity v of elastic waves.

Now let us determine the term I_2 in (17), which corresponds to the first transverse wave. Let the vector $\mathbf{a}_{\vec{\varkappa}2}$ be normal to $\varkappa$ and lie in the plane of the vectors $\mathbf{e}_{is}$ and $\vec{\varkappa}$. Then, it can readily be shown that

$$I_2 = \frac{2}{15}\cdot\frac{V}{(2\pi)^2}\cdot\frac{k^4\theta^4}{\hbar^3 mNv^5}\left[F\,(T/\theta) + \frac{1}{2}\right]. \tag{23}$$

The term I_3 which corresponds to the second transverse wave, vanishes, since the vector $\mathbf{a}_{\vec{\varkappa}3}$ is always perpendicular to $\mathbf{e}_{is}$ and $(\mathbf{e}_{is}\mathbf{a}_{\vec{\varkappa}3}) = 0$.

The maximum wave number $\varkappa_m$ is given, as is known, by the equation

$$\frac{V}{(2\pi)^3}\cdot\frac{4}{3}\pi\varkappa_m^3 = N. \tag{24}$$

Therefore $v = \omega_m/\varkappa_m$ can be written in the form

$$v = \frac{k\theta v_0^{1/3}}{2\pi\hbar}\sqrt[3]{4\pi/3}, \tag{25}$$

where $v_0 = V/N$ is the volume per atom.

Now we can rewrite (17) in the form

$$\sum_{\vec{x}j} (e_{is}\vec{a}_{\vec{x}j})^2 (e_{is}\vec{\varkappa})^2 = 7.7\,\frac{\hbar^2}{k}\cdot\frac{F(T/\theta)+1/2}{m\theta v_0^{2/3}}. \qquad (26)$$

Thus the final expression for the variable part of the absorption coefficient becomes (Ref.16):

$$\bar{\mu} = \sum_s A_s N_s \sin B_s \exp\left\{-7.7\cdot\frac{\hbar^2}{k}\cdot\frac{K^2 r_s^2}{m\theta v_0^{2/3}}\left[F(T/\theta)+\frac{1}{2}\right]\right\}. \qquad (27)$$

Discussion

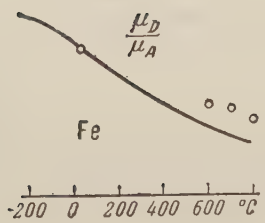

Fig.1

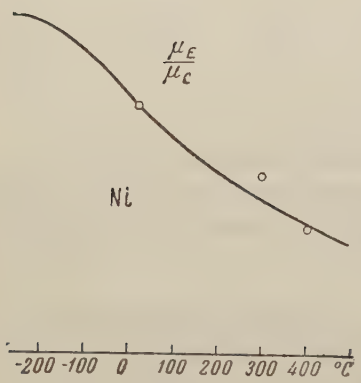

Fig.2

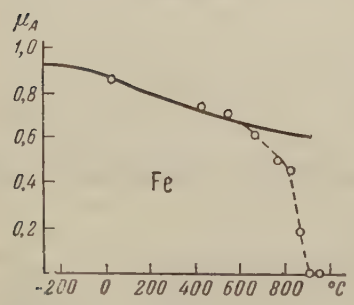

Fig.3

1. First, we note that at $T = 0$, when $F(0) = 0$, the exponent is not zero due to the term 1/2 in the brackets. This term appears because the zero-point vibrations of the lattice have been taken into account. The decrease of contrast due to the zero-point vibrations is by no means small. They have a particularly strong suppressing effect on the far short wavelength extrema. Thus the height of the D peak in the Cu K absorption spectrum (located 147 ev from the absorption edge) at 0°K is only 63% the height it would have if the atoms in the lattice were completely at rest. This example shows that whereas the theory[2] of fine structure is based on the assumption that the atoms are at rest, in comparison of the calculated peak intensities with experiment, one must take into account both the zero-point vibrations of the lattice and the thermal vibrations of the atoms.

2. Equation (27) describes the well known experimental fact that with rise of temperature the far short wavelength peaks of the fine structure disappear before the peaks nearer the edge. Indeed, the K^2 term in (27) considerably strengthens the temperature dependence of the peak height.

3. The hyperfine structure, which is due to the scattering of the electron waves from outer coordination spheres, must vanish sooner than the fine structure caused by scattering from the first coordination sphere. This too is confirmed by experiment.

4. Finally, it is interesting to carry out a direct comparison of the deductions from theory with experiment. Trapeznikov & Nemnonov[6] measured the ratios of the peak heights μ_D/μ_A for Fe and μ_E/μ_C for Ni. These data are indicated by the open circles in Figs.1 & 2. We measured the height of the peak A for Fe at different temperatures; the results are shown in Fig.3. The solid curves in all the figures were calculated using Eq.(27).

It will be evident from Fig.3 that above 700°C the experimental and theoretical data diverge sharply. This indicates that at this temperature the thermal vibrations become highly anharmonic and therefore are no longer described by the Debye-Born theory of elastic vibrations.

Summarizing, we may conclude that the proposed theory yields satisfactory agreement with experiment.

I am deeply grateful to I.B.Borovskii and A.I.Kozlenkov for discussions and valuable suggestions.

References

1. A.I.Kostarev, Zhur.eksp.i teor.fiz., 20, 811 (1950); 21, 917 (1951).
2. A.I.Kozlenkov, Present issue of the Bulletin, p.968.
3. T.Shiraiwa, T.Ishimura & M.Sawada, J.Phys.Soc.Japan, 13, 847 (1958).
4. R.W.James, Optical Principles of the Diffraction of X-Rays. London, 1948.
5. F.Seitz, The Modern Theory of Solids, N.Y., 1940.
6. V.A.Trapeznikov & S.A.Nemnonov, Fiz.metallov i metallovedenie (Physics of Metals & Metallography), 3, 314 (1956).

INFLUENCE OF TUNGSTEN IMPURITIES ON THE TEMPERATURE DEPENDENCE OF THE FINE STRUCTURE OF THE K ABSORPTION SPECTRUM OF IRON

- I.B.Borovskii & V.V.Shmidt

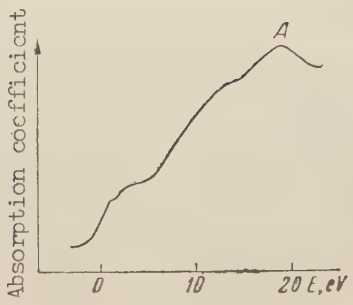

Fig.1

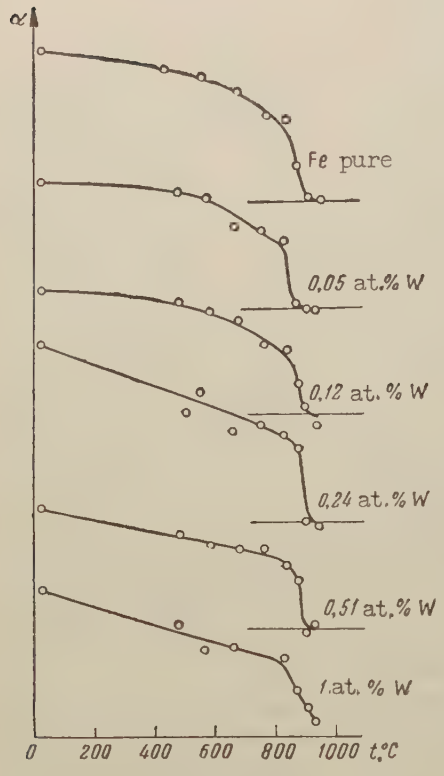

Fig.2

An earlier study[1] of the influence of minor admixtures of Sn and Tl on the temperature dependence of the fine structure of the L_{III} absorption spectrum of Pb showed that at some optimum impurity concentrations the temperature at which the fine structure disappears increases. In other words, these impurities tend to "stabilize" the fine structure.

In addition, we have studied the influence of minor amounts of W on different physical properties of Fe: the self-diffusion coefficient[2], the coefficient of linear expansion[3], the elastic constants and internal friction coefficient[4], the optical constants[5] and the temperature coefficient of electric resistance[6]. In all these experiments we found that at a W content of 0.05-0.1 atomic percent there appears a maximum or minimum in the "property vs concentration" curve.

In connection with the above, we felt it would be of interest to study the temperature dependence of the fine structure of the x-ray absorption spectrum of iron in alloys with a low W content.

We used the alloys that had been employed in the experiments mentioned above.

The study was carried out on a double-crystal spectrometer by the procedure described in Ref.7. The absorber-foil was heated in a high vacuum (10^{-5} mm Hg) by passing an electric current through it.

To study the temperature dependence of the fine structure we measured the magnitude of τd (the product of the linear absorption coefficient by the absorber thickness) at the points E = 18 ev ($\tau_1 d$) and E = 23 ev ($\tau_2 d$) in the range from 20 to 950° C (the energies E were reckoned from the absorption edge to the short wavelength side).

The ratio $\mu_A = (\tau_1 d - \tau_2 d)/\tau_2 d$, obviously, does not depend on absorber thickness and characterizes the height of peak A (Fig.1). The temperature dependence of μ_1 for all the investigated alloys is shown in Fig.2.

The value of the derivative $d\mu_A/dT$ can serve as a characteristic of the rate of "melting" (effacement) of the fine structure. This quantity was determined by means of graphic differentiation at the t = 20°C points of the curves shown in Fig.2. These curves were first approximated by polynomials by means of the method of least squares.

The concentration dependence of $d\mu_A/dT$ is shown in Fig.3, where the concentration dependence of the self-diffusion coefficient obtained in Ref.2 is also given for the purpose of comparison.

We now turn to a discussion of the results. Shmidt[8] deduced the following formula for the temperature dependence of the intensity of the short wavelength fine structure peaks:

$$\mu = \sum_s N_s A_s \sin(2Kr_s + 2\eta_1) \exp\left\{-7.7\frac{\hbar^2}{k}\cdot\frac{K^2 r_s^2}{m\theta v_0^{2/3}}\left[F\left(\frac{T}{\theta}\right)+\frac{1}{2}\right]\right\} \qquad (1)$$

$$F\left(\frac{T}{\theta}\right) = (e^{\theta/T}-1)^{-1} + \frac{1}{3}\cdot\frac{T}{\theta} f_D\left(\frac{T}{\theta}\right);$$

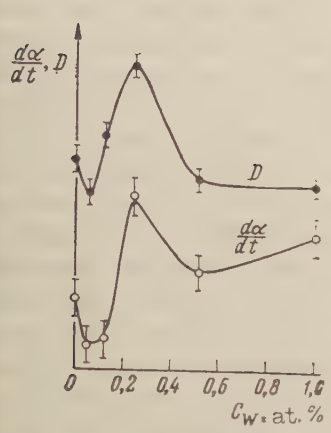

Fig.3

here N_s is the number of atoms in the s-th coordination sphere; A_s is the scattering amplitude of the electron wave by the atoms of the s-th coordination sphere at the point of the absorbing atom; η_1 is the scattering phase; K is the wave number of the electron; r_s is the radius of the s-th coordination sphere; k is the Boltzmann constant; m is the atomic mass; θ is the Debye temperature; v_0 is the volume per atom; f_0 is Debye's specific heat function.

We assume that peak A in the fine structure of the iron spectrum is due mainly to scattering of electron waves by atoms of the first coordination sphere. Then instead of Eq.(1), we can use the simpler formula:

$$\mu = \mu_0 \exp\left\{-7.7\frac{\hbar^2}{k}\cdot\frac{K^2 r_1^2}{m\theta v_0^{2/3}}\left[F\left(\frac{T}{\theta}\right)+\frac{1}{2}\right]\right\}. \qquad (2)$$

The θ dependence of $d\mu/dT$ is rather complicated. It follows from analysis of this quantity at T = 300°K that $d\mu_A/dT$ decreases with increasing θ at least more rapidly than θ^{-2}.

Consequently, among the investigated specimens those containing 0.05-0.1 and 0.24 atomic percent W have the maximum and minimum Debye temperature, respectively.

The impurity concentration dependence of $d\mu_A/dT$ is identical with the corresponding dependence of the self-diffusion coefficient D.

The present results can be interpreted in terms of the theory of the influence of impurities on the spectrum of thermal vibrations of the crystal lattice of transition elements.[9]

"A.A.Baikov" Metallurgical Institute,
Academy of Sciences of the USSR

References

1. I.B.Borovskii & G.N.Ronami, Izv.AN SSSR, Ser.fiz., 21, 1397 (1957). (Trans. Bulletin, 21, 1385.)

2. I.B.Borovskii, K.P.Gurov & Yu.G.Miller, Doklady AN SSSR, 118, 280 (1958). (Trans.Soviet Physics - Doklady.)

3. Yu.G.Miller, Doklady AN SSSR, 119, 488 (1958). (Trans.Sov.Physics - Doklady.)

4. Yu.G.Miller, Trudy (Proceedings), Inst.of Metallurgy, USSR Ac.of Sci., 6, 20 (1960).

5. I.B.Borovskii & O.V.Neklyudova, Ibid., 6, 25 (1960).

6. E.G.Okonnikov, Ibid., 6, 32 (1960).

7. I.B.Borovskii & V.V.Shmidt, Izv.AN SSSR, Ser.fiz., 24, 428 (1960). (Trans. Bulletin, 24, 438.)

8. V.V.Shmidt, Present issue of the Bulletin, p.988.

9. K.P.Gurov & I.B.Borovskii, Fizika metallov i metallovedenie, 10, 513 (1960). (Trans.Physics of Metals & Metallography.)

INFLUENCE OF THE CHEMICAL BOND ON THE ENERGY AND INTENSITY OF THE X-RAY LINES OF ATOMS IN COMPOUNDS

- A.T.Shubaev

Formation of chemical bonds and changes in their character are accompanied by redistribution of the valence electrons in states and in particular by redistribution of the electrons between atoms. Inasmuch as valence electrons contribute to the electron density in the inner as well as outer regions of an atom, any such redistribution will affect the height and relative location of the atomi energy levels. Karal'nik[1-3] called attention to this fact in a number of papers. Thus, incident to removal of an outer electron from a free atom, for example, or "withdrawal" of valence electrons to a neighboring atom in a compound, the electron density in the region of the given atom decreases. As a result, incident to ionization of any shell or transitions between shells the electrons will move in a stronger field, which leads to increase of the ionization potential and the ene gy of the emitted photons, i.e., to a rise of all the energy levels and a short wavelength shift of the lines in the x-ray spectrum of the atom. In the case of the formation of negative ions analogous changes will occur, but in the opposite direction. It is quite clear that the character of atomic interaction will also have a substantial and, often, decisive effect on the position of the last lines in the x-ray spectra of atoms in compounds. For example, in going from a metal to a compound, exchange interaction increases sharply owing to localization of the valence electrons in a few preferential directions. This means that the ener gy of the valence band is reduced and the last line is shifted to the long wavelength side, even in the case of increase of the field throughout the region of the atom.

As far as the principal x-ray lines are concerned, save for a few special exceptions, their shifts are determined solely by changes in the density of the valence electrons in the inner regions of the atom. When it is feasible to measure them, these shifts may yield information on the distribution of valence elec trons between atoms bound in compounds. In the present work we estimated the shifts of atomic levels for some types of redistribution of valence electrons.

Level Shifts Incident to Ionization of Free Atoms

By way of example let us consider the change in level energies and in the position of the lines of the K series incident to removal of one valence electron from the calcium atom. The starting-point of our calculations was the Schrödinger equation in the usual form employed in using the Hartree self-consistent field:

$$\frac{d^2P_{n,l}(r)}{dr^2} - l(l+1)\frac{P_{n,l}(r)}{r^2} + 2\frac{Z-\sigma_p}{r}P_{n,l}(r) = \varepsilon_{n,l}P_{n,l}(r); \qquad (1)$$

here $P_{n,l}(r) = r\Psi_{n,l}(r)$, where $\Psi_{n,l}(r)$ is the radial wave function of electrons in the state with quantum numbers n and l,

$$\sigma_p(r) = \sum_{n,\,l} N_{n,l} r \int_0^\infty \frac{\sigma_{n,l}(r)}{r^2}\,dr,$$

$N_{n,l}$ is the number of electrons in the $n,\ l$ state without taking into account the electron whose energy is being investigated; $\sigma_{n,l}(r) = \int_0^r P_{n,l}^2(r)\,dr$, and $\varepsilon_{n,l}$ is the level energy taken with opposite sign.

As follows from Eq.(1), the change in level energy for some redistribution of electrons is given by the following relation:

$$\Delta\varepsilon_{n,l} = -\int_0^\infty \Delta\left(\frac{dP_{n,l}(r)}{dr}\right)^2 dr - l(l+1)\int_0^\infty \frac{\Delta(P^2_{n,l}(r))}{r^2}\,dr + \\ + 2\int_0^\infty \Delta(P^2_{n,l}(r))\frac{Z-\sigma_p}{r}\,dr - 2\int_0^\infty P^2_{n,l}\frac{\Delta\sigma_p}{r}\,dr, \qquad (2)$$

where Δ denotes the change of the function, corresponding to the given redistribution of electrons. For our calculations we used the wave functions of Ca and Ca^+ deduced in the work of Hartree[4]. Table 1 gives the results of calculating level shifts ($\Delta\varepsilon$) and line shifts (ΔE) for the $Ca \rightarrow Ca^+$ transition.

Table 1

Level	$\Delta\varepsilon$, Ry	Line	ΔE, eV
K	+0,497	K_α	+0,03
L	+0,495	K_{β_1}	+0,13
M	+0,485	K_{β_2}	+0,62
N	+0,440	K_1	+0,62
O	+0,286	K_2	+2,02

As can be seen, the levels are shifted by several electronvolts. The shift of the Kα line is insignificant (the accuracy of experimental determination of the position of lines in the K series of Ca is of the order 0.1 ev). The shift of the Kβ line can already be detected experimentally. The position of the K_1 and K_2 absorption lines (transitions from the K level to the $4p$ and $5p$ levels) and their separation change especially sharply, i.e., the absorption spectrum is particularly sensitive to a change in the charge of the atom. Analogous level and line shifts will be observed in going from metallic calcium and other elements to the corresponding oxides inasmuch as this is accompanied by "withdrawal" of the valence electron cloud from the metal atom to the oxygen atom. The magnitudes of these shifts are different, however, inasmuch as the contribution of the valence electrons to the electron density in the inner regions of an atom in a metal and of a free atom differs.

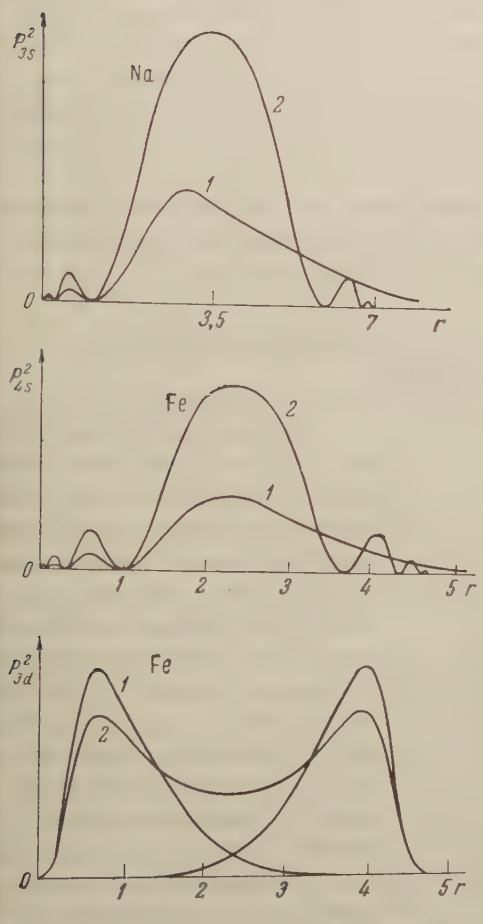

Fig.1. Distribution in density of valence electrons in free atoms (1) and between neighboring atoms in a metal (2).

Change in the Contribution of Electrons to the Electron Density in Going to a Metal

Fig.1 depicts the distribution in density of valence electrons $\rho_{n,l}(r) = P^2_{n,l}(r)$ in a free atom and between neighboring atoms in the metallic state for sodium and iron, according to the data of Wigner[5] and Seitz[5] and Nikiforov[6,7]. As may be seen, in going from the free atom to the metal the density of the cloud of outer valence electrons in the inner region of the atom increases by a factor of 2 or 3. If inner electrons participate in the chemical bonding (for example, the d electrons of iron), the cloud of these electrons is "drawn out" in the direction of the neighboring atom and the density of this cloud in the inner regions is somewhat diminished. The ratio of electron densities $\rho_{n,l}$ in an atom bound in a metal and in a free atom is determined by the conditions of normalization of the wave function of the val-

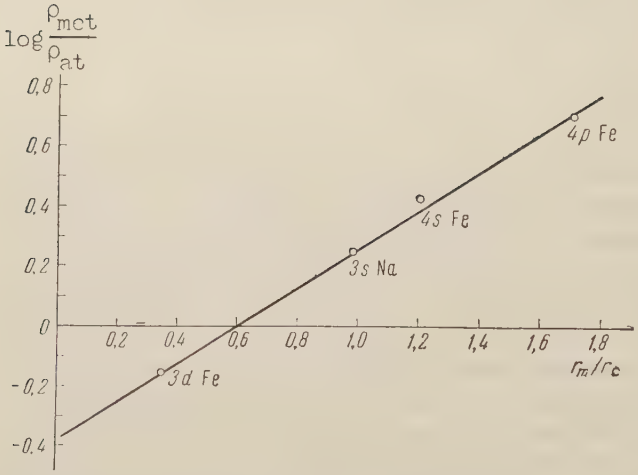

Fig.2. Variation of the logarithm of the ratio of the density of valence electrons in an atom in the metal and in the free atom as a function of r_m/r_c,

ence shown in Fig.2 yields the relation

ence electrons in the volume of the atomic polyhedron in the metal and, consequently, depends on the relation between the dimensions of the valence shell of the free atom and the interatomic separations in the metal. We note that the indicated ratio of electron densities is constant in the region $r<0.8\,r_m$, where r_m is the radius corresponding to the maximum of the $\rho_{n,l}$ function for the valence electron of the free atom.

Fig.2 shows the r_m/r_c, dependence of the logarithm of the ratio of the $\rho_{n,l}$ functions of an atom in a metal and of a free atom for the different types of valence electrons in different atoms. Here r_c is the covalent radius (half the distance between neighboring atoms in the metal). Potentialization of the linear depend

$$\frac{\rho_{n,l}(r)_{met}}{\rho_{n,l}(r)_{at}} = 0.4e^{1.65\frac{r_m}{r_c}}, \qquad (3)$$

valid for $r<0.8\,r_m$.

This semiempirical relation allows of approximate evaluation of the contribution of valence electrons to the electron density in the inner regions of an atom in a metal on the basis of the wave functions of the free atom.

Influence of the Type of Chemical Bond on the Position of Lines for the Elements from Sodium to Chlorine

Table 2

A_nB_n	$\Delta EK_{\alpha}{}_A$	$\Delta EK_{\alpha}{}_B$
Na_2S	+0,09	—0,16
MgS	+0,19	—0,25
MgSi	+0,05	—0,15
Al_2S_3	+0,27	—0,19
AlP	+0,16	—0,29
SiC	+0,22	
SiS_2	+0,50	
SiO_2	+0,59	
Na_2SiF_6	+0,87	

Table 3

Compound	$\Delta\lambda K_{\beta_1}$, X	Δd, A
Co_2O_3	—0,10	+0,05
FeO	—0,08	+0,25
Fe_2O_3	—0,17	+0,09
MnO	—0,28	+0,31
MnO_2	—0,28	+0,03
$KMnO_4$	+0,21	—0,29
Cr_2O_3	—0,21	+0,10
K_2CrO_4	+0,35	—0,31
V_2O_3	+0,15	+0,05
V_2O_5	+0,20	—0,30
TiO_2	+0,12	—0,09

Using relations (2) and (3) and the wave functions from Refs.8-11, we calculated the shifts of the Kα lines incident to "withdrawal" of one electron from atoms of Na, Si and Cl in the solid state. The calculated values of ΔE_{K_α} proved to be 0.26 ev for Na, 0.36 ev for Si and 0.31 ev for Cl. These shifts amount to some tenths of an electronvolt and, inasmuch as the accuracy of experimental determination of the K series lines of these elements lies within 0.01-0.

ev, the shifts can be measured with adequate precision. A number of students have in fact detected various shifts of the Kα lines of the elements from Na to Cl in going from some of their compounds to others. In Table 2 we list the shifts of the Kα lines (in ev) in going from the pure elements (A and B) to compounds for a number of binary compounds, according to the data of Johnson[12].

The causes of these shifts were not clear. It follows from the present work that these shifts are proportional to the changes in density of valence electrons inside the L shell; in other words, they can serve as a measure of the redistribution of valence electrons between the atoms in a compound. It will be evident from the cited data that for "donor" atoms the Kα line is shifted to the short wavelength side, and the greater the electronegativity of the second component, the more appreciable the shift. For "acceptor" atoms, the corresponding changes have the opposite sign.

Causes of Shifts of the Principal Lines of Transition Elements

Besides being influenced by the redistribution of electrons between atoms, the position of the principal lines of transition elements is substantially affected by the marked changes in interatomic separations that take place in going from one compound to another. As a rule, with increasing valence of the transition metal these separations diminish, the atomic volume decreases and the density of valence electrons at all points in this volume increases. As a result, there appear long wavelnegth shifts of the principal x-ray lines. In Table 3 we list the pertinent data of Sanner[13]; it follows from these data that the sign of the shift of the $K\beta_1$ line in the majority of cases is determined by the sign of the deviation Δd of the interatomic separation in the compound from the sum of the covalent radii. In addition, as Wood[14] and Pratt[14] have shown, the position of the levels of transition elements and, consequently, the lines of the x-ray spectrum are substantially influenced by the presence of or a change in spin of the atom.

Influence of the Type of Chemical Bond on the Intensity of the Last Lines

The integral intensity of the last line of the x-ray spectrum is given by

$$I \sim \int_0^\infty N(E) W(E)\, dE, \tag{4}$$

where $N(E)$ is the distribution in energy of the electrons in the valence band, E and $W(E)$ is the probability for an electron transition to an inner level of the atom. If the last line of the K series is being considered, the transition probability

$$W(E) \sim \left| \int_0^\infty P_{1s}(r)\, r P_v(r, E)\, dr \right|^2, \tag{5}$$

where $P_{1s}(r)$ and $P_v(r, E)$ are the wave functions of the $1s$ level and the valence band, respectively.

As follows from the results of a number of authors[5-7], the form of the wave function of valence electrons in the inner regions of atoms does not change even for sharp changes in the type of chemical bond, so that the function $P_v(r, E)$ can be written in the form

$$P_v(r, E) = A(E) f(r),$$

where $A(E)$ is a coefficient that depends on the character of the chemical bond and the energy distribution of the electrons in the valence band, while $f(r)$ is a function that does not depend on the type of bond. Inasmuch as in Eq.(5) the variation of function $P_v(r, E)$ is significant only in the region of r where $P_{1s}(r)$ differs appreciably from zero, we can write

$$W(E) \approx A^2(E) \quad \text{and} \quad I \approx \int_0^\infty N(E)\, A^2(E)\, dE.$$

On the other hand, the electron density due to the valence electrons inside the $1s$ shell equals

$$\rho_{v,1s} = \int_0^\infty N(E)\, dE \int_0^{r_{1s}} P^2(r,\ E)\, dr \approx \int_0^\infty N(E)\, A^2(E)\, dE,$$

where r_{1s} is the radius corresponding to the maximum of $P_{1s}(r)$. Thus $I \sim \rho_{v,1s}$, i.e., the integral intensity of the last line in the x-ray spectrum of atoms bound in chemical compounds is proportional to the electron density attributable to the valence electrons in the region of the K shell.*

Table 4

Compound	$I_{K_{\beta_1}}/I_{K_{\alpha_{1,2}}}$	Compound	$I_{K_{\beta_2}}/I_{K_{\beta_1}}$	Compound	$I_{K_{\beta_1}}/I_{K_{\alpha_{1,2}}}$
KCl	0,141	Cu_2Se	0,071	MoS_2	0,099
$KClO_3$	0,072	SeO_2	0,057	As_2S_3	0,093
$KClO_4$	0,069	KBr	0,170	Na_2SO_3	0,069
FeS	0,105	$Ba(BrO_3)_2$	0,138	$CaSO_4$	0,064
FeS_2	0,090				

As we have already noted above, the density of valence electrons in the inner regions of an atom varies with changes in the type of chemical bond; consequently, the integral intensity of the last line must also change by a corresponding amount. In view of the absence in the literature of data on the influence of the type of chemical bond on the intensity of the last lines, the present author, in order to check the validity of the concepts set forth above, undertook to obtain such data for some compounds. The measurements were carried out on DRUS and KPFS spectrographs. Specifically, there were determined the relative intensities $I_{K_{\beta'}}/I_{K_{\alpha_{1,2}}}$ of Cl and S ions and $I_{K_{\beta_2}}/I_{K_{\beta_1}}$ of Se and Br ions in compounds differing markedly as regards the character of the chemical bands. Table 4 gives the results (the uncertainty in all cases is ±0.005).

It will be evident that the intensity of the last line is highly sensitive to the character of the chemical bonds.

Rostov-on-the-Don State University

References

1. S.M.Karal'nik, Izv.AN SSSR, Ser.fiz., 20, 815 (1956). (Trans.Bulletin 20, 739.)

2. S.M.Karal'nik & S.Nizhnik, Ukr.fiz.zhur. (Ukrainian Physics Journal), No. 2, 4 (1957).

3. S.M.Karal'nik, Izv.AN SSSR, Ser.fiz., 21, 1445 (1957). (Trans.Bulletin, 21, 1432.)

4. D.Hartree & W.Hartree, Proc.Roy.Soc., A, 164 (1938).

---

*Our reasoning applies exclusively to the case when all valence electrons are in the $p\ (l = 1)$ state. If electrons in other states are present in the valence band, the intensity of the last line will be proportional to that part of the electron density which is due to the p electrons only.

5. E.Wigner & F.Seitz, Phys.Rev., 43, 804 (1933).
6. I.Ya.Nikiforov, Materialy vtoroi nauchnoi konferentsii aspirantov (Transactions of the Second Scientific Conference of Graduate Students), Rostov Univ., 33 (1960).
7. I.Ya.Nikoforov, Present issue of the Bulletin, p.1048.
8. D.Hartree & W.Hartree, Proc.Roy.Soc., A, 193, 299 (1948).
9. H.Donley, Phys.Rev., 50, 1012 (1936).
10. W.Hartree & D.Hartree, Phys.Rev., 60, 857 (1941).
11. D.Hartree & W.Hartree, Proc.Roy.Soc., A 156, 45 (1936).
12. N.Johnson, Dissertation, Lund, 1939.
13. V.Sanner, Dissertation, Uppsala, 1941.
14. J.Wood & G.Pratt, Phys.Rev., 107, 995 (1957).

* * * * * * *

INVESTIGATION OF THE K ABSORPTION SPECTRA OF CALCIUM IN SOME COMPOUNDS

- A.T.Shuvaev & V.F.Demekhin

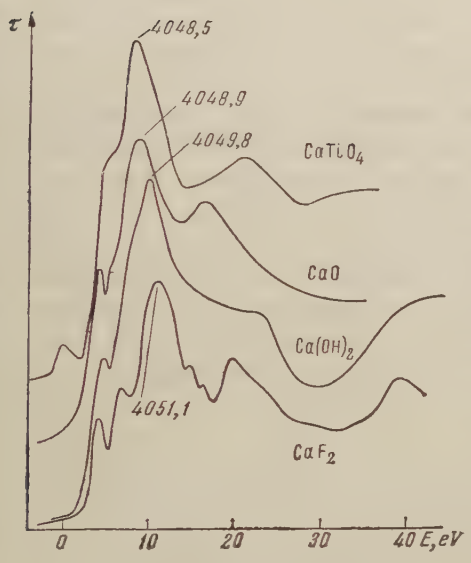

K absorption spectra of Ca in compounds.

We investigated the K absorption spectra of calcium in a number of its compounds by means of a DRS vacuum x-ray spectrograph. The analyzer was a quartz crystal with reflection from the $(10\bar{1}0)$ planes, bent to a radius of 500 mm. The x-ray tube was operated at a potential of 7 kv (i = 30 ma). The exposure time was 3-4 hours in recording the spectra of CaO, CaF_2 and $Ca(OH)_2$ and 7-8 hours in recording the spectrum of $CaTiO_3$. The resolution of the instrument in the region of the K spectrum of Ca is 10 000. The spectrograms were scanned on an MF-4 microdensitometer. After conversion of blackenings to intensities and averaging over 3-4 spectrograms we obtained the log I vs photon energy curves reproduced in the accompanying figure.

The purpose of the present work was to investigate the influence of the charge of the Ca ion in compounds on its absorption spectrum and to determine the charge of the Ca ion in $CaTiO_3$. This dictated the choice of compounds: the electronegativity of the second component in the series CaO, $Ca(OH)_2$ and CaF_2 increases; consequently, so does the charge of the Ca ion.

As will be evident from the figure, the position of the principal absorption peaks in this series of compounds shifts to the short wavelength side. This is in agreement with the deductions drawn in Ref.1 regarding the influence of ionic charge on the position of absorption lines. The structure beyond the principal absorption peak does not exhibit any direct relation to the ionic charge and is, apparently, determined by the type of lattice.

The principal peak of $CaTiO_3$ is displaced to the long wavelength side relative to the peaks of the other investigated compounds; consequently, the charge of the Ca ion in this compound must be even smaller than in CaO. For rough evaluation of

the ionic charge in $CaTiO_3$ one can use the values of the charge of the Ca ion in CaO and CaF_2, determined according to Pauling, assuming linear variation of the position of the principal absorption peak as a function of the ionic charge. Using this procedure we obtained a value of 1.0 for the charge of the Ca ion in $CaTiO_3$ (the charge values taken for CaO and CaF_2 were 1.1 and 1.4 respectively).

The more precise procedure for determining the ionic charge from absorption spectra, developed by Barinskii & Nadzhakov[2], could not be used in the given case owing to the great complexity of the spectra, which is presumably due to surposition of the spectrum of the excited states and the spectrum due to transitions to levels of the lattice.

In the long wavelength region of the investigated absorption spectra there appear a number of weak peaks, the position of which is the same in all the compounds, within the limits of the measurement error. In addition, in the spectrum of $CaTiO_3$ there is clearly evinced an absorption peak which is commonly associated with the presence of unoccupied states in the $3d$ band. It must be noted, however, that this peak does not appear in the spectra of the other compounds, although one can scarcely assume that the $3d$ bands in these compounds are completely filled. This would indicate that the presence or absence of this absorption peak is only indirectly related with filling of the $3d$ band.

Rostov-on-the-Don State University

References

1. A.T.Shuvaev, Present issue of the Bulletin, p.996.
2. R.L.Barinskii & E.G.Nadzhakov, Izv.AN SSSR, Ser.fiz., 24, 407 (1960). (Trans.Bulletin, 24, 419.)

INVESTIGATION OF THE BINDING FORCES IN Ni-Mo SOLID SOLUTIONS BY OBSERVING THE FINE STRUCTURE OF THE ABSORPTION SPECTRA

- V.A.Trapeznikov

Information on the variation of the binding forces in solid solutions can be obtained by observing the fluctuations of the fine structure of their absorption spectra. This was demonstrated on the basis of the theory of Kostarev[1,2] in the experimental study of Ref.3 and by calculations[4,5] in two variants. Both variants of the calculations show that the binding forces increase or decrease with increase or decrease of the ratio $\Phi_{K''}/\Phi_{K'}$, where $\Phi_{K''}$ is the amplitude of the short wavelength fluctuation and $\Phi_{K'}$ is the amplitude of the long wavelength fluctuation $(K'' > K')$. Variation of $\Phi_{K''}/\Phi_{K'}$ in the treatment of Ref.4 occurs owing to change of the characteristic temperature θ, while in Ref.5 it is assumed to occur owing to variation of the mean radial electron density with changes in the amplitude of the thermal vibrations of the atoms in the lattice.

It must be noted that now the inferences we arrived at in Refs.3 & 4 regarding the variation of the binding forces in a given specimen with variation of the temperature T of the experiment owing to decrease of θ with increase of T do not seem convincing, as was noted in formulating the problem in Ref.5. Only the negative aspects of the arguments set forth in Ref.4 now seems pertinent, namely, our proof of the inapplicability of the temperature variant of Kostarev's theory to the entire temperature range, inasmuch as taking into account the temperature coefficient S, proposed by Kostarev, yields a temperature dependence of $\Phi_{K''}/\Phi_{K'}$ of opposite sign to that observed experimentally. In positive agreement as regards the temperature variant are the deductions of Ref.5 and the results of the recent work of Shmidt[6], carried out on the basis of the work of Kozlenkov[7], who developed the theory of the fine structure of absorption spectra from the standpoint of the determining influence of short range order on the structure.

In the present work there were obtained experimental data on the ratio of the amplitudes of the fluctuations in the K edge of nickel in Ni-Mo solid solutions with molybdenum concentrations of 0, 0.5, 1, 2, 4, 5 and 16% by weight. Specifically, we measured the ratio of the fifth fluctuation E to the third fluctuation C at room temperature (see figure). The experimental procedure and method of calculation were the same as in work in Ref.3. The obtained values of the ratio Φ_E/Φ_C for different concentrations are listed in the accompanying table.

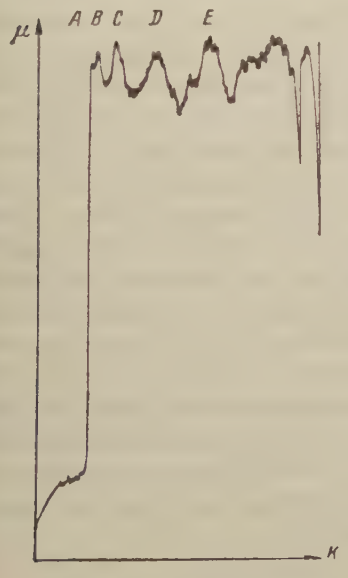

K absorption edge of nickel.

% Mo	Φ_E/Φ_C	% Mo	Φ_E/Φ_C
0	1,36±0,03	4	1,63±0,06
0,5	1,39±0,07	8	1,60±0,04
1	1,41±0,03	16	1,63±0,08
2	1,56±0,03		

It will be evident from the tabulated data that the $\Phi_E/\Phi_C = f(c)$ curve rises up to 4% Mo and then levels off. The rise of the curve corresponds to the first concentration case in Ref.4, i.e., indicates increase of θ $\left(\frac{d}{d\theta}\left(\frac{\Phi_{K''}}{\Phi_{K'}}\right) > 0\right)$, or, according to Ref.5, corresponds to decrease in the amplitude of the thermal vibrations, i.e., alloying of the nickel by molybdenum increases the binding forces. This increase of the binding forces continues with increase of the Mo concentration up to 4%; the forces then remain constant within the limits of the experimental error up to the limiting solubility.

The fact that the binding forces remain constant in a certain region of soli solutions is not new; thus, for example, Badaeva[8] showed experimentally that many solid solutions have the same heat of formation as the following intermetallic compounds.

The increase of the binding forces in Ni-Mo solid solutions agrees with the experimental data obtained by other methods[9-11]. But the latest data on the strength characteristics, and in particular on the heat resistance, show a monotonic increase in strength up to the solubility limit. This disagreement between the data on the binding forces and on the strength characteristics for the region above 4% Mo can be explained if it is assumed that the increase in the strength of the material depends on two factors, namely, the binding forces and structural factors. The results of our x-ray spectroscopic investigation of Ni-Mo solid solutions, which show increase of the binding forces only up to 4% Mo, indicate that in these solutions the role of binding forces is limited and that the dominant role is played by structural factors.

Analogous investigations of the binding forces in iron-molybdenum solid solutions[3] indicate that in this case "saturation" of the binding forces occurs at 2% Mo, whereas the limiting solubility of Mo in iron is 6%. On the other hand, for a number of solid solutions, as for the Ni-Mo system, it has been demonstrated[9-1] that the strength characteristics increase up to the solubility limit. From this it may be concluded that within the range of a given solution the role of binding forces in the general increase in strength is limited or overshadowed by structural factors.

Nevertheless, binding forces should play a decisive role in the initial choice of the base for the alloy; further improvement of the characteristics, including heat resistance, through alloying is then determined by structural factor and such factors as the size of the grains and blocks, the state of their boundaries, the degree of imperfection of the crystal lattice, the number and density o dislocations, the presence of impurities on grain boundaries, etc. (see, for example, Ref.12). Thus, we believe that the best way to obtain a material with hig heat resistance is, first, careful choice of a suitable base with strong binding forces and a potential for utilization of the structural factors, and then improvement of this base by varying the different structural factors through alloying and heat treatment.

In earlier discussions of the x-ray spectroscopic data on the fine structure of absorption spectra we did not take into account the possible influence of loca concentrational inhomogeneities in the solid solution on the attenuation of the fluctuations. The possibility of local distribution of molybdenum in Ni-Mo solid solutions owing to formation of the K state has been noted by Polotskii & Benieva In the work of Ref.14 we pointed out that concentrational inhomogeneity may reduc the contrast of the spectrum, but we did not consider to what extent this decreas in contrast can affect the different fluctuations (intensities of the fine structure peaks). The influence of concentrational inhomogeneity as regards nonunifor attenuation of the fine structure will be evinced in the position of the fluctuations for the "local" edge and for the edge due to the main part of the solution; these edges do not in general coincide. Nonuniform decrease in the contrast for different fluctuations with alloying may be due to the dependence of the attenuation on two factors, namely, on the binding forces and nonuniform distribution of the alloying element. Hence in further investigations in this field one must bea in mind the possible influence of local concentrational inhomogeneities on the ratio of amplitudes of fluctuations of the fine structure.

Institute of the Physics of Metals,
Academy of Sciences of the USSR

References

1. A.I.Kostarev, Zhur.eksp.i teor.fiz., 11, 60 (1941).
2. A.I.Kostarev, Ibid., 20, 811 (1950).
3. V.A.Trapeznikov & S.A.Nemnonov, Fizika metallov i metallovedenie, 3, 314 (1956).
4. V.A.Trapeznikov, Ibid., 5, 8 (1957). (Trans.Physics of metals and metallography).
5. V.A.Trapeznikov, Izv.AN SSSR, Ser.fiz., 23, 582 (1959). (Trans.Bulletin, 23, 563.)
6. V.V.Shmidt, Present issue of the Bulletin, p.988
7. A.V.Kozlenkov, Present issue of the Bulletin, p.968.
8. T.A.Badaeva, Doklady AN SSSR, 64, 533 (1949).
9. I.I.Kornilov & N.T.Domodenko, Issledovanie po zharoprochnym splavam (Investigations of heat resistant alloys), Vol.V, p.3, M., 1959.
10. I.I.Kornilov & K.P.Myasnikova, Tezisy dokladov na XII Vses. sessii po zharoprochnym materialam i splavam (Abstracts of reports presented at the 12th All-Union Session on Heat Resistant Materials and Alloys), p.50, M. 1958.
11. I.G.Polotskii, T.Ya.Benieva & Z.A.Khodov, Issledovanie po zharoprochnym splavam, Vol.III, p.310, M. 1958.
12. M.V.Pridantsev, Ibid., p.12.
13. I.G.Polotskii & T.Ya.Benieva, Issledovanie po zharoprochnym spavam, Vol. IV, p.202, M. 1959.
14. S.A.Nemnonov & V.A.Trapeznikov, Trudy (Proceedings), Institute of the Physics of Metals, USSR Ac.of Sci., No.16, 223 (1955).

X-RAY SPECTROSCOPIC INVESTIGATION OF INTERMETALLIC COMPOUNDS IN THE Cu-Zn SYSTEM

- V.A.Batyrev

It has been shown in a number of studies[1,2] that the fine structure in the x-ray absorption spectra of different intermetallic compounds differs markedly from the structure in the spectra of the pure constituent metals. Most of the earlier investigations, however, were carried out on compounds of different classes with different properties and in some cases with inadequately known crystal structure.

The purpose of the present work was to investigate the fine structure of the K absorption spectra of copper and zinc in the Cu-Zn system. Our choice of this system was dictated by the fact that these classic electronic compounds have been thoroughly studied as regards both their physical properties and their crystal structure. The latter has been successfully explained in the framework of the band model. Konobeewski[3] and Jons[4] established the relation between the Hume-Rothery electron concentration rules[5] and the filling of the Brillouin zones.

We investigated the K absorption edges of copper and zinc in the β-phase (CuZn; electron concentration 1.5), the γ-phase (Cu_5Zn_8; electron concentration 1.62) and the ϵ-phase ($CuZn_3$; electron concentration 1.75). The β-phase has a body-centered cubic lattice of the CsCl type; the γ-phase has a complex cubic structure with 52 atoms per unit cell; the ϵ-phase is characterized by a close packed hexagonal structure similar to that of pure zinc.

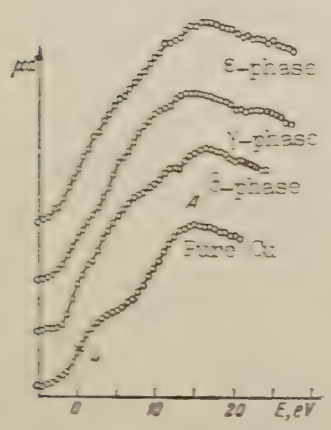

Fig.1

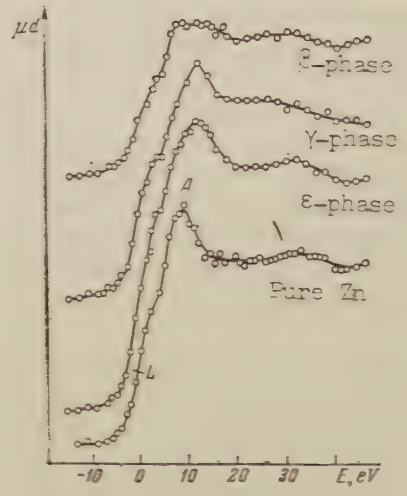

Fig.2

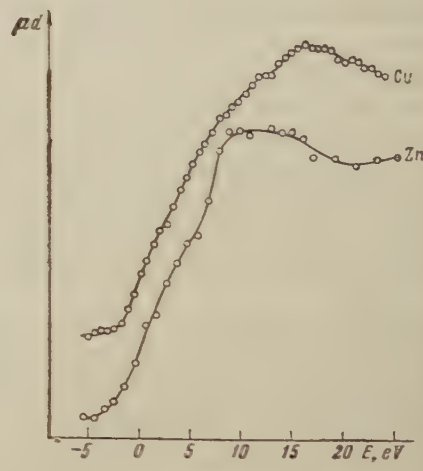

Fig.3

Fig.1 shows the K absorption edges of pure copper and copper in the enumerated compounds. The spectra were recorded by the ionization procedure (at least 25 000 pulses were recorded at each point) on an RSDI spectrometer[6] in the first order of reflection from the $(13\bar{4}0)$ plane of a quartz crystal. The resolution was ~5000 as determined with reference to the Zn $K\alpha_1$-$K\alpha_2$ doublet.

The K absorption edges of pure zinc and zinc in the investigated alloys are shown in Fig.2. These spectra were recorded on a double crystal spectrometer wit a resolution of ~10 000. At least 15 000 pulses were recorded at each point. Th absorbers (specimens) were in powder form.

As will be evident from Fig.1, the K absorption edges of copper in the β-, γ-, and ϵ-phases differ substantially from the K edge of pure copper. The extrem long wavelength structure is increasingly smeared out with rise of the Zn concentration. The position of the point of inflection (point L), which is usually

associated with the location of the Fermi surface, remains constant within the limits of the experimental error (0.2-0.3 ev). The short wavelength peak A also changes little in position; it remains at a distance of 15-17 ev from the inflection point.

In contrast, the shape of the K edges of zinc changes little. A minor change in shape is observed only for the β-phase. The position of the inflection point L remains virtually constant within the limits of the experimental error (0.3-0.5 ev). The short wavelength peak A remains virtually fixed at a distance of 10-12 ev from the inflection point.

If we assume that the shape of the absorption spectrum characterizes the density distribution of unfilled states, the main absorption edges of copper and zinc in the same alloy should be similar, inasmuch as these spectra yield information on the shape of the same bands belonging to the same alloy. Some differences should be observed only in the separation of the individual fluctuations (fine structure peaks).

Fig.3 gives a comparison of the K absorption edges of copper and zinc in the β-phase. These curves have been plotted to the same scale with the inflection points aligned. The difference between the two spectra cannot be explained by different degrees of resolution. One can justifiably speak of similarity of the curves only in the vicinity of the inflection point, i.e., in a range of 3-5 ev from point L. For the γ- and ε-phases the difference between the edge curves for copper and zinc in the same alloy is even more substantial. This indicates that attempts[7] to interpret the fine structure of the main absorption edge only in terms of the distribution in density of states is unjustified. One must take into account a second factor, namely, the transition probability. However, in order to take this factor into account it is not enough to know only the main absorption edge; one must also thoroughly study the short wavelength fine structure.

I desire to express my gratitude to I.B.Borovskii for valuable suggestions and helpful discussion.

References

1. S.A.Nemnonov & M.F.Sorokina, Izv.AN SSSR, Ser.fiz., 24, 455 (1960). (Trans. Bulletin, 24, 462.)
2. S.A.Nemnonov & A.Z.Men'shikov, Ibid., 23, 578 (1959). (Trans.Ibid., 23, 559.)
3. S.T.Konobeewski, Ann.Physik. 26, 97 (1936).
4. Jons, Proc.Roy.Soc.A144, 225 (1934).
5. W.Hume-Rothery, Nature, 135, 1038 (1926).
6. V.A.Batyrev & V.G.Bogdanov, Present issue of the Bulletin, p.944.
7. W.W.Beeman & H.Friedman, Phys.Rev., 56, 392 (1939).

INFLUENCE OF THERMAL VIBRATIONS OF ATOMS ON THE PROCESS OF "MELTING" OF THE FINE STRUCTURE OF X-RAY ABSORPTION SPECTRA. I. INVESTIGATION OF A COPPER-PLATINUM SOLID SOLUTION

- I.B.Borovskii & G.N.Ronami

Investigations of the influence of temperature on the fine structure of the absorption spectra of pure metals were begun about 30 years ago.[1] The results of these investigations were somewhat surprising and were in conflict with the theories generally accepted at the time. In particular, it turned out that there was no correlation whatsoever between the melting point and the intensity of "melting of the short wavelength fine structure.

One of us (Borovskii) was the first to suggest that the process of "melting" of the fine structure is determined by the rms amplitudes of the vibrations of th atoms, i.e., by elastic constants, and, consequently, by the Debye temperature as well; whence it could be concluded that the process should depend on the mass of the vibrating atoms, which agreed with the Debye-Waller theory[2].

Theoretical investigations of the influence of temperature on the fine structure were first undertaken by Kostarev[3] and then developed and made more precise by Shmidt[4]. These authors obtained a clear dependence of the process o "melting" of the fine structure on the atomic mass and the characteristic temperature; Shmidt[4] showed in addition that zero-point vibrations have a great influence on the relative intensity of fluctuation of th absorption coefficient within the range of the short wavelength fine structure. It was assumed in the calculations that the spectrum of the thermal vibrations corresponded to the Debye spectrum.

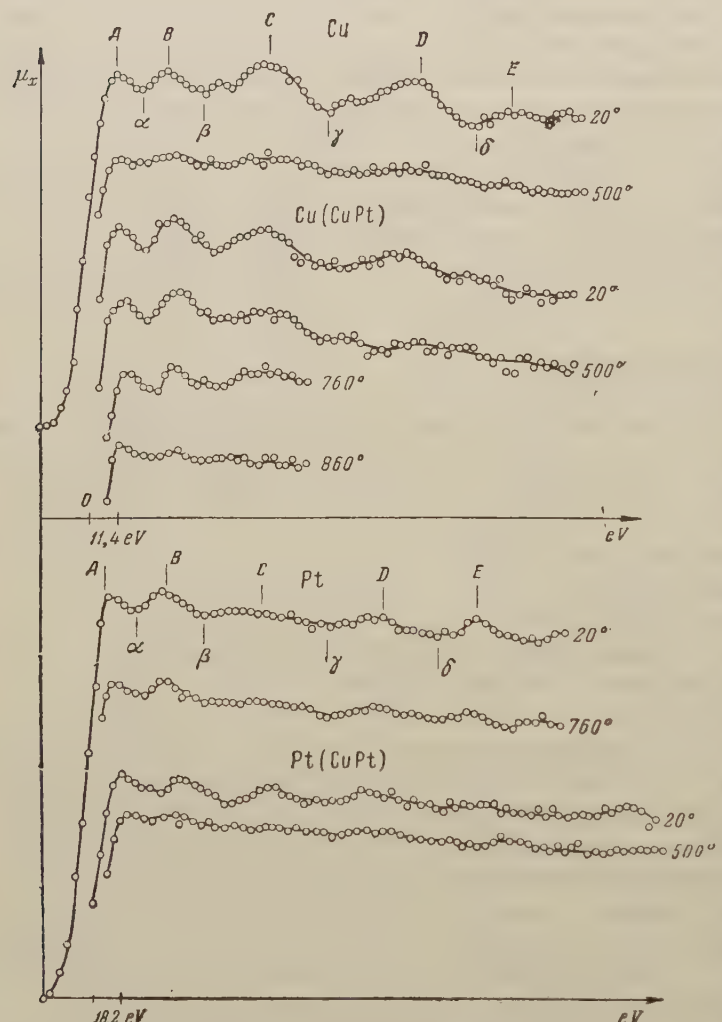

X-Ray absorption spectra

Up to the present, however, it has proved impossible to calculate the spectrum of the thermal vibrations of two-component and more complex metallic compounds, and there is no chance of constructing a theory characterizing the temperature dependence of the "melting" of the fine structure of these systems. Nevertheless, investigation of the temperature spectrum of complex metallic compounds, in addition to its undeniable scientific interest, is also of great practical interest. It is therefore very important to obtain experimental facts that migh help elaborate new models.

In our previous investigations we demonstrated the great influence of minor impurities on the temperature dependence of the short wave-

Table 1

Distances (in ev) of extrema from the point of inflection

Extremum	Cu	Cu in Cu—Pt	Pt	Pt in Cu—Pt	Extremum	Cu	Cu in Cu—Pt	Pt	Pt in Cu—Pt
A	15	13	18	20	γ	110	104	146	144
α	26	23	30	32	*D*	148	133	171	172
B	37	34	48	49	δ	175	—	208	210
β	55	52	72	76	*E*	—	—	234	236
C	82	75	110	110	Edge	0	0	0	0

length fine structure. At certain "optimum" impurity concentrations the fine structure of the host atoms is preserved up to the melting point, whereas in the pure metal it "melts" altogether some 150-200° below this temperature.

Below we give the results of studies carried out on Cu-Pt alloy of stoichiometric composition. We chose this alloy because its components differ in mass by about a factor of three ($m_{Pt}/m_{Cu} = 3.07$); the pure metals have the same crystal structure (face-centered cubic; $a_{Pt} = 3.916$ Å; $a_{Cu} = 3.608$ Å) and close interatomic separations ($r_{Cu-Cu} = 2.55$ Å; $r_{Pt-Pt} = 2.77$ Å). Cu-Pt alloy has the structure of a somewhat distorted face-centered cubic lattice with $a = 3.85$ Å ($r_{Cu-Pt} = 2.75$ Å) and each copper and platinum atom is surrounded by six copper and six platinum atoms (in the pure metals each atom has twelve equidistant nearest neighbors). According to data in the literature[6], $(\bar{u}^2)^{1/2}_{Cu} = 0.15$ Å, $(\bar{u}^2)^{1/2}_{Pt} = 0.12$ Å, $\theta_{Cu} = 320°K$ and $\theta_{Pt} = 230°K$.

If we follow short-range order theory, which was first developed for metals by Kostarev[7], and assume that in alloys also to the first approximation the rms displacements of atoms differing in mass are inversely proportional to the square root of the atomic masses, we should expect the behavior of the fine structure as a function of temperature to differ for atoms in compounds and in pure metals: the fine structure of the K absorption spectrum of copper in Cu-Pt alloy should be less sensitive to temperature than in the pure metal; the fine structure of the L absorption spectrum of platinum, on the other hand, should begin to "melt" at a lower temperature than in pure platinum.

Table 2

Ratios of the amplitudes of fluctuations of absorption

Ratio	Cu		Cu in Cu—Pt
	Exper.	Theory	
$A_{20°}/A_{500°}$	1,7	1,37	1,3
$B_{20°}/B_{500°}$	1,6	1,75	1,0
$C_{20°}/C_{500°}$	3	3,0	1,5
$D_{20°}/D_{500°}$	3,4	7,1	

For study of the absorption spectra we prepared 7-9 μ thick foils for pure Cu and Cu in Cu-Pt and 6-8 μ foils for pure Pt and Pt in Cu-Pt. Prior to spectrometry, the foils were vacuum annealed for 10 hours at 500°C.

The spectra were obtained on a Cauchois spectrograph (transmission method) with ionization recording. The analyzer was a quartz crystal (R = 1000 mm) with reflection from the $(10\bar{1}0)$ planes. The dispersion in the investigated regions was 57 ev/mm for Cu and 91 ev/mm for Pt. At least 26 000 pulses were counted for each point with the x-ray table operated at 13.5 kv & 20 ma for the K absorption spectrum of Cu and 21 kv & 20 ma for the L absorption edge of Pt. The specimens were investigated in the temperature range from 20 to 860° (temperature measurements accurate to within ±5°). The results are shown in the figure and in Tables 1 and 2.

It follows from the results that 1) the fine structure of the K absorption spectrum of pure Cu disappears at 500°C, while the fluctuations of the absorption coefficient in the case of Cu in Cu-Pt change but little with temperature in the

range from 20° to 860°C, and 2) the fine structure of the L_{III} edge of pure Pt persists up to 760°C, while in the case of Pt in Cu-Pt the fine structure disappears completely at 500°C.

We note that the positions of the extrema (peaks and valleys) of the fine structure relative to the point of inflection in the main L_{III} edge of Pt in Cu-Pt and in the pure metal coincide, while the analogous extrema in the K absorption spectrum of Cu in Cu-Pt are shifted to the side of longer wavelengths as compared with the pure metal.

Thus, experimental results fully substantiate our initial premises. It also follows from our results that the relative intensity of the extrema of the absorption coefficient as well as of the "hyperfine" structure (small variations of the absorption coefficient within the fine structure extrema) depends substantially on the type of atoms involved. The rate of "melting" of the fine structure of the K absorption spectrum of Cu is substantially reduced in the presence of Pt as compared with the pure metal (see Table 2).

Moscow State University

References

1. Hanawalt, Z.Phys., 70, 293 (1931).
2. I.Waller, Dissertation, Uppsala, 1927.
3. A.I.Kostarev, Zhur.eksp.i teor.fiz., 20, 811 (1950).
4. V.V.Shmidt, Present issue of the Bulletin, p.988.
5. I.B.Borovskii & G.N.Ronami, Izv.AN SSSR, Ser.fiz., 21, 1397 (1957). (Trans Bulletin, 21, 1385.)
6. K.Lonsdale, Acta crystallogr., 1, 142 (1948).
7. A.I.Kostarev, Zhur.eksp.i teor.fiz., 21, 917 (1951); 22, 628 (1952).

CONCERNING THE ELECTRON CONFIGURATION IN METALS OF THE IRON GROUP

- N.D.Borisov and V.V.Nemoshkalenko

Weiss and DeMarco[1] presented new values for the number of $3d$ electrons per atom in the iron transition group elements as obtained by x-ray measurements of the atomic scattering factors (table).

Element	Structure	Number of electrons per atom
Cu	Face-centered cubic	9.8 ± 0.3
Ni	"	9.7 ± 0.3
Co	Close-packed hexagonal	8.4 ± 0.3
Fe	Body-centered cubic	2.3 ± 0.3
Cr	"	0.2 ± 0.4

Whereas the data for Co, Ni, and Cu were close to the accepted values, those for Cr and Fe were quite different. They naturally attracted much attention and became the subject of extensive scientific discussion.

Hume-Rothery and co-workers[2], while recognizing the experiments of Weiss & DeMarco to be faultless and thorough, nevertheless advised theoreticians to approach the values in the table with great caution, in view of the fact that each measurement was based on one reflection only, namely (110) for Cr and Fe, (100) for Co, and (111) for Ni and Cu. In the absence of data on the symmetry of the electron cloud, one can speak only of the electron density in the corresponding direction in the crystal. Hence the assumption by Weiss & DeMarco of spherical symmetry of the electron cloud in Cr, Fe, Co and Ni is highly debatable.

To support their point of view, Hume-Rothery et al refer to the paper by Deslattes[3], who pointed out the discrepancy between the data of Weiss & DeMarco[1] and Nilsson's data[4] on the isochromates of the x-ray spectra of transition metals.

We felt it desirable to obtain additional data on the structure of the electron spectrum of the iron group metals by a procedure different from that employed by Weiss & DeMarco, particularly since Hume-Rothery's reference to the Deslattes paper[3] is not well chosen. There can be no doubt that the isochromate method employed by Nilsson[4] can be used to study the distribution of unoccupied states in metals and alloys. The fine-structure feature - "h-structure" - observed by Nilsson in the isochromates of the transition group metals was a partially resolved line, the intensity of which decreased in going from Ti to Cu, i.e., with filling of the $3d$ band. This enabled Nilsson to correlate this feature with states in the unfilled part of the $3d$ band. He found the "h-structure" intensity ratio for iron and cobalt to be 4/3, which is in good agreement with the accepted electron configuration in the outer energy band of these metals. This enabled Deslattes to refute the data of Weiss and DeMarco, which would yield a ratio 4/1.

It can be shown, however, that Deslattes' deduction is incorrect, owing to an error in treating the "h-structure". In fact, the "h-structure" cannot be juxtaposed with the unfilled part of the band described by the atomic $3d$ wave functions, as was done by Deslattes[3]. The relatively high intensity of the $K\beta 5$ band in the spectra of transition group metals points to considerable overlapping of the wave functions of the $3d$, $4s$ and $4p$ states in the occupied part of the outer energy band. This overlapping will, obviously, be even greater in the unoccupied part of the band. Consequently, the "h-structure" must be matched not with the states in the unoccupied part of the $3d$ band, but with the states in the unfilled parts of the $3d$, $4s$ and $4p$ bands.

The data of Weiss & DeMarco and the general aspects of the electron-band

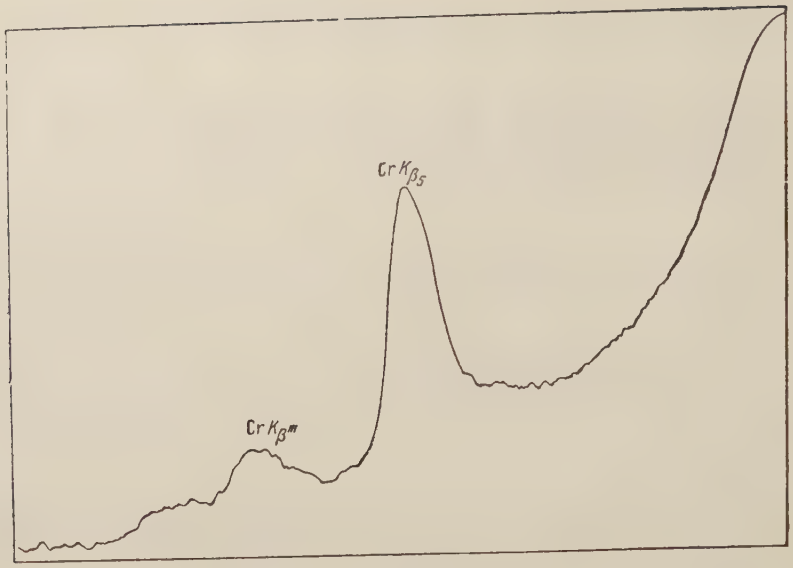

Fig.1. Cr spectrum.

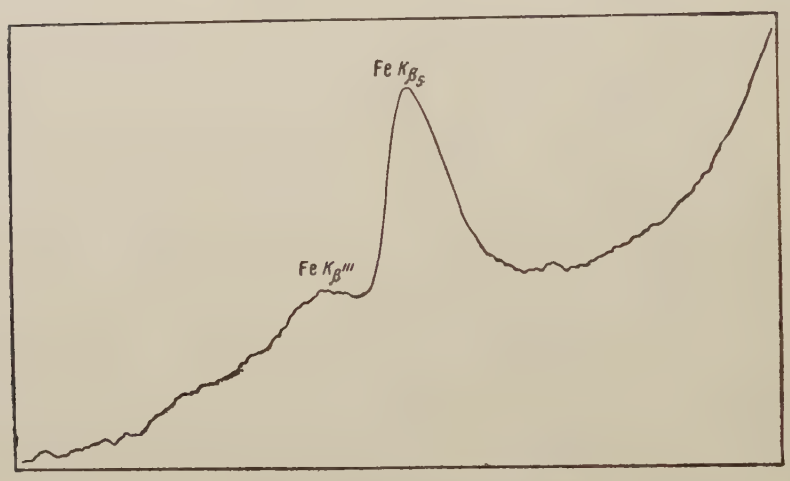

Fig.2. Fe spectrum.

structure, as described by Mott and Stevens[5], indicate that in iron two electrons are in states described by atomic $3d$ wave functions and do not participate in the conduction and formation of the Fermi surface, but are responsible only for the magnetic properties of the metal. The remaining electrons form a band located above the $3d$ electron band, and are described by $3d$ (xy symmetry), $4s$ and $4p$ wave functions; consequently their radial parts extend far out in space. Hence the contribution of these electrons to scattering is negligible. Inasmuch as the total number of electrons in both bands is now known to be eight, the unoccupied parts of the conduction bands of iron and cobalt should be related as 4/3, as was indeed observed by Nilsson.

It follows from the foregoing that neither the data on absorption spectra nor the data on the isochromates can be used directly to check on the validity of the Weiss-DeMarco results inasmuch as they cast light on only one aspect of the problem — the distribution of unoccupied states in metals and alloys — but yield no specific information on the distribution of the occupied states. In our

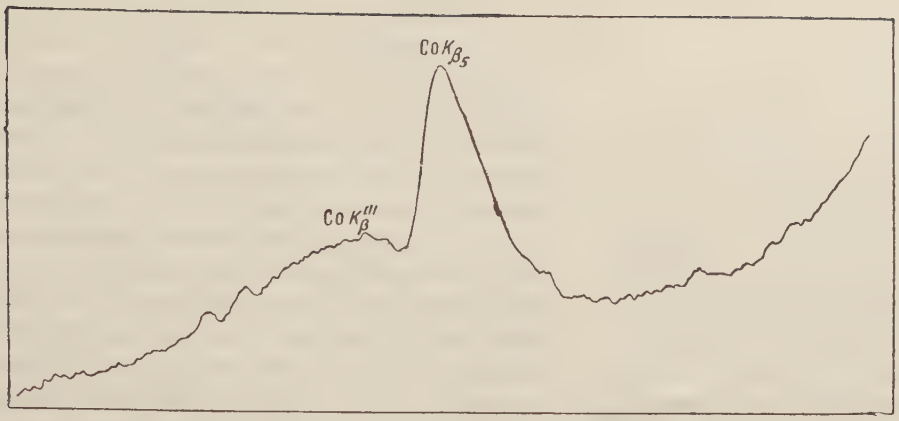

Fig.3. Co spectrum.

opinion, this problem can be resolved by investigating the x-ray emission spectra.

Accordingly, in the present work we investigated a number of parameters (integral intensity and intensity at the peak) of the $K\beta_5$ emission bands of pure Cr, Fe and Co (Figs.1,2 and 3). We used a high-transmission x-ray spectrograph of our own design[6] employing a Johann mount with a quartz crystal bent to a radius of 500 mm (reflection from the $(10\bar{1}0)$ planes).

Under our experimental conditions the $K\beta'''$ satellite was clearly resolved, so that we could subtract its intensity from the overall intensity of the Fe $K\beta_5$ and Co $K\beta_5$ bands. This is of great importance in comparing the integral intensities of the last two emission bands.

We developed a special procedure for comparing the intensities of the $K\beta_5$ bands when using photographic recording. This procedure consisted essentially of recording the $K\beta_5$ emission bands on a "sandwich" consisting of two films separated by an aluminum absorber. The absorber thickness for neighboring elements was chosen so as to make the density of the $K\beta_1$ line recorded on the second film not greater than 0.7. Inasmuch as each line pair ($K\beta_5$ - $K\beta_1$) was recorded with the same exposure time, this automatically excluded the effect of variation of the exposure time and fluctuation of the beam intensity in the process of recording. Inasmuch as the x-radiation recorded on the second film passed not only through the aluminum absorber but also through a double layer of silver bromide and the film backing, to compare the $K\beta_5$ line intensities it was necessary to determine the ratio of the absorption coefficients for the $K\beta_1$ line wavelengths of the compared elements. This was done by photographing the $K\beta_1$ lines from a 50% alloy of each of the compared elements with and without the absorber. The spectrograms were scanned on an MF-4 microphotometer, coupled to an EPP-09 recording potentiometer.[7]

This method of recording has two significant advantages over registration on photographic paper. First, the microphotometric curves are obtained directly in intensity vs energy coordinates, and therefore require no further conversion. Second, the area under the curves is larger than obtained with photographic paper, which enhances the accuracy of area measurement. The correctness of the procedure employed was checked by comparing our data with those obtained with spectrometers using ionization recording.

Fig.4 shows a plot of the relative intensity of the $K\beta_5$ bands vs atomic number Z, taken from Ref.8. The crosses denote our values. The good agreement indicates that the assumed invariance of the integral intensity of the $K\beta_1$ lines with

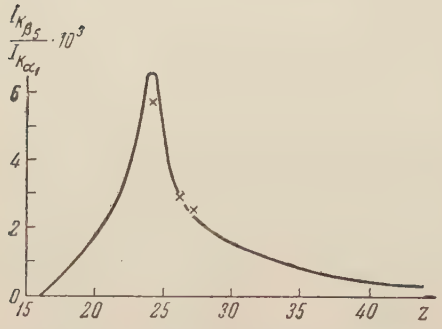

Fig.4. Relative intensity of the $K\beta_5$ bands vs atomic number.

change in atomic number (at least for $Z \geqslant 24$) is justified.

To explain the curve of Fig.4 we must assume that a decrease in atomic number is accompanied not only by a reduction in the number of electrons in the outer energy band, but also by a change in the probability for transition of electrons from the conduction band to the K level.

This being the case, to determine the number of outer electrons, in addition to the data on the integral intensities of the $K\beta_5$ bands, we must know the corresponding transition probabilities. In our case, as will be shown below, it is sufficient to have data on the ratio of the transition probabilities for the two pairs of the compared elements, rather than the absolute probability values.

Element	$I_{K\beta_5}/I_{K\beta_1}$	$I_{K\beta_5\ max}/I_{K\beta_1\ max}$
Cr	0.618	0.641
Fe	0.289	0.339
Co	0.198	0.290

Indeed, since the shapes of the Brillouin zones are determined, within the framework of the band model, by the structure of the lattice, crystals having the same crystal lattice will have the same $N = f(E)$ curves. Then, bearing in mind that chromium and iron (in the α-phase) have the same crystal structure, and that the zones in chromium and iron are filled beyond the maximum, the ratio of the corresponding transition probabilities of these elements will be determined by the ratio of the intensities of the Cr and Fe $K\beta_5$ bands at the peaks. It follows from the cited data that for chromium and iron the value of this ratio is ~2.

Knowing the transition probability ratio, we can estimate the ratio of the number of electrons in chromium and iron. According to our data this ratio is close to unity; this means that chromium and iron have an equal number of electrons in the outer energy band, which is in good agreement with the data of Weiss & DeMarco[1].

Unfortunately, it is impossible at present to make an analogous evaluation for cobalt, since we do not know the character of the $N = f(E)$ curve for this metal.

Institute of Metal Physics,
Academy of Sciences of the Ukrainian SSR

References

1. R.J.Weiss & J.J.DeMarco, Revs.Mod.Phys., 30, 59 (1958).
2. W.Hume-Rothery, P.J.Brown, J.B.Forsyth & W.H.Taylor, Phil.Mag.,3, No.36, 1466 (1958).
3. R.D.Deslattes, Phys.Rev., 110, 1471 (1958).
4. A.Nilsson, Arkiv.fys., 6, 513 (1953).
5. N.F.Mott & K.W.H.Stevens, Phil.Mag., 2, No.23,(1957).
6. N.D.Borisov & Ya.M.Fogel', Zhur.telh.fiz., 7, No.2, 164 (1937).
7. V.K.Latyshev & A.K.Felinger, Zavodskaya laboratoriya (Industrial Laboratory), No.5, 630 (1953).
8. M.A.Blokhin, Fizika rentgenovskikh luchey (X-ray Physics), Moscow, 1957.

THE $K\beta_X$ EMISSION BAND AND K ABSORPTION EDGE OF ALUMINUM IN SOME ALLOYS WITH TRANSITION METALS

- S.A.Nemnonov & L.D.Finkel'shtein

We have already studied[1,2] the nature of atomic interaction in compounds of transition metals with aluminum in connection with the ever-growing practical importance of metalloid compounds of this type. However, in order to judge of the character of interatomic interaction and the structure of the energy bands in the alloys and compounds of interest, it is necessary to examine not only the x-ray spectroscopic characteristics reflecting the state of atoms of the transition metal but also those connected with the behavior of the second component, viz. aluminum. In the present work we investigated the emission and absorption spectra of aluminum in a number of alloys and compounds with transition metals. In view of the complexity of recording long wavelength absorption spectra, the K edges were recorded only for compounds with a relatively low transition metal content*. For the same reason we were obliged to limit ourselves to a study of the main absorption edges. In this paper we also report on the results of investigations of the $K\beta_X$ emission band and the K absorption edge of pure aluminum.

Experimental Procedure

The K emission and absorption spectra of aluminum were recorded in the first order of reflection from the $(10\bar{1}0)$ planes of a quartz crystal ($d_1 = 4.24$ Å). The linear dispersion in the investigated region of the spectrum was 14 X/mm (voltage dispersion - 2.8 v/mm).

Excitation of the $K\beta_X$ emission band was effected by the primary method at a potential of 3 kv (i = 10 ma). A nitrogen trap helped maintain a vacuum in the $3\cdot10^{-6}$ to $3\cdot10^{-7}$ mm Hg range. The absorption edges were recorded with the instrument operated at 2.5 kv and 50 ma, which precluded the appearance of second and higher orders of reflection.

$K\beta_X$ Emission Band and K Absorption Edge of Pure Aluminum

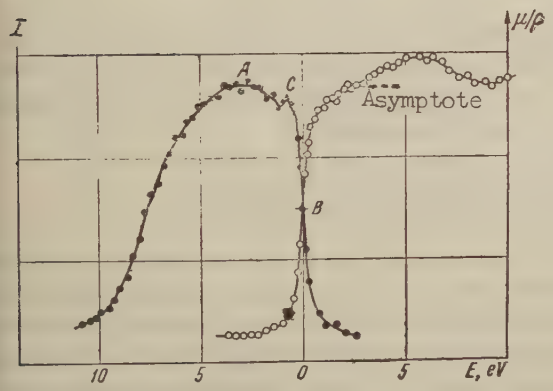

Fig.1

Fig.1 shows the $K\beta_X$ emission band and K absorption edge of pure aluminum. The midpoint of the short wavelength side of the $K\beta_X$ emission band and the point of inflection of the arc tangent section of the absorption edge coincide (point B). This coincidence of the end of emission and beginning of absorption is characteristic of metals, and the position of point B corresponds to the Fermi level. The shape of the $K\beta_X$ band and absorption edge in conjunction give (after exclusion of the influence of the width of the inner level) an approximate characterization of the distribution of p electron states in the filled and unfilled parts of the conduction band.

The $K\beta_X$ band is the last emission band of aluminum. It arises incident to electron transitions from the collective $3s3p$ band

---

*The highest content of transition metal at which it was still possible to record the absorption edge of aluminum was 40 atomic percent (the compound Ni_2Al_3).

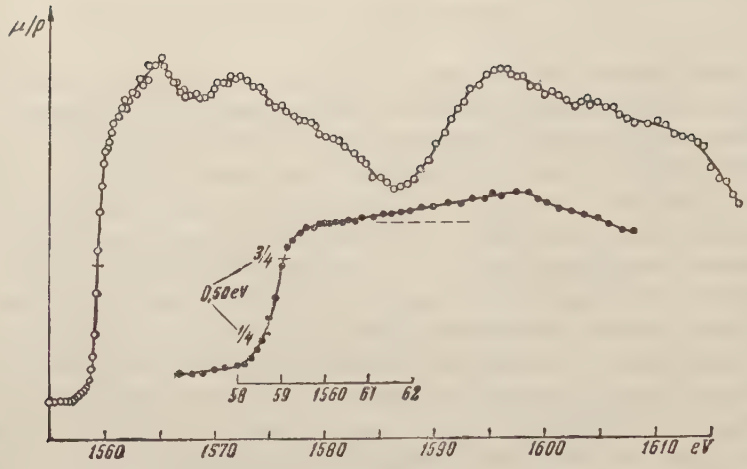

Fig.2

to the 1s level. Our shape of the $K\beta_x$ band in general agrees with the results of Nordfors[3], except that in his work the peaks which we designate by A and C are united into a single maximum. According to Farinea the long wavelength side of th emission band exhibits an addi tional peak that purportedly corresponds to the first fille Brillouin zone. This peak was not observed in the present study or in the work of Nord- fors[3]. We found that at an in adequate vacuum there appears on the long wavelength side of the $K\beta_x$ band a hump due to the $K\beta_1$ band of Al_2O_3, at the loca tion of the peak reported by Farineau[4].

According to Farineau[4], the valence electrons of aluminum are distributed i two Brillouin zones, only the first of which is completely occupied. The zone model predicts a decrease in density of states incident to transition from the first to the second zone, which corresponds to an energy interval of between 7 a 11 ev from the long wavelength end of the band. The distances of peaks A and C from the long wavelength end of the band, taking into account broadening of low- lying states of the band owing to nonradiative transitions, are about 8.5 and 11 ev, respectively, i.e., are in satisfactory agreement with the concepts of the zone theory model.

Fig.2 shows the K absorption edge of aluminum, recorded with a 2 μ thick ab sorber. The shape of the edge and the position of the extrema agree well with the results of Shaw's work[5] carried out on a double-crystal spectrometer. The a sorption edges for absorbers of other thicknesses differ only as regards the dep of the extrema. For a 3 μ absorber the depth is less, while for a 1 μ absorber it is greater.

The width of the initial absorption level was determined with reference to the short wavelength edge of the emission curve and to the main absorption edge (Fig.2, lower curve). Both values equal 0.50 ev, which agrees with the value of the width of the K level calculated by Blokhin and Sachenko[6].

$K\beta_x$ Band of Aluminum in Alloys of Transition Metals

Fig.3 shows the $K\beta_x$ band of aluminum in a number of alloys and compounds wi the transition metals Cr, Fe and Ni. It will be evident that the character of t change in the emission band as one goes from higher to lower intermetallic com- pounds is identical for all three systems: with increasing content of the transi tion metal the intensity of the short wavelength part of the $K\beta_x$ falls off con- sistently, and for alloys with the maximum transition metal content (Cr_2Al, Fe_3A and Ni_3Al) the band becomes narrower, almost symmetric, and is shifted to the lo energy side relative to its position in the spectrum of pure Al. For the purpos of quantitative evaluation of the alterations we drew a vertical dashed line through the A peak of pure aluminum and measured the areas of the short waveleng parts of the bands (i.e., to the right of the dashed line). The measurement re-

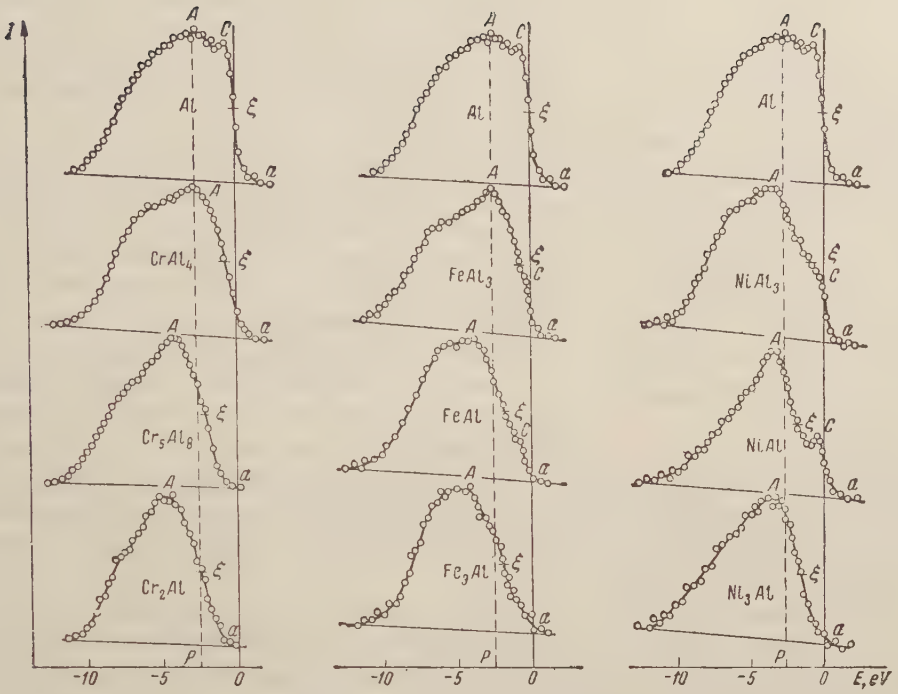

Fig.3

Some characteristics of the $K\beta_x$ band of aluminum in the investigated alloys

Compound	Area of short wavelength part of band, arb.units	ξ, eV	A, eV
Pure Al	420	1558,9	1556,2
$NiAl_3$	330	1558,1	1555,2
NiAl	285	1557,0	1555,2
Ni_3Al	250	1557,1	1555,2
$FeAl_3$	340	1558,0	1556,2
FeAl	235	1557,0	1554,7
Fe_3Al	200	1556,9	1554,7
$CrAl_4$	360	1558,2	1556,1
Cr_5Al_8	195	1556,6	1554,6
Cr_2Al	160	1556,2	1554,0

sults are given in the table.

On the basis of these data we conclude that for all systems, increase of the transition metal content leads to consistent decrease in the intensity of the short wavelength part of the band, and shift of the point ξ (the midpoint of the short wavelength side) and the peak A to the low energy side. The extent of these changes is greatest for alloys in the chromium-aluminum system, somewhat less for iron-aluminum and least for nickel-aluminum (for identical component concentrations).

It is obvious that this betrays the influence of the different degrees of filling of the *3d* shell of chromium, iron and nickel atoms.

The general aspect of the bands for alloys with high transition metal content is reminiscent of the $K\beta_1$ band of Al_2O_3. Fig.4 shows the $K\beta_x$ bands of pure aluminum, aluminum in Al_2O_3 and aluminum in Ni_3Al. It is obvious that the last occupies an intermediate position.

It seems to us that the similarity in shape of the bands in the spectra of the alloys and Al_2O_3 is not fortuitous, that in alloys and compounds of aluminum with transition metals the predominant metallic type of bond is supplemented by interaction between the transition metal atoms and the aluminum atoms, the nature of which is somewhat similar to the ionic-covalent bonding between aluminum and oxygen in Al_2O_3. It should be noted that the difference between the electronegativities of aluminum and oxygen exceeds that between aluminum and transition metals by at least a factor of seven.*

*Electronegativity values[7]: O - 3.5, Al - 1.6, Ni - 1.8.

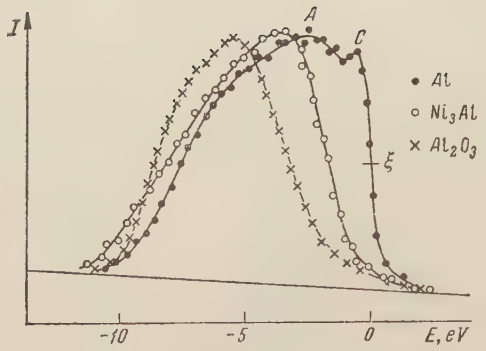

Fig.4

Hence the polar-covalent interaction between the transition metal and aluminum atoms and, consequently, the degree of alteration of the emission band in the alloys should be considerably weaker than in the predominantly ionic compound Al_2O_3.

Earlier[1,2] we developed the concept of ionic-covalent interaction in alloys and compounds of transition metals with aluminum, basing our views on the aggregate of physical properties, structural peculiarities and x-ray spectral characteristics of transition metals in these compounds. The present work, it seems to us, yields the most direct x-ray spectroscopic confirmation of this concept. In fact, the character of the change in the $K\beta_x$ emissio band of aluminum in alloys points to withdrawal of part of the high energy electrons of the aluminum atoms to the transition metal atoms with an unfilled $3d$ she The lower energy resulting from this interaction is evinced by the shift of the e tire band to the low energy side.

We can get a clear idea of the polar-covalent interaction in the alloys only on the basis of investigation of the $K\beta_x$ band of aluminum in alloys with a high transition metal content, wherein the metallic aluminum-aluminum interaction is weakened owing to the great separations between the aluminum atoms and does not mask the polar-covalent interaction between the aluminum and transition metal atoms. Thus, in the alloy $NiAl_3$ there are twelve nickel atoms in the immediate ambiance of each aluminum atom; six aluminum atoms are located in the second coordination sphere, and their distance from the central Al atom substantially exceeds the interatomic separations in pure aluminum. In the compound $NiAl_3$ each emitting aluminum atom is surrounded by only three nickel atoms and eight aluminu atoms, whose distances virtually do not differ from the interatomic separations i pure aluminum. Hence, here the strong metallic interaction between the aluminum atoms masks the polar-covalent interaction with the transition metal atoms. An analogous situation obtains in compounds of the other systems as well.

K Absorption Edge of Aluminum in Some Compounds with Transition Metals

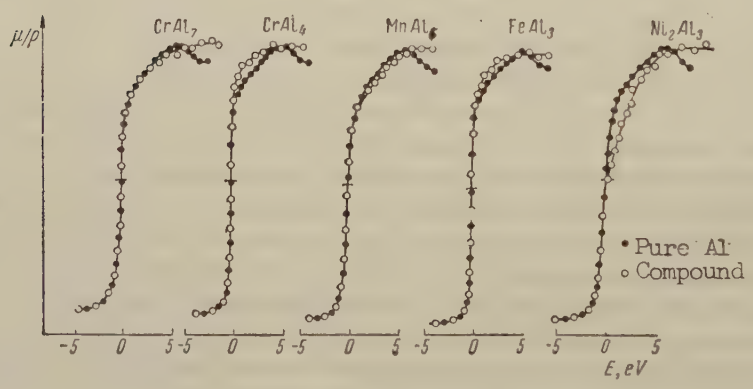

Fig.5

As we saw above, the alterations that the $K\beta_x$ emi sion band undergoes in the direction of the $K\beta_1$ band of Al_2O_3 are convincing evidenc of the presence of polar-covalent interaction in the investigated compounds. It is natural to expect the absorption edges also to evinc changes bringing them closer to the edge of Al_2O_3. Accor ing to the data of Rudström[8] the K absorption edge of alu minum in Al_2O_3 is shifted 5. ev to the short wavelength

side relative to the edge of pure aluminum. Owing to experimental difficulties we succeeded in recording the main absorption edges of aluminum only in compounds with a relatively low transition metal content. Fig.5 shows the main absorption edges of aluminum in these compounds with the main absorption edge of pure aluminum superposed on them for the purpose of comparison. It will be evident that a shift of the edge to the short wavelength side is noticeable only for the compound Ni_2Al_3, which has the highest transition metal content of all the investigated compounds (40 atomic percent). It would be interesting to study the absorption spectra of aluminum in other compounds with an even higher content of transition metal. We plan to undertake such studies in the near future.

Institute of the Physics of Metals,
Academy of Sciences of the USSR

References

1. S.A.Nemnonov, L.D.Finkel'shtein & K.M.Kolobova, Fizika metallov i metallovedenie, 9, 243 (1960). (Trans.Physics of Metals & Metallography.)
2. S.A.Nemnonov & M.F.Sorokina, Izv.AN SSSR, Ser.fiz., 24, 455 (1960). (Trans. Bulletin, 24, 462.)
3. B.Nordfors, Arkiv fys., 10, 279 (1956).
4. J.Farineau, Ann.phys., 10, 20 (1938).
5. C.H.Shaw, Theory of Alloy Phases, p.35, Cleveland, 1956.
6. M.A.Blokhin & V.P.Sachenko, Izv.AN SSSR, Ser.fiz., 21, 1343 (1957). (Trans. Bulletin, 21, 1333.)
7. M.A.Fineman & R.Daignault, J.Inorg.Nucl.Chem., 10 (3/4), 205 (1959).
8. L.Rudström, Arkiv fys., 12, 287 (1957).

COMPUTER FOR CORRECTING THE SHAPE OF EMISSION SPECTRA

- M. I. Korsunskii & Ya. E. Genkin

Distortions of emission spectra due to interaction of the x-ray photons with the instrument and the width of the inner levels are usually allowed for by methods[1,2] involving the use of special tables, charts or matrices. In such calculations it is particularly convenient to employ accumulator or storage devices capable of algebraic summation (mechanical or electrical calculators).

In general, the corrected ordinate f_i is given by

$$f_i = \sum_{k=1}^{n} b_{ik} F_k \qquad (i = 1, 2, \ldots, s), \tag{1}$$

where $\| b_{ik} \|$ is a s by n transformation matrix, and F_k is the corresponding ordinate of the experimental spectrum.

We have designed a simple computer for correcting x-ray spectra for distortions introduced by the instrument and the width of inner levels. This device can easily be constructed in any laboratory. Fig.1 gives a schematic of the computer for correcting spectra (CCS). The matrix elements are made of manganin wire resistors r_{ik}. The CCS consists of n cells. Each k-th cell comprises s series connected resistors (the elements of the k-th column of the $\| b_{ik} \|$ matrix), a dc source (battery), an adjusting potentiometer, a ballast resistor and a resistor with a resistance equal to that of the instrument measuring the current in the circuit of the given cell. The potentiometers are used to adjust the current in each cell to the value corresponding to the ordinate at each point of the experimental spectrum ($j_k \sim F_k$). Then the potential drop across each resistor is $V_{ik} = r_{ik} j_k = \alpha b_{ik} F_k$, where α is a constant of the instrument. The sum of the potential drops across all the i-th resistors of all the cells is then proportional to the i-th ordinate of the corrected spectral curve:

$$V_i = \sum_{k=1}^{n} v_{ik} = \alpha f_i. \tag{2}$$

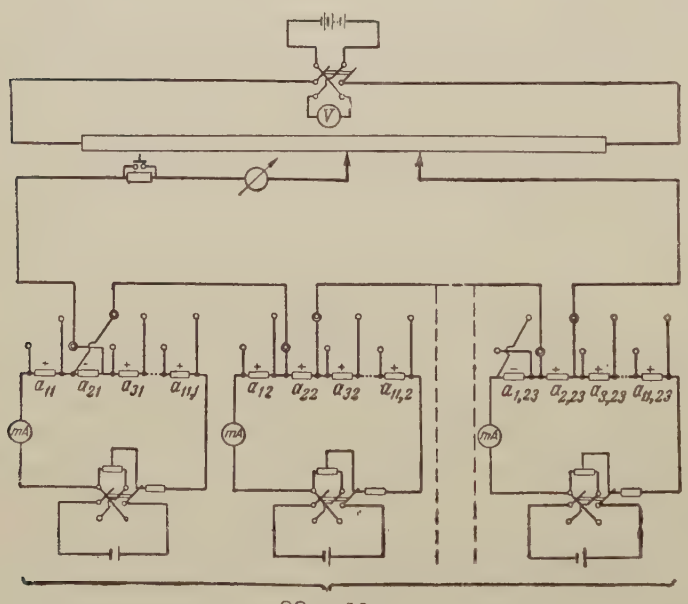

Fig.1. Schematic of the computer for correcting spectra.

The potential drops are added by setting a special movable contact panel (MCP) successively into s positions; thus there are obtained s values of the corrected spectrum at s points.

The total potential drop at each point is determined by the compensation method. Fig.2 shows the electric circuit of the CCS. It will be seen that each matrix element ik is connected to a stationary contact panel (SCP). The diagram shows the MCP in the position in which there is realized summation of the voltage drops over the 11, 12, 13, ...1,23 matrix element, i.e., there is determined the potential drop proportional to the first corrected ordinate f_1.

This voltage is taken off the ends of resistors 11 and 1,23 and

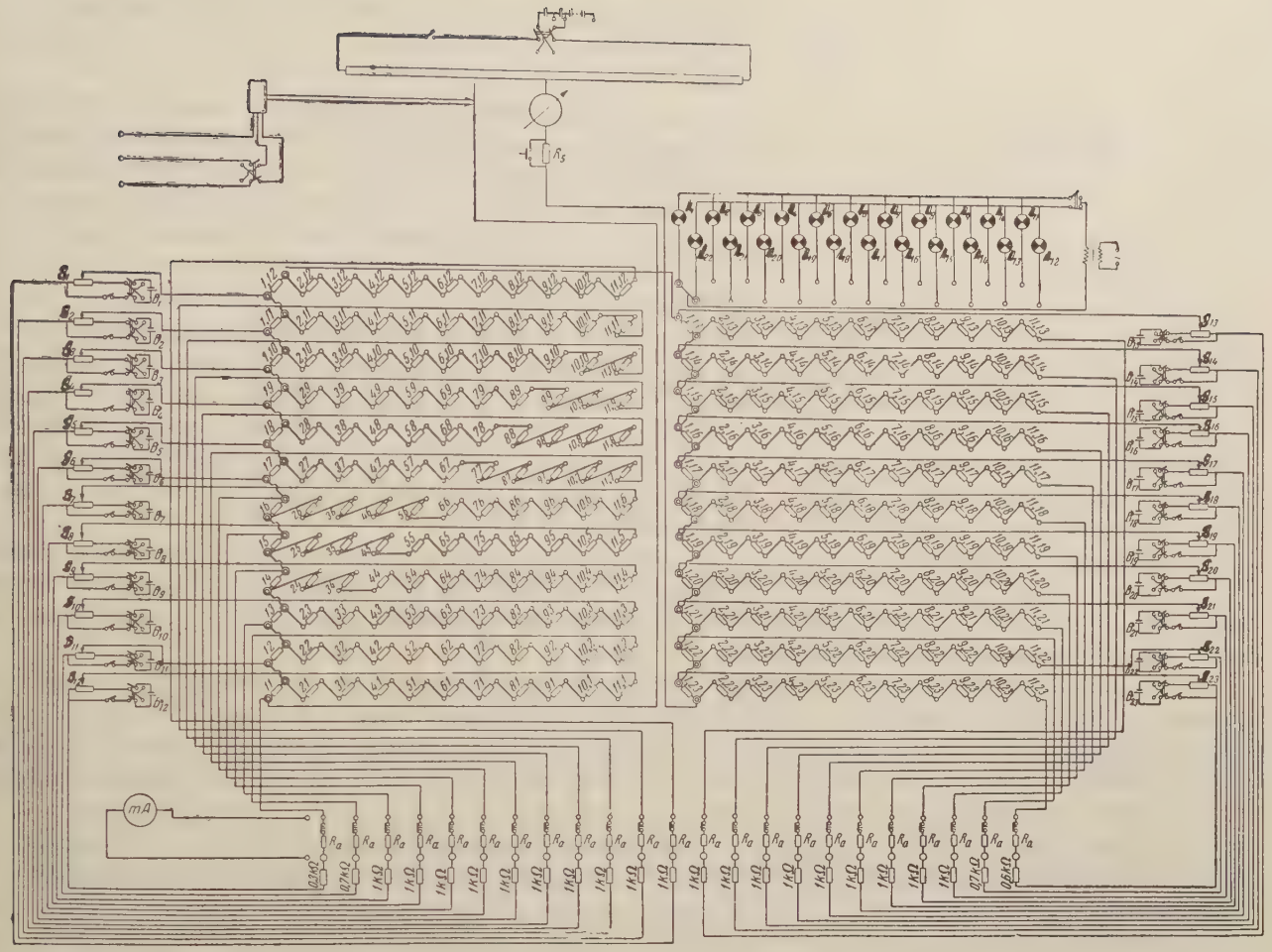

Fig.2. Electric circuit of the CCS.

is applied to the movable contact of the compensating potentiometer and to its midpoint. If the potential difference between the midpoint and the movable contact of the potentiometer is not equal to the voltage difference taken off resistors 11 and 1,23, the galvanometer will show a deflection. By pressing the appropriate button one actuates a reversible motor mechanically coupled to the moving contact of the potentiometer. This motor operates until the galvanometer returns to the null position. Then the voltage drop across the potentiometer will be equal to the applied voltage difference, i.e., will be proportional to f_1. The moving contact of the potentiometer is connected to a pointer moving over a dial with the zero mark corresponding to the center of the potentiometer. The potentiometer contact is moved by means of a screw connected to the motor shaft through a reducing gear. There is a circular scale on the axis of this screw. Thus, together with the potentiometer scale, this circular scale gives the position of the moving contact to four significant figures. The length of the potentiometer wire is 1 meter. The potentiometer circuit includes a current reversing switch.

After determining the first corrected ordinate f_1, the MCP is moved to position 2, in which the potential drop across the ends of resistors 21, and 2,23 is applied to the potentiometer. Compensation of this voltage gives the value of the corrected ordinate for the second point, etc. The MCP is moved into successive

positions by means of a Maltese cross mechanism. An appropriate switch causes the corresponding signal lamp L_i to light up, thereby indicating that the i-th ordinate is being corrected.

Our CCS was programed with an 11 x 23 matrix designed for correcting spectra directly from microdensitograms without previous conversion to intensities. This matrix was obtained from a matrix of the 22nd order "with translation".[2]

In practice, a matrix for correcting any spectral intervals can readily be constructed. The summing circuit remains the same; only the r_{ik} are changed. It should be noted that when the matrix elements in any column have opposite signs they are connected to the SCP as shown in Fig.2 (for instance, the 25 and 65 matrix elements have opposite signs, whereas the 65 and 85 elements have the same sign).

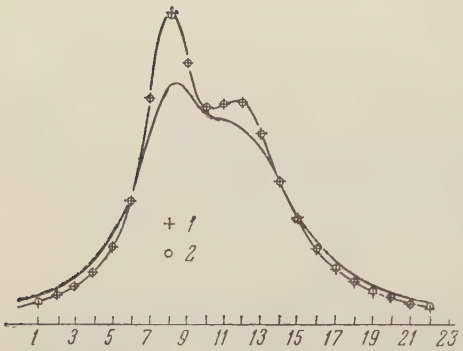

Fig.3. Corrected spectra obtained by direct calculation (1) and by means of the CCS (2). Solid line - experimental spectrum.

Corrected spectra are shown in Fig.3. The crosses give the values obtained by direct calculations; the circles are the points obtained by means of the CCS. It will be seen that the agreement is satisfactory.

Use of the CCS greatly reduces the time necessary for processing microphotograms. Thus, for example, correction of a section of the spectrum equal to about 16 dispersion widths by the matrix method[2] requires about 4 hours; correction by the column method takes about 36 hours, whereas only some 30-40 min are required to correct the same section by means of the CCS.

A positive feature of the CCS is that all the matrix elements are made of wire resistors so that the apparatus is relatively insensitive to temperature changes.

We take this opportunity to express our deep gratitude to L. I. Lukashenko for assistance in the work, V.F.Balditsyn and I.A.Belenko for their craftsman-like workmanship in assembling the CCS.

"V.I.Lenin" Kharkov Polytechnic Institute

References

1. M.A.Blokhin, Metody rentgeno-spektral'nykh issledovanii (Methods of x-ray spectroscopic investigation), p.236, M., 1959.

2. Ya.E.Genkin & I.A.Rumyantsev, Izv.AN SSSR, Ser.fiz., 24, 384 (1960). (Trans.Bulletin, 24, 398.)

COMPARISON OF TWO METHODS OF CORRECTING EXPERIMENTAL CURVES (Column and Matrix Methods)

- Ya.E.Genkin & I.A.Rumyantsev

The column and matrix methods of correcting experimental curves have been described elsewhere.[1,2] The purposes of the present paper are to establish the advantages and disadvantages of each method and to determine its range of applicability.

1. Column Method

As is known,[1] the column method consists essentially of using successive approximations to find a function $f(x)$ satisfying a convolution equation of the form

$$F(x) = \int_{-\infty}^{\infty} f(z)\,\varphi(x-z)\,dz, \tag{1}$$

where

$$F(x) = \begin{cases} 1 \text{ for } -\frac{a}{2} < x < \frac{a}{2}, \\ 0 \text{ for } |x| > \frac{a}{2}, \end{cases}$$

$$\varphi(x-z) = \frac{1}{\pi\beta} \cdot \frac{1}{1+\left(\frac{z-x}{\beta}\right)^2};$$

here a is the width of a unit column, and β is the half-width of the dispersive distortion.

This function as obtained in the tenth or fifteenth approximation will be found in the table below for those values of x for which it is no less than $5 \cdot 10^{-5}$. By using this function (p_{10} or p_{15}) one can correct any experimental curve. In the process, that part of the curve which is outside the correction interval is taken into account by approximating the dropped parts of the experimental curve by semi-infinite step functions and then using the special tables of q_{10} (or q_{15}) obtained by solving Eq.(1) for

$$F(x) = \begin{cases} 1 \text{ for } x > 0 \\ 0 \text{ for } x < 0. \end{cases}$$

This method is universal in the sense that it can be applied to a spectrum section of any length and to either emission or absorption spectra.

If the uncertainty in determining the ordinate of the experimental curve is ε, the maximum uncertainty in the ordinate of the corrected curve is $N\varepsilon$, where N is the sum of the absolute values of the coefficients in the computation table. An advantage of the method is the possibility of obtaining relatively small coefficients (<10) in the computation table, and this makes it possible to reduce the uncertainty by appropriate choice of the approximation.

The tables given by Blokhin[1] are calculated for a subdivision interval equal to $\beta/2$. Such a small interval, however, is of no particular advantage, as will be shown below. Furthermore, the smaller the interval, the longer the time required for correcting the curve (30-35 hours for correcting a spectrum of width $10.5\,\pi\beta \approx 33\,\beta$).

A disadvantage of the method is that the experimental curve is approximated by a histogram; what is corrected is in fact an approximate step-function type of curve, which does not correspond to physical reality.

Another disadvantage (in our view the most important) is that Blokhin gives

no rule for obtaining the heights of the semi-infinite step function used to approximate those parts of the spectrum which are outside the correction section. This may cause deviations of the area and shape from those of the true curve, depending on the choice of the height of the step function.

2. Matrix Method

The matrix method[2] is based on approximating sections of the true $f(x)$ curve in the correction section by polynomials of degree two. The sections of the true curve outside the correction section are taken into account by approximating them by hyperbolas also of degree two; one then integrates the approximating functions within the correction section over small subintervals of appropriate width, and outside the correction section over the entire range of the variable, reducing Eq.(1) to the form

$$F_k = \sum_{i=1}^{n} a_{ki} f_i. \qquad (2)$$

The $\| b_{ik} \|$ matrix, which is the inverse of the linear transformation matrix $\| a_{ki} \|$ in (2), is the one used in developing the matrix method for correctin experimental emission spectra.

In Ref.2 we also gave a method for finding the $\| b'_{ik} \|$ matrix, which can be used to correct experimental emission spectra even if the datum of the ordinates is not known.

The primary advantage of this method is that it is the true curve, rather than the experimental one, which is approximated. Further, the approximation by parabolas can be used to obtain not only the ordinate, but also the slope and curvature of the true curve, and this makes it possible to reduce the number of subdivisions. Thus the matrix method gives not only the values of the ordinate at the points of correction, but whole sections of the true curve in the neighborhood of these points (or more accurately, sections of parabolas approximating the true curve). It should be borne in mind, however, that correction by any method makes sense only if the area under the experimental curve in the correction section amounts to at least 70-80% of the area under the true curve.

Since all known correction methods assume the datum of the ordinates to be known, the matrix method has the additional advantage that one can obtain the $\| b'_{ik} \|$ matrix "with translation", which can be used to perform corrections when this condition is not satisfied, i.e., to find the true value of the ordinates measured from the true datum.

The matrices tabulated in Ref.2 were calculated to the fourth or fifth decimal place, and have now been made more exact at the Computation Center of the Academy of Sciences, Ukrainian SSR on the "Ural" electronic computer. They can be used to obtain the exact values of points on the corrected curve. When these matrices are used, the time necessary to correct a curve of width $10.5\ \pi\beta$ is about three to four hours.

Another advantage of the method is that the results can easily be checked by making use of the appropriate matrices themselves, rather than their inverses.

A disadvantage of the method is the inflexibility of the correction section (equal to the product of the subdivision interval by the order of the matrix), which limits the range of applicability of a matrix of given order.

As has been mentioned, as the subdivision interval is decreased, the magnitude of the matrix elements increases. When using matrices with large elements, however, the ordinates of the experimental curve must be known to good accuracy.

Let us consider the extent to which it is worthwhile to reduce the subdivisio

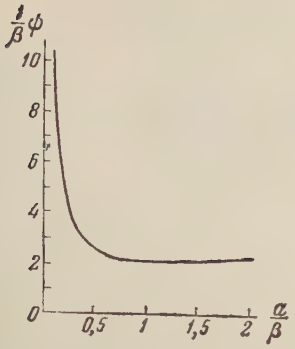

Fig.1. Plot of $\psi(a)$.

interval in correcting an experimental curve. To this end we consider what happens to a column of height 1 and width equal to the subdivision interval under dispersive distortion for subdivision intervals in the range from 0.1 β to 2 β. It is natural that as the subdivision interval is reduced, the column will "diffuse", becoming less and less sharp and identifiable. As the distinguishability criterion we use the function $\Phi(x) = \left|\frac{2F(x)}{F'(x)}\right|$. We chose this function because it takes into account both the ordinate and the slope of the curve. Values of this function have been calculated for several subdivision intervals (a) at points a distance a from the center of the column.

The function $\psi(a)$ obtained in this way is plotted in Fig.1. It will be seen that as the subdivision interval is decreased from 2 β to 0.7 β, there is essentially no change in $\psi(a)$, but as the subdivision interval is further decreased, $\psi(a)$ increases rapidly. This shows that it is not expedient to reduce the subdivision interval below a certain value (~0.7 β).

A disadvantage common to both methods is that they do not work very well on curves with abrupt rises and drops.

3. Extending the range of application of the matrix method

We have calculated matrices of order 12 and 50 with subdivision intervals πβ/2 for correction of 5.5 πβ and 24.5 β wide sections, respectively (the matrix of order 50 is given in Table 1).

In addition, we have calculated matrices of order 12 and 20 with a subdivision interval πβ/4 (the matrix of order 20 is given in Table 2).

Examples of the use of the matrix of order 20 with a subdivision interval πβ/4 and of the use of the column method (subdivision interval 0.5 β) are given in Figs.2 and 3.

What is usually corrected is not the original photometric curve, but the curve obtained from it by converting to intensities. It is found, however, that this intensity conversion can be included in a matrix with translation.[2] This gives a matrix which makes it possible to obtain the correct values of the ordinates, using only the ordinates of the microdensitometer trace, as measured from the zero line (i.e., the line obtained when the photocell is covered). This matrix can be used to crrect spectra with densities of less than 0.5, i.e., when the blackening is proportional to the radiation intensity.

The zero line of the microdensitometer trace is broken up into subintervals of width πβ/2. Measurements (in mm)* are made at all integral ordinates from 0 to 23, i.e., at 24 points. Then the 23 values of $t_k = \frac{n_k - n_{k-1}}{n_k + n_{k-1}}$ are obtained, starting with $k = 1$. The corrected ordinate f_i at the i-th point is given by T_i:

$$T_i = \sum_{k=1}^{23} b_{ik} t_k = \alpha f_i \quad (i = 1, 2, \ldots, 22)$$

The $\|b_{ik}\|$ matrix is given in Table 3. The sum of the elements in each row of this matrix vanishes, which provides for taking into account a linearly varying background.

---

*The ordinates are measured at right angles to the zero line.

i \ k	1	2	3	4	5	6	7	8	9	10	11	12
1	2,523	—0,982	—0,153	—0,082	0,000	0,003	—0,007	—0,005	—0,004	—0,004	—0,002	—0,003
2	—1,103	3,216	—1,212	0,229	—0,096	0,003	—0,007	—0,005	—0,004	—0,002	—0,003	—0,001
3	0,179	—1,211	3,247	—1,226	0,232	—0,095	0,004	—0,007	—0,005	—0,004	—0,002	—0,003
4	—0,088	0,232	—1,226	3,247								
5	—0,004	—0,094	0,232	—1,226								
6	—0,011	0,005	—0,095	0,232								
7	—0,009	—0,006	0,004	—0,095								
8	—0,006	—0,004	—0,007	0,004								
9	—0,006	—0,003	—0,005	—0,007								
10	—0,004	—0,003	—0,004	—0,005								
11	—0,004	—0,002	—0,002	—0,004								
12	—0,003	—0,002	—0,003	—0,002								
13	—0,003	—0,001	—0,001	—0,003								
14	—0,002	—0,001	—0,002	—0,001								
15	—0,002	—0,001	—0,001	—0,002								
16	—0,001	—0,001	—0,001	—0,001								
17	—0,001	—0,001	0,000	—0,001								
18	—0,001	—0,001	—0,001	0,000								
19	—0,001	—0,001	—0,001	—0,001								
20	—0,001	—0,001	—0,001	—0,001								
21	—0,001	0,000	—0,000	—0,001								
22	0,000	—0,001	—0,001	0,000								
23	—0,001	0,000	0,000	—0,001								
24	—0,001	0,000	—0,001	0,000								
25	0,000	0,000	0,000	—0,001								
	1	2	3	4	5	6	7	8	9	10	11	12

	26	27	28	29	30	31	32	33	34	35	36	37
1	0,000	—0,001	0,000	—0,001	0	0	0	0	0	0	0	0
2	—0,001	0,000	—0,001	0,000	—0,001							
3	0,000	—0,001	0,000	—0,001	0,000	—0,001						
4	0,000											
5	—0,001											
6	0,000											
7	—0,001											
8	0,000											
9	—0,001											
10	—0,001											
11	—0,001											
12	0,000											
13	—0,001											
14	—0,001											
15	—0,002											
16	—0,001											
17	—0,003											
18	—0,002											
19	—0,004											
20	—0,005											
21	—0,007											
22	0,004											
23	—0,095											
24	0,232											
25	—1,226											
i / k	26	27	28	29	30	31	32	33	34	35	36	37

Note: The unfilled boxes of the table contain matrix elements found from the relation $b_{i+m,\ k+m} = b_{ik}$ $(m = 1, 2, 3, \ldots)$, **where** $i > 2$, $k > 3$). **The matrix elements in the second half of the table** $(i > 25)$ **are obtained from the relation** $b_{51-i,\ 51-k} = b_{ik}$.

Table 1

13	14	15	16	17	18	19	20	21	22	23	24	25	k / i
—0.002	—0,002	—0,001	—0,001	—0,001	—0,001	—0,001	—0,001	—0,000	—0,001	0,000	—0,001	—0,001	1
—0,002	—0,001	—0,002	—0,001	—0,001	—0,001	—0,001	0,000	—0,001	0,000	—0,001	0,000	—0,001	2
—0,001	—0,002	—0,001	—0,001	0,000	—0,001	—0,001	—0,001	0,000	—0,001	0,000	—0,001	0,000	3
													4
													5
													6
													7
													8
													9
													10
													11
													12
													13
													14
													15
													16
													17
													18
													19
													20
													21
													22
													23
													24
													25
13	14	15	16	17	18	19	20	21	22	23	24	25	

Table 1 continued

38	39	40	41	42	43	44	45	46	47	48	49	50	
0	0	0	0	0	0	0	0	0	0	0	0	0	1
													2
													3
													4
													5
													6
													7
													8
													9
													10
													11
													12
													13
													14
													15
													16
													17
													18
									—0,001				19
									0,000	—0,001			20
									—0,001	0,000	—0,001		21
									0,000	—0,001	0,000	—0,001	22
									—0,001	0,000	—0,001	0,000	23
									0,000	—0,001	0,000	—0,001	24
									0,000	0,000	0,000	—0,001	25
38	39	40	41	42	43	44	45	46	47	48	49	50	i / k

Table 2

i \ k	1	2	3	4	5	6	7	8	9	10	k \ i
1	3,94213	—3,63951	1,69617	—0,83682	0,34794	—0,17293	0,04910	—0,01949	—0,00953	—0,00146	1
2	—6,24230	14,83773	—11,05945	5,22204	—2,47160	1,07156	—0,47387	0,14251	—0,02932	—0,01991	2
3	2,71507	—10,87905	17,96553	—12,53734	5,90371	—2,77218	1,19454	—0,51103	0,14519	—0,02483	3
4	—1,67525	5,43901	—12,68297	18,80958	—12,92447	6,07278	—2,83933	1,21387	—0,51080	0,14252	4
5	0,71035	—2,57215	5,96734	—12,92560	18,92036	—12,97754	6,09341	20,84632	1,21429	—0,51153	5
6	—0,52986	1,28236	—2,87829	6,10848	—12,99061	18,95625	—12,98960	6,09785	—2,84609	1,21488	6
7	0,12228	—0,50573	1,21242	—2,84143	6,09336	—12,98890	18,95368	—12,98985	6,09717	—2,84742	7
8	—0,13976	0,23856	—0,55779	1,23687	—2,86855	6,13325	—13,06206	19,06233	—13,06064	6,12985	8
9	—0,03883	0,00695	0,13179	—0,50283	1,20793	—2,84516	6,09622	—12,98940	18,95407	—12,98978	9
10	—0,03169	0,00622	—0,03856	0,14556	—0,51130	1,21539	—2,84678	6,09796	—12,98951	18,95495	10
11	—0,04511	0,03868	—0,03853	—0,01480	0,13800	—0,51029	1,21468	—2,84771	6,09819	—12,99025	11
12	—0,03226	0,02868	—0,01505	—0,01358	—0,02644	0,14469	—0,51188	1,21503	—2,84728	6,09762	12
13	—0,03552	0,01201	—0,00117	—0,00192	—0,02026	—0,02440	0,14353	—0,51363	1,22054	—2,86081	13
14	—0,02581	0,02725	—0,03468	0,02300	—0,01201	—0,01514	—0,02634	0,14356	—0,51188	1,21477	14
15	—0,03183	0,01935	—0,00181	—0,02097	0,01672	—0,00935	—0,01602	—0,02594	0,14402	—0,51166	15
16	—0,01152	0,00287	—0,00530	0,00980	—0,02686	0,01923	—0,01042	—0,01644	—0,02571	0,14287	16
17	—0,02798	0,02898	—0,02530	0,00574	0,00580	—0,02525	0,01866	—0,00968	—0,01690	—0,02431	17
18	—0,00970	—0,00292	0,01251	—0,01455	0,00014	0,00910	—0,02617	0,01692	—0,00703	—0,02008	18
19	—0,01231	0,01888	—0,01863	0,01670	—0,01720	—0,00200	0,00630	—0,02281	0,01150	—0,00156	19
20	—0,01637	0,01143	—0,00539	—0,00314	0,00059	—0,00359	—0,00408	0,00144	—0,00913	—0,00113	20
i \ k	1	2	3	4	5	6	7	8	9	10	k \ i

Table 2 continued

i \ k	11	12	13	14	15	16	17	18	19	20	k \ i
1	—0,00113	—0,00913	0,00144	—0,00408	—0,00359	0,00059	—0,00314	—0,00539	0,01143	—0,01637	1
2	—0,00156	0,01150	—0,02281	0,00630	—0,00200	—0,01720	0,01670	—0,01863	0,01888	—0,01231	2
3	—0,02008	—0,00703	0,01692	—0,02617	0,00910	0,00014	—0,01455	0,01251	—0,00292	—0,00970	3
4	—0,02431	—0,01690	—0,00968	0,01866	—0,02525	0,00580	0,00574	—0,02530	0,02898	—0,02798	4
5	0,14287	—0,02571	—0,01644	—0,01042	0,01923	—0,02686	0,00980	—0,00530	0,00287	—0,01152	5
6	—0,51166	0,14402	—0,02594	—0,01602	—0,00935	0,01672	—0,02097	—0,00181	0,01935	—0,03183	6
7	1,21477	—0,51188	0,14356	—0,02634	—0,01514	—0,01201	0,02300	—0,03468	0,02725	—0,02581	7
8	—2,86081	1,22054	—0,51363	0,14353	—0,02440	—0,02026	—0,00192	—0,00117	0,01201	—0,03552	8
9	6,09762	—2,84728	1,21503	—0,51188	0,14469	—0,02644	—0,01358	—0,01505	0,02862	—0,03226	9
10	—12,99025	6,09819	—2,84771	1,21468	—0,51029	0,13800	—0,01480	—0,03853	0,03862	—0,04511	10
11	18,95495	—12,98951	6,09796	—2,84678	1,21539	—0,51130	0,14556	—0,03856	0,00622	—0,03169	11
12	—12,98978	18,95407	—12,98940	6,09622	—2,84516	1,20793	—0,50283	0,13179	0,00695	—0,03883	12
13	6,12985	—13,06064	19,06233	—13,06206	6,13325	—2,86855	1,23687	—0,55779	0,23856	—0,13976	13
14	—2,84742	6,09717	—12,98985	18,95368	—12,98890	6,09336	—2,84143	1,21242	—0,50573	0,12228	14
15	1,21488	—2,84609	6,09785	—12,98960	18,95625	—12,99061	6,10848	—2,87829	1,28236	—0,52986	15
16	—0,51153	1,21429	—2,84632	6,09341	—12,97754	18,92036	—12,92560	5,96734	—2,57215	0,71035	16
17	0,14252	—0,51080	1,21387	—2,83933	6,07278	—12,92447	18,80958	—12,68297	5,43901	—1,67525	17
18	—0,02483	0,14519	—0,51103	1,19454	—2,77218	5,90371	—12,53734	17,96553	—10,87905	2,71507	18
19	—0,01991	—0,02932	0,14251	—0,47387	1,07156	—2,47160	5,22204	—11,05945	14,83773	—6,24230	19
20	—0,00146	—0,00953	—0,01949	0,04910	—0,17293	0,34794	—0,83682	1,69617	—3,63951	3,94213	20
i \ k	11	12	13	14	15	16	17	18	19	20	i \ k

Table 3

i \ k	1	2	3	4	5	6	7	8	9	10	11	12	k \ i
1	10,43411	—6,10955	1,60710	—0,86065	—0,10889	—0,27294	—0,21742	—0,22017	—0,21585	—0,21185	—0,20897	—0,20801	1
2	8,77020	—2,30046	0,06060	—0,57312	—0,26197	—0,29219	—0,26264	—0,25575	—0,25014	—0,24550	—0,24210	—0,24037	2
3	8,52411	—3,28880	3,16824	—1,79137	—0,06416	—0,41671	—0,28573	—0,29757	—0,28482	—0,27873	—0,27526	—0,27202	3
4	8,07957	—2,92211	1,86526	1,45582	—1,32483	—0,20719	—0,41281	—0,31949	—0,32624	—0,31285	—0,30769	—0,30445	4
5	7,73965	—2,88468	2,00995	0,21520	1,89966	—1,46520	—0,20708	—0,44821	—0,35006	—0,35601	—0,34351	—0,33877	5
6	7,37643	—2,73950	1,83073	0,43931	0,63923	1,76713	—1,46495	—0,24064	—0,47730	—0,37840	—0,38532	—0,37336	6
7	7,04974	—2,63326	1,76210	0,32678	0,84353	0,51004	1,76582	—1,49859	—0,27010	—0,50592	—0,40790	—0,41578	7
8	6,70433	—2,50596	1,66596	0,32115	0,71160	0,71888	0,50748	1,73236	—1,52791	—0,29854	—0,53529	—0,43728	8
9	6,36910	—2,38566	1,58223	0,29523	0,68656	0,59248	0,71500	0,47467	1,70308	—1,55634	—0,32789	—0,56517	9
10	6,04370	—2,26768	1,49798	0,27630	0,64132	0,57154	0,58711	0,68186	0,44460	1,67402	—1,58612	—0,35714	10
11	5,71810	—2,15015	1,41643	0,26016	0,60139	0,53061	0,56406	0,55391	0,65167	0,41600	1,64453	—1,61538	11
12	5,39607	—2,03129	1,33426	0,24223	0,56505	0,49700	0,52215	0,53130	0,52420	0,62341	0,38695	1,61538	12
13	5,06981	—1,91115	1,25576	0,22616	0,52991	0,46557	0,48815	0,49055	0,50258	0,49597	0,59418	0,35714	13
14	4,75910	—1,79425	1,17375	0,20840	0,49358	0,43256	0,45421	0,45529	0,46043	0,47359	0,46663	0,56517	14
15	4,44282	—1,67850	1,09459	0,19363	0,45772	0,40217	0,42068	0,42228	0,42554	0,43163	0,44422	0,43728	15
16	4,11624	—1,55528	1,01497	0,17912	0,42464	0,37258	0,38991	0,38981	0,39334	0,39783	0,40330	0,41578	16
17	3,80512	—1,44330	0,93555	0,16214	0,38830	0,34126	0,35654	0,35717	0,35889	0,36382	0,36751	0,37336	17
18	3,47410	—1,31787	0,85393	0,14946	0,35400	0,31203	0,32569	0,32599	0,32778	0,33072	0,33511	0,33877	18
19	3,16137	—1,19484	0,78594	0,13224	0,31868	0,28104	0,29305	0,29339	0,29427	0,29763	0,30022	0,30445	19
20	2,84350	—1,08426	0,69616	0,11737	0,28575	0,25201	0,26306	0,26311	0,26429	0,26682	0,26938	0,27202	20
21	2,51327	—0,96044	0,61432	0,10133	0,25094	0,22067	0,23021	0,23067	0,23125	0,23628	0,23809	0,24037	21
22	2,22118	—0,85834	0,54123	0,08437	0,21670	0,19243	0,20007	0,20082	0,20106	0,20350	0,20535	0,20801	22
i \ k	1	2	3	4	5	6	7	8	9	10	11	12	k \ i

Table 3 continued

k / i	13	14	15	16	17	18	19	20	21	22	23	k / i
1	—0,20535	—0,20350	—0,20106	—0,20082	—0,20007	—0,19243	—0,21670	—0,08437	—0,54123	0,85834	—2,22118	1
2	—0,23809	—0,23628	—0,23125	—0,23067	—0,23021	—0,22067	—0,25094	—0,10133	—0,61432	0,96044	—2,51327	2
3	—0,26938	—0,26682	—0,26429	—0,26311	—0,26306	—0,25201	—0,28575	—0,11737	—0,69616	1,08426	—2,84350	3
4	—0,30022	—0,29763	—0,29427	—0,29339	—0,29305	—0,28104	—0,31868	—0,13224	—0,78594	1,19484	—3,16137	4
5	—0,33511	—0,33072	—0,32778	—0,32599	—0,32569	—0,31203	—0,35400	—0,14946	—0,85393	1,31787	—3,47410	5
6	—0,36751	—0,36382	—0,35889	—0,35717	—0,35654	—0,34126	—0,38830	—0,16214	—0,93555	1,44330	—3,80512	6
7	—0,40330	—0,39783	—0,39334	—0,38981	—0,38991	—0,37258	—0,42464	—0,17912	—1,01497	1,55528	—4,11624	7
8	—0,44422	—0,43163	—0,42554	—0,42228	—0,42068	—0,40217	—0,45772	—0,19363	—1,09459	1,67850	—4,44282	8
9	—0,46663	—0,47359	—0,46043	—0,45529	—0,45421	—0,43256	—0,49358	—0,20840	—1,17375	1,79425	—4,75910	9
10	—0,59418	—0,49597	—0,50258	—0,49055	—0,48815	—0,46557	—0,52991	—0,22616	—1,25576	1,91115	—5,06981	10
11	—0,38695	—0,62341	—0,52420	—0,53130	—0,52215	—0,49700	—0,56505	—0,24223	—1,33426	2,03129	—5,39607	11
12	—1,64453	—0,41600	—0,65167	—0,55391	—0,56406	—0,53061	—0,60139	—0,26016	—1,41643	2,15015	—5,71810	12
13	1,58612	—1,67402	—0,44460	—0,68186	—0,58711	—0,57154	—0,64132	—0,27630	—1,49798	2,26768	—6,04370	13
14	0,32789	1,55634	—1,70308	—0,47467	—0,71500	—0,59248	—0,68656	—0,29523	—1,58223	2,38566	—6,36910	14
15	0,53529	0,29854	1,52791	—1,73236	—0,50748	—0,71888	—0,71160	—0,32115	—1,66596	2,50596	—6,70433	15
16	0,40790	0,50592	0,27010	1,49859	—1,76582	—0,51004	—0,84353	—0,32678	—1,76210	2,63326	—7,04974	16
17	0,38532	0,37840	0,47730	0,24064	1,46495	—1,76713	—0,63923	—0,43931	—1,83073	2,73950	—7,37643	17
18	0,34351	0,35601	0,35006	0,44821	0,20708	1,46520	—1,89966	—0,21520	—2,00995	2,88468	—7,73965	18
19	0,30769	0,31285	0,32624	0,31949	0,41281	0,20719	1,32483	—1,45582	—1,86526	2,92211	—8,07957	19
20	0,27526	0,27873	0,28482	0,29757	0,28573	0,41671	0,06416	1,79137	—3,16824	3,28880	—8,52411	20
21	0,24210	0,24550	0,25014	0,25575	0,26264	0,29219	0,26197	0,57312	—0,06060	2,30046	—8,77020	21
22	0,20897	0,21185	0,21505	0,22017	0,21742	0,27294	0,10889	0,86065	—1,60710	6,10955	—10,43411	22
i / k	13	14	15	16	17	18	19	20	21	22	23	i / k

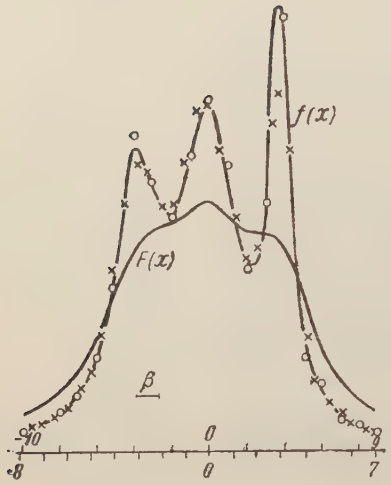

Fig.2

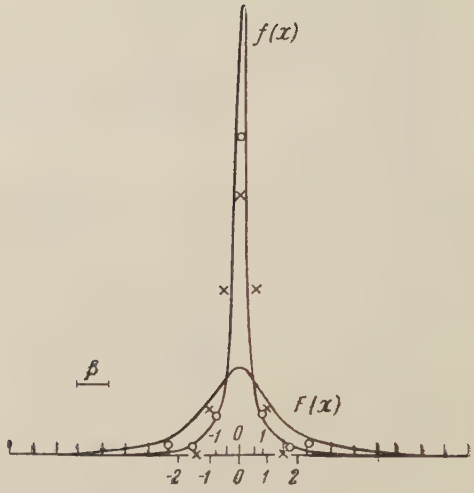

Fig.3

Fig.2. An example of the use of both methods of correcting an experimental curve: $f(x)$ is the true curve, $F(x)$ is the distorted curve. Points obtained by the matrix method are denoted by circles; points obtained by the column method are denoted by crosses.

Fig.3. Another example of correction by the two methods being compared. Designations are the same as in Fig.2.

Conclusions

1. It makes no sense, in any correction method, to try to use information concerning experimental points separated by less than 0.6-0.7 β.

2. Both methods satisfactorily correct emission curves without abrupt rises and drops. It is impossible, however, to avoid errors due to the way the curves are approximated outside the correction interval.

3. The error of the approximation is easily evaluated in the matrix method. In the column method this evaluation is impossible due to uncertainty in the choic of the height of the approximating semi-infinite step functions.

4. Sections of spectra close to abrupt changes are poorly approximated in both methods.[1,2]

5. Experiment shows that the time needed to correct an experimental curve of width 10.5 πβ is 3-4 hours when using the matrix method, and 30-35 hours in using the column method.

"V.I.Lenin" Kharkov Polytechnic Institute

References

1. M.A.Blokhin, Metody rentgenospektral'nykh issledovanie (Methods of x-ray spectroscopic investigations), M., 1959.

2. Ya.E.Genkin & I.A.Rumyantsev, Izv.AN SSSR, Ser.fiz., 24, 384 (1960). (Trans.Bulletin, 24, 398.)

CORRECTED $L\beta_2$ EMISSION BAND IN THE SPECTRA OF PURE NIOBIUM AND ITS COMPOUNDS

- M.I.Korsunskii & Ya.E.Genkin

The present authors have described elsewhere[1,2] investigations of the fluorescent L-series spectra of pure niobium and niobium in the Nb-N system. According to measurements of Brauer[3], specimens containing 6.32 and 6.8% nitrogen by weight belong in the region of the homogeneous β phase, characterized by the formula Nb_2N; specimens with 8.1% N lie in the region of the β + γ phase; those with 11.9% nitrogen in the region of the γ + ε phase; those with 13% nitrogen (stoichiometric NbN) consist of the ε phase.

Significant changes in the character of the $L\beta_2$ and $L\gamma_1$ emission bands were observed in the spectra of these compounds (as compared to pure Nb). The other L lines showed no noticeable shifts and little change in relative intensity.

We arrived at the conclusion that the disappearance of some parts of the emission bands in these compounds indicates that the relative density of occupied d states is not constant, and changes in different ways in going to different compounds. In order to clarify the character of the alterations in the $L\beta_2$ band, we undertook a correction of this band for the width of the internal L_{III} level and the apparatus distortion. We assume the L_{III} level to have the classical dispersion (Lorentzian) shape with a half-width equal to 1.04 ev.[4] The shape of the apparatus distortion was checked by observing the Kα line of Mo in the seventh order[5] and the $L\beta_1$ line of Ag in the first and second orders.[6] These lines had the classical dispersion shape within the limits of our measurement error. The apparatus broadening deduced from these measurements was 0.58 ev for a Bragg angle of ~38°, at which the $L\beta_2$ bands of niobium were recorded.

From the fact that the substances in question have a relatively high conductivity and become superconductors at low temperatures, one may conclude that the $L\beta_1$ emission band should have a sharp edge (Fermi level). This is substantiated by the data on the distortion parameter β for the short-wavelength side of the $L\beta_2$ band.

In all cases β was found to equal, within limits of experimental error, the sum of the half-width of the internal L_{III} level and the apparatus half-width. As indicated in Ref.7, this is a good criterion for the existence of the Fermi level. The same paper defines β and describes the method by which the Fermi level is found. Further calculations were performed with the aid of a 20-by-20 matrix which was applied to the experimental curve using intervals of width $\pi\beta/4$.[8] The distortion parameter was taken equal to 1.33 ev. In using this matrix, however, true values are not obtained for points close to the limit (edge) because of the poor approximation resulting for regions of abrupt rise and fall. We therefore corrected the $L\beta_2$ band using the special matrix "with abrupt drop", which will give reliable corrections close to the limit. This matrix can be used only after the Fermi level has been determined and the spectrogram has been processed by any of the "conventional" correction methods[8-10].

In constructing the matrix "with abrupt drop" we based our procedure on the following considerations. The ordinate of the experimental curve at the i-th point is given by

$$F_i = \sum_{k=1}^{n} a_{ik} f_k, \qquad (1)$$

where the a_{ik} are the elements of the $\|a_{ik}\|$ correction matrix and f_k is the ordinate of the true curve at the k-th point. It should be borne in mind that f_n is the ordinate at the limit, and that $f_k = 0$ for $k > n$.

Thus in any one of the correction methods the information about the experimental curve must be obtained from points an integral number of subdivision inter-

vals distant from the limit. We chose these points at distances which were multiples of $\pi\beta/4$ from the limit point. After using the 20-by-20 matrix, we assumed the ordinates f_k for $k \leqslant n-4$ to have their correct values. Then

$$\Delta F_{n-s} = \sum_{k=n-3}^{n} a_{n-s,k} f_k, \quad \text{where} \quad s = 3, 2, 1, 0, \tag{2}$$

and

$$\Delta F_{n-s} = F_{n-s} - \sum_{k=1}^{n-4} a_{n-s,k} f_k \equiv F_{n-s} - F'_{n-s}. \tag{3}$$

The F'_{n-s} are obtained from the $\| a_{ik} \|$ matrix. After this, the ΔF_{n-s} are determined from the experimental curve. From the set of linear equations (2) it follows that

$$f_{n-s} = \sum_{k=n-s}^{n} b_{n-s,k} \Delta F_k, \tag{4}$$

where b_{ik} are the elements of the inverse matrix $\| b_{ik} \|$ of linear transformation (2).

For a subdivision interval equal to $\pi\beta/2$, this matrix is

$$\begin{array}{rrrr} 9.14527 & -8.53313 & 4.23426 & -1.99158 \\ -8.58090 & 17.24132 & -12.94146 & 5.69902 \\ 4.39040 & -13.07057 & 20.96031 & -13.24616 \\ -3.55158 & 9.59240 & -21.75649 & 23.97369, \end{array} \tag{5}$$

so that, for instance,

$$f_{n-2} = -8.58090\, \Delta F_{n-3} + 17.24132\, \Delta F_{n-2} - 12.94146 \times \Delta F_{n-1} + 5.69902 \cdot \Delta F_n.$$

For subdivision at intervals equal to $\pi\beta/2$, the matrix "with abrupt drop" is

$$\begin{array}{rrrr} 3.2716 & -1.6292 & 0.4040 & -0.2209 \\ -1.6330 & 4.1007 & -1.9416 & 0.6816 \\ 0.4062 & -1.9018 & 4.5964 & -0.6910 \\ -0.3081 & 0.8222 & -3.6817 & 7.4282 \end{array} \tag{6}$$

The results of the calculations performed as described above for the $L\beta_2$ band in the emission spectra of pure niobium and niobium nitrides are shown in the figure. The differences between the corrected and experimental spectrum are clearly discernible. The corrected spectra show more clearly the two parts of the band arising either from the redistribution of the d level densities or the altered symmetry of the ψ function, which is equivalent to altered transition probabilities to the collective band. From the corrected spectrum one can determine more accurately the width of the filled part of the band, which requires finding the limit of occupation on the long wavelength side. Such determination by the method described in Ref.7 is impossible, since the distortion parameter on the long wavelength side may be significantly larger due to nonradiative transitions within the collective band itself. Nevertheless, the results of the above described calculations indicate that incident to formation of niobium nitrides the collective band is broadened, the Fermi level shifts to higher energies as the nitrogen concentration is increased. The magnitudes of this shift for different concentrations of nitrogen by weight are (in ev)

6.32%	6.8%	8.1%	11.9%	13.1%
0.5	1.1	1.8	1.9	2.1

Thus, using niobium-nitrogen as an example, we have shown that one cannot arrive at definitive inferences regarding the degree of filling of the valence or conduction band without first correcting the experimental curves. This observation undoubtedly applies to absorption spectra as well.

Our study of the $L\beta_2$ band of niobium leads us to assert that in the formation of the nitrides the nitrogen atoms are to a certain extent "metalized", by which

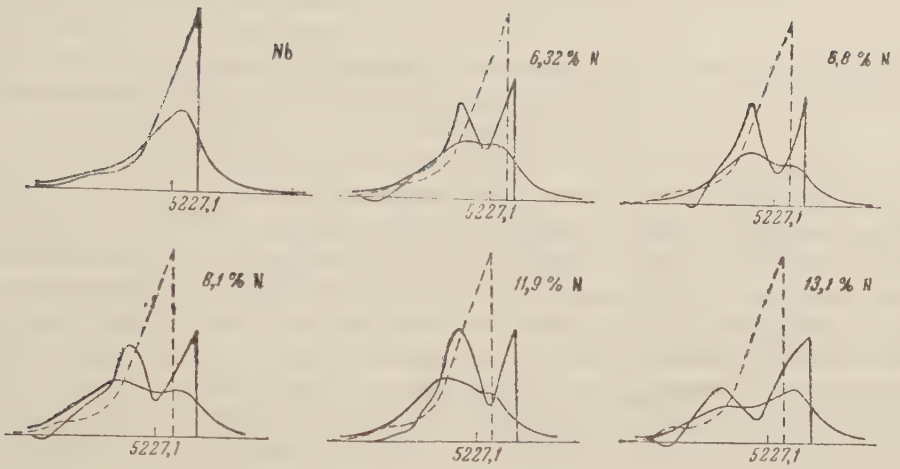

Results of correcting of the experimental $L\beta_2$ band in the emission spectra of pure niobium and niobium nitrides.

we mean that the nitrogen atoms give up some of their electrons to the "collective system."[11,12]

References

1. M.I.Korsunskii & Ya.E.Genkin, Izv.AN SSSR, Ser.fiz., 24, 461 (1960). (Trans.Bulletin, 24, 467.)

2. M.I.Korsunskii & Ya.E.Genkin, Ibid., 24, 470 (1960). (Trans.Ibid., 24, 475.)

3. G.Brauer, Conference on Niobium, Tantalum, Molybdenum and Tungsten, Sheffield Univ., Sept.1960.

4. M.A.Blokhin, Metody rentgeno-spektral'nykh issledovanii (Methods of x-ray spectroscopi investigation), p.370, M., 1959.

5. L.G.Parratt, Phys.Rev., 50, 1 (1936).

6. L.G.Parratt, Phys.Rev., 54, 99 (1938).

7. M.I.Korsunskii & Ya.E.Genkin, Present issue of the Bulletin, p.1036.

8. Ya.E.Genkin & I.A.Rumyantsev, Present issue of the Bulletin, p.1023.

9. M.A.Blokhin, Metody rentgeno-spektral'nykh issledovanii (Methods of x-ray spectroscpic investigation), p.238, M., 1959.

10. Ya.E.Genkin & I.A.Rumyantsev, Izv.AN SSSR, Ser.fiz., 24, 384 (1960). (Trans.Bulletin, 24, 398.)

11. A.R.Ubbelohde, Proc.Roy.Soc., A159, 295 (1937).

12. Ya.S.Umanskii, B.N.Finkel'shtein & M.E.Blanter, Fizicheskie osnovy metallovedeniya (Physical fundamentals of metallography), M.1949.

ON DETERMINING THE FERMI LEVEL FROM X-RAY EMISSION BANDS

- M.I.Korsunskii & Ya.E.Genkin

Investigation of emission spectra provides a means for determining the density $N(E)$ of filled electron states by solving the integral equation

$$I_q(E_0) \sim \int_{-\infty}^{\infty} N(E) W_q(E_0 - E)\, dE, \tag{1}$$

where $I_q(E_0)$ is the spectral intensity, $W_q(E_0 - E)$ is the probability that an atom excited to an internal level q will have an energy in the interval E_0 to $E_0 + dE$.

If we assume that the shape of the internal levels may be characterized by a classical (Lorentzian) dispersion curve with half-width β_q, then in the case of dispersion apparatus distortions with a half-width β_a, the density of the filled electron states may be found from the integral equation[1]:

$$I_q(E_0) \sim \frac{1}{\pi(\beta_q + \beta_a)} \int_{-\infty}^{\infty} N(E) \frac{dE}{1 + \left(\frac{E_0 - E}{\beta_q + \beta_a}\right)^2}. \tag{2}$$

In considering emission bands it should be borne in mind that the function under the integral vanishes only in a certain energy interval, the extent of which is equal to the width a of the filled part of the outer energy band.* Then

$$I_q(E_0) \equiv \alpha F(z), \tag{3}$$

where

$$F(z) = \frac{1}{\pi\beta} \int_{-a}^{0} \frac{f(x)\, dx}{1 + \left(\frac{z - x}{\beta}\right)^2} \tag{4}$$

here α is a proportionality constant, $\beta = \beta_q + \beta_a$ and $f(x) \equiv N(E)$. At present there have been developed several methods for finding the function $f(x)$ from the known experimental intensity curve $F(z)$ in a limited section of the spectrum.[1-6]

In general, solution of Eq.(2) with respect to $f(x)$ over the entire axis is possible only with an accuracy to first order terms. Hence to obtain a single solution one must impose certain conditions on the functions $f(x)$ and $F(z)$.

Such a condition may be

$$\int_{-\infty}^{\infty} f(x)\, dx = \int_{-\infty}^{\infty} F(z)\, dz < A, \tag{5}$$

where $A = \text{const}$.

In the most general case the solution will be of the form

$$f = \check{B}F, \tag{6}$$

where $\check{B}$ is an operator containing known parameters of the distortion β, and F is an experimental function known over the entire axis. Inasmuch as in any actual case the function F is known only over a limited section of the spectrum and is always measured with some uncertainty, no precise solution exists. Nevertheless, reasonable approximation of the function f or F beyond the limits of the section of correction (for example, taking into account (5)) narrows the number of solutions, which are grouped close to the true shape of the distribution.

However, in the above mentioned methods of correction it is impossible to use continuous information on the function F; only the values of this function

---

*In this treatment we neglect the width of each of the levels forming the band.

at a limited number of points are used. This leads to different solutions depending on the selection of the points along the experimental curve. Increase in the number of experimental points used in the mathematical formalism leads to an appreciable increase of the coefficients of operator $\check{B}$, and this can lead to the awkward situation where the resultant "corrected" curve will differ from the true curve to a greater extent than the curve being corrected.

Particularly great divergences from the true solution are observed in the case of "cut-off" curves, in particular, in the case of the presence of the Fermi level (brim). In such cases there appear in the corrected curve "dips" and a high "hump" located to different sides of the cut-off. Such "dips" and "humps" are observed only in the case of abruptly varying curves. This criterion enables us to establish the position of the Fermi level with an accuracy to within the distortion parameter β. Use in the correction of an inaccurate value of β increases the error in determining the position of the Fermi level. Inasmuch as knowledge of the location of the Fermi level helps elucidate many properties of the material under investigation, enhancement of the accuracy in determining the level energy is important.

In the present contribution we propose a method for determining the position of the Fermi level and refining the value of the distortion parameter β in the region of the level, based on the properties of the function $\varphi(z) = \left|\frac{2F(z)}{F'(2)}\right|$, obtained by plotting the subtangents to the experimental curve.

Method of Determining the Fermi Level

At temperatures above absolute zero, the Fermi brim is not sharp. The "smearing out" in the electron distribution has a width $\sim kT$, and for temperatures at which spectra are commonly recorded this value is appreciably smaller than the sum of the apparatus distortion and the width of the internal level. Hence, hereinafter we approximate the true curve close to the Fermi level by a vertical drop at the level.

To clarify the fundamentals of the proposed method for determining the Fermi level let us consider the properties of the function $\varphi(z)$.

Differentiating (4) and utilizing the mean value theorem, we obtain

$$\varphi(z) = \left|\frac{\beta^2 + (z - x_{av})^2}{z - x_{av}}\right|, \tag{7}$$

where x_{av} depends on $f(z)$ and z and lies in the interval $0 \geqslant x_{av} \geqslant -a$. It follows from Eq.(7) that regardless of the course of $f(x)$ within the limits of the interval a, the function $\varphi(z)$ will have not less than two minima located at points satisfying the equation

$$(z_{min} - x_{av})^2 - \beta^2 = 0). \tag{8}$$

From Eq.(8) it follows that

$$z_{1min} \leqslant \beta \quad \text{and} \quad z_{2min} \geqslant -(\beta + a), \tag{9}$$

i.e., the minima of the function $\varphi(z)$ do not extend outside the boundaries of the interval a by more than the magnitude of the distortion parameter β for any width of filling of the last energy band.

Let us see how the position of the minimum of $\varphi(z)$ changes with change in

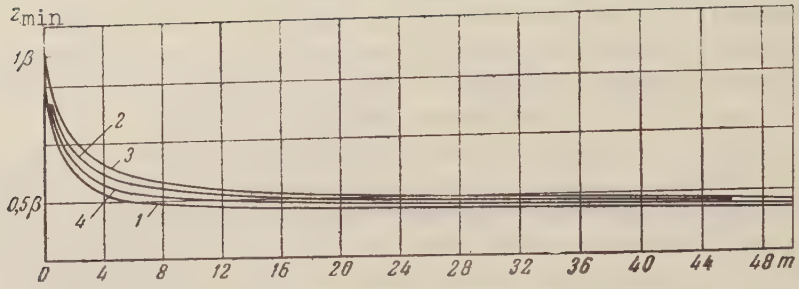

Fig.1.

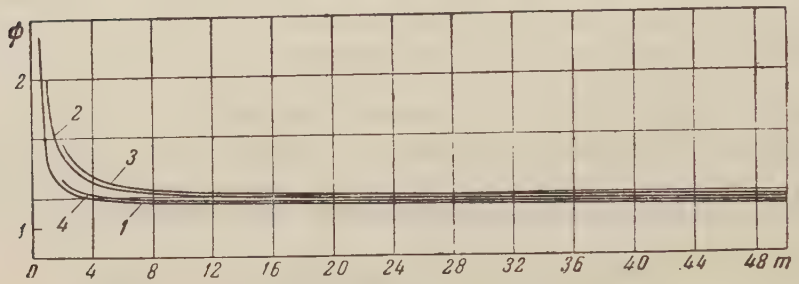

Fig.2.

the interval a for some forms of the function $f(x)$. We restrict our consideration to cases of filling of the last energy band in the form of a rectangle or triangle with a sharp cut-off (edge) on the high energy side.

Fig.1 shows a series of curves illustrating the dependence of the position of the minimum on the width of the filled band. Curve 1 pertains to filling of the rectangular type: $f(x) = c$ in the interval $0 \geqslant x \geqslant -m\beta$, where $m = a/\beta$, and $f(x) = 0$ outside this interval; curve 2 pertains to filling of the triangular type: $f(x) = \frac{c}{m\beta}(x + m\beta)$ in the interval $0 \geqslant x \geqslant -m\beta$ and $f(x) = 0$ outside this interval. It will be evident from the appearance of these curves that the position of the minimum of $\varphi(z)$ changes little even with $m \geqslant 5$; the value of z_{min} may be taken equal to 0.5 β with an accuracy to within 0.05 β. From this it may be inferred that in the case when the density of states is characterized by a function of any form contained between a triangle of width $m = 5$ and a semiinfinite rectangle, $z_{min} \approx 0.5\ \beta$.

Thus, if the half-width of the dispersion distortion is known, then from the determined position of the minimum one can establish the location of the Fermi level.

One can, however, determine the position of the Fermi level even when the value of the distortion parameter β is unknown. To this end let us determine the values of $\varphi(z_{min})$ and $\varphi(0)$ for the above mentioned approximate shapes of the emission bands.

Fig.2 shows a family of curves representing $\frac{\varphi(0)}{\varphi(z_{min})} \equiv \psi(m)$. It will be evident from these curves that for emission bands of the indicated type the function $\psi(m)$ varies little and equals approximately 1.2.

In view of this one can employ the following method for determining the Fermi level:

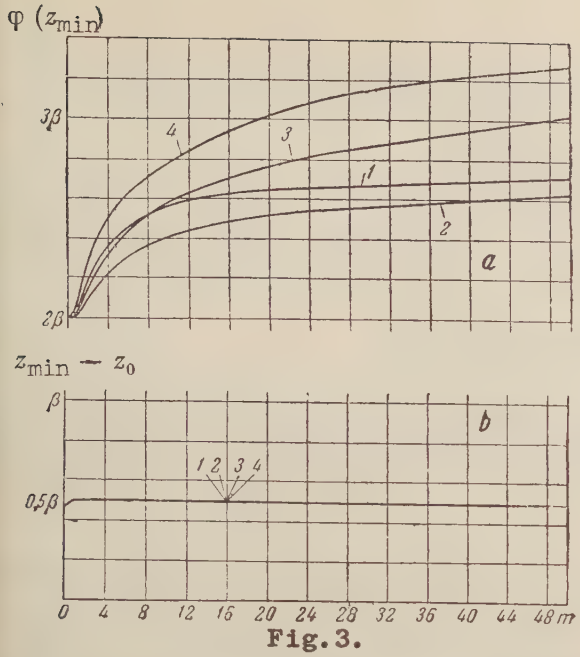

Fig.3.

1) plot the $\varphi(z)$ curve in the region of the Fermi limit and determine $\varphi(z_{min})$;

2) multiply the value of $\varphi(z_{min})$ determined in this manner by 1.2;

3) determine the abscissae at which $\varphi(z)$ has the value 1.2 $\varphi(z_{min})$. There are two such abscissae. The one nearest to the spectrum represents the Fermi level:

$$\varphi(z_0) = 1.2\,\varphi(z_{min}). \qquad (10)$$

The position of the Fermi level $z = z_0$ determined in this manner differs from its true position $z = 0$; however, for a width $m \geqslant 5$ this difference does not exceed 0.1 β.

As noted above the position of z_{min} and also of z_0 changes relatively little with variation of a; moreover, their difference $z_{min} - z_0$ is even less sensitive to variation of a.

Fig.3 a shows the variation of $\varphi(z_{min})$ with the filling width: curve 1 is for filling of the rectangular type; curve 2 for filling of the triangular type.

Fig.3 b shows the variation of $z_{min} - z_0$ for the two types of filling of the energy bands. Curves 1 and 2 for triangular and rectangular filling, respectively, virtually coincide and within the accuracy of the calculations (0.01 β) do not depend on the filling width. For $m \geqslant 2$

$$z_{min} - z_0 = \beta/2. \qquad (11)$$

From this we derive a method for determining the distortion parameter: β is equal to twice the difference $z_{min} - z_0$.

Case when β is not Constant

In the above treatment the width of the levels forming the energy band was not taken into account. Actually, however, owing to nonradiative transitions inside the band these levels may have a substantial width and may vary over the band.

It is obviously of interest to consider the question on how z_{min}, $\varphi(z_{min})$, $\psi(m)$ and $z_{min} - z_0$ change in the case of variation of β.

Let us consider the case when β varies linearly over the band (i.e., within the limits of the interval $0 \geqslant x \geqslant -m\beta_0$):

$$\beta(x) = \beta_0 - \frac{n}{m}x, \qquad (12)$$

where $n > 0$. Outside the band $\beta(x) = \beta_0$. Obviously, $n\beta_0 = \Delta\beta$ represents the magnitude of the variation of the distortion parameter over the band.

Curves 3 & 4 (curve 3 for triangular and curve 4 for rectangular filling) in Figs.1-3 represent the variation of z_{min}, $\varphi(z_{min})$, $\psi(m)$ and $z_{min} - z_0$ over the filled part of the energy band with $n = 0.1m$, i.e., under the condition that the width of the levels at the bottom of the energy band is equal to 0.2 the width a of the filled part of the band. Even with this very appreciable variation of the distortion parameter the location of the z_{min} $\varphi(z_{min})$ and $\psi(m)$ curves changes

relatively little as compared with the location in the case when β = const, while the $z_{min} - z_0$ curve does not change at all within the limits of the calculation accuracy (0.01 β), i.e., the value of $z_{min} - z_0$ with variable β determines the value of the distortion parameter at the Fermi level.

Further, from the data of Fig.2 it follows that although the function $\psi(m)$ does change with variation of the distortion parameter β, the change is insignificant, and the position of the Fermi level may be determined with an accuracy to within 0.1 β in the manner described above, i.e., by means of Eq.(10).

Comparison with Experimental Data

In order to check the above inferences we carried out determinations of the position of the Fermi level and the magnitude of the distortion parameter β from the intensity distribution curve (Fig.4) obtained by dispersion distortion with a parameter β for the density of states curve in the form of a trapezoid with width $a = 10\,\beta$.

As will be evident, the determined value of β agrees with the value of the distortion parameter, and the determined Fermi level is located at a distance of 0.02 β from the true position of the brim. In addition, we determined the position of the Fermi level and the distortion parameter β from the $L\beta_2$ emission band of niobium. Fig.5 shows the shape of the Nb $L\beta_2$ emission band and the function $\varphi(z)$; in this figure we also show the position of the Fermi level determined by means of Eq.(10). That this determination is essentially correct is substantiated by the following juxtaposition of the value of β determined from (11) and the known experimental data for the width of the internal level and the apparatus distortion:

	β_a	β_q	$\beta_a + \beta_q$	β
Nb L_{β_2}	0.29 ev	1.04 ev	1.33 ev	1.32 ev

Agreement of the value of β determined by the above procedure with the value of $\beta_a + \beta_q$ indicates the presence of the Fermi level. In order to illustrate this, using the above method, we determined the distortion parameters for the $L\beta_1$ and $L\alpha_2$ lines of niobium. In order to avoid the influence of the satellites of the $L\beta_1$ line and the effect of the $L\alpha_1$ line, the distortion parameters in each case were determined with reference to the long wavelength side of the line. There were obtained the following results:

	β_a, ev	β_q ev	$\beta_a + \beta_q$, ev	β, ev	$\beta - (\beta_a + \beta_q)$ ev
L_{β_1}	0.30	0.85	1.15	2.43	1.28
L_{α_2}	0.30	1.04	1.34	2.66	1.32

The fact that the calculated value of the distortion parameter β proved to be greater than the half-sum of the width of the internal level and the apparatus distortion indicates that in this case there is no band ($m \approx 0$) terminating with a sharp brim. Here the value of β includes the half-width of the internal and outer levels as well as the half-width of the apparatus dispersion distortion.

Inasmuch as the widths of the $L\beta_1$ and $L\alpha_2$ lines include the width of the outer M_{IV} level, it follows from the deduced value of the distortion parameter that the width ΔE of the M_{IV} level of Nb equals 2.6 ev.

Discussion

As will be evident from the above data, the values of the distortion parameter β obtained by the proposed procedure are in good agreement with the data

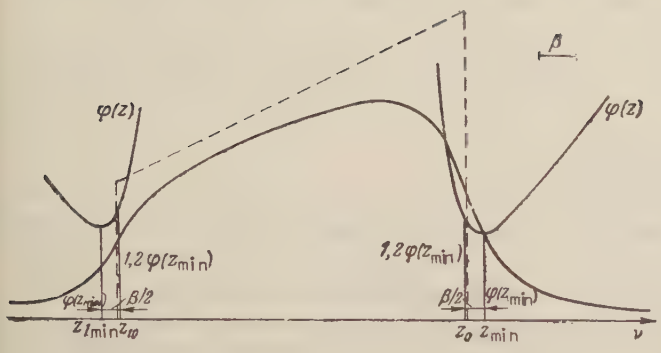

Fig.4

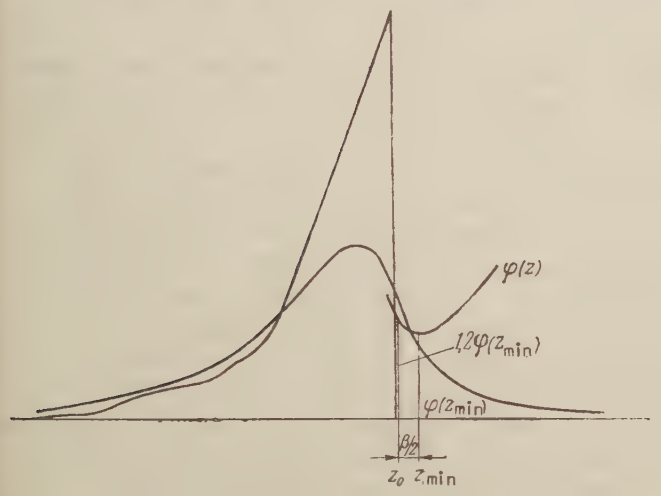

Fig.5

on the half-widths of the internal levels[1] and the apparatus distortion, determined experimentally with reference to classical dispersion emission lines. This shows that our determination of the distortion parameter by means of Eq.(1) is essentially correct, and so consequently is the determination of the Fermi level with the indicated uncertainty.

The described method of determining the Fermi level can be used as the first approximation. The position of the level can be determined with higher accuracy by using the relation

$$\varphi(0) = \psi(m)\varphi(z_{\min}), \qquad (13)$$

following from determination of the function $\psi(m)$.

The value of $\psi(m)$ is determined from Fig.2 in accord with the shape and width of the filled part of the energy band. It must be emphasized that in view of the weak dependence of $\psi(m)$ on a, in refining the position of the Fermi level there is no need to establish the precise value of the width of the filled part of the energy band and its shape: one need only know the approximate value of a and the form of the function $f(x)$. In the curve reproduced in Fig.4 the value of a was taken equal to 12 rather than 10.

Correct determination of the Fermi level makes it possible to use a special "matrix with cut-off" for re-establishing the true shape of the outer energy band.

It also appears feasible to develop the proposed method for determining the limit of the density of the filled states on the side of low energies and for determining the distortion parameter in the long wavelength part of the emission bands, which is very important for explaining the nature of long wavelength tails and determining the spectrum of electron states in different substances.

The above described method of determining the Fermi level and distortion parameter β is also applicable to absorption spectra. Where the width of the apparatus distortion is known, one can determine the width of the internal level of the investigated spectrum.

It should be noted that this method can be applied only when the intensity of the emission band is not distorted by reabsorption. Hence before attempting to determine the precise position of the Fermi level, one must either correct the emission band for self-absorption or measure the spectrum under experimental conditions that insure negligible self-absorption. (The Nb $L\beta_2$ emission band reproduced in Fig.5 is virtually free of distortion due to self-absorption.[7])

The presence of short wavelength satellites will naturally affect the accuracy in determining the Fermi level; hence where such satellites occur they should be subtracted from the emission band curve beforehand.

Chair of General & Experimental Physics,
"V.I.Lenin" Kharkov Polytechnic Institute

References

1. M.A.Blokhin, Metody rentgenospektral'nykh issledovanii (Methods of X-ray Spectroscopic Investigation), M., 1959.
2. M.A.Blokhin, Doklady AN SSSR, 107, 33 (1956). (Trans.Doklady.)
3. M.A.Blokhin, Ibid., 107, 229 (Trans.Doklady.)
4. M.A.Blokhin, Izv.AN SSSR, Ser.fiz., 20, 142 (1956). (Trans.Bulletin, 20, 127.)
5. I.Ya.Nikiforov, Ibid., 21, 1362 (1957). (Trans.Bulletin, 24, 1351.)
6. Y.E.Genkin & I.A.Rumyantsev, Ibid., 24, 384 (1960). (Trans.Ibid., 24, 398.)
7. M.I.Korsunskii & Ya.E.Genkin, Ibid., 24, 470 (1960). (Trans.Ibid., 24, 475.)

ON FINDING THE TRUE SHAPE OF SPECTRA USING THE SHANNON APPROXIMATION

- V.P.Sachenko

To find the true shape of spectra, as well as to solve many other problems in different fields of physics and information theory, one must solve the integral equation of the convolution type

$$F(x) = \int_{-\infty}^{+\infty} f(t)\,\varphi(x-t)\,dt, \tag{1}$$

where $F(x)$ is the experimentally observed shape of the spectrum, $f(x)$ is its true shape, and $\varphi(x)$ is the distortion function. Difficulties arising in solution of (1) are related to the fact that in reality $F(x)$ is always given either graphically or in tabular form and always with some (experimental) uncertainty. There exist many approximation methods for solving this equation (see Rautian's review article[1]), differing as regards the way in which $F(x)$ is approximated. None of these methods, however, can be used to find which is the best approximation for $f(x)$, whose existence follows from the instability of the solution of (1) with respect to experimental error. Further, it is not clear which of the methods is best from the point of view of the time expended and the accuracy of the results obtained. In this paper we propose a new method for solving (1), a method which may be used to answer these questions.

We assume that the values of $F(x)$ are given at a set of discrete, equally spaced points with a separation interval d. We shall call these the given points. The set of values of $F(x)$ at these points represents the entire information on $F(x)$ obtained from the experiment. Therefore any approximation of $F(x)$ which reproduces or approximates sufficiently well its values at the given points is as good as any other in solving (1). From this point of view, no particular method of solution has an advantage over any other, but from the standpoint of the amount of work involved the simplest will be those approximations whose parameters are the values of $F(x)$ at the given points. Examples of such methods may be found in the literature[2,3] and may be contrasted with more complicated ones.[4]

Applying the convolution theorem to (1), we obtain

$$\widetilde{F}(t) = \widetilde{f}(t)\,\widetilde{\varphi}(t), \tag{2}$$

where $\widetilde{F}(t)$, $\widetilde{f}(t)$ and $\widetilde{\varphi}(t)$ are Fourier transforms of the corresponding functions.

Ordinarily $\varphi(x)$ has either a limited spectrum of frequencies (as in the case of $\frac{\sin x}{x}$), or $\widetilde{\varphi}(t)$ decreases with increasing frequency so rapidly that one can introduce a certain maximum frequency (as, for instance, for the case of classical dispersion and Gaussian curves, for which $\widetilde{\varphi}(t)$ decreases as e^{-t} and e^{-t^2}, respectively). Further, even if $f(x)$ has discontinuities or δ function singularities, its spectrum will in any case not increase with increasing t. It therefore follows from (2) that the spectrum of $F(x)$ will decrease with t no less rapidly than does $\widetilde{\varphi}(t)$, so that it will be essentially different from zero only in a certain bounded frequency region. The approximation for $F(x)$ will be the better, the more nearly the spectra of the approximating expression and of $F(x)$ coincide. On the basis of these considerations, let us choose the approximating function $F^*(x)$ (henceforth the asterisk will denote the approximating expressions) in the form

$$F^*(x) = \sum_n F(nd)\,\frac{\sin\omega(x-nd)}{\omega(x-nd)}, \tag{3}$$

where n is an integer and $\omega = \pi/d$.

Equation (3) represents an approximation satisfying the above-mentioned conditions. In particular, the spectrum of $F^*(x)$ is bounded by the frequency ω:

$$\tilde{F}^*(t) = \frac{\pi}{\omega} \sum_n F(nd) \exp(intd)\, \theta(t/\omega), \tag{4}$$

where

$$\theta(x) = \begin{cases} 1 \text{ for } |x| < 1 \\ 0 \text{ for } |x| > 1 \end{cases}.$$

The sum in (3) contains a finite number of terms if there is a finite number of given points, and an infinite number of terms if the number of given points is infinite. Therefore the present approximation is not restricted by the assumption that the section over which $F(x)$ is given is finite. With increasing ω, i.e., with increasing density of the given points, the information on $F(x)$ also increases. Therefore ω determines the information density, and the total information given is obtained from the product of ω and the magnitude of the section containing the given points.

Inserting (4) into (2), we obtain

$$\tilde{f}^*(t) = \frac{\pi}{\omega} \frac{1}{\tilde{\varphi}(t)} \sum_n F(nd)\, e^{indt} \theta(t/\omega), \tag{5}$$

whence

$$f^*(x) = \frac{1}{2\omega} \sum_n F(nd) \int_{-\infty}^{+\infty} \frac{e^{i(nd-x)t}}{\tilde{\varphi}(t)} \theta(t/\omega)\, dt. \tag{6}$$

The θ function in the integrand makes the integral converge for finite ω. The frequency spectrum of $f^*(x)$ as given by (5) is bounded by the same maximum frequency ω as is the spectrum of $F^*(x)$. This is quite natural, since ω determines the amount of information we have on $F(x)$, which cannot be increased by mathematical operations. From this point of view $F(x)$ represents the information contained in $f(x)$, encoded according to Eq.(1). Solving Eq.(1) then corresponds to deciphering of the code.

Let us consider some examples.

1. Let $\varphi(x)$ be

$$\varphi(x) = \frac{1}{\pi} \frac{\sin x}{x}; \tag{7}$$

then

$$\tilde{\varphi}(t) = \begin{cases} 1 \text{ for } t < 1 \\ 0 \text{ for } t > 1, \end{cases} \tag{8}$$

and Eq.(2) can be fulfilled only for $\omega \leqslant 1$. In this case (6) leads to

$$f^*(x) = \sum_n F(nd) \frac{\sin \omega(x - nd)}{\omega(x - nd)} = F^*(x).$$

If, therefore, the distortion function is given by (7), "correction" of $F(x)$ is a meaningless procedure.

These results can be understood quite simply. Because of the particular characteristics of $\tilde{\varphi}(t)$ as given by (8), all frequencies greater than 1 are cut off in the spectrum of $F(x)$. The information contained in $f(x)$ for frequencies greater than 1 is irrevocably lost. Once $\omega = 1$ further increase of ω does not increase the information about $F(x)$ and therefore also about $f(x)$, since in this case $F(x)$ is completely defined at any point by its values at the given points.

Thus if the spectrum is obtained by means of an instrument with a distortion function given by (7), the optimum separation d between the given points is π.

2. Consider the case in which

$$\varphi(x) = \frac{1}{\pi}\frac{1}{1+x^2} \tag{9}$$

and

$$\varphi(t) = e^{-|t|}.$$

Inserting this into (6) and integrating, one obtains

$$f^*(x) = \frac{1}{\omega}\sum_n F(nd)\left\{\frac{e^{\omega}[\cos\omega(x-nd)+(x-nd)\sin\omega(x-nd)]-1}{1+(x-nd)^2}\right\}.$$

Let us attempt to find $f^*(x)$ at the given points md. Without loss of generality one may set $m = 0$. Then

$$f^*(0) = \frac{1}{\omega}\sum_n F(nd)\frac{(-1)^n e^{\omega}-1}{1+n^2d^2}$$

or

$$f^*(0) = \frac{1}{\omega}\left\{F(0)(e^{\omega}-1) + \sum_{n=1}^{\infty}[F(nd)+F(-nd)]\frac{(-1)^n e^{\omega}-1}{1+n^2d^2}\right. . \tag{10}$$

Thus to find the values of f at the given points it is sufficient to know the set of numbers k_n given by

$$k_n = \frac{(-1)^n e^{\omega}-1}{\omega(1-n^2d^2)}. \tag{11}$$

n	k_n	n	k_n
0	+7,048	9	—0,094
1	—3,842	10	+0,070
2	+1,410	11	—0,063
3	—0,768	12	+0,049
4	+0,415	13	—0,045
5	—0,296	14	+0,036
6	+0,190	15	—0,034
7	—0,154	16	+0,027
8	+0,108		

Further calculations are carried through in complete analogy with the method of columns.[2] As is seen from (11), the k_n alternate in sign. This property makes it very easy to approximate the errors due to discarding terms with large n. If, however, the discarded terms are of the order of 2 to 5, better results are obtained by the method of Blokhin[2]. The accompanying table gives the values of k_n for $d = 1$ $(\omega = \pi)$.

3. Assume $\varphi(x)$ is a Gaussian. Calculations similar to the above will lead to k_n that can be used to solve Eq.(1). It need only be mentioned that in this case the k_n decreases much more rapidly than in the above case.

The method here described can be used to answer the question of which is the best approximation. For the special case of the method of columns this question is treated elsewhere.[5] Let us consider it in application to the dispersive distortion curve of Eq.(9). Since the spectrum of this function is unbounded, in distinction from case (1), no matter how large ω, its further increase will increase the information on $F(x)$ (assuming that the $f(x)$ spectrum is not limited) and would therefore seem expedient. This conclusion is valid, however, only if the ordinates of $F(x)$ can be measured with arbitrarily high accuracy. When this is not the case, the situation is substantially different. Let us assume for simplicity that the error in the $F^*(x)$ at the given points is the same in absolute value and equal to ε_c. We shall call this a chance error. Then the maximum change error A_c in the values obtained for $f^*(x)$ will be

$$A_c = \varepsilon_c \sum_n |k_n|.$$

In addition to this error, the $F^*(x)$ values will contain an additional error ε_a due to the approximation of (3). Let us call this the approximation error. Then the values of $f^*(x)$ will also have some approximation error A_a. As ω increases, the approximation error decreases, but the chance error A_c increases sharply. Therefore ω should have an optimum value ω_{opt} given by $\varepsilon_c = \varepsilon_a$. In order to estimate the error of approximation, one can use the asymptotic properties of the spectrum of $F(x)$. As has been shown above, the spectrum of $F(x)$ should decrease as ce^{-t}, where c is some constant. We may write the Fourier transform of the error function

$$\tilde{\varkappa}(t) = \tilde{F}(t) - \tilde{F}^*(t)$$

in the form

$$\tilde{\varkappa}(t) = \begin{cases} 0 & \text{for } |t| < \omega \\ ce^{-t} & \text{for } |t| > \omega. \end{cases}$$

Then

$$\varkappa(x) = \frac{c}{\pi} e^{-\omega} \left[\frac{\cos x\omega - x \sin x\omega}{1 + x^2} \right]$$

and the maximum approximation error will be given by

$$\varepsilon_a = \frac{c}{\pi} e^{-\omega},$$

from which we arrive at the conclusion that

$$\omega_{opt} = -\ln \frac{\pi}{c} \varepsilon_c. \qquad (12)$$

Equation (12) is valid for $f(x)$ containing discontinuities or δ function singularities. The constant c is the magnitude of the discontinuity or the factor multiplying the δ function. In this case, however, (12) is only locally valid in the neighborhood of the singularity. If $f(x)$ contains no discontinuities or δ function singularities the spectrum of $F(x)$ decreases much more rapidly than e^{-t} and the estimate given in (12) is far too high. In this case the optimum approximation can be found by trial and error. It is natural to suppose that the largest value of ε_a will be at the $x = nd/2$ points located midway in between the given points. To find the approximation error, one must calculate the value of the approximation function (3) at points located at a distance $\pm d/2$ from the points at which the $f^*(x)$ values are given. One may then say that the difference between the calculated and the known values of $F(x)$ at these points is ε_a. The approximation (or ω) should then be increased (or decreased) until ε_a becomes equal to ε_c. A more rigorous method for finding the optimum approximation involves using A_c. Let $f^*_{\omega_1}$ and $f^*_{\omega_2}$ denote the values of f obtained at a given point for two different values of ω, namely, ω_1 and ω_2, with $\omega_1 < \omega_2$. Then ω should be increased until

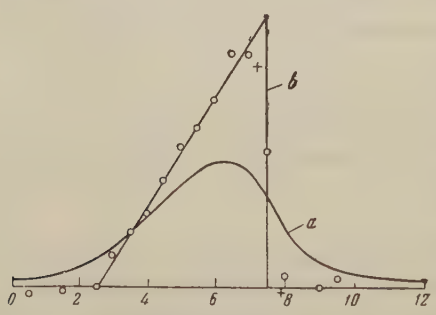

Reestablishment of a "smeared out" triangle.

$$|f^*_{\omega_2} - f^*_{\omega_1}| > |A_c(\omega_2) - A_c(\omega_1)|.$$

The above methods can be used to find the optimum approximation or to verify the reality of some hump or peak in the $f^*(x)$ curve after correction. It should be emphasized that all the above calculations are essentially local, and that the value of ω_{opt} they give will be different for different points.

Our method has been applied to a specific case, with the results shown in the figure. The curve b is $f(x)$ and curve a is $F(x)$; the distortion function $\varphi(x)$ is assumed to have the classical dispersion shape. The points give the values f^* for $d = 1$. The value of ε_c was 0.3 for the maximum ordinate of 150. At points 7 and 8 the approximation error ε_a was 0.9, which is considerably greater than ε_c. Therefore two points were calculated with $d = 0.7$ (denoted by crosses on the figure). As one may have expected, these points lie closer to the true $f(x)$ curve.

Rostov-on-the-Don State University

References

1. S.G.Rautian, Uspekhi fiz.nauk, 66, 475 (1958). (Trans.Soviet Physics - Uspekhi.)

2. M.A.Blokhin, Metody rentgeno-spektral'nykh issledovanii (Methods of x-ray spectrographic investigations.), M. 1959.

3. Ya.E.Genkin & I.Ya.Rumyantsev, Izv.AN SSSR, Ser.fiz., 24, 384 (1960). (Trans.Bulletin, 24, 398.)

4. M.A.Blokhin, Ibid., 20, 142 (1956). (Trans.Bulletin, 20, 147.)

5. M.Ya.Nikiforov, Ibid., 24, 380 (1960). (Trans.Bulletin, 24, 394.)

CONCERNING THE SHAPE OF THE $K\beta_5$ EMISSION BAND OF IRON. Part I.

- I.Ya.Nikiforov

One of the most complicated and least understood aspects of x-ray spectroscopy is the energy dependence of the transition probability in emission bands and at absorption edges. The first problem of x-ray spectroscopy is to explain the energy dependence $N(E)$ of the electron-state density in different substances. This function enters into the expression for the intensity of the emission band together with the matrix element $P(E,\mathrm{k})$ of the transition (usually called the transition probability):

$$I(E) \approx h\nu \int_S [P(E,\mathrm{k}) / \operatorname{grad} E]\, dS, \tag{1}$$

where the integration is taken over isoenergetic surfaces in reciprocal space. It is often assumed that one can use the directional average of $P(E,\mathrm{k})$ for a given energy, thus taking it out from under the integral sign. Then as a result there is obtained the product of $P(E)$ and

$$N(E) = \frac{v_a}{4\pi^3} \int_{(S)} \frac{dS}{\operatorname{grad} E},$$

$$I(E) \approx h\nu\, P(E)\, N(E). \tag{2}$$

To calculate $P(E)$ one must know the wave function Ψ of an electron in the conduction band of the crystal. It is known from group theoretical considerations[1] that this function is completely specified by the reduced wave vector k and the number of the energy band. The transition probability for different values of k but for a single irreducible diagram will, of course, be the same. The wave function is usually calculated only for points in the reciprocal lattice with a high order of symmetry, since then the symmetry greatly simplifies the solution. There exist at present a number of methods for finding Ψ in the single-electron theory, among which one may mention the Wigner-Seitz-Slater method[2] (often called the cell method), which has been applied successfully to many elements (Ref.3-5) and compounds[6,7], the strong coupling method[8], the method of orthogonalized plane waves[9], and others.

The many results obtained by the cell method and their frequent use in the interpretation of x-ray spectra has led naturally to studies of $P(E)$ using wave functions calculated in this approximation. The probability of transition to an internal level is determined by the values of Ψ inside the atom, where the cell method gives the best approximation for Ψ. In the method of orthogonalized plane waves, on the other hand, this would not seem to be the case. As a result, this method leads to strange results, as for instance, a width of 1.2 eV for the conduction band of iron[10] instead of the experimentally determined 5 eV.

In the cell method one attempts to find the wave function in the form

$$\Psi = \sum_{m=-l}^{l} \sum_{l=0}^{\infty} a_{m,l} R_l(r,E)\, Y_{lm}\,, \tag{3}$$

where $Y_{l,m}$ is a spherical harmonic, and $R_l(r,E)$ is a radial function with l-fold symmetry. More accurately, the sum is taken over several functions which, in turn, are combinations of spherical harmonics and are called the lattice harmonics. The $a_{m,l}$ are found from the boundary conditions.

As has been shown elsewhere,[11] the transition probability in the cell method can be written as the product of two factors: the radial factor

$$P_1(E) = \left| \int_0^{r_{sph}} R_i(r)\, rR_l(r, E)\, r^2 dr \right|^2$$

and the factor $P_2(E) \approx \overline{a_l^2(E)}$, representing the fraction of electrons in an l state. Here $R_i(r)$ is the radial wave function of an electron on an inner shell, and l is the index of the harmonic whose symmetry corresponds to a dipole transition to the level with symmetry i.

The transition probability for x-ray emission bands has been studied for the case of a simple cubic lattice[12] and a face-centered cube,[13] for which $P_2(E)$ was obtained for the beginning of the K and the $L_{II,III}$ bands. The present paper is devoted to evaluating $P(E)$ in $K - V$ transitions for several directions in k space in a body-centered cubic lattice (Fig.1). We use standard notation[1,14] and the results obtained by Chodorow and Manning,[14] who used group theory to study the way the a_l coefficients, chosen to approximate Ψ to the 14th harmonic, vanish at points in k space possessing a high order of symmetry.

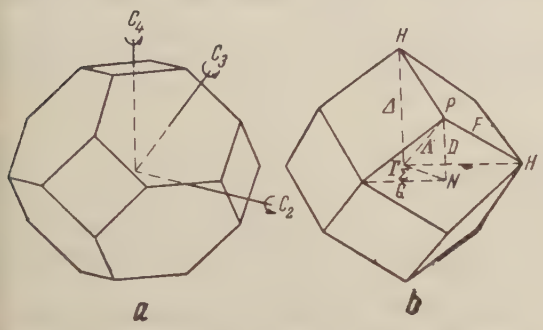

Fig.1. Symmetric unit (a) and reciprocal cells (b) of a body-centered lattice.

Sets of homogeneous equations for the a_l were obtained by using the boundary conditions in various directions in k space. When the determinants of these sets of equations are equated to zero, one obtains equations for the dispersion curves, and the a_l are found by using the additional normalization condition. To date we have considered only those representations which lead to vanishing of all coefficients except those multiplying the functions possessing p, d and f symmetries. These are Δ_2, $\Delta_5(2)$, and Δ_2 for the [001] direction, Σ_2, Σ_3 and Σ_4 for the [110] direction, and $\Lambda_3(2)$ for the [111] direction. One first determines the ratios a_p/a_d and a_f/a_d and then obtains the absolute values of the coefficients from the normalization condition.

For $\Delta_5(2)$, [001] we obtained

$$\frac{a_p}{a_d} = \frac{\sqrt{3}\, T d_1 f_2}{3p_1 f_2 + 2p_2 f_1} \frac{1}{\sqrt{5}}, \quad \frac{a_f}{a_p} = -\left(\frac{p_2}{2f_2}\right)\sqrt{\frac{7}{12}}, \tag{4}$$

where the indices 1 and 2 indicate that the value of the function (or its first derivative) is taken half-way between the nearest and next nearest neighbors, respectively (for instance, $p_2 = R_p(r_2)$, where $r_2 = a/2$), $T = \mathrm{tg}\,(ka/4)$, a is the lattice parameter, and $k = |\mathbf{k}|$.

For Σ_4, [110] the relations between the coefficients are of the same form as (4), except that in the first of them d_1 is replaced by d_2, f_2 by f_1, and $T = \mathrm{tg}\,(ka/2)$, where $k = \sqrt{2}\,|\mathbf{k}|/2$.

For the Σ_3 representation the wave function will be the sum of four lattice harmonics

$$(\Psi = a_p i\sqrt{3/4\pi}\, zp + a_d \sqrt{15/8\pi}\,(xz + yz)\, d + a_f i\sqrt{7/16\pi}\, z(5z^2 - 3)\, f + a_f' i\sqrt{105/4\pi}\, xyzf,$$

where x, y and z represent the direction cosines x/r, y/r and z/r, so that the number of relations is larger:

$$\frac{a_p}{a_d} = \frac{\sqrt{3}\, T d_1 f_2}{2p_1 f_2 + 3p_2 f_1} \frac{1}{\sqrt{5}}; \quad \frac{a_f}{a_p} = -\left(\frac{p_2}{2f_2}\right)\sqrt{\frac{7}{12}}; \quad \frac{a_f'}{a_p} = \frac{\sqrt{3}\, T d_1}{2f_1}\sqrt{35}, \tag{5}$$

where T and k have the same meaning as for Σ_4.

For Λ_2 there were obtained analogous, but more complicated expressions. In

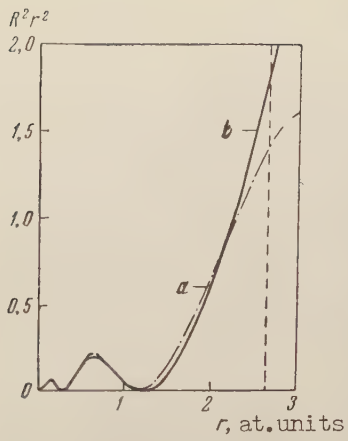

Fig.2. Normalized $R^2 r^2$ functions for the p electrons in the conduction band of iron for energy eigenvalues $\epsilon = 0$ (a) and $\epsilon = 0.6$ (b) (in Rydbergs).

this representation Ψ is a combination of eight functions

It is interesting that in all the cases we have studied a_p, the coefficient which determines the probability of ns—V transitions, increases as the function $p = R_p(r)$ and its derivative decrease at the boundary points, which are the centers of the faces of the atomic polyhedron (Fig.1a

The formulas obtained were used to calculate $P(E)$ for the $K\beta_5$ band in Fe. As the potential field of metallic iron we used the self-consistent field obtained by Manning[15] (which he used to calculate the density of electron states as a function of energy). The wave functions were calculated by solving the Schrödinger equation using Numerov's method of finite differences.[16] The equation was written in the form suggested by Hartree,[17] which is particularly convenient for numerical integration:

$$Y''_\rho(\rho) - [2rZ_p - \varepsilon r^2 - (l-0{,}5)^2]\, Y(\rho) = 0, \qquad (1$$

where $Y = Rr^{1/2}$, $\rho = \ln 1000\, r$, $\varepsilon = -E$ (in Rydbergs), and Z_p is the effective charge for the potential, as tabulated by Manning.[15]

For the initial values of $R_p(r)$ and $Rf(r)$ we use the hydrogen-like functions of Slater. As opposed to the d functions, described elsewhere,[11] which are highly energy dependent, the normalized p and f functions hardly depend on the energy (Fig.2). This is particularly true of the f function, as a result of the large value of $(l-0.5)^2 = 12.25$ in Eq. (6). It is clear that the higher harmonics will have a radial part virtually independent of the energy, which simplifies the otherwise rather difficult calculation at points where the symmetry is poorest.

The overlap factor $P_1(E)$ for the $K\beta_5$ band of Fe is found to be virtually energy independent as a result of the above mentioned property of the p function, whereas for the L_{III} band it changes by a factor of 2 from one end of the band to the other.[11]

The values and first derivatives of the radial functions for nine values of the energy (from 0 to 0.4), as obtained by graphic interpolation of the solution to (6), were used to calculate a_p^2 from formulas such as those of Eqs.(4) and (5) (normalized).

Fig.3 shows the results for three representations corresponding to different directions and subbands: III, IV — (Δ_5), V — (Σ_4) and VI — (Σ_3).[15] These subbands lie close to the Fermi limit and would seem to have the comparatively largest fraction of p electrons. Indeed, the deeper subbands (I and II) correspond most closely to the atomic d states, and are therefore occupied primarily by d electrons. As may be seen by studying Chodorow and Manning,[14] the II band contains only d electrons in the $\Delta(\Delta_2)$ and $\Sigma(\Sigma_2)$ representations (i.e., in the [110] direction). In all cases treated the energy dependence of a_p^2 is of roughly the same character; namely, a_p^2 increases up to the Fermi limit and then drops rapidly. The fraction of p electrons was found to be very low and to depend strongly on directi

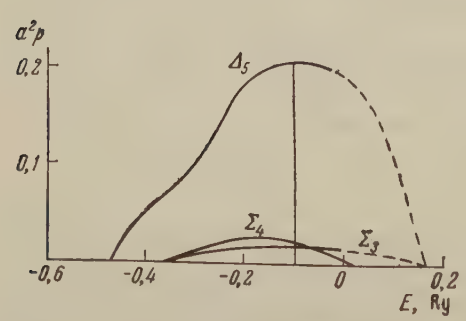

Fig.3. Probability of K→V transitions in the various directions in k space: Δ, [001]; Σ, [110]

In order to calculate the total probability $P(E)$ in the $K\beta_5$ band of Fe, one must know $a_p^2(E)$ for all the important directions and subbands. From the coefficients we have so far obtained (Fig.3), however, we may already assert that when $P(E)$ is properly allowed for, the theoretical $I(E) \approx P(E)N(E)$ curve will at least in general agree with experiment.[18]

In order to compare the theoretical and experimental shapes of the $K\beta_5$ band of Fe, one will have to allow for the smearing out of the theoretical curves due to nonradiative transitions within the band[19] and to correct the experimental curve for self-absorption and the broadening due to the finite thickness of the inner level and to instrumental distortions. This requires obtaining the experimental band with high accuracy and under well-defined conditions.

Rostov-on-the-Don State University

References

1. L.P.Bouckaert, R.Smoluchowski & E.Wigner, Phys.Rev., 50, 58 (1936).
2. J.C.Slater, Phys.Rev., 45, 794 (1934).
3. H.M.Krutter, Phys.Rev., 48, 664 (1935).
4. M.F.Manning & H.M.Krutter, Phys.Rev., 51, 761 (1937).
5. D.J.Howarth, Proc.Roy.Soc., 220A, 513 (1953).
6. W.Shockley, Phys.Rev., 50, 754 (1936).
7. D.G.Bell, D.M.Hum, L.Pincherle, D.W.Sciama & P.M.Woodward, Proc.Roy.Soc., 217A, 71 (1952).
8. G.C.Fletcher, Proc.Phys.Soc., A65, 192 (1952).
9. C.Herring, Phys.Rev., 57, 1169 (1940).
10. J.Callaway, Phys.Rev., 99, 500 (1955).
11. I.Ya.Nikiforov, Materialy vtoroi nauchnoi konferentsii aspirantov (Transactions of the 2nd Sci.Conf.of Graduate Students), Rostov Un.1960.
12. H.Jones, N.F.Mott & W.B.Skinner, Phys.Rev., 45, 379 (1934).
13. J.Farinaux, Ann.phys., 10, 20 (1938).
14. M.I.Chodorow & M.F.Manning, Phys.Rev., 52, 731 (1937).
15. M.F.Manning, Phys.Rev., 63, 190 (1943).
16. W.E.Milne, Numerical Solution of Differential Equations, N.Y., 1953.
17. D.R.Hartree & W.Hartree, Proc.Roy.Soc., A149, 210 (1935).
18. J.A.Bearden & C.H.Shaw, Phys.Rev., 48, 18 (1935).
19. M.A.Blokhin & V.P.Sachenko, Izv.AN SSSR, Ser.fiz., 24, 397 (1960). (Trans. Bulletin, 24, 410.)

ON THE "DERIVATIVE METHOD" FOR CORRECTING THE SHAPE OF SPECTRA

- V.P.Sachenko

The convolution type of equation

$$F(x) = \int_{-\infty}^{+\infty} f(t)\,\varphi(x-t)\,dt \tag{1}$$

is encountered in many fields of physics. For this reason much work (see Rautian review article[1]) has been devoted to numerical procedures for solving this equati In the present paper we suggest a new method for solving the equation, a method i which the solution is obtained as a series of derivatives of $F(x)$.

Let us write a solution of (1) in the form

$$f(x) = \int_{-\infty}^{+\infty} F(t)\,\psi(x-t)\,dt; \tag{2}$$

here $\psi(x)$ is a new function satisfying the equation

$$\delta(x) = \int_{-\infty}^{+\infty} \psi(t)\,\varphi(x-t)\,dt, \tag{3}$$

where $\delta(x)$ is the delta function. It follows from (3) that $\psi(x)$ is a generalized function.

Applying the convolution theorem to (3), we obtain (the tilda denotes the Fourier transform):

$$\sqrt{2\pi}\,\widetilde{\varphi}(t)\,\widetilde{\psi}(t) = 1. \tag{4}$$

Then $\psi(x)$ is obtained from (4) by taking the inverse Fourier transform

$$\psi(x) = \frac{1}{(2\pi)^{3/2}} \int_{-\infty}^{+\infty} \frac{1}{\widetilde{\varphi}(t)}\, e^{-ixt}\,dt. \tag{5}$$

We may write $1/\widetilde{\varphi}(t)$ in the form

$$\frac{1}{\widetilde{\varphi}(t)} = u(t) + iv(t),$$

where $u(t)$ is an even function and $v(t)$ is an odd one.

Assume that $u(t)$ and $v(t)$ can be expanded in a power series

$$\begin{aligned} u(t) &= \sum_{n=0}^{\infty} a_n t^{2n}, \\ v(t) &= \sum_{n=0}^{\infty} b_n t^{2n+1}. \end{aligned} \tag{6}$$

We now insert (6) into (5) and use the fact that

$$\widetilde{x^n} = 2\pi\,(i)^n\,\delta^{(n)}(t), \tag{7}$$

where

$$\widetilde{x^n} = \int_{-\infty}^{+\infty} x^n\, e^{-ixt}\,dt.$$

Then

$$\psi(x) = \frac{1}{\sqrt{2\pi}} \sum_{n=0}^{\infty} (-1)^n \left[a_n \delta^{(2n)}(x) - b_n \delta^{(2n+1)}(x)\right], \tag{8}$$

and the solution of the integral equation can be written in the form

$$f(x) = \frac{1}{\sqrt{2\pi}} \sum_{n=0}^{\infty} (-1)^n [a_n F^{(2n)}(x) - b_n F^{(2n+1)}(x)]. \tag{9}$$

Let us consider in detail two cases of practical importance:

1. Let $\varphi(x)$ be

$$\varphi(x) = \frac{1}{a} \sqrt{\frac{\ln 2}{\pi}} e^{-\frac{\ln 2}{a^2} x^2}, \tag{10}$$

where the parameter a is the half-width of the curve at half-height of the peak. Then

$$\frac{1}{\tilde{\varphi}(t)} = \sqrt{2\pi} \exp\left(\frac{a^2 t^2}{4 \ln 2}\right) = \sqrt{2\pi} \sum_{n=0}^{\infty} \frac{1}{n!} \left(\frac{a}{2\sqrt{\ln 2}}\right)^{2n} t^{2n},$$

$$\psi(x) = \sum_{n=0}^{\infty} \frac{(-1)^n}{n!} \left(\frac{a}{2\sqrt{\ln 2}}\right)^{2n} \delta^{(2n)}(x)$$

and

$$f(x) = \sum_{n=0}^{\infty} \frac{(-1)^n}{n!} \left(\frac{a}{2\sqrt{\ln 2}}\right)^{2n} F^{(2n)}(x). \tag{11}$$

A similar solution was obtained for the same case in a less general way by Paisakhson.[2]

2. Let $\varphi(x)$ be

$$\varphi(x) = \frac{1}{\pi a} \frac{1}{1 + \left(\frac{x}{a}\right)^2}. \tag{12}$$

Then the function

$$\frac{1}{\tilde{\varphi}(t)} = \sqrt{2\pi}\, e^{a|t|}$$

has a singularity at $t = 0$.

The expression for $\psi(x)$ is

$$\psi(x) = \frac{1}{2\pi} \int_{-\infty}^{+\infty} e^{a|t|} e^{-ixt}\, dt = \frac{1}{\pi} \int_{0}^{\infty} e^{at} \cos xt\, dt. \tag{13}$$

Let us consider the real part of the integral

$$\int_{-\infty}^{+\infty} e^{at} e^{-ixt}\, dt.$$

Expanding e^{at} in a series and making use of (7), we arrive at

$$\mathrm{Re} \int_{-\infty}^{+\infty} e^{at} e^{-ixt}\, dt = 2\pi \sum_{n=0}^{\infty} \frac{(-1)^n}{(2n)!} a^{2n} \delta^{(2n)}(x). \tag{14}$$

On the other hand,

$$\mathrm{Re} \int_{-\infty}^{+\infty} e^{at} e^{-ixt}\, dt = \int_{0}^{\infty} e^{at} \cos xt\, dt + \frac{1}{a} \frac{1}{1 + \left(\frac{x}{a}\right)^2}. \tag{15}$$

Comparing (13), (14), and (15) we arrive at

$$\psi(x) = 2\sum_{n=0}^{\infty} \frac{(-1)^n}{(2n)!} a^{2n} \delta^{(2n)}(x) - \frac{1}{\pi a} \frac{1}{1+\left(\frac{x}{a}\right)^2}. \tag{16}$$

By making use of this expression, we obtain the solution to the integral equation with the kernel given by (12), namely,

$$f(x) = 2\sum_{n=0}^{\infty} \frac{(-1)^n}{(2n)!} a^{2n} F^{(2n)}(x) - \frac{1}{\pi a} \int_{-\infty}^{+\infty} \frac{F(t)}{1+\left(\frac{x-t}{a}\right)^2} dt. \tag{17}$$

Calculation of the derivatives

Equations (11) and (17) are exact solutions of Eq.(1) with the corresponding kernels. Thus the solution of the integral equation is reduced to finding the derivatives of $F(x)$. If $F(x)$ is given graphically or is tabulated with some experimental error, the errors will increase in obtaining the derivatives. This instability with respect to errors is characteristic for equations of the type of (1).[1]

Difference methods may be used to calculate the derivatives of the graphed or tabulated $F(x)$. Without loss of generality we may set $a = 1$ in Eqs.(10) and (12). Then Stirling's formula can be used to obtain the derivatives at the interpolation points in terms of central differences:

$$\begin{aligned}
F^{(2)} &= \frac{2}{h^2}\left(\frac{\Delta^2 F_{-1}}{2!} - \frac{\Delta^4 F_{-2}}{4!} + \frac{4}{6!}\Delta^6 F_{-3} - \frac{36}{8!}\Delta^8 F_{-4} + \ldots\right);\\
F^{(4)} &= \frac{4!}{h^4}\left(\frac{\Delta^4 F_{-2}}{4!} - \frac{5}{6!}\Delta^6 F_{-3} + \frac{49}{8!}\Delta^8 F_{-4} + \ldots\right);\\
F^{(6)} &= \frac{6!}{h^{(6)}}\left(\frac{\Delta^6 F_{-3}}{6!} - \frac{14}{8!}\Delta^8 F_{-4} + \ldots\right);\\
F^{(8)} &= \frac{8!}{h^8}\left(\frac{\Delta^8 F_{-4}}{8!} + \ldots\right);
\end{aligned} \tag{18}$$

here $\Delta^n F_{-2n}$ is the central difference of n-th order, and h is the tabulation interval of $F(x)$ (in units of a). If ε is the absolute error in the values given for $F(x)$, the maximum error of the difference of n-th order is

$$\varepsilon_n = 2^n \varepsilon.$$

The squared error in the n-th difference is given by

$$\varepsilon_n^{sq} = \sqrt{c_{2n}^n}\,\varepsilon:$$

$$\varepsilon_2^{sq} = 2.45\varepsilon; \quad \varepsilon_4^{sq} = 8.36\varepsilon; \quad \varepsilon_6^{sq} = 30.4\varepsilon; \quad \varepsilon_8^{sq} = 113.6\varepsilon.$$

In calculating the derivatives one should use only finite differences for which

$$\Delta^n \geqslant \varepsilon_n^{sq}. \tag{19}$$

The finite difference will decrease with h, while the error in it remains constant for constant ε. From this point of view, therefore, it is better to use large values of h. But as h is increased, so is the error in the derivatives, due to the diminished accuracy of the approximation. There must therefore exist an optimum value of h, depending both on ε and on the differential properties of

$F(x)$. Unfortunately, we have been unable to establish any general criteria for this optimum h. All we can do is to recommend values of h such that (19) will limit the differences used up to the 8-th order.

Numerical solution of the convolution-type integral equation with a dispersive kernel

Let us consider in greater detail the solution of Eq.(1) with the kernel given by (12). We express the solution obtained in (17) by central differences, going only to the 8-th order ($a = 1$):

$$f(x) = 2F - \frac{1}{\pi}\int_{-\infty}^{+\infty} \frac{F(t)}{1+(x-t)^2}\,dt - A\Delta^2 F_{-1} + B\Delta^4 F_{-2} - C\Delta^6 F_{-3} + D\Delta^8 F_{-4}. \qquad (20)$$

Here A, B, C and D depend on h. Table 1 gives the values of these coefficients for several values of h.

Table 1

h	A	B	C	D
0,1	100	841,667	2917,78	5679,25
0,2	25	54,167	52,361	31,791
0,25	16	22,667	15,111	6,746
0,3	11,111	11,214	5,648	2,028
0,4	6,250	3,776	1,290	0,3513
0,5	4,000	1,6667	0,44444	0,10317
0,6	2,778	0,87448	0,19757	0,04155
0,7	2,041	0,51714	0,10413	0,020530
0,8	1,5625	0,38365	0,061866	0,011669
1,0	1	0,16667	0,027778	0,0049603

Table 2

i	$a_{0.5i}$	A_i	i	$a_{0.5i}$	A_i	i	$a_{0.5i}$	A_i
0	$2a_{0.5} = 0,106$	0,447	11	0,007	0,055	22	0,001	0,030
1	0,170	0,277	12	0,003	0,052	23	0,001	0,029
2	0,053	0,224	13	0,005	0,047	24	0,001	0,028
3	0,065	0,159	14	0,002	0,045	25	0,001	0,027
4	0,021	0,138	15	0,003	0,042	26	0,001	0,026
5	0,029	0,109	16	0,002	0,040	27	0,001	0,025
6	0,011	0,098	17	0,003	0,037	28	0,001	0,024
7	0,016	0,082	18	0,001	0,036	29	0,001	0,023
8	0,006	0,076	19	0,002	0,034	30	0,001	0,022
9	0,010	0,066	20	0,001	0,033	31	0,001	0,021
10	0,004	0,062	21	0,002	0,032	32	0,001	0,020

The integral term in the solution can be calculated numerically. Writing the integral $I(x_k)$ at the point x_k in terms of integral sums (with $h = 0.5$), we have

$$I(x_k) = \sum_{i=0}^{n} a_{0.5i} F(x_k + 0.5i) + \sum_{i=0}^{m} a_{0.5i} F(x_k - 0.5i) + A_n \bar{F}_n + A_m \bar{F}_m,$$

where $\bar{F}_n$ and $\bar{F}_m$ are the "effective" values of $F(x)$ to the right and to the left of the interval $(x_k - 0.5m,\ x_k + 0.5n)$, respectively.

Table 2 gives the values of a as obtained by Simpson's rule, the values of A and those of $2a_{0.5}$. Thus it is no more difficult to calculate the integral term than to solve Eq.(1) by the column method.[3]

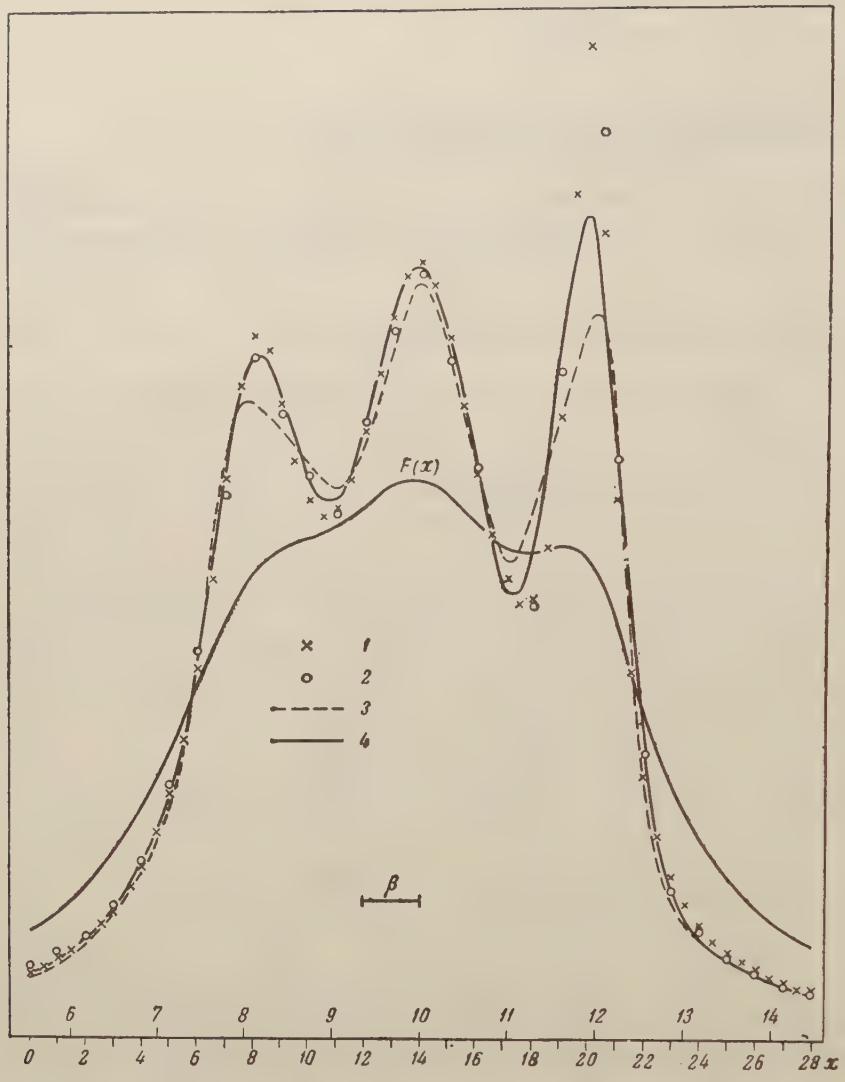

Comparison of different methods for solving Eq.(1). $F(x)$ is the "distorted" curve. 1 - points of the true curve, 2 - points obtained by the derivative method, 3 - points obtained by the matrix method[5], 4 - points obtained by the column method.

It takes very little time to make up the finite difference tables for all the x_k. Further, one need calculate only the differences of second and fourth order for most of the points. For this reason our method requires very little more time than the column method.[3] On changing h one need only recalculate the finite difference table, since in all cases of practical interest $h = 0.5$ gives sufficient accuracy for the integral term. The A, B, C and D coefficients on the derivatives can be combined with the a coefficients on the derivatives can be combined with the coefficients used in calculating the integral term. The coefficients then obtained are almost the same as those in Shannon's method[4] with the same interval. However, by separating out the irregular term and using (19), one obtains a more or less automatic choice of the required approximation. The figure gives an example of the use of our method.

Rostov-on-the-Don State University

References

1. S.G.Rautian, Usp.fiz.nauk, 66, 475 (1958). (Trans.Soviet Physics - Uspekhi
2. I.V.Peisakhsov, Izv.AN SSSR, Ser.fiz., 18, 680 (1954). (Trans.Bulletin, 18, 363.)
3. M.A.Blokhin, Metody rentgeno-spektral'nykh issledovanii (Methods of x-ray spectroscopic investigation), M., 1959.
4. V.P.Sachenko, Present issue of the Bulletin, p.1043.
5. Ya.E.Genkin & I.A.Rumyantsev, Izv.AN SSSR, Ser.fiz., 24, 384 (1960). (Trans.Bulletin, 24, 398.)

COMPARISON OF DIFFERENT METHODS OF CORRECTING THE SHAPE OF SPECTRA

- I.Ya.Nikiforov, V.P.Sachenko & M.A.Blokhin

There exist at present several effective methods for correcting the shape of x-ray spectra for dispersive and other distortions. Among these are the methods of trigonometric series[1,2], step functions[3], columns[4], matrices[5], derivatives[6], Shannon's method[7], and others[8,9].

The trigonometric-series method can be used to correct spectra for distortions of any kind. The method of derivatives was developed to deal with dispersive (Lorentzian) and Gaussian distortions, as well as for distortions in the shape of a hyperbolic secant, which is intermediate to these. All the other methods apply primarily to dispersive distortions; any other form of distortion requires preliminary calculations which, in principle at least, can always be performed.

All these methods give the true spectrum only approximately, and no two of them give the same results. This is essentially because these methods differ in the way that they approximate the initial experimental curve $F(x)$. In fact $F(x)$ is replaced by some analytic function, and it is for this analytic function that one obtains an "exact" solution.

In the trigonometric-series method this analytic function is a finite trigonometric series; in the step-function and column methods (using successive approximations) it is a series of arc tangents for a dispersive distortion; in Shannon's method it is the functions (sin x)/x, and in the derivative method it is polynomials.

Thus one might say that in all these methods an inexact curve is corrected exactly, the main difference between the methods being the way in which the experimental curve is approximated. If, as is often the case for small distortion, one has a good approximation of $F(x)$, correction by any of the methods will give a spectrum very close to the true one.

From the calculational point of view, all the methods are also quite similar. In the column, matrix, and Shannon methods the ordinate $f(x_i)$ of the corrected curve is a linear expression in the values of $F(x)$ at equally spaced points, i.e.,

$$f(x_i) = \sum_k F(x_k)\, a_j, \qquad (1)$$

where the coefficients have been previously calculated and where $j = |k - i|$. The coefficients a_j depend on the subdivision interval chosen; this is equal to $\beta/2$ in the column method (where β is the half-width of the Lorentzian distortion curve, and $2\pi\beta/2$ or $\pi\beta/4$ in the matrix method; in Shannon's method these coefficients are easily calculated for any interval. In the column method they are also easily calculated for any subdivision interval other than $\beta/2$. In the matrix method, however, this involves a great deal of computation.

It should be remarked that all the matrices given by Genkin and Rumyantsev[5] involved a fixed set of the a_j arranged symmetrically about a_0, in each row, with a_0 on the main diagonal. The a_j are somewhat different only near the edges of the matrix (to take account of edge effects).

The trigonometric-series method is considerably more complicated and can be used successfully only with the aid of a harmonic analyzer.

In the step-function method the ordinates do not have to be multiplied by any coefficients. A special ruler is used to obtain numbers whose algebraic sum gives the correction at the chosen point (which lies half way up the step). Finally, this process is easily mechanized (eliminating the necessity for algebraic addition) with the aid of a curvometer. To do this one must construct the correction function for a step as shown in Fig.1. According to data given by one of

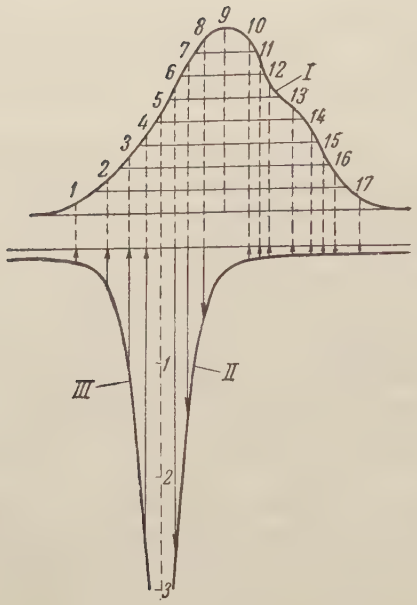

Fig.1. Correction of a curve by rectangular step functions at point 5: I - experimental $F(x)$ curve, II and III - correction curves for positive and negative step functions (the scale of curve II and III has been increased arbitrarily compared with curve I.

authors[3], one can also calculate this function by using the coefficients of the columns in the fifteenth approximation[4] (or one can calculate them from the coefficients obtained by Shannon's method[7]).

To obtain the correction to the ordinate of the experimental curve at point 5 (Fig.1) the correction curves are placed as shown in the diagram, and the curvometer is moved successively over the ordinates of these curves in the directions shown by the arrows. The upward direction denotes a positive correction, and the downward direction, a negative correction. The reading on the curvometer scale is then the desired correction.

Since each division of the curvometer scale represents 10 mm, and the correction is good only to 1/4 division, that is, to 2.5 mm; correction to within 1 percent of the maximum ordinate of the experimental curve requires the following scale for Fig.1. Curve I should be drawn so that its maximum ordinate be no less than 150-200 mm; the abscissa scale is chosen so that β = 20 mm. This curve is then broken up into 10-20 steps of equal height.

Curves II and III are drawn to the same abscissa scale, and the unit on the ordinate is chosen no less than 60-100 mm. If these curves are constructed in the ninth approximation in accord with Nikiforov's data[3], their maximum ordinate will be 240 to 400 mm.

After performing the above (Fig.1) measurements with the aid of a curvometer, the result must be divided in the ratio of the scales of the ordinates of curves II, III and I. The unit for curves II and III should be equal to the height of each separate step into which curve I is broken up.

It is thus seen that from the point of view of the work involved, the step-function method differs sharply from all the others in that it takes relatively little time. With a certain amount of practice, however, the other methods are also fairly rapid.

One of the advantages of the step-function method is that it can be applied directly to an experimental curve of any shape, and specifically to either an emission or an absorption spectrum (for which it is particularly convenient).

Before correcting any curve, one decides what energy interval or section is to be corrected. From this point of view all the methods can be divided into two groups, namely, those that can be used for any arbitrary interval, and those which have been developed for a certain standard interval (in units of β). The matrix method belongs in the latter category; all the other methods mentioned above can be used for an arbitrary interval. It should be noted, however, that although the trigonometric-series method does not in principle restrict the energy interval, good results are obtained only for an interval not much larger than the main part of the curve. This is because if there is a long tail (even if weak) the approximation will be poorer with the same number of terms in the series. On the other hand, an increase in the number of terms increases the contribution from experimental errors.

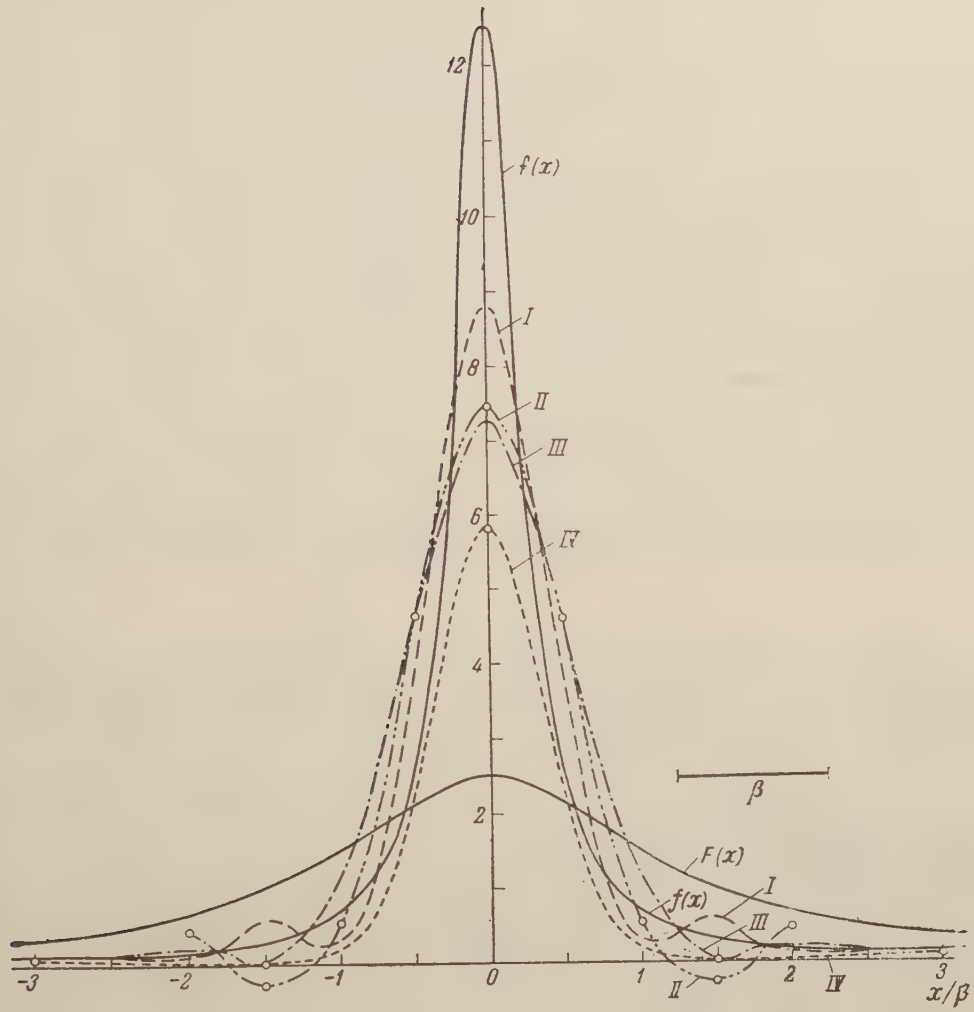

Fig.2. Correction of a classical dispersion curve. $f(x)$ is the true curve, and $F(x)$ is the experimental curve, I - correction by the derivative method, II - Shannon's method, III - column method, IV - matrix method. β is the half-width of the distortion curve.

In all cases of correction in the neighborhood of the boundaries of the interval there occurs some distortion (edge effects). If the method is not associated with a standard interval, one may always extend the energy range being corrected so that the point of interest lies outside the edge-effect region and the corrected ordinate will be obtained with an error no greater than that for the other points of the range. In the matrix method, the use of a preselected standard energy interval makes it expedient to correct experimental curves only when the part of the curve of interest coincides with this standard interval.

If the experimental curve is narrow compared to the width of the standard interval, or if it has small fluctuations, there will be too few points on the section of the curve of interest. If, on the other hand, the curve is too wide at the base, the standard interval may be too small. Thus, the use of the matrix method requires a large number of different matrices corresponding to various intervals with different subdivisions. If we assume, for instance, that it would be

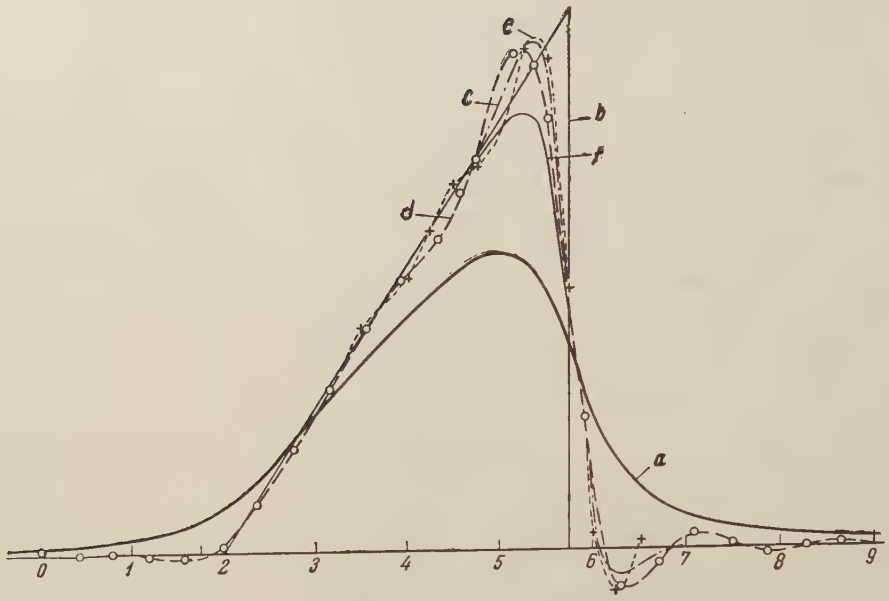

Fig.3. Triangle (b) dispersively distorted to the shape (a). Corrected curves: c - column method, d - Shannon's method with subdivision interval $\pi\beta/2$, and matrix method with the same subdivision interval, e - Shannon's method with a subdivision interval β.

sufficient to have matrices for four different intervals with four subdivisions, we would need altogether sixteen matrices.

The potentialities of the above-mentioned methods were further clarified by applying them to two examples of "distorted" analytic curves whose correct shape was known beforehand. The first of these (Fig.2) was an experimental curve of classic dispersion shape with a half-width of 1.25 β, which represents a very great distortion. (For small distortions all the methods give almost the same result, and it becomes quite difficult to pinpoint the difference between them.) It will be seen that in this particularly "bad" case the curves yielded by all the methods differ considerably from the true one. The derivative method gives the best results, while the matrix method (with a subdivision interval of $\pi\beta/2$) gives the worst. Not only that, but the points in this latter method are so greatly separated (by 1.5 half-widths) that the curve is poorly defined, i.e., there is an appreciable degree of arbitrariness in drawing the curve.

The second example involves a smeared out triangle (Fig.3). Bearing in mind the last point mentioned above, three sets of points were used in the matrix method, all with a subdivision interval of $\pi\beta/2$; this was accomplished by shifting the standard interval by $\pi\beta/6$ and $\pi\beta/3$. The curve obtained exhibits rather strong fluctuations. Almost the same curve is obtained by Shannon's method[7] with the same subdivision interval. Shannon's method with a subdivision interval of β gives a shape more nearly that of the triangle, but also with fluctuations (of higher frequency and smaller amplitude). The column and step-function methods give smoother curves which, at most of the points, lie closer to the original triangle than do the results of the matrix calculation.

The similarity of the results obtained by the matrix method and by Shannon's method with the same subdivision interval can be explained by the fact that the first coefficients are almost the same for both methods, and these play a deter-

mining role. Thus, the matrix method suffers in comparison with Shannon's method (with the same subdivision interval) in that it has a restricted interval and that the calculation for smaller subdivisions (which is quite simple in Shannon's method) is quite difficult and involves a further narrowing of the corrected interval. This is because the number of equations (the number of rows in the matrix) is in practice restricted, for as the number of equations is increased, the calculations rapidly become more cumbersome.

The fact that fluctuations occur in Shannon's method is related to the approximation of the experimental curve by functions of the form (sin x)/x. It would seem that the form of the approximation in the matrix method is quite similar to this, although this is difficult to show explicitly. In any method the curve obtained also has fluctuations, their magnitude depending essentially on the value of the second derivative and increasing with it. In the trigonometric-series method this effect is known and has been called the Gibbs effect. All the methods require the development of a criterion for the reality of such fluctuations, as well as fluctuations due to experimental errors.

As a necessary, but not sufficient, condition one may use the following criterion: since $F(x)$ cannot contain fluctuations with half-width β_1 (at the midpoint of the peak ordinate) less than the half-width β of the distortion curve, the corrected $f(x)$ curve can contain fluctuations only if

$$\beta_2 \Delta f > \beta \Delta F, \qquad (2)$$

where ΔF is the level of experimental errors, Δf is the amplitude of the fluctuations in the corrected curve, and β_2 is the half-width of such fluctuations. This criterion is established on the assumption of the fluctuations having the classical dispersion shape, and will therefore not always be strictly valid.

In all these methods, when the experimental ordinates are multiplied by the a_j, these same coefficients will multiply the experimental errors. These coefficients depend on the subdivision interval and (in the column method) on the number of approximations; therefore the optimum result is obtained by varying either the subdivision interval or the number of approximations according to the level of experimental error. In the matrix method this is virtually impossible. In order to obtain the optimum result one would, in general, have to look for the corrected ordinate at each point with respect to a different origin and with a different optimum subdivision interval or in a different approximation. This is, of course, impossible in practice; a curve can only be approximated in a single definite approximation[10] and a single subdivision interval, but then the most important points can be further corrected to optimize the approximation.

In order to minimize the role played by experimental errors and to obtain the best possible approximation, we may recommend the following procedure. From the experimental curves subtract a curve whose corrected shape is known, for instance, an arc tangent, a Lorentzian curve, or a smeared out triangle. The remainder can then be corrected and added to the analytic correction of the curve previously subtracted. Subtraction of a smeared out triangle is particularly helpful in the case of emission bands. We also recommend a check on the correction by smearing out the curve obtained and comparing it with the original one.

In summation, we may say that all the above methods are of some use in correcting the shape of spectra. In choosing the correct method for each specific case, however, one should bear in mind the peculiarities and disadvantage of each of them, as discussed above.

Rostov-on-the-Don State University

References

1. M.A.Blokhin, Doklady AN SSSR, 17, 33 (1956). (Trans.Doklady.)
2. M.A.Blokhin, Ibid., 107, 229 (1956). (Trans.Ibid.)
3. I.Ya.Nikiforov, Izv.AN SSSR, Ser.fiz., 21, 1362 (1957). (Trans.Bulletin, 21, 1351.)
4. M.A.Blokhin, Metody rentgeno-spektral'nykh issledovanii (Methods of x-ray spectroscopic investigation), M. 1959.
5. Ya.E.Genkin & I.A.Rumyantsev, Izv.AN SSSR, Ser.fiz., 24, 384 (1960). (Trans.Bulletin, 24, 398.)
6. V.P.Sachenko, Present issue of the Bulletin, p.1052.
7. V.P.Sachenko, Present issue of the Bulletin, p.1043.
8. R.N.Bracewell, Austral.J.Phys., 8, No.1, 61 (1955).
9. L.G.Parratt, Revs.Mod.Phys., 31, 616 (1959).
10. I.Ya.Nikiforov, Izv.AN SSSR, Ser.fiz., 24, 380 (1960). (Trans.Bulletin, 24, 394.)

CONCERNING THE USE OF SECONDARY-EMISSION MULTIPLIERS FOR INVESTIGATING SOFT X-RAY SPECTRA

- M.A.Rumsh, A.P.Lukirskii & V.N.Shchemelev

In connection with the use of secondary-emission multipliers for detecting x-rays in vacuum x-ray spectrometers there is considerable interest in the regularities governing the external photoeffect produced by x-rays of different wavelengths in photocathode materials. We have carried out a number of studies[1,2] for elucidating the basic regularities; these provide the justification for some recommendations regarding the choice of photocathode and its mounting in the multiplier.

The basic experimental regularities observed[3] are consistent with the phenomenological theory of secondary electron emission and can satisfactorily be explained by simple phenomenological calculations.

Such calculations are based on the assumption that the radiation intensity absorbed in each microvolume of the photocathode leads to the appearance of mobile electrons in this microvolume. It is further assumed that the energy acquired by the mobile electrons is due not only to the energy of the primary electrons but also to the energy of nonradiative transitions excited in the absorbing atoms and to the fluorescence energy absorbed in the photocathode.

We denoted the mean energy per mobile electron by E; then in a photocathode layer of thickness dx, situated at a depth x, there appear $dn = dE/E$ mobile electrons, where dE is the energy absorbed in the layer. Thus with the x-ray beam incident at an angle θ to the photocathode surface (Fig.1) there will be produced in the layer

$$dn = \frac{I_0[1 - R\theta]}{E} e^{-\frac{\mu}{\sin\theta}x} \frac{\mu}{\sin\theta} dx \qquad (1)$$

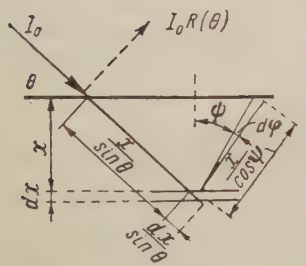

Fig.1.

electrons per second; here I_0 is the intensity of the incident beam, μ is the linear x-ray absorption coefficient of the photocathode material, and $R(\theta)$ is the coefficient of reflection from the face of the photocathode; this coefficient begins to differ from zero at a certain small θ and tends to unity with further decrease of θ (complete external reflection).

The electrons appearing in the layer dx are, apparently, characterized by more or less uniform distribution in angles; hence the fraction of electrons emerging from the layer in directions in the angular range from ψ to $\psi + d\psi$ to the normal to the photocathode surface will be given by

$$d^2n = \frac{I_0[1 - R(\theta)]}{2E} e^{-\frac{\mu}{\sin\theta}x} \frac{\mu}{\sin\theta} \sin\psi \, d\psi \, dx. \qquad (2)$$

If it is assumed that the energy of the electrons is appreciably greater than the work function, then for determining the emission one must, as is done in the theory of secondary emission, multiply (2) by $e^{-\frac{\alpha}{\cos\psi}x}$, where α is the linear coefficient of attenuation of the electron flux, and then integrate the resultant expression with respect to ψ in the limits from 0 to $\pi/2$ and with respect to x from 0 to ∞. Extending the limit of integration to infinity is necessary because the factor $e^{-\left(\frac{\mu}{\sin\theta} + \frac{\alpha}{\cos\psi}\right)x}$ under the integral vanishes even for small x inasmuch as the

coefficient α, as will be shown below, is of the order of 10^6 cm^{-1}.

The above integration leads to the equation

$$n_B = \frac{I_0[1-R(\theta)]}{2E}\left[1 - \frac{1}{\frac{\mu}{\alpha \sin\theta}} \ln\left(1 + \frac{\mu}{\alpha \sin\theta}\right)\right], \quad (3)$$

where n_B is the number of electrons emitted per second. Inserting $I_0 = N_0 \frac{hc}{\lambda}$, where N_0 is the number of x-ray photons incident per second, and writing for the quantum efficiency defined as n_B/N_0, we obtain

$$\varkappa = \frac{[1-R(\theta)]hc}{2E\lambda}\left[1 - \frac{1}{\frac{\mu}{\alpha \sin\theta}} \ln\left(1 + \frac{\mu}{\alpha \sin\theta}\right)\right]. \quad (4)$$

According to the data of Partsch & Hellwachs[5], $\alpha = 10^6$ cm^{-1}, while μ for not excessively long wavelength radiation does not exceed 10^4 cm^{-1}. Hence, $\frac{\mu}{\alpha \sin\theta} < 1$ and Eq.(4) can be simplified by expansion of $\ln\left(1 + \frac{\mu}{\alpha \sin\theta}\right)$ into a series. Such expansion yields

$$\varkappa = \frac{[1-R(\theta)]hc}{4E\lambda} \cdot \frac{\mu}{\alpha \sin\theta}\left[1 - \frac{2}{3}\left(\frac{\mu}{\alpha \sin\theta}\right) + \frac{2}{4}\left(\frac{\mu}{\alpha \sin\theta}\right)^2 - \ldots + (-1)^n \frac{2}{n+2}\left(\frac{\mu}{\alpha \sin\theta}\right)^n + \ldots\right], \quad (4a)$$

or in the first approximation we can write

$$\varkappa = \frac{[1-R(\theta)]hc}{4E\lambda} \frac{\mu}{\sin\theta}. \quad (4b)$$

Two significant inferences may be drawn from the last equation. First, the quantum efficiency differs for different angles, and for not excessively small angles, where external reflection can be neglected [$R(\theta) = 0$], the quantum efficiency will vary with angle as $\operatorname{cosec}\theta$. Second, if one assumes that α and E are independent of the wavelength λ, the variation of the quantum efficiency over the spectrum will be determined by the variation of μ/λ.

Both these inferences were checked experimentally. Fig.2 shows the variation of the quantities $\varkappa$ and $\varkappa \sin\theta$ as functions of θ, plotted on the basis of the experimental data for an aluminum photocathode and Si K_α radiation. Similar dependences were observed for all photocathodes and for all wavelengths with minor variations in the degree of decrease of $\varkappa \sin\theta$ in approaching the range of small angles. Comparison of the very rapid increase of $\varkappa$ with decrease of angle and the almost constant value of $\varkappa \sin\theta$ substantiates the first inference following from Eq.(4b). Some decrease of $\varkappa \sin\theta$ observed in reducing θ from 20 to 5° is explained by the more precise formula (4a), according to which

$$\varkappa \sin\theta = \frac{[1-R(\theta)]hc}{4E\lambda} \frac{\mu}{\alpha}\left[1 - \frac{2}{3}\frac{\mu}{\alpha \sin\theta} + \ldots\right]. \quad (5)$$

The additional factor in Eq.(5) decreases with decrease of θ. Variation in the degree of deviation of $\varkappa \sin\theta$ from the "constant" value, observed in changing photocathodes and in going from one wavelength to another is explained by variation in the value of the ratio μ/α, which enters as a parameter into the angular dependence. The substantial decrease of $\varkappa \sin\theta$ at angles $\theta < 5°$ is explained by the presence of the factor $[1 - R(\theta)]$, which decreases rapidly with reduction of the angle in this range.

The variation of log $\varkappa$ with log λ for Be, Mo and Al photocathodes is shown

Fig.2. Variation of κ and $\kappa \sin\theta$ with θ for an Al photocathode and Si K_α radiation.

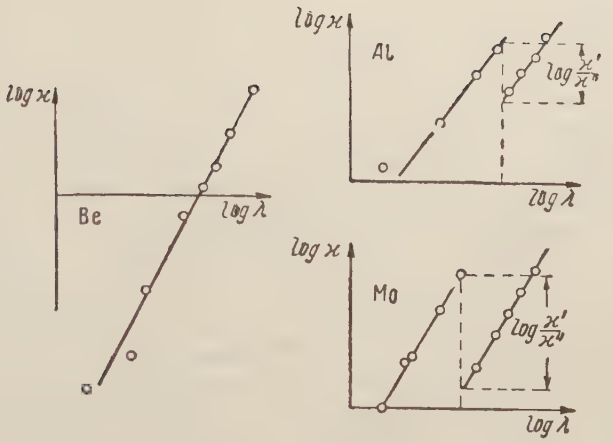

Fig.3. Variation of log κ with log λ for Be, Mo and Al photocathodes.

in Fig.3. It will be evident from the figure that at the wavelength equal to the wavelength of the absorption edge there is evinced a jump or discontinuity of the quantum efficiency κ, analogous to the discontinuity of the absorption coefficient μ. In the wavelength ranges between the absorption discontinuities there obtains linear dependence of log κ on log λ, indicating that

$$\kappa \approx \lambda^n. \tag{6}$$

We determined the values of the exponent from the slope of the rectilinear sections of the plots and found that $n = 2$ for Be, $n = 1.8$ for Mo, and $n = 1.3$ for Al.

Whereas the values of n for Be and Mo correspond to proportionality between κ and μ/λ, inasmuch as $\mu \approx \lambda^m$, where m lies in the range from 2.8 to 3, the value $n = 1.3$ obtained for Al indicates the absence of proportionality between κ and μ/λ in this case. The value of n obtained for Al, as well as for a number of other photocathodes, indicates that κ varies over the spectrum not only owing to variation of μ/λ, but also owing to change of α and E as functions of the wavelength.

From the plot for Al in Fig.3 one can determine the change in log κ in going through the wavelength of the K absorption edge. Having the values of κ' and κ'', the quantum efficiencies to either side of the absorption edge, we could readily calculate $\sigma_K = \kappa'/\kappa''$ (the efficiency jump or discontinuity) and compare this with the absorption discontinuity S_K.

In a similar manner, using the curves for Mo in Fig.3, we determined the common efficiency discontinuity $\sigma_{L_I M_I}$ at the L absorption edges, and compared this value with the analogous absorption discontinuity $S_{L_I M_I}$. We carried out such determinations for a number of other photocathodes as well. The results are summarized in the accompanying table together with the corresponding absorption discontinuities.

It will be evident from the table that the efficiency discontinuities are consistently larger than the absorption discontinuities. This lack of correspondence may be due to abrupt change in the values of E and α in going through the absorption edge. This is plausible since the mechanisms of transformation of the

Photocathode	Absorption edge	S	σ
Al	K	12.6	2.1
Ti	K	9	1.6
Ni	K	8.3	5
Ge	L	8	5.6
Mo	L	5.6	5.2
Te	L	4.9	2.3
W	M	6.3	5
SrF_2	L	6.2	3.1

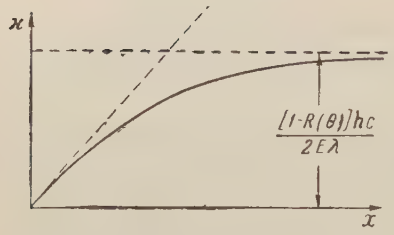

Fig.4. Variation of $\varkappa$ with $x = \mu/\alpha \sin\theta$. The solid curve is based on Eq.(4); the dashed line is given by Eq.(4b).

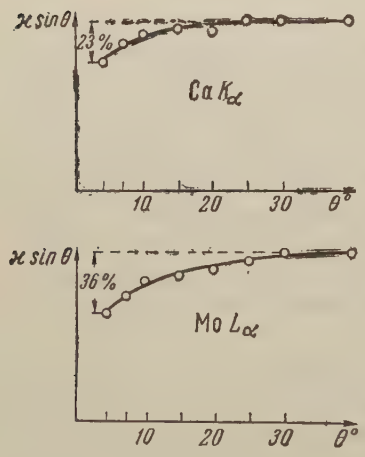

Fig.5. Variation of $\varkappa$ with θ for an Mo photocathode and Ca K_α and Mo L_α radiation.

absorbed radiation into the energy of electron motion may be different to either side of the absorption discontinuity. On the other hand, it is also possible that the proportionality between $\varkappa$ and μ, implicit in the simplified Eq.(4b), actually does not obtain in reality as characterized by the more accurate formula (4); if this is the case there should not be correspondence between the discontinuities σ and S.

Fig.4 shows the variation of $\varkappa$ with $x = \mu/\alpha \sin\theta$, as given by Eqs.(4) and (4b). If α is assumed to be constant, then in going through the absorption edge, μ, and, consequently, x, should change by a factor of S_K. It will be evident from Fig.4 that a S_K-fold decrease of x is accompanied by a S_K-fold decrease of $\varkappa$ according to (4b) (dashed line), whereas according to Eq.(4) $\varkappa$ changes by a smaller factor (solid curve).

In order to check the validity of this explanation for the noncorrespondence between σ and S we determined the magnitude of the efficiency discontinuities for Mo and W at different angles: θ = 20, 10 and 5°. It was expected that σ would decrease in going to smaller angles inasmuch as according to the curves of Fig.4 the values of $\Delta\varkappa$ corresponding to two separate values of x differing by a factor of S should decrease with increase of x. The measurement results showed, however, that the values of $\sigma_{20°}$, $\sigma_{10°}$ and $\sigma_{5°}$ are the same within the limits of the experimental error. Consequently, the noncorrespondence of σ and S cannot be explained by the accurate formula (4), but must be attributed to abrupt change of E and α in going through the absorption edge.

In order to determine how E and α change in going through the absorption edge we recorded the variation of $\varkappa$ with θ for two wavelengths located at different sides of the absorption edge. From Eq.(5), which gives the decrease of $\varkappa \sin\theta$ in going from θ = = 20° to θ = 5°, it is apparent that the decrease will be the more appreciable, the greater the parameter μ/α. The curves obtained for an Mo photocathode are reproduced in Fig.5. It will be evident that the decrease of $\varkappa \sin\theta$ in the case of Ca K_α radiation is smaller than in the case of Mo L_α radiation. This can obtain only on condition that $(\mu/\alpha)_{Ca\,K_\alpha} < (\mu/\alpha)_{Mo\,L_\alpha}$, and inasmuch as $(\mu)_{Ca\,K_\alpha} > (\mu)_{Mo\,L_\alpha}$, the inferred inequality can only obtain with $(\alpha)_{Ca\,K_\alpha} > (\alpha)_{Mo\,L_\alpha}$. Thus in the case of Mo, α in going through the absorption edge changes abruptly in the same direction as μ, but to a greater degree.

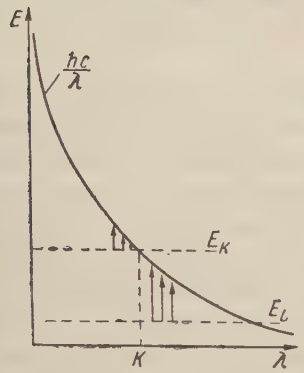

Fig.6. Diagram clarifying the abrupt change in E in going through the K absorption edge.

A similar variation of α is observed for Al photocathodes. For Ni, Te and MgO photocathodes $(\mu/\alpha)_{\lambda<\lambda_K}$ is somewhat greater than $(\mu/\alpha)_{\lambda>\lambda_K}$; hence α in going through the absorption edge changes abruptly and in the same direction as μ, but in this case to a lesser degree. For rough evaluation in the change in the parameter μ/α in going through the absorption edge one can make use of Eq.(5), retaining only the first term of the expansion. Using the curves of Fig.5 to determine the percent reduction of $\varkappa \sin\theta$ that obtains for $\theta = 5^\circ$, one can readily calculate the values of μ/α and the change in this parameter in going through the absorption edge. Evaluations show that in all cases μ/α changes by an amount not exceeding 50%, whereas $\varkappa$ changes by a factor of 2-3 (and even 5 in the case of nickel), and that the change is always a decrease in going from shorter to longer wavelengths through the absorption edge. Comparison of the changes of μ/α with the changes of $\varkappa$ leads to the inference that the electron energy E also changes abruptly in going through the absorption edge, increasing in going through the edge from shorter to longer wavelengths.

All these facts are clarified in Fig.6, where in addition to the curve characterizing the variation of the photon energy with wavelength (solid line), we have plotted the energies of the x-ray levels (horizontal dashed lines). Near the absorption edge we have drawn a group of arrows, departing in the $\lambda<\lambda_K$ region from the K x-ray level and in the $\lambda > \lambda_K$ region from the L x-ray level. These arrows symbolize photoelectrons ejected primarily from the K shell with $\lambda < \lambda_K$ and from the L shell with $\lambda > \lambda_K$. The length of the arrows indicates that for $\lambda < \lambda_K$ most of the photoelectrons are characterized by a low energy (small E) and hence an appreciable attenuation coefficient α (it will be recalled that the attenuation coefficient increases with decreasing energy). In the $\lambda>\lambda_K$ region the photoelectron energy proves to be appreciably greater, and, consequently, the coefficient α is smaller. This qualitative explanation of the results does not take into account Auger electrons, but it must be noted that regardless of the role played by the Augers, the above argument remains valid.

Thus the variation of the quantum efficiency over the spectrum is determined not only by changes in the parameter μ/λ, but also by changes in α and E. In fact, it would appear that the values of α and E affect the quantum efficiency to a greater extent than the value of μ, which explains why such photocathodes as Be, LiF and MgO, which have a small x-ray absorption coefficient μ, are characterized by an appreciably higher efficiency than W, Bi_2Te and HgSe photocathodes for which μ is appreciable.

We can now turn to certain deductions that follow from the above data, deductions that are of practical interest in choosing photocathodes for experimental purposes. In general it will be recalled that secondary-emission multipliers have a number of advantages over Geiger counters. Secondary-emission multipliers can be used for detecting radiation in any vacuum wavelength interval and are also suitable for recording in the ultralong wavelength x-ray region, where the applicability of Geiger counters is limited by absorption in the counter window. In addition, secondary-emission multipliers are capable of incomparably higher counting rates than Geiger counters inasmuch as the pulse rise time in multipliers

is of the order of 10^{-9} sec, while the "dead time" of the recording circuit can be reduced to 10^{-6} sec or less. By appropriate choice of the photocathode and mounting it at a suitable angle relative to the beam, one can always attain a high detecting efficiency in a wide spectral range.

In working with secondary-emission multipliers, however, it must be borne in mind that the efficiency of the tube varies over the spectrum and undergoes an abrupt change in the region of the absorption edges. This distinctive feature of multipliers must be borne in mind in setting up the spectroscopic experiments, that is, one must strive to choose a photocathode that will not have any absorption edges in the investigated wavelength range. From this standpoint, BeO, LiF, and MgO photocathodes are preferable inasmuch as they are characterized by a minimum number of absorption edges and distinguished by high efficiency.

On the other hand, the strong wavelength dependence of the efficiency of secondary-emission multipliers, particularly in the region of the absorption edge can be utilized to practical purposes. Thus the discontinuities in the quantum efficiency can be utilized for determining the location of the absorption edge of the investigated substance. In this case the investigated substance is used as the photocathode, which obviates the experimental difficulties connected with the preparation of thin layers. Undoubtedly investigation of the fine structure of the quantum efficiency of photocathodes, which should be evinced in the vicinity of the absorption edge, can yield additional data to further our understanding of the interaction of radiation with matter.

We desire to express our gratitude to Academician A.A.Lebedev for his interest in the work.

Physics Faculty,
Leningrad State University

References

1. A.P.Lukirskii, M.A.Rumsh & L.A.Smirnov, Optika i spektroskopiya, 9, 512 (1960). (Trans.Optics & Spectroscopy.)

2. A.P.Lukirskii, M.A.Rumsh & I.A.Karpovich, Ibid., 9, 653 (1960). (Trans. Ibid.)

3. M.A.Rumsh, A.P.Lukirskii & V.N.Shchemelev, Doklady AN SSSR, 135, 55 (1960 (Trans.Doklady.)

4. H.Bruining, Die Sekundärelektronenemission fester Körper. (Secondary emission from solids), Berlin, 1942.

5. A.Partsch & W.Hellwachs, Ann.Phys., 41, 247 (1913).

QUANTUM SENSITIVITY OF PHOTOGRAPHIC MATERIALS TO X-RADIATION WITH WAVELENGTHS FROM 1.54 TO 113 Å

- M.A.Rumsh, V.N.Shchemelev & A.P.Lukirskii

We investigated the sensitivity of six different types of photographic film to x-ray radiation. The studies in the soft part of the x-ray spectrum (1.5 to 14 Å) were carried out by means of a vacuum x-ray monochromator[1]; the studies in the ultrasoft region (20 to 113 Å) were carried out by means of a monochromator with a diffraction grating[2]. Both these instruments originally had provision for detection of the radiation by two detectors, namely, a Geiger counter and an Allen type secondary-emission multiplier. The Geiger counters in both monochromators were of the retractable type so that they could be introduced into the beam for measuring its intensity and withdrawn from the beam in exposing the film. The Geiger counters were calibrated to yield absolute intensity values in terms of the number of photons per second.

For investigating the photographic emulsions the secondary-emission multipliers were replaced by a cassette equipped with a feed mechanism for advancing the film. By virtue of this mechanism it was feasible to expose on each film strip the requisite number of "markers" with a known integral flux, as measured beforehand by the Geiger counter. Depending on the sensitivity of the film and the sensitivity of the monochromatic beam, the exposure time for different "markers" varied from 10 sec to 2 hours.

Specifically, we investigated samples of the following films: RT-1 (PT-1), RT-2 (PT-2)(Shostka Plant), RT-2 (Kazan' Plant), RM-1 (PM-1)(Shostka Plant), Agfa-Laue, and the experimental NIKFI-45 film (NIKFI = Scientific Research Cinematographic & Photographic Institute). In developing the films we rigorously adhered to the conditions and developer formulation recommended by the respective manufacturers. For the experimental NIKFI-45 film we used Chibisov's[3] negative developer No.1; the developing time was 4 min. Since the photographic density over the area of the "markers" was not uniform (owing to mosaicity of the crystal and astigmatism of the diffraction grating), in determining the number of photons incident per 1 mm^2 of marker, we reduced the marker area to the value corresponding to uniform density equal to the maximum density in the given marker. This normalizing procedure has been described in Ref.4.

As a measure of the sensitivity we took $1/N_o$, where N_o is the number of photons per mm^2 of marker with optical density D = 0.2. The variation of log $(1/N_o)$ as a function of log λ for the RT-1 film is shown in Fig.1,a.

Similar curves were obtained for the RT-2 (Shostka), RM-1 (Shostka), RT-2 (Kazan') and Agfa-Laue films. A curve of different character was obtained for the NIKFI-45 film; this is reproduced in Fig.1,b. The maximum sensitivity of the films characterized by a sensitivity curve of the type shown in Fig.1,a lies in the region of 3.5 Å. The decrease in sensitivity to the short wavelength side of the maximum is explained by decrease of absorption in the emulsion with decrease of λ; the decrease in sensitivity on the long wavelength side of the maximum is explained by that fact that with increase of λ the fraction of radiation absorbed in the gelatin, particularly in the gelatin of the superficial, covering layer, increases. In the ultrasoft region the radiation is completely absorbed in part of the top layer of the emulsion, wherein the relative proportion of gelatin is high. In going from O K_α to C K_α radiation the absorption in gelatin diminishes owing to the absorption discontinuity in carbon. In connection with this, the relative absorption in AgBr increases, with resultant increase in the sensitivity.

Thus the observed jump in sensitivity is explained by the presence of the

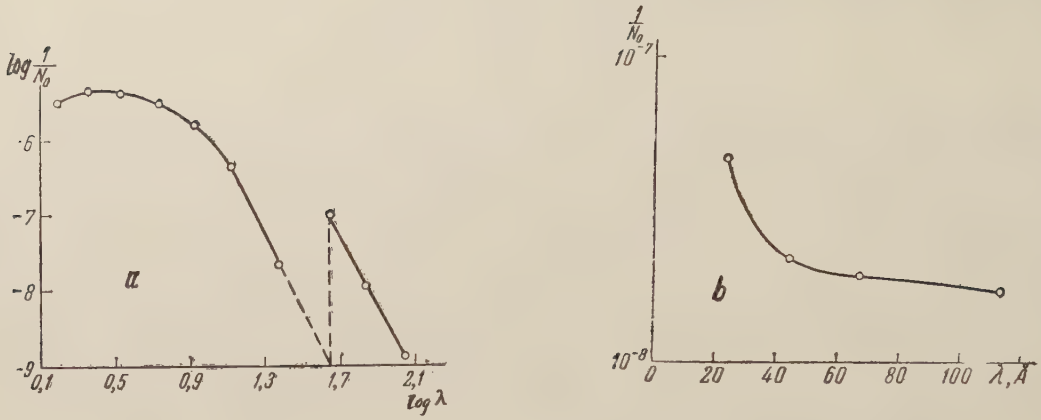

Fig.1. Quantum spectral sensitivity curves for two films: a) RT-1 (Shostka), b) NIKFI-45.

absorption discontinuity of carbon on the short wavelength side of the C K_α line. The spectral sensitivity curve for the NIKFI-45 film is characterized by a monotonic decrease in going to longer wavelengths; the absence of a sensitivity jump at C K_α in the case of this film can readily be understood, inasmuch as this film does not have a protective gelatin coating.

In the accompanying table we list the values of N_0, the number of photons per mm^2 corresponding to an optical density D = 0.2, for ten characteristic x-ray lines for all six of the investigated films. It will be evident that N_0 varies in the range from 10^5 to 10^8 photons/mm^2. Experimental difficulties were encountered in determining the sensitivity of the films to Cu L_α (13.3 Å) radiation. In order to eliminate fogging of the films by the visible and ultraviolet light coming from the tube and reflected from the crystal, the tube window was covered with an aluminized celluloid film. Whereas for the hard part of the radiation the aluminum layer could be made sufficiently thick to eliminate fogging, in the case of Cu L_α radiation use of an optically opaque aluminum layer results in reduction of the line contrast, i.e., to increase in the relative intensity of the higher orders of the hard radiation. Hence we had to compromise and use an aluminum layer thickness which did not completely eliminate the effect of visible light

Values of N_0 (in 10^5 photons/mm^2) corresponding to density D = 0.2

λ, A	RT-1	RT-2 (Shostka)	RM-1	RT-2 (Kazan')	Agfa Laue	NIKFI-45
1,537 (CuK_α)	3,2	9,4	8	9,6	1,2·10	—
2,278 (CrK_α)	2,2	6,0	3,7	4,0	5,5	—
3,35 (CaK_α)	2,5	4,8	2,5	2,8	4,4	—
5,395 (MoL_α)	3,4	5,1	3,3	3,7	6,1	—
8,32 (AlK_α)	6,2	8,4	5,3	4,6	8,5	—
13,33 (CuL_α)	2,4·10	2,5·10	1,1·10	1,3·10	1,4·10	—
23,6 (OK_α)	$4,7·10^2$	$5,1·10^2$	$2,34·10^2$	$3,9·10^2$	$7,2·10^2$	$1,5·10^2$
44 (CK_α)	$1,1·10^2$	$1,15·10^2$	1,90·10	3,0·10	$1,7·10^2$	$2,92·10^2$
67 (BK_α)	$9,5·10^2$	$9,1·10^2$	$2,2·10^2$	$1,2·10^3$	$8,8·10^2$	$3,52·10^2$
113 (BeK_α)	$7,8·10^3$	$6,6·10^3$	$1,57·10^3$	—	$5,2·10^3$	$4,4·10^2$

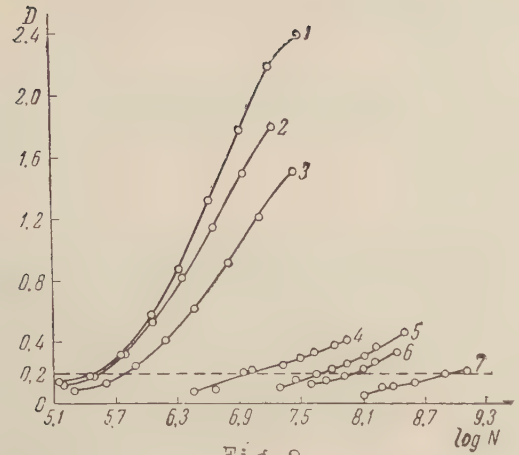

Fig.2

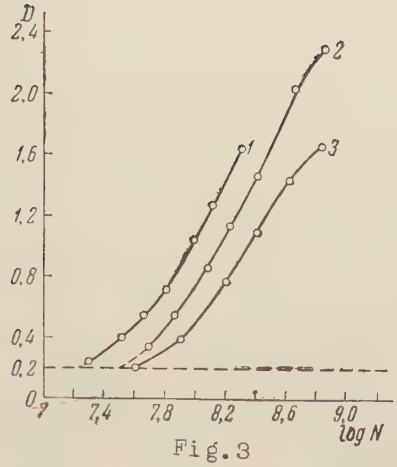

Fig.3

Fig.2. Blackening curves for the RT-1 (Shostka) film: 1 - 1.537 Å (Cu K_α), 2 - 5.395 Å (Mo L_α), 3 - 8.32 Å (Al K_α), 4 - 44 Å (C K_α), 5 - 23.6 Å (O K_α), 6 - 67 Å (B K_α), 7 - 113 Å (Be K_α).

Fig.3. Blackening curves for the NIKFI-45 film: 1 - 23.6 Å (O K_α), 2 - 44 Å (C K_α), 3 - 113 Å (Be K_α).

but still provided a reasonable degree of contrast. Consequently, there is reason to assume that the sensitivity values for Cu L_α radiation are overestimates (this is evident from the spectral curves).

It should be noted that the sensitivity of the experimental NIKFI-45 film in the 100 Å region is more than an order of magnitude higher than the sensitivity of the other films. The blackening curves for the RT-1 (Shostka) and NIKFI-45 films are reproduced in Figs.2 and 3. It will be evident from these figures that with increase of the wavelength the blackening curves shift to the side of larger N, i.e., the sensitivity decreases; in addition, the rectilinear section of the curves diminishes. The values of gamma ($\gamma = dD/d(\log N)$) determined for the RT-1 and NIKFI-45 films at different wavelengths are the following:

Film	1.54 Å	5.4 Å	8.32 Å	23.6 Å	44 Å	67 Å	113 Å
RT-1	1.36	1.2	1	-	-	-	-
NIKFI-45	--	--	-	2.0	1.95	1.9	1.6

We desire to express our gratitude to Academician A.A.Lebedev for his advice and interest in the work.

Physics Faculty,
Leningrad State University

References

1. M.A.Rumsh, A.P.Lukirskii, I.A.Karpovich & V.N.Shchemelev, PTE, No.5, 67 (1960). (Trans.Instruments & Experimental Techniques.)

2. A.P.Lukirskii, M.A.Rumsh & L.A.Smirnov, Optika i spektroskopiya, 9, 505 (1960). (Trans.Optics & Spectroscopy.)

3. Sensitometricheskii spravochnik, (Sensitometric handbook), Edited by Yu. N.Gorokhovskii and S.S.Gilev, M., 1955.

4. A.P.Lukirskii & I.A.Karpovich, Optika i spektroskopiya 4, 685 (1959). (Trans.Optics & Spectroscopy.)

Bulletin of the Academy of Sciences of the USSR - Physical Series
Vol.25, No.8 - August 1961

Transactions of the Fifth Conference on X-ray Spectroscopy

Table of Contents

	Page Orig.	Trans.
Use of x-ray bremsstrahlung for investigation of absorption spectra in the ultrasoft region - A.P.Lukirskii	910	923
Spectrometer for ultrasoft x-radiation with combined detection by means of secondary-electron multipliers and a Geiger counter - A.P.Lukirskii	913	926
Microfocus x-ray spectrograph - I.B.Borovskii, S.A.Ditsman & V.G.Bogdanov	919	932
Investigation of the region of a microfocus source in an x-ray microanalyzer - S.A.Ditsman	923	935
On the possibility of quantitative analysis by means of x-ray spectra without the use of standards - N.P.Il'in	929	940
Vacuum x-ray spectrometer with ionization recording - V.A.Batyrev & V.G.Bogdanov	933	944
Constant vacuum x-ray tube for a long-wavelength x-ray spectrometer - K.I.Narbutt, E.M.Fridman & G.M.Nikolaenko	936	947
Reflection of hard x-radiation by bent crystals - S.A.Ditsman	939	949
Regarding the resolution of Johann mounting single-crystal spectrographs - N.D.Borisov & V.V.Nemoshkalenko	943	954
Experimental investigation and calculation of the L absorption spectra of noble gases - R.L.Barinskii	947	958
Regarding the asymmetry of the $K\alpha_1$ and $K\alpha_2$ lines of atoms of the iron group - L.K.Izraileva	954	965
Theory of the fine structure of x-ray absorption spectra - A.I.Kozlenkov	957	968
Contribution to the theory of the temperature dependence of the fine structure of x-ray absorption spectra - V.V.Shmidt	977	988
Influence of tungsten impurities on the temperature dependence of the K absorption spectrum of iron - I.B.Borovskii & V.V.Shmidt	983	994
Influence of the chemical bond on the energy and intensity of the x-ray lines of atoms in compounds - A.T.Shuvaev	986	996
Investigation of the K absorption spectra of calcium in some compounds - A.T.Shuvaev & V.F.Demekhin	992	1001
Investigation of the binding forces in Ni-Mo solid solutions by observing the fine structure of the absorption spectra - V.A.Trapeznikov	994	1003
X-Ray spectroscopic investigation of intermetallic compounds in the Cu-Zn system - V.A.Batyrev	997	1006
Influence of thermal vibrations of atoms on the process of "melting" of the fine structure of the x-ray absorption spectra. I. Investigation of a Cu-Pt solid solution - I.B.Borovskii & G.N. Ronami	999	1008
Concerning the electron configuration in metals of the iron group - N.D.Borisov & V.V.Nemoshkalenko	1002	1011
The $K\beta_x$ emission band and K absorption edge of aluminum in some alloys with transition metals - S.A.Nemnonov & L.D.Finkel'shtein	1007	1015

Computer for correcting the shape of emission spectra - M.I.Korsunskii & Ya.E.Genkin	1013	1020
Comparison of two methods of correcting experimental curves (column and matrix methods) - Ya.E.Genkin & I.A.Rumyantsev	1017	1023
Corrected $L\beta_2$ emission band in the spectra of pure niobium and its compounds - M.I.Korsunskii & Ya.E.Genkin	1028	1033
On determining the Fermi level from x-ray emission bands - M.I.Korsunskii & Ya.E.Genkin	1031	1036
On finding the true shape of spectra using the Shannon approximation - V.P.Sachenko	1038	1043
Concerning the shape of the $K\beta_5$ emission band of iron. Part I - I.Ya.Nikiforov	1043	1048
On the "derivative method" for correcting the shape of spectra - V.P.Sachenko	1048	1052
Comparison of different methods of correcting the shape of spectra - I.Ya.Nikiforov, V.P.Sachenko & M.A.Blokhin	1054	1057
Concerning the use of secondary-emission multipliers for investigating soft x-ray spectra - M.A.Rumsh, A.P.Lukirskii & V.N. Shchemelev	1060	1063
Quantum sensitivity of photographic materials to x-radiation with wavelengths from 1.54 to 113 Å - M.A.Rumsh, V.N.Shchemelev & A.P.Lukirskii	1066	1069

Translated in 1962 by
Columbia Technical Translations
5 Vermont Ave., White Plains, N.Y.

Transactions

of the

Eleventh Annual Conference on Nuclear Spectroscopy

(Riga, 25 January - 3 February, 1961)

(Continued from Vol.25, Nos.2 & 7; to be continued in Vol.25, No.10 & Vol.26, No.1)

MAGNETIC SPECTROMETER FOR DETECTING INTERNAL CONVERSION ELECTRONS FROM THE (n,γ) REACTION

- V.I.Pelekhov & A.F.Malov

Spectrometry of internal conversion electrons, appearing as a result of absorption of slow neutrons by nuclei, can yield information on transitions in the radiating nucleus, information which supplements the results of investigation of neutron capture γ-rays by means of a γ-spectrometer. In the case of transitions with large conversion coefficients, in addition to energy and intensity values, there can also be obtained data on the multipolarity of the radiation. Moreover, one can detect transitions of the $0^+ \rightarrow 0^+$ type, for which emission of single γ-rays is absolutely forbidden.[1,2]

Hibdon & Muehlhauser[3] and later Church & Goldhaber[4] used a Danysz (180° focusing, constant magnetic field) β-spectrometer with photographing recording to detect conversion electrons from neutron bombarded targets. Motz[1] investigated conversion electrons emitted from a bombarded target by means of a lens spectrometer. Groshev et al[5] used the magnetic spectrometer commonly employed in their laboratory for measuring γ-rays emitted in thermal neutron capture by observation of Compton recoils. The referred to investigation of Groshev et al was undertaken primarily for the purpose of evaluating the possibility of studying internal conversion electron spectra from thermal neutron capture by means of a spectrometer with recording of electrons by means of two widely separated counters connected in coincidence. All the spectrometers used in the investigations mentioned to above were characterized by a relatively low transmission factor, an unsatisfactory effect-to-background ratio and in the case of the studies of Refs.1 and 5 relatively low resolution. Actually, measurements were carried out only for Cd, Sm, Gd, Dy and Hg isotopes with a large thermal neutron capture cross section. The lower bound of the capture cross section for which it was feasible to investigate conversion electron spectra was 500-1000 barns.

Aside from a spectrometer detecting conversion electrons emitted in the (n,γ) reaction, designed to utilize a neutron beam for radiating the target, one can also construct a spectrometer with the target located in the immediate proximity of the reactor core. The latter variant was recently described by Meier-Leibnitz[6]. However, we chose the former variant. Below we describe the experimental set-up operated in conjunction with the Institute of Reactor Technology reactor[7] and consisting of a special magnetic spectrometer designed specifically for analysis of internal conversion electrons emitted by nuclei as a result of radiative thermal neutron capture. We give some of the electron-optical characteristics of the spectrometer and present an example of the internal conversion electron spectrum obtained with a Cd^{113} target.

Arrangement of the Spectrometer

The experimental set-up is diagramed in Fig.1. Neutrons from the reactor pass through a 10 cm diameter channel in the shielding and strike the target. The system of collimators is assembled of boron carbide-loaded paraffin, steel and lead, mounted in the channel, limits the neutron beam at the target to 3 x 3.3 cm. Since together with neutrons there are incident on the target γ-rays from the reactor, to minimize the background of Compton electrons, photoelectrons and electrons from the electron-positron pairs produced by these γ-rays, the focusing of the conversion electrons from the target is realized in the direction opposite to that of incidence of the neutron beam.

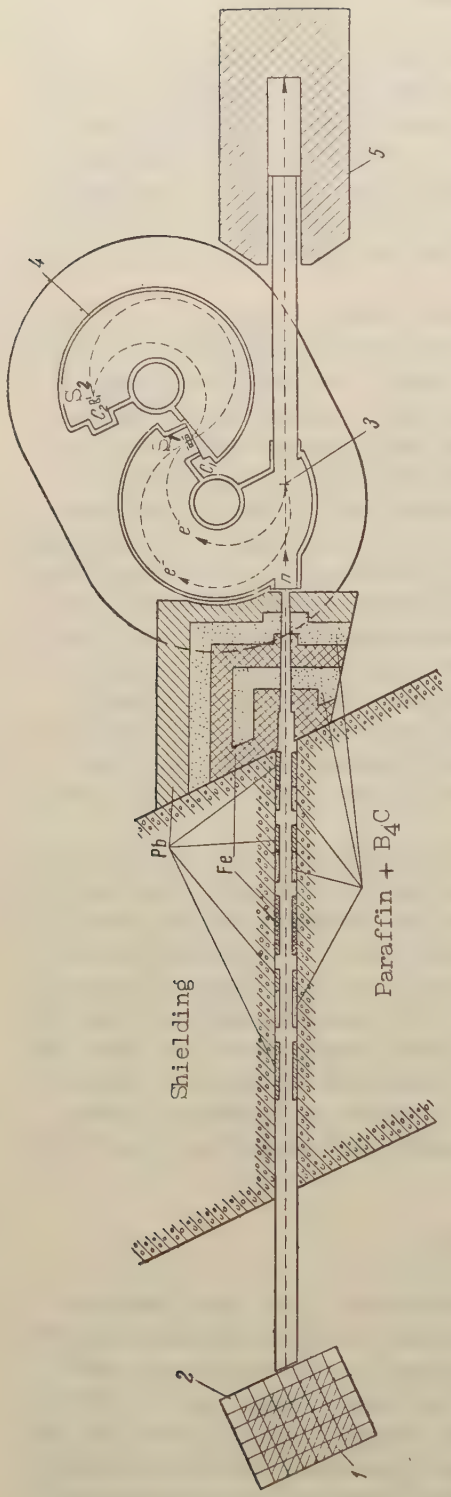

Fig.1. Diagram of experimental arrangement for investigating internal conversion electrons emitted in radiative thermal neutron capture: 1) reactor core, 2) graphite reflector, 3) target, 4) spectrometer, 5) beam catcher.

The electron trajectories in the spectrometer are shown in Fig.2. The spectrometer consists of two equal electromagnets with an axially symmetric field, realizing $\pi/2$ focusing of the electrons with a central orbit radius r_0 = 30 cm. The two magnets have a common magnetic circuit and are connected in series; the magnetic fields in the magnets are opposed. Optimum design requires complete identity of the electromagnets. The common intermediate focus of the magnetic field is located at the point of intersection of the central orbit with the plane containing the axis of symmetry of the magnetic fields. The principle of focusing the electrons in two directions was deliberately chosen in order to obtain an appreciable acceptance angle without sacrifice in resolution.[8] This is necessary in view of the relatively weak neutron flux to the target (~10^9 neutrons cm^{-2} sec^{-1}) inasmuch as it is located at a distance of about 4 meters from the reactor core.

A projection of the electron trajectories on the symmetry plane of the spectrometer is shown in the upper part of Fig.2. The lower drawing shows a projection of the electron trajectories onto the surface of a cylinder (unrolled) perpendicular to the symmetry plane and passing through the optical axis of the electron beam. The internal conversion electrons, emitted from the target T located in the field of the first magnet, are collected by the magnetic field to the intermediate focus, i.e., onto slit S_1 behind which is located counter C_1 with thin windows. Passing through the counter and entering the oppositely directed field in the second magnet, the electrons are focused onto the receiving slit S_2 and are detected by counter C_2. The counters C_1 and C_2 are connected in coincidence. Thus the experimental result is the variation in number of coincidences between pulses from counters 1 and 2 as a function of the strength of the magnetic field.

The field of the magnets in the symmetry plane $z = 0$ near the central

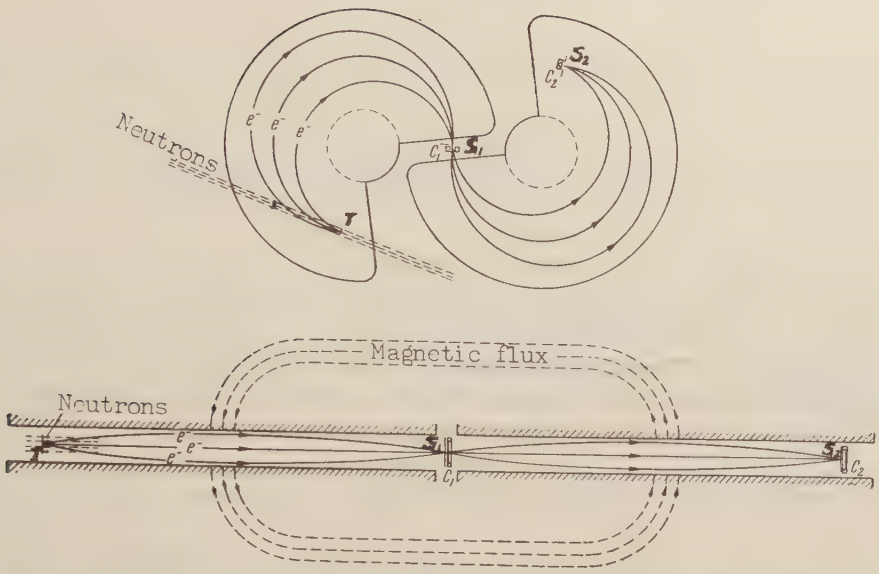

Fig.2. Electron trajectories in the spectrometer: above - projection of the trajectories on the symmetry plane of the instrument; below - projection of the electron trajectories on a cylindrical surface (unrolled) perpendicular to the symmetry plane and passing through the optical axis of the electron beam. T - target, S_1 and S_2 - spectrometer slits, C_1 and C_2 - Geiger-Müller counters. The target T is located in the field of the first magnet; the receiving slit S_2 is located in the field of the second magnet.

orbit $r = r_0$ (r and z are cylindrical coordinates) can be represented by the series

$$H_z(r, 0) = H_0\left\{1 + \alpha\frac{r - r_0}{r_0} + \beta\left(\frac{r - r_0}{r_0}\right)^2 + \ldots\right\}, \qquad (1)$$

where $\alpha = -1/2$. The coefficient β in the third term was chosen equal to 1/8, inasmuch as in this spectrometer the radial divergence of the electron beam is appreciably greater than the axial divergence[9-12].

Below we give some of the electron-optical characteristics of the spectrometer. First, however, we must define the designations and quantities necessary for calculating the spectrometer parameters; we also introduce separate systems of coordinates for each of the magnets. The z axes of the r, φ, z coordinate systems coincide with the symmetry axes of the fields and are oriented in the directions of the magnetic flux in the magnet, as indicated by the arrows in the lower part of Fig.2. The angle φ is measured from the intermediate focus, and is assumed to be positive in the second magnet and negative in the first. The electron trajectories are shown in relative coordinates, which are related with the cylindrical coordinates by the expressions

$$^k\rho_i = \frac{^kr_i - r_0}{r_0} \quad \text{and} \quad ^k\xi_i = \frac{^kz_i}{r_0}, \qquad (2)$$

where the index i corresponds to the number of the magnet (1 or 2), and the index k is introduced only for designating the coordinates and other quantities at the three foci: 1 identifies the target focus, 2 stands for the intermediate focus and 3 denotes the focus at the receiving slit S_2. The tangent $^k\psi_{ri}$ of the radial angle and the tangent $^k\psi_{zi}$ of the axial angle of the electron trajectories at the

point $({}^k\rho_i,\ {}^k\xi_i)$ are given by the formulas

$$ {}^k\psi_{ri} = \frac{{}^k\left(\frac{d\rho}{d\varphi}\right)_i}{1 + {}^k\rho_i}, \tag{3a} $$

$$ {}^k\psi_{zi} = \frac{{}^k\left(\frac{d\xi}{d\varphi}\right)_i}{1 + {}^k\rho_i}\left\{1 - \frac{1}{2}\left[\frac{{}^k\left(\frac{d\rho}{d\varphi}\right)_i}{1 + {}^k\rho_i}\right]^2\right\} \tag{3b} $$

We designate the maximum values of the tangents of the radial and axial angles of the electron trajectories at the initial point (i.e., at the target T) by ψ_r^0 and ψ_z^0, respectively. At the intermediate focus $(k = 2)$ the coordinates and tangents for the first magnet $(i = 1)$ in accord with the choice of coordinate systems, are related to the corresponding coordinates and tangents for the second magnet $(i = 2)$ by the expressions

$$ {}^2\rho_2 = -{}^2\rho_1, \quad {}^2\xi_2 = -{}^2\xi_1, \quad {}^2\psi_{r2} = -{}^2\psi_{r1} \quad \text{and} \quad {}^2\psi_{z2} = -{}^2\psi_{z1}. \tag{4} $$

Dispersion

The dispersion of electrons in momentum can be determined by considering the particular case of electron motion in the central plane $z = 0$ of the magnetic field $H(r, z)$. In this case, according to Baranov et al[9], the equation of motion of an electron in the first and second magnets for small values of momentum $\Delta p_0 = p - p_0$ can be written in the form

$$ \left(\frac{d^2\rho}{d\varphi^2}\right)_i + (1 + \alpha)\,\rho_i = \frac{\Delta p_0}{p_0}, \tag{5} $$

where p is the momentum of the electron, and p_0 is its momentum in moving along the central orbit with $r = r_0$ in the field $H_0(r_0, 0)$.

The solution of (5), defining the electron trajectory in the first magnet for the initial conditions ${}^1\rho_1 = {}^1\psi_{r1} = 0$ is given by

$$ \rho_1(\varphi, p) = \frac{\Delta p_0}{p_0(1 + \alpha)}(1 + \cos\sqrt{1 + \alpha}\,\varphi). \tag{6} $$

From (6), using Eqs.(3a) and (4), for $\varphi = 0$ we obtain the initial conditions for electron motion in the second magnet:

$$ {}^2\rho_2 = -\frac{2\,\Delta p_0}{p_0(1 + \alpha)} \quad \text{and} \quad {}^2\psi_{r2} = 0. \tag{7} $$

Solving Eq.(5) for the initial conditions (7), we obtain the following expression for the electron trajectory in the second magnet:

$$ \rho_2(\varphi, p) = \frac{\Delta p_0}{p_0(1 + \alpha)}(1 - 3\cos\sqrt{1 + \alpha}\,\varphi). $$

The dispersion γ of electrons in momentum in the spectrometer[13], defined by the linear dispersion

$$ \Delta r_0 = r_0\{{}^3\rho_2(\pi\sqrt{2}, p) - {}^3\rho_2(\pi\sqrt{2}, p_0)\} = 8r_0\frac{\Delta p_0}{p_0}, $$

is given by the expression

$$\gamma = \frac{e}{c} \cdot \frac{\Delta r_0}{\Delta p_0} = \frac{e}{c} \cdot \frac{8 \cdot r_0}{p_0} = \frac{8}{H_0}, \qquad (8)$$

where e is the electron charge and c is the velocity of light.

This value of the dispersion is twice the dispersion ($\gamma = 4/H_0$) obtaining in the case of single $\pi\sqrt{2}$ focusing.[14]

In all our calculations we have neglected distortion of the electron trajectories in the narrow section between magnets, as well as electron scattering in the target, films and gas of counter C_1 and the residual gas in the spectrometer chamber.

Resolution of the Spectrometer

The line half-width $\Delta(Hr_0)$ (width at half-height) for monoenergetic electrons can be determined on the basis of the spectrometer geometry, taking into account multiple scattering of the electrons in the target and the windows and gas of counter C_1.

The relative line half-width $\frac{\Delta(Hr_0)}{Hr_0}$ associated with the geometry of the instrument, has been calculated theoretically. According to our evaluations (and those of Daniel[15]), the electron trajectories in the field of the second and first magnets, which does not depend on the azimuthal angle φ and is determined in the $z = 0$ plane by the series (1) with $\alpha = -1/2$, can be represented by the equations:

$$\begin{aligned}
\rho_i(\varphi) = {} & \left[{}^k\rho_i + \frac{2\beta-1}{3}({}^k\rho_i)^2 + \frac{3-4\beta}{6}({}^k\xi_i)^2 + \frac{8\beta-1}{3}({}^k\psi_{ri})^2 + \right. \\
& \left. + \frac{3-8\beta}{3}({}^k\psi_{zi})^2\right]\cos\frac{\varphi}{2^{1/2}} + \left[2^{1/2}\,{}^k\psi_{ri} + \frac{2^{1/2}(1-2\beta)}{3}\,{}^k\rho_i\,{}^k\psi_{ri} + \frac{2^{3/2}\beta}{3}\,{}^k\rho_i\,{}^k\psi_{zi}\right]\sin\frac{\varphi}{2^{1/2}} + \\
& + \left\{\frac{\beta}{3}\left[2({}^k\psi_{zi})^2 - ({}^k\xi_i)^2\right] - \frac{1+4\beta}{12}\left[2({}^k\psi_{ri})^2 - ({}^k\rho_i)^2\right]\right\}\cos(2^{1/2}\varphi) + \\
& + \left[\frac{1+4\beta}{2^{1/2}\cdot 3}\,{}^k\rho_i\,{}^k\psi_{ri} + \frac{2^{3/2}\beta}{3}\,{}^k\xi_i\,{}^k\psi_{zi}\right]\sin(2^{1/2}\varphi) + \\
& + \frac{1-4\beta}{4}\left[2({}^k\psi_{ri})^2 + ({}^k\rho_i)^2\right] + \frac{2\beta-1}{2}\left[2({}^k\psi_{zi})^2 + ({}^k\xi_i)^2\right]; \qquad (9)
\end{aligned}$$

$$\begin{aligned}
\xi_i(\varphi) = {} & \left[{}^k\xi_i + \frac{6-16\beta}{3}\,{}^k\psi_{ri}\,{}^k\psi_{zi} - \frac{4\beta}{3}\,{}^k\rho_i\,{}^k\xi_i\right]\cos\frac{\varphi}{2^{1/2}} + \\
& + \left[2^{1/2}\,{}^k\psi_{zi} - \frac{2^{1/2}(3-4\beta)}{3}\,{}^k\xi_i\,{}^k\psi_{ri} - \frac{2^{3/2}\beta}{3}\,{}^k\rho_i\,{}^k\psi_{zi}\right]\sin\frac{\varphi}{2^{1/2}} + \\
& + \frac{4\beta-3}{3}\left[{}^k\psi_{ri}\,{}^k\psi_{zi} - \frac{{}^k\rho_i\,{}^k\xi_i}{2}\right]\cos(2^{1/2}\varphi) + \\
& + \frac{3-4\beta}{2^{1/2}\cdot 3}\left[{}^k\xi_i\,{}^k\psi_{ri} + {}^k\rho_i\,{}^k\psi_{zi}\right]\sin(2^{1/2}\varphi) + \\
& + (4\beta-1)\left[{}^k\psi_{ri}\,{}^k\psi_{zi} + \frac{{}^k\rho_i\,{}^k\xi_i}{2}\right]. \qquad (10)
\end{aligned}$$

The trajectory equations were calculated to second order terms relative to the initial coordinates ${}^k\rho_i$ and ${}^k\xi_i$ and tangents ${}^k\psi_{ri}$ and ${}^k\psi_{zi}$ of the initial angles of emergence of the electron from the target ($k = 1$) for the first magnet and the intermediate focus ($k = 2$) for the second magnet.

Applying Eqs. (9) and (10) to the first magnet ($i = 1$) and using Eqs. (3) and (4), we find the initial conditions for motion of an electron in the second magnet ($i = 2$) in terms of the coordinates ${}^1\rho_1$ and ${}^1\xi_1$ and the tangents ${}^1\psi_{r1}$ and ${}^1\psi_{z1}$ of the angles

of emergence of the electron at the initial point on the target:

$$^2\rho_2 = {}^1\rho_1 - \frac{2-4\beta}{3}({}^1\rho_1)^2 - \frac{4\beta-3}{3}({}^1\xi_1)^2 - \frac{2-16\beta}{3}({}^1\psi_{r1})^2 - \frac{16\beta-6}{3}({}^1\psi_{z1})^2;$$

$$^2\xi_2 = {}^1\xi_1 - \frac{8\beta}{3}{}^1\rho_1\,{}^1\xi_1 - \frac{32\beta-12}{3}{}^1\psi_{r_1}\,{}^1\psi_{z1};$$

$$^2\psi_{r2} = \frac{{}^1\psi_{r1} + {}^1\rho_1\,{}^1\psi_{r1} + \frac{8\beta}{3}{}^1\xi_1\,{}^1\psi_{z1}}{1 - {}^1\rho_1 + \frac{2-4\beta}{3}({}^1\rho_1)^2 + \frac{4\beta-3}{3}({}^1\xi_1)^2 + \frac{2-16\beta}{3}({}^1\psi_{r1})^2 + \frac{16\beta-6}{3}({}^1\psi_{z_1})^2}; \qquad (11)$$

$$^2\psi_{z2} = \frac{{}^1\psi_{z1} + \frac{3-8\beta}{3}{}^1\rho_1\,{}^1\psi_{z1}}{1 - {}^1\rho_1 + \frac{2-4\beta}{3}({}^1\rho_1)^2 + \frac{4\beta-3}{3}({}^1\xi_1)^2 + \frac{2-16\beta}{3}({}^1\psi_{r1})^2 + \frac{16\beta-6}{3}({}^1\psi_{z1})^2} \times$$

$$\times\left\{1 - \frac{1}{2}\left[\frac{{}^1\psi_{r1} + {}^1\rho_1\,{}^1\psi_{r1} + \frac{8\beta}{3}{}^1\xi_1\,{}^1\psi_{z1}}{1 - {}^1\rho_1 + \frac{2-4\beta}{3}({}^1\rho_1)^2 + \frac{4\beta-3}{3}({}^1\xi_1)^2 + \frac{2-16\beta}{3}({}^1\psi_{r1})^2 + \frac{16\beta-6}{3}({}^1\psi_{z1})^2}\right]^2\right\}.$$

Inserting the initial conditions (11) into Eqs.(9) and (10) and setting $\varphi = \pi\sqrt{2}$, we determined the coordinates $^3\rho_2$ and $^3\xi_2$ of the point of intersection of the electron trajectory with the $\varphi = \pi\sqrt{2}$ plane, containing the receiving slit S_2. The results of calculation carried out to second order terms relative to the coordinates $^1\rho_1$ and $^1\xi_1$ and tangents $^1\psi_{r1}$ and $^1\psi_{z1}$ of the angles of emergence from the initial point on the target can be presented in the form

$$^3\rho_2 = -{}^1\rho_1 + \frac{4-8\beta}{3}({}^1\rho_1)^2 + \frac{8\beta-6}{3}({}^1\xi_1)^2 + \frac{4-32\beta}{3}({}^1\psi_{r1})^2 + \frac{32\beta-12}{3}({}^1\psi_{z1})^2; \qquad (12)$$

$$^3\xi_2 = -{}^1\xi_1 + \frac{16\beta}{3}{}^1\rho_1\,{}^1\xi_1 + \frac{64\beta-24}{3}{}^1\psi_{r1}\,{}^1\psi_{z1}. \qquad (13)$$

Comparison of Eqs.(12) and (13) with the analogous expressions for the coordinates for the point of intersection of the electron trajectory with the $\varphi = \pi\sqrt{2}$ plane for a β-spectrometer with simple $\pi\sqrt{2}$ focusing (see Refs.16, 13 & 8), shows that all the aberration terms in (12) and (13) are increased by a factor of 2. Addition of the aberrations in the case of the double spectrometer under consideration occurs owing to the opposite orientation of the fields in the magnets and the two-fold inversion of the image of the target relative to the coordinates r and z, in accord with first order focusing.

The width Q^{**} and height h^{**} of the image of the target T at the focus of the receiving slit S_2 can be calculated by means of Eqs.(12) and (13). For a target of area $Q \times h$, where h is the height, for the tangent ψ_r^0 of the radial angle and the tangent ψ_z^0 of the axial angle of acceptance, which determine the aperture of the electron beam, we obtain

$$Q^{**} = Q + \frac{|4\beta-3|}{6}\cdot\frac{h^2}{r_0} + \frac{|4-32\beta|}{3}r_0(\psi_r^0)^2 + \frac{|32\beta-12|}{3}r_0(\psi_z^0)^2; \qquad (14)$$

$$h^{**} = h + \frac{8\beta}{3}\cdot\frac{Qh}{r_0} + \frac{|128\beta-48|}{3}r_0\psi_r^0\psi_z{}^0. \qquad (15)$$

The basic resolution R_0 (Ref.13) of a spectrometer with receiving slit S_2 of width Q is given by

$$R_0 = \frac{Q+Q^{**}}{\gamma H r_0} = \frac{Q+Q^{**}}{8r_0}, \qquad (16)$$

where γ is the dispersion (see Ref.8) and Q^{**} is the width of the image of the target T at the slit S_2. The relation between the basic resolution R_0 and the resolution $R_{1/2}$, determined by the relative line half-width $\frac{\Delta(Hr_0)}{Hr_0}$ for monoenergetic electrons, depends on the intensity distribution over the line. For practical purposes a sufficiently good approximation[8,13,16] is given by

$$R_{1/2} = \frac{\Delta(Hr_0)}{Hr_0} \approx \frac{1}{2} R_0. \tag{17}$$

Using Eqs.(14), (16) and (17), we find the resolution of the spectrometer as a function of the dimensions of the target $Q \times h$, the width Q of the receiving slit S_2, the tangent ψ_r^0 of the radial and tangent ψ_z^0 of the axial aperture angles and the field coefficient β:

$$R_{1/2} = \frac{2Q}{16\, r_0} + \frac{|4\beta - 3|}{96}\left(\frac{h}{r_0}\right)^2 + \frac{|1 - 8\beta|}{12}(\psi_r^0)^2 + \frac{|8\beta - 3|}{12}(\psi_z^0)^2. \tag{18}$$

The above calculations of the resolution $R_{1/2}$ of the spectrometer were carried out on the assumption that there is no collimation or limiting of the electron beam by the slit S_1. The maximum opening of slit S_1, satisfying this assumption, is determined as follows. We establish at the central orbit $r = r_0$ a magnetic field H_0 for which the centers of the images of the target T on the slits S_1 and S_2 coincide with the centers of the slits. The width of the target image on the slit S_1 (see Ref.13) $Q^* = Q + \Delta$, where Δ is the sum of all the aberration terms; according to Eq.(14) the width of the image at slit S_2 is $Q^{**} = Q + 2\Delta$. For small variations of the field H about the H_0 value for the central orbit, the difference $^k(r - r_0)_i$ between the radial coordinates of the center of the slit (r_0) and the edge (r) corresponding to the image of the target will vary as

$$\begin{aligned} {}^2(r - r_0)_1 &= -4r_0 \frac{H - H_0}{H_0} \pm \frac{Q^*}{2} \quad \text{for slit } S_1, \text{ and} \\ {}^3(r - r_0)_2 &= -8r_0 \frac{H - H_0}{H_0} \pm \frac{Q^{**}}{2} \quad \text{for slit } S_2. \end{aligned} \tag{19}$$

where the plus sign in both equations is taken for the edge of the image located at the greater radius.

Fig.3 shows the radial coordinates of the points of the image of the target T on the slits S_1 bounded by solid lines) and S_2 (bounded by dashed lines) as a function of small changes in the magnetic field, as deduced by means of Eq.(19). The edges of the receiving slit S_2 are indicated by the lines with hatching in the figure. The width d of slit S_1, as determined from the condition that slit S_1, defining the electron beam, covers the image of the target at slit S_2 outside the boundaries of slit S_2, is shown in Fig.3 by the solid heavy line. As will be evident from the figure, on this condition the width d and position of slit S_1 depend on the strength of the magnetic field. If we choose the width of S_1 to be constant and equal to Q (see Fig.3), the image of the target T on slit S_2 will appear only in the region indicated by hatching in the figure. In this case the image of the target within the range of slit S_2 is not limited by slit S_1 and is focused onto slit S_2 as though slit S_1 were absent. The resolution $R_{1/2}$ of the spectrometer with this width of slit S_1 is given by Eq.(18). As will readily be evident from analysis of Fig.3, the resolution of the spectrometer does not depend on the width of slit S_1. The width of slit S_1 determines only the height of the monoenergetic electron peak.

We calculated the resolution of the spectrometer by means of Eq.(18) for the following parameters: widths of target T and slits S_1 and S_2 $Q = 1$ cm, height

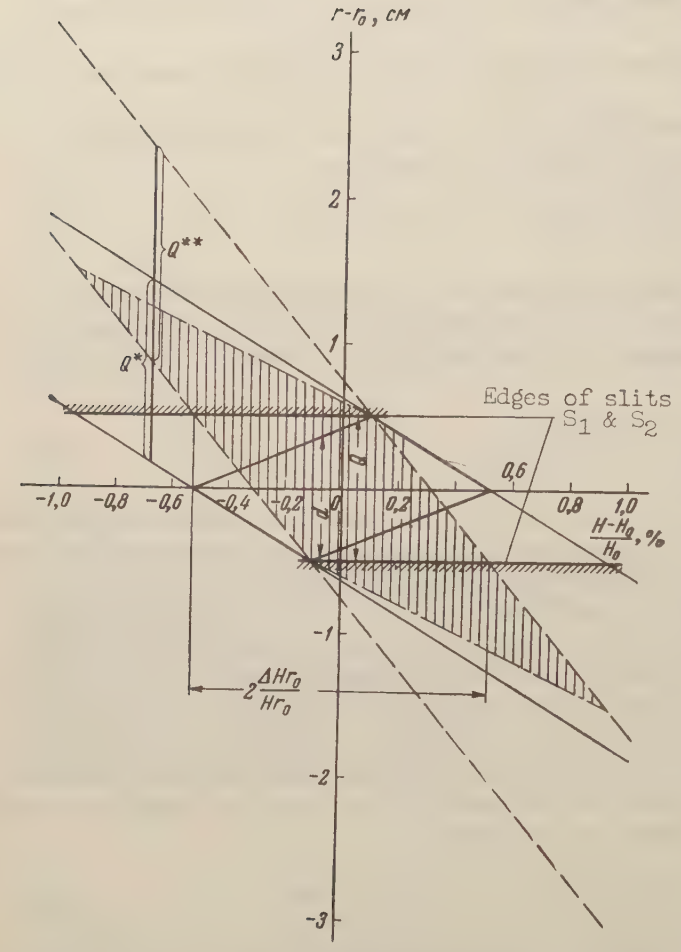

Fig.3. Variation of the radial coordinates of the points of the image of the target on slits S_1 and S_2 as a function of small changes of the magnetic field. Q is the width of slits S_1 and S_2. Q^* is the width of the image on slit S_1. Q^{**} is the width of the image on slit S_2. The region of appearance of the image of the target on slit S_2 is hatched. $2\frac{\Delta(Hr_0)}{Hr_0}$ is the relative basic line width.

of target h = 3 cm, central orbit radius r_0 = 30 cm, tangent of the radial aperture angle ψ_r^0 = 0.24, tangent of the axial aperture angle ψ_z^0 = 0.068 and field coefficient β = = 1/8, and obtained $R_{1/2}$ = 0.52%. This part of the resolution was also found experimentally from the half-width of the K conversion electrons of 624 kev energy emitted by Ba^{137}. These measurements were carried out with the electrons being detected only by counter C_2, i.e., without counter C_1. The section of the conversion electron spectrum shown in Fig.4,a was measured with a Cs^{137} source having an area of 1 x 3 cm and slits S_1 and S_2 set to a width of 1 cm. The experimental resolution (0.56%) differs from the theoretical value (0.52%) mainly owing to scattering of the electrons by the cladding and backing of the Cs^{137} source.

Scattering of electrons in the films and gas of counter C_2 leads to loss of electrons, reduction of their energy by an amount equal to the probable energy loss in films and gas with a common thickness of ~1 mg/cm^2, and broadening of the energy distribution of the electrons owing to appreciable fluctuation of the energy loss.[16,17] Fig.4,b shows the K line of conversion electrons from the 558 keV transition in Cd^{114}. In this case the electrons were detected using both counters and the widths of the target and slits S_1 and S_2 were all 1 cm. According to evaluations[16] the fraction of the line half-width associated with broadening of the electron energy distribution in passing through counter C_1 amounts to about 0.05%. This increases with decrease of the electron energy and attains the value of ~0.1 at 300 keV.[16]

The influence of the thickness of the matter and backing of the target on the half-width of the detected line is close to the analogous influence of the thickness of the source in β-spectroscopy, which has been considered by a number of authors[16,18,19]. The thickness of the matter of the target may vary from 0.01 to 5 mg/cm^2.

The natural width of the conversion line, associated with the width of the corresponding atomic levels[20,21], may be evinced in measurements with the given

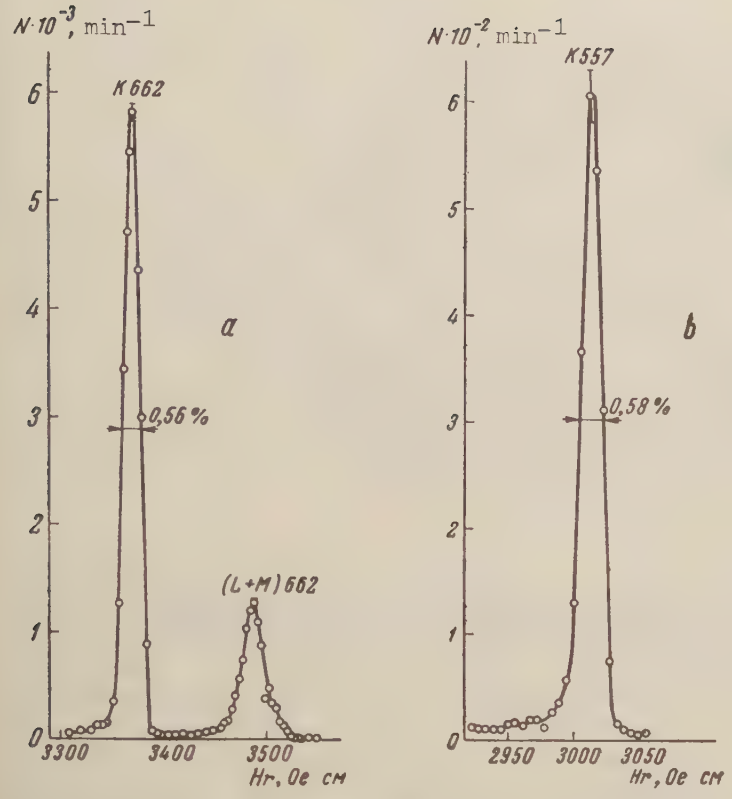

Fig.4. Conversion electron lines recorded on the spectrometer: a - transition in Ba^{137}, b - transition in Cd^{114}.

spectrometer only for transitions of low energy (~50 keV) in nuclei with a high atomic number. For $Z \approx 90$ the natural width Γ_K of the K line exceeds the width of the L lines.[20-23] For Z = 96 the width $\Gamma_K \approx 100$ eV.[23] The natural conversion line width for nuclei with $Z > 40$ varies according to the $Z^{3.4}$ law.[23,24]

Doppler broadening owing to nuclear recoils due to γ-rays preceding the converted transition can virtually be neglected.

Relative Solid Angle

The electron beam focused by the spectrometer with a 1 x 3 cm target is defined by two 5.8 x 20 cm apertures mounted in the gaps of the first and second magnets in the $|\varphi| = \pi\sqrt{2}$ planes. At the intermediate focus the electron beam is virtually not limited in the z direction. The mean relative solid angle of the spectrometer under the given conditions is given by the formula

$$\overline{\Omega} \approx \frac{S}{8\pi r_0^2} \varkappa_1 \varkappa_2, \qquad (20)$$

where $\frac{S}{8\pi r_0^2}$ is the relative solid angle for a point of the target with coordinates $^1\rho_1 = {}^1\xi_1 = 0$ (Ref.9), and $\varkappa_1$ and $\varkappa_2$ are numerical coefficients. By introduction of the coefficient $\varkappa_1$, calculated by means of Eqs.(9) and (10) and equal to 0.95, there was taken into account the dependence of the relative solid angle on the coordinates of points on the target. The coefficient $\varkappa_2$ determines the fraction of the intensity of the image of the target within the limits of the height of slit S_2, inasmuch as the image of the target on slit S_2 is substantially magnified in the z direction (see Eq.(15)). For a slit height of 4 cm the coefficient $\varkappa_2$ obtained from the z intensity distribution calculated by means of Eqs.(12) and (13) equals 0.9; the corresponding values for a slit height of 6 cm is 0.99. The mean relative solid angle $\overline{\Omega}$ of the spectrometer, as given by Eq.(20) for a height of slit S_2 equal to 4 cm is 0.44%, and for a height of 6 cm 0.48%.

Design of the Spectrometer

A vertical section through the spectrometer along the symmetry axis of the fields of the first and second magnets is shown in Fig.5.

The pole pieces are made of Armco iron, and simultaneously serve as covers of the vacuum chamber. The side walls of the chamber are made of 1Kh18N9T stainless steel. The outside diameter of the pole pieces is 92 cm. The width of the

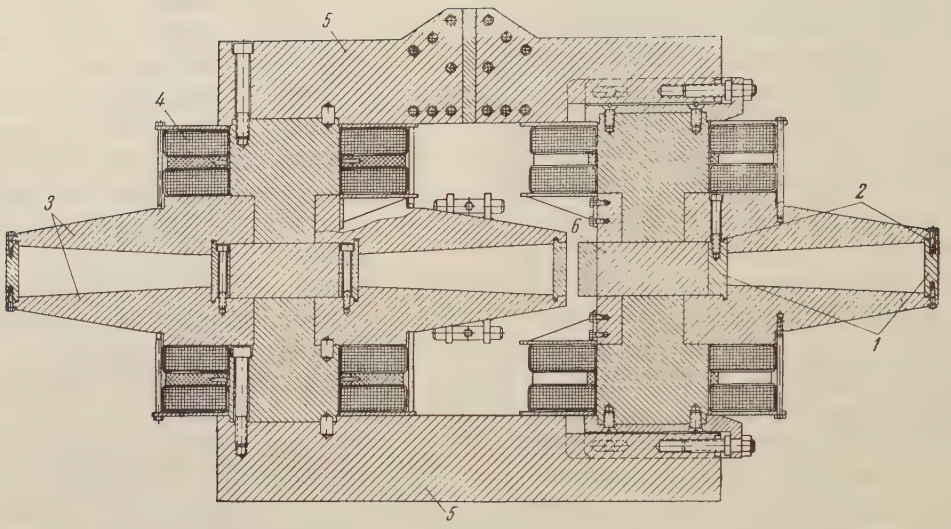

Fig.5. Vertical section of the spectrometer in the plane passing through the symmetry axes of the magnets: 1 - wall of vacuum chamber, 2 - rubber gasket, 3 - pole pieces, 4 - magnet winding, 5 - yoke, 6 - lead block.

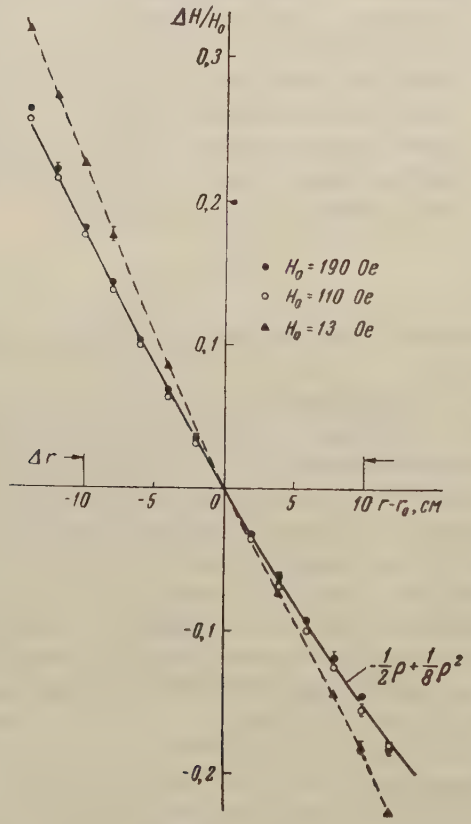

Fig.6

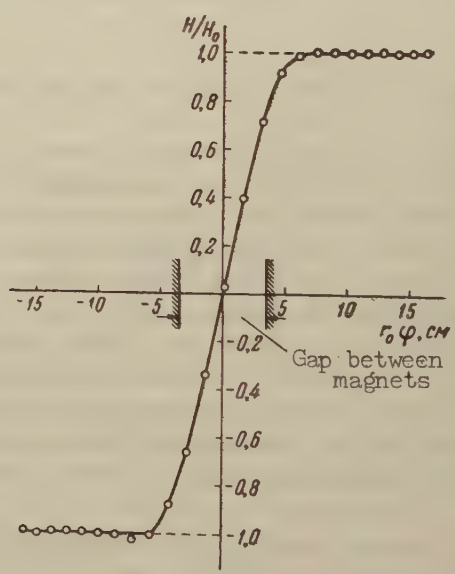

Fig.7

Fig.6. Radial distribution of the magnetic field in the magnet gap. The solid line ($-\frac{1}{2}\rho + \frac{1}{8}\rho^2$) gives the theoretical distribution; Δr is the maximum width of the magnetic path occupied by the electron orbits.

Fig.7. Magnetic field distribution in the intermediate focus, measured along the central electron orbit $r = r_0$.

gap at the central orbit is 7 cm. The magnets are connected in series in a common magnetic circuit by means of a yoke of steel 3. The cross section of the yoke perpendicular to the magnetic flux is 324 cm^2. The length of the electron trajectory along the central orbit (Fig.2) is 267 cm. The magnet windings, which consist of eight sections of 800 turns each provide a magnetic field of up to ~400 oersted at a current of 1250 ma, which corresponds to focusing of electrons of ~3 MeV energy. The total weight of the spectrometer including the transport dolly, the shielding plate and the lead blocks inside the chamger protecting the counters is about 3 metric tons.

The radial field distribution was measured in the gaps of both magnets of the spectrometer along the lines of intersection of the $z = 0$ plane with the $|\varphi| = \pi\sqrt{2}$ planes. In the $|\varphi| = \pi\sqrt{2}$ planes the distance of the investigated points of the field from the radial section of the pole pieces exceeds twice the magnet gap. At the given excitation current the field distributions in all the indicated directions measured by the ballistic method agree within 0.5% for the two magnets. Fig. 6 shows the radial field distribution in the gaps of the first and second magnets for the $|\varphi| = \pi\sqrt{2}$ planes obtained at different field strengths at the central orbit $r = r_0$. In the figure the vertical axis is scaled in $\frac{H(r) - H(r_0)}{H(r_0)}$. The solid line shows the calculated theoretical distribution (see Eq.(1)). The maximum width of the magnetic path Δr, occupied by the electron orbits, is indicated in the figure. As will be evident, at field strength of 190 and 110 oersted the experimental and theoretical distributions agree within the limits of the calculation and experimental errors. For a field of ~13 oersted the radial distribution changes. The variation of the field configuration with field strength in the range of weak fields is due to nonlinearity of the magnetic characteristics of the iron.[12,25,26] As a result of this variation the resolution of the spectrometer $R_{1/2} \approx$ 0.6% decreases for electrons with energies under ~300 keV (H_0 = 70 oersted) owing to nonagreement of the radial and axial foci of the fields of the first and second magnets. Correlation of the fields by means of special coils allows of improving the fraction of the resoltuion associated with the geometry of the instrument to ~0.8% for electrons of ~50 keV energy.*

Fig.7 shows the magnetic field distribution at the intermediate focus, measured in the $z = 0$ plane along the central electron orbit $r = r_0$. Here the vertical axis is scaled in terms of H/H_0, where H_0 is the field at the central orbit in the $|\varphi| = \pi\sqrt{2}$ plane ($H_0 \sim$ 110 Oe); the horizontal scale is laid off in terms of the distance $r_0\varphi$ along the central orbit from the intermediate focus to the given point. The gap between the neighboring radial sections of the pole pieces of the first and second magnets is shown to scale. As will be evident from the figure, the transition section of the field has a length of ~13 cm, which equals approximately 5% of the total length of the electron trajectory along the central orbit.

---

*After the present report was written and presented at the Eleventh Annual Conference on Nuclear Spectroscopy we carried out further work on improving the correlation windings. As a result at present the spectrometer is adjusted for conversion electrons with energies in the range from 20 to 300 keV as well. The part of the relative half-width of the apparatus K electron line dependent on the spectrometer geometry equals ~1.9 and 0.8% for conversion electrons of 29 and 132 keV energy, respectively, when the width of the target T and the slits S_1 and S_2 are all 1 cm.

The current feeding the electromagnets is stabilized to within 1 in 10^4. The magnetic field is measured by the compensation method with a permalloy saturated probe with an accuracy of $\sim 5 \cdot 10^{-5}$. The probe is located in the stray field of the second magnet. The electromagnet is demagnetized prior to each measurement by means of an automatic circuit in order to minimize the influence of residual magnetization on the field configuration.

The pressure in the vacuum chamber of the spectrometer is maintained at $\sim 5 \cdot 10^{-3}$ mm Hg. In detecting electrons with energy below ~300 keV the vacuum in increased to $\sim 5 \cdot 10^{-5}$ mm Hg. At these pressures one can neglect the effect of scattering of the electrons in the residual gas in the entire range of measured electron energies. The windows of the Geiger-Müller counters C_1 and C_2 are made of 3 μ thick terilene film. The counters are filled with a mixture of 80% argon plus 20% alcohol to a pressure of 80 mm Hg. The electron loss in the first counter (C_1) amounts to ~50% at electron energy of 531 keV and to ~30% at an energy of 1278 keV.

In order to insure the highest specific activity, the targets to be used in the spectrometer will be prepared of isotopes enriched to the highest possible degree.

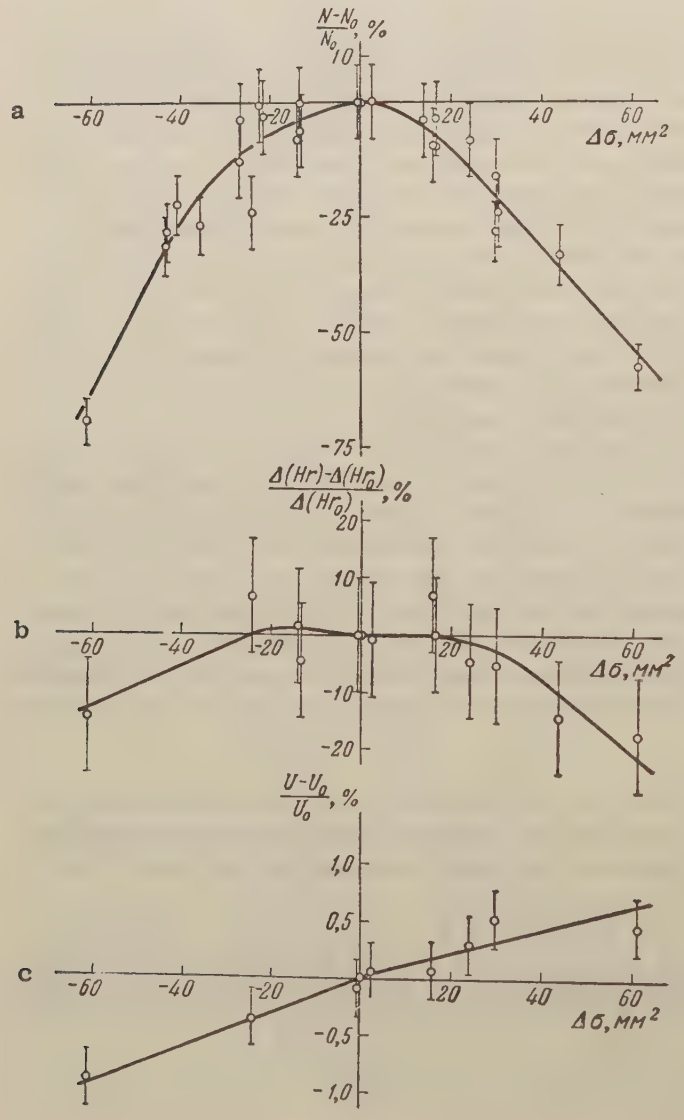

←Fig.8. Variation of the height N_0 (a), half-width $\Delta(Hr)_0$ (b) and position U_0 on the calibration scale (c) of the 531 keV conversion line (K line of the 558 keV transition in Cd^{114}) as a function of the cross section of the shunt used to obtain the optimum relation between the magnet fields.

Adjustment of the Spectrometer

For adjustment of the spectrometer one must determine the position of the foci of the first and second magnets relative to the intermediate focus (the location of slit S_1) and to establish over the entire investigated electron energy range the optimum relation between the magnet fields, providing the maximum height of the recorded conversion line. Alignment of the symmetry planes of the fields of the first and second magnets and correct relative location of the target T and the slits S_1 and S_2 is insured by the design, machining and assembly of the spectrometer.

Here we shall consider only the requirement as regards setting the optimum relation between the fields of the two magnets, a requirement common to all double systems.[27] The

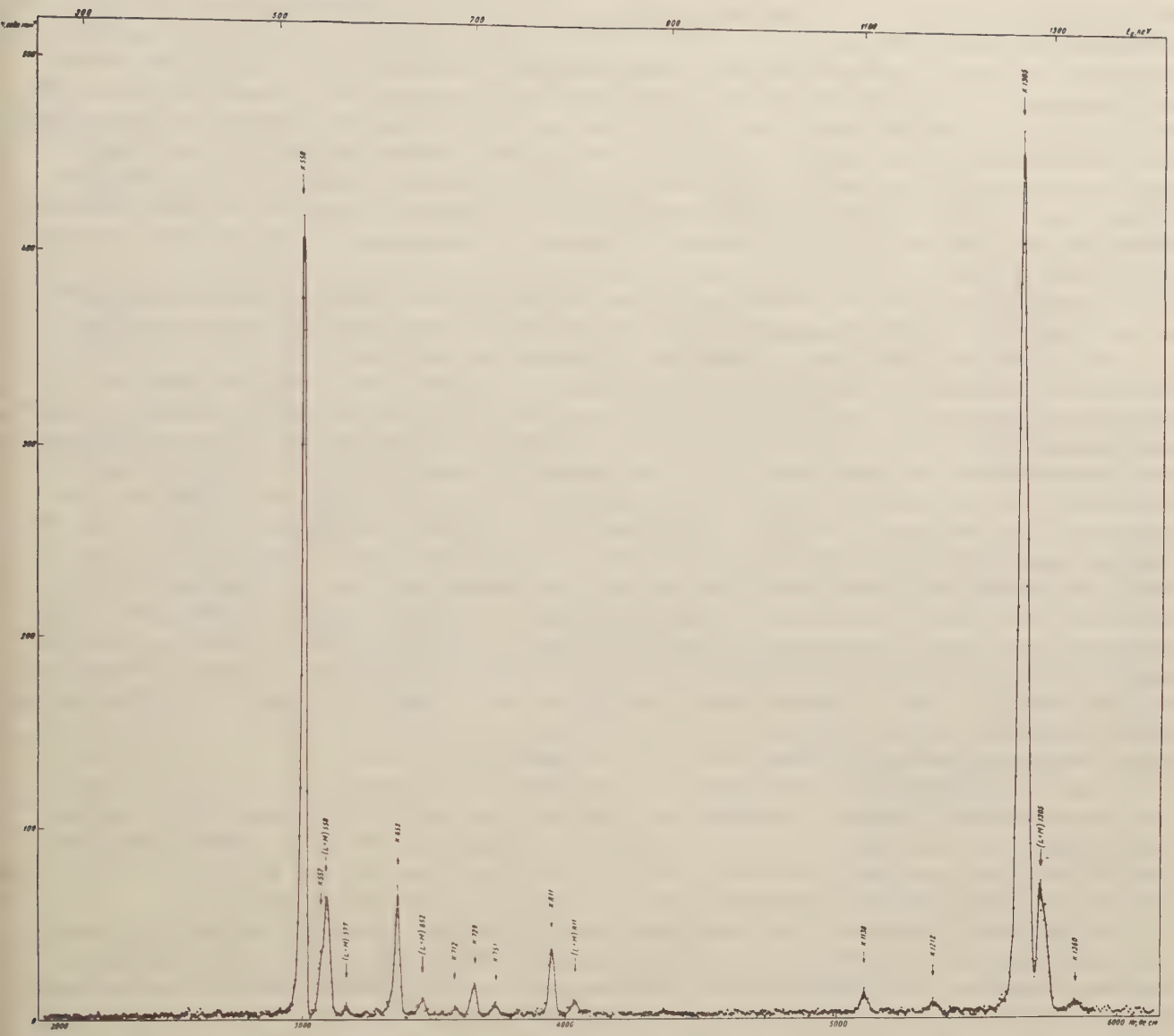

Fig.9. Experimental spectrum of internal conversion electrons from the $Cd^{113}(n,\gamma)Cd^{114}$ reaction.

optimum relation of the fields must be found experimentally owing to possible differences (0.1-0.2 mm) between the gaps in the magnets, the presence of an external magnetic field, the presence of steel objects in the vicinity of the spectrometer and the appreciable energy loss by the electrons in the films and gas of counter C_1. Inasmuch as the energy loss varies with the electron energy[16,17], the optimum relation between the fields also depends on the electron energy. Variation in the relation between the fields of the magnets is realized by means of magnetic shunts - a set of steel plates with a cross section of 10-15 mm^2 - which are used to "short" the gap of one of the magnets. The shunts are applied to the outside circumference of the pole pieces at the maximum distance from the electron trajectory. Tests showed that shunting does not affect the focusing of the electrons by the given magnet. Fig.8 shows the relative variation in the height N_0, half-width

$\Delta(Hr)_0$, and position U_0 on the calibration scale of the K conversion line of the 558 keV transition in Cd^{114} as a function of $\Delta\sigma$, the transverse cross section of the shunt in the first magnet, used to obtain the optimum field relation. The character of these dependences can be explained by means of Fig.3, if one takes into account the intensity distribution over the image of the target on slits S_1 and S_2. As will be evident from Fig.8, for establishing the optimum relation between the magnet fields one must select the proper cross section of the shunt with an accuracy of ~5 mm^2. The variation of the cross section of the shunt as a function of the strength of the magnetic field was obtained for conversion electrons of 290, 531 and 1278 keV energy by means of curves similar to that reproduced in Fig.8,a.

To evaluate relative energies in investigating conversion electron spectra we have plotted calibration curves on the basis of electrons of known energy.

To illustrate the type of spectra obtained by the spectrometer in Fig.9 we reproduce the experimental spectrum of internal conversion electrons emitted in the thermal neutron irradiation of cadmium. The ~0.8 mg/cm^2 thick target of cadmium oxide, enriched to ~85% Cd^{113}, was located at a distance of ~9 meters from the reactor core, in distinction to the geometry shown in Fig.1. The background measured with the neutron beam shuttered by a ~1 mm thick cadmium plate at the exit from the reactor shielding, amounted to 0.3 coincidences per min and was subtracted in plotting the reproduced spectrum. This low background is attained mainly by using the coincidence procedure for detecting the conversion electrons, focusing them from the target in the direction opposite to that of incidence of neutron beam, high dispersion of the instrument, the presence of slit S_2, and the appreciable separation between the counters (48 cm) as well as between counter C_2 and the beam (85 cm). Chance coincidences do not exceed 0.05 per min. The individual loadings of counters C_1 and C_2 in measuring sections of the spectrum between intense conversion lines differ by a factor of ~13.

The low background level makes it feasible to use the described instrument for investigating internal conversion electron spectra of isotopes with a relatively small cross section for slow neutron absorption. With a thermal neutron flux of $\sim 10^9$ neutron cm^{-2} sec^{-1} to the target, the lower bound for the neutron absorption spectrum for bombarded nuclei with $Z \geqslant 50$ is ~50 barns.

We desire to express our gratitude to L.V.Groshev and A.M.Demidov for guidance in the work, D.V.Pavlov for useful suggestions in discussing the design of the spectrometer, I.M.Kamyshev for working out certain design details and preparing the drawings, A.C.Volkov for designing the control equipment and supervising its installation, and F.V.Nemtsov for high quality workmanship in assembling the spectrometer.

References

1. H.T.Motz, Phys.Rev., 104, 1353 (1956).

2. L.V.Groshev, A.M.Demidov, V.N.Lutsenko & V.I.Pelekhov, Report presented at the Second All-Union Conference on Nuclear Reactions at Low and Medium Energies, Moscow, July, 1960.

3. C.T.Hibdon & C.O.Muehlhause, Phys.Rev., 88, 943 (1952).

4. E.L.Church & M.Goldhaber, Phys.Rev., 95, 626 (1954).

5. L.V.Groshev, A.M.Demidov & V.A.Naidenov, Izv.AN SSSR, Ser.fiz., 21, 1619 (1957). (Trans.Bulletin, 21, 1606.)

6. H.Maier-Leibnitz, Symposium on Pile Neutron Research in Physics, Vienna, 1962. (Pub.Vienna, 1962.)

7. V.V.Goncharov, E.N.Babulevich, Yu.G.Nikolaev & Yu.F.Chernilin, Report No.2185 presented at the Second International Conference on the Peaceful Uses of Atomic Energy, Geneva, 1958.
8. C.DeVries & A.H.Wapstra, Nucl.Instr. and Meth., 8, 121 (1960).
9. S.A.Baranov, A.F.Malov & K.N.Shlyagin, PTE (Instruments & Experimental Techniques), No.1, 3, (1956).
10. E.Huster, G.Lehr & W.Walcher, Z.Naturforsch., 10A, 83 (1955).
11. G.E.Lee-Whiting & E.A.Taylor, Canad.J.Phys., 35, 1 (1957).
12. H.Wild & O.Huber, Helv.phys.acta, 30, 3 (1957).
13. E.Persico & C.Geoffrion, Rev.Sci.Instr., 21, 945 (1950).
14. N.Svartholm & K.Siegbahn, Arkiv.Mat.Astr.Fys., 33A, No.21 (1946).
15. H.Daniel, Rev.Sci.Instr., 31, 249 (1960).
16. Kai Siegbahn (ed.), Beta- and Gamma-Ray Spectroscopy, N.Y., 1955.
17. E.Segrè (ed.), Experimental Nuclear Physics, N.Y., 1953.
18. B.N.Subba Rao, Proc.Ind.Acad.Sci., 51A, 28 (1960).
19. L.V.Groshev & I.S.Shapiro, Spektroskopiya atomnykh yader (Spectroscopy of Atomic Nuclei), M., 1952.
20. H.Slätis & G.Lindstrom, Phys.Rev., 88, 1429 (1952).
21. H.Slätis, Arkiv fys., 6, 415 (1953).
22. M.Mladjenovic, Arkiv fys., 8, 27 (1954).
23. R.L.Graham, G.T.Ewan & J.S.Geiger, Nucl.Instr. and Meth., 9, 245 (1960).
24. B.G.Gokhale, Ann.phys., 7, 852 (1952).
25. K.E.Bergkvist, Arkiv fys., 12, 381 (1957).
26. P.H.Stoker, Ong ping hok, E.F.DeHaan & G.J.Sizoo, Physica, 20, 337 (1954).
27. L.V.Groshev, A.M.Demidov, V.N.Lutsenko & A.F.Malov, Izv.AN SSSR, Ser.fiz., 24, 791 (1960). (Trans.Bulletin, 24, 794.)

INVESTIGATION OF THE POSITRON AND CONVERSION ELECTRON SPECTRA OF Tb^{152}

- K.Ya.Gromov, B.S.Dzhelepov, Zh.T.Zhelev & A.V.Kudryavtseva

The present work was devoted to investigation of the β^+ and conversion electron spectra of Tb^{152} by means of a triple focusing β-spectrometer[1].

The terbium fraction was separated from a tantalum target bombarded for two hours with 660 MeV protons. The fraction contained several groups of terbium isotopes with close periods: Tb^{150} (3.5 hr) & Tb^{149} (4.1 hr), Tb^{154}, Tb^{152} & Tb^{151} (17-20 hr), Tb^{153} (62 hr) and Tb^{155} (5.6 day) & Tb^{156} (5.2 day).

The conversion electron spectrum and β^+-spectrum of the terbium fraction are rather complicated; hence difficulties are encountered in attempting to interpret them. Actually, for correct identification of the lines one should investigate the spectra of the separated isotopes. In the present case, in order to obtain Tb^{152} in almost pure form we separated the terbium from the dysprosium fraction extracted in the usual manner from the tantalum target. The dysprosium fraction was first held for four hours; during this time there could build up in it Tb^{152} from 2.5-hr Dy^{152} and smaller amounts of Tb^{153} from 6.3-hr Dy^{153} and Tb^{155} from 10-hr Dy^{155}.

Conversion Electron Spectrum

The conversion electron spectrum of Tb^{152} has been investigated repeatedly[2-7]. The results of different authors as regards the region up to 600 keV are generally in good agreement. The 600 to 1100 keV section has been investigated only in the work of Anton'eva et al[2] and Toth et al[7]. Anton'eva et al observed lines with energies of 977 ± 5 keV (T = 8 hr) and 1050 ± 5 keV (T = 18 hr), which they attributed to decay of Tb^{154} (at the time Tb^{152} was not known). Toth et al observed only one of these: the K line of the 1047 keV transition.

We investigated the conversion electron spectrum of Tb^{152} in the energy range from 530 to 1550 keV, and detected 12 conversion lines. The conversion spectrum

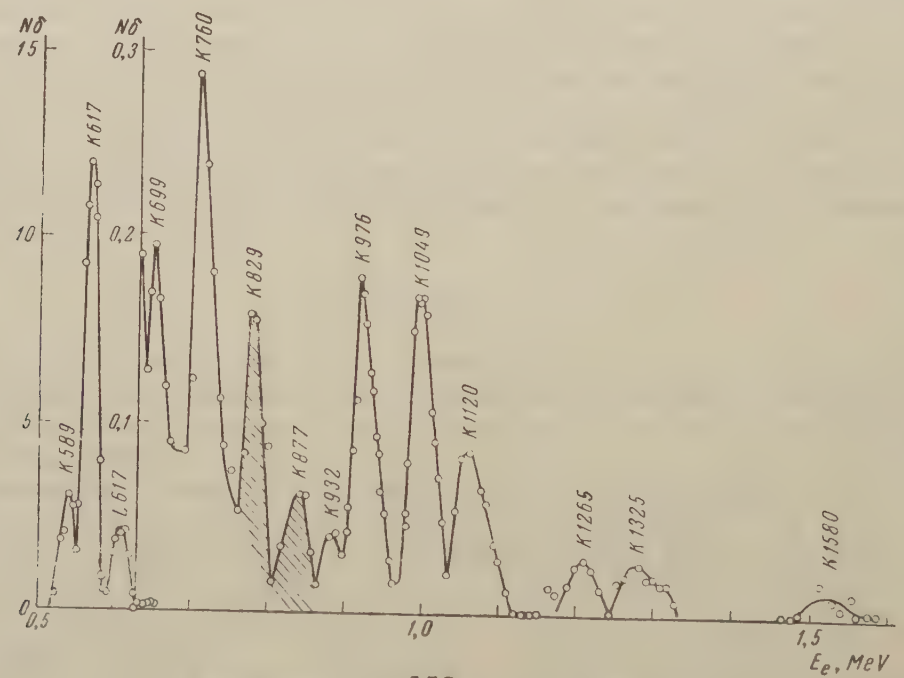

Fig.1 Conversion electron spectrum of Tb^{152} in the 530 to 1550 keV energy range. The hatched lines belong to Tb^{153}.

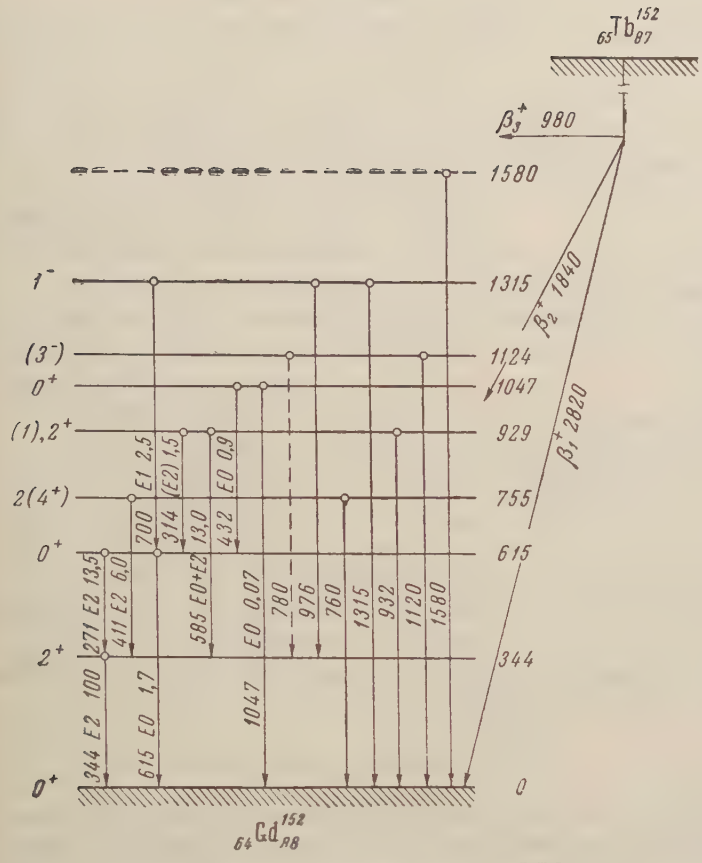

Fig.2. Decay scheme for Tb^{152}.

is reproduced in Fig.1; the data pertaining to the detected lines are listed in Table 1. Our data for all the lines observed by Toth et al[7] are in agreement, within the limits of the experimental error, with the energy and intensity values of these authors except for the K1047 line, for which Toth et al reported an intensity twice as great as ours.

The newly detected transitions with energies 699, 760, 932, 976, 1120 and 1325 keV and the earlier known 589, 617 and 1049 keV transitions can readily be accomodated in the level diagram for Gd^{152} (daughter of Tb^{152} and Eu^{152}) given by Toth et al[7] (Fig.2). In addition to the earlier known levels in Gd^{152}, which are excited in β^--decay of Eu^{152} (Ref.8), Toth et al introduced two new levels at 929 keV (1+ or 2+) and 1047 keV (0+). In the recorded conversion electron spectrum there appear lines corresponding to crossover transitions from these two levels to the ground state of Gd^{152}; this substantiates the low spin values assigned to these levels. The 760 ± 4 keV transition apparently departs from the 755 keV level to the ground state. If this is the case, the spin of the 755 keV level cannot be 4 (Toth et al give $2,(4)^+$); accordingly, we opt for 2. Toth et al report that they observed 780 keV γ-rays that are in cascade with γ-rays of 344 keV energy. We were unable to distinguish the K780 line; it must be at least four times weaker than the K760 line.

In the investigated energy region we also detected two lines, apparently, K829 and K887, the intensity of which fell off with a period of 2.5-3 days. Probably, these belong to Tb^{153}.

Table 1

Data on the conversion electrons of Tb^{152}

E_e, keV	Identification	$I/I_{\beta+}$,%	$T_{1/2}$, hr	Transition energy according to other authors [Ref]
539±3	K 589	2,1	18	85 [7], 588 [5], 589 [2] 587,3 [6], 586 [4]
567±2	K 617	9,2	18	616 [2, 5]
609±3	L 617	2,0	19	615 [4, 7], 615,9 [6]
649±4	K 699	0,22	21	—
710±4	K 760	0,32	20	—
882±5	K 932	0,039	~20	—
926±4	K 976	0,19	18	977 [2]
998,5±4	K 1049	0,22	18	1050 [2], 1047 [7], 1050 [4], 1049 [5]
1070±7	K 1120	0,11	~18	—
1215±8	K 1265	0,035	~18	—
1275±10	K 1325	0,039	~20	—
1530±14	K 1580	—	—	—

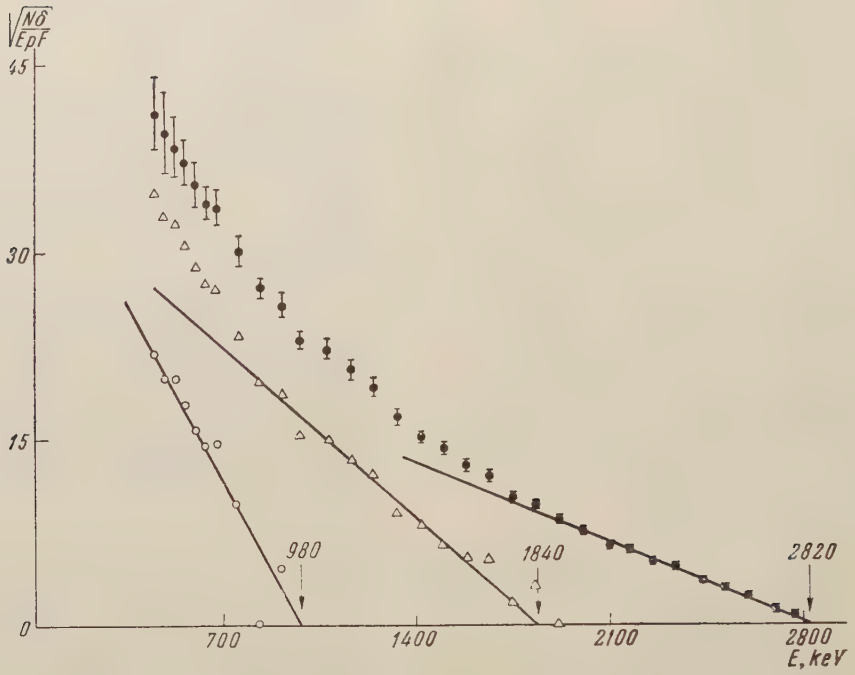

Fig.3. Kurie plot of the β^+-spectrum of Tb^{152}.

Table 2
Data on the positron spectrum of Tb^{152}

Component	E_{ep}, keV	β_i/β_1
β_1	2820±40	1
β_2	1840±100	0,65
β_3	980±120	0,18

β^+-Spectrum

In 1958 Anton'eva et al[2] observed a positron spectrum with T ≈ 18 hr consisting of components with end-point energies 750 ± 100, 1650 ± 80 and 2800 ± 50 keV and relative intensities 0.15:0.25:1. At the time they attributed this spectrum to Tb^{154}.

In 1960, Bonch-Osmolovskaya et al[11] in working with a dysprosium fraction observed build up of a positron spectrum, which they attributed to Tb^{152} on the basis of the available data. The end-point energies were determined as 1650 ± 100 and 2700 ± 100 keV, and the relative intensities as 0.33:1.

As noted above, in the present work we investigated the positron spectrum of Tb^{152}. The Kurie plot is reproduced in Fig.3. It will be evident that the β^+-spectrum is complex and consists of at least three components. The data on the positron spectrum are listed in Table 2.

According to the calculations of Riddel[9] and Cameron[10] the Tb^{152} - Gd^{152} mass difference equals 2181 and 3278 keV, respectively. As will be evident from the table, according to our data, the mass difference for these isobars is at least 2820 ± 40 keV. The accuracy in determining the end-point energies of the other two components is relatively low and it is impossible at present to determine what levels they feed.

We desire to express our gratitude to I.A.Yutlandov and Yu.Norseev for preparing the sources.

Joint Institute for Nuclear Research, &
Leningrad State University

References

1. B.S.Dzhelepov, Zh.T.Zhelev, A.V.Kudryavtseva, O.V.Larionov, M.K.Nikitin & R.Stepich, Preprint OIYaI (Preprint Joint Inst.for Nucl.Research), P-587, Dubna 1960.

2. N.M.Anton'eva, A.A.Bashilov, B.S.Dzhelepov & B.K.Preobrazhenskii, Doklady AN SSSR, 119, 241 (1958). (Trans.Doklady.)

3. K.S.Toth, K.T.Faler & J.O.Rasmussen, Phys.Rev., 115, 158 (1959).

4. A.S.Basina, K.Ya.Gromov & B.S.Dzhelepov, Preprint, Joint Inst.for Nuclear Research, No.595, Dubna, 1960.

5. A.A.Abdurazakov, K.Ya.Gromov, B.S.Dzhelepov & G.Ya.Umarov, Ibid., 595.

6. A.T.Strigachev, L.S.Novikov, A.A.Sorokin, B.S.Shpinel' & V.A.Khalkin, Doklady na III soveshchanii po neitrono-defitsitnym izotopam redkikh zemel' (Report presented at the Third Conference on Neutron-Deficient Rare Earth Isotopes), Dubna, 1960.

7. K.S.Toth, O.B.Nielson & O.Skilbreid, Nucl.Phys., 19, 389 (1960).

8. B.S.Dzhelepov & L.K.Peker, Skhemy raspada radioaktivnykh yader (Decay schemes of radioactive nuclei), M., 1958.

9. J.Riddel, A Table of Levy's Empirical Atomic Masses, SRP-654, Chalk River, 1957.

10. A.Cameron, A Revised Semi-Empirical Atomic Mass Formula, No.433, Chalk River, 1957.

11. N.A.Bonch-Osmolovskaya, B.S.Dzhelepov & O.E.Kraft, Izv.AN SSSR, Ser.fiz., 24, 283 (1960). (Trans.Bulletin, 24, 270.)

INTERNAL CONVERSION COEFFICIENTS OF SOME TRANSITIONS IN Yb^{171}

- N.M.Anton'eva & B.S.Dzhelepov

Lutetium-171 decays by electron capture to different excited states of Yb^{171}. Investigators[1-3] have reported over 30 transitions in Yb^{171} with energies in the range from 19 to ~900 kev. Accordingly, the decay scheme is very complicated and in order to plot it one must know the spin assignments, and to establish these it is essential to determine the multipole orders of the transitions in Yb^{171}.

In view of this we undertook to measure the internal conversion coefficients for some of the transitions in Yb^{171} by means of the photoelectron-conversion electron procedure developed by Adamchuk, Bashilov & Preobrazhenskii[4]. In this procedure α_K is determined by measuring for the same source the number n_e of conversion electrons and the number n_γ of photoelectrons ejected from a calibrated radiator by means of a magnetic spectrometer. The value of the internal conversion coefficient is given by the formula[4]

$$\alpha_K = g\tau\frac{n_e}{n_\gamma},$$

where τ is the photoelectric absorption coefficient and g is a function of the energy and the parameters of the instrument and can be determined by means of special calibration experiments using sources emitting γ-rays with known conversion coefficients. In the present experiments we used a bismuth target (σ = 1.6 mg/cm^2), i.e., the same radiator as was employed by Adamchuk, Bashilov & Preobrazhenskii[4]. However, in view of the fact that in our experiments with Yb^{171} we used an appreciably larger source it was necessary to correct the calibration of the radiator; this was done with reference to Cs^{137} γ-rays from a source of appropriate size.

We determined the internal conversion coefficients for two nuclear transitions in Yb^{171}: the 668.2 and 740.9 keV transitions. The activity was obtained from a tantalum target bombarded with 660 MeV protons in the Joint Institute for Nuclear Research synchrocyclotron for 12 hours. The rare earths were extracted from the Ta target and then separated chromatographically into elementary fractions. The lutetium fraction was held for ~10 days prior to measurement.

The conversion electron and photoelectron spectra with the background subtracted are reproduced in Fig. 1 and Fig.2. It must be noted that the photoelectron peaks were observed against a substantial background due mainly to Compton recoils from the hard γ-rays.

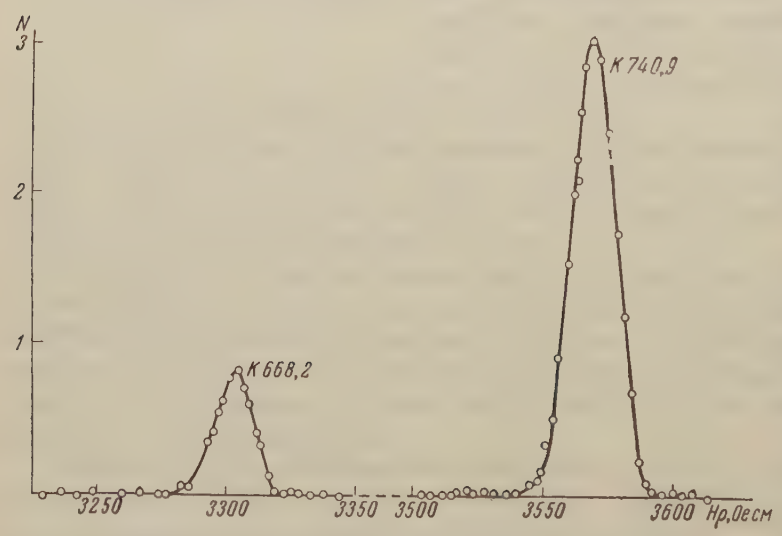

Fig.1. Conversion electron spectrum of Lu^{171} in the region of the K668.2 and K740.9 lines. N = thousands of pulses per min.

Our experimental results are summarized in Table 1. The figures represent averages for several series of measurements. The intensity ratio $K_{668.2}/K_{740.9}$ = = 0.29 ± 0.01. According to the data of Harmatz, Handley & Mihelich[3] this ratio equals 0.32. This divergence is probably explained by the fact that Harmatz et al recorded their spectra photographically, a procedure that involves ap-

Table 1

Experimental data for the 668.2 and 740.9 keV γ-transitions in Yb^{171}

E_γ, keV	τ, см$^{-1}$	$g\cdot10^4$, см	$\frac{n_e}{n_{e_1}}\cdot100$	$\frac{n_\gamma}{n_{\gamma_1}}\cdot100$	$\frac{n_e}{n_\gamma}$	$\alpha_K\cdot10^4$
668,2	0,457	1,73	29±1	32±3	34±3	27±4
740,9	0,364	1,76	100	100	38±3	24±3

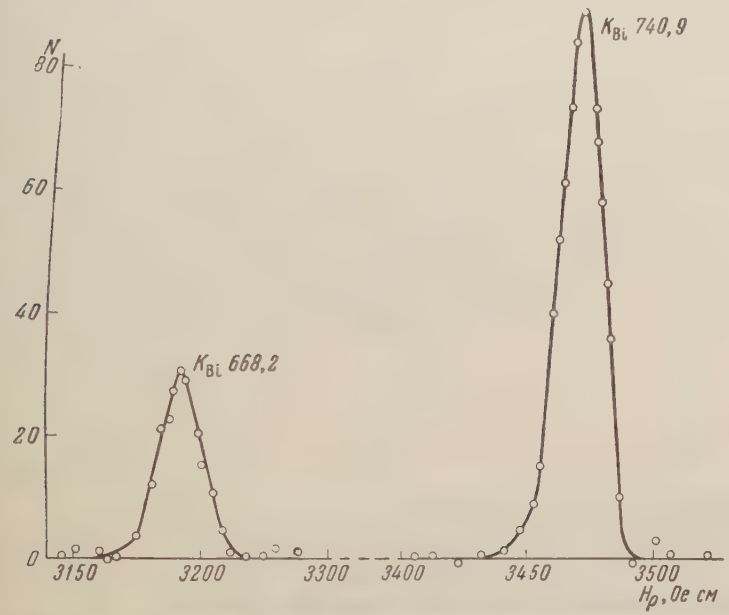

Fig.2. Spectrum of photoelectrons ejected by the 668.2 and 740.9 kev γ-rays of Lu^{171} from a bismuth radiator (τ = 1.6 mg/cm^2). N = = pulses per min.

preciable errors.

Our results also allow of calculating the relative γ-rays intensities: $I_{668.2}/I_{740.9}$ = 0.26 ± ± 0.03. Hitherto the relative intensities of the γ-rays of Lu^{171} have been measured only in the work of Lebedev et al[5] by means of a scintillation spectrometer. The 668.2 and 740.9 keV γ-transitions were not resolved in this investigation.

Our experimental values for the internal conversion coefficient are compared with the theoretical values[6] in Table 2 and in Fig.3. It will be evident that both transitions can definitely be identified as E1.

Harmatz, Handley & Mihelich[3] propose a decay scheme for Lu^{171} in which the 668.2 keV transition is located between levels with 7/2- and 9/2+, and the 740.9 keV transition is shown in two alternate locations: between 7/2- and 7/2+ and between 9/2- and 7/2- states. Our results are in agreement with these assignments for the 668.2 keV transition and with the first alternative for the 740.9 keV transition.

Table 2

Multipole orders of the transitions in Yb^{171}

E_γ, keV	Experimental value $\alpha_K\cdot10^2$	Theoretical values $\alpha_K\cdot10^2$					Assignment
		E1	E2	E3	M1	M2	
668,2	0,27±0,04	0,28	0,71	1,7	1,7	4,6	E1
740,9	0,24±0,03	0,23	0,57	1,3	1,3	3,4	E1

Scientific-Research Physical Institute at
Leningrad State University

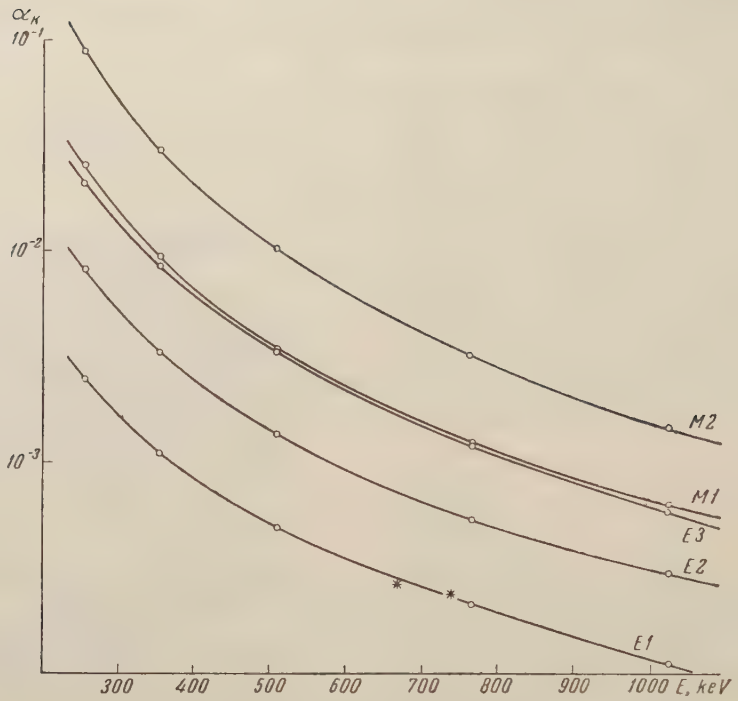

Fig.3. Theoretical values of α_K according to Sliv & Band[6] for different multipole orders as a function of energy for Z = 70. The two asterisks represent the experimental values of α_K for the 668.2 and 740.9 keV transitions.

References

1. K.Ya.Gromov, B.S.Dzhelepov, Materialy II Soveshchaniya po neitrono-defitsitnym izotopam redkikh zemel' (Transactions of the 2nd Conference on Neutron-Deficient Rare Earth Isotopes. I. Lutetium fraction.), Dubna, 1959.

2. J.W.Mihelich, B.Harmatz & T.H.Handley, Phys.Rev., 108, 989 (1957); Ibid 114, 1082 (1959).

3. B.Harmatz, T.H.Handley & J.W.Mihelich, Ibid., 119, 1345 (1960).

4. V.K.Adamchuk, A.A.Bashilov & B.K.Preobrazhenskii, Izv.AN SSSR, Ser.fiz., 22, 919 (1958). (Trans.Bulletin, 22, 911.)

5. A.N.Lebedev, A.N.Silant'ev & I.A.Yutlandov, Ibid., 22, 839 (1958). (Trans.Bulletin, 22, 833.)

6. L.A.Sliv & I.M.Band, Tablitsy koeffitsientov vnutrennei conversii γ-izlucheniya (Tables of internal conversion coefficients), Part I, K-shell. M.-L, 1956.

CONVERSION ELECTRON SPECTRUM OF Tm^{165}

- Kang Meng-Hua, K.Ya.Gromov, B.S.Dzhelepov, V.Zvol'ska & I.Zvol'skii

The conversion electron spectrum of Tm^{165} has been investigated by Gromov et al[1,2] and by Mihelich & co-workers[3,4]. Dzhelepov & Peker[6] in their book analyze the decay schemes for Tm^{165} given by different authors and propose a more complete level diagram. The existence of levels with energies with 77.2, 243.0, 296.2, 297.5 and 356.6 keV has been proved by e^--e^- coincidence measurements in the work of Dzhelepov & Sergienko[8]. Of the 65 transitions now known to occur in Er^{165}, 41 do not fit into this scheme. It is obvious that one must introduce new levels - primarily high-lying levels. Accordingly, the present work was concerned with determining the energies of the γ-transitions in Er^{165} to within 0.1%, mainly with a view to introducing new levels into the decay scheme for Tm^{165}.

We investigated the conversion electron spectrum on a double focusing β-spectrometer with the magnetic field being monitored by the method of proton resonance in the electron energy range above 55 keV and by the method of a saturated probe in the lower energy range. The thulium activity was obtained by chromatographic separation from a mixture of rare earth elements produced by bombardment of a tantalum target with 660 MeV protons.

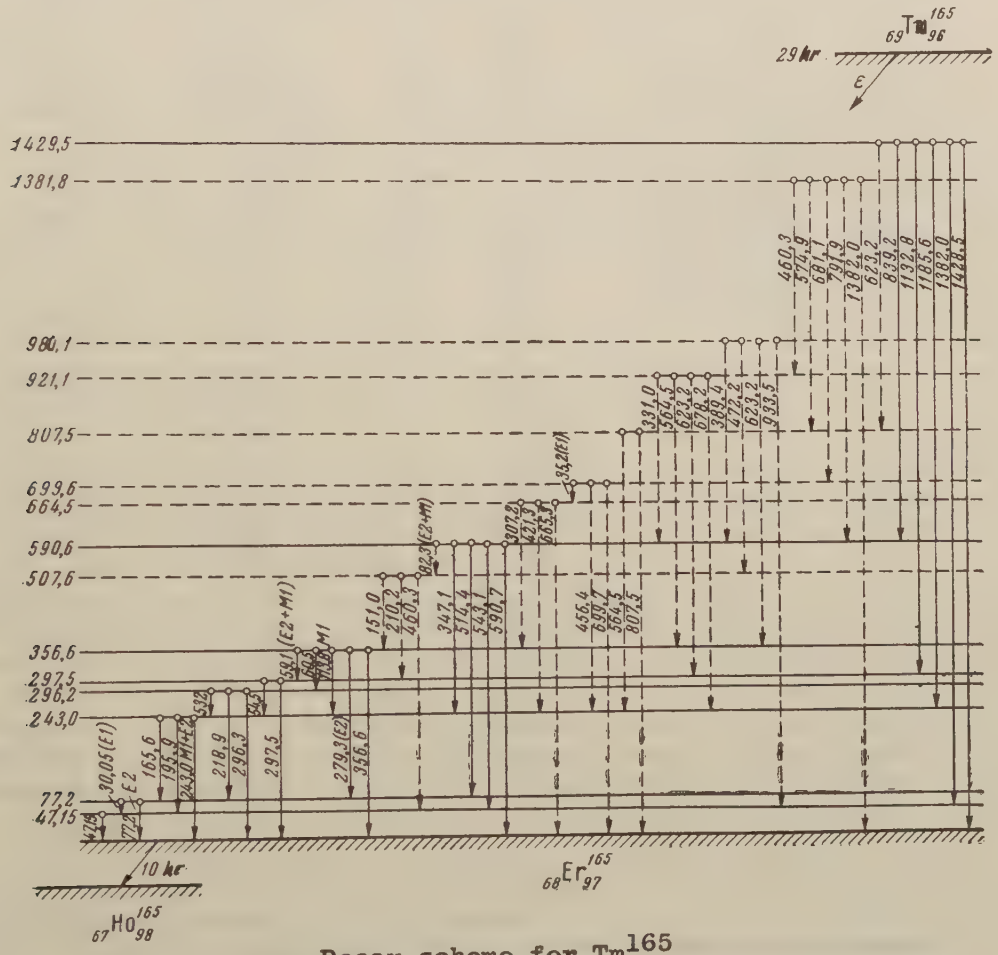

Decay scheme for Tm^{165}

Table 1

Energies of γ-transitions in Er^{165} and relative intensities of the K conversion lin

No.	Gromov et al[1,2,5]		Harmatz et al[4]		Our data	
	hν, keV	I	hν, keV	I	hν, keV	I
1*	—	—	15,45	—	—	—
2	—	—	30,05	—	—	—
3	—	—	35,2	—	—	—
4	—	—	47,15	—	47,15	—
5	} 53,2	—{	53,2	—	53,2	—
6			54,45	—	54,50	—
7	—	—	59,15	—	—	—
8	—	—	60,4	—	60,5	—
9*	—	—	70,6	250	70,6	—
10	77,4	140	77,2	90	77,2	—
11	82,3		82,25	~1,9	82,3	—
12*	—		86,9	weak	—	—
13*	—		88,2	20	—	—
14	112,8	59	113,6	300	113,8	—
15	—	—	151,0	8	151,0	9±1
16	165,4	7	165,8	7	165,6	8±1
17	—	—	196,0	5	195,9	4,5±0,8
18	—	—	210,3	4,5	210,2	4,6±0,6
19	219,5	157	219,3	132	218,9	132±10
20	242,8	1000	243,3	1000	243,0	1000
21	279,0	7	279,4	6,6	279,3	5,7±0,6
22	}298	—{	296,5	70	296,3	74±10
23			297,8	115	297,5	125±14
24	307,0	4	307,3	2,5	307,2	2,6±0,3
25*	312,1	10	312,7	10	312,3	8,0±1,5
26	330,7	4	331,1	2,7	331,0	2,5±0,3
27	347		347,3	35	347,1	36±9
28	356,9		356,9	20	356,6	19±2
29*	366,0	6,0	365,9	6,1	365,6	4,4±0,9
30*	(~378)	4	—	—	—	—
31*	389,4	4,3	389,7	4,4	389,4	4,3±0,9
32	421,9	1,5	420,7	1,3	421,3	1,1±0,2
33*	443,6	2,2	442,6	1,5	443,2	1,4±0,5
34*	(449,1)	2,4	448,4	1,3	448,7	1,4±0,3
35	457,2	}17	456,1	5,7	456,4	6,9±1,5
36	460,4		460,3	11,3	460,3	13,0±1,7
37	471,6	2,7	471,5	1,9	472,2	1,5±0,3
38*	(478,5)	2,8	477,4	2,1	478,1	1,9±0,3
39*	488,2	6,0	487,1	5,3	487,8	4,7±1,4
40	—	—	513,4	1,6	514,4	1,4±0,3
41*	—	—	526,8	1,9	527,2	2,1±0,3
42	543,5	5,1	542,6	4,6	543,1	4,3±0,4
43*	—		558,4	1,1	559,4	1,5±0,3
44	566,0	1,0	564,3	8,5	564,5	8,9±1
45*	—	—	575,0	<1,4	574,9	<1,4**
46	—	—	590,0	<3,4	590,7	<3,3***
47	—	—	623,5	~0,6	623,2	0,7±0,3
48	—	—	665,3	1,0	665,3	1,0±0,3
49	—	—	677,5	0,45	678,2	0,32±0,13
50	—		681,3	~0,3	681,1	0,29±0,12
51			699,3	1,4	699,7	1,57±0,5
52			791,5	~0,3	791,9	0,42±0,13
53	807,1	17	807,4	14,5	807,5	21±2
54	838,3	1,2	838,4	0,7	839,2	0,9±0,2
55*	—	—	893,1	0,1	—	—
56	—	—	933,5	0,1	—	—
57*	—	—	953,4	0,15	954,1	0,25±0,08
58	1132,9	0,3	1132,6	0,3	1132,8	0,5±0,15
59*	~1146	~0,1			—	—
60*	~1154	~0,1			1154,7	0,13±0,07
61	1179	0,5				
62	1187	0,5	1186,0	0,44	1185,6	0,5±0,1
63	—	—	1381,4	0,17	1382	0,17±0,08
64	—	—	—	—	1428,5	0,35±0,15

*Transition not accomodated in the decay scheme.

**Together with the L526.8 line. ***Together with the L542.6 line.

Table 2

Energy balances in the proposed Er^{165} level diagram

Assumed level energy, keV	Energy of cross-over transition or sum of energies of transitions departing from the given level, keV		Assumed level energy, keV	Energy of cross-over transition or sum of energies of transitions departing from the given level, keV	
	Cascade	Sum		Cascade	Sum
47,15	Cross-over transition	47,15	664,5	Cross-over transition	665,3
				243,0+421,3	664,3
77,2	Cross-over transition	77,2		356,6+307,9	663,8
	47,15+30,05*	77,2	699,6	Cross-over transition	699,7
243,0	Cross-over transition	243,0		243,0+456,4	699,4
	47,15+195,9	243,0		664,5+35,2*	699,7
	77,2+165,6	242,8	807,5	Cross-over transition	807,5
296,2	Cross-over transition	296,3		243,0+564,5	807,5
	77,2+218,9	296,1			
	243,0+53,2	296,2	921,1	243,0+678,2	921,2
297,5	Cross-over transition	297,5		297,5+623,2	920,7
	243,0+54,4	297,4		356,6+564,5	920,7
				590,8+331,0	921,8
356,6	Cross-over transition	356,6	980,1	47,15+933,5*	980,6
	77,2+279,3	356,5		356,6+623,2	979,8
	243,0+113,8	356,8		507,6+472,2	979,8
	296,2+60,5	356,6		590,6+389,4	980,0
	297,5+59,1*	356,6	1381,8	Cross-over transition	1382,0
507,6	Cross-over transition	507,4		590,6+791,9	1382,5
	297,5+210,2	507,4		699,6+681,1	1380,7
	356,6+151,0	507,6		807,5+574,9	1382,4
				921,1+460,3	1381,4
590,6	Cross-over transition	590,7	1429,5	Cross-over transition	1428,5
	47,15+543,1	590,2		47,15+1382,0	1429,1
	77,2+514,4	591,6		243,0+1185,6	1428,5
	243,0+347,1	590,1		297,5+1132,8	1430,3
	507,6+82,3	589,9		590,6+839,2	1429,7
				807,5+623,2	1430,7

*The energy values for the 30.05, 35.2, 59.1 and 933.5 keV transitions have been taken from Harmatz et al[4].

The relative intensities of the K conversion lines and the corresponding transition energies are listed in Table 1, together with the data of Gromov et al[1,2,5] and Harmatz et al[4]. It will be evident that our data on the energies are in good agreement with the results of Harmatz et al.

On the basis of the transition energies listed in Table 1 we attempted to identify new high-lying levels in Er^{165}. The most plausible level diagram is shown in the accompanying figure. We cannot claim, however, that this diagram is definitive. In view of the great number of transitions in Er^{165}, even with the relatively high accuracy in determining transition energies attained in the work of Harmatz et al[4] and in the present experiments, there are many cases when the the sum of the energies of two transitions is equal within the limits of the error to the energy of a third transition. In many such cases identification of true cascades is a difficult problem. This is illustrated by the fact that some transitions can be located in the proposed scheme in several places: thus, for example, the 623.2 keV transition can be inserted in any one of three locations.

Different ways for arriving at the energy values for the levels in Er^{165} are shown in Table 2. It will be evident that the level energies determined by sum-

ming the energies of different transitions are in good agreement. It will be evident from Table 2 that our data on the transition energies substantiate the existence of levels with energies of 590.0, 665.3 and 807.4 keV proposed by Gromov & Dzhelepov[5]. According to our measurements the more accurate values for the energies of these levels are 590.6, 664.5 and 807.5 keV. On the basis of the energy balance one can also infer the existence of levels with energies of 507.6, 699.6, 921.1, 980.1, 1381.8 and 1429.5 keV (see figure). The level at 47.15 keV was introduced at the suggestion of L.K.Peker.

It will be obvious that for establishing the complete and definite decay scheme for Tm^{165} there is need for further experiments on γ-ray and conversion electron coincidences and measurements aimed at determining the multipole orders of the transitions.

References

1. K.Ya.Gromov, B.S.Dzhelepov & B.K.Preobrazhenskii, Izv.AN SSSR,Ser.fiz., 21, 918 (1957).(Trans. Bulletin, 21, 920.)

2. K.Ya.Gromov, B.S.Dzhelepov, A.G.Dmitriev, V.A.Morozov & K.I.Yakovlev, Ibid.,24, 272 (1960).(Trans. Bulletin, 24, 260).

3. J.W.Mihelich, B.Harmatz & T.H.Handley, Bull.Amer.Phys.Soc.,3, 358 (1958).

4. B.Harmatz, T.H.Handley & J.W.Mihelich, Phys.Rev.,114, 1082 (1959).

5. K.Ya.Gromov & B.S.Dzhelepov, Materialy II soveshchaniya po yadernoi spektroskopii neitronodefitsitnykh izotopov redkikh zemel' (Transactions of the 2nd Conference on Nuclear Spectroscopy of Neutron-Deficient Rare Earth Isotopes), Part II, Dubna, 1959.

6. B.S.Dzhelepov & L.K.Peker, Skhemy raspada radioaktivnykh yader (Decay schemes of radioactive nuclei), M.-L., 1958.

7. B.R.Mottelson & S.G.Nilsson, Mat.-Fys.Skr.Danske Videnskab Selskab, 1, No.8 (1959).

8. B.S.Dzhelepov & V.A.Sergienko, Transactions of the 2nd Conference on Nuclear Spectroscopy of Neutron-Deficient Rare Earth Isotopes, Part II, Dubna, 1959.

CONVERSION ELECTRONS FROM THE ERBIUM FRACTION FORMED IN SPALLATION OF TANTALUM

- A.A.Abdurazakov, K.Ya.Gromov, B.S.Dzhelepov & V.A.Khalkin

The following decay chains beginning with erbium are now known:

1. $Er^{165} \xrightarrow[EC]{10\ hr} Ho^{165}$ (stable),

2. $Er^{163} \xrightarrow[EC]{75\ min} Ho^{163} \xrightarrow{?} Dy^{163}$ (stable),

3. $Er^{161} \xrightarrow[EC,\beta^+]{3.5\ hr} Ho^{161} \xrightarrow[EC]{2.5\ hr} Dy^{161}$ (stable),

4. $Er^{160} \xrightarrow[EC]{29\ hr} Ho^{160} \xrightarrow[EC,\ \beta^+]{5\ hr;\ 22\ min} Dy^{160}$ (stable),

5. $Er^{158} \xrightarrow[EC]{2.5\ hr} Ho^{158} \xrightarrow[EC,\beta^+]{27\ min} Dy^{158}$ (stable),

(we list only the chains starting with neutron-deficient erbium isotopes; neutron-rich isotopes virtually do not form under the bombardment conditions employed in our experiments).

The erbium fraction was obtained by chromatographic separation from the rare earths formed by spallation of tantalum under bombardment with 660 MeV protons (bombardment time ~2 hrs). The conversion electron spectra were investigated by means of a uniform magnetic field β-spectrograph. The primary purpose of the measurements was to obtain more accurate transition energy values. We used two erbium sources. In exposing the plates in using the first source the field was set to record electrons with energies from 20 to 180 keV; in the exposures with the second source there were recorded electrons with energies from 135 to 900 keV. The exposures were started some 3-4 hours after the end of proton bombardment and approximately one hour after chromatograph separation of the erbium. Three plates were successively exposed with each source; the exposure time was chosen so as to provide for the possibility of distinguishing the lines of isotopes with different half-lives. For calibrating the spectrograms in energy we used the energy values for some of the transitions occurring in the decay of Er^{160}, determined by Grigor'ev et al[1]. Our data for the energies of the transitions in the $Er^{160} \rightarrow Ho^{160} \rightarrow Dy^{160}$ decay chain are compared with the data of Grigor'ev et al in Table 1.

Table 1

Energies (keV) of transitions evinced in $Er^{160} \rightarrow Ho^{160} \rightarrow Dy^{160}$

Our data	Ref. 1	Our data	Ref.1
60,1±0,1	60,1±0,1	*	645,5±0,4
*	86,84±0,07	*	728,5±0,5
*	197,0±0,2	754,1±1,0	754,5±0,6
297,4±0,5	297,7±0,3	765,5±1,0	765,7±0,6
298,6±0,5	298,8±0,3	873,1±1,0	872,5±0,8
406,0±0,6	405,7±0,4	*	879,8±0,6
513,9±0,6	513,5±0,4	*	962,8±0,6
*	538,7±0,4	966,1±1,0	966,4±0,6

*Transitions, the conversion lines of which were used for calibration in energy.

Table 2

Results of investigation of the conversion electron spectrum of the chain $Er^{161} \rightarrow Ho^{161} \rightarrow Dy^{161}$

$H\rho$, Oe cm	E_e, keV	Identification	Transition energy, keV
		$Er^{161} \rightarrow Ho^{161}$	
1427	155,4	K211,0	
1660	202,2	$(L_I + L_{II})$211,1	
1664	203,1	L_{III}211,2	211,1±0,3
1693	209,2	M_{III}211,1	
1700	210,6	N_I211,0	
3053	537,0	K592,6	
3228	583,2	L_I592,6	592;6±0,6
3925	771,6	K827,2	
4092	817,7	L_I827,0	827,1±1,0
4117	824,6	M_I826,7	
		$Ho^{161} \rightarrow Dy^{161}$ (stable)	
912,0	68,53	L_I77,61	
915,0	68,95	L_{II}77,57	
920,0	69,67	L_{III}77,52	77,6±0,1
960,4	75,51	M_{II}77,36	

For analysis of the experimental data we used the results of photometric scanning of the spectrograms. Processing of the photometry results for the purpose of determining the relative conversion line intensities has not yet been completed.

We did not observe any conversion lines that, on the basis of our rough data or the data in the literature, could be attributed to erbium isotopes with A = = 165 or A = 163. Thus we assign all the detected lines to the chains starting with Er^{161} and Er^{158}.

1. $Er^{161} \rightarrow Ho^{161} \rightarrow Dy^{161}$

The conversion lines attributed to the chain starting with Er^{161} are listed in Table 2. The 77.6 keV transition has been observed by a number of investigators, and in particular by Harmatz et al[2]. According to the data of these authors, this is the most intense transition occurring in the decay of Ho^{161}. Other, weaker transitions in Dy^{161} were not evinced in our plates. We attributed the transitions with energies of 211.1, 592.6 and 827.1 keV to the decay of Er^{161} to Ho^{161} on the basis of the studies of Dneprovskii[3,4], in which there was determined the period of decay in intensity of the conversion lines of these transitions. Moreover, the energy differences between the K, L and M conversion electron lines (Table 2) clearly indicate that these transitions occur in Ho^{161}.

2. $Er^{158} \rightarrow Ho^{158} \rightarrow Dy^{158}$

The conversion electron groups that we attribute to the $Er^{158} \rightarrow Ho^{158} \rightarrow Dy^{158}$ chain are listed in Table 3.

67.3 keV transition. According to our data, the energy difference between the L_{III} and N conversion lines of this transition gives reason to assert that this transition occurs in the holmium nucleus. According to Dneprovskii[4], the intensity of the conversion lines of this transition in the spectrum of the erbium fraction falls off with a period of 130 ± 25 min. Basina et al[5] observed the L line of this transition in the spectrum of their holmium fraction (from spallation of Ta) and established that its intensity falls off with a period of ~30 min. These facts show that the 67.3 keV transition takes place in Ho^{158}.

The conversion lines of the 67.3 keV transition are the most intense of the lines we have assigned to the $Er^{158} \rightarrow Ho^{158} \rightarrow Dy^{158}$ chain.

Table 3

Results of investigation of the conversion electron spectrum of the chain $Er^{158} \rightarrow Ho^{158} \rightarrow Dy^{158}$

$H\rho$, Oe cm	E_e, keV	Identification	$h\nu$, keV
		$Er^{158} \rightarrow Ho^{158}$	
838,2	58,43	L_{II} 67,35	67,3±0,1
844,0	59,20	L_{III} 67,27	
890,0	65,45	M_{II} 67,37	
900,0	66,84	N_I 67,28	
2234	331,2	K386,8	387,0±0,5
2426	377,8	L_I 387,2	
		$Ho^{158} \rightarrow Dy^{158}$ (stable)	
732,5	45,18	K98,97	99,0±0,1
1055	89,94	L_I 99,02	
1058	90,41	L_{II} 99,03	
1062	91,05	L_{III} 98,90	
1100	97,15	M_{II} 99,0	
1109	98,61	N_I 99,03	
1472	164,2	K218,03	218,1±0,2
Coincides with M211,1 Er^{161}		$(L_I + L_{II})$ 218,3	
Coincides with N211,1 Er^{161}		L_{III} 218,5	
1726	216,2	M_I 218,0	
1733	217,7	N_I 218,1	
1956	266,7	K320,5	320,5±0,5
2113	302,8	K356,6	356,6±0,5
2150	311,4	L_I 320,5	—
2304	348,1	L_I 357,2	
3172	568,5	K622,3	622,3±1,0
3265	593,0	K646,8	646,8±0,7
3579	677,3	K731,1	731,0±0,8
4006	794,0	K847,8	847,8±0,9
4014	796,3	K850,1	850,1±0,9
4359	891,9	K945,7	945,7±1,0
4369	894,7	K948,5	948,5±1,0

387.0 keV transition. This transition was observed by Dneprovskii[3] in investigating the conversion electron spectrum of a similar erbium fraction. He established on the basis of the decay period and the energy differences between the K, L and M lines that this transition occurs in Ho^{158}. Our value for the K - L line energy difference substantiates this deduction.

99.0 and 218.1 keV transitions. The energy differences between the conversion electrons of these transitions (Table 3) agree exactly with the corresponding tabular values for Dy. These transitions were observed in the spectrum of an erbium fraction by Dneprovskii[3] and in that of a holmium fraction by Gromov et al[6] and Basina et al[5]. It may therefore be asserted that these transitions occur in $Ho^{158} \rightarrow Dy^{158}$ decay.

320.5 and 356.6 keV transitions. Transitions of these energies were observed by Dneprovskii[3]. The period corresponding to the decrease in intensity of the conversion lines of these transitions is 2.5 hr. It was determined from the energy differences between the K, L and M electrons that these transitions occur in Dy^{158}. Our data on the energy differences between the K and L lines substantiate this. A 356.6 keV transition (T ≈ 30 min) was observed by Basina et al[5] in investigating the holmium fraction extracted from the spallation products of tantalum.

The transitions with energies of 622.3, 646.8, 731.0, 847.8, 850.1, 945.7 and

948.5 keV were attributed to the decay of Ho^{158} to Dy^{158} on the basis of the following considerations:

a) Transitions with energies of ~619, ~848 and ~947 keV were observed by Basina et al[5] in investigating the conversion electron spectrum of their holmium fraction. The decay period for the conversion lines of these transitions prove to be ~30 min.

b) The K line of a 647 keV transition was observed by Grigor'ev et al[7] in the spectrum of a holmium fraction. These authors did not determine the period.

c) Transitions with energies of 731.0, 847.8, 850.1, 945.7 and 948.5 keV are readily accomodated in the decay scheme of Ho^{158} shown in the accompanying figure.

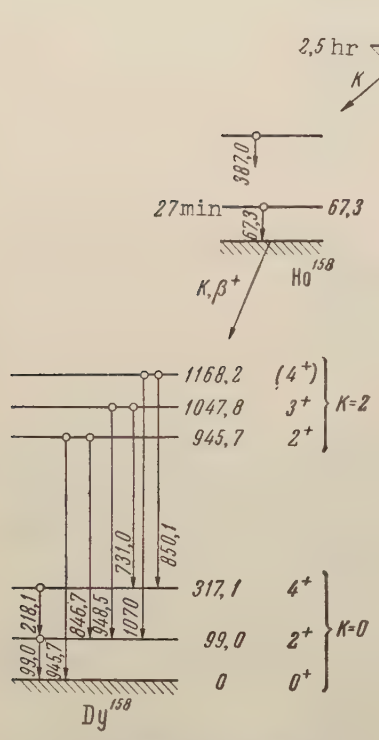

Proposed scheme for $Er^{158} \rightarrow Ho^{158} \rightarrow Dy^{158}$ decay.

3. Unidentified lines

The following 22 conversion lines were detected in the plates but have not been identified: 36.58, 37.33, 38.05, 38.50, 44.11, 62.56, 139.7, 180.4, 182.7, 185.3, 190.4, 192.3, 230.8, 238.5, 247.9, 255.3, 259.1, 364.6, 371.9, 408.2, 416.9, 451.2 and 876.0 keV.

4. Discussion of the Decay Scheme

In view of the data available on the radiation accompanying the $Er^{158} \rightarrow Ho^{158} \rightarrow Dy^{158}$ decay chain one can draw the following inferences regarding the decay scheme. Two transitions occur in the decay of Er^{158} to Ho^{158}, namely, 67.3 and 387.0 keV. In all probability the 67.3 keV level in Ho^{158} is analogous to the 60.1 keV level in Ho^{160}.

The probable arrangement of levels in Dy^{158}, excited in the decay of Ho^{158}, is shown in the figure. This scheme was constructed on the basis of the data on transition energies listed in Table 3 by analogy with the level diagram of Dy^{160}. It is assumed that the 99.0 and 218.1 keV transitions are transitions between the first rotational level of Dy^{158} - 99.0 keV (2, 0^+) - and the ground state, and between the second rotational level - 317.1 keV (2, 0^+) - and the first rotational level, respectively. This inference is upheld by the fact that on the basis of the data of Dneprovskii[3] on the intensity ratio of the ($L_I + L_{II}$) and L_{III} lines of the 99 keV transition the most probable multipole order of this transition is E2. It is difficult to determine the multipole order of the 218.1 keV transition on the basis of the available data because the L lines of this transition in the spectrum of the erbium fraction coincide with the M and N lines of the 211.1 keV transition occurring in the decay of Er^{161}. The only argument in favor of this location of the 218.1 keV transition is therefore the good agreement of the energy ratio of the 317.1 and 99 keV levels (3.2) with the theoretical ratio for rotational levels (3.33).

The locations of the 945.7 (2, 2^+) and 1047.8 (3, 2^+) keV levels are determined by the 945.7 and 846.7 keV transitions and the 948.5 and 731.0 keV transitions, respectively. According to preliminary evaluations, the relative intensities of these transitions are close to the relative intensities of the analogous transitions in the decay of Ho^{160} to Dy^{160}. Basina et al[5] in investigating the

decay of Ho^{158} (T = 27 min) observed a γ-transition with an energy of 1070 keV. This transition and the 850 keV transition can be located in the decay scheme of Ho^{158} if one postulates the existence of a level at 1168.2 keV. By analogy with the decay scheme of Ho^{160} this level may be characterized by $I = 4^+$, $K = 2$ and identified as the third level of the second rotational band of Dy^{158}.

Central Asian Polytechnic Institute &
Joint Institute for Nuclear Studies

References

1. E.P.Grigor'ev, B.S.Dzhelepov, V.Zvol'ska & A.V.Zolotavin, Program of the Present Conference.

2. B.Harmatz, T.H.Handley & J.W.Mihelich, Phys.Rev.,114, 1082 (1959).

3. I.S.Dneprovskii, Materialy II Soveshchaniya po yadernoi spektroskopii neitrono-defitsitnykh izotopov redkikh zemel' (Transactions of the 2nd Conference on Nuclear Spectroscopy of Neutron-Deficient Rare Earth Isotopes),Dubna,June,1959.

4. I.S.Dneprovskii, Transactions of the 3rd Conference on Nuclear Spectroscopy of Neutron-Deficient Rare Earth Isotopes, Dubna, June, 1960.

5. A.S.Basina, K.Ya.Gromov, B.S.Dzhelepov & V.A.Morozov, Izv.AN SSSR,Ser.fiz., 25, 194 (1961).(Trans. Bulletin, 25, 188.)

6. K.Ya.Gromov, B.S.Dzhelepov, Zeong Chong Pai &V.G.Chumin, Transactions of the 2nd Conference on Nuclear Spectroscopy of Neutron-Deficient Rare Earth Isotopes, Dubna, June, 1959.

7. E.P.Grigor'ev, Transactions of the 3rd Conference on Neutron-Deficient Rare Earth Isotopes, Dubna, June, 1960.

DECAY SCHEME OF Eu^{147}

- I.Vizi, K.Gromov, B.Dzhelepov,
Zh.Zhelev & Yu.Yazvitskii

We investigated the high-energy part of the conversion electron spectrum of Eu^{147} and the γ-γ coincidences in the decay of this isotope by means of a triple focusing β-spectrometer[1] and a cascade selector circuit[2].

Our radioactive source was the europium fraction extracted from a tantalum target bombarded for 12 hours with 660 MeV protons in the Joint Institute for Nuclear Research synchrocyclotron. The europium was separated from the tantalum 2 days after the end of bombardment; the measurements were started 40 days after the end of bombardment. Specifically, we investigated the section of the conversion electron spectrum in the range from 750 to 1100 keV (Fig.1). We carried out two series of measurements with an interval of 48 days between them. The list of detected lines attributed to Eu^{147} on the basis of the fall off in intensity is given in the accompanying table together with the data of other investigators. The observed conversion electrons are associated with 800, 900, 957 and 1082 keV γ-transitions. That there occur in the decay of Eu^{147} transitions with energies of 800, 957 and 1082 keV and of 76.5, 121, 198, 603 and 676 keV has been reported earlier by Anton'eva et al[3] and Schwerdtfeger[4]. The data on the 900 keV transition are conflicting: Schwerdtfeger et al report detecting this transition, while Anton'eva et al do not mention it. Our data give reason to affirm that a 900 keV transition is excited in the decay of Eu^{147}.

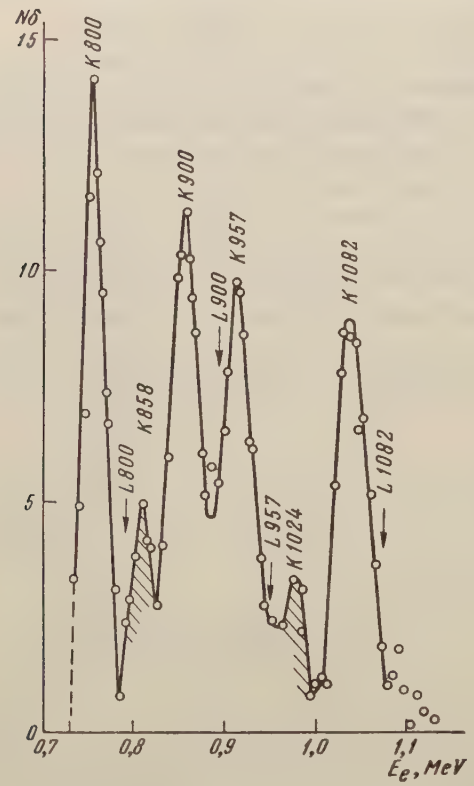

Fig.1. Conversion electron spectrum of Eu^{147} in the 730 to 1120 keV region. The hatched lines belong to Eu^{148}.

Data on the K conversion lines of Eu^{147} in the high energy region

$\frac{K}{K_{800}}\cdot 100$	E_γ, keV		
	Our data	Ref.3	Ref.4
100	800±3	800±4	800
113	900±4	—	900
87	957±4	957±4	976
93	1082±5	1080±5	1100

In investigating the γ-γ coincidence spectra we looked for cascades departing from levels at about 198, 800, 900 and 1080 keV. There were detected coincidences between γ-rays of the following energies: 76.5—121, 121—676, 198—603, 121—780, 198—700, 121—957 and 198—880 keV (Figs.2-5). Thus our results substantiate the existence of levels at 198, 800 and 1080 keV.[3] The fact that there are 198—700 and 121—780 keV coincidences and a cross-over transition of 900 keV energy gives reason to introduce a level at 900 keV into the diagram for Sm^{147} (Fig.6).

Schwerdtfeger et al[4] report observing positron radiation in the decay of Eu^{147}, give end-point energies of 270 and 150 keV for the components of the positron spectrum, and note that the low energy positrons yield coincidences with the

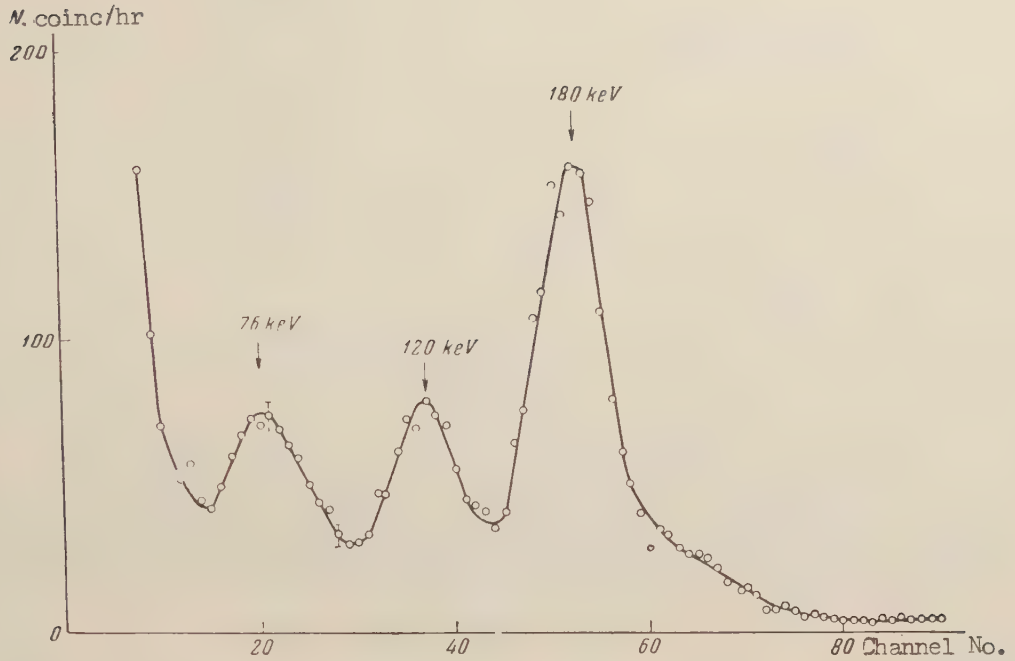

Fig.2. Coincidence spectrum of the 76.5—121 keV γ-transitions with the coincidence circuit set for a sum energy of 198 keV. $\tau_p = 2 \cdot 10^{-7}$ sec. Gate width 12 keV. The 180 keV peak is due to coincidence of x-rays with the 178 keV γ-rays of Eu^{149}, which was present in our source.

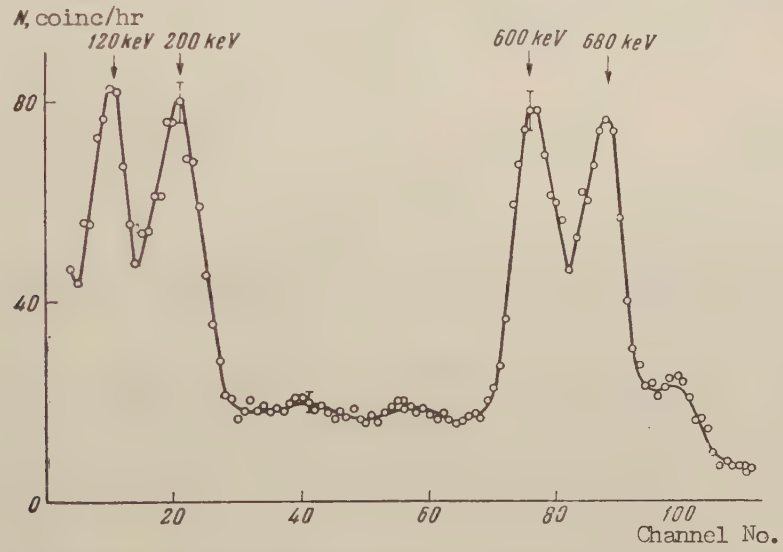

Fig.3. Coincidence spectrum of the 121—676 and 198—603 keV transitions with the circuit set for a sum energy of 800 keV. $\tau_p = 2 \cdot 10^{-7}$ sec. Gate width 40 keV.

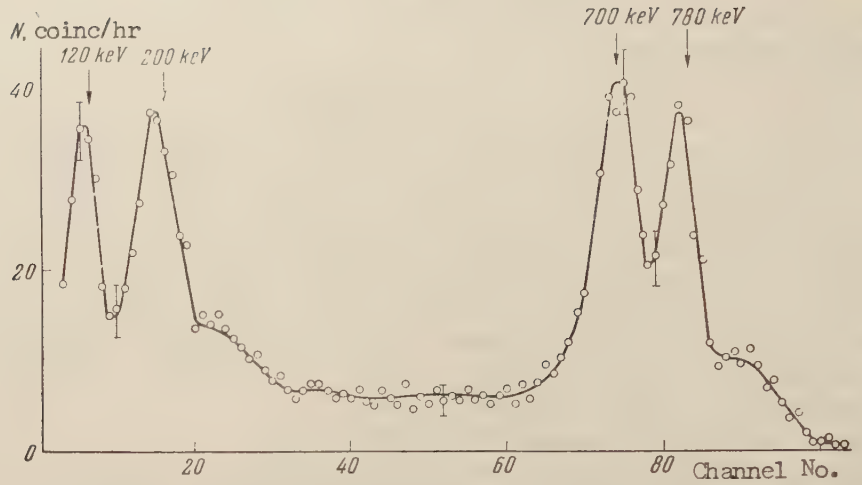

Fig.4. Coincidence spectrum of the 121—780 and 198—700 keV transitions with the circuit set for a sum energy of 900 keV. $\tau_p = 2 \cdot 10^{-7}$ sec. Gate width 70 keV.

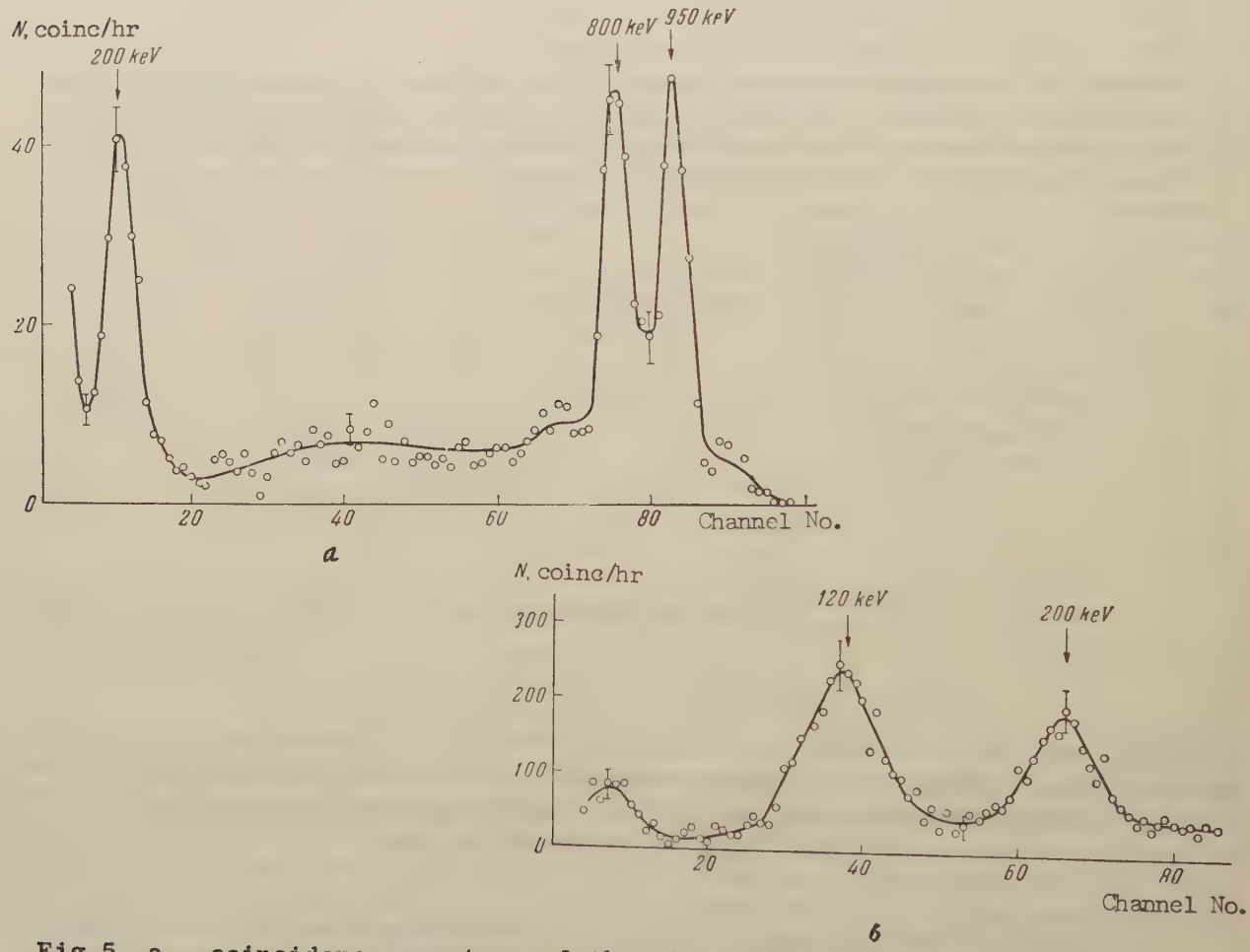

Fig.5. a - coincidence spectrum of the 121—957 and 198—880 keV transitions with the circuit set for a sum energy of 1080 keV. $\tau_p = 2 \cdot 10^{-7}$ sec. Gate width 70 keV. b - low energy section of the coincidence spectrum of the 121—957 and 198—880 keV transitions with the circuit set for an energy sum of 1080 keV.

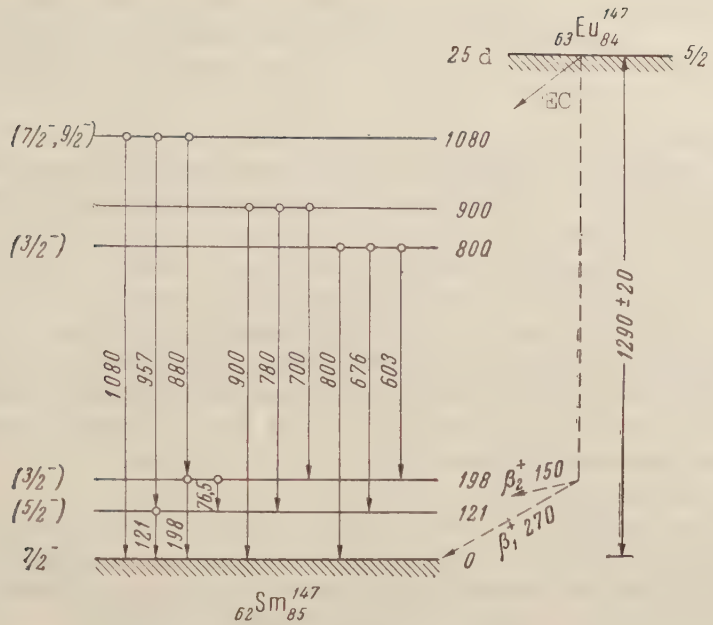

Fig.6. Decay scheme of Eu^{147}.

122 keV γ-rays. We did not detect positrons in the decay of Eu^{147}. According to our evaluations, the upper bound for the intensity of the positron spectrum is 16 ± 5% relative to the intensity of the K conversion line of the 121 keV γ-transition.

We take this opportunity to express our gratitude to V.A.Khalkin, Van Fu-Tszyun' and Kang Meng-Hua for preparing the sources.

Joint Institute for Nuclear Research &
"V.G.Khlopin" Radium Institute,
Academy of Sciences of the USSR

References

1. B.S.Dzhelepov, Zh.Zhelev, A.V.Kudryavtseva, O.V.Larionov, M.K.Nikitin & R.Stepich, Preprint OIYaI (Preprint, Joint Inst. for Nucl.Research), P-587, Dubna, 1960.

2. Van Fu-Tszyun', I.Vizi, K.Gromov, B.Dzhelepov, Zh.Zhelev, A.Kudryavtseva & Yu.Yazvitskii, Izv.AN SSSR,Ser.fiz., 26, 114 (1962).(Trans.Bulletin,26, No.1.)

3. N.M.Anton'eva, A.A.Bashilov, B.S.Dzhelepov, K.G.Kaun, A.F.Meier & V.B. Smirnov, Doklady na III soveshchanii po neitronodefitsitnym izotopam redkikh zemel' (Transactions of the 3rd Conference on Neutron-Deficient Rare Earth Isotopes), Dubna, 1960.

4. C.F.Schwerdtfeger, J.W.Mihelich & B.Harmatz, Bull.Amer.Phys.Soc., 4, 426 (1959).

INVESTIGATION OF THE CONVERSION ELECTRON SPECTRA OF NEUTRON-DEFICIENT ISOTOPES OF ERBIUM AND HOLMIUM

- K.Ya.Gromov & I.S.Dneprovskii

The investigated erbium isotopes were obtained by bombardment of tantalum targets with 660 MeV protons in the Joint Institute for Nuclear Research synchrocyclotron for periods of from 0.5 to 2 hours. The procedures employed in extracting the rare earths from the Ta target and separating them into elementary fractions are described in Ref.1. The erbium fraction was, as a rule, separated from the other rare earths some 2-3 hours after the end of bombardment.

The conversion electron spectra of the neutron-deficient erbium isotope were investigated by means of a double focusing $\pi\sqrt{2}$ β-spectrometer (type BPP-1).[2] The instrumental half-width of the conversion lines was 0.2-3%. The sources were prepared by evaporation of erbium lactate on 20 x 0.8 mm aluminum foils 0.005 mm thick The measurements on the β-spectrometer were started from 2.5 to 3.5 hours after the end of bombardment of the tantalum target.

It is known that spallation of tantalum results in formation of neutron-deficient isotopes; the yield of neutron-rich isotopes is negligible. In the conversion electron spectra of the erbium activities used in the present study there were observed electrons emitted in the following decay chains:

$$Er^{165} \xrightarrow[EC]{10\ hr} Ho^{165}\ (stable),$$

$$Er^{161} \xrightarrow[EC]{3.1\ hr} Ho^{161} \xrightarrow[EC]{2.5\ hr} Dy^{161}\ (stable),$$

$$Er^{160} \xrightarrow[EC]{30\ hr} Ho^{160} \xrightarrow[EC,\beta^+]{5\ hr} Dy^{160}\ (stable),$$

$$Er^{158} \xrightarrow[EC]{2.4\ hr} Ho^{158} \xrightarrow[EC,\beta^+]{27\ min} Dy^{158}\ (stable).$$

It has been shown in earlier investigations[3,4] that no γ-rays are emitted in the decay of Er^{165}. The presence of Er^{165} in our sources was evinced only by the appearance of a component with a corresponding period (~10 hr) in the curve characterizing the falling off in intensity of the Auger electron lines. The conversion electrons spectrum emitted in the decay chain starting with Er^{160} has been investigated by Grigor'ev[5]. Our results for the conversion electron spectrum of Er^{165} are in good agreement with their data.

The new results obtained in the present study pertain to $Er^{161} \rightarrow Ho^{161}$ decay and the $Er^{158} \rightarrow Ho^{158} \rightarrow Dy^{158}$ chain. There were also detected a number of electron lines, the intensity of which fell off with a period of about 1 hour.

1. $Er^{161} \rightarrow Ho^{161}$

The spectrum of conversion electrons emitted in the decay of Er^{161} was investigated earlier by one of the present authors.[6-8] There were observed conversion lines associated with γ-transitions of 210.9 and 826.2 keV energy. In Ref.7 there was inferred the existence of a 592 keV γ-transition. The existence of this transition has been definitely proved in the present study. The results of the present investigation of the conversion electron spectrum emitted in the decay of Er^{161} are given in Table 1.

The listed lines were attributed to the decay of Er^{161} on the basis of the decrease in intensity with time. By way of illustration, in Fig.1 we show how the intensity of the K592.3 line fell off with time; the value of the period as determined from this plot is 3.2 ± 0.2 hours, which is in good agreement with the mean

Table 1
Conversion electron lines pertaining to $Er^{161} \rightarrow Ho^{161}$

No.	E_e, keV	Identification	Relative intensity I_e
1	155,40	K211,0	100±10
2	201,6	$(L_I + L_{II})$210,5	70±7
3	202,15	L_{III}210,2	35±3
4	536,6	K592,1	0,90±0,15
5	583,0	L592,1	0,26±0,12
6	773,2	K827,0	13±1
7	816,5	L825,6	2,0±0,25
8	824,5	M826,0	0,4±0,2

value of the period corresponding to the other lines of Er^{161} (3.1 ± 0.1 hrs). The dash-dot curve in Fig.1 shows the character of variation in intensity of the lines of daughter Ho^{161}. It will be seen that the experimental points diverge greatly from the dash-dot line and, consequently, the K592.3 line cannot be attributed to the decay of Ho^{161}. The values obtained for the γ-transition energies are in good agreement with the results of Harmatz et al[9] and Abdurazakov et al[10].

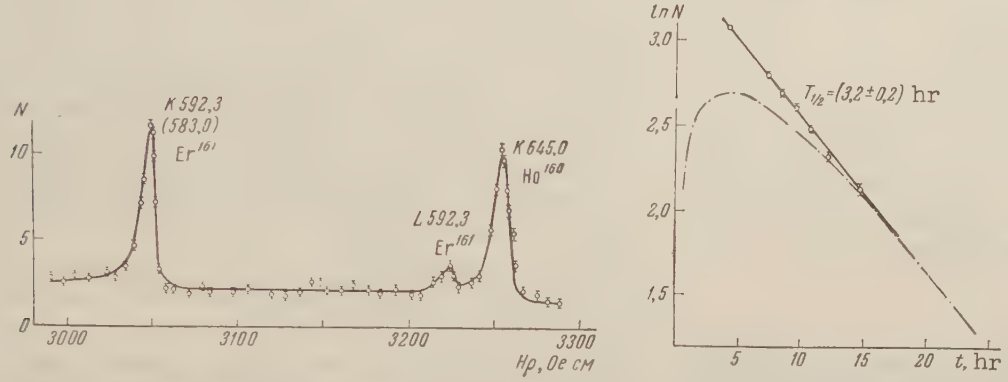

Fig.1. Conversion electrons of the 592.3 keV γ-transition following decay of Er^{161}. At right - decrease in intensity of the K line. The dash-dot line shows the calculated variation in intensity of the conversion electrons following decay of Ho^{158} for observation of the erbium fraction.

As was shown in Ref.6, the intensity ratios of the K, $(L_I + L_{II})$ and L_{III} lines of the 210.9 keV transition allow of establishing the multipole order of this transition as E3. Analogously, in Ref.8, the multipole order assignment for the 826.2 keV transition was found to be M1.

The γ-spectrum of Er^{161} was investigated by Dalkhsuren et al[11]. These authors observed γ-rays with energies of 210, 825 and ~1200 keV and relative intensities (13 ± 2):100:(~5). Dalkhsuren et al did not observe 592 keV γ-rays, and according to their evaluation the upper bound for these must be less than 5% the intensity of the 825 keV γ-rays. They determined the abundances of the 210 and 825 keV transitions in percent per disintegration by means of a 4π scintillation spectrometer and obtained 23 and 77%, respectively.

On the basis of the above data one can draw certain inferences regarding the Er^{161} decay scheme.

It was established by Dalkhsuren et al[11] that the sum of the intensities of the 210.9 and 826.2 keV transitions amounts to 100% per disintegration. Accepting this value and utilizing the data on the relative intensities of the conversion electron lines listed in Table 1, we calculated the abundances of the 210.9 and 826.2 keV transitions; these are given in Table 2. The intensities of the 592 and ~1200 keV transitions are taken from Ref.11.

Table 2
Intensities of γ-transitions in $Er^{161} \rightarrow Ho^{161}$

$h\nu$, keV	Multipole order	Abundance per disintegration, %
210,9	$E3$	18
592,3	—	<4
826,2	$M1$	82
1200	—	~4

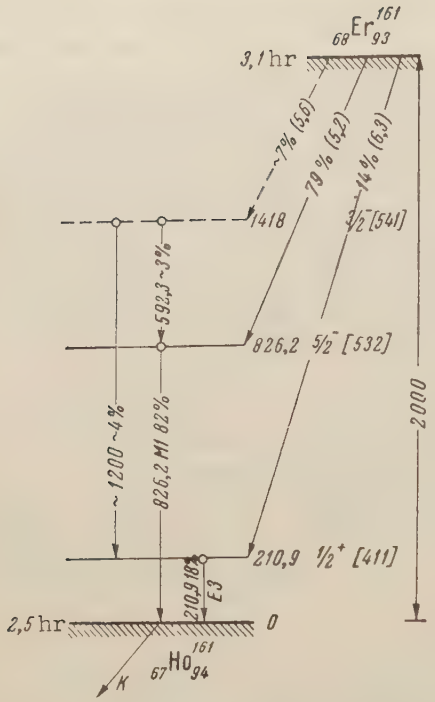

Fig.2. Decay scheme for Er^{161}. The figures in parentheses are for the log ft values for electron capture to the indicated levels in Ho^{161}.

The decay scheme of Er^{161} was discussed in Ref.8. It was assumed that in the decay of this isotope there are excited levels at 210.9 and 826.2 keV (Fig.2). The 592.3 and ~1200 keV transitions referred to above can be accomodated in the scheme if one postulates the existence of a level at 1418 keV. Admittedly, the only argument in favor of this location is the coincidence within the limits of the experimental error of the sums of the transition energies: 826.2 + 592.2 = = 1418.4 keV and 210.9 + ~1200 = 1410 keV. In Fig.2 we have indicated the abundances of the γ-transitions in percent per disintegration and the ensuing intensities of the K capture branches to the levels in Ho^{161}. The log ft values of the K capture branches are given in parentheses.

The $Er^{161} \rightarrow Ho^{161}$ disintegration energy is taken from Cameron's table[12]. The deduced log ft values for K capture to the 210.9 and 826.2 keV levels are consistent with the spin assignments for these levels.

The transition to the 210.9 keV level: $3/2^-$ [521] $\xrightarrow{K} 1/2^+$ [411] (log ft = 6.3) is first forbidden, unhindered; the transition to the 826.2 keV level: $3/2^-$[521] $\xrightarrow{K} 5/2^-$ [532] (log ft = 5.3) is allowed, hindred. The log ft value for the K capture branch to the 1418 keV level equals 5.6, which indicates that this transition is allowed, i.e., the assignment for the 1418 keV level should be $1/2^-$, $3/2^-$ or $5/2^-$. On the basis of Nilsson's level scheme it may be inferred that the most probable assignment for the 1418 keV level is $3/2^-$ [541]. Accordingly, K capture to this level must be allowed, hindered.

2. $Er^{158} \rightarrow Ho^{158} \rightarrow Dy^{158}$

In 1958 one of us[6] in investigating the conversion electron spectrum of erbium isotopes detected the lines of a 98.6 keV transition. The intensity of these lines fell off with a period of 2.5 hours. It was inferred that there exists a new erbium isotope with T = 2.5 hours.

Subsequently, there were detected many conversion lines with the same decay period.[7,13] Bonch-Osmolovskaya et al[14], investigating the spectrum of a similar erbium fraction, observed a positron spectrum with end-point energy 1350 keV, the intensity of which fell off with a period of ~2.5 hours. The mass number of the erbium isotope with T = 2.5 hours and of its Ho daughter was established on the basis of the following facts.

1. Gamma-transitions of 98 and 218 keV energy were observed in investigating the erbium and holmium fractions and in investigating daughter holmium separated from the erbium fraction. The intensities of the conversion lines of these transitions fell off with a period of 2.5 hours in the spectrum of the erbium fraction[7], and with a period of 27 min in the spectrum of the holmium fraction separated directly from the rare earths formed in the Ta target. In the spectrum of the daughter holmium separated from the erbium fraction the intensity of these lines decreased with a period of 27 min.[13]

In the case of the erbium fraction there was observed increase in the intensity of the positron spectrum with end-point energy 1350 keV.[14] The build-up period was about 0.5 hours; the fall-off period after going through the maximum was ~2.5 hours. These data indicate that we are dealing here with a decay chain comprising an erbium isotope with a period of 2.5 hours and a holmium isotope with a period of 27 min. The 98 and 218 keV transitions take place in the final dysprosium nucleus. This is substantiated by the values of the differences between the energies of the K, L, M and N conversion lines.

2. The intensity ratios of the K, $(L_I + L_{II})$ and L_{III} conversion lines of the 98 keV transition (see Table 4) definitely indicate that the multipole order of this transition is E2. The energy ratio of the 218.3 and 98.6 keV transitions, namely, 2.22, is close to the theoretical ratio (2.33) for $4^+ \to 2^+$ and $2^+ \to 0^+$ transitions in the ground state rotational band of even-even deformed nuclei. Assuming that the 98.6 keV transition departs from the first rotational level of an even-even dysprosium nucleus, one can readily determine the mass number of this nucleus. The energies of the first rotational levels of the even-even dysprosium isotopes are 138 keV for Dy^{156}, 87 keV for Dy^{160}, 81 keV for Dy^{162} and 73 keV for Dy^{164}. If we assume that the isotope in question has A = 158, we find that the 98.6 keV transition energy value falls on a smooth curve characterizing the A dependence of the transition energies.

In view of the above argument one can safely assert that there exists the decay chain

$$Er^{158} \xrightarrow[EC]{2.4\ hr} Ho^{158} \xrightarrow[EC]{27\ min} Dy^{158}.$$

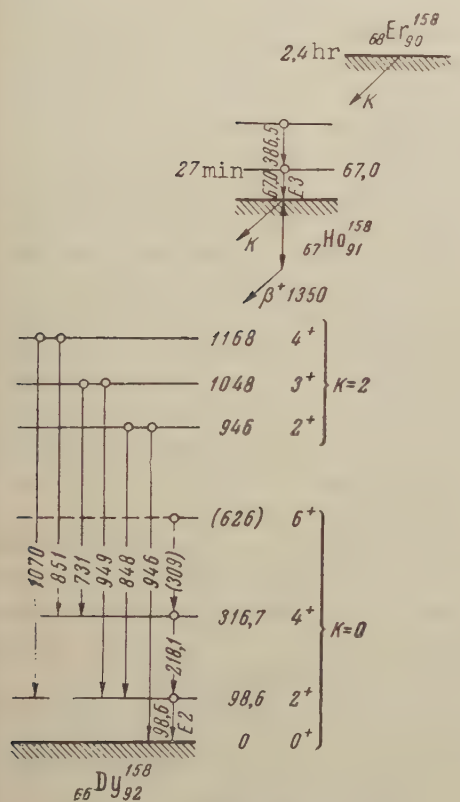

Fig.3. Decay scheme for $Er^{158} \to Ho^{158} \to Dy^{158}$.

In Table 3 we list the conversion lines that we believe pertain to this chain.

Admittedly, the attribution of some of the lines listed in Table 3 to the $Er^{158} \to Ho^{158} \to Dy^{158}$ decay chain is not reliable. One can only safely assert that γ-transitions of energies 67.0, 98.6, 218.1, 356.8, 847.8, 851.1, 946.3 and 948.7 keV occur in this chain, inasmuch as they have been observed in investigating the conversion electron spectrum of the erbium fraction in our work (T = = 2.5 hours) and by Basina et al[16] in investigating the spectrum of a holmium fraction (T ≈ 30 min). Where the other lines are concerned one can only make the assignment on the basis of the decay period. In this manner it proved feasible to determine that the 71.5, 320.3 and 386.5 keV γ-transitions belong to the chain beginning with Er^{158}. We were unable to determine with adequate accuracy the decay periods corresponding to the relatively weak conversion lines of the γ-transitions with energies of 130.6, 194, 309.0, 313.5, 461.8, 470.6, 505.3, 731, 931.1 and 987 keV. Hence it is not impossible that these γ-transitions occur in the decay of Er^{161} (T = 3.1 hours). Nevertheless, it is more probable that these lines are associated with transitions taking place in the chain starting with Er^{158}.

From the energy differences between the conversion electron lines associated with them it may be

Table 3

Results of investigating the conversion electron spectrum of the $Er^{158} \rightarrow Ho^{158} \rightarrow Dy^{158}$ decay chain

No.	E_e, keV	Identification	Relative intensity, I_e
		$Er^{158} \rightarrow Ho^{158}$	
1*	57,7	$(L_I + L_{II})66,6$	130±30
2*	58,9	$L_{III}66,9$	100
3**	65,2	$M67,3$	65±15
4***	66,6	$N67,0$	15±3,5
5	330,4	$K386,0$	1,3±0,15
6	377,3	$L386,7$	0,21±0,05
7	384,8	$M386,9$	0,15±0,05
		$Ho^{158} \rightarrow Dy^{158}$	
1	44,7	$K98,5$	430±70
2	61,18	L_I 71,25	110±25
3	71,25	$N71,67$	6±2
4***	76,6	$K130,4$	
5	89,8	$(L_I + L_{II})98,4$	400±80
6	90,65	$L_{III}98,5$	300±60
7	96,9	$M98,9$	150±30
8	98,2	$N98,6$	35±7
9***	121,7	$(L_I + L_{II})130,3$	14±2
10	122,7	$L_{III}130,6$	5,2±0,8
11	128,80	$M130,8$	2,5±0,8
12	130,30	$N130,7$	0,6±0,3
13	139,7	$K193,5$	10±4
14	164,5	$K218,3$	100±5
15	—	L (~218,1)	—
16	216,0	$M217,8$	3,7±1,0
17	217,6	$N217,9$	1,1±0,3
18****	255,3	$K309,1$	2,5±1,0
19	259,0	$K312,8$	2,2±0,6
20	266,0	$K319,8$	4,0±0,8
21	302,2	$K356,4$	2,0±0,5
22	311,8	$L320,9$	1,0±0,3
23	318,3	$M320,3$	0,20±0,08
24	348,0	$L357,1$	0,3±0,1
25	408,0	$K461,8$	0,15±0,07
26	416,8	$K470,6$	0,3±0,15
27	451,5	$K505,3$	0,3±0,15
28	671,0	$K724,5$	0,3±0,2
29	675,5	$K731,0$	0,6±0,3
30	794,1	$K847,9$	2,4±0,4
31	797,0	$K850,8$	1,2±0,2
32	838,5	$L847,6$	0,6±0,2
33****	842,3	$L851,4$	0,3±0,1
34	876,0	$K929,8$	1,0±0,2
35	892,2	$K946,0$	2,0±0,4
36	894,5	$K948,3$	1,8±0,4
37	933,5	$K987,3$	0,40±0,15
38	937,6	$L946,7$	0,40±0,15
39****	940,0	L 949,1	0,30±0,15

*This line coincides with others; in the work of Ref.6 it was erroneously attributed to the decay of Er^{161}.

**In the work of Ref.6 this line was erroneously attributed to the decay of Er^{161}.

***Line incorrectly identified in Ref.6.

****Line coincides with others.

Table 4

Intensity ratios of the conversion electron lines of the 67.0 and 98.6 keV γ-transitions and the corresponding theoretical ratios for different multipole orders

Ratio	Theory						Experiment
	*E*1	*E*2	*E*3	*M*1	*M*2	*M*3	
$h\nu = 67$ keV							
$(L_I + L_{II})/L_{III}$	3,2	0,91	1,01	80,4	4,2	0,64	1,3±0,3
$K/\Sigma L$	5,6	0,28	0,015	5,1	2,1	0,33	<0,10
$h\nu = 98,6$ keV							
$(L_I + L_{II})/L_{III}$	4,34	1,17	1,07	80,6	5,12	1,11	1,2±0,1
$K/\Sigma L$	6,21	0,855	0,094	6,3	3,5	1,11	0,65±0,20

inferred that the 67.0 and 386.5 keV γ-transitions occur in the holmium nucleus, while the 98.6, 218.1 and 320.3 keV transitions occur in the dysprosium nucleus. The presence of 356.8, 847.9, 851.1, 946.3 and 948.7 keV transitions in the spectrum of the holmium fraction shows that these transitions occur in the dysprosium nucleus. The energies of the transitions for which we were unable to determine the atomic number of the nucleus were calculated on the assumption that they occur in the dysprosium nucleus.

In the investigated conversion electron spectra there were observed weak lines with energies of 49.3, 53.8, 74.0, 92.3, 93.9, 132.3, 145.1, 510, 565, 594, 784, 841, 845, 940 and 944 keV. At present we are unable to identify these lines.

On the basis of the experimental results we propose the decay scheme for the $Er^{158} \rightarrow Ho^{158} \rightarrow Dy^{158}$ decay chain shown in Fig.3. Er^{158} converts by K capture and, possibly β^+-decay[14] to Ho^{158}. De-excitation of the levels in Ho^{158} gives rise to the 67.0 and 386.5 keV transitions. The multipole order of the 67.0 keV transition can be unambiguously determined as E3 from the relative intensities of the K and L conversion lines (see Table 4 and Fig.4). The 67.0 keV transition is very intense; according to our evaluations its intensity amounts to ~50% per disintegration of Er^{158}. Hence it may safely be assumed that the 67.0 keV transition feeds the ground state of Ho^{158} and determines the location of the isomeric level (67 keV). The period of Ho^{158} (27 min) determined in our earlier study[13] and in the work of Gromov et al[15] apparently belongs to this isomeric state. The decay period of the ground state of Ho^{158} is probably even shorter. It will be evident that we have here a situation analogous to that observed in the decay of Er^{160}, where the E3 type 60 keV γ-transition determines the position of the isomeric level with a period of 5 hours.

One may reasonably expect the decay scheme for $Ho^{158} \rightarrow Dy^{158}$ to bear many similarities to the decay scheme for $Ho^{160} \rightarrow Dy^{160}$. On the basis of the available data we propose the level diagram for Dy^{158} shown in Fig.3. As noted above, there can be little doubt that the 98.6 and 316.7 keV levels are the first two levels of a rotational band based on the ground state.

The levels of 946.3, 1047.3 and 1167.8 keV apparently are the levels of a second rotational band and have spins 2, 3 and 4, respectively. The location of each of these levels is determined by two γ-transitions. One of the γ-transitions (1070 keV) determining the position of the 1167.8 keV level was observed only in the work of Basina et al[16]. Using the conversion line intensities listed in Table 3 and assuming that all the γ-transitions between the levels of the first and second rotational bands are E2, we evaluated the relative intensities of these transitions. No significant discrepancies appear in the balance of intensities for the proposed scheme.

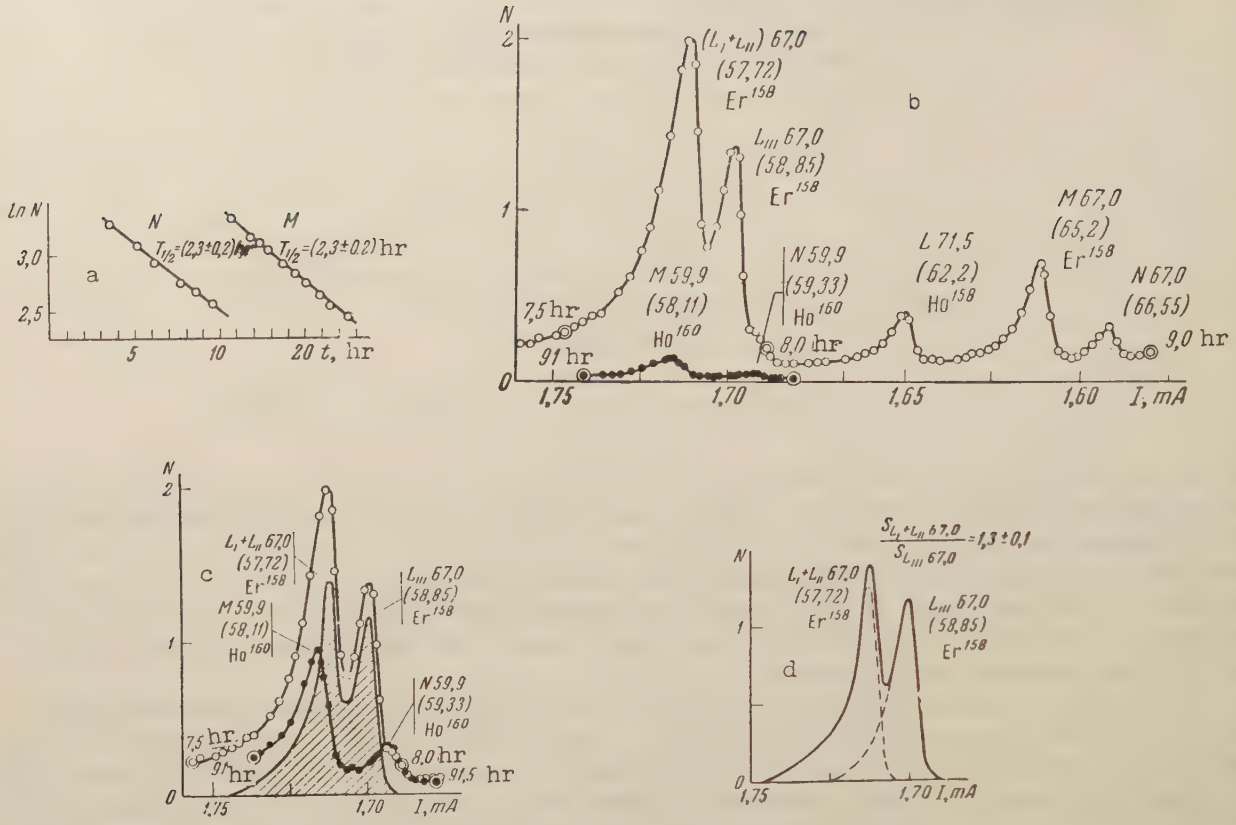

Fig.4. Conversion electrons of the 67.0 keV γ-transition: a - decrease in intensity of the N67 and M67 lines with time; b - section of the conversion spectrum in which the lines in question are located. The horizontal scales are the values of the current readings of the magnetometer measuring the field strength in the β-spectrometer.[2] The energies of the conversion electrons are given in parentheses. The figures at the double circle points indicate the time elapsed from the instant of separation of the erbium fraction. The solid circle points represent the series of measurements giving the height and shape of the M60 and N60 lines evinced in the decay of Ho^{160}. c - determination of the height and shape of the L67.0 line; solid circles - lines of Ho^{160} reduced to the time of measurement of the first series; the hatched area corresponds to the graphic difference between the series, i.e., the L67.0 line. d - resolution of the integral L67.0 line into components: $L_I + L_{II}$ and L_{III}.

In Table 5 we compare the experimental energy values of the levels of the first and second rotatinnal bands with the values calculated according to the theory of Bohr & Mottelson[17] for axial nuclei and the theory of Davydov & Filippov[18,19] for nonaxial nuclei. Comparison of the theoretical and experimental values leads to the following deductions:

1. The relatively good agreement of the values calculated in the adiabatic approximation using the theory of axial (axially-symmetric) nuclei (4; 0^+, and 4, 2^+ levels) and according to the theory of nonaxial nuclei (4, 0^+; 3, 2^+ and 4, 2^+ levels) is evidence in favor of the proposed scheme.

2. Calculations in the nonadiabatic approximation of the theory of axial

Table 5

Comparison of the experimental energy values for the levels of the rotational bands in Dy^{158} with the theoretical values calculated on the basis of the theory of axial nuclei and according to the theory of nonaxial nuclei

I, K^{π} of level	Experiment	Theory			
		Adiabatic approximation		Nonadiabatic approximation	
		Axial nuclei	Nonaxial nuclei	Axial nuclei	Nonaxial nuclei
		$A_1 = 16{,}43$ keV $A_2 = 16{,}83$ keV	$\mu = 0$ $\gamma = 12{,}8°$	$A_1 = 16{,}68$ keV $A_2 = 17{,}58$ keV $B_1 = -0{,}043$ $B_2 = -0{,}126$	$\gamma = 12{,}2°$ $\mu = 0{,}27$
$2\ 0^+$	98,6	98,6*	98,6*	98,6*	98,6*
$4\ 0^+$	316,7	328,3	325,4	316,7*	316,7*
$6\ 0^+$	625 or 630	690,2	671,8	625,1	632,0
$8\ 0^+$	—	1183	1131	978	1055,0
$2\ 2^+$	946,3	946,3*	946,3*	946,3*	945,3*
$3\ 2^+$	1047,3	1047,3*	1046	1047,3*	1021
$4\ 2^+$	1167,8	1181,9	1178	1167,8*	1183
$5\ 2^+$	—	1350,2	1341	1295,8	1257

*Energy values used in the calculations.

nuclei cannot be compared with experiment, inasmuch as all the experimental energy values must be used for calculating the parameters in the formulas of this theory. The energies of the 3, 2^+ and 4, 2^+ levels calculated according to the theory of nonaxial nuclei in the nonadiabatic approximation differ from the experimental values to a greater extent than in the adiabatic approximation.

Thus if the proposed level scheme is correct, recourse to the nonadiabatic approximation in the theory of nonaxial nuclei in this case does not improve agreement with experiment.

The energy value of the 6, 0^+ level calculated in the nonadiabatic approximation according to the theories of axial and nonaxial nuclei equals 625.1 and 632.0 keV, respectively. It is possible that a 309 or 313 keV transition departs from this level. The former value is in better agreement with the calculations according to the theory of axial nuclei; the second agrees better with the calculations according to the theory of nonaxial nuclei. At present, however, there are no data to indicate reliably that the 6, 0^+ level is excited in the decay of Ho^{158}.

Table 6

Comparison of the experimental values of ratios of the reduced transition probabilities between rotational bands in Dy^{158} with the corresponding theoretical ratios

Reduced probability ratio	Experiment	Theory		
		Axial nuclei		Nonaxial nuclei $\gamma = 12{,}8°$
		Acc. Alaga	With Mottelson's correction $z = 0{,}040$	
$B(2_2, 0) : B(2_2, 2_1)$	0,55	0,70	0,55*	0,45
$B(3_2, 4_1) : B(3_2, 2_1)$	0,63	0,40	0,67	0,64

*Value used for calculating the parameter in Mottelson's correction factor.

In Table 6 we compare the experimental values of the reduced probabilities for transitions from the 2, 2^+ and 3, 2^+ levels to the levels of the first rotational band with the theoretical values calculated according to the theories of axial[20,21] and nonaxial[19] nuclei. It may be noted that here there is observed a situation analogous to that obtaining for neighboring even-even isotopes[22]: the experimental values lie between the values calculated according to the theory of nonaxial nuclei and the values computed according to the theory of axial nuclei using Alaga's rule, but are closer to the former. Introduction of Mottelson's[21] correction to the theory of axial nuclei yields improved agreement with experiment.

3. Conversion electron lines with T ≃ 1 hour

Earlier[6,7] we reported that in the conversion electron spectrum of the erbium fraction extracted from proton-bombarded tantalum there were observed conversion lines the intensity of which fell off with a period of about 1 hour. Some of these were attributed[6] to the 138 keV γ-transition in Ho^{156} (T ≈ 1 hr). Now we have established that the presence of the lines of this transition in the early experiments was due to contamination of the erbium sources with holmium.

Table 7

Conversion electron lines with a period of ~1 hr

E_e, keV	118.9	123.5	255.8*	301.0	307.4
Identification	-	L132	K309.6	L310.6	M309.4

*The period corresponding to this line given in Ref.7 was erroneous.

In Table 7 we list the conversion electron lines in the spectrum of the erbium fraction, the intensity of which fell off with a period of 50 ± 10 min. These lines cannot be attributed to any known isotope. Possibly, they are due to the decay of a new isotope with T ≈ 50 min. At present we do not have sufficient data to make a mass number assignment; one can, however, exclude A = 155, 156 and 157 in view of the fact that in the experiments we did not observe the strong lines of the daughter isotopes with these mass numbers, namely, Dy^{155} (K227), Dy^{156} (K138) and Dy^{157} (K326). If the new erbium isotope had any one of these mass numbers, the corresponding K line would undoubtedly have been detected.

We desire to express our deep gratitude to B.S.Dzhelepov for his interest in the work and valuable suggestions, V.A.Khalkin and I.A.Yutlandov for preparing the sources, and L.N.Nikityuk for assistance in carrying out the measurements and processing the results.

Joint Institute for Nuclear Research &
"V.I.Vernadskii" Institute of Geochemistry and Analytic Chemistry,
Academy of Sciences of the USSR

References

1. B.K.Preobrazhenskii, O.M.Lilova, A.N.Dobronravova & E.D.Teterin, Zhur. neorgan.khimii (Journ.Inorg.Chem.), 1, 2294 (1956).

2. I.M.Bekkerman, B.A.Gumenyuk & I.S.Dneprovskii, Beta-spektrometr tipa BPP (Type BPP Beta-spectrometer), VINITI, M.,1959.

3. G.M.Gorodinskii, A.N.Murin, B.N.Pokrovskii & B.K.Preobrazhenskii, Izv. AN SSSR,Ser.fiz.,21, 1004 (1957).(Trans. Bulletin, 21, 1005.)

4. O.I.Grigor'ev, B.S.Kuznetsov, N.S.Shimanskaya & I.A.Yutlandov, Ibid.,22, 850 (1958).(Trans. Bulletin, 22, 845.)

5. E.P.Grigor'ev, B.S.Dzhelepov, A.V.Zolotavin, O.E.Kraft, B.Kratsik & L.K. Peker, Ibid.,22, 101 (1958).(Trans. Bulletin, 22, 99); E.P.Grigor'ev, B.S.Dzhelepov, A.V.Zolotavin, B.Kratsik & G.Bitterlikh, Ibid.,23, 868 (1959).(Trans. Bulletin 23, 859).

6. I.S.Dneprovskii & G.M.Kolesov, Ibid.,22, 935 (1958).(Trans. Bulletin,22, 927.)

7. I.S.Dneprovskii, Materialy II soveshchaniya po yadernoi spektroskopii neitronodefitsitnykh izotopov redkikh zemel' (Transactions of the 2nd Conference on Nuclear Spectroscopy of Neutron-Deficient Rare Earth Isotopes), Dubna, 1959.

8. I.S.Dneprovskii, L.Nemet & L.K.Peker, Zhur.eksp.i teor.fiz., 39, 13 (1960).(Trans. Soviet Physics - JETP.)

9. B.Harmatz, T.H.Handley & J.W.Mihelich, Phys.Rev.,114, 1082 (1959).

10. A.Abdurazakov, K.Ya.Gromov & B.S.Dzhelepov, Materialy III soveshchaniya po neitronodefitsitnym izotopam redkikh zemel' (Transactions of the 3rd Conference on Neutron-Deficient Rare Earth Isotopes), Dubna, 1960.

11. B.Dalkhsuren, M.L.Kuznetsova, I.Yu.Levenberg, Yu.V.Nerseev, V.N.Pokrovskii & I.A.Yutlandov, Ibid.

12. A.G.W.Cameron, A Revised Semi-Empirical Atomic Mass Formula, CRP-690, Chalk River, Ontario, 1957.

13. I.S.Dneprovskii, Atomnaya energiya, 8, 46 (1960).(Trans.Soviet Journal of Atomic Energy.)

14. N.A.Bonch-Osmolovskaya, B.S.Dzhelepov & O.E.Kraft, Doklad na XI Ezhegodnom soveshchanii po yadernoi spektroskopii (Program of the 11th Conference on Nuclear Spectroscopy), Riga, 1961.

15. K.Ya.Gromov, B.S.Dzhelepov, Zeong Chong Pai & V.G.Chumin, Transactions of the 2nd Conference on Nuclear Spectroscopy of Neutron-Deficient Rare Earth Isotopes, Dubna, 3, 37 (1959).

16. A.S.Basina, K.Ya.Gromov, B.S.Dzhelepov & V.A.Morozov, Izv.AN SSSR,Ser. fiz.,25, 194 (1961).(Trans. Bulletin, 25, 188.)

17. A.Bohr & B.R.Mottelson, in Beta- and Gamma-Ray Spectroscopy, edited by Kai Siegbahn, N.Y., 1955.

18. A.S.Davydov & G.F.Filippov, Zhur.eksp.i teor.fiz.,35, 440 (1958).(Trans. Soviet Physics - JETP.)

19. A.S.Davydov, Izv.AN SSSR,Ser.fiz.,23, 792 (1959).(Trans. Bulletin 23, 788.)

20. G.Alaga, K.Alder, A.Bohr & B.Mottelson, Kgl.Danske Videnskab Selskab, Mat.-fys.Medd., 29, 9 (1955).

21. P.G.Hansen, O.B.Nielsen & P.K.Sheline, Nucl.Phys.,12, 4 (1959).

22. E.P.Grigor'ev & M.P.Avotina, Doklad na XI Ezhegodnom soveshchanii po yadernoi spektroskopii (Program of the 11th Conference on Nuclear Spectroscopy), Riga, 1961.

INVESTIGATION OF THE RADIATION OF Mn^{56}

- S.S.Vasil'ev, No Sen Ch'ang & L.Ya.Shavtvalov

Radioactive decay of 2.6-hour Mn^{56} has been the subject of many investigations.[1-9] In none of these, however, was an attempt made to separate the partial β^--spectra by measuring β-γ coincidences. This is explained by the experimental difficulties encountered in studying an activity with so short a period. Hence we felt it would be of interest to resolve the partial β^--spectra correlating with the different γ-rays in order to establish the definitive decay scheme.

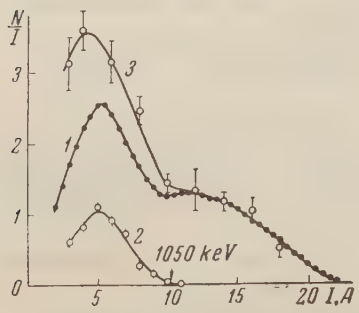

Fig.1. 1 - β^--spectrum of Mn^{56}, 2 - β^--spectrum correlating with 1.81 MeV γ-rays, 3 - β^--spectrum correlating with 0.845 MeV γ-rays.

The Mn^{56} activity was obtained by the $Mn^{55}(d,p)Mn^{56}$ reaction, i.e., by bombarding a 0.6 mg/cm^2 manganese foil with 13.7 MeV deuterons in the cyclotron of the Scientific Research Institute of Nuclear Physics of Moscow State University.

The β^--spectrum recorded by means of a thin magnetic lens β-spectrometer is shown in Fig.1 (curve 1). Resolution of this β-spectrum by means of the usual Fermi-Kurie plot showed that it is comprised of three partial spectra with end-point energies 2830 ± 40, 1030 and 750 keV and relative intensities 60, 28 and 12%, respectively.

The γ-spectrum of Mn^{56} was investigated by means of a scintillation γ-spectrometer (Cs^{137} 662 keV γ-line half-width 8.7%). The experimental γ-spectrum is shown in Fig.2. There are discernible sharp peaks at 845, 1810 and 2100 keV and less clearly pronounced peaks at 2530 and 2660 keV.

The β-γ coincidences were investigated by means of the magnetic lens spectrometer and the scintillation γ-spectrometer connected into a coincidence circuit. The resolving time of the coincidence circuit was determined periodically in the process of measuring true coincidences and proved to be 0.27 microsec.

The Fermi-Kurie plot of the β^--spectrum correlating with the 2.1 MeV γ-rays is shown in Fig.1. The end-point energy obtained from this plot is 780 ± 60 keV, which is in good agreement with the end-point energy obtained by resolution of the singles β^--spectrum. The β^--spectrum correlating with the 1810 keV γ-rays is shown in Fig.1 (curve 2). Naturally, in this case there passed through the analyzer gate Compton recoils from harder γ-rays (namely, the 2.1 MeV gammas). However, the deduced end-point energy (1050 keV) is determined primarily by coincidences with the 1810 keV γ-rays inasmuch as the 2100 keV γ-rays yield coincidences only with the partial β^--spectrum with 750 keV end-point energy. Lastly, we also investigated coincidences of the electrons with 845 keV γ-rays. The resultant β^--spectrum (curve 3 in Fig.1) almost coincides with the β^--spectrum recorded on the β-spectrometer alone. This indicates that the entire complex β^--spectrum correlates with the 845 keV γ-rays. Some increase in the number of counts in the coincidence measurements in the $E_\beta < 1$ MeV region is apparently connected with additional coincidences produced by Compton electrons from the harder γ-rays. As will be evident from Fig.2, the contribution of hard-

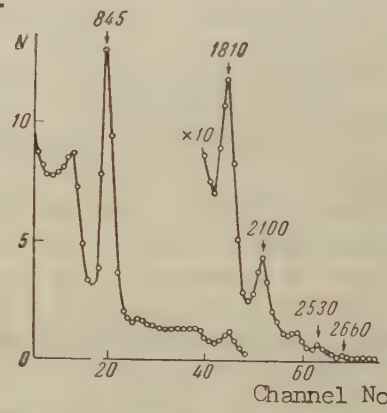

Fig.2. Gamma-spectrum of Mn^{56} recorded on a scintillation spectrometer.

gamma Compton recoils amounts to ~20% in the 850 keV region. The "additional" number of coincidences amounted to approximately the same percentage.

Our experimental data substantiate the decay scheme for Mn^{56} that is commonly accepted at present. Fig.4 shows this decay scheme, taken from Ref.5, with the β-γ correlation results obtained in the present investigation indicated by double lines.

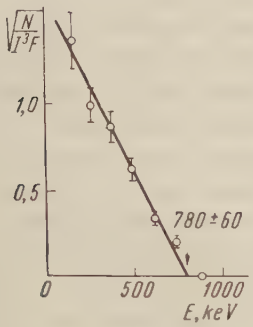

Fig.3. Fermi-Kurie plot of the β^--spectrum correlating with the 2100 keV γ-rays.

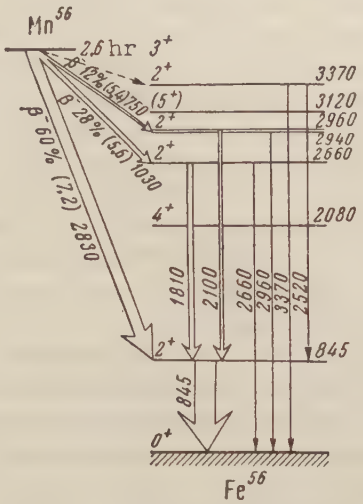

Fig.4. Decay scheme of Mn^{56}.

We desire to express our gratitude to V.S.Zazulin and Yu.A.Vorob'ev for assistance in the work.

Scientific Research Institute of Nuclear Physics,
Moscow State University

References

1. L.G.Elliott & M.Deutsch, Phys.Rev., 64, 321 (1943).
2. K.Siegbahn, Arkiv Mat.Ast.Fys., 33A, No.10 (1946).
3. G.R.Bishop, R.Wilson & H.Halban, Phys.Rev.,77, 416 (1950).
4. F.R.Metzger & W.B.Todd, Phys.Rev.,92, 904 (1953).
5. L.V.Groshev, A.M.Demidov, V.N.Lutsenko & V.I.Pelekhov, Atomnaya energiya, 3, 187 (1957).(Trans. Soviet Journal of Atomic Energy).
6. C.S.Cook, Nucl.Phys., 7, 480 (1958).
7. P.Dagley, M.A.Grace, T.M.Gregory & T.S.Hill, Proc.Roy.Soc., A250, 550 (1959).
8. P.Kienle & R.E.Segel, Phys.Rev.,114, 1554 (1959).
9. R.W.Bauer & M.Deutsch, Phys.Rev.,117, 519 (1960).

PROPERTIES OF LOW-LYING STATES OF Li^5 AND Be^8 EVINCED IN DISINTEGRATION REACTIONS INVOLVING LIGHT NUCLEI

- S.S.Vasil'ev, V.V.Komarov & A.M.Popova

In the energy distribution of the products of reactions with simultaneous emission of several particles there may appear a specific structure due to interaction of the reaction products with each other. Thus, for example, if as a result of a nuclear reaction there form three simultaneously emitted particles, the energy distribution of one type of particles, which in general is described by statistical laws, may have a complex form: there may be evinced in it maxima corresponding to potential interaction of the two other reaction products or to their resonance interaction in different states, if such interactions are energetically possible. The greater the number of particles formed simultaneously in the nuclear reaction and the greater the possibilities of different variants of their interaction with each other in the final state, the more complex will be the form of the energy distribution.

If we consider the simplest reaction with simultaneous formation of three particles, for example, disintegration of a deuteron under the action of protons or neutrons, there will appear in the energy spectrum of nucleons of one type two peaks, corresponding to proton-neutron, proton-proton or neutron-neutron interaction in the final state.

In earlier contributions[1-4] it was shown that as regards height, these maxima depend on the angle of emergence of the investigated reaction product, and as regards width, on the magnitude of the energy constant characterizing the interaction of the particle pair.

This example of a simple reaction with the formation of several nucleons (see Refs.2 & 3) is an illustration of the influence of pair interactions of reaction products in the final state on their energy distribution. In more complicated reactions, when there can occur cascade processes, the energy spectrum is further complicated by the appearance of maxima corresponding to different states of the intermediate and final nuclei. In addition to the above mentioned cascade maxima, one may expect the appearance of maxima due to interaction of the reaction products in the final state when the reaction is one of direct disintegration.

Let us consider how one can take into account the influence of interaction of reaction products in the final state in investigating the integral energy distributions of particles forming as a result of reactions occurring by direct disintegration of a compound nucleus. The differential cross section for disintegration of a compound nucleus with spin I and parity π into n particles with given energy E_i and momentum p_i can be written in the form

$$d\sigma \sim \delta\left[\sum_{i=1}^{n}(E_i - E)\right]\delta\left(\sum_{i=1}^{n} p_i\right)\prod_{i=1}^{n} d^3p_i\,|H_{a\sigma}|^2, \qquad (1)$$

where E is the total energy of the system and H_{ab} is the matrix element of the transition from the initial state a to the final state b, which is of the form

$$\langle\prod_{i=1}^{n}\psi_i\,\varkappa(S_i)\,|\,V\,|\,\Psi_{jjz}\rangle, \qquad (2)$$

where Ψ_{jjz} is the wave function of the compound nucleus and $\psi_i\varkappa(S_i)$ is the wave and spin function of the i-th particle formed as a result of the reaction.

If the particles do not react with each other in the final state, their wave functions ψ_i are plane waves and the motion of any two particles i and j can be written in the form of the product of plane waves

$$\exp(-i\vec{q\rho}/\hbar)\ \exp(-ipR/\hbar),$$

where $q = {}^1/_2(p_i - p_j)$ is the momentum of the relative motion of the particles:

$$P = (p_i + p_j),\ \vec{\rho} = (r_i - r_j) \text{ and } R = {}^1/_2\ (r_i + r_j).$$

If one takes into account the interaction of the particles i and j, the wave function $\varphi(\rho)$ of their relative motion will be a distorted wave. The radial part of the wave function of the relative motion of the scattered particles can be approximated in the form[5]

$$\varphi(\rho) = f(E_{rel})\, g(\rho), \tag{3}$$

where $f(E_{rel})$ is a function depending only on the relative energy of the interacting particles. The form of this function can be determined from the data on scattering, so that if we take $\varphi(\rho)$ in the form of a scattered wave and use the boundary condition at $\rho = a$, where a is the range of the nuclear forces, we can obtain

$$f(E_{rel}) = \frac{A}{q}\sin(\delta + \Phi), \tag{4}$$

where

$$A^2 = F_L^2(a) + G_L^2(a), \text{ and } \Phi = \operatorname{arctg}\ F_L(a)/G_L(a),$$

wherein $F_L(a)$ and $G_L(a)$ are Coulomb functions.

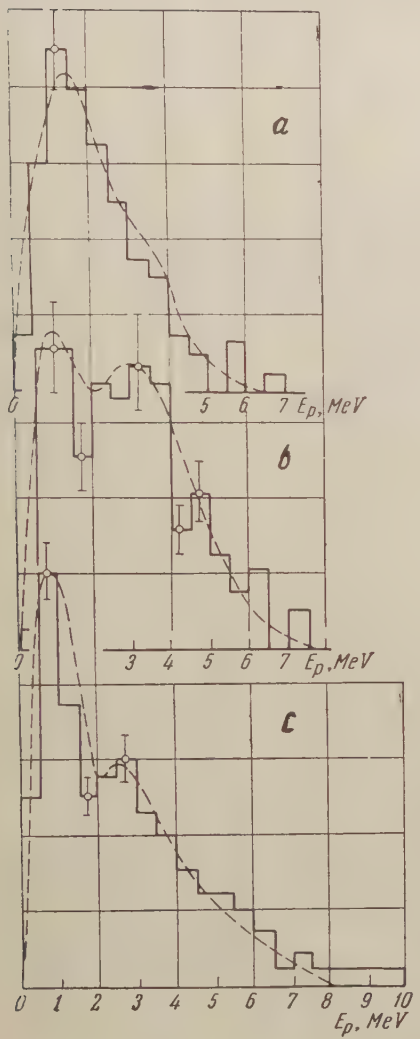

Energy distributions of protons from the $C^{12}(p,p')-3\alpha$ reaction for three different energy ranges of the incident particles in the center of mass system: a - 15-20 MeV, b - 21-33 MeV, c - 24-29 MeV protons. The solid lines are the theoretical curves constructed on the assumption of four-particle simultaneous disintegration taking into account the following interactions: a) two α-particles on the ground and 2.9 MeV levels of the Be^8 nucleus and an α-particle and proton on the ground level of the Li^5 nucleus for a primary proton energy of 15-20 MeV, b) two α-particles on the ground, 2.9 and 11.7 MeV levels of Be^8 and an α-particle and proton on the ground level of Li^5 at a primary proton energy of 21-23 MeV, c) two α-particles on the ground, 2.9 and 11.7 MeV levels of Be^8 and an α-particle and proton on the ground level of Li^5 for a primary proton energy of 24-29 MeV.

Using Eq.(3) for the radial wave function of the relative motion of the interacting particles, one can, following Chew-Hart-Brueckner[6], write the differential cross section for the reaction in the form

$$\frac{d\sigma}{dE_i} \sim f(E_i)\ \frac{\sin^2(\delta + \Phi)}{q^2}. \tag{5}$$

If there can occur simultaneous interaction of two pairs of particles in the final state, the differential cross section will be of the form

$$\frac{d\sigma}{dE_i} \sim f(E_i) \frac{\sin^2(\delta_1 + \Phi_1)}{q_1^2} \cdot \frac{\sin^2(\delta_1 + \Phi_2)}{q_2^2}. \quad (6)$$

By way of illustration let us consider the energy distribution of protons forming in the reaction of disintegration of C^{12} into three α-particles under the influence of primary protons with energies from 15 to 30 MeV.

As was shown in Ref.7, disintegration of a carbon nucleus into three α-particles under proton bombardment occurs with low probability by cascade through the C^{12} compound nucleus, for its levels are very weakly evinced. Direct interactions for the investigated primary proton range begin to play a substantial role only at an energy of ~22 MeV. This means that the main modes of disintegration of the C^{12} nucleus at primary proton energies in the range from 15 to 30 MeV are the following:

$$C^{12} + p \rightarrow Be^8 + Li^5;$$
$$C^{12} + p \rightarrow Be^8 + p + \alpha;$$
$$C^{12} + p \rightarrow Li^5 + \alpha + \alpha;$$
$$C^{12} + p \rightarrow p + \alpha + \alpha + \alpha.$$

It should be noted that from the standpoint of energy considerations in the above listed four- and three-particle disintegrations there can occur interaction of two α-particles on the ground, 2.9 and 11.8 MeV levels of the Be^8 nucleus and interaction of an α-particle and a proton on the ground level of the Li^5 nucleus, i.e., the Li^5 and Be^8 nuclei may be evinced not as intermediate nuclei of the cascade but as a result of interaction of the reaction products.

Then in the histograms of the excitation energies of Be^8 and Li^5 there will be evinced the levels of these nuclei, and the spectra of the protons and α-particles will be described by statistical distributions calculated on the assumption of four-particle disintegration taking into account interaction of two α-particles on the listed levels of the Be^8 nucleus and an α-particle and proton on the ground level of the Li^5 nucleus, respectively.

To verify this inference we investigated the energy distributions of protons from the $C^{12}(p,p')3\alpha$ reaction in the primary proton energy range from 15 to 30 MeV. The experimentally observed proton spectra in the indicated primary proton energy range have peaks in the region of low proton energies (see figure), which cannot be explained by manifestation of the levels of the compound C^{12} nucleus, if the decay mode is $C^{12} + p \rightarrow C^{13} \rightarrow C^{12} + p \rightarrow p + 3\alpha$.

It is natural to assume that this structure of the spectrum of the protons forming in the $C^{12}(p,p')3\alpha$ reaction is due to simultaneous interaction in the final state of two α-particles on the levels of the Be^8 nucleus and an α-particle and proton on the ground state of the Li^5 nucleus in direct disintegration of the compound nucleus.

Under this assumption the energy distributions of the protons from the C^{12}-$(p,p')3\alpha$ reaction should be characterized by Eq.(6). In the case of resonance scattering $\operatorname{tg}(\delta + \Phi) = -{}^1/_2 F_L/(E_{res} - E_{rel})$. In this case Eq.(6) can be rewritten in the form

$$\frac{d\sigma}{dE_p} = Af(E_p) \frac{\Gamma_L'^2}{(E'_{res} - E'_{rel})^2 - {}^1/_4 \Gamma_L'^2} \cdot \frac{\Gamma_L''^2}{(E''_{res} - E''_{rel})^2 - {}^1/_4 \Gamma_L''^2}, \quad (7)$$

where E_p is the proton energy, E'_{res} is the energy of the level in the Be^8 nucleus and E''_{res} is the energy of the level in the Li^5 nucleus involved in the scatter-

ing of the particles, E'_{rel} is the relative energy of the two interacting α-particles, E''_{rel} is the relative energy of the interacting α-particle and proton, and Γ_L is the level width.

For comparison with the experimental energy distributions of protons formed in the $C^{12}(p,p')3\alpha$ reaction we plotted the theoretical sum curves. The addends for these were the curves of the energy distributions of the protons calculated on the assumption of simultaneous four-particle disintegration taking into account possible interactions of the α-particles on one of the levels of Be^8 and an α-particle with protons on the levels of Li^5.

The relative areas under the individual statistical curves (addends) were in agreement with the relative probability of manifestation of the levels of the Be^8 nucleus and the Li^5 nucleus in the investigated primary proton energy ranges. The probability for manifestation of a level in each energy range of the primary protons was investigated in the work of Ref.7.

The calculated sum curves are shown in the figure. It will be evident that the shape of the experimental spectra of the protons is in agreement with the theoretical curves plotted on the assumption of simultaneous four-particle disintegration of the compound nucleus, taking into account resonance interaction of the particles in the final state. It was found from the calculation that the peak of the energy distribution of the protons in the 2-3, 2.5-3.5 and 3-4 MeV regions for primary protons of energies in the 15-20, 21-23 and 24-29 MeV intervals, respectively, is due to interaction in the final state of two α-particles on the 0 and 2.9 MeV levels of Be^8 and an α-particle and a proton on the ground level of Li^5.

The maximum in the energy distribution of the protons in the 1-2 and 0.5-1.5 MeV regions for primary proton energies in the 21-23 and 26-27 MeV intervals, respectively, is due to resonance interaction of two α-particles on the 11.8 MeV level of Be^8 and interaction of an α-particle and proton on the ground level of Li^5.

Institute of Nuclear Physics,
Moscow State University

References

1. V.V.Komarov & A.M.Popova, Zhur.eksp.i teor.fiz.,38, 253 (1960).(Trans. Soviet Physics - JETP.)

2. V.V.Komarov & A.M.Popova, Ibid.,38, 1559 (1960).(Trans. Ibid.)

3. V.V.Komarov & A.M.Popova, Nucl.Phys., 18, 296 (1960).

4. V.V.Komarov & A.M.Popova, Izv.AN SSSR,Ser.fiz.,24, 1145 (1960).(Trans. Bulletin,24, 1147.)

5. E.W.Hamburger, Thesis, University of Pittsburgh, 1959.

6. K.Brueckner, Phys.Rev., 82, 598 (1951).

7. S.S.Vasil'ev, V.V.Komarov & A.M.Popova, Izv.AN SSSR,Ser.fiz.,24, 1153 (1960).(Trans. Bulletin, 24, 1154.)

ELECTRON-NEUTRINO ANGULAR CORRELATION IN FREE NEUTRON DECAY

- V.V.Vladimirskii, V.K.Grigor'ev, V.A.Ergakov, D.P.Zharkov, & Yu.V.Trebukhovskii

Hitherto the angular correlation coefficient for free neutron decay has been measured twice. Robson[1] published the value $\lambda = +0.07 \pm 0.12$, whereas we obtained[2] $\lambda = -0.06 \pm 0.13$. The error in these measurements was so large that we decided to measure λ again using an improved set-up.

In the present work we studied the recoil proton energy spectra by the time-of-flight technique; the momentum of the decay electron, and, hence, that of the neutrino, were fixed. Proton spectra corresponding to various values of λ for electron momentum $p_e = 2mc$ are shown in Fig.1. Since the proton spectrum is very sensitive to λ, measurement of the spectrum is a convenient means of studying angular correlation.

A diagram of the experimental set-up is shown in Fig.2. The collimated 35 mm diameter neutron beam, emanating from the USSR Academy of Sciences heavy water reactor, passed into an aluminum vacuum chamber containing the detectors and spectrometers for analyzing the decay electrons and recoil protons. The electrons were momentum selected by a double toroidal β-spectrometer.[3] The resolution of this system is 6%. At the intermediate focus of the spectrometer there was mounted a thin-walled (3 mg/cm^2 terylene) Geiger-Müller counter filled with circulating methylal. A plastic scintillator 90 mm in diameter and 1 mm thick was located at the second focus and coupled by a light pipe to a BS photomultiplier. Our coincidence circuit selected only those electrons which passed through both detectors. Use of a double toroidal spectrometer made it possible to reduce substantially the chance coincidence background and to limit the volume in which decays were recorded.

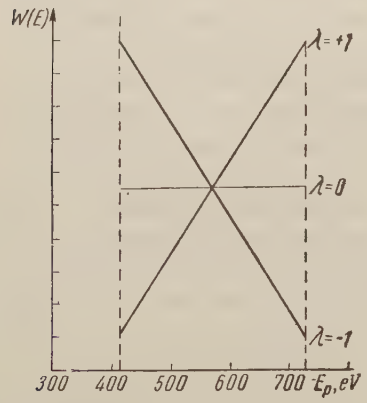

Fig.1. Recoil proton spectra at fixed values of the decay electron momentum for different values of the angular correlation coefficient λ. The dashed lines indicate the limits of the proton spectrum for the specified electron momentum.

The recoil protons were focused by an electrostatic spectrometer[4] onto an electron multiplier with an axially symmetric Al-Mg alloy[5] window 24 cm^2 in area.

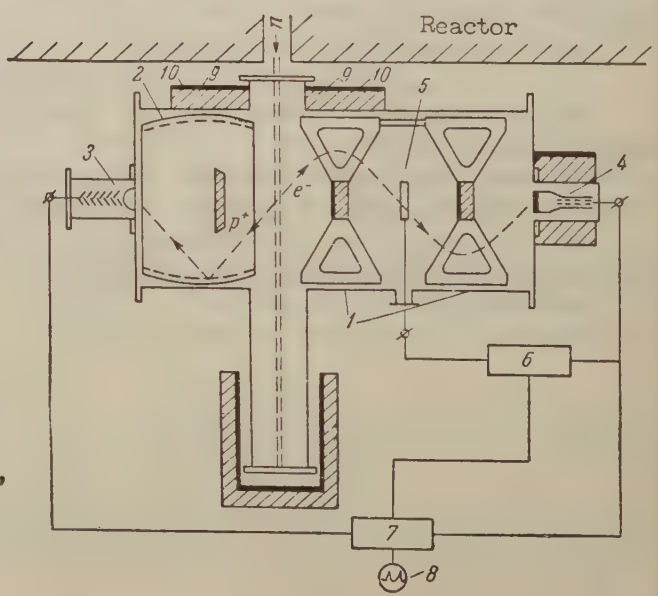

Fig.2. Diagram of the set-up for studying angular correlation in free neutron decay: 1) double toroidal β-spectrometer, 2) electrostatic time-of-flight analyzer, 3) electron multiplier, 4) scintillation counter, 5) counter, 6) coincidence circuit, 7) time analyzer, 8) oscilloscope, 9) lead, 10) boron carbide shielding.

The electrostatic spectrometer was a capacitor with cofocal ellipsoid plates. It operates on the principle of an electrostatic mirror. The inner plate, made of screen mesh, was grounded; a positive potential was applied to the outer plate.

The proton spectra were studied by the time-of-flight technique, inasmuch as the paths of particles in an elliptical field are the same regardless of the particle energy and angle of emergence from the source volume.

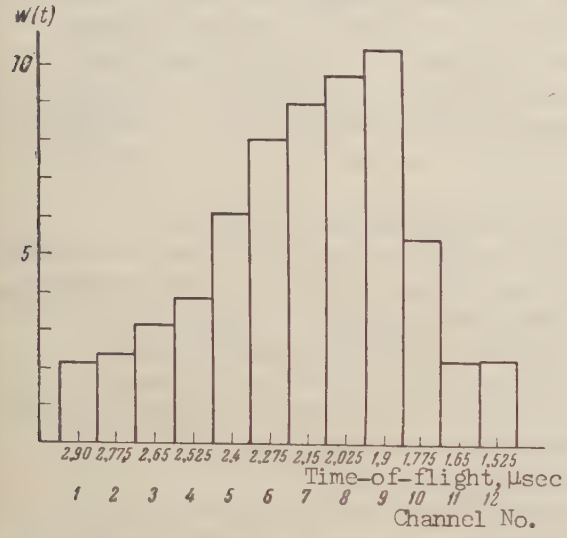

Fig.3. Experimental pulse distribution as recorded by the 12-channel time analyzer.

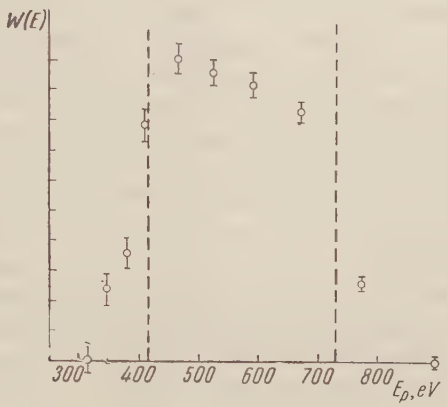

Fig.4. Experimental energy distribution of pulses due to the decay protons. Electron momentum $p_e = 2mc$. The dashed lines, as in Fig.1, represent the limits of the spectrum.

Two cofocal spherical screens were mounted in front of the multiplier cathode. To reduce the background a potential of +35 V was applied to the outer sphere, while the inner sphere was maintained at -4 kV. This field accelerated the protons and markedly improved the focusing onto the electron multiplier.

The pulses due to protons and electrons were recorded on a 12-channel time analyzer with a 0.125 microsec channel width. The measurement range was from 1.5 to 3 microsec. The counting rate was as high as 20 pulses per hour. The average ratio of chance to true coincidences was 1:3.

The pulse distribution obtained experimentally is shown by the histogram of Fig.3. Channels 1, 2, 11 and 12 recorded the chance coincidence background. Fig.4 shows the same data replotted to an energy scale. A least square analysis of the results gave the value of $\lambda = -0.12 \pm 0.04$. The indicated uncertainty is comprised of the statistical (0.02) and instrumental (0.03) errors.

If we assume that tensor and scalar forms of interaction are absent, the value obtained for λ corresponds to

$$R = \frac{|g_{\Gamma-T}|^2}{|g_{\Phi}|^2} = 1.75^{+0.48}_{-0.33}.$$

References

1. I.M.Robson, Canad.J.Phys.,36, 1450 (1958).

2. Yu.V.Trebukhovskii, V.V.Vladimirskii, V.K.Grigor'ev & V.A.Ergakov, Zhur. eksp.i teor.fiz.,36, 1314 (1959).(Trans. Soviet Physics - JETP.)

3. V.V.Vladimirskii, E.K.Tarasov & Yu.V.Trebukhovskii, PTE , 1, 13 (1956).

4. V.K.Grigor'ev, Ibid.,5,33 (1960).(Trans. Instruments & Exper.Techniques.)

5. V.A.Ergakov, G.E.Levin, A.E.Melamid, Yu.V.Trebukhovskii & N.S.Khlebnikov, Ibid., No.3, 157 (1961).(Trans. Ibid.)

REMARKS ON THE EXCITED STATES OF THE ODD-ODD NUCLEI Ho^{166} AND Cs^{134}

- L.F.Kalinkin, A.S.Melioranskii & I.V.Estulin

Holmium-166

Low-lying states of $_{67}Ho^{166}$ form in β-decay of Dy^{166} (80.2 hr) and as a result of neutron radiative capture by Ho^{165}. Earlier we[1] considered the γ-transitions between the Ho^{166} levels evinced in these two processes. Helmer & Burson[2] and Rusinov et al[3] supplied new detailed data on the decay of Dy^{166}, showing that the single-particle characteristics of an odd proton (Ω_p) and neutron (Ω_n) could account for the energy levels of Ho^{166}, in agreement with the theory of strongly deformed nuclei. The results of detailed analysis of the new data are shown in Fig.1.

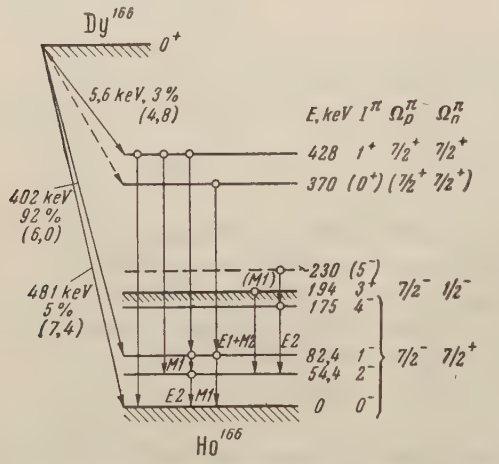

Fig.1. Low-lying energy levels and γ-transitions observed in $Dy^{166} \xrightarrow{\beta^-} Ho^{166}$ and $Ho^{165}(n,\gamma)Ho^{166}$.

The ground state of Ho^{166} has a $(^7/_2^-,\ ^7/_2^+)$ configuration in agreement with the experimental data on the spins of the ground states of the neighboring nuclei Ho^{165} $(\Omega_p^\pi = {}^7/_2^-)$ Dy^{165} and Er^{167} $(\Omega_n^\pi = {}^7/_2^+)$ and Nilsson's[4] level scheme. The levels of Ho^{166} with energies 54.4 (2^-), 82.4 (1^-) and 175 (4^-) keV are rotational states of configuration $(^7/_2^-,\ ^7/_2^+)$ with K = 0 and odd parity[1,2].

The isomeric level of Ho^{166} at 194 keV can be interpreted, by analogy with the isomeric states of $_{66}Dy^{165}$ (108 keV) and $_{68}Er^{167}$ (208 keV), by single-particle excitation of a neutron with $\Omega_n^\pi = {}^1/_2^-$. The appearance of such a state does not conflict with Nilsson's level scheme. According to the theoretical calculations of Nilsson[4] and Lemmer and Green[5], the value of Ω_p^π corresponding to single-particle excitation of an odd proton is $^7/_2^+$. The allowed character of the β-decay of Dy^{166} to the 428 keV level of Ho^{166} ($\log ft = 4.8$) indicates that this level is reached by a single particle β-transition of a neutron without reorientation of the angular momentum and with $\Delta\Lambda = 0$.[6] Therefore it is natural to assigne to this level the configuration $(^7/_2^+,\ ^7/_2^+)$, which would also explain the absence of a transition from this level to the 194 keV (3^+) level. The 370 keV level, which also forms in β-decay of Dy^{166}, probably has $I^\pi = 0^+$, which would allow of simple explanation of the peculiarities of the observed γ-transitions. This explanation assumes that the 428 and 370 keV levels are the initial states of a rotational band with K = 0 and even parity for the $(^7/_2^+,\ ^7/_2^+)$ configuration.

Thus most of the levels of Ho^{166} shown in Fig.1 agree fairly well with the theoretical calculations of level assignments and level sequences for strongly deformed nuclei.[4,5] At the same time the nature of the 230 keV level remains ambiguous. The experimental data do not exclude an E1 transition from this level[1]; then its parity would be even. In this event the level could be considered a consequence of excitation of a proton with $\Omega_p^\pi = {}^1/_2^+$ in accord with Nilsson's level scheme.[4] It is also possible that this state is associated with a configuration of several nucleons in unfilled shells.

Cesium-134

Previously we suggested that some of the low-lying excited levels of Cs^{134}, detected in studying the $Cs^{133}(n,\gamma)Cs^{134}$ reaction, could be interpreted as nuclear multiplet states.[7] The theoretical calculations of Varshalovich[8] permit us to state with much greater certainty that multiplet structure is present in the low-lying levels of Cs^{134}.

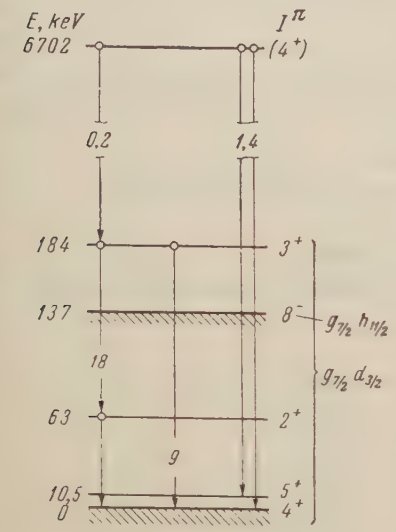

Fig.2. Some levels and γ-transitions in Cs^{134}. The γ-transition intensities are shown in the gaps in percent referred to neutron capture.

Figure 2 shows γ-transitions from the initial state, which is formed in thermal neutron capture[9] by Cs^{133}, to lower levels of Cs^{134}. A comparison of the experimentally measured intensities of these transitions[9] with Varshalovich's calculations[8] (the experimental and theoretical ratios of the reduced probabilities are respectively ~0.15 and 0.11) confirms that the 184 keV excited state belongs to a nuclear multiplet characterized by the $(g_{7/2}, d_{3/2})$ configuration of the odd proton and neutron, just as are the ground state[10] and the first (10.5 keV) level[11]. This configuration allows of states with spin and parity 5^+, 4^+, 3^+, and 2^+. If we assume that all the lower levels with even parity shown in Fig.2 comprise a multiplet, then for pure M1 and E2 transitions from the 184 keV (3^+) level to the 63 keV (2^+) level and to the ground state (4^+) the experimental reduced probability ratio is approximately an order of magnitude greater than the theoretical ratio[8]. A favorable relative mixture of these radiations in the transitions could reduce the discrepancy. The assumption that the 184 keV level has the odd nucleon configuration $(d_{5/2}, d_{3/2})$ leads to a difference of about three orders of magnitude between the experimental and theoretical ratios of the reduced probabilities.

The energy splitting and the spin sequence of the nuclear multiplet levels can be compared with theoretical predictions by using Schwartz's approximate calculations[12]. From a calculation taking into account all the nucleons in unfilled shells, i.e., for $(g_{7/2})^5_{7/2}, d^1_{3/2}$ configurations, and the reasonable value of 0.1 for α (α is a parameter which characterizes the admixture of spin forces[13]), one obtains the correct level splittings and spin sequence: 4^+ (ground state), 5^+ (10.5 keV), and 2^+ (63 keV). However, the location of the 3^+ (184 keV) level fails to agree with Schwartz's theory.

It should be noted that Kaliteevskii et al[14] attributed the $(h_{11/2})^{10}_0 (d_{3/2})^3_{5/2}$ configuration to the neutrons in the unfilled shells of $_{55}Ba^{135}$. The assumption that the neutron configuration is conserved in $_{55}Cs^{134}$ requires a proton configuration $(d_{5/2})^2_0 (g_{7/2})^3_{7/2}$, which explains the spins of the ground state (4^+) and isomeric state (8^-) in agreement with Nordheim's "weak" rule as revised by Brennan & Bernstein[13].

Scientific Research Institute of Nuclear Physics,
Moscow State University

References

1. A.S.Melioranskii, I.V.Estulin & L.F.Kalinkin, Zhur.eksp.i teor.fiz.,40, 64 (1961).(Trans. Soviet Physics - JETP.)

2. R.G.Helmer & S.B.Burson, Phys.Rev., 119, 788 (1960).

3. L.I.Rusinov, A.V.Borovikov, V.S.Gvozdev, G.D.Porsev, S.L.Sakharov & Yu. L.Khazov, Zhur.eksp.i teor.fiz., 39, 1529 (1960).(Trans.Sov.Physics - JETP.)

4. S.G.Nilsson, Deformation of nuclei (cited in Russian trans.), 1958.

5. R.H.Lemmer & A.E.S.Green, Phys.Rev.,119, 1043 (1960).

6. M.E.Voikhanskii & L.K.Peker, Programma i tezisy dokladov XI Ezhegodnogo soveshchaniya po yadernoi spektroskopii v Rige (Program of the Eleventh Annual Conference on Nuclear Spectroscopy, Riga, 1960), p.28, M.,1960.

7. A.S.Melioranskii, I.V.Estulin, L.F.Kalinkin & B.S.Kudinov, Zhur.eksp. i teor.fiz., 38, 758 (1960).(Trans. Soviet Physics - JETP.)

8. D.A.Varshalovich, Ibid., 38, 173 (1960).(Trans. Ibid.)

9. R.Balzer, H.Knoepfel, J.Lang, P.Stoll & W.Wölfli, Helv.phys.acta, 32, 264 (1959).

10. E.H.Bellamy & K.F.Smith, Phil.Mag., 44, 33 (1953).

11. A.W.Sunyar, J.W.Mihelich & M.Goldhaber, Phys.Rev.,95, 570 (1954).

12. C.Schwartz, Phys.Rev.,94, 95 (1954).

13. M.H.Brennan & A.M.Bernstein, Phys.Rev.,120, 927 (1960).

14. N.I.Kaliteevskii, E.E.Fradkin & M.P.Chaika, Zhur.eksp.i teor.fiz., 39, 954 (1960).(Trans. Soviet Physics - JETP.)

LEVELS IN Cu^{64}, EXCITED IN THE $Ni^{64}(p,n\gamma)Cu^{64}$ REACTION

- A.K.Val'ter, I.I.Zalyubovskii, A.P.Klyucharev & V.A.Lutsik

Information on the level structure of Cu^{64} can be obtained only from nuclear reactions. Investigation of the energy spectrum of protons from the $Cu^{63}(d,p)Cu^{64}$ reaction made it possible to establish the level structure of Cu^{64} above 3800 keV.[1] However, the decay of these levels has not been studied. Some scant data on the decay of some states of Cu^{64} have been obtained from studies of thermal neutron capture by Cu^{63}. However, it is difficult to identify γ-transitions following this reaction when, as was the case in most investigations[2-5], the natural Cu isotope mixture is used as the target.

Results of γ-ray energy measurements and comparison of our results with the data of others (energies in keV)

$Cu^{63}(d,p)$ (1)	$Cu^{63}(n,\gamma)$ Ref.2	Ref.3	Ref.4	Ref.5		$Ni^{64}(p,n\gamma)$ Our data
158 (8)	150?				155 (5)	162 (3)
			202 (10)		205 (10)	205 (6)
277 (8)		280 (8)	280 (10)	280 (25)	276 (10)	279 (2)
343 (8)						349 (3)
360 (8)						367 (7)?
574 (8)						
607 (8)		618 (11)	620 (25)	600 (50)		
664 (8)						
743 (8)		754 (21)	770 (25)			
877 (8)						
894)8)		}904 (21)?	910 (33)?			
925 (8)						

Note: The figures in parentheses are the uncertainties in units of the last digit.

To investigate the low-lying levels of Cu^{64} and their decay one can use the hitherto uninvestigated $Ni^{64}(p,n\gamma)Cu^{64}$ reaction. The threshold of this reaction as calculated from the nuclear masses[6] is 2450 ± 6 keV (Q = -2412 keV), while the experimentally measured[7] threshold is 2500 keV (Q = 2460 keV), i.e., 50 keV higher than the calculated value.

Instead of detecting neutrons, the usual procedure in studying energy levels excited in $(p,n\gamma)$ reactions, we used a scintillation γ-spectrometer (a 30 x 15 mm NaI(Tl) crystal coupled to an FEU-42 photomultiplier) and a 60-channel pulse height analyzer.

The target was a metallic foil 1 μ thick prepared by electrolytic deposition. Its composition was: 9.7% Ni^{58}, 6.1% Ni^{60}, 0.4% Ni^{61} and 79.8% Ni^{64}. This target was bombarded with 2.3 to 3.0 MeV protons accelerated in the 4 MeV electrostatic accelerator of the Physical-Technical Institute of the Academy of Sciences of the Ukrainian SSR. The γ-ray spectrum obtained when bombarding the target with 3.0 MeV protons is shown in Fig.1. The results of the energy measurements are listed and compared with the data of other authors[1-5] in the table. The γ-spectrometer was calibrated with reference to the following sources: radioactive Hg^{203} (279 keV) and Hf^{181} (480 keV) and the $Co^{59}(p,n\gamma)Ni^{59}$ (E_γ = 342 ± 2 keV) and $Cu^{65}(p,n\gamma)Zn^{65}$ (E_γ = 115 and 155 keV) reactions. The thresholds for excitation of the 162, 279 and 349 keV levels were determined from the excitation functions shown in Fig. 2 and found to equal 2656 ± 4, 2782 ± 5 and 2850 ± 5 keV, respectively. The threshold, calculated from these data, for the $Ni^{64}(p,n\gamma)Cu^{64}$ reaction is 2496 ± 6 keV,

which is in agreement with the value of 2500 keV reported earlier by Blaser et al and 44 ± 8 keV higher than the computed threshold. Apparently, the value of the atomic mass of Cu^{63} and/or Ni^{64} given by Kravtsov[6] is erroneous.

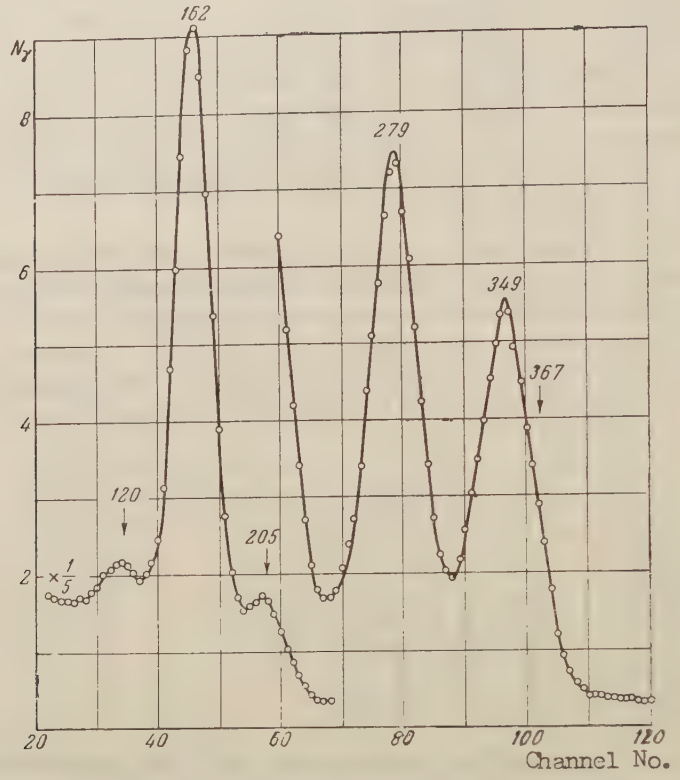

Fig.1. Gamma-ray spectrum obtained in bombarding a Ni^{64} target with 3.0 MeV protons.

Fig.2.presents the integral yield of γ-rays with $E_\gamma \geq 600$ keV (triangle-point curve) emitted as a result of the (p,γ) and $(p,p'\gamma)$ reactions mainly on Ni^{64}. It will be seen that the maximum yield of these reactions is reached at a proton energy below the threshold of the (p,n) reaction and that each "partial" threshold is accompanied by a significant decrease in the yield of the (p,γ) and $(p,p'\gamma)$ reactions.[8] This circumstance can be utilized for determining the $(p,n\gamma)$ reaction thresholds. However, in this case, the target thickness has a significant effect on the accuracy of the threshold determinations; this is why one observes a decrease in the γ-yield for proton energies some 20-30 keV above each $(p,n\gamma)$ threshold. However, such accuracy in the determination of thresholds is entirely sufficient to demonstrate that the 162, 279 and 349 keV γ-rays correspond to cross-over γ-transitions from the respective levels in Cu^{64} to the ground state (Fig.3).

The behavior of the integral γ-ray excitation function indicates that as a result of the competition of the $(p,n\gamma)$ reaction the yields of the (p,γ) and $(p,p'\gamma)$ reactions decrease sharply with increase of proton energy. Consequently, the proton elastic scattering cross section for reactions going through a Ni^{64} compound nucleus stage should also be smaller compared to the cross section for other nickel isotopes. This has been observed by one of us.[9]

The relative probabilities for exciting the 162, 279 and 349 keV levels in the $Ni^{64}(p,n\gamma)Cu^{64}$ reaction can be determined from the excitation functions for

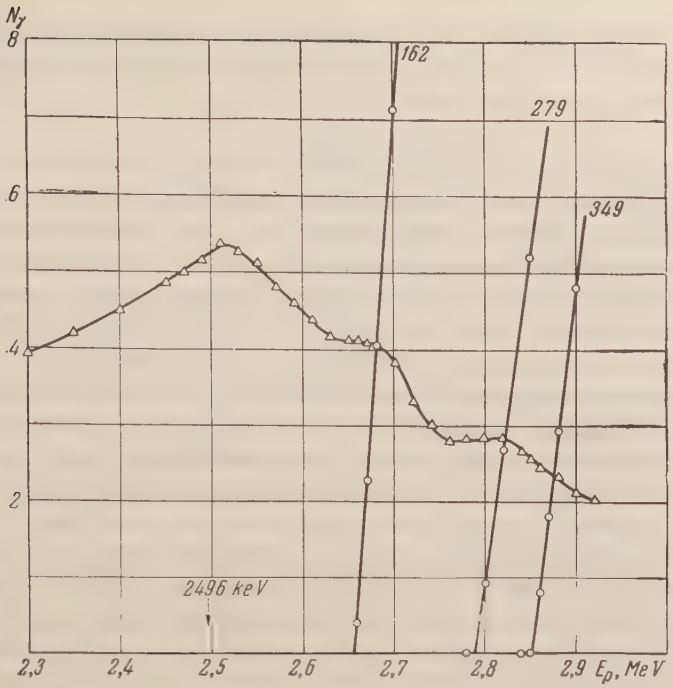

Fig.2. Excitation functions of the 162, 279 and 349 keV γ-rays and the excitation function of the integral γ-radiation with $E_\gamma > 600$ keV.

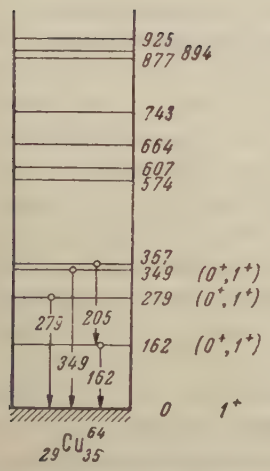

Fig.3. Energy level diagram of Cu^{64}.

the corresponding γ-peaks. With corrections for the differences in the sensitivity of the γ-spectrometer to γ-rays of of these energies, the slopes of the yield curves (Fig.2) should be the same near the $(p,n\gamma)$ threshold for each γ-line. Since our method precludes direct comparison to the intensities of neutron groups to the ground and excited states of Cu^{64}, we compared the relative decrease of the integral yield of the (p,γ) and $(p,p'\gamma)$ reactions near the (p,n) threshold and near the threshold for excitation of the 162 keV level. Such a comparison (Fig.2) indicates that the intensities of these neutron groups are probably equal. But then the ground and first three excited states of Cu^{64} are excited with the same probabilities in the $(p,n\gamma)$ reaction. Consequently, the spins of these states can differ from each other and from the ground state of Ni^{64} by no more than one unit. Inasmuch as the assignment for the ground state of Ni^{64} is 0^+ and since according to Nilsson's level diagram the parities of the low-lying states of Cu^{64} are even, the states with 0^+ or 1^+ must be excited with the greatest abundance.

In this connection, some results of investigations of high energy γ-transitions in the $Cu^{63}(n,\gamma)Cu^{64}$ reaction[3,5] should be mentioned. Thermal neutrons are known to be captured by the 7915 keV level of Cu^{64}, which has the characteristics 1^- or 2^- since the spin and parity of the ground state of Cu^{63} are $3/2^-$. But the only γ-transitions departing from the 7915 keV level are transitions to the ground state and to the 279 and 607 keV levels; no γ-transitions to the 162 and 349 keV levels have been detected. Hence the spin of the 7915 keV level is most probably

2^-, and γ-transitions to the 162 and 349 keV levels would not be detected if the spins of these levels are 0^+. It is possible that the assignments for the ground state and the first three excited states of Cu^{64} are 1^+, 0^+, 1^+ and 0^+, respectively.

In addition to the 162, 279 and 349 keV γ-rays corresponding to levels of these energies in Cu^{64}, a 205 keV γ-ray was also observed to be excited in the (p,nγ) reaction. This γ-line was observed at $E_p > 2.85$ MeV. Consequently, it could appear only as a result of a cascade transition from the 349 keV or the next higher level of Cu^{64} via the 162 keV level, for it is known[1] that the fourth level of Cu^{64} lies less than 20 keV above the 349 keV level. Because of unfavorable conditions for calculating the excitation function of the 205 keV γ-rays, it is impossible to establish reliably from which of the two levels the 205 keV transition departs. Consequently, to identify the departure level we turned to the data of Reier & Shamos[4] and Groshev et al[5] who observed this γ-transition. But these researchers did not detect a 349 keV γ-line. Hence the 205 keV γ-line is not associated with a cascade transition from the 349 keV level. On the other hand, the sum of the energies of the 205 and 162 keV γ-transitions is the same as the energy of the fourth level[1] to within the limits of the accuracy with which the energies were determined; therefore the 205 keV γ-transition must be attributed to de-excitation of the 367 keV rather than the 349 keV level. A cross-over transition from the 367 keV level to the ground state has not been observed either by us or by others.[4,5]

The 120 ± 6 keV γ-peak (Fig.1) was observed below the threshold of the (p,nγ) reactions. By means of our method for identifying γ-transitions in (p,nγ), (p,p'γ) and (p,γ) reactions[8] it was shown that the 120 keV γ-peak is not associated with any of these reactions on Ni^{64}.

We desire to express our gratitude to A.Ya.Taranov and A.A.Tsygikalo for permission to use the electrostatic generator and the V.N.Medyanik for preparing the isotopic nickel foils.

Physical-Technical Institute,
Academy of Sciences of the Ukrainian SSR

References

1. R.P.DeFigueiredo, M.Mazari & W.W.Buechner, Bull.Amer.Phys.Soc.,3, 38 (1958); Phys.Rev.,112, 873 (1958).

2. B.Hamermesh & V.Hummel, Phys.Rev.,88, 916 (1952).

3. G.A.Bartholomew & B.B.Kinsey, Phys.Rev.,89, 386 (1953).

4. M.Reier & M.H.Shamos, Phys.Rev.,95, 636 (1954); 100, 1302 (1955).

5. L.V.Groshev, A.M.Demidov, V.N.Lutsenko & V.I.Pelekhov, Atlas spektrov - γ-luchei radiatsionnogo zakhvata teplovykh neitronov (Atlas of thermal neutron capture γ-ray spectra), M.,1958.

6. V.A.Kravtsov, Uspekhi fiz.nauk, 65, 451 (1958).(Trans.Sov.Physics - Uspekhi.)

7. J.P.Blaser, F.Boehm, P.Marmier & P.Scherrer, Helv.phys.acta, 24, 441 (1951).

8. A.K.Val'ter, I.I.Zalyubovskii, A.P.Klyucharev & V.A.Lutsik, Zhur.eksp.i teor.fiz.,39, 1159 (1960).(Trans. Soviet Physics - JETP.)

9. A.P.Cliutcharev, Proceedings of the International Conference on Nuclear Structure, p.169, Univ. of Toronto Press, 1960.

POLARIZATION OF THE γ-RAYS FROM THE $Si^{30}(p,\gamma)P^{31}$ REACTION

- P.M.Tutakin

Introduction

Measurement of level spins and parities is of interest from many standpoints including that of verification and improvement of nuclear models.

In cases when the nuclei emit linearly polarized γ-rays, the level parities can be determined by measuring the polarization. For measurement of the polarization of γ-rays with energies from 4 to 12 meV one can use photodisintegration of the deuteron. As is known[1], the process of deuteron photodisintegration in this energy range occurs almost entirely owing to electric dipole absorption. The yield of photoprotons at an angle Φ to the vector E is proportional to $\cos^2\Phi$.[2] Taking advantage of this dependence and employing the nuclear emulsion technique, a number of authors[3,4] have investigated the polarization of γ-rays from nuclear reactions.

In the present work we measured the polarization of γ-rays from the $Si^{30}(p,\gamma)P^{31}$ reaction. For the 773, 939 and 979.5 keV resonances[5] we investigated the transitions from the resonance levels to the ground state of P^{31}. These are the resonances observed by Broude, Green & Willmott[6] at 775, 955 and 1000 keV. It has been shown[5,6] that all these transitions are $^3/_2 \rightarrow {}^1/_2$ transitions. For the 1393 keV resonance[7] we investigated the transition from the resonance level to the 1.26 meV level ($^5/_2 \rightarrow {}^3/_2$ transition).

Experimental Part

The beam of monoenergetic H_2^+ ions, accelerated by the electrostatic generator of the Physical-Technical Institute (USSR Academy of Sciences), was incident on a thin isotopic target of Si^{30} prepared by magnetic separation. The γ-rays emitted from the target at an angle of 90° to the direction of the beam were intercepted by the plates containing heavy water. The plates were arranged around the target in a steel annular cassette with a mean diameter of 80 mm. The cassette accomodated 12 plates measuring 12 x 14 mm. The thickness of the emulsion was 200 μ. The exposure time was 30-40 hours with an average current of 20-25 μA to the target. The energy loss in the target by 1 MeV protons attaned ~5 keV. In order to determine the photon track background, simultaneously with the plates soaked in heavy water, there were exposed plates soaked with ordinary water. Inasmuch as the high voltage generator was not used earlier for accelerating deuterons, the background of recoil proton tracks formed by neutrons from the $D(d,n)He^3$ reaction was nil. The general background from all possible sources was very low and hence was neglected in processing the experimental results.

The direction and length of the photoproton tracks appearing in the emulsion as a result of disintegration of deuterons were determined by means of a microscope. The photoproton tracks were measured at all angles α in the plane of the emulsion. The angle α was measured from the direction of the particle beam. For counting, we accepted all photoproton tracks lying wholly within the emulsion, the entrance angle of which did not exceed 30°.

Experimental Results

If the radiation from a nucleus is partially polarized, the azimuthal distribution of photoprotons is of the form

$$W(\alpha) = 1 + (R - 1)\cos^2\alpha, \tag{1}$$

where R is the ratio of the intensity of the γ-rays polarized in the plane P, defined by the direction of the accelerated proton and the emitted γ-ray, to the intensity of the γ-rays polarized at 90° to the plane P.

Hamilton[8] showed that the value of the ratio R for each type of radiation is related with the coefficients of the polar angular distribution of the γ-rays, written in the form

$$W(\theta) \sim 1 + a_2\cos^2\theta + a_4\cos^4\theta + \ldots .$$

For electric dipole and quadrupole radiation of the value of R is given by

$$R_{E1} = \frac{1 + a_2\cos 2\theta}{1 + a_2} \tag{2}$$

and

$$R_{E2} = \frac{(1 + a_2 + a_4) - {}^1/_2\, a_4 \sin^2 2\theta}{1 + (a_2 + a_4)\cos 2\theta} . \tag{3}$$

For magnetic dipole and quadrupole radiation the values of R_{M1} and R_{M2} are the reciprocals of R_{E1} and R_{E2}.

Photoproton track length distribution

Comparison of the experimental angular distribution of photoprotons with that calculated by means of Eq.(1) allows of determining the character of the radiation (for example, E1 or M1) and, consequently, whether parity change is involved in the transition.

The photoproton range distribution is shown in the accompanying figure. The photoproton energies corresponding to the centers of the peaks, determined from the ratio between the range and the energy for the wet emulsion, correspond to the energies of the γ-rays associated with the transitions from the excited state of P^{31} to the ground state (E_p = 773, 939 and 979.5 keV) and to the first excited level at 1.26 MeV (E_p = 1393 keV). The presence of some short tracks can be explained by transitions to low lying levels in P^{31}.

The values of the level energies E^*, the γ-ray energies E_γ, and the calculated coefficients a_2 and a_4 for dipole and quadrupole transitions and the measured coefficients a_2 are shown in Table 1. The divergence of the measured coefficients from the calculated values for pure dipole radiation always indicates a mixture of M1 + E2. For this reason a number of authors[6,9], on the basis of analysis of the transition probabilities and the results of measurements of the angular distributions of the γ-rays attributed even parity to the 8.04, 8.20 and 8.24 MeV levels of P^{31}.

The results of the present measurements of the polarization of the γ-rays allow of obtaining further information on the multipole orders of the radiation. In Table 2 we list the measured and calculated by means of Eqs.(1), (2) and (3) numbers of photoproton tracks for pure E1, M1, E2 and M2 transitions in each 30° interval of α. In the last column of Table 2 we give the type of pure transition that is in agreement with the measured angular distribution of photoprotons.

Table 1

Level and γ-ray energies and value of the coefficients a_2 and a_4

E_p, keV	E^*, MeV	E_γ, MeV	Transition	$a_2$theo		$a_4$theo	$a_2$exp		
				Dipole rad.	Quadrup. rad.		[6]	[5, 7]	[10]
773	8,04	8,04	3/2→1/2	−0,6	+1	0	−0,40±0,01	−0,44	−0,47±0,03
939	8,20	8,20	3/2→1/2	−0,6	+1	0	−0,80±0,02	−0,61	—
979,5	8,24	8,24	3/2→1/2	−0,6	+1	0	−0,64±0,03	−0,47	—
1393	8,64	8,64	5/2→3/2	−0,5	−1,87	+2,5	—	−0,45	—

Table 2

Measured and calculated numbers of photoproton tracks*

E_p, keV	E_γ, MeV	Experiment			Calculated						Assignment
		0—30°	31—60°	61—90°	0—30°	31—60°	61—90°	0—30°	31—60°	61—90°	
					*E*1			*M*1			
773	8,04	109	73	34	111	73	35	35	73	111	*E*1
939	8,20	124	183	228	278	183	88	88	183	278	*M*1
979,5	8,24	173	116	73	176	116	56	56	116	176	*E*1
1393	8,64	26	60	109	86	60	34	34	60	86	*M*1
					*M*2			*E*2			
773	8,04	109	73	34	10	73	136	136	73	10	*E*2
939	8,20	124	183	228	24	183	340	340	183	24	*M*2
979,5	8,24	173	116	73	15	116	216	216	116	15	*E*2
1393	8,64	26	60	109	28	60	92	92	60	28	*M*2

*The calculated and experimental data are equated for the 31 to 60° angular interval.

Conclusions

The following conclusions may be drawn on the basis of the polarization measurements of the γ-radiation emitted in the $Si^{30}(p,\gamma)P^{31}$ reaction.

1. The radiations emitted in the transitions from the 8.03, 8.20 and 8.24 MeV resonance levels (I = 3/2) of P^{31} to the ground level ($I = 1/2^+$) and in the transition from the 8.64 MeV level (I = 5/2) to the 1.26 MeV level ($I = 3/2^+$) are noticeably polarized.

2. Measurements of the angular distributions of the photoprotons show that

a) for the 939 and 1393 keV resonances the transitions are primarily M1 with a small admixture of E2 radiation; from this it follows that the P^{31} nucleus in the 8.20 and 8.64 MeV states has even parity;

b) for the 773 and 979.5 keV resonances the transitions are primarily E2 with an admixture of M1, and hence the 8.04 and 8.24 MeV levels also have even parity (for the 979.5 keV resonance this assertion may be open to question inasmuch as the coefficient a_2 has been measured with low accuracy).

I desire to express my gratitude to the group working under A.A.Tsygikalo and S.P.Tsytko for assistance in carrying out the experiments.

References

1. H.A.Bethe, Elementary Nuclear Theory, N.Y., 1947.
2. H.A.Bethe & R.F.Bacher, Revs.Mod.Phys., 8, 122 (1936).
3. L.W.Fagg & S.S.Hanna, Phys.Rev., 92, 372 (1953).
4. J.S.Hughes & D.Sinclair, Proc.Phys.Soc., A69, 125 (1956).

5. Yu.P.Antuf'ev, A.K.Val'ter, V.Yu.Gonchar, E.G.Kopanets, A.N.L'vov, P.M. Tutakin & S.P.Tsytko, in "Yadernye reaktsii pri malykh i srednikh energiyakh" (Nuclear reactions at low and medium energies), pp.294, M., 1958.
6. C.Broude, L.L.Green & J.C.Willmott, Proc.Phys.Soc., A72, 1097, 1115, 1122 (1958).
7. A.K.Val'ter, S.P.Tsytko, and others, Izv.AN SSSR, Ser.fiz., 25, 854 (1961). (Trans.Bulletin 25, 862.)
8. D.R.Hamilton, Phys.Rev., 74, 782 (1948).
9. P.M.Endt & C.M.Braams, Revs.Mod.Phys., 29, 683 (1957).
10. P.M.Endt, M.Suffert & A.M.Hoogenboom, Physica, 25, 659 (1959).

* * * * * * *

LEVELS EXCITED IN THE $F^{19}(\alpha,p)Ne^{22}$ REACTION

- A.M.Romanov, E.V.Myakinin & M.P.Konstantinova

Most of the available information on the energies of the low-lying levels of Ne^{22} has been obtained in investigating the $F^{19}(\alpha,p)Ne^{22}$, $N^{22}(p,p')Ne^{22}$, and $Na^{22}(\gamma,p)Ne^{22}$ reactions and studying β-decay of Na^{22}. Some data on levels in Ne^{22} above 11 MeV have been obtained by observing the neutron yield resonances for the $O^{18}(\alpha,n)Ne^{21}$ reaction.

The data on the levels of Ne^{22} have been systematized in the review by Ajzenberg-Selove & Lauritsen[1]. Analysis of these data gives reason to assert that the energies of only two of the excited levels of Ne^{22} have been reliably established.

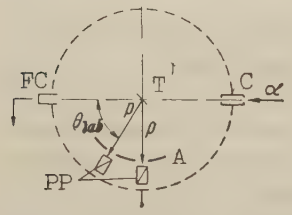

←Fig.1. Diagram of the experiment: C - collimator, T - target, FC - Faraday cup, PP - photographic plate, A - apertures.

With a view to obtaining further information on the level diagram of Ne^{22}, particularly in the excitation energy range above 3.3 MeV, we investigated the energy spectra of protons from the $F^{19}(\alpha,p)Ne^{22}$ reaction at incident α-particle energies of 10.3, 13.6 and 14.7 MeV.

The experimental arrangement is diagramed in Fig.1. The α-particle beam from the cyclotron of the Physical-Technical Institute of the USSR Academy of Sciences was focused by means of quadrupole lenses and collimated. The target was located in the center of the brass chamber at an angle of 45° to the beam. The target was a fluoroplastic film with a superficial density of 1.3 mg/cm^2. The photographic cassettes with Ya-2 nuclear plates (emulsion thickness 100 μ) were mounted inside the chamber at a distance of 206 mm from the target. The cassette windows were covered with aluminum foil, which protected the photographic plates from light and stopped α-particles scattered from the target.

The photographic plates were processed in the usual manner and scanned by means of an MBI-2 microscope. Typical range distribution histograms are shown in Figs.2 and 3. The mean energies of the proton groups from the $F^{19}(\alpha,p)Ne^{22}$ reaction were determined by means of range-energy curves for aluminum and photographic emulsions. As the energy scale references we used the position of the

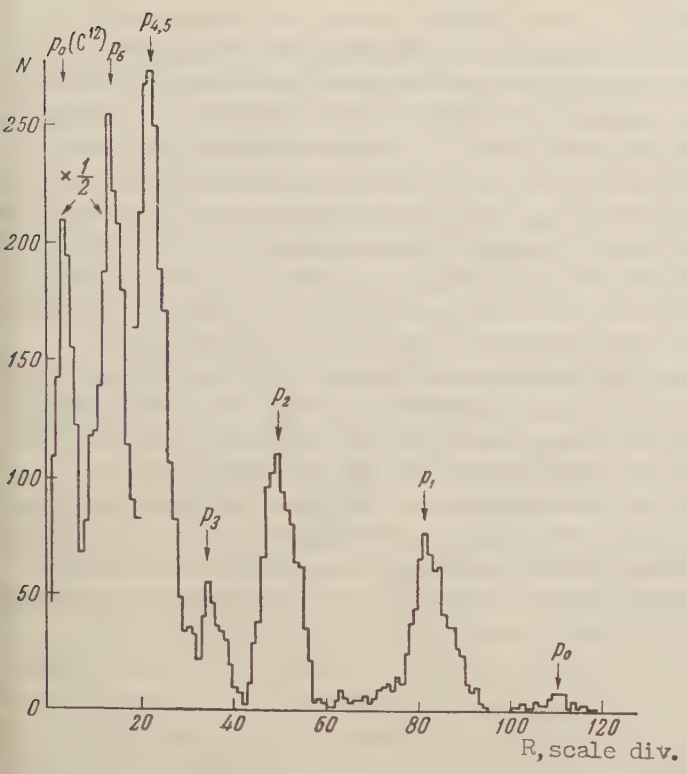

Fig.2. Histograms of tracks of protons from the $F^{19}(\alpha,p)Ne^{22}$ reaction at E_α = = 10.3 MeV and $\theta_{lab} = 60^\circ$.

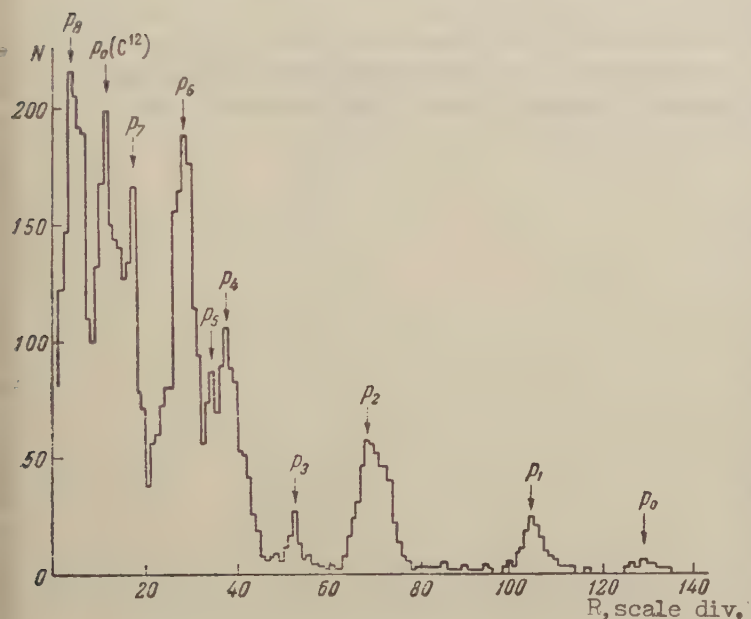

Fig.3. Histogram of tracks of protons from the $F^{19}(\alpha,p)Ne^{22}$ reaction at E_α = 13.6 MeV and $\theta_{lab} = 90^\circ$.

proton group from the $C^{12}(\alpha,p)N^{15}$ reaction (Q_0 = -4.965 MeV) and the position of the p_2 proton group from the $F^{19}(\alpha,p)Ne^{22}$ reaction corresponding to formation of Ne^{22} in the second excited state (we assumed Q_2 = -1.67 MeV). Analogous measurements were carried out for two emission angles (θ_{lab} = 60 and 90°) and three α-particle energies (E_α = 10.3, 13.6 and 14.7 MeV). This enabled us to identify more reliably the proton groups from the $F^{19}(\alpha,p)Ne^{22}$ reaction and to establish the mean proton energies. For determining the excitation energy of the levels in Ne^{22} we used the relation

$$Q_i = E_{pi}\left(1+\frac{m_p}{m_r}\right) - E_\alpha\left(1-\frac{m_\alpha}{m_r}\right) - \frac{2\sqrt{E_{pi}E_\alpha m_p m_\alpha}}{m_r}\cos\theta,$$

where Q_i is the reaction energy in excitation of the i-th level of the final nucleus, m_p, m_α and m_r are the masses of the proton, α-particle and final nucleus, respectively, E_α is the α-particle energy (laboratory system), E_{pi} is the mean energy of the proton group produced in the reaction with formation of the final nucleus in the i-th state, and θ is the angle of emission of the protons in the laboratory system.

The reaction energy Q_0, in accord with the masses of the nuclei participating in the reaction, was taken equal to 1.69 MeV.

The results of analysis of the experimental data are given in the accompanying table together with the results of other authors[2,3]. It may be noted that the existence of levels at 6.37, 7.52 and 8.54 MeV has not been reported hitherto. The energy of the third excited level as determined in our experiments is in good agreement with the data of Ophel & Wright[3], but differs substantially from the value reported by Foster, Stanford & Lee[2].

Energies of levels in Ne^{22} (MeV)

Level No.	Ref. 2	Ref. 3	Our data
1	1,28	1,3	1,30±0,05
2	3,3	3,3	3,36±0,05
3	4,9	4,4	4,46±0,10
4	—	5,4	5,40±0,10
5	—	5,7	5,76±0,15
6	—	—	6,37±0,12
7	—	—	7,52±0,15
8	—	—	8,54±0,15

In all cases the intensity of the p_0 proton group associated with formation of Ne^{22} in the ground state was appreciably lower than the intensity of the proton groups corresponding to formation of Ne^{22} in higher excited states. Thus, for example (see Fig.2), the intensity of the p_0, p_1, p_2 and p_3 proton groups at E_o = 10.3 MeV and $\theta_{lab} = 60^o$ are related as 1:10:12:4. At E_α = 13.6 MeV and $\theta_{lab} = 60^o$ the intensity ratios of the p_0, p_1 and p_2 groups are 1:7:20, and at E_α = 14.7 MeV and $\theta_{lab} = 90^o$ the ratios are 1:6:22.

The fact that the intensity of the p_0 proton groups is some 6-12 times lower than the intensity of the p_1 group is, apparently, connected with the character of the shell structures of the initial (F^{19}) and final (Ne^{22}) nuclei. To clarify this matter we are undertaking a further investigation of the distribution of the p_0, p_1 and p_2 proton groups in a wide range of angles. In this connection, we note that in the case of the $Al^{27}(\alpha,p)Si^{30}$ reaction, investigated by us earlier[4], the proton energy spectra have the same peculiarities, and the angular distribution of the p_0 and p_1 group protons indicated that direct interaction mechanisms play a substantial role.

Physical-Technical Institute,
Academy of Sciences of the USSR

References

1. Fay Ajzenberg-Selove & T.Lauritsen, Nucl.Phys., 11, 1 (1959).
2. B.P.Foster, G.S.Stanford & L.L.Lee, Phys.Rev., 93, 1069 (1954).
3. Ophel & Wright, Proc.Phys.Soc., A71, 389 (1958).
4. T.V.Tsareva, A.M.Romanov, E.V.Myakinin & M.P.Konstantinova, Doklad II Svesoyuznoi konferentsii po yadernym reaktsiyam (Report presented at the 2nd All-Union Conference on Nuclear Reactions), Moscow, 1960; A.M.Romanov, Zhur. eksp.i teor.fiz., 39, 1540 (1960). (Trans.Soviet Physics - JETP.)

SPIN AND PARITY ASSIGNMENTS FOR SOME STATES OF Cd^{112}, Sn^{118} AND Sn^{120}

- O.F.Nemets & V.V.Tokarevskii

Excitation of collective levels in stripping reactions has been considered theoretically by Satchler[1] who showed that the probabilities for the reactions with excitation of the successive levels of one vibrational band should differ by approximately an order of magnitude for neighboring levels. To verify Satchler's inferences, we chose Cd^{112}, Sn^{118} and Sn^{120}, inasmuch as the relative energies and spins of the first two levels in these nuclei (the first level is obviously a triplet one) give reason to assume that they are vibrational levels. Moreover, the angular distributions of protons from stripping reactions on Cd^{111}, Sn^{117} and Sn^{119} have not hitherto been studied.

The measurements were carried out using 13.6 MeV deuterons; the experimental procedure has been described in Ref.2. The unbacked targets, enriched to at least 90%, were prepared in the laboratory of A.P.Klyucharev at the Physical-Technical Institute of the Ukrainian SSR Academy of Sciences.

The proton angular distributions are shown in Figs.1,2 and 3. In all figures the solid curves represent the results of calculations according to Butler's theory[3].

For all three nuclei transitions to the ground state are accompanied by transfer of momentum $l_n = 0$, while the transitions to the first excited states involve $l_n = 2$. Inasmuch as the spins of the ground states of the initial nuclei are all $1/2^+$, the $l_n = 0$ value is consistent with the 0^+ assignment for the ground states of the even-even final nuclei.

The possible assignments for the first two excited states are 1^+, 2^+ and 3^+, which is consistent with the value 2^+ obtained from β-decay for the 0.618 MeV level of Cd^{112}, the 1.210 MeV level of Sn^{118} and the 1.180 MeV level of Sn^{120}. The ratios of the probabilities of the reactions corresponding to transitions to

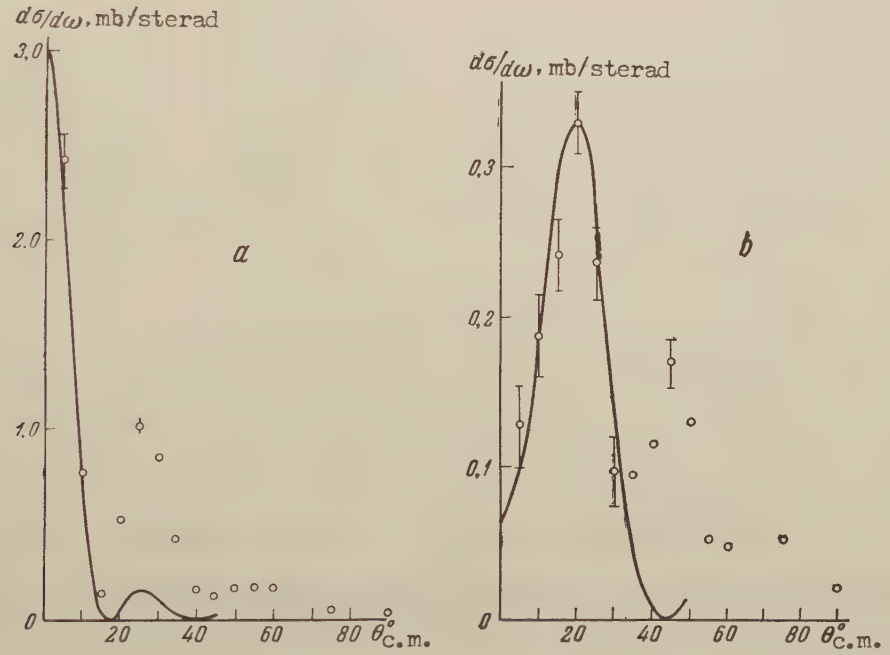

Fig.1. Angular distributions of protons from the reactions: a - $Sn^{117}(d,p)Sn^{118}_{g.s}$ ($l_n = 0$, $r_0 = 7.67$ f); b - $Sn^{117}(d,p)Sn^{118m}$ ($l_n = 2$, $r_0 = 6.3$ f). Curves calculated according to Butler[3].

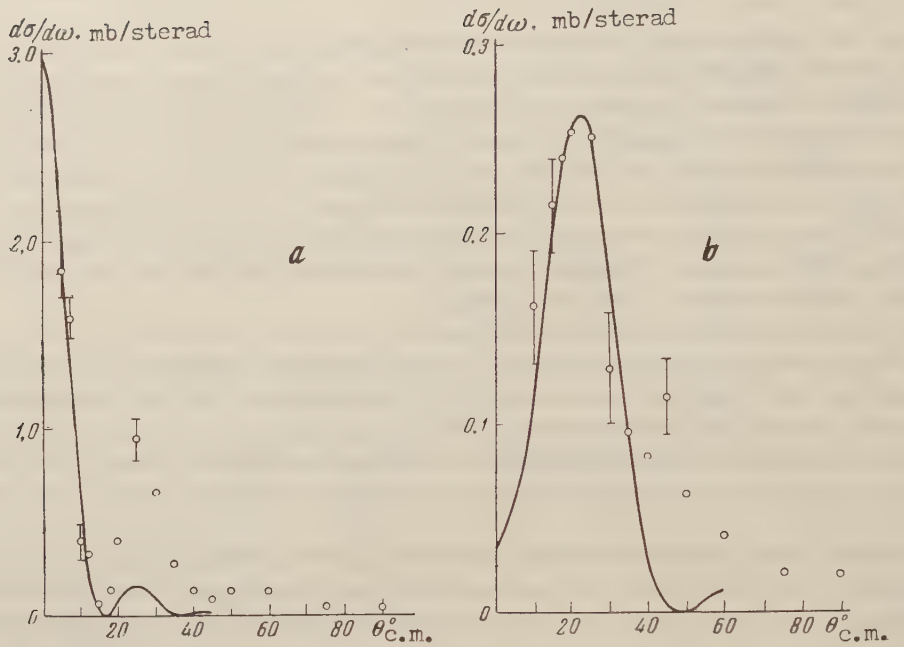

Fig.2. Angular distributions of protons from the reactions: a - $Sn^{119}(d,p)Sn^{120}_{g.s}$ ($l_n = 0$, $r_0 = 7.70$ f); b - $Sn^{119}(d,p)Sn^{120m}$, ($l_n = 2$, $r_0 = 5.65$ f).

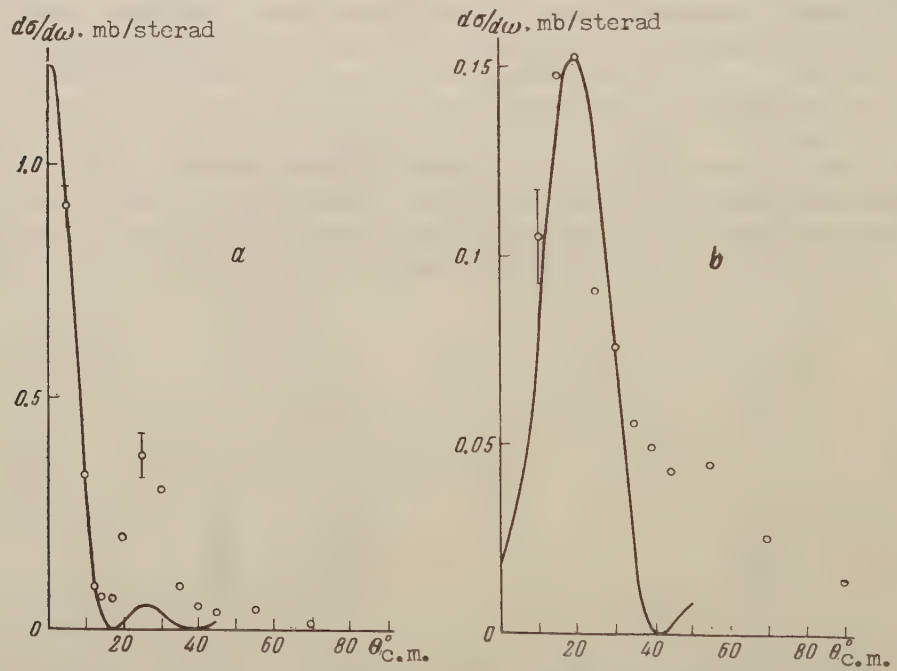

Fig.3. Angular distributions of protons from the reactions: a - $Cd^{111}(d,p)Cd^{112}_{g.s}$ ($l_n = 0$, $r_0 = 7.57$ f); b - $Cd^{111}(d,p)Cd^{112m}$ ($l_n = 2$, $r_0 = 6.60$ f).

the ground states of the final nuclei to the probabilities of reactions corresponding to transitions to the first excited states multiplied by the statistical factor proved to be 4.4 ± 0.2, 4.8 ± 0.1 and 5.7 ± 0.1 for Cd^{112}, Sn^{118} and Sn^{120},

respectively; this is an approximate agreement with the value of ~10 predicted by Satchler.[1]

A noticeable feature in the angular distributions is the greater height of the secondary peak as compared with that predicted by Butler's[3] plane wave theory. Both the great dip between the first and second peaks for $l_n = 0$ and the very small contribution of the isotropic part of the angular distribution indicate that the process of formation of a compound nucleus plays an insignificant role. To obtain agreement with the simple plane wave theory of stripping as regards the location of peaks in the angular distribution for $l_n = 2$, one must assume smaller than usual values for the interaction radius ($r_0 = (1.7 \pm 1.22\, A^{1/3})f$). Such deviations can be explained in the framework of the theory taking into account nuclear and electric interaction.[4]

We desire to express our gratitude to A.P.Klyucharev for preparation of the targets and the personnel of the cyclotron laboratory for insuring operation of the equipment.

Institute of Physics,
Academy of Sciences of the Ukrainian SSR

References

1. G.R.Satchler, Ann.Phys., 3, 275 (1958).
2. N.I.Zanka & O.F.Nemets, Izv.AN SSSR, Ser.fiz., 23, 1460 (1959). (Trans. Bulletin, 23, 1447.)
3. S.T.Butler, Proc.Roy.Soc., A208, 559 (1951).
4. W.Tobocman & M.H.Kalos, Phys.Rev., 97, 132 (1955); G.R.Satchler & W. Tobocman, Ibid., 118, 1566 (1960).

ANGULAR DISTRIBUTION OF PHOTOELECTRONS EJECTED FROM Ag AND Bi TARGETS BY Cs^{137} GAMMA-RAYS

- K.K.Aglintsev, V.V.Mitrofanov, A.A.Rimskii-Korsakov & V.V.Smirnov

Introduction

The angular distribution of photoelectrons from γ-radiation is described by Sauter's formula[1], which should be valid for hard γ-rays and converters with small Z. Inasmuch as in deducing the formula, Sauter did not take into account the influence of the field of the nucleus, this formula will not be correct in the range of large angles θ of emission of the photoelectrons relative to the direction of the incident photons.

Sliv[2] developed a method of calculating the angular distribution of photoelectrons in the relativistic region, taking into account the Coulomb field of the nucleus. The expression deduced by Sliv is a series that converges rapidly for small Z and large θ. Calculations for substances with Z = 20 and 47 yield angular distribution curves differing significantly from the curves given by Sauter's formula. In a later paper[3], Sauter showed that for $\theta = 0$, i.e., in the direction of the incident photons, the photoelectron yield must differ from zero. The results of calculation of I_o/I_{max}, the ratio of the photoelectron flux in $\theta = 0$ direction to the maximum flux corresponding to a certain optimum angle, for the case of a lead target and Co^{60} γ-rays are close to the experimental value obtained by Hedgran & Hultberg[4].

Experimental investigation of the angular distribution of photoelectrons for the purpose of checking the theoretical formulas is difficult owing to strong smearing out of the angular distribution because of multiple scattering of the electrons in the converter. The use of thin converters leads to sharp decrease of the photoelectron flux, which makes it impossible to obtain reliable data, particularly in the range of small and large angles where the intensity is minimal. The experimental curves obtained in the work of Refs.4-7 are strongly smeared out and do not correspond to the true angular distribution. The experimenters referred to were able to obtain angular distribution curves close to the theoretical curves of Sauter only by introducing large corrections for the geometry of the instrument, etc.

The purpose of the present work was experimental investigation of the angular distribution of photoelectrons ejected by Cs^{137} γ-rays from thin layers (~0.05 mg/cm^2) of silver and bismuth and comparison of the results with the theoretical data.

Experimental procedure

The angular distribution experiments were carried out on a Ritron type magnetic spectrometer, the design of which allows of obtaining the spectrum of electrons ejected by γ-rays from a target at different angles.[8] This instrument is diagramed in Fig.1. The electrons with momentum satisfying the detecting conditions, ejected from the target T by the collimated γ-ray beam emerge in the direction TB at an angle θ to the incident beam and are detected by counters 1 and 2 which are connected into a coincidence circuit. The spectrometer had the following parameters: design radius 11 cm, height of main slit 46 cm, width of main slit 2 mm. The source - 6 curie of Cs^{137} - was mounted in a massive lead collimator, which by means of special device could be rotated about the vertical axis through the center of the target (converter) in the range of angles from 0 to 80°.

The character of the photoelectron spectrum from a 25 μ thick Bi target is

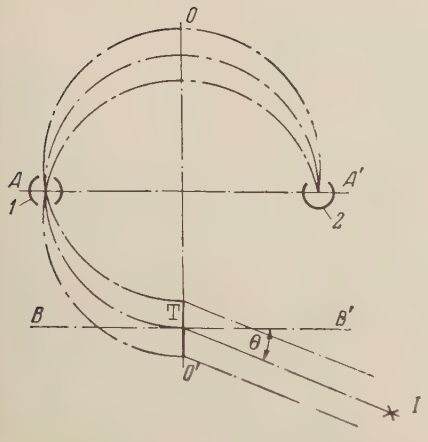

Fig.1. Diagram of the spectrometer: I - Cs^{137} source, T - target(converter), A & A' - slits, 1 & 2 - counters.

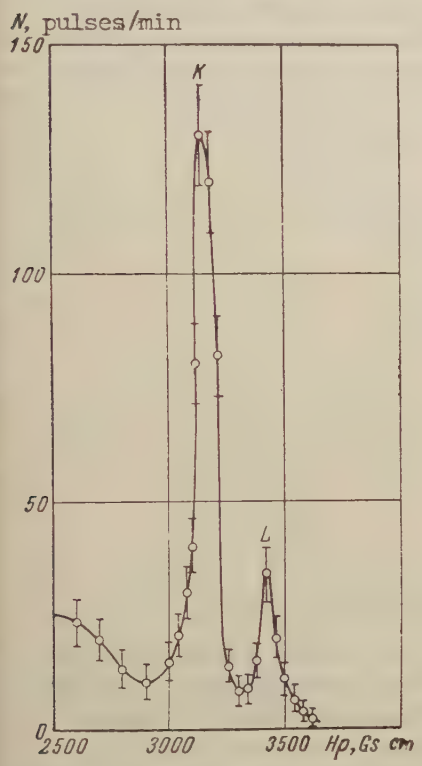

Fig.2. Spectrum of photoelectrons ejected by Cs^{137} γ-rays from a 25 μ thick Bi target.

shown in Fig.2. The half-width of the K photoelectron line equalled 2.5%. To elucidate the influence of electron scattering in the converter on the character of the angular distribution, we performed experiments with converters of different thickness. The silver converters 15 μ (16 mg/cm^2) and 6 μ (6.3 mg/cm^2) thick were foils, the 0.70 μ (0.74 mg/cm^2), 0.21 μ (0.22 mg/cm^2), 0.08 μ (0.08 mg/cm^2) and 0.06 μ (0.06 mg/cm^2) converters were prepared by sputtering silver onto thin collodion films. The bismuth targets, all which were prepared by sputtering, had thicknesses of 0.37 μ (0.36 mg/cm^2), 0.05 μ (0.05 mg/cm^2) and 0.02 μ (0.02 mg/cm^2). The thickness of the deposited layers was determined by weighing coated and uncoated sections of the backing. The angular distribution of photoelectrons was determined from the intensity of the K line at different angles of incidence of the γ-ray beam in the range from 0 to 50°. The photoelectron flux at the given angle was determined as the difference between the area under the corresponding peak and the background recorded under the same conditions but with an uncoated collodion film. The indicated uncertainties are statistical.

Results and discussion

The experimental angular distribution curves obtained with the 6, 0.21 and 0.06 μ thick Ag converters are shown in Fig.3. The analogous curves for 0.37 and 0.05 μ thick Bi converters are given in Fig.4. The solid line in the figures represent the angular distribution curves calculated according to Sauter's formula for the given γ-ray energy and Z of the converter. As will be evident from Fig.3,a the experimental points in the case of the Ag target with a superficial density of 0.06 mg/cm^2 fall on the Sauter curve within the limits of the statistical uncertainty. With increase in the target thickness (Figs.3,b & c) and experimental points depart ever further from the theoretical curve, particularly in the range of angles close to $\theta = 0$. In the case of the Bi targets the experimental curves differ markedly from the curves given by Sauter's formula.

It will be noted that even for the Ag target with a superficial density of 0.22 mg/cm^2 there is observed a substantial photoelectron flux at $\theta = 0$. In order to establish the correspondence between the experimental angular distribution curves and the theoretical curves one must carefully analyze all the factors that may distort the experimental results. One group of factors is connected with the instrument used for the measurements. In the Ritron, as in most spectrometers, there are detected not only the electrons emitted from the target at the

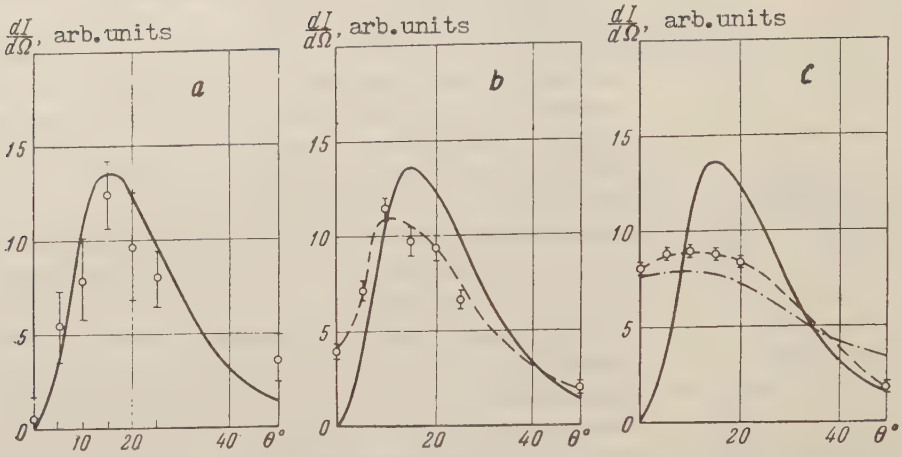

Fig.3. Angular distribution of K photoelectrons ejected by Cs^{137} γ-rays from Ag targets of different thickness: a) superficial density σ = 0.06 mg/cm^2, b) σ = = 0.22 mg/cm^2, c) σ = 6.30 mg/cm^2. Solid lines - theoretical curves calculated by means of Sauter's formula. Dashed lines - curves through the experimental points. Dash-dot lines - calculated curve according to Sauter but taking into account electron scattering in the target.

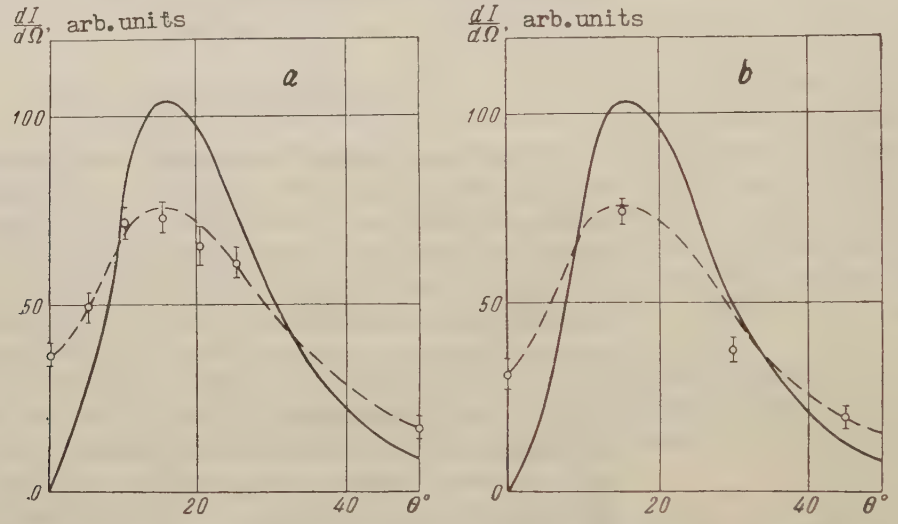

Fig.4. Angular distribution of K photoelectrons ejected by Cs^{137} γ-rays from Bi targets of different thickness: a) σ = 0.05 mg/cm^2, b) σ = 0.36 mg/cm^2. Solid lines - curve calculated according to Sauter's formula; dashed lines - curve drawn through the experimental points.

measured angle θ, but also electrons moving at other angles close to θ. This leads to smearing out of the angular distribution. The results of calculations[9] of the efficiency of "capture" (acceptance and detection) of electrons as a function of the angle for $\theta = 0$ and $\theta \geqslant 15^\circ$ in working with the given spectrometer are presented in the form of curves in Fig.5,a. In Fig.5,b, together with the original distribution curve calculated according to Sauter's formula, we show the curve recalculated taking into account the efficiency of electron "capture" in the spectrometer. It will be evident that the introduced distortion cannot have a significant influence on the results.

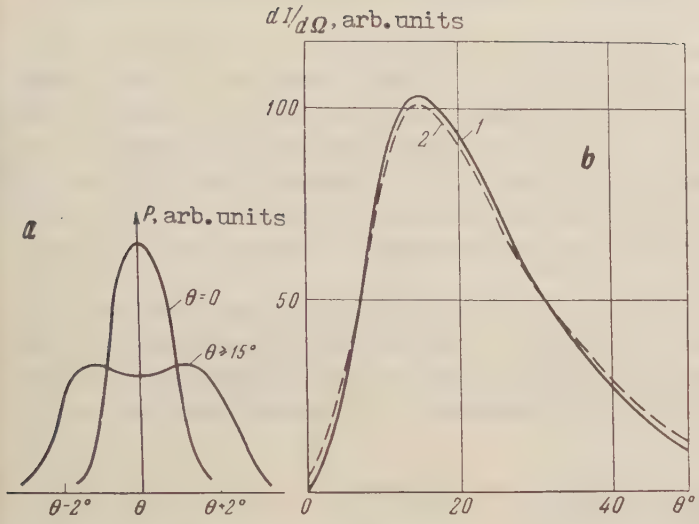

Fig.5. a - Efficiency of electron "capture" in the spectrometer for different angles of emission; b - comparison of Sauter's theoretical curve (1) and the same curve corrected for the efficiency of electron "capture" in the spectrometer (2).

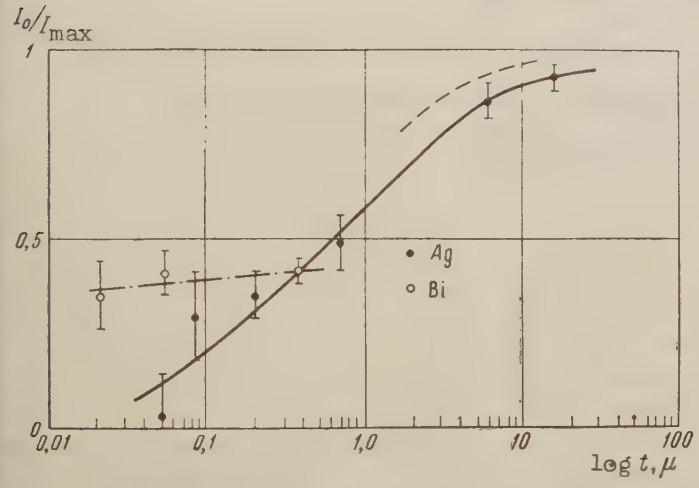

Fig.6. Variation of the ratio I_o/I_{max} with the target thickness t. Dashed line - calculated data for Ag converters.

Distortion of the initial angular distribution of photoelectrons can also occur because of electron scattering in the films covering the entrance and exit windows of counter 1 (in our case collodion films <1 μ thick). In order to evaluate the effect of this factor, we compared the photoelectron spectra recorded at different angles with and without films on the windows of counter 1; in the latter case the electrons were detected only by counter 2. Comparison of the results showed that the presence of films on the windows of counter 1 has no significant effect on the character of the angular distribution.

Another, more significant factor distorting the angular distribution is electron scattering in the material of the converter. The scattering factor can be characterized by the ratio I_o/I_{max}. Approaching the distribution corresponding to Sauter's formulas, this ratio will tend to zero with decrease of the converter thickness. When I_o/I_{max} does not equal 0, as occurs in the case of Bi targets, this ratio must tend to a certain constant value. Fig.6 shows the variation of I_o/I_{max} as a function of the target thickness t. It will be evident that in the case of the 0.06 μ thick Ag converter the photoelectron scattering is virtually nil. In contrast, for Bi targets the ratio remains virtually constant at 0.4 ± 0.1. Theoretical evaluation of the electron scattering in the converter was carried out by the method proposed by Dzhelepov[10]. This method is based on Williams[11] scattering theory and allows of calculating the distortion of the initial angular distribution owing to scattering in the converter with a mean number of collisions $N \geq 10$.

In our case this method is applicable to targets having a thickness greater than 2 μ. In Fig.3,c the dash-dot line represents the calculated curve characterizing the angular distribution of photoelectrons undergoing scattering in the converter. The calculated values of I_o/I_{max} for thick targets are given by the dashed line in Fig.6. Comparison of the calculated data with the experimental results

showed that calculations by Dzhelepov's method apparently yield overestimates for the scattering cross section.

For thin converters, where the number of collisions N = 0.04 to 0.14, the Dzhelepov method of calculation is not applicable. In this case an approximate evaluation of the electron scattering in thin layers was carried out using Mott's formula. These calculations showed that in a 0.2 μ thick Ag layer virtually all the 0.6 MeV electrons are scattered through angles in the range from 0.05 to 0.2°. Thus it may be asserted that the curves reproduced in Figs.3,a and 4,a represent the actual angular distribution of K photoelectrons ejected from Ag and Bi converters by Cs^{137} γ-rays.

The presence in the case of Bi converters of photoelectrons emitted at $\theta = 0^{\circ}$ substantiates the results of Sauter & Wüster[3]; further investigation of this effect would be of interest from the standpoint of the theory of the photoeffect.

We desire to express our gratitude to M.N.Chubarov for assistance in carrying out the measurements.

References

1. F.Sauter, Z.Phys., 11, 454 (1931).
2. L.A.Sliv, Thesis, Physical-Technical Inst., USSR Ac.of Sci., 1955.
3. F.Sauter & H.Wüster, Z.Phys., 141, 83 (1955).
4. A.Hedgran & S.Hultberg, Phys.Rev., 94, 498 (1954).
5. G.D.Latyshev, Zhur.eksp.i teor.fiz., 14, 65 (1944).
6. R.Roy, M.L.Goes & J.Berger, Compt.rendu, 241, 1936 (1955).
7. S.Hultberg, Arkiv fys., 15, No.27, 307 (1959).
8. V.V.Mitrofanov & V.V.Smirnov, PTE, No.1, 22 (1960). (Trans.Instruments & Experimental Techniques.)
9. Yu.V.Khol'nov, Thesis, Radium Institute, USSR Ac.of Sci., 1952.
10. B.S.Dzhelepov, Izv.AN SSSR, Ser.fiz., 18, 95 (1954).
11. E.W.Williams, Proc.Roy.Soc., 169, 531 (1939).

EXCITED STATES OF Li^7 WITH ENERGIES UP TO 9 MeV

- V.G.Shevchenko & B.A.Yur'ev

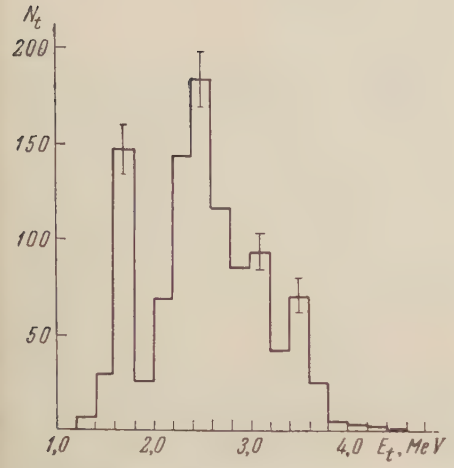

Fig.1. Energy distribution of tritons from the $Li^7(\gamma,t)He^4$ reaction. The curve represents the sum of the measurements at angles of 30°, 60°, 90°, 120° and 135°.

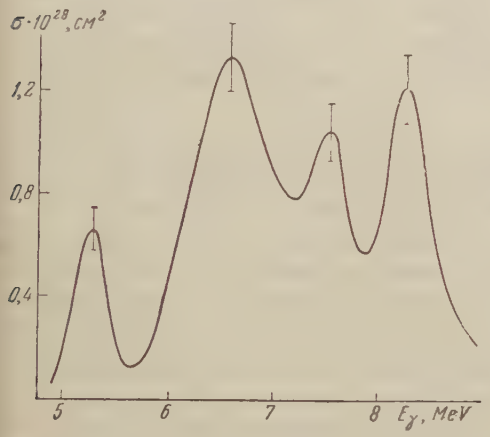

Fig.2. Cross section for the $Li^7(\gamma,t)He^4$ reaction.

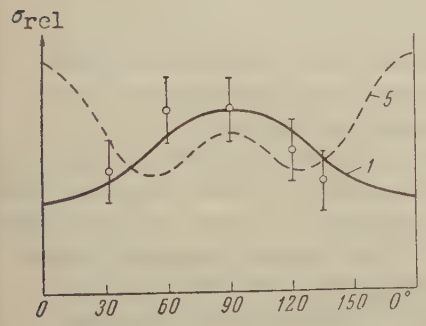

At present, attempts to explain the positions and spins of the low-lying excited states of Li^7 on the basis of the shell model meet with certain difficulties. The shell model calculations of Inglis[1], Kurath[2] and Balashov[3], assuming intermediate coupling, indicate that there should be a $5/2^-$ level in the energy range from 5.5 to 6.5 MeV. However, the experimental data reveal in this region only a single broad level with even parity, which Lane has interpreted as a $1s^4 1p^2 2s_{1/2}$ single particle level. Attempts have been made to determine the level scheme of Li^7 by observing the $Li^7(\gamma, t)He^4$ reaction at different values of $E_{\gamma\ max}$.[4,5] Erdos et al[4] found levels at 4.7, 5.5, 6.8, 7.4, 8.3 and 9.0 MeV, and attempted to determine the spin and parity of the first three levels from the angular distribution of the reaction products. Miwa and Yamanouchi[5] investigated Li^7 for excitations above 6 MeV and found levels at 6.6, 7.8 and 8.8 MeV. However, in both studies inadequate statistics and the presence of stars from other reactions made it impossible to obtain truly unambiguous results.

In the present work we investigated the $Li^7(\gamma,t)He^4$ reaction with a spectrum of bremsstrahlung having a maximum energy of 9.5 MeV in order to elucidate in more detail the characteristics of the excited states of Li^7 in this energy region. Our γ-source was the Moscow State University Scientific Research Institute of Nuclear Physics betatron, which produces a bremsstrahlung spectrum with a maximum energy of 35 MeV. The maximum energy of the γ-radiation, $E_{\gamma\ max}$ = 9.5 MeV, was chosen to assure that the $Li^7(\gamma,t)He^4$ reaction would be the only reaction producing charged particles.

The target was made of 2.4 mg/cm^2 natural lithium foil and was mounted in the vacuum chamber at an angle of 30° to the direction of the collimated γ-ray beam. The radiation dose was monitored with an ionization chamber which was calibrated with reference to the

← Fig.3. Angular distribution of tritons corresponding to the 5.3 MeV state of Li^7 (points). The theoretical curve numbers in this and the following figures correspond to those in the table.

Triton angular distributions in the $Li^7(\gamma,t)He^4$ reaction

Multipole order of transition	J	L_K	$f(\vartheta)$	Curve No. in Figs. 3–5
$E1$	$^5/_2$	2	$1+\sin^2\vartheta$	1
	$^3/_2$	2	$1-0{,}43\cdot\sin^2\vartheta$	2
	$^1/_2$	0	const	3
$M1$	$^5/_2$	3	$1+\sin^2\vartheta$	1
	$^3/_2$	1	$1-0{,}43\cdot\sin^2\vartheta$	2
	$^1/_2$	1	const	3
$E2$	$^7/_2$	3	$1+3{,}528\cdot\cos^2\vartheta-2{,}647\cdot\cos^4\vartheta$	4
	$^5/_2$	3	$1-1{,}875\cdot\cos^2\vartheta+2{,}5\cdot\cos^4\vartheta$	5
	$^3/_2$	1	const	3
	$^1/_2$	1	const	3

Note. J is the spin of the excited state, L is the relative orbital angular momentum of the triton and the α-particle.

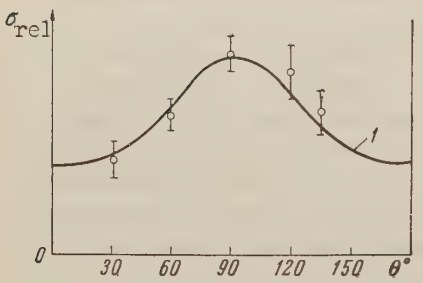

Fig.4. Angular distribution of tritons corresponding to the 66 MeV state of Li^7 (points).

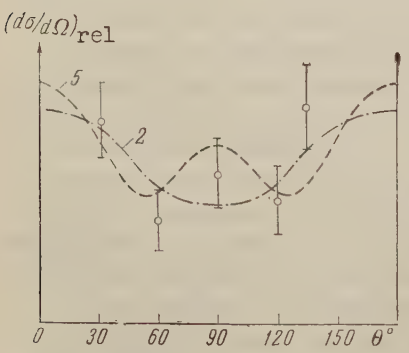

Fig.5. Angular distribution of tritons corresponding to the 8.3 MeV state of Li^7 (points).

indications of a thick-walled aluminum chamber.[6] In view of the low intensity of the γ-radiation, the error in the calibration was ~20%. The tritons from the target were recorded on NIKFI type T-3 photographic plates with 100 μ thick emulsion; the plates were positioned in the chamber at 30°, 60°, 90°, 120° and 135° relative to the direction of the γ-ray beam. We scanned a total plate area of about 53 cm^2 and observed and measured 998 triton tracks.

The integral energy distribution of tritons at 30°, 60°, 90°, 120° and 135° is shown in Fig.1. It will be evident that rather sharply defined groups appear at triton energies of 1.7, 2.5 and 3.5 MeV; also there is a weakly resolved group at 3.1 MeV. The positions of these groups correspond to levels in Li^7 at 5.3 ± 0.2, 6.6 ± 0.2, 7.5 ± ± 0.25 and 8.3 ± 0.3 MeV. The $Li^7(\gamma,t)$ reaction cross section, shown in Fig.2, was calculated on the basis of the triton energy distribution. The uncertainty in the values of the absolute cross section is ~40%. The relative error, upon which the shape of the curve is dependent, is determined only by the statistical uncertainty (indicated by vertical bars in Fig.2).

Figs.3,4 & 5 show the angular distributions obtained for distinct groups of phototritons, corresponding to Li^7 excitation energies of 5.3, 6.6 and 8.3 MeV. Because the 3.1 MeV phototriton group (E_γ = 7.6 MeV) is poorly separated from the more intense 2.5 MeV group (E_γ = 6.6 MeV), the corresponding angular distribution was not plotted. Theoretically calculated angular distributions are given in the table and are plotted in Figs.3-5 (numbered curves). A comparison of these curves with the experimental results shows that the possible assignments for the 5.3 MeV state are $5/2^-$ or $5/2^+$, for the 6.6 MeV state

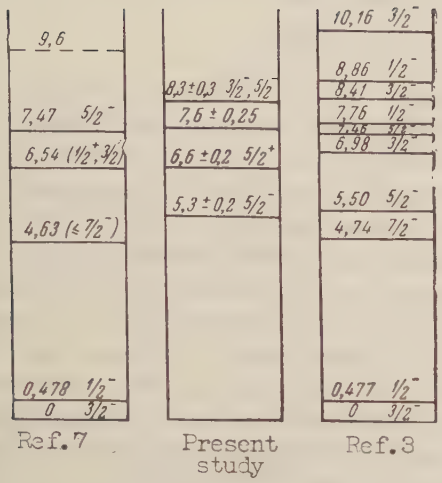

Fig.6. Li^7 level diagrams.

$5/2^+$ or $5/2^-$, and for the 8.3 MeV level $3/2^-$, $3/2^+$ or $5/2^-$. Comparison of the experimentally determined intensities of the electromagnetic transitions with the previously mentioned LS coupling shell model calculations of the intensities of E1, M1, and E2 transitions to the listed levels showed that the 6.6 MeV level is excited by E1 absorption, while the 5.3 and 8.3 MeV levels are excited by either M1 or E2 absorptions. The calculations indicate that the 5.3 MeV level has spin and parity $5/2^-$, the 6.6 MeV level $5/2^+$ and the 8.3 MeV level $3/2^-$ or $5/2^-$. The experimental energies of the 5.3 and 8.3 MeV levels are in good agreement with the results of Balashov's calculations[3] (Fig.6).

Scientific Research Institute of Nuclear Physics, Moscow State University

References

1. D.R.Inglis, Revs.Mod.Phys., 25, 390 (1953).
2. D.Kurath, Phys.Rev., 101, 216 (1956).
3. V.V.Balashov, Zhur.eksp.i teor.fiz., 36, 1123 (1959) (Trans.Soviet Physics - JETP.); Thesis, Moscow State University, 1958.
4. P.Erdös, P.Stoll, M.Wächter & V.Watagin, Nuovo cimento, 12, No.5, 639 (1954).
5. M.Miwa & M.Yamanouchi, J.Phys.Soc.Japan, 15, No.6, 947 (1960).
6. B.H.Flowers, J.D.Lawson & E.B.Fossey, Proc.Phys.Soc., 65B, 286 (1952).
7. F.Ajzenberg-Selove & T.Lauritsen, Nucl.Phys., 11, 1 (1959).

ON THE INFLUENCE OF COLLECTIVE EXCITATIONS OF THE SUPERFLUID PHASE IN NUCLEI ON THE NUCLEAR MOMENTS OF INERTIA

- B.B.Dotsenko

Application to nuclei of the methods of Bogolyubov[1] and the ideas of the theory of superconductivity has made it possible to explain a number of experimentally observed properties of nuclei[1-4]. In particular, the values of the moments of inertia of nuclei have been explained by Migdal[5], who also considered the superfluid nucleonic condensate in nuclei in the ground state, taking into account elementary excitations and fluctuations. Migdal hypothesized that the nucleus consists of a proton (p) and a neutron (n) subsystem, in which, in addition to a self-consistent field, there are residual $p-p$ and $n-n$ correlations. These systems have their own Fermi energies $E_F(p)$ and $E_F(n)$. The moment of inertia of the nucleus $J = J_n + J_p$, where J_n and J_p are the moments of inertia of the respective subsystems which, according to Migdal, depend on the width of the energy gaps Δ_n and Δ_p of the subsystems (the width of the gaps must be determined from experiment). The gyromagnetic ratio $g_r = J_p/(J_n + J_p)$ for Sm^{152}, Sm^{154} and Nd^{150}, according to Migdal, equals 0.21 ± 0.04. Whence $J_n/J_p \approx 3.5 \pm 1$. Inasmuch as $J_n/J_p = (N/Z)^{4/3}\Delta_p/\Delta_n$ (where N is the number of neutrons in the nucleus and Z is the number of protons), we have

$$1.5 \leqslant \Delta_p/\Delta_n \leqslant 2.5.$$

Thus according to experiment, the effective width of the energy gap Δ_n of the neutron subsystem is substantially smaller than the width of the gap Δ_p of the proton subsystem, although for ground states of the subsystems $\Delta_{n0} \approx \Delta_{p0}$ would appear more probable (the influence of the excess kinetic energy in the neutron subsystem on Δ_{n0} is approximately equivalent to the reducing effect of the Coulomb repulsion in the proton subsystem on Δ_{p0} - see Bogolyubov[1]).

In this connection let us consider qualitatively in the semiclassical approximation the collective excitations in the n and p subsystems according to the scheme proposed by Migdal[5] (also see Ref.6). We assume that the nucleons occupy states with momenta $\mathbf{P} = \mathbf{p} + M[\mathbf{r}\vec{\Omega}]$ in a system rotating with angular velocity Ω. We use the Bogolyubov-Fock method and introduce the correlation functions for the distribution of the particle-particle and particle-hole complexes[7]

$$F(f, f') \equiv \langle a_f^+ a_{f'} \rangle_0 = v_f^* v_{f'}; \quad \Phi(f_1, f_2) \equiv \langle a_{f_1} a_{f_2} \rangle_0 = u_{f_1} v_{f_2}, \tag{1}$$

where a_f^+ and a_f are the Fermi amplitudes of the particles in the state $f = (\mathbf{P}, \sigma)$ (as regards spins the states of the particle pairs are singlet[8]), and u and v are the coefficients of Bogolyubov's[1,7] canonical transformation. If there acts upon the system a weak perturbation with momentum $q \ll p_F$ (p_F is the Fermi momentum), tending to change the momentum p of the paired nucleons, then according to Bogolyubov[7]

$$F = F_0 + \delta F; \quad \Phi = \Phi_0 + \delta\Phi, \tag{2}$$

where F_0 and Φ_0 describe the ground state of the system,

$$\delta F(f_1, f_2) = v_{f_1}^* u_{f_2} \lambda(-f_1, f_2) + u_{f_1}^* v_{f_2} \lambda^*(-f_2, f_1),$$
$$\delta\Phi(f_1, f_2) = u_{f_1} u_{f_2} \lambda(f_1, f_2) + v_{f_1} v_{f_2} \lambda(-f_2, -f_1); \quad \lambda(f, f') = -\lambda(f', f), \tag{3}$$

and λ is a parameter describing the collective excitations. Representing λ in the form of a superposition of normal oscillations[7]

$$\lambda(f_1, f_2) = \sum_E e^{-iEt}\xi_E(f_1, f_2); \quad \lambda^*(f_1, f_2) = \sum_E e^{-iEt}\eta_E(f_1, f_2) \tag{4}$$

and operating according to Bogolyubov[7], we obtain for the functions

$$\theta_q(\mathbf{p}) = \xi(\mathbf{p}_1, \mathbf{p}_2) - \eta(-\mathbf{p}_1, -\mathbf{p}_2) \text{ and } \zeta_q(\mathbf{p}) = \xi(\mathbf{p}_1, \mathbf{p}_2) + \eta(-\mathbf{p}_2, -\mathbf{p}_1) \tag{5}$$
$$(\mathbf{p}_1 + \mathbf{p}_2 = \mathbf{q})$$

the following equations

$$\begin{aligned} \{\Xi(\mathbf{p}) + \Xi(\mathbf{p}-\mathbf{q})\}\theta(\mathbf{p}) + \sum_{p'} Q_q(\mathbf{p}, \mathbf{p}')\theta(\mathbf{p}') &= E\zeta(\mathbf{p}), \\ \{\Xi(\mathbf{p}) + \Xi(\mathbf{p}-\mathbf{q})\}\zeta(\mathbf{p}) + \sum_{p'} R_q(\mathbf{p}, \mathbf{p}')\zeta(\mathbf{p}') &= E\theta(\mathbf{p}), \end{aligned} \tag{6}$$

where $\Xi(p) = \sqrt{(\varepsilon(p)-\mu)^2 + C^2(p)}$, $\varepsilon(p)$ is the energy of one particle, μ is the chemical potential ($\mu \approx E_F$), $C(p) \approx \Delta$,

$$\begin{aligned} Q_q(\mathbf{p}, \mathbf{p}') &= g(\mathbf{p}, \mathbf{p}')L(\mathbf{p})L(\mathbf{p}') + I_q(\mathbf{p}, \mathbf{p}')M(\mathbf{p})M(\mathbf{p}'), \\ R_q(\mathbf{p}, \mathbf{p}') &= g(\mathbf{p}, \mathbf{p}')S(\mathbf{p})S(\mathbf{p}') + G_q(\mathbf{p}, \mathbf{p}')T(\mathbf{p})T(\mathbf{p}'), \\ L(\mathbf{p}) &= u(\mathbf{p})u(\mathbf{p}-\mathbf{q}) + v(\mathbf{p})v(\mathbf{p}-\mathbf{q}), \\ M(\mathbf{p}) &= v(\mathbf{p})u(\mathbf{p}-\mathbf{q}) - u(\mathbf{p})v(\mathbf{p}-\mathbf{q}), \\ S(\mathbf{p}) &= u(\mathbf{p})u(\mathbf{p}-\mathbf{q}) - v(\mathbf{p})v(\mathbf{p}-\mathbf{q}), \\ T(\mathbf{p}) &= v(\mathbf{p})u(\mathbf{p}-\mathbf{q}) + u(\mathbf{p})v(\mathbf{p}-\mathbf{q}); \end{aligned} \tag{6'}$$

$g(\mathbf{p}, \mathbf{p}') = g(\mathbf{p}, -\mathbf{p}+\mathbf{q}; -\mathbf{p}'+\mathbf{q}, \mathbf{p}')$ is the "normalized" effective correlative interaction of two nucleons,

$$\begin{aligned} I_q(\mathbf{p}, \mathbf{p}') &= g(\mathbf{p}, \mathbf{p}'-\mathbf{q};\ \mathbf{p}', \mathbf{p}-\mathbf{q}) - g(\mathbf{p}, \mathbf{p}'-\mathbf{q};\ \mathbf{p}-\mathbf{q}, \mathbf{p}') - g(\mathbf{p}, \\ &\quad -\mathbf{p}'; \mathbf{p}'+\mathbf{q}, \mathbf{p}-\mathbf{q}), \\ G_q(\mathbf{p}, \mathbf{p}') &= g(\mathbf{p}, \mathbf{p}'-\mathbf{q};\ \mathbf{p}', \mathbf{p}-\mathbf{q}) - g(\mathbf{p}, \mathbf{p}'-\mathbf{q};\ \mathbf{p}-\mathbf{q}, \mathbf{p}') + \\ &\quad + g(\mathbf{p}, -\mathbf{p}'; -\mathbf{p}'+\mathbf{q},\ \mathbf{p}-\mathbf{q}). \end{aligned} \tag{6''}$$

We note that Marumori[4] independently derived for jj coupling and the shell model equations analogous to the expressions for ξ and η, from which there was deduced the set (6). The secular equation for the set (6) has a root lying inside the energy gap (see Ref.7 and Ref.4), i.e., the corresponding collective excitations are peculiar to the superfluid state. According to Marumori[4] and Bogolyubov[7], the entire subsystem participates in the collective excitations, and its state of superfluidity is somewhat modified (a detailed investigation of this question is now underway). In experiments the effect of the above mentioned collective excitations should, apparently, be qualitatively evinced as decrease in the width of the energy gap and increase in the moment of inertia of the subsystems. This argument is true for the neutron subsystem.

An entirely different situation obtains in the proton subsystem where, in addition to pair correlative interaction, there is Coulomb repulsion between the nucleons. Taking into account this proton repulsion, according to Bogolyubov[7], we find that in the ground state it leads only to shift of the levels without changing their relative locations. Upon appearance of collective excitations, however, the situation changes: according to Bogolyubov[7] in the expression for G in (6'') there appears an addition term $8\pi e^2/q^2$ so that the expression becomes divergent for small q. Then the corresponding secular equation will not have a root inside the energy gap Δ, i.e., such collective excitations with energy

$\leqslant \Delta$ cannot appear in the superfluid proton subsystem. Thus, in the proton subsystem the width of the energy gap Δ_p corresponds to the ground state, whereas in the neutron subsystem the gap width Δ_n is effectively reduced owing to the energy of the collective excitations. This apparently explains the smaller width of the gap Δ_n as compared with Δ_p (see paragraph 6 in Ref.5).

The collective excitations considered above can probably be qualitatively interpreted as follows. Inasmuch as in transition to the superfluid state (phase transition), there appear holes and bound particle pairs in the neutron subsystem[7], the subsystem changes its structure, since there occurs a change in its correlation function and therefore in the distribution of the particle density in the outer region of the nucleus corresponding to the layer near the Fermi surface (the inner region of the nucleus is incompressible) compared with the normal state of the subsystem. Collective excitations associated with weak perturbation q, as has been shown by Bogolyubov[7], correspond to oscillations in the particle density (function $\zeta(p)$) and momentum density ($\theta(p)$), i.e., in the neutron subsystem there can apparently appear weak oscillations of the distribution and density of particles in the superfluid phase (from the density distribution corresponding to the superfluid state to the normal and vice versa) as well as oscillations in the distribution in density of momentum. In the proton system, on the other hand, owing to the presence of Coulomb forces which tend to "push apart" the system within the bounds of its potential well, there can appear only momentum oscillations without changes in the particle density. Thus the proton subsystem remains incompressible in the state of superfluidity as well, whereas the neutron subsystem, owing to change in structure in transition to the superfluid phase, becomes partially compressible (within narrow limits corresponding to transition from the superfluid state to the normal state and vice versa) for weak perturbations. This "loosening" of the neutron subsystem may serve to explain the experimental fact that the density distribution of neutrons close to the nuclear surface falls off more slowly than the proton density so that one may, roughly speaking, think of the nucleus as being wrapped in a loose neutron layer, in which there may arise oscillations in particle density.

A more rigorous analysis of the questions touched upon in this paper is now underway.

The writer is deeply grateful to N.N.Bogolyubov for his interest in the work, to A.S.Davydov for fruitful discussions and to V.G.Solov'ev for valuable suggestions.

Institute of Physics,
Academy of Sciences of the Ukrainian SSR

References

1. N.N.Bogolyubov, V.V.Tolmachev & D.V.Shirkov, Novyi metod v teorii sverkhprovodimosti (A new method in the theory of superconductivity), M., 1958.

2. V.G.Solov'ev, Doklady AN SSSR, 23, 652 (1958). (Trans.Doklady.)

3. S.Belyaev, Kgl.Danske Videnskab.Selskab, Mat.-fys.Medd., 31, No.11 (1959).

4. T.Marumori, Progr.Theoret.Phys., v.24, 331 (1960).

5. A.B.Migdal, Zhur.eksp.i teor.fiz., 37, 249 (1959). (Trans.Soviet Physics - JETP.)

6. D.Inglis, Phys.Rev., 96, 1059 (1954); 103, 1786 (1956).

7. N.N.Bogolyubov, Usp.fiz.nauk, 67, 549 (1959). (Trans.Soviet Physics - Uspekhi.)

8. V.F.Weisskopf, Proceedings of the International Conference on Nuclear Structure, p.890, Kingston, Canada, Univ.of Toronto Press, 1960.

PAIR CORRELATIONS IN SINGLE-NUCLEON REDUCED LEVEL WIDTHS IN NUCLEI

- V.B.Belyaev & B.N.Zakhar'ev

Reduced level widths β^2 are important spectroscopic characteristics of nuclear states. For light nuclei, expressions for the reduced widths, derived from the shell model, were presented by Lane[1], while formulas based on the collective model were calculated by Yoshida[2]. An exhaustive discussion of the problems connected with reduced width will be found in reviews of Lane and Macfarlane & French[3].

Let us consider the state Ψ_s of a nucleus, characterized by the set of quantum numbers s. We shall characterize different modes (channels) of separation of the system by the set of quantum numbers k (k comprises both the internal characteristics of the product of separation and the quantum numbers of their relative motion). The state Ψ_s can be expanded at the nuclear boundary Σ (outside the range of action of nuclear forces) in terms of functions Φ_{sk} of the different channels:

$$\Psi_s(\Sigma) = \sum_k \beta_k \Phi_{sk}. \tag{1}$$

The squares of the coefficients of this expansion are the reduced widths. Equation (1) can be rewritten in the form

$$\beta_k = \int_\Sigma \Psi_s \Phi_{sk}^*. \tag{2}$$

Thus the single-nucleon reduced width represents the square of the "projection" of the state Φ (residual nucleus + free nucleon) on the given state Ψ of the nucleus. The significance of the reduced widths is that in terms of them there can be expressed the cross sections for reactions not going through the compound nucleus stage.

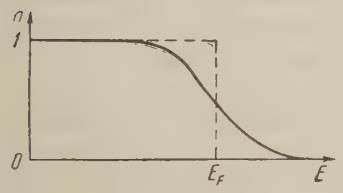

Fig.1. Distribution of nucleons in energy: dashed line - according to Eq.(3); solid line - according to Eq.(4).

The purpose of the present work was to obtain corrections to the formulas for β^2, deduced on the basis of the individual particle model, corrections that result from taking into account residual pair interactions (self-consistent field subtracted) between the nucleons.

The wave function of the neutron or proton shell of the nucleus (for example, with an even number of particles N) in the independent particle model can be written in requantized form as

$$\Psi_{\mathrm{IPM}} = \prod_{\nu=\nu_0}^{\nu_{\max}} a_{\nu_+}^+ a_{\nu_-}^+ \Psi_0, \tag{3}$$

where Ψ_0 is the nucleon vacuum ($a_{\nu\pm}^+ \Psi_0 = 0$), ν is the quantum number characterizing the level; $\pm$ indicates that the particles on one level have opposite projections of momenta. Equation (3) corresponds to the distribution of the nucleons in energy shown schematically by the dashed line in Fig.1. Inclusion of residual pair interactions changes the wave function (3). It is feasible to find it in this case only if we give up precise conservation of the number of particles (N is conserved only on the average). Then, according to Solov'ev[4], the function becomes

$$\Psi = \prod_\nu (u_\nu + v_\nu a_{\nu_+}^+ a_{\nu_-}^+) \Psi_0, \tag{4}$$

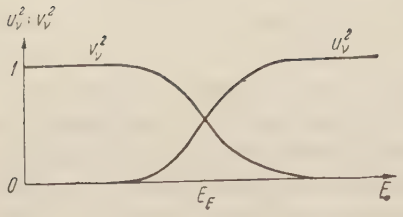

←Fig.2. Qualitative dependence of the coefficients v_ν^2 and u_ν^2 on the excitation energy (i.e., on ν). The factors under the product sign in (7) and (8) do not substantially change the quantitative dependence of the correlation corrections on ν. For odd nuclei the energy of the ground state lies close to the Fermi surface E_F, while for even nuclei (all nucleons paired) on the ground state lies below E_F.

where u_ν^2 is the probability that there are no particles on the given level ν, and v_ν^2 is the probability that there is a pair of nucleons on the level ν. The energy distribution of nucleons corresponding to Eq.(4) is shown by the solid line in Fig.1. Fig.2 gives the quantitative dependence of u_ν^2 and v_ν^2 on the excitation energy. Precise values of these coefficients for different nuclei can be obtained by solving the corresponding integral equations, as was done by Solov'ev[5] for strongly deformed nuclei.

A large number of single-nucleon reduced widths have been determined from the cross sections for (d, n) and (d, p) stripping reactions.[3] When pair correlations are taken into account, however, an additional factor A appears in the expression for the stripping reaction cross section:

$$\sigma_{st} \sim |\langle \Psi_f^* | a_{\nu_1}^+ | \Psi_i \rangle|^2 \sim \beta_{\nu_1}^2 A; \tag{5}$$

here Ψ_i and Ψ_f are the wave functions of the nucleus before and after the stripping reaction, $a_{\nu_1}^+$ is the creation operator for the picked off nucleon in the state ν_1, and $\beta_{\nu_1}^2$ is the reduced width of the level ν_1 for the picked off nucleon in the final nucleus.

Let us determine the factor A for the case when, for example, the neutron in the process of stripping settles on a nucleus with an even number of neutrons. Then

$$\begin{aligned} \Psi_i &= \prod_\nu (u_\nu^i + v_\nu^i a_{\nu_-}^+ a_{\nu_+}^+) \Psi_{0i}; \\ \Psi_f &= \prod_{\nu \neq \nu_1} (u_\nu^f + v_\nu^f a_{\nu_-}^+ a_{\nu_+}^+) a_{\nu_1}^+ \Psi_{0f}. \end{aligned} \tag{6}$$

By means of these functions we obtain

$$A = (u_{\nu_1}^i)^2 \prod_{\nu \neq \nu_1} (u_\nu^i u_\nu^f + v_\nu^i v_\nu^f)^2. \tag{7}$$

The factor $(u_{\nu_1}^i)^2$ shows that A is proportional to the probability that the level ν_1 in the residual nucleus remains unoccupied, while the expression under the product sign appears owing to rearrangement in the other levels of the neutron shell. The contribution from rearrangement of the proton shell is small and we shall neglect it.

If the neutron is captured into a nucleus with an odd number of neutrons and is paired in the process, then for A we obtain

$$A = (v_{\nu_1}^f)^2 \prod_{\nu \neq \nu_1} (u_\nu^i u_\nu^f + v_\nu^i v_\nu^f)^2. \tag{8}$$

If the neutron is not paired, in which case the wave function is

$$\Psi_f = \prod_{\nu \neq \nu_1} (u_\nu^f + v_\nu^f a_{\nu_+}^+ a_{\nu_-}^+)(u_{\nu_1}^f a_{\nu_{1+}}^+ a_{\nu_{1-}}^+ - v_{\nu_1}^f) \Psi_{0f}, \tag{9}$$

the expression for A is obtained from (8) by replacing $(v^f_{\nu_1})^2$ by $(u^f_{\nu_1})^2$.

In the independent particle model "direct" reactions as a result of which the nucleon settles on a level located below the Fermi surface are rigorously forbidden, inasmuch as in this model all levels with energy $<E_F$ are fully occupied. (Such processes are usually interpreted as "direct" reactions with excitation of the target nucleus.) Taking into account residual interactions has the effect of "allowing" such processes, inasmuch as levels below the Fermi surface are occupied only with a probability $v^2_\nu \leqslant 1$ (Fig.1). The cross section for the process

$$\sigma \sim B\beta^2_{\nu\,\mathrm{exc}}\,, \tag{10}$$

where $\beta^2_{\nu\,\mathrm{exc}}$ is the single-nucleon reduced width for the system: excited target nucleus + nucleon on the ν level ($E_\nu < E_F$). The factor B has a form analogous to (7) (taking into account residual interactions, the processes with settling of the nucleon on levels with energies $>E_F$ and $<E_F$ do not differ substantially). However, in this case there will correspond to the factor $(u^i_\nu)^2$ in Fig.2 the part of the curve to the left of E_F.

Inasmuch as reduced widths are calculated from the experimental data by means of formulas that do not take into account pair correlations, the factors responsible for these correlations should enter into the numerical values for the reduced widths (see Table 1 in the review of Macfarlane & French[3]).

Let us consider the behavior of reduced widths for a nucleon in a given nucleus as a function of the level energy. We will be interested primarily in the ratios $\beta^2/\beta^2_{\mathrm{g.s}}$. Let us analyze the simplest case, when the odd nucleon in the process of the stripping reaction settles on the free shell. In this case in the independent particle model $\beta^2/\beta^2_{\mathrm{g.s}} = 1$ for all levels. According to Eq.(7) (also see the behavior of the function u^2_ν in Fig.2; the factor under the product sign does not significantly change the qualitative dependence of A on the excitation energy of the level), taking into account pair correlations leads to $\beta^2_\nu/\beta^2_{\mathrm{g.s}}$ increasing with energy. This is substantiated by the experimental data. In F^{17} there is one proton outside the closed double magic O^{16} core. The widths for two levels - the ground $(d_{5/2})$ and 0.5 MeV $(s_{1/2})$ levels are known: $\frac{\beta^2_{0.5\,\mathrm{MeV}}}{\beta^2_{\mathrm{g.s}}} \approx 4$. In the O^{17} nucleus (one neutron +O^{16}) $\frac{\beta^2_{0.871\,\mathrm{MeV}}(s_{1/2})}{\beta^2_{\mathrm{g.s}}(d_{5/2})} \approx 2$. The small relative width for the 4.56 MeV level is explained by rearrangement of the configuration of the core in the process of the stripping reaction. This is in agreement with the small relative value of the correlation factor (10). In Ca^{41} (one neutron outside the double magic Ca^{40} core) $\frac{\beta^2_{1.95\,\mathrm{MeV}}(2p_{3/2})}{\beta^2_{\mathrm{g.s}}(f_{7/2})} \approx 1.5$. The relative widths for the 2.677 and 3.405 MeV levels (the configuration in both cases is $2s^3_{1/2}\, f^2_{7/2}$) are small owing to rearrangement of the core (capture of the nucleon into a level below E_F). Gradual increase of the reduced width with increasing excitation energy is observed for the eight levels of K^{40} (the configurations of the first four are $d^7_{3/2}$ and $f_{5/2}$, and of the others, $d^7_{3/2}$ and $2p_{3/2}$).

The reduced width of the levels in B^{12}, C^{13}, Zn^{69} and S^{33} can be interpreted analogously. When there is more than one particle in the last orbit, interpretation of the experimental data becomes more complicated; however, the influence of pair correlation can be followed even in these cases. Thus, for example, for the two levels in Cr^{54} (magic neutron number core + 2 paired neutrons in the $2p^2_{3/2}$

shell) $\frac{\beta^2_{0.86\,MeV}}{\beta^2_{g.s}} = 0.44$, which correspond to the correlation factor (8) (see also the behavior of v_ν^2 in Fig.2).

We desire to thank V.G.Neudachin, V.G.Solov'ev, N.I.Pyatov & V.I.Furman for valuable discussions.

Laboratory of Theoretical Physics,
Joint Institute for Nuclear Research

References

1. A.M.Lane, Proc.Phys.Soc., A66, 977 (1953).
2. S.Yoshida, Progr.Theor.Phys., 12, 141 (1954).
3. A.M.Lane, Revs.Mod.Phys., 32, 519 (1960); M.H.Macfarlane & J.B.French, Revs.Mod.Phys., 32, 567 (1960).
4. V.G.Solov'ev, Zhur.eksp.i teor.fiz., 35, 823 (1958); Ibid., 36, 1869 (1959), (Trans.Soviet Physics - JETP); S.T.Belyaev, Klg.Danske Videnskab,Selskab, Mat.-fys.Medd., 31, 11 (1959).
5. V.G.Solov'ev, Doklady AN SSSR, 133, 325 (1960) (Trans.Doklady); Liu Yuan, I.N.Silin, V.G.Solov'ev, N.I.Pyatov & V.I.Furman, Zhur.eksp.i teor.fiz.,40,1503 (1961) (Trans.Soviet Physics - JETP.)

* * * * * * *

PROBABILITIES FOR E2 AND E1 TRANSITIONS FROM SOME EXCITED LEVELS IN Tb^{159}, Ho^{165} AND Tm^{169}

- V.I.Popov

1. The known excited states in odd-A deformed nuclei are satisfactorily interpreted from the standpoint of the unified nuclear model and can, as a rule, be classified in one of two categories: vibrational states of an axially symmetric nucleus or single-particle states in a deformed potential well.[1] Until recently, however, there were no definite indications of the existence in odd nuclei of vibrational states, analogous to the β and γ vibrational states in even-even nuclei. Development of the theory of such states in odd nuclei encounters certain difficulties in view of the complexity of the problem of taking into account interaction of the odd nucleon with the vibrational motion.

In the recent work of Gallagher & Edwards[2] it was hypothesized that the 511 and 686 keV levels in Re^{187}, interpretation of which in the framework of Nilsson's level scheme encounters certain difficulties, are γ-vibrational in character. In the experimental study of Nathan and the writer[3] there was observed in a number of deformed odd-Z nuclei Coulomb excitation of one or two levels in the 500 to 900 keV region, among which was the 511 keV level in Re^{187}. The reduced transition probabilities B(E2) in all cases are close to the probability for a single-particle transition, according to the theoretical evaluation for a spherical nucleus[4]. There is reason to assert, as was noted in Ref.3, that at least some of the excited levels may be due to γ-vibrations.

It may be of interest to analyze in greater detail the experimental data for Tb^{159}, Ho^{165} and Tm^{169} obtained in the work of Ref.3. From the 560, 515 and 565

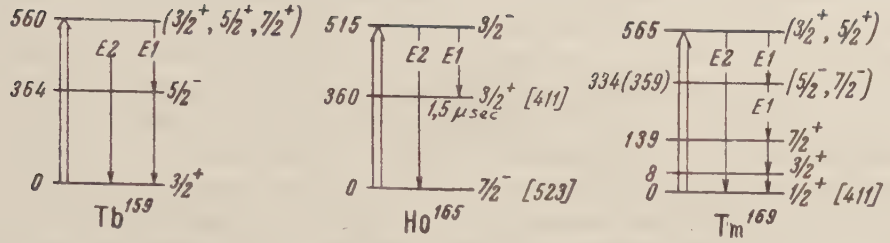

Fig.1. Transitions in Tb^{159}, Ho^{165} and Tm^{169}. The double-line arrow indicates Coulomb excitation of the level.

Table 1

Data on transitions in Tb^{159}, Ho^{165} and Tm^{169}

Nucleus	Transition (level energies in keV)	Relative intensity	$B(E2)_{Coul}$ $e^2 \cdot 10^{-48}$ см^4
Tb^{159}	560 → 0	60	0.03
	560 → 364	40	
Ho^{165}	515 → 0	80	0.016
	515 → 361	20	
Tm^{169}	565 → 0	20	0.05
	565 → 334(359)	80	

keV levels excited in Tb^{159}, Ho^{165} and Tm^{169}, respectively, there occur both a cross-over transition to the ground state and a transition to an intermediate state. The multipole orders and probabilities of these transitions allow of drawing certain inferences regarding the nature of these levels.

2. Data on the above mentioned transitions in Tb^{159}, Ho^{165} and Tm^{169} are listed in Table 1; the corresponding transition schemes are shown in Fig.1. The multipole orders of the transitions and the values of the spins and parities of the levels which were detected for the first time in the work of Ref.3 (the spins are given in parentheses) are discussed below. For the levels of Ho^{165} and Tm^{169}, which are satisfactorily described by Nilsson's model[1], there are given the corresponding wave functions. The $B(E2)_{Coul}$, listed in the fourth column of Table 1, are the reduced transition probabilities from the ground state to the indicated level, determined on the assumption that the Coulomb excitation is an E2 transition. The experimental error does not exceed 50%. The relative transition intensities are characterized by a better accuracy and, in particular, for Ho^{165} are in agreement with the data obtained by Tornau[5] in investigating the decay scheme of Dy^{165}.

The results for Ho^{165} are the easiest to interpret, inasmuch as the observed transitions take place between levels with known spins and parities* (see Fig.1). The ensuing multipole order assignments (E2 for the cross-over transition and E1 for the transition to the 360 keV level) are in agreement with the observed Coulomb excitation intensities**.

In the case of Tb^{159}, although the spin and parity assignments have been made only for the ground state and the intermediate 364 keV level[1], the proposed decay scheme follows unambiguously from the experimental results, and the corresponding cross-over and cascade transitions have the same multipole orders as in Ho^{165}.

The situation is less clear in the case of Tm^{169}, for the assignments for the levels involved in the observed transitions in this nucleus are not known except

---

*The spin and parity of the 515 keV level in Ho^{165} (3/2-) have been reliably established in the studies of Refs.5 and 6.

**As will be evident from evaluations of the partial lifetimes (see below), the admixture of M2 and E1 to the transition in Ho^{165} (as well as to the transitions in Tb^{159} and Tm^{169}) must be small.

for the ground state (1/2+) and the 139 keV rotational level (7/2+)(Fig.1). However, by analogy with Ho^{165} and Tb^{159}, it can be assumed that the cross-over and cascade transitions from the 565 keV level in Tm^{169} have multipole orders E2 and E1, respectively. In this case the transition between the 334 (or 359) and 139 keV levels, which have opposite parity, is in all probability E1, inasmuch as the lifetime of this level must be $\leqslant 10^{-8}$ sec (upper bound obtained from the resolving time of the experimental set-up), which cannot be the case for an M2 or E3 transition. Any other assumptions regarding the multipole orders of these transitions in Tm^{169} would be difficult to reconcile with the observed intensities. The parity and possible spins of the three levels in Tb^{159} and Tm^{169}, as determined on the basis of the above mentioned multipole orders, are shown in Fig.1 in parentheses. Of the three possible indicated values for the 560 keV level in Tb^{159}, one can reject 3/2+, inasmuch as one cannot find a corresponding single-particle or collective state with a relatively low energy and large E2 transition probability. It must be noted that the inferences regarding the decay scheme of Tm^{169} cannot be regarded as definitive, although they are not in conflict with the data now available.

Some substantiation of the decay scheme for Tm^{169} proposed in Ref.3 is furnished by the results of Johansson[7], according to which in the spectrum of γ-rays emitted in K capture by Yb^{169} there may be ~195 keV γ-rays in coincidence with the γ-rays from de-excitation of the 139 keV level. This γ-line was attributed to a transition from a level at 336 keV to the 139 keV level. The 336 keV energy value is in good agreement with the calculated excitation energy for a 9/2+ rotational level belonging to the K = 1/2+ ground state rotational band. On the basis of this, Johansson[7] concluded that the 336 keV level is characterized by I = 9/2 and K = 1/2. At the same time, it must be noted that in the work of Hatch et al[8] in which the spectrum of γ-rays from K capture in Yb^{169} was investigated by means of a crystal spectrometer no 195 keV γ-line was observed. It must be borne in mind, however, that this γ-line may have escaped detection against the background of the strong 198 keV line if the actual energy difference between the two lines is $\leqslant 2$ keV. The level diagram obtained in investigating K capture in Yb^{169} is shown in Fig.2. The 336 keV level inferred by Johansson[7] is indicated by a dashed line.

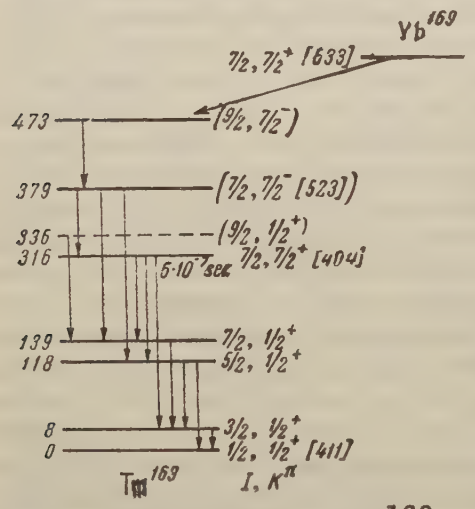

Fig.2. Decay scheme of Tb^{169}.

The 336 keV level energy is in good agreement with one of the possible energy values for the intermediate state in Tm^{169} indicated in Fig.1. At the same time, the characteristics of this state, which follow from the results of Ref.3, are inconsistent with the assignment 9/2+ proposed by Johansson. It must be noted that excitation of a rotational level with I = 9/2 and K = 1/2 in K capture by Yb^{169} with an appreciable probability (a few percent, as follows from Ref.7) is in conflict with the strong forbiddenness as regards the selection rules for K ($\Delta K = 3$) and the asymptotic quantum numbers in Nilsson's model (see Fig.2). At the same time, if this level is characterized by K = 5/2 or 7/2, as indicated in Fig.1, the transition in question must have an appreciable probability. According to Nilsson's scheme, in Tm^{169} one can expect single-particle excited states with $7/2^-$ [523] and $5/2^-$ [532]. The level corresponding to one of these states is the 379 keV level. In the work of Ref.1 this level was identified as 7/2 [523], although the other alternative cannot be excluded on the basis of the available experimental data.

Thus the level fed by the decay from the 565 keV state may be a single-particle level with one of the two above listed sets of quantum numbers.

3. The above described experimental data allow of drawing certain inferences regarding the nature of the states in odd-Z nuclei excited in the work of Ref.3 by E2 transitions. The hypothesis advanced in Ref.3 that some of these levels can be attributed to γ-vibrations was based, first, on the fact that the location of the 515 keV level in Ho^{165}, like that of the 511 keV level in Re^{187} (Ref.2), is in conflict with Nilsson's scheme, and second, the fact that the spin, parity and E2 transition probabilities for these two levels correspond to the expected characteristics for a γ-vibrational state in an odd nucleus.

One can adduce further arguments in favor of the collective nature of the states under discussion.

A. The excitation energies of these levels in different nuclei have close values comparable with the excitation energy of the second 2+ levels in deformed even-even nuclei.

B. The probability for an E2 transition from the ground state in all cases amounts to 1-2 times the probability given by single-particle evaluation for a spherical nucleus*, whereas transitions between single-particle levels of a deformed nucleus, if they do not satisfy the asymptotic quantum number selection rules[1], and have much lower probabilities as compared with the case of a spherical nucleus (hindered transitions). In particular, hindered E2 transitions have been observed in Eu^{153} and Ta^{181}, for which the corresponding retardation factor amounts to 10-100.**

Violation of the asymptotic number selection rules will also obtain for the Ho^{165} and Tb^{159} levels under consideration, if one attributes to them the wave functions of the state closest to the ground state in Nilsson's scheme.

As was noted above, the spins of the earlier known levels in Ho^{165}, Re^{185} and Re^{187} agree with the expected values for γ-vibrational states, which can be approximately characterized by the quantum number $K = K_o \pm 2$, where K_o is the projection of the total angular momentum of the nucleus on the symmetry axis in the ground state. One of the possible assignments for the analogous levels in Tb^{159} and Tm^{169} (7/2 and 5/2, respectively) also satisfies this condition. The same spin values can be expected in rotational states of a nucleus with a nonaxial and equilibrium shape, analogous to the second 2+ levels in even-even nuclei in the Davydov-Filippov model[10]. Thus the collective character of the levels under discussion may be due to γ-vibrations and/or to deviation of the equilibrium shape of the nucleus from axial symmetry.

Davydov[11] recently showed that the second 2+ levels in strongly deformed even-even nuclei can be described as states due to γ-vibrations of an axially symmetric nucleus, i.e., taking into account γ-vibrations in this case is equivalent to introduction of a certain equilibrium nonaxial deformation. Hence there is reason to expect that γ-vibrations and axial symmetry will be evinced in a like manner in the case of odd nuclei as well.***

If the coupling between the odd nucleon and the γ-deformation is small, the wave function of the nucleon in the ground state and the corresponding excited

---

*The probability of the reverse transition can be obtained from these values by multiplication by the statistical factor, which for the 515 keV level in Ho^{165} equals 2.

**The question of the probabilities of E2 transitions between single-particle levels in deformed nuclei is discussed in Ref.9.

***Hereinafter for brevity we will speak of γ-deformation, having in mind both γ-vibrations and axial asymmetry of the equilibrium shape of the nucleus.

Table 2

Partial lifetimes of the levels in Tb^{159}, Ho^{165} and Tm^{169}

Nucleus	Multipole order	Spins & parities of initial & final states	Partial lifetime τ, 10^{-10} sec	$\frac{\tau}{\tau_{sp}}$
Tb^{159}	$E2$	$(7/2^+) \rightarrow 3/2^+$	0.9	1.6
	$E1$	$(7/2^+) \rightarrow 5/2^-$	1.3	$5 \cdot 10^3$
Ho^{165}	$E2$	$3/2^- \rightarrow 7/2^-$	0.6	0.8
	$E1$	$3/2^- \rightarrow 3/2^+$	2.5	$4 \cdot 10^3$
Tm^{169}	$E2$	$(5/2^+) \rightarrow 1/2^+$	0.9	1.6
	$E1$	$(5/2^+) \rightarrow (5/2^-, 7/2^-)$	0.2	10^3

state will be approximately the same and may be characterized (in the case of small γ-deformation) by the quantum number Ω, i.e., projection of the angular momentum of the nucleon on the symmetry axis of the axial nucleus. In the case of strong coupling of the odd nucleon with the γ-deformation Ω will no longer be a good quantum number. Bohr[12], regarding the effect of axial asymmetry of the nucleus on the nucleon motion as a perturbation, showed that such coupling leads to the appearance in the wave function of the nucleon of an admixture of $\Omega \pm 2$, K states, where Ω and K are the quantum numbers of the unperturbed state.

Our data on the E2 and E1 transitions allow of drawing certain inferences regarding the role of coupling of the nucleon with the γ-deformation in the case of the investigated odd-Z nuclei. From the experimental data on B(E2) and the relative transition probabilities (Table 1) one can calculate the partial lifetimes τ of the corresponding levels. These values of τ are listed in Table 2.

In the cases of Tb^{159} and Tm^{169} it was assumed that the spins of the levels from which the transition depart are 7/2 and 5/2, respectively. If one uses the other possible spin values, namely, 5/2 for Tb^{159} and 3/2 for Tm^{169}, then owing to the statistical factor the values of τ are decreased by 4/3 and 3/2, respectively. The experimental error in the cited values of τ amounts to about 50%. In the fifth column of Table 2 we list the ratios of the experimental values of τ to the values of τ_{sp} calculated by means of the single-particle formulas for a spherical nucleus[4]. As will be evident from the data in the table, the lifetime for E1 transitions exceeds the single-particle lifetime by a factor of 10^3–10^4, i.e., there obtains a retardation similar to that observed for other E1 transitions in deformed nuclei[1].

The case of Ho^{165} is of particular interest. If it is assumed that the 3/2- level is a pure $\Omega = 7/2$, K = 3/2- state, E1 transitions from it to the single particle 3/2+ level ($\Omega = 3/2$, K = 3/2) would be forbidden. The fact that an E1 transition does occur indicates an admixture of a $\Omega = 3/2$-, K = 3/2- state. The probability for this E1 transition, as will be evident from Table 2, is comparable with the probability that can be expected for single-particle E1 transitions in a deformed nucleus. If it is assumed that the 3/2- level in Ho^{165} is a single-particle state with 3/2- [532] (the state closest to the ground state in Nilsson's scheme), the calculated E1 transition probability to the 3/2+ [411] level is close to the experimental value, namely, $4.3 \cdot 10^3$ times lower than the probability for a single-particle transition in a spherical nucleus. Thus the experimental probabilities for E2 and E1 transitions from the 515 keV level in Ho^{165} show that a collective $\Omega = 7/2$, K = 3/2 state and a single-particle $\Omega = 3/2$, K = 3/2 state can make comparable contributions to the wave function of this level. The same conclusion can be drawn in the case of Tm^{169} if the decay scheme proposed for this nucleus is valid. Consequently, it may be concluded that in the given nuclei there obtains strong interaction of the odd proton with the γ-deformation, leading to shift of the energy levels and mixing of the single-particle and collective wave functions.

Of considerable interest would be further investigation of the levels in deformed odd nuclei with similar properties, and, in particular, verification of the above-proposed spins for the levels of Tm^{169}. As will be evident from the above discussion of the experimental results of Ref.3, investigation of γ-transitions occurring as a result of Coulomb excitation of high-lying levels in odd nuclei provides possibilities for analysis of the character of such excited states.

"P.N.Lebedev" Physical Institute,
Academy of Sciences of the USSR

References

1. B.R.Mottelson & S.G.Nilsson, Kgl.Danske Videnskab.Salskab., Mat.-fys. Medd., 31, No.8 (1959).
2. C.J.Gallagher & W.F.Edwards, Nucl.Phys., 19, 18 (1960).
3. O.Nathan & V.I.Popov, Nucl.Phys., 21, 631 (1960).
4. S.A.Moszkowski, in Beta- and Gamma-Ray Spectroscopy, edited by Kai Siegbahn, N.Y. 1955.
5. R.Tornau, Z.Phys., 159, 101 (1960).
6. Cranston, Bunker & Starner, Bull.Amer.Phys.Soc., 5, 255 (1960).
7. S.A.E.Johansson, Phys.Rev., 100, 835 (1955).
8. E.N.Hatch, F.Boehm, P.Marmier & J.W.M.DuMond, Phys.Rev., 104, 745 (1956).
9. D.Bogdan, Nuovo cimento, 15, 709 (1960).
10. A.S.Davydov & G.F.Filippov, Zhur.eksp.i teor.fiz., 35, 440 (1958). (Trans.Soviet Physics - JETP.)
11. A.S.Davydov, Vestnik, Moscow University, Series 3, No.1, 56 (1961).
12. A.Bohr, Kgl.Danske Videnskab.Selskab, Mat.-fys.Medd., 26, No.14 (1952).

ON THE POSSIBILITY OF DETERMINING REDUCED WIDTHS FROM POLARIZATION EFFECTS IN DIRECT NUCLEAR REACTIONS

- G.L.Vysotskii

As is known, reduced widths, which are used in the theory of direct nuclear reactions, are extremely important shell model parameters that characterize the amplitude with which the given single-particle state is represented in the wave function of the captured nucleon.[1] In the theory of polarization effects in direct nuclear reactions[2-4] - to be specific, we shall consider the (d,p) stripping reaction - the reduced widths are encountered along with other quantities, calculation of which is connected with certain drastic simplifications. Polarization effects are particularly sensitive to the choice of a model for the interaction of deuterons and protons with a nucleus. Hence we may inquire whether one cannot by appropriate polarization experiments exclude the quantities that depend on model concepts for the purpose of determining reduced widths?

It can be shown that in this case, when the captured nucleon is characterized by one value of the orbital momentum l (configuration mixing with regard to l is not, as a rule, taken into account in the shell model with intermediate coupling), and in the case of the variant of the theory of polarization effects that neglects spin-orbit interaction of the proton and deuteron waves with the nucleus, for determining the ratio of the reduced widths it is sufficient to carry out measurements of the polarization of the proton and p-γ correlation with polarized deuterons.

In the case of a pure multipole transition the angular distribution of γ-rays is described by

$$w(\vartheta,\ \varphi) \sim \sum_{k\,\mathrm{par}} \begin{Bmatrix} j_f j L \\ k L j \end{Bmatrix} (L-1L1\,|\,k0) \sum_q \rho_{kq}(P_d) Y_{kq}(\vartheta,\varphi), \qquad (1)$$

where j and j_f are the spins of the excited and ground states, L is the multipole order of the transition, and ϑ and φ are the angles of emission of the photon in the system of coordinates with the z axis perpendicular to the plane of the reaction and the x axis aligned with the deuteron beam. The spin tensors $\rho_{kq}(P_d)$ determine the alignment of the nucleus and are measured in the experiment. They depend on the polarization P_d of the deuterons and the angle of emission of the proton.

The analysis is particularly simple in the $l = 1$ case, when it is sufficient to carry out experiments with deuterons polarized either perpendicular to the plane or in the plane of the reaction.

For $l = 1$, we have $\rho_{4q} = 0$. For deuterons polarized along the z axis

$$\rho_{22}(P_d) = \rho_{22}(0)(1 + 3P_pP_d)^{-1},$$

where P_p is the proton polarization, and $\rho_{21} = 0$. As for ρ_{20}, the change in this quantity in going to polarized deuterons depends on the ratio of the reduced widths It can be shown that the combination

$$\frac{\rho_{20}(P_d)(1+3P_pP_d) - \rho_{20}(0)}{P_pP_d} = 2\sqrt{6} f(1) \qquad (2)$$

does not depend on the angle of emergence of the proton and represents a simple algebraic function of the ratio of reduced widths. If one uses the set of reduced widths ϑ_{ls} (s is the channel spin ($s = i + 1/2$), i is the spin of the initial nucleus, then ($[j] \equiv 2j + 1$):

$$f(l)=\frac{3}{2}(-)^{l}\frac{\sum_{ss'}\theta_{ls}\theta_{ls'}(-)^{s-j}[s]^{1/2}[s']^{1/2}\begin{Bmatrix}s' & s & 1\\ 1/2 & 1/2 & i\end{Bmatrix}\begin{Bmatrix}s' & j & l\\ 1 & 2 & 1\\ s & l & l\end{Bmatrix}}{\sum_{ss'}\theta_{ls}\theta_{ls'}(-)^{s+s'}[s]^{1/2}[s']^{1/2}\begin{Bmatrix}1/2 & 1/2 & 1\\ s' & s & i\end{Bmatrix}\begin{Bmatrix}l & l & 1\\ s & s' & j\end{Bmatrix}}. \qquad (3)$$

The relation between the reduced widths θ_{lj_n} and the set ϑ_{ls} is given by

$$\theta_{ls}=\sum_{j_n}(-)^{j_n+i+j}[s]^{1/2}[j_n]^{1/2}\begin{Bmatrix}1/2 & i & s\\ l & j & j_n\end{Bmatrix}\theta_{lj_n}.$$

where j_n is the total momentum of the captured nucleon $\left(j_n=l+1/2\right)$.

For l = 1, but with deuterons polarized in the plane of the reaction, for example, along the x axis, the quantities ρ_{20} and ρ_{22} do not change in going to polarized deuterons $(\rho_{20}(P_d)=\rho_{20}(0);\ \rho_{22}(P_d)=\rho_{22}(0))$, but a term with q = 1 appears in the correlation function; moreover, $\rho_{21}(P_d)P_p^{-1}P_d^{-1}=-3f(1)$ also does not depend on the angle of emission of the proton and is expressed in terms of the ratio of reduced widths. In the case when $l>1$ it is necessary to carry out experiments with deuterons polarized perpendicular to the plane of the reaction and to follow the variation of ρ_{20} and ρ_{22}, and then carry out experiments with deuterons polarized in the plane of the reaction (for example, along the x axis) and measure Then the combination

$$\frac{\rho_{20}(P_d)(1+3P_pP_d)-\rho_{20}(0)}{\sqrt{6}P_pP_d}-\frac{\rho_{22}(P_d)(1+3P_pP_d)-\rho_{22}(0)}{P_pP_d}-\frac{\rho_{21}(P_d')}{P_pP_d'}=f(l) \qquad (4)$$

does not depend on the angle of emission of the proton and is expressed in terms of the ratio of reduced widths. We emphasize the fact that the present analysis makes minimal use of model concepts. We feel that the matter may be of topical interest in view of the recent announcement[5] of construction of an effective source of polarized deuterons.

Khar'kov Physical-Technical Institute

References

1. G.R.Satchler, Ann.Phys., 3, 275 (1958).
2. R.Huby, M.Refai & G.Satchler, Nucl.Phys., 9, 94 (1958).
3. G.Vysotskii & A.Sitenko, Zhur.eksp.i teor.fiz., 36, 1143 (1959). (Trans. Soviet Physics - JETP.)
4. G.Vysotskii, Ukr.fiz.zhur. (Ukrainian Physics Journal), 5, 289 (1960).
5. E.Baumgartner, L.Brown, P.Huber, H.Rudin & H.Striebel, Phys.Rev.Letters, 5, 154 (1960).

ROTATIONAL STATES OF NONSPHERICAL EVEN-EVEN NUCLEI

- V.I.Belyak & D.A.Zaikin

Introduction

Significant successes have recently been scored by the theory of nonaxial nuclei, proposed by Davydov & Filippov[1-3]. Even the simple nonaxial rigid rotator model satisfactorily explains the energies of the levels and the probabilities of electromagnetic transitions between them in a number of nuclei.[4] Subsequently there were investigated the corrections for this model due to departure from adiabaticity of the rotation owing to β-oscillations[5-7]; Davydov[7] has also taken into account γ-oscillations for nuclei with large deviations from axial symmetry ($\gamma_0 > 10^\circ$). However, the cases of axial symmetry and small deviations from it require special investigation. Such investigation is of interest in that it may lead to clarification of whether small deviations from axial symmetry are an equilibrium state or are a consequence of γ-oscillations of an axially symmetric nucleus. Collective excitations of axially symmetric nuclei were investigated by Davydov[7] and Birbrair, Peker & Sliv[8] in the approximation when the projection of the angular momentum of the nucleus on the symmetry axis is an integral of motion.

In the present paper we consider the interaction of rotation with the γ-oscillations for axially symmetric even-even nuclei without postulating a priori constancy of the projection of the angular momentum on the nuclear symmetry axis.*

The wave functions of the collective states and the energies corresponding to them are obtained in the form of expansions in inverse powers of the rigidity parameter of the γ-oscillations; a noteworthy result is that for high rigidity of the nucleus with respect of γ-oscillations, in the first approximation, the projection of the nuclear momentum on the symmetry axis is a good quantum number. Using the deduced wave functions, we evaluate the probabilities for electromagnetic transitions between the states of the first two rotational bands. The results of the calculations are compared with the experimental data. Finally, we discuss the relation between the results obtained and the deductions from the theory of nonaxial nuclei.

1. Equation for γ-oscillations and rotation

The Hamiltonian for an axial asymmetric even-even nucleus, averaged over the wave functions of the individual motion of the nucleons, can be written in the form[10,11]

$$\hat{H} = \hat{T}_\beta + \frac{C(\beta-\beta_0)^2}{2} + \frac{\hbar^2}{2B\beta^2}(\hat{T}_\gamma + \hat{T}_{rot}) + \beta V(\gamma), \tag{1.1}$$

where B and C are, respectively, the mass parameter and the deformation parameter of the nucleus with respect to β-oscillations,

$$\hat{T}_\beta = -\frac{\hbar^2}{2B\beta^4}\frac{\partial}{\partial\beta}\beta^4\frac{\partial}{\partial\beta}, \qquad \hat{T}_\gamma = -\frac{1}{\sin 3\gamma}\frac{\partial}{\partial\gamma}\sin 3\gamma\frac{\partial}{\partial\gamma},$$
$$\hat{T}_{rot} = \sum_{\varkappa=1}^{3}\hat{J}_\varkappa^2/\tau_\varkappa, \quad \tau_\varkappa = 4\sin^2(\gamma - 2\pi\varkappa/3). \tag{1.2}$$

---

*Investigations of this type were undertaken earlier but in an inconsistent manner (see, for example, Ref.9).

From symmetry consideration it follows that the potential energy of the γ-oscillations $V(\gamma)$ is a periodic even function of γ with a period $2\pi/3$. In the case of axially symmetric nuclei the potential energy $V(\gamma)$ has a minimum at $\gamma = 0$. Assuming the β-oscillations to be small, i.e., $|\beta - \beta_0| \ll \beta_0$, we retain in (1.1) only the first terms of the expansion in $\beta - \beta_0$; then

$$\begin{aligned} \hat{H} &= \hat{H}_\beta + \hat{H}_{\gamma\theta}, \\ \hat{H}_\beta &= \hat{T}_\beta + \frac{C(\beta-\beta_0)^2}{2}, \\ \hat{H}_{\gamma\theta} &= \frac{\hbar^2}{2B\beta_0^2}\hat{L}, \quad \hat{L} = \hat{T}_\gamma + \hat{T}_{rot} + W(\gamma), \\ W(\gamma) &= D\gamma^2 + F\gamma^4 + \dots . \end{aligned} \tag{1.3}$$

Thus in the given approximation we neglect the coupling between the β-oscillations and the γ-oscillations and rotation. Accordingly, the wave function of the collective motion may be written in the form

$$X(\beta, \gamma, \theta) = f(\beta)\,\Psi(\gamma, \theta_i),$$

where

$$\hat{H}_\beta f(\beta) = E_\beta f(\beta), \tag{1.4}$$

$$\hat{L}\Psi(\gamma, \theta_i) = \Lambda\Psi(\gamma, \theta_i), \tag{1.5}$$

and the collective energy motion

$$E = E_\beta + \frac{\hbar^2}{2B\beta_0^2}\Lambda.$$

Equation (1.4) for the β-oscillations is an ordinary harmonic oscillator equation so that hereinafter we shall consider only Eq.(1.5) describing γ-oscillations and rotation. Assuming the γ-oscillations to be small ($|\gamma| \ll 1$), i.e., that the rigidity of the nuclear surface with respect to γ-oscillations is great ($D \gg 1$), one can in the expansion of the operator $\hat{L}$ in powers of γ restrict ourselves to the leading terms and after introduction of the variable $y = D^{1/4}\gamma$ go over to the following equation for $\Psi(y, \theta_i)$:

$$(\hat{\mathcal{H}}_0 + \hat{\mathcal{H}}_1 - \lambda)\Psi = 0, \tag{1.6}$$

where

$$\hat{\mathcal{H}}_0 = -\frac{\partial^2}{\partial y^2} - \frac{1}{y}\cdot\frac{\partial}{\partial y} + y^2 + \frac{\hat{J}_3^2}{4y^2} + D^{-1/2}\left(\frac{\hat{J}^2}{3} - \frac{\hat{J}_3^2}{4}\right), \tag{1.7}$$

$$\hat{\mathcal{H}}_1 = -D^{-3/4}\frac{2y}{3\sqrt{3}}(\hat{J}_1^2 - \hat{J}_2^2), \tag{1.8}$$

$$\lambda = D^{-1/2}\Lambda.$$

It should be borne in mind that if the expansion of $\hat{L}$ one successively takes into account all terms of equal order, then additional terms appear in Eqs.(1.7) and (1.8). It can be shown, however, that neither the ratio of probabilities of electromagnetic transitions nor the corrections to the integral rule for the energy in a given rotational band depend on these terms in the given approximation.

2. Rotational and β-vibrational states of an axially symmetric nucleus

In Eq.(1.8) $\hat{H}_1 \sim D^{-3/4}$ can be regarded as a perturbation, inasmuch as $D \gg 1$. Solutions of the unperturbed problem

$$(\hat{\mathcal{H}}_0 - \lambda_0)\Phi = 0 \tag{2.1}$$

are the functions

$$\Phi_{nK}^{JM} = g_{nK}(y)\, \mathcal{D}_{MK}^{J}(\vartheta_i), \tag{2.2}$$

corresponding to the eigenvalues

$$\lambda_0^{nKJ} = 4n + K + 2 + D^{-1/2}[J(J+1)/3 - K^2/4], \tag{2.3}$$

where K is the projection of the total angular momentum on the nuclear symmetry axis, and n is a non-negative integer. In (2.2) the $\mathcal{D}_{MK}^{J}$ are the normalized and symmetrized Wigner D functions;

$$\mathcal{D}_{MK}^{J}(\vartheta_i) = \sqrt{\frac{2J+1}{16\pi^2(1+\delta_{K0})}}\,[D_{MK}(\vartheta_i) + (-1)^J D_{M-K}(\vartheta_i)],$$

and the normalized functions $g_{nK}(y)$ have the form

$$g_{nK} = \frac{D^{1/4}}{\Gamma(K/2+1)}\sqrt{\frac{2\Gamma(n+K/2+1)}{3\Gamma(n+1)}}\, e^{-y^2/2} y^{K/2} F(-n,\ K/2+1,\ y^2),$$

where $F(\alpha, \beta, z)$ is a confluent hypergeometric function.

An analogous approximation is used by Davydov[7] and Birbrair et al[8]. In this approximation the quantum number K is an integral of motion. Inclusion of the perturbation $\hat{\mathcal{H}}_1$ leads to the appearance of an admixture of functions pertaining to other K. Owing to the rigidity of the γ-oscillations, however, this admixture is quite small and K can be regarded as an approximate quantum number. The specific form of the wave functions in the first approximation of perturbation theory is the following

$$\begin{aligned}\Psi_{nK}^{JM} = \Phi_{nK}^{JM} + D^{-3/4}(3\sqrt{3})^{-1}\{&\sqrt{1+(-1)^J\delta_{K0}}\,\alpha_+(JK)\,[\sqrt{n}\,\Phi_{n-1\,K+2}^{JM} + \\ &+ \sqrt{n+K/2+1}\,\Phi_{nK+2}^{JM}] - \sqrt{1+(-1)^J\delta_{K2}}\,\alpha_-(JK)\,[\sqrt{n+K/2}\,\Phi_{nK-2}^{JM} + \\ &+ \sqrt{n+1}\,\Phi_{n+1\,K-2}^{JM}]\},\end{aligned}$$

$$\alpha_\pm(JK) = {}^1\!/_2\sqrt{(J\mp K)(J\mp K-1)(J\pm K+1)(J\pm K+2)}. \tag{2.4}$$

In particular, the wave functions of the ground state and the state with $J = 3$ are of the form

$$\Psi_{00}^{00} = \Phi_{00}^{00}, \quad \Psi_{02}^{3M} = \Phi_{02}^{3M};$$

the first two states with $J = 2$ are described by the functions

$$\Psi_{00}^{2M} = \Phi_{00}^{2M} + (2/3D^{1/4})\,\Phi_{02}^{2M}, \quad \Psi_{02}^{2M} = \Phi_{02}^{2M} - (2/3D^{1/4})(\Phi_{00}^{2M} + \Phi_{10}^{2M})$$

and so on.

For the energy (in $\hbar^2/2B\beta_0^2$ units) in the first approximation of perturbation theory, we obtain

$$\Lambda^{nKJ} = D^{1/2}\lambda^{nKJ} = D^{1/2}(4n + K + 2) + \varepsilon_J,$$

$$\varepsilon_J = J(J+1)/3 - (27D)^{-1}\{[1+(-1)^J\delta_{K0}]\,(K+2)\,\alpha_+^2(JK) - (K-2)(1-\delta_{K0})\,\alpha_-^2(JK)\}. \tag{2.5}$$

In this expression for the energy we have dropped terms not depending on J, smaller in order of magnitude than the leading term $\propto D^{1/2}$. Inclusion of these terms leads to an equal shift of all the energy levels in a given rotational band. We have also omitted the terms yielding a correction proportional to $D^{-1/2}$ to $J(J+1)/3$ that are not dependent on J. The effect of these terms as regards deviations from the energy interval rule is insignificant. For the rotational energy of the ground state band ($n = K = 0$) there is obtained from (2.5) the usual expression:

$$\varepsilon_J(n=K=0)=J(J+1)/3-(27D)^{-1}J(J-1)(J+1)(J+2)\approx$$
$$\approx J(J+1)/3-(27D)^{-1}J^2(J+1)^2. \qquad (2.6)$$

It is found that Eq.(2.6) correctly describes the experimentally observed deviations from the interval rule in the ground state rotational band.

3. Electric quadrupole transition probabilities

The reduced probability for an electric quadrupole transition $nKJ\to n'K'J'$, expressed in $e^2Q_0^2/16\pi$ units, equals

$$b(E2, nKJ\to n'K'J')=\frac{5}{2J+1}\sum_{MM'\mu}|\langle nKJM\,|\,\hat{q}_{2\mu}\,|\,n'K'J'M'\rangle|^2, \qquad (3.1)$$

where the nuclear quadrupole moment operator (in eQ_0 units) is

$$\hat{q}_{2\mu}=D^2_{\mu 0}\cos\gamma+(D^2_{\mu 2}+D^2_{\mu -2})\sin\gamma/\sqrt{2}.$$

By means of (3.1) there were calculated the probabilities for E2 transitions between the states described by the wave functions (2.4). Below we give the more important ratios of these probabilities in the notation of (3.1) and Davydov et al[1-4]:

$$\frac{b(E2,022\to 000)}{b(E2,002\to 000)}\equiv\frac{b(E2,22\to 0)}{b(E2,21\to 0)}=D^{-1/2}, \qquad (3.2)$$

$$\frac{b(E2,022\to 002)}{b(E2,022\to 000)}\equiv\frac{b(E2,22\to 21)}{b(E2,22\to 0)}=\frac{10}{7}(1+4D^{-1/2}), \qquad (3.3)$$

$$\frac{b(E2,022\to 004)}{b(E2,022\to 002)}\equiv\frac{b(E2,22\to 41)}{b(E2,22\to 21)}=\frac{1}{20}\left(1+\frac{28}{3}D^{-1/2}\right), \qquad (3.4)$$

$$\frac{b(E2,023\to 004)}{b(E2,023\to 002)}\equiv\frac{b(E2,3\to 41)}{b(E2,3\to 21)}=\frac{2}{5}\left(1+\frac{28}{3}D^{-1/2}\right). \qquad (3.5)$$

Comparison of the experimental and theoretical probability ratios for E2 transitions

Nucleus	E_{21}, keV	E_{22}, keV	$\mu\equiv\frac{E_{22}}{E_{21}}$	$\frac{b(E2,22\to 21)}{b(E2,22\to 0)}$ Theory	$\frac{b(E2,22\to 21)}{b(E2,22\to 0)}$ Experiment	$\left[\frac{b(E2,22\to 41)}{b(E2,22\to 21)}\right]_{\text{theo}}$	$\left[\frac{b(E2,3\to 41)}{b(E2,3\to 21)}\right]_{\text{theo}}$
Sm^{152}	122	1092	8,95	2,07	2,2±0,3	0,10	0,82
Gd^{154}	123	998	8,12	2,13	1,8	0,11	0,86
Gd^{156}	89	1240	13,94	1,84	1,9±0,9	0,08	0,67
Dy^{160}	86,5	966,5	11,2	1,94	2,0±0,1	0,09	0,73
Er^{166}	80,6	787,4	9,76	2,02	2,0±0,3	0,10	0,78
Er^{168}	79,8	822	10,3	1,98	1,8±0,3	0,10	0,76
W^{182}	100,1	1222	12,2	1,90	1,8±0,1	0,09	0,70
W^{184}	111,1	904	8,16	2,13	1,8±0,3	0,11	0,86
W^{186}	122,5	733	5,98	2,38	2,5±0,3	0,13	1,02
Os^{186}	137,2	768	5,61	2,45	2,7±0,6	0,13	1,06
Os^{188}	155,0	168	4,08	2,83	2,7±0,2	0,16	1,31
Os^{190}	187,0	557	2,98	3,34	6,8±1,2	0,20	1,65
Th^{228}	57,5	965	16,8	1,77	2,5±0,5	0,08	0,62
Th^{230}	52,8	1060	20,1	1,71	—	0,07	0,58
Th^{232}	52,8	790	14,95	1,81	2,1±0,3	0,08	0,65
U^{232}	47	868	18,5	1,74	—	0,08	0,60
Pu^{238}	44,2	1031	23,4	1,67	1,5±0,2	0,07	0,56
Pu^{240}	42,9	1020	23,8	1,67	—	0,07	0,56

These ratios depend on the single parameter D, which is directly connected with the energy ratio of the first two levels with $J = 2$, namely, $\mu \equiv E_{022} / E_{002} \equiv \equiv E_{22} / E_{21} \approx D^{1/2}$. Determining μ for each nucleus from the experimental data on the location of the levels with $J = 2$, one can calculate the ratio of the reduced probabilities for E2 transitions between the collective levels in these nuclei. The results of such calculations for the ratios (3.3) and (3.5) are listed in the accompanying table together with the experimental data for the ratio (3.3) taken from the work of Van Patter[4]; it will be seen that in this case there is good agreement between the experimental and theoretical values.

We must emphasize that all the present results were obtained on the assumption of high rigidity of the γ-oscillations. Hence, for example, in the case of Os^{190}, for which $\mu \approx 3$, one cannot expect good agreement with experiment. We note that in Eqs.(3.2)—(3.5) there were rejected terms of order D^{-1}, inasmuch as taking into account anharmonicity of the potential energy of the γ-oscillations leads to corrections of the same order of magnitude.

4. Comparison of the present results with the theory of nonaxial nuclei

The experimental data pertaining to low-lying levels in nuclei for which the ratio $E_{22}/E_{21} \equiv \mu$ is large, are satisfactorily explained by means of the model of a nonaxial rotator[1-3] with a small degree of nonaxiality ($\gamma_0 \leqslant 15°$). In this case the expressions for the energies and the transition probabilities can be expanded in series in powers of γ_0; however, restricting ourselves to the first terms of this expansion, we obtain

$$\mu \approx 1/(2\gamma_0^2),$$

$$\frac{b(E2,22 \to 21)}{b(E2,22 \to 0)} \approx \frac{10}{7}(1 + 8\gamma_0^2) = \frac{10}{7}\left(1 + \frac{4}{\mu}\right), \tag{4.1}$$

$$\frac{b(E2,22 \to 0)}{b(E2,21 \to 0)} = \gamma_0^2 = \frac{1}{2\mu} \tag{4.2}$$

Eq.(4.1) agrees with (3.3). This identity of the results of the present work and those following from the model of a nonaxial rotator is explained by the fact that for axially symmetric nuclei, i.e., for nuclei the potential energy of deformation of which is minimal for $\gamma = 0$, as a result of γ-oscillations even in the ground state $\overline{\gamma^2} \neq 0$. This leads to the possibility of rotation about the 3 axis.

In a number of cases, however, the results of the present investigation differ from the corresponding results following from the model of a nonaxial rotator. Thus, the values of the reduced probabilities for E2 transitions between levels pertaining to different rotational bands differ by a factor of 2 in the first order in $1/\mu$. This is explained by the fact that

$$\frac{b(E2, J'2 \to J\,0)_{\text{nonaxi}}}{b(E2, J'2 \to J\,0)_{\text{axi}}} \approx \frac{\sin^2\gamma_0}{|\langle g_{02}(\gamma)|\sin\gamma|g_{00}(\gamma)\rangle|^2} \approx \frac{1}{2}, \tag{4.3}$$

inasmuch as

$$|\langle g_{02}(\gamma)|\sin\gamma|g_{00}(\gamma)\rangle|^2 \approx \mu^{-1};\ \sin^2\gamma_0 \approx (2\mu)^{-1}.$$

In particular, the probability ratio $\frac{b(E2,22 \to 0)}{b(E2,21 \to 0)}$ for axial nuclei is about twice as great as the corresponding ratio deduced from the model of a nonaxial rotator (in the first order in $1/\mu$). This difference may make it impossible to decide experimentally whether there exist small equilibrium deviations from axial symmetry in atomic nuclei. To this end one must measure with adequate accuracy the ratio

(3.3) (we note that the scanty experimental data available for this ratio[4] are better explained from the standpoint of the theory of nonaxial nuclei). On the other hand, it would be desirable to drop the restrictions used in the present work and, in particular, to take into account deviations from the hydrodynamic dependence of the moments of inertia on γ.

We desire to express our gratitude to A.S.Davydov for his interest in the work and stimulating discussion.

"P.N.Lebedev" Physical Institute,
Academy of Sciences of the USSR

References

1. A.S.Davydov & G.F.Filippov, Zhur.eksp.i teor.fiz., 35, 440 (1958). (Trans.Soviet Physics - JETP.)
2. A.S.Davydov & V.S.Rostovskii, Ibid., 36, 1783 (1959). (Trans.Ibid.)
3. A.S.Davydov, Izv.AN SSSR, Ser.fiz., 23, 792 (1959). (Trans.Bulletin, 23, 788.)
4. D.M.Van Patter, Nucl.Phys., 14, 42 (1959/60).
5. A.A.Chaban, Zhur.eksp.i teor.fiz., 38, 1630 (1960). (Trans.Sov.Phys. - JETP.)
6. A.S.Davydov & A.A.Chaban, Nucl.Phys., 20, 499 (1960).
7. A.S.Davydov, Vestnik, Moscow State Univ., Series 3, No.1, 56 (1961).
8. B.L.Birbrair, L.K.Peker & L.A.Sliv, Zhur.eksp.i teor.fiz., 36, 803 (1959). (Trans.Soviet Physics - JETP.)
9. T.Tamura & T.Udagawa, Nucl.Phys., 16, 460 (1960).
10. A.Bohr, Kgl.Danske Videnskab.Selskab, Mat.-fys.Medd., 26, No.14 (1952).
11. A.Bohr & B.Mottelson, Ibid., 27, No.16 (1953).

ON COLLECTIVE EXCITATIONS IN NONSPHERICAL NUCLEI

- Yu.T.Grin' & D.F.Zaretskii

1. Where excitations of deformed nuclei are concerned, in addition to studies of rotational levels, there have been fairly thorough experimental investigations of other collective levels, for example, β- and γ-vibrational levels. Beta-vibrational levels correspond to internal excitations with $k = 0$, while γ-vibrational levels correspond to excitations with $k = 2$ (k is the projection of the angular momentum on the nuclear axis). The energies of these levels lie in the range from 0.5 to 1.2 MeV, while the reduced probabilities for electric quadrupole transitions from these levels to the ground state are somewhat higher than the probabilities for transitions from single-particle levels. These levels have been interpreted theoretically either from the standpoint of the hydrodynamic model[1] or in the framework of the independent particle model[2]. In the case of the hydrodynamic model, the oscillation energy comes out to be 1.5 to 2.5 MeV, which is appreciably higher than the observed values. Moreover, in the hydrodynamic model one cannot take into account shell effects. On the other hand, calculations by means of the independent particle model yield an oscillation energy of the order of the separation between shells.

Recently there has been developed the theory of collective excitations in spherical nuclei[3-5]. This theory is based on the introduction, in addition to interaction leading to pairing, of a residual quadrupole-quadrupole interaction between the particles. The existence of quadrupole-quadrupole interaction between nucleons follows from experiment. Actually, near magic nuclei with an odd number of nucleons have an additional quadrupole moment as compared with the single-particle case. Moreover, the probabilities for E2 transitions are heightened in odd-nucleon near magic nuclei as compared with the probabilities for single-particle transitions. In the case of nonspherical nuclei there is also observed enhancement of the probabilities for E2 transitions between different internal states, as compared with the single-particle probabilities calculated on the basis of Nilsson's scheme[6].

In the present paper we give a generalization of the theory for the case of nonspherical nuclei. We deduced an equation for finding the frequencies of the collective excitations and obtain a relation between the frequencies of the β- and γ-excitations in the semi-classical approximation.

2. The bound state of two quasi-particles can be described by means of the two-particle Green's function.[7] In the case of a spherical nucleus this treatment was initially proposed by Belyaev[4]. The two-particle Green's function is defined by

$$K = \langle \Phi_0 | T (a_1 a_2^+ a_3 a_4^+) | \Phi_0 \rangle, \qquad (1)$$

where T is the time ordering operator, Φ_0 is the wave function of the ground state and a_i and a_k^+ are the Fermi annihilation and creation operators for particles in the Heisenberg representation; these obey the usual commutation rules when $t = 0$. The state of a particle i is characterized by the set of quantum numbers pertaining to the deformed nucleus. The quadrupole-quadrupole interaction between particles, taking into account the exchange term, is of the form

$$V (12; 34) = \varkappa [(q_{2\mu})_{12} (q_{2\mu})_{34} - (q2_{\mu})_{14} (q_{2\mu})_{23}]. \qquad (2)$$

Here $\varkappa < 0$ is a constant (dimensionality MeV/cm^4) which characterizes the strength of the interaction, and $(q_{2\mu})_{ik}$ is the matrix element of the quadrupole moment operator. Then the equation for K in the first approximation in interaction will have the form

$$K(12;34) = K^{\circ}(12;34) + i\,[G(15)\,G(72) + F(17)\,F^{+}(25)] \times \\ \times V(56;78)\,K(86;34), \tag{3}$$

where $K^{\circ}(12;34)$ is the two-particle Green's function neglecting interaction (2), and G and F are single-particle Green's functions, which in the zeroth approximation for the interaction (2), have the form[8,9]:

$$G(1.1;\omega) = \frac{\frac{1}{2}\left(1+\frac{\varepsilon_1}{E_1}\right)}{\omega - E_1 + i\delta} + \frac{\frac{1}{2}\left(1-\frac{\varepsilon_1}{E_1}\right)}{\omega + E_1 - i\delta}, \\ F(1,1;\omega) = -F^{+}(1,1;\omega) = -\frac{i\Delta}{2E_1}\left(\frac{1}{\omega - E_1 + i\delta} - \frac{1}{\omega + E_1 - i\delta}\right), \tag{4}$$

where $\delta \to +0$, $E_1 = \sqrt{\Delta^2 + \varepsilon_1^2}$, ε_1 is the energy of level 1 reckoned from the Fermi surface ε_0, and Δ is a parameter characterizing the pair correlation energy. Let $t_1, t_2 > t_3, t_4$, then

$$K(12;\ 34) = \sum_s \varphi_s(12)\,\tilde{\varphi}_s(34), \tag{5}$$

where $\varphi_s(2) = \langle 0 | T(a_1 a_2^{+}) | s \rangle$, $\tilde{\varphi}_s(34) = \langle s | T a_3 a_4^{+} | 0 \rangle$ and $|s\rangle$ is the wave function of the intermediate state.

In investigating bound states, one must discard the free term in (3). After this Eq.(3) can be "reduced" by eliminating $\tilde{\varphi}_s(34)$ and becomes

$$\varphi_s(12) = i\,[G(15)\,G(72) + F(17)\,F^{+}(25)]\,V(56;78)\,\varphi_s(86). \tag{6}$$

Going over to the Fourier representation with respect to time in the functions φ_s, G and F, and making use of the fact that G and F are diagonal, we obtain

$$\varphi(12;\omega k) = i\int d\omega'\,[G(1,1;\omega + \omega')\,G(2,2;\omega') + F(1,1;\omega + \omega')\,F^{+}(22;\omega')]\,V(16;28)\,\varphi(86;\omega' k), \tag{7}$$

where ω is the excitation frequency and k is the projection of the total angular momentum on the nuclear axis for the given state. Equation (7) was deduced on the assumption of a prompt potential V.

Integrating in (7) and neglecting the exchange term in V, we obtain

$$\varphi(12;\omega k) = \varkappa \frac{\omega\left(\frac{\varepsilon_1}{E_1} - \frac{\varepsilon_2}{E_1}\right) + (E_1 + E_2)\left(1 - \frac{\varepsilon_1\varepsilon_2}{E_1 E_1} + \frac{\Delta^2}{E_1 E_2}\right)}{2\,[\omega^2 - (E_1 + E_2)^2]} \times (q_{2k})_{12}\,(q_{2k})_{68}\,\varphi(86;\omega k). \tag{8}$$

Neglect of the exchange term in (8) yields an error $\sim A^{-1/3}$. Actually in the expressions connected with the exchange term summation extends over all quantum numbers except Ω, the projection of the angular momentum on the nuclear axis in the single-particle states. This limitation does not apply to the sums containing a leading term.

Multiplying (8) by $(q_{2k})^{*}_{21}$ and summing over 2 and 1, we obtain the following expression for determining ω:

$$1 = \varkappa \sum_{12} \frac{(E_1 E_1 - \varepsilon_1\varepsilon_2 + \Delta^2)}{2E_1E_2\,[\omega^2 - (E_1 + E_1)^2]}\,|\,(q_{2k})_{12}\,|^2. \tag{9}$$

Eq.(9) is a relationship for determining the frequencies of the bound states. When $\Delta = 0$, the equation for ω becomes

$$1 = -\varkappa \sum_{12} \frac{n_1 - n_2}{\omega - (\varepsilon_1 - \varepsilon_2)}\,|\,q_{12}\,|^2, \tag{10}$$

where

$$n_i = \begin{cases} 1, & \text{if } \varepsilon_i < \varepsilon_0. \\ 0, & \text{if } \varepsilon_i > \varepsilon_0. \end{cases}$$

3. Equation (9) can be solved in the framework of the realistic Nilsson model only numerically. Hence we shall attempt to find the solution of this equation in the model of an axially symmetric deformed oscillator potential. In this model the energy of the single-particle level λ in the semi-classical approximation is of the form

$$\varepsilon_\lambda + \varepsilon_0 = h\omega_x (n_x + n_y) + h\omega_z n_z = h\omega_x n_\perp + h\omega_z n_z, \tag{11}$$

where ω_x, ω_y and ω_z are the frequencies of oscillation along the axes, and n_x, n_y and n_z are the oscillator quantum numbers. The quadrupole moment operators are of the form

$$\begin{aligned} q_{20} &= r^2 Y_{20} = \sqrt{\frac{5}{16\pi}} (2z^2 - x^2 - y^2), \\ q_{2\pm2} &= r^2 Y_{2\pm2} = \mp \sqrt{\frac{15}{32\pi}} (x \pm iy)^2. \end{aligned} \tag{12}$$

The matrix elements of these operators are nonzero for transitions inside the given shell $N = n_x + n_y + n_z$ and through the shell $N' = N \pm 2$. Transitions through the shell are "far" transitions in the sense that

$$\varepsilon_\lambda - \varepsilon_{\lambda'} \sim 2h\omega_0 \gg 2\Delta,$$

where $h\omega_0$ is the separation between shells in the spherical nucleus.

The diagonal matrix elements of the operators (12) can readily be calculated. In the semi-classical approximation we have

$$\begin{aligned} (q_{20})_{\lambda\lambda} &= \sqrt{\frac{5}{16\pi}} \left(\frac{2n_z}{\omega_z} - \frac{n_\perp}{\omega_\perp} \right), \\ (q_{2\pm2})_{\lambda\lambda} &= \mp \sqrt{\frac{15}{32\pi}} \left(\frac{n_x - n_y}{\omega_x} \right). \end{aligned} \tag{13}$$

The nondiagonal matrix elements of the operator q_{20} correspond to "far" transitions only. The operator $q_{2\pm2}$ has nondiagonal matrix elements, which correspond to transitions not involving change in energy:

$$(q_{2\pm2})_{\lambda\lambda'} = 2i \sqrt{\frac{15 n_x n_y}{32\pi 4\omega_x^2}}, \tag{14}$$

where the state λ' is described by the quantum numbers $n'_x = n_x \pm 1$, $n'_y = n_y \mp 1$ and $n'_z = n_z$; here $n'_\perp = n_\perp$. All the other nondiagonal matrix elements of this operator correspond to "far" transitions.

Eq.(9) can be rewritten in the form

$$1 = \varkappa \sum_{\lambda\lambda'} \frac{2\Delta^2 |q_{\lambda\lambda'}|^2}{E_\lambda (4E_\lambda^2 - \omega^2)} + \varkappa \sum_{\lambda\lambda'}{}' \frac{(E_\lambda E_{\lambda'} - \varepsilon_\lambda \varepsilon_{\lambda'} - \Delta^2)(E_\lambda + E_{\lambda'})}{2E_\lambda E_{\lambda'} [(E_\lambda + E_{\lambda'})^2 - \omega^2]} |q_{\lambda\lambda'}|^2, \tag{15}$$

where $\sum_{\lambda\lambda'}$ indicate summation over all transitions occurring without change in energy, while $\sum_{\lambda\lambda'}{}'$ represents summation over all "far" transitions. In the last

sum one can neglect ω, after which the entire sum over the "far" transitions can be included in the renormalization of the constant $\varkappa$. Then

$$1 = \varkappa' \sum_{\lambda\lambda'} \frac{2\Delta^2}{E_\lambda (4E_\lambda^2 - \omega^2)} |q_{\lambda\lambda'}|^2,$$

where

$$\varkappa' = \frac{\varkappa}{1 - \varkappa \sum_{\lambda\lambda'}' \frac{E_\lambda E_{\lambda'} - \varepsilon_\lambda \varepsilon_{\lambda'} + \Delta^2}{2E_\lambda E_{\lambda'} (E_\lambda + E_{\lambda'})} |q_{\lambda\lambda'}|^2}. \tag{16}$$

For a fixed transition energy $(\varepsilon_\lambda - \varepsilon_\lambda)$, $|q_{\lambda\lambda'}|^2$ varies considerably with the state λ over the interval $\sim \varepsilon_0 A^{-1/3}$. At the same time the function $\frac{1}{E_\lambda (4E_\lambda^2 - \omega^2)}$ has a maximum of width $\sim 2\Delta$ at $\varepsilon_\lambda = 0$. Hence, with semi-classical accuracy we can write

$$1 = \varkappa' \frac{4\Delta^2}{\omega^2 \sqrt{\frac{4\Delta^2}{\omega^2} - 1}} \operatorname{arctg} \frac{1}{\sqrt{\frac{4\Delta^2}{\omega^2} - 1}} \sum_{\lambda\lambda'} |q_{\lambda\lambda'}|^2 \delta(\varepsilon_\lambda). \tag{17}$$

Solution of the transcendental equation (17) can be found in explicit form in the two limiting cases: $\omega \ll 2\Delta$ and $2\Delta - \omega \ll 2\Delta$.

In the first case

$$\omega = 2\Delta \sqrt{\frac{3}{2}} \cdot \sqrt{1 - \varkappa' \sum_{\lambda\lambda'} |q_{\lambda\lambda'}|^2 \delta(\varepsilon_\lambda)}, \tag{18}$$

and in the second case

$$\omega = 2\Delta \left\{1 - \frac{\pi}{8} \varkappa'^2 \left[\sum_{\lambda\lambda'} |q_{\lambda\lambda'}|^2 \delta(\varepsilon_\lambda)\right]^2\right\}. \tag{19}$$

The order of magnitude of $\varkappa$ and, consequently, of $\varkappa'$ is known[4]: $\varkappa \sim \frac{\varepsilon_0}{AR_0^4}$ (A is the number of nucleons and R_0 is the nuclear radius). Moreover we can use the evaluation

$$\sum_{\lambda\lambda'} |q_{\lambda\lambda'}|^2 \delta(\varepsilon_\lambda) \approx R_0^4 \rho_0,$$

where ρ_0 is the level density at the Fermi surface. On the basis of the foregoing evaluation we can write

$$\varkappa' \sum_{\lambda\lambda'} |q_{\lambda\lambda'}|^2 \delta(\varepsilon_\lambda) \approx 1;$$

consequently, the difference between ω and 2Δ can be $\sim \Delta$.

Thus we find that in deformed nuclei there can exist collective excitations with an energy substantially lower than 2Δ. Clearly, this deduction is valid provided $\varkappa' \sum_{\lambda\lambda'} |q_{\lambda\lambda'}|^2 \delta(\varepsilon_\lambda) < 1$. Otherwise, the theory is inapplicable.

4. We now turn to the problem of finding the ratio of frequencies of β- and γ-oscillations. To this end we return to Eq.(9) and rewrite it in the form

$$\varkappa' \omega^2 \sum_{\lambda\lambda'} \frac{(E_\lambda E_{\lambda'} - \varepsilon_\lambda \varepsilon_{\lambda'} + \Delta^2) |q_{\lambda\lambda'}|^2}{2E_\lambda E_{\lambda'} (E_\lambda + E_{\lambda'}) [(E_\lambda + E_{\lambda'})^2 - \omega^2]} = 1, \tag{20}$$

where

$$\varkappa' = \frac{\varkappa}{1-\varkappa\sum_{\lambda\lambda'}\frac{E_\lambda E_{\lambda'}-\varepsilon_\lambda\varepsilon_{\lambda'}+\Delta^2}{2E_\lambda E_{\lambda'}(E_\lambda+E_{\lambda'})}|q_{\lambda\lambda'}|^2}.$$

It can readily be shown that the sum over all states λ and λ' in the definition of $\varkappa'$ does not depend on the type of oscillations. Thus in the semi-classical approximation and for deformations $\beta \ll 1$:

$$\sum_{\lambda\lambda'}\frac{E_\lambda E_{\lambda'}-\varepsilon_\lambda\varepsilon_{\lambda'}+\Delta^2}{2E_\lambda E_{\lambda'}(E_\lambda+E_{\lambda'})}|q_{\lambda\lambda'}|^2 \approx \sum_{\lambda\lambda'}|q_{\lambda\lambda'}|^2\delta(\varepsilon_\lambda) = \int \rho(\bar{\varepsilon}_0, r)\, r^6 dr,$$

where $\rho(\varepsilon_0, r) = \sum_\lambda \varphi_\lambda^* \varphi_\lambda \delta(\varepsilon_\lambda)$ is the particle density near the Fermi surface.

On the approximating assumption that $\omega \ll 2\Delta$, we obtain from (20) the following ratio for the frequencies of β- and γ-excitation:

$$\frac{\omega_\beta^2}{\omega_\gamma^2} = \frac{\sum_{\lambda\lambda'}\frac{E_\lambda E_{\lambda'}-\varepsilon_\lambda\varepsilon_{\lambda'}+\Delta^2}{2E_\lambda E_{\lambda'}(E_\lambda+E_{\lambda'})^3}(q_{22})^2_{\lambda\lambda'}}{\sum_{\lambda\lambda'}\frac{E_\lambda E_{\lambda'}-\varepsilon_\lambda\varepsilon_{\lambda'}+\Delta^2}{2E_\lambda E_{\lambda'}(E_\lambda+E_{\lambda'})^3}(q_{20})^2_{\lambda\lambda'}}. \tag{21}$$

The sums in (21) can readily be calculated in the semi-classical approximation[9]:

$$\sum_{\lambda\lambda'}\frac{E_\lambda E_{\lambda'}-\varepsilon_\lambda\varepsilon_{\lambda'}+\Delta^2}{2E_\lambda E_{\lambda'}(E_\lambda+E_{\lambda'})^3}q^2_{\lambda\lambda'} \approx \sum_{\lambda\lambda'}\frac{1-g\left(\frac{\varepsilon_\lambda-\varepsilon_{\lambda'}}{2\Delta}\right)}{4\Delta^2\left(\frac{\varepsilon_\lambda-\varepsilon_{\lambda'}}{2\Delta^2}\right)^2}|q_{\lambda\lambda'}|^2\delta(\varepsilon_\lambda), \tag{22}$$

where $g(x) = \frac{\ln|x+\sqrt{1+x^2}|}{x\sqrt{1+x^2}}$.

Invoking (22), we obtain

$$\frac{\omega_\beta^2}{\omega_\gamma^2} = \frac{\sum_{\lambda\lambda'}\frac{1-g\left(\frac{\varepsilon_\lambda-\varepsilon_{\lambda'}}{2\Delta}\right)}{\left(\frac{\varepsilon_\lambda-\varepsilon_{\lambda'}}{2\Delta}\right)^2}(q_{22})^2_{\lambda\lambda'}\delta(\varepsilon_\lambda)}{\sum_{\lambda\lambda'}\frac{1-g\left(\frac{\varepsilon_\lambda-\varepsilon_{\lambda'}}{2\Delta}\right)}{\left(\frac{\varepsilon_\lambda-\varepsilon_{\lambda'}}{2\Delta}\right)^2}(q_{20})^2_{\lambda\lambda'}\delta(\varepsilon_\lambda)}. \tag{23}$$

Let us now find the relation between the frequencies of β- and γ-excitations in the model of a deformed axially symmetric oscillator potential.

"Far" transitions make a negligibly small contribution to (23). On the other hand, when $\beta \ll 1$

$$\sum_\lambda (q_{20})^2_\lambda \delta(\varepsilon_\lambda) = \sum_{\lambda\lambda'}(q_{22})^2_{\lambda\lambda'}\delta(\varepsilon_\lambda) = \frac{5}{64\pi}\cdot\frac{h^2}{m^2\omega_0^2}\left(\frac{\varepsilon_0}{h\omega_0}\right)^2\frac{1}{h\omega_0}. \tag{24}$$

Consequently, in the model of an axially symmetric oscillator potential the frequencies of β- and γ-excitations agree. This agreement occurs owing to degeneracy of the levels in the given potential.

Next let us consider a more realistic model, namely, the Nilsson model without spin-orbit coupling[6]. In this case the Hamiltonian is

$$H = H_0 + Dl^2,$$

where

$$H_0 = \frac{p^2}{2m} + \frac{m}{2}(\omega_x^2 x^2 + \omega_y^2 y^2 + \omega_z^2 z^2), \tag{25}$$

m is the mass of the nucleon and D is a constant known from experiment (D equals about $-0.025\,\hbar\omega_0$).

In the case of deformations $\beta \gtrsim A^{-1/3}$ the term Dl^2 can be taken into account by means of perturbation theory.[10] In this case the single-particle levels can be classified by the quantum numbers n_z, $n_\perp$, Λ, where Λ is the projection of the angular momentum on the nuclear axis ($\Lambda = \pm 1, \pm 3 \ldots$ if Λ is odd, and $\Lambda = 0, +2, +4, \ldots$ if Λ is even). In the semi-classical approximation

$$\langle n_\perp \Lambda n_z | l^2 | n_\perp \Lambda n_z \rangle = \Lambda^2 + 2n_\perp n_z. \tag{26}$$

Introduction of the term Dl^2 into the Hamiltonian thus leads to removal of the degeneracy. As a result there appear "near" nondiagonal transitions in the case of γ-excitations (n_z, $n_\perp$, $\Lambda \to n_z$, $n_\perp$, $\Lambda \pm 2$). The difference between the corresponding energies $\varepsilon_\lambda - \varepsilon_{\lambda'} = \pm 4D\Lambda$. In the case of β-excitations, introduction of this term does not lead to the appearance of "close" nondiagonal transitions.

As a result the ratio of the frequencies of the γ- and β-excitations in Nilsson's model without spin-orbit coupling can be obtained from (23) in the form

$$\frac{\omega_\beta^2}{\omega_\gamma^2} = 3\int_0^1 \frac{1 - g\left(\frac{2D\varepsilon_0 x}{\omega_0 \Delta}\right)}{\left(\frac{2D\varepsilon_0}{\omega_0 \Delta} x\right)^2}(1 - 3x^2 + 2x^3)\,dx. \tag{27}$$

In going from Eq. (23) to (27) we have replaced summation over quantum numbers by integration and used the explicit form of the matrix element $q_{\lambda\lambda'}$.

It follows from (25) that in the limit as $D \to 0$, the ratio $\omega_\beta/\omega_\gamma \to 1$. Evaluation in terms of our notation gives $D \sim \varepsilon_0/A$, $\Delta \sim \varepsilon_0 A^{-2/3}$ and, consequently, $\frac{2D\varepsilon_0}{\omega_0\Delta} \sim 1$; hence there is no explicit notational difference between ω_β and ω_γ. However, it is evident from (25) that $(\omega_\beta/\omega_\gamma)^2 < 1$, i.e., that the levels corresponding to β-excitations must lie below levels corresponding to γ-excitations.

The dependence of the ratio $\omega_\beta/\omega_\gamma$ on the parameter $\alpha = \frac{2D\varepsilon_0}{\omega_0\Delta}$ is indicated by the following figures:

α	1.8	2.25	3.0	4.5
$\frac{\omega_\beta}{\omega_\gamma}$	0.90	0.86	0.80	0.72

5. Present reliable data on levels corresponding to β- and γ-excitations are available mainly for heavy nuclei in the region of thorium, uranium and plutonium.[11] It is found in all these cases that the energy of the β-oscillations is less than the energy of the γ-oscillations by 0.1-0.3 MeV. This experimental fact is in qualitative agreement with the results of our calculations. It also follows from the theory that β- and γ-vibrational levels may have excitation energies substantially lower than 2Δ.

Thus the microscopic interpretation of β- and γ-levels proposed above appears to be plausible. In contrast, the hydrodynamic model and the independent particle model are incapable of explaining either the absolute energies or the relative locations of the levels in question.

Unfortunately, comparison of the theory with experiment in the region of rare earths is difficult owing to the lack of systematic data on the positions of the levels corresponding to β-excitations. In view of this it would be of interest to search for low-lying β-levels in this nuclear region.

References

1. A.Bohr & B.Mottelson, in "Problemy sovremenyi fizikii" (Problems of modern physics), No.9 (1955).
2. D.Inglis, Ibid., No.1 (1956).
3. T.Marumori, Progr.Theoret.Phys., 24, 331 (1960).
4. S.T.Belyaev, Kgl.Danske Videnskab.Selskab, Mat.-fys.Medd., 31, No.11 (1959); S.T.Belyaev, Zhur.eksp.i teor.fiz., 39, 1387 (1960). (Trans.Soviet Physics - JETP.)
5. M.Baranger, Phys.Rev., 120, 957 (1960); R.Arvien & M.Veneroni, Compt. rendu, 250, 992, 2155 (1960).
6. S.Nilsson, in "Deformathiya atomnykh yader" (Deformation of atomic nuclei), M., 1958.
7. V.M.Galitskii & A.B.Migdal, Zhur.eksp.i teor.fiz., 34, 139 (1958). (Trans.Soviet Physics - JETP.)
8. L.P.Gor'kov, Ibid., 34, 735 (1958). (Trans.Ibid.)
9. A.B.Migdal, Ibid., 37, 249 (1959). (Trans.Ibid.)
10. O.Prior, Arkiv fys., 14, 451 (1959).
11. I.Perlman, Proceedings of the International Conference on Nuclear Structure, p.547, Kingston, Canada, 1960.

INVESTIGATION OF THE DECAY SCHEME OF Eu^{145}

- Yu.A.Aleksandrov & M.K.Nikitin

In the present work, using a coincidence scintillation spectrometer, we investigated the γ-transitions and γ-γ coincidences evinced in the decay of the europium fraction separated chromatographically from a tantalum target bombarded with 660 MeV protons. It must be noted that the presence of a mixture of isotopes in the europium fraction greatly hampered interpretation of the experimental results.

The γ-spectrum and γ-γ coincidences were investigated twice with an interval of about two months between measurements under identical conditions. Thus, through analysis of the spectra we were able to distinguish between the radiations of the long-lived isotopes Eu^{147}, Eu^{148} and Eu^{149} and the radiations of the relatively short-lived isotopes Eu^{145} and Eu^{146}. The problem of separating the radiations of Eu^{145} and Eu^{146} is more complicated inasmuch as the periods of these isotopes are close. In the given case we used the results of our earlier work[1] in which there were carefully investigated the γ-spectrum and γ-γ coincidences in the decay of Eu^{146} separated from a gadolinium fraction (also extracted from proton bombarded tantalum).

Moreover, in investigating the γ-γ coincidences we used the following procedure. The fixed channel of the coincidence spectrometer was set to discriminate narrow gamma energy intervals (~50 keV). In investigating coincidences with a region of the γ-spectrum wherein transitions close in energy are not resolved by the scintillation spectrometer, we shifted the setting of the fixed channel in successive steps. Then by comparison and analysis of the experimental coincidence curve, in some cases we were able to draw unambiguous inferences regarding the presence of cascade γ-transitions in the decay of Eu^{145}.

The most reliable identifications of Eu^{145} were made in the studies of Grover[2] and Bashilov et al[3], wherein there were established the mass number and the period (5.6 days). In the work of Bashilov et al it was shown that γ-transitions with energies 2000, 1880, 1660 and 890 keV belong to Eu^{145}. Grover[2], who used the $Sm^{144}(\alpha,p,2n)Eu^{145}$ reaction, observed γ-transitions with energies of 530, 645, 890, 1300 and 1650 keV. The conversion electron spectrum of Eu^{145} was investigated by Anton'eva et al[4]; there were identified the following γ-transitions: 1990, 1867, 1652, 1142, 886, 757, 647 and 110 keV. The positron spectrum and conversion electron spectrum were investigated by Dzhelepov et al[5] on a triple focusing magnetic spectrometer; it was established that there are β^+-components with end-point energies of 740 and 1740 keV.

We carried out a further investigation of the γ-spectrum of Eu^{145} particularly in the high energy range (to 3 MeV). We detected γ-transitions with energies of 110, 190, 530, 655, 765, 895, (1140), (1300), (1870), 2000, (2200) and 2420 keV, which are, apparently, transitions between levels of Sm^{145}. One cannot positively affirm the existence of the 1140 and 1300 keV transitions in view of their low intensity and the presence of γ-transitions close in energy in the decay of Eu^{146}. The 1870 and 2200 keV transitions are evinced explicitly only after resolution of the experimental γ-spectrum, using standard line shapes.

We obtained the following values for the relative intensities of the γ-rays:

E_γ, keV	530	655	765	895	1660	1870	2000	2200	2420
I_γ	7.3±2.7	27±7	10±3	100	15.6±0.8	1.5	8±1	1	1

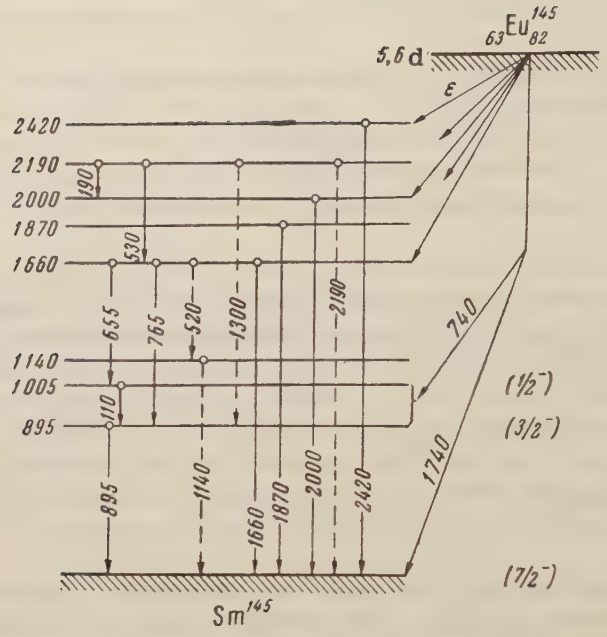

Decay scheme of Eu^{145}.

Investigation of the γ-γ coincidences revealed the existence of the following cascade transitions: 895—665—530—110; 895—765; 530—765; 530—520 keV; 2000 keV-(K x-rays); 1660 keV-(K x-rays). We did not detect 1660—110, 2000—110 of 2000—895 keV coincidences.

On the basis of the experimental results we propose the decay scheme for Eu^{145} shown in the figure. Without further investigation of the decay of Eu^{145} and the angular correlation in the cascade transitions one cannot draw any definitive inferences regarding the nature of the levels of Sm^{145} and the spin assignments for them.

We desire to express our deep gratitude to the staff of the Laboratory of Nuclear Problems of the Joint Institute for Nuclear Research for making available the europium fraction.

Scientific-Research Physical Institute at
Leningrad State University

References

1. Yu.A.Aleksandrov, V.Kroga & M.K.Nikitin, Materialy III Soveshchaniya po neitrondefitsitnym izotopam (Transactions of the Third Conference on Neutron-Deficient Isotopes), Dubna, 1960.

2. J.R.Grover, Phys.Rev., 116, 406 (1959).

3. A.A.Bashilov, O.V.Larionov, M.K.Nikitin & V.B.Smirnov, Izv.AN SSSR, Ser. fiz., 24, 788 (1960). (Trans.Bulletin 24, 791.)

4. N.M.Anton'eva, A.A.Bashilov & B.S.Dzhelepov, Materialy X Ezhegodnogo soveshchaniya po yadernoi spektroskopii (Transactions of the Tenth Annual Conference on Nuclear Spectroscopy), M., 1960.

5. B.S.Dzhelepov, Zh.T.Zhelev & A.V.Kydryavtseva, Transactions of the Third Conference on Neutron-Deficient Isotopes, Dubna, 1960.

QUADRUPOLE MOMENTS AND ISOTOPE SHIFTS OF BARIUM ISOTOPES

- N. I. Kaliteevskii, E. E. Fradkin & M. P. Chaika

The purpose of the present work was to determine the nuclear quadrupole moments and isotope shifts of barium isotopes by the method of optical spectroscopy using separated isotopes (80-90% enrichment).

For determining the quadrupole moments of the odd isotopes we investigated the deviations from the hyperfine structure (hfs) interval rule for the Ba I $6s6p^3P_1$ term, for which we studied the hfs of the two Ba I lines: λ = 4599 Å $(6p^2\ ^1S_0 - 6\ ^3P_1)$ and λ = 4573.9 Å $(6p^2\ ^3P_0 - 6\ ^3P_1)$, the upper levels of which are not split. There were obtained the following values for the quadrupole moments[1]:

$$Q(Ba^{135}) = (0.25 \pm 0.12)\cdot 10^{-24}\ cm^2,$$
$$Q(Ba^{137}) = (0.2 \pm 0.1)\cdot 10^{-24}\ cm^2.$$

According to the generally accepted shell model classification[2] the configuration of the ground state of Ba^{135} is $2d_{3/2}$ and that of the Ba^{137} is $(2d_{3/2})^3$. Our results ($Q > 0$ for both isotopes) indicates that in both Ba^{137} and Ba^{135} there is a hole in the $2d_{3/2}$ neutron level. Consequently, one must assign the configuration $(3s_{1/2})^2(1h_{11/2})^{10}(2d_{3/2})^3$ or the configuration $(3s_{1/2})^0(1h_{11/2})^{12}(2d_{3/2})^3$ to the ground state of Ba^{135}. It is interesting to note that Xe^{131}, the ground state configuration of which is $(2s_{1/2})^2(1h_{11/2})^{10}2d_{3/2}$ has a negative quadruople moment[3].

The absolute value of the quadrupole moments of the odd barium isotopes cannot be explained in the framework of the single-particle shell model, inasmuch as according to the evaluation based on this theory even an odd proton nucleus with A = 135 and the ground state $d_{3/2}$ would have a smaller value of Q than the quadrupole moment found by us for Ba^{135}.

For determining the isotope shifts of the barium isotopes we investigated the shift of the Ba I $(6s^2\ ^1S_0 - 6s6p\ ^1P_1)$, λ = 5535.6 Å line. The measured shifts in 10^{-3} cm^{-1} were the following:

Ba^{138}	Ba^{136}	Ba^{134}	Ba^{137}	Ba^{135}
-4.7 ± 0.5	-0.5 ± 0.5	0	1 ± 0.7	2.9 ± 0.4

These data on the relative position of the isotopes differ from those of previous investigations (see Ref.4) as regards the position of Ba^{136}, which was measured in the present work with particular care.

Theoretical calculations[5] yield the following evaluation for the shift of this line due to the isotopic mass difference: $\nu_A - \nu_{A+2} = -6.3\cdot 10^{-3}$ cm^{-1}. Subtracting the mass shift from the experimental values, we obtain the following figures for the volume isotope shift (in 10^{-3} cm^{-1}):

Ba^{138}	Ba^{137}	Ba^{136}	Ba^{135}	Ba^{137}
0	8,8	10.5	17.0	17.3

Two important inferences follow from the cited data, namely, there exists a pronounced even-odd shift when the positions of the even isotopes are not equidistant.

The relative isotope shifts for the isotope pairs

$$(\nu_{134} - \nu_{136}) : (\nu_{135} - \nu_{137}) : (\nu_{136} - \nu_{138}) = 0{,}65 : 0{,}78 : 1$$

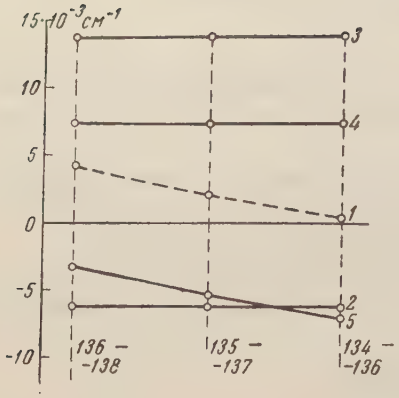

←Isotope shift at the 5535 Å line. The isotope shift of the line for three pairs of isotopes is laid off along the vertical scale: 1 - shift obtained from experiment, 2 - mass shift evaluated theoretically, 3 - regular part of the volume shift, 4 - shift equal to the sum of shifts 2 and 3 (follows from the spherical nucleus model), 5 - difference between shifts 1 and 4, equal to the deformation shift.

show an appreciable increase of the shift for the 136—138 pair, i.e., with closing of the neutron shell (N = 82), which is inconsistent with the concept of the shell model that does not take into account nonstatic deformations of the nuclear core.

Using the method outlined by Kopfermann[6], we calculated the isotope shift constant:

$$\beta C_{\exp} = \frac{\beta \delta T_s}{\pi a_0^3 \psi_s^2(0)/Z} = \frac{\beta \delta T_s}{a_s/G},$$

where δT_s is the isotope shift due to the s electron, and a_s is the $6s$ magnetic hfs constant (this is determined experimentally from measurement of the hfs of the $6s6p\,^3P_1$ term). The constant G was calculated by means of the formula

$$G = R_\infty \alpha^2 Z \frac{m_e}{m_p} \cdot \frac{\mu}{I} F_r(jZ)(1-\delta)(1-\varepsilon).$$

There were obtained, with an error estimated not to exceed 20%, the following values for the isotope shift constant for the barium isotopes (in 10^{-3} cm^{-1}):

$Ba^{136-138}$	$Ba^{135-137}$	$Ba^{134-136}$
67	52	44

These values, while greater than those published earlier[5,7], are still anomolously low, which indicates a small change of the root mean square radii of the barium nuclei. Possibly the anomolously small isotope shift and the nonequidistant positions of the isotopes can be explained by effective deformation and decrease thereof from Ba^{134} to Ba^{138} (nucleus with a closed neutron shell) which is illustrated in the accompanying figure. This hypothesis is supported by the fact that apparently $Q_{137} < Q_{135}$, although, admittedly, these quantities have been measured with an appreciable uncertainty.

Scientific-Research Physical Institute at
Leningrad State University

References

1. N.I.Kaliteevskii, E.E.Fradkin & M.P.Chaika, Zhur.eksp.i teor.fiz., 39, 954 (1960). (Trans.Soviet Physics - JETP.)
2. I.P.Elliott & A.M.Lane, Handbuch der Physik, B.39, 1957.
3. A.Bohr, J.Koch & E.Rasmussen, Arkiv fys., 4, 455 (1952).
4. J.E.Mack, Phys.Rev., 109, 820 (1958).
5. I.I.Gol'dman, Zhur.eksp.i teor.fiz., 24, 177 (1953).
6. H.Kopfermann, Kernmomente, Frankfurt, 1956. (Trans.Nuclear Moments, N.Y. 1958.)
7. P.Brix & H.Kopfermann, Revs.Mod.Phys., 30, 517 (1958).

GENERATOR OF SHORT LIGHT PULSES

- G.S.Vil'dgrube, Yu.A.Kolosov & Zh.M.Ronkin

It is superfluous to point out the importance of objective methods of investigating the pulse characteristics of photomultipliers. The need for such a method is particularly great in laboratories of plants producing photomultiplier tubes. The lack of a stable yet flexible (in the sense of a wide control range) source of light pulses is holding up the development of commercial automatic equipment for testing multipliers and greatly hinders laboratory tests of such tubes.

All pulsed light sources now available, such as neon tubes, spark gaps, mechanical modulators and tubes in which there is utilized fluorescence of glass, either do not provide the necessary stability or have only a limited range of use owing to a restricted pulse duration range or other shortcomings. We have tested some of the enumerated sources with negative results. Thus, for example, krypton tubes prepared especially for this purpose proved to be highly unstable: the amplitude of the light pulses varied by 20-30% or more. Neon lamps (types MN5 and MN8), despite careful selection and aging, showed even worse characteristics. A cathode-ray tube prepared especially for this purpose, in which there was no screen and use was made of the effect of fluorescence of glass, proved to be somewhat more stable; nevertheless, the light pulses varied in the range of 10-15% and there was observed pronounced fluctuation of the fluorescence spot over the screen.

With a view to developing a better light pulse source we investigated a miniature ZLK-1 kinescope with a helenite screen, developed in our organization. Admittedly the use of a cathode-ray tube as a pulse light source is not in itself new, but all the phosphors commonly employed in such tubes have a substantial shortcoming, namely, an appreciable build-up time and, what is more important, a long persistence. The ZLK-1 kinescope is free of this shortcoming by virtue of use of a phosphor with a very short persistence - helenite.

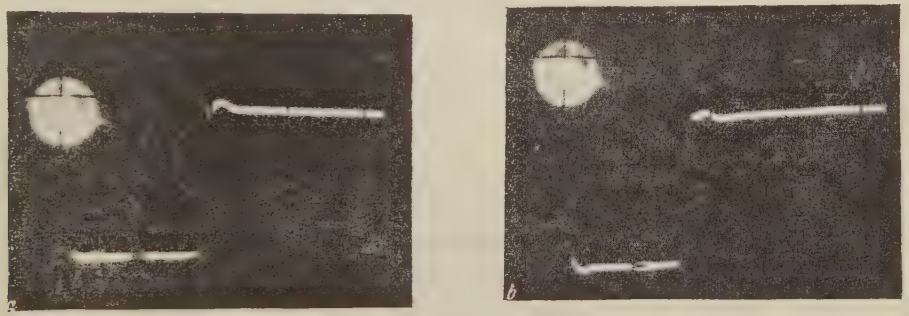

Fig.1. Oscillograms of 2 μsec pulses: a - on the modulator of the ZLK-1 tube and b - on the collector of the photomultiplier.

Fig.1 shows oscillograms of two pulses of 2 microsec duration: a) a triggering pulse on the modulator of the ZLK-1 tube and b) a pulse on the collector of the photomultiplier; from these one can judge of the simulation of the triggering pulse. As will be evident from the figure there is not noticeable distortion of the pulse shape; the rise time of the pulse is $(1\text{-}2)\cdot10^{-7}$ sec.

The emission of the helenite screen has a highly desirable composition; the radiation peaks at about 4000 Å. The spectral characteristics of a cesium-antimony photocathode and of the radiation from a helenite screen are shown in Fig.2.

These desirable characteristics plus good stability made it possible to use a ZLK-1 tube with a helenite screen in a circuit (Fig.3) for measuring the intrinsic amplitude resolution of photomultipliers.

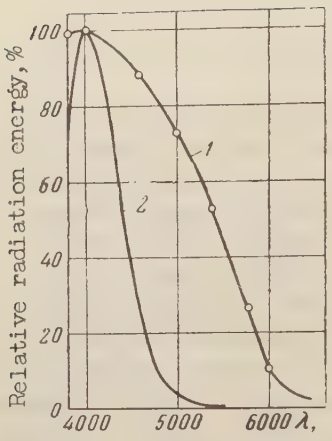

←Fig.2. Spectral characteristics of 1 - cesium-antimony photocathode, and 2 - radiation from helenite screen.

During the dark interval the tube is cut off by part of the voltage from the divider connected into the circuit of the high voltage rectifier VS-10 (ВС-10); the tube is unblocked by pulses from a precision limiter designed about a 6N6P (6Н6П) tube, calibrated in amplitude. The limiter circuit in turn is triggered by a pulse from a GI-2A (ГИ-2А) generator, which is applied to the "start" terminal. The amplitude spectra are recorded by means of a 100-channel pulse height analyzer (type AI-100). The stability of the precision pulses is better than 0.1% over a period of 8 hours operation. The stability of the light pulses is 1.5% as determined over the same period.

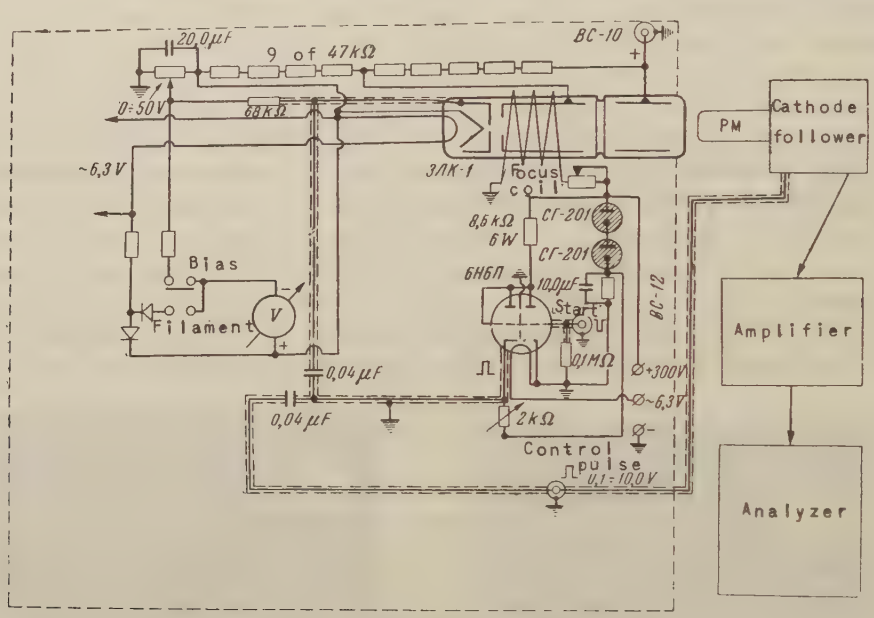

Fig.3. Circuit of set-up for measuring the intrinsic resolution of photomultipliers.

Fig.4 shows two histograms: a) recorded for an FEU-13 photomultiplier viewing a NaI(Tl) crystal exposed to radiation from a Cs^{137} source (the amplitude resolution is 10%) and b) for the same FEU-13 photomultiplier but with a ZLK-1 tube (amplitude resolution of the photomultiplier 5.5%; flash intensity equivalent to the scintillations in the NaI(Tl) crystal). For determining the intrinsic amplitude resolution of the tube we recorded the variation of the square of the resolution of the photomultiplier plus tube combination as a function of the reciprocal of the flash energy; the intrinsic amplitude resolution of the tube was found to be 0.5-1%.

The great range of brightnesses available from the tube (the maximum light flux in a pulse is 0.3-0.5 lm) made it possible to use this tube for investigating the light pulse characteristics of photomultipliers. In this case the ZLK-1 tube is operated under the same conditions but the triggering pulse has a higher

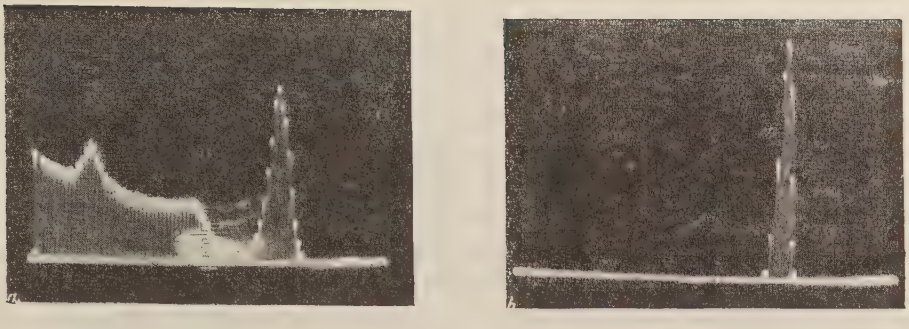

Fig.4. Histograms recorded by means of the AI-100 pulse height analyzer for a FEU-13 photomultiplier: a - with an NaI(Tl) crystal and a Cs^{137} source, and b - with a ZLK-1 tube with a helenite screen (flash brightness equivalent to the scintillations produced in the NaI(Tl) crystal by Cs^{137}).

amplitude (300-350 V). The photocathode of the tested photomultiplier is irradiated with powerful light flashes, the brightness of which can be regulated by means of a set of neutral filters or by varying the height of the triggering pulse.

In conclusion, it may be noted that the use of a ZLK-1 tube with a helenite screen for the purpose of obtaining microsecond light pulses offers great possibilities in the field of investigation of photomultipliers and other photoelectric devices.

We take this opportunity to express our deep gratitude to N.N.Nordstrem for assitance in preparing the sample tubes.

LIGHT-PULSE CHARACTERISTICS OF LOUVRE TYPE PHOTOMULTIPLIERS

- G.S.Vil'dgrube, N.K.Dalinenko, N.V.Dunaevskaya & Zh.M.Ronkin

1. Procedure

We constructed a special set-up and developed a test procedure for investigating the linearity of the light characteristics of photomultipliers (PM) operated under conditions where the photocathode is illuminated by brief light pulses.

By way of pulse light source we used a ZLK-1 (ЗЛК-1) cathode-ray tube with a helenite screen.[1] The tube is triggered by square pulses from a GI-2A (ГИ-2А) generator, preamplified by an amplifier designed about a GU-50 (ГУ-50) tube.

The amplitude of the PM output current is determined from the voltage of the square pulse measured by an MVIlM crest voltmeter with a load of 100 ohms in the anode circuit of the PM. To determine the optimum supply regime for the PM we use a voltage divider made of potentiometers; the shape of the pulse on the anode is observed by means of an I0-4 synchroscope. Inasmuch as in addition to evaluating the linearity of the light characteristic, we felt it would be of interest to investigate the stability of the photomultipliers under conditions of high output current (≥1 A), a special highly stabilized power unit was used for supply for the entire set-up.

Pulses of 2 μsec duration are applied to the ZLK-1 tube; the maximum brightness regime is found by varying the modulator potential. The resultant maximum brightness flux is taken as unity or 100%. The light flux is weakened as necessary by means of a set of neutral light filters. The pulse repetition rate in the measurements was 50 pps. In some measurements we also used single pulses (1 pulse per min). In the process of measurement by successive variation of the voltage divider potentiometer settings we obtained the maximum output pulse, which was observed on the screen of the I0-4 synchroscope.

2. Experimental results

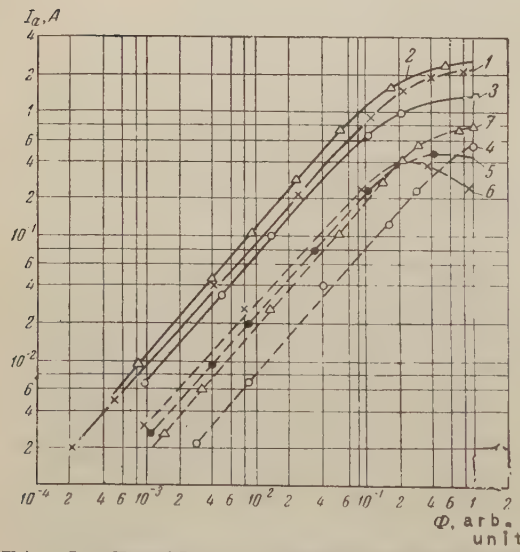

Fig.1. Family of light pulse characteristics for different photomultipliers: 1) FEU-49, 2) FEU-53, 3) FEU-11, 4) EMI-9558, 5) FEU-19M (alloy type), 6) FEU-19, 7) FEU-IV.

Using the developed procedure, we investigated samples of FEU-11, FEU-12, FEU-52 and FEU-53 photomultipliers. The family of light characteristics for different PM louvre designs is shown in Fig.1. For purpose of comparison in the same figure we give the light characteristics obtained for samples of FEU-19, FEU-IV and EMI-9558 photomultiplier tubes.

On the basis of the test results we carried out an analysis of the influence of the design and electric parameters of photomultipliers on the linearity of the light pulse characteristics.

As follows from the curves of Fig.1, photomultipliers with alloy emitters, which allow of high average output currents, can be used under "forced conditions" with longer durations and higher repetition frequencies (curves 1-5 & 7) as compared with photomultipliers with cesium-antimony emitters (curve 6). The louvre type design has limitations as regards the output assembly both because

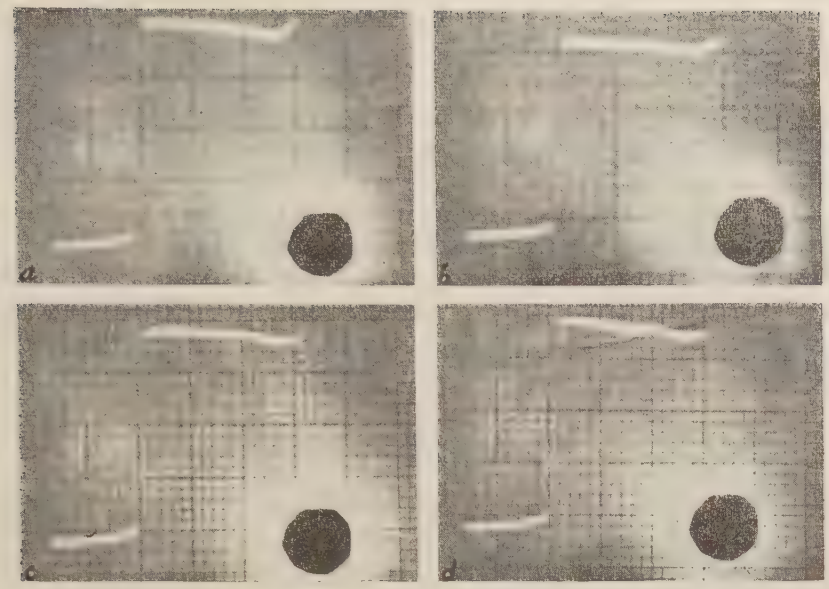

Fig.2. Oscillograms of output pulses from FEU-52 photomultiplier tube No.83: a) unaged photomultiplier after 30 min operation, b) unaged photomultiplier after 8 hours operation, c) aged photomultiplier after 30 min operation, d) aged photomultiplier after 8 hours operation.

of geometric conditions and because of limitation of the applied anode potential.

If one regards the output stage of the PM as a diode with a flat cathode (the last stage of the multiplication system) and an anode (the collector), then, under conditions of limitation of the current by space charge, there appears a retarding field that holds back the electrons emitted from the cathode with low initial velocities, which determines the steady state PM current. With change in the anode potential the strength of the retarding field changes and with it the PM output current. If the electron transit time is shorter than the duration of the light pulse, one can consider the electron current at any cross section from the cathode to the anode to be virtually constant. In this case for determining the current at the PM output one can use the 3/2-power law. Thus the limit of linearity of the light characteristic in our case is imposed by the internal resistance of the gap between the last stage and the anode.

It must be borne in mind that the voltage between the last stage and the anode at the time of flow of current will be equal to the sum of the voltages on the load resistance in the last stage-anode gap, while during the dark interval the entire anode voltage proves to be applied to the last stage-anode gap. In designing the output assembly of a multiplier, bringing the last stage closer to the anode increases the linearity of the light characteristic by decrease of R_i, but at the same time the electric strength of the gap is reduced, which means that the magnitude of the maximum anode voltage must also be diminished.

As was noted, the light characteristics were investigated using a voltage divider with potentiometers adjusted to the optimum positions. On the basis of extensive statistical material we chose an "average" voltage divider which can be recommended for general operational use (the value of the anode current should not differ by more than 10% from the maximum value):

Characteristics of the "average" voltage divider (relative units):

Stage 1	1-2	2-3	3-4	4-5	5-6	6-7	7-8	8-9	9-10	10-11	11-12	12-A
0.7	0.8	0.9	1.0	1.0	1.0	1.0	1.0	1.0	1.2	1.5	1.6	Rated

In photomultipliers with fourteen multiplication stages the ratio of the resistances for the last stages remains the same, while for the intermediate stages (3-11) it is set equal to unity.

We investigated the stability of the photomultiplier output current with an amplitude of 1 A over a period of 8 hours both with single pulses and at a pulse repitition frequency of 50 pps. In both cases the stability of the PM output current after 8 hours of continuous operation was no worse than 5%. Fig.2 shows the oscillograms of the first and last pulses obtained in testing an FEU-52 tube before and after aging.

References

1. G.S.Vil'dgrube, Yu.A.Kolosov & Zh.M.Ronkin, Present issue of the Bulletin, p.1185.

NUMBERS OF PHOTONS PER DECAY OF Ce^{144} AND Eu^{155}

- A.N.Silant'ev and B.S.Kuznetsov

In the present work we measured the numbers of photons per decay of Ce^{144} and Eu^{155} using the $4\pi\beta$-γ coincidence procedure described in Ref.1. The cerium and europium were purified chromatographically. In order to check the purity of the specimens we carried out additional measurements after the passage of four months. The results of the repeat measurements agreed with those of the initial ones.

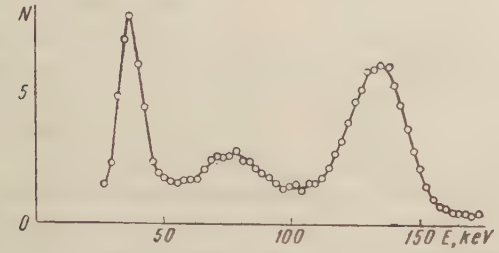

Fig.1. Gamma-spectrum of Ce^{144} in equilibrium with Pr^{144}.

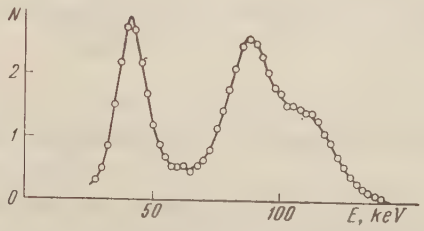

Fig.2. Gamma-spectrum of Eu^{155}.

The experimental spectrum of Ce^{144} in equilibrium with Pr^{144} is shown in Fig.1. There are evident peaks corresponding to γ-rays with energies of 36, 80 and 134 keV. In order to evaluate the contribution from the radiation of Pr^{144}, we carried out chromatographic separation of Pr from the Ce and recorded its spectrum. In the low energy region the γ-spectrum of Pr^{144} consists of the Compton distribution from the hard γ-rays of Pr^{144}. There is also some contribution from bremsstrahlung. From the experimental spectrum there was subtracted the spectrum of γ-rays belonging to Pr^{144}. Then we determined the area under the peak corresponding to the 134 keV γ-rays. In the region of the 80 keV γ-ray peak there is some contribution from the 134 keV γ-rays as well as from the hard γ-rays and bremsstrahlung of Pr^{144}. In order to evaluate the contribution of the 134 keV γ-rays to the peaks corresponding to the 80 and 36 keV γ-rays we carried out three series of measurements using different absorbers.

The resultant numbers of photons per disintegration are shown in Table 1; the estimated uncertainty is 15%.

Table 1

Numbers of photons per decay of Ce^{144} (in %)

E_γ, keV	Ref. 2	Ref. 3	Ref. 4	Our data
36	—	—	—	8,2
80	—	4	—	1,6
134	15,4	13	13,9	9,7

Table 2

Conversion coefficients for the γ-rays of Ce^{144}

Transition energy, keV	Shell	Ref. 6	Ref. 3	Ref. 7	Our data
80	K	1,2	1,4	2,14	2,1
	L	—	—	0,29	0,3
134	K	0,71	0,76	0,49	0,55
	L	—	—	0,07	0,08

Geiger et al[5] determined the number of conversion electrons per disintegration and also showed that the 80 and 134 keV γ-transitions are pure M1. On the basis of our results and the data of Geiger et al one can calculate the conversion coefficients for the 80 and 134 keV γ-rays. The resultant values are listed in

Table 2 from which it will be seen that the conversion coefficients deduced from experiment are in agreement with the theoretical values[7] for M1 transitions.

Fig.2 shows the γ-ray spectrum of Eu^{155}. The spectrum comprises a peak corresponding to γ-rays of 41 keV energy and a peak corresponding to γ-rays with energies of 86 and 105 keV. We resolved this peak into components. The percentages of 41, 86 and 105 keV γ-rays per disintegration of Eu^{155} proved to be 25, 32 and 16%, respectively. Inasmuch as resolution into components introduces a certain error, the sum of the values for the last two transitions is relatively more accurate.

"V.G.Khlopin" Radium Institute,
Academy of Sciences of the USSR

References

1. A.Silant'ev, Izv.AN SSSR, Ser.fiz., 25, 270 (1961). (Trans.Bulletin, 25, 256.)
2. W.Kreger & C.Cook, Phys.Rev., 196, 1276 (1954).
3. R.Hickok, W.McKinley & S.Fultz, Phys.Rev., 109, 113 (1958).
4. F.Porter & P.Day, Phys.Rev., 114, 1286 (1959).
5. J.Geiger, R.Graham & G.Ewan, Nucl.Phys., 16, 1 (1960).
6. I.Pullmann & P.Axel, Phys.Rev., 102, 1366 (1956).
7. L.A.Sliv & I.N.Band, Tablitsy koeffitsientov vnutrennei konversii gamma-izlucheniya (Tables of internal conversion coefficients) Part I, K shell; Part II, L shell, M.-L., 1956/8.

USE OF AN IONIZATION ALPHA-SPECTROMETER WITH A TIME ANALYZER FOR DETERMINING DECAY PERIODS

- Yu.M.Volkov, A.P.Komar, G.A.Korolev & G.E.Kocharov

Introduction

Generally, a number of difficulties are encountered in experimental measurements of the lifetime of short-lived α-emitters. Most of these difficulties can be avoided through the use of an ionization α-spectrometer[1,2] in conjunction with a time analyzer.

The decay period is determined from the time distribution of the pulses of the α-particles from the investigated element relative to the distribution of pulses of α-particles from the parent substance. This procedure has the following merits.

1. Energy discrimination of the investigated α-particles substantially reduces the chance coincidence background and makes it possible to carry out measurements in the presence of particles of other energies.

2. Simultaneously with measurement of the decay period, one can with high accuracy determine the energy of the α-particles.

3. Use of a multiple channel time analyzer substantially reduces the measuring time as compared with that necessary in using integral and differential methods of delayed coincidences.

4. For long periods one can use a 4π chamber with a low intrinsic background (1 pulse per hour per 1 MeV energy interval), which makes it possible to measure periods of up to 10 sec.

To check the potentialities of the equipment and procedure we carried out measurements of the period of Po^{215} with high accuracy (0.3%). Po^{215} (AcA) is a member of the actinium series. It forms in α-decay of 3.92-sec Rn^{219} (An) and converts by α-emission to Pb^{211} (AcB). The first direct measurements of the period of Po^{215} were carried out by Moseley & Fajans[3] by the method of a rotating disk; they obtained 0.002 sec. Subsequently, Ward[4] used the integral method of delayed coincidences and obtained a value of $(1.83 \pm 0.04) \cdot 10^{-3}$ sec. Inasmuch as the method proposed herein allows of attaining considerably higher accuracy, we felt that new measurements of the period of Po^{215} would be of considerable interest.

1. Description of the Equipment

A block diagram of the set-up is shown in Fig.1. The ionization chamber, containing the actinium series activity, was filled with a mixture of 97% argon + 3% CH_4 at a pressure of 1.8 atm.

The pulses due to all α-particles were amplified, after which the pulses due to Rn^{219} and Po^{215} α-particles were selected in amplitude by means of differential discriminators. For selecting the α-lines we used a 28-channel pulse height analyzer and a precise-amplitude pulse oscillator.

The section of the α-spectrum containing the lines of Rn^{219} and Po^{215} is shown in Fig.2.

The discriminator output pulses due to α-particles from the parent Rn^{219} were fed into input I of the 49-channel time analyzer; the pulses due to the α-particles of the daughter Po^{215} were applied to input II. From the distribution of the pulses of the α-particles of Po^{215} in time relative to the pulses of the α-particles of Rn^{219} one can determine the period of Po^{215}.

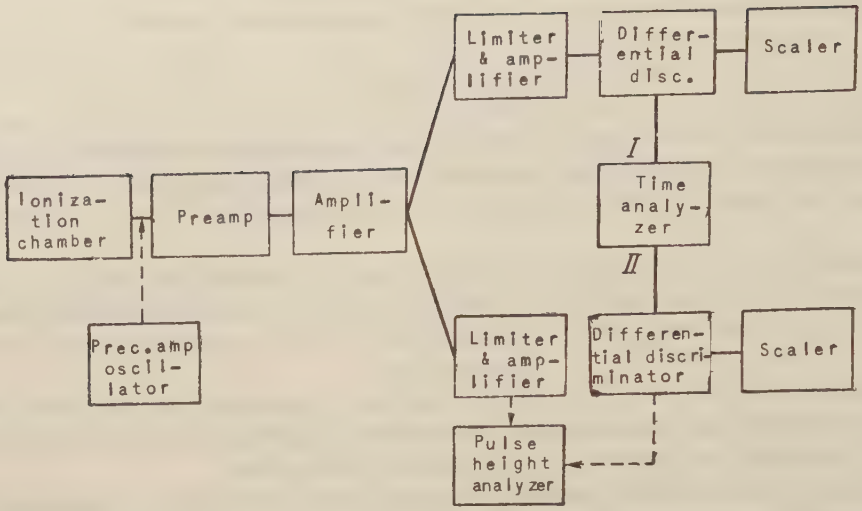

Fig.1. Block diagram of the set-up.

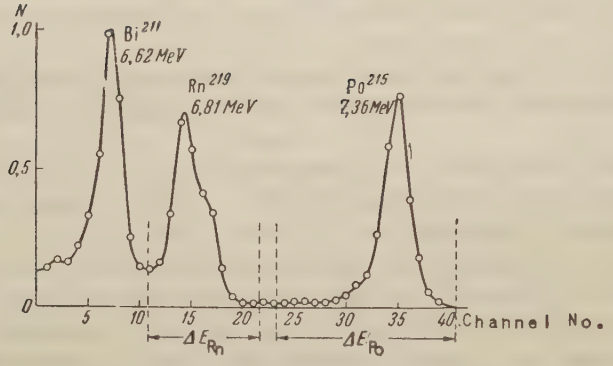

Fig.2. Section of the α-spectrum of the actinium series. ΔE_{Rn} - gate of the discriminator channel for Rn^{219} α-particles; ΔE_{Po} - gate of discriminator channel for Po^{215} α-particles.

In the course of the experiment the relative position of the α-lines and the discriminator gates was checked periodically. The drift of the discriminator levels and amplification factors and, consequently, the variation in the loading in the channels was negligible during the entire period of measurements.

2. Time Analyzer

The pulses from the outputs of the discriminators for the α-particles of the parent and daughter activities are fed, respectively, into inputs I and II of the time analyzer converter unit (Figs.3 & 4).

The pulses entering input I, after shaping, trigger the shock oscillator, while the pulses fed into input II cut off the oscillator. Thus the shock oscillator operates during the time corresponding to the interval between the appearance of pulses produced by α-particles from the parent and daughter elements. The 105 kc sinusoidal oscillations of the shock oscillator are limited and shaped into narrow (total duration about 1 μsec) unipolar pulses, which are sent into the divider unit consisting of three frequency dividers with division factors of 3,3 and 4, respectively. Thus, at the output of the last frequency divider there is obtained a series of pulses, the separation between which corresponds to the product of the period of the shock oscillator by the total division factor (342 μsec).

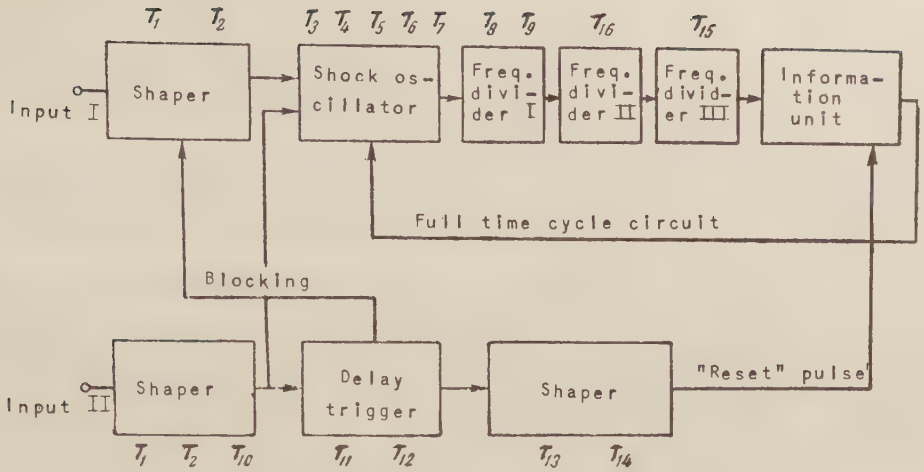

Fig.3. Block diagram of time analyzer.

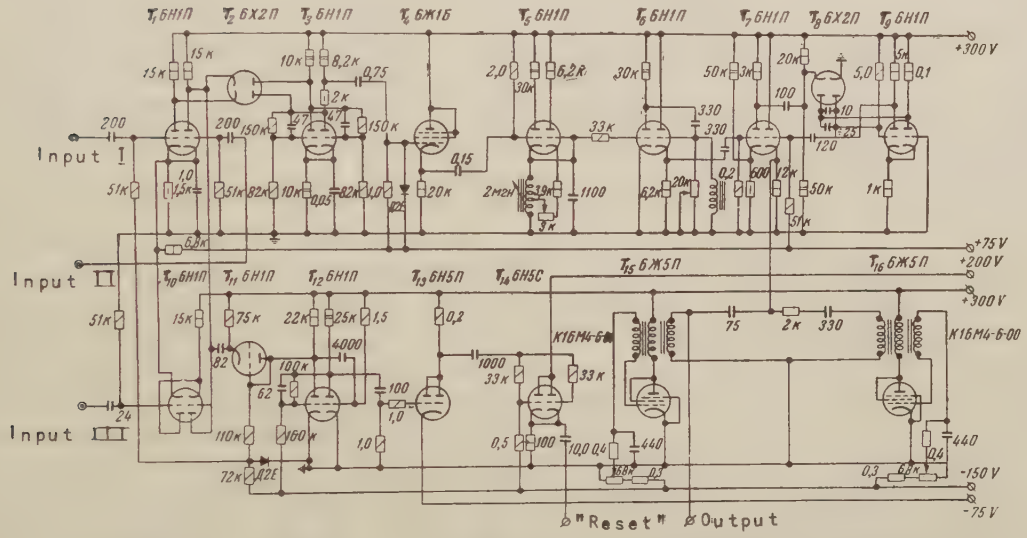

Fig.4. Circuit of time analyzer converter unit.

The information unit counts the number of pulses in the series and performs registration in the channel, the number of which is equal to the number of pulses in the series. After recording, the information unit is brought back to the initial state by a "reset" pulse which arrives 10 μsec (the dead time of the mechanical register) after appearance of the daughter element pulse. The "reset" pulse is shaped from the trailing edge of the delay trigger pulse, set off from the side of input II.

After being triggered from the side of input I, the analyzer is insensitive to α-particle pulses from the parent substance up to the instant of triggering from input II and then for a further 10 μsec. The first blocking is provided by a diode circuit incorporating a two position relay, which controls the operation of the shock oscillator; the second blocking is provided by the circuit of the delay trigger. This second blocking eliminates the possibility of a count being missed owing to the dead time of the mechanical register.

After recording of a pulse due to an α-particle of the daughter substance, the analyzer is insensitive to pulses from the side of input II up to the time it is reactivated by a pulse from input I. If during the time of the complete cycle of the analyzer no pulse arrives at input II, then by means of a circuit acting on input III (Fig.4) from the side of the information unit, the analyzer is brought back to the initial sensitive state.

The information unit consists of two ring scalers (with scaling factors of 5 and 10, respectively), connected in series and actuated by the series pulses. Coincidences between the states of the cells of the first and second scalers provide for 50 effective time channels.

The given analyzer was converted to a time analyzer from the pulse height analyzer 1 described in Ref.5. The conversion unit of this analyzer utilizes some of the components of the conversion unit of the pulse height analyzer, while the information unit has not been changed, except for replacement of the SB-1M mechanical registers by MES-54 registers.

3. Calibration of the Analyzer Time Scale

The time scale of the analyzer was calibrated, and its stability periodically checked in the course of the experiments by comparison of the frequency of the shock generator with the frequency of a quartz crystal oscillator (a 271M range calibrator). The frequency of the quartz crystal oscillator was checked beforehand to determine its precise value; to this end the pulses from the 271M were recorded for a period of 24 hours by a scaler switched on and off by signals from a time standard radio station.

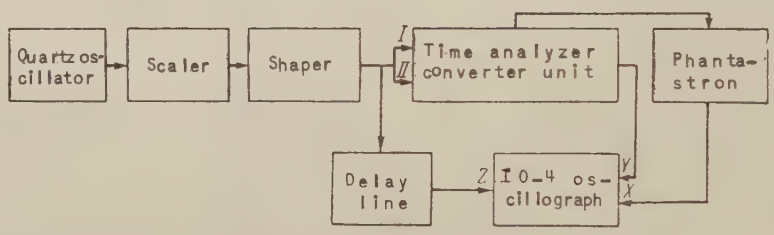

Fig.5. Block diagram of the calibration set-up.

With a quartz crystal frequency of 7495.53 ± 0.12 cps, the 271M oscillator yielded calibration pulses with a spacing of 133.413 μsec; these were recorded by a 100:1 scaler (Fig.5). The first calibration pulse excited the shock oscillator; the second cut off the oscillation. The series of output pulses from the converter unit was applied to the Y channel of an I0-4 oscillograph. The possibility of observing the last pulse of the output series was realized by triggering the sweep from a special phantastron (time delay tube) oscillator. Calibration pulses were also fed through a delay line to the Z channel of the I0-4 oscillograph and produced marker pips.

The frequency of the shock oscillator was set so that the last pulse of the series corresponded to the boundary between the 39th and 40th channels. A 0.01% change in the frequency of the shock oscillator yielded a 5 mm deviation of the last output pulse relative to the marker pip on the screen of the I0-4. Thanks to measures taken to insure a constant temperature and stabilized supply voltages, the frequency of the shock oscillator over a period of 24 hours did not drift beyond these limits and was periodically adjusted with the calibrating set-up connected to the inputs and outputs of the analyzer converter unit.

Comparison of the positions of the first and last output pulses of a series with the calibration pips made it possible to measure the interval corresponding to the full 39 channels; this proved to be equal to 13 348.0 ± 1.0 μsec. It follows from this that the channel width is 342.254 ± 0.025 μsec. Analogous measurements with closer spacing of the calibration pulses showed that the greatest nonuniformity of the channel widths (for the first two channels) did not exceed 0.2-0.4 μsec. We also determined that the instability of the channel boundaries corresponds to a time interval of the order of 0.3 μsec.

4. Measurements and Processing of the Results

Preliminary measurements of the period of Po^{215} yielded a value of $1.79 \cdot 10^{-3}$ sec. These measurements enabled us to choose the optimum counting rate and duration of the experiment for the main measurements.

For calculating the decay period we used the method of processing the results described by Peierls[6]. This method of processing is applicable to any set of exponentially decreasing quantities, measured at small equal intervals. This condition is satisfied by the time distribution of pulses from Po^{215} α-particles relative to the pulses from Rn^{219} α-particles, as recorded by the time analyzer. The method of Peierls[6] also requires that the time intervals not exceed 0.5 the decay period of the investigated isotope. This requirement was satisfied in choosing the channel width of the time analyzer.

Inasmuch as at high coincidence counting rates there could occur strong distortion of both the exponential distribution of true coincidences and the distribution of chance coincidences (see Sections 5 and 6, below), the coincidence counting rate was chosen so that the correction allowing for this distortion would not exceed 0.5% the decay period of Po^{215}.

At a counting rate of 2.5 pulses per sec in the Rn^{219} α-particle pulse channel and 3.0 pulses per sec in the Po^{215} α-particle pulse channel, the counting rate of true coincidences was 1.0 pulses per sec and the counting rate of chance coincidences amounted to only 0.06 pulses per sec. The Rn^{219} 6.81 MeV α-line onto which the differential discriminator was set corresponds to the α-transition to the ground state of Po^{215} and has an intensity of 82%. Hence the counting rate in the Rn^{219} α-particle pulse channel is somewhat lower than in the channel of the Po^{215} α-particle pulses. The total measurement time was 411 hours.

During an interval in the range of the first channel of the time analyzer there may occur superposition of the pulses from Rn^{219} and Po^{215} α-particles. As a result the number of counts in the first channel is reduced. Hence in processing the results, the indications of the first channel of the analyzer are not used.

The background of chance coincidences due to the intrinsic background of the chamber was negligibly small. The effective solid angle of the ionization chamber was 2π; half of all the Rn^{219} α-particles entering the working volume of the chamber were accompanied by the corresponding α-particles of Po^{215}. If the second α-particle of such a regular pair enters the working volume of the chamber during a time shorter than T (the time of the complete cycle of the time analyzer), there is recorded a true coincidence.

The optimum number of channels that should be used for carrying out the calculations by the method of Peierls depends on the ratio of the background to the exponential component and in our case was 36.

After triggering of the analyzer from the side of input I (Fig.3) of the two or more impulses arriving at input II during the time T only the first pulse is recorded. The resultant counting loss leads to distortion of the true coincidence

spectrum and the chance coincidence background; hence appropriate corrections must be introduced.

5. Correction for the Background of Chance Coincidences

A coincidence is recorded as a chance one if during the interval T after triggering of the analyzer by an α-particle from the parent element there arrives at input II a pulse from an α-particle that does not constitute a regular pair with the triggering particle.

The chance coincidence background can be regarded as consisting of two parts. The first part is comprised of the cases of recording the second particles of regular pairs, the first particles of which do not arrive in the interval T. The probability of recording such pulses is the same for all channels. The second part of the chance background is due to recording of second pulses of pairs the first pulses of which arrive within the interval T. Inasmuch as the first pulse of such a regular pair may arrive only after starting of the analyzer (otherwise the pulse itself will trigger the analyzer), its second pulse has the probability of arriving in the interval T proportional to $(1 - e^{-\lambda t})$, where t is reckoned from the instant of triggering the analyzer.

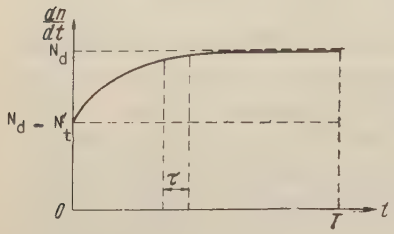

Fig.6. Distribution in time of the total number of background pulses arriving during one triggering of the analyzer.

Fig.6 shows the distribution in time of the total number of background pulses arriving during one period of operation (triggering) of the analyzer; this distribution is characterized by the function

$$\frac{dn}{dt} = N_d - N_t' e^{-\lambda t},$$

where λ is the decay constant, N_d is the counting rate for pulses arriving at input II of the analyzer, and N_t' is the number of such regular α-particle pairs entering the working volume of the chamber per unit time in which the second particle is emitted after the first within the interval T. This quantity is somewhat greater than the counting rate of true coincidences and can readily be calculated.

The mean number of background pulses entering the i-th channel during one triggering of the time analyzer is obtained from the above equation and is given by

$$n_i = N_d \tau - \frac{N_t'}{\lambda} [e^{-(i-1)\lambda\tau} - e^{-i\lambda\tau}], \qquad (1)$$

here τ is the width of the time analyzer channel. The probability for recording a chance coincidence in the i-th channel will be

$$q_i = e^{-\sum_{j=1}^{i-1} n_j} (1 - e^{-n_i}), \qquad (2)$$

where n_j is given by Eq.(1). The first factor in this expression is the probability that the background pulse will not arrive in the preceding channel; the second factor is the probability that at least one background pulse will arrive in the i-th channel.

The background recorded in the individual channels of the time analyzer is proportional to q_i. Having determined graphically the background in the last

channels in which the exponential component is small and using Eq.(2), one can find the background in all the channels. The background in the last channels was determined by successive approximations so that the experimental points would fit a straight line plotted in semilogarithmic coordinates. This proecture gives a more precise determination of the background than the method described in Ref.7.

6. Correction for Distortion of the Spectrum

A true coincidence is recorded if the pulse due to the second α-particle of a regular pair enters input II of the analyzer during the time T after arrival of the first particle pulse, triggering the analyzer. However, appearance of a background pulse before the pulse of the second particle of a regular pair will lead to recording of a background pulse. Let us agree, however, to consider such cases to be true coincidences but recorded in the wrong channel. In this case superposition of background pulses does not change the total number of true coincidences but only distorts the exponential distribution. This distortion can be calculated.

If a regular pair is emitted in the interval T, the probability of arrival of a coincidence pulse in the i-th channel is given by

$$p_i = \frac{e^{-(i-1)\lambda\tau} - e^{-i\lambda\tau}}{1 - e^{-\lambda\tau}}.$$

By taking into account the possibility of arrival of background pulses, the probability of recording of coincidences in the i-th channel will be given by

$$p_j^{\text{rec}} = p_i\left(1 - \sum_{j=1}^{i-1} q_j\right) + q_i \sum_{j=i+1}^{m} p_j, \qquad (3)$$

where m is the number of channels, and q_j is given by Eq.(2). The first term in this equation is the probability of recording a true coincidence in the i-th channel in the absence of a background coincidence in any of the preceding channels; the second term is the probability of recording a background pulse in the i-th channel when simultaneously with it there arrives in one of the subsequent channels a pulse from the second particle of the regular pair.

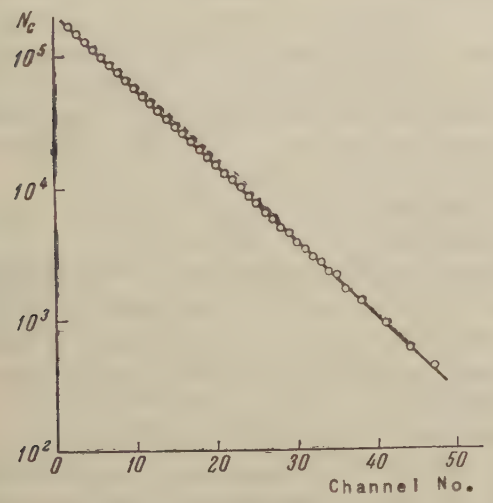

Fig.7. Time distribution of pulses due to Po^{215} α-particles relative to the pulses due to α-particles of the parent substance.

It will be evident from Eq.(3) that the recorded distribution differs from the exponential by increase in the number of counts in the first channels and decrease in the number of counts in the last channels.

After introduction of the correction for distortion of the spectrum, we carried out graphic determination of the background in the last channels. The background in the 47th channel was found to be equal to 2020 ± ± 20. The recorded exponential distribution giving the period of Po^{215} with the corrections allowed for is shown in Fig.7.

Thus processing the experimental data by the method of Peierls we determined the period and obtained 1778 ± 2.0 μsec. The

uncertainty here is the root mean square error due to statistical fluctuations and the presence of background, which was also evaluated according to Peierls. Possible systematic errors will be considered below. The decay period was also calculated by the method of Hole[8] with the same result.

7. Measurement Errors

For evaluating the systematic errors in determining the period of Po^{215} we must consider a number of different factors.

Error in determining the background. The method of Peierls, which, as noted, was used for the calculations, is highly sensitive to the value taken for the chance coincidence background. Inasmuch as the value of the background was taken with an accuracy of within ±20 counts for the last channel, this introduces an uncertainty of ±1.6 μsec into the measured decay period.

Ambiguity of the correction for distortion of the spectrum and background. The accuracy in determining this correction was 5%. Taking the absolute value of this to be 7 μsec, this leads to an additional uncertainty of ±0.35 μsec in determining the decay period.

Inaccuracy of calibration of the time scale of the analyzer. The sources of error here are inaccuracy of the process of calibration (±0.13 μsec), instability of the shock oscillator (±0.26 μsec) and inaccuracy in determining the frequency of the quartz crystal oscillator (±0.03 μsec).

Influence of multiple differentiation in the amplifier on the counting rate of pulses due to daughter element α-particles. In the common amplification channel the pulses from the daughter element α-particles can be superimposed on the overshoot or tail of the pulse triggering the analyzer. Such superposition is equivalent to displacement of the α-line relative to the gate of the differential discriminator and, consequently, leads to a different change in the counting rate in different channels of the time analyzer. To reduce the overshoot the ratio of the smallest differentiation constant of the intermediate circuit to the differentiation constant of the shaping circuit was taken larger than 10^4. In this case the distortion of the time analyzer spectrum should not exceed 0.02%, which corresponds to an error not exceeding 0.35 μsec in determining the decay period.

Such a factor as the scatter in the rise times of the pulses, which depends on the conditions of collection of the electrodes in the ionization chamber and on the properties of the electronic equipment, leads to an insignificant additional uncertainty as regards the boundaries of the time channels. This uncertainty under the given conditions could not introduce an appreciable error.

Thus the total systematic measurement error should not exceed ±3 μsec. Hence the final value for the period of Po^{215} may be given as 1778 ± 5 μsec.

A check for the reliability of the results obtained for individual channels in the absence of any other noticeable errors was carried out by the same procedure as used in the work of Dardel[7]. Using the obtained number of counts in the second channel and the calculated value of the decay period there was found the theoretical exponential distribution for all channels.

The ratios of the experimental to the theoretical values were plotted on a graph and it was found that all the points except those corresponding to the first channel fell on a straight line within the limits of the statistical fluctuations.

Conclusions

Let us evaluate the range in which the described set-up is suitable for determining lifetimes. The limitation on the side of short lifetimes is set by the

finite pulse rise time in the ionization chamber; evaluations from this standpoint show that the lower bound for measurable lifetimes lies somewhat below 10^{-4} sec. Of greater value would appear to be the possibility of measuring lifetimes of the order of a second. In working in this range it would be desirable to modify the equipment, namely, to use a 4π chamber with a film source and a time analyzer with an electronic commutator. Under favorable experimental conditions when the equipment can be set on the detected α-line so as to insure 100% efficiency in recording, the only limitation imposed is that of an excessive measurement time.

With increase in the number N of disintegrations per unit time the counting rate N_c of chance coincidences increases faster than the counting rate N_t of true coincidences. These quantities are related by the expression

$$N = \frac{1}{T} \cdot \frac{N_c}{N_t},$$

where T is the time of one cycle of the time analyzer. It is expedient to take N_c/N_t not larger than 1. Thus the upper bound for measuring decay periods is determined by the time required to accumulate a sufficient number of counts. At any rate, it lies somewhere in the region of 1 minute. Thus, it is evident that periods of up to 10 sec can be measured with a high degree of accuracy.

The potentialities of the described set-up are, in general, not limited to measurement of α-α coincidences. There should be no difficulty in providing channels for detecting β-particles and γ-rays. Thus, the possibility of simultaneous measurement of the energy of α-emitters and the decay period provides a reliable method for identifying new radioactive isotopes.

We desire to express our gratitude to A.V.Kulikov for a number of valuable suggestions and to Z.A.Isaeva for assistance in the work. V.V.Pashuk, graduate student at Leningrad Polytechnic Institute, participated in the measurements.

"A.F.Ioffe" Physical-Technical Institute,
Academy of Sciences of the USSR

References

1. G.E.Kocharov, A.P.Komar & G.A.Korolev, Zhur.eksp.i teor.fiz., 36, 68 (1959). (Trans.Soviet Physics - JETP.)
2. G.E.Kocharov & G.A.Korolev, Izv.AN SSSR, Ser.fiz., 25, 237 (1961). (Trans. Bulletin, 25, 227.)
3. H.G.T.Moseley & K.Fajans, Phil.Mag., 22, 629 (1911).
4. A.G.Ward, Proc.Roy.Soc., A181, 183 (1942).
5. S.N.Nikolaev, Yu.M.Volkov, A.V.Kulikov & V.A.Kireev, Peredovoi nauchno-tekhnicheskii i proizvodstvennyi opyt, TsITEI (Advanced practice in technology and production, Central Institute of Information on Technology & Economics), Theme 36, (1960).
6. R.Peierls, Proc.Roy.Soc., A149, 467 (1935).
7. G.Dardel, Arkiv fys., 2, 337 (1950).
8. N.Hole, Arkiv fys., 3, 471 (1952).

Bulletin of the Academy of Sciences of the USSR - Physical Series

Vol.25, No.9 - September 1961

Transactions of the Eleventh Conference on Nuclear Spectroscopy
(Continued from Vol.25, Nos.2 & 7;
to be continued in Vol.25, No.10 and Vol.25, No.1)

Table of Contents

	Page Orig.	Trans.
Magnetic spectrometer for detecting internal conversion electrons from the (n,γ) reaction - V.I.Pelekhov & A.F.Malov	1069	1077
Investigation of the positron and conversion electron spectra of Tb^{152} - K.Ya.Gromov, B.S.Dzhelepov, Zh.T.Zhelev & A.V. Kudryavtseva	1084	1092
Internal conversion coefficients of some transitions in Yb^{171} - N.M.Anton'eva & B.S.Dzhelepov	1088	1096
Conversion electron spectrum of Tm^{165} - Kang Meng-Hua, K.Ya.Gromov, B.S.Dzhelepov, V.Zvol'ska & I.Zvol'skii	1092	1099
Conversion electrons from the erbium fraction formed in spallation of tantalum - A.A.Abdurazakov, K.Ya.Gromov, B.S.Dzhelepov, & V.A.Khalkin	1096	1103
Decay scheme of Eu^{147} - I.Vizi, K.Gromov, B.Dzhelepov, Zh.Zhelev, & Yu.Yazvitskii	1101	1108
Investigation of the conversion electron spectra of neutron-deficient isotopes of erbium and holmium - K.Ya.Gromov & I.S.Dneprovskii	1105	1112
Investigation of the radiation of Mn^{56} - S.S.Vasil'ev, No Sen Ch'ang & L.Ya.Shavtvalov	1115	1122
Properties of low-lying states of Li^5 and Be^8 evinced in disintegration reactions involving light nuclei - S.S.Vasil'ev, V.V. Komarov & A.M.Popova	1117	1124
Electron-neutrino angular correlation in free neutron decay - V.V.Vladimirskii, V.K.Grigor'ev, V.A.Ergakov, D.P.Zharkov, & Yu.V.Trebukhovskii	1121	1128
Remarks on the excited states of the odd-odd nuclei Ho^{166} and Cs^{134} - L.F.Kalinkin, A.S.Melioranskii & I.V.Estulin	1124	1130
Levels in Cu^{64}, excited in the $Ni^{64}(p,n\gamma)Cu^{64}$ reaction - A.K. Val'ter, I.I.Zalyubovskii, A.P.Klyucharev & V.A.Lutsik	1127	1133
Polarization of the γ-rays from the $Si^{30}(p,\gamma)P^{31}$ reaction - P.M.Tutakin	1131	1137
Levels excited in the $F^{19}(\alpha,p)Ne^{22}$ reaction - A.M.Romanov, E.V. Myakinin & M.P.Konstantinova	1135	1140
Spin and parity assignments for some states of Cd^{112}, Sn^{118} and Sn^{120} - O.F.Nemets & V.V.Tokarevskii	1138	1143
Angular distribution of photoelectrons ejected from Ag and Bi targets by Cs^{137} γ-rays - K.K.Aglintsev, V.V.Mitrofanov, A.A.Rimskii-Korsakov & V.V.Smirnov	1141	1146
Excited states of Li^7 with energies up to 9 MeV - V.G.Shevchenko & B.A.Yur'ev	1146	1151
On the influence of collective excitations of the superfluid phase in nuclei on the nuclear moments of inertia - B.B.Dotsenko	1149	1154

Pair correlations and single-nucleon reduced level widths in nuclei - V.B.Belyaev & B.N.Zakhar'ev	1152	1157
Probabilities for E2 and E1 transitions from some excited levels in Tb^{159}, Ho^{165} and Tm^{169} - V.I.Popov	1156	1160
On the possibility of determining reduced widths from polarization effects in direct nuclear reactions - G.L.Vysotskii	1161	1166
Rotational states of nonspherical even-even nuclei - V.I.Belyak & D.A.Zaikin	1163	1168
On collection excitations in nonspherical nuclei - Yu.T.Grin' & D.F.Zaretskii	1169	1174
Investigation of the decay scheme of Eu^{145} - Yu.A.Aleksandrov & M.K.Nikitin	1176	1181
Quadrupole moments and isotope shifts of barium isotopes - N.I.Kaliteevskii, E.E.Fradkin & M.P.Chaika	1178	1183
Generator of short light pulses - G.S.Vil'dgrube, Yu.A.Kolosov & Zh.M.Ronkin	1180	1185
Light-pulse characteristics of louvre type photomultipliers - G.S.Vil'dgrube, N.K.Dalinenko, N.V.Dunaevskaya & Zh.M.Ronkin	1183	1188
Numbers of photons per decay of Ce^{144} and Eu^{155} - A.N.Silant'ev & B.S.Kuznetsov	1186	1191
Use of an ionization α-spectrometer with a time analyzer for determining decay periods - Yu.M.Volkov, A.P.Komar, G.A. Korolev & G.E.Kocharov	1188	1193

Translated in 1962 by
Columbia Technical Translations
5 Vermont Ave., White Plains, N.Y.

Transactions

of the

Eleventh Annual Conference on Nuclear Spectroscopy

(Riga, 25 January - 3 February, 1961)

(Continued from Vol.25, Nos.2,7 & 9)

INVESTIGATION OF THE PROPERTIES OF STRONGLY DEFORMED NUCLEI ON THE BASIS OF A NUCLEAR MODEL TAKING INTO ACCOUNT PAIR CORRELATIONS

- V.G.Solov'ev

The mathematical methods developed by Bogolyubov[1] in constructing the theory of superfluidity and superconductivity can be extended to a number of other fields. In particular, they allow of solving the problem of taking into account residual interactions of fermions, leading to pair correlations, as a many-body problem. The application of these methods to nuclear theory proved to be extremely fruitful inasmuch as pair correlations of nucleons are clearly evinced in nuclei.

The long-range part of the forces is responsible for the average field of the nucleus, which is fundamental to the independent particle model. The short-range part of the forces leads to formation of pair correlation of nucleons. Taking these short-range forces into account leads to a better insight into the properties of nuclei than was afforded by the shell and unified nuclear models.

It is known that residual interactions between nucleons of the superconducting type cannot be included in the self-consistent potential. This fact was clearly demonstrated in Ref.2, where the self-consistent field was explicitly defined. We note that no modifications of the potential well can lead to the appearance of the effects that are yielded by short-range pair forces.

Investigations[3-8] of interactions of the superconducting type made it possible to explain a number of properties of nuclei, which could not be interpreted in the framework of the independent particle model. On the basis of such investigations, one can regard as proved that residual short-range forces between nucleons are attractive forces and that the ground state of any nucleus is the superfluid state. This state is energetically more advantageous than the state with successive filling of levels of the independent particle model. We note, as was shown in Ref.9, that the ground state of a light nucleus is a state with quadruple correlation of the nucleons.

The properties of the ground state and the superfluid excited states of a nucleus exert a great influence on a number of nuclear processes. These properties must be taken into account in investigating nuclear structure and in studying nuclear reactions.

In the present work, on the basis of the "superfluid nuclear model" formulated in Ref.10, we investigate the properties of strongly deformed nuclei. In the first part of the paper we briefly formulate the basic premises underlying this model, discuss the basic regularities involved and give the general results of calculation of the level spectra of even and odd systems, as well as the corrections to the probabilities for β- and γ-transitions. In addition, we give the initial premises for carrying out detailed investigations. In the second part of the paper we consider the properties of strongly deformed nuclei in the $174 \leqslant A \leqslant 188$ region on the basis of the proposed model.

I. Basic Regularities of the "Superfluid Model"

1. Fundamental equations

The significant features of the proposed nuclear model are the following.[10] The model, while based on the average field of the shell or unified nuclear model, takes into account short-range forces leading to pair correlations under the following assumptions.

1. The residual interactions both between neutrons and between protons are described by a Hamiltonian of the form

$$H = \sum_{s\sigma} \{E_0(s) - \lambda\} a^+_{s\sigma} a_{s\sigma} - G \sum_{s,\, s'} a^+_{s+} a^+_{s-} a_{s'-} a_{s'+}. \qquad (1)$$

2. The calculations are carried out for each given nucleus neglecting the fact of averaging connected with conservation of the number of particles on the average:

$$n = \sum_{s\sigma} \langle a^+_{s\sigma} a_{s\sigma} \rangle. \qquad (2)$$

3. The basic equations are found by means of the variational principle of Bogolyubov[11]; for the ground state, as well as for the excited states of the nucleus, there are obtained separate sets of equations, which characterize the properties of the superfluidity of these states. The influence of their excitation on the superfluid properties of the system has come to be called the blocking effect.

The most important distinctions of the given model as compared with earlier treatments of pair correlations[3-6] are a) taking into account changes in the superfluid properties of the nucleus in going from the ground state to excited states, and b) conservation of the number of particles on the average. We note that in the initial formulation of the properties of superfluidity[3-6] the number of particles was not conserved even on the average.

The difference between the results of investigation on the basis of the proposed "superfluid model" and the results of investigation on the basis of the initial formulation of pair correlations is most significant in the region of strongly deformed nuclei.

We described the state of the nucleon by the set of quantum numbers $(s\sigma)$, determined by the form of the average field; $\sigma = \pm 1$; degenerate states differing as regards the sign of σ are conjugate with respect to the operation of time reversal; $a^+_{s\sigma}$ and $a_{s\sigma}$ are the nucleon creation and annihilation operators, $E_0(s)$ is the single particle energy in the state s of the average field, λ is a parameter that plays the role of the chemical potential, and n is the number of nucleons in the system under consideration. We regard the matrix element of the pair interaction G to be constant in view of the short range of the forces leading to pair correlation.

As in Refs.5 & 12, let us deduce the equations, wave functions and energies of the ground and excited states of even and odd systems. Inasmuch as in Eq.(1) there is contained part of the interaction making a contribution to the average field, we carry out the renormalization

$$E(s) = E_0(s) - \frac{G}{2} v_s^2. \qquad (3)$$

Let us write out the wave functions, energies and basic equations describing the properties of superfluidity of nuclei.

Ground state of an even system.

The wave function is

$$\Psi = \prod_s (u_s + v_s a^+_{s+} a^+_{s-}) \Psi_0; \qquad (4)$$

the energy is

$$\mathcal{E} = \sum_s E(s) \left\{ 1 - \frac{E(s) - \lambda}{\sqrt{C^2 + [E(s) - \lambda]^2}} \right\} - \frac{C^2}{G}; \qquad (5)$$

the equations for determining C and λ are

$$\frac{2}{G} = \sum_s \frac{1}{\sqrt{C^2 + \{E(s) - \lambda\}^2}}, \tag{6}$$

$$n = \sum_s \left\{1 - \frac{E(s) - \lambda}{\sqrt{C^2 + [E(s) - \lambda]^2}}\right\}, \tag{7}$$

where

$$a_{s\sigma}\Psi_0 = 0, \quad u_s^2 = \frac{1}{2}\left\{1 + \frac{E(s) - \lambda}{\sqrt{C^2 + [E(s) + \lambda]^2}}\right\},$$

$$v_s^2 = \frac{1}{2}\left\{1 - \frac{E(s) - \lambda}{\sqrt{C^2 + [E(s) - \lambda]^2}}\right\}.$$

Two-quasiparticle excited states of an even system.
The wave functions are

$$\Psi(s_1, s_2) = a^+_{s_1\sigma_1} a^+_{s_2\sigma_2} \prod_{s \neq s_1, s_2} (u_s(s_1, s_2) + v_s(s_1, s_2)\, a^+_{s+} a^+_{s-})\, \Psi_0, (s_1 \neq s_2), \tag{8}$$

$$\Psi(s_1, s_1) = (u_{s_1}(s_1, s_1)\, a^+_{s_1+} a^+_{s_1-} - v_{s_1}(s_1, s_1)) \prod_{s \neq s_1} (u_s(s_1, s_1) + v_s(s_1, s_1)\, a^+_{s+} a^+_{s-})\, \Psi_0; \tag{8'}$$

the energy is

$$\mathcal{E}(s_1, s_2) = E(s_1) + E(s_2) + \frac{G}{2}\left(v_{s_1}(s_1, s_2)^2 + v_{s_2}(s_1, s_2)^2\right) + \sum_{s \neq s_1, s_2} E(s)\, v_s(s_1, s_2)^2 - \frac{C(s_1, s_2)^2}{G}; \tag{9}$$

the basic equations are

$$\frac{2}{G} = \sum_{s \neq s_1, s_2} \frac{1}{\sqrt{C(s_1, s_2)^2 + \{E(s) - \lambda(s_1, s_2)\}^2}}, \tag{10}$$

$$n = 2 + \sum_{s \neq s_1, s_2} \left\{1 - \frac{E(s) - \lambda(s_1, s_2)}{\sqrt{C(s_1, s_2)^2 + [E(s) - \lambda(s_1, s_2)]^2}}\right\}. \tag{11}$$

One-quasiparticle ground and excited states of an odd system.
The wave function is

$$\Psi(s_i) = a^+_{s_i\sigma_i} \prod_{s \neq s_i} (u_s(s_i) + v_s(s_i)\, a^+_{s+} a^+_{s-})\, \Psi_0; \tag{12}$$

the energy is

$$\mathcal{E}(s_i) = E(s_i) + \frac{G}{2} v_{s_i}(s_i)^2 + \sum_{s \neq s_i} E(s)\, v_s(s_i)^2 - \frac{C(s_i)^2}{G}; \tag{13}$$

the basic equations are

$$\frac{2}{G} \sum_{s \neq s_i} \frac{1}{\sqrt{C(s_i)^2 + [E(s) - \lambda(s_i)]^2}}, \tag{14}$$

$$n = 1 + \sum_{s \neq s_i} \left\{1 - \frac{E(s) - \lambda(s_i)}{\sqrt{C(s_i)^2 + [E(s) - \lambda(s_i)]^2}}\right\}. \tag{15}$$

Three-quasiparticle excited states of an odd system.
The wave function is

$$\Psi(s_1, s_2, s_3) = a^+_{s_3\sigma_3} a^+_{s_2\sigma_2} a^+_{s_1\sigma_1} \prod_{s \neq s, s_2, s_3} (u_s(s_1, s_2, s_3) + v_s(s_1, s_2, s_3)\, a^+_{s+} a^+_{s-})\, \Psi_0 \qquad (s_1 \neq s_2 \neq s_3); \tag{16}$$

the energy is

$$\mathscr{E}(s_1, s_2, s_3) = E(s_1) + E(s_2) + E(s_3) + \frac{G}{2}(v_{s_1}(s_1, s_2, s_3)^2 + v_{s_2}(s_1, s_2, s_3)^2 + v_{s_3}(s_1, s_2, s_3)^2) + \sum_{s \neq s_1, s_2, s_3} E(s)\, v_s(s_1, s_2, s_3)^2 - \frac{C(s_1, s_2, s_3)^2}{G}; \quad (17)$$

the basic equations are

$$\frac{2}{G} = \sum_{s \neq s_1, s_2, s_3}' \frac{1}{\sqrt{C(s_1, s_2, s_3)^2 + [E(s) - \lambda(s_1, s_2, s_3)]^2}}, \quad (18)$$

$$n = 3 + \sum_{s \neq s_1, s_2, s_3}' \left\{1 - \frac{E(s) - \lambda(s_1, s_2, s_3)}{\sqrt{C(s_1, s_2, s_3)^2 + [E(s) - \lambda(s_1, s_2, s_3)]^2}}\right\}. \quad (19)$$

For determining the principal characteristics of superfluidity of the above listed states, i.e., the correlation functions C and the chemical potentials λ, we solved, as in the work of Refs.12 & 13, the corresponding sets of equations with the aid of a computer.

In the calculations, described in the first part of the article, for the levels of the average field we took slightly corrected energy values for the levels of Nilsson's scheme[14], while in the calculations in the second part we used the experimental data on single-particle levels of odd nuclei.

2. Pairing energies and single-particle levels of odd nuclei

The general regularities governing the behavior of single-particle levels of odd nuclei in the "superfluid model" were investigated in Ref.10. A more detailed investigation of the spectra of the transuranium elements was carried out in Ref. 12, and of the odd rare earth elements in Ref.13. The energies of the single-particle levels in Nilsson's scheme, given in Ref.15, were somewhat corrected by application of the corresponding parameters on the basis of analysis of the experimental data on odd nuclei and taking into account the influence of superfluidity. The corrected energy values for the single-particle levels are close to those given by Nilsson & Prior[8] except for the $^{11}/_{2}^{-}$ [505] state in the neutron system, which in our case is located about 0.3 $\hbar\mathring{\omega}_0$ lower than in Ref.8 ($\hbar\mathring{\omega}_0 = 41A^{-1}/_{3}$ MeV). The influence of superfluidity on the behavior of single-particle levels in odd nuclei amounts essentially to the following.

1. Superfluidity does not lead to change in the spin of the ground state of the nucleus given by Nilsson's scheme, except in cases when a hole level is very close to the K level (K is the last filled level of the nucleus according to the independent particle model, i.e., with $G = 0$).

2. With increase of the pair interaction constant G, the excitation energy decreases.

3. Hole and particle levels behave differently with increase of G, however, the sequence of hole (particle) levels (relative position of the levels) remains the same.

4. Compression of the excitation spectra for a given G as compared with the $G = 0$ case occurs nonuniformly. Thus, at values of G found from experimental data on pairing energies, for levels lying below 0.5 MeV the excitation energies change by a factor of about 3; for levels up to 1 MeV they change by a factor of about 2; for higher-lying states by about 1.5

We write the energy difference between a given excited state s_i and the ground state s_0 in the form

$$\mathcal{E}(s_i) - \mathcal{E}(s_0) = \varepsilon_{s_i}(s_i) - \varepsilon_{s_0}(s_0) +$$

$$+ \frac{G}{2}\left[\frac{E(s_0) - \lambda(s_0)}{\varepsilon_{s_0}(s_0)} - \frac{E(s_i) - \lambda(s_i)}{\varepsilon_{s_i}(s_i)}\right] + \frac{C(s_i)^2 - C(s_0)^2}{2G} - \sum{}' [\varepsilon_s(s_i) - \varepsilon_s(s_0)], \qquad (20)$$

where

$$\varepsilon_{s_i}(s_k) = \sqrt{C(s_k)^2 + [E(s_i) - \lambda(s_k)]^2}.$$

It can readily be seen that if C and λ are the same for both the states, their energy difference equals $\varepsilon_{s_i}(s_0) - \varepsilon_{s_0}(s_0)$ (neglecting the small correction connected with renormalization of the average field). In this case, among the excited states of a system consisting of an odd number N of particles, there are states corresponding to $N-2$ particles if $\lambda < K$ and $N+2$ particles if $\lambda > K$.

The pair interaction constants for a neutron system (G_N) and for a proton system (G_Z) can be determined from the pairing energies:

$$P_N = 2\mathcal{E}(Z, N-1) - \mathcal{E}(Z, N) - \mathcal{E}(Z, N-2). \qquad (21)$$

From comparison of the calculated values of the pairing energies with the experimental data there were obtained the following mean values of the pair interaction constants:

a) $G_N = 0.024\,\hbar\mathring{\omega}_0$, $G_Z = 0.026\,\hbar\mathring{\omega}_0$ (region of rare earth elements[13]),

b) $G_N = 0.020\,\hbar\mathring{\omega}_0$, $G_Z = 0.022\,\hbar\mathring{\omega}_0$ (region of transuranium elements[12]).

We note that the values of the pair interaction constants depend on the number of levels over which the summation in (6) & (7) and (14) & (15) is carried out (in the computations in Refs.12 & 13 there were used 24-28 levels). Analysis shows that the physical properties of the system virtually do not depend on the number of levels over which the summation is carried out provided this number exceeds 10-12 both above and below the K level. Hence to obtain more reliable results the number of levels summed over was increased to 36, which led to some decrease of the constants G_N and G_Z.*

In Refs.12 & 13, there were calculated the energies of the single-particle levels of odd nuclei; the calculated excitation energies proved to be in better agreement with the experimental data than the values deduced from Nilsson's scheme. However, in view of the strong dependence of the energy of the levels in odd nuclei on the behavior of the energy levels of the average field, primary attention was turned to investigation of the density of the single-particle levels. It was shown[12,13] that in the region of both rare earths and transuranium elements the density of low-lying levels, obtained by calculation, agrees with the experimental data and is about twice the value of the density given by Nilsson's scheme. We note that the effect of increase in the level density is connected with the properties of superfluidity of the ground and excited states and cannot be obtained by changing the position of the single-particle levels in the independent particle model.

In the excitation spectrum of an odd system, in addition to one-quasiparticle levels, there should also be observed three-quasiparticle levels, the excitation

---

*The expediency of increasing the number of levels in the summation was brought to my attention by Dr.Nilsson, whom I take this opportunity to thank.

energy of which is somewhat higher than the excitation energy of an even system. However, in the case when there is one particle and one hole level close to the K level, i.e., close to the point of intersection of the three levels of the average field, the energy of the three-quasiparticle state $K-1$, $K+1$, K is strongly reduced. This is connected with the fact that in the $K-1$, K,$K+1$ state the superfluidity of the system is close to zero, and the energy difference in the $K+1$ and $K-1$ states is small.

By way of example let us consider the case of Dy^{161}. If the $^{11}/_{2}^{-}[505]$ level is located 0.3 $\hbar\omega_0$ lower than in Nilsson's scheme[15], then the K, $K-1$ and $K+1$ levels will be $^{5}/_{2}^{+}[642]$, $^{3}/_{2}^{-}[521]$ and $^{5}/_{2}^{-}[523]$, respectively, and the separation between the hole and particle excited states in the level scheme of the average field will be ~0.2 MeV. Evaluations show that the three-quasiparticle states $^{3}/_{2}^{+}$, $^{7}/_{2}^{+}$ and $^{13}/_{2}^{+}$ must have an energy of the order of 1 MeV. We note that experimentally these levels are most easily detected by the method of Coulomb excitation of Dy^{161}, inasmuch, as it will be shown below, in β-decay they can be populated only in the case of transitions from those two-quasiparticle states in which the quasiparticles are located in any two of the three states $K-1, K$ and $K+1$.

3. Superfluidity properties of an even system

The advantages of the "superfluid model" as compared with the unified nuclear model are evinced particularly clearly in investigating the properties of even-even nuclei. The spectra of single-particle levels of even-even nuclei, calculated in Refs.10, 12 & 13, illustrate the basic regularities in the behavior of the levels of these nuclei and as a whole agree with the corresponding experimental data. We note that in the "superfluid model" the number of particles is conserved on the average and all the calculated excited states pertain to one and the same system of particles. In contrast, in the initial treatment of pair correlations[3-5] among the calculated excited states of the system, which in the ground state comprises N particles, there are present levels corresponding to systems consisting of $N-2, N$ and $N+2$ particles.

The change in the positions of the levels in an even system with increase in G, as calculated on the basis of the "superfluid model" differs from the change in the position of the levels calculated according to the initial treatment of pair correlations[3-5]. Whereas the energy of the ground state with increase of G decreases in both cases according to the same law, the energies of the excited states behave differently. According to the initial treatment[3-5], the energies of the excited states increased as compared with their values for $G = 0$, and the difference between the excited and ground state energies is always greater than the width of the energy gap $2C$. In the "superfluid model" the energies of the excited states decrease with increase of G relative to their value at $G = 0$, and the degree of decrease depends on the change in the properties of the superfluidity of these states as compared with the ground state. The excitation energy of one, and in a number of cases, of several states calculated on the basis of the "superfluid model" takes on values that are smaller than the width of the energy gap ($2C$). In Ref.12 it was shown that in the excited $K, K+1$ state of an even system, (i.e., in the state where one quasiparticle is on the K level and the other on the following higher level $K+1$ the role of pair correlations greatly decreases, and the excitation energy is always less than the gap width $2C$. The diminution of superfluidity in this state is connected with the fact that in view of the Pauli exclusion principle the correlated pairs cannot occupy the K and $K+1$ levels and hence in states available to the pairs there is evinced a wider gap in the case of strongly deformed nuclei. Inasmuch as below this gap the number of states is equal to

the number of particles and in view of kinetic energy considerations it is disadvantageous for the pairs to occupy the $K+2$ and higher states, the superfluidity in the excited $K, K+1$ state is strongly reduced. The fact that the $K, K+1$ states sink below the energy gap is substantiated by calculations of the spectra of more than ten different even-even nuclei and is in good agreement with the experimental data. In fact, the agreement of theory with experiment as regards the decrease in the energy of the $K, K+1$ level to below the energy gap is one of the most significant confirmations of the initial premises of the "superfluid model" and is one of the advantages of this model in considering strongly deformed nuclei as compared with the initial treatment of pair correlations.

4. Correction for superfluidity and supplementary classification of β-transitions

On the basis of the "superfluid model" one can take into account changes in the structure of the nucleus as a many-body system in β- and γ-transitions of certain nuclei. It was shown in earlier papers[10,12] that the role of superfluidity corrections to the probabilities for β- and γ-transitions in strongly deformed nuclei is very important. In the present section we shall formulate the general rules for introducing corrections to β-decay[16], connected with superfluidity of the nucleus in the ground and excited states and shall carry out classification[16] of the probabilities for β-decay of strongly deformed nuclei in supplement to Alaga's selection rules. The role of the corrections for superfluidity will be investigated in the second part of the article by analysis of the $\log ft$ values for β-transitions between like pairs of single-particle states in different nuclei.

We write the matrix element describing β-decay of a complex nucleus in symbolic form:

$$M \sim \Psi^{*}_{2n_N}\Psi^{*}_{2n_Z+1}(s_2)\sum_{\nu,\,\nu'}\langle \nu|\Gamma|\nu'\rangle a^{+}_{\nu}b_{\nu'}\Psi_{2n_Z}\Psi_{2n_N+1}(s_1) = \langle s_2|\Gamma|s_1\rangle L; \qquad (22)$$

here $\langle s_2|\Gamma|s_1\rangle$ is the single-particle matrix element of the transition and $L = (\Psi^{*}_{2n_N}\Psi_{2n_N})(\Psi^{*}_{2n_Z}\Psi_{2n_Z})$ where Ψ_N is the wave function of the system N particles. We obtain the values of ft characterizing the β-decay in the form

$$ft = \frac{\text{const}}{|\langle s_2|\Gamma|s_1\rangle|^2}L^{-2}; \qquad (23)$$

here we write L^2 in the form $L^2 = R_Z R_N \equiv R$. The quantities R_Z and R_N characterize rearrangement of the nucleus incident to the β-transition; the former pertains to rearrangement of the proton system; the latter to rearrangement of the neutron system. We shall consider the proton and neutron systems separately. Let us find R_i (i.e., R_Z or R_N) for β-decays involving any number of quasiparticles in the initial and final states, except for the cases when there are two quasiparticles on one and the same level. We write

$$R_i = \gamma\prod_{s\neq f_1,\ldots,f_k}(u_s u'_s + v_s v'_s)^2, \qquad (24)$$

where the functions u_s and v_s pertain to the initial state, and the functions u'_s and v'_s to the final state. In the product $\prod_{s\neq f_1,\ldots,f_k}(u_s u'_s + v_s v'_s)^2$ there are no factors corresponding to the level on which there are quasiparticles, and this product is

closer to unity, the more similar the properties of the superfluidity of the initial and final states. In the initial formulation[3-5] of pair correlations this product was assumed equal to unity. Further, if the number of paired particles in the initial and final states is the same, as obtains, in the case of $^{108+1}_{72}Hf^{181} \rightarrow {}^{108}_{72+1}Ta^{181}$ β-decay, $\gamma = u_f^2$, while if the number of paired nucleons changes in the process of decay, as in the $^{110}_{72+1}Ta^{183} \rightarrow {}^{108+1}_{74}W^{183}$ case, then $\gamma = v_f^2$; here f pertains to the level on which the quasiparticle disappeared or appeared. The functions u_f^2 or v_f^2 in (24) characterize the properties of superfluidity of the system with the smaller number of quasiparticles. Thus, for example, in β-decay of an odd system to the ground state of an even system u_f^2 and v_f^2 pertain to the even system, while in β-decay of a one-quasiparticle odd state to a two-quasiparticle excited state v_f^2 and u_f^2 pertain to the odd system, and so on.

Let us consider the case when the pair interaction constant G tends to zero, i.e., when the "superfluid model" transforms to the independent particle model. Then the correction R_i takes on one of two values, namely, R_i = 1 or R_i = 0; the former corresponds to the case when β-decay occurs without change in the position of all the nucleons except one, while the latter case corresponds to β-decay with change in the position of more than one nucleon in the independent particle model. For β-decay in which the number of pairs remains unchanged R_i = 1 for particle transitions and R_i = 0 for hole transitions, while for β-decay in which the number of pairs changes by one, R_i = 1 for hole and R_i = 0 for particle transitions. Under "particle transitions" we understand transitions in which a quasiparticle appears or disappears on single particle levels f with an energy greater than λ, pertaining to the system with the smaller number of quasiparticles. For hole transitions the energy of the single-particle levels f is smaller than λ. Let us now carry out a classification of β-transitions in strongly deformed complex nuclei, supplementary to the selection rules of Alaga formulated in Ref.15. We divide all β-transitions into three groups[16]:

$$\text{first group:} \quad R_i = 1 \ (G = 0), \quad 0 < R_i < 1 \ (G \neq 0);$$

$$\text{second group:} \quad R_i = 0 \ (G = 0), \quad 0 < R_i < 1 \ (G \neq 0);$$

$$\text{third group:} \quad R_i = 0 \ (G = 0), \quad R_i = 0 \qquad (G \neq 0).$$

In the first group we put

a) β-transitions, the initial and final states of which are the ground states of the respective systems,

b) particle transitions involving no change in the number of pairs, and

c) hole transitions with change in the number of pairs by one.

We note that the 1060.1 keV β-transition to the $^7/_2^-$ [503] state of Hf^{177} and the 1226.7 and 1045.5 keV β-transitions to the $^9/_2^-$ [505] and $^7/_2^-$ [503] states of Hf^{175}, detected by Harmatz et al[17], and other similar transitions belong in group 1.

In the second group we classify

a) hole transitions involving no change in the number of pairs, and

b) particle transitions in cases when the number of particle pairs changes by one.

For β-transitions classified in group 2, the "superfluid model" gives non-zero transition probabilities, whereas these transitions are strongly forbidden according to the independent particle model. We note that the corrections R_i calculated on the basis of the "superfluid model" for β-transitions to low-lying states ($\lesssim$ 0.3 MeV) are of the same order of magnitude for transitions of the first

and second groups; in the case of transitions to high-lying states ($\gtrsim$1 MeV) there appears an appreciable difference between the corrections for transitions of the first and second groups.

Analysis of the available experimental data shows that there are more than twenty reliably established β-transitions that can be classed in the second group. For example, decay of Ta^{177} to the $^5/_2^-[512]$ state of Hf^{177}, β-decay of Hf^{181} to the $^1/_2^+[411]$ state of Ta^{181} and decay of W^{187} to the $^1/_2^+[411]$ state of Re^{187} are all transitions belonging to the second group. In fact the experimental detection of β-transitions belonging to the second group is evidence of the superiority of the "superfluid model" over any independent particle model and is yet another substantiation of the existence of significant short-range pairing forces.

Whereas in the first and second groups we have β-transitions in which only one quasiparticle appears or disappears in the proton (or neutron) system and the position of the other particle remains unchanged, in the third group we classify

a) transitions involving change in the number of quasiparticles in the proton (or neutron) system by more than one,

b) transitions where in addition to the change in the number of quasiparticles by one there occurs a change in the position of some of the other quasiparticles.

The "superfluid model" is a nuclear model of independent quasiparticles; consequently, in the framework of this model transitions involving rearrangement of the quasiparticles are rigorously forbidden. It is of interest to investigate the question of the degree of forbiddenness of transitions classified in the third group. It is probable that they are greatly retarded as compared with transitions in the first and second groups. For determining the degree of forbiddenness of β-transitions classed in the third group one should experimentally investigate the possibility of β-transitions of one-quasiparticle states of an odd system to such two-quasiparticle excited states of an odd system where all three quasiparticles will be located on different single-particle levels.

The above supplementary classification of β-transitions proved to be useful in identifying excited states of odd nuclei and in analysis of the levels in even-even nuclei. For rough evaluation of the retardation of β-transitions in odd nuclei in Table 1 we give the averaged values of v_s^2, characterizing this retardation as a function of the excited energy of the odd system (which should be reckoned from the K level); we have taken into account the increase in the level density in the given nuclear model as compared with the independent particle model.

Table 1

Values of v_s^2

	Hole states			K	Particle states		
	2,0 MeV	1,0 MeV	0,5 MeV		0,5 MeV	1,0 MeV	2,0 MeV
v_s^2	0,98	0,95	0,90	0,50	0,15	0,08	0,02

The importance of taking into account corrections for superfluidity where γ-transitions are concerned was emphasized in Refs.10 and 12 and in a number of other contributions. The rules for calculating superfluidity corrections to γ-transitions are similar to those for β-decay. We can represent the correction to an electromagnetic transition in the form

$$R_\gamma = \gamma \prod_{s \neq j_1, \ldots, j_k} (u_s u_s' + v_s v_s')^2, \qquad (25)$$

where

$$\gamma = [u_{f_1}(f_2\ldots)u_{f_2}(f_1\ldots) - \eta v_{f_1}(f_2\ldots)v_{f_2}(f_2\ldots)]^2, \quad \eta = \pm 1, \tag{26}$$

if the number of quasiparticles in the initial and final states is the same, and

$$\gamma = (u_{f_1}v_{f_2} - \eta v_{f_1}u_{f_2})^2, \tag{27}$$

if the number of quasiparticles changes by two in the transition. The quantities u_f and v_f, entering into γ, pertain to single-particle states in which there appeared or disappeared a quasiparticle, and belong to the systems in which there is no quasiparticle on these levels. As regards the behavior of R_γ, in the limit as $G \to 0$, as in the case of β-decay, there is introduced a supplementary classification of electromagnetic transitions, the utility of which is now being evaluated.

5. Basic premises for carrying out detailed calculations

In the work of Refs.10, 12 & 13, there were carried out calculations of the characteristics of the ground and excited superfluid states of even and odd systems. On this basis there were computed the spectra of single-particle states of most odd and a number of even-even strongly deformed nuclei, as well as the corrections to the β- and γ-transition probabilities. In these papers there was illustrated the necessity of taking into account the superfluid properties of nuclei, inasmuch as the determined regularities characterizing the behavior of complex nuclei agree with the available experimental data. It was also shown that the specific attributes of the "superfluid model" are particularly important in the case of strongly deformed nuclei, i.e., for the corresponding case of the density of single-particle levels of the average field and the values of the pair interaction constants G_Z and G_N.

Let us consider the question of what limits the accuracy of calculations and whether one can on the basis of the "superfluid model" investigated not only the general regularities in the behavior of nuclei but also the specific properties of each particular nucleus. Let us also evaluate the reliability and definiteness of such calculations. Inasmuch as in the "superfluid model" the number of particles is conserved on the average, in calculating the characteristics of superfluidity of each state there was simultaneously computed the root mean square fluctuation in the number of particles Δn. Analysis showed that the error involved in assuming conservation of the number of particles on the average, i.e., of the ratio $\Delta n/2\Omega$ (where Ω is the number of summed over levels) nowhere exceeds 5-6% and in most cases amounts to only 2-4%.

The superfluidity properties of a system depend greatly on the behavior of several levels of the average field near the K level and on the magnitude of the pair interaction constant G. Our earlier calculations were based on slightly corrected energy values for the single-particle levels in Nilsson's scheme, which does not in all cases give the correct level sequence and, particularly, the separation between levels. Hence the accuracy of the calculations was limited not by the accuracy with which the number of particles on the average is actually conserved, but by the rough description of the behavior of the levels of the average field. Thus the calculations suffer from the shortcomings, first, inherent in Nilsson's scheme itself, second, those connected with imperfect knowledge of the parameters of equilibrium deformations, and, third, those associated with failure to take into account variation of the average field of the proton (neutron) system with increase (decrease) in the number of particles in the neutron (proton) system,

etc. Thus the basic premises for detailed calculations must be formulated so as to exclude to the greatest degree possible indefiniteness and inaccuracies connected with inadequate knowledge of the levels and wave functions of the average field.

Accordingly, we shall carry out detailed calculations of the properties of superfluidity of strongly deformed nuclei and thus determinations of the excitation spectra of even-even nuclei, corrections to the β- and γ-transition probabilities, moments of inertia of the ground and excited states and other effects according to the "superfluid model" on the basis of experimental data on the single-particle levels of odd nuclei and pairing energies. To this end we must modify the position of some of the levels close to the K level in Nilsson's scheme and choose the pair interaction constant G so as to obtain a spectrum of single-particle states in odd nuclei and pairing energies in agreement with the experimental data. Inasmuch as we shall take the position of several levels close to the K state in accord with experiment, and the position of the other levels virtually does not influence the superfluidity properties of the system, the calculations in which wave functions are not used do not depend on the specific choice of the potential of the average field. Thus the calculations of the relative quantities which depend only weakly and indirectly on the parameters of the average field are free of the shortcomings connected with poor knowledge of the parameters of the average field, equilibrium deformations and the like. The principal shortcoming and main limitation as regards the accuracy of the calculations by the proposed method is that we do not take into account the change in the average field for neighboring nuclei, inasmuch as the same conjunction or set of single-particle levels must be used for calculating the characteristics of the superfluidity of a number of nuclei. However, with this approach it becomes possible to investigate the changes in the average field in going from one nucleus to another.

We note that with the given system of levels of the average field and the fixed value of the pair interaction constant, the calculations based on the "superfluid model" are entirely unambiguous. This formulation of the problem, in which the same set of single-particle levels is used for calculating the properties of a number of nuclei, completely eliminates any element of adjustment or fitting of the results of calculation to experiment.

II. Investigation of the Properties of Strongly Deformed Nuclei in the $174 \leqslant A \leqslant 188$ Region

1. Choice of single particle levels and pair interaction constants

In accord with the calculation program formulated above, we choose one set of single-particle level energies and one pair interaction constant for all neutron systems in the $102 \leqslant N \leqslant 112$ region and for proton systems in the $70 \leqslant Z \leqslant 76$ region. In Table 2 we list the relative positions of the six most important single-particle levels in the proton and neutron systems.

Inasmuch as the pairing energies in the region under consideration, given by experiment, change from nucleus to nucleus, we carried out rather rough averaging and after appropriate calculations obtained the following values for the pair interaction constant:

$$G_N = 0{,}020\hbar\dot{\omega}_0 \approx 0{,}145\ \text{MeV} \approx \frac{26}{A}\ \text{MeV},$$
$$G_Z = 0{,}021\hbar\dot{\omega}_0 \approx 0{,}152\ \text{MeV} \approx \frac{2{,}8}{A}\ \text{MeV} \qquad (28)$$

It is possible that the above value for the proton pair interaction constant G_Z is an underestimate. The summation in the equations for determining C and λ was carried out over 36 single-particle levels. With increase in the number of summed over levels the values of the pair interaction constant in the given nuclear region decreased from $G_N = 0.023\,\hbar\mathring{\omega}_0$ to $G_N = 0.020\,\hbar\mathring{\omega}_0$ and from $G_Z = 0.025\,\hbar\mathring{\omega}_0$ to $G_Z = 0.021\,\hbar\mathring{\omega}_0$, as compared with the values given in Figs.2 and 3 in Ref.13. However, despite the decrease of the constants G_N and G_Z, the values of the correlation functions C and $C(s_i)$ on the average did not change as compared with the values given in Ref.13. The values of the correlation functions of the proton system are virtually constant in the $70 \leqslant Z \leqslant 76$ region: $C \approx 0.114\ \hbar\mathring{\omega}_0$ and $\frac{C(s_K)}{C} \approx 0.65$. In the case of the neutron system, the value of the correlation function increases in going from N = 102 to N = 112 by about 15%: $C \approx 0.13\ \hbar\mathring{\omega}_0$; the ratio $\frac{C(s_K)}{C} \approx 0.75$.

Table 2

Single particle levels of the average field

Neutron system			Proton system		
N	Level assignment	Energy $\hbar\mathring{\omega}_0$	Z	Level assignment	Energy $\hbar\mathring{\omega}_0$
103	$^5/_2^-$ [512]	0	67	$^7/_2^-$ [523]	0
105	$^7/_2^-$ [514]	0,04	69	$^1/_2^+$ [411]	0,07
107	$^9/_2^+$ [624]	0,12	71	$^9/_2^-$ [514]	0,17
109	$^1/_2^-$ [510]	0,19	73	$^7/_2^+$ [404]	0,18
111	$^3/_2^-$ [512]	0,26	75	$^5/_2^+$ [402]	0,30
113	$^7/_2^-$ [503]	0,30	77	$^1/_2^+$ [400]	0,39

The choice of a single set of levels of the average field and of one value of G for a comparatively extensive group of nuclei is in the nature of an approximation, inasmuch as in the given nuclear range the behavior of the levels of the average field, the equilibrium deformation and the pairing energies vary. This was done mainly in order a) to minimize arbitrariness in calculating the spectra of even-even nuclei and b) to exclude the influence of the average field for comparison of relative values of $\log ft$ for β-transitions and for finding $\log ft$ for transitions in even nuclei on the basis of the experimental data for odd nuclei. This choice of a single set of levels and one pair interaction constant was also dictated by the fact that the single-particle levels of odd nuclei are not known with a sufficient accuracy to allow of separating the groups of nuclei into subgroups corresponding to different single-particle level schemes.

Calculations based on the assumed scheme of single-particle energies of the average field and chosen values of G lead to relatively good prediction of the behavior of levels in odd nuclei, except for the change in sequence of the $^7/_2^+$ [404] and $^9/_2^-$ [514] levels in some odd-Z nuclei. It is possible that these two levels do not intersect in the given nuclear region but are very close to each other; in this case superfluidity leads to the situation where the energy of the hole state will be lower than the energy of the state with a quasiparticle on the K level. Undoubtedly, further experimental studies are necessary to clarify the behavior of these levels.

2. Analysis of β-transition probabilities

The purpose of the present section is, on the one hand, to clarify the role of superfluidity corrections to the β-transition probabilities and, on the other hand, to explain the changes in the experimental values of $\log ft$ for transitions between like single-particle states in different nuclei and calculate the $\log ft$ values for β-transitions in even nuclei on the basis of the experimental data on β-transitions in odd nuclei. In order to exclude to the greatest extent the influence of the average field, let us analyze the values of $\log ft$ for β-transitions between pairs of like single-particle states in different nuclei. Obviously, in such a transition the influence of the single-particle matrix element $\langle s_1|\Gamma|s_2\rangle$ on the relative values of $\log ft$ is not completely excluded inasmuch as in going from one nucleus to another the average field changes somewhat. Following the supplementary classification of β-transitions, introduced above, we use I to designate transitions pertaining to the first group and II to indicate transitions classified in the second group. After the usual classification of β-transitions, we will indicate the supplementary classification, first for the proton system and then for the neutron system. Thus, for example, *ah* I II indicates that the proton transition belongs to the first group and the neutron transition to the second.

Table 3

Calculation of corrections for β-transitions in odd nuclei

Initial & final states	β-transition	Classification	$(\log ft)_{exp}$	R	$(\log ft)_{rel}$
$s_Z = \{^7/_2^+[404]\}$ $s_N = \{^7/_2^-[503]\}$	$^{102}_{73}Ta^{175} \rightarrow {}^{103}_{72}Hf^{175}$	*1u* I I	6,2 [17]	0,41	6,2
	$^{104}_{73}Ta^{177} \rightarrow {}^{105}_{72}Hf^{177}$	*1u* I I	6,4 [17]	0,40	6,2
	$^{112}_{73}Ta^{185} \rightarrow {}^{111}_{74}W^{185}$	*1u* I II	6,5 [18]	0,19	6,5
	$^{110}_{73}Ta^{183} \rightarrow {}^{109}_{74}W^{183}$	*1u* I II	6,9 [15]	0,11	6,8
$s_Z = \{^7/_2^+[404]\}$ $s_N = \{^7/_2^+[633]\}$	$^{102}_{73}Ta^{175} \rightarrow {}^{103}_{72}Hf^{175}$	*ah* I II	6,7 [17]	0,12	6,7
	$^{104}_{73}Ta^{177} \rightarrow {}^{105}_{72}Hf^{177}$	*ah* I II	7,8 [17]	0,06	7,0
$s_Z = \{^7/_2^+[404]\}$ $s_N = \{^9/_2^-[505]\}$	$^{102}_{73}Ta^{175} \rightarrow {}^{103}_{72}Hf^{175}$	*1u* I I	6,4 [17]	0,41	6,4
	$^{112}_{73}Ta^{185} \rightarrow {}^{111}_{74}W^{185}$	*1u* I II	~7,3 [18]	0,15	6,8
$s_Z = \{^1/_2^+[411]\}$ $s_N = \{^1/_2^-[510]\}$	$^{108}_{75}Re^{183} \leftarrow {}^{107}_{76}Os^{183}$	*1u* I II	6,3 [19]	0,27	6,3
	$^{108}_{73}Ta^{181} \leftarrow {}^{109}_{72}Hf^{181}$	*1u* II I	7,1 [15]	0,07	6,9

First, let us consider β-transitions in odd nuclei. We carried out calculations of the corresponding superfluidity corrections. The results are given in Table 3, in the last column of which we list the values of $(\log ft)_{rel}$, i.e., the values of $\log ft$ calculated relative to the first transition of the given series between like states in different nuclei. If the average field does not change in going from nucleus to nucleus, the variation in $\log ft$ must be attributed to superfluidity of the ground and excited states. Thus, the experimental value $(\log ft)_{exp}$ for transitions between the $^7/_2^+[404]$ and $^7/_2^-[503]$ states varies in the range

$$6.2 < (\log ft)_{exp} \leqslant 6.9,$$

whereas if one takes into account the correction for superfluidity, the quantity

$(\log ft)_{\exp} - \log \frac{1}{R}$ varies little, namely,

$$5.8 \leqslant \log [(ft)_{\exp} R] \leqslant 6.0.$$

For the above mentioned transition there was obtained good agreement between calculated and experimental values of $\log ft$. For two other transitions the superfluidity corrections reduced the difference between the probabilities of the first and second transitions and also increased the value of the corresponding matrix elements; for example, for the transition between the $^{7}/_{2}^{+}[404]$ and $^{7}/_{2}^{+}[633]$ states, $(\log ft)$ = 6.7 and 7.8, while $\log [(ft)_{\exp} \cdot R]$ = 5.8 and 6.6, respectively.

Table 4

$s_Z = \{^{5}/_{2}^{+}[402]\} \leftrightarrows s_N = \{^{3}/_{2}^{-}[512]\}$ β-transitions

State	β-transition	State	Classification	$(\log ft)_{\exp}$ [Ref.]	R	$(\log ft)_{rel}$
	$^{112}_{75}Re^{187} \leftarrow {}^{113}_{74}N^{187}$		1*u* II	7,9 [20]	0,3	7,9
	$^{110}_{75}Re^{185} \leftarrow {}^{111}_{74}N^{185}$		1*u* II	7,5 [15]	0,38	7,8
1^- $s_Z = \{^{5}/_{2}^{+}[402]\}$ $s_N = \{^{3}/_{2}^{-}[512]\}$	$^{111}_{75}Re^{186} \rightarrow {}^{112}_{74}W^{186}$	ground	1*u* II	7,1÷7,7 [21]	0,23	8,0
	$^{111}_{75}Re^{186} \rightarrow {}^{110}_{76}Os^{186}$	ground	1*u* II	7,7 [21]	0,34	7,8
1^- $s_Z = \{^{5}/_{2}^{+}[402]\}$ $s_N = \{^{3}/_{2}^{-}[542]\}$	$^{113}_{75}Re^{188} \rightarrow {}^{112}_{76}Os^{188}$	ground	1*u* II	8,0 [21]	0,30	7,9

Table 5

$s_Z = \{^{9}/_{2}^{-}[514]\} \rightleftarrows s_N = \{^{7}/_{2}^{-}[514]\}$ β-transitions

State	β-transition	State	Classification	$(\log ft)_{\exp}$ [Ref.]	R	$(\log ft)_{rel}$
	$^{104}_{71}Lu^{175} \leftarrow {}^{105}_{70}Yb^{175}$		*au* II	4,5 [15]	0,32	4,5
	$^{106}_{73}Ta^{179} \leftarrow {}^{105}_{74}W^{179}$		*au* II	4,5 [22]	0,44	4,4
7^- $s_Z = \{^{7}/_{2}^{+}[404]\}$ $s_N = \{^{7}/_{2}^{-}[514]\}$	$^{105}_{73}Ta^{178} \rightarrow {}^{106}_{72}Hf^{178}$	8^- $s_Z = \{^{7}/_{2}^{+}[404]\}$ $s'_Z = \{^{9}/_{2}^{-}[514]\}$	*au* II	4,9 [23]	0,34	4,5
	$^{105}_{73}Ta^{178} \leftarrow {}^{104}_{74}W^{178}$	ground	*au* II		0,36	4,6
1^+ $s_Z = \{^{9}/_{2}^{-}[514]\}$	$^{105}_{75}Ta^{178} \rightarrow {}^{106}_{72}Hf^{178}$	ground	*au* II	4,6 [23]	0,22	4,6
$s_N = \{^{7}/_{2}^{-}[514]\}$	$^{105}_{73}Ta^{178} \rightarrow {}^{106}_{72}Hf^{178}$	0^+ $s_Z = s'_Z = \{^{9}/_{2}^{-}[514]\}$	*au* II	5,1 [23]	0,41	4,4
	$^{105}_{73}Ta^{178} \rightarrow {}^{106}_{72}Hf^{178}$	0^+ $s_N = s'_N = \{^{7}/_{2}^{-}[514]\}$	*au* II	4,7]23]	0,46	4,6

A comparison of the reduced probabilities for β-transitions between like states in odd and even nuclei is feasible only in cases when all these transitions are allowed, first forbidden, etc. Only in such cases can one calculate the $\log ft$ values for the β-transitions in even nuclei on the basis of the experimental data on odd nuclei. In Table 4,5 & 6, we give the results of calculations

for transitions of the given types. In Table 4, for example, we give the data for the β-transition between the $^5/_2^+[402]$ and $^3/_2^-[512]$ states, classified as $1u$; the transition between the states with spins 1^- and 0^+ are also $1u$ type transitions and hence one can carry out a comparison of these transitions in even and odd nuclei. For determining the configuration of odd-odd nuclei we use the rule formulated by Gallagher & Moszkowski[24], which states that the state with the lowest energy will be that with parallel projections of the spins of the odd neutron and proton on the nuclear symmetry axis. For determining the configuration of two-quasiparticle excited states we used Gallagher's rule, according to which the system with antiparallel spins has the lowest energy. The calculated values of $(\log ft)_{rcl}$ for β-transitions in even nuclei, listed in Table 4, are in satisfactory agreement with the experimental data.

In Table 5 we list the values of $(\log ft)$ for β-transitions in even nuclei calculated on the basis of the data on $Yb^{175} \rightarrow Lu^{175}$ β-decay; it will be seen that the calculated values of $(\log ft)_{rcl}$ are in good agreement with the experimental data. The β-transitions to two-quasiparticle states with 0^+ were calculated by means of the usual formulas without taking into account the specific attributes of these states. In Table 6 we list the transitions between the $s_Z = \{^7/_2^+[404]\}$ and $s_N = \{^9/_2^+[624]\}$ states which cannot be reconciled with each other. This is apparently connected with the change in the relative positions of the $^7/_2^+[404]$ and $^9/_2^-[514]$ levels, which we have not taken into account. We have divided the known transitions between these states into two parts, associating the first with the $Yb^{177} \rightarrow Lu^{177}$ transition, and the second with $Os^{183} \rightarrow Re^{183}$ decay.

Table 6

$s_Z = \{^7/_2^+[404]\} \rightleftarrows s_N = \{^9/_2^+[624]\}$ β-transitions

State	β-transition	State	Classification	$(\log ft)_{exp}$ [Ref]	R	$(\log ft)_{rcl}$
	$^{106}_{71}Lu^{177} \leftarrow {}^{107}_{70}Yb^{177}$		*ah* II	6,2 [15]	0,41	6,2
	$^{106}_{71}Lu^{177} \rightarrow {}^{105}_{72}Hf^{177}$		*ah* I II	6,3 [15]	0,13	6,7
	$^{108}_{73}Ta^{181} \rightarrow {}^{107}_{74}W^{181}$		*ah* II	6,6 [22]	0,34	6,3
1^+ $s_Z = \{^7/_2^+[404]\}$ $s_N = \{^9/_2^+[624]\}$	$^{105}_{71}Lu^{176} \rightarrow {}^{104}_{72}Hf^{176}$	ground	*ah* II	6,5 [21]	0,31	6,3
3^- $s_Z = \{^7/_2^+[404]\}$ $s_N = \{^1/_2^-[510]\}$	$^{109}_{73}Ta^{182} \rightarrow {}^{108}_{74}W^{182}$	4^- $s_N = \{^1/_2^-[510]\}$ $s'_N = \{^9/_2^+[624]\}$	*ah* II	6,9 [22]	0,22	6,9 (7,9)
7^- $s_Z = \{^7/_2^+[404]\}$ $s_N = \{^7/_2^-[514]\}$	$^{105}_{73}Ta^{178} \rightarrow {}^{106}_{72}Hf^{178}$	8^- $s_N = \{^7/_2^-[514]\}$ $s'_N = \{^9/_2^+[624]\}$	*ah* I II	4,9 [23]	0,21	6,5 (7,4)
1^+ $s_Z = \{^7/_2^+[404]\}$ $s_N = \{^9/_2^+[624]\}$	$^{107}_{73}Ta^{180} \rightarrow {}^{108}_{72}Hf^{180}$	ground	*ah* II	6,0 [21]	0,23	6,4 (7,4)
	$^{107}_{73}Ta^{180} \rightarrow {}^{106}_{74}W^{180}$	ground	*ah* II	6,8 [21]	0,38	6,3 (7,2)
	$^{108}_{75}Re^{183} \leftarrow {}^{107}_{76}Os^{183}$		*ah* II	7,1 [19]	0,46	7,1
	$^{104}_{73}Ta^{177} \rightarrow {}^{105}_{72}Hf^{117}$		*ah* II	$\geqslant$7,9 [17]	0,33	7,3
	$^{106}_{73}Ta^{179} \rightarrow {}^{107}_{72}Hf^{179}$		*ah* II	~6,9 [15]	0,25	7,4

Table 7

K, K + 1 levels in Hf^{178} and W^{182}

Nucleus	System	Gap $2C$, MeV	Spin & parity K, K + 1	Energy of K, K + 1 level, MeV	
				Calc.	Exper.
Hf^{178}	Proton	1,66	8^-	1,03	1,148
Hf^{178}	Neutron	1,85	8^-	1,46	1,480
W^{182}	"	1,89	4^-	1,46	1,554
W^{182}	Proton	1,61	6^+	1,3	—
W^{182}	"	1,61	2^-	1,4*	1,290
W^{184}	"	1,61	2^-	1,3	1,150

*K - 1, K + 1 level.

Recently, Gallagher[21] showed that single-particle transitions in even nuclei occur with approximately the same probabilities as transitions in the corresponding odd nuclei. Our calculations substantiate this. The values of $\log[(ft)_{exp}R]$, which are the quantities that should be compared with each other and with the results of calculation of β-transition probabilities according to the independent particle model, are approximately the same for even and odd nuclei. There is less difference between the quantities $\log[(ft)_{exp}R]$ for even and odd nuclei than between the values of $(\log ft)_{exp}$.

In cases when the change in spin incident to β-transitions in even and odd nuclei is different, as, for example, in the case of the β-transition between the $s_Z = \{^9/_2^-[514]\}$ and $s_N = \{^1/_2^-[510]\}$ states of Re^{182} (3⁻) to W^{182} (2⁻), where $(\Delta I)_{odd} = 4$, while $(\Delta I)_{even} = 1$, one cannot calculate the β-transition probabilities for even nuclei on the basis of the probabilities for odd nuclei. However, in such cases one can and should carry out calculations of the relative β-transition probabilities in different even nuclei.

In the work of Mottelson & Nilsson[15] observed β-transition probabilities in strongly deformed nuclei were systematized and linked with the classification of β-transition as follows

$$4.5 < \log(ft)_{exp} < 5.0\ au,$$
$$6.0 < \log(ft)_{exp} < 7.5\ ah,$$
$$5.5 < \log(ft)_{exp} < 7.5\ 1u,$$
$$7.5 < \log(ft)_{exp} < 8.5\ 1h.$$

Inasmuch as the asymptotic quantum number selection rules are based on the independent particle model in the form of Nilsson's potential, one should formulate the limitations not on $\log(ft)_{exp}$, but on the quantity $\log[(ft)_{exp}R]$, since it is necessary to exclude the influence of superfluidity. Calculations carried out on the basis of the "superfluid model" show that the range of values of $\log[(ft)_{exp}R]$ narrows as compared with the range of values of $\log(ft)_{exp}$ and is shifted to the side of smaller values.

3. Two-quasiparticle levels in Hf^{178} and W^{182}

Using the "superfluid model" formulas, we calculated the two-quasiparticle levels of Hf^{178} and W^{182} and the reduced β-transition probabilities. We note that such calculations are completely unambiguous and are based on the experi-

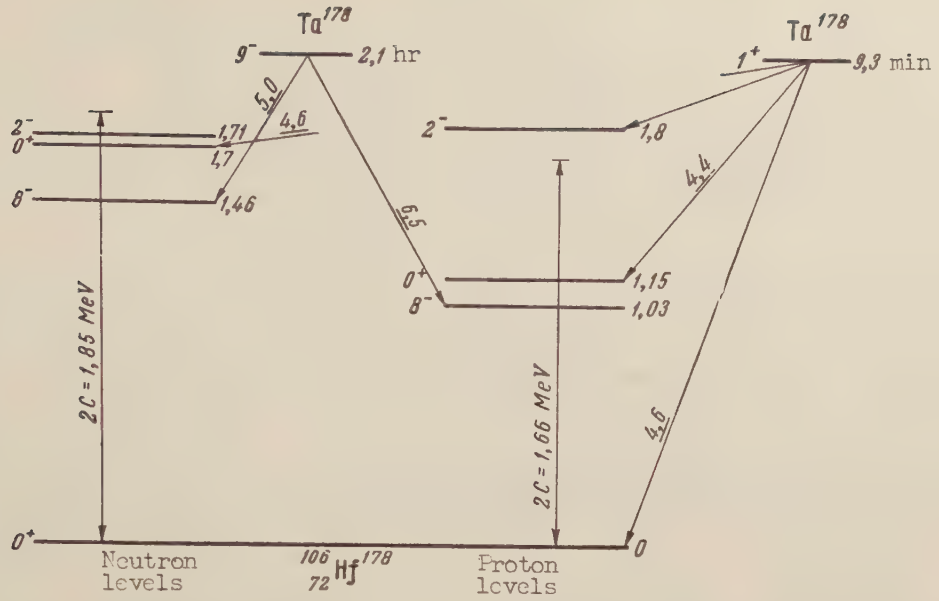

Fig.1. Calculated two-quasiparticle levels in Hf^{178} and values of $(\log ft)_{rel}$ (Relative values of $\log ft$ underlined.)

mental data on odd nuclei and pairing energies.

The calculated two-quasiparticle levels of Hf^{178} and values of $(\log ft)_{rel}$ for β-transitions of 2.1-hr Ta^{178} in the 9^- state, where $s_Z = \{^9/_2^-[514]\}$ and $s_N = \{^9/_2^+[624]\}$ and 9.3-min Ta^{178} in the 1^+ state, where $s_Z = \{^9/_2^-[514]\}$ and $s_N = \{^7/_2^-[514]\}$ are shown in Fig.1. The calculated values of $(\log ft)_{rel}$ for β-decay of 9.3-min Ta^{178} for transitions to the ground and neutron (0^+) states are in good agreement with experiment[23]; in addition, we have predicted the probabilities for β-decay of 2.1-hr Ta^{178} to the 8^- state. If it is assumed that the assignment for 2.1-hr Ta^{178} is 7^-, where $s_Z = \{^7/_2^+[404]\}$ and $s_N = \{^7/_2^-[514]\}$, then for β-decay to the 8^- neutron level we obtain $(\log ft)_{rel} = 6.9$ and to the 8^- proton level $(\log ft)_{rel} = 4.7$. The calculated energy of the 8^- proton state is in good agreement with the experimental value of 1.148 MeV, and that of the 8^- neutron level with the experimental determined value of 1.480 MeV.

The numerical agreement can be improved by introducing the $\frac{G}{2}(v_K^2 + v_{K+1}^2)$ corrections; the magnitude of these, however, lies within the limits of accuracy of the calculations. The 0^+ states with energies 1.197 MeV (this state in Ref.23 is regarded as a β-vibrational state) and 1.440 MeV can, on the basis of our calculations, be considered as two-quasiparticle states: the first a proton state (E = 1.15 MeV), and the second a neutron state (E = 1.7 MeV). We note that the calculations of the energies of the 0^+ two-quasiparticle states are carried out with appreciably lower accuracy than that characterizing the calculations of the other states. The 1^+ level with energy 1.430 MeV, detected by Gallagher et al[23], cannot be found among the two-quasiparticle levels in this energy region. We predicted a 2^- proton level with an energy of 1.8 MeV, which may be observed in $1h$ β-decay of 9.3-min Ta^{178}, if this process is energetically possible.

The calculated energy of the two-quasiparticle levels in W^{182} and values of $(\log ft)_{rel}$ for β-decays of 115-day Ta^{182}, 60-hr Re^{182} and 13-hr Re^{182} are shown in Fig.2. Apparently, 60-hr Re^{182} has spin 7^+ and $s_Z = \{^5/_2^+[404]\}$ and $s_N = \{^9/_2^+[624]\}$;

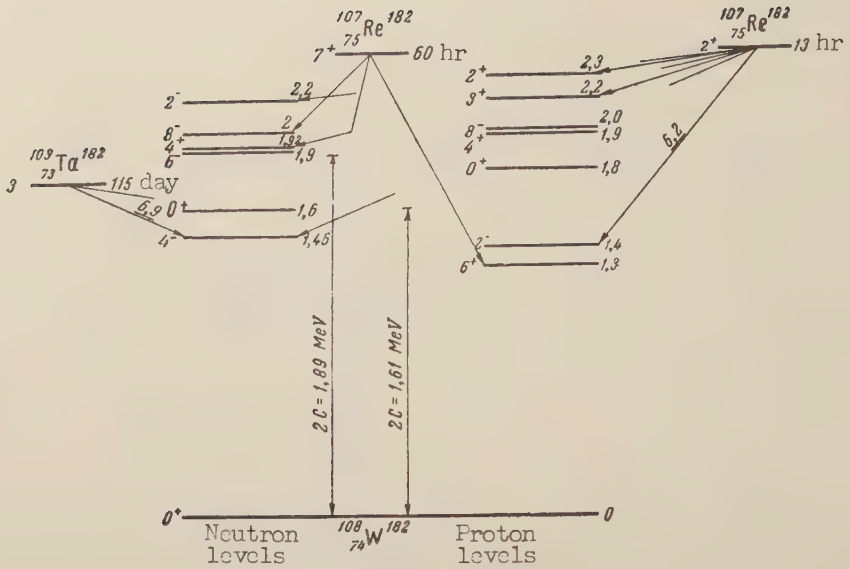

Fig.2. Calculated two-quasiparticle levels in W^{182} and values of $(\log ft)_{rel}$.

13-hr Re^{182} has spin 2^+ and the same s_Z and s_N; 115-day Ta^{182} with spin 3^- is assigned $s_Z = \{^7/_2{}^+[404]\}$ and $s_N = \{^1/_2{}^-[510]\}$ by Gallagher & Moszkowski[24]; however, in this case β-transitions to the 2^- proton levels are forbidden according to the model under consideration, whereas $(\log ft) \approx 8.3$ (Ref.22). More accurate experimental determination of the probability of this transition is essential, first, for determining the configuration of 115-day Ta^{182}, and second, for determining to what extent β-transitions belonging in the third group are retarded as compared with β-transitions classified in the first and second groups.

The calculated energy of the 2^- proton level (1.4 MeV) and the value of $(\log ft)_{rel}$ (6.2) are in satisfactory agreement with the measured energy (1.255 MeV) and $(\log ft)_{exp}$ (6.3). The calculated relative probability of the β-transition ($(\log ft)_{rel} = 6.8$) to the 4^- neutron level and the energy of this level (1.46 MeV) are in good agreement with the experimental values of Gallagher et al[25]: $(\log ft)_{exp}$ = = 6.8 and E = 1.554 MeV.

It will be seen from the calculated level spectra of Hf^{178} and W^{182} that two or three single-particle levels in each nucleus lie below the top of the energy gap $2C$. In Table 7 we list the widths of the gap, the calculated energies of the $K, K+1$ levels and the experimentally determined values of the energies of these levels. The 2^- proton level in W^{182} is the $K-1, K+1$ state in the single-particle level scheme; if, however, the $^7/_2{}^+[404]$ and $^9/_2{}^-[514]$ levels are interchanged this will be the $K, K+1$ level. It will be evident from Table 7 that the calculated dropping of the $K, K+1$ level below the width of the energy gap is substantiated by the experimental data. This effect cannot be explained by means of the initial formulation of pair correlation.

Conclusions

In the first part of the present paper we have formulated the "superfluid model" as a nuclear model based on the average field of the unified model in the form of a Nilsson potential, which takes into account pair correlations. We then investigated the general regularities involved in the model; in carrying out detailed studies, our calculations were based on the experimental data on single-

particle levels of odd nuclei, pairing energies and some reduced β-transition probabilities in odd nuclei. This basis for our calculations does not depend on the shortcomings of the unified model, and the calculations themselves are entirely unambiguous and do not involve recourse to any new parameters. We have calculated relative quantities, excluding or minimizing the influence of the average field. Calculations of this type are being continued along the line of investigation of other strongly deformed nuclei and along the line of calculating other parameters, primarily the reduced probabilities for electromagnetic transitions.

The results set forth in the second part of the work show that the proposed method makes it possible to carry out quantitative calculations of the energies of single-particle levels in even-even nuclei and the reduced probabilities of β-transitions in the region of strongly deformed nuclei.

I desire to express my deep gratitude to N.N.Bogolyubov for fruitful discussions and N.N.Govorun, I.N.Silin, Liu Yuan and N.I.Pyatov for assistance in carrying out the computations. Part of the present work was carried out during my stay at the institute of Theoretical Physics at the University of Copenhagen. I desire to thank Prof.N.Bohr for his hospitality and A.Bohr, B.Mottelson and C. Gallagher for useful discussions.

Laboratory of Theoretical Physics,
Joint Institute for Nuclear Research

References

1. N.N.Bogolyubov, Lektsii po kvantovoi statistike (Lectures on quantum statistics), Kiev, 1947; N.N.Bogolyubov, V.V.Tolmachev & D.V.Shirkov, Novyi metod v teorii sverkhprovodimosti (New method in the theory of superconductivity), M.-L. 1958.

2. N.N.Bogolyubov & V.G.Solov'ev, Doklady AN SSSR, 124, 1011 (1959). (Trans. Doklady.)

3. V.G.Solov'ev, Zhur.eksp.i teor.fiz., 35, 823 (1958)(Trans.Soviet Physics - JETP); Nucl.Phys., 9, 655 (1958/59).

4. S.T.Belyaev, Kgl.Danske Videnskab Selskab, Mat.-fys.Medd., 31, No.11 (1959).

5. V.G.Solov'ev, Zhur.eksp.i teor.fiz., 36, 1869 (1959). (Trans.Sov.Phys.-JETP.)

6. A.B.Migdal, Ibid., 37, 249 (1959) (Trans.Ibid.); Yu.T.Grin', S.I.Drozdov & D.F.Zaretskii, Ibid., 38, 222 (1960) (Trans.Ibid.); J.J.Griffin & M.Rich, Phys. Rev.Letters, 3, 342 (1959).

7. L.S.Kisslinger & R.Sorensen, Kgl.Danske Videnskab Selskab, Mat.-fys.Medd., 32, No.9 (1960).

8. S.G.Nilsson & O.Prior, Ibid., 32, No.16 (1961).

9. V.G.Solov'ev, Doklady AN SSSR, 131, 286 (1950); Nucl.Phys., 18, 161 (1960).

10. V.G.Solov'ev, Doklady AN SSSR, 133, 325 (1960) (Trans.Doklady).

11. N.N.Bogolyubov, Ibid., 119, 224 (1958) (Trans.Ibid.).

12. V.G.Solov'ev, Zhur.eksp.i teor.fiz., 40, 654 (1961) (Trans.Soviet Physics - JETP).

13. Liu Yuan, N.I.Pyatov, V.G.Solov'ev, I.N.Silin & V.I.Furman, Ibid., 40, 1503 (1961) (Trans.Ibid).

14. S.G.Nilsson, Kgl.Danske Videnskab Selskab, Mat.-fys.Medd, 29, No.16 (1955).

15. B.Mottelson & S.G.Nilsson, Mat.-fys.Skr.Dan.Vid.Selsk., 18, No.8 (1959).

16. V.G.Solov'ev, Doklady AN SSSR, 137, 1358 (1961). (Trans.Doklady.)
17. B.Harmatz, T.H.Handley & J.W.Mihelich, Phys.Rev., 119, 1345 (1960).
18. H.Morinaga & K.Nagatani, Nucl.Phys., 119, 334 (1960).
19. J.O.Newton, Phys.Rev., 117, 1520 (1960).
20. C.J.Gallagher, W.F.Edwards & G.Manning, Nucl.Phys., 19, 18 (1960).
21. C.J.Gallagher, Ibid., 16, 215 (1960).
22. Nuclear Data Sheets, Nat.Acad.Sci.Nat.Res.Council, Washington, 1960.
23. C.J.Gallagher, H.L.Nielsen & O.B.Nielsen, Preprint.
24. C.J.Gallagher & S.A.Moszkowski, Phys.Rev., 111, 1282 (1958).
25. C.J.Gallagher, J.O.Newton & V.Shirley, Ibid., 113, 1298 (1959).
26. Felber, Stephens & Asaro, J.Inorg. & Nucl.Chem., 7, 153 (1958).

$Yb^{166} \rightarrow Tm^{166} \rightarrow Er^{166}$ DECAY CHAIN

- E.P.Grigor'ev, K.Ya.Gromov, B.S.Dzhelepov, Zh.T.Zhelev, V.Zvol'ska & I.Zvol'skii

The transformations and transitions occurring in the $Yb^{166} \rightarrow Tm^{166} \rightarrow Er^{166}$ chain have been studied and checked by many authors.[1-12] Investigation of the sequence of excited states in the even-even deformed nucleus Er^{166} is of great interest inasmuch as the experimental data in this case can be compared with the predictions of the unified model theory. The principal purpose of the present investigation was to refine and supplement the available data on the levels in Er^{166}.

1. Experimental Conditions

The sources used for investigating the conversion electron spectra of Yb^{166} and Tm^{166} were prepared of the ytterbium fraction obtained by chromatographic separation from the rare earths produced in spallation of a tantalum target with 660 MeV protons. In the conversion electron spectrum of the ytterbium fraction, in addition to Yb^{166} and Tm^{166} electrons, there are evinced conversion electrons from Yb^{169}; however, identification of these presents no difficulties inasmuch as the conversion electron spectrum of Yb^{169} has been thoroughly investigated, and moreover, the half-life of Yb^{169} is relatively long (33 days). Measurements were carried out with several sources obtained as the result of 2 hour bombardment of the tantalum target and with two sources extracted from targets bombarded for 12 hours. We investigated most of the transitions by means of a double focusing β-spectrometer; the spectrometer field was monitored by the method of proton magnetic resonance, which made it feasible to determine the conversion electron energies with an accuracy to 0.05-0.10%. The apparatus half-width of the conversion lines in these measurements was ~0.2%. The positron spectrum was investigated by means of a triple focusing β-spectrometer.

2. Measurement Results

Our data on the energies of the γ-transitions in Er^{166} and the relative intensities of the K conversion lines are shown in Table 1, where, for comparison, we also give the data of Brabets et al[2] and Jacob et al[6]. Jacob et al estimate the error in their energy values as 0.15%; our data agree with their results within the limits of this error. There is, however, an appreciable divergence between our data and those of Brabets et al in the range of high energies. We also obtained a more accurate value for the energy of the transition from the excited level of Tm^{166} to the ground state. The line at 690 keV, which was identified by Brabets et al as K749, is, apparently, the M line of a 691.9 keV transition.

Successive sections of the conversion electron spectrum of Tm^{166} are shown in Figs.1, 2 & 3.

The measured transition energies allow of determining the energies of the excited levels in Er^{166}. The results of different ways of evaluating the level energies are listed in Table 2. It will be seen that there is good agreement as regards the level energy values deduced on the basis of different cross-over and cascade transitions.

We feel there can be no doubt regarding the existence of the levels and transitions listed in Table 2 and shown in the decay scheme of Fig.4. Of the 47 transitions listed in Table 1, 32 have been fitted into the decay scheme; it is obvious, therefore, that the proposed decay scheme requires further elaboration.

Table 1

Energies of γ-transitions in Er^{166} and relative intensities of the K conversion lines

No.	Brabets et al[2]		Jacob et al[6]		Our data	
	hν, keV	I	hν, keV	I	hν, keV	I
1	80	L1640 (M+N)450	80,6	L1200 (M+N)435	82,3 in Tm^{166} 80,6	1670 420
2	—	—	84,1	1,1	—	—
3	—	—	147,2	0,97	147,4	0,59
4	153,4	4	154,3	3,64	154,6	3,1
5	—	—	170,0	0,79	170,1	0,48
6	183,9	100	184,5	100	184,4	100
7	193,6	11	194,7	10,3	194,8	8,3
8	214,1	8,4	215,1	8,7	215,4	7,3
9	282	0,84	280,2	0,81	280,5	0,56
10	299	0,77	—	—	298,3	0,57
11	347	—	345,5	2,1	346,1	1,2
12					390,4	0,12
13	405	1,0	403,8	2,0	403,9	1,2
14	—	—	—	—	410,6	0,09
15	—	—	—	—	412,8	0,06
16	433	0,45	—	—	430,4	0,12
17	459	2,7	459,3	4,9	459,7	3,3
18	—	—	—	—	472,5	0,10
19	522	0,13	—	—	521,2	0,08
20	—	—	—	—	530,4	0,09
21	596	1,0	595,0	1,5	594,8	0,97
22	598	0,27	—	—	599,0	0,27
23	—	—	—	—	604,7	0,1
24	674	0,77	672,9	0,91	673,1	0,52
25	—	—	675,4	0,39	675,5	0,17
26	693	1,45	692,3	2,2	691,9	1,76
27	707	2,4	706,2	3,4	705,8	2,8
28	749	0,18	—	—	—	—
29	760	0,77	758,9	1,4	758,9	0,80
30	782	2,7	780,0	4,4	779,6	3,6
31	789	1,2	787,1	2,3	786,8	1,77
32	(807)	—	—	—	811,1	0,15
33	877	0,55	876,9	0,73	875,9	0,66
34	—	—	1081,6	weak	1080,0	0,18
35	1158	0,23	1155,2	0,43	1153,8	0,32
36	1181	1,2	1179,8	1,3	1178,2	1,3
37	1209	0,14	—	—	1204,5	0,18
38	1277	1,7	1276,9	1,9	1275,0	2,0
39	1309	0,1	1304,3	0,13	1302,7	0,20
40	—	—	1350,4	0,14	1348,1	0,17
41	1380	0,59	1377,6	0,57	1375,9	0,60
42	(1423)	0,1	—	—	—	—
43	—	—	—	—	1433,5	0,10
44	—	—	1451,2	0,15	1450,1	0,17
45	—	—	1508,5	0,10	1507,2	0,12
46	—	—	—	—	1624*	0,08
47	1878	0,37	—	—	1868,9	0,16
48	—	—	—	—	1898**	0,05
49	2060	0,68	—	—	2053,6	0,65
50	2088	0,27	—	—	2080,2	0,2

*This transition was first detected in the measurements with the triple focusing β-spectrometer.

**This transition was detected by V.G.Chumin by means of a uniform field β-spectrometer.

Er^{166} level energies determined on the basis of different transition cascades

Table 2

Level energy, keV	Sum of energies determining the level, keV
80,6	Cross-over 80,6
265,0	80,6+184,4= 265,0
545,5	265,0+280,5= 545,5
786,5	Cross-over 786,8
	80,6+705,8= 786,4
	265,0+521,2= 786,2
860,0	80,6+779,6= 860,2
	265,0+594,8= 859,8
956,5	80,6+875,9= 956,5
	265,0+691,9= 956,9
	786,5+170,1= 956,6
	545,5+410,6= 956,1
1075,8	265,0+811,1=1076,1
	545,5+530,4=1075,9
	860,0+215,4=1075,4
1535,4	860,0+ 675,5=1535,5
	1075,6+ 459,7=1535,2
1940,0	786,5+1153,8=1940,3
	860,0+1080,0=1940,0
	1535,4+ 403,9=1939,3
2134,6	80,6+2053,6=2134,2
	265,0+1868,9=2133,9
	786,5+1348,1=2134,6
	860,0+1275,0=2135,0
	956,5+1178,2=2134,7
2161,7	80,6+2080,2=2160,8
	265,0+1898,0=2163,0
	786,5+1375,9=2162,4
	860,0+1302,7=2162,7
	956,5+1204,5=2161,0

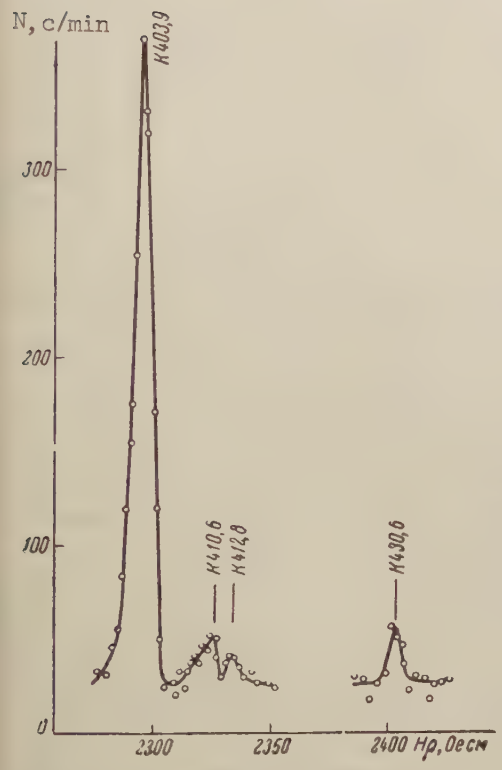

Fig.1. 350 to 380 keV section of the conversion electron spectrum.

The positron spectrum proved to be complex. It consists of two components with end-point energies 1940 ± 20 and 1080 ± 100 keV (Fig.5). The intensity ratio $I_{1940}/I_{1080} = 6.7$. There may also be a weak component with end-point energy ~450 keV.

We also determined the intensity ratio of the positron spectrum and the conversion lines:

$$\frac{I_{\beta+}}{I_{K+L+M\,(2054+2080)}} = 0.0145.$$

Using the data of Table 3, we find that the number of positrons per 100 disintegrations is 1.8. The 1940 keV component of the β^+-spectrum may be either an allowed or a unique transition depending on the parity of the ground state of Tm^{166}.

The $I_K/I_{\beta+}$ ratio for a β-decay energy of 2 MeV is 3.2 for allowed transitions and 10 for unique ones. The fraction of transitions to the 80.6 keV level for the high energy component of the positron spectrum is unknown; consequently, in the decay scheme (Fig.4) we have indicated the extreme values for the intensity of this component. Analogous observations apply to the β^+-spectrum with end-point energy 1080 keV, which feeds the levels of the second rotational band.

3. Intensity Balance of the Transitions between the Levels of Er^{166}

Knowing the intensities of the conversion lines and the multipole orders of the transitions, one can, on the basis of the theoretical conversion coefficients, determine the total relative transition intensities:

$$I = I_K + I_L + I_{M+N} + I_\gamma.$$

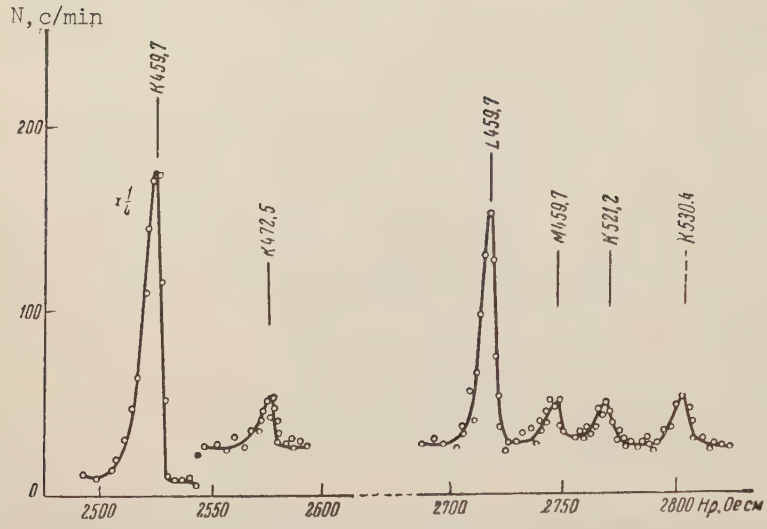

Fig.2. 400 to 415 and 445 to 480 keV sections of the conversion electron spectrum.

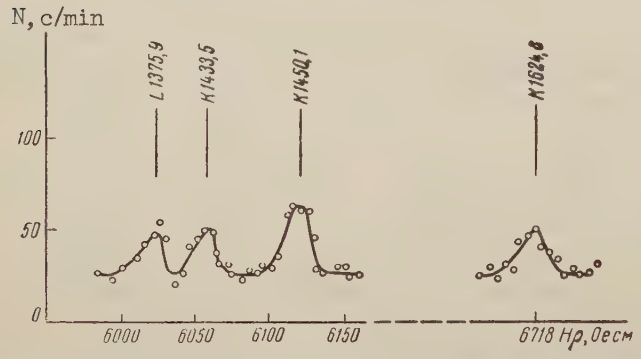

Fig.3. 1360 to 1400 and 1570 keV sections of the conversion electron spectrum.

The uncertainty in determining the conversion line intensities amounts to 5-10% for the strong transitions and up to 20% for the weak ones. The error in the calculated transition intensities equals ~10% if the multipole order is known precisely; this is often the case inasmuch as transitions between rotational levels in even-even nuclei are generally E2 or E2 with a small admixture of M1. On the basis of the γ-ray intensities reported by Baranovskii & Pokrovskii[1] and the measured intensities of the conversion lines one can evaluate the conversion coefficients for a number of transitions and hence draw certain inferences regarding their multipolarity. Precise determination of the conversion coefficients is impossible because the γ-ray intensities have as yet not been determined with adequate accuracy, owing to the complexity of the γ-spectrum. For calculating the transition intensities we assume the multipole orders obtained from the data on the conversion coefficients. We assume that the transitions between rotational levels are pure E2. The intensities of the γ-lines associated with the transitions from the two upper levels of Er^{166} were calculated on two assumptions regarding the multipolarities, namely, E2 and M1; the figures given first in Table 3 are for E2.

There are transitions to the ground state of Er^{166} from only two levels; 80.6 (2^+) and 786.5 keV (2^+); no cross-over transitions to the ground state from any of the other nine levels listed in Tables 2 and 4 have been observed. Neglecting β-transitions to the ground state (evaluations show that their abundance does not exceed 5%) and possible γ-transitions from the highest lying levels to the ground state, we conclude that the total intensity of the two transitions to the ground state $I_{80.6} + I_{786.5} = 100\%$. The intensities of the other transitions accomodated in the decay scheme (Fig.4 & Table 3) were calculated on this assumption.

The total intensity of the 15 transitions that were detected but not accomodated in the proposed decay scheme (Fig.4) is 50% if it is assumed that all these transitions are E1, 20% if E2 and 11% if M1; these figures indicate the magnitude of the error that may arise owing to the above assumption. The intensities of the transitions arriving and departing from the various levels can be balanced if of the two possible multipole orders for the 1178.2 and 1275.0 keV transitions one chooses M1 (Table 4).

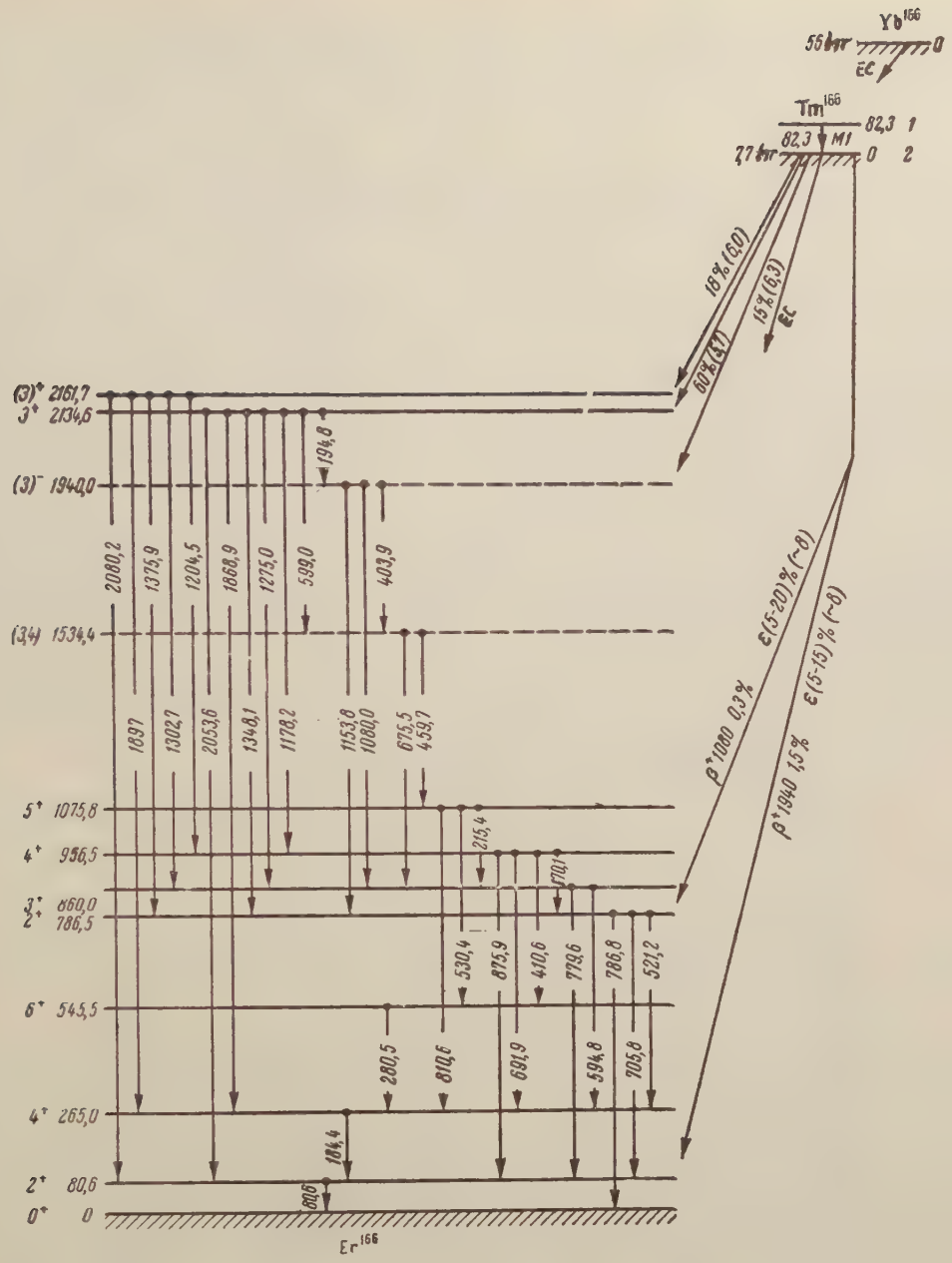

Fig.4. $Yb^{166} \rightarrow Tm^{166} \rightarrow Er^{166}$ decay scheme.

4. Er^{166} Level Diagram

The existence of two rotational bands in Er^{166} was proved in earlier investigations.[6,9,12] On the basis of our data one can draw the further inference that there is a 5^+ level in the second rotational band, the energy of which is defined by three transitions to lower lying levels and is in good agreement with the results of calculations by the formula for rotational levels.

The locations of the higher lying levels were inferred from the energies of the transitions arriving from these levels (Fig.4). The following inferences

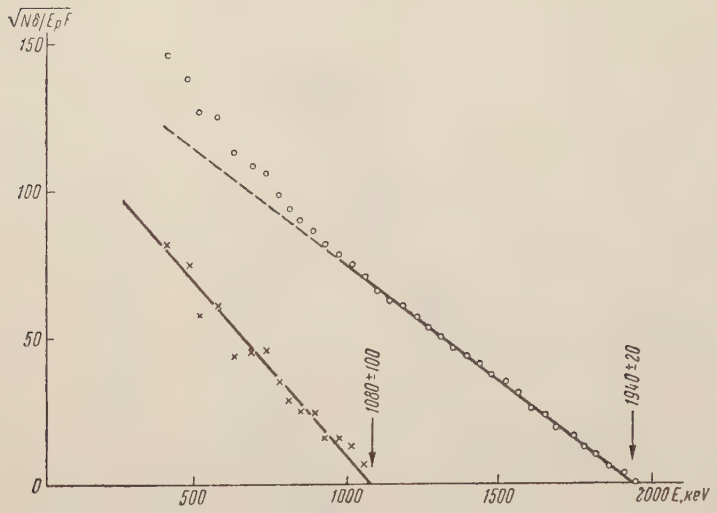

Fig.5. Kurie plot for the β^+-spectrum of Tm^{166}.

regarding the characteristics of the levels in Er^{166} may be drawn from the data of Table 4:

1. The multipole order of the 1778.2 keV transition departing from the 2134.6 keV level to the 956.5 keV (4^+) level is M1. This follows from the intensity balance for the 956.5 keV level. Hence of the two possible spin values for the 2134.5 keV level - 2 and 3 - there remains only the latter (the spin cannot be 4, inasmuch as this level is strongly populated in the decay of Tm^{166}, the spin of which is known to be 2 (Ref.5)).

2. The intensity balance for the 786.5, 860.0, 856.5 and

Table 3

Intensities of conversion electrons and γ-rays and total transition abundances per 100 disintegrations

E_γ, keV	I_K	Multipole order	$\alpha_K \cdot 10^3$	I_γ	I
80,6	77,2*	*E*2	—	12	89,2
170,1	0,014	*E*2	250	0,056	0,07
184,4	2,79	*E*2	200	14,0	18,7
194,8	0,24	*E*1	45	5,3	5,6
215,4	0,21	*E*2	128	1,63	1,9
280,5	0,016	*E*2	61	0,26	0,28
403,9	0,033	*E*1	7,4	4,5	4,55
410,6	0,0026	*E*2	21,8	0,12	0,12
459,7	0,092	*E*2, *M*1	15,6; 38	5,9; 2,4	6,0; 2,5
521,2	0,0023	*E*2	11,8	0,2	0,2
530,4	0,0026	*E*2	11,2	0,23	0,23
594,8	0,028	*E*2	8,8	3,2	3,2
599,0	0,0075	*E*2, *M*1	8,6; 18,5	0,87; 0,40	0,87; 0,40
675,5	0,0047	*E*2, *M*1	6,4; 13,5	0,74; 0,35	0,74; 0,35
691,9	0,049	*E*2	6,2	7,9	7,9
705,8	0,078	*E*2	5,8	13,4	13,4
779,6	0,10	*E*2	4,7	21,3	21,3
786,8	0,0495	*E*2	4,6	10,7	10,8
811,1	0,004	*E*2	4,2	1,0	1,0
875,9	0,019	*E*2	3,7	5,1	5,1
1080,0	0,0050	*E*1	0,98	5,1	5,1
1153,8	0,0089	*E*1	0,88	10,1	10,1
1178,2	0,036	*E*2, *M*1	2,0; 3,5	18; 10	18; 10
1204,5	0,005	*E*2, *M*1	1,95; 3,3	2,5; 1,5	2,5; 1,5
1275,0	0,056	*E*2, *M*1	1,72; 2,9	33; 19	33; 19
1302,7	0,0056	*E*2, *M*1	1,65; 2,7	3,4; 2,1	3,4; 2,1
1348,1	0,0048	*E*2, *M*1	1,55; 2,5	3,1; 1,9	3,1; 1,9
1375,9	0,017	*E*2, *M*1	1,48; 2,4	11,5; 7,1	11,5; 7,1
1868,9	0,0045	*E*2, *M*1	0,87; 1,18	5,3; 3,8	5,3; 3,8
1898	0,0014	*E*2, *M*1	0,84; 1,15	1,7; 1,2	1,7; 1,2
2053,6	0,0186	*E*2, *M*1	0,72; 0,96	24; 19,4	24; 19,4
2080,2	0,0056	*E*2, *M*1	0,70; 0,93	8; 6	8; 6

* I_{e^-}.

2161.6 keV levels clearly indicates that the multipolarities of the transitions departing from the 2161.7 keV level cannot be E1, inasmuch as in this case their intensities would be two times higher than in the E2 case. From this it follows that the parity of the 2161.7 keV level is even.

5. Comparison of the experimental Data with the Deductions from the Theories of Axial and Nonaxial Nuclei

According to the Bohr-Mottelson unified nuclear model, the four lowest levels in Er^{166} constitute a rotational band with K = 0, and the four next levels belong to the band with K = 2 based on the 786.5 keV level, which is a γ-rotational level. According to the Davydov-Filippov theory of nonaxial nuclei, all these levels belong to one ground state rotational band. In Table 5 we give the comparison of the experimental energy values of these rotational levels with the theoretical values tabulated according to the two theories.[13,14] We calculated the theoretical data both in the adiabatic approximation and with corrections for nonadiabaticity .

Precise determination of the level energies allows of calculating the parameters A and B for the rotational bands, i.e., the moments of inertia of the nucleus and the magnitude of the coupling between the rotation of the nucleus and its other forms of motion. These parameters are given by the familiar Bohr-Mottelson formula:

$$E^* = E_0 + A\,[I(I+1) - I_0(I_0+1)] - B\,[I(I+1) - I_0(I_0+1)]^2.$$

For the lower rotational band:

$$A_1 = 13.51 \pm 0.03 \text{ keV},$$
$$B_1 = 0.013 \pm 0.003 \text{ keV}.$$

For the rotational band based on the 786.5 keV level:

$$A_2 = 12.33 \pm 0.13 \text{ keV},$$
$$B_2 = 0.014 \pm 0.008 \text{ keV}.$$

The small values of the parameter B are characteristic of isotopes in the middle of the region of deformed nuclei.

For the nonaxiality parameter γ in the Davydov-Filippov theory (this parameter is determined from the experimental ratio of the excitation energies of the two lowest 2^+ type levels) we obtained $\gamma = 12.68^\circ$. We determined the theoretical value of $E_i/E(2_1^+)$ from the tables of Moore & White[15]. In taking into account the correction for nonadiabaticity[14], we obtained a value of 12.56° for γ for a nonadiabaticity parameter $\mu = 0.172$.

The comparison presented in Table 5 shows that corrections for nonadiabaticity substantially improve both theories as far as agreement with experiment is concerned.

From the measured intensities of the conversion lines one can calculate the reduced transition probabilities and compare their ratios with the theoretical ratios calculated on the basis of the unified model (Alaga's rules) and the theory of nonaxial nuclei. The experimental and theoretical reduced probability ratios for the transitions between the levels of the first and second rotational bands are compared in Table 6. It was assumed that the multipole order of all the transitions is E2.

In column 6 of Table 6 we list the theoretical values calculated according to Alaga's rules but with the correction $f(z, I_i, I_f)$, which takes into account mixing

Table 4

Intensity balances in the Er^{166} decay scheme

Level	Arriving from higher levels		Departing lower levels		Percent electron capture
	E_γ, keV	I, %	E_γ, keV	I, %	
0	80,6 786,8	89,2 10,8 100 (assumed)		0	<5
80,6	184,4 705,8 779,6 811,1 875,9 2053,6 2080,2	18,7 13,4 21,3 1,0 5,1 24; 19,4 8; 6 91,0; 84,4	80,6	89,2 89,2	~(1—5)
265,0	280,5 521,2 594,8 691,9 1868,9 1898	0,28 0,2 3,2 7,9 5,3; 3,8 1,7; 1,2 18,6; 16,6	184,4	18,7 18,7	~(1—5)
545,5	410,6 530,4	0,12 0,23 0,35	280,5	0,28 0,28	0
786,5	170 1153,8 1348,1 1375,9	0,07 10,7 3,1; 1,9 11,5; 7,1 25,4; 19,8	521,2 705,8 786,8	0,2 13,4 10,8 24,4	~(1—5)
860,0	215,4 675,5 1080 1275,0 1302,7	1,9 0,74; 0,35 5,1 33; 19 3,4; 2,1 44,2; 28,4	594,8 779,6	3,2 21,3 24,5	~(1—5)
956,5	1178,2 1204,5	18; 10 2,5; 1,5 20,5; 11,5	170,1 410,6 691,9 875,9	0,07 0,12 7,9 5,1 13,2	~(1—3)
1075,8	459,7	6,0; 2,5 6,0; 2,5	215,4 530,4 811,1	1,9 0,23 1,0 3,1	—
1535,4	403,9 599,0	4,55 0,9; 0,4 5,5; 5,0	459,7 675,5	6,0; 2,5 0,74; 0,35 6,7; 2,9	—
1940,0	194,8	5,6 5,6	403,9 1080,0 1153,8	4,55 5,1 10,7 20,3	15

(Table 4 continued)

Level	Arriving from higher levels		Departing lower levels		Percent electron capture
	E_γ, keV	I, %	E_γ, keV	I, %	
2134,6	—	—	194,8 599,0 1178,2 1275,0 1348,1 1868,9 2053,6	5,6 0,9; 0,4 18; 10 33; 19 3,1; 1,9 5,3; 3,8 24; 19,4	
				89,9; 60,1	90; 60
2161,7	—	—	1204,5 1302,7 1375,9 1898 2080,2	2,5: 1,5 3,4; 2,1 11,5; 7,1 1,7; 1,2 8; 6	
				27,1; 17,9	27; 18
					132; 93

Table 5

Energies (in keV) of the rotational levels in Er^{166} (Comparison of the experimental results with the data calculated on the basis of the theories of axial and nonaxial nuclei)

Level	Experiment	Theory			
		Adiabatic approximation		With correction for nonadiabaticity	
		axial nuclei	nonaxial nuclei	axial nuclei	nonaxial nuclei
		A_1=13,43 (for 4_1^+ & 6_1^+) A_2=12,25 (for 4_2^+ & 5_1^+)	μ=0 γ=12,68	A_1=13,51 B_1=0,013 (for 4_1^+ & 6_1^+) A_2=12,33 B_2=0,014 (for 4_2^+ & 5_1^+)	μ=0,173 γ=12,56
2_1^+	80,6	80,6*	80,6*	80,6*	80,6*
4_1^+	265,0	268,6	266,0	265,0*	265,0*
6_1^+	545,5	564,0	551,5	544,5	545,0
2_2^+	786,5	786,5*	786,5*	786,5*	786,5*
3_1^+	860,0	860,0*	867,3	860,0*	864,8
4_2^+	956,5	958,0	978,5	956,4	968,8
5_1^+	1075,8	1080,5	1108,2	1074,3	1090,5

*Taken from experiment.

Table 6

Ratio of reduced probabilities for γ-transitions in Er^{166} (Comparison of experimental and theoretical data)

Ratio of reduced transition probabilities	Experiment			Theory		
				Axial nuclei		Nonaxial nuclei
	Our data	Ref.6	Ref.2	no correction	with Mottelson's correction z = 0.032	γ=12,7°
$B(2_2^+ \to 4_1^+) : B(2_2^+ \to 2_1^+) : B(2_2^+ \to 0)$	0,07 : 1 : 0,58	—:1 : 0,51	—:1 : 0,37	0,05 : 1 : 0,70	0,074:1: 0,58*	0,06 : 1 : 0,45
$B(4_2^+ \to 6_1^+) : B(4_2^+ \to 4_1^+) : B(4_2^+ \to 2_1^+)$	0,20 : 1 : 0,21	—:1 : 0,17	—:1 : 0,13	0,09 : 1 : 0,34	0,16 : 1 : 0,21	0,15 : 1 : 0,11
$B(3_1^+ \to 4_1^+) : B(3_1^+ \to 2_1^+)$	0,57	0,71	0,78	0,40	0,61	0,64

*The $B(2_2^+ \to 2_1^+) : B(2_2^+ \to 0)$ ratio was used for determining z.

of the states with K = 2 and K = 0. The form of the correction $f(z, I_i, I_f)$ for transitions from levels of a band where K = 2 to the levels of a band with K = 0 was determined by Mottelson[16]. It will be evident from Table 6 that the experimental results are in best agreement with the values determined according to Alaga's rule with the Mottelson correction. Apparently, in Er^{166} there is mixing of the states of different rotational bands. For a number of other even-even nuclei, for example, Gd^{156} and Dy^{160}, introduction of the correction $f(z, I_i, I_f)$ also leads to improvement of the agreement between the experimental and theoretical reduced transition probability ratios. As a rule, the experimental values lie between the theoretical values calculated according to the theories of axial and nonaxial nuclei.[17]

I take this opportunity to thank V.A.Khalkin for preparing the source.

Leningrad State University &
Joint Institute for Nuclear Research

References

1. V.I.Baranovskii & V.P.Pokrovskii, Izv.AN SSSR, Ser.fiz., 23, 819 (1959). (Trans.Bulletin, 23, 813.)

2. V.Brabets, K.Ya.Gromov, B.S.Dzhelepov, A.G.Dmitriev & V.A.Morozov, Ibid., 23, 812 (1959). (Trans.Bulletin, 23, 805.)

3. E.P.Grigor'ev, B.S.Dzhelepov & A.V.Zolotavin, Ibid., 23, 188 (1959). (Trans.Bulletin, 23, 180.)

4. E.P.Grigor'ev, B.S.Dzhelepov & A.V.Zolotavin, Ibid., 23, 864 (1959). (Trans.Bulletin, 23, 855.)

5. J.C.Walker & D.L.Harris, Phys.Rev.Letters, 5, 453 (1960).

6. K.P.Jacob, J.W.Mihelich, B.Harmatz & T.H.Handley, Phys.Rev., 117, 1102 (1960).

7. P.Boskma & H.deWaard, Nucl.Phys., 12, 533 (1959).

8. E.Bozek, H.Niewodniczanski, Yu.V.Norseev, S.Ogaza & S.Szymczyk, Energy Levels in Er^{166}, Report No.163/OFJ, Polska Akademia Nauk.

9. R.Wilson & M.Pool, Phys.Rev., 119, 262 (1960).
10. B.S.Dzhelepov & L.K.Peker, Skhemy raspada radioaktivnykh yader (Decay schemes of radioactive nuclei), M., 1958.
11. K.Jacob, J.Mihelich, B.Harmatz & T.Handley, Bull.Amer.Phys.Soc., Ser.2, 3, 358 (1958).
12. K.Ya.Gromov, B.S.Dzhelepov & V.P.Pokrovskii, Izv.AN SSSR, Ser.fiz., 23, 821 (1959). (Trans.Bulletin, 23, 815.)
13. A.S.Davydov & G.F.Filippov, Zhur.eksp.i teor.fiz., 35, 440 (1958). (Trans.Soviet Physics - JETP.); Nucl.Phys., 8, 237 (1959).
14. A.S.Davydov & A.A.Chaban, (?), 20, 499 (1960).
15. R.B.Moore & W.White, Canad.J.Phys., 38, No.9 (1960).
16. P.G.Hansen, O.B.Nielsen & R.K.Sheline, Nucl.Phys., 12, No.4 (1959).
17. E.Grigor'ev & M.P.Avotina, Izv.AN SSSR, Ser.fiz., 24, 324 (1960). (Trans. Bulletin, 24, 311.)

COINCIDENCES BETWEEN CONVERSION ELECTRONS EMITTED IN THE DECAY OF Ho^{160} TO Dy^{160}

- B.S.Dzhelepov, I.Zvol'skii & V.A.Sergienko

Decay of Ho^{160} to Dy^{160} has been investigated by several groups.[1-12] It has been established that in the process of electron capture and β^+-decay of Ho^{160} there form many excited states of Dy^{160}, between which there occur more than 70 different transitions. On the basis of the radiations emitted in $Ho^{160} \xrightarrow{EC,\beta^+} Dy^{160}$ decay[1-9] and $Tb^{160} \xrightarrow{\beta^-} Dy^{160}$ decay[13-25], as well as the inferences following from the unified nuclear model, there was proposed a level diagram for Dy^{160} (see Refs. 7 & 9). The purpose of the present work was to check and refine the $Ho^{160} \rightarrow Dy^{160}$ decay scheme by the method of e-e coincidences.

I. Experimental Conditions

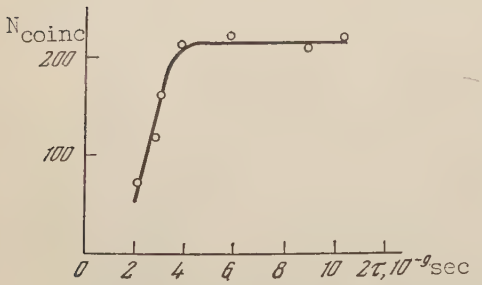

Fig.1. Variation of the coincidence counting rate as a function of the resolving time 2τ of the coincidence circuit.

We investigated the coincidences between the conversion electrons emitted in decay of Ho^{160} on the twin lens β-spectrometer described in Ref.26. By way of electron source we used Er^{160}(T = 29.4 hrs) which converts by electron capture to Ho^{160}(T = = 4.6 hrs). The conversion electron spectrum of the $Er^{160} \rightarrow Ho^{160} \rightarrow Dy^{160}$ chain differs from the electron spectrum of $Ho^{160} \rightarrow Dy^{160}$ only by the presence of the conversion lines from the 60.1 keV transition in Ho^{160}.

The Er^{160} was obtained by chromatographic separation from the rare earths formed as a result of bombardment of a tantalum target with 660 meV protons. The activity in the form of the lactate was deposited on a thin lightly aluminized collodion film. The diameter of the sources was 4-5 mm. The films were sufficiently thin so that electron scattering in them had virtually no effect on the line shape. The singles electron spectra recorded by both halves of the spectrometer had virtually the same appearance; the counting rate for the two halves in detecting electrons of the same energy did not differ by more than 10%.

By way of electron detectors we used scintillation counters coupled to FEU-33 photomultipliers. The operation of the counters and associated electronic circuit is illustrated in Fig.1, the curve in which characterizes the variation of the coincidence counting rate with the resolving time 2τ of the coincidence circuit for ~60 keV electrons (coincidence between the K114.5 and K115.3 electrons of Gd^{146}). It will be evident that for resolving times shorter than $4 \cdot 10^{-9}$ sec the coincidence counting efficiency remains virtually constant.

II. Results

The levels of Dy^{160}, excited in the decay of Ho^{160} (Fig.2), form one of the most complicated diagrams known at present. The 0 (0^+), 86.7 (2^+), 283.7 (4^+) and 581.4 keV (6^+) levels constitute a first rotational band with K = 0, while the 966.5 (2^+), 1049.5 (3^+), 1156.4 (4^+) and 1289 keV (5^+) levels make up a second rotational band with K = 2. In addition to these levels, there are many higher lying levels up to 2922 keV.[9]

We investigated coincidences between conversion electrons with energies to 1000 keV, namely,

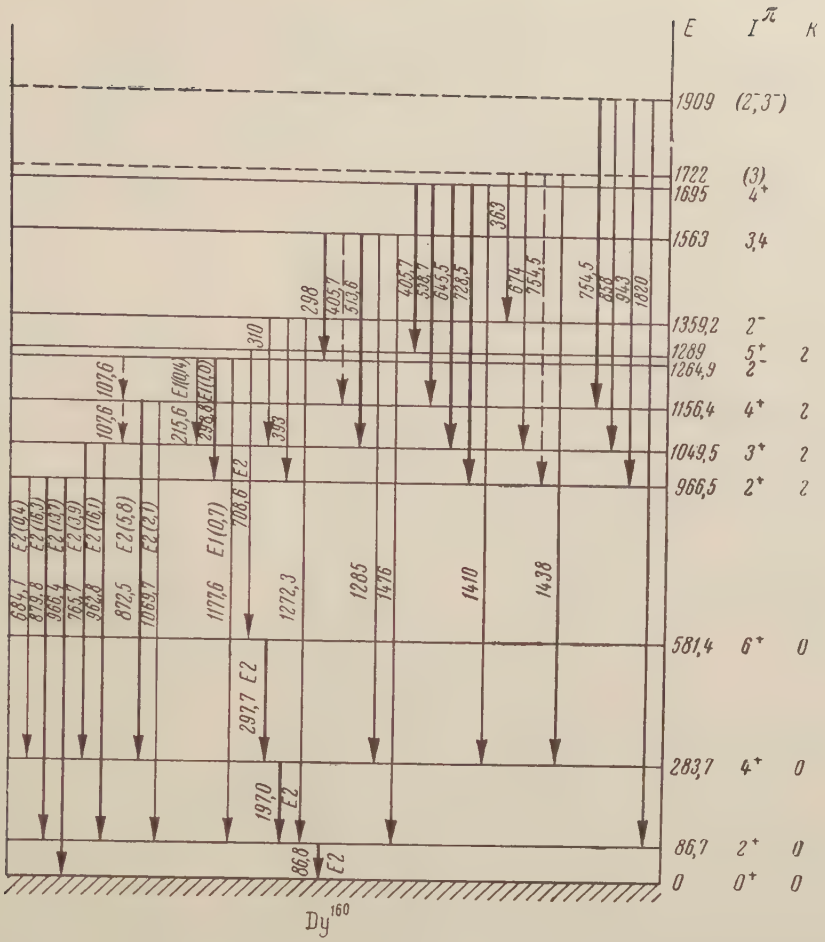

Fig.2. Investigated section of the level diagram of Dy^{160} (levels excited in the decay of Ho^{160}). The figures in parentheses indicate the relative intensities of the transitions in percent referred to the transitions to the ground state. The heavy lines denote the transitions of the detected and investigated cascades.

1) coincidences between conversion electrons from the 86.8, 197.0 and 297.7 keV transitions departing from the levels of the first rotational band;

2) coincidences of conversion electrons from the transitions between the levels of the first and second rotational bands (765.7, 872.5, 879.8, 962.8 and 966.4 keV transitions) with the conversion electrons of the 86.8 and 197.0 keV transitions;

3) coincidences of the conversion electrons from the transitions feeding the levels of the second rotational band (the 107.6, 298.8, 405.7, 513.6, 538.7, 645.5, 728.5 and 754.5 keV transitions) with the electrons of the transitions de-exciting the levels of the first and second rotational bands (transitions with $h\nu$ = 86.8, 197.0, 297.7, 872.5, 879.8, 962.8 and 966.4 keV);

4) coincidences between the electrons of the components of the complex K(297.7 + 298.8) line.

The conversion electron spectrum up to 1000 keV recorded in the half of the spectrometer viewing the activity side of the source is reproduced in Fig.3. There are clearly discernible Ho^{160} conversion electrons from transitions with

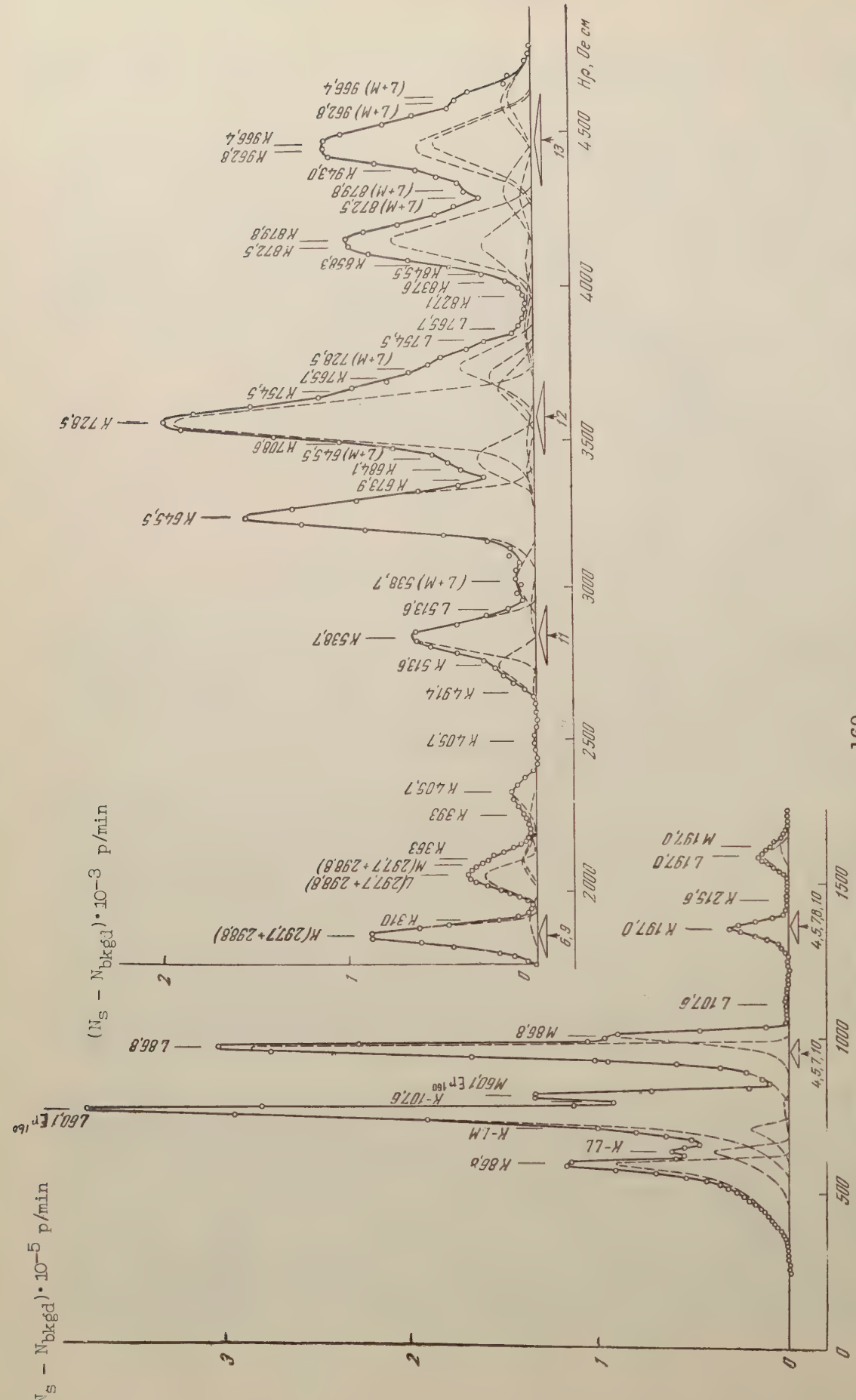

Fig.3. Conversion electron spectrum of Er^{160} to 1000 keV, recorded by one half of the spectrometer one day after separation of the erbium fraction. The dashed curves give the resolved components of the complex lines; the resolution was carried out on the basis of the data on the relative intensities of the conversion electrons determined in the work of Ref.9. The triangles with arrows under the spectrum indicate the energy settings of the "fixed" half of the spectrometer in measuring coincidences; the numerals under the arrows denote the numbers of the figures in which the corresponding coincidence spectra are presented.

Table 1

Results of investigation of the coincidences between the conversion electrons emitted in $Ho^{160} \rightarrow Dy^{160}$ decay

Line detected by first spectrometer	Counting rate at peak $(N_1-N_{bkgd})\cdot 10^{-3}$, p/min	Line detected in second spectrometer	Counting rate at peak (N_2-N_{bkgd}) 10^{-3} p/min	Coincidences per hour		
				Total	Chance	True
*L*86,8	3100	*L*107,6	5,8	1 061	247	814
		*K*197,0	220	35 954	854	35 100
		*K*298	6,4	1 100	85	1 015
		*K*513,6	~1,5	~263	13	~250
		*K*538,7	4,8	892	42	850
		*K*645,5	11	1 912	63	1 849
		*K*728,5	14,8	1 663	63	1 600
		K(754,5+765,7)+*L*728,5	~5	817	29	789
		K(872,5+879,8)	7,2	1 406	42	1 364
		K(962,8+966,4)	8,2	854	53	801
*K*197,0	220	*L*107,6	5,8	112	6	120
		*K*298	6,4	252	7	245
		*K*405,7	1	66	10	56
		*K*513,6	~1,5	~33	3	~30
		*K*538,7	4,8	178	6	172
		*K*645,5	11	135	8	127
		*K*728,5	14,8	⩽22	8	⩽14
		K(754,5+765,7)+*L*728,5	~5	132	8	124
		K(872,5+879,8)	7,2	109	10	99
*K*298	6,8	*K*298	6,4	14,2	5,6	8,6
*K*298	6,4	*K*405,7	1	8	2	6
*K*538,7	5,2	*K*(872,5+879,8)	7,2	9,4	2,8	6,6
*K*728,5	14,4	*K*(872,5+879,8)	7,2	20	5	15
*K*962,8+ +*K*966,4	8,4	*K*645,5	11	10	2,8	7,2
		*K*728,5	14,8	8,7	2,2	6,5

energies 86.8, 107.6, 197.0, (297.7 + 298.8), 405.7, 538.7, 645.5, 728.5, (872.5 + + 879.8), and (962.8 + 966.4) keV (the transition energies here and below are given in accord with the measurements of Grigor'ev et al[11] carried out on a $\pi\sqrt{2}$ double focusing β-spectrometer, the magnetic field in which was monitored by the method of nuclear resonance). The energies and relative intensities of these conversion lines agree within the limits of the experimental error with the data of Refs.7 & 9. It will be evident that some of the lines are complex. The dashed curves in Fig.3 and the following figures give the separate components. In resolving the complex lines we used the relative conversion electron intensities given in Ref.9. The resolution was carried out so that the line shape in the reduced coordinates would be the standard shape; in the electron energy range above 140 keV as the standards we used the K197.0 and K645.5 lines, the shapes of which in the reduced coordinates are virtually identical. The triangles with arrows under the spectrum in Fig.3 denote the energy intervals isolated in the different coincidence experiments, i.e., the energy intervals on which the constant field half of the spectrometer was set (hereinafter we refer to this as the "fixed" half of the spectrometer.

The results of our experiments are summarized in Table 1 (the data have been normalized to the same source activity).

The true coincidence counting rates at the line peaks in the coincidence spectra differed substantially in different experiments: the coincidence rates varied from 6 to 35 000 coinc/hr; the counting rate in individual channels varied from 10^3 to $3 \cdot 10^6$ pulses/min. The ratio of true to chance coincidences varied in

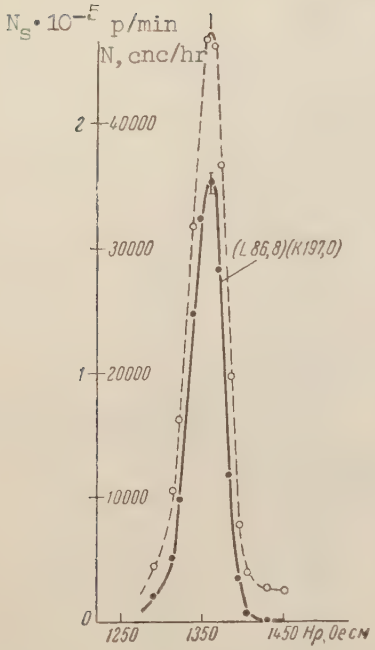

Fig.4

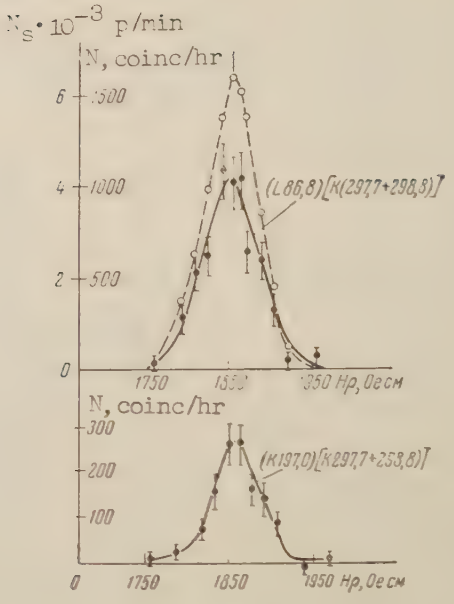

Fig.5

Fig.4. Coincidences of L86.8 electrons with K197.0 electrons. The dashed line indicates the section of the K197.0 conversion electron spectrum recorded by means of the "movable" half of the spectrometer. The solid line represents the coincidence counting rate. The "fixed" half of the spectrometer was set to isolate the section of the spectrum denoted by arrow 4 in Fig.3.

Fig.5. Coincidences of K(297.7 + 298.8) electrons (the singles spectrum of which is shown by the dashed line) with the L86.8 electrons (upper solid curve) and K197.0 electrons (lower solid curve). "Fixed" half of spectrometer set on energy interval indicated by arrow 5 in Fig.3.

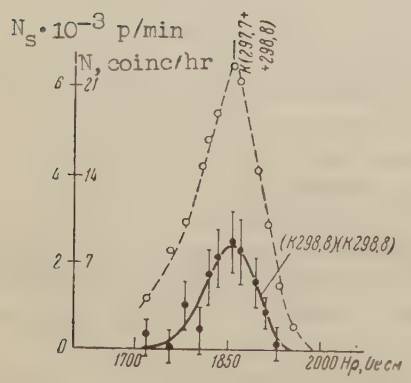

Fig.6. Self-coincidences of K(297.7 + 298.8) electrons.

the range from 1.5 to 41. The weakest transition cascade that we were able to detect (coincidences of K538.7 electrons with K872.5 electrons) is realized (with respect to conversion) with a probability of $3 \cdot 10^{-6}$ per disintegration of Ho^{160}.

In all we investigated 25 different cascades (Figs.4-13).

1. Coincidences between the L86.8 and K197.0 conversion electrons are shown by the curve in Fig. Here the "fixed" half of the spectrometer was set to accept the L86.8 line, while the "movable" half of the spectrometer was swept over the region of the spectrum where the K197.0 line is located. The recorded rate of true coincidences in this case (35 100 coinc/hr) was the highest encountered in all the experiments with Ho^{160}. These coincidences are associated with the 197.0-86.8 keV cascade via the 86.8 keV level of the first rotational band.

2. Coincidences between the K(297.7 + 298.8) electrons with the electrons of

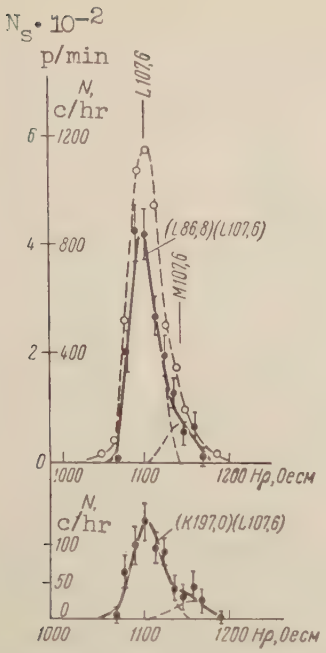

Fig.7. Coincidences of L107.6 electrons (upper curve) and K197.0 electrons (lower curve).

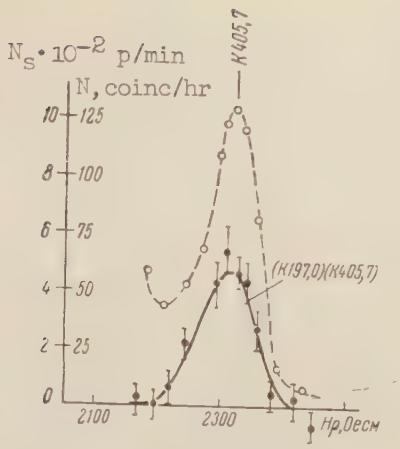

Fig.8

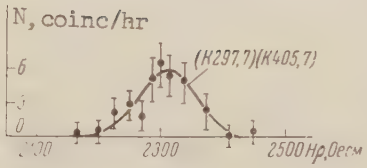

Fig.9

←Fig.8. Coincidences of K405.7 electrons with K197.0 electrons.

←Fig.9. Coincidences of K405.7 electrons with K(297.7 + 298.8) electrons.

the 86.8 and 197.0 keV transitions are characterized by the curves of Fig.5. In detecting these coincidences the "fixed" channel was set on 1) the L86.8 line (upper curve) and 2) the K197.0 line (lower curve). These coincidences are evidence of existence of the triple cascade ~298-197.0-86.8 keV.

3. Fig.6 shows the K(297.7 + 298.8)-K(297.7 + 298.8) self-coincidences. The "fixed" half of the spectrometer was set to accept the K(297.7 + 298.8) electrons and some of the K310 electrons (the gate is indicated by arrow 6 in Fig.3); however, the number of K310 electrons detected was so small that they mat be disregarded. The fact that there occur these "self-coincidences" substantiates the complex structure of the K298 line and shows that at least two components of this line stem from transitions located one above the other in the Ho^{160} decay scheme.

4. Fig.7 gives the curves obtained in recording coincidences of the L107.6 electrons with the L86.8 and K197.0 electrons. The "fixed" half of the spectrometer was set on the L86.8 line and on the K197.0 line, respectively. These coincidences are evidence for the triple cascade: 107.6-197.0-86.8 keV.

5. Coincidences of the K405.7 electrons with the K197.0 electrons are shown in Fig.8 and with the K(297.7 + 298.8) electrons in Fig.9. In the first case, the "fixed" half of the spectrometer was set to detect the K197.0 electrons; in the second case the K(297.7 + 298.8) electrons. The existence of these coincidences indicates that the 405.7 keV transition forms a cascade with the 197.0 keV transition and with at least one of the components of the complex ~298 keV transition. Below we shall show that this is the soft 297.7 keV component.

6. Fig.10 shows the coincidence spectra of the L86.8 electrons (curve b) and K197.0 electrons (curve c) with the electrons from transitions with energies from 500 to 1000 keV. The five peaks in curve b are evidence of the following coincidences: (L86.8)-(K538.7), (L86.8)-(K645.5), (L86.8)-(K728.5), (L86.8)-[K(872.5 + + 879.8)] and (L86.8)-[K(962.8 + 966.4)]. The broadening of the (L86.8)-(K538.7) peak to the low energy side indicates that there are also present (L86.8)-(K513.7) coincidences. It will also be evident from curve b of Fig.10 that there are appreciable numbers of coincidences with the L86.8 electrons at the locations of the following lines in the singles spectrum (curve a): L538.7, [K(754.5 + 765.7) +

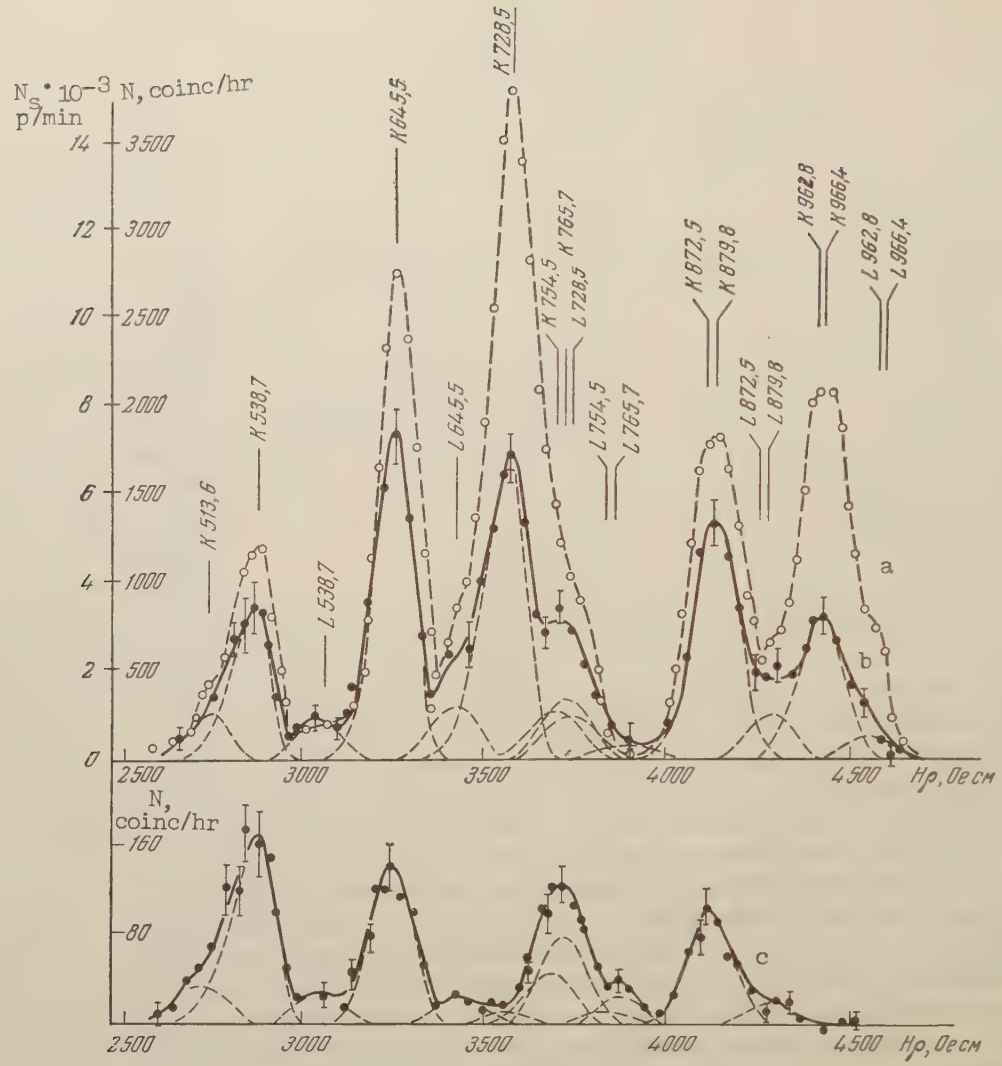

Fig.10 Coincidences of L86.8 electrons (curve b) and K197.0 electrons (curve c) with electrons with energies from 430 to 960 keV. Curve a - singles spectrum.

+ L728.5], L(872.5 + 879.8) and L(962.8 + 966.4). Apparently, the (L86.8) - - [K(754.5 + 765.7) + L728.5] coincidences are complex: if one compares the ratio of the coincidence counting rate for (L86.8)-[K(754.5 + 765.7) + L728.5]: (L86.8)- -(K728.5) $\approx$ 0.45:1 with the intensity ratio L728.5:K728.5 $\approx$ 0.16:1 (Ref.9), it becomes obvious that in the given coincidences there participate not only L728.5 electrons but also electrons from at least one of the components of the K(754.5 + + 765.7) doublet.

Curve c in Fig.10 characterizes the coincidences between the K197.0 electrons and electrons of higher energies; in this curve there are present peaks at the locations of the following electron lines in the singles spectrum (curve a): K538.7, K645.5, K(754.5 + 765.7) and K(872.5 + 879.8). There are also evident rises at the locations of the L538.7, L645.5, L(754.5 + 765.7) and L(872.5 + + 879.8) lines. From the shape of the (K197.0)-(K538.7) coincidence line on the low energy side it is evident that there are present (K197.0)-(K513.6) coincidences as well.

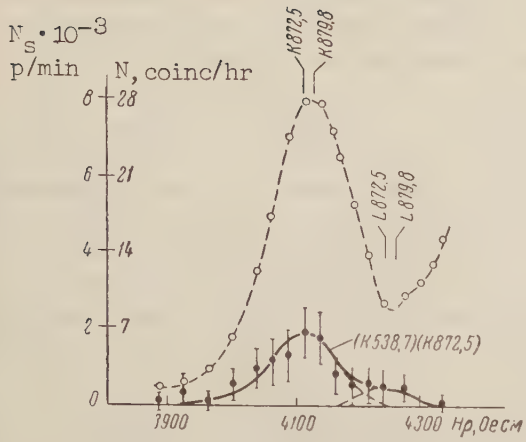

Fig.11

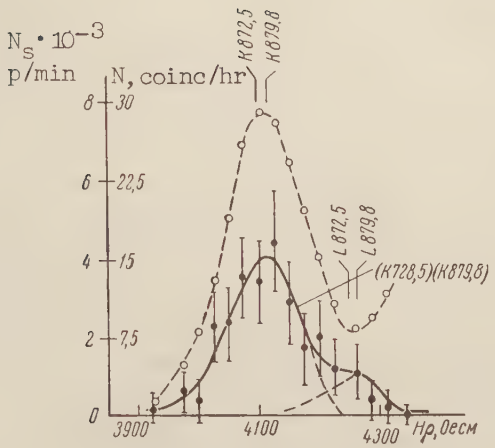

Fig.12

Fig.11. Coincidences of K538.7 electrons with K(872.5 + 879.8) electrons.
Fig.12. Coincidences of K728.5 electrons with K(872.5 + 879.8) electrons.

The (K197.0)-[K(754.5 + 765.7)] coincidence curve is probably complex and is the sum of the peaks due to (K197.0)-(K754.5) and (K197.0)-(K765.7) coincidences. Evidence of this is the minor but noticeable broadening of this line. Below it will be shown that analysis of the rate of build up of the coincidence rate leads to the same inference. It will also be evident from curve c of Fig.10 that there are no coincidences between the K197.0 electrons and K(926.8 + 966.4) electrons.

The results of resolution of the coincidence spectrum into individual lines are shown by the dashed cufves in Fig.10. In resolving the complex lines we utilize the results of quantitative analysis of the coincidences (see below). On the basis of the presented data it may be asserted 1) that there exist the following transition cascades: 513.6-197.0-86.8, 538.7-197.0-86.8, 645.5-197.0-86.8, 728.5-86.8, 754.5-197.0-86.8 and 765.7-197.0-86.8 keV, 2) that at least one of the components of the 872.5 + 879.8 keV doublet forms a triple cascade with the 197.0 and 86.8 keV transitions, and 3) at least one component of the 962.8 + 966.4 keV doublet is in cascade with the 86.8 keV transition.

7. Fig.11 shows the spectrum of coincidences between the K538.7 and K(872.5 + + 879.8) electrons. In this case the "fixed" half of the spectrometer was set to detect the K538.7 line (arrow 11 in Fig.3). The admixture of K513.6 and L513.6 electrons that could be detected by the "fixed" channel was so small that it may be neglected. According to the Ho^{160} decay scheme (Fig.2), the observed coincidences are realized between the K538.7 and K872.5 electrons, i.e., the 538.7 and 872.5 keV γ-transitions are in cascade.

8. The observed coincidences between the K728.5 and K(872.5 + 879.8) electrons are shown in Fig.12. The "fixed" half of the spectrometer detected K728.5 electrons and a small fraction of the L645.5, K708.6, K754.5 and K765.7 electrons (arrow 12 in Fig.3). However, the last could not yield many coincidences with the K(872.5 + 879.8) electrons, as will be evident from their low intensity and the location of the corresponding transitions in the Ho^{160} decay scheme. The 728.5 keV and at least one of the components of the 872.5 + 879.8 keV doublet should form a cascade. This follows from the fact that there were observed (K728.5)-[K(872.5 + 879.8)] coincidences.

9. Fig.13 shows the coincidences between the K(962.5 + 966.4) electrons, detected by the "fixed" channel, and the K645.5 and K728.5 electrons. In the de-

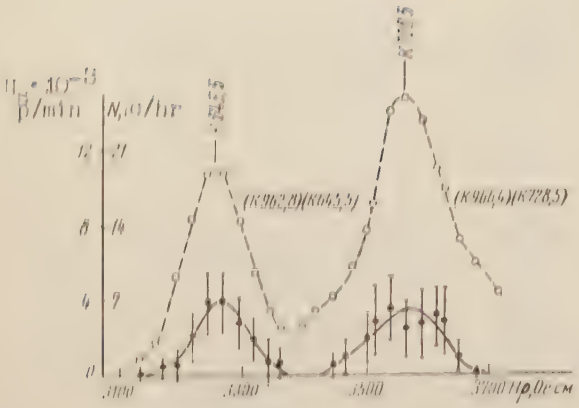

Fig.13. Coincidences of K(962.8 + + 966.4) electrons with K645.5 and K728.5 electrons. Dashed line - singles curve; solid line - coincidence curve.

cay scheme for Ho^{160} (Fig.2) the 645.5 and 962.8 keV transitions and the 728.5 and 966.4 keV transitions form cascades; this is substantiated by our experiments.

We note that the counting rates for the coincidences discussed in paragraphs 3,5,7,8 and 9 above were low: the counting rates with the strongest sources amounted to only from 8 to 20 coinc/hr. Inasmuch, however, as the ratio of true to chance coincidences was always greater than one, there can be no doubt that the enumerated coincidences actually occur.

III. Quantitative Analysis of the Coincidences

In some cases one cannot draw unambiguous deductions regarding the position of transitions in the decay scheme solely on the basis of observed coincidences. Hence in using the method of coincidences to check a decay scheme it is important to compare the experimental counting rates with the counting rates (abundances) calculated on the basis of the variant of the decay scheme being checked.

One can compute the counting rates on the basis of a given decay scheme when there is available sufficient information on the intensities and multipole orders of the transitions involved in the decay of the isotope under investigation. Although the amount of information on the γ-radiations emitted in the decay of Ho^{160} to Dy^{160} is relatively limited, there are available sufficient precise data on the relative intensities of the conversion electrons of Ho^{160}, on the internal conversion coefficients and on the relative probabilities for different branches of de-excitation of the intermediate levels for calculation of the relative counting rates of coincidences in the investigated cases.

In order to clarify the method of calculation let us consider two transitions "1" and "2" forming a cascade. We shall designate the conversion coefficients on different shells i (K, L, M, etc.) of the "1" and "2" transitions by α'_{i1} and α'_{i2} and the fraction of corresponding electrons in each transition by α'_{i1} and α'_{i2}. The counting rate for coincidences of electrons from the "1" and "2" transitions can be calculated by means of the formula

$$N_{coinc} = N_1 \alpha'_{i2} \delta_{12} \omega_2 \varepsilon_2 \varepsilon_{12} \varkappa, \qquad (1)$$

where N_1 is the counting rate for electrons of the first group, $\alpha'_{i2} = \dfrac{\alpha_{i2}}{1 + \sum \alpha_{i2}}$, δ_{12} is the probability for the occurrence of a "2" transition after a "1" transition (referred to one "1" transition), ω_2 is the effective solid angle of the half of the spectrometer detecting the electrons of the "2" transition, ε_2 is the efficiency of the counter for electrons of the "2" transition, ε_{12} is the efficiency of the coincidence circuit, and $\varkappa$ is a factor taking into account the effect of angular correlation (this factor depends on the spins of the levels, the multipole orders of the transitions, the energy and type of electrons and the geometry of the instrument).

Table 2

Experimental and calculated values of the counting rate of e-e coincidences in $Ho^{160} \rightarrow Dy^{160}$ decay

No.	Coincidences	Counting rate coinc/hr		Value of the coefficient		
		Exper.	Calc.	α'_{i2}	δ_{12}	Intensity of convers. electrons, $N_1 \cdot 10^{-3}$, p/min
1	(L107,6) (L86,8)	814	918	0,44	1	5,8
2	(K197,0) (L86,8)	35 100	35 100	0,44	1	220
3	(K297,7) (L86,8)	1 015	750	0,44	1	6,4
4	(K513,6) (L86,8)	250	238	0,44	1	1,5
5	(K538,7) (L86,8)	850	750	0,44	1	4,8
6	(K645,5) (L86,8)	1 849	1 750	0,44	1	11
7	(K728,5) (L86,8)	1 600	1 290	0,44	0,55	14,8
8	(L728,5) (L86,8)	788	209	0,44	0,55	2,4
9	(K754,5) (L86,8)		222	0,44	1	1,4
10	(K765,7) (L86,8)		285	0,44	1	1,8
11	(K872,5) (L86,8)	1364	317	0,44	1	2,0
12	(K879,8) (L86,8)		902	0,44	1	5,7
13	(K962,8) (L86,8)	801	728	0,44	1	4,6
14	(K966,4) (L86,8)		0	0,44	0	4,0
15	(L107,6) (K197,0)	120	56	0,14	0,19	5,8
16	(K297,7) (K197,0)	245	323	0,14	1	6,4
17	(K405,7) (K197,0)	56	50	0,14	1	1,0
18	(K513,6) (K197,0)	~30	14	0,14	0,19	1,5
19	(K538,7) (K197,0)	172	174	0,14	0,72	4,8
20	(K645,5) (K197,0)	127	105	0,14	0,19	11,0
21	(K728,5) (K197,0)	⩽14	7	0,14	0,01	14,8
22	(L728,5) (K197,0)	124	1	0,14	0,01	2,4
23	(K754,5) (K197,0)		51	0,14	0,72	1,4
24	(K765,7) (K197,0)		91	0,14	1	1,8
25	(K872,5) (K197,0)	99	101	0,14	1	2,0
26	(K879,8) (K197,0)		0	0,14	0	5,7
27	(K298) (K298)	8,6	6	0,015	0,56	1,0
28	(K405,7) (K298)	6	16	0,046	1	1,0
29	(K538,7) (K872,5)	6,6	4,6	0,0034	0,72	5,2
30	(K538,7) (K879,8)		0	0,0034	0	5,2
31	(K645,5) (K962,8)	7,2	9	0,0028	0,81	11
32	(K645,5) (K966,4)		0	0,0028	0	11
33	(K728,5) (K872,5)	15	0	0,0034	0	14,8
34	(K728,5) (K879,8)		10	0,0034	0,55	14,8
35	(K728,5) (K962,8)	6,5	0	0,0028	0	14,8
36	(K728,5) (K966,4)		6,7	0,0028	0,45	14,8

It is assumed in Eq.(1) that the lifetime of all the intermediate levels is much shorter than the resolving time of the coincidence circuit. This condition was always fulfilled in our experiments. The longest lifetime, apparently, is that of the 86.7 keV state: according to the data of McGowan[27], its lifetime $\tau = 1.8 \cdot 10^{-9}$ sec. The resolving time 2τ of our coincidence circuit was $\sim 1 \cdot 10^{-8}$ sec in all the experiments except those involving coincidences with the L86.8 electrons in which case the resolving time was increased to $2 \cdot 10^{-8}$ sec. In addition, in derivation of (1) it is assumed that the conversion lines for which the electron coincidences are being determined do not overlap at all.

The coincidence counting rates determined experimentally and calculated by means of Eq.(1) are listed in Table 2. In designating the coincidences (column 2) the electrons of the first group are given in the first parentheses; the electrons of the second group in the second parentheses. In Table 2 we also list the values of the coefficients α'_{i2} and δ_{12} and of the counting rate N_1 for electrons of the first group. The values of α_{i2} are known for the 86.8, 197.0, 298.8, 879.8, 962.8 and 966.4 keV transitions. According to the most accurate measurements[25,28], carried out with a Tb^{160} source, the experimental values of the internal conversion

coefficients for these γ-transitions (except for the 298.8 keV transition) agree within 10% with the theoretical values for E2 transitions (the 298.8 keV transition is E1). As for the 297.7 and 872.8 keV transitions, occurring between the 6^+ & 4^+ and 4^+ & 4^+ rotational levels (see Fig.2), it may be inferred that they are also E2. On the basis of these data one can calculate the coefficients α_{i2} for all the investigated cases of coincidences.

For calculating the probabilities δ_{12}, the values of which depend on the relative location of the transitions in the decay scheme, one must know the relative intensities of the transitions de-exciting the intermediate levels of the cascade. Inasmuch as at present there is a lack of adequate data on the γ-spectrum of Ho^{160}, we calculated the relative intensities of the γ-transitions from the intensity of the conversion electrons[9] and the corresponding internal conversion coefficients (Refs.25,28). In Fig.2 together with the energies and multipole orders of the transitions, we show in parentheses the relative intensities of the transitions used in calculating the δ_{12}.

Using these values we find, for example, for the (K645.5)-(K197.0) coincidences (No.20 in Table 2):

$$\delta_{645,5;\,197,0} = \delta_{645,5;\,765,7}\delta_{765,7;\,197,0},$$

$$\delta_{645,5;\,765,7} = \frac{I_{765,7}}{I_{765,7}+I_{962,8}} = \frac{3.9}{3.9+16.1} = 0.19$$

(19% of the 645.5 transitions are followed by a 765.7 keV transition), $\delta_{765,7;197,0} = 1$ (a 197.0 keV transition always follows a 765.7 keV transition), and $\delta_{645,5;197,0} = 0.19$ (in 19% of the cases a 645.5 keV transition is followed by a 197.0 keV transition).

In Table 2 we also list the experimental counting rates for electrons of the first group. In the case of complex lines, the resolution of the components was carried out according to the data on the relative intensities of the conversion electrons given in Ref.9.

The product of the efficiencies $\varepsilon_2 \cdot \varepsilon_{12}$ in our experiments may be regarded as constant: as was mentioned in Refs.26 & 29, the efficiencies ε_2 and ε_{12} in our instrument are virtually energy independent above 40 keV.

In comparing experimental counting rates with calculated rates it must be borne in mind that, owing to electron scattering in the source, conversion lines of low energy are broadened, which leads to decrease of the counting rate at the line peak. In our experiments, in recording the softest electrons (L86.8) this effect attained ~35%, which is equivalent to a like reduction of the effective solid angle ω. To be able to regard the product $\omega_2\varepsilon_2\varepsilon_{12}$ in Eq.(1) as constant, we introduced appropriate corrections to the experimental counting rates for electrons and coincidences. The experimental values given in Tables 1 and 2 have been corrected in this way.

The factor $\varkappa$, taking into account the influence of angular correlation, equals 1 for an isotropic distribution of the direction of emergence of one electron relative to another. The values of $\varkappa$ for the case of coincidences between K conversion electrons can be calculated using the data of Biedenharn & Rose[30]. Calculations carried out for the different cases of coincidences investigated in the present experiment showed that $\varkappa$ varies in the range from 0.75 to 1.23. It must be borne in mind that owing to multiple scattering of electrons in the source and backing the angular dependence for low energy electrons is smeared out and $\varkappa$ approaches 1. Inasmuch as in our experiment the sources were of different thickness and it was impossible to take into account the effect of smoothing out of the angular anisotropy, in calculating the coincidence counting rate we assumed $\varkappa = 1$.

The errors involved in this assumption do not exceed 20% and virtually do not alter the inferences drawn from comparison of the calculated and experimental counting rate. The question to what extent the experimental counting rates agree with the calculated coincidence counting rate is discussed below.

IV. Discussion of the Results and Ho^{160} Decay Scheme

1. Coincidences between the conversion electrons from the 86.8, 197.0 and 297.7 keV transitions in the first rotational band

As was noted above, the fact that there are (L86.8)-(K197.0), (L86.8)-[K(297.7 + 298.8)] and (K197.0)-[K(297.7 + 298.8)] coincidences proves that the 86.8 and 197.0 keV transitions and at least one of the components of the ~298 keV doublet form a triple cascade. There can be little doubt that the 86.8 and 197.0 keV transitions are located between the lowest levels of Dy^{160}. This was established in the first studies of the decay of Tb^{160} by the method of γ-γ and β-γ coincidences[14-23], and also follows from the intensity balance[9] of the transitions in the decay of Ho^{160} and, moreover, is consistent with the model concept for rotational transitions in even-even nuclei in this mass number region.

The situation is more complicated when it comes to the ~298 keV transition. The complex structure of the K298 line was noted in one of the early investigations of the conversion spectrum of Ho^{160} (Grigor'ev et al[7] - 1958). Subsequently (1960), it was substantiated by studies carried out on instruments with higher resolution: Grigor'ev et al[11] detected the doublet structure of the line by means of a magnetic spectrometer and gave the transition energies as 297.7 and 298.8 keV; Abdurazakov et al[12] evaluated the transition energies as 297.7 and 299.0 keV. Grigor'ev et al reported that the soft component of the K298 doublet is 3-6 times more intense than the hard component.

In the $Ho^{160} \rightarrow Dy^{160}$ decay scheme (Fig.2) there are level energy differences of about 298 keV at three points, namely, between the 1563 and 1264.9 levels (difference 298.1), between the 1264.9 and 966.5 keV levels (difference 298.4) and between the 581.4 and 283.7 keV levels (difference 297.7 keV). The 581.4 keV level is the expected 6^+ third level of the first rotational band. Given the data[11] on the energies of the transitions in Dy^{160}, the theory of axial deformed nuclei predicts a value of 586 keV for the energy of this level, while the theory of non-axial nuclei yields 597 keV. Obviously, these values are close to the sum 283.7 + + 298 = 581.7 keV.

It follows from our experiments that the more intense component of the complex K298 line is associated with the transition between the 581.4 (6^+) and 283.7 keV (4^+) rotational levels. This follows from the intensity of the (K298)-(K197.0) coincidences: the corresponding transitions in the rotational band are in cascade; using Eq.(1) one can calculate the coincidence counting rate on the basis of the intensity of the K298 electrons and the value of α_K for the 197.0 keV transition. The calculated value given in Table 2 (No.16) - 323 coinc/hr - was obtained on the assumption that all the K298 electrons are emitted in the transition between the 581.4 and 283.7 keV levels.

It can be shown that K298 electrons emitted in transitions between high lying levels virtually will not give (K298)-(K197.0) coincidences, for de-excitation of the upper levels occurs mainly via the 966.5 keV level and it de-excites in such a way that the 197.0 keV transition occurs in few cases. Let us assume that the 298 keV transition is realized only 1) between the 1264.9 and 966.5 keV levels or 2) between the 1563 and 1264.9 keV levels. In the former case (K298)--(K197.0) coincidences can be realized through the intermediary of the 684.1 keV

transition; in the latter case mainly via the 215.6 and 765.7 keV cascade. Using the known relative intensities of the transitions de-exciting the 966.5 and 1049.5 keV levels, we can calculate the counting rate for (K298)-(K197.0) coincidences for both alternatives. In the former case we obtain a value of 1.6 coinc/hr; in the second case 7 coinc/hr. These rates are much lower than the experimental counting rate of 245 coinc/hr. A similar situation was encountered in investigating the decay of Tb^{160}: here the 298 keV transition occurs mainly or solely between high lying levels and few 298-197 coincidences are observed.[21]

Thus, it may safely be asserted that the 581.4 keV (6^+) level is excited in the decay of Ho^{160} and that the most intense component of the complex K(297.7 + + 298.8) line is evinced in de-excitation of this level to the 283.7 keV (4^+) level. The intensity of the K297.7 component amounts to ~70% of the total intensity of the K298 electrons.

This assertion is further substantiated by the following facts.

1. The intensity ratio $I_K/I_L = 3.4$ observed[7] for the 298 keV transition in the decay of Ho^{160} is closer to the value for an E2 type transition, whereas in the decay of Tb^{160}, where apparently the 581.4 keV (6^+) level is not excited, we have $I_K/I_L = 6.7$ and α_K ($\gamma 298$) = $1.3 \cdot 10^{-2}$ (Ref.25), i.e., values in good agreement with the theoretical ones for E1 transition.

2. If in the decay of Tb^{160} there occurs a 298 keV transition between the 1264.9 and 966.5 keV levels, the 215.6 keV transition competes with it. Comparing the intensities of the K298 and K215.6 electrons in Tb^{160} and Ho^{160}, we obtain $I_{K298} : I_{K215,6}$ = 2.7:1 for Tb^{160} (Ref.25) and $I_{K298} : I_{K215,6}$ = 10:1 for Ho^{160} (Ref. 9), i.e., in Ho^{160} the intensity ratio is 3.7 times higher than in Tb^{160}. Hence in the decay of Ho^{160} ~70% of the K298 electrons originate not in the transition between the 1264.9 and 966.5 keV levels but elsewhere.

2. Coincidences between the electrons of the components of the complex 298 keV transition. Structure of the K298 line

Above it was shown that the K298 line is a doublet and that the most intense component is evinced in the transition between the 6^+ and 4^+ levels of the first rotational band. It was also noted that the second, weaker component may be emitted in the transition between the 1264.9 and 966.5 keV levels or/and the transition between the 1563 and 1264.9 keV levels.

Actually, the K298 line is apparently a triple one. The hypothesized structure of this line in the decay of Ho^{160} is shown in the upper part of Fig.14. This structure follows from the occurrence of "self-coincidences" of the K298 electrons. The softest component (K297.7), which appears in the 581.4 (6^+) $\rightarrow$ $\rightarrow$283.7 keV (4^+) transition, cannot give rise to a substantial number of (K298)-(K298) coincidences, inasmuch as the multipole orders of the intermediate 1264.9 (2^-) $\rightarrow$581.4 (6^+) and 966.5 (2^+) $\rightarrow$581.4 (6^+) transitions (Fig.2) are very high and these transitions are not observed. Hence the (K298)-(K298) coincidences must be attributed to two transitions between high lying levels. If we assume that these transitions are in direct cascade and use the relative intensities of the three branches of de-excitation of the 1264.9 keV state and the conversion coefficient for the 298 keV γ-transition in the decay of Tb^{160}, we can calculate the counting rate for (K298)-(K298) coincidences.

The results of these calculations are given in Table 2 (No.27). In the calculations it was assumed that there are involved in the cascade 30% of all the K298 electrons (15% in the upper and 15% in the lower parts of the cascade). The listed counting rate (6 coinc/hr) is necessarily approximate, but, as will be seen, it is not in conflict with the experimental rate of 8.6 coinc/hr.

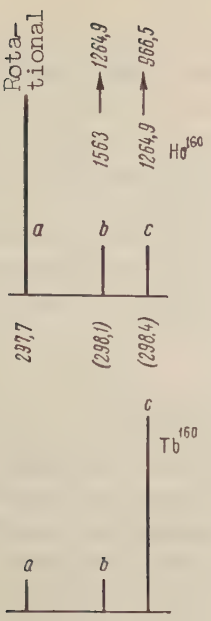

←Fig.14. Hypothesized structure of the K298 triplet in Ho^{160} and Tb^{160}. The relative location of the lines is taken from the work of Grigor'ev et al[11]. The intensity ratios $b:c$ in Ho^{160} and $a:b$ in Tb^{160} are not known but $a:(b+c) =$ = 3-6 in Ho^{160} and $(a+b) \ll c$ in Tb^{160}.

The situation in the decay of Tb^{160} is, apparently, different (Fig.14, lower part); here the most intense component of the triplet is the one associated with the transitions between the 1264.9 and 966.5 keV levels. From the high abundance of (γ298)-(γ880) and (γ298)-(γ966) coincidences[18,21,23], the low intensity of (γ298)-(γ197) coincidences[21] and the absence of (β859)-(γ298) coincidences[18,20,21] it follows that the 298 keV γ-transition occurs between high lying levels. From occurrence of (β570)-(γ298) coincidences[18-21] it follows that the 298 keV transition is a transition between the 1264.9 and 966.5 keV levels (the 859 and 570 keV components of the β-spectrum in the decay of Tb^{160} to Dy^{160} feed the 966.5 and 1264.9 keV levels, respectively.)

3. Coincidences of electrons from the 765.7, 872.5, 879.8, 962.8 and 966.4 keV transitions between levels of the two rotational bands with electrons of the 86.8 and 197.0 keV transitions

In our experiments the conversion electron lines from the 872.5 and 879.8 keV transitions and from the 962.8 and 966.4 keV transitions were not separated from each other and in detecting K765.7 electrons there were simultaneously counted K754.5 and L728.5 electrons. Hence merely the fact that there were observed coincidences of these electrons with the L86.8 and K19710 electrons does not solve the question which of the components of the (962.8 + 966.4), 872.5 + 879.8) and (754.5 + 765.7) keV doublets form cascades with the 86.8 and 197.0 keV γ-transitions.

Comparing the experimental coincidence counting rates with the calculated rates (Table 2), we see that there is obtained good agreement under the following assumptions:

1. Of the components of the 962.8 + 966.4 keV doublet only one (apparently the softer one) is in cascade with the 86.8 keV transition (Nos.13 & 14 in Table 2) and the observed (L86.8)-[K(962.8 + 966.4)] coincidences must be interpreted as (L86.8)-(K966.4) coincidences.

2. Both components of the 872.5 + 879.8 keV doublet form cascades with the 86.8 keV transition (Nos.11 & 12 in Table 2), but only the softer component is also in cascade with the 197.0 keV transition (Nos.24 & 26). Hence the observed (L86.8)-[K(872.5 + 879.8)] coincidences must be interpreted as (L86.8)-(K872.5) & (L86.8)-(K879.8) coincidences, and the (K197.0)-[K(872.5 + 879.8)] coincidences must be interpreted as (K197.0)-(K872.5) coincidences.

3. The 765.7 keV transition is in cascade with the 86.8 and 197.0 keV transitions (Nos.10 & 24). More detailed analysis of the counting rates of coincidences of the (K754.5 + K765.7 + L728.5) electrons with the L86.8 and K197.0 electrons will be given below.

In calculating the coincidence counting rates in all three cases it was assumed that the 765.7, 872.5, 879.8 and 962.8 keV transitions are always followed by an 86.8 or a 197.0 keV transition ($\delta_{12} = 1$), i.e., that the 765.7, 872.5, 879.8 and 962.8 keV γ-transitions feed levels of the first rotational band. Hence it

follows from our results that the 765.7 and 872.5 γ-transitions go to the 283.7 keV level, the 879.8 and 962.8 keV γ-transitions go to the 86.8 keV level, and the 966.4 keV transition goes to the ground state of Dy^{160}.

Thus, by the method of e-e coincidences we have established the existence of excited states with energies 966.5 (2^+), 1049.5 (3^+) and 1156.4 (4^+) keV in full agreement with the accepted decay scheme for Ho^{160}.

Earlier experiments on γ-γ, β-γ (Refs.18-23) and e-γ (Ref.28) coincidences in the decay of Tb^{160} to Dy^{160} led to analogous inferences regarding the location of the 879.8, 962.8 and 966.4 keV γ-transitions in the scheme for Dy^{160}. The 872.5 keV transition is not excited in the decay of Tb^{160}.

4. Coincidences of K754.5 electrons with L86.8 and K197.0 electrons

As noted under Section II above, the small broadening of the peak of (K197.0)-[K(754.5 + 765.7)] coincidences leads to the inference that these coincidences are actually the sum of (K197.0)-(K754.5) + (K197.0)-(K765.7) coincidences. Comparison of the experimental coincidence counting rate with the calculated one leads to the same deduction.

In the decay scheme for Ho^{160} (Fig.2) an energy difference of ~755 keV is encountered at two points, namely, between the 1909 and 1156.4 keV levels and between the 1722 and 966.5 keV levels. For either location of the 754.5 keV γ-transition there may arise (K197.0)-(K754.5) coincidences, but their probability will be different in the two cases.

In Table 2 we list the calculated (K754.5)-(K197.0) (No.23) and (K754.5)-(L86.8) (No.9) coincidences calculated on the assumption that the 754.5 keV transition is located between the 1909 and 1156.4 keV levels. In this case the (K754.5)-(K197.0) coincidences are realized by the intermediary of the 872.5 γ-transition and the (K754.5)-(L86.8) coincidences occur through the 872.5 + 197.0 and 1069.7 keV γ-transitions. In this case the sum of the calculated counting rates for (K754.5)-(K197.0) + (K765.7)-(K197.0) + (L728.5)-(K197.0) coincidences equals 51 + 91 + 1 = 143 coinc/hr (Nos.22, 23 & 24), and the rate for (K754.5)-(L86.8) + (K765.7)-(L86.8) + (L728.5)-(L86.8) coincidences equals 222 + 285 + + 209 = 716 coinc/hr (Nos.8, 9 & 10), which is in good agreement with the experimental counting rates: (K754.5 + K765.7 + L728.5)-(K197.0) = 124 coinc/hr and (K754.5 + K765.7 + L728.5)-(L86.8) $\approx$ 788 coinc/hr.

If the 754.7 keV transition occurs mainly between the 1722 and 966.5 keV levels, there would be very few (K754.5)-(K197.0) coincidences owing to the low probability for de-excitation of the 956.5 keV level by the 684.1 keV transition (δ_{12} = 0.01; calculations lead to a coincidence rate of 0.7 coinc/hr). The experimental counting rate for K(754.5 + 765.7) -(K197.0) coincidences in this case turns out to be 40% greater than the calculated rate, which exceeds the experimental error.

Hence we consider it more probable that the 754.5 keV transition occurs mainly between the 1909 and 1156.4 keV levels.

5. Coincidences with electrons from the 728.5, 645.5 and 538.7 keV transitions

In the accepted decay scheme for Ho^{160} (Fig.2) transitions of energies 728.5, 645.5 and 538.7 keV are evinced in de-excitation of the 1695.0 keV (4^+) level to the levels of the second rotational band. In Table 2 we list the counting rates for coincidences of the K728.5, K645.5 and K538.7 electrons with the L86.5 electrons (Nos.7,6 & 5, respectively) and with the K197.0 electrons (Nos.21, 20 & 19); these were calculated for the above described location of the 728.5, 645.5 and

538.7 keV transitions. Comparing the calculated and experimental coincidence counting rates we find good agreement. The low rate for (K728.5)-(K197.0) coincidences (No.21) is in accord with the low probability for de-excitation of the 966.5 keV level by the 684.1 γ-transition ($\delta_{12} = 0.01$).

In agreement with the decay scheme for Ho^{160} one can then interpret the observed coincidences of the K728.5, K645.5 and K538.7 electrons with the electrons of the 872.5 + 879.8 keV and 962.8 + 966.4 keV doublets as follows:

$$(K728.5)-[K(872.5 + 879.8)] = (K728.5)-(K879.8);$$
$$(K728.5)-[K(962.8 + 966.4)] = (K728.5)-(K966.4);$$
$$(K645.5)-[K(962.8 + 966.4)] = (K645.5)-(K962.8);$$
$$(K538.7)-[K(872.5 + 879.8)] = (K538.7)-(K872.5).$$

It will be evident from a comparison of the calculated coincidence counting rates with the experimental ones (Nos.29-36) that this interpretation is not inconsistent with experiment.

Thus we have proved the existence of the following γ-transition cascades departing from the 1695.0 keV level:

728.5-879.8-86.8 keV, 645.5-962.8-86.8 keV, and
728.5-966.4 keV, 538.7-872.5-197.0-86.8 keV.

6. Coincidences of K405.7 electrons with the electrons from the 197.0 and 297.7 keV transitions

In the decay scheme for Ho^{160} a level energy difference of ~406 keV is encountered in two locations, namely, between the 1563 and 1156.4 keV levels and between the 1695.0 and 1289 keV levels. The 1289 keV level is presumably the 5^+ type level of the second rotational band. Using the data of Grigor'ev et al[11], the Bohr-Mottelson theory gives an energy of 1284 keV for this level, while the Davydov-Filippov theory leads to a value of 1312 keV. Our data on the coincidences of the K405.7 electrons with the K197.0 and K298 electrons allow of deciding which of these two variants for the location of the 405.7 keV level in the Dy^{160} diagram is realized in the decay of Ho^{160}.

A. (K405.7)-(K197.0) coincidences. In both locations of the 405.7 keV transition there should be observed coincidences of the electrons from the 405.7 keV transition with the electrons associated with 197.0 keV transition in the first rotational band. For a different location of the 405.7 keV transition (K405.7)-(K197.0) coincidences may arise in the following cascades:

a) 405.7-708.6-297.7-197.0-86.8 keV (100% 197.0 keV transitions after the 405.7 keV transition),

b) 405.7-872.5-197.0-86.8 keV (70% 197.0 keV transitions after the 405.7 keV transition).

The experimental counting rate for (K405.7)-(K197.0) coincidences agrees with that calculated on the assumption that every 405.7 keV transition is followed by a 197.0 keV transition (experimental rate - 56 coinc/hr; calculated rate - 50 coinc/hr; No.17 in Table 2).

We are inclined to give preference to cascade a) and, consequently, the higher location of the 405.7 keV transition due to the fact that there are observed (K405.7)-(K298) coincidences (in the case of cascade b) these coincidences should not occur).

B. K(405.7)-(K298) coincidences. If the 405.7 keV transition is located between the 1695.0 and 1289 keV or 1563 and 1156.4 keV levels there would not be

realized coincidences of the K405.7 keV electrons with the electrons of those components of the 298 keV triplet which occur in the upper part of the decay scheme (1563→1264.9 and 1264.9→966.5 keV transitions). There can, however, be realized coincidences between the K405.7 keV electrons and the K297.7 electrons from the transition in the first rotational band.

If the 405.7 keV transition occurs between the 1695.0 and 1289 keV levels, the (K405.7)-(K297.7) coincidences should occur by the intermediary of the 708.6 keV transition, which was observed (by detection of conversion electrons) in the work of Ref.9. In case of location of the 405.7 keV transition between the 1563 and 1156.4 keV levels, (K405.7)-(K297.7) coincidences should be realized only in the presence of a transition or transitions linking the 1156.4 (4^+) and 581.5 keV (6^+) levels. However, a cross-over transition with an energy of ~575 keV has not yet been observed. If it existed but had a low intensity, de-excitation of the 1156.4 keV level would take place past it (primarily by means of the 872.5 keV transition) and virtually no (K405.7)-(K297.7) coincidences would be observed. Hence we feel it more probable that the 405.7 keV transition is located between the 1695.0 and 1289 keV levels.

The counting rate for (K405.7)-(K297.7) coincidences in our experiments amounted to 6 coinc/hr. If one calculates the counting rate for these coincidences according to the cascade a) (see under A above) on the assumption that the 1289 keV level is de-excited only by the 708.6 keV transitions, one obtains a value of 16 coinc/hr (No.28 in Table 2). The depression of the experimental counting rate as compared with the calculated (by about 1:2.5) can be connected with the existence of a transition between the 1289 (5^+) and 283.8 keV (4^+) levels with an energy of 1005.2 keV and an intensity of the same order of magnitude as the intensity of the 708.6 keV transition. Such a transition may have escaped detection. In the conversion electron spectrum of Ho^{160} the K1005.2 and L962.8 lines should have a separation of only 2 keV, and to explain the observed divergence it is sufficient to assume that the K1005.2 line exists but is considerably weaker than the L962.8 line ($I_{L962,8}/I_{K709} \approx 5$ (Ref.9)). If this assumption is correct, it then follows from our data that the 1289 keV level is de-excited 40% by the 708.6 keV transition and 60% by the 1005.2 keV transition. This is not in conflict with theory: the Bohr-Mottelson theory taking into account mixing of the K = 0 and K = 2 states[31] gives a value of ~30:70 for the intensity ratio of the 708.6 ($5^+ \rightarrow 6^+$) and 1005.2 keV ($5^+ \rightarrow 4^+$) transitions.

It was established by Ewan et al[28] that in the decay of Tb^{160} there is excited a 1286.5 keV (3^-) level, which de-excites by 1199.8 and 1002.7 keV transitions to the 86.7 (2^+) and 283.7 keV (4^+) levels. Probably the 1286.5 keV level is also excited in the decay of Ho^{160}, inasmuch as there was observed (conversion electrons) a 1200 keV transition.[9] In this case there may be realized a 408.5 keV transition between the 1695.0 (4^+) and 1286.5 keV (3^-) levels. However, the K408.5 keV electrons cannot yield coincidences with electrons of the K298 triplet. Coincidences of the K408.5 electrons with the K297.7 electrons of the first rotational band can in principle be realized by the intermediary of a 705.1 keV transition (1286.5 (3^-)→581.4 keV (6^+)). But the 705.1 keV transition should be a transition of high multipole order. No transition of this energy is observed in the decay of Tb^{160} and the probability for de-excitation of the 1286.5 keV level by a 705.1 keV transition is negligibly small. Hence introduction of a 1286.5 keV (3^-) level will change nothing significant in the above interpretation of the observed (K405.7)-(K298) coincidences.

Thus, it follows from our data that in the decay of Ho^{160} there is excited a 1289 keV level which may be interpreted as the 5^+ level of the second rotational band, and the observed 405.7 keV γ-transition occurs at least partially in de-

excitation of the 1695.0 keV level to this level.

7. Coincidences of L107.6 electrons with L86.8 and K197.0 electrons

In Ref.7 it was inferred that the 107.6 keV transition occurs between the 1156.4 (4^+) and 1049.5 keV (3^+) levels of the second rotational band. The counting rates for (L107.6)-(L86.8) and (L107.6)-(K197.0) coincidences for this location of the 107.6 keV γ-transition are shown in Table 2 (Nos.1 & 15). It will be noted that in the case of the (L107.6)-(K197.0) coincidences the experimental and calculated rates differ by a factor of 2 (experimental rate: 120 coinc/hr; calculated rate: 56 coinc/hr). The difference is greater than the estimated experimental error (~30%) and gives reason to question the inferred location of the 107.6 keV transition between the 1156.4 and 1049.5 keV rotational levels.

The 107.6 keV γ-transition is a relatively intense one. Hence it is strange that there are not observed other transitions between the levels of the second rotational band, for example, a 1156.4 (4^+)→966.4 keV (2^+) transition.

An energy difference close to 108 keV is also encountered in the Ho^{160} decay scheme between the 1264.9 (2^-) and 1156.4 keV (4^+) levels. However, location of the 107.6 keV transition between these levels in the decay scheme for Ho^{160} is in conflict with the data obtained in studying the decay of Tb^{160}. No transition of 107.6 keV energy in Tb^{160} was ever observed, whereas 215.6 and 1177.6 keV transitions departing from the 1264.9 keV level are observed, and the intensity of their conversion lines in the decay of Ho^{160} is an order of magnitude lower than the intensity of the L107.6 electrons.

Inasmuch as so far no other coincidences with the electrons of the 107.6 keV transition have been observed, the question of its location in the decay scheme remains open.

Conclusions

Summarizing the results of our measurements, it may be said that they in general substantiate the decay scheme for Ho^{160} proposed by Grigor'ev et al[7,9].

We showed that in the decay of Ho^{160} there are excited the rotational levels 581.4 (6^+) and 1289 keV (5^+).

It follows from our experiment that the 405.7 keV transition is realized, at least partially, between the 1695.0 (4^+) and 1289 keV (5^+) levels and that location of the 754.5 keV transition between the 1909 and 1156.4 keV levels is more reasonable and probable than between the 1695.0 and 966.5 keV levels.

It follows from analysis of the coincidence spectra that the K298 line is a triple one. The most intense component (~70%) is associated with the transition between the 581.4 (6^+) and 283.7 keV (4^+) levels of the ground state rotational band. The other two components pertain to transitions located in the upper part of the decay scheme: one is probably a transition between the 1264.9 (2^-) and 966.5 keV (2^+) levels and the second a transition between the 1563 and 1264.9 keV (2^-) levels.

Our experiments substantiate the earlier inferences that in the decay of Ho^{160} there are excited levels at 966.5 (2^+), 1049.5 (3^+), 1156.4 (4^+) and 1695.0 keV (4^+).

We desire to express our gratitude to M.K.Nikitin for chemical separation and preparation of the sources and to A Gorzhak, A.L.Popeko and E.N.Rozhin for assistance for carrying out the measurements.

Leningrad State University &
Joint Institute for Nuclear Research

References

1. J.W.Mihelich & B.Harmatz, Phys.Rev., 106, 1232 (1957).
2. J.W.Mihelich, B.Harmatz & T.H.Handley, Phys.Rev., 108, 989 (1957).
3. G.M.Gorodinskii, A.N.Murin, V.N.Pokrovskii, B.K.Preobrazhenskii & N.E. Titov, Doklady AN SSSR, 112, 405 (1956). (Trans.Doklady.)
4. B.S.Dzhelepov, O.E.Kraft & B.K.Preobrazhenskii, Ibid., 116, 581 (1957). (Trans.Ibid.)
5. B.S.Dzhelepov, B.K.Preobrazhenskii, I.M.Rogachev & P.A.Tishkin, Izv.AN SSSR, Ser.fiz., 21, 962 (1957). (Trans.Bulletin, 21, 964.)
6. E.P.Grigor'ev, B.S.Dzhelepov, A.V.Zolotavin, B.Kratsik, B.K.Preobrazhenskii & I.S.Yanchevskaya, Doklady AN SSSR, 117, 53 (1957). (Trans.Doklady.)
7. E.P.Grigor'ev, B.S.Dzhelepov, A.V.Zolotavin, O.E.Kraft, B.Kratsik & L.K. Peker, Izv.AN SSSR, Ser.fiz., 22, 101 (1958). (Trans.Bulletin 22, 99.)
8. E.P.Grigor'ev, B.S.Dzhelepov & A.V.Zolotavin, Ibid., 22, 821 (1958). (Trans.Bulletin, 22, 815.)
9. E.P.Grigor'ev, B.S.Dzhelepov, A.V.Zolotavin, B.Kratsik & G.Bitterlikh, Ibid., 23, 868 (1959). (Trans.Bulletin, 23, 859.)
10. K.S.Toth & J.O.Rasmussen, Phys.Rev., 115, 150 (1959).
11. E.P.Grigor'ev, B.S.Dzhelepov, V.Zvol'ska & A.V.Zolotavin, Materialy III soveshchaniya po neitronodefitsitnym izotopam (Transactions of the Third Conference on Neutron-Deficient Isotopes), Dubna, 1960.
12. A.A.Abdurazakov, K.Ya.Gromov, B.S.Dzhelepov & V.A.Khalkin, Ibid.
13. S.B.Burson, K.W.Blair & D.Saxon, Phys.Rev., 77, 403 (1950).
14. J.M.Cork, C.E.Branyan, W.C.Rutledge, A.E.Stoddard & J.M.LeBlanc, Phys. Rev., 78, 304 (1950).
15. L.Ya.Shavtvalov, Izv.AN SSSR, Ser.fiz., 17, 503 (1953).
16. V.Keshishian, H.W.Kruse, R.J.Klotz & C.M.Fowler, Phys.Rev. 96, 1050 (1954).
17. H.Jaffe, Nucl.Sci.Abstrs., 9, 12B, 276 (1955).
18. S.B.Burson, W.C.Jordan & J.M.LeBlanc, Phys.Rev., 94, 103 (1954).
19. I.P.Stepanenko & L.Ya.Shavtvalov, Izv.AN SSSR, Ser.fiz., 19, 318 (1955). (Trans.Bulletin, 19, 289.)
20. G.Bertolini, M.Bettoni & E.Lazzarini, Nuovo cimento, 3, 754 (1956).
21. O.Nathan, Nucl.Phys., 4, 125 (1957).
22. M.A.Clark & J.W.Knowles, Bull.Amer.Phys.Soc., 2, 231 (1957).
23. S.Ofer, Nucl.Phys., 5, 331 (1958).
24. M.P.Avotina, E.P.Grigor'ev, A.V.Zolotavin & B.Kratsik, Doklady AN SSSR, 119, 1127 (1958). (Trans.Doklady.)
25. E.P.Grigor'ev, A.V.Zolotavin & B.Kratsik, Izv.AN SSSR, Ser.fiz., 23, 191 (1959). (Trans.Bulletin, 23, 183.)
26. V.A.Sergienko, Ibid., 22, 198 (1958). (Trans.Bulletin, 22, 195.)
27. F.K.McGowan, Phys.Rev., 85, 142 (1952).
28. G.T.Ewan, R.L.Graham & J.S.Geiger, Nucl.Phys., 22, 610 (1961).
29. B.S.Dzhelepov, B.K.Preobrazhenskii & V.A.Sergienko, Izv.AN SSSR, Ser.fiz., 22, 795 (1958). (Trans.Bulletin, 22, 789.)
30. L.C.Biedenharn & M.E.Rose, Revs.Mod.Phys., 25, 729 (1953).
31. P.Gregers Hansen, O.B.Nielsen & R.K.Sheline, Nucl.Phys., 12, 389 (1959).

COINCIDENCES BETWEEN CONVERSION ELECTRONS OF THE DYSPROSIUM FRACTION FROM PROTON BOMBARDED TANTALUM

- B.S.Dzhelepov. I.Zvol'skii, M.K.Nikitin & V.A.Sergienko

We investigated coincidences between the conversion electrons emitted by the dysprosium fraction separated from a tantalum target bombarded with 660 MeV protons. The measurements were carried out on the twin lens β-spectrometer described in Ref.1, and were started 20 hours on the average after the end of bombardment.

In earlier studies[2-4] devoted to the dysprosium fraction in the spallation products of tantalum it was established that there are present in this fraction Dy isotopes with A = 152, 153, 155, 157 and 159. In our experiments by the time of separation of the fraction short-lived (2.6 hr) Dy^{152} had almost completely decayed; as for Dy^{159} (T = 144 days), in the case of 3-4 hr bombardment of the Ta target the amount of this isotope is too small for its activity to be detectable by our instrument.

Thus, in our measurements there were observed the conversion electrons of Dy^{157} (T = 8 hr), Dy^{155} (T = 10 hr), Dy^{153} (T = 6.4 hr) and of the daughter nuclides Tb^{155} (T = 5 days) and Tb^{153} (T = 62 hr).

The conversion electron spectrum of the dysprosium fraction comprises a large number of lines. The resolution of our spectrometer (~3.5%) was inadequate for the separation of many of these lines, which naturally complicated analysis of the coincidence measurement results.

The part of the conversion electron spectrum that was investigated in the present work is shown in Fig.1; this spectrum was recorded by means of one half of our instrument. The thin vertical bars in the figure show the positions and relative intensities of the individual conversion lines according to the data of Ref.5.

Our measurements were carried out over a period of some 20 hours after separation of the dysprosium fraction. During this time, naturally, there built up some amount of Tb^{155} and Tb^{153}, so that part of the detected coincidences could pertain to the decay of these isotopes. In order to separate the coincidences associated with the decay of Dy to Tb all the measurements were repeated after the passage of 4 to 8 days to allow for decay of the Dy isotopes. The coincidence curves pertaining to Dy→Tb were then obtained by subtraction. These are shown in Figs.2,3,5,6,7,9 and 10 by the heavy solid lines. The dashed curves in these figures represent the sections of the singles spectrum recorded by the first half of our spectrometer (hereinafter we refer to this as the "movable" half or channel, to distinguish it from the "fixed" half). Inasmuch as the shape of these curves depends on the time elapsed from the end of bombardment of the Ta target and the time elapsed after separation of the dysprosium fraction, these dashed curves do not fully agree with the singles spectrum shown in Fig.1. The energy intervals isolated in the different experiments by the "fixed" half of the spectrometer are indicated by the triangles and arrows in Fig.1.

Coincidences between conversion electrons emitted in Dy^{157}--Tb^{157} decay

The conversion electrons, first detected by Mihelich et al[6] in investigating the decay of Dy^{157}, were also observed[5-7] in the conversion electron spectrum of the dysprosium fraction. The corresponding transitions have energies of 60.77, 83.01, 143.9, 182.5, 265.5 and 326.4 keV (the transition energies here and below are given on the basis of the results of the work of Ref.5, carried out by means of a double-focusing $\pi\sqrt{2}$ β-spectrometer with measurement of the magnetic field by the method of nuclear resonance). Harmatz et al[8] also mentioned transitions of

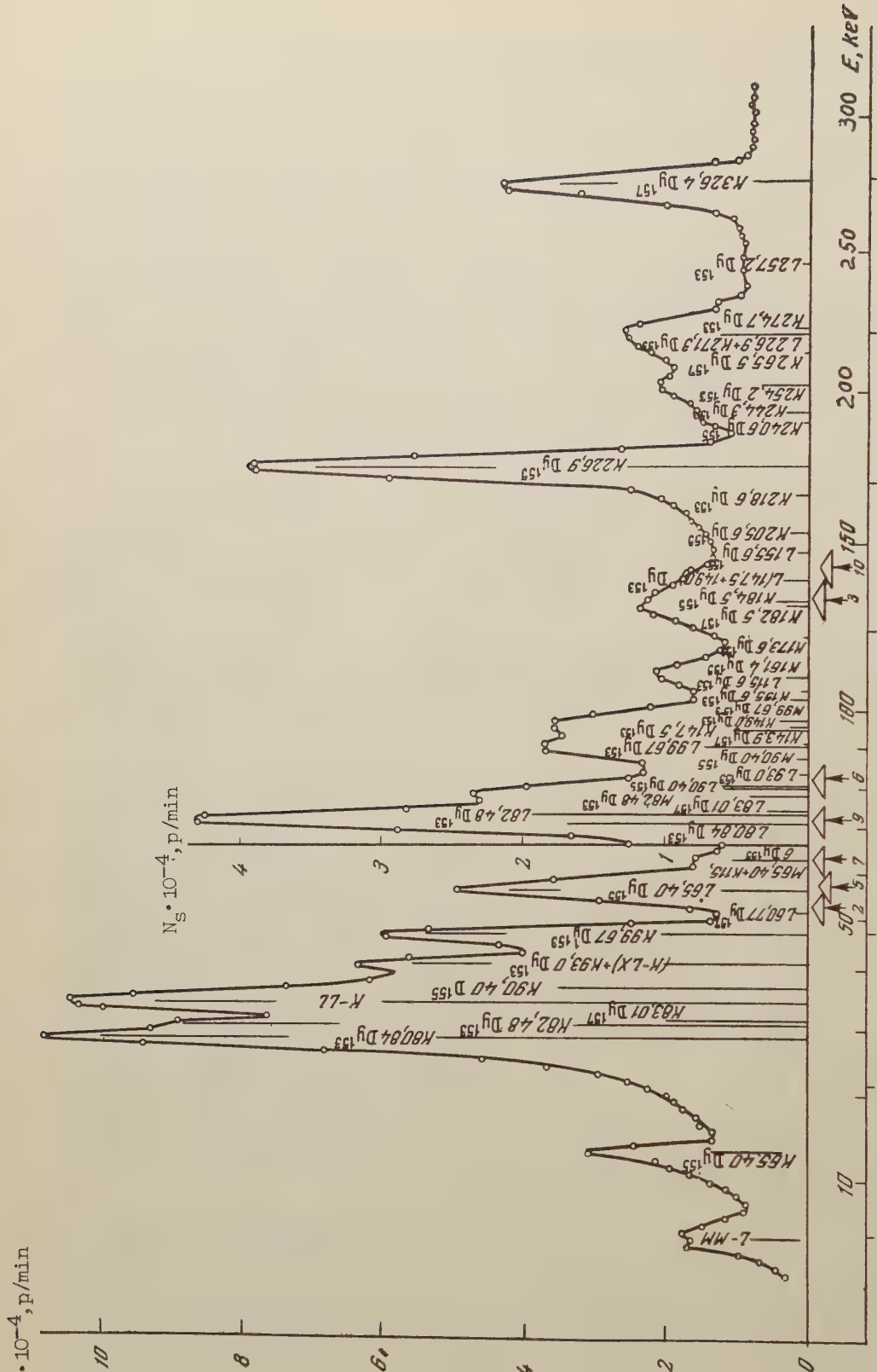

Fig.1. Conversion electron spectrum of the dysprosium fraction (up to 300 keV) recorded by means of one half of our spectrometer some two hours after separation of the fraction and 24 hrs after the end of bombardment of the Ta target. The recording time was ~2.5 hr; the background has not been subtracted. The thin vertical bars indicate the positions and relative intensities of the individual conversion lines according to the data of Ref.5, as recorded in that investigation 3 hrs after separation of the dysprosium fraction. (The lines of Tb had not yet appeared.) The arrows and triangles along the energy scale indicate the energy intervals encompassed by the second "fixed" half of the spectrometer in the various series of coincidence measurements; the numbers under the arrows correspond to the numbers of the figures in which the coincidence spectra are shown.

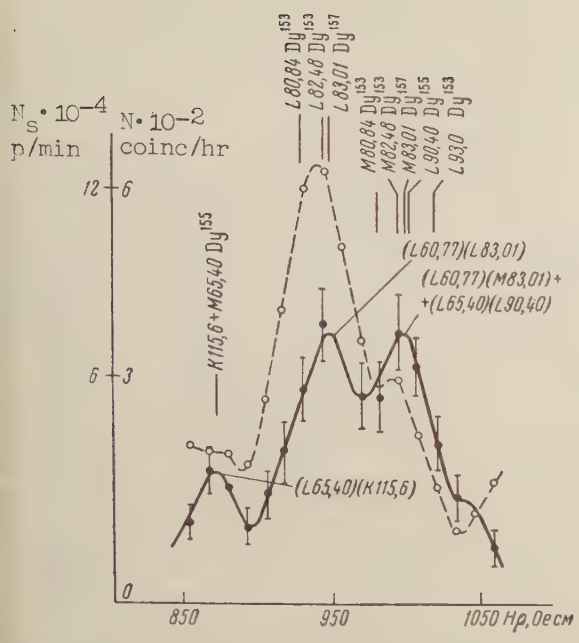

Fig.2. Coincidences with Dy^{157} L60.77 + Dy^{155} L65.40 electrons. Solid curve - coincidence counting rate; "fixed" half of the spectrometer set on the energy interval indicated by arrow 2 in Fig.1. The dashed line shows the singles conversion electron spectrum recorded at the same time by means of the "movable" half of the spectrometer; inasmuch as it contains lines belonging to Dy and daughter Tb isotopes with different periods, the shape of this spectrum depends greatly on the history of the source.

545, 554 and 576 keV energy which, however, so far have not been accomodated in the decay scheme for Dy^{157}. Possibly some of these transitions are identical with the transitions observed in the work of Ref.5 in the decay of the dysprosium fraction isotopes (the relatively weak electron lines: K544.7 (T = 6.2 ± 2 hr), K549.9 (T = 10.8 ± ± 2 hr), K559.2 (T = 6.4 ± 3 hr) and K570.8 (T ≈ 12 hr).

In the present work we investigated coincidences between the most intense lines of Dy^{157}, namely, L60.77, K83.01, L83.01, K182.5 and K326.4. It was established that the following electrons coincide as regards time of emission (resolving time of our coincidence circuit $2\tau \approx 10^{-8}$ sec): L60.77 with L83.01, L60.77 with K182.5, and K182.5 with K83.01 and L83.01. There were detected no coincidences of the K326.4 electrons with the L60.77, L83.01 and K182.5 electrons.

The spectrum of (L60.77)(L83.01) coincidences is shown in Fig.2. In this case the "fixed" channel of the spectrometer detected the Dy^{157} L60.77 electrons and some fraction of the Dy^{155} L65.40 electrons (triangle 2 in Fig.1). Hence the peak in Fig. 2 in the region of the Dy^{153} L80.84 + Dy^{153} L82.48 + Dy^{157} L83.01 line group belongs to Dy^{157} (L60.77)(L83.01) coincidences. The other two peaks in the coincidence curve in the regions of the Dy^{155} K115.6 + Dy^{155} M65.40 and Dy^{153} M80.84 + Dy^{153} M82.48 + + Dy^{157} M83.01 + Dy^{155} L90.40 + Dy^{153} L93.0 lines correspond to Dy^{155} (L65.40)(K115.6) and Dy^{155} (L65.40)(L90.40) + Dy^{157}(L60.77) (M83.01) coincidences.

Coincidences of K182.5 electrons with L60.77 and K83.01 electrons of Dy^{157} are shown in Fig.3. In this case the "fixed" half of the spectrometer was set on the energy interval indicated by triangle 3 in Fig.1 and hence detected by Dy^{157} K182.5 and Dy^{155} K184.5 electrons and partially the Dy^{157} L143.9, Dy^{153} L147.5 and Dy^{153} L149.0 electrons. In Fig.3 in the regions of the K83.01 and L60.77 conversion lines there are evinced peaks pertaining to Dy^{157} (K83.01)(K182.5) and (L60.77)(K182.5) coincidences.

On the basis of our results one can draw the following inferences regarding the decay scheme of Dy^{157}:

1. The 182.5, 83.01 and 60.77 keV γ-transitions form a triple cascade.

2. The 326.4 keV transition is located parallel to this triple cascade in the Dy^{157} decay scheme. This is indicated by the following facts: a) the energy of this transition is close to the sum of the three cascade transitions, and b) no coincidences between the K326.4 and L60.77, K83.01 or K182.5 electrons were detected despite a careful search.

3. In view of the fact that the 326.4 keV transition is the most intense[9,5]

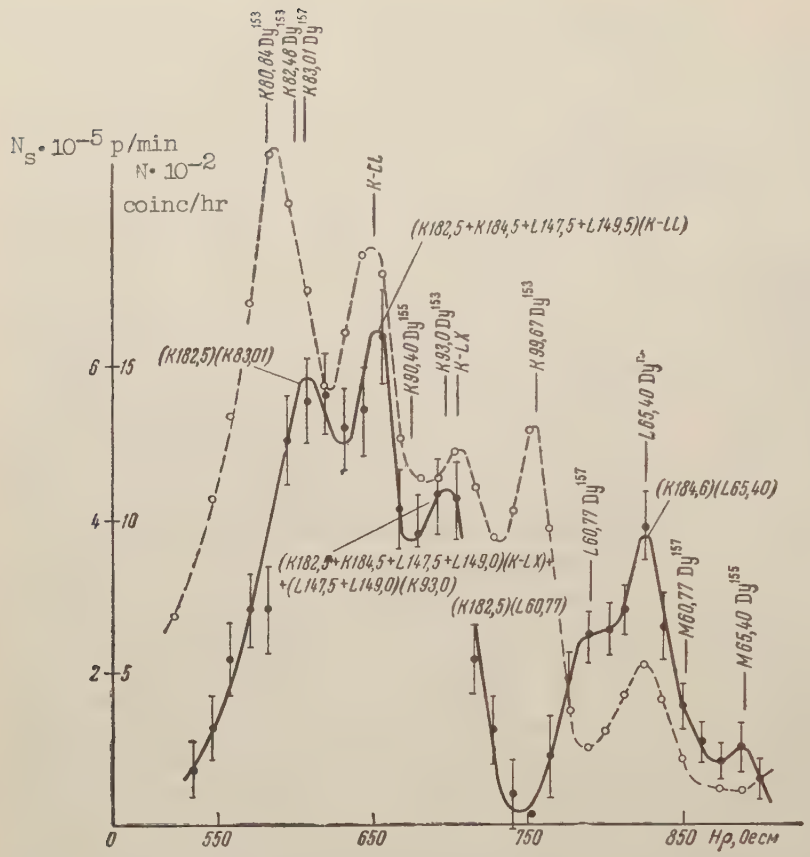

Fig.3. Coincidences with Dy^{157} K182.5 + Dy^{155} K184.5 + + Dy^{157} L143.9 + Dy^{153} L147.5 + Dy^{153} L149.0 electrons. Designations - see captions of Figs.1 & 2.

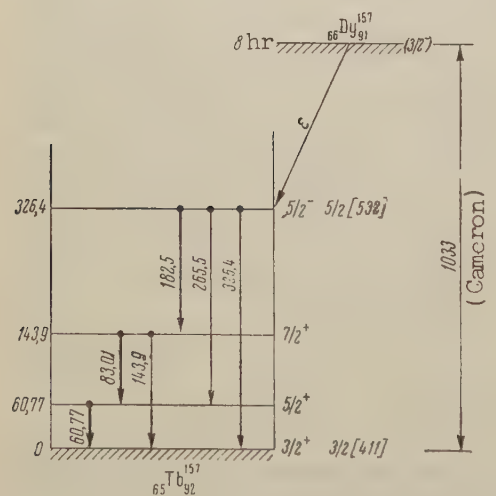

Fig.4. Decay scheme for Dy^{157}.

one excited in the $Dy^{157} \rightarrow Tb^{157}$ decay process, there undoubtedly exists a 326.4 keV level in Tb^{157}.

Thus, our results substantiate the decay scheme for Dy^{157} proposed by Mihelich et al[6] and reproduced in Fig.4, and are in complete agreement with the data of Toth & Nielsen[9], obtained in investigating e-γ coincidences.

The first two excited levels of Tb^{157} are apparently the levels of a rotational band based on the ground state for which Nilsson's scheme predicts the assignment $3/2^+$ ([411] $3/2^+$ state for the 65th proton). The ground state spin of Tb^{159}, a close analog of Tb^{157}, is known from experiment to have the same value (3/2). The assignments for the first two excited states are $5/2^+$ and $7/2^+$.

The spin and parity of the 326.4 keV state was established by Toth & Nielsen[9]. They found that the multipole orders of all three transitions from this level to the levels of the ground state rotational band are E1. It follows that the assignment for the 326.4 keV level should be $5/2^-$; possibly this state is characterized by $5/2^-$ [532].

It is of interest to compare the experimental and theoretical reduced probabilities for transitions between the 326.4 keV level and the levels of the rotational band: 0 ($3/2^+$), 60.77 ($5/2^+$) and 143.9 keV ($7/2^+$). According to the data of Toth & Nielsen[9], the ratios of the reduced probabilities $\gamma_{326.4} : \gamma_{265.5} : \gamma_{182.5} = 1:0.0075:0.105$, while the theoretical ratios (Alaga's rules) are 1:0.43:0.07. It will be evident that the 265.5 keV γ-transition is greatly retarded. A similar situation is encountered in the case of Tb^{159} (Ref.14), where the 364

keV ($5/2^-$) level is de-excited to the 0 ($3/2^+$), 57 ($5/2^+$) and 137 keV ($7/2^+$) levels of the ground state rotational band by 364, 305 and 255 keV γ-transitions. The reduced probability ratios $\gamma_{364} : \gamma_{305} : \gamma_{225} = 1:0.016:0.11$. Nielsen et al[14] attribute the difference between the theoretical and experimental ratios to the retardation of E1 type transitions as compared with the evaluations of Weisskopf for single-particle transitions. It was noted by Mottelson & Nilsson[10] that the retardation in the case of Tb^{159} is connected with forbiddenness with respect to the asymptotic quantum numbers.

The characteristics of the ground state of Dy^{157} are determined by its 91st neutron. By analogy with Gd^{155} (Ref.10) it follows that the assignment for the ground state of Dy^{157} should be $3/2^-$ [521]. In this case orbital electron capture should be realized primarily to the 326.4 keV ($5/2^-$) level (allowed transition). This has been substantiated by experiment: Toth & Nielsen[5] on the basis of measurements of e-γ coincidences give an intensity balance for the low lying levels evinced in $Dy^{157} \rightarrow Tb^{157}$ decay; it follows from this balance that if one neglects transitions from higher lying levels the numbers of transitions arriving at and departing from the 326.4 keV level are 0 and 10 100 ($\epsilon \approx 10\,000$), 190 arriving at and 250 departing from the 143.9 keV level ($\epsilon < 60$), and 280 arriving at and 280 departing from the 60.77 keV level ($\epsilon \approx 0$) (all the indicated numbers are relative).

Coincidences between conversion electrons emitted in Dy^{155}--Tb^{155} decay

It has been established in studies devoted to the decay of Dy^{155} (Refs.9 & 11) and the conversion electron spectrum of the dysprosium fraction from spallation of tantalum (Refs.5,7 & 12) that in $Dy^{155} \rightarrow Tb^{155}$ decay there are excited transitions with energies of 65.40, 90.40, 115.6, 155.6, 161.4, 184.5, 205.6, 226.9, 271.3, 371.7, 433.0, 484.0, 498.6, 508.4, 664.7, 906.5 and probably, 549.9 keV.

In the present work we studied coincidences between the L65.40, L90.40, K115.6, K155.6, K161.4, K184.5 and K226.9 electrons. It was found that the following electrons yield coincidences: L65.40 & L90.40, L65.40 & K115.6, L65.40 & K161.4, L65.40 & K184.5, L90.40 & L115.6, and K115.6 & K155.6. No coincidences were detected between the K226.9 electrons and the L65.40, L90.40, K115.6, K155.6 and K161.4 electrons.

The curve for coincidences with the L65.40 electrons of Dy^{155} is shown in Fig.5. There are evident three peaks located in the regions of the following line groups: Dy^{155} M65.40 + Dy^{155} K115.6, Dy^{153} M80.84 + Dy^{153} M82.48 + Dy^{157} M83.01 + + Dy^{155} L90.40 + Dy^{153} L93.0 and Dy^{155} L115.6 + Dy^{155} K161.4. In these experiments the "fixed" half of the spectrometer was set as indicated by arrow 5 in Fig. 1 so that it detected primarily L65.40 electrons. The admixture of L60.40 and K115.6 electrons was insignificant. Hence it may safely be asserted that the peaks in the curve pertain to (L65.40)(K115.6), (L65.40)(L90.40) and (L65.40) (K161.4) coincidences, respectively.

Fig.6 shows the curve for (L90.40)(L115.60) coincidences (peak in the region of the L115.6 and K155.6 lines). In this case the "fixed" half of the spectrometer was set as indicated by arrow 6 in Fig.1 and detected the Dy^{155} L90.40 electrons and a major portion of the Dy^{153} M80.84, Dy^{153} M82.48, Dy^{157} M83.01 and Dy^{153} L93.0 electrons.

Fig.7 illustrates the coincidences between the K115.6 + M65.40 electrons of Dy^{155}, detected by the "fixed" half of the spectrometer, and the K155.6, L115.6, and K161.4 electrons. The coincidence curve obviously has a width greater than

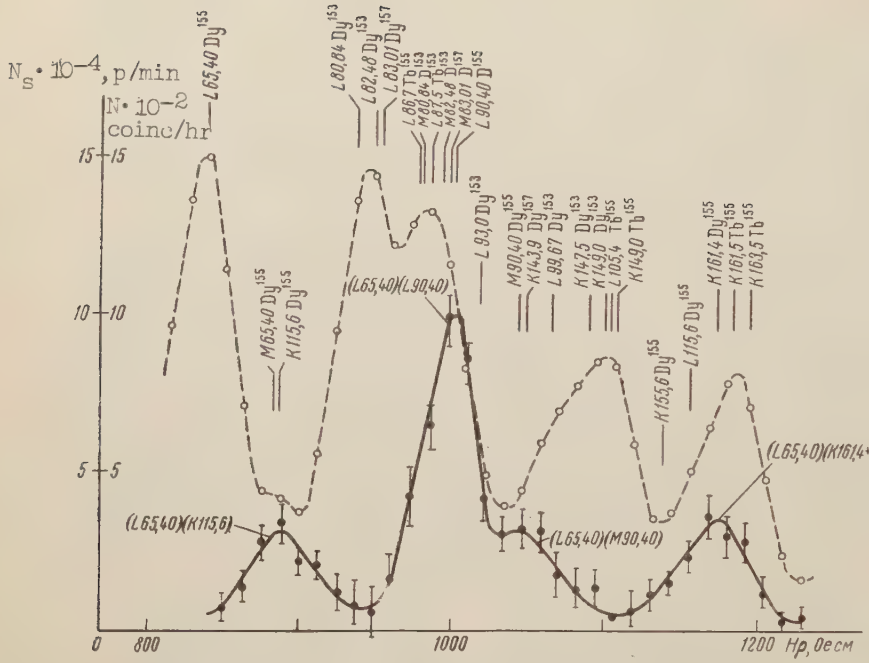

Fig.5. Coincidences with Dy^{155} L65.40 electrons.

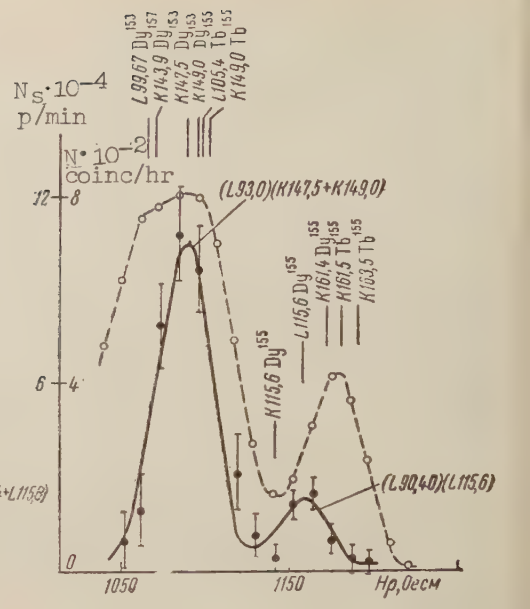

Fig.6. Coincidences with Dy^{155} L90.40 + Dy^{153} L93.0 + Dy^{153} M80.84 + Dy^{153} M82.48 + Dy^{157} M83.01 electrons.

the instrumental width and represents the sum of the (K115.6)(K155.6) + (M65.40)·(L115.6) + (M65.40)(K161.4) coincidence curve. The tentative resolution into components is shown by the dashed lines under the solid cufve in Fig.7.

The peak in the region of the Dy^{155} L65.40 line in Fig.3 is evidence for the existence of (L65.40)(K184.5) coincidences. In this case the "fixed" half of the spectrometer detected Dy^{155} K184.5 + Dy^{157} K182.5 electrons and partially Dy^{157} L143.9, Dy^{153} L147.5 and Dy^{153} L149.0 electrons.

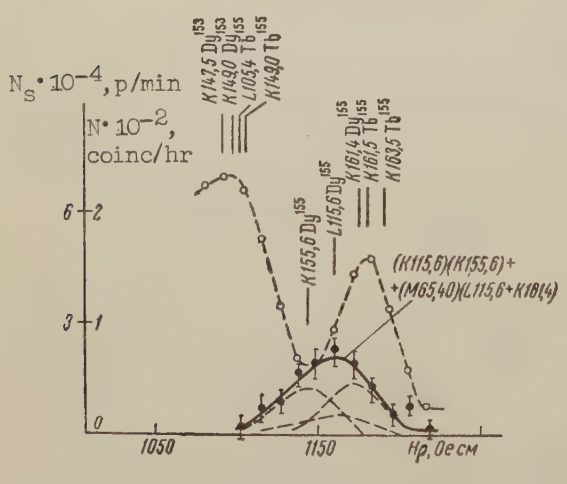

Fig.7. Coincidences with Dy^{155} K115.6 + Dy^{155} M65.40 electrons.

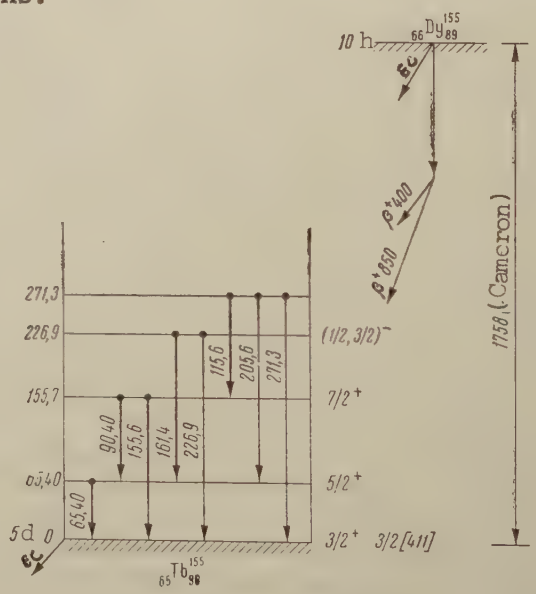

Fig.8. Decay scheme for Dy^{155}. (Spin & parit of the 226.9 keV level are probably $5/2^-$.)

Thus our experiments on coincidences between the conversion electrons of Dy^{155} lead to the following conclusions:

1. It may be asserted that the 65.40, 90.40 and 115.6 keV γ-transitions form a triple cascade, inasmuch as there are observed coincidences between the electrons of these transitions, and there exists a 271.3 keV transition, the energy of which is approximately equal to the sum of the energies of the 65.40, 90.40 and 115.6 keV transitions. In the decay scheme of Dy^{155} these transitions must be located one above the other, and the 271.3 keV transition parallel to this triple cascade.

2. The 115.6 and 155.6 keV transitions form a cascade, the energy of which is also close to that of the 271.3 keV transition.

3. Our detection of a 65.40-184.5 keV γ-transition cascade indicates that a 184.5 keV transition occurs in the decay of Dy^{155}, but so far this transition has not been accomodated in the Dy^{155} decay scheme.

4. The 65.40 and 161.4 keV transitions form a cascade. These transitions must be in series inasmuch as there exists a 226.9 keV transition, the energy of which is approximately equal to their sum and coincidences between the K226.9 electrons and the L65.40 and K161.4 electrons are not observed.

5. The 65.40 and 226.9 keV γ-transitions are the most intense of all the transitions excited in $Dy^{155} \rightarrow Tb^{155}$ decay.[5,9] Hence it may be assumed that the 65.40-90.40-115.6, 115.6-155.6 and 65.4-161.4 γ-transition cascades all feed the ground state of Tb^{155} and that there must exist excited levels with energies of 226.9 and 271.3 keV.

All these results are in agreement with the data of Toth & Nielsen[9] on e-γ coincidences in the decay of Dy^{155} and substantiate the Dy^{155} decay scheme (Fig. 8) which was first proposed by Toth & Rasmussen[11].

The first two excited levels of Tb^{155} (65.40 and 155.7 keV) together with the ground state apparently form a rotational band. By analogy with Tb^{159} and Tb^{157}, they may be assigned the following characteristics: $3/2^+$, $5/2^+$, $7/2^+$, K = = 3/2 and the asymptotic quantum numbers [411].

If, as inferred by Toth & Nielsen, the multipole order of the 226.9 keV γ-transition is E1, the possible assignments for the 226.9 keV level are $1/2^-$, $3/2^-$ and $5/2^-$. The last spin is more probable, inasmuch as $1/2^-$ and $3/2^-$ levels do not occur in the corresponding location in Nilsson's diagram.

Assuming that the spin and parity of the 226.9 keV level are $5/2^-$, we can evaluate the intensity of the 71 keV (E1) transition which should occur between the 226.9 and 155.7 keV ($7/2^+$) levels. The theoretical reduced probability ratio $B(E1; \gamma 226.9) : B(E1; \gamma 71) = 1:0.07$. From this it follows that the intensity ratio of the K226.9 and L71 conversion electrons $I_{K226.9}(E1) : I_{L71}(E1) = 1000:5.1$. Although Toth & Nielsen did not observe an L71 line, it will be evident that a line of this intensity could readily escape detection. The upper bound for its intensity may be evaluated from our data: the L71 electrons should yield coincidences with the L65.40 electrons (71-90.40-65.40 keV γ-cascade). Inasmuch as in 94% of the cases after formation of an L71 electron there is excited a 65.40 keV transition[9], which always accompanies formation of L90.40 electrons, the ratio of the (L65.40)(L71) and (L65.40)(L90.40) coincidence counting rates will be virtually equal to the intensity ratio of the L71 and L90.40 electrons. The coincidences of the L65.40 electrons with the L90.40 and the hypothesized L71 electrons are illustrated in Fig.5. In the region of the L71 electron energy (~62 keV) there is evinced a peak in the coincidence curve, which we initially attributed to (L65.40)(K115.6) coincidences (the energy of the K115.6 electrons is 63.6 keV). The intensity ratio (L65.40)(L90.40)/(L65.40)(K115.6) $\approx$ 3. If the "(L65.40)(K115.6)" coincidences are actually the sum of (L65.40)(K115.6) + (L65.40)(L71) coincidences, then in

the extreme case, assuming the intensity of the former coincidences to be zero, we obtain $I_{L90,40}/I_{L71} \approx 3$ and in units in which the intensity of the K226.7 electrons is 1000, the intensity of the L71 electrons $\leqslant 60$.

Toth & Nielsen[9] introduced into the Tb^{155} level scheme a 880 keV level on the basis of observation of 227-660 keV γ-ray coincidences and 880 keV γ-rays. If such a level actually exists, its energy according to the data of Ref.5 should be 226.9 + 664.7 = 891.6 keV, but it must be noted that no conversion electrons from a transition of this energy have as yet been observed. (In this energy region there was detected the relatively intense K906.5 line.) Using the relative conversion line intensities from Ref.5 and the γ-ray intensities from Ref.9 we can evaluate the internal conversion coefficient for the 665.0 keV γ-transition:

$$\alpha_{K\,664.7} = \frac{I_{K664.7} I_{\gamma\,226.9}}{I_{\gamma\,664.7} I_{K226.9}} \alpha_{K226.9}\,(E1) = \frac{13.0 \cdot 1000}{73 \cdot 1000}\, 0.0028 = 0.0050.$$

The theoretical values for $\alpha_{K664.7}$, are 0.0022 for E1, 0.0060 for E2 and 0.012 for M1; the closest to the experimental value is obviously the value for E2. If we accept that the spin and parity of the 226.9 keV level are $1/2^-$ or $3/2^-$, the probable assignment for the 891.6 keV level is $5/2^-$ or $7/2^-$.

In the work of Ref.7 there was introduced a 662.0 keV level on the basis of the sums of the energies of the 434.0 + 227.0 γ-transitions (661.0 keV) and the 508.0 + 155.8 keV transitions (663.8 keV) and the energy of the cross-over transition (662.0). We are of the opinion that the introduction of this level was incorrect. According to the data of Ref.5, the energy difference between the sums 433.0 + 226.9 = 659.9 keV and 508.4 + 155.6 = 664.0 keV is outside the limit of the experimental error ($\leqslant$0.1%) and location of the 664.7 keV transition in parallel with the 508.4-155.6 keV γ-cascade is in conflict with the existence of 665-227 keV γ-ray coincidences[9].

Coincidences between conversion electrons emitted in $Dy^{153} \rightarrow Tb^{153}$ decay

According to the data of Abdurazakov et al[7], Adam et al[5] and Basina et al[13], the electron lines from 80.84, 82.48, 99.67, 147.5, 149.0, 173.6, 218.6, 240.6, 244.3, 254.3, 274.7, 389.6, 512.4 and 544.7 keV transitions and the electron line with energy 84.27 keV, appearing in the conversion electron spectrum of the dysprosium fraction, should be attributed to $Dy^{153} \rightarrow Tb^{153}$ decay.

As a result of our investigation of the coincidences between the conversion electrons from Dy^{153} there were established the following facts:

1. There occur coincidences between the electrons from the 80.84 and 82.48 keV transitions. Fig.9 illustrates the (L80.84 + L82.48)(K80.84 + K82.48) coincidences (peak in the vicinity of the Dy^{153} K80.84 + Dy^{153} K82.48 + Dy^{157} K83.01 line group) and (L80.84 + L82.48)(L80.84 + L82.48) "self-coincidences" (peak in the region of the Dy^{153} L80.84 + Dy^{153} L82.48 + Dy^{157} L83.01 lines). In both cases the "fixed" half of the spectrometer detected Dy^{153} L80.84 + Dy^{153} L82.48 + + Dy^{157} L83.01 electrons (arrow 9 in Fig.1). The existence of these coincidences proves that the 80.84 and 82.48 keV transitions form a cascade.

2. There are observed coincidences between the K147.5 + K149.0 electrons and the electrons with energy 84.27 keV and coincidences of the L147.5 + L149.0 electrons with electrons having an energy of ~41 keV. The corresponding coincidence curves are shown in Figs.6 and 10. The existence of the former coincidences is evinced by the peak in Fig.6 in the region of the Dy^{153} L99.67 + Dy^{157} K143.9 + + Dy^{153} K147.5 + Dy^{153} K149.0 electron group. It is evident from the position of this peak that these coincidences pertain to K147.5 + K149.0 electrons rather than L99.67 electrons. The "fixed" half of the spectrometer detected the Dy^{153}

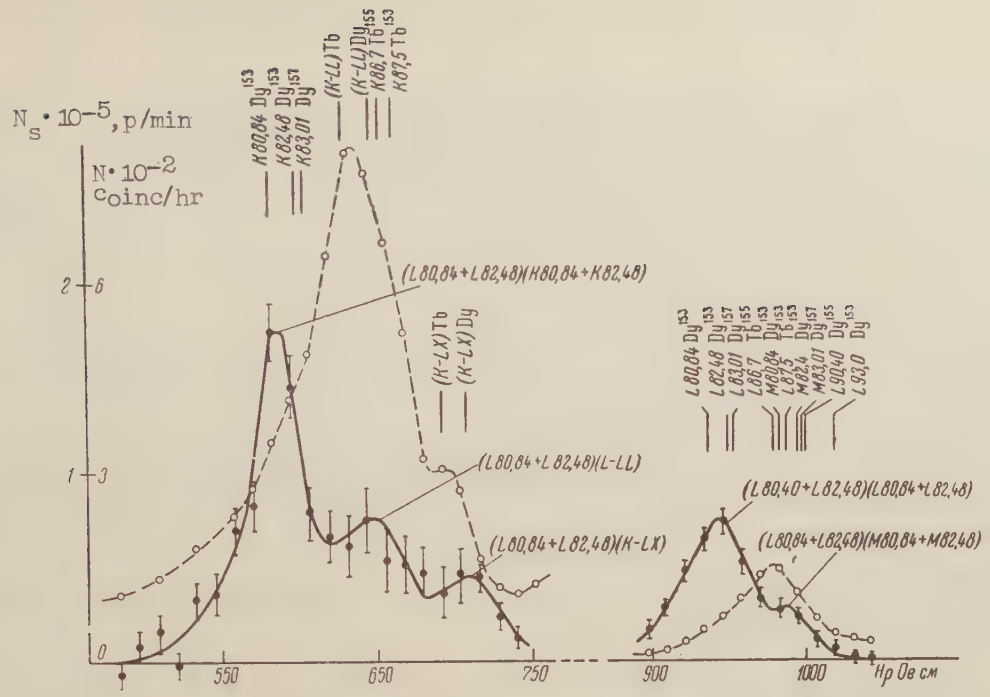

Fig.9. Coincidences with Dy^{153} L80.84 + Dy^{153} L82.48 + Dy^{157} L83.01 electrons.

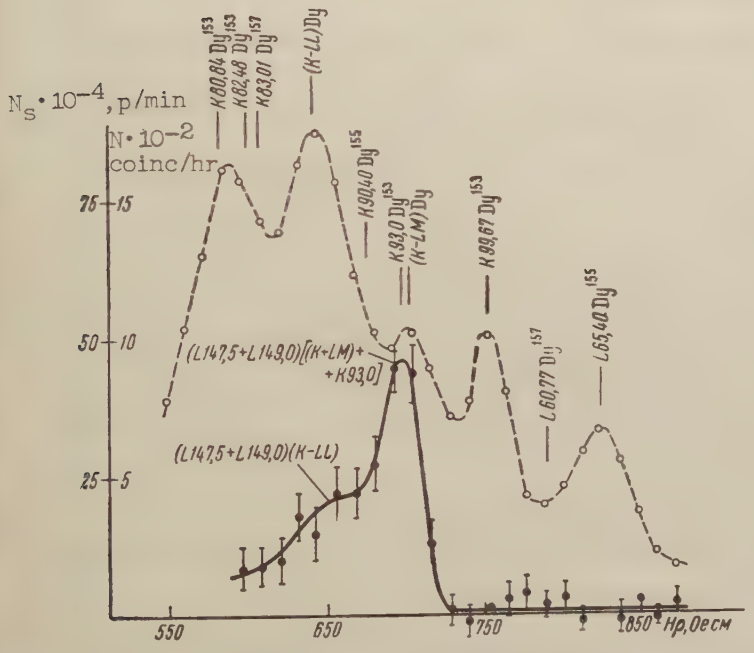

Fig.10. Coincidences with Dy^{153} L147.5 + Dy^{153} L149.0 electrons.

84.27 keV electrons (data of Ref. 5) and the close in energy Dy^{155} L90.40, Dy^{153} M80.84, Dy^{153} M82.48 and Dy^{157} M83.01 electrons. In order to make sure that the observed coincidences are produced by the 84.27 keV electrons and not by electrons from the 80.84 and 82.48 keV γ-transitions, we set the "fixed" channel of the spectrometer on the Dy^{153} L80.84 + Dy^{153} L82.48 + Dy^{157} L83.01 electron group; in this case no coincidences were observed. Hence it may be regarded as certain that the K147.5 + + K149.0 electrons coincide in time of emission with the 84.27 keV electrons.

Fig.10 shows the coincidence curve in the region of electrons with energy ~41 keV. This is the region of K - LM Auger electron. The "fixed" half of the spectrometer was set so that there were detected mainly the L147.5 + L149.0 electrons and partially the L155.6 electrons (arrow 10 in Fig.1). Inasmuch as in the region of medium-Z elements the (K - LL)/(K - LX) Auger intensity ratio is about 2 (Ref.15), and the observed (L147.5 + L149.0)(K - LL) to (L147.5 + L149.0)(K - LX) coincidence counting rate ratio was ~0.4,

it becomes clear that together with (L147.5 + L149.0)(K - LX) coincidences there were detected coincidences between the K147.5 + K149.0 electrons and conversion electrons with an energy close to the energy of the $(K - LX)_{Dy-Tb}$ Auger electrons (~41 keV).

Thus, it has been established that there exist coincidences between the K147.5 + K149.0 electrons and the ~41 and 84.27 keV conversion electrons. The energy difference between 84.27 and ~41 keV agrees with the difference between the electron binding energies on the K and L shells of terbium (43.3 keV). Hence it may be assumed that the 84.27 keV electrons detected in the studies of Refs. 5 & 7 are the L conversion electrons of a 93.0 keV transition and that in the second case there was observed the K93 line.

In the investigations of Refs.5 & 7 there were observed conversion electrons from a 240.6 keV transition. This energy is close to the transition energies sum 93.0 + 147.5 keV = 240.5 keV. On the basis of this it may be assumed that the 93.0 and 147.5 keV transitions are located one above the other.

3. There were not observed any coincidences between the L147.5 + L149.0 electrons and the K80.84, K82.48 and K99.67 electrons (see Fig.10). Also there were detected no coincidences between the M80.84 + M82.48 + L93.0 electrons and the L99.67 electrons (see Fig.6).

We take this opportunity to thank V.Bunakov, L.Popeko and E.N.Rozhin for assistance in the measurements.

Leningrad State University &
Joint Institute for Nuclear Research

References

1. V.A.Sergienko, Izv.AN SSSR, Ser.fiz., 22, 198 (1958). (Trans.Bulletin, 22, 195.)

2. G.M.Gorodinskii, A.N.Murin, V.N.Pokrovskii & B.K.Preobrazhenskii, Ibid., 21, 1624 (1957). (Trans.Bulletin, 21, 1011.)

3. A.N.Dobr9nravova, L.M.Krizhanskii, A.N.Murin & V.N.Pokrovskii, Ibid., 22, 815 (1958). (Trans.Bulletin, 22, 809.)

4. M.A.Bonch-Osmolovskaya, B.S.Dzhelepov & O.E.Kraft, Program of the Tenth All-Union Conference on Nuclear Spectroscopy, M., 1960.

5. I.Adam, E.P.Grigor'ev, B.S.Dzhelepov, V.Zvol'ska, I.Zvolskii & V.A.Khalkin, Materialy III soveshchaniya po neitronodefitsitnym izotopam (Transactions of the Third Conference on Neutron-Deficient Isotopes), Dubna, 1960.

6. J.W.Mihelich, B.Harmatz & T.H.Handley, Phys.Rev., 108, 989 (1957).

7. A.A.Abdurazakov, K.Ya.Gromov, B.S.Dzhelepov & G.Ya.Umarov, Izv.AN SSSR, Ser.fiz., 24, 1126 (1960). (Trans.Bulletin, 24, 1130.)

8. B.Harmatz, T.H.Handley & J.W.Mihelich, Phys.Rev., 114, 1082 (1959).

9. K.S.Toth & O.B.Nielsen, Nucl.Phys., 22, 57 (1961).

10. B.R.Mottelson & S.G.Nilsson, Kgl.Danske Videnskab Selskab, Mat.-fys.Medd, 1, 8 (1959).

11. K.S.Toth & J.O.Rasmussen, Phys.Rev., 115, 150 (1959).

12. B.S.Dzhelepov, O.E.Kraft, B.K.Preobrazhenskii & G.F.Yushkevich, Izv.AN SSSR, Ser.fiz., 22, 208 (1960). (Trans.Bulletin 22, 205.)

13. A.S.Basina, K.Ya.Gromov & B.S.Dzhelepov, Ibid., 24, 811 (1960). (Trans. Bulletin, 24, 813.)

14. K.O.Nielsen, O.B.Nielsen & O.Skilbreid, Nucl.Phys., 7, 561 (1958).

15. M.A.Listengarten, Izv.AN SSSR, Ser.fiz., 24, 1041 (1960). (Trans.Bulletin, 24, 1050.)

SUPPLEMENTARY DATA ON NEUTRON-DEFICIENT OSMIUM ISOTOPES

- T.V.Malysheva & B.A.Khotin

In papers[1,2] presented at the preceding conference on nuclear spectroscopy, mention was made of the existence in specimens of daughter osmium, separated from iridium, of a short-lived activity with a period of ~20 min. It was hypothesized[1] that this activity belongs to the isomer Os^{184m}, forming in the decay of 3-hr Ir^{184}.

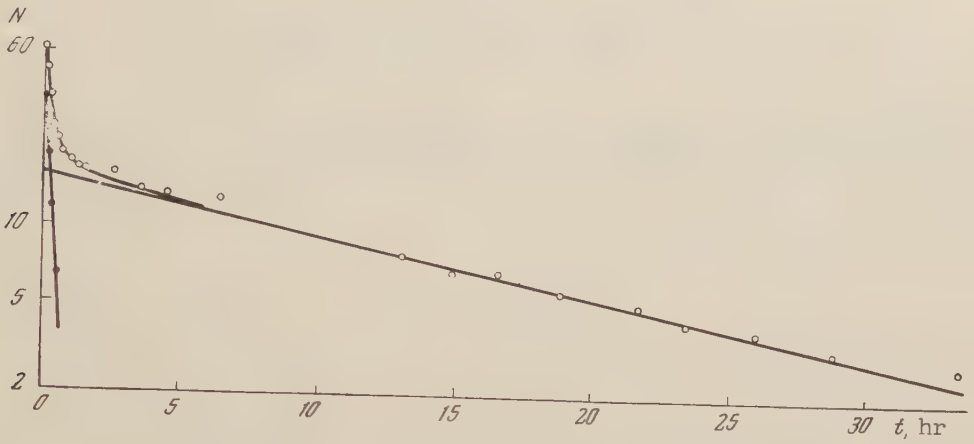

Fig.1. Decay curve for daughter osmium.

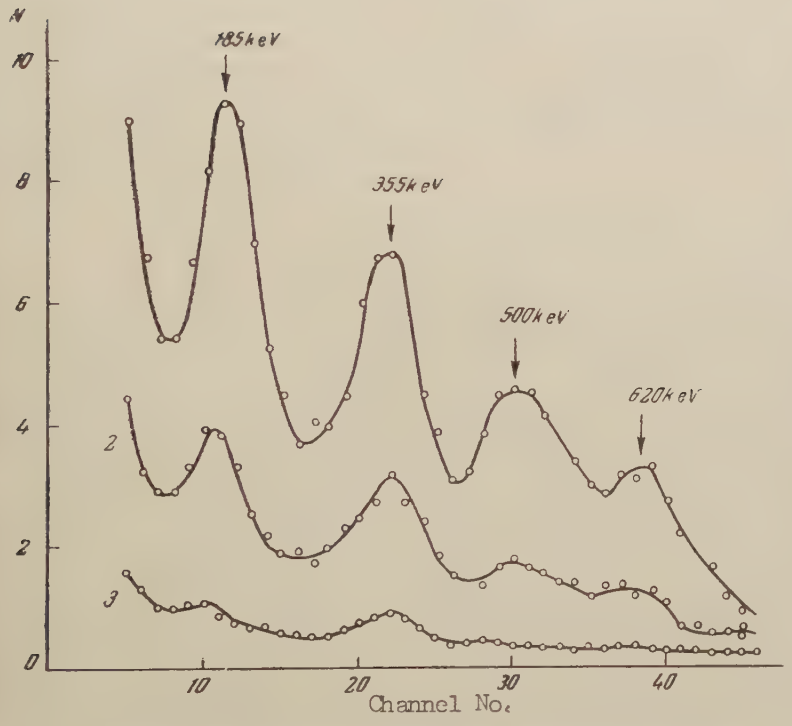

Fig.2. Gamma-spectra of daughter osmium recorded 1) immediately after separation from the parent iridium, 2) 20 min after separation, and 3) 20 h after separation.

In measuring the total activity of the daughter osmium we obtained a more accurate value for the period of the short-lived activity. As will be evident from the decay curve shown in Fig.1, the half-life equals 10 ± 0.5 min.

We also measured the γ-spectrum of the daughter osmium on a scintillation spectrometer with a 100-channel pulse height analyzer. The measurements were carried out immediately after separation of the osmium (an operation which requires 10-15 min). There were detected γ-lines with energies of 185, 355 and 620 keV (Fig.2), the activity of which fell off with a period of ~10 min. According to the data of Nielsen et al[3] this activity should be attributed to the isomer Os^{190m}.

Thus, if there do exist isomers of other even neutron-

deficient osmium isotopes, they apparently have periods shorter than 2 min.

We desire to express our gratitude to K.Ya.Gromov and V.G.Chumin for valuable advice in setting up the experiment and helpful discussions.

"V.I.Vernadskii" Institute of Geochemistry and Analytic Chemistry,
Academy of Sciences of the USSR

References

1. V.I.Baranov, K.Ya.Gromov, B.S.Dzhelepov, Zyong Chong Bai, T.V.Malysheva, V.A.Morozov, B.A.Khotin & V.G.Chumin, Izv.AN SSSR, Ser.fiz., 24, No.9, 1079 (1960). (Trans.Bulletin, 24, 1086.)

2. Yu.A.Surkov, G.M.Chernov, A.K.Lavrukhina & Z.V.Khromchenko, Izv.AN SSSR, Ser.fiz., 24, 1119 (1959). (Trans.Bulletin, 24, 1123.)

3. O.B.Nielsen, N.O.Roy Poulsen, R.K.Sheling & B.S.Yensen, Nucl.Phys., 10, 475 (1959).

INVESTIGATION OF THE CONVERSION ELECTRON SPECTRUM OF NEUTRON-DEFICIENT PLATINUM ISOTOPES

- L.N.Kryukova, V.V.Murav'eva, L.Duda, T.V.Malysheva & B.A.Khotin

In the present work, using a spiral magnetic β-spectrometer, we investigated the conversion electron spectrum of neutron-deficient platinum isotopes forming as a result of spallation of gold under bombardment with 660 MeV protons. We also investigated γ-γ and e-γ coincidences in the decay of 10-day Pt^{188} by means of a two-lens β-spectrometer and a scintillation γ-spectrometer.

1. Conversion electron spectrum

The chemical procedure of carrier-free separation of the platinum from the spallation products was described in Ref.1. The platinum sources were prepared by evaporation from hydrochloric solution onto 1 x 12 mm strips of platinum foil. With the utilized 0.6% of 4π acceptance angle the instrumental resolution was 0.4%. However, the appreciable thickness of the sources increased the relative half-width of the electron lines, which, as a result, attained 0.8% in the 30-40 keV energy region. The first results of our investigation of the conversion electron spectrum of the platinum fraction were published in Ref.1. In the present work, we extended the investigated energy range and also obtained more accurate data on some of the electron lines. In all, we carried out five series of measurements in the electron energy range from 30 to 360 keV. (Under a series of measurements we mean a number of measurements of the spectrum using a source or sources obtained from one irradiation.) The composite spectrum is shown in Fig.1. The lines were identified by observation of the decay periods and on the basis of the data in the literature on the energies of the known γ-transitions in platinum and daughter iridium. The results of investigation of the conversion electron spectrum are shown in Table 1. The list of electron lines can be divided into five groups on the basis of their periods.

Group I: Lines with T = 10-11 days

Of the 34 lines in this group*, 17 lines may be attributed to known transitions occurring in the decay of the daughter isotopes Ir^{188} and Ir^{189} (Table 1). The other 17 lines belong to Pt^{188}. Identification of the lines in this group was facilitated by the fact that, in addition to measurements of the spectrum immediately after irradiation, there were carried out measurements with Pt sources separated from the Ir two to four weeks after bombardment. No lines corresponding to the decay of Ir^{189} appear in this spectrum; the lines of Ir^{188} exhibit an increase in intensity during the first days after separation. Our data substantiate the existence[5] in the decay of Pt^{188} of γ-transitions with energies of 54.6, 139.9, 187.0, 194.7, 281, 410 and 472.5 keV. The 56.8 keV electron line cannot be identified with any known γ-transition; we assume that it is the K line of a new 132.9 keV transition, the L line of which lies between the intense Pt^{188} 118.4 keV and Pt^{193m} 121.4 keV lines and is masked by them. The 132.9 keV transition may occur between the 187.0 and 54.6 keV levels, inasmuch as its energy equals, within the limits of the experimental error, the energy difference between the 187.0 and 54.6 keV transitions (Fig.2).

---

*The 23.4 and 28.6 keV lines were observed only in the spectrum recorded on the two-lens β-spectrometer.

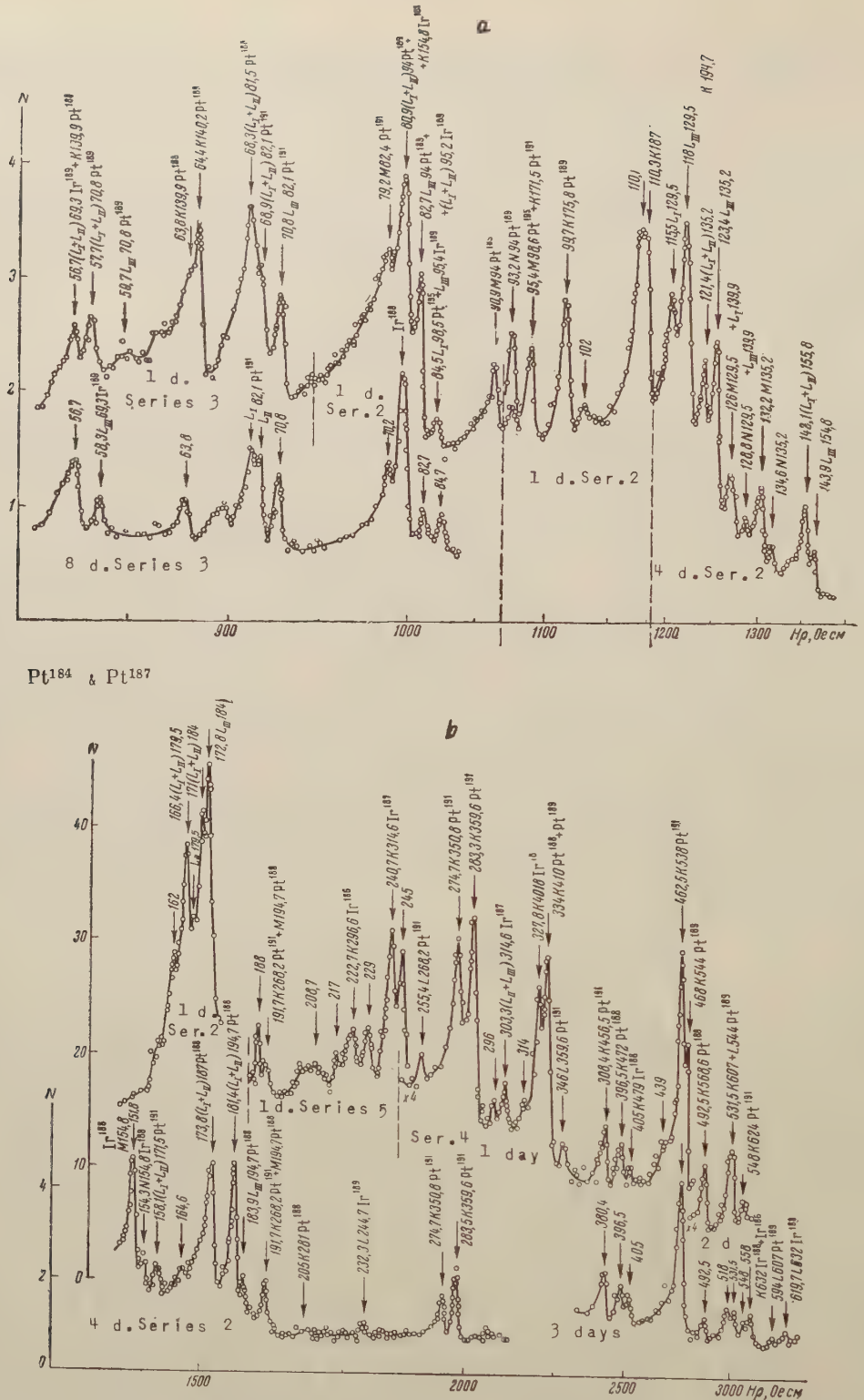

Fig.1. Conversion electron spectrum of the platinum fraction: a - 55 to 144 keV energy range, b - 154 to 620 keV range. The individual parts of the spectrum have been taken from different series of measurements carried out on sources irradiated for different times (see Table 1 for additional data on identification of the lines in the 1200 to 1300 Oe cm region).

Table 1

Results of investigation of the conversion electron spectra of the platinum fraction

E_e, keV	Period		Identification	E_γ, keV		Isotope
	Our data	Refs. 1–4		Our data	Refs. 1–3, 5	
1	2	3	4	5	6	7
Group I						
41,3±0,2	10±1 days		L_I 54,7			
41,9±0,2	»		L_{II} 54,7			
43,4±0,2	»		L_{III} 54,6	54,6±0,2	55	
51,2±0,1	»		M 54,4			
56,8±0,1	»		K 132,9	132,9±0,1	—	
63,8±0,1	»		K 139,9			
126,3±0,5	»		$(L_I + L_{II})$ 139,4	139,9±0,1	140	
128,7±0,4	»	10 days	L_{III} 139,9			
110,9±0,2	»		K 187,0			
173,8±0,2	»		$(L_I + L_{II})$ 186,9	187,0±0,2	188,5	Pt^{193}
118,4±0,3	»		K 194,5			
181,4±0,2	»		$(L_I + L_{II})$ 194,5			
183,9±0,2	»		L_{III} 195,1	194,7±0,3	195,7	
191,6±0,3	~10 days		M 194,7			
205,0±1,5	10±1 days		K 281	281±1,5	279	
334,0±0,5	4–8 days		K 410	410±0,5	410	
396,5±2	~10 days		K 472,5 + L 410	472,5±2	470	
80,9±0,2	10±1 days	10 days	K 154,8			
142,1±0,2	»	T of Pt^{188}	$(L_I + L_{II})$ 154,8			
143,9±0,3	»		L_{III} 154,8	154,8±0,2	155	Ir^{194}
151,8±0,2	»		M 154,8			
154,3±0,3	»		N 155,0			
405±1,5	Several days		K 478,8	479±1,5	478,5	
558±2	build-up observed		K 632	632±2	633,5	Ir^{188} + Ir^{194}
23,4±0,4	10 days		L 36	36,1±0,4	36,2	
28,6±0,4	»		M 31,3	31,3±0,4	30,8	
45,7±0,3	11±1 days		$(L_I + L_{II})$ 58,4	58,4±0,3	59,0	
56,7±0,1	»	11 days	$(L_I + L_{II})$ 69,4			
58,3±0,2	»		L_{III} 69,2	69,3±0,2	69,5	Ir^{195}
66,5±0,2	9±1,5 days		M 69,5			
82,6±0,2	11±1 days		$(L_I + L_{II})$ 95,4	95,4±0,3	95,2	
84,5±0,3	»		L_{III} 95,4			
170,8±0,4	10±1 days		K 244,7			
232±1	Several days		$(L_I + L_{II})$ 244,7	244,7±0,4	245	
Group II						
51,2±0,1	4±1 days	3,3–4,4 d.	K 129,6			
115,5±0,3	»		L_I 129,4			
118,0±0,2	»		L_{III} 129,6	129,5±0,2	129,5±0,2	Pt^{193*}
126±0,5	»		M 129,5			
128,8±0,3	5±1 days		N 129,5			
84,5±0,3	4±1 days		L_I 98,4	98,5±0,2	97–99	
95,4±0,1	»		M 98,6			
121,4±0,3	4±1 days	3,4–4,5 d.	$(L_I + L_{II})$ 135,0			
123,4±0,3	»		L_{III} 135,0	135,2±0,3	135,5	Pt^{193*}
132,2±0,2	»		M 135,5			
134,6±0,2	»		N 13*,5			
52,9±0,2	3,5±1 days		K 129,0	129,0±0,2	129,4–129,6	
68,9±0,4	»		$(L_I + L_{II})$ 82,0			
70,8±0,2	»		L_{III} 82,0	82,1±0,4	82,5	
79,2±0,4	»		M 82,4			

Table 1 continued

E_e, keV	Period		Identification	E_γ, keV		Isotope
	Our data	Refs. 1–4		Our data	Refs. 1–3, 5	
1	2	3	4	5	6	7
95,5±0,2	3,5±1 days		K 171,6	171,5±0,3	172	
158,1±0,3	»		$(L_I + L_{II})$ 171,4			
191,7±0,3	3,5±0,5 days	2,9–3,2 d.	K 267,8	268,2±0,5	267–268	
255,4±0,4	3,2±0,5 days		$(L_I + L_{II})$ 268,5			
274,7±0,4	»		K 350,8	350,8±0,4	351–352	Pt^{191}
283,5±0,4	2,6±0,5 days		K 359,6	359,6±0,4	360–361	
246±1	Several days		$(L_I + L_{II})$ 359			
334,0±0,5	4,4–8 days		K 410,1	410,1±0,5	410	
380,4±0,6	5–8 days		K 456,5	456,5±0,6	456–458	
462,5±1,5	2,5–4 days		K 538,6	538±2	539–540	
548±1,5	~2 days		K 624	624±1,5	623	
			Group III			
57,7±0,1	10± 2 hrs		$(L_I + L_{II})$ 70,8	70,8±0,2	—	
59,7±0,1	10± 3 hrs		L_{III} 70,9			
68,3±0,1	9±1 1 hrs		$(L_I + L_{II})$ 81,4	81,5±0,3	—	
70,6±0,2	Several hours		L_{III} 81,8			
80,9±0,2	10±1 hrs		$(L_I + L_{II})$ 94,0			
82,7±0,2	9±1 hrs		L_{III} 93,9	94,0±0,2	94,0	
90,9±0,1	10±0,5 hrs		M 94,1			
93,2±0,2	10±1 hrs		N 93,9			
64,4±0,2	11±1,5 hrs	11 hrs	K 140,5	140,2±0,3	140	Pt^{189}
126,9±0,4	Several hours		$(L_I + L_{II})$ 140			
99,7±0,2	10±0,5 hrs		K 175,8	175,8±0,3	—	
162,7±0,4	Several hours		$(L_I + L_{II})$ 175,7			
468,0±1	~11 hrs		K 544	544±1	—	
492,5±1	9–14 hrs		K 568,6	568,6±1	—	
531,5±1	10–14 hrs		K 607,6 + L 544	607±1	—	
594±1	»		L 607			
37,3±0,1	11±2 hrs		—	—	—	
229,7±0,2	10–14 hrs		—	—	—	
222,7±0,3	14±1 hrs	411–6 hrs	K 296,9	296,6±0,3	297	Ir^{188}
240,7±0,3	12±1 hrs	13 hrs	K 314,6	314,6±0,3	314,4	Ir^{187}
303,3±0,5	10 hrs		$(L_{II}+L_{III})$ 314,9			
327,8±0,5	11±2 hrs		K 401,8	401,8±1	401	
102,0±0,2	15–20 hrs					
110,1±0,2	15 hrs					
208,7±0,4	11–16 hrs		Not identified			
217,2±0,3	Several hours					
205,4±0,6	»					
			Group IV			
103,4±0,2	⩽2 hrs		K 179,5	179,5±0,3	—	Pt^{184} or Pt^{187}
166,4±0,4	3±1 hrs		$(L_I + L_{II})$ 179,5			
168,3±0,4	3 hrs	2–3 hrs	L_{III} 179,5			
171,0±0,4	2,5±0,5 hrs		184,1	184,0±0,4	—	
172,8±0,4	2,5±0,5 hrs		184,0			
188,0±0,3	3 hrs		Not identified			
245,6±0,6	3–4 hrs					

Table 1 continued

E_e, keV	Period		Identification	E_γ, keV		Isotope
	Our data	Refs. 1–4		Our data	Refs. 1–3, 5	
1	2	3	4	5	6	7
			Group V			
249,5±0,5	Long (days)	10 days	K 323,4	323,4±0,5	323	Ir^{188}
261±1	"	—	—	—	—	—
268±0,7	"	10 days	$(L_I + L_{II})$ 281	281±0,7	279	Pt^{188}
296–296,5	Pos. build up	—	—	—	—	—
314±1	Unknown	—	—	—	—	—
439±2	"	—	—	—	—	—
518±2	Pos. build up	—	—	—	—	—
620±2	Unknown	10 days	L 632,4	632,4±2	633,5	Ir^{188}

Table 2

Relative intensities of the K conversion lines of Pt^{188}

E_γ, keV	132,9	139,9	187	194,7	281	380	410	472,5
I_K	5	10	100	90	1,5	$\leqslant 3$	$\leqslant 3$	3

Table 3

Multipole order assignments for some transitions

E_γ, keV	Relative conversion coefficient	Multipole order assignments
54,7	$L_I : L_{II} = 0,7$ $L_{II} : L_{III} = 0,9$ $L_I : L_{III} = 0,5$ $L_{III} : M = 1,3$	$E2 + M1$
139,9	$K : (L_I + L_{II}) \geq 1,7$	not higher than $E2$
187,0	$K : (L_I + L_{II}) = 5$	$E2 + M1$ $(M2 + E1)$
194,7	$(L_I + L_{II}) : L_{III} = 4$ $K : (L_I + L_{II}) = 3,5$ $L_{III} : M = 1$	$E2 + M1$

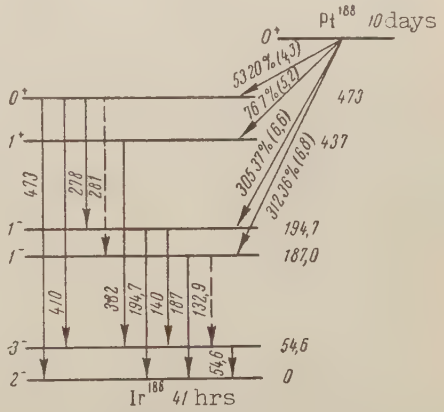

Fig.2. Decay scheme for Pt^{188} The 132.9 and 281 keV γ-transitions, inferred from the present conversion electron data, are indicated by dashed lines.

The relative intensities of the K conversion lines of Pt^{188} are listed in Table 2. We were able to evaluate the multipole orders of the 54.6, 139.9, 187.0 and 194.7 keV γ-transitions by comparing the ratios of the heights of the K, L and M shell and L_I, L_{II} and L_{III} subshell conversion peaks with the corresponding theoretical conversion coefficient ratios; the resultant assignments are listed in Table 3.

Group II: Lines with T = 3-4 days

The 26 conversion lines in this group correspond to well known γ-transitions: the 98.5 and 129.5 keV transitions in Pt^{195m}, the 135.2 keV transition in Pt^{193m}, and the 82.1, 129.0, 171.5, 268.2, 350.8, 359.6, 410.1, 538 and 624 keV transitions occurring in the decay of Pt^{191}.

Group III: Lines with T = 10-15 hours

Of the 27 lines in this group, we associate 4 lines with the known[3] 296.6 keV transition in Ir^{186} and the 314.6 and 401.8 keV transitions in Ir^{187}; we attribute 18 lines to Pt^{189}; hence 5 lines remain unidentified. In addition to the known transitions with energies of 140.2 (Ref.2) and 94 keV (Ref.1), we hypothesized the existence of 6 additional transitions in the decay of Pt^{189}, transitions with energies of 70.8, 81.4, 175.8, 544, 568.6 and 607 keV. It must be noted, however, that the data on these transitions are still inadequate and require further verification.

Group IV: Lines with T = 2-3 hours

Five lines in this group were identified earlier[1] as the conversion lines of 179.5 and 184.0 keV γ-transitions occurring in the decay of Pt^{184}, Pt^{186} or Pt^{187} (Ref.4). According to Ref.6, the decay of Pt^{186} goes to the ground state of Ir^{186} and, consequently, these γ-transitions should be attributed to the decay of Pt^{184} or Pt^{187}. Accordingly, the 188.0 and 245.6 keV conversion lines detected in the present work should also be attributed to the same isotopes. In view of the fact that measurements of the spectra were started some 8-9 hours after bombardment, the present data on the 2-3 hour isotopes are necessarily less complete than for the longer lived isotopes.

Group V

We were unable to determine the decay period with reasonable accuracy for some of the conversion lines; we have put these lines in Group V. Three of these lines can be attributed to the 281 keV transition in the decay of Pt^{188} and the 323.4 and 632.4 keV transitions in the decay of Ir^{188}. The remaining 5 lines have so far not been identified (see Table 1).

2. Results of investigation of the decay of Pt^{188}

In decaying, Pt^{188} converts to the odd-odd nucleus Ir^{188}. The γ-radiation of Pt^{188} was investigated on a scintillation γ-spectrometer with a relative line half-width of 9% (Cs^{137} 661 keV line). The γ-spectrum was investigated with a platinum source separated from the iridium some 4 weeks after bombardment. However, even in this case analysis of the spectrum was rendered difficult owing to the presence of intense lines of daughter Ir^{188} (T = 41 hr). Fig.3 shows the γ-spectrum obtained during the first day after separation; Fig.4 shows the γ-spectrum of Pt^{188} in equilibrium with daughter Ir^{188}. For measuring γ-γ coincidences we used a scintillation coincidence spectrometer[7] with a resolving time 2τ = $= (1.5\text{-}2)\cdot 10^{-7}$ sec.

As a result of these measurements we feel safe in asserting the following:

a) There are no coincidences between the 187.0 and 194.7 keV γ-rays, which is in agreement with the data of Ref.5.

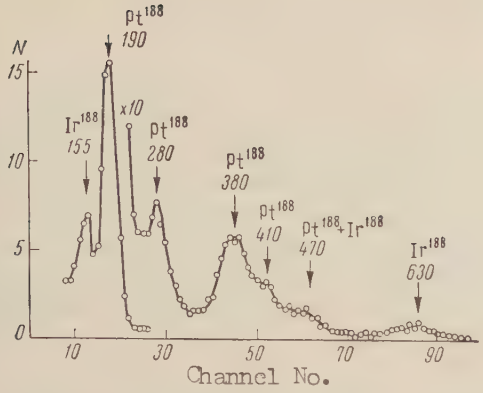

Fig.3

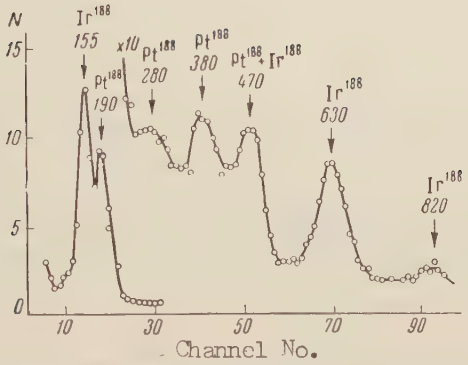

Fig.4

Fig.3. Gamma-spectrum of Pt^{188} recorded on a scintillation spectrometer the first day after separation from Ir.

Fig.4. Gamma-spectrum of Pt^{188} in equilibrium with daughter Ir^{188}.

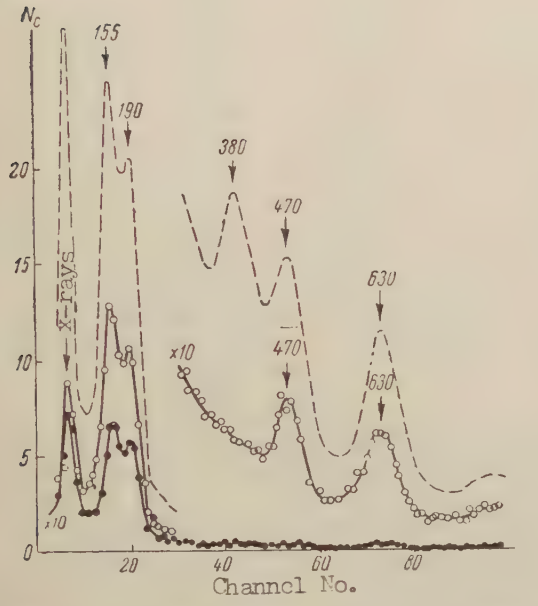

Fig.5. Coincidences with K x-rays (open circles). Solid circles - chance coincidences; dashed line - singles spectrum.

b) There are no coincidences between the K x-rays and the 381 keV γ-rays (Fig.5), which is also in agreement with Ref.5 and is connected with the fact that only L capture goes to the 437 keV level (Fig.2). On the basis of energy considerations it may be assumed that the 473 keV level is also fed only by L capture. The peak at 470 keV appearing in our spectrum of coincidences with K x-rays is probably due to Ir^{188}.

There are evinced with low intensity coincidences between the 281 keV γ-rays and the unresolved 187-194.7 and 139.9-132.9 keV γ-rays, which is not in conflict with the proposed decay scheme.

As noted above, we also carried out measurements of e-γ coincidences using the two-lens β-spectrometer in conjunction with the scintillation γ-spectrometer[8]. The conversion electron spectrum obtained on the two-lens β-spectrometer is shown in Fig.6. The results of e-γ coincidence measurements substantiate the data obtained by observation of γ-γ coincidences and, moreover, indicate the existence of low intensity coincidences between the L54.6 electrons and the unresolved 140-133 and 380-410 keV γ-rays.

On the basis of our evaluations of the multipole orders (Table 3) and the values of log ft given in Ref.5, we made tentative spin assignments for the excited levels of Ir^{188}; these are indicated at the left in Fig.2. The difference between the spins of the ground state and the first excited level and the value of the energy of the first excited level give reason to assume that this 54.6 keV level is a rotational one (see Ref.9). The moment of inertia of the Ir^{188} nucleus in this case proved to be 2.5 times greater than the moment of inertia of the neighboring even-even Os^{186} nucleus.

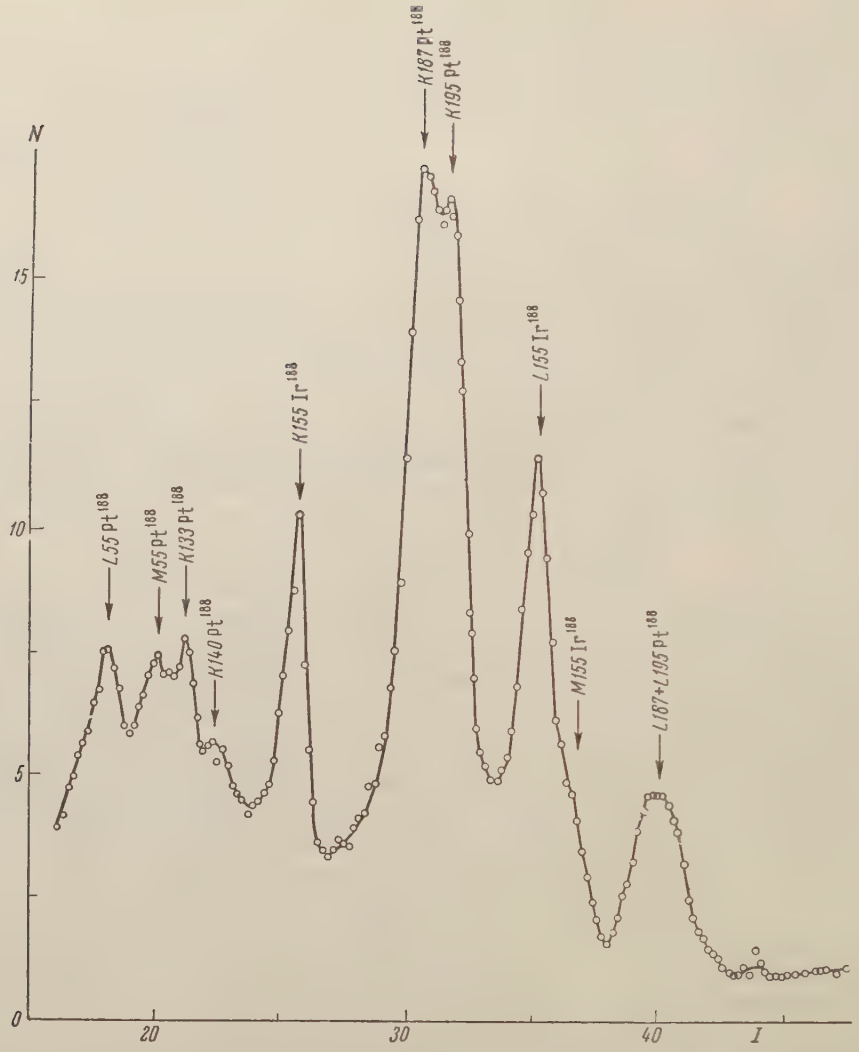

Fig.6. Conversion electron spectrum in the 40 to 220 keV region, recorded on the two-lens β-spectrometer.

Scientific-Research Institute of Nuclear Physics.
Academy of Sciences of the USSR

References

1. T.V.Malysheva, B.A.Khotin, A.K.Lavrukhina, L.N.Kryukova & V.V.Murav'eva, Izv.AN SSSR, Ser.fiz., 24, 1109 (1960). (Trans.Bulletin, 24, 1113.)

2. D.Strominger, J.M.Hollander & G.T.Seaborg, Revs.Mod.Phys., 30,585 (1958).

3. R.M.Diamond & J.M.Hollander, Nucl.Phys.,8, 143 (1958).

4. V.I.Baranov, K.Ya.Gromov, B.S.Dzhelepov, Zyong Chong Bai, T.V.Malysheva, V.A.Morozov, B.A.Khotin & V.G.Chumin, Izv.AN SSSR, Ser.fiz., 24, 1079 (1960). (Trans.Bulletin, 24, 1086.)

5. Nuclear Data Sheets, 3 (1959).

6. Nuclear Data Sheets, 5 (1959).

7. N.N.Delyagin & A.A.Sorokin, Zhur.eksp.i teor.fiz., 38, 1106 (1960). (Trans. Soviet Physics - JETP.)

8. V.P.Parfenova, N.V.Forafontov & V.S.Shpinel', Izv.AN SSSR, Ser.fiz., 21, 1601 (1957). (Trans.Bulletin, 21, 1590.)

9. L.K.Peker, Ibid., 24, 365 (1960). (Trans.Bulletin, 24, 350.)

INVESTIGATION OF THE RADIATION FROM NEUTRON-DEFICIENT HAFNIUM ISOTOPES

- V.Brabec, B.Kracik, T.Kracikova, Z.Miligi, M.Weis, A.Mashtalka, M.Vobecky & V.Gnatovicz

The investigated neutron-deficient hafnium isotopes were obtained by spallation of tantalum bombarded with 660 MeV protons in the synchrocyclotron of the Joint Institute for Nuclear Research in Dubna.

The measurements were carried out on an intermediate focusing β-spectrometer[1] and an NaI(Tl) scintillation spectrometer coupled to a 200-channel pulse height analyzer. The resolution of the β-spectrometer was 2.5%; that of the scintillation spectrometer was 9% (Cs^{137} 661 keV line).

Table 1

Lines identified in the conversion electron spectrum of Hf^{171} and Hf^{173}

E_e, keV	Identification	Isotope	E_e, keV	Identification	Isotope
35	$K98$	Hf^{171}	145	$K208$	Hf^{171}
43	$K-L\bar{L}$	—	152 **	$L162$	Hf^{173}
51	$K-LM$	—	154	$L164$	Hf^{171}
61	$K124$	$Hf^{171}+Hf^{173}$	182 ***	?	—
72 *	$K135$	Hf^{173}	198 ****	$L208$	Hf^{171}
77 *	$K140$	Hf^{173}	206	K270	Hf^{171}
83	?	—	234	$K297$	Hf^{173}
88	$L98$	Hf^{171}	244 **	$K307$	Hf^{173}
99 *	$K162$	Hf^{173}	249 **	$K312$	Hf^{173}
101 *	$K164$	Hf^{171}	260	$L270$	Hf^{171}
114	$L124$	Hf^{173}	287	$L297$	Hf^{173}
125 *	$L135$	Hf^{173}	297 **	$L307$	Hf^{173}
130 *	$L140$	Hf^{173}	302 **	$L312$	Hf^{173}
138 **	$M140$	Hf^{173}			

*Line not fully resolved. **Line located in the high-energy tail of a more intense line. ***Double line. ****Line located in the low energy tail of a more intense line.

The hafnium fraction was separated from the bombarded target by the carrier-free procedure described in Ref.2. The activity was deposited on a thin collodion film and then covered with a thin layer of aluminum by vacuum evaporation. The diameter of the source was 3 mm.

There were identified the following isotopes in the hafnium fraction: 16-hour Hf^{171}, 24-hour Hf^{173} and 70-day Hf^{175} and their daughter isotopes 8.1-day Lu^{171}, 1.4-year Lu^{173}. The present work was concerned primarily with investigation of the short-lived part of the hafnium fraction (Hf^{171} and Hf^{173}). We studied the 30 to 350 keV region of the spectrum.

Hf^{173} has been thoroughly investigated in the work of Harmatz et al[3]; although Hf^{171} has been studied by a number of authors[4-9], its conversion electron spectrum has so far not been investigated.

The results of our measurements of the conversion electron spectrum are shown in Table 1 and in Figs.1 & 2.

The spectrometer was calibrated with reference to the lines of Hf^{173}, the energies of which were accurately determined in the work of Harmatz et al[3]. The relative intensities of the Hf^{171} lines were obtained by graphic resolution of the conversion spectrum and subtraction of the lines belonging to Hf^{173}, Hf^{175}, Lu^{171} and Lu^{173}.

In order to determine the contribution from the long-lived isotopes the conversion electron spectrum of the hafnium fraction was studied for a period of over

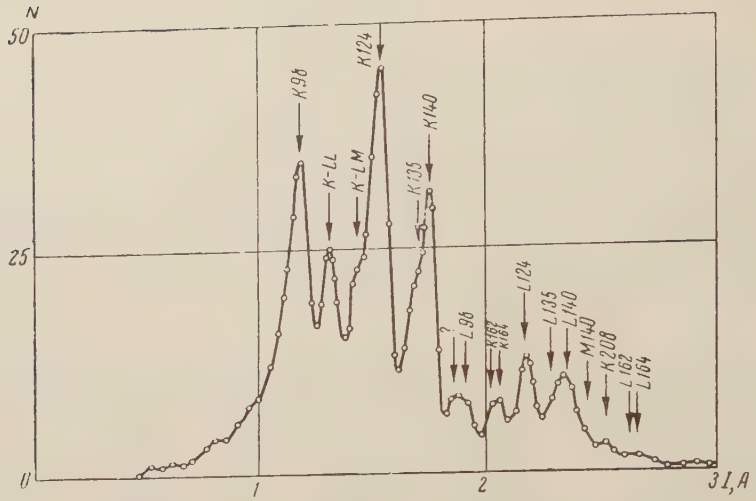

Fig.1. Conversion electron spectrum of the hafnium fraction in the 0 to 195 keV energy region.

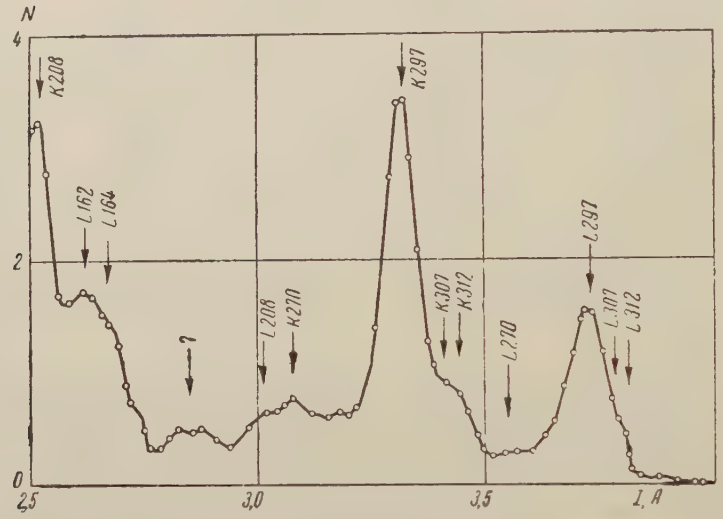

Fig.2. Conversion electron spectrum of the hafnium fraction in the 140 to 330 keV region.

Table 2

Relative intensities of the conversion lines of Hf^{171}

Line	Relative intensity	K/L
K98	100	7
K124	80	~9
K164	10	—
K208	5	—
K270	1	—

a month. In the case of Hf^{173} we also utilized the intensity data of Harmatz et al.

The resultant relative intensities of the K conversion lines of Hf^{171} and the K/L ratios are listed in Table 2. The error in determining the intensities of the K98 and K124 lines may be as great as 50%. In the case of the other lines, the indicated intensities are order of magnitude values.

In the γ-spectrum investigated on the scintillation spectrometer there were observed the following transitions: 100 and 170 keV belonging to Hf^{171} and 130 and 310 keV belonging to Hf^{173}. In addition there were observed indications of lines with energies of about 210 and 250 keV. If these γ-rays exist they are probably associated with the γ-transitions giving rise to the K and L208 and K and L270 conversion lines of Hf^{171}.

Institute of Nuclear Studies
Czechoslovak Academy of Sciences, Rzesz &
Department of Technical and Nuclear Physics,
Czechoslovak Technical College, Prague

References

1. Z.Plajner & V.Brabec, Ceskosl.casop.fys., 10, 115 (1960).
2. M.Vobecky & A.Mashtalka, Materialy III Soveshchaniya po neitronodefitsitnym izotopam (Transactions of the Third Conference on Neutron-Deficient Isotopes), Dubna, 1960.
3. B.Harmatz, T.H.Handley & J.W.Mihelich, Phys.Rev., 114, 1082 (1959).
4. G.Wilkinson & H.G.Hicks, Phys.Rev., 81, 540 (1951).
5. A.H.Wapstra & C.Jongejans, Physica, 20, 36 (1954).
6. W.E.Nervik & G.T.Seaborg, Phys.Rev., 97, 1092 (1955).
7. W.H.Johnson, Jr. & V.B.Bhanot, Phys.Rev., 107, 1669 (1957).
8. V.I.Baranovskii & A.V.Kalyamin, Izv.AN SSSR, Ser.fiz., 23, 831 (1959). (Trans.Bulletin, 23, 825.)
9. E.P.Grigor'ev, O.V.Larionov, M.K.Nikitin, L.S.Sakharov & V.O.Sergeev, Materialy II Soveshchaniya po yadernoi spektroskopii neitronodefitsitnykh izotopov redkikh zemel' (Transactions of the Second Conference on Nuclear Spectroscopy of Neutron-Deficient Rare Earth Isotopes), Dubna, 1959.

PHOTODISINTEGRATION OF Li^7 BY BREMSSTRAHLUNG OF UP TO 9.5 MeV

- V.G.Shevchenko & B.A.Yur'ev

At present certain difficulties are encountered in attempting to explain the energies of the low-lying states of Li^7 and their spins and parities on the basis of the shell model. The results of calculations carried out by Inglis[7], Kurath[2] and Balashov[3], using intermediate coupling and Meshkov & Ufford[4] in the LS limit, indicate that at ~5.5 MeV there should be a $5/2^-$ level with the classification $^{22}F_{5/2}$ in the LS coupling scheme. Experimental data on reactions with particles indicate[5], however, that in this region there is only one wide level with even parity, which Lane has interpreted as a single-particle level with the configuration $1s_{4}1p^{2}2s_{1/2\ 1/2}$.

Erdös et al[6] made an attempt to determine the level diagram of Li^7, using the $Li^7(\gamma,t)He^4$ reaction with $E_{\gamma max}$ = 31 MeV. These authors detected levels with energies of 4.7, 5.5, 6.8, 7.4, 8.3 and 9.0 MeV and made an attempt to determine the spins and parities of the first three levels on the basis of the angular distributions. However, they were unable to obtain unambiguous results, owing to inadequate statistics. Moreover, the possible admixture of stars from the $N^{14}(\gamma,\alpha)B^{10}$ and $O^{16}(\gamma,\alpha)C^{12}$ reactions, which these authors were unable to separate from the investigated cases, and some contribution from the $Li^6(n,\alpha)H^3$ reaction increased the uncertainty of their results.

In the present work we investigated the $Li^7(\gamma,t)He^4$ reaction at a maximum bremsstrahlung energy of 9.5 MeV for the purpose of more precise determination of the characteristics of the excited states of Li^7, lying in this energy range.

Experimental procedure

Our γ-ray source was the 35 MeV betatron of the Scientific Research Institute of Nuclear Physics at Moscow State University. The 9.5 MeV maximum γ-ray energy was chosen so that the $Li^7(\gamma,t)$ reaction would be the only reaction on Li^7 with emission of charged particles. The experimental arrangement is shown in Fig.1. The bremsstrahlung beam, before impinging on the target, passed through a collimator 32 cm long, and a magnetic field which deflected the electrons from the beam. The target was made of metallic lithium in the form of 2.4 mg/cm^2 thick foil and was mounted in the vacuum chamber at an angle of 30° to the direction of the γ-ray beam.

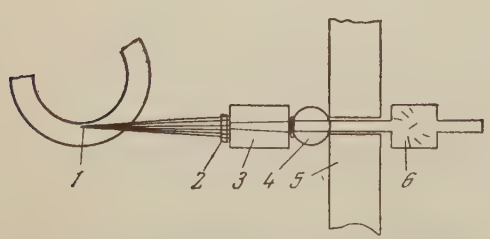

Fig.1. Arrangement of the experiment: 1) betatron target, 2) thin walled ionization chamber, 3) collimator, 4) deflecting magnet, 5) shielding wall, 6) vacuum chamber.

The radiation dose was determined by means of an ionization chamber, the absolute calibration of which was carried out with reference to the indications of a thick walled aluminum chamber[7]; the calibration error, in view of the low intensity, attained ~20%.

The tritons emitted from the target were detected by NIKFI photographic plates with 100 μ thick type T-3 emulsion; these plates were mounted in the chamber at angles 30, 60, 90, 120 and 135° relative to the direction of the γ-ray beam. The position of the beam axis relative to the center of the target was determined by an x-ray film and checked by comparison of the effects in two photographic plates mounted symmetrically relative to the center of the target at an angle of 90° to each other. The absolute magnitude of the solid angles was determined graphically and by calculation. In scanning the plates we

selected the tracks, corresponding to $\geq$1.2 MeV tritons, that began from the surface of the emulsion and lead from the irradiated part of the target. The triton energy was determined from the range-energy curves for Ilford C-2 emulsion with a ~6% correction for the difference between the thickness of the T-3 and C-2 emulsions.

We measured the background in the chamber in the absence of the target. It proved to be isotropic for all angles and in all directions and amounted to ~40% of the investigated effect. In view of the high level of the background we took special pains to determine it accurately with good statistics. In all, we scanned 53 cm^2 of emulsion and found 998 triton tracks.

Experimental results

The total energy distribution of tritons for all the measurement angles is shown in Fig.2. It will be seen that there are clearly evinced individual triton groups with energies of 1.7, 2.5 and 3.5 MeV and a poorly resolved group with an energy of 3.1 MeV. In view of the fact that our target consisted of a natural mixture of lithium isotopes (92% Li^7 and 7.5% Li^6), at the chosen maximum γ-ray energy there could have occurred the $Li^6(\gamma,p)He^5$ and $Li^6(\gamma,np)He^4$ reactions. The cross sections for these reactions near the threshold have not been accurately determined. According to our evaluations, their contribution could amount to no more than 10% relative to the yield of the investigated reaction. Actually, however, this contribution was much smaller, inasmuch as otherwise in the obtained spectrum above the maximum allowable energy for tritons there would have been present longer tracks that could be mistaken for triton tracks. Such tracks are not present in the energy distributions. The α-particles from the investigated reaction had ranges much shorter than the range of the lowest energy tritons and hence could readily be discriminated. The energy distribution shown in Fig.2 contains corrections taking into account the triton energy loss in the target and thus improving the resolution. The positions of the individual phototriton groups correspond to individual levels in Li^7 lying at 5.3 ± 0.2, 6.6 ± 0.2, 7.5 ± 0.25 and 8.3 ± 0.3 MeV.

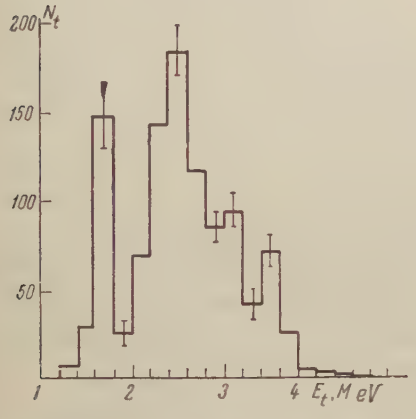

Fig.2. Distribution of tritons in energy.

The obtained energy distribution of phototritons enabled us to calculate the cross section for the $Li^7(\gamma,t)He^4$ reaction, inasmuch as the reaction products do not have excited states so that the energy and angle of emission of the triton uniquely determine the energy of the photon inducing the reaction. The calculations were carried out using the Schiff spectrum for bremsstrahlung in the case of a fixed target. The resultant cross section curve is shown in Fig.3. The accuracy of determining the absolute values of the cross section was limited by the accuracy of absolute measurement of the dose, errors in determining the thickness of the target, the solid angles and by statistical errors, so that the total measurement error attained 40%. The relative error, which may affect the shape of the cross section curve, was determined only by the statistical uncertainties, the magnitudes of which are indicated by the vertical bars in Figs.2 and 3.

The angular distributions for the 5.3, 6.6 and 8.3 MeV phototriton groups are shown in Figs.4,5 & 6. Inasmuch as the 3.1 MeV phototriton group (E_γ = 7.5 MeV) was poorly separated from the more intense 2.5 MeV group, we did not plot

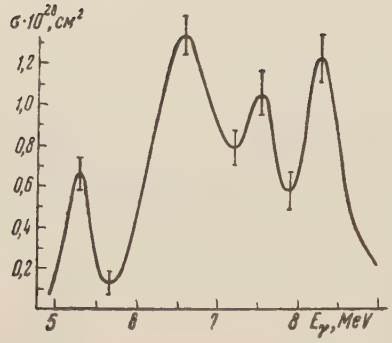

Fig.3

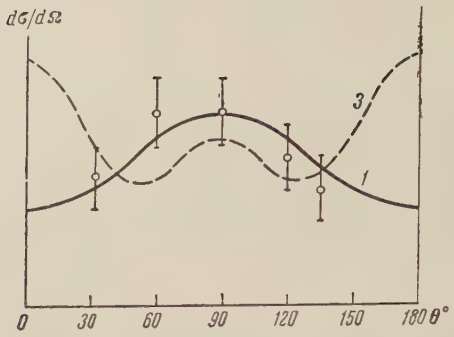

Fig.4

Fig.3. Variation of the cross section for the $Li^7(\gamma,t)He^4$ reaction as a function of the γ-ray energy.

Fig.4. Angular distribution of tritons from the 5.4 MeV state of Li^7. The solid and dashed curves, identified by the figures, represent the calculated angular distributions given in Table 1.

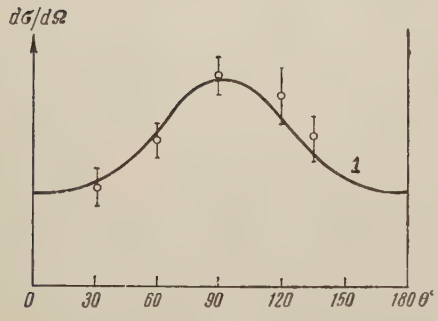

Fig.5

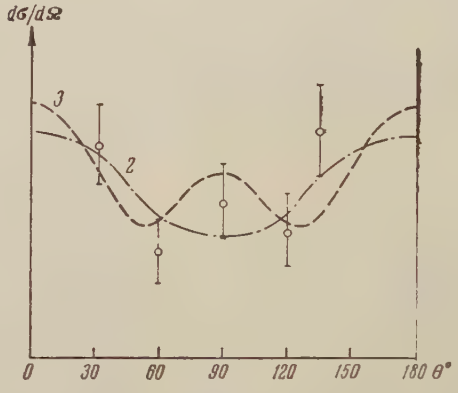

Fig.6

Fig.5. Angular distribution of tritons from the 6.6 MeV state of Li^7.

Fig.6. Angular distribution of tritons from the 8.3 MeV state of Li^7. The numbered curves represent the calculated angular distributions given in Table 1.

the angular distribution for this group. The vertical bars in the figures represent only the statistical uncertainties.

Discussion

The calculated angular distributions and radiation widths are given and compared with the experimental data in Figs.4,5 & 6 and in Tables 1 and 2. The radiation widths were calculated on the basis of the shell model with LS coupling. This is justified, inasmuch as for Li^7 the wave functions in the intermediate coupling approximation are very close to the wave functions in the LS coupling limit.

5.3 MeV level. Comparison of the calculated angular distributions with the experimental results (Fig.4) shows that the assignment for the 5.3 MeV level is 5/2; the value of the radiation width indicates that this level is excited by M1 and E2 transitions (Table 2) and is characterized by odd parity. Thus the 5.3 MeV level may be classified as $5/2^-$ and is, apparently, the level predicted in the calculations[1-4] mentioned in the introductory paragraph and identified as $^{22}F_{5/2}$

Table 1

Angular distributions of tritons in the $Li^7(\gamma,t)$ reaction

Multipole order of γ-transition	I*	L_K**	$f(\vartheta)$	Curve No. in Figs. 4–6
$E1$	$^5/_2$	2	$1+\sin^2\vartheta$	*1*
	$^3/_2$	2	$1-0{,}43\sin^2\vartheta$	*2*
	$^1/_2$	0	const	—
$M1$	$^5/_2$	3	$1+\sin^2\vartheta$	*1*
	$^3/_2$	1	$1-0{,}43\sin^2\vartheta$	*2*
	$^1/_2$	1	const	—
$E2$	$^7/_2$	3	$1+3{,}528\cos^2\vartheta-2{,}647\cos^4\vartheta$	—
	$^5/_2$	3	$1-1{,}875\cos^2\vartheta+2{,}5\cos^4\vartheta$	*3*
	$^3/_2$	1	const	—
	$^1/_2$	1	const	—

*I - spin of the excited state of Li^7.

**L_K - relative orbital momentum of the triton and α-particle.

Table 2

Comparison of the calculated and experimental radiation widths of the Li^7 levels

Level energy, MeV	$\Gamma_{\gamma theo}$, MeV			$\Gamma_{\gamma exp}$, MeV
	$E1$	$M1$	$E2$	
5,3	$2{,}2\cdot10^{-6}$	$4{,}2\cdot10^{-8}$	$1{,}1\cdot10^{-9}$	$(2{,}5\pm1{,}2)\cdot10^{-8}$
6,6	$4{,}2\cdot10^{-6}$	$7{,}7\cdot10^{-8}$	$5{,}0\cdot10^{-9}$	$(0{,}9\pm0{,}4)\cdot10^{-6}$
8,3	$1{,}08\cdot10^{-6}$	$0{,}8\cdot10^{-7}$	—	$(1{,}3\pm0;6)\cdot10^{-7}$

Table 3

Ratios of the reduced α-particle widths of the Li^7 levels to the Wigner limit

Level energy, MeV	γ^2/γ_0^2			
	$L=0$	$L=1$	$L=2$	$L=3$
5,3	0,041	0,057	0,13	0,56
6,6	0,105	0,14	0,23	0,93
8,3	0,04	0,05	0,07	0,20

in the LS coupling scheme. This inference is substantiated by analysis of the α-particle reduced widths, from which it follows that the reduced width is close to the single-particle width for $L = 3$ (Table 3).

In the intermediate coupling approximation allowance is made for mixing of states. Hence, in addition to E2 transitions, which alone cannot explain the experimentally measured width Γ_γ for this level, it may be excited by M1 absorption, owing to admixture of states. In this case, inasmuch as the intensity of M1 transitions is some 40 times greater than the intensity of E2 transitions, even a small admixture of p states (5-10%) is sufficient for M1 absorption to predominate and determine the intensity of the transition; this apparently obtains in our case (see Fig.4 and Tables 1 & 2).

6.6 MeV level. The angular distribution of phototritons for the 6.6 MeV level obtained experimentally is in good agreement with the curves calculated for spin 5/2 in the case of E1 and M1 transitions. The experimental width Γ_γ for this level is some 4-5 times smaller than the calculated width in the case of E1 transitions, and ~10 times greater than the calculated width in the case of M1 transitions. Apparently, the 6.6 MeV level is excited by E1 absorption and has even

parity. In several investigations of the $Li^6(d,p)Li^7$ reaction there was also observed a level at 6.5 MeV (Ref.5). It was interpreted as a level with configuration $1s^4 1p^2 2s_{1/2}$. However, detailed examination of the characteristics of the analogous level in the mirror nucleus Be^7 showed that identification of it as a $1s^4 1p^2 2s_{1/2}$ level encounters certain difficulties, primarily difficulties in explaining the large α-particle reduced widths obtained in experiment. We hypothesize that the observed 6.6 MeV ($5/2^+$) level has the configuration $1s^3 1p^4$. In this case it has an α-particle width close to the single-particle width and a small reduced width for nucleons. The last, apparently, is the reason why this level is so weakly evinced in the $Li^6(d,p)$ reaction and was not detected at all in a recent investigation[8] of this reaction. Inasmuch as the 6.6 MeV ($5/2^+$) level in the LS coupling scheme has $L = 2$, there should at a lower energy be an analogous level with $L = 0$ and $I^\pi = 1/2^+$.

There are certain indications that there exists a level at ~3 MeV, but its attributes are not known.[5] Moreover, if the 6.6 MeV level has the above mentioned configuration, somewhat above it in the energy scale there should be an analogous level with $I^\pi = 3/2^+$. Possibly this level is the 7.5 MeV level. Unfortunately, owing to the poor resolution we were unable to determine the spin of this level with certainty. However, the angular distribution obtained for it does not conflict with the assignment 3/2. As for the known[5] 7.45 MeV ($5/2^-$) level, the cross section for absorption of photons to this level is presumably small and it is impossible to detect it against the background of the above mentioned dipole transitions.

It must be noted that calculations in the framework of the shell model indicate that levels with the $1s^3 1p^4$ configuration should lie in the range of low energies. The fact that the radiation width for the E1 transition proved to be greater than the experimentally observed width may be due to mixing of configurations, as a result of which there may occur weakening of the transitions to the low-lying states and enhancement of transitions to high-lying levels.

8.3 MeV level. From analysis of the angular distributions (Fig.6) it follows that the possible assignments for this level are $3/2^+$, $3/2^-$ and $5/2^-$. Comparison of the calculated radiation widths for E1, M1 and E2 transitions with the experimental values shows that the integral cross section corresponds to the intensity of M1 transitions. This is also indicated by comparison of the reduced α-particle widths (Table 3) which shows that the reduced width is close to the single-particle width for $L = 1$ and that in the LS coupling scheme the 8.3 MeV level may be identified as [21] $^{24}P_{2/2}$. From this it follows that the 8.3 MeV level has spin and parity $3/2^-$.

Thus we have established that there may exist the following levels in the Li^7 nucleus: 5.3 ± 0.2 ($5/2^-$), 6.6 ± 0.2 ($5/2^+$) and 8.3 ± 0.3 MeV ($3/2^-$). The indicated energies, as will be evident from Table 4, are in good agreement with the results of Erdös et al[6]; moreover, the position of the 5.3 and 8.3 MeV levels with odd parity is in agreement with the level scheme for Li^7 proposed by Balashov[3].

We desire to express our deep gratitude to V.V.Balashov, V.G.Neudachin, N.P.Yudin and Yu.F.Smirnov for valuable discussions, to A.V.Rudchenko for assistance in processing the experimental data and to the personnel of the betatron for assistance in the work.

Scientific-Research Institute of Nuclear Physics,
Moscow State University.

Table 4

Energies and spins and parities of the Li^7 levels according to different data

Ref.5		Ref.6		Our work		Ref.8	
E, MeV	I^π	E, MeV	I^π	E, MeV	I^π	E, MeV	I^π
0	$3/2^-$	—	—	—	—	0	$3/2^-$
0,478	$1/2^-$	—	—	—	—	0,477	$1/2^-$
4,63	$7/2^-$	4,7	$5/2^-$	—	—	4,74	$7/2^-$
—	—	5,5	$5/2^-, 3/2^-, 1/2^-$,	5,3±0,2	$5/2^-$	5,50	$5/2^-$
6,54	$(1/2^+,$ $3/2^+)$	6,8	$1/2^+, 5/2^-, 3/2^-,$ $1/2^-, 1/2^+$	6,6±0,2	$5/2^+$	—	—
—	—	—	—	—	—	6,98	$3/2^-$
7,47	$5/2^-$	(7,4)	—	(7,5±0,25)	—	7,46	$5/2^-$
—	—	—	—	—	—	7,76	$1/2^-$
—	—	(8,3)	—	8,3±0,3	$3/2^-$	8,41	$3/2^-$
—	—	(9,0)	—	—	—	8,86	$2/2^-$

References

1. D.R. Inglis, Revs.Mod.Phys., 25, 390 (1953).
2. D.Kurath, Phys.Rev., 101, 216 (1956).
3. V.V.Balashov, Zhur.eksp.i teor.fiz., 36, No.4, 1123 (1959). (Trans.Soviet Physics - JETP.); Thesis, Moscow State University, 1958.
4. S.Meshkov & C.W.Ufford, Phys.Rev., 101, 734 (1956).
5. F.Ajzenberg-Selove & T.Lauritzen, Nucl.Phys., 11, N 1, 1 (1959).
6. P.Erdös, P.Stoll, M.Wächter & V.Watagin, Nuovo cimento, 12, N 5, 639 (1954).
7. B.H.Flowers, I.D.Lawson & E.B.Fossey, Proc.Phys.Soc., 65B, 286 (1952).
8. E.W.Hamburger & J.R.Cameron, Phys.Rev., 117, 781 (1960).

PROBABILITIES FOR SINGLE-PARTICLE TRANSITIONS IN Yb^{173}

- E.E.Berlovich, M.P.Bonitz, Yu.K.Gusev & M.K.Nikitin

The results of measurements of the probabilities for single-particle transitions in deformed nuclei can be compared with the simple Weisskopf[1] single-particle evaluation and with the more rigorous formula of Nilsson[2] for ellipsoidal nuclei.

In the present work we investigated the mean lifetimes of the 351 and 637 keV levels in Yb^{173}, which forms from 480-day Lu^{173} by K capture. The decay scheme for Lu^{173} (see Refs.3-5) is given in Fig.1.

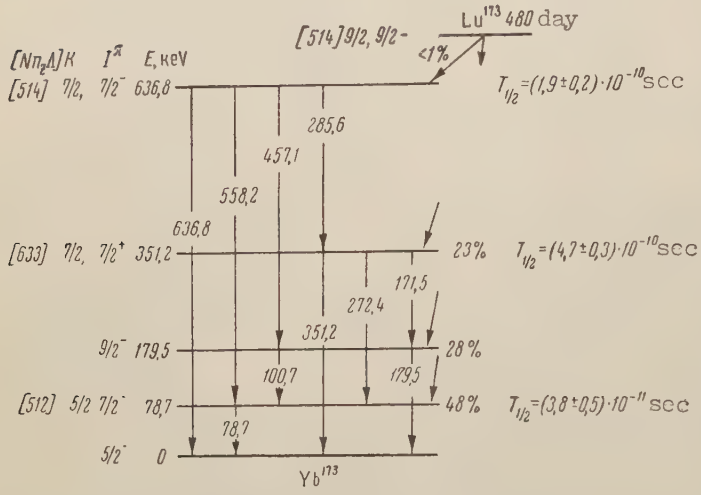

Fig.1. Decay scheme for Lu^{173} (Bichard et al[4]).

In the literature there can be found only the lifetimes of the first two excited states of Yb^{173} (79 and 179 keV), which were determined from Coulomb excitation experiments by de Boer et al[6]. The accuracy of these data is low, inasmuch as the E2 component in these transitions is very weak (4.5% according to Romanov et al[7]). Recently we determined the lifetime of the 79 keV level directly by the method of delayed coincidences[8] and obtained $T_{79} = (3.8 \pm 0.5) \cdot 10^{-11}$ sec, in agreement with the de Boer et al. This enabled us to determine the gyromagnetic ratios for Yb^{173}; in addition, knowledge of the lifetime of the 79 keV state is essential for determining the lifetimes of the 351 and 637 keV levels.

1. Experimental part

For determining the level lifetimes we used the "multichannel time analyzer procedure"; this has been described in detail in Refs.9 & 10; hence here we shall only mention the distinctive features of the present experiment. As in earlier measurements, we made sure that the measured (Lu^{173}) and reference (Na^{22}) sources had nearly the same strength. In addition, we insured virtual identity of the "single-pulse curves" for the measured and reference sources; hence the observed shifts of the coincidence curves were due only to the finite lifetimes of the investigated levels.

We recorded coincidences between the x-radiation accompanying K capture (by a 30 x 30 mm stilbene crystal) and the γ-rays accompanying de-excitation of the excited states (by a 30 x 30 mm NaI(Tl) crystal). A 1 mm thick phosphor bronze absorber in front of the NaI(Tl) crystal served to reduce the x-ray flux comprising an appreciable portion of the radiation from Lu^{173} ($\lesssim$20%). By way of reference source in both cases we used Na^{22} (annihilation radiation). The measurements with the investigated and reference sources were alternated repeatedly; this minimized the influence of slow drift of the electronic circuits on the results. An idea of the time resolution of the set-up may be obtained from the insert in Fig. 2, which shows the resolution curve obtained with two NaI(Tl) crystals at an energy of 511 keV in each branch (Na^{22} source).

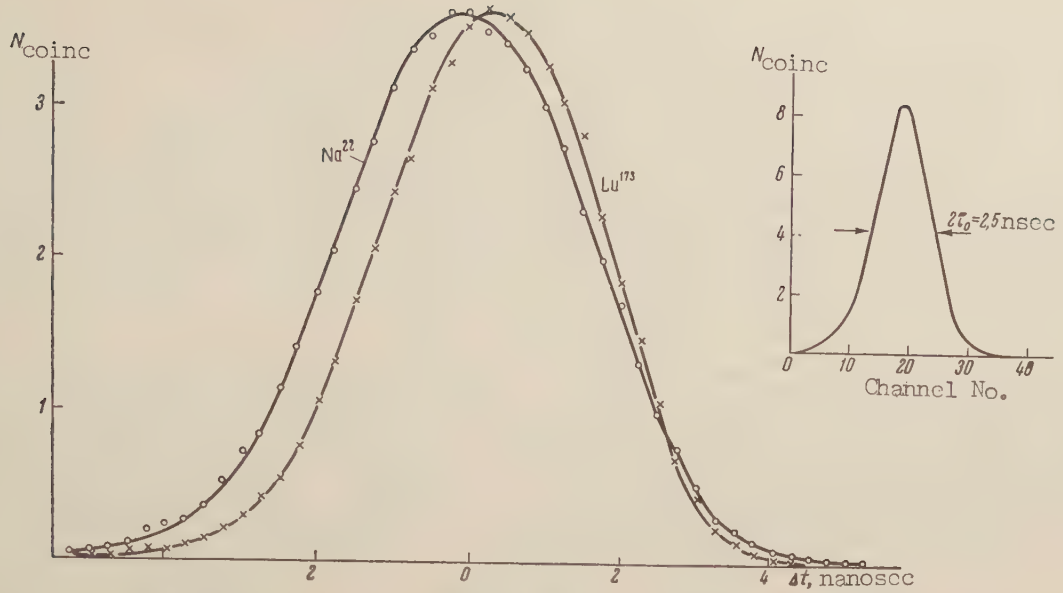

Fig.2. Coincidence curves for determining the lifetime of the 351 keV state of Yb^{173} (Δt = delay). Insert - curve of prompt coincidences of the annihilation photons from the Na^{22} source. Channel width $2.3 \cdot 10^{-10}$ sec.

351 keV level

The 351 keV level is de-excited by three E1 type transitions - 351, 272 and 171 keV - of which the second is the most intense; hence in our experiment the gate of the differential discriminator in the channel detecting the γ-rays was set on the 272 keV line, while the gate in the other channel was set on the x-ray peak, which is clearly evinced in the spectrum recorded by means of a stilbene crystal[11]. By control experiments with an Hg^{203} source, which emits only one γ-line of close energy (279 keV), it was established that under the conditions of our experiment there are no spurious coincidences with back-scattered photons. However, the coincidences of 272 keV γ-rays with x-rays accompanying K capture are inseparable from coincidences of the 272 keV γ-rays with the x-rays accompanying the internal conversion electrons of the 79 keV transition, which is in cascade with the 272 keV transition. Coincidences of the second type gave rise to an additional shift of the coincidence curve in the direction opposite to the shift produced by coincidences of the first type. However, knowing the K conversion coefficient for the 79 keV transition, which determines the number of accompanying x-ray photons, and the lifetime of the 79 keV level (Ref.8), we could allow for this effect. After introduction of the appropriate correction to the experimental results (Fig.2), we obtained a value of $(4.7 \pm 0.3) \cdot 10^{-10}$ sec for the mean lifetime of the 351 keV level.

A certain asymmetry of the curves is explained by the use of crystals with different characteristics (NaI(Tl) and stilbene). A somewhat greater width of the "prompt" coincidence curve (with the Na^{22} source) as compared with the investigated curve is explained by the fact that the shapes of the Na^{22} and Lu^{173} spectra within the limits of the chosen "gate" differ from each other, although the "energy centroids" of the Na^{22} and Lu^{173} peaks coincide: the Na^{22} spectrum varies smoothly (Compton distribution section), while the Lu^{173} spectrum contains a photopeak in the region of the gate, which is equivalent to effective reduction of the

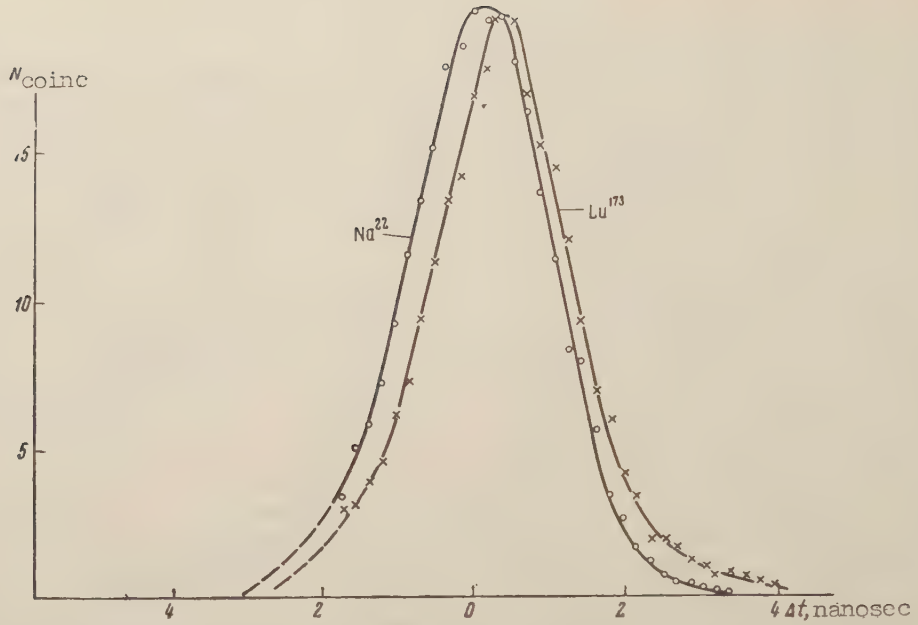

Fig.3. Coincidence curve for determining the lifetime of the 631 keV state of Yb^{173}.

gate width. Naturally, the steeper coincidence curve for the Lu^{173} source at a certain value of the relative bias can intersect the coincidence curve for the Na^{22} source. The time resolution in our experiments was about $4 \cdot 10^{-9}$ sec; the duration of the experiment was 10 hours.

637 keV level

The 637 keV state is de-excited by four low intensity transitions: 637, 558, 457 (M1 + E2) and 285 keV (E1).

The gate of the differential discriminator in one channel was set on the region encompassing the photopeaks of the two highest energy γ-rays (637 & 558 keV), while the other channel detected the x-radiation. In addition to the coincidences of interest, in this case there were also present a few coincidences of the 558 keV γ-rays with the x-rays accompanying the internal conversion electrons of the 79 keV transition; these additional coincidences were corrected for in processing the experimental results (Fig.3). Owing to the low coincidence counting rate the duration of the experiment in this case was about 27 hours. Thanks to the high energy of the γ-rays the time resolution in this experiment proved to be better than in the preceding case and equaled $2 \cdot 10^{-9}$ sec. After introducing the appropriate corrections we obtained $T_{637} = (1.9 \pm 0.2) \cdot 10^{-10}$ sec.

These experiments show that the important attributes of our time-to-amplitude converter, namely, the lower sensitivity to variation in the pulse rise time[9], favors use of NaI(Tl) crystals without any additional measures such as, for example, employment of wide band amplifiers between the photomultipliers and the pulse limiters.

2. Discussion

For calculating the radiative lifetimes for E1 type transitions with energies of 171, 272 and 351 keV (from the 351 keV level) and M1 type transitions with energies of 457, 558 and 637 keV and an E1 type transition with an energy of 285 keV (from the 637 keV level) we used the relative intensities of the K conversion lines taken from the work of Bichard et al[4] and the internal conversion coefficients from the tables of Sliv & Band[12]. We did not take into account the possible admixture of higher multipole orders, for according to Bichard et al such admixture in the case of the E1 transitions does not exceed 7%. The radiative lifetimes listed in column 6 of Table 1 were calculated by means of the formula

$$\tau_{\gamma i} = \tau_{\exp} \frac{1+\alpha_i}{N_i} \sum_k N_k,$$

where N_i is the total intensity and α_i is the total conversion coefficient of the i-th transition. In columns 7 & 8 of Table 1, we list the theoretical values of the radiative lifetimes calculated according to the Weisskopf[1] single-particle formulas and according to the Nilsson[2] formulas for single-particle transitions in deformed nuclei. In columns 9 & 10 we give the values of retardation factors relative to the results of both types of calculation, namely,

$$F_W = \frac{\tau_\gamma}{\tau_{\gamma W}} \text{ and } F_N = \frac{\tau_\gamma}{\tau_{\gamma N}}.$$

It will be evident from Table 1 that in six cases the experimental data are in good agreement with calculations by Nilsson's formulas, but in the case of the E1 transition from the 351 keV level to the ground state the retardation factor F_N is very appreciable: ~2200.

Table 1

Radiative lifetimes and retardation factors

E_γ, keV	Multipole order	N_e [4]	N_i	α_i [12]	τ_γ, sec	$\tau_{\gamma W}$, sec	$\tau_{\gamma N}$, sec	F_W	F_N
171,5	*E*1	25	15	0,088	$1{,}01\cdot10^{-8}$	$6{,}3\cdot10^{-14}$	$4{,}1\cdot10^{-9}$	$1{,}6\cdot10^{5}$	2,5
272,4	*E*1	100	1,13	0,029	$7{,}6\cdot10^{-10}$	$1{,}6\cdot10^{-14}$	$1{,}3\cdot10^{-10}$	$4{,}8\cdot10^{4}$	5,9
351,2	*E*1	1,0	57	0,013	$3{,}85\cdot10^{-8}$	$7{,}3\cdot10^{-15}$	$1{,}76\cdot10^{-11}$	$5{,}3\cdot10^{6}$	2200
457,1	*M*1	1,4	18,8	0,059	$5{,}23\cdot10^{-9}$	$3{,}4\cdot10^{-13}$	$5{,}15\cdot10^{-8}$	$1{,}5\cdot10^{4}$	0,1
558,1	*M*1	2,2	7,15	0,033	$1{,}98\cdot10^{-9}$	$1{,}9\cdot10^{-13}$	$3{,}52\cdot10^{-9}$	$1{,}0\cdot10^{4}$	0,6
636,8	*M*1	5,8	1,9	0,024	$5{,}37\cdot10^{-10}$	$1{,}26\cdot10^{-13}$	$2{,}98\cdot10^{-10}$	$4{,}2\cdot10^{3}$	1,8
285,6	*E*1	2,8	3,8	0,023	$1{,}05\cdot10^{-9}$	$1{,}4\cdot10^{-14}$	$4{,}53\cdot10^{-9}$	$7{,}5\cdot10^{4}$	0,2

Table 2

Comparison of the retardation factors for the transitions in Yb^{173}, Lu^{175} and Hf^{177}

Nucleus	F_N factors		
	To ground level	To first excited level	To second excited level
$_{70}Yb^{173}$	2200	5,9	2,5
$_{71}Lu^{175}$	31	3,5	0,5
$_{72}Hf^{177}$	400	0,6	1,0

In Table 2 we give a comparison of the F_N retardation factors for E1 transitions in Yb^{173} with factors for the neighboring nuclei Lu^{175} and Hf^{177} (values taken from Refs.13 & 14, respectively). It will be seen that anomaly of the transition to the ground level is observed in these nuclei as well (the retardation factors equal 31 and 400, respectively).

A number of authors[4,14,15] have called attention to violation

of the Alaga intensity rules[16] for single-particle transitions to different levels of a rotational band. Some authors[14,15] have hypothesized that the departure from the intensity rules occurs because transitions to rotational levels are favored. It follows, however, from our measurement results that the probabilities for transitions to rotational levels are in satisfactory agreement with those given by Nilsson's formula and that the departure from the Alaga intensity rules occurs because of strong retardation of E1 transitions to the ground level. The character of this anomaly and the great strength of the effect do not allow of explaining them on the basis of the assumption of shift of the levels, as was successfully done by Hansen et al[17] for 2^+ transitions in even-even nuclei. For the same reasons, recourse to the hypothesis of inaccuracy of the adiabatic approximation for explaining the observed anomaly is also unsatisfactory. Apparently, this anomaly cannot be explained in the framework of the unified nuclear model; probably there are involved here certain effects that are not taken into account by this model. It is not impossible that it may prove feasible to explain the anomaly by taking into account the effect of superfluidity[18-20].

"A.F.Ioffe" Physical-Technical Institute

References

1. V.F.Weisskopf, Phys.Rev., 83, 1073 (1951).
2. S.G.Nilsson, Kgl.Danske Videnskab Selskab Mat.-fys.Medd., 29, No.16 (1955).
3. Materialy II Soveshchaniya po yadernoi spektroskopii neitrondefitsitnykh izotopov redkikh cemel' (Transactions of the Second Conference on Nuclear Spectroscopy of Neutron-Deficient Rare Earth Isotopes), Dubna, 1959.
4. J.W.Richard, J.W.Mihelich & B.Harmatz, Phys.Rev., 116, 720 (1959).
5. R.G.Wilson & M.L.Pool, Phys.Rev., 117, 807 (1960).
6. J.de Boer, M.Martin & P.Marmier, Helv.phys.acta, 32, 377 (1959).
7. V.A.Romanov, M.G.Iodko & V.V.Tuchkevich, Zhur.eksp.i teor.fiz., 38, 1019 (1960). (Trans.Soviet Physics - JETP.)
8. E.E.Berlovich, M.P.Bonitz & M.K.Nikitin, Ibid., 40, 749 (1961).(Trans. Ibid.)
9. M.Bonitz & E.E.Berlovich, Nucl.Instrum., 9, 13 (1960).
10. M.Bonitz, E.E.Berlovich & V.V.Nikitin, Izv.AN SSSR, Ser.fiz., 25, 218 (1961). (Trans.Bulletin, 25, 210.)
11. E.E.Berlovich, K.Grotovski, M.Bonitz, V.I.Breslav & B.K.Preobrazhenskii, Nucl.Phys., 6, 672 (1958).
12. L.A.Sliv & I.M.Band, Tablitsy koeffitsientov vnutrennei konversii gamma-izlucheniya (Tables of internal conversion coefficients), Part I, K shell; Part II,L shell, M.-L., 1956/8.
13. Program of the Tenth Annual Conference on Nuclear Spectroscopy, p.64, M.-L., 1960.
14. G.A.Vartapetyan, Zhur.eksp.i teor.fiz., 38, 1916 (1960). (Trans.Soviet Physics - JETP.)
15. A.V.Gnedich, L.N.Kryukova & V.V.Murav'eva, Ibid., 38, 726 (1960).(Trans. Ibid.)
16. G.Alaga, K.Alder, A.Bohr & B.Mottelson, Kgl.Danske Videnskab Selskab Mat. -fys.Medd., 29, No.9 (1955).
17. P.G.Hansen, O.B.Nielsen & R.K.Sheline, Nucl.Phys., 12, 389 (1959).
18. M.G.Urin, Zhur.eksp.i teor.fiz., 38, 1852 (1960). (Trans. JETP.)
19. Yu.G.Grin', Ibid., 39, 138 (1960). (Trans.Ibid.)
20. A.B.Migdal, Program of the Eleventh Annual Conference on Nuclear Spectroscopy, M.-L., 1961.

GAMMA-RAYS PRODUCED IN INELASTIC SCATTERING OF 2.95 MeV NEUTRONS BY I^{127}, La^{139} AND Bi^{209}

- L.Ya.Graudynya, K.A.Petrzhak & A.V.Sorokina

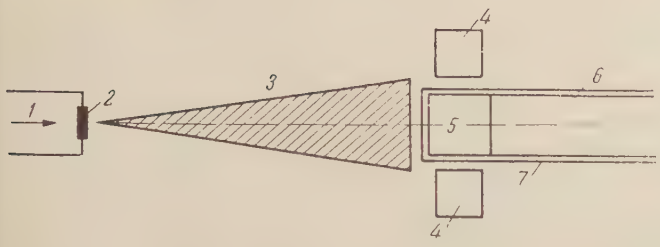

Fig.1. Diagram of the experiment: 1) deuteron beam, 2) deuterium target, 3) lead cone, 4) scatterer, 5) crystal, 6) photomultiplier, 7) black paper light shield.

One of the convenient methods of investigating energy levels of stable nuclei is study of the γ-rays emitted as a result of inelastic neutron scattering. In recent years there have been published a number of experimental papers on the subject, but the results reported are frequently in conflict.

In the present work we investigated the spectra of γ-rays produced in inelastic scattering of 2.95 MeV neutrons by I^{127}, La^{139} and Bi^{209}.

The source was a neutron generator operated at a voltage of 180 kV. The neutrons were obtained by the $D(d,n)He^3$ reaction on a thick Zr-Mo target with adsorbed deuterium. The neutron flux was monitored by a long boron counter calibrated with reference to a standard Ra-Be neutron source.

The γ-ray spectra were investigated by means of a scintillation spectrometer with annular geometry. The experiment is diagramed in Fig.1. The scatterer (4) was a thin-walled ring-shaped container of plexiglas which was filled with the scattering substance. In the case of I^{127} this was crystalline iodine (286 g), in the case of La^{139} - lanthanum oxide (220 g), and in the case of Bi^{209} - bismuth granules (1000 g). All the substances were of the chemically pure grade.

The scintillation spectrometer proper consisted of an NaI(Tl) crystal 40 mm in diameter and 40 mm thick, a FEU-13 photomultiplier and a 63-channel pulse height analyzer. The energy resolution of the spectrometer was 10-11% (Cs^{137} 660 keV γ-rays). A lead cone (3) served to protect the crystal from the direct beam of neutrons and γ-rays. The background due to neutrons elastically scattered in the crystal, scatterer and surrounding objects was determined by measuring the γ-ray spectrum with the element-filled scatterer replaced by a solid ring of plexiglas. The number of scattering atoms in the different scatterers was the same.

The γ-ray spectrum emitted in the case of inelastic neutron scattering by Bi^{209} has been thoroughly investigated by a number of authors[1-6], and accordingly, in the present work was used as a control for the operation of our experimental set-up. The recorded γ-spectrum (Fig.2) is in agreement with the data of other authors, except that the 1.29 MeV line observed by Androsenko et al[6] was not detected in the present work. The peak evidenced in Fig.2 in this region is due entirely to the Compton distribution.

The γ-ray spectrum obtained in the experiments with La^{139} is shown in Fig.3; there are evident γ-lines with energies of 0.64, 0.79, 1.24, 1.43, 1.75 and 2.08 MeV.

Two excited levels in La^{139} - 0.163 and 1.43 MeV - are known[7] from radioactive decay of Ba^{139}. It may be assumed that the 1.24 MeV line is due to a cascade transition from the 1.43 MeV level to the ground state via the 0.163 MeV level. The 0.79 MeV line is in all probability due to inelastic scattering of neutrons in the lead shield. The number of neutrons elastically scattered at large angles and entering the lead cone, in the case of a lanthanum scatterer, must be greater than in the case of a ring of solid plexiglas; hence one can expect the appearance of

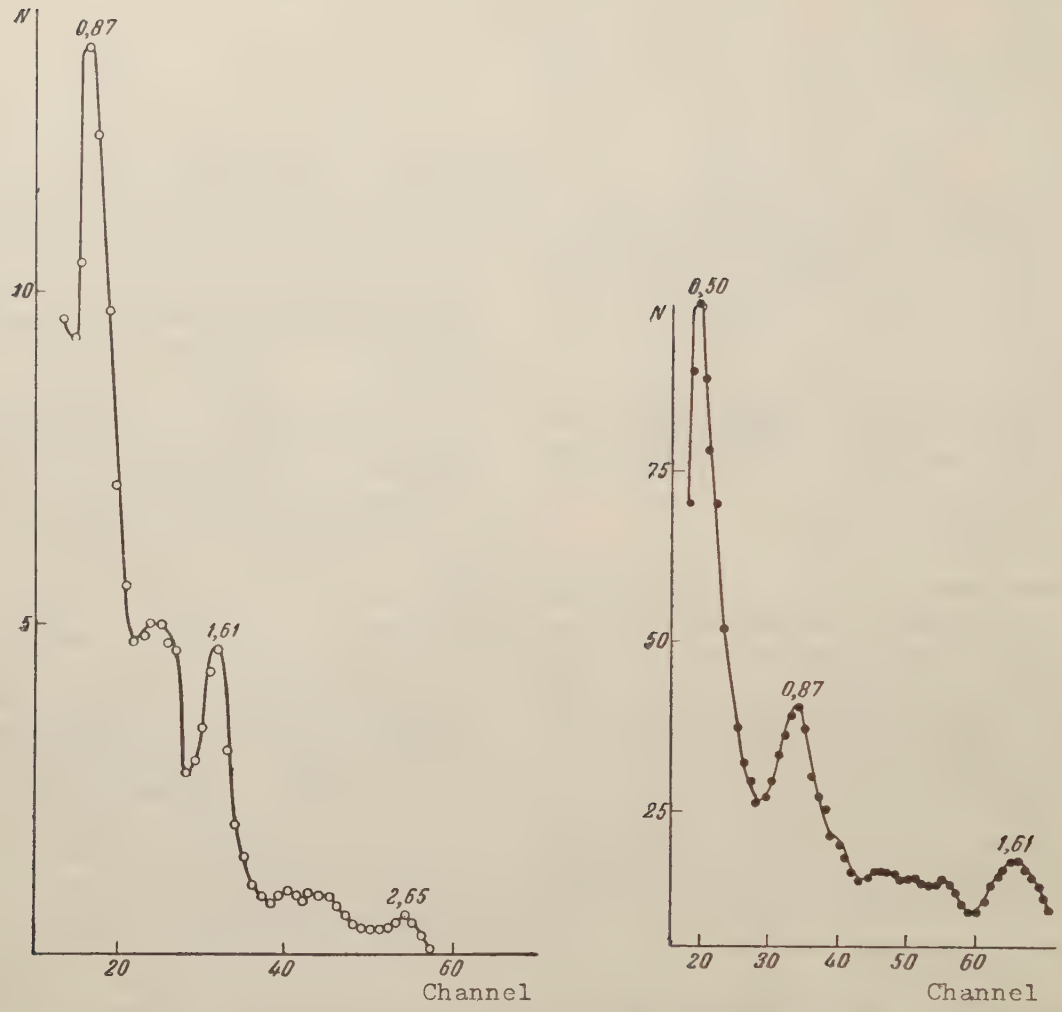

Fig.2. Spectrum of γ-rays emitted in inelastic scattering of 2.95 MeV neutrons in Bi^{209}.

a more intense γ-line from the lead. Upon replacement of the lead shielding cone by an aluminum cone, there appeared in the La^{139} γ-ray spectrum, in place of the 0.79 MeV γ-line, 0.83 and 1.02 MeV lines, i.e., the most intense lines in the spectrum of Al^{27}.

As compared with Bi^{209} and La^{139}, the γ-ray spectrum in the case of I^{127} is rather complex (Fig.4). In addition to the familiar γ-lines, there were detected three γ-transitions with energies of 0.49, 2.13 and 2.66 MeV. A transition of 0.49 MeV energy was first detected in the work of Day[4] in investigating the spectrum of γ-rays produced in an NaI(Tl) crystal, but was not definitely attributed to I^{127}. It also follows from the work of Day that this γ-transition appears at neutron energies above 2.12 MeV and is associated with excitation of high-lying levels in the iodine nucleus. The 2.13 MeV γ-line may appear as a result of photoproduction of pairs in the NaI(Tl) crystal by 2.66 MeV γ-rays and emission of an annihilation photon. However, the intensity of such a line, if it is determined relative to the intensity of the similar "pair" γ-line in the spectrum of Na^{24} should be 5-6 times lower than the measured intensity. This fact is substantiated by the presence of an independent 2.13 MeV γ-transition in the γ-ray spectrum of I^{127}.

Energies (MeV) of γ-rays observed in inelastic scattering of neutrons by I^{127}, La^{139} and Bi^{209}

Isotope	Our data $E_n = 2,95$ MeV	Ref. 1 $E_n = 3,9$ MeV	Ref. 2 $E_n = 2,5$ MeV	Ref. 3 $E_n = 3,2$ MeV	Ref. 4 $E_n = 2,56$ ÷ 3,13 MeV	Ref. 5 $E_n = 2,48$ MeV	Ref. 6, 10 $E_n = 3$ MeV	Ref. 8 $E_n = 0,8$ MeV	Ref. 9 $E_n = 1,2$ MeV
Bi^{209}	0,50±0,02	—	—	0,49±0,02	—	—	0,57±0,03		
	0,87±0,03	0,91±0,04	0,85±0,03	0,94±0,05	0,904±0,009	0,899±0,002	0,90±0,03		
	—	—	—	—	—	—	1,29±0,03	—	—
	1,61±0,03	1,63±0,04	1,57±0,07	1,62±0,07	1,66±0,016	1,66±0,05	1,61±0,03		
	2,65±0,05	2,60±0,06	—	2,6±0,1	2,60±0,02	—	2,53±0,04		
La^{139}	0,64±0,02						0,87±0,03		
	1,24±0,03						1,21±0,04		
	1,43±0,04	—	—	—	—	—	—	—	—
	1,75±0,04						1,78±0,04		
	2,06±0,05						2,17±0,04		
I^{127}	—			—	—		—	—	0,031±0,002
	—			—	0,058		—	—	0,063±0,002
	—			—	0,138		—	0,134	0,145±0,005
	—			0,21±0,01	0,204		—	0,21	0,208±0,002
	0,33±0,02			0,33±0,01	—		0,35±0,03	—	—
	—			—	0,396		—	—	0,390±0,01
	0,42±0,03			0,42±0,02	0,441		0,42±0,03	0,41	0,435±0,04
	0,49±0,03			—	—		—	—	—
	0,625±0,03	—	—	0,63±0,03	0,634	—	0,62±0,03	0,62	0,632±0,006
	0,74±0,04			—	0,742		0,76±0,06	0,78	0,750±0,02
	0,84±0,04			—	—		—	—	—
	1,02±0,04			1,04±0,05	—		0,98±0,04	—	0,950±0,02
	1,21±0,05			—	—		1,25±0,04	—	—
	1,78±0,05			—	—		1,78±0,04	—	—
	2,13±0,05			—	—		—	—	—
	2,66±0,06			—	—		—	—	—

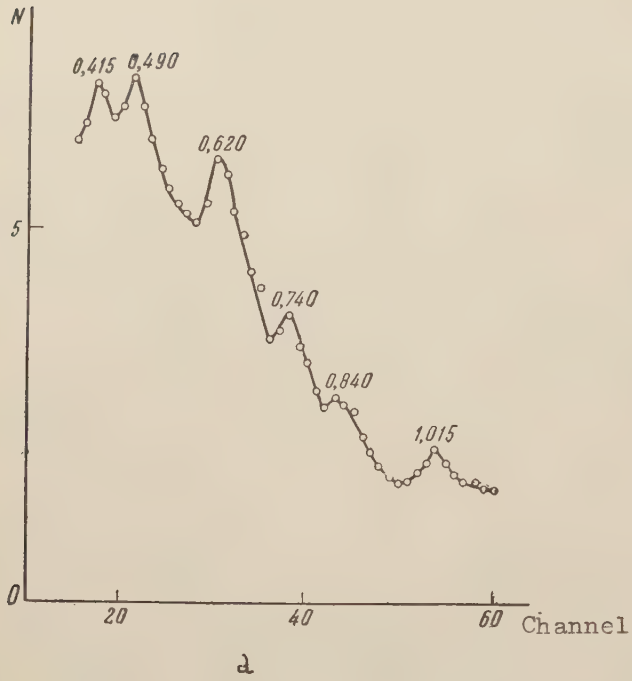

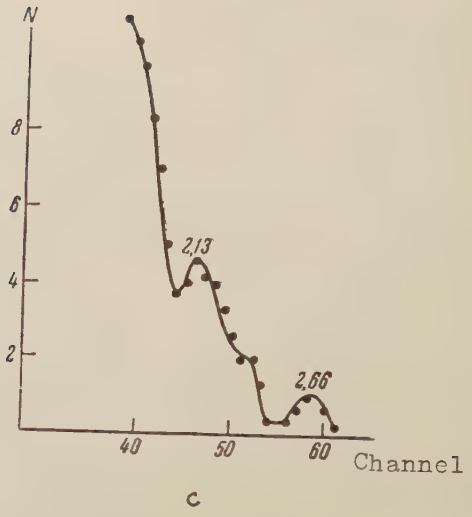

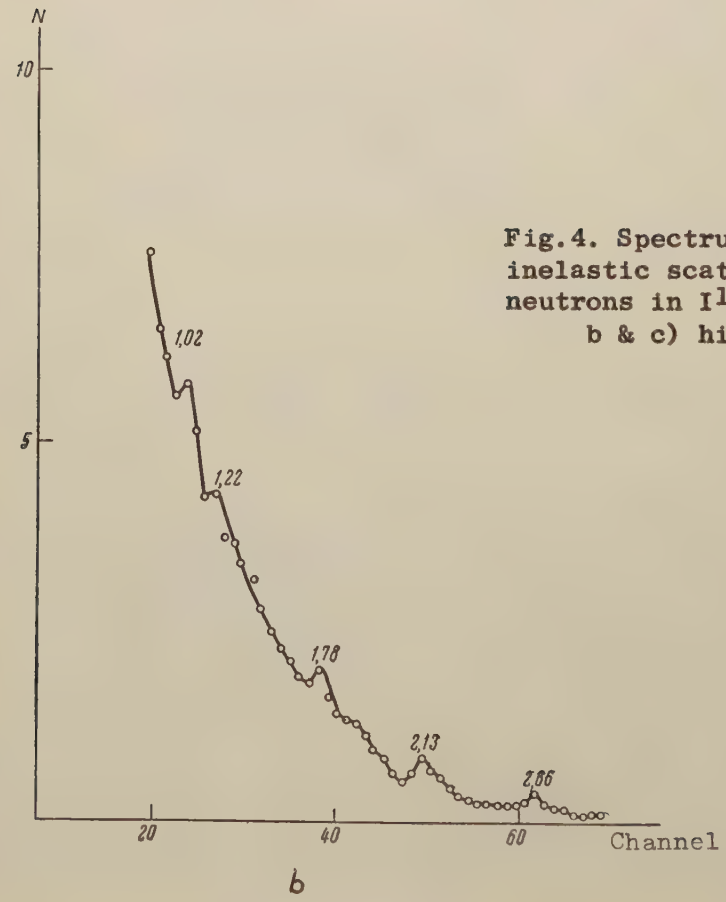

Fig.4. Spectrum of γ-rays emitted in inelastic scattering of 2.95 MeV neutrons in I^{127}: a) low energy part, b & c) high energy part.

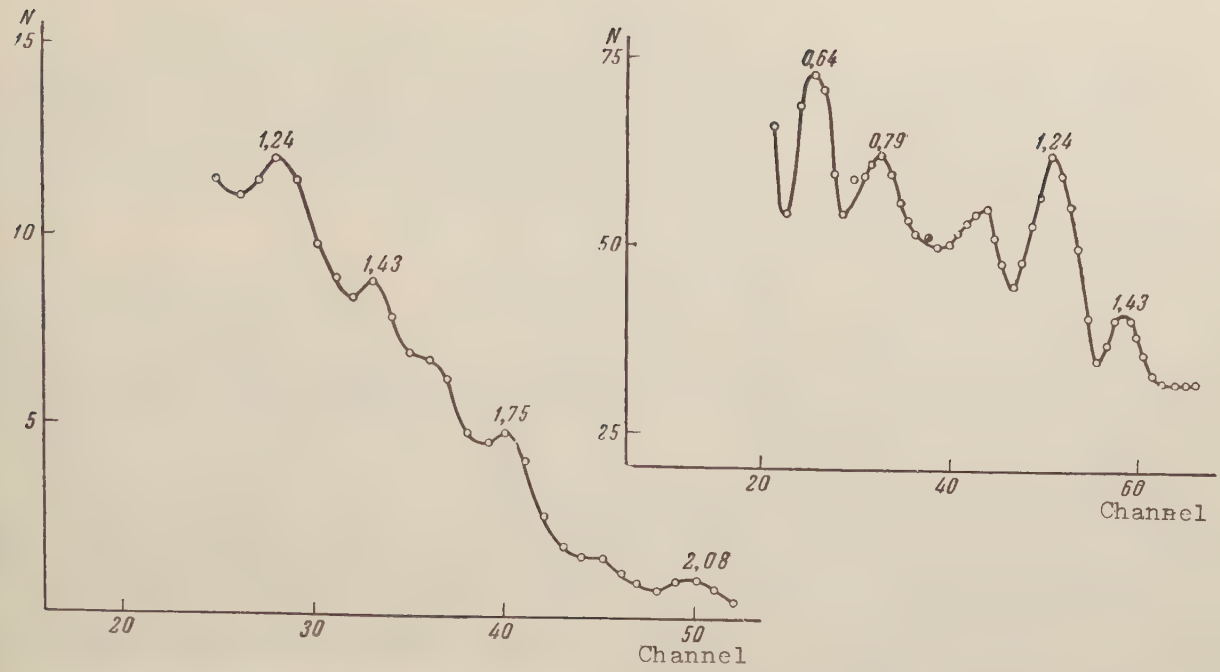

Fig.3. Spectrum of γ-rays emitted in inelastic scattering of 2.95 MeV neutrons in La^{139}.

The results of the present work are listed and compared with the data of other authors in the accompanying table.

We desire to express our gratitude to O.I.Kostochkin and S.N.Korshun for assistance in carrying out the experiment.

References

1. M.A.Rothman & C.E.Mandeville, Phys.Rev., 93, 796 (1954).
2. E.A.Eliot, D.Hicks, L.E.Beghian & H.Halban, Phys.Rev., 94, 144 (1954).
3. V.E.Scherrer, B.A.Allison & W.R.Faust, Phys.Rev., 96, 386 (1954).
4. R.B.Day, Phys.Rev., 102, 767 (1956).
5. F.I.Boley, E.H.Thorndike & A.T.Moffet, Phys.Rev., 110, 915 (1958).
6. A.L.Androsenko, D.L.Broder & A.I.Lashchuk, Atomnaya energiya, 7, No.3, 268 (1959). (Trans.Soviet Journal of Atomic Energy.)
7. B.S.Dzhelepov & L.K.Peker, Skhemy raspada radioaktivnykh yader (Decay schemes of radioactive nuclei), M.-L., 1958.
8. I.L.Morgan, Phys.Rev., 103, 1031 (1956).
9. J.J.Van Loef & D.A.Lind, Phys.Rev., 101, 103 (1956).
10. A.L.Androsenko, D.L.Broder & A.I.Lashchuk, Atomnaya energiya, 9, No.5, 403 (1960). (Trans.Soviet Journal of Atomic Energy.)

SEMICONDUCTOR SPECTROMETERS FOR CHARGED PARTICLES

- L.A.Zubritskii, A.I.Popov, P.V.Sorokin & V.F.Samoilov

Introduction

In recent years there have been published several papers[1-7] describing the use of semiconductor devices for detecting charged particles. Such spectrometers are in many respects superior to scintillation spectrometers and ionization chambers. The sensitive element in a semiconductor spectrometer is the space charge region formed in the junction under reverse bias. The width of the space charge region is given by the formula

$$D = \sqrt{\frac{\varepsilon(\varphi_0 + V)\rho\mu}{2\pi}} \cdot 10^{-6} \text{ cm}, \qquad (1)$$

where ε is the dielectric constant of the semiconductor, φ_0 is the contact difference of potentials, V is the voltage on the junction, ρ is the resistivity of the semiconductor, which depends on the impurity concentration, and μ is the mobility of the majority current carriers.

In passing through the space charge layer of a p-n junction a charged particle expends part of its kinetic energy on production of electron-hole pairs. Owing to the strong electric field in the space charge region, the current carriers produced along the path of the moving particle are swept to the junction boundary, giving rise to an increase of the current in the bias-providing circuit. This leads to appearance of a pulse on the p-n junction, if there is a sufficiently large load resistance in the supply circuit.

P-n junctions can be used for spectrometry only provided the particle range lies within the dimensions of the space charge region, i.e., when all the current carriers produced by the charge particle are in a strong electric field and are drawn out of the volume of the semiconductor at a high rate. This insures a steep rise of the pulse and the absence of recombination losses of the carriers produced in the volume of the semiconductor. In this case virtually all the minority carriers produced by a charged particle reach the junction boundary and the amplitude of the pulse is proportional to the particle energy:

$$V_{\text{pul}} = \frac{E}{\varepsilon_0 C_{\text{in}}}; \qquad (2)$$

here E is the particle energy, ε_0 is the pair production energy in the semiconductor (for silicon ε_0 = 3.6 eV; in germanium - 2.9 eV), and C_{in} is the input capacitance which is comprised of the junction capacitance and the capacitance of the associated circuit.

Such detectors can be utilized as spectrometers for heavy particles (protons, α-particles, fission fragments, etc.) inasmuch as the space charge region of a p-n junction prepared of high purity materials cannot be greater than 1 mm. Investigations[1,3,6] have shown that the pair production energy and, consequently, the height of the pulse do not depend on the type of ionizing particles.

Semiconductor spectrometers have good time characteristics, inasmuch as by virtue of the strong electric field in the space charge region (10^4-10^5 V/cm), the carrier collecting time is very short: $5 \cdot 10^{-10}$ to $5 \cdot 10^{-9}$ sec.

We prepared a number of semiconductor spectrometers and investigated some of their properties using Po^{210} α-particles. The output pulses were amplified by a linear amplifier with an expander and analyzed by means of a 100-channel pulse height analyzer (type AI-100).

Germanium spectrometers

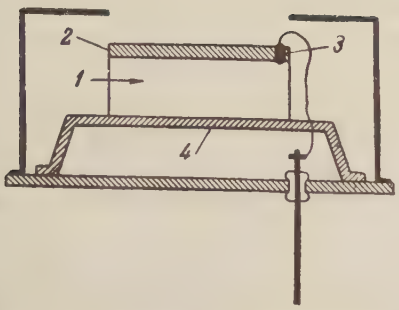

Fig.1. Design of the semiconductor spectrometer: 1 - 5 x 5 x 1 mm germanium plate, 2 - 500 A thick gold coating, 3 - melted-in indium pellets, 4 - kovar (fernico) crystal holder.

The germanium spectrometers were prepared using electronic grade germanium with a resistivity of 40-45 ohm-cm. The surface barrier p-n junctions were produced by sputtering gold on the germanium surface. For fabricating the semiconductor spectrometers the germanium was cut into 5 x 5 x 1 mm plates. The plates were etched in SR-4 (CP-4) solution to formation of a specular surface, washed, dried and soldered (tin solder with a small amount of antimony) to a kovar (fernico) crystal holder. Simultaneously with the soldering, there was melted into the plates an indium pellet, which produced an alloyed p-n junction about 0.3 mm in diameter. After soldering to the holder, the plates were etched in boiling H_2O_2 (for 0.5-1 min), washed twice in distilled water and dried. The edges of the plates were then coated with a protective layer of BF-2 varnish, which limited the region of the p-n junction and served to prevent shorting of the gold layer to the holder. After this, the plates were mounted in a vacuum unit, cleansed by ion bombardment and coated with a ~500 Å thick layer of gold. The gold film provides for making reliable contact with the external circuit.

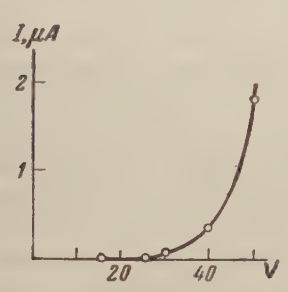

Fig.2

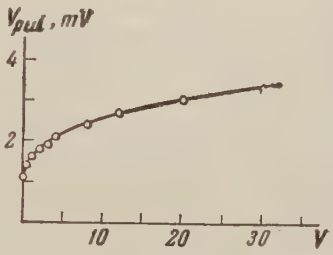

Fig.3

Fig.2. Current-voltage characteristic of gold-germanium spectrometer.

Fig.3. Variation of the pulse height as a function of the bias voltage on the p-n junction.

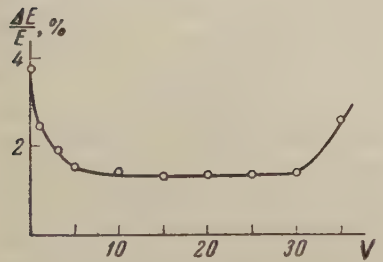

Fig.4

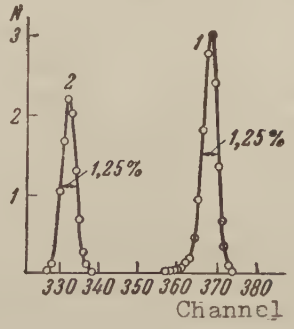

Fig.5

Fig.4. Variation of the resolution of the gold-germanium spectrometer as a function of the voltage on the p-n junction.

Fig.5. Spectra of Po^{210} α-particles (1) and pulses from a pulse generator (2).

The design of the semiconductor spectrometer is shown schematically in Fig. 1. The gold-germanium spectrometer was investigated at liquid nitrogen temperature. The current-voltage characteristic of the spectrometer is shown in Fig.2. Comparing the current-voltage characteristic of our spectrometer with that described by Halbert & Blankenship[3], it may be noted that our spectrometer has a higher quality junction. This makes it possible to apply to the junction an appreciably higher reverse bias and to form a larger space charge region.

Fig.3 shows the variation of the pulse height as a function of the bias voltage on the junction. The rapid increase in pulse amplitude with increase of the voltage from 0 to 5 volts is due both to decrease in the capacitance of the junction and to appreciable improvement in collection. Above 5 volts the increase in pulse height is connected mainly with decrease of the junction capacitance.

Fig.4 shows the variation of $\Delta E/E$ as a function of the voltage on the junction. With increase of the voltage from 0 to 5 volts, the resolution improves owing to improvement of current carrier collection. At a low voltage on the junction the width of the space charge layer is less than the α-particle range in germanium and collection of carriers is realized mainly owing to diffusion. In this case an appreciable fraction of the carriers can recombine. Under these conditions the fluctuation in the number of nonrecombining carriers is greater and the resolution poorer than in the case of complete collection of current carriers Above 30 volts the resolution is impaired owing to the appearance of noise connected with increase of the current flowing through the junction.

It should be noted that the indicated 1.25% resolution is not the intrinsic resolution of the spectrometer, but is determined by the noise level of the amplifier. Fig.5 shows the spectrum of pulses from α-particles and from a pulse generator. It will be seen that the relative half-widths of both peaks are equal. Hence the resolution of our spectrometer is better than 0.5%, inasmuch as with an intrinsic spectrometer resolution of 0.5% the relative line width for α-particles would be 1.35%, which would be readily noticeable.

Silicon spectrometers

The silicon spectrometers were prepared by a somewhat different procedure. The initial material was electronic grade silicon with a resistivity of 100 ohm-cm. The silicon single crystal was cut into 4 x 4 x 1 mm plates which were etched in a mixture of nitric and hydrofluoric acids. The junctions were prepared by vacuum evaporation of boron onto the silicon plates heated to 1200°C, with subsequent diffusion of the boron to a depth of $\leqslant$1 micron. After diffusion, the excess p-layer was etched off, the plate was washed and soldered, using gold solder with 2% antimony, to a tantalum crystal holder. At the same time there was soldered to the p-layer an aluminum contact. The design of the silicon instrument is analogous to the design of the germanium spectrometer with the difference that the gold layer was replaced by a thin diffused layer of p-silicon. The silicon spectrometer were investigated both at room temperature and a liquid nitrogen temperature.

The variation of the resolution $\Delta E/E$ as a function of the voltage on the spectrometer, recorded at room temperature, is shown in Fig.6. It will be seen that such a spectrometer has a resolution of 3% at a voltage of 5 to 10 volts. Above 10 volts the resolution is impaired owing to increase of noise. The variations of pulse height and resolution as a function of the voltage on the junction at liquid nitrogen temperature are shown in Figs.7 and 8. The resolution remains constant at about 2.5% with variation of the voltage from 50 to 180 volts. The current through the junction up to 200 volts is less than 0.01 μA. At a voltage in excess of 200 volts there is observed a sharp increase in current. However, after removal of the voltage the spectrometer recovers its initial characteristics.

In the case of the silicon spectrometers we also determined the effective thickness of the sensitive (depleted) layer. For determining the effective depth of the sensitive layer we recorded, with the spectrometer at liquid nitrogen temperature, the pulses from protons elastically scattered by a thick beryllium target. The maximum energy of the scattered protons was 2.2 MeV. The pulse spectra

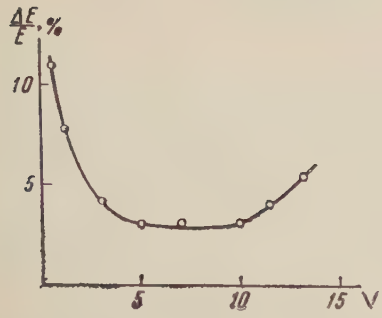

Fig.6. Variation of the resolution ΔE/E of a silicon spectrometer at room temperature as a function of the voltage on the p-n junction.

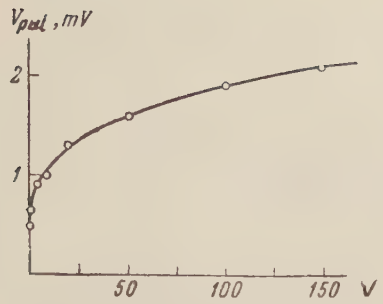

Fig.7. Variation of the pulse height as a function of the voltage on the p-n junction at liquid nitrogen temperature.

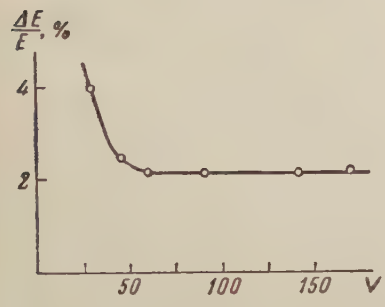

Fig.8. Variation of the resolution of the silicon spectrometer at liquid nitrogen temperature as a function of the voltage on the p-n junction.

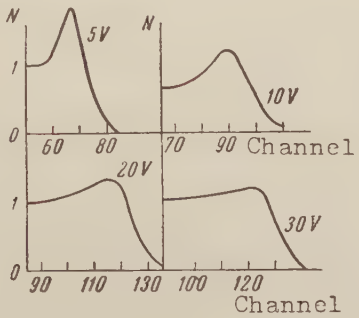

Fig.9. Spectra of pulses from protons scattered in a thick beryllium target at different voltages on the p-n junction of the silicon spectrometer.

at different voltages on the junction are shown in Fig.9. At a voltage of 5 volts the high-energy protons lose only part of their energy in the sensitive layer and in the pulse spectrum there appears a peak corresponding to the energy lost in the layer. At a voltage of 30 V on the junction this peak disappears. This means that at this point the thickness of the sensitive layer becomes equal to the proton range. From this it follows that the effective thickness of the sensitive layer of the detector at a voltage of 30 V amounts to 55 microns. The width of the space charge layer calculated by means of Eq.(1) equals 27 microns. Thus it is found that the effective depth of the sensitive layer is 28 microns greater than the thickness of the space charge region in the p-n junction. This is explained by the fact[3] that an appreciable fraction of the current carriers produced by the charged particles outside the space charge region diffuses into this region and participates in the formation of the pulses.

We desire to express our gratitude to A.K.Val'ter and A.Ya.Taranov for guidance in carrying out the work.

Physical-Technical Institute,
Academy of Sciences of the Ukrainian SSR &
Khar'kov State University

References

1. J.M.McKenzie & D.A.Bromley, Proc.Inst.Electr.Engrs., 106, 731 (1959).
2. J.J.Mayer, Appl.Phys., 30, 1937 (1959).
3. M.L.Halbert & J.L.Blankenship, Nucl.Instr.and Method, 8, 106 (1960).
4. G.Amsetl, P.Baruch & O.Smulkowski, Nucl.Instr.and Method, 8, 92 (1960).
5. S.Fridland, J.Mayer & J.Wiggins, Nucleonics, 18, 2, 54 (1960).
6. E.Almen, G.E.Larsh, T.Gordon & Sikkeland, Rev.Sci.Instrum., 31, 1114 (1960).
7. Nucleonics, 18, 5, 98 (1960).

ELEVEN-COUNTER INSTRUMENT FOR MEASURING γ-γ ANGULAR CORRELATION

- A.I.Belyaevskii & Yu.A.Gur'yan

1. Principle of operation

Investigations of γ-γ angular correlation can yield information in the spins of nuclei in excited states, on multipole orders and on the mixing coefficients for mixed radiations. Using the dependence of the angular correlation on external fields one can determine the magnitude and sign of g (the gyromagnetic ratio) or $Q\frac{\partial^2 V}{\partial z^2}$ (the product of the nuclear quadrupole moment in the given state by the gradient of the electric field). There are other uses for this type of correlation.

For example, Jacobsohn & Henley[1] proposed measurement of triple β-γ-γ angular correlation for testing time-reversal invariance. For carrying out such experiments within a reasonable time one must have available an instrument with a high efficiency, inasmuch as here one must deal with the products of three small solid angles.

The ordinary two-counter instrument usually employed for measuring angular correlations is unsatisfactory in this case, as it is in cases when the radiation source is short-lived (<10 min) or weak.

In Ref.2 one of us proposed a new method for investigating angular correlation; in employing it, when there are used 11 counters, coincidence measurements are realized simultaneously at five angles and the overall efficiency of the operation is increased by a factor of 110. Below we describe briefly the principle of operation of this instrument (a detailed description will be found in Ref.2).

The scintillation γ-spectrometers are positioned uniformly on a circle. Coincidences between two γ-rays emitted in cascade and detected by any pair of counters are recorded by a mechanical register corresponding to the angle of divergence of the given pair. The pulses from the γ-rays must satisfy the conditions for amplitude set by the thresholds and widths of the analyzer channels and must be simultaneous to within the resolving time of the coincidence circuit.

In principle, for this purpose, one must have 11 counters, 55 fast pair coincidence circuits corresponding to all combinations of the 11 counters taken two at a time, and 22 single-channel analyzers. In addition, there must be a unit, called an angular selector in Ref.2, which distributes the pulses among the mechanical registers according to the divergence angle attribute. In this case there are five such registers for divergence angles of $32^\circ 44'$, $65^\circ 28'$, $98^\circ 10'$, $130^\circ 54'$ and $163^\circ 38'$. The first two angles actually correspond to angles of $147^\circ 32'$ in the second quadrant inasmuch as the angular correlation function is expressed in terms of $\cos^2\theta$ (i.e., $\cos^2 m\theta = \cos^2(180^\circ - m\theta)$, where m is the angle multiplicity factor.

In this arrangement all the counters are identical. Variation in the efficiency of one of them leads to a proportional change in the number of coincidences counted at all the angles. Since we are interested only in the ratios of intensities, such a change in efficiency does not affect the sought angular correlation function. More accurately, it is evinced in appreciably weakened form owing to the effect of equalization. This effect of equalization of the ratios of the coincidence counting efficiencies at different angles $\varepsilon(m\theta)/\varepsilon(0)$, where

$$\varepsilon(m\theta) = \sum_{i=1}^{n} e_i' e_{i+m}'' + e_i'' e_{i+m}', \qquad (1)$$

was calculated in Ref.2 on the assumption that the efficiency γ of the coincidence

circuits equals unity. Below we remove this restricting assumption and calculate the effect on the general case when $\gamma < 1$. The first term in the sum (1) corresponds to "direct" coincidences (55 pairs), the second term to "cross" coincidences; the single and double primes indicate that the given γ-rays belong to different transitions in the cascade; m takes on the values 1,2,3,4 & 5, and

$$e_i = \bar{e}(1 + \delta_i),$$

where the δ_i are the relative deviations from the mean value for each of the 11 counters.

Analogously, let us write the efficiencies for detecting individual "pair" coincidences ($\gamma_{i,\,i+m}$) and "cross" coincidences ($\gamma_{i+m,\,i}$) in terms of the mean efficiency $\bar{\gamma}$ for all 110 pair combinations and the relative deviation from it $D_{i,\,i+m}$:

$$\gamma_{i,\,i+m} = \bar{\gamma}(1 + D_{i,\,i+m}),$$
$$\gamma_{i+m,\,i} = \bar{\gamma}(1 + D_{i+m,\,i}).$$

Inserting these in (1), we obtain

$$\varepsilon(m\theta) = \sum_{i=1}^{n} e'_i e''_{i+m}\gamma_{i,\,i+m} + e''_i e'_{i+m}\gamma_{i+m,\,i} =$$
$$= \bar{e}'\bar{e}''\bar{\gamma}\sum_{i=1}^{n}(1+\delta'_i)(1+\delta''_{i+m})(1+D_{i,\,i+m}) + (1+\delta''_i)(1+\delta'_{i+m})(1+D_{i+m,i}) =$$
$$= \bar{e}'\bar{e}''\bar{\gamma}\sum_{i=1}^{n}\left\{1 + \frac{1}{2}[\delta'_i\delta''_{i+m} + \delta''_i\delta'_{i+m} + D_{i,\,i+m}(1+\delta'_i+\delta''_{i+m}) + D_{i+m,\,i}(1+\delta''_i+\delta'_{i+m})]\right\}. \qquad (2)$$

In opening the parentheses we have discarded all third order and higher terms.

The ratio characterizing the uniformity of the total efficiencies in counting coincidences at different angles will be (the $2\bar{e}'\bar{e}''\bar{\gamma}$ term cancels out):

$$\frac{\varepsilon(m\theta)}{\varepsilon(0)} = \frac{\sum_i \{1 + 1/2[\delta'_i\delta''_{i+m} + \delta''_i\delta'_{i+m} + D_{i,\,i+m}(1+\delta'_i+\delta'_{i+m}) + D_{i+m,\,i}(1+\delta''_i+\delta'_{i+m})]\}}{\sum_i \{1 + 1/2[\delta'_i\delta''_{i+1} + \delta''_i\delta'_{i+1} + D_{i,\,i+1}(1+\delta'_i+\delta''_{i+1}) + D_{i+1,\,i}(1+\delta''_i+\delta'_{i+1})]\}}. \qquad (3)$$

Let us find the minimum and maximum possible values for this ratio, using absolute values and assuming

$$|\delta_i| \leqslant \delta; \quad |D_{i+m,\,i}| = |D_{i,\,i+m}| \leqslant D.$$

Substituting in (3), we obtain

$$\frac{1 - \delta^2 - D(1+2\delta)}{1 + \delta^2 + D(1+2\delta)} \leqslant \frac{\varepsilon(m\theta)}{\varepsilon(\theta)} \leqslant \frac{1 + \delta^2 + D(1+2\delta)}{1 - \delta^2 - D(1+2\delta)}. \qquad (4)$$

If all the $\gamma_{i,\,i+m}$ and $\gamma_{i+m,\,i}$ equal 1, then $D = 0$, and we obtain the expression

$$\frac{1-\delta^2}{1+\delta^2} \leqslant \frac{\varepsilon(m\theta)}{\varepsilon(\theta)} \leqslant \frac{1+\delta^2}{1-\delta^2}, \qquad (5)$$

which is in agreement with that deduced earlier in Ref.2.

D enters into (4) linearly; hence the requirement that the efficiency of all the coincidence circuits be close to 100% is highly important, inasmuch as in this case the efficiencies will also be close to each other, which is essentially what we require. In principle, extremum values are, of course, possible, but in practice little probable as a result of chance deviation of the 110 quantities from the mean value. This makes it necessary to use coincidence circuits with a resolving time of not less than $\sim 4 \cdot 10^{-8}$ sec in order not to lose any true coincidences.

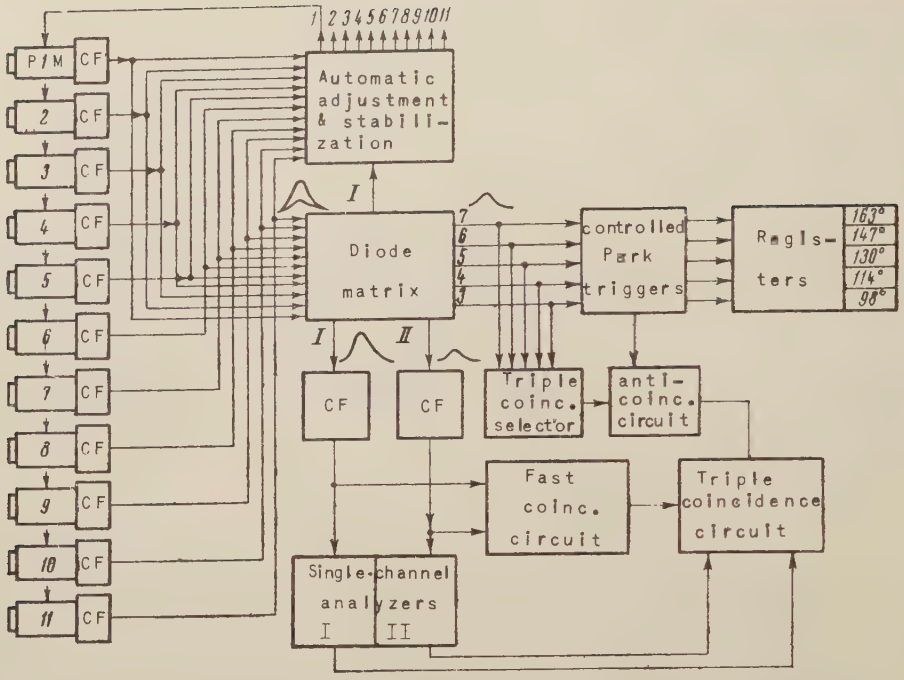

Fig.1. Block diagram of the 11-counter instrument for measuring γ-γ angular correlations. CF = cathode follower.

2. Block diagram of the 11-counter instrument

In practice, of course, it is not necessary to build an instrument with 55 separate coincidence circuits and 22 individual single-channel analyzers; we have described the circuit in this way only to clarify the principle of operation. In practice it is necessary to have only one double coincidence circuit with a resolving time of $4 \cdot 10^{-8}$ sec, as shown in Fig.1, and only two single-channel analyzers. This economy is gained by using a diode matrix, which concurrently fulfills several functions.

The pulses from the last dynodes of the FEU-13 photomultipliers are fed through low input impedance cathode followers CF to the 11 inputs of the matrix. The maximum height of the pulses is 30-50 V, which allows of carrying out amplitude and time selection without having 11 amplifiers following the photomultipliers (such amplifiers could introduce additional straggle or distortion into the leading edges of the pulses).

The matrix used in our instrument has 7 outputs. At output I, by means of an 11 diode "or" circuit, there is separated the larger of the two simultaneously arriving pulses, while at output II there is selected the smaller pulse. These pulses go to the single-channel analyzers[3] I and II, respectively, and to the two inputs of the fast coincidence circuit, which is a modification of the Weinzierl[4] circuit. If both pulses have an amplitude between the thresholds for which the analyzers are set and the fast coincidence circuit is triggered, there appears a pulse on the output of the triple coincidence circuit ($\tau \approx 1$ μsec); this pulse then goes to the anticoincidence circuit. The second (blocking) pulse on the second input of this circuit appears when a γ-ray is detected simultaneously by three rather than two γ-counters. Such cases may occur in the event of cascades

consisting of three or more transitions and are rejected by means of the anticoincidence circuit and the triple coincidence selector.

The main part of the matrix consists of 55-diode pair coincidence circuits ("and" type circuits), the outputs of which are connected through separator diodes (Fig.2) to five common bus bars (11 per conductor), each of which corresponds to a certain angle of divergence (also see Fig.1 in Ref.2). The smaller of the pulses appearing on one of these bars goes through a cathode follower (outputs 3-7) to the inputs of the 5 controllable Park triggers and to the triple coincidence selector. In addition, from these CF the pulses go through a 5-diode "or" circuit to the above mentioned matrix output II.

The controlled Park triggers are actuated by an arriving pulse only when there also arrives a "controlling" pulse from the anticoincidence circuit. In this case the output pulse from the Park trigger is recorded by the mechanical register corresponding to the angle of divergence of the given pair of photons.

The automatic adjustment and stabilization unit is not functionally connected with the other assemblies of the instrument. It serves for automatic matching of the spectra on the outputs of the photomultipliers; this is necessary because the amplitude and time selection of the pulses from all the photomultipliers is realized by common analyzers and the common double-coincidence circuit. This unit operates on the principle of counting rate difference feed-back[7] and simultaneously with adjustment realizes stabilization of the multiplication of all the photomultiplier tubes.

3. Matrix

In Fig.2 at the left we show one of the 11 cathode followers CF designed about 6Zh9P tubes. The input is connected with the last dynode of the corresponding FEU-13 photomultiplier; the output is connected to one of the inputs of the matrix. Through the lower tube there flows the current of the 10 diodes connected with the given input (10 mA). The CF must provide a low input impedance so that the matrix, which is a network of diode coincidence circuits and "or" circuits, can transfer the pulses with the least possible distortion. The distortion is determined by the ratio of the pulse u_c produced by a coincidence to the pulse v_0 arriving at the output from a single pulse on the input. As is known, this ratio equals

$$\frac{u_c}{v_0} = \frac{u_c \cdot 2R}{E\,(r_d + r_F)}; \quad r_F \approx \frac{1}{S_1 S_2 R_a}, \tag{6}$$

where R is the load of the coincidence circuit (120 kilohm), E is the dc supply voltage (240 V), r_d is the normal resistance of the diode in the region of the working characteristic, r_F is the output resistance of the CF and R_a is the load of the upper tube. In practice for 35 V pulses this ratio proved to be about 100.

Of the 55 such circuits in the instrument, in Fig.2 we show only 5 circuits, corresponding to the five divergence angles, indicated (without minutes) at the bottom of the matrix. On the left we show the above mentioned 11-diode "or" circuits; although they have only a common input with the coincidence circuits, we show them together with the matrix.

It will be evident from what has been said above that two pulses arriving at any two of the eleven inputs of the matrix are passed by it to the two outputs I and II depending on their amplitude ratio. The smaller pulse simultaneously carries information on the angle of divergence of the photons and appears on the bus bar which corresponds to the given angle of divergence. Information on the time relation of the γ-rays in our case is carried by the leading edge of the pulses.

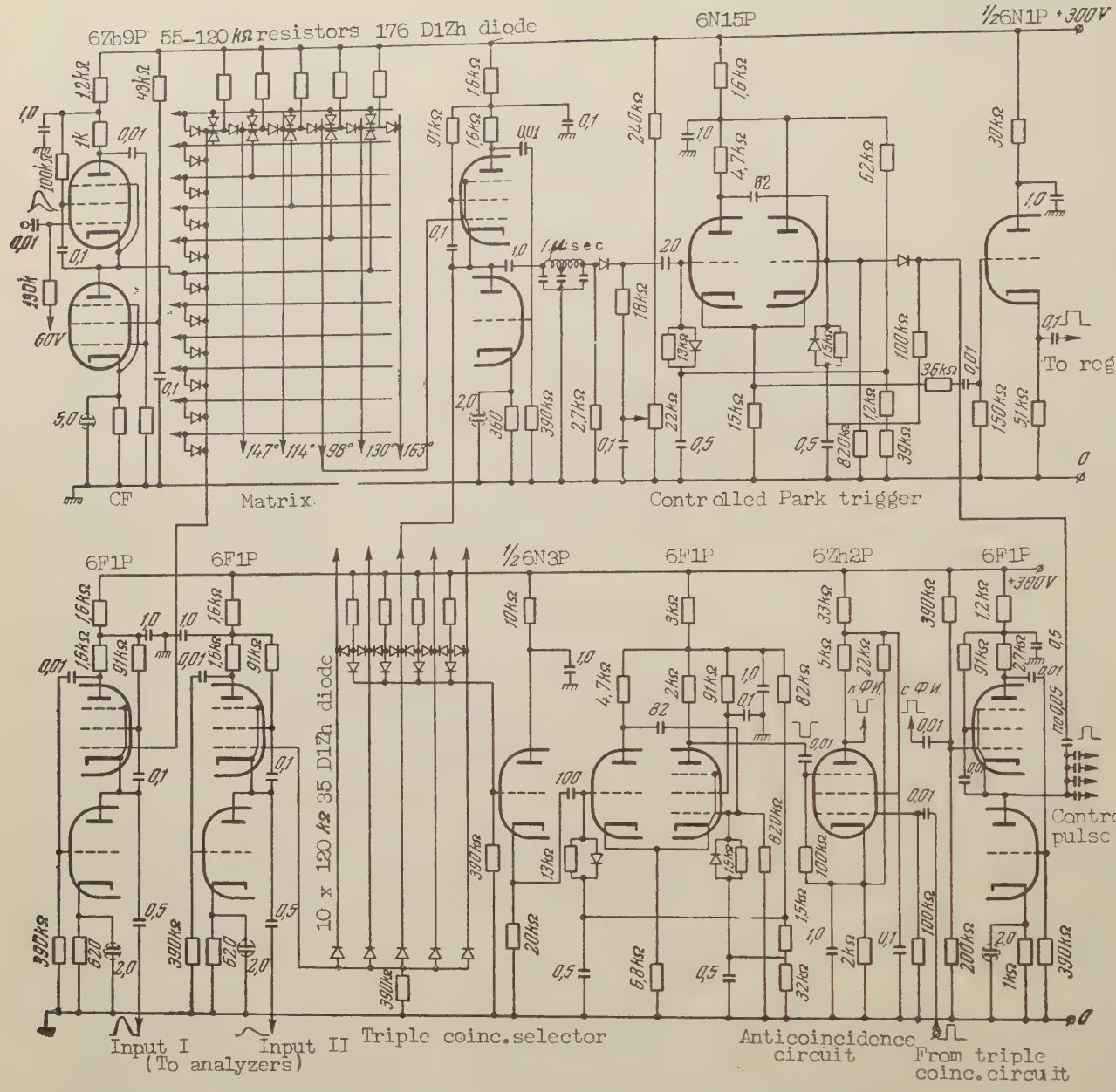

Fig.2. Matrix and controlled Park trigger assembly.

Thus it is essential that distortion of the pulse in going through the matrix be minimal.

The distortion of the leading edge of the larger pulse is determined by integration in the $r_d C_{pair}$ circuit. The transfer resistance of the diode amounts to hundreds of ohms, and the spurious capacitance is determined by the total capacitance of the 11 diodes, since the input capacitance of the CF is smaller than the total capacitance of the diodes.

The "and" circuit also transmits the leading edge of the smaller pulse, even if it does not coincide with the leading edge of the larger pulse, which serves in the given case as the "gating pulse", but the shape of the smaller pulse is

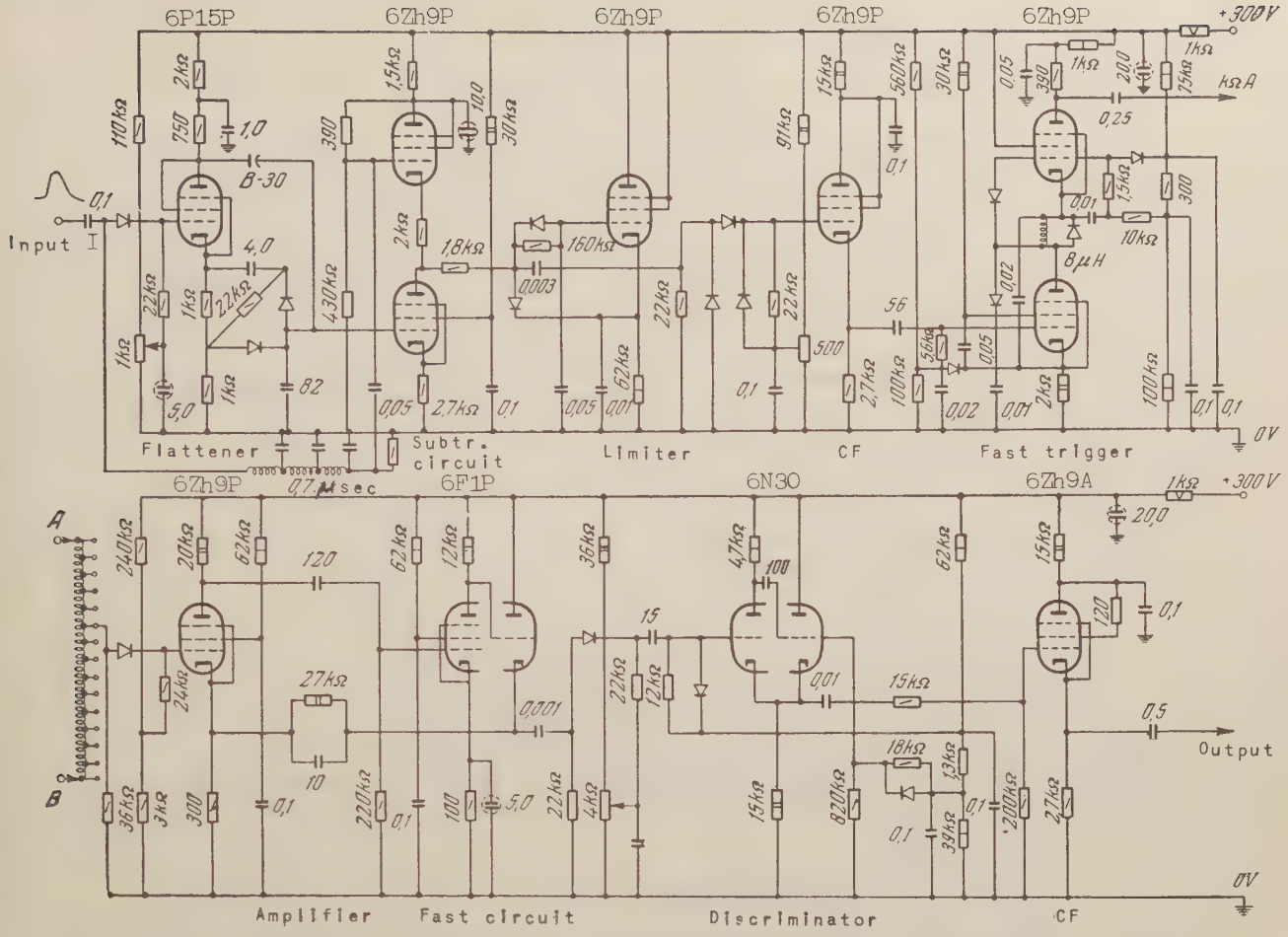

Fig.3. Fast coincidence circuit.

distorted in this case. There is transferred only the overlapping part of the pulses. The distortion of the leading edge of the smaller pulse is approximately the same as that for the larger pulse. The fast coincidence circuit into which the two pulses are fed selects only the overlapping pulses and rejects the others.

In assembling the matrix and cathode followers we paid particular attention to reducing all stray capacitances. The D1Zh diodes were selected for minimum forward and maximum back resistance in the working current-voltage region.

4. Fast coincidence circuit

As was noted above, a basic requirement is that the efficiency of the fast coincidence circuit be high. Circuits described in the literature for working with "slow" scintillators (for example, NaI(Tl) crystals) do not utilize in full the theoretical possibilities as regards the resolving time ($\sim 5 \cdot 10^{-9}$ sec at an energy of ~500 keV).

Our fast coincidence circuit, which is diagramed in Fig.3, is a modification of a circuit with compensation of the time scatter in the operation of the shaping triggers (owing to the difference between the pulse heights) by means of a special pedestal pulse, which is subtracted from the working pulse.[4,6] In contrast to the

Weinzierl[4] circuit, where there are used high power tubes with a heavy current, we used an adding (more accurately subtracting) circuit designed about two series-connected 6Zh9P tubes. The pedestal pulse, which is formed in the cathode circuit of the first tube and equals $u' = u\left(\frac{\Delta v}{u_0}u - \Delta v\right)$, where Δv is the trigger threshold, u is the pulse amplitude and u_0 is the least amplitude of the compensated pulse, is applied to the grid of the second tube (lower tube in Fig.3), appears in the plate circuit of the tube in opposite phase and is subtracted from the positive pulse transmitted directly from the input through a delay line. The third 6Zh9P tube limits the height of the pulses that then go to the input of the fast shaping trigger. In the Weinzierl circuit secondary emission tubes are employed for this purpose, but the instability inherent in this design forced us to seek another solution. The trigger shown in Fig.3 yields a flat topped pulse with a duration of $\sim 4 \cdot 10^{-8}$ sec at the base and an amplitude of ~5 V at a load of 200 ohm. Series dc supply of the tubes in this case is a convenience. The threshold of the trigger is set at about 0.1 V.

To the plates of the upper trigger tubes there is connected a variable delay line, in which the pulses are propagated in opposite directions. In the case of coincidences they are added at the point where they are taken off, yielding a pulse with double amplitude. By way of delay line we used a section of RKZ-400 cable with taps every 7 cm. The cable was wound in a spiral about an 11-contact stepping switch; the pulse taken off the arm of the switch goes to the selector diode. Then it is amplified by an amplifier with negative feed-back assembled about 6Zh9P and 6F1P tubes and is sent via the diode discriminator to a shaper and then goes to the triple coincidence circuit. The delay curves recorded by means of this circuit with an Sc^{46} source have three-four points in the flat part and show that the efficiency of the coincidence circuit is close to 100 with $\tau \approx (4\text{-}6) \cdot 10^{-8}$ sec.

5. Controlled trigger unit

From the five bus bars the pulses are fed through cathode followers to the delay lines and then to the grids of the left tubes of the five controlled Park triggers (Fig.2). So that the pulse itself (without a "gating pulse") would not actuate the trigger, the grid circuit of the tube contains an additional diode, which is normally open and has its positive terminal connected to the grid. The pulse from the plate is differentiated and attenuated by the capacitance and resistance of this diode. The amplification factor of the closed loop comprised of the plate of the left tube, coupling circuit, the cathodes of the two tubes (the right tube operates as a cathode follower), and the plate of the left tube, is less than unity. Under these conditions the trigger is not actuated by even relatively large pulses. Even if there arrives from the coincidence circuit a positive pulse, the controlling diode remains blocked and the circuit operates further as a conventional Park trigger. One controlling pulse also cannot actuate the trigger, which thus becomes a very useful unit. The pulses from the cathode of the triggers through cathode followers are transmitted to the recording unit, which consists of scalers and mechanical registers.

As noted above, a control pulse is produced by the anticoincidence circuit when there arrives a pulse from the triple coincidence circuit and no pulse comes from the triple coincidence selector. The triple coincidence circuit is assembled about diodes. The triple coincidence selector (Fig.2) consists of 10-diode coincidence circuits, which include all the pair combinations of the five outputs of the matrix. In Fig.2 we show only four such elementary circuits. As usual, the pulses from them are taken off through decoupling diodes.

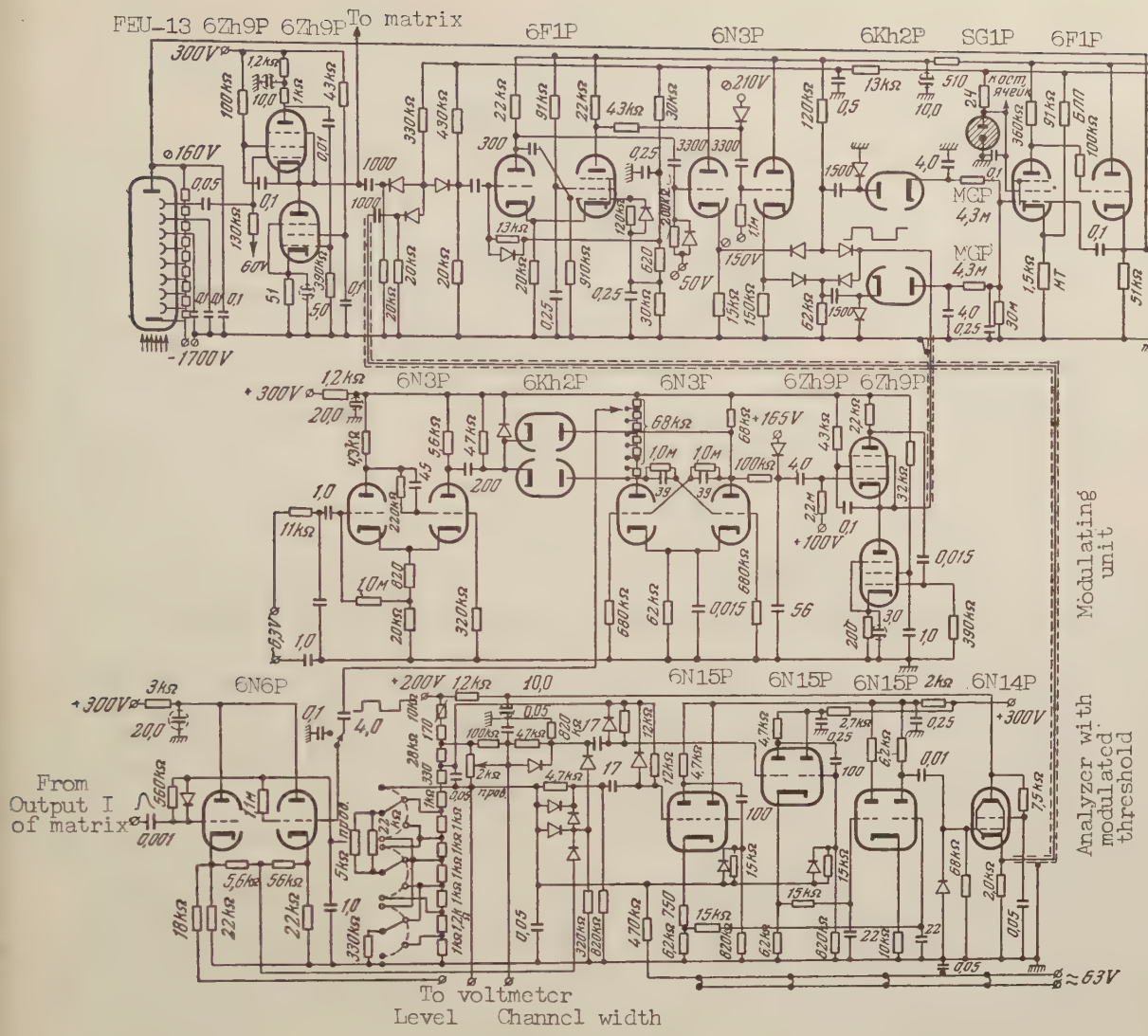

Fig.4. Circuit of the automatic adjustment and stabilization unit.

Three pulses arriving simultaneously from different photomultipliers at the input of the matrix yield pulses on two of its output bars; the third pulse may not satisfy the conditions of amplitude and simultaneity inasmuch as the controlling pulse is produced by the first two pulses. In the presence of pulses on two bus bars in one of the "and" circuits, there appears a signal which triggers the shaper (6F1P tube). A negative pulse from the plate of the right tube blocks the 6Zh2P tube, and the controlling pulse from the triple coincidence circuit cannot pass to the controlled trigger.

6. Automatic adjustment and stabilization unit

The numerical example given in Ref.2 shows that in principle one can reduce the effect of nonuniformity and instability of the efficiencies of the individual counters, but not the efficiency of the coincidence circuits, to a fraction of a percent. To this end the adjustment of the photomultipliers and selection and

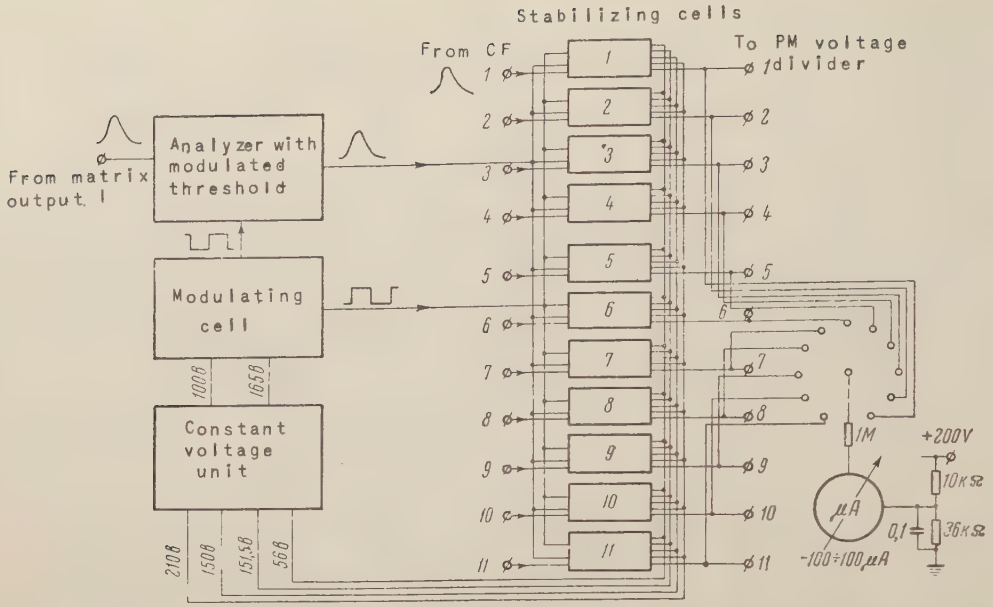

Fig.5. Block diagram of the automatic adjustment and stabilization unit.

matching of the NaI(Tl) crystals should be such that the efficiency scatter will not exceed 3-5%, inasmuch as otherwise the differences, which are smoothed out according to the square law, become appreciable. Attainment of this accuracy of adjustment manually is difficult, and in the case of short-lived sources impossible. Hence we decided to develop a unit for automatic adjustment; at the same time this unit was also designed to stabilize the multiplication factor of all the photomultipliers.

In designing this unit we utilized the work of de Waard[5] but supplemented his circuit with our own method of modulation (Fig.4). The storage circuits are based on a circuit designed in our Institute by A.V.Kulikov. The main problem, however, was utilization of the principle of counting rate difference feed-back[5] with simultaneous stabilization and matching of the spectra of a large number of scintillation spectrometers. This was achieved by introduction of diode coincidence circuits at the inputs of the stabilizing cells (Figs.4 & 5). A pulse arrives at such a cell only when the pulse from the photomultiplier lies between the thresholds of the analyzers with a modulated channel. In this case there appears a positive pulse from the analyzer at one of the inputs of the coincidence circuit of each cell. The second input of the coincidence circuit of each cell is connected with its photomultiplier (Fig.5). Hence there is actuated the coincidence circuit only of the cell which is connected with the counter detecting the given photon. Thus there is found the "address" of the stabilizing cell corresponding to the given γ-rays.

As was noted above, the larger pulses from any given photomultiplier arrive at output I of the matrix. They then go to analyzer I, and to the single-channel analyzer with a modulated channel. Modulation of the channel is realized by square pulses taken off the left anode of the binary cell (tube 6N3P - Fig.4). This cell is flipped by a Schmidt trigger actuated by the filament voltage, as shown in the figure.

The process of stabilization of a photomultiplier may be described as follows. The analyzer with the modulation switched off is set on the photopeak of

the reference line. Then the width of its channel is increased to about half the line width at half-height and the modulation is switched on; the modulation amplitude is made approximately equal to the line width at half-height. The pulses from the output of the analyzer are fed into the coincidence circuit of the cell and from it to the Park trigger. The positive and negative charge storage circuits, corresponding to the lower and upper positions of the analyzer channel, are assembled about 6Kh2P diode tubes in order to reduce leakage. These storages are charged alternately by positive pulses from the left anode of the Park trigger and negative pulses from the right anode. The switching is realized by two "and" type circuits in each cell, which operate as follows. Square modulation pulses with a frequency of 25 cps, an amplitude of 100 V and a duty factor of 1/2 enter through the cathode follower at the inputs of both "and" type circuits. The dc potentials on both inputs are held rigorously constant (by the constant voltage unit - see Fig.5). At the upper level of the modulating voltage there is blocked the right diode of the coincidence circuit for positive pulses (upper "and" circuit in Fig.4). In this case there can only pass positive pulses to the storage circuit from the trigger. At the output of the "and" circuit for negative pulses with proper selection of the constant voltages there are observed only small bumps on the leading edges of the modulating pulses.

The second "and" circuit operates in an analogous fashion, passing negative pulses at the lower level of modulation to the negative charge storage circuit.

If the adjustment is accurately made, the counting rates to either side of the reference line will be equal, and equal but opposite charges will be built up in the storages. The divider of two 4.7 megohm resistors serves as an adding circuit for the voltages on the storage capacitors. In the case considered above the potential difference at its midpoint with reference to the ground should be zero. In this case, at the output of the dc amplifier (6F1P tube) there is established a voltage of ~160 V, which is applied directly to the anode of the corresponding photomultiplier tube. Any change in the multiplication factor of the photomultiplier gives rise to a shift of the photopeak and the appearance of a difference in counting rates to either side of the line and, consequently, to change in the voltages on the storage capacitors. The modulation phases of the analyzer and "and" circuits are selected so that shift of the line to the side of smaller amplitudes gives rise to an increase of the voltage on the anode of the photomultiplier, so that the amplification of the PM is re-established. The linear region of the dynamic characteristic of the dc amplifier equals ±100 V. Change in the stabilization coefficients of the cells with artificial variation of the photomultiplier voltage by ±100 V yielded values no worse than 10 at a counting rate of 25 pulses/sec over the entire area of the photopeak. The duration of the pulses taken off the Park triggers is about 80 μsec. During this time the 1500 pF capacitors have time to charge to saturation through the load resistors of the coincidence circuits.

The method of modulation of the channel of the analyzer itself can be understood from Fig.4 and the above description. Mixing of pulses from output I of the matrix with the modulating voltage is effected by the adding circuit (cathodes of tubes 6N6P). From the midpoint of this circuit the pulse goes to the diode discriminator of the single-channel analyzer (Park circuit). In our circuit the coupling capacitor used by de Waard[5], recharging of which interferes with using square pulse modulation, is left out. During the initial adjustment the switch shown in Fig.4 above tube 6N6P is turned to the "ground" position and the modulation is cut off.

The voltmeter shown in Fig.5 serves as an indicator of drift of the amplification of the photomultipliers and indicates the value of the additional voltage

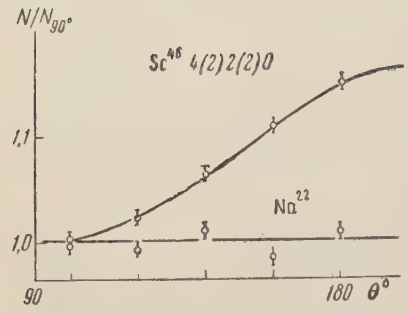

Fig.6. Results of measurement of γ-γ angular correlation with Sc^{46} and Na^{22} sources.

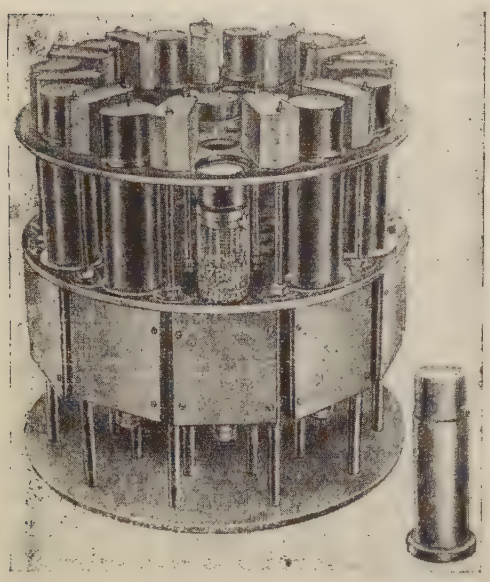

Fig.7. Scintillation spectrometer assembly of the 11-counter instrument.

applied to the photomultiplier anodes. All the photomultipliers are supplied from a common high voltage source which yields a current of 4 μA. Individual adjustment of the voltages is realized by a set of resistors, part of which are variable.

7. Tests of the instrument

The described instrument was tested with sources previously investigated by other authors, namely, Sc^{46} (892—118 keV cascade) and Na^{22} (511 keV annihilation γ-rays—1270 keV transition). The results of 4-hour measurements with each of these sources are shown in Fig.6. In the first case there were about $2 \cdot 10^4$ counts per point; in the second case, about $1.6 \cdot 10^4$.

It will be seen that the experimental points for the Sc^{46} source fell exactly on the theoretical curve for the 4(2)2(2)0 cascade (solid line) corrected for angular resolution. The solid angle was taken equal to 1/170 of 4π. The points for Na^{22} do not fit as well on the straight line to be expected in this case. This may be the result of impairment of the efficiency of the fast coincidence circuit with decrease of energy or/and due to the operation of chance factors.

Conclusions

The principle utilized in the construction of the described 11-channel instrument for measuring γ-γ angular correlation is applicable to investigation of other forms of correlation in cases when the individual radiations of the cascade are isotropic or have axial symmetry.

As compared with two-counter (single-channel) instruments the 11-channel instrument insures a two orders of magnitude higher efficiency, makes it possible to work with short-lived and weak sources and to measure triple correlations.

The principal sub-assemblies of the instrument are the following:

1) a matrix which makes it possible to use a conventional two-channel fast-slow coincidence circuit for amplitude and time selection of pulses arriving from a large number of scintillation spectrometers,

2) a unit for simultaneous stabilization and adjustment of a large number of photomultiplier tubes, and

3) controlled Park triggers.

A photograph of the scintillation spectrometer assembly is reproduced in Fig. 7.

We desire to express our deep gratitude to G.S.Vil'dgrube for making available 12 matched FEU-13 photomultipliers and to I.F.Bugakov for assistance in

assembling the instrument.

"A.F.Ioffe" Physical-Technical Institute,
Academy of Sciences of the USSR

References

1. B.A.Jacobsohn & E.M.Henley, Phys.Rev., 113, 234 (1959).
2. A.I.Belyaevskii, PTE (Instruments & Exper.Techniques), No.3, 25 (1957).
3. J.Park, Scient.Instrum., 33, 257 (1956).
4. P.Weinzierl, Rev.Scient.Instrum., 27, 226 (1956).
5. H.de Waard, Nucleonics, 13, 36 (1955).
6. B.Johansson, Nucl.Instrum., 1, 274 (1957).

BETA-SPECTROMETER WITH TWO-FOLD $\pi\sqrt{2}$ FOCUSING

- S.A.Shestopalova

The basic requirements set for modern β-spectrometers are good resolution and high luminosity. Best, judged from this standpoint, are spectrometers with double-focusing through an angle of $\pi\sqrt{2}$.[1-3]

Where solution of a number of specific physical problems is concerned, however, in addition to meeting the above requirements, the instrument must have a number of other characteristics, for example, absence of scattering inside the instrument, and minimum interfering background. Elimination or weakening of the effects associated with scattering is generally realized by using multiple focusing, as for example, in spectrometers with triple focusing[4,5] and in spectrometers with two-fold focusing[6]. Location of thin-walled Geiger-Müller counters behind the foci and use of the method of coincidences make it possible to solve the problem of minimizing the background at the same time.

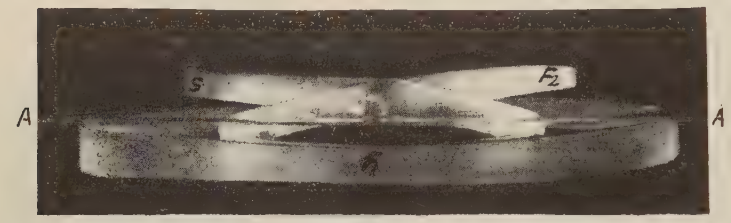

Fig.1. Model showing path of the electron beam in the two-fold focusing spectrometer (side view): S - source, F_1 and F_2 - foci, AA - symmetry plane of the magnetic field.

Inasmuch as $\pi\sqrt{2}$ focusing spectrometers generally have the best electron-optical properties, it is desirable in using multiple focusing to retain this focusing angle. This proves to be feasible by virtue of the fact that in a magnetic field falling off along the radius and possessing axial symmetry, the electrons oscillate in both ρ and Z. Hence, if the source is located above the plane of symmetry of the magnetic field, the focal points prove to be located alternately above and below this plane.

Fig.2. Path of electron beam (top view).

Models of the electron beam in the new spectrometer are shown in Figs.1 and 2. As will be evident from Fig.1, the first focus is located below the plane of symmetry of the magnetic field; for calculating its shape one can use the usual formulas and tabulated values for a field with focusing over an angle of $\pi\sqrt{2}$. As is known[2] this focus is curved; accordingly, the first slit must be curved. The shape of the outer edge of the slit and the contours of three apertures were calculated by M.A.Listengarten with an accuracy to third order terms (the other necessary apertures were calculated by us, using the first approximation formulas given in Ref.3).

After passing through the first slit and the first G-M counter with thin windows, the electron beam begins to rise, passes above the source and is focused $\pi\sqrt{2}$ (254.5°) after the second source at a point as high above the symmetry plane as the source. Behind the second focus there are located two G-M counters, in which there are counted triple coincidences. As Listengarten's calculations showed, the second focus of the instrument proves to be more rectilinear and narrower than the first focus. However, the second focusing can be regarded only as a

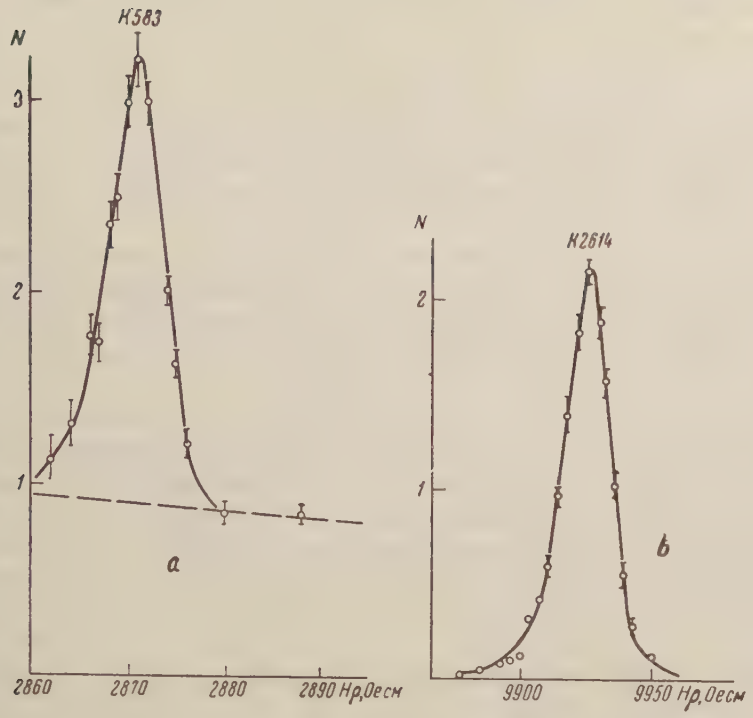

Fig.3. Conversion electron lines of radiothorium active deposit: a - from the 583 keV γ-transition, b - from the 2614 keV γ-transition. $\Delta H\rho/H\rho$ = = 0.21%.

means for eliminating background and reducing the probability of detecting electrons scattered in the first half of the spectrometer. In this case the slit at the second focus can be widened so as to accept electrons scattered in the first part of the counter; the resolution of the spectrometer is still determined by the first slit, the dimensions of the source and the geometry of the beam at the first focus. The radius of the equilibrium orbit in our instrument is 140 mm. We were able to obtain a field distribution in the entire working region agreeing to within 0.2% (the accuracy of field measurement) with the theoretical configuration. The height of the source is 15 mm; the center of the source is located 24 mm above the symmetry plane of the magnetic field. The width of the slit at the first focus is 1 mm; the width at the second focus 14 mm. Under these conditions the relative line half-width amounts to 0.21% (Fig.3) (0.5 mm wide radiothorium active deposit source).

We investigated some of the attributes of the instrument using a Cs^{137} source. Unfortunately, owing to inadequate quality of the source, the conversion lines of Cs^{137} measured under the same conditions as the lines of radiothorium deposit had a half-width of 0.32 ± 0.02% (Fig.4).

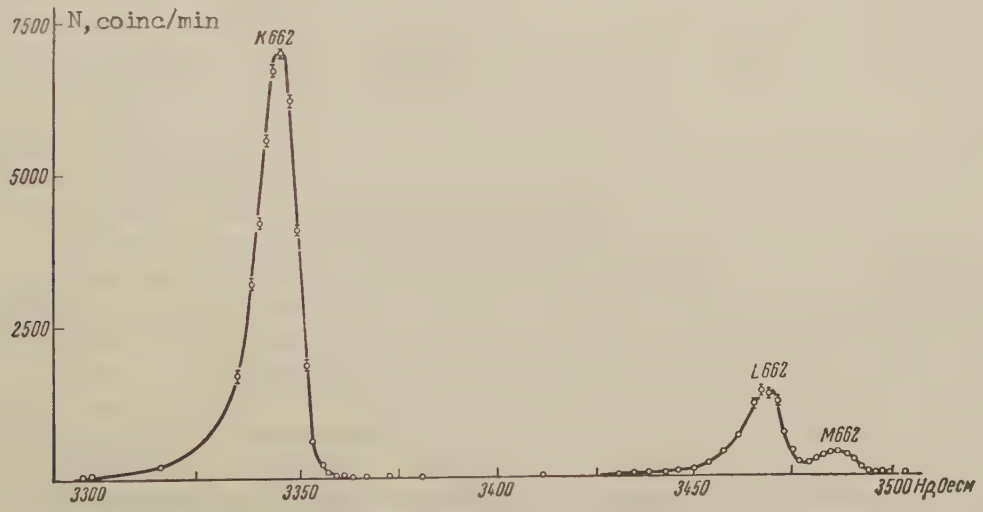

Fig.4. Spectrum of Cs^{137} conversion electrons. $\Delta H\rho/H\rho$ = 0.32%.

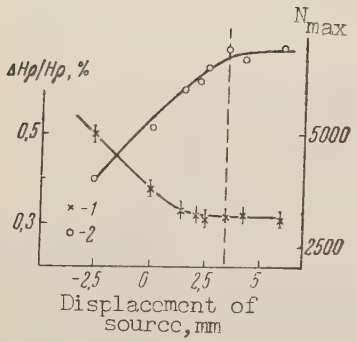

←Fig.5. Results of experiment aimed at finding the optimum focusing conditions. 1 - relative line half-width, 2 - counting rate at the peak of the Cs^{137} K line. Dashed line - working conditions.

The instrument was first adjusted mechanically and then by moving the source along the optical axis to find the optimum focusing conditions. The results are shown in Fig.5.

With the Cs^{137} source the background of chance of cosmic coincidences at zero current in the magnet amounted to less than one coincidence per 40 hours; the background behind a hard β-spectrum proved to be less than one coincidence per 10 hours.

We desire to express our deep gratitude to B.S.Dzhelepov for a number of valuable suggestions and constant interest in the work, A.F.Malov for valuable discussions, M.A.Listengarten for valuable advice and for calculating the shape of the focus and of some of the apertures, I.F.Uchevatkin and A.I.Medvedev for assistance in adjusting and testing the spectrometer, and A.V.Zolotavin and E.P. Grigor'ev for useful advice on obtaining the requisite configuration of the magnetic field.

"D.I.Mendeleev" All-Union Scientific Research Institute of Metrology

References

1. Beta- and gamma-ray Spectroscopy, edited by Kai Siegbahn, Chapt.3, N.Y. 1955.

2. A.V.Zolotavin, Izv.AN SSSR Ser.fiz., 18, 127 (1954); Thesis, Radium Institute, USSR Ac.of Sci., 1960.

3. S.A.Baranov, A.F.Malov & K.N.Shlyagin, PTE (Instruments & Exper.Techniques), No.1, 3 (1956).

4. B.S.Dzhelepov, N.M.Anton'eva & S.A.Shestopalova, Doklady AN SSSR, 64, 309 (1949); B.S.Dzhelepov, I.F.Uchevatkin & S.A.Shestopalova, Zhur.eksp.i teor. fiz., 37, 858 (1959). (Trans.Soviet Physics - JETP.)

5. B.S.Dzhelepov & O.E.Kraft, Izv.AN SSSR, Ser.fiz., 20, 318 (1956). (Trans. Bulletin, 20, 293.)

6. M.G.Kaganskii, Thesis, Radium Inst., Radium Inst., USSR Ac.of Sci., 1960.

USE OF AN IONIZATION CHAMBER FOR PARTICLE SELECTION BY MEASURING E(dE/dx)

- Yu.V.Gofman, V.N.Dobrikov, N.I.Zaika & O.F.Nemets

For selective detection of particles in investigating deuteron-induced reactions experimenters frequently utilize a procedure that follows from Bethe's[1] formula, according to which $E(dE/dx) \propto Z^2 m$, where E is the energy of the particle, dE/dx is the specific energy loss, m is the mass of the particle and Z is its charge. Simultaneous measurement of E and dE/dx and obtaining their product allows of separating such particles as protons, deuterons and tritons, i.e., particles with identical charges but different masses. It can be shown[2], on the basis of range-energy curves, that if the particle energy lies in the range from 5 to 25 MeV, the ratios of the product E(dE/dx) for protons, deuterons and tritons are 1:1.8:2.6 in a number of different substances.

This method of particle selection has been realized by a number of authors[2,3] by means of scintillation counters consisting of a combination of thick and thin crystals (or a plastic scintillator); the thin crystal serves for measuring the loss, the thick crystal for measuring E. Aside from low resolution, which is peculiar to all scintillation spectrometers, crystal selectors have the additional drawback that the preparation of thin crystals for measuring dE/dx is very difficult inasmuch as the thickness of such crystals in working at energies of the order of 10-20 MeV must be only 0.05-0.1 mm. On the other hand, plastic scintillators are characterized by nonlinear dependence of the pulse height on the particle energy for large dE/dx and hence for plastic scintillators the E(dE/dx) ratios deviate from the above mentioned values with change in the particle energy. This seriously impairs particle separation and necessitates further complication of the experimental set-up.

In view of this we felt it would be of interest to use for particle selection an ionization chamber with two collecting electrodes, one of which (the short) can serve for measuring dE/dx and the other (long) for measuring the particle energy. A particularly great convenience in this case is the possibility of varying the particle energy loss at the first plate by changing the gas pressure in the chamber, which allows of separating particles in a wide energy range. Moreover, in principle, an ionization chamber allows of obtaining better energy resolution.

The ionization chamber used in the present work was a modification of the flat grid-type chamber described in Ref.4. On the basis of the fact that the maximum energy of our cyclotron-accelerated deuterons was 13.6 MeV, the lengths chosen for the electrodes were 5 and 31 cm. Both electrodes were connected to linear amplifiers, which were located on the wall of the chamber; from these the pulses were sent via coaxial cables and additional amplifiers to the pulse adding and multiplying circuits. The chamber was filled with argon with an admixture of methane; the pressure could be varied from 1 to 12 atm.

A block diagram of the experimental arrangement is shown in Fig.1. The pulses from the chamber were amplified by two identical amplifiers 1 and 1', and then fed via the adding circuit 2 to the multiplying circuit 4. The adding circuit proved to be necessary inasmuch as a particle entering the chamber with energy E, in approaching the small electrode, loses a part of its energy dE; hence in the absence of an adding circuit there is applied to the multiplying circuit a pulse proportional to E - dE, rather than E, which substantially impairs the particle separation. The adding circuit, which sums the two pulses, sends to the multiplying circuit a pulse proportional to E, so that proportionality of E(dE/dx) to the particle mass is conserved. When there simultaneously arrive two positive pulses, the coincidence circuit 3 produces the pulse necessary for actuating the two coincidence circuits with conservation of amplitude, located at both outputs

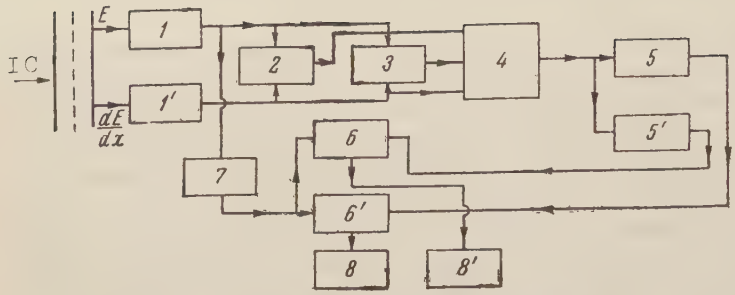

Fig.1. Block diagram of the spectrometer: IC - ionization chamber, 1 & 1' - amplifiers, 2 - adding circuit, 3 - coincidence circuit, 4 - multiplying circuit, 5 & 5' - discriminators, 6 & 6' - coincidence circuits with conservation of amplitude, 7 - stretcher, 8 & 8' - multiple channel analyzers.

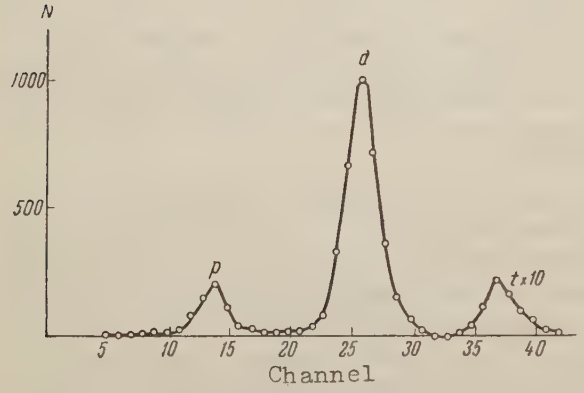

Fig.2. Spectrum of pulses with amplitude proportional to E(dE/dx). Deuteron reaction on Be^9; θ_{lab} = = 20°.

of the multiplication circuit.

The utilized principle of multiplication consists in shaping of a square pulse, the amplitude of which is proportional to the amplitude of one of the input signals and the duration of which is proportional to the amplitude of the second input signals. After integration there is obtained a pulse with amplitude proportional to the product of the amplitude of both the input signals.[5]

At the output of the multiplication circuit by appropriate discrimination one can segregate the particles of given mass. The equipment has provision for simultaneous observation of the spectra of particles of two different masses; to this end there are provided two discriminators 5 and 5' and two multiple channel analyzers 8 and 8'.

A typical spectrum of pulses with amplitude proportional to the product E(dE/dx) is shown in Fig.2; this spectrum was obtained in bombardment of Be^9 with 13.6 MeV deuterons. As will be evident from the figure, the proton, deuteron and triton groups are satisfactorily separated.

Lastly, for obtaining the energy spectra of particles of a given type, mass selected by means of the discriminator, the equipment includes the coincidence circuits with conservation of amplitudes 6 and 6', which are actuated by the E(dE/dx) pulses and pass pulses proportional to E through to the analyzer. The pulse stetcher 7 extends the pulses to the duration necessary for proper operation of the other components.

Institute of Physics,
Academy of Sciences of the Ukrainian SSR

References

1. E.Segre (ed.), Experimental Nuclear Physics, N.Y., 1953.
2. F.A.Aschenbrenner, Phys.Rev., 98, 657 (1955).
3. J.L.Yntema, Phys.Rev., 113, 261 (1959).
4. N.I.Zaika & O.F.Nemets, Izv.AN SSSR, Ser.fiz., 23, 1460 (1959). (Trans. Bulletin, 23, 1447.)
5. B.Wolfe, A.Silverman & J.W.deWire, Rev.Sci.Instr., 26, 504 (1955).

SPIN AND PARITY ASSIGNMENTS FOR SOME STATES OF Si^{30}, Zr^{91}, Zr^{92} AND Cd^{114}

- N.I.Zaika & O.F.Nemets

Investigation of the angular distribution of the products of stripping reactions allows of finding the value of the angular momentum transferred to the nucleus and determining the spin and parity of the final state.[1] If the deuteron energy exceeds the height of the Coulomb barrier, in most cases the value of the transferred angular momentum can be determined unambiguously. Hence from the standpoint of nuclear spectroscopy it is useful to increase the deuteron energy in studying stripping reactions.

In the present work we investigated the angular distributions of protons from the (d,p) reactions on Si^{29}, Zr^{90}, Zr^{91} and Cd^{113}. The 13.6 MeV deuterons were extracted from the Institute of Physics (Ukrainian SSR Ac.of Sci.) cyclotron. The protons were detected by an ionization chamber[2], in front of which was mounted an appropriate absorber to stop all deuterons. The targets were prepared in the form of thin polystyrene films loaded with the oxides of the enriched isotopes in powdered form. A Zr^{91} target was also available in the form of a thin metallic film. The isotope contents of the targets are listed in Table 1.

Table 1

Isotope content of targets

Target	Isotope content, %				
Si^{29}	Si^{28} — 29,3	Si^{29} — 69,7	Si^{30} — 1,0		
Zr^{90}	Zr^{90} — 96,1	Zr^{91} — 1,5	Zr^{92} — 1,2	Zr^{94} — 1,2	
Zr^{91}	Zr^{90} — 11,0	Zr^{91} — 79,5	Zr^{92} — 6,1	Zr^{94} — 3,0	Zr^{96} — 0,4
Cd^{113}	Cd^{111} — 0,2	Cd^{112} — 3,8	Cd^{113} — 73,9	Cd^{114} — 22,1	$Cd^{106, 108, 110, 116}$ — $<0,2$

$Si^{29}(d,p)Si^{30}$

The proton distributions corresponding to the ground and first excited (2.24 MeV) states of Si^{31} are shown in Fig.1. In this and the following figures the points represent the experimental results; the curves - the results of calculation using Butler's formulas[1].

Inasmuch as our target contained 29.3% Si^{28}, the protons corresponding to the first excited state of Si^{30} were detected together with the Si^{29} ground state group of protons from the $Si^{28}(d,p)Si^{29}$ reaction. The energy difference between these two proton groups is 90 keV; hence these groups could not be distinguished in our experiment. However, the angular distribution of protons corresponding to the first excited state of Si^{30} could be obtained by subtracting the contribution from the $Si^{28}(d,p)Si^{29}_{g.s}$ reaction from the total angular distribution. The angular distribution of protons corresponding to the ground state of Si^{29} was measured by us earlier[2]; it corresponds to $l_n = 0$. We carried out a repeat measurement in the present work.

Our results are in agreement with the data of Sukharevskii[3] obtained at a deuteron energy of 4.3 MeV. As might have been expected the angular distributions obtained with 13.6 MeV deuterons evince the splitting process more clearly.

$Zr^{90,91}(d,p)Zr^{91,92}$

The angular proton distributions corresponding to the ground and first excited states of the final nuclei are shown in Fig.2, together with the values of

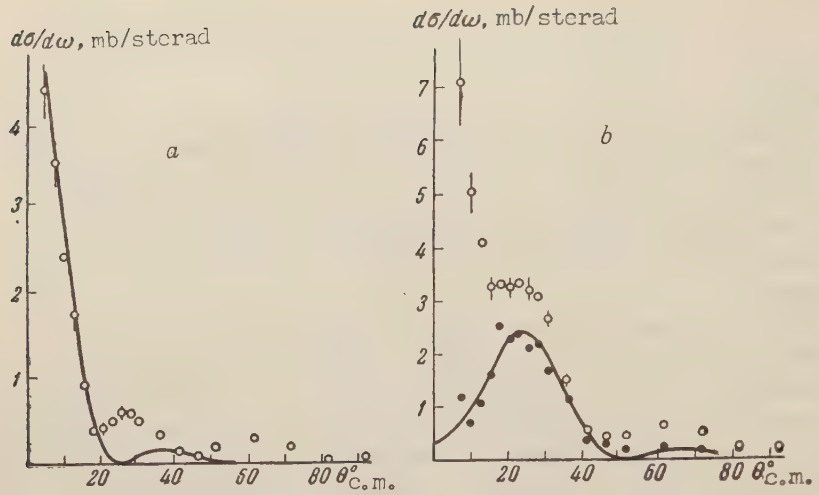

←Fig.1. Angular distributions of protons from the $Si^{29}(d,p)Si^{30}$ reaction: a - protons corresponding to the Si^{30} ground state: Q = 8.39 MeV, $l_n = 0$, $r_0 = 5.45$ f; b - protons corresponding to the first excited state; Q = 6.15 MeV, $l_n = 2$. Solid points - results of subtraction of the distribution from the $Si^{28}(d,p)Si^{29}_{g.s}$ reaction; solid curves - distribution calculated according to Butler[1].

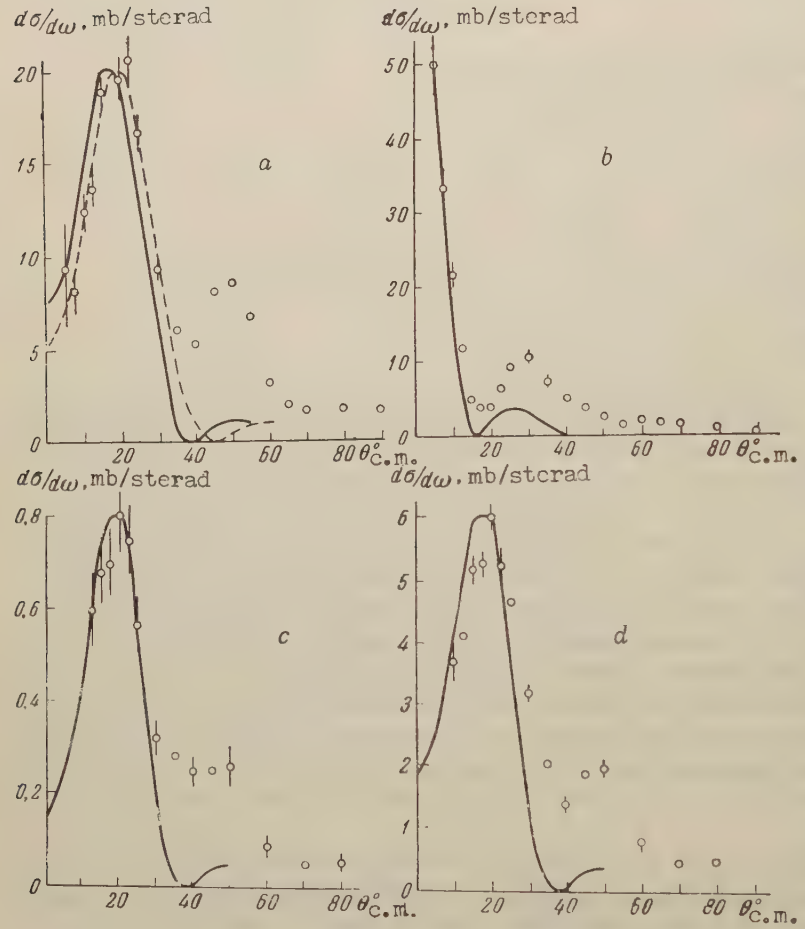

←Fig.2. Angular distributions of protons from the reactions: a - $Zr^{90}(d,p)Zr^{91}_{g.s}$, Q = 5 MeV, $l_n = 2$; b - $Zr^{90}(d,p)Zr^{91*}$, Q = 3.79 MeV, $l_n = 0$; c - $Zr^{91}(d,p)Zr^{92}_{g.s}$, Q = 6.5 MeV, $l_n = 2$; d - $Zr^{91}(d,p)Zr^{92*}$, Q = 5.57 MeV, $l_n = 2$.

the transferred angular momentum.

In the level scheme proposed by Klinkenberg[4] in the presence of 50 neutrons in the nucleus there are successively filled the $d_{5/2}$, $g_{7/2}$, $h_{11/2}$, $d_{3/2}$ and $s_{1/2}$ states. The calculations of Nilsson[5] for the spherical case lead to the following order of filling: $d_{5/2}$, $g_{7/2}$, $s_{1/2}$, $d_{3/2}$ and $h_{11/2}$.

Of the two assignments obtained by us for the ground state of Zr^{91} - $3/2^+$ and $5/2^+$ - the latter is in agreement with the $d_{5/2}$ state predicted by both models; the $5/2^+$ assignment is also in agreement with the results of direct measurements of the spin carried out by Brun et al[6]. As for the $1/2^+$ assignment for the first excited state of Zr^{91} (1.21 MeV), it is not consistent with either of the above schemes. We note that in the case of the $Sr^{88}(d,p)Sr^{89}$ reaction[7] for the transition to the first excited level the 51st neutron is also picked up in the $s_{1/2}$ state.

In view of the fact that Sr^{88} and Zr^{90} have a close neutron shell, it may be expected that the states excited in the (d,p) reaction (at least the lowest lying states) will be single-particle ones and that their sequence will be that required by the shell model, namely, $d_{5/2}$, $g_{7/2}$ and so on.

On the other hand, in the successive filling of the states by nucleons in no case is there one nucleon in the $g_{7/2}$ state: at first there occurs pair filling of the $g_{7/2}$ state, with which there is an odd number of nucleons in the $d_{5/2}$ state, and beginning with Cd^{111} there occurs filling of the $s_{1/2}$ state with the $g_{7/2}$ state remaining unfilled.[8] It is possible that in both cases violation of the predicted filling sequence is due to the same causes. There is no reason to assume that the $g_{7/2}$ level was simply not detected in our experiments, say, owing to inadequate resolution, inasmuch, first, according to all available data[9-11] there are no additional levels close to 1.07 MeV in Sr^{89} and 1.21 MeV in Zr^{91}, and, second, it cannot be concluded from the appearance of the angular distribution of protons corresponding to the first excited states of Sr^{89} (Ref.7) and Zr^{91} that there is a component of noticeable intensity corresponding to $l_n = 4$, i.e., to the $g_{7/2}$ state.

In their book, Dzhelepov & Peker[9] give $5/2^+$ for the spin of the first excited level of Zr^{91}; this also is difficult to interpret from the standpoint of the shell model. They also give a value of 2^+ for the first excited state (0.93 MeV) of Zr^{92}. If the ground state spin of Zr^{91} is $5/2^+$, according to the selection rules for stripping reactions[1], this state can form with $l_n = 0$, 2 and 4. The fact that it is evinced only with $l_n = 2$ (Fig.2,d) indicates that the $l_n = 0$ value is forbidden by the shell model selection rules. That such forbiddenness may obtain for transitions to the ground state of the final nuclei was inferred by Bethe & Butler[12], and this inference was substantiated experimentally by King & Beach[13]. We know of no other example of such inhibition for transitions to excited states.

$Cd^{113}(d,p)Cd^{114}$

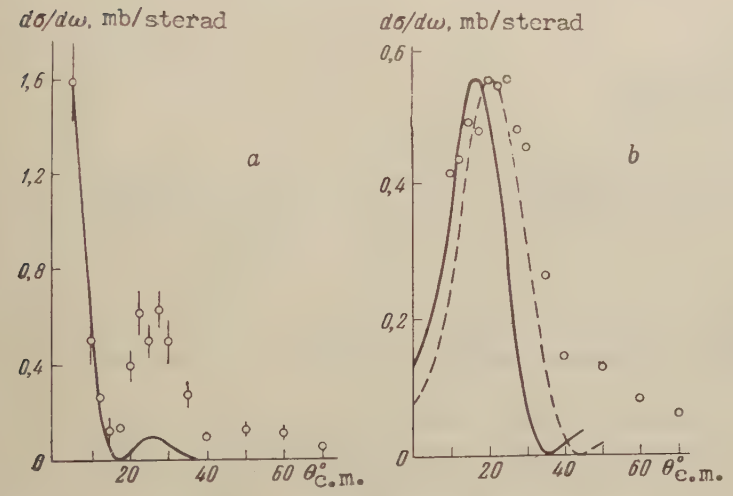

Fig.3. Angular distributions of protons from the reactions: a - $Cd^{113}(d,p)Cd^{114}_{g.s.}$, Q = 6.75 MeV, $l_n = 0$; b - $Cd^{113}(d,p)Cd^{114*}$, Q = 6.19 MeV, $l_n = 2$.

As will be evident from Fig.3, the angular momenta transferred to the neutron nucleus are 0 to 2 for the transitions to the ground and first excited (0.56 MeV) states of Cd^{114}.

As regards their attributes the low lying levels of Cd^{114} are vibrational levels; hence measurements for Cd^{113} are of interest also from the standpoint of testing the inferences of Satchler[14] that the probabilities of excitation of successive levels belonging to one vibrational band must differ by approximately an order of magnitude for neighboring levels.

In our case the ratio of the transition probability to the first excited level (reduced width) to the transition probability to the

Table 2

Results of investigation of the (d,p) reaction on Si^{29}, Zr^{90}, Zr^{91} and Cd^{113}

Target	I^{π}_{init}	Final nucleus state, (MeV)	l_n	Possible assignments	Interaction radius r_0, f
Si^{29}	$1/2^+$	0	0	$\underline{0}^+$, 1^+	5,45
		2,24	2	1^+, $\underline{2}^+$, 3^+	5,45
Zr^{90}	0^+	0	2	$3/2^+$, $\underline{5/2}^+$	7,16(6,15)*
		1,21	0	$1/2^+$	7,16
Zr^{91}	$5/2^+$	0	2	$\underline{0}^+$, 1^+, 2^+, 3^+, 4^+, 5^+	7,19
		0,98	2	0^+, 1^+, $\underline{2}^+$, 3^+, 4^+, 5^+	7,19
Cd^{113}	$1/2^+$	0	0	$\underline{0}^+$, 1^+	7,6
		0,56	2	1^+, $\underline{2}^+$, 3^+	7,6 (6)*

*The figures in parentheses are the values of the radius used in calculating the dashed curves in Figs.2,a and 3,b.

ground state proved to be 0.43, instead of 0.1 as predicted by Satchler.

The results obtained in the present work are summarized in Table 2.

Measurements of the absolute differential cross sections were carried out by means of a current integrator.[15] The uncertainty in determining the cross sections was evaluated as ±50%.

It should be noted that in some cases for obtaining better agreement of theory with experiment we took smaller values for the interaction radius than follows from the usual formula $r_0 = (1.7 + 1.22\ A^{1/3})f$. This, in our opinion, is a consequence of the influence of Coulomb interaction. However, the influence of Coulomb interaction was not so great as to introduce ambiguity into determination of the values of l_n.

Institute of Physics,
Academy of Sciences of the Ukrainian SSR

References

1. S.T.Butler, Proc.Roy.Soc., A208, 559 (1951).

2. N.I.Zaika & O.F.Nemets, Izv.AN SSSR, Ser.fiz., 23, 1460 (1959). (Trans. Bulletin, 23, 1447.)

3. V.G.Sukharevskii, Zhur.eksp.i teor.fiz., 36, 52 (1959). (Trans.Soviet Physics - JETP.)

4. P.F.A.Klinkenberg, Revs.Mod.Phys., 24, 63 (1952).

5. S.G.Nilsson, Kgl.Danske Videnskab Selskab, Mat.-fys.Medd., 29, No.16 (1955).

6. E.Brun, J.Oeser & H.H.Staub, Phys.Rev., 105, 1929 (1957).

7. N.I.Zaika & O.F.Nemets, Izv.AN SSSR, Ser.fiz., 24, 865 (1960). (Trans. Bulletin, 24, 868.

8. M.G.Mayer & J.H.D.Jensen, Elementary Theory of Nuclear Shell Structure, N.Y.1955.

9. B.S.Dzhelepov & L.K.Peker, Skhemy raspada radioaktivnykh yader (Decay schemes of radioactive nuclei), M.-L., 1958.

10. C.E.McFarland & F.B.Shull, Phys.Rev., 89, 489 (1953).

11. B.L.Cohen & R.E.Price, Nucl.Phys., 17, 129 (1960).
12. H.A.Bethe & S.T.Butler, Phys.Rev., 85, 1045 (1952).
13. J.S.King & E.H.Beach, Phys.Rev.Letters, 90, 381 (1953).
14. G.R.Satchler, Ann.Phys., 3, 275 (1958).
15. V.N.Dobrikov, N.I.Zaika & O.F.Nemets, PTE, 4, 23 (1958). (Trans.Instruments & Experimental Techniques.)

Bulletin of the Academy of Sciences of the USSR - Physical Series
Vol.25, No.10 - October 1961
Transactions of the Eleventh Conference on Nuclear Spectroscopy
(Continued from Vol.25, Nos.2, 7 & 9; to be continued in Vol.26, No.1)

TABLE OF CONTENTS

	Page Orig.	Trans.
Investigation of the properties of strongly deformed nuclei on the basis of a nuclear model taking into account pair correlations - V.G.Solov'ev	1198	1207
$Yb^{166} \rightarrow Tm^{166} \rightarrow Er^{166}$ decay chain - E.P.Grigor'ev, K.Ya.Gromov, B.S.Dzhelepov, Zh.T.Zhelev, V.Zvol'ska & I.Zvolskii	1217	1227
Coincidences between conversion electrons emitted in the decay of Ho^{160} to Dy^{160} - B.S.Dzhelepov, I.Zvol'skii & V.A.Sergienko	1228	1238
Coincidences between conversion electrons of the dysprosium fraction from proton bombarded tantalum - B.S.Dzhelepov, I.Zvol'skii, M.K.Nikitin & V.A.Sergienko	1246	1257
Supplementary data on neutron-deficient osmium isotopes - T.V.Malysheva & B.A.Khotin	1256	1267
Investigation of the conversion electron spectrum of neutron-deficient platinum isotopes - L.N.Kryukova, V.V.Murav'eva, L.Duda, T.V.Malysheva & B.A.Khotin	1257	1269
Investigation of the radiation from neutron-deficient hafnium isotopes - B.Brabec, B.Kracik, T.Kracikova, Z.Miligi, M.Weis, A.Mashtalka, M.Vobecky & V.Gnatovicz	1266	1277
Photodisintegration of Li^7 by bremsstrahlung of up to 9.5 MeV - V.G.Shevchenko & B.A.Yur'ev	1269	1280
Probabilities for single-particle transitions in Yb^{173} - E.E.Berlovich, M.P.Bonitz, Yu.K.Gusev & M.K.Nikitin	1275	1286
Gamma-rays produced in inelastic scattering of 2.95 MeV neutrons by I^{127}, La^{139} and Bi^{209} - L.Ya.Graudynya, K.A.Petrzhak & A.V.Sorokina	1280	1291
Semiconductor spectrometers for charged particles - L.A.Zubritskii, A.I.Popov, P.V.Sorokin & V.F.Samoilov	1286	1296
Eleven-counter instrument for measuring γ-γ angular correlation - A.I.Belyaevskii & Yu.A.Gur'yan	1291	1300
Beta-spectrometer with two-fold $\pi\sqrt{2}$ focusing - S.A.Shestopalova	1302	1312
Use of an ionization chamber for particle selection by measuring E(dE/dx) - Yu.V.Gofman, V.N.Dobrikov, N.I.Zaika & O.F.Nemets	1305	1315
Spin and parity assignments for some states of Si^{30}, Zr^{91}, Zr^{92} and Cd^{114} - N.I.Zaika & O.F.Nemets	1308	1317

Translated in 1962 by
Columbia Technical Translations
5 Vermont Ave., White Plains, N.Y.

Transactions

of the

(First) Conference on Ferromagnetism & Antiferromagnetism

(5-11 March 1961, Leningrad)

(To be continued in Vol.25, No.12 & Vol.26, No.1)

SOME ASPECTS OF THE MODERN THEORY OF FERRO- AND ANTIFERROMAGNETISM
(Condensation of a Review)

- S.V.Vonsovskii

Of outstanding importance in any consideration of present-day theory of substances with atomic magnetic order are a) genesis of the magnetic order and the criteria determining its different forms - ferro- and antiferromagnetism, and b) model and phenomenological treatments of ferro- and antiferromagnetic materials from the standpoint of quantum theory.

Ferromagnetism and antiferromagnetism are distinctive forms of spin (and possibly orbital) paramagnetism with a certain spatially ordered distribution of electronic magnetic moments. The "suppliers" of these moments are atoms (ions) with unfilled inner (d or f) electron shells which, in accord with Hund's rule, at the same time have uncompensated magnetic moments.

For the most part these are atoms of the transition elements (d metals: elements of the iron group, palladium and platinum, and f metals: the rare earths and actinides). Two opposed tendencies operate in crystals: one hampers realization of atomic magnetic order (Fermi energy), the second favors magnetic order (ex-change interaction). Owing to the appreciable difference between the effective radii of the incomplete d and f layers, an entirely different situation obtains in d as compared with f metals.

In d metals, the d electrons are collectivized, and only in some of the iron group metals is there realized magnetic order (Fe, Co and Ni - ferromagnetism; Cr and Mn - antiferromagnetism). In Sc, Ti and V and in metals of the palladium and platinum group we encounter Pauli paramagnetism. In f metals, the f layers retain their atomic localization but, owing to their small radii, cannot interact with each other to any significant extent. Hence the atomic magnetic order is determined by their indirect or so-called superexchange interaction through the conduction electrons.

At present one can tentatively distinguish four different types of ferro- and antiferromagnetic substances:

1) ferro- and antiferromagnetic metals and metal alloys of the d type with collectivized d and s electrons;

2) ferro- and antiferromagnetic metals of the f type with localized f layers and superexchange interaction via the conduction electrons;

3) ferro- and antiferromagnetic greatly dilute solutions of d metal ions in diamagnetic metals with superexchange interaction via the conduction electrons;

4) nonmetallic ferromagnetic and antiferromagnetic compounds in which at least one of the components among the d or f metals present participates in indirect interaction of the Kramers type.

(In the report there are also considered the electronic properties of different types of crystals with atomic magnetic order. There are discussed and evaluated different models of collectivized electrons (Frenkel-Block-Stoner) and localized spins. Finally there are indicated the possibilities of more rigorous treatments making use of the new quantum-statistical methods - Green's functions, etc.).

**Institute of the Physics of Metals,
Academy of Sciences of the USSR**

NON-COLLINEAR FERRO- AND ANTIFERROMAGNETISM

- E.A.Turov

The purpose of this paper is to formulate certain general conditions by means of which, knowing the specific crystallographic structure of the magnetic material, one can single out, from among the various possible antiferromagnetic spin configurations, the particular configurations that allow of realization of weak (non-collinear) ferromagnetism of relativistic origin.[1]

(There is omitted here the review part of the report, devoted to methods of calculating spin configurations.)

1. Let us consider a system of spins located at crystallographically equivalent lattice sites, (i.e., at points that transform into each other by the usual operations of space group symmetry). We assume that the exchange forces acting between these spins are such that in themselves they lead to collinear antiferromagnetic structure.

For complete description of the ordered spin system one must take into consideration, in general, as many magnetic sublattices as there are spins contained in a magnetic unit cell of the crystal. If, however, we are interested in the properties of the antiferromagnet only as regards weak external influences, the energy of which is low compared with the exchange energy responsible for the spin ordering, these properties in the case of collinear (or weakly non-collinear) configuration of the spin system under consideration can always be described by means of two magnetic sublattices.* We must attribute all sites with the same direction of spin to the same sublattice. Accordingly, the two sublattices may be characterized by two spin densities, such that

$$S_1^2(\mathbf{r}) = S_2^2(\mathbf{r}) = S_0^2 = \text{const.} \qquad (1)$$

2. Forces of magnetic (relativistic) origin can disturb the rigorous collinearity of the spins in an antiferromagnet.[2,3] Deflections of the spins from the collinear orientation, due to magnetic forces, are usually small, inasmuch as these forces are weak compared with exchange forces. Hence if the non-collinearity of the spins does not lead to the appearance of a nonzero magnetic moment, it will not have any substantial effect on the properties of the antiferromagnet and can therefore be neglected.[4] Below, however, we shall be concerned precisely with the case of appearance of a spontaneous magnetic moment connected with non-collinearity of the spins.

Inasmuch as we shall be concerned only with weakly non-collinear antiferromagnetic structures, for their description we again need consider only two magnetic sublattices with spin densities $S_1(\mathbf{r})$ and $S_2(\mathbf{r})$. We introduce the antiferro-

---

*From the physical standpoint this possibility is connected with the fact that in this case introduction of a larger number of sublattices can lead only to the appearance of optical modes of the spin system (in addition to the two acoustical modes, which are always present in the energy spectrum of an antiferromagnet). The energy slits for the optical spin vibrations are determined by exchange forces so that these vibrations cannot be excited by the above mentioned weak external influences (among which we include thermal motion at low temperatures). Hence as regards both static and dynamic properties the system behaves like a system consisting of two magnetic sublattices.

magnetism vector

$$\mathbf{l} = (\mathbf{S}_1 - \mathbf{S}_2)/2S_0, \tag{2}$$

which defines the direction of the antiferromagnetic ordering axis, and the ferromagnetism vector

$$\mathbf{m} = (\mathbf{S}_1 + \mathbf{S}_2)/2S_0, \tag{3}$$

which determines the relative total spin density. From condition (1) it follows that

$$m^2 + l^2 = 1 \quad \text{and} \quad (\mathbf{m} \cdot \mathbf{l}) = 0. \tag{4}$$

We note the following distinctive features of the transformation properties of the antiferromagnetism and ferromagnetism vectors. If the initial collinear antiferromagnetic structure (hereinafter referred to as simply "structure") is allowed by the symmetry of the crystal lattice, the corresponding vector l under all space group symmetry operations for the given lattice must transform only through itself. Here one must distinguish two cases. If some symmetry operation lead to exchange (permutation) of the spins within one and the same magnetic sublattice, then under it l transforms like an ordinary axial vector. If, on the other hand, the symmetry operation involves interchange of spins pertaining to different magnetic sublattices (which corresponds to permutation of the indices 1 and 2 in the right hand part of (2)), then with regard to such an operation the vector l must undergo (in addition to the axial vector transformation) a change of sign. In the first case we shall characterize the structure as even, in the second case as odd with respect to the symmetry operation.

In contrast to l, the vector m is invariant under any exchange of spins, hence it always transforms like an ordinary axial vector.

The appearance of $\mathbf{m} \neq 0$ in an antiferromagnetic crystal is connected with the presence in its spin Hamiltonian of terms of the form

$$l_\alpha m_\beta \, (\alpha, \beta = x, y, z)$$

or terms of higher order in l and linear in m. These terms must be invariant under all symmetry operations. From this requirement, taking into account the above mentioned properties of l and m, one can obtain the following results.

3. Weak ferromagnetism (WFM) is possible only in structures which are even with respect to all translations of the lattice and also relative to the center of symmetry, if there is one in the lattice. From this it follows that

a) for structures allowing of WFM, the chemical and magnetic unit cells must coincide;

b) there must obtain alignment of the spins at all the sites pertaining to the same Bravais lattice and also at sites transforming into each other by means of a center of symmetry;

c) WFM is impossible when all the spins belong to one and the same Bravais lattice (or two Bravais lattices linked by a center of symmetry) and, in particular, when there is only one spin in a chemical unit cell.

4. One can construct the following table of invariants in the spin Hamiltonian, allowed by different symmetry elements and responsible for WFM in even (+) and odd (-) structures:

Symmetry elements	Parity of structure	Invariants*
$2_z, \sigma_z$	+	$m_x l_y,\ m_y l_x,\ m_z l_x l_y l_z$
	−	$m_x l_z,\ m_y l_z,\ m_z l_x,\ m_z l_y$
$3_z, \bar{3}_z$	+	$m_x l_y - m_y l_x,\ m_z(l_x \pm i l_y)^3$
	−	
$4_z, \bar{4}_z$	+	$m_x l_y - m_y l_x$
	−	$m_x l_y + m_y l_x,\ m_x l_x - m_y l_y,\ m_z l_x l_y l_z,$ $m_z (l_x^2 - l_y^2)\ l_z$
$6_z, \bar{6}_z$	+	$m_x l_y - m_y l_x$
	−	$m_z(l_x \pm i l_y)^3$

*Actual combinations are comprised of these complex invariants.

In this table n_z denotes the symmetry axis (simple or screw), and $\bar{n}_z$ is an inversion axis of the n-th order; σ_z is a symmetry plane (simple or glide). The invariants are given in the Cartesian system of coordinates, the z axis of which is parallel to the symmetry axis under consideration (or perpendicular to the symmetry plane). For each of the m components we have written only the lowest order invariants.

We call attention to the fact that if the spins are located on a simple symmetry axis or on a simple (mirror) symmetry plane, the structure is always even with respect to these symmetry elements.

By means of the above table (knowing the specific crystallographic structure of the magnetic material and taking into account the conditions formulated above in Section 3) one can readily find the structures allowing of WFM, and also the directions of the vector l for which $m \neq 0$. In doing so one must look in the table for each symmetry element of the crystal.* This will also give us the terms in the spin Hamiltonian, necessary for quantitative description of WFM.

5. We now consider a number of consequences following from the table.

A. Orthorhombic crystals. For realization of WFM in orthorhombic crystals the necessary and sufficient conditions are fulfillment of the requirement outlined in Section 3 above and the additional requirement (also with appropriate direction of the vector l - see below) that the structure be even only with respect to one of the independent symmetry elements (axis or plane). If such a symmetry element is 2_z (or σ_z), the terms of the Hamiltonian, responsible for the WFM, have the following general form**:

$$d_1 m_x l_y + d_2 m_y l_x + d_3 m_z l_x l_y l_z. \qquad (5)$$

---

*It is sufficient to consider only the independent symmetry operations, beginning with the symmetry axis of highest order.

**The corresponding terms for the cases when the symmetry element is 2_x (σ_x) or 2_y (σ_y) are obtained from (5) by cyclic permutation of x, y, z.

This means, in particular, that in orthorhombic crystals (except in the rare cases when all three components of l are nonzero) $m \neq 0$ only on condition that the vector l is perpendicular to the given symmetry axis (parallel to the symmetry plane).[5] We note also that if the spins lie at the intersection of two simple symmetry axes (planes), WFM in such a crystal is impossible.

Example 1: The D_{2h}^{16} group has 4-fold positions of three types (a, b and c - Ref.6). Positions of the a and b type (coinciding with the center of symmetry) permit WFM in each of three possible structures. The c position (located in the mirror plane σ_y) allows of WFM only in one of the structures, namely, in the structure in which the sites linked by the center of symmetry have parallel spins (i.e., in the structure that is even with respect to the center of symmetry). Positions of type b are occupied by magnetic ions of the iron group elements in rare earth orthoferrites.* The rare earth ions in these compounds, as well as the Mn ions in MnP and MnB, are located in positions of type c.[4,5,8]

Example 2: The D_{2h}^{17} group also has three 4-fold positions (a, b and c - Ref. 6). Two of these - a and b (for which the sites lie in the mirror plane σ_x) - allow of WFM, but in only one (of the three possible) structure, namely, in that which is odd with respect to the center of symmetry. For the third position - c - the sites lie at the intersection of two mirror planes (σ_x and σ_z), and, consequently, for it WFM cannot be realized. We note that the low temperature modification of $CoSO_4$, which was investigated by Borovik-Romanov & Kreines[9], has magnetic ions in positions b of the D_{2h}^{17} group, so that the transition from the antiferromagnetic to the weakly magnetic state (in a magnetic field), observed by these investigators, is a transition to the structure that is even with respect to the center of symmetry.

B. Uniaxial crystals. In all uniaxial crystals $m = 0$, when l is parallel to the principal symmetry axis. The invariant of second order yielding WFM in all cases, except for that of odd structure in a tetragonal crystal, is of the form[3,10]:

$$m_x l_y - m_y l_x = [\mathbf{m} \times \mathbf{l}]_z. \tag{6}$$

It can readily be shown that under the condition $\mathbf{m} \perp \mathbf{l}$ following from the second relation under (4), Eq.(6) does not depend on the direction of the vector l in the basal plane. This means that the magnitude of the spontaneous moment m in the given approximation will not depend on its direction in this plane. Among crystals of this type[3] are $MnCO_3$ and α-Fe_2O_3.

For odd structures in tetragonal crystals the following two invariants may be responsible for WFM in the basal plane:

$$m_x l_y + m_y l_x, \tag{7}$$
$$m_x l_x - m_y l_y. \tag{8}$$

For different crystals they may be present in the spin Hamiltonian either separately or both together.** These expressions do depend on the direction of l, as a result of which the magnitude of m also proves to be a function of the angle φ in the basal plane. The first invariant gives rise to a spontaneous

---

*Orthoferrites are compounds of the $MFeO_3$ type with a rhombically distorted perovskite structure. We note that in contrast to orthoferrites the compound $BiFeO_3$ with a rhombohedrally distorted perovskite structure (group D_{3d}^5)[7] should not exhibit WFM, inasmuch as in it the Fe ions occupy a 1-fold position.

**(See footnote on following page.)

moment varying according to the law $m = C_1 |\cos 2\varphi|$, while the second gives a spontaneous moment described by $m = C_2 |\sin 2\varphi|$, where C_1 and C_2 are constants. Nickel fluoride, NiF_2, furnishes an example of a tetragonal crystal in which WFM is described by an invariant of form (7).[3,10]

C. In the presence in a crystal of axes of the 3 or $\bar{3}$ type WFM is possible only in structures in which all the sites transforming into each other by means of these axes have parallel spins.

D. Cubic crystals. In cubic crystals WFM is impossible. We recall that we are dealing here with antiferromagnets in which the initial structure is collinear. If, nevertheless, there is observed WFM in a cubic crystal, this means that its structure has substantial non-collinearity (presumably of exchange character). An example of such a crystal is, apparently, furnished by UO_2.[11]

6. So far we have considered only WFM of the transverse type, inasmuch as it follows from condition (1) or (4) that m is perpendicular to l. There can, however, exist longitudinal WFM ($\mathbf{m} \parallel \mathbf{l}$) both by itself and in conjunction with transverse WFM.[12] Above we were unable to consider the existence of longitudinal WFM mainly because this would reduce the generality of the considerations; these were based on condition (1), which does not follow directly from the requirements of symmetry and which is essentially a model assumption. It is characteristic that in the thermodynamic theory of Dzyaloshinskii[3], in which no restrictions are imposed on the spins, WFM may be both transverse and longitudinal. In particular, the spontaneous moment m given by an invariant of the form (7) (for example, in an NiF_2 type crystal) in this case will be transverse when l is directed along the side of the basal square, and longitudinal when l is parallel to the diagonal of this square; here the magnitude of m, in contrast to the inference in Section 5 above, must be isotropic (in the approximation linear in l). Thus experimental investigation of the anisotropy of m in NiF_2 crystals would be of great interest and value from the standpoint of checking the basic model assumptions of the modern theory of ferro- and antiferromagnetism, among which is condition (1).

Among the obvious physical reasons for the existence of longitudinal WFM one can cite the following:

A. Nonequivalence of the magnetic sublattices. In this case even with fulfillment of condition (1) for the local spin densities the mean thermodynamic spin moments of the sublattices at $T \neq 0^\circ K$ can differ owing to different temperature dependences. Moreover, in this case with rigorous antiferromagnetic compensation of the magnetic spin moments of the sublattices there may appear a longitudinal magnetic moment due to differences between the effective magnetomechanical relations (g factors) of these sublattices.[2,12]

B. Anisotropy of the g factor. Even in the case of equivalent magnetic sublattices (i.e., in the case when the sublattice sites transform into each other by the symmetry operations for the space group under consideration) the tensor g may differ by rotation through a certain angle for sites pertaining to differ-

---

**(from previous page) We note that sometimes in one and the same tetragonal crystal, but for different types of antiferromagnetic ordering, WFM can be due to different invariants: of the form (6), (7) or (8). Thus, for example, for space group D_{4h}^5 when the magnetic ions occupy 8-fold positions i (Ref.6), there may exist three structures even with regard to the center of symmetry and permitting WFM (one even and two odd with respect to the 4_z axis). To each structure there corresponds a different invariant: (6), (7) or (8). The C_4^1 group (for position $2c$) is the simplest example allowing of existence of both invariants (7) and (8) for the same structure. It must be noted that invariants (7) and (8) are obtained from each other by simple 45° rotation of the system of coordinates about the z axis.

ent Bravais lattices.[10] In this case for a certain orientation of the vector l there may appear a longitudinal spontaneous magnetic moment (inasmuch as the g factor in this direction will be different for different Bravais lattices).

An analogous reason can lead to the appearance of a mechanical longitudinal moment due to anisotropy of the temperature dependence of the mean sublattice spin, owing to the fact that this anisotropy is "shifted in phase" for one sublattice relative to the other.

In conclusion it must be noted that the general requirement necessary for the existence of WFM in a system of equivalent spins, formulated in Section 3, is also applicable to the case of longitudinal WFM, inasmuch as in deduction of this condition perpendicularity of m and l was not utilized.

Institute of the Physics of Metals,
Academy of Sciences of the USSR

References

1. E.A.Turov, Compt.rend., 252, 3420 (1961).
2. A.S.Borovik-Romanov & M.P.Orlova, Zhur.eksp.i teor.fiz., 31, 579 (1956). (Trans.Soviet Physics - JETP.)
3. I.E.Dzyaloshinskii, Ibid., 32, 1547 (1957); 33, 1454 (1957). (Trans.Ibid.)
4. V.E.Naish & E.A.Turov, Fizika metallov i metallovedenie, 11, 161, 321 (1961). (Trans.Phys.of Metals & Metallography.)
5. E.A.Turov & V.E.Naish, Ibid., 9, 10 (1960). (Trans.Ibid.)
6. G.V.Bokii, Kristallokhimiya (Crystallochemistry), M., 1960.
7. A.I.Zaslavskii & A.G.Tutov, Doklady AN SSSR, 135, 815 (1960). (Trans. Doklady.)
8. N.G.Guseinov & E.A.Turov, Izv.AN Azerbaidzhan SSR, No.4, 85 (1960).
9. A.S.Borovik-Romanov & N.M.Kreines, Zhur.eksp.i teor.fiz., 33, 1119 (1957); 40, 762 (1961). (Trans.Soviet Physics - JETP.)
10. T.Moriya, Phys.Rev., 117, 635 (1960); Ibid., 120, 91 (1960).
11. Henstan & Brockhause, Bull.Amer.Phys.Soc., 2, 9 (1957).
12. E.A.Turov, Zhur.eksp.i teor.fiz., 36, 1254 (1959). (Trans.Sov.Phys. - JETP.)

INFLUENCE OF THE MAGNETIC SUBLATTICE STRUCTURE OF FERRITES ON THEIR PHYSICAL PROPERTIES

- K.P.Belov

1. By now it has been firmly established that ferrites have a magnetic sublattice structure. This has been demonstrated by magnetic experiments as well as by neutron diffraction studies. The presence of sublattices engenders various anomalies in the behavior of ferrites as compared with ordinary ferromagnets. The influence of sublattices is evinced particularly clearly in the case of ferrite compositions having a "compensation point" θ_c. The anomalous physical properties of ferrites consist not only in heteroclite behavior of the magnetic characteristics near θ_c, but also in unusual temperature dependence of the magnetic and nonmagnetic properties in the low temperature region. In the present paper we would like to call attention to these low temperature anomalies of the physical attributes of ferrites having a compensation point.

2. Fig.1 shows the results of measurements[1] of the magnetic and resonance characteristics of gadolinium ferrite with the garnet structure. It will be evident that near 100°K (i.e., 180° below θ_c) the paraprocess* (high field) susceptibility χ_p and normal (low field) susceptibility χ go through a maximum, while the coercive force H_c and width ΔH of the ferromagnetic resonance absorption curve pass through a minimum. Fig.2 shows the results obtained by Goryaga and Lin Chang-ta[2] for lithium ferrite-chromite. As may be seen, in the region of liquid nitrogen temperatures (i.e., 200° below θ_c) there occurs a break in the σ_s versus T curve, a dip of H_c and a peak of χ, as well as a break in the electric resistance curve (log R versus 1/T) and maxima in the curves of the longitudinal and transverse galvanomagnetic effects $(\Delta R/R)_{\parallel}$ and $(\Delta R/R)_{\perp}$ (both effects have a negative sign, owing to the influence of the paraprocess). The character of all these anomalies resembles that generally observed at the ferromagnetic Curie point. We also note that low temperature anomalies of physical properties are observed only in the lithium ferrite-chromite compositions (many different compositions were studied) that have a compensation point.

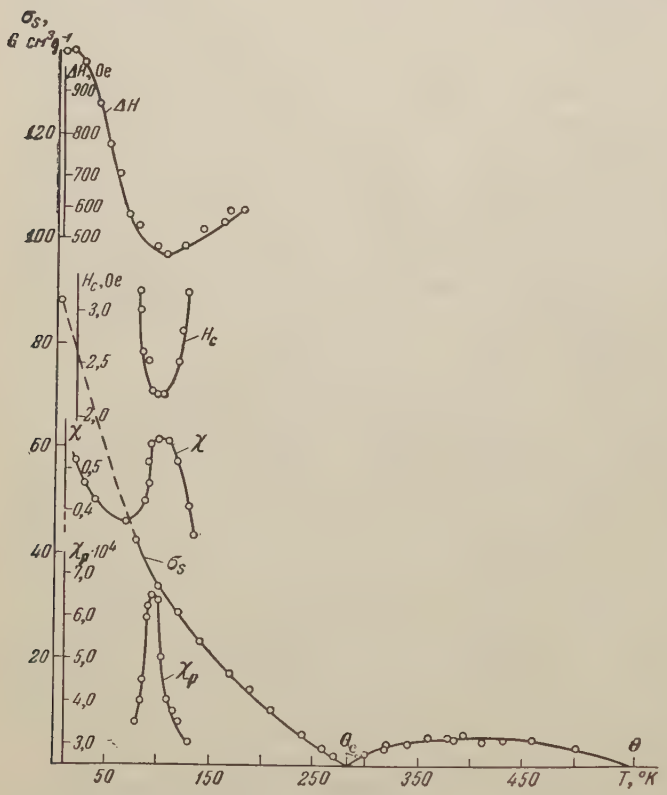

Fig.1. Temperature anomalies of the physical properties of gadolinium ferrite-garnet $3Gd_2O_3 \cdot 5Fe_2O_3$ in the low temperature region: σ_s - spontaneous magnetization, χ_p - paraprocess (high-field) susceptibility, χ - magnetic susceptibility in weak fields, H_c - coercive force, ΔH - width of the ferromagnetic resonance absorption peak.

3. In order to gain a better understanding of the causes responsible for these anomalies, let us analyze the temperature variation of

*Paraprocess = change in the absolute value of the magnetization due to realignment of the spin magnetic moments.

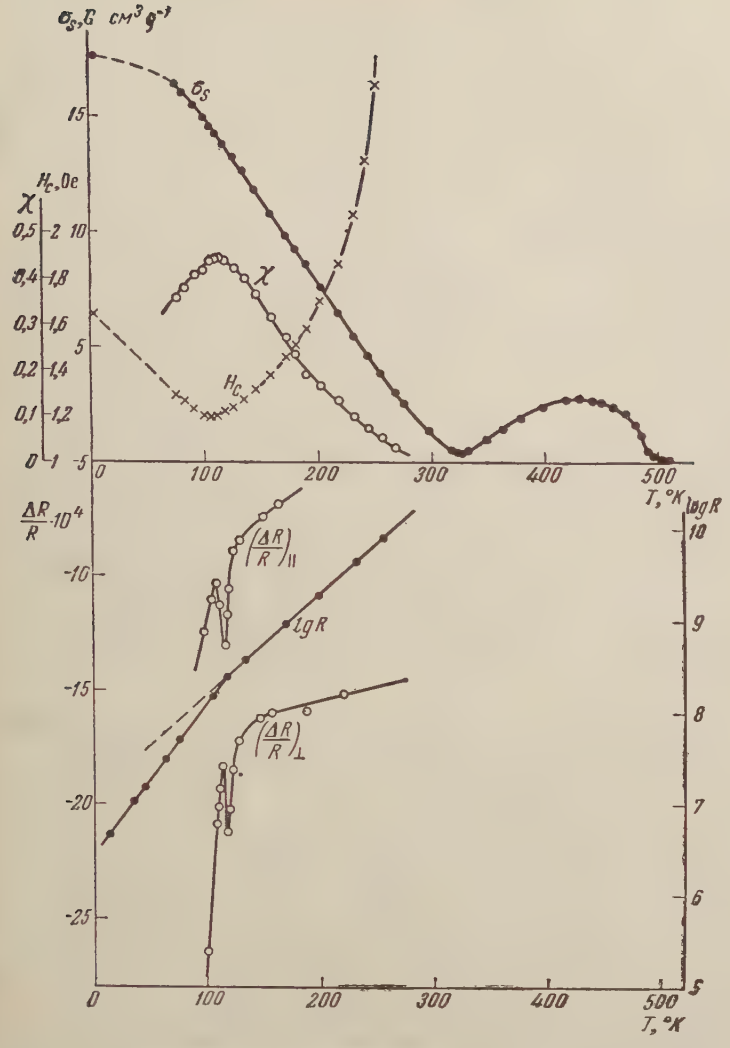

Fig.2. Temperature anomalies of the physical properties of lithium ferrite-chromite ($Li_2O \cdot 2.5Fe_2O_3 \cdot 2.5Cr_2O_3$) in the low temperature region: $(\Delta R/R)_{\parallel}$ and $(\Delta R/R)_{\perp}$ are the longitudinal and transverse galvanomagnetic effects, respectively.

the spontaneous magnetization in ferrites possessing a compensation point. For example, consider gadolinium ferrite-garnet $\{Gd_3^{3+}\}(Fe_3^{3+})[Fe_2^{3+}]O_{12}$. As is known, this ferrite has a triple sublattice structure. The Gd^{3+} ions form a dodecahedral sublattice (with eightfold coordination - braces), while the Fe^{3+} ions form a tetrahedral (parentheses) and an octahedral (brackets) sublattice. In view of the strong exchange interaction of the Fe ions, at low temperatures the two last-mentioned sublattices can be regarded as a single sublattice. In what follows, therefore, we shall speak of the gadolinium ferrite as consisting of two sublattices: a "gadolinium" sublattice and an "iron" sublattice. We now turn to a discussion of the temperature variation of σ_s for the iron sublattice. To do this, we must "exclude" the action of the gadolinium sublattice by replacing the Gd^{3+} ions by some nonmagnetic ions, for example, Y^{3+} or Lu^{3+}, Yttrium ferrite-garnet (Y-Fe garnet) is such a ferrite; the temperature dependence of σ_s for it is given by curve 1 in Fig.3. It will be evident that the iron sublattice has the normal Weiss temperature dependence of σ_s; at the same time its Curie point is rather high, which attests to strong exchange interaction between the Fe^{3+} ions. Knowing the shape of σ_s versus T curve for the iron sublattice, we can approximate the temperature dependence of σ_s for the gadolinium sublattice by simple addition of the ordinates of the gadolinium ferrite and yttrium ferrite curves (Fig.3, curves 3 and 1, respectively). The dash curve (2) represents the approximate temperature variation of σ_s for the gadolinium sublattice. It will be evident that this temperature dependence is extremely smeared out; it is even difficult to determine the location of the Curie point on this curve (the entire curve has the character of a "tail"). This smearing out cannot be explained by the effect of fluctuation of the ion concentration in the sublattice, as is often the case in ferromagnetic alloys, inasmuch as it is known that in iron-garnets the ions are distributed in the lattice in an ordered manner. The reason for this smearing out is that establishment of long-range magnetic order in the gadolinium sublattice depends not

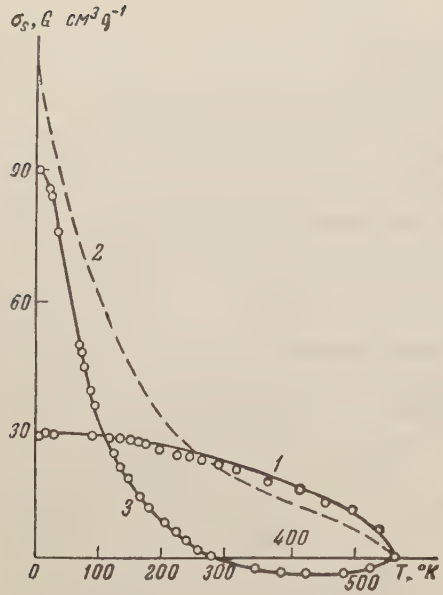

Fig.3. Temperature dependence of spontaneous magnetization: 1) "iron" sublattice (yttrium ferrite-garnet), 2) "gadolinium" sublattice, 3) gadolinium ferrite-garnet.

only on the intrinsic positive exchange interaction between the Gd^{3+} ions but also on the negative exchange interaction between the Gd^{3+} and Fe^{3+} ions. It is clear that the weaker the positive interaction within the gadolinium sublattice, the greater will be the effect on Gd^{3+} of negative exchange interaction from the iron sublattice. There is little positive interaction in the Gd sublattice. Hence at low temperatures the effect of this interaction becomes negligible with the result that there occurs a marked change in the long-range magnetic order in the Gd sublattice. At higher temperatures, the long-range order persists in part owing to the effect of the negative interaction, which, as it were, inhibits definitive breakdown of long-range order. The negative interaction between the iron and gadolinium sublattices is far stronger, as is borne out by the high value of θ_c (without this interaction the appearance of θ_c would be impossible). In our opinion, this is the explanation for the smearing out of the σ_s versus T curve for the Gd sublattice.

The anomalies in the temperature dependences of the physical properties near 100°K that are observed for gadolinium ferrites correspond exactly to the temperature of "exclusion" of the effect of the weak positive interaction in the gadolinium sublattice. This temperature can be regarded as a sort of "Curie point" peculiar to the gadolinium sublattice, which explains why the anomalies of its physical properties are similar to those observed at the Curie point of ordinary ferromagnets. Strictly speaking, from the standpoint of the thermodynamic theory of second order phase transitions this temperature cannot be regarded as a magnetic phase transition point, inasmuch as the gadolinium sublattice is located in the intense "magnetizing" field of the iron sublattice (in order to emphasize this difference we have put "Curie point" in quotation marks).

Analysis of the temperature dependence of σ_s for lithium ferrite-chromites possessing a compensation point leads to the same result. Here the "weak" sublattice (in which the Cr^{3+} and Fe^{3+} ions are distributed) is octahedral and its σ_s versus T curve is smeared out, while the "strong" sublattice (which contains only Fe^{3+} ions) is tetrahedral and has a Weiss type σ_s versus T curve.

4. The above concepts also help to explain the "mechanism" of appearance of a compensation point in ferrites. The condition for the appearance of θ_c is the presence of a sublattice that has a large magnetic moment (at 0°K) and weak exchange interaction, i.e., a smeared out σ_s versus T curve (curve 2, Fig.4,a), while the sublattice with the smaller magnetic moment has strong exchange interaction, i.e., a Weiss type σ_s versus T curve (curve 1, Fig.4,a). Under this condition there exists a high probability of appearance of θ_c even at low temperatures, which is precisely what one observes experimentally. According to the Néel phenomenological theory[3], in which only sublattices that have Weiss type σ_s versus T curves are considered, the θ_c point can only appear near θ (see Fig.4,c);

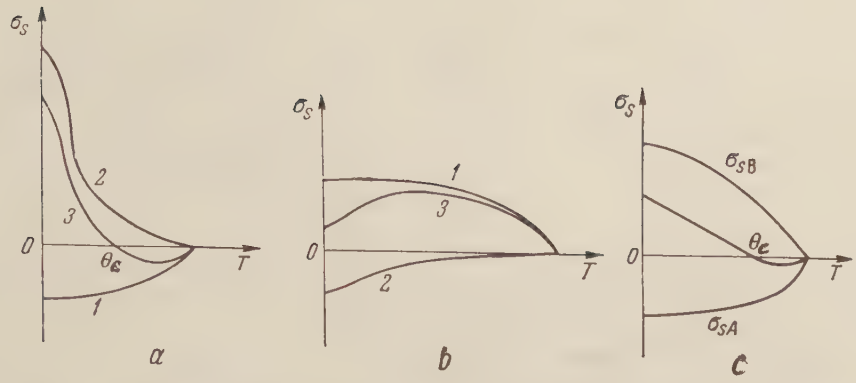

Fig.4. Diagram pertaining to the discussion concerning the appearance of a compensation point.

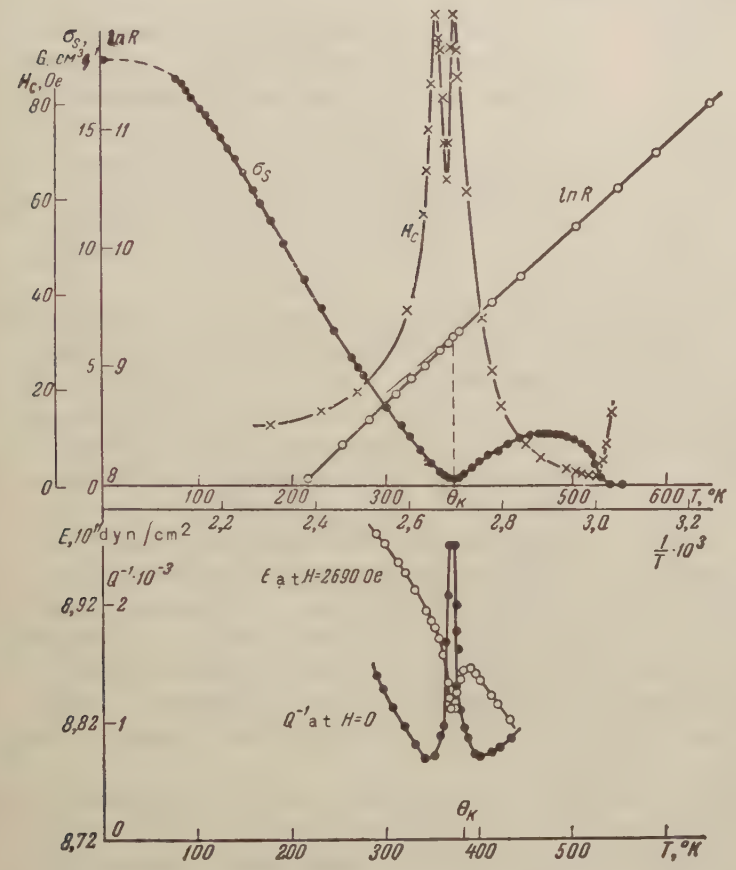

←Fig.5. Temperature anomalies of the physical properties of lithium ferrite-chromite in the region of θ_c (E - modulus of elasticity; Q^{-1} - internal friction).

there is scant probability for θ_c appearing at low temperatures.*

5. If the "weak" sublattice has a lower magnetic moment at 0°K than the "strong" one, there appears an anomalous temperature dependence of σ_s (in Néel's classification, type M; see Fig.4,b). In the particular case when the magnetic moments of both sublattices are equal, we may get a σ_s versus T curve that "issues" from the origin, i.e., θ_c lies at or near 0°K. In this case it is difficult to determine the "Curie point" of the "weak" sublattice inasmuch as ferrimagnetic magnetization in such a ferrite is determined mainly by the "strong" sublattice. The "weak" sublat-

---

*Nor does Néel's theory enable us to explain the appearance of low temperature anomalies of the physical properties of lithium ferrite-chromites, because in his theory it is assumed that the exchange interaction both within the sublattices (AA and BB) and between the sublattices (AB) are negative. If, however, we assume that in at least one of the sublattices there exists positive interaction (as we do in the present article), the appearance of low temperature anomalies in lithium ferrite-chromites having a compensation point becomes understandable.

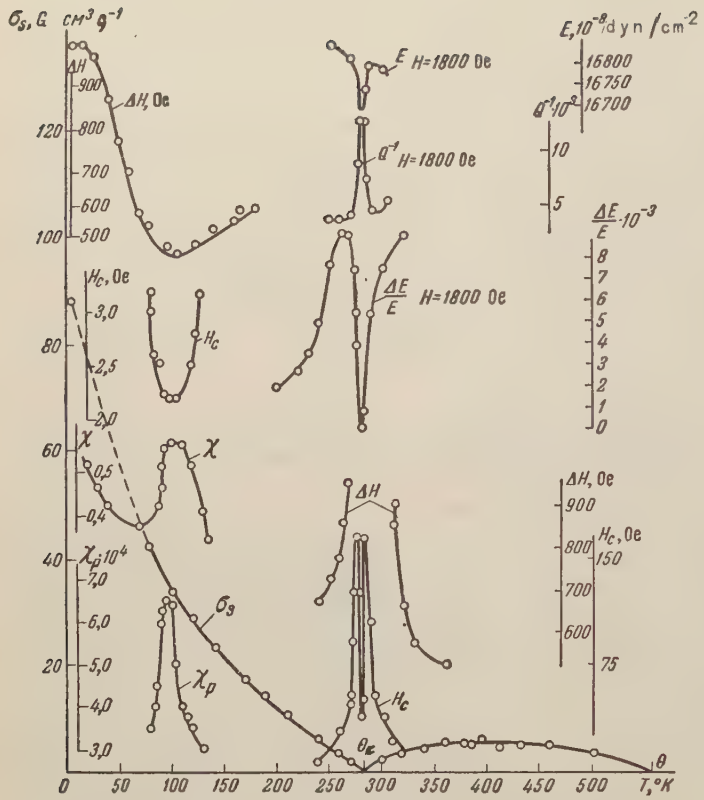

Fig.6. Temperature anomalies of the physical properties of gadolinium ferrite-garnet at low temperatures and in the region of θ_c ($\Delta E/E$ - relative change of E in a magnetic field: the "ΔE effect").

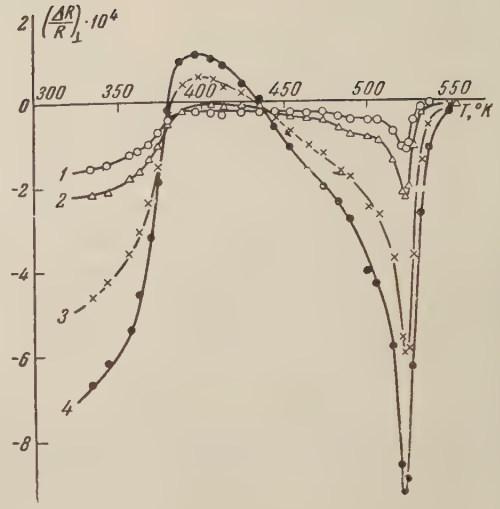

Fig.7. Temperature dependence of the longitudinal $(\Delta R/R)_\parallel$ and transverse $(\Delta R/R)_\perp$ galvanomagnetic effects in lithium ferrite-chromite ($Li_2O \cdot 2.7Fe_2O_3 \cdot 2.3Cr_2O_3$), recorded in different magnetic fields: 1) 1083 Oe, 2) 2260 Or, 3) 6800 Oe, 4) 11 070 Oe.

tice has little effect on the shape of the σ_s versus T curve for the ferrite.

6. Owing to the difference between the exchange (and, obviously, magnetic) interactions in the sublattices, the physical properties of ferrites below and above θ_c must differ in character. This applies to all properties: magnetic, resonance, electric, galvanomagnetic, magnetoelastic, etc. Near the compensation point, where the sublattices, so to speak, exchange roles, there are observed marked anomalies of all the enumerated characteristics (Figs. 5 & 6). The behavior of the indicated characteristics does not resemble that which is observed at the ferromagnetic or antiferromagnetic Curie points; therefore, θ_c should not be regarded as the temperature of a second order phase transition.

7. Finally, we would like to call attention to the behavior of the magnetization curves of and even effects in ferrites with θ_c in high fields. By virtue of the fact that these ferrites have a sublattice with "weak" exchange interaction, at low temperatures there are observed a strong paraprocess (especially near the low temperature "Curie point") and the usual associated effects: volume magnetostriction, high-field galvanomagnetic effects, etc.

In the region of temperatures above θ_c, inasmuch as the "weak" sublattice is magnetized antiparallel to the "strong" sublattice, a strong magnetic field can lead to the effect of spin "flip out" from the "weak" sublattice, with the result that the magnetization curves will not evince saturation.

Fig.7 shows the temperature dependences of the longitudinal and transverse galvanomagnetic effects in lithium ferrite-chromite, measured[4] in strong fields. Whereas below θ_c and near θ these effects are due to the paraprocess (both effects are negative and equal), above θ_c (but close to it) both effects are positive, which is unusual for ferromagnets. We ascribe the appearance of this anomaly to the effect of spin "flip out". A longitudinal and a transverse field will rotate the spin in the same direction (decrease the angle between the spin and the field), which accounts for the appearance of longitudinal and transverse galvanometric effects of the same (positive) sign.

We note that the spin "flip out" effect can also be observed in ferromagnets that do not have θ_c but do have a "weak" sublattice (curve 3, Fig.4,b). L.A. Malevskaya in our laboratory detected this phenomenon in $2.7Yt_2O_3 \cdot 0.3Tb_2O_3 \cdot 5Fe_2O_3$ in the process of recording magnetization curves. Saturation was not observed on these curves even at very low temperatures, although the magnetic anisotropy constant was approximately the same as in $3Yt_2O_3 \cdot 5Fe_2O_3$ ferrite.

Thus, in order to understand the physical properties of ferrites, it is important to take into account not only the magnitudes of the magnetic moments of the sublattices but also the character and strength of the exchange interactions in and between the sublattices.

Moscow State University

References

1. A.V.Ped'ko, Zhur.eksp.i teor.fiz., 41, 700 (1961). (Trans.Soviet Physics - JETP.)
2. A.N.Goryaga & Lin Chang-ta, Ibid., 41, 696 (1961). (Trans.Ibid.)
3. L.Néel, Ann.Phys., 3, 137 (1948).
4. K.P.Belov, A.N.Goryaga & Lin Chang-ta, Zhur.eksp.i teor.fiz., 38, 1941 (1961). (Trans.Soviet Physics - JETP.)

REGARDING THE NORMAL ENERGY STATE OF FERRITE WITH THREE MAGNETIC SUBLATTICES

- A.A.Gusev & A.S.Pakhomov

1. Consistent quantum mechanical treatment of the magnetic properties of ferromagnets provides the basis for extending to such systems the phenomenological method of molecular fields.[1,2] The advantage of the microscopic treatment is that it allows of immediate introduction of the atomic characteristics of the system and enhances the possibilities of analysis and explanation of the behavior of specific substances as well as the prediction of new effects.

Quantum mechanical treatments of the ferrite model with two sublattices have already been published by a number of authors.[1-4] In particular, Tyablikov[3] investigated the general ferrite model near absolute zero by the method of approximate secondary quantization; then this treatment was extended[2] to finite temperatures by the variational method. In the present paper, proceeding by analogy with the work of Ref.2, we consider the general case of a ferrite model with three sublattices, with a view to applying the results to interpretation of the properties of rare earth ferrites with the garnet structure. In this first stage of the investigation we consider the normal energy states corresponding to stable configurations of the magnetic moment at absolute zero with different assumptions regarding the signs of the exchange integrals. We also touch on the question of the dependence of the magnetization on the intensity of the external field. For the sake of simplifying the calculations and convenience in comparing the theoretical results with experimental data for garnets, in addition to the assumptions inherent in the given model, we make only the assumption that the exchange interactions of one of the sublattices (the rare earth sublattice) with the other two (iron) are approximately equal and appreciably weaker than the exchange interaction between the two iron sublattices.

This assumption, however, is physically resonable, inasmuch as experiment shows that all rare earth garnets have approximately the same Curie point.

2. The investigated system - a magnetic single crystal - may be regarded as a conjunction of three sublattices, one inserted into the other, at the sites of each of which there are located magnetic ions of one type with given spins (s_1, s_2, s_3) and magnetic moments (μ_1, μ_2, μ_3). The numbers of magnetic ions in the sublattices equal N_1, N_2 and N_3, respectively. Each of the sublattices is ferromagnetic, i.e., the exchange integrals $J_{11}, J_{22}, J_{33} > 0$.

The exchange interaction between the sublattice can, in general, be either ferromagnetic (positive) or antiferromagnetic (negative).

The Hamiltonian of the system can be written in the form

$$\hat{H} = -\frac{1}{2}\sum_{\substack{i=1\\ f_1, f_2}}^{3} I(f_1^{(i)}, f_2^{(i)})(\hat{\mathrm{S}}_{f_1^{(i)}}\hat{\mathrm{S}}_{f_2^{(i)}}) - \sum_{\substack{i\neq j;\, i,\, j=1\\ f,g}}^{3} I(f^{(i)}, g^{(j)})(\hat{\mathrm{S}}_{f^{(i)}}\mathrm{S}_{g^{(j)}}) - \sum_{\substack{k=1\\ f^{(k)}}}^{3}\mu_k(\mathrm{H}\hat{\mathrm{S}}_{f^{(k)}}). \qquad (1)$$

Transformation of (1) to Bose operators[2] allows of separating out the energy of the ground state:

$$E = -\frac{1}{2}\sum_{\substack{i=1\\ f_1, f_2}}^{3} I(f_1^{(i)}, f_2^{(i)})(\vec{\sigma}_{f_1^{(i)}}\vec{\sigma}_{f_2^{(i)}}) - \sum_{\substack{i\neq j;\, i,\, j=1\\ f,\,g}}^{3} I(f^{(i)}, g^{(j)})(\vec{\sigma}_{f^{(i)}}\vec{\sigma}_{g^{(j)}}) - \sum_{\substack{k=1\\ f^{(k)}}}^{3}\mu_k(\mathrm{H}\vec{\sigma}_{f^{(k)}}), \qquad (2)$$

which, as can readily be shown, can be written out on the basis of (1) by formal replacement of the $S_{f^{(i)}}$ operators by classical vectors $\sigma_{f^{(i)}}$. Introducing the sums over the lattice

$$J_{ii} = \sum_{f_2^{(i)}} I(f_1^{(i)}, f_2^{(i)});\ J_{ij} = \sum_{f_2^{(j)}} I(f_1^{(i)}, f_2^{(j)});\ J_{ji} = \sum_{f_1^{(i)}} I(f_1^{(i)}, f_2^{(j)}), \qquad (3)$$

invoking the relations

$$N_1 J_{12} = N_2 J_{21} = K_{12}, \quad N_2 J_{23} = N_3 J_{32} = K_{23}, \quad N_3 J_{31} = N_1 J_{13} = K_{31}, \tag{4}$$

and assuming that in each of the sublattices the spins are approximately parallel and, therefore, that the classical vectors $\vec{\sigma}_{f(i)}$ do not depend on the site index f, i.e., assuming that $\vec{\sigma}_{f(i)} = \vec{\sigma}_i$, we can introduce the partial magnetizations

$$\mathbf{M}_i = \mu_i N_i \vec{\sigma}_i \quad (i = 1, 2, 3) \tag{5}$$

and rewrite (2) in the form

$$E = -E_0 - \sum_{\substack{i>j \\ i,\, j=1}}^{3} k_{ij} (\mathbf{M}_i \mathbf{M}_j) - \sum_{i=1}^{3} (\mathbf{H}\mathbf{M}_i), \tag{6}$$

where

$$E_0 = \frac{1}{2} \sum_{i=1}^{3} N_i J_{ii} \sigma_i^2, \quad k_{ij} = \frac{K_{ij}}{\mu_i \mu_j N_i N_j}. \tag{7}$$

According to (4), the constants K_{ij} are symmetrical as regards commutation of their indices; the same thing obviously is valid for k_{ij}, i.e., $k_{ij} = k_{ji}$.

On the basis of Eq.(1) and utilizing the Bogolyubov variational theorem, we can, by a procedure analogous to that employed in Ref.1, write equations describing the temperature dependence of the magnetization. We note that these equations allow of considering the question of compensation points, the behavior of the magnetization in the region of the Curie point and in the paramagnetic region. However, these questions will be examined in another paper.

According to (6), the ground state energy of the system is a function of the spatial arrangements of the vectors $\mathbf{M}_i$. The external magnetic field H can be regarded as a parameter $(0 < H < \infty)$. The behavior of E is determined by the microscopic characteristics of the system: the exchange interaction, the k_{ij}, the values of the atomic constants μ_i and σ_i, and the cation distribution N_i.

3. For determining the equilibrium configurations of $\mathbf{M}_i$ we make use of Lagrange's method of multipliers. The lengths of the spin vectors are fixed:

$$\sum_{\alpha=1}^{3} (M_i^\alpha)^2 = M_{i0}^2 = \text{const}_i \quad (i = 1, 2, 3). \tag{8}$$

The energy (6) must be investigated taking into account Eq.(8), i.e., extremum conditions of the form

$$F = E - \frac{1}{2} \sum_{i=1}^{3} \lambda_i M_i^2. \tag{9}$$

Writing the total differential of F, setting $dF = 0$ and equating the coefficients at the $d\mathbf{M}_i$ to zero, we obtain

$$\begin{aligned} \lambda_1 \mathbf{M}_1 + k_{12}\mathbf{M}_2 + k_{13}\mathbf{M}_3 &= -\mathbf{H}, \\ k_{21}\mathbf{M}_1 + \lambda_2 \mathbf{M}_2 + k_{23}\mathbf{M}_3 &= -\mathbf{H}, \\ k_{31}\mathbf{M}_1 + k_{32}\mathbf{M}_2 + \lambda_3 \mathbf{M}_3 &= -\mathbf{H}. \end{aligned} \tag{10}$$

Eqs.(10) together with conditions (8) form a complete system for determining the M_i^α and λ_i, corresponding to the extremum given by (9).

Carrying out vector multiplication of each of Eqs.(10) by the corresponding $\mathbf{M}_i$ and adding, we obtain

$$\sum_{i=1}^{3}\left(\mathbf{M}_i\times\mathbf{H}\right)=0. \tag{11}$$

For $H\neq 0$ the condition characterized by (11) will obtain provided

$$\sum_{i=1}^{3}\mathbf{M}_i=0 \tag{12}$$

or

$$\left(\sum_{i=1}^{3}\mathbf{M}_i\right)\parallel\mathbf{H}. \tag{13}$$

The results (11)-(13) are, obviously, general properties of our postulated model, which should be borne in mind in solving the set (10) in different specific cases. Incidentally, without imposing any restrictions, it may be assumed that the field H is in the direction of the z axis.

Regarding Eq.(12) we note that this case corresponds to a closed "triangular" configuration of the magnetic moments with the resultant magnetization equal to zero, a case which we will not consider here.

4. The matrices of the cofficients of the set (10) are

$$K=\begin{pmatrix}\lambda_1 & k_{12} & k_{13}\\ k_{21} & \lambda_2 & k_{23}\\ k_{31} & k_{32} & \lambda_3\end{pmatrix}, \tag{14}$$

$$K'=\begin{pmatrix}\lambda_1 & k_{12} & k_{13}-1\\ k_{21} & \lambda_2 & k_{23}-1\\ k_{31} & k_{32} & \lambda_3-1\end{pmatrix} \tag{15}$$

We denote the determinant of matrix K by $\Delta_3=\mathrm{Det}\,K$ and the determinants of the adjoint matrix K' through $\Delta_3^{(i)}$. Accordingly, we shall use $\Delta_2^{(i)}$ for denoting the determinants of the square second order matrices that can be constructed from K'

Depending on the characteristics of the ions, the values of the J_{ij}, the relations between them and the geometric structure of the crystal, i.e., type of lattice, the determinant Δ_3 may or may not vanish. Let us consider the case when it does not vanish.

Solution of the set (10) yields

$$\mathbf{M}_i=\frac{\Delta_3^{(i)}}{\Delta_3}\mathbf{H}. \tag{16}$$

Consequently, all the $\mathbf{M}_i$ are parallel to the field H; hence in view of conditions (8) we obtain

$$M_i^x=M_i^y=0,\quad M_i^z=\pm M_{i0}\quad (i=1,2,3), \tag{17}$$

i.e., eight solutions (for all possible combinations of signs). Among these we must choose those that actually correspond to extremum values of E. This is achieved by successive insertion of each solution α into (6) and comparison of the E_α with each other.

The Lagrangian multipliers λ_i will, obviously, depend on k_{ij}, M_{i0} and H. Their explicit form can be determined from the set of equations

$$\Delta_3 M_{i0}-\Delta_3^{(i)}H=0\quad (i=1,2,3),$$

however, we will not solve them here inasmuch as in our case we do not require the λ_i in explicit form.

Let us now consider the three physically most natural cases of distribution of the signs of the exchange integrals J_{ij}, which determine the character of the interaction between the ions of different sublattices, namely,

$$\left.\begin{array}{l} \text{A. } J_{12},\ J_{13}<0,\quad J_{23}>0, \\ \text{B. } J_{12},\ J_{23}<0,\quad J_{31}>0, \\ \text{C. } J_{12},\ J_{23},\ J_{31}<0. \end{array}\right\} \tag{18}$$

Carrying out the above level selection operation for each of these cases on the assumption that $|k_{12}|>|k_{13}|, |k_{23}|$, we obtain the following minimum energies (for not excessively strong magnetic fields):

$$E_{\mathrm{I}}^{\mathrm{A}} = -E_0 - k_{12}M_{10}M_{20} - k_{13}M_{10}M_{30} - k_{23}M_{20}M_{30} - (-M_{10}+M_{20}+M_{30})H, \tag{19}$$

$$E_{\mathrm{I}}^{\mathrm{B}} = -E_0 - k_{12}M_{10}M_{20} - k_{13}M_{10}M_{30} - k_{23}M_{20}M_{30} - (M_{10}-M_{20}+M_{30})H, \tag{20}$$

$$E_{\mathrm{I}}^{\mathrm{C}} = -E_0 - k_{12}M_{10}M_{20} - k_{13}M_{10}M_{30} + k_{23}M_{20}M_{30} - (-M_{10}+M_{20}+M_{30})H. \tag{21}$$

The M_i configuration corresponding to $E_{\mathrm{I}}^{\mathrm{A}}$ and $E_{\mathrm{I}}^{\mathrm{C}}$ is shown in the figure (a); we note, however, that in general $E_{\mathrm{I}}^{\mathrm{A}}<E_{\mathrm{I}}^{\mathrm{C}}$. The resultant magnetization in these two cases (A and C) equals

$$M_{res} = -M_{10}+M_{20}+M_{30}, \tag{22}$$

and in the case B (figure b)

$$M_{res} = M_{10}-M_{20}+M_{30}. \tag{23}$$

In superstrong fields, capable of overcoming the spin forces, there will be realized a different extremum solution (solution II), corresponding to a maximum value of the energy. It will correspond to the configuration in which all the M_i are aligned with the field H; this configuration (figure c) will be common for all cases: A, B and C. The energy levels in this case, obviously, will be different. Thus the energy for case C will be

$$E_{\mathrm{II}}^{\mathrm{C}} = -E_0 + k_{12}M_{10}M_{20} + k_{13}M_{10}M_{30} + k_{23}M_{20}M_{30} - (M_{10}+M_{20}+M_{30})H. \tag{24}$$

It may be of interest to compare the deduced expressions for the magnetization with the available data for rare earth ferrites with the garnet structure.

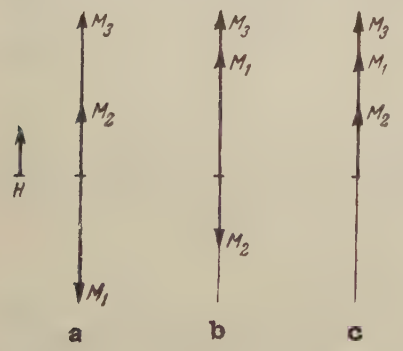

It can readily be seen that Eq.(22), which was obtained as a result of successive solution of the problem of the stable, minimum energy arrangement of the magnetization vectors of the sublattices of the system, agrees with Néel's empirical formula for garnets, (see, for example, Ref.7):

$$M_{res} = 6M_c - (6M_d - 4M_a). \tag{25}$$

The similarity between Eqs.(25) and (22) becomes obvious if we set $M_{10}=6M_d$ (rare earth sublattice), $M_{30}=6M_c$ (tetrahedral Fe^{3+} lattice), and $M_{20}=4M_a$ (octahedral Fe^{3+} sublattice). Equation (25), as is known, is in agreement with the experimental results for gadolinium and yttrium garnets.

Inasmuch as the configuration given by (22) is realized both in the case when all the exchange interactions between the sublattices are assumed to be negative

(case C) and in the case when it is assumed that one exchange interaction (namely, J_{23}) is positive, these circumstances should be borne in mind in interpreting experimental data and carrying out experimental tests of the theory.

Equation (25) proved to be inapplicable to other (other than Gd and Yt) rare earth garnets. For example, in the case of dysprosium garnet Eq.(25) yields $M_{theo} \approx 10\mu_B$, whereas the experimental value $M_{exp} = 32{,}5\ \mu_B$; for holmium garnet the divergence is even greater: ($M_{theo} \approx 5\mu_B$, $M_{exp} = 27{,}5\ \mu_B$). If, however, we assume that for these garnets there is realized the case B configuration given by Eq.(23), we obtain appreciably better agreement: for Dy garnet $M_{theo} \approx 30\ \mu_B$, and for Ho garnet $M_{theo} \approx 25\ \mu_B$. In this connection there may arise the question of the mechanism of appearance of a compensation point. Although here we are not considering temperature dependences, we may note that this difficulty can be overcome if it is assumed that collinearity does not persist with increasing temperature or that the magnetization of the Fe^{3+} sublattices is characterized by its own compensation point.

5. Obviously, the linear configuration (solution I) in a very strong external magnetic field will be disarrayed even at absolute zero, so that in final analysis, as was noted above, in all cases we obtain solution II, i.e., orientation of all the M_i along the field ("absolute" saturation). It is found that the region intermediate between solutions I and II is also described by Eqs.(10) in the so far unexamined case when $\Delta_3 = 0$ (solution III). To be specific, let us consider the case C (all the $J_{ij} < 0$).

So that for $\Delta_3 = 0$ the equations of set (10) will be compatible there must be fulfilled the conditions $\Delta_3^{(i)} = 0$ $(i = 1, 2, 3)$. This gives us the following set of equations for the Lagrangian multipliers:

$$\left.\begin{aligned} \Delta_3^{(1)} &= \lambda_1\lambda_2 + k_{23}\lambda_1 + k_{13}\lambda_2 + k_{12}(k_{23} + k_{31} - k_{12}) = 0, \\ \Delta_3^{(2)} &= \lambda_2\lambda_3 + k_{31}\lambda_2 + k_{21}\lambda_3 + k_{23}(k_{31} + k_{12} - k_{23}) = 0, \\ \Delta_3^{(3)} &= \lambda_3\lambda_1 + k_{12}\lambda_3 + k_{32}\lambda_1 + k_{31}(k_{12} + k_{23} - k_{31}) = 0. \end{aligned}\right\} \tag{26}$$

Equations (26), as well as (10), are not independent. Let us first consider the limiting case when there obtain not only conditions (26) but all the $\Delta_2^{(i)} = 0$, i.e., when among Eqs.(10) only one is independent. Then we obtain the condition

$$k_{12} = k_{13} = k_{23} = k, \quad \lambda_1 = \lambda_2 = \lambda_3 = -k. \tag{27}$$

The arrangement of the magnetization vectors with $H \parallel 0z$ must satisfy the condition

$$\sum_{i=1}^{3} M_i^x = \sum_{i=1}^{3} M_i^y = 0, \ \sum_{i=1}^{3} M_i^z = \frac{1}{k} H. \tag{28}$$

The energy of this state is

$$E_{III}^{\parallel m} = -E_0 - \frac{k}{2}\sum_{i=1}^{3} M_{i0}^2 - \frac{1}{2k} H^2, \tag{29}$$

and the resultant magnetization is

$$M_{res}^{\parallel m} = \frac{1}{k} H. \tag{30}$$

The magnetization increases linearly with the field, but there is always retained the condition (28). Physically this limiting case can be realized only under an exceptional conjunction of circumstances, namely, when

$$\frac{J_{12}}{\mu_1} = \frac{J_{21}}{\mu_2} = \frac{J_{23}}{\mu_2} = \frac{J_{32}}{\mu_3} = \frac{J_{31}}{\mu_3} = \frac{J_{13}}{\mu_1}. \tag{31}$$

Hence the limiting case is only of abstract interest; mainly it establishes the important fact that the field dependence of M_{res} is linear. This result, as we shall see, remains valid in more complicated cases.

Still bearing in mind ferrites with the garnet structure, let us assume that

$$k_{23} = k_{31} = k', \quad k_{12} = k \text{ and } k > k', \tag{32}$$

then Eqs.(26) become

$$\begin{aligned} &(\lambda_1 + k')(\lambda_2 + k') = (k - k')^2, \\ &(\lambda_2 + k)(\lambda_3 + k') = 0, \\ &(\lambda_1 + k)(\lambda_3 + k') = 0. \end{aligned} \tag{33}$$

It will be obvious that there can be two intermediate solutions:

$$1.\quad \lambda_1 = \lambda_2 = -k, \quad \lambda_3 \neq -k'; \tag{34}$$

$$2.\quad \lambda_1,\ \lambda_2 \neq -k, \quad \lambda_3 = -k'. \tag{35}$$

The mathematically possible case $\lambda_1 = \lambda_2 = -k$, $\lambda_3 = -k'$ leads to incompatibility of Eqs.(10) with $k \neq k'$ and must be rejected.

Case 1. If conditions (34) are fulfilled, then having solved (10), we obtain for the energy

$$E_{III}^{C_1} = -E_0 - \frac{1}{2k}[k^2(M_{10}^2 + M_{20}^2) + k'^2 M_{30}^2] - \left(1 - \frac{k'}{k}\right) H M_{30} - \frac{1}{2k} H^2, \tag{36}$$

and, accordingly, for the magnetization

$$M_{res} = \left(1 - \frac{k'}{k}\right) M_{30} + \frac{1}{k} H. \tag{37}$$

We note that with $k' \approx k$ we arrive at the limiting case characterized by Eqs. (27)-(31), i.e., $k' \approx k$ corresponds to strong coupling between the rare earth lattice and the iron lattices. On the other hand, for very small k' there will be such weakening of the coupling that we will essentially have the intermediate case of a two-sublattice model[2], when M_3 will always be oriented along the field, while for components M_1 and M_2, which are oriented perpendicular to the field (hereafter we denote them by M'_1 and M'_2) there will be fulfilled the condition $M'_1 = -M'_2$ (obviously, in this case $M'_3 = 0$). Break up of the linear configuration will occur in a critical field

$$H_{cr}^{(1)} = k(M_{20} - M_{10}) + k' M_{30}, \tag{38}$$

which is obtained by joining Eqs.(21) and (36).

Case 2. If there are fulfilled the conditions of Eq.(35), then having solved the set (10), we obtain for the energy

$$E_{III}^{C_2} = -E_0 - \frac{k'}{2} \sum_{i=1}^{3} M_{i0}^2 - (k - k') M_{10} M_{20} - \frac{1}{2k'} H^2, \tag{39}$$

and for the magnetization

$$M_{res} = \frac{1}{k'} H. \tag{40}$$

Thus the orientation of the rare earth sublattice magnetization M_3 is inti-

mately related with the directions of M_1 and M_2 (for a given direction of the field H), but the resultant magnetization for all distributions of the M_i in the entire region of the validity of this solution is a linear function of the field; the difference from the limiting case characterized by Eqs.(28)-(30) is that the susceptibility in the intermediate state III will equal $1/k'$ (rather than $1/k$) and that this state forms from state I at the critical value of the field

$$H_{cr}^{(2)} = k'(M_{20} + M_{30} - M_{10}),$$

which is obtained by joining Eqs.(21) and (39).

Institute of Crystallography,
Academy of Sciences of the USSR &
Physics Faculty, Moscow State University

References

1. K.B.Vlasov & B.Kh.Ishmukhametov, Zhur.eksp.i teor.fiz., 27, 75 (1954).
2. A.A.Gusev, Kristallografiya, 4, 695 (1959); 5, 420 (1960). (Trans.Soviet Physics - Crystallography.)
3. S.V.Tyablikov, Fizika metallov i metallovedenie, 3, 3 (1956); 8, 152 (1959). (Trans.latter, Physics of Metals & Metallography.)
4. S.V.Vonsovskii & Yu.M.Seidov, Izv.AN SSSR, Ser.fiz., 18, 319 (1954). (Trans.Bulletin, 18, 14.)
5. T.Shiklosh, Acta Physica, 8, 141 (1954).
6. E.I.Kondorskii, A.S.Pakhomov & T.Shiklosh, Radiotekhnika i elektronika (Radio-engineering & electronics) 2, 134 (1957).
7. K.P.Belov & M.A.Zaitseva, Usp.fiz.nauk, 66, 141 (1958). (Trans.Soviet Physics - Uspekhi.)

CONCERNING THE COEXISTENCE OF THE FERROELECTRIC AND FERRIMAGNETIC STATES

- G.A.Smolenskii, V.A.Isupov, N.N.Krainik & A.I.Agranovskaya

In a previous investigation[1] of ferroelectrics of complex composition we demonstrated the possibility of coexistence in crystals of the antiferromagnetic and ferroelectric states.

One can assume that substances that simultaneously have ferroelectric and ferromagnetic or antiferromagnetic properties will exhibit a number of interesting, distinctive attributes. Depending on the character of the spin ordering, we shall call these substances ferroelectric-ferromagnets, ferroelectric-antiferromagnets or ferroelectric-ferrimagnets. The appearance of magnetic ordering will obviously affect the ferroelectric properties, and, conversely, the appearance of the ferroelectric state will affect the magnetic properties. From the point of view of thermodynamics this means that in expansion of the thermodynamic potential of a single-domain ferroelectric-ferromagnet or ferroelectric-antiferromagnet into a series in terms of the components of the polarization vector P_i, the magnetization vector M_j and the deformation tensor u_{ij}, mixed terms, for example, terms of the $P_i^2 M_j^2$, as well as the $P_i^2 M_j^2 u_{ij}$ type, must be taken into account.

Among the different types of crystal structure known at present only the perovskite class comprises a large number of ferroelectrics and substances with magnetic ordering. ABO_3 type crystals with the perovskite structure are characterized by the strong internal electric fields necessary for the appearance of ferroelectricity. In addition, the angles in the B cation - oxygen - B cation chains are equal or very close to 180°, which is the optimum condition for the appearance of magnetic ordering in the B sublattice, owing to superexchange interaction. In view of this, crystals with the perovskite structure are the ones among which we are most likely to find coexistence of electric and magnetic ordering.

It is perfectly clear that for magnetic ordering to appear in crystals with the perovskite structure, there must be present in the B sublattice a certain concentration of transition element ions with noncompensated spins. Such ions, however, are not distinguished by high polarizability. At the same time, ferroelectricity appears, if the A and B ions are distinguished by high electronic and ionic polarizability in the crystal lattice. This condition is most fully satisfied if in the B sublattice there are transition metal ions having in their ground states the s^2p^6 shell of a noble gas (Ti^{4+}, Zr^{4+}, Nb^{5+}, Ta^{5+}, W^{6+}), while in the A sublattice there are ions with an unshared pair of $6s$ electrons; such pairs, apparently, are stereochemically active (Pb^{2+}, Bi^{3+}, Tl^{1+}). The ions of these groups, however, do not have a magnetic moment. As a result of careful search, we[5] discovered a substance that simultaneously satisfies the above requirements. Our investigations showed that $Pb(Fe_{2/3}W_{1/3})O_3$ is a ferroelectric-antiferromagnet with a ferroelectric Curie temperature of -90°C and a Néel temperature of about 100°C. Our next problem was to obtain a ferroelectric-ferrimagnet based on this compound.

Ferrimagnetism can be induced in substances with the perovskite structure by a certain ordering of the ions in the B sublattice in solid solutions. In the $(1-x)\,A'B'O_3 - x\,A''B_{0.5}''B_{0.5}'''O_3$ system* of solid solutions let the first compound be an antiferromagnet, each B′ cation of which is surrounded by six B′ cations with spins antiparallel to that of the first cation, and let the second compound be paramagnetic with ordered arrangement of the B″ and B‴ ions alternating along all three fourth-order axes of the cubic lattice. At small values of x, the ions in the octahedral positions are distributed statistically. With increasing content

---

*Here and in what follows x is the concentration (in mole %) of the second component.

of the second component, however, there occurs partial ordering of the ions (at sufficiently high concentrations of the second component this ordering may become complete). Let us examine the case when the B'' ion has a magnetic moment, while the B''' ion does not. In this case (provided magnetic ordering is maintained) the solid solutions can be represented by the formula:

$$A'_{1-x}A''_x(\vec{B}'_{\frac{1-x}{2}}\vec{B}''_{\frac{x}{2}})(\overleftarrow{B}'_{\frac{1-x}{2}}B'''_{\frac{x}{2}})O_3,$$

where the arrows indicate the directions of the magnetic moments of the ions.

Establishment of magnetic ordering leads to the appearance of the ferrimagnetic state. Let us calculate the saturation magnetic moment per formula unit as a function of component concentration for the idealized case of complete ordering of the ions at any concentration.

The calculations are carried out on the assumption that the only magnetic ions that contribute to the magnetic moment of the crystal are those that have no less than two neighboring magnetic ions in the other sublattice. We do not take into account the possibility of weak ferromagnetism, and assume collinear orientation of spins. This assumption is justified by the fact that in substances with the perovskite structure exchange interaction within each of the sublattices forming as a result of ordering of the B ions can be neglected and only the interaction between sublattices need be taken into account. Analogous calculations[6,7] were carried out for ferrimagnets with the structure of rock salt and garnet.

The magnetic moment per ABO_3 formula unit equals

$$m_s = 0.5(m_I - m_{II}) = 0.5\{[m'(1-x) + m''x][1 - E(k_{II})] - m'(1-x)[1 - E(k_I)]\};$$

here and in what follows m_I and m_{II} are the magnetic moments of the sublattices, m' and m'' are the moments of the B' and B'' ions, k_I and k_{II} are the fractions of nonmagnetic ions in sublattices I and II relative to the total number of ions in the given sublattice (in the present case $k_I = 0$ and $k_{II} = x$) and $E(k) = 6k^5 - 5k^6$ is the probability that a magnetic ion in one sublattice has no more than one nearest neighbor from among the magnetic ions in the other sublattice (for $k_I = 0$ and $E(k_I) = 0$).

The results of our calculations are shown in Fig.1. In spite of the fact that the number of ions with uncompensated spins in sublattice I is always greater than the number in sublattice II, at high concentrations of the second component there occurs a change in direction of the macroscopic magnetic moment. This is explained by the fact that, when there is a high concentration of diamagnetic ions in the second sublattice, most of the magnetic ions in the first sublattice do not have among their neighbors a sufficient number of magnetic ions. As was pointed out above, such ions do not take part in the magnetic ordering. $LaFeO_3 - SrNi_{0.5}W_{0.5}O_3$ solid solutions can serve as an example of ferrimagnetic solid solutions of this type. These solid solutions, however, do not have ferroelectric properties.

We investigated $(1-x)Pb(Fe_{2/3}W_{1/3})O_3 - xPb(Mg_{1/2}W_{1/2})O_3$ ferroelectric solid solutions. Polycrystalline specimens were prepared by means of sintering of the appropriate mixtures of the oxides (chemically pure and reagent grade) at 900-920°C. Petrographic analyses and x-ray diffraction studies disclosed the formation of solid solutions in the entire range of concentrations with a low content (up to 5%) of the second, nonmagnetic Pb_2WO_5 phase. The first component of these solid solutions, as was pointed out above, is ferroelectric and antiferromagnetic, while the second component is antiferroelectric with ordered arrangement of dia-

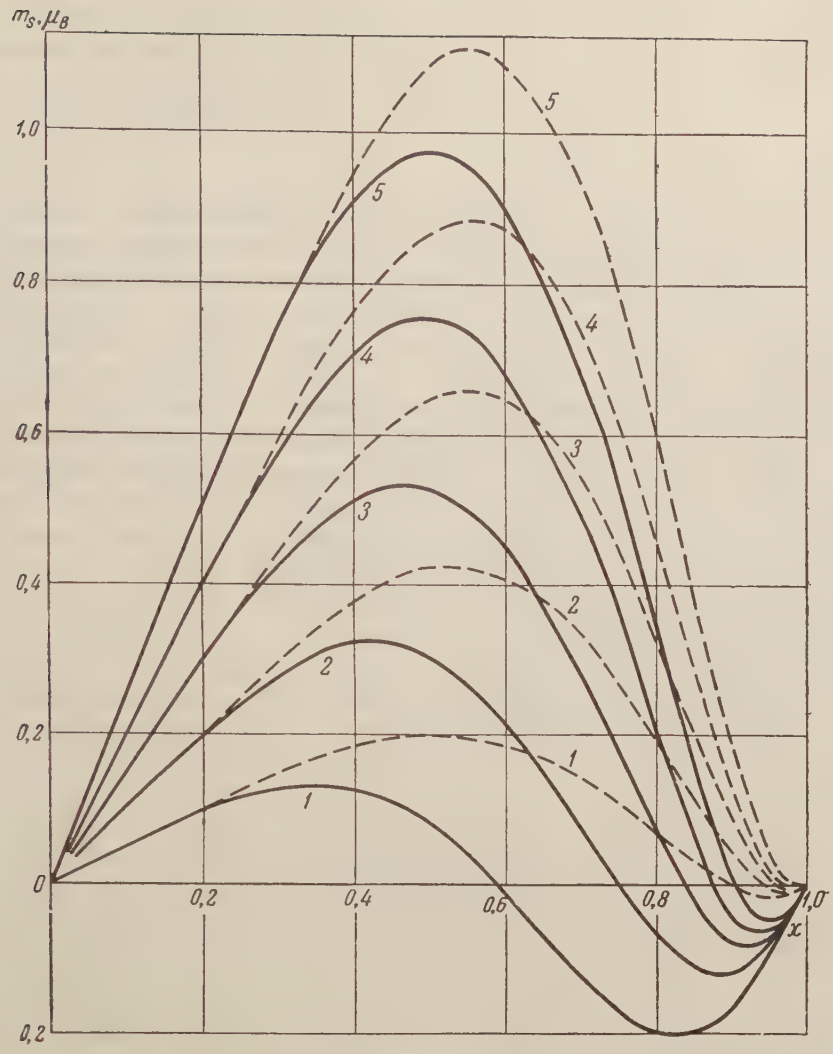

Fig.1. Calculated values of the magnetic moment of $A'_{1-x}A''_x(\vec{B}'_{\frac{1-x}{2}}\vec{B}''_{\frac{x}{2}})(\overleftarrow{B}'_{1-x}B'''_{\frac{x}{2}})O_3$ **type solid solutions for different values of** x **for the cases when the magnetic moment of the** B' **ion equals** $5\mu_B$ **(solid lines) and** $1\mu_B$ **(dash lines). The figures at the curves indicate the magnetic moment of the** B'' **ion.**

magnetic Mg^{2+} and W^{6+} ions. This case differs from the one discussed above in that the second compound contains no magnetic ions but causes ordering of the Fe^{3+} and W^{6+} ions in the solid solution. X-ray diffraction studies carried out by M.F. Bryzhina showed that already at a second component concentration of $x \geqslant 0.20$ there is observed ordering of the ions in octahedral positions. The volume of the crystal and magnetic unit cell equals $\sim 8a_0^3$, where a_0 is the cubic cell parameter in the absence of ordering. The chemical formula describing the completely ordered solid solutions is

$$Pb(Fe_{3/6(1-x)}Mg_{3/6x})(Fe_{\frac{1}{6}(1-x)}W_{\frac{1}{6}(2+x)})O_3.$$

The investigated solid solutions are ferroelectric in the range $x = 0$ to 0.88.

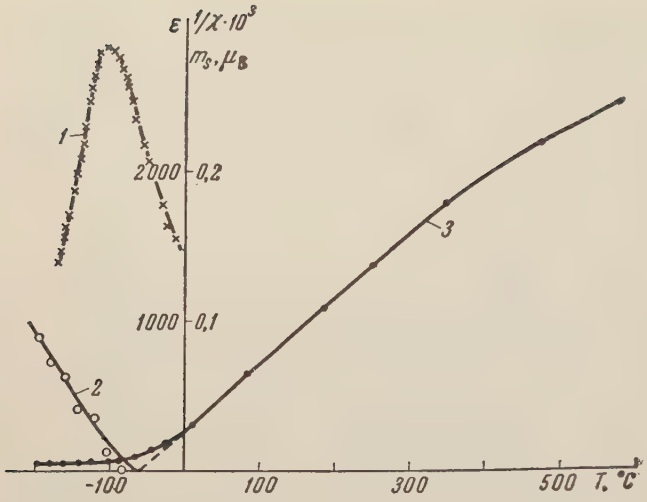

←Fig.2. Temperature dependence of the dielectric constant ε (1), spontaneous magnetic moment (2) and reciprocal of the susceptibility $1/\chi$ (3) of $0.7\,Pb(Fe_{2/3}W_{1/3})O_3 - 0.3\,Pb(Mg_{1/2}W_{1/2})O_3$ solid solution.

At temperatures below θ_f (the ferroelectric phase transition temperature) there are observed dielectric hysteresis loops. For $x > 0.88$ the solid solution are antiferroelectric. Curve 1 of Fig.2 shows temperature dependence of the dielectric constant for solid solutions with $x = 0.3$. The magnetic moment measurements were carried out by the Faraday method using spherical specimens. The field dependences of the magnetic moment

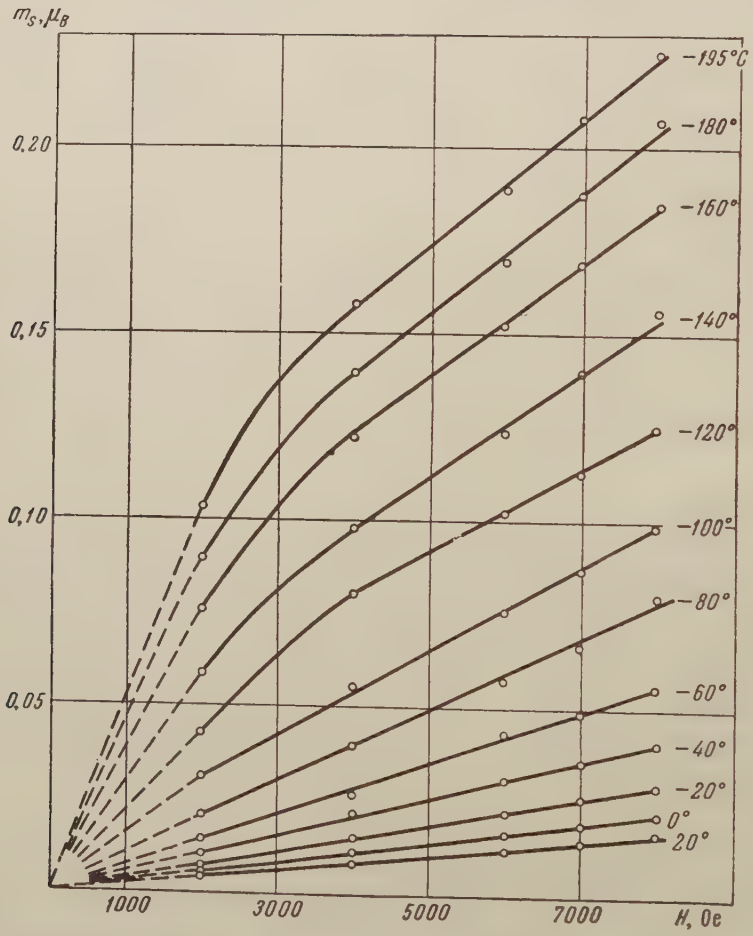

Fig.3. Field dependences of the magnetic moment of $0.7Pb(Fe_{2/3}W_{1/3})O_3 - 0.3Pb(Mg_{1/2}W_{1/2})O_3$ solid solution at different temperatures.

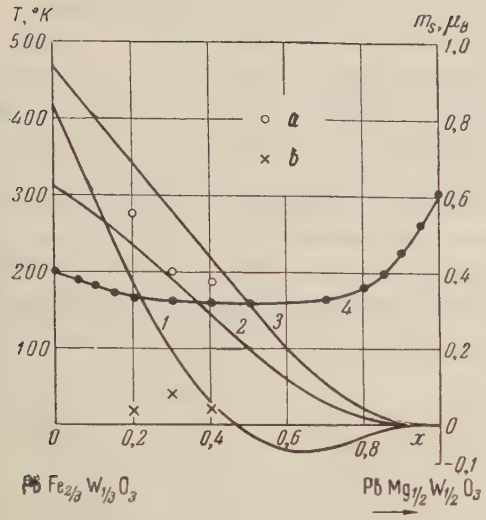

Fig.4. Results of calculating the magnetic moment m_s (1), magnetic Curie temperature with complete ordering of the B ions (2) and the Néel temperature for statistical distribution of ions (3) of $(1-x)\,Pb\,(Fe_{2/3}W_{1/3})\,O_3 - x\,Pb\,(Mg_{1/2}W_{1/2})\,O_3$ solid solutions. Curve 4 represents the experimental variation of the ferroelectric Curie temperature θ_f with composition in the given solid solutions system: a) experimental value of θ_M, b) experimental value of m_s.

of this solid solution at different temperatures are shown in Fig.3. The spontaneous moment m_s (curve 2, Fig.2) was determined from the resultant curves by means of the formula $m = m_s + \chi H$, where $H = H_{ext} - \frac{4\pi}{3} I$ Curve 3 in Fig.2 shows the temperature dependence of $1/\chi$. The curve is characteristic of ferrimagnets. The phase transition to the paramagnetic state is smeared out; hence in this case it is more appropriate to speak of a phase transition region rather than a transition point. In Ref.8 we attempted to give the reason for smearing out of the phase transition.

Gilleo[7] assumed that the exchange interaction energy in a crystal (and, consequently, the Curie temperature) is proportional to the average number of magnetic couplings or the number of interacting Fe-O-Fe pairs per "active" Fe ion, and calculated the Curie temperature θ_M of ferrites with the garnet and spinel structures. Similarly, we can evaluate the number of interactions in perovskite:

$$n(k_I, k_{II}) = (1-k_I)\,[1-E(k_{II})]\,(1-k_{II})\,[1-E(k_I)].$$

The number of ions participating in the ferrimagnetism:

$$N = 0.5\,\{(1-k_I)\,[1-E(k_{II})] - (1-k_{II})\,[1-E(k_I)]\};$$

from which it follows that the Curie temperature equals

$$\theta_M(k_I, k_{II}) = \frac{n(k_I, k_{II})}{N} \cdot \theta_M(0,0),$$

where $\theta_M(0.0)$ is the Néel temperature of the substance not containing any nonmagnetic ions.

Composition (value of x)	Magnetic moment per formula unit at 77°K, μ_B (experimental)	Magnetic moment at 0°K, μ_B (calculated)
0.2	0.034	0.36
0.3	0.085	0.18
0.4	0.046	0.05

Fig.4 shows the results of calculating the magnetic moment (curve 1) and Curie temperature (curve 2) of solid solutions for the case of complete ordering, and the Néel temperature (curve 3) for the case of statistical distribution of the ions. Fig. 4 also shows the experimental composition dependence of the ferroelectric phase transition temperature as indicated by the maximum of ϵ (curve 4).

As can be seen from the accompanying table, the values of the magnetic moments of the compositions with x = 0.3 and 0.4, determined experimentally at

-196°C, are somewhat lower than the values calculated for the case of complete ordering at 0°K and taking only spin moments into account. The magnetic moment of the $x = 0.20$ material is substantially lower than the calculated value. This points to incomplete ordering of ions in the given solid solution, which is substantiated by x-ray diffraction data on the intensity of the superstructure lines.

The experimental Curie temperatures are in satisfactory agreement with the calculated values.

In 1960 a number of authors (see, for example, Ref.9) reported the discovery of ferrimagnetic and ferroelectric properties in some compounds with the structure of tetragonal potassium-tungsten bronzes. Our experiments showed that these compounds are indeed ferroelectrics, but we found no evidence of ferrimagnetism.

Institute of Semiconductors,
Academy of Sciences of the USSR

References

1. G.A.Smolenskii, A.I.Agranovskaya, S.N.Popov & V.A.Isupov, Zhur.tekh.fiz., 28, 2152 (1958). (Trans.Soviet Physics - Technical Physics.)

2. W.Shokley, Phys.Rev., 73, 1273 (1948).

3. L.E.Orgel, J.Chem.Soc., No.12, 3815 (1959).

4. G.A.Smolenskii, V.A.Isupov, A.I.Agranovskaya & N.N.Krainik, Fiz.tverdogo tela 2, 2982 (1960). (Trans.Soviet Physics - Solid State.)

5. G.A.Smolenskii, A.I.Agranovskaya & V.A.Isupov, Ibid., 1, 990 (1959). (Trans.Ibid.)

6. J.B.Goodenough, D.G.Wickham & W.J.Croft, J.Phys.Chem., 5, 107 (1958).

7. M.A.Gilleo, J.Phys.Chem.Solids, 13, 33 (1960).

8. G.A.Smolenskii, V.A.Isupov, A.I.Agranovskaya & S.N.Popov, Fiz.tverdogo tela, 2, 2906 (1960). (Trans.Soviet Physics - Solid State.)

9. P.H.Fang, R.S.Roth & H.S.Schofer, Bull.Amer.Phys.Soc., Ser.II, 5, No.1, Part I, 57 (1960).

ENERGY SPECTRUM OF CURRENT CARRIERS IN FERRO- AND ANTIFERROMAGNETS

- E.K.Kudinov & A.G.Samoilovich

Investigations of the temperature dependence of the conductivity of some antiferromagnetic materials reveal a change in the character of the conductivity incident to transition through the Curie point: below the Curie point the conductivity is typical of semiconductors:

$$\sigma \sim \exp\left(-\frac{\Delta E_a}{kT}\right),$$

while above the Curie point the conductivity is metallic, i.e., $\sigma \sim 1/T$. Values for some compounds are given in the accompanying table.

Compound	T_c, °K	ΔE_a, eV
VO	120	0,23
V_2O_3	160	0,32
VO_2	340	0,23

It will be evident from these data that the activation energy ΔE_a is much greater than the exchange interaction energy leading to antiferromagnetic ordering. It is significant that in these substances the s electrons do not participate in the conduction, inasmuch as they go over to the oxygen atoms. We shall assume that conduction here is due to the remaining d electrons of the metal.

In the present work we propose an explanation for the existence of ΔE_a. We shall use the polar model to describe conduction, and assume that the electrons in going from lattice site to lattice site obey Hund's rule.

In the zeroth approximation the lower level of nonpolar states is separated from one-hole levels by a gap ΔE_0 equal in order of magnitude to the energy of electrostatic interaction of an excess electron and the rest of the atom's electrons. Taking into account interaction between neighbors, these levels broaden into bands. If the band width of the polar states depends on magnetic ordering, the activation energy will vary with the magnetization of the sublattice. In particular, if the lower edge of the band of polar states overlaps the lower edge of a nonpolar band, the conductivity will be metallic in character.

We shall determine the width of the zone of polar states with a single excitation as a function of the magnetization and shall consider a crystal with a single excess electron. We assume that the excess electron occupies an orbit lying somewhat outside the orbits occupied by the atomic electrons; we also assume that the atomic shell is filled. In most actual cases these conditions are, apparently, not satisfied inasmuch as the atomic d electrons do not fill the d orbits, while the extra electron does occupy these orbits; but taking such degenerated states into account makes the problem practically unsolvable. Nor is it clear just how taking degeneration into account would affect the result.

We assume that the excess electron, in occupying the states with maximum total spin, obeys Hund's rule. We shall look for splitting of the degenerate level into a band (whose width agrees in order of magnitude with the width of a band with a single hole). We shall allow for electron-electron interaction only by selecting wave functions that take into account exchange interaction between neighboring atoms (spin ordering) and within the atom (Hund's rule); we shall consider the splitting of the level into a band by means of the one-electron Hamiltonian:

$$\hat{H} = \sum_{\alpha\alpha';\sigma} F_{\alpha\alpha'} a^+_{\alpha\sigma} a_{\alpha'\sigma}, \qquad (1)$$

where σ is the spin index and the α are the other quantum numbers describing the electron, i.e., f_n - the radius vector of the n-th lattice site, m - the magnetic sublattice number, γ - the quantum numbers of atomic orbits $\gamma(l; l')$ (the l are the

quantum numbers of the filled orbits and l' is the quantum number of the excess electron's orbit). In the case of ferromagnets, the zeroth approximation wave functions can be schematically represented as follows (we have in mind the case of only two sublattices):

$$\Phi^{(1)}(f_n) \rightarrow \begin{array}{ccccc} S_z = S & S_z = -S & S_z = S + 1/2 & & \\ \uparrow & \downarrow & \uparrow\uparrow & \downarrow & \uparrow\ \downarrow \\ \underbrace{m=1\ m=2}_{f_{n-1}} & & \underbrace{m=1}_{f_n} & \underbrace{m=2}_{} & \underbrace{m=1\ m=2}_{f_{n+1}} \end{array},$$

$$\Phi^{(2)}(f_n) \rightarrow \begin{array}{ccccc} S_z = -S & S_z = S & S_z = -S + 1/2 & & \\ \uparrow & \downarrow & \uparrow & \downarrow\uparrow & \uparrow\ \downarrow \\ \underbrace{m=1\ m=2}_{f_{n-1}} & & \underbrace{m=1}_{f_n} & \underbrace{m=2}_{} & \underbrace{m=1\ m=2}_{f_{n+1}} \end{array},$$

i.e., the function $\Phi^{(1)}(f_n)$ describes the location of the extra electron at site f_n in the first sublattice, while $\Phi^{(2)}(f_n)$ describes its location at site f_n in the second sublattice.

In the second quantization representation these functions can be written in the form

$$\Phi^{(2)}(f_n) = \sum_{m=-1/2}^{+1/2} C^{S+1/2;\ -S+1/2}_{S;\ -S+1/2-m;\ 1/2;\ m}\ a^{+}_{f_n\beta 2m}\ \hat{A}_{f_n 1S;\ S} \prod_{f_{n'}\neq f_n} \prod_{m=1;\ 2} \hat{A}_{f_{n'}mS;S_m}\Phi_0; \qquad (2)$$

here $\hat{A}_{f_n 1S;\ S_m}$ is a linear combination of the products of the creation operators, which, acting on the vacuum function, yields the atomic state with a total momentum S and component S_m, for example

$$\hat{A}_{f_n m10} = \frac{1}{\sqrt{2}}\left(a^{+}_{f_n m\alpha_1 1/2} a^{+}_{f_n m\alpha_2 -1/2} + a^{+}_{f_n m\alpha_1 -1/2} a^{+}_{f_n m\alpha_2 1/2}\right),$$

where the $C^{J;J_z}_{j_1;j_{1z};j_2;j_{2z}}$ are Clebsch-Gordan coefficients:

$$\Phi^{(1)}(f_n) = a^{+}_{f_n\beta 1 1/2}\ \hat{A}_{f_n 1S;\ S}\ \hat{A}_{f_n 2S;-S} \prod_{f_{n'}\neq f_n} \prod_{m=1;\ 2} \hat{A}_{f_{n'}mSS_m}\Phi_0. \qquad (3)$$

We shall seek the solution of the Schrödinger equation with operator (1) in the form of a series in the functions (2) and (3), taking translational symmetry into account. As a result of simple operations, we obtain in the nearest-neighbor approximation an energy band of the form

$$\Delta E_a = \frac{F_{\beta 1;\beta 2}}{\sqrt{2S+1}} f(\mathrm{k}), \qquad (4)$$

where the function $f(\mathrm{k})$ depends only on the geometric structure of the lattice ($F_{\beta 1;\beta 2} = F_{f_n\beta 1;f_n\beta 2}$).

The dependence of the band width of the excess electron on the state of magnetic ordering, which is characterized by the factor $\frac{1}{\sqrt{2S+1}}$ and embodies the gist of the obtained result, is a consequence of the assumption that the excess electron interacts so strongly with the electrons of the given atom that in effect it obeys Hund's rule. The probability for transition of the electron to a neighboring atom will depend on the state of ordering of the lattice.

Calculations for ferromagnetic ordering are carried out in an analogous manner (for the sake of convenience we consider a ferromagnet consisting of two identical sublattices):

$$\Delta E_f = F_{\beta_1;\beta_2} f(k). \tag{5}$$

In the paramagnetic case we obtain an energy band for each given arrangement of the spin moments and then average this band over all possible arrangements with equal weight. This yields the following:

$$\Delta E_n = \frac{F_{\beta_1;\beta_2}}{(2S+1)^3}\left\{\left(\sum_{S_z=-S}^{+S}\sqrt{S+S_z+1}\right)^2+\left(\sum_{S_z=-S}^{+S}\sqrt{S-S_z}\right)^2\right\} f(k). \tag{6}$$

Thus, in all three cases splitting of the energy level is of the form

$$\Delta E_p = J_p f(k), \tag{7}$$

where J_p has different indices for the ferromagnetic, antiferromagnetic and paramagnetic cases; by definition

$$J_p = \alpha_p J_0, \tag{8}$$

where $J_0 = F_{\beta_1;\beta_2}$.

The values of α_p for different S are given in the table.

S	α_f	α_p	α_a
1/2	1	0,85	0,7
1	1	0,85	0,6
3/2	1	0,85	0,5

As will be evident, incident to transition from the antiferromagnetic to the paramagnetic state, the zone width increases and, in principle, transition from the state with semiconductor conductivity to the state with metallic conductivity becomes possible. Incident to transition from the ferromagnetic to the paramagnetic state, on the other hand, the zone narrows, and transition from metallic to semiconductor conductivity can ensue.

Institute of Semiconductors,
Academy of Sciences of the USSR

CONTRIBUTION TO THE THEORY OF KINETIC EFFECTS IN NiO TYPE SEMICONDUCTORS

- M. I. Klinger

The phenomenon of electron transfer in semiconductors of the NiO type at elevated temperatures exhibits a number of distinctive quantitative attributes; among other things the carrier mobility U is anomalously low and $U(T) \sim \exp(-Q/T)$.[1-3] Usually these are substances in which the electron zone Δ_e is relatively narrow (the d or f zone of the transition metal, i.e., Ni in the case of NiO). Accordingly the theory of electron transfer should be capable of explaining observed experimental facts and predicting others, and should adequately describe the mechanism of transfer in such substances.*

According to Ioffe[1], who was the first to study this problem, the current carriers in these substances move by jumps from one lattice site s to another s' between the ions of the transition metal; later, Heikes & Johnston[2] hypothesized that the current carriers are "small" polarons (polarons of small radius). Subsequently, Yamashita & Kurosawa[4], using the theory of quantum transitions, calculated the mean probability $\overline{W}_{ss'}$ for such a jump, accompanied by many-phonon transitions with conservation of the phonon energy (we are dealing here with a crystal having ideal periodicity, when the polaron energy at identical transition metal ions in different sites is the same, i.e., when $\varepsilon_s = \varepsilon_{s'}$. It was found[4] that the expression for $\overline{W}_{ss'}$ diverges

$$W_{ss'} \sim \int_{-\infty}^{\infty} \frac{d\xi}{2\pi} \exp(\zeta \cos \xi) = \infty;$$

the divergence was eliminated by the somewhat arbitrary and in no way justified substitutions

$$\int_{-\infty}^{\infty} \to \int_{-\pi}^{\pi} \quad \text{and} \quad \overline{W}_{ss'} \to \overline{W}'_{ss'} \sim I_0(\zeta).$$

Holstein[5] carried out a more thorough analysis of $\overline{W}_{ss'}$ for the particular case of a one-dimensional molecular chain (alternating "+" and "-" ions in the molecule), and elucidated the reason for the divergence; however, even Holstein was unable to eliminate the divergence in a physically justified, unambiguous manner. In the approach employed in the work of Refs.4 & 5 there arises the important question of compatability of the polstulated jump mechanism with translational symmetry of the crystal and the presence of a polaron zone; it was shown[4-6] that the width of this zone

$$\Delta_{\text{pol}} = \Delta_e \exp\left(-\lambda \frac{kT}{\hbar\omega_0}\right) \qquad (1)$$

for $kT > \hbar\omega_0$ (ω_0 is the limiting frequency of the polarization phonons and λ is a parameter of the polaron coupling, which is appreciable).

The basic argument underlying the investigations of Refs.4,5 & 7 is the following: inasmuch as $\Delta_{\text{pol}} \ll \Delta_e$ and Δ_{pol} rapidly decreases with increasing temperature, the zone treatment and the alternative transfer mechanism - jumps - are inapplicable for such narrow zones. This approach, however, is unsatisfactory, for no quantitative criterion was established. Although in Refs.4 & 5 there were obtained formulas for $\overline{W}'_{ss'}(T)$ and some other interesting specific results, it follows

---

*We shall not touch here on the question of the character of the spectrum of the quasiparticles - current carriers (why, for example, NiO is not metallic), inasmuch as we are interested primarily in the transfer mechanism; the existence of such virtually noninteracting carriers is assumed a priori.

from what has been said above that the theory for the probability of jumps, developed by these authors, cannot be regarded as consistent and satisfying in principle. Finally, in Refs.4 & 5 the general theory of kinetic effects was not considered, and it was assumed only that the diffusion coefficient $D = a^2 \overline{W}'_{ss'}$ (a is the lattice constant, while the mobility $U(T) = eD/kT$.

In the present paper we propose a general theory for transfer with low mobility, in which all the above mentioned difficulties and questions simply do not arise or are automatically solved.*

For the sake of brevity we do not consider the influence of magnetic transitions inasmuch as we are concerned in the main with the region where $T > T_N$ or T_C: these and other questions can also be examined in the framework of the given theory. On the basis of general expressions for the kinetic coefficients σ_{AB} (Ref.8) and using equations (I.4-8 from Ref.9) we consider only stationary processes for which $\sigma^{(s)}_{AB} = \frac{1}{2}(\tilde{\sigma}_{AB} + \tilde{\sigma}_{BA})$ (and the analogous expression for $\sigma^{(a)}_{AB}$):

$$\tilde{\sigma}_{AB} = \frac{\beta N_e}{2} \int_{-\infty}^{\infty} dt e^{-\nu|t|} \operatorname{Re} \langle BA(t) \rangle, \tag{2}$$

where the B, A are the fluxes (charge, energy and the like), $A(t) = \exp\left(\frac{iH}{\hbar} t\right) \times$ $\times A \exp\left(-\frac{iH}{\hbar} t\right)$, H is the Hamiltonian of the system, $\langle \ldots \rangle \equiv \operatorname{Sp} \exp(\beta F - \beta H)(\ldots)$, N_e is the carrier concentration, and $\beta \equiv 1/kT$.

Specifically, our system consists of a small polaron located at a transition metal ion site and weakly interacting with the fields of the other (stationary) ions, i.e.,

$$H = H_0 + \lambda_0 H',$$

wherein

$$H_0 | sn^{(s)} \rangle = \varepsilon(n^{(s)}) | sn^{(s)} \rangle; \quad (sn^{(s)} | H' | s'n'^{(s')}) = (sn^{(s)} | V_{s'} | s'n'^{(s')});$$

$$(sn^{(s)} | H' | sn^{(s)}) = 0; \quad \dot{\lambda}_0 V_{s'} = \sum_{t' (\neq s')} V_{t'}(\mathbf{x} - \mathbf{a}_{t'}); \tag{3}$$

here $n^{(s)}$ is the aggregate number of phonons that can change incident to a $s \to s'$ transition; the function $|sn^{(s)})$ can be orthagonalized and it can be assumed that $(sn^{(s)} | s'n^{(s')}) = \delta_{ss'}\delta_{nn'}$. In calculating $\tilde{\sigma}_{AB}$ we regard $\lambda_0 H'$ as a small perturbation and formally expand $\tilde{\sigma}_{AB}$ in terms of λ_0, taking Sp in the $|sn^{(s)})$ system for different $s, n^{(s)}$, which to good approximation we regard as complete (in case of necessity one can readily take into account other states as well). Inasmuch as continuity of the spectrum of the system is a necessary condition for transfer, important in principle here is continuity of the phonon spectrum; then for calculating the $\tilde{\sigma}_{AB}$ we used the theory of perturbations in a continuum. This is conveniently done for the resolvents R_l:[9,10]

$$R_l^{\pm} = \lim_{\varepsilon \to +0} (H_0 + \lambda_0 H' - l \pm i\varepsilon)^{-1}, \quad \exp\left(\pm \frac{iH}{\hbar} t\right) = \frac{\pm i}{2\pi} \int_{-\infty}^{\infty} dl \exp\left(\pm \frac{it}{\hbar} l\right) R_l^{\pm}.$$

In formal expansion of $R_l^{\pm}$ in terms of λ_0 it proved feasible to realize partial

---

*We are dealing here with one "excess" carrier, so that the question of the relation between the methods of Heitler-London and Bloch, associated mainly with taking into account Coulomb correlation, simply does not arise.

summation of some of the subsequences; we utilized the specific properties of the elements

$$(sn^{(s)} \mid \lambda_0 H' \mid s'n'^{(s')}),$$

namely,

$$(sn^{(s)} \mid \lambda_0 H' \mid s'n'^{(s')}) \sim \begin{cases} 0\,(N^0) & \text{for } s \neq s', n^{(s)} = n'^{(s')}, \\ 0\,(N^{-z/2}),\ z \geqslant 1, & \text{for } n^{(s)} \neq n'^{(s')},\ s \neq s' \end{cases} \tag{4}$$

and

$$(sn^{(s)} \mid \lambda_0 H' A_1 \lambda_0 H' \ldots A_k \lambda_0 H' \mid s'n'^{(s')}) \sim \begin{cases} 0\,(N^0) & \text{for } n^{(s)} = n'^{(s')} \\ 0\,(N^{-z/2}) & \text{for } n^{(s)} \neq n'^{(s')}, \end{cases}$$

if $A_i \mid sn^{(s)}) = A_i(sn^{(s)}) \mid sn^{(s)})$ and N is the number of ions (atoms) in the crystal (in the limit as $N \to \infty$, $\Omega \to \infty$ for $\Omega / N = \text{const}$). The partially summed new series $R_l^{\pm}$ takes into account "attenuation" of the $\mid sn^{(s)})$ states (owing to $sn^{(s)} \to s'n'^{(s')}$ transitions); detailed analysis shows that

$$\eta(T) \equiv \frac{\Delta_{\text{pol}}(T)}{\hbar \bar{\Gamma}(T)},$$

is actually a small parameter; here $\bar{\Gamma}(T)$ is the mean (for the ensemble) width of the unperturbed level of the polaron; moreover $\bar{\Gamma}(T)$ is finite (no divergences).

The developed theory of transfer effects in a system with strong coupling (electrons with phonons) contains the following basic small parameters:

$\eta(T) < 1$, $\Lambda \equiv \frac{\Delta_e}{kT} \lesssim 1$*, and also $\frac{\hbar \bar{\Gamma}}{kT} < 1$ and $\Gamma \ (\omega_{\text{characteristic}})^{-1}$ (as a consequence $\Delta_{\text{pol}} \ll kT$). Inasmuch as Δ_{pol} decreases, while $\bar{\Gamma}(T)$ increases with increasing T, at appropriate values of Δ_e, λ and ω_0 the condition $\eta < 1$ can be fulfilled for $T > T_{\text{cr}}$; also $\Delta_{\text{pol}}(T_{\text{cr}}) = \hbar \Gamma(T_{\text{cr}})$. In the region where $T \gtrsim \Delta_e$ and $T > T_{\text{cr}}$ the correction to the leading term in $\tilde{\sigma}_{AB}$ is small and thus the theory is valid, while the difficulties encountered in the investigations of Refs.3 & 4 do not arise. Moreover, in case of reasonable interpretation of the condition $\eta(T) < 1$ it may be assumed that the jumps are essentially a form of polaron-zone motion (i.e., transitions of trapped zone packets between sites), which is possible provided the width of the packet $\sim \Delta_{\text{pol}} < \hbar \bar{\Gamma}(T)$. This is possible for the zone of a small polaron (but not an electron), if the phonon spectrum is continuous.**

Before concluding we would like to mention some of the other results ensuing from the developed theory.

1. The phenomenon of transfer with low mobility may occur not only in ionic crystals but in crystals of the homopolar type in which there can form current carriers - condensons of small radius, which is possible at certain values of the parameters of the system (small condenson-electron strongly interacting with the phonons of the homopolar crystal). Such effects have much in common with polaron

---

*For expansion of $\exp(-\beta H)$ in terms of λ_0.

**If the phonon spectrum were discrete, we would have transitions between discrete levels at nearest neighbor sites (tunneling type transitions, and it would be necessary to take into account degeneration of $(n^{(s)})$ in energy, which is not required in the case of a continuous spectrum of phonons) and then it would be assumed that $\Delta_{\text{pol}} \sim \exp(-Q/T)$ and that the theory does not contain the small parameter η, and consequently, transfer could not have the character of jumps (see above, regarding the continuity of the spectrum as a necessary condition for transfer).

transfer but also exhibit certain distinctive features (this matter will be discussed in a future paper).

2. Only the principal approximation in terms of η and Λ can be interpreted as transfer by independent jumps between nearest neighbor sites; higher order approximations may be said to take into account the quantum-statistic correlation of real jumps and virtual transitions over intermediate sites, involving an ever greater number of such events, but their contribution decreases rapidly for $\eta < 1$. Thus for $\eta \gtrsim 1$ there occurs a transition from jumps of packets to zonal motion of the Bloch type.

3. In the principal approximation the Hall mobility $U_{xy} = 0$, and the mobility

$$U(T) = (s \mid (x - a_s)^2 \mid s) \frac{e}{kT} \overline{\Gamma}(T),$$

moreover, at high temperatures

$$U(T) \sim \exp(-Q/T), \quad Q \approx \frac{\lambda \omega_0}{4};$$

from this there follow the formulas for $U(T)$ deduced in Refs.4 and 5 for some particular cases; usually $(s \mid (x - a_s)^2 \mid s) \lesssim a^2$ and, together with Δ_e, the element $(s \mid (x - a_s)^2 \mid s)$ can be used to take into account the influence of magnetic transitions.

4. In an ideal crystal (with transition element ions of one type) the thermo-emf $\alpha = \frac{k}{e} \mu$ and $\Delta\alpha \equiv \alpha - \frac{k}{e} \mu = 0$ (μ is the chemical potential) and the zero-point heat conductivity $\tilde{\varkappa} = 0$. The inequalities $\frac{k}{e} |\mu| \gg |\Delta\alpha| \neq 0$ and $\tilde{\varkappa} \neq 0$ can obtain under certain conditions in a nonideal crystal (or in the presence of several different types of transition ions with close energies

Thus our theory explains the basic experimental facts and predicts certain other facts; it also provides a basis for quantitative description of the mechanism of transfer with low mobility of the carriers.

References

1. A.F.Ioffe, Canad.Phys., 34, 1393 (1956).
2. R.R.Heikes & W.D.Johnston, J.Chem.Phys., 26, 582 (1957).
3. F.I.Morin, Bell System Techn.J., 37, 1047 (1958); G.H.Jonker, J.Phys. Chem.Sol., 9, 165 (1959); van Houten, Ibid., 17, 7 (1960).
4. J.Yamashita & T.Kurosawa, Ibid., 5, 34 (1958).
5. T.Holstein, Ann.Phys., 8, 343 (1959).
6. G.L.Sewell, Philos.Mag., (8), 3, 1361 (1958).
7. H.Fröhlich & G.L.Sewell, Proc.Phys.Soc., 74, 643 (1959).
8. R.Kubo, J.Phys.Soc.Japan, 12, 570 (1957); R.Kubo, M.Jokota & S.Nakajama, J.Phys.Soc.Japan, 12, 1207 (1957); M.I.Klinger, Fizika tverdogo tela, 1, 1225 (1959). (Trans.Soviet Physics - Solid State.)
9. M.I.Klinger, Ibid., 2, 309 (1960). (Trans.Ibid.)
10. L.Van Hove, Physica, 21, 901 (1955).

CONTRIBUTION TO THE THEORY OF NONRESONANCE ABSORPTION OF AN ALTERNATING MAGNETIC FIELD BY A FERROMAGNETIC DIELECTRIC AT LOW TEMPERATURES

- M. I. Kaganov & V. M. Tsukernik

Introduction

If the applied homogeneous high frequency magnetic field is circularly polarized in the plane perpendicular to the equilibrium magnetic moment of the ferromagnetic specimen, the field vector can rotate either in the direction of free rotation of the magnetization vector or in the opposite sense. In the first case the most significant role in the absorption is played by ferromagnetic resonance associated with coincidence of the frequency of the field with the frequency of precession of the magnetic moment; in this case there is excited a spin wave with zero momentum owing to absorption of a photon (the momentum of the photon is assumed to be zero).

In the second case ferromagnetic resonance does not occur, and absorption of the magnetic field is possible only due to interaction in the spin wave system (this applies to the range of temperatures substantially lower than the Curie point).

The spin waves interact with each other, with phonons and with impurities. In the present work we take into account the first two types of interaction, which occur even in an ideal ferromagnetic dielectric. In this case the Hamiltonian of the system in the spin-wave approximation with accuracy to fourth order terms in the spin-wave creation and destruction operators $a_{\mathbf{k}}^{+}$ and $a_{\mathbf{k}}$ is of the form (see, for example, Ref.1):

$$\varkappa = \varkappa_0 + \varkappa_{ss} + \varkappa_{sl} + \varkappa_h. \tag{1}$$

here the first term $\varkappa_0$ is the Hamiltonian of the system of noninteracting spin-waves

$$\varkappa_0 = \sum_{\mathbf{k}} \varepsilon_{\mathbf{k}} a_{\mathbf{k}}^{+} a_{\mathbf{k}}, \quad \varepsilon_{\mathbf{k}} = \varepsilon_0 + \theta_c (ak)^2, \tag{2}$$
$$\varepsilon_0 = \mu H_0 + \beta \mu M_0,$$

where H_0 is the constant field applied in the direction of the easy magnetization axis, M_0 is the equilibrium moment, β is the anisotropy constant, θ_c is a quantity of the order of the Curie temperature, a is the lattice constant, and $\mu = g\hbar$ (g is the gyromagnetic ratio).

$\varkappa_{ss}$ is the operator of the interaction of the spin-waves with each other

$$\varkappa_{ss} = \sum_{123} \Phi_{12;3} a_1^{+} a_2^{+} a_3 + \sum_{1234} \Phi_{12;34} a_1^{+} a_2^{+} a_3 a_4 + \sum_{1234} \Phi_{1;234} a_1^{+} a_2 a_3 a_4 + \text{comp. conj.} \tag{3}$$

In performing the summation one must bear in mind the obvious laws of conservation of momentum:

$$\Phi_{12;3} = -\frac{\pi\mu}{2}\left(\frac{2\mu M_0}{V}\right)^{1/2} (\sin 2\theta_1 e^{-i\varphi_1} + \sin 2\theta_2 e^{-i\varphi_2}), \tag{4}$$

$$\Phi_{12;34} = -\frac{\mu^2}{8V}\left\{2\beta + \pi(\sin^2\theta_1 + \sin^2\theta_2 + \sin^2\theta_3 + \sin^2\theta_4) - \right.$$
$$\left. - 2\pi\left[\frac{(k_{1z}-k_{4z})^2}{(\mathbf{k}_1-\mathbf{k}_4)^2} + \frac{(k_{1z}-k_{3z})^2}{(\mathbf{k}_1-\mathbf{k}_3)^2} + \frac{(k_{2z}-k_{4z})^2}{(\mathbf{k}_2-\mathbf{k}_4)^2} + \frac{(k_{2z}-k_{3z})^2}{(\mathbf{k}_2-\mathbf{k}_3)^2}\right]\right\}, \tag{5}$$

$$\Phi_{1;234} = -\frac{\pi\mu^2}{6V}(\sin^2\theta_2 e^{2i\varphi_2} + \sin^2\theta_3 e^{2i\varphi_3} + \sin^2\theta_4 e^{2i\varphi_4}), \tag{6}$$

V is the volume of the specimen, θ and φ are the polar angles of the vector k; the polar axis is chosen along the easy magnetization axis.

$\varkappa_{sl}$ is the Hamiltonian of the interaction of the spin-waves with the phonons:

$$\varkappa_{sl} = \sum_{123j} \{\psi_{12;3} a_1^+ a_2^+ b_{3j} + \psi_{123} a_1^+ a_2 b_{3j}\} + \text{comp.conj.}, \tag{7}$$

$$\psi_{12;3} = \frac{i}{2}\gamma\mu M_0 \left(\frac{\hbar}{2\rho V \omega_{3j}}\right)^{1/2} e_{3j}^- f_3^-; \quad f_3^- = f_3^x - i f_3^y;$$

$$e_{3j}^- = e_{3j}^x - i e_{3j}^y; \tag{8}$$

$$\psi_{123} = i\gamma\mu M_0 \left(\frac{\hbar}{2\rho\omega_{3j}V}\right)^{1/2} (f_3 e_{3j} - 3 f_{3z} e_{3j}^z), \tag{9}$$

where γ is the magnetostriction constant, e_{3j} is the unit vector of the polarization of the accoustic wave vector f_3 and polarization j (j takes on three values), $\omega_{3j} = c_j f$ (c_j is the speed of sound), and ρ is the density of the specimen.

$\varkappa_h$ is the Hamiltonian of the interaction with the alternating magnetic field circularly polarized as described above*:

$$\varkappa_h = -\left(\frac{\mu M_0 V}{2}\right)^{1/2} h_0 (a_0 e^{-i\omega t} + a_0^+ e^{i\omega t}), \tag{10}$$

here h_0 is the amplitude of the alternating field, and ω is its frequency. Inasmuch as the photon momentum in the radiofrequency range is appreciably smaller than the momenta of quasiparticles (spin-waves and phonons), the alternating field may be regarded as homogeneous.

In Eqs.(5) and (9) we have omitted terms associated with exchange interaction (see Eqs.(3.15') in Ref.1 and (11.5) in Ref.2). In addition, we have neglected terms of higher orders in the expression for $\varkappa_h$, appearing in the expansion of the moment operators in powers of a^+a (see Eq.(3.4) in Ref.1). This is justified inasmuch as with accuracy to second order perturbation theory (to which we restrict our consideration), these terms make no significant contribution to the absorption of the magnetic field.[3,4]

For calculating the transition matrix elements it is convenient to use expansion of the S matrix in powers of interaction. The absorption coefficients are determined by first order terms in the expansion of the S matrix. Terms not containing interaction, as will be evident from Eq.(10), vanish. Hence in the approximation of lowest order in interaction and of first order in the alternating field the expansion of the S matrix is of the form

$$S = 1 - \frac{1}{\hbar^2} \iint_{-\infty}^{\infty} dt_1\, dt_2 T \varkappa_{int}(t_1)\, \varkappa_h(t_2), \tag{11}$$

where $\varkappa_{int} = \varkappa_{ss} + \varkappa_{sl}$; the operators $\varkappa_{int}$ and $\varkappa_h$ are taken in the interaction representation for which the time dependence of the operators a_k and a_k^+ is given by the factors $e^{-\frac{i\varepsilon_k t}{\hbar}}$ and $e^{\frac{i\varepsilon_k t}{\hbar}}$, respectively, and T is the time ordering operator.

1. Interaction of spin-waves with each other

It can readily be shown that third order terms in $\varkappa_{ss}$ make no contribution to the S matrix, inasmuch as for the processes involved (see Fig.1a) conservation of

---

*The transition to resonance polarization corresponds to change of the sign of ω in Eq.(10).

momentum and energy do not obtain simultaneously.

Processes described by fourth order terms that make a nonzero contribution to the S matrix are shown in Fig.1b and 1c. For these processes, using Wick's theorem and the fact that the relation between the operators a_λ^+ and a_μ is described by

$$\overrightarrow{a_\lambda^+(t_1)}\,a_\mu(t_2) = \frac{i}{2\pi}\,\delta_{\lambda\mu}\int_{-\infty}^{\infty}\frac{e^{i\omega'(t_1-t_2)}}{\omega'-\omega_\lambda+i\delta}\,d\omega',\ (\delta\to+0),$$

we can calculate the corresponding transition probabilities. The probability W_1 of break up of a spin-wave into two spin-waves with emission of a photon (Fig.1,b) is given by the following expression

$$W_1 = \frac{64\pi}{\hbar}\,\mu M_0 V h_0^2\,\frac{|\Phi_{0\lambda;\mu\nu}|^2}{(\varepsilon_0+\hbar\omega)^2}\,n_\lambda(n_\mu+1)(n_\nu+1)\,\delta(\hbar\omega+\varepsilon_\mu+\varepsilon_\nu-\varepsilon_\lambda), \tag{12}$$

$$\mathbf{k}_\lambda = \mathbf{k}_\mu + \mathbf{k}_\nu.$$

The expression for the probability W_2 of merging of two spin-waves into one with emission of a photon (Fig.1,c) is given by

$$W_2 = \frac{36\pi}{\hbar}\,\mu M_0 V h_0^2\,\frac{|\Phi_{\mu;\varkappa\lambda 0}|^2}{(\varepsilon_0+\hbar\omega)^2}\,n_\varkappa n_\lambda(n_\mu+1)\,\delta(\varepsilon_\varkappa+\varepsilon_\lambda-\varepsilon_\mu-\hbar\omega), \tag{13}$$

$$\mathbf{k}_\varkappa + \mathbf{k}_\lambda = \mathbf{k}_\mu.$$

The zero index on the amplitudes Φ corresponds to the wave vector of the photon, which we neglected; in our case of a field circularly polarized perpendicular to the easy magnetization axis $\theta_0 = 0$.

From Eqs.(5) and (6), invoking the laws of conservation of momentum, we obtain

$$\Phi_{0\lambda;\mu\nu} = -\frac{\mu^2}{8V}\,[2\beta+3\pi-\pi\cos^2\theta_\lambda-5\pi(\cos^2\theta_\mu+\cos^2\theta_\nu)],$$

$$\Phi_{\mu;\,\varkappa\lambda 0} = -\frac{\pi\mu^2}{6V}\,(\sin^2\theta_\varkappa e^{2i\varphi_\varkappa}+\sin^2\theta_\lambda e^{2i\varphi_\lambda}). \tag{14}$$

The absorption coefficient is expressed in terms of the probabilities of the "forward" and "reverse" transitions:

$$\Gamma = \frac{8\pi\hbar\omega}{h_0^2 V}\sum\{W_{if}-W_{fi}\}, \tag{15}$$

where W_{if} is the probability for a "forward" and W_{fi} is the probability for a "reverse" transition. The summation is carried out over the wave vectors of the spin-waves participating in the given process, and also over all the processes.

Making use of Eqs.(12)-(15) and going over from summation to integration and replacing the spin-wave occupation numbers by Bose functions, we obtain

$$\Gamma_{ss} = \Gamma_{ss}^{(1)} + \Gamma_{ss}^{(2)},\quad \Gamma_{ss}^{(1)} = \frac{8\omega\mu M_0}{\pi^4(\varepsilon_0+\hbar\omega)^2}\,V^2\left(e^{\frac{\hbar\omega}{T}}-1\right)\iint\frac{dk_\mu\,dk_\nu\,|\Phi_{0\lambda;\,\mu\nu}|^2\,e^{\frac{\varepsilon_\mu+\varepsilon_\nu}{T}}\,\delta(\varepsilon_\mu+\varepsilon_\nu-\varepsilon_\lambda+\hbar\omega)}{\left(e^{\frac{\varepsilon_\mu}{T}}-1\right)\left(e^{\frac{\varepsilon_\nu}{T}}-1\right)\left(e^{\frac{\varepsilon_\mu+\varepsilon_\nu+\hbar\omega}{T}}-1\right)},$$

$$\Gamma_{ss}^{(2)} = \frac{9\omega\mu M_0}{4\pi^4(\varepsilon_0+\hbar\omega)^2}\,V^2\left(1-e^{-\frac{\hbar\omega}{T}}\right)\iint\frac{dk_\mu\,dk_\nu\,|\Phi_{\lambda;\,\mu\nu_0}|^2\,e^{\frac{\varepsilon_\mu+\varepsilon_\nu}{T}}\,\delta(\varepsilon_\mu+\varepsilon_\nu-\varepsilon_\lambda-\hbar\omega)}{\left(e^{\frac{\varepsilon_\mu}{T}}-1\right)\left(e^{\frac{\varepsilon_\nu}{T}}-1\right)\left(e^{\frac{\varepsilon_\mu+\varepsilon_\nu}{T}}-1\right)}, \tag{16}$$

$$\mathbf{k}_\lambda = \mathbf{k}_\mu + \mathbf{k}_\nu.$$

the δ-functions are most conveniently eliminated by integration over the difference $\varphi_\mu - \varphi_\nu$. Carrying out, in addition, all the other integrations, after rather

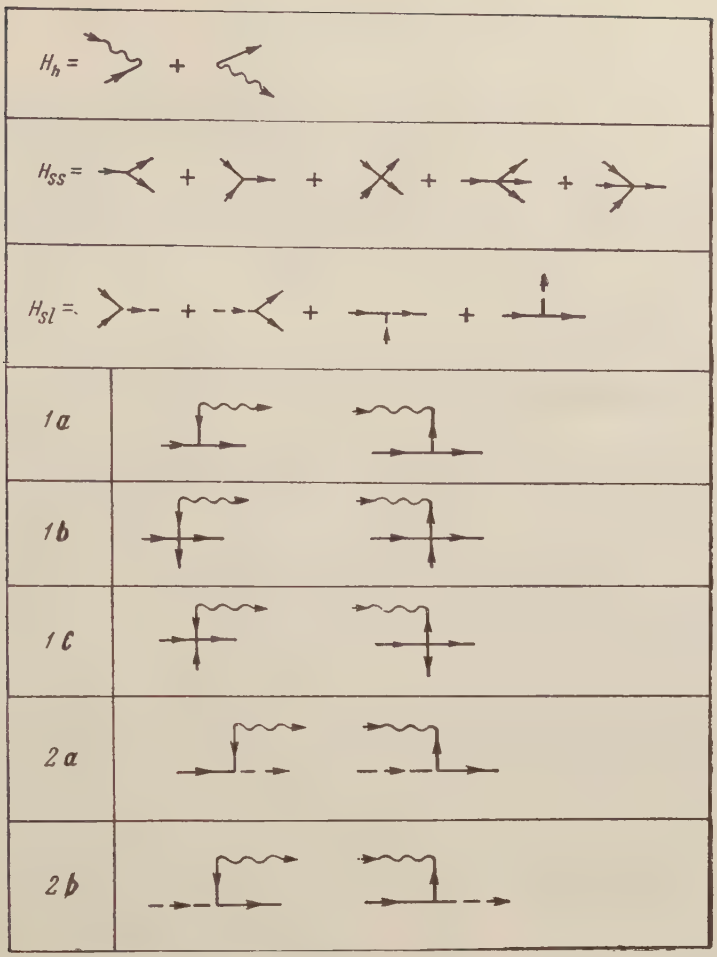

Schematic representation of processes. The solid lines represent spin-waves, the wavy lines represent a photon with zero momentum and energy $\hbar\omega$; the dashed lines correspond to phonons.

cumbersone computations, we obtain for the different limiting cases:

a) "high temperatures"* ($T \gg \varepsilon_0$):

$$\Gamma_{ss} \approx \begin{cases} A_1\omega \left(\frac{w}{\theta_c}\right)^2 \frac{\mu M_0}{\theta_c} \cdot \frac{\hbar\omega T^2}{\varepsilon_0^3}, & \hbar\omega \ll \varepsilon_0, \\ A_2 g M_0 \left(\frac{w}{\theta_c}\right)^2 \frac{T^2}{\hbar\omega\theta_c}, & \varepsilon_0 \ll \hbar\omega \ll T, \\ \frac{4}{15}\sqrt{\frac{\pi}{2}}\,\zeta(3/2)\, g M_0 \left(\frac{w}{\theta_c}\right)^2 \frac{T^{3/2}}{(\hbar\omega)^{1/2}\theta_c}, & \hbar\omega \gg T, \end{cases} \tag{17}$$

where $w = \frac{\mu^2}{a^3}$ is the dipole-dipole interaction energy; rough evaluation of the numerical coefficients yields $A_1 \approx A_2 \approx 10^3$;

b) low temperatures ($T \ll \varepsilon_0$):

---

*We recall that in all cases the temperature is assumed to be much lower than the Curie point ($T \ll \theta_c$).

$$\Gamma_{ss} \approx \begin{cases} B_1 \omega \left(\frac{w}{\theta_c}\right)^2 \frac{\mu M_0}{\theta_c} \frac{\hbar\omega T^{1/2}}{\varepsilon_0^{3/2}} e^{-\frac{3\varepsilon_0}{T}}, & \hbar\omega \ll \varepsilon_0, \\ \frac{4}{15}\sqrt{\frac{\pi}{2}}\,\omega \left(\frac{w}{\theta_c}\right)^2 \frac{\mu M_0}{\theta_c} \left(\frac{T}{\hbar\omega}\right)^{3/2} e^{-\frac{3\varepsilon_0}{T}}, & \hbar\omega \gg \varepsilon_0, \end{cases} \tag{18}$$

where

$$B_1 = \frac{15\pi^{7/2}}{8\sqrt{2}}\left\{121 + \frac{1}{15}\left[\left(\frac{2\beta}{\pi} - \frac{2}{3}\right)^2 + \frac{121}{45}\right]\right\} + \frac{4}{15}\sqrt{\frac{\pi}{2}} \approx 10^4$$

(for not excessively large β).

2. Interaction of spin-waves with phonons

Let us now consider the influence of the interaction of spin-waves with phonons on the absorption in the magnetic field. Absorption in this case occurs because of transformation of a phonon and a photon into a spin-wave and also because of merging of a spin-wave and photon with the formation of a phonon (see Eqs.(1), (7) and (11) and Figs.2a and 2b). We denote the corresponding field absorption coefficients by $\Gamma_{sl}^{(1)}$ and $\Gamma_{sl}^{(2)}$, respectively.

Proceeding much as above, we obtain

$$\Gamma_{sl}^{(1)} = \frac{2\hbar\omega\,(\mu M_0)^3\gamma^2}{\pi\rho\,(\varepsilon_0+\hbar\omega)^2}\left(e^{\frac{\hbar\omega}{T}}-1\right)\sum_j \int \frac{|e_j^- f^-|^2 e^{\frac{\hbar\omega_j(f)}{T}}\,\delta(\varepsilon_f - \hbar\omega_j(f) - \hbar\omega)}{\omega_{fj}\left(e^{\frac{\hbar\omega_j+\hbar\omega}{T}}-1\right)\left(e^{\frac{\hbar\omega_j}{T}}-1\right)}\,df, \tag{19}$$

$$\Gamma_{sl}^{(2)} = \frac{\hbar\omega\,(\mu M_0)^3\gamma^2}{2\pi\rho\,(\varepsilon_0+\hbar\omega)^2}\left(1-e^{-\frac{\hbar\omega}{T}}\right)\sum_j \int \frac{(fe_j - 3f_z e_j^z)^2 e^{\frac{\hbar\omega_j}{T}}\,\delta(\hbar\omega_j - \varepsilon_f - \hbar\omega)}{\omega_j\left(e^{\frac{\hbar\omega_j-\hbar\omega}{T}}-1\right)\left(e^{\frac{\hbar\omega_j}{T}}-1\right)}\,df, \tag{20}$$

The δ-functions in this case are best eliminated by integration over f. Using the explicit form of the f dependences of ε_f and $\hbar\omega_j$, we obtain

$$\delta(\hbar\omega_j - \varepsilon_f \pm \hbar\omega) = \frac{1}{\theta_c a^2}\,\delta[(f-f_1)(f-f_2)], \tag{21}$$

where

$$f_1 = \frac{\hbar c_j}{2\theta_c a^2} + \sqrt{\left(\frac{\hbar c_j}{2\theta_c a^2}\right)^2 - \frac{\varepsilon_0 \mp \hbar\omega}{\theta_c a^2}}, \tag{22}$$

$$f_2 = \frac{\hbar c_j}{2\theta_c a^2} - \sqrt{\left(\frac{\hbar c_j}{2\theta_c a^2}\right)^2 - \frac{\varepsilon_0 \mp \hbar\omega}{\theta_c a^2}} \tag{23}$$

(the upper signs correspond to $\Gamma_{sl}^{(1)}$; the lower signs to $\Gamma_{sl}^{(2)}$).

After integration over f in the denominators in the expressions under the integrals above, as will be evident from Eqs.(21)-(23), there appears the factor

$$\sqrt{\left(\frac{\hbar c_j}{2\theta_c a^2}\right)^2 - \frac{\varepsilon_0 \mp \hbar\omega}{\theta_c a^2}}\,.$$

If the speed of sound c_j were independent of the direction of propagation, this root could be taken out from under the integral. Then at frequencies

$$\hbar\omega = \mp\frac{\theta_j^2}{4\theta_c} \mp \varepsilon_0 \quad \left(\theta_j = \frac{\hbar c_j}{a}\right)$$

the absorption coefficient would have singularities. Actually, however, even in a cubic crystal the speed of sound depends on the direction of the vector f. After integration over angles the singularities vanish. From Eqs.(22) and (23) it is evident that the absorption coefficient $\Gamma_{sl}^{(1)}$ is nonzero for all frequencies if $\varepsilon_0 < \frac{1}{4} \cdot \frac{\hbar^2 c_{\max}}{\theta_c a^2}$, while if $\varepsilon_0 > \frac{1}{4} \cdot \frac{\hbar^2 c_{\max}^2}{\theta_c a^2}$ it is nonzero only at frequencies greater than $\omega_g^{(1)} = \frac{\varepsilon_0}{\hbar} - \frac{1}{4} \cdot \frac{\hbar c_{\max}^2}{\theta_c a^2}$. Near the point $\omega = \omega_g^{(1)}$ the coefficient $\Gamma_{sl}^{(1)} \sim \sqrt{\omega - \omega_g^{(1)}}$.

Analogously, if $\varepsilon_0 > \frac{1}{4} \cdot \frac{\hbar^2 c_{\max}^2}{\theta_c a^2}$, the coefficient $\Gamma_{sl}^{(2)} = 0$ at all frequencies, while if $\varepsilon_0 < \frac{1}{4} \cdot \frac{\hbar^2 c_{\max}^2}{\theta_c a^2}$, the coefficient $\Gamma_{sl}^{(2)} \neq 0$ for $\omega < \omega_g^{(2)} = \frac{1}{4} \cdot \frac{\hbar c_{\max}^2}{\theta_c a^2} - \frac{\varepsilon_0}{\hbar}$. Near the point $\omega = \omega_g^{(2)}$ the absorption coefficient $\Gamma_{sl}^{(2)} \sim \sqrt{\omega_g^{(2)} - \omega}$. The absorption coefficient $\Gamma_{sl}^{(1)}$ goes to zero at $\omega = \omega_g^{(1)}$ and $\omega = \infty$, while $\Gamma_{sl}^{(2)} = 0$ at $\omega = 0$ and $\omega = \omega_g^{(2)}$. This means that each of these coefficients has a maximum. The less the speed of sound depends on the direction of vector f, the higher will be these maxima and the closer they will be located to the frequencies $\omega_g^{(1)}$ and $\omega_g^{(2)}$.

Comparison of the coefficients Γ_{sl} and Γ_{ss} shows that for the usual values of the constants entering into the expressions for Γ the absorption due to interaction with phonons is appreciably less than the absorption due to interaction of the spin-waves with each other.

We take this opportunity to thank I.M.Lifshits for valuable discussions.

Physical-Technical Institute,
Academy of Sciences of the Ukrainian SSR

References

1. A.I.Akhiezer, V.G.Bar'yakhtar & M.I.Kaganov, Uspekhi fiz.nauk, 71, 533 (1960). (Trans.Soviet Physics - Uspekhi.)

2. A.I.Akhiezer, V.G.Bar'yakhtar & M.I.Kaganov, Ibid., 72 (1960). (Trans. Ibid.)

3. A.I.Akhiezer, V.G.Bar'yakhtar & M.I.Kaganov, Zhur.eksp.i teor.fiz., 40, 365 (1961). (Trans.Soviet Physics - JETP.)

4. M.I.Kaganov & V.M.Tsukernik, Ibid., 39, 518 (1960). (Trans.Ibid.)

CONCERNING A MECHANISM OF ABSORPTION OF THE LONGITUDINAL MAGNETIC FIELD BY A FERROMAGNETIC DIELECTRIC

- M.I.Kaganov & V.M.Tsukernik

In an earlier contribution[1] we investigated absorption by a ferromagnetic dielectric of the energy of an alternating magnetic field polarized along an easy magnetization axis. The absorption of the field for $\omega\tau_{ss} \ll 1$, where τ_{ss} is the relaxation time in the system, was calculated by means of a kinetic equation for the distribution of the spin-waves (it was assumed that the temperature of the material is appreciably below the Curie point θ_c). In the case of higher frequencies the predominant role in absorption is played by break up of the photon into two spin-waves with opposite momenta. This process was also considered in Ref.1. However, as was noted in this contribution, the break up of a photon into two spin-waves occurs only at frequencies ω greater than $\frac{2\varepsilon_0}{\hbar}$, where ε_0 is the energy of a spin-wave with zero momentum. Yet there is a broad frequency range $\frac{1}{\tau} \ll \omega < \frac{2\varepsilon_0}{\hbar}$, which was not considered.

The subject of the present communication is the absorption in this frequency range. The interaction Hamiltonian of the spin-waves with each other and also with the longitudinal alternating magnetic field in the lowest order approximation in spin-waves is of the form

$$H' = H_{int} + H_h, \tag{1}$$

where

$$H_{int} = \sum_{132}' \Phi_{12;3} a_1^+ a_2^+ a_3 + \text{compl. conj.}, \tag{2}$$

$$H_h = \frac{1}{2}\mu h_0 (e^{i\omega t} + e^{-i\omega t}) \sum_{\mathbf{k}} a_{\mathbf{k}}^+ a_{\mathbf{k}}, \tag{2'}$$

h_0 is the amplitude of the alternating field; for the other notations see Ref.2. As for the strong exchange interaction between the spin-waves, it can be shown that in the given approximation (second approximation of perturbation theory) it makes no significant contribution to the absorption.

It will be evident from Eqs.(1) and (2) that the matrix elements of the transitions are linear in the alternating field and nonzero only in the second (and higher) approximation of perturbation theory; the corresponding processes are a) merging of a photon with a spin-wave with the formation of two spin-waves and b) merging of two spin-waves and a photon into one spin-wave.

The calculations of the corresponding absorption coefficients Γ_a and Γ_b are analagous to those described in Ref.3. Here we give only the final results for the total absorption coefficient $\Gamma = \Gamma_a + \Gamma_b$ with an accuracy to within a numerical factor of the order of unity.

At high temperatures $(\varepsilon_0 \ll T \ll \theta_c)$;

$$\Gamma \sim \begin{cases} gM_0 \dfrac{w^2}{\varepsilon_0 \theta_c} \left(\dfrac{T}{\theta_c}\right)^2, & \dfrac{\hbar}{\tau_{ss}} \ll \hbar\omega \ll \varepsilon_0, \\ gM_0 \dfrac{w^2}{\hbar\omega\theta_c} \left(\dfrac{T}{\theta_c}\right)^2, & \varepsilon_0 \ll \hbar\omega \ll T, \\ gM_0 \dfrac{w^2}{\theta_c^{3/2}(\hbar\omega)^{1/2}} \left(\dfrac{T}{\theta_c}\right)^{3/2}, & T \ll \hbar\omega \ll \theta_c. \end{cases}$$

At low temperatures ($T \ll \varepsilon_0$) :

$$\Gamma \sim \begin{cases} gM_0 \dfrac{w^2}{\theta_c^2} \left(\dfrac{\varepsilon_0}{\theta_c}\right)^{1/2} \left(\dfrac{T}{\theta_c}\right)^{1/2} e^{-\frac{3\varepsilon_0}{T}}, & \dfrac{\hbar}{\tau_{ss}} \ll \hbar\omega \ll \varepsilon_0, \\ gM_0 \dfrac{w^2}{\theta_c^{3/2}(\hbar\omega)^{1/2}} \left(\dfrac{T}{\theta_c}\right)^{3/2} e^{-\frac{\varepsilon_0}{T}}, & \hbar\omega \gg \varepsilon_0. \end{cases}$$

Comparison of these results with the coefficient of absorption due to break up of a photon into two spin-waves[1] shows that the process considered here is significant only when $\hbar\omega < 2\varepsilon_0$.

Physical-Technical Institute,
Academy of Sciences of the Ukrainian SSR

References

1. M.I.Kaganov & V.M.Tsukernik, Zhur.eksp.i teor.fiz., 37, 823 (1959). (Trans.Soviet Physics - JETP.)
2. A.I.Akhiezer, V.G.Bar'yakhtar & M.I.Kaganov, Uspekhi fiz.nauk, 71, 533 (1960). (Trans.Soviet Physics - Uspekhi.)
3. M.I.Kaganov & V.M.Tsukernik, Present issue of the Bulletin, p.1358.

TEMPERATURE DEPENDENCE OF THE WIDTH OF FERROMAGNETIC RESONANCE PEAKS

- Mêng Hsein-Cheng

Van Vleck[1] was the first to advance the notion that broadening of ferromagnetic resonance peaks may be caused by disorder of the ions in the lattice. Clogston et al[2] later used this notion in the first quantum mechanical analysis, investigating elementary excitations in which energy is, but momentum is not conserved. They assumed that the scattering of spin waves with $k=0$ and the appearance of spin waves with $k\neq 0$ are due to variations in the pseudodipolar interaction in a lattice with chaotic distribution of the ions. In the spin wave approximation they found that $2\Delta H\sim\sqrt{M_0}$. Hypothesizing the same mechanism, P'u Fu-Chue and the author[3] employed Green's functions to calculate the magnetic susceptibility tensor, from which $2\Delta H$ was determined. The result is in agreement with that of Clogston et al. Izyumov[4] also postulated the same mechanism but at a certain stage in the analysis he replaced the spin operator $\hat{s}_j^z$ by its mean value and found that in the spin-wave approximation $\Delta H\sim M$. It is evident from the work of White[5], however, that the factor mainly responsible for the width of the resonance peaks cannot be pseudodipolar interactions.

Callen & Pittelli[6] recently took into account the dependence of the internal spin-spin and spin-orbit coupling energy on the position of the ion in the crystal lattice.[7,8] In view of this, the perturbation due to disordering of the ions can give rise to intense scattering of spin waves with $k=0$. On the basis of this mechanism, Callen & Pittelli found the same dependence of $2\Delta H$ on M_0 as in Ref.2, along with anisotropy of $2\Delta H$.

By adopting the Callen-Pittelli[6] model but without restricting ourselves to the spin-wave approximation, we can use Pauli operators to arrive at a result that hypothetically should be valid for all temperatures.

Let us assume that only two kinds of ions, A and B, are found in the octahedral sites of the spinel lattice. We then separate these ions into four groups according to the directions of their crystallographic fields, namely parallel to: 1) $[111]$; 2) $[\bar{1}\bar{1}1]$; 3) $[1\bar{1}\bar{1}]$; 4) $[\bar{1}1\bar{1}]$. We designate the unit vectors in these directions by E_t $(t=1,\ 2,\ 3,\ 4)$.

According to Callen & Pittelli[6], the first and second order perturbation energy due to internal spin-spin and spin-orbit coupling is equal to $D(\mathbf{E}_t\cdot\hat{\mathbf{S}}_j)^2$. The Hamiltonian of the system is of the form:

$$\hat{H}=\hat{H}_0+(D_A-D_B)\sum(q_j-c)\,P_{tj}\,(\mathbf{E}_t\hat{\mathbf{S}}_j)^2, \tag{1}$$

where $\hat{H}_0$, c, q_j and P_{tj} have the same meanings as in Ref.6.

Consider the most general case of a ferrite ellipsoid. The crystallographic axes are directed along ξ_i and the principal axes of the ellipsoid along $x_i'(i=1,2,3)$. The resultant magnetization is parallel to the x_3 axis (one axis of the coordinate system $x_i(i=1,2,3)$). In general, M is not parallel to the external field.

We now transform from the operators $\hat{S}_j$ to the operators $\hat{b}_j$ and $\hat{b}_j^+$:[9]

$$\hat{S}_j^x+\hat{S}_j^y=\sqrt{2S}\left(1-\frac{\hat{n}_j}{2S}\right)^{\frac{1}{2}}\hat{b}_j,\quad \hat{S}_j^x-i\hat{S}_j^y=\sqrt{2S}\,\hat{b}_j^+\left(1-\frac{\hat{n}_j}{2S}\right)^{\frac{1}{2}}, \tag{2}$$

$$\hat{S}_j^z=S-\hat{n}_j\,(\hat{n}_j=\hat{b}_j+\hat{b}_j);$$

these operators obey the following rules:

$$[\hat{b}_j, \hat{b}_{j'}] = 0,$$
$$[\hat{b}_j, \hat{b}_j^+] = \delta_{jj'}\left(1 - \frac{2S+1}{(2S)!}\hat{b}_j^{+2S}\hat{b}_j^{2S}\right), \tag{3}$$
$$\hat{b}_j^{2S+1} = \hat{b}_j^{+2S+1} = 0.$$

Unfortunately, there is at present no suitable method to determine the explicit form of Green's functions for the $S \neq 1/2$ case, which compels us to apply the method developed for the $S = 1/2$ case in Ref.10. We introduce the operators $\hat{a}_k$, $\hat{a}_k^+$, $\hat{\sigma}_k$ and $\hat{\sigma}_k^+$, which are defined as follows:

$$\hat{b}_j = N^{-1}\sum l^{ikn_j}\hat{a}_k.$$
$$\hat{b}_j^+ = N^{-1}\sum e^{-ikr_j}\hat{a}_k^+, \tag{4}$$
$$\hat{a}_k = \operatorname{ch}\frac{\lambda_k}{2}\hat{\sigma}_k - \operatorname{sh}\frac{\lambda_k}{2}e^{2i\Phi k}\hat{\sigma}_{-k}^+,$$
$$\hat{a}_k^+ = \operatorname{ch}\frac{\lambda_k}{2}\hat{\sigma}_k^+ - \operatorname{sh}\frac{\lambda_k}{2}e^{-2i\Phi_k}\hat{\sigma}_{-k}. \tag{5}$$

It must be stressed that here $\hat{a}_k$, $\hat{a}_k^+$, $\hat{\sigma}_k$ and $\hat{\sigma}_k^+$ are not Bose operators, inasmuch as $\hat{b}_j$ represents a Pauli operator. It can be shown that the following commutation relations hold:

$$[\hat{a}_k, \hat{a}_{k'}^+] = \delta_{kk'} - \frac{1}{N^2}\sum e^{-i(k-k'+k_1-k_2)r_j}\hat{a}_{k_1} + \hat{a}_{k_2},$$
$$[\hat{a}_k, \hat{a}_{k'}] = 0,$$
$$[\hat{\sigma}_k, \hat{\sigma}_{k'}^+] = \left(\operatorname{ch}\frac{\lambda_k}{2}\operatorname{ch}\frac{\lambda_{k'}}{2} - \operatorname{sh}\frac{\lambda_k}{2}\operatorname{sh}\frac{\lambda_{k'}}{2}e^{2i(\Phi_k - \Phi_{k'})}\right)[\hat{a}_k, \hat{a}_{k'}^+],$$
$$[\hat{\sigma}_k, \hat{\sigma}_{k'}] = \frac{1}{N}\left(\operatorname{ch}\frac{\lambda_k}{2}\operatorname{sh}\frac{\lambda_{k'}}{2}e^{2i\Phi_{k'}} - \operatorname{sh}\frac{\lambda_k}{2}\operatorname{ch}\frac{\lambda_{k'}}{2}e^{2i\Phi_k}\right)\sum e^{-i(k+k')r_j}(1 - 2\hat{n}_j). \tag{6}$$

It can readily be shown that

$$\langle[\hat{a}_k, \hat{a}_{k'}^+]\rangle = 2\sigma S\delta_{kk'},$$
$$\langle[\hat{\sigma}_k, \hat{\sigma}_{k'}^+]\rangle = 2\sigma S\delta_{kk'}, \tag{7}$$
$$\langle[\hat{\sigma}_k, \hat{\sigma}_{k'}]\rangle = 0\ (\langle S_j^z\rangle = \sigma S).$$

At a certain stage of the calculations we use (7) instead of (6). It is apparent that this approximation is equivalent to the one used by Tyablikov[10].

The Hamiltonian is finally written as follows:*

$$\hat{H} = \hat{H}_0 + \sum f_1(k, k')\hat{\sigma}_k^+\hat{\sigma}_{k'} + \sum f_1^*(k, k')\hat{\sigma}_k\hat{\sigma}_{k'}^+ +$$
$$+ \sum f_2(k, k')\hat{\sigma}_k\hat{\sigma}_{k'} + \sum f_2^*(k, k')\hat{\sigma}_k^+\hat{\sigma}_{k'}^+; \tag{8}$$

here

$$f_1(k, k') = \frac{1}{4N}(D_A - D_B)\sum(q_j - c)P_{tj}e^{-i(k-k')r_j}\left\{U_t\left(\operatorname{sh}\frac{\lambda_k}{2}\operatorname{ch}\frac{\lambda_{k'}}{2}\times\right.\right.$$
$$\times e^{2i\Phi_k} + \operatorname{ch}\frac{\lambda_k}{2}\operatorname{sh}\frac{\lambda_{k'}}{2}e^{-2i\Phi_{k'}}\Big) + V_t\left(\operatorname{sh}\frac{\lambda_k}{2}\operatorname{sh}\frac{\lambda_{k'}}{2}e^{2i(\Phi_k - \Phi_{k'})} + \right.$$
$$\left.\left. + \operatorname{ch}\frac{\lambda_k}{2}\operatorname{ch}\frac{\lambda_{k'}}{2}\right) + 2iQ_t\left(\operatorname{sh}\frac{\lambda_k}{2}\operatorname{ch}\frac{\lambda_{k'}}{2}e^{2i\Phi_k} - \operatorname{ch}\frac{\lambda_k}{2}\operatorname{sh}\frac{\lambda_{k'}}{2}e^{-2i\Phi_{k'}}\right)\right\}, \tag{9}$$

---

*The Hamiltonian is given incorrectly in Ref.6.

$$f_2(k, k') = \frac{1}{4N}(D_A - D_B)\sum (q_j - c)\, P_{tj} e^{-i(\mathbf{k}+\mathbf{k}')\mathbf{r}_j}\left\{-U_t\left(\operatorname{ch}\frac{\lambda_k}{2}\operatorname{ch}\frac{\lambda_{k'}}{2} + \right.\right.$$
$$+ \operatorname{sh}\frac{\lambda_k}{2}\operatorname{sh}\frac{\lambda_{k'}}{2} e^{-2i(\Phi_k - \Phi_{k'})} - 2V_t \operatorname{ch}\frac{\lambda_k}{2}\operatorname{sh}\frac{\lambda_{k'}}{2} e^{-2i\Phi_{k'}} +$$
$$\left. + 2iQ_t\left(\operatorname{sh}\frac{\lambda_k}{2}\operatorname{sh}\frac{\lambda_{k'}}{2} e^{2i(\Phi_k - \Phi_{k'})} - \operatorname{ch}\frac{\lambda_k}{2}\operatorname{ch}\frac{\lambda_{k'}}{2}\right)\right., \tag{10}$$

where

$$\begin{aligned} V_t &= (\mathbf{E}_t\mathbf{e}_1)^2 - (\mathbf{E}_t\mathbf{e}_2)^2, \\ V_t &= (\mathbf{E}_t\mathbf{e}_1)^2 + (\mathbf{E}_t\mathbf{e}_2)^2 - 2(\mathbf{E}_t\mathbf{e}_3)^2, \\ Q_t &= (\mathbf{E}_t\mathbf{e}_1)(\mathbf{E}_t\mathbf{e}_2), \end{aligned} \tag{11}$$

$\mathbf{e}_i$ (i = 1,2,3) are unit vectors in the directions x_i (i = 1,2,3).

Assuming that the time derivative of $\hat{\sigma}_k$ is primarily dependent upon $\hat{\sigma}_k$ and $\hat{\sigma}_0$, i.e., neglecting all remaining terms with $\mathbf{k}' \neq \mathbf{k}$, we obtain

$$\begin{aligned} i\hbar\dot{\hat{\sigma}}_0 &= \omega_0\hat{\sigma}_0 + 2\sigma S\sum \alpha^*(k)\hat{\sigma}_k + 2\sigma S\sum \beta(k)\hat{\sigma}_k^+, \\ i\hbar\dot{\hat{\sigma}}_k &= \omega_k\hat{\sigma}_k + 2\sigma S\alpha(k)\hat{\sigma}_0 + 2\sigma S\beta(k)\hat{\sigma}_0^+, \end{aligned} \tag{12}$$

where

$$\begin{aligned} \alpha(k) &= f_1(k, 0) + f_1^*(0, k), \\ \beta(k) &= f_2(k, 0) + f_2^*(0, k), \end{aligned} \tag{13}$$

The following expressions are obtained for the frequencies ω_0 and ω_k:

$$\omega_0 = \gamma\sqrt{[H_0 + (N_{11} - N_{33})M][H_0 + (N_{22} - N_{33})M - N_{12}M^2]}, \tag{14}$$

$$\omega_k = \gamma\sqrt{(H_0 - N_{33}M + \sigma H_l a^2k^2)(H_0 - N_{33}M + \sigma H_l a^2k^2 + 4\pi M\sin^2\vartheta_k}, \tag{15}$$

where H_0 is the x-component of the external field and $\overleftrightarrow{N}$ is the demagnetization tensor.

Here, in contrast to the familiar expressions for ω_0 and ω_k, obtained in the spin-wave approximation, M is the magnetization at the given temperature, rather than at absolute zero. Moreover, the exchange term in ω_k depends on σ.

We now introduce the following Green's functions:[3]

$$\begin{aligned} G^{(1)}(t - t') &= \theta(t - t')\langle[\hat{\sigma}_0(t),\ \hat{\sigma}_0^+(t')]\rangle, \\ G^{(2)}(t - t') &= \theta(t - t')\langle[\hat{\sigma}_0^+(t),\ \hat{\sigma}_0(t)]\rangle. \end{aligned} \tag{16}$$

Making use of the general formula for the susceptibility tensor[10]

$$\chi_{xx} = \frac{N\pi g^2\beta^2 i}{2}(G_n^{(1)}(E) + G_n^{(2)}(E))_{E=\hbar\omega+i\varepsilon}, \tag{17}$$

it can be shown that near resonance

$$\chi_{xx}^{\cdot} = \frac{M\gamma^0}{2\omega_0}[H_0 + (N_{22} - N_{33})M]\frac{\Gamma_+}{(\omega - \omega_0)^2 + \Gamma_+^2}. \tag{18}$$

where

$$\Gamma_+ = \gamma\Delta H = \frac{\pi}{\hbar^2}\sum |\alpha(k)|^2\,\delta(\omega - \omega_k). \tag{19}$$

Finally, the following expression can be written for the width of the resonance line:

$$2\Delta H = 2\Delta H_0 + 2\Delta H_1 (\alpha_1^2\alpha_2^2 + \alpha_2^2\alpha_3^2 + \alpha_3^2\alpha_1^2), \tag{20}$$

where α_1, α_2 and α_3 are the direction cosines of M relative to the ξ_i axes,

$$2\Delta H_0 = \frac{4}{9} A\sigma^2 \int_0^{\pi} \left[\mathrm{sh}^2 \frac{\lambda_k}{2} k^2 \frac{\partial k}{\partial \omega} \right]_{\omega_k = \omega_0} \sin \vartheta_k \, d\vartheta_k; \tag{21}$$

$$2\Delta H_1 = 2A\sigma^2 \int_0^{\pi} \left[\left(\mathrm{ch}^2 \frac{\lambda_k}{2} + \frac{1}{9} \mathrm{sh}^2 \frac{\lambda_k}{2} \right) k^2 \frac{\partial k}{\partial \omega} \right]_{\omega_k = \omega_0} \sin \vartheta_k \, d\vartheta_k; \tag{22}$$

$$A = \frac{V}{N} \frac{S^2}{\pi\gamma\hbar^2} (D_A - D_B)^2 c (1 - c),$$

These equations can be rewritten in the form

$$2\Delta H_0 = 2S^2 c (1 - c) \left(\frac{D_A - D_B}{\gamma\hbar} \right)^2 \left(\frac{4\pi M_0}{He^3} \right)^{\frac{1}{2}} [I_1(\sigma) - I_2(\sigma)] \sigma, \tag{23}$$

$$2\Delta H_1 = 5S^2 c (1 - c) \left(\frac{D_A - D_B}{\gamma\hbar} \right)^2 \left(\frac{4\pi M_0}{He^3} \right)^{\frac{1}{2}} [2I_1(\sigma) + I_2(\sigma)] \sigma; \tag{24}$$

the functions $I_1(\sigma)$ and $I_2(\sigma)$ differ from their counterparts in Ref.6 in that M_0 is replaced by the magnetization M at the given temperature.

The deduced σ dependence of $2\Delta H$ differs from the results of the calculations in Refs.2 and 6. The latter involve the spin-wave approximation, so that only M_0 appears, and the final result essentially lacks any temperature dependence. Our analysis shows that these expressions cannot be extrapolated by the simple substitution of M for M_0 as was done in Ref.2. In the limit when $\sigma = 1$, i.e., at 0°K, our equations reduce to those obtained in the spin-wave approximation.* There is qualitative agreement with the final result of Ref.4 only provided $H \gg 4\pi M$.

In view of the fact that for many ferrites other mechanisms[11-13] come into play at low and high temperatures (near the Curie point), direct verification of the above deduced temperature dependence obviously presents great difficulties. The mechanism of line broadening near the Curie point[12,13] is isotropic. Therefore, in order to verify the proposed theory it is expedient to investigate the temperature variation of the anisotropic part of the line width.

I desire to express my gratitude to S.V.Tyablikov and A.G.Gurevich for their interest in the work; I must also thank P'u Fu-Chue for his help.

References

1. J.H.Van Vleck, Phys.Rev., 74, 1168 (1948); Ibid., 78, 266 (1950).

2. S.M.Clogston et al, J.Phys.Chem.Solids, 1, 129 (1956).

3. P'u Fu-Chue & Meng Hsien-Cheng, Doklad na soveshchanii po ferromagnitnomu rezonansu (Report presented at the Conference on Ferromagnetic Resonance), Leningrad, 1960.

4. Yu.A.Izyumov, Fizika metallov i metallovedenie, 10 No.1140 (1960). (Trans. Physics of Metals & Metallography.)

---

*Throughout the derivation we have used Eqs.(3) for the operators $\hat{b}_j$ and $\hat{b}_j^+$ with $S = 1/2$. If we adhere to these relations consistently, the results in the limit as T → 0 will not agree with those obtained in the spin-wave approximation.

5. R.L.White, Phys.Rev., 115, 1519 (1959).
6. H.B.Callen & E.Pittelli, Phys.Rev., 119, 1523 (1960).
7. A.Abraham & M.H.Pryce, Proc.Roy.Soc., A205, 135 (1951).
8. K.Yoshida & M.Tachiki, Progr.Theoret.Phys., 17, 331 (1957).
9. Yu.A.Izyumov, Doklady AN SSSR, 125, 1227 (1959). (Trans.Doklady.)
10. S.V.Tyablikov, Fizika tverdogo tela, 2, 2, 361 (1960). (Trans.Soviet Physics - Solid State.)
11. A.M.Clogston, Bell System Tech.J., 34, 739 (1955).
12. G.V.Skrotskii & L.V.Kurbatov, Fizika metallov i metallovedenie, 10, No.3, 335 (1960). (Trans.Physics of Metals & Metallography.)
13. P.G.De Gennes, C.Kittel & A.M.Portis, Phys.Rev., 116, 323 (1959).

FERROMAGNETIC RESONANCE IN FERRITES IN STRONG ALTERNATING MAGNETIC FIELDS

- A.G.Gurevich & S.S.Starobinets

For the purpose of investigating some of the features of ferromagnetic resonance at high power levels we measured χ''_{res}, $2\Delta H$ and H_{res} in yttrium garnet single crystals in a wide range of magnetic field amplitudes.

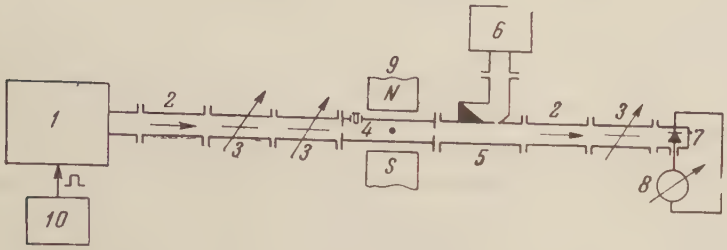

Fig.1. Diagram of set-up for measuring ferromagnetic resonance at high power levels: 1) pulse magnetron, 2) ferrite rectifier, 3) precision attenuator, 4) cavity with specimen, 5) directional coupler, 6) 45-I power meter, 7) crystal detector, 8) M-95 microammeter, 9) permanent magnet, 10) 26-I pulse generator.

The measurements were carried out at a frequency of 9375 Mc at room temperature and liquid nitrogen temperature and at different orientations of the constant external field in the (110) plane. The experimental set-up is diagramed in Fig.1. In order to avoid heating of the specimen we used a pulse generator for the high frequency oscillations: duty factor 1/4000 or lower; pulse duration 0.5 microsec. The specimen in the form of a ~0.5 mm diameter sphere was mounted in the antinode of the magnetic field in the TE_{106} rectangular cavity with two coupling holes. The cavity was tuned in the process of measurement by means of a piston. The precision attenuator located at the cavity input made it possible to carry out all measurements at a constant output power. The setting of the attenuator (attenuation) gave the power absorbed in the specimen and, consequently, the value of χ''. A similar method for measuring ferromagnetic resonance at high power levels was used earlier in our work[1] and in the experiments of Weiss[2] and Green & Schlömann[3]. The advantages of this procedure are that 1) the amplitude of the alternating magnetic field is the same at every point on the resonance curve, and 2) the measurement results do not depend on the characteristics of the crystal detector.

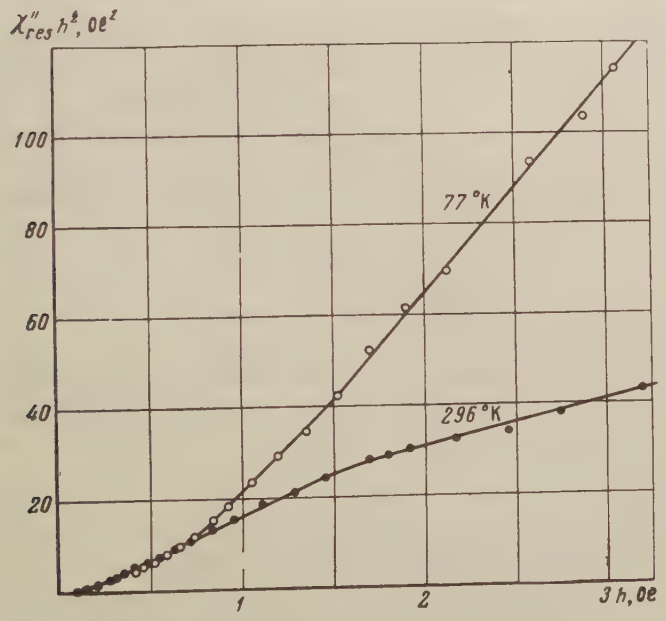

Fig.2. Variation of the resonance absorption $\chi''_{res}h^2$ with the amplitude of the alternating field h in an yttrium garnet single crystal. Constant field oriented in the [111] direction.

Fig.2 shows typical curves characterizing the variation of the absorbed power at resonance ($\chi''_{res}h^2$) with the amplitude of the alternating field. It will be seen that after a small initial section with χ''_{res}=const, , which is quadratic in the given coordinates, the absorbed power depends linearly on h, but there are evinced several linear

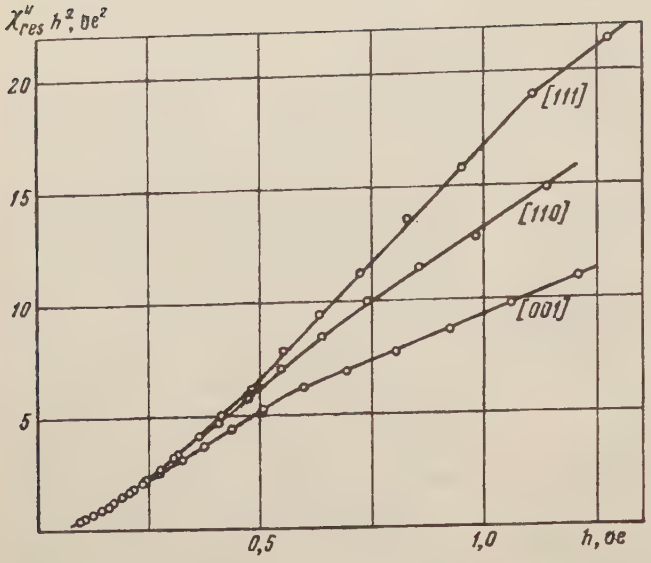

Fig.3. Variation of the resonance absorption with the alternating field amplitude for three crystallographic directions at 296°K.

sections with different slopes. According to the theory of Suhl[4], at sufficiently high field amplitudes, $\chi''_{res} \sim \frac{1}{h}$. It follows from our results that $\chi''_{res} = \frac{m}{h}\left(1 + \frac{h_1}{h}\right)$ where m and h_1 are constant quantities for each linear section. It may be assumed[1] that this h dependence of χ''_{res} is explained by increase in the amplitude of the uniform precession above the threshold of instability of the spin waves.

Noteworthy is the significant increase of the resonance loss in strong alternating fields with decrease of the temperature from 296 to 77°K (Fig.2), despite the fact that this decrease in temperature leads to broadening of the resonance curve at low power levels. We assume that this is explained by the influence of the rare earth impurities, which, as is known[5], becomes stronger with decrease in temperature. Earlier[1] we showed that increase in the rare earth impurity concentration also leads to growth of the resonance absorption in the range of high alternating fields.

The variation of the absorbed power with h for three different crystallographic directions is shown in Fig.3. Despite the fact that the anisotropy field, as we shall show below, virtually does not depend on h, the anisotropy of the resonance losses increases substantially with increase in amplitude of the alternating field.

Fig.4 shows the variation of the resonance field H_{res} with the angle θ rela-

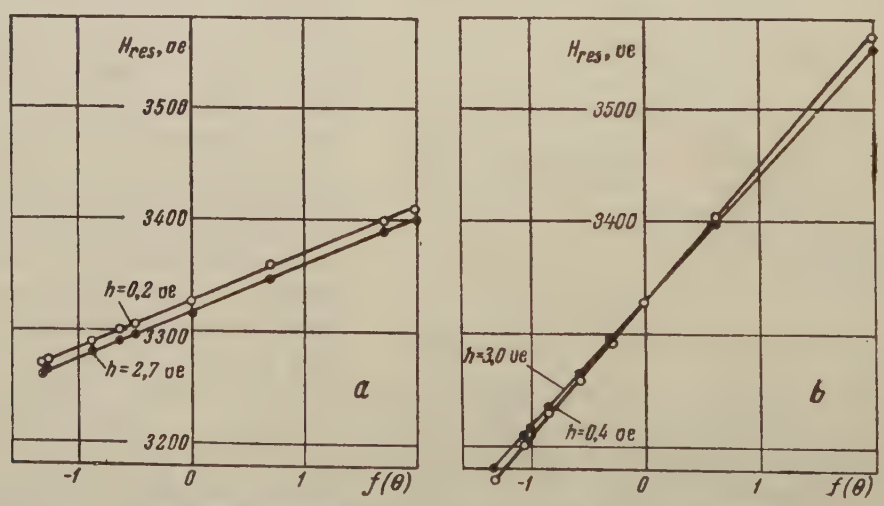

Fig.4. Variation of the resonance field H_{res} with the orientation in the (110) plane at low and high power levels: a) at 296°K, b) at 77°K.

tive to the [001] direction in the (110) plane for low and high power levels. Here the horizontal scale is laid off in terms of the function

$$f(\theta) = \frac{3}{16} + \frac{5}{4}\cos 2\theta + \frac{15}{16}\cos 4\theta$$

so that

$$H_{res} = \frac{\omega}{\gamma} - \frac{|K_1|}{M} f(\theta) \qquad (1)$$

Intersection of the line (1) with the vertical axis gives the value of the spectroscopic splitting factor g, while the slope of the line gives the anisotropy field.

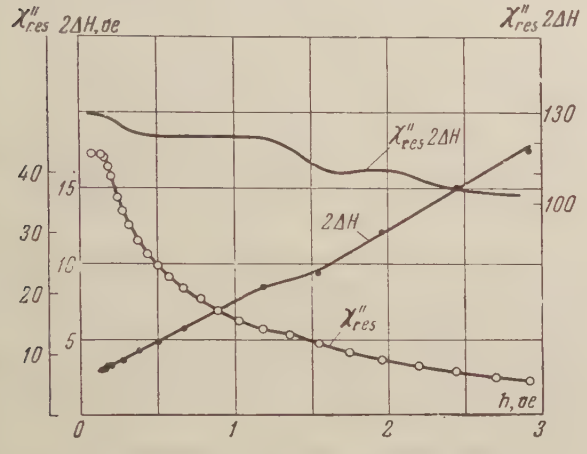

Fig.5. Variation of χ''_{res}, 2ΔH and $\chi''_{res}\cdot 2\Delta H$ with the amplitude of the alternating magnetic field at 296°K.

At room temperature (Fig.4,a) the g factor increases with increase of the power level. Weiss[6] found that with variation of the power level and, consequently, the spin temperature, the g factor behaves in the same way as with variation of the lattice temperature. The variation of the g factor with the lattice temperature for yttrium iron garnet was obtained by Dillon[7]. Evaluation shows that the spin system must heat up several hundred degrees to explain the increase of the g factor from 2.005 to 2.011, observed in our experiment.

At 77°K (Fig.4,b) the splitting factor does not depend on the power up to fields of the order of 3 oersted. This is in agreement with the independence of the g factor of the lattice temperature in the vicinity of 77°K.[7]

As will be evident from Fig.4, the value of $|K_1|/M$ at room temperature does not depend on the power level, but at liquid nitrogen temperature decreases from 118 oe at h = 0.4 to 112 oe at h = 3.0 oe. This result is obviously not consistent with the assumption that the anisotropy field depends identically on the spin and on the lattice temperature.

Fig.5 shows the variation of χ''_{res} and 2ΔH and of their product with the amplitude of the alternating field. As is known, in weak alternating fields $\chi''_{res}\cdot 2\Delta H = M$, where M is the permanent magnetization. The noticeable decrease of $\chi''_{res}\cdot 2\Delta H$ with increase in the field amplitude apparently indicates decrease of the magnetization as a result of increase in the amplitude of the spin waves.

References

1. A.G.Gurevich & S.S.Starobinets, Fizika tverdogo tela, 3, 1995 (1961). (Trans.Soviet Physics - Solid State.)
2. M.T.Weiss, J.Appl.Phys., 31, 778 (1960).
3. J.J.Green & E.Schlömann, IRE Trans.Microwave Theory and Techn., 8, N 1, (1960).
4. H.Suhl, Phys.Chem.of Solids, 1, 209 (1957).
5. P.-G. de Gennes, C.Kittel & A.M.Portis, Phys.Rev., 116, 323 (1959).
6. M.T.Weiss, J.Appl.Phys., 30, 12, 2013 (1959).
7. J.F.Dillon, Phys.Rev., 105, 759 (1957).

EFFECT OF INDUCED ANISOTROPY ON FERROMAGNETIC RESONANCE

- A.G.Gurevich, A.P.Safant'evskii, V.I.Solov'ev & E.S.Sher

Induced anisotropy develops in some ferrites as a result of ion or electron diffusion.[1-3] In polycrystalline specimens this anisotropy is uniaxial. When ion diffusion is responsible[1,2], at room temperature there is observed quasi-stable anisotropy, the axis of which is oriented in the direction of the magnetic field applied during heat treatment. Anisotropy due to electronic processes[3] does not "freeze" even at liquid nitrogen temperature: for several tens of seconds its axis at this temperature orients in the direction of the applied field. At room temperature this anisotropy is not observed. Electronic processes, similar to those giving rise to induced anisotropy, have at this temperature a relaxation time of the order of 10^{-5} sec and exert a substantial influence on the magnetic spectra[4].

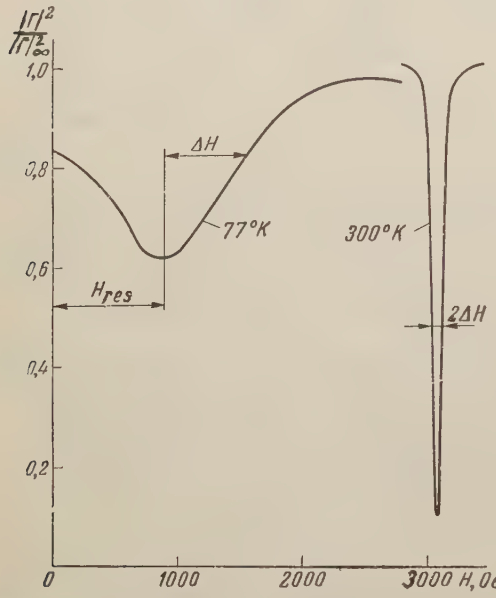

Fig.1. Variation of the reflection factor $|\Gamma|$ of the cavity containing the ferrite specimen with the magnetic field. Undoped specimen sintered at 1450°. $|\Gamma|_\infty$ - reflection factor far from ferromagnetic resonance. The levels at which $2\Delta H$ was determined were calculated according to Ref.6.

The purpose of the present work was to investigate the influence of induced anisotropy due to electronic processes on ferromagnetic resonance. The studies were carried out on polycrystalline specimens of yttrium garnet.

The ferromagnetic resonance measurements were carried out in the temperature range from 4.2 to 300°K at a wavelength of 3.2 cm. The measurement procedure in the 77 to 300°K temperature range was similar to that described in Ref.5. For measurements in the 4.2 to 77°K temperature range the rectangular cavity with the specimen was immersed in liquid helium, and the temperature variation recorded after boiling out of the helium.

The resonance field H_{res} and the width of the resonance curve $2\Delta H$ were determined from the reflection factor $|\Gamma|$ versus magnetic field curves, which were recorded by means of an EPP-09 recording potentiometer. Two such curves are shown in Fig.1. The temperature dependences of H_{res} and $2\Delta H$ for several specimens are reproduced in Fig.2. It will be evident from these curves that for specimens (without Mn impurity) sintered at a high temperature there obtains sharp increase of $2\Delta H$ with decrease of temperature. This growth of $2\Delta H$ in our case cannot be attributed to the influence of rare earth impurities[7] inasmuch as our initial yttrium oxide was ~99.995% pure. This growth also cannot be explained by broadening of the resonance curves in polycrystalline specimens owing to the influence of anisotropy and porosity (our specimens had a density $\geqslant$95% the theoretical value).

The reason for the broadening of the resonance curves for ferrites may be the presence of Fe^{2+} ions. There are two mechanisms capable of explaining the influence of Fe^{2+} ions. The first mechanism[8] links the additional source of relaxation with electron transitions between Fe^{2+} and Fe^{3+} ions. According to the second mechanism[9], the Fe^{2+} ions, which have a very high paramagnetic relaxation

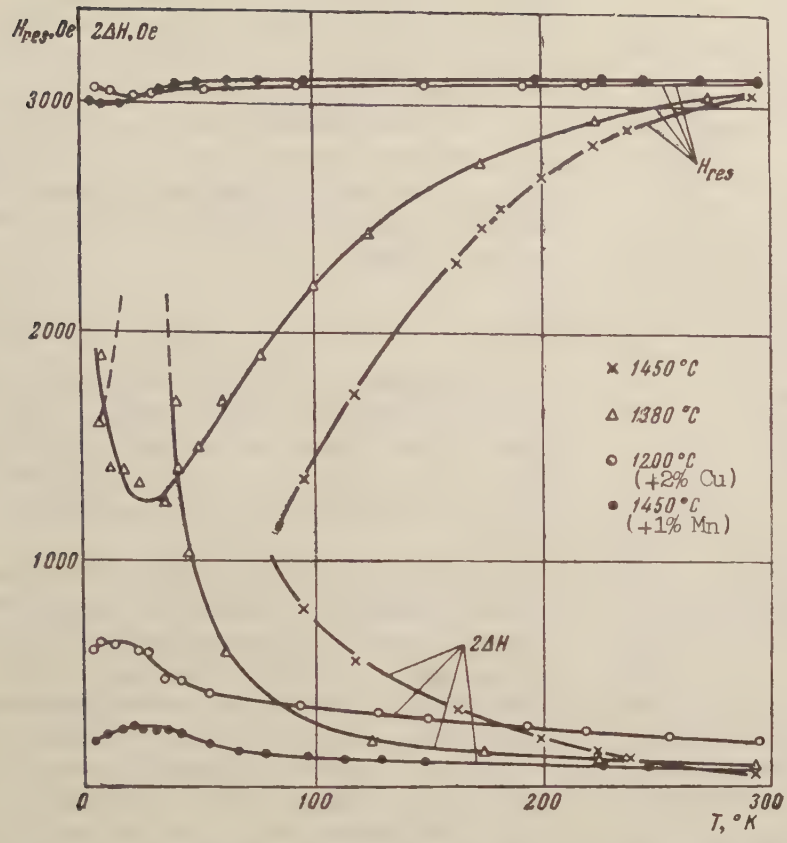

Fig.2. Temperature dependences of H_{res} and $2\Delta H$ for specimens sintered at different temperatures and specimens doped with Cu and Mn. (The impurity concentrations are indicated in percent by weight.)

frequency, like rare earth ions[7], transfer energy from the lattice spin system. Both mechanisms should yield a low temperature maximum of $2\Delta H$, which is actually evinced in the experimental curves (Fig.2). The theory based on the first mechanism[8] does not allow of determining the width of this peak. The width of the peak evaluated on the basis of the second mechanism[7] proves to be much smaller than the experimental value. Thus, for example, in the case of the specimen sintered at 1450° the content of Fe^{2+} amounted to 0.35% by weight* and the calculated value of $2\Delta H$ was ~100 Oe. The experimental value for the same specimen is greater than 2000 Oe (see Fig.2).

Thus the actual mechanism responsible for the broadening of the resonance peaks of the investigated specimens with decrease in temperature remains obscure. But, as will be shown below, this broadening is undoubtedly connected with the presence of Fe^{2+} ions.

As will be evident from Fig.2, simultaneously with increase of $2\Delta H$ with decrease of temperature, there occurs a marked decrease of H_{res}. For example, for the above mentioned specimen this decrease δH_{res} (referred to ω/γ) amounts to 2200 Oe (at 77°K).

The decrease in the value of the resonance field may, in general, be caused by one or more of the following factors:

1. The general dependence of the resonance frequency on attenuation (see, for example, Ref.10), which leads to the expression

$$H_{res} = \sqrt{H_{res_0}^2 - (\Delta H)^2}, \qquad (1)$$

where H_{res_0} is the resonance field in the absence of attenuation. In our case for the above mentioned specimen at 77°K $H_{res_0} - H_{res} \approx 40$ Oe.

2. Displacement of the resonance absorption peak in a polycrystalline specimen as a result of averaging over the grains. This shift is of the order of magnitude of K_1/M.[10] In our case at 77°K this shift equaled ~120 Oe.

---

*The chemical analyses were carried out by N.N.Parfenova, whom we take this opportunity to thank.

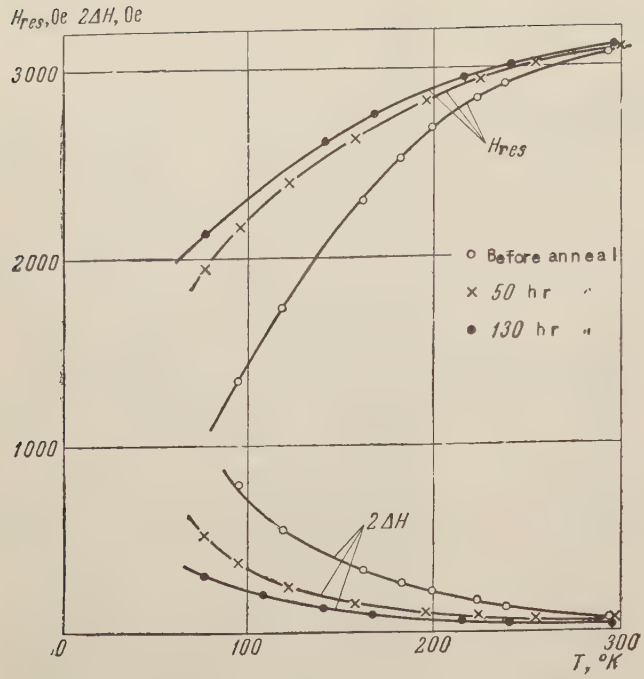

Fig.3. Effect of annealing in an atmosphere O_2 on H_{res} and $2\Delta H$. The undoped specimen sintered at 1450° was annealed in O_2 at 1000° for 50 hours and then for a further 80 hours.

3. Shift of the absorption peak due to porosity, which according to Ref.10 equals $2\pi M\rho$, where ρ is the relative porosity. In our case this shift could not exceed 60 Oe.

4. The presence of an effective induced anisotropy field. This field $H_{i.an}$, neglecting the above enumerated sources of decrease of H_{res}, can be evaluated as

$$H_{i.an} = \frac{\omega}{\gamma} - H_{res} \qquad (2)$$

Inasmuch as the first three factors can explain only a small fraction of the observed decrease of H_{res} at low temperatures, this decrease must be due mainly to induced anisotropy.

The induced anisotropy in this case is connected with the presence of Fe^{2+} ions. It is known[4,11] that the number of Fe^{2+} ions decreases with reduction of the sintering temperature, and, as will be evident from Fig.2, this decrease is accompanied by a substantial decrease of H_{res}. We note that a fairly high density at low sintering temperatures can be obtained through the addition of a small amount of Cu.

By preparing polycrystalline specimens of yttrium garnet with small amounts of Mn one can obtain[4,6,11] electric and magnetic properties characteristics of specimens with few or no Fe^{2+} ions even at high sintering temperatures. It will be evident from Fig.2 that the addition of 1% Mn by weight virtually eliminates induced anisotropy as well as the broadening of the curves at low temperatures due to the presence of Fe^{2+} ions. The number of Fe^{2+} ions can be reduced[4,11] by prolonged heating in an atmosphere of oxygen. This results in reduction of the induced anisotropy and $2\Delta H$ at low temperatures (Fig.3).

Thus all our experimental data substantiate the inference that the induced anisotropy in polycrystalline yttrium garnet is due to the presence of Fe^{2+} ions.

In order to determine how the induced anisotropy becomes established with time, we recorded the time variation of the reflection factor $|\Gamma|$ in the case of rapid (~0.1 sec) 90° rotations of the specimen in a constant field H_o.

At temperatures above about 130°K no change of $|\Gamma|$ was noted. At lower temperatures there are obtained time characteristics similar to those shown in Fig. 4: upon rotation of the specimen $|\Gamma|$ changes abruptly and then slowly returns to its initial value.

The H_o dependence of the sign and amplitude of the reflection factor jumps can be qualitatively explained if it is assumed that at the first instant after rotation the induce anisotropy is not fully established and the resonance curve is shifted a distance H_c to the side of higher fields relative to the position of the "static" curve at the given temperature (Fig.1). Assuming that this small shift of the curve occurs without change in its shape we can, on the basis of the

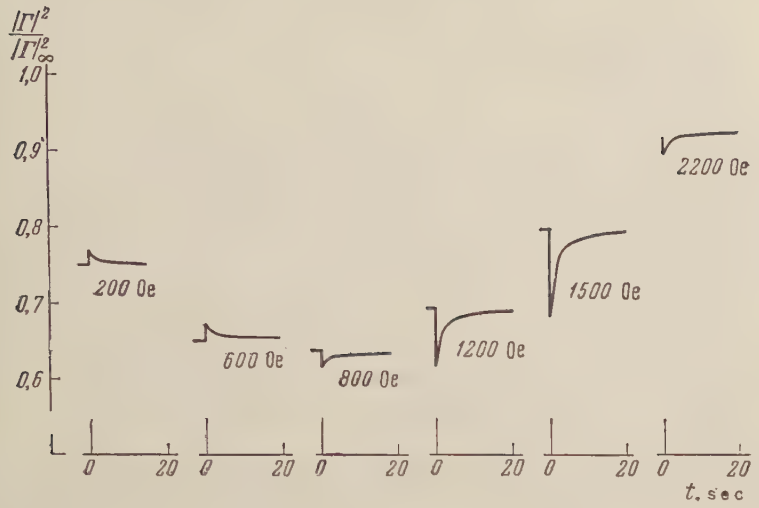

Fig.4. Time dependences of the reflection factor $|\Gamma|$ with rotation of the specimen by 90°. The figure at the curves are the values of the constant magnetic field H_0. Temperature 77°K. Undoped specimen sintered at 1450°. The static $|\Gamma|$ versus H curves for this specimen are shown in Fig.1.

magnitude of the jumps, evaluate H_c. The values of H_c determined in this manner proved to be 350 Oe at 77°K and 200 Oe at 90°K. These values are substantially smaller than the values of $\omega/\gamma - H_{res} \approx H_{i.an}$ for the same specimen at the corresponding temperatures. From this it follows that in addition to the temporal processes that we observe after rotation of the specimen, there also occur other processes with time constants appreciably shorter than the rotation time; as a result of these processes there is established a major part of the induced anisotropy field.

The observed temporal processes, as will be evident from Fig.5, are not characterized by a single time constant. If one approximates the initial sections of the curves shown in Fig. 5 by exponential plots, there are obtained the temperature dependences for the time constants shown in Fig.6. These are characterized by an activation energy of

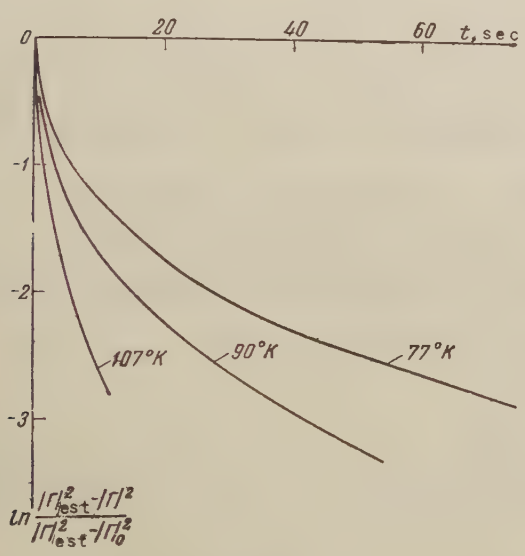

Fig.5

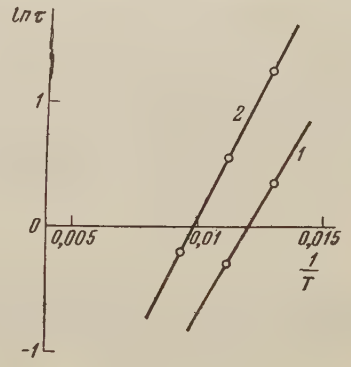

Fig.6

Fig.5. Time dependences of the reflection factor upon rotation of the specimen for different temperatures. Undoped specimen sintered at 1450° after annealing in O_2. $|\Gamma|_{ste}$ - steady state value of $|\Gamma|$.

Fig.6. Temperature dependences of the time constants. The time constants τ were determined from the initial sections of the time characteristics $\frac{|\Gamma|^2}{|\Gamma|^2_\infty}(t)$ 1 - same specimen as in Fig.4; 2 - same specimen as in Fig.5.

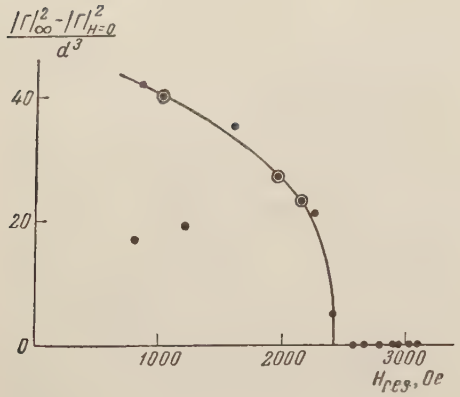

Fig.7. Variation of the reflection factor $|\Gamma|_0$ in the absence of a constant field, which characterizes the initial loss, as a function of the resonance field for a number of specimens. Temperature 77°K; d = specimen diameter. The circled points correspond to the same specimen before and after annealing in oxygen (Fig.3).

~0.05 eV. Approximating the last sections of the curves in Fig.5 by exponentials, we obtain appreciably larger values of the time constants - values of the order of tens of seconds at 77°K - and an activation energy of the same order of magnitude as for the initial sections.

At 4.2°K upon rotation of specimens with a large induced anisotropy we observed time characteristics analogous to those shown in Fig.4, but with smaller amplitude and a time constant of 1-2 sec. Clearly, these characteristics can be connected only with processes that at 77°K proceed very rapidly, while the processes responsible for the evident establishment of anisotropy (see Figs.4 & 5) are completely "frozen" at 4.2°K.

Thus the time characteristics of the induced anisotropy in yttrium garnet are due to superposition of processes with different time constants and activation energies of the order of 0.05 eV. This value of the activation energy is substantially lower than the value of 0.375 eV obtained by Smolenskii et al[4] for electronic processes accompanying domain wall motion. These processes, apparently, differ substantially from the processes responsible for induced anisotropy, although all are apparently associated with Fe^{2+} ions. In the case of displacement of domain walls, there occurs diffusion of electrons from one iron ion to another[4]. In our case, with change in the direction of the magnetic field there apparently occurs deformation of the electron cloud of the Fe^{2+} ions. Naturally, this deformation requires a lower activation energy.

The role of the external field consists, of course, only in changing the direction of the magnetization. From this it follows that in the absence of an external field there obtains induced anisotropy within each domain. This is substantiated by the appearance of initial losses (intrinsic ferromagnetic resonance) connected with this anisotropy.

As is known, the initial loss boundary is determined by the condition

$$\frac{\omega}{\gamma} = 4\pi M + H_{an}. \qquad (3)$$

Comparing this relation with Eq.(2), we see that the boundary value of H_{res} at which initial losses appear equals

$$H_{res.bound.} = 4\pi M. \qquad (4)$$

As will be evident from Fig.7, initial losses at 77°K appear at $H_{res} < 2400$ Oe, i.e., at $H_{i.an} > 800$ Oe, which is in satisfactory agreement with the above evaluation ($4\pi M = 2300$ G at 77°K).

We note that the induced anisotropy due to electronic processes may be evinced in ferromagnetic resonance in single crystals as well. This apparently occurred in the work of Dillon[12]. In polycrystalline ferrites, in particular in yttrium garnet, as follows from the above described experimental results, the effect

of induced anisotropy can be substantial at low temperatures.

We desire to express our gratitude to G.A.Smolenskii and Ya.M.Ksendzov for helpful discussions.

References

1. R.Bozorth, Phys.Rev., 99, 1788 (1955).
2. R.F.Penoyer & L.R.Bickford, Jr., Phys.Rev., 108, 271 (1957).
3. D.J.Epstein, B.Frackiewicz & R.P.Hunt, J.Appl.Phys., 32, 217 (1961).
4. G.A.Smolenskii, Chang Tsung & A.K.Stankevich, Fizika tverdogo tela, 3, No.2, 663 (1961). (Trans.Soviet Physics - Solid State.)
5. A.G.Gurevich, I.E.Gubler & A.G.Titova, Ibid., 3, No.1, 19 (1961). (Trans. Ibid.)
6. A.G.Gurevich & I.E.Gubler, In "Ferrity" (Ferrites), p.539, Minsk, 1960.
7. C.Kittel, Phys.Rev., 115, 1587 (1959).
8. A.M.Clogston, Bell System Techn.J., 34, 739 (1955).
9. R.L.White, Phys.Rev.Letters, 2, 465 (1959).
10. A.G.Gurevich, Ferrity na sverkhvysokikh chastotakh (Ferrites at microwave frequencies), M., 1960.
11. Ya.M.Ksendzov & Stogova, In "Ferrity" (Ferrites), p.286, Minsk, 1960.
12. J.F.Dillon, Bull.Amer.Phys.Soc., 6, No.2, 160 (1961).

EXPERIMENTAL INVESTIGATION OF THE EFFECTS IN YTTRIUM FERRITE SINGLE CRYSTALS, ASSOCIATED WITH NUTATIONAL OSCILLATIONS OF THE MAGNETIZATION OF THE MATERIAL UNDER CONDITIONS OF FERROMAGNETIC RESONANCE

- V.A.Fabrikov, V.I.Kozlov, V.T.Kadeev & V.D.Kudryavtsev

Introduction

In the present work we investigated certain effects connected with the nonlinear gyromagnetic properties of ferrites at high frequencies; the experiments were performed on yttrium garnet single crystals.

Under the influence of a transverse high frequency magnetic field there is established in a magnetized ferrite specimen precession of the magnetic moments[1]. If the high frequency field is circularly polarized, the precession occurs with a constant frequency and at a fixed angle relative to the direction of the field. Nonlinear gyromagnetic properties of ferrites are evinced in the case of simultaneous action on the ferrite specimen of two or more electromagnetic signals of different frequency (or different polarization). Each of the signals affects the parameters of the medium as far as the other signals are concerned. In the first approximation, all the linear gyromagnetic effects in ferrites can be divided into two groups: the first group is connected with frequency modulation (periodic disturbance) of the precessional motion established in the material; the second group is connected with modulation in angle.

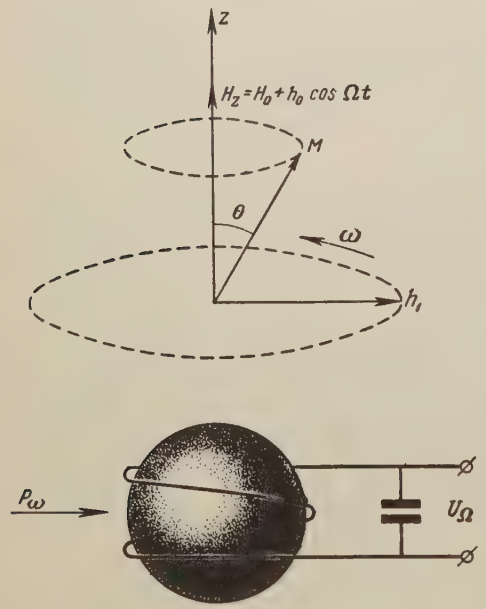

Fig.1. Orientation of the interacting magnetic fields involved in the experiment.

The effects investigated in the present study are of the second type. They are connected with the appearance in the ferrite specimen of nutational oscillations of the magnetization, i.e., oscillations of the precession angle. In other words, we investigated the interaction with the ferrite specimen of two electromagnetic signals, namely, a high frequency (10 000 Mc) wave with transverse (relative to the magnetization of the material) polarization of the magnetic field and a low frequency signal (0.5 to 8 Mc) with longitudinal polarization. The relative orientation of the magnetic fields is shown in Fig.1. The z axis in Fig.1 agrees with the direction of the constant magnetic field H_0 and the permanent magnetization M_0 of the material.

The theory of the effects under consideration has been set forth in Refs.2,3 & 4. Here we shall mention only some of the general physical concepts involved.

General physical concepts

The variation of the precession angle with the magnitude of the applied constant magnetizing field has a resonance character, i.e., is characterized by a resonance type curve such as that shown in normalized form in Fig.2. Here the horizontal scale is laid off in values of the precession angle in relative units.

It will be evident from Fig.2 that the periodic variation of the magnetizing field must lead to periodic variation of the precession angle θ and, consequently, to variation of the magnetization of the material in the direction of this

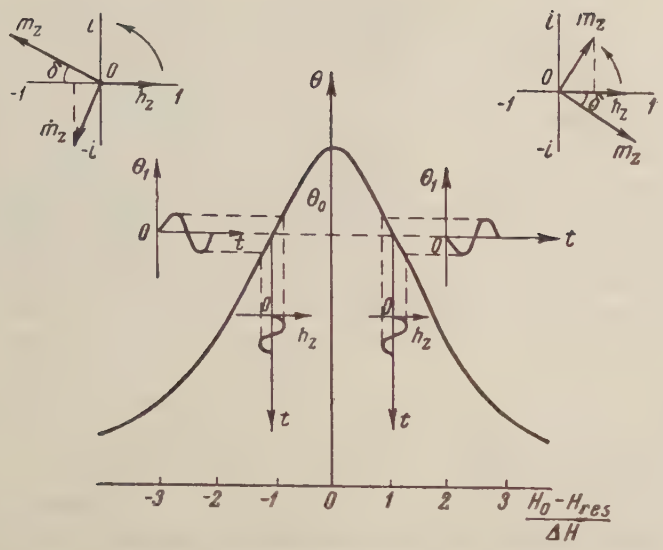

Fig.2. Diagram illustrating the phase relationship between the variation of the magnetizing field H_z and the precession angle θ of the magnetic moments in the material.

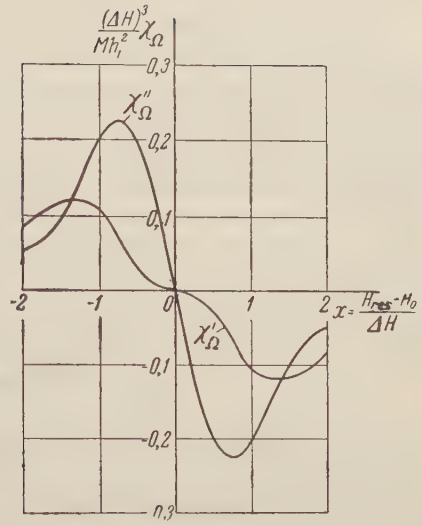

Fig.3. Complex magnetic susceptibility χ_Ω of magnetized ferrite material relative to a low frequency modulating field h_z as a function of the constant applied magnetizing field H_0.

field: $M_z = M\cos\theta$. The variation of the field and magnetization occurs in phase or antiphase, depending on whether the magnetizing field is greater or smaller than the corresponding resonance value. Strictly speaking, however, the above is valid only for relatively slow changes of the magnetizing field. Under dynamic conditions in the presence of magnetic losses the actual changes in magnetization will lag a certain angle δ behind the changes of the corresponding "equilibrium" values.

In the inserts in Fig.2 we show in the complex plane the relation between the field oscillation vector $h_z = H_z - H_0$, the magnetization oscillation vector $m_z = M_z - M_0$ and the time derivative of the magnetization dm_z/dt in the direction of the z axis. The magnetization derivative is of interest in that it enters into the expression for the mean power[5]:

$$P = \frac{1}{T}\int_0^T h_z \frac{dm_z}{dt}\,dt = \frac{\chi''_\Omega h_1^2}{2}, \qquad (1)$$

absorbed (or generated) by the specimen at the frequency Ω of the modulating field h_z. The direction of energy transfer (given by the sign of P) depends on the phase relationships between the oscillations of the "force" h_z and the "velocity" dm_z/dt.[6] It will be evident from Fig.2 that if the value of the magnetizing field is greater than the resonance value, the phase angle between the field and the derivative of the magnetization will be less than 90°, while if the value of the magnetic field is smaller than the resonance value, the phase angle will exceed 90°. This means that in the case of variation of the magnetizing field about the resonance value the imaginary part of the low frequency susceptibility χ''_Ω of the ferromagnetic material changes sign. At the same time the direction of the energy flux between the field h_z and the precessing moment also changes direction.

At negative values of χ''_Ω the energy of the field h_z is no longer absorbed, but is "amplified" by the medium.*

The above physical reasoning is substantiated by analysis of the corresponding equations of motion.[2,3] The variation of the low frequency susceptibility of a ferrite specimen exposed to the simultaneous influence of a high frequency signal as a function of the magnetizing field is shown in Fig.3. On the assumption that the absolute magnitude of the magnetic moment M is invariable, this dependence is described by an expression of the form

$$\chi_\Omega = -\frac{Mh_1^2}{(\Delta H)^3}\frac{x}{1+x^2}\frac{1+x^2-y^2-2iy}{(1+x^2-y^2)^2+4y^2}; \qquad (2)$$

here h_1 is the amplitude of the circularly polarized high frequency field, $\Delta H = 1/\gamma T_2$ is the half-width of the ferromagnetic resonance peak for the material, γ = 2.8 Mc Oe^{-1} is the electron spin gyromagnetic ratio, x and y are dimensionless parameters defined by $x = \frac{H_{res} - H_0}{\Delta H}$ and $y = \Omega T_2$, and χ' and χ'' are the real and imaginary parts of the magnetic susceptibility. The curves in Fig.3 are plotted for the case when the frequency of the modulating field $\Omega = 2\pi f$ equals the relaxation frequency $1/T_2$ in the material. This is the case when one can expect the greatest interaction of the two signals.

The reproduced curves were calculated on the assumption that the amplitude of the modulating field is small compared with the half-width of the resonance peak. With increase in the amplitude of the modulating field there must be observed a certain "saturation" effect connected with decrease in the intensity of the ferromagnetic resonance line. This effect is also susceptible of quantitative analysis[4] and experimental verification.

Experimental procedure and results

The experiments were carried out on yttrium ferrite single crystal specimens with a ferromagnetic resonance line width of 1-2 Oe. The experimental specimen in the form of a sphere 0.5 to 1 mm in diameter was cemented in position at the center of a coil consisting of several turns and connected into the low frequency (0.5 to 10 Mc) resonance circuit supplied from a standard signal oscillator. The coil with the specimen was introduced into a section of rectangular wave guide coupled to a Klystron generator.

The parameters of the test circuit were periodically varied under the influence of a high frequency signal (wavelength 3 cm). To observe these changes the voltage from the inductance of the circuit was applied through an appropriate detecting and amplifying circuit to an indicator or an oscillograph. In some cases the low frequency part of the circuit was replaced by a standard set-up for observing the susceptibility in nuclear resonance (IMI-2). In this case the "probe" was the coil with the ferrite specimen exposed to the microwave field. On the screen of the oscillograph in this case there was observed a curve characterizing the law of modulation of the losses introduced by the ferrite specimen into the generator circuit under the influence of the microwave signal. An oscillogram characterizing the variation of the loss as a function of the constant magnetic field is shown in Fig.4; it will be seen that it closely duplicates the curves in Fig.3. The magnitude of the effect depends linearly on the power of the microwave signal.

*At a sufficiently high value of χ''_Ω the system may go over to "generation" of energy.[7]

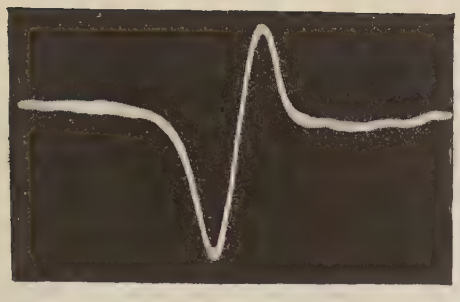

Fig.4. Oscillogram characterizing the variation of χ''_Ω of a ferrite specimen, under the influence of a high frequency field, in the case of slow sinusoidal variation of the magnetizing field H_0 about the resonance value.

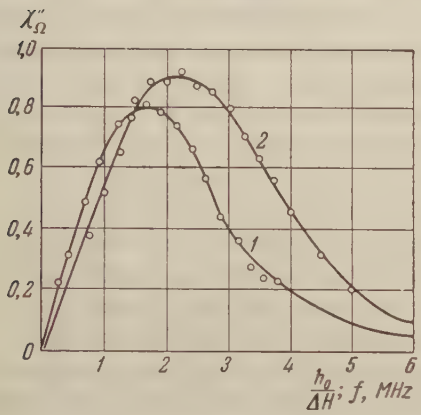

Fig.5. Experimental (points) and theoretical (curves) dependences of χ''_Ω on the amplitude h_0 (1) and frequency f (2) of the low frequency field h_z.

In Fig.5 we show the dependence of the effect on the frequency f and the amplitude h_0 of the modulating field. The experimental and theoretical curves shown in these figures can be compared only to within a proportionality factor, inasmuch as the experimental curves were recorded in relative units and were superimposed on the theoretical curves by matching two points. Under the influence of the modulating field the ferromagnetic resonance peak broadens and changes shape. This explains the dependence of the effect on the value of h_0.

Conclusions

The described experimental results are in agreement with the theoretical inferences drawn in Refs. 2,3 & 4. The investigated effect is of interest in two respects: first, it is observed at relatively low power levels of the applied high-frequency field (of the order of a milliwatt or even a fraction of a milliwatt at a wavelength of 3 cm), and, second, it is due to relaxation processes and its characteristics are intimately related with the relaxation characteristics of the material. The effect can be utilized for investigating the processes of relaxation in ferrite materials with a narrow resonance absorption line and should prove useful for determining the corresponding parameters.

We desire to thank K.M.Polivanov for his interest in the work.

References

1. A.G.Gurevich, Ferrity na sverkhvysokikh chastotakh (Ferrites at microwave frequencies), M., 1960.

2. V.A.Fabrikov, Radiotekhnika i elektronika, 3, No.2, 190 (1958).

3. V.A.Fabrikov, Ibid., 4, No.7, 1203 (1959). (Trans.Radio Engineering & Electronics.)

4. V.A.Fabrikov, Ibid., 6, No.10, 1707 (1961). (Trans.Ibid.)

5. K.M.Polivanov, Ferromagnetiki (Ferromagnets), M., 1957.

6. A.A.Kharkevich, Avtokolebaniya (Self-oscillations), M., 1954.

7. L.K.Mikhailovskii, V.P.Makarishchev, B.P.Pollak & V.A.Fabrikov, Radiotekhnika i elektronika, 6, No.7, 1178 (1961). (Trans.Radio Engineering & Electronics.)

MAGNETIC AND RESONANCE PROPERTIES OF YTTRIUM-IRON GARNET WITH THE Yt^{3+} IONS REPLACED BY Tb^{3+}, Nd^{3+} AND Lu^{3+} IONS

- K.P.Belov & L.A.Malevskaya

The standpoint of the theory of ferromagnetism rare earth and particularly yttrium-iron garnets are of interest in view of their complex magnetic sublattice structure. For the purpose of elucidating the influence of this structure on the magnetic properties of ferrites we investigated the magnetic and resonance characteristics of yttrium-iron garnet in which the yttrium ions were partially or completely replaced by terbium, neodymium or lutetium ions.

1. The yttrium sublattice in yttrium-iron garnet is nonmagnetic. It is of interest to follow the gradual "involvement" in the resultant spontaneous magnetization of the ferrite by successive partial replacement of the nonmagnetic Yt^{3+} ions (ionic radius 1.06 Å) by magnetic Tb^{3+} ions (ionic radius 1.09 Å). The resultant magnetization at $0^{\circ}K$ can be calculated by means of Néel's theory[1]. According to Néel's model, with increase of the Tb content the magnetization should decrease, and this is borne out by experiment.

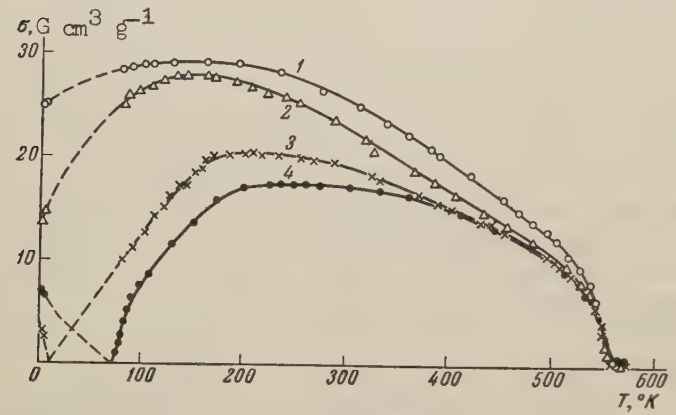

Fig.1. Temperature dependence of the spontaneous magnetization of mixed garnets: 1) $2.9Yt_2O_3 \cdot 0.1Tb_2O_3 \cdot 5Fe_2O_3$, 2) $2.7Yt_2O_3 \cdot 0.3Tb_2O_3 \cdot 5Fe_2O_3$, 3) $2.2Yt_2O_3 \cdot 0.8Tb_2O_3 \cdot 5Fe_2O_3$, 4) $2Yt_2O_3 \cdot Tb_2O_3 \cdot 5Fe_2O_3$.

Iron-garnets described by the formula $(3 - x)Yt_2O_3 \cdot xTb_2O_3 \cdot 5Fe_2O_3$ in the range of small x exhibit an anomalous temperature variation of the spontaneous magnetization (Fig. 1, curves 1 and 2) in the range of low temperatures (type M according to Néel's classification). With increase of the terbium content (to $x = 0.8$) there appears in the spontaneous magnetization versus temperature curve a compensation point in the region of liquid helium temperatures ($10^{\circ}K$) (curve 3). (The compensation point is the temperature at which the magnetization goes through zero and changes). According to Néel's model, the compensation point of this ferrite should be observed in the vicinity of $0^{\circ}K$. A $\sim 10^{\circ}$ shift may be explained by the influence of other rare earth ions present as impurities. With further increase of the Tb content ($x = 1$) the compensation point is shifted to still higher temperatures ($70^{\circ}K$) (curve 4). Moreover, with increase in the Tb content in the ferrite there is observed strong growth of the coercive force H_c in the region of low temperatures. Whereas at room temperature H_c in all Yt-Tb ferrites is of the order of 10 Oe, at liquid helium temperature H_c increases to 1000 Oe or higher. One can hardly explain this great increase of H_c by increase of the magnetic anisotropy owing to the introduction of the Tb ions. The reason for the noted increase of H_c, in our opinion, is closeness of the compensation point. According to the studies of Ref.2, upon approach to the compensation point, owing to strong decrease of the magnetization, there are created in ferrites conditions for the appearance of magnetic inhomogeneities (a magnetically heterogeneous state) which hinder the processes of magnetization reversal and lead to increase of H_c. In investigating the temperature dependence of ferromagnetic resonance in yttrium-iron garnet there was observed a strong increase in the absorption linewidth in the tempera-

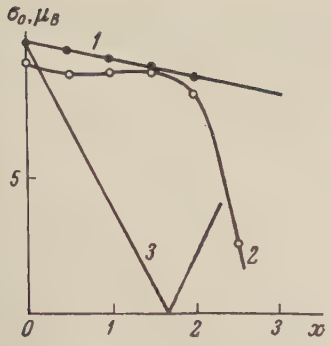

←Fig.2. Variation of the magnetization σ_0 at 4.2°K as a function of the Nd content in yttrium-iron garnet: 1) curve calculated on the assumption of coexistence of two ferrites (see Ref.7), 2) experimental curve, 3) curve calculated according to Néel.

ture interval from 4 to 60°K. Theoretical calculations[3], substantiated by experiment[4], showed that in the region of low temperatures the resonance linewidth ΔH has a maximum upon introduction into the ferrites of minor amounts of Tb.

As experiment showed, with increase of the Tb concentration the low temperature anomaly of the linewidth is extended over the temperature scale and in the region of very low temperatures (2°K) there is observed no decrease in the linewidth ΔH. This smearing out of the low temperature anomaly of ΔH in the temperature scale in ferrites with a relatively high content of Tb can, in our opinion, be explained by the fact that at low temperatures broadening of the resonance line is produced not only by the Kittel-Dillon mechanism but also by the presence of a magnetically heterogeneous state owing to closeness to the compensation point.

2. Bertaut & Forrat[5], who carried out a thorough investigation of iron-garnets, indicated that the existence of garnets having the formula $3A_2O_3 \cdot 5B_2O_3$ is possible provided the ionic radius ratio r_A/r_B does not exceed a certain critical value α. This value, calculated for the ionic radii given by Goldschmidt, proved to be 1.70 for iron-garnets. The rare earth element neodymium, the trivalent ion of which has a large ionic radius (1.15 Å) does not satisfy this requirement, and, as has been established experimentally, does not form the garnet structure. However, if in yttrium-iron garnet $3Yt_2O_3 \cdot 5Fe_2O_3$ the Yt^{3+} ions are partially replaced by Nd^{3+} ions, it is found that the garnet structure persists up to the composition $Yt_2O_3 \cdot 2Nd_2O_3 \cdot 5Fe_2O_3$.

We prepared polycrystalline ferrites with the general formula $(3 - x)Yt_2O_3 \cdot x Nd_2O_3 \cdot 5Fe_2O_3$. Debye patterns recorded for these ferrite shows that up to $x = 2$ these ferrites have the garnet structure. The lattice constants of the mixed Yt-Nd garnets increases with increase of the Nd content from 12.37 Å for $3Yt_2O_3 \cdot 5Fe_2O_3$ to 12.50 Å for $Yt_2O_3 \cdot 2Nd_2O_3 \cdot 5Fe_2O_3$. With complete replacement of the Yt^{3+} ions by Nd^{3+} there was obtained a specimen with a perovskite-like structure, described by the formula $NdFe_2O_3$ and having a lattice period of 3.88 Å. No other phases in these mixed garnets were disclosed by x-ray diffraction analysis.

According to Néel the magnetic moment of ferrites with the garnet structure at absolute zero can be calculated by means of the formula

$$\sigma_s = [6\sigma_c - (6\sigma_d - 4\sigma_a)],$$

where σ_c, σ_d and σ_a are, respectively, the magnetic moments of the sublattices of the rare earth and iron ions located at the c, d and a sites. The trivalent neodymium ions, which have a magnetic moment equal to $3\mu_B$, occupying the c sites in the sublattice, should lead to the appearance of anomalous magnetization curves similar to those observed for mixed Yt-Tb ferrites (Fig.1). Actually, however, the spontaneous magnetization versus temperature curves for Yt-Nd ferrites have the ordinary appearance characteristic of yttrium ferrite and do not exhibit compensation points. In the investigated ferrites the measured values of the saturation magnetization in the vicinity of absolute zero diverged from the values calculated according to Néel (Fig.2). This divergence can be explained if it is

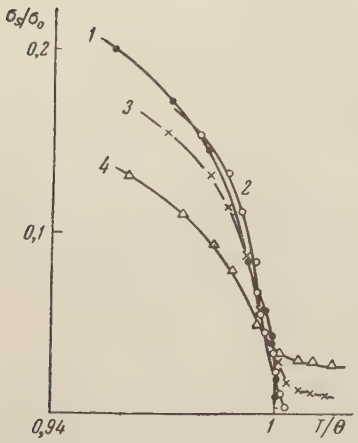

←Fig.3. Tails on the spontaneous magnetization versus temperature curves in the vicinity of the Curie point: 1) $3Yt_2O_3 \cdot 5Fe_2O_3$, 2) $3Lu_2O_3 \cdot 5Fe_2O_3$. 3) $2.5Yt_2O_3 \cdot 0.5Lu_2O_3 \cdot 5Fe_2O_3$, 4) $1.5Yt_2O_3 \cdot 1.5Lu_2O_3 \cdot 5Fe_2O_3$.

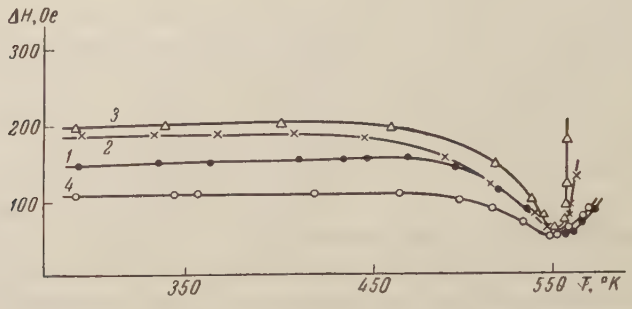

Fig.4. Temperature dependence of the resonance linewidth for ferrites: 1) $2Yt_2O_3 \cdot 5Fe_2O_3$, 2) $2.5\ Yt_2O_3 \cdot 0.5Lu_2O_3 \cdot 5Fe_2O_3$, 3) $1.5Yt_2O_3 \cdot 1.5Lu_2O_3 \cdot 5Fe_2O_3$, 4) $3Lu_2O_3 \cdot 5Fe_2O_3$.

assumed that in these ferrites the magnetic moments of the Nd^{3+} ions entering into the c sublattice do not produce ferromagnetic order in this sublattice, inasmuch as the exchange interaction is inadequate for such ordering. It is also possible that there arises in this sublattice antiferromagnetic ordering of the magnetic moments of the Nd ions. As a result of this, the properties of mixed Yt-Nd ferrites, like those of pure yttrium-iron garnet, are determined only by the Fe^{3+} ions (also see Refs.7 & 8).

3. We also investigated a number of mixed Yt-Lu ferrites. It is known that Lu ions (ionic radius 0.99 Å) do not have a magnetic moment. Hence we did not expect to observe an appreciable change in the magnetic properties as a result of introduction of lutetium ions. Actually, in ferrites described by the formula $(3 - x)\text{-}Yt_2O_3 \cdot xLu_2O_3 \cdot 5Fe_2O_3$ little change in the magnetic moment is observed with increase of x. There is observed a minor ($<10^{\circ}$) decrease of the Curie temperature, which is probably connected with change in the lattice parameter. Replacement of the Yt ions by Lu ions, which have a smaller radius, leads to the appearance in the mixed ferrite of structural inhomogeneities, which in turn give rise to magnetic inhomogeneities. The development of these inhomogeneities is responsible for the appearance of tails on the spontaneous magnetization versus temperature curves (Fig.3, curves 3 & 4) and significant increase of the resonance linewidth ΔH in the vicinity of the Curie point (Fig.4, curves 2 & 3). In the case of the "pure" ferrites $3Yt_2O_3 \cdot 5Fe_2O_3$ and $3Lu_2O_3 \cdot 5Fe_2O_3$ the increase in linewidth is insignificant (Fig.4, curves 1 & 4). A discussion of the influence of structural and magnetic inhomogeneities on the ferromagnetic linewidth in the region of the Curie temperature will be found in Ref.6.

4. In investigating the magnetic properties of yttrium ferrites with replacement of the Yt ions by Tb and Nd ions we observed the phenomenon of magnetic viscosity at low temperatures. In the case of mixed Yt-Tb ferrites it was established that in the temperature interval from 4 to 60°K, upon the application of a weak (~10 Oe) magnetic field, the net magnetization is established not immediately but only after the passage of 5-10 min, i.e., there obtains in these ferrites an appreciable magnetic viscosity in the indicated temperature range. In contrast, virtually no magnetic viscosity was detected in yttrium ferrite prepared of purified (99.99% pure) yttrium oxide.

In the Yt-Nd mixed ferrite system magnetic viscosity is evinced in strong fields (4000 Oe). When the ferrites $2Yt_2O_3 \cdot Nd_2O_3 \cdot 5Fe_2O_3$, $1.5Yt_2O_3 \cdot 1.5Nd_2O_3 \cdot 5Fe_2O_3$ and $Yt_2O_3 \cdot 2Nd_2O_3 \cdot 5Fe_2O_3$ are cooled down to 4.3°K the hysteresis loops fail to close. The appearance of open hysteresis loops is connected with the influence of magnetic viscosity. Upon reversal of the applied magnetic field the specimen does not have time to reverse and hence the value of the saturation magnetization evaluated from the lower branch of the loop is an underestimate. Upon passage of a certain time (30 to 40 min) the hysteresis loop closes. The hysteresis loops become rectangular in character; moreover, in the region of residual magnetization there are evident "steps", i.e., the value of the magnetization does not change with increase of the magnetizing field. The greatest width of the step (400 Oe) is observed in the case of $1.5Yt_2O_3 \cdot 1.5Nd_2O_3 \cdot 5Fe_2O_3$ ferrite. One cannot explain the appearance of the "steps" by magnetic viscosity, inasmuch as with the passage of time the width of the "steps" does not change.

Strong magnetic viscosity in the region of helium temperatures was also observed in the mixed Yt-Lu ferrites. This viscosity is probably due to purely structural factors, inasmuch as Lu ions, like Yt ions, have no magnetic moment.

Moscow State University

References

1. L.Néel, Compt.rendu, 239, No.8 (1954).
2. K.M.Bol'shova & T.A.Elkina, Fiz.metallov i metallovedenie, 8, 461 (1959). (Trans.Physics of Metals & Metallography); K.P.Belov & A.V.Pek'ko, Zhur.eksp.i teor.fiz., 39, 10, 961 (1960). (Trans.Soviet Physics - JETP.)
3. C.Kittel, A.Portis & P.de Gennes, Phys.Rev., 116, 323 (1959).
4. J.F.Dillon,Jr., Phys.Rev., 111, 1476 (1958); K.P.Belov, L.A.Malevskaya & V.I.Sokolov, Zhur.eksp.i teor.fiz., 39, 1542 (1960). (Trans.Sov.Physics - JETP.)
5. F.Bertaut & J.Forrat, Compt.rendu, 243, 17, 1219 (1956).
6. K.P.Belov, Zhur.eksp.i teor.fiz., 40, 2, 711 (1961). (Trans.Sov.Phys. - JETP.)
7. K.P.Belov, M.A.Zaitseva & L.A.Malevskaya, in "Ferrity" (Ferrites), p.212, Minsk, 1960.
8. R.J.White, J.Appl.Phys., 32, 1178 (1961).

EFFECT OF THE BOUNDARY CONDITION FOR THE MAGNETIC MOMENT ON SPIN-WAVE RESONANCE IN METALS

- M.I.Kaganov & Yü Liu

It is known[1] that the high frequency characteristics of ferromagnetic dielectrics are not sensitive to exchange effects. In metals, if the effective permeability is large and the anisotropy energy small, the "exchange" term in the Landau-Lifshits equation becomes comparable to or even greater than the Zeeman term, owing to significant homogeneity of the magnetic moment in the skin layer. Exchange shift of the resonance frequency and broadening of the resonance line were observed experimentally by Rado & Wertman[2,3]. They called the ferromagnetic resonance observed under these conditions "spin-wave resonance". Ament & Rado[4] elaborated the macroscopic theory of this effect by simultaneous solution of Maxwell's equations and the Landau-Lifshits equation.

Taking into account exchange effects, i.e., spatial dispersion of the magnetic susceptibility, makes it necessary to formulate the boundary condition for the magnetic moment. Ament & Rado arrived at the boundary condition $\partial m/\partial n = 0$, which corresponds to predominance of exchange interaction. Kittel[5] used the condition $m = 0$ at the boundary for considering standing spin-wave resonance in a film. This corresponds to predominance of surface anisotropy energy. Apparently, there actually obtains the more general boundary condition

$$\frac{\partial m}{\partial n} + \alpha m = 0 \qquad (1)$$

here α is a parameter characterizing the quality of the surface.

Comparison of theory with experiment[3,4] showed that the theory satisfactorily describes the line shape at room temperatures, but that the value of the exchange factor obtained from experiments is appreciably higher than the values following from other experiments (spin-wave resonance experiments yield $A = 2.88 \cdot 10^{-6}$ erg/cm at a frequency of $3 \cdot 10^{9}$ cps and $A = 3.8 \cdot 10^{-6}$ erg/cm at a frequency of $4 \cdot 10^{-9}$ cps, whereas measurements of the temperature dependence of the magnetization[6] yield $A = (1 \pm 0.2) \cdot 10^{-9}$ erg/cm). The physical justification of the frequency dependence of the microscopic characteristic A deduced by Ament & Rado[4] is obscure.

It must be noted that the above mentioned comparison[3,4] was carried out on the assumption that at the boundary $\sigma m/\sigma n = 0$. Consideration of the other limiting case ($m = 0$ at the boundary) showed that the theoretical formulas in this case fail to describe the line shape.

The purpose of the present communication is to show that by appropriate choice of the values of $\alpha (\alpha \neq 0$ and $\alpha \neq \infty)$ one can satisfactorily describe the experimental results (for example, those of Ref.2) with one value of the exchange integral taken from magnetic measurements.

Earlier one of us[7] showed that the spin-wave resonance excitation curve is extremely sensitive to the boundary condition; moreover, experiments indicate that in the case of films the parameter α is large.

We calculate the surface impedance using the general boundary condition (1) and investigate its dependence on the parameter α. We restrict our consideration to normal skin effect.

The problem is solved by the same method as employed in the work of Ament & Rado; for convenience we shall also utilize their notation. If it is assumed that m, h and e are proportional to $\exp(i\omega t - ky)$, then by combined solution of the Landau-Lifshits equation and Maxwell's equations one can readily obtain the approximate dispersion equation

$$K^6 - K^4 - (\eta - \Omega^2 + i\Omega L)\,K^2 - 2i\varkappa^2 = 0, \tag{2}$$

where

$$\eta = \frac{H_z}{4\pi M_s}; \quad \Omega = \frac{\omega}{4\pi M_s \gamma}; \quad L = \frac{\lambda}{M_s \gamma}; \quad \varkappa^2 = \frac{A}{2\pi M_s^2 \delta^2};$$

$$K = k\varkappa\delta; \quad \delta = c/\sqrt{2\pi\sigma\omega};$$

γ is the gyromagnetic ratio, A is the exchange factor (exchange stiffness constant), and λ is the relaxation constant.

In deducing Eq.(2) it was assumed that under conditions of spin-wave resonance all the parameters entering into this equation are appreciably smaller than unity: $\eta\Omega^2,\ L\Omega,\ \varkappa \approx 10^{-3}$. The approximate solution of Eq.(2) is of the form

$$K_{1,2}^2 = \frac{1}{2}\{(\eta - \Omega^2 + i\Omega L) \pm [(\eta - \Omega^2 + i\Omega L)^2 - 8i\varkappa^2]^{1/2}\}, \tag{3}$$

$$K_3^2 = 1, \ \mathrm{Re}\, K > 0.$$

The conditions of continuity of e_z and h_x at the boundary and condition (1) can be written in the following form

$$\begin{gathered} h_{1x} + h_{2x} + h_{3x} = h_{0x}, \\ K_1 h_{1x} + K_2 h_{2x} + K_3 h_{3x} = Z' h_{0x}, \\ K_1^2 (K_1 + \beta\sqrt{\varkappa})\, h_{1x} + K_2^2 (K_2 + \beta\sqrt{\varkappa})\, h_{2x} + K_3^2 (K_3 + \beta\sqrt{\varkappa})\, h_{3x} = 0, \\ (K_1 + \beta\sqrt{\varkappa})\,[(K_1^2 - \eta) K_1^2 + 2i\varkappa^2]\, h_{1x} + (K_2 + \beta\sqrt{\varkappa})\,[(K_2^2 - \eta) K_2^2 + \\ + 2i\varkappa^2]\, h_{2x} + (K_3 + \beta\sqrt{\varkappa})\,[(K_3^2 - \eta) K_3^2 + 2i\varkappa^2]\, h_{3x} = 0, \end{gathered} \tag{4}$$

where

$$Z' = \frac{4\pi\sigma\varkappa\delta}{c} Z, \quad \beta = \delta\sqrt{\varkappa\alpha}. \tag{5}$$

From the condition of existence of a nontrivial solution of the set (4) we find with the same accuracy

$$Z' = \frac{K_1 K_2 (K_1 + K_2 + \beta\sqrt{\varkappa})}{K_2^2 + K_1 K_2 + K_1^2 + \beta\sqrt{\varkappa}\,(K_1 + K_2)}; \tag{6}$$

inserting K_1 and K_2 from (4), we obtain

$$Z' = \frac{\varkappa(1+i)\,[\sqrt{\eta - \Omega^2 + i\Omega L + 2\varkappa(1+i)} + \beta\sqrt{\varkappa}]}{\eta - \Omega^2 + i\,\Omega L + \varkappa(1+i) + \beta\sqrt{\varkappa}\sqrt{\eta^2 - \Omega^2 + i\Omega L + 2\varkappa(1+i)}}. \tag{7}$$

The real part of the impedance is positive for any arbitrary value of β, if it is assumed that $\sqrt{\varkappa} > 0$ and $\mathrm{Re}\sqrt{\eta - \Omega^2 + i\Omega L + 2\varkappa(1+i)}$ (this corresponds to the condition $\mathrm{Re}\, K_{1,2} > 0$).

Following Ament & Rado[5], we introduce the effective dielectric constant:

$$\varepsilon_{\mathrm{eff}} = -\frac{4\pi i\sigma}{\omega}.$$

then

$$Z = \left(\frac{\mu_{\mathrm{eff}}}{\varepsilon_{\mathrm{eff}}}\right)^{1/2}, \tag{8}$$

here $\mu_{\mathrm{eff}} = \mu_1 - i\mu_2$, in accord with Eqs.(5), (7) and (8), is defined as follows:

$$\varkappa\mu_{\mathrm{eff}} = \left[\frac{\sqrt{N + 1 + 2i} + \beta}{N + i + \beta\sqrt{N + 1 + 2i}}\right]^2, \tag{9}$$

where

$$N = \frac{1}{\varkappa}(\eta - \Omega^2 + \varkappa + i\Omega L).$$

If $\beta = 0$, i.e., $\frac{\partial m}{\partial y} = 0$ at the boundary, we have

$$\varkappa\mu_{eff} = \frac{N+1+2i}{(N+i)^2}; \tag{10}$$

while if $\beta = \infty$, i.e., $m = 0$ at $y = 0$, we obtain

$$\varkappa\mu_{eff} = \frac{1}{N+1+2i}. \tag{11}$$

Equations (10) and (11) agree with the results given in Ref.3. Setting $L = 0$, i.e., neglecting the influence of relaxation as compared with exchange effects, we have shown the relation between μ_1 and μ_2 at different values of β in the accompanying figure. It is found that by varying β one can describe the experimental data for values of A consistent with the results of other experiments. The values of β (or α) appear to depend on the strength of the resonance field.

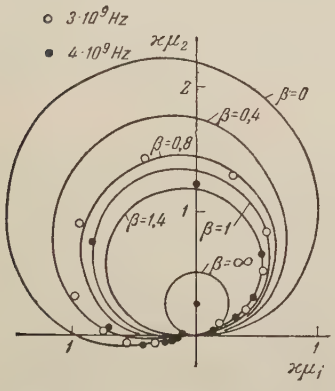

Relation between μ_1 and μ_2 at different values of β at room temperature[3].

As will be evident from the figure, the experimental results (these have been taken from Ref.3) can be described assuming that $A = 1.2\cdot10^{-6}$ erg/cm* and that β varies in the range from 0.4 to 1.0, depending on the strength of the external magnetic field and the frequency (each point in the figure corresponds to a certain value of the magnetic field).

We note that the value $\beta \approx 1$ signifies that exchange interaction and surface anisotropy at the boundary play approximately equal roles.

It must be pointed out that inasmuch as the impedance is highly sensitive to the boundary condition for the magnetic moment (actually two parameters, A and α, must be determined) one cannot regard the method of determining A from spin-wave resonance as unambiguous. Hence in practice it is essential to combine this method with other methods (excitation of spin-waves by a uniform field[5], temperature dependence of the magnetization, etc.). In our opinion, it would be of great interest to carry out experiments on specimens with different surface finishes.

"A.M.Gor'kii" Kharkov State University &
Physical-Technical Institute of the
Academy of Sciences of the Ukrainian SSR

References

1. A.I.Akhiezer, V.G.Bar'yakhtar & M.I.Kaganov, Uspekhi fiz.nauk, 71, 533 (1960). (Trans.Soviet Physics - Uspekhi.)
2. G.T.Rado & J.P.Wertman, Phys.Rev., 94, 1386 (1954).
3. G.T.Rado & J.P.Wertman, Phys.Chem.Solids, 11, 315 (1959).
4. W.S.Ament & G.T.Rado, Phys.Rev., 97, 1558 (1955).
5. C.Kittel, Phys.Rev., 110, 1295 (1958).
6. E.I.Kondorskii & L.N.Fedotov, Izv.AN SSSR, Ser.fiz., 16,432 (1952).
7. M.I.Kaganov, Zhur.eksp.i teor.fiz., 39, 158 (1960). (Trans.Sov.Phys. - JETP.)

*We have recently learned from a private communication that the value of A deduced from standing wave resonance measurements is $(1.02\text{-}1.05)\cdot10^{-6}$ erg/cm.

TEMPERATURE DEPENDENCE OF THE CONDUCTIVITY AND HALL EFFECT IN METALLIC GADOLINIUM

- N.V.Volkenshtein & G.V.Fedorov

Experimental studies of the electric and galvanomagnetic properties of ferromagnets have disclosed a number of "anomalies" characteristic of elements whose free atoms have an unfilled $3d$ shell. The particular energy spectrum of these ferromagnets gives rise to spontaneous magnetization, which is responsible for these "anomalies".[1]

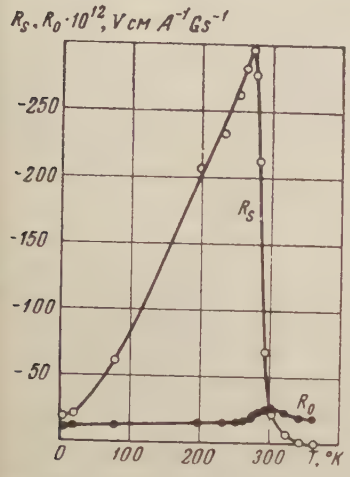

Fig.1. Temperature dependences of the Hall coefficients R_s and R_0 for Gd.

Most experimental studies have been carried out on $3d$-transition elements and their alloys. We felt it would be of interest to measure the electric and galvanomagnetic properties of a rare earth ferromagnetic element, namely, gadolinium, which is a transition element with an unfilled $4f$ rather than $3d$ shell. Owing to its distinctive electronic structure the exchange interaction mechanism in gadolinium may differ from that in ferromagnetic $3d$-transition elements.

Fig.1 shows the temperature dependences of the Hall coefficients for gadolinium. It can be seen that the spontaneous Hall coefficient R_s has a maximum near the Curie point. The character of the R_s curve differs in the paramagnetic and ferromagnetic regions. In the paramagnetic region R_s drops sharply in a very narrow temperature interval and then falls off to zero in a range of about 50°; this terminal decrease is associated with the "tail" in the temperature dependence of the spontaneous magnetization σ_s extending beyond the Curie point. In the ferromagnetic region there is a clearly pronounced temperature dependence, due presumably to the temperature dependence of σ_s, as follows from the relationship

$$R_s = a\,(\sigma_{s_0}^2 - \sigma_{s_T}^2), \tag{1}$$

where σ_{s_0} is the spontaneous magnetization at 0°K, and σ_{s_T} is the spontaneous magnetization at temperature T. This relationship was established experimentally by Komar & Volkenshtein[2] and Kikoin et al[3] and theoretically by Vonsovskii et al[4] and Patrakhin[5].

In view of the relation established[1,6] between $\Delta\rho$, the decrease in resistance of a ferromagnet below the Curie point (see Fig.2), and the square of the spontaneous magnetization:

$$\Delta\rho = c + b\sigma_{s_T}^2, \tag{2}$$

there should obtain a linear relation between R_s and $\Delta\rho$, provided relationship (1) holds.

It follows from Fig.3 that for gadolinium there is in fact a linear relation between R_s and $\Delta\rho$ in the range from 78 to 270°K. However, it should be noted that in the limit when $\sigma_{s_T} \to \sigma_{s_0}$ the coefficient R_s does not tend to zero, but remains finite, as found by Belov and Ped'ko[7] for the temperature dependence of the change in resistance in a magnetic field. Relationship (1) is therefore no longer valid at low temperatures.

As regards the temperature dependence of the usual Hall coefficient R_0, a characteristic feature is the presence of a maximum near the Curie point, which

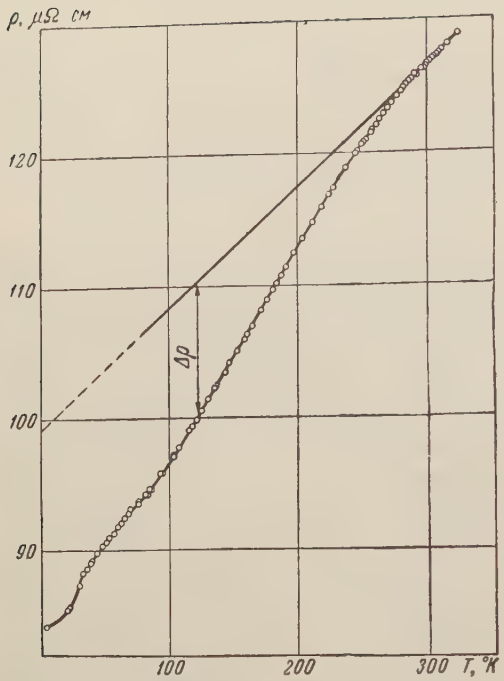

Fig.2. Temperature dependence of the resistivity of Gd.

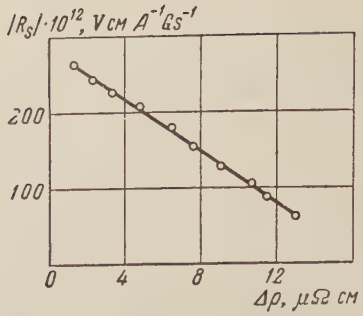

Fig.3. Relation between R_s and $\Delta\rho$.

can be attributed to the paraprocess in the saturation region. It therefore follows that the so-called usual Hall coefficient in ferromagnets may differ from R_0 in nonferromagnetic metals. The presence of a maximum of R_0 near the Curie point was reported earlier[3] in the case of nickel-copper alloys.

Fig.4 shows the variation of R_s for nickel and gadolinium as a function of the reduced temperature T/θ, where T is the temperature of the measurements and θ is the Curie point. It will be evident that the sign of the effect and the character of the temperature dependence for them are the same. However, the magnitude of the effect for gadolinium is about 20 times greater than for nickel. Thus, the particular electron structure of gadolinium does not affect the character of the temperature dependence of the Hall effect but only increases its magnitude. It therefore follows that the unusual Hall effect owes its origin only to the effective internal field and that its temperature dependence is connected with the temperature dependence of this effective magnetic field, which is determined by the spontaneous magnetization.

In fact, in the transition metals of the $3d$ group the electrons responsible for the magnetic properties are fairly closely coupled with the conduction electrons, owing to overlapping of the s- and d-bands, and themselves participate in the conductivity and hence in galvanomagnetic phenomena. In transition metals of the $4f$ group the electrons responsible for the magnetic properties are not coupled to the conduction electrons, since the s- and f-bands do not overlap. However, this does not affect the temperature dependence of R_s.

The anomalously high values of R_s for gadolinium compared with iron and nickel, and hence the high value of the spin-orbit interaction in gadolinium is not inconsistent with the generally accepted ideas regarding the strength of this interaction in the rare earths with their particular electronic structure.

In most theoretical investigations[4,9,10] of the Hall effect in ferromagnets its anomalies are attributed to spin-orbit interaction. Numerical calculations are based on some form of electron scattering, i.e., some particular relation between R_s and the resistivity ρ. For example, Karplus & Luttinger[10] assume

$$R_s = a\rho^n. \tag{3}$$

Other authors[11,12], however, give an empirical or theoretically based relationship of the form

$$R_s = a\rho + b\rho^2. \tag{4}$$

Luttinger[12] relates the first term of this relationship with scattering by impurities, while Irkhin & Shavrov[13] associate the second term with scattering by phonons and by ferromagnons (fluctuations of the spontaneous magnetization).

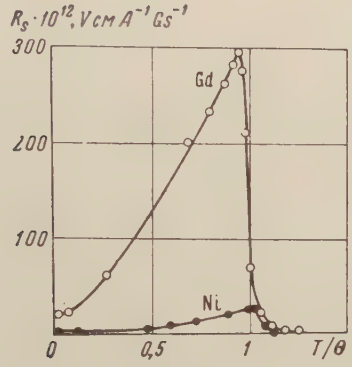

Fig.4.

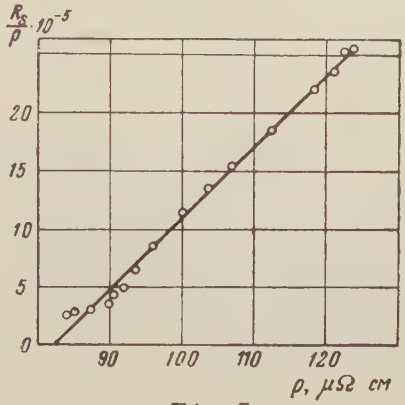

Fig.5.

Fig.4. Temperature dependence of R_s for Gd and Ni (θ is the Curie point of the given metal).

Fig.5. R_s/ρ versus ρ for Gd.

If we assume that Eq.(4) is valid, there should be a linear relationship between R_s/ρ and ρ. As can be seen from Fig.5, the relationship is in fact linear in the range from 90 to 270°K. For a detailed investigation of relationship (4) we would have to conduct experiments on metals with known amounts of impurities and over a wider range of temperatures (particularly higher temperatures).

If we assume, as follows from most theoretical treatments, that the Hall effect in ferromagnets is determined by spin-orbit interaction, it would appear that measurements of the Hall effect can be used to study spin-orbit interaction. It would be desirable, however, to compare the experimental results based on the Hall effect with the data of other experiments which also provide information on spin-orbit interaction.

Institute of Physics of Metals,
Academy of Sciences of the USSR

References

1. S.V.Vonsovskii, Izv.AN SSSR, Ser.fiz., 11, 618 (1947).
2. A.P.Komar & N.V.Volkenshtein, Doklady AN SSSR, 60, 785 (1948).
3. I.K.Kikoin, E.M.Buryak & Yu.A.Muromkin, Doklady AN SSSR, 125, 1011 (1959). (Trans.Soviet Physics - Doklady.)
4. S.V.Vonsovskii, L.Ya.Kobelev & K.P.Rodionov, Izv.AN SSSR, Ser.fiz., 16, 569 (1952).
5. N.P.Patrakhin, Izv.AN SSSR, Ser.fiz., 16, 584 (1952).

6. W.Gerlach & K.Schneiderhan, Ann.Phys., 6, 772 (1930).
7. K.P.Belov & A.V.Ped'ko, Zhur.eksp.i teor.fiz., 33, 815 (1957). (Trans. Soviet Physics - JETP.)
8. F.E.Allison & E.M.Pugh, Phys.Rev., 102, 1281 (1956).
9. V.Rudnitskii, Zhur.eksp.i teor.fiz., 9, 262 (1939).
10. R.Karplus & J.M.Luttinger, Phys.Rev., 95, 1154 (1954).
11. N.S.Akulov & A.V.Cheremushkina, Doklady AN SSSR, 98, 35 (1954).
12. J.M.Luttinger, Phys.Rev., 112, 739 (1959).
13. Yu.P.Irkhin & V.G.Shavrov, Tezisy Soveshchaniya po ferro- i antiferromagnetizmu (Program of the Conference on Ferro- and Antiferromagnetism), L., 1961.

* * * * * * *

MAGNETOELASTIC PROPERTIES OF TERBIUM AND HOLMIUM*

- K.P.Belov, R.Z.Levitin & S.A.Nikitin

In contrast to metals of the iron group, the rare earth metals (Dy, Ho, Tb, Tm, Er and Gd) are characterized by a complex dependence of the magnetic properties on the temperature and field. At low temperature these metals are ferromagnetic; then at a certain temperature θ_1 they change from the ferromagnetic state to the antiferromagnetic state with a Curie point θ_2. However, this antiferromagnetism between θ_2 and θ_1 can be comparatively easily removed by an external magnetic field.

In the present article we give data on the magnetoelastic properties of Tb and Ho.

For Tb, $\theta_1 = 223^\circ K$, $\theta_2 \approx 234^\circ K$.[4] The antiferromagnetic interaction is very weak and is removed by a field of about 200 Oe. Measurements of Young's modulus and the internal friction of terbium showed that below 230° there is a considerable anomaly in Young's modulus and at 223°K there is a maximum of the internal friction (Fig.1). These anomalies do not disappear in fields up to about 2500 Oe. The inset in Fig.1 shows the temperature dependence of Young's modulus near θ_1 and θ_2, plotted to a larger scale. It can be seen that there are two temperatures at which anomalies in Young's modulus are evinced: a large anomaly at $\theta_2 = 234^\circ K$ and a small anomaly at $\theta_1 = 223^\circ K$. This confirms the data of magnetic measurements on the presence of two Curie points θ_1 and θ_2 in Tb.

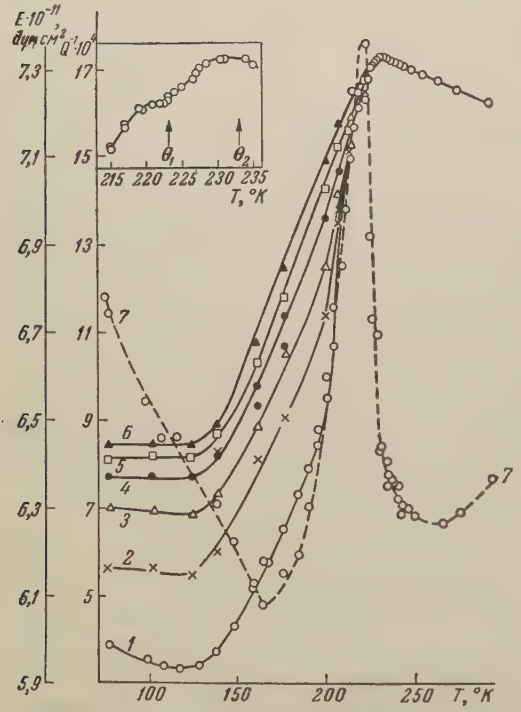

Fig.1. Young's modulus E(1-6) and internal friction Q^{-1} (7) in terbium: 1 - H = 0, 2 - H = 500, 3 - H = 1000, 4 - H = 1500, 5 - H = = 2000, 6 - H = 2500 Oe; 7 - H = = 0.

Fig.2 shows the results of measurements of magnetostriction in Tb. At liquid nitroger

---

*The present paper only gives part of the material presented at the Conference; the remainder appears in Refs.1, 2 & 3.

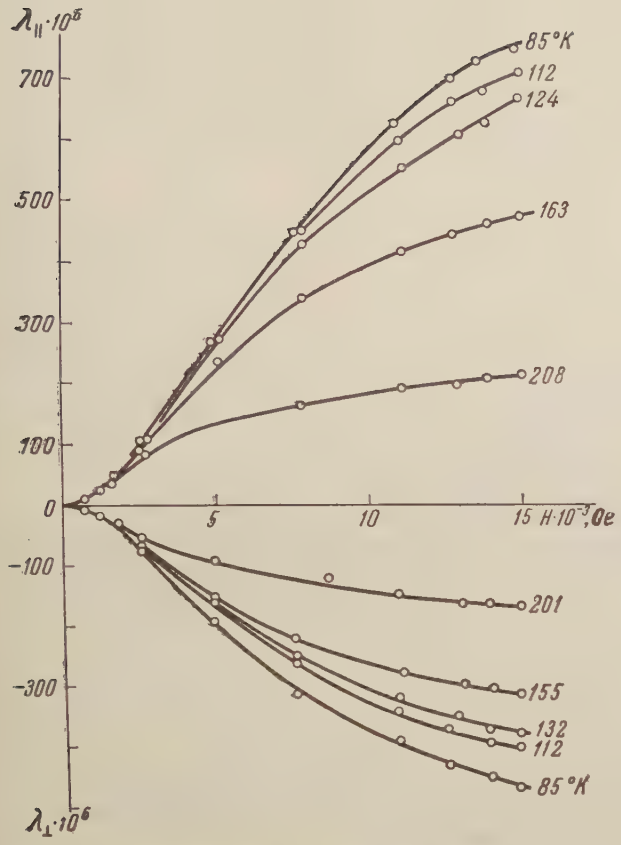

Fig.2. Isotherms of longitudinal and transverse magnetostriction in terbium.

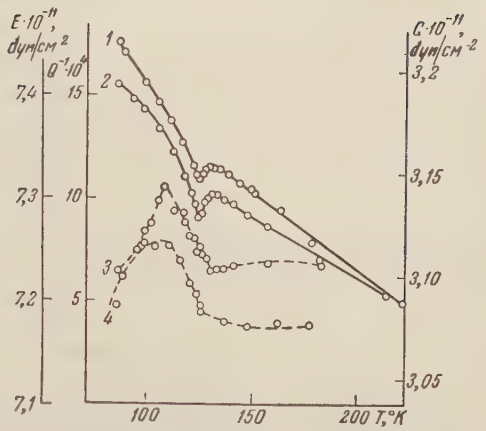

Fig.3. Moduli of elasticity and internal friction Q^{-1} in holmium: 1 - shear modulus G, 2 - Young's modulus E, 3 - internal friction in longitudinal vibrations, 4 - internal friction in torsional vibrations.

nitrogen temperature the magnetostriction is very high ($750\cdot10^{-6}$) and the λ versus H curves do not show saturation for fields up to 15 000 Oe. The magnetostriction decreases monotonically with increase of temperature.

The temperature dependences of the modulus of elasticity and internal friction in Ho were studied only in the neighborhood of the θ_2 point (Fig.3). At $\theta_2 = 196^{\circ}K$ there are anomalies in the moduli of elasticity. It is an interesting fact that anomalies are observed not only for Young's modulus but also for the shear modulus (a similar phenomenon was found in Dy). This shows that in the transition at θ_2 there occur other changes in addition to purely volume deformations. This is confirmed by the x-ray diffraction studies of Banister, Legvold & Spedding[5], who showed that the ratio of the unit axes a/c of Dy changes in going below θ_2.

Recent neutron diffraction studies by Koehler & Wollan[6] have shown that in the antiferromagnetic region (i.e., above θ_1) there is observed in Dy crystals the so-called helicoidal spin structure: the spins in neighboring basal planes of the hexagonal Dy lattice are turned relative to one another, forming a "spiral" arrangement. At temperatures below θ_1 the spins lying in these planes are parallel. It may be assumed that the other rare earth metals, in particular Ho and Tb, have the same spin structure. Measurements[1,2] of magnetostriction in Tb and Dy show that these metals have a high magnetoelastic energy (in a field of 15 000 Oe, $\lambda \approx 1000\cdot10^{-6}$ for Dy and $\lambda \approx 750\cdot10^{-6}$ for Tb), and great magnetic anisotropy, since there is no leveling off of the magnetostriction isotherms in fields up to 15 000 Oe. At temperatures below θ_1 the internal effective magnetic field, resulting from the great magnetic and magnetoelastic anisotropy, produces parallel orientation of the magnetic spins in the basal planes of the crystal, i.e., the ferro-

magnetic state. This effective field decreases with increase in temperature; at temperatures above θ_1 there abruptly forms the helicoidal spin configuration which is responsible for the antiferromagnetic behavior of the metal. However, if an external field is superimposed on this field, at a certain critical field value the helicoidal spin structure breaks down and the ferromagnetic state is restored. The value of the critical field increases with temperature inasmuch as the effective anisotropy field decreases greatly with temperature.

Physics Faculty,
Moscow State University

References

1. K.P.Belov, R.Z.Levitin, S.A.Nikitin & A.V.Ped'ko, Zhur.eksp.i teor.fiz., 40, 155 (1961). (Trans.Soviet Physics - JETP.)
2. R.Z.Levitin & S.A.Nikitin, Fizika metallov i metallovedenie, 11, 948 (1961). (Trans.Physics of Metals and Metallography.)
3. K.P.Belov & S.A.Nikitin, Ibid., 1961. (Trans.Ibid.)
4. W.Thoburn, S.Legvold & F.Spedding, Phys.Rev., 112, 56 (1958).
5. J.R.Banister, S.Legvold & F.H.Spedding, Phys.Rev., 94, 1140 (1954).
6. W.Koehler & E.Wollan, Report at the Seminar on Rare Earth Elements, California, Oct.1960.

* * * * * * * * *

DETERMINATION OF THE PARAMETERS CHARACTERIZING THE CATION DISTRIBUTION IN MULTIPLE COMPONENT SPINELS

- A.N.Men'

We shall consider a spinel structure containing N_i i-type cations. Let one parameter λ be sufficient for characterizing the distribution of cations among the tetrahedral (A) and octahedral (B) sites.* To determine the dependence of λ on the composition c_i we must solve the equation

$$\frac{dF}{d\lambda} = 0, \tag{1}$$

where

$$F = K(\lambda, C_i, T) - kT \ln w(\lambda, c_i). \tag{2}$$

In Eq.(2) we separated the configuration entropy (the second term); this will help us to analyze the existing experimental data and discuss theoretical studies. From (1) and (2) we obtain

$$\frac{d \ln w}{d\lambda} = \frac{1}{kT} \frac{dK}{d\lambda}. \tag{3}$$

---

*The existing experimental data[1] on $\lambda = f(T,c)$ are consistent with this assumption.

The existing experimental data on the c_i dependence of λ (see Table 4 in Ref.2) pertains to the following distributions:

$$\begin{pmatrix} \lambda_1 & 1-\lambda_1-r & \frac{N_3^A}{N}\dots\frac{N_n^A}{N} \\ 3c_1-\lambda_1 & 3c_2-1+\lambda_1+r & \frac{N_3^B}{N}\dots\frac{N_n^B}{N} \end{pmatrix}, \tag{4a}$$

$$\begin{pmatrix} 3c_1-\lambda_2 & 1-3c_1+\lambda_2-r & \frac{N_3^A}{N}\dots\frac{N_n^A}{N} \\ \lambda_2 & 3(c_1+c_2)-1-\lambda_2+r & \frac{N_3^B}{N}\dots\frac{N_n^B}{N} \end{pmatrix}, \tag{4b}$$

where

$$\lambda_1=\frac{N_1^A}{N};\quad \lambda_2=\frac{N_1^B}{N};\quad c_i=\frac{N_i}{3N};$$
$$r=\frac{1}{N}\sum_{i=3}^{h}N_i^A;\quad \sum_{i=1}^{n}N_i=3N. \tag{5}$$

Here N_i^μ is the number of i atoms at sites of type μ ($\mu = A, B$). If we neglect the correlation between the cations, then

$$w=\frac{N!}{\prod_{i=1}^{n}N_i^A!}\,\frac{(2N)!}{\prod_{i=1}^{n}N_i^B!}; \tag{6}$$

and in view of (6) and (4), Eq.(3) becomes

$$\frac{\lambda_1(3c_2-1+\lambda_1+r)}{(1-\lambda_1-r)(3c_1-\lambda_1)}=\alpha_1,$$
$$\frac{\lambda_2(1-3c_1+\lambda_2-r)}{(3c_1-\lambda_2)(3c_1+3c_2-1-\lambda_2+r)}=\alpha_2, \tag{7}$$

where

$$\alpha_i=\exp\left\{-\frac{f_i}{kT}\right\},\qquad f_i=f_i(\lambda c_i T)=\frac{dK}{d\lambda_i}. \tag{8}$$

If f is independent of λ for the case $\lim_{T\to 0}\alpha=0$ (low temperatures), then from (7) we readily obtain the explicit form of $\lambda_i = f(c)$:

$$\lambda_i=\frac{1}{2(1-\alpha)}[-(a_i+\alpha b_i)+\sqrt{(a_i+\alpha b_i)^2+4\alpha(1-\alpha)d_i}], \tag{9}$$

where

$$a_1=3c_2+r-1,\quad a_2=1-3c_1-r;$$
$$b_1=3c_1+1-r,\quad b_2=6c_1+3c_2-1+r;$$
$$d_1=3c_1(1-r),\quad d_2=3c_1(3c_1+3c_2-1+r). \tag{10}$$

For the case of high temperatures we obtain

$$\lambda_1\approx\frac{1-r}{1-\sum_{i=3}^{n}c_i}c_1,\qquad \lambda_2=3c_1-\lambda_1. \tag{11}$$

The assumption as to the independence of f of λ is valid for the $Fe_{1-\lambda}Mg_\lambda$-$(Fe_{1+\lambda}Mg_{1-\lambda})O_4$ (Ref.3) $MgFe_{2-c}Mn_cO_4$ $(0.8\leqslant c\leqslant 1.2)$ (Ref.4) and $Fe_{1-\lambda}Ti_\lambda$ $(Ni_{1+c}Fe_{1-2c+\lambda}$-$-Ti_{c-\lambda})O_4$ (see Table 1 in Ref.2) systems. Magnesium ferrite shows good agreement

between the theoretical $\lambda = f(T)$ curve and experiment[5], if we assume that f is a linear function of λ*; in this case the theory will contain two parameters. As regards the $Ni_{1+c}Fe_{2-2c}Ti_cO_4$ system, good agreement can be obtained between the theoretical $\lambda = f(c)$ curve and experiment[8], if f is considered as a linear function of λ and c, and three parameters are introduced.** There are a number of systems for which $\lambda(c_0) = 0$ when $T \neq 0$ (see table).

No.	System	c_0	Explicit form of Eq.(7)	Value of $\alpha\,\big|_{\substack{\lambda=0\\c=c_0}}$
1	$Ni_{1,5-c}Zn_cFeTi_{0,5}O_4$ See Ref.1, Fig.18b	0,5	$\frac{\lambda(0,5-c+\lambda)}{(0,5-\lambda)(0,5+c-\lambda)}=\alpha$	0
2	$Ni_{1,5-c}Mn_cFeTi_{0,5}O_4$ See Ref.1, Fig.20c	1	$\frac{\lambda(\lambda+c)}{(0,5-\lambda)(1-c-\lambda)}=\alpha$	$2\lim\limits_{\substack{\lambda\to0\\c\to1}}\frac{\lambda}{1-c-\lambda}$
3	$Li_{0,5}Fe_{2,5-c}Cr_cO_4$ See Ref.1, Fig.22b	0,5	$\frac{\lambda(1,5+\lambda-c)}{(0,5-\lambda)(1-\lambda)}=\alpha$	0
4	$Mg_cMn_{1-c}Fe_2O_4$ See Ref.6, Fig.4	0,1	$\frac{\eta[1+1,8c(\eta-0,8)]}{(1-\eta)[0,2+c(0,8-\eta)]}=\alpha$ See Ref.6, Eq.(9)	0

It follows from Eq.(8) that for $\alpha(\lambda = 0,\ c = c_0) = 0$ when $T \neq 0$, the function f should contain a term*** of the form $1/\lambda^p (1 > p > 0)$, i.e., when considering the systems listed in the table, in the concentration region containing c_0 in evaluating K it is not sufficient to take into account only the Coulomb energy u_c and the repulsion energy u_v associated with overlapping of ion cores, if Eq.(6) is assumed to be valid.

The analysis shows that to obtain agreement between theory and experiment for some systems it is sufficient to set $K = U_v\,(f = \text{const})$, for other systems we must assume that $\lambda = f(c)$, choosing $K = U_c + U_v\,(f = A_1\lambda + A_2c + A_3,\ A_i = \text{const})$. Finally, we should bear in mind that there are systems for which $K \neq U_c + U_v$. If we take into account short-range order in spinels, then Eqs.(7) will change inasmuch as the parameters characterizing the distributions will be Q_{ij} - the number of pairs of i and j atoms, and the parameters λ will be found from equations such as (1), but with the equilibrium values $Q_{ij}^{(0)} = Q_{ij}^{(0)}(\lambda)$ (Ref.9).

Even in the case of the simplest spinels calculation of the correlation parameters is very complicated, inasmuch as here for the first coordination sphere we must consider three different separations[10] between the cations. We will deal with this problem at a later date.

To arrive at a refined model, which would enable us to describe the configuration properties, we must determine $\lambda = f(c)$ experimentally at high temperatures; we must also determine the dependence of the specific heat[11] at the equilibrium vapor pressure of oxygen[12] on c, and the variation of the lattice constant as a function of c and λ.[13] For meaningful comparison of theory with experiment we should have available the results of direct measurements characterizing the dis-

---

*The dependence of f on λ for $MgFe_2O_4$ and $Mg_{0.75}Mn_{0.25}Fe_2O_4$, obtained from magnetic measurements[6] using the Néel model[7], is also linear.

**For the $Li_{0.5}Fe_{2.5-c}Cr_cO_4$ system there is no quantitative agreement between theory and experiment over the entire concentration range for any three constants (see Fig.2 of Ref.8).

***The function f can also become infinite in the presence of the term $\frac{1}{c-c_0}$ but in this case $K = \infty$, which has no physical meaning.

tribution of cations among the sublattices as a function of the temperature and composition.

Institute of Metallurgy,
Ural Branch of the
USSR Academy of Sciences

References

1. E.V.Gorter, Uspekhi fiz.nauk, 57, 435 (1955).
2. A.N.Men', Fizika tverdogo tela (In press). (Trans.Soviet Phys. - Solid State.)
3. R.Pauthenet & L.Bochirol, J.Phya.et radium, 12, 249 (1951).
4. K.Muramori & S.Miyahara, J.Phys.Soc.Japan, 15, 2354 (1960).
5. A.N.Men' & A.N.Orlov, Fizika metallov i metallovedenie (Physics of Metals and Metallography), 1, 410 (1955).
6. C.J.Kriessman & S.F.Harrison, Phys.Rev., 103, 857 (1956).
7. L.Néel, Ann.Phys., 3, 137 (1948).
8. A.N.Men' & A.N.Orlov, Issledovaniya po zharoprochnym splavam (Investigation of heat-resistant alloys), 2, 44, Publ.USSR Ac.of Sci., 1957.
9. A.N.Men', Fizika metallov i metallovedenie, 8, 450 (1959). (Trans.Physics of Metals and Metallography.)
10. A.N.Men', Ibid., 9, 801 (1960). (Trans.Ibid.)
11. A.N.Men', Fizika tverdogo tela, 3, 2466 (1961). (Trans.Soviet Physics - Solid State.)
12. A.N.Men', Ibid., 3, 1101 (1961). (Trans.Ibid.)
13. A.N.Men', Fizika metallov i metallovedenie, 6, 781 (1958). (Trans.Physics of Metals and Metallography.)

MAGNETIZATION AND THE MAGNETOCALORIC EFFECT IN URANIUM HYDRIDE AND DEUTERIDE

- A.I.Karchevskii & E.M.Buryak

Uranium hydride and deuteride were the first ferromagnets discovered among the chemical compounds of the actinide group[1]. In investigating these compounds it became feasible for the first time to observe a change in the magnetic properties of a substance associated with a difference in isotopic composition. Both substances have a simple cubic lattice with constants[2] $a_{UH_3} = 6.632$ Å and $a_{UD_3} = 6.625$ Å.

Several authors[3-6] have studied the magnetic, thermal and other properties of UH_3 and UD_3. Henry[4] has shown that the molar magnetization of UH_3 at 1.3°K is much greater than that of UD_3 (by about 30%); the relative difference in the magnetization decreases somwehat with increase of the magnetic field.

Investigations of the magnetocaloric effect by Abraham et al[5] showed the presence of an isotope shift of the Curie point: whereas $\theta_{fUH_3} = 182$°K, $\theta_{fUD_3} = 178.4$°K. Measurements of the specific heat by Abraham et al[6] threw doubt on the large difference between magnetizations of UH_3 and UD_3 at low temperatures, found by Henry[4], and confirmed the existence of an isotope shift of the Curie point.

The present paper gives the results of a detailed investigation of the magnetization of UH_3 and UD_3 at 4.2 and 77.4°K in magnetic fields of up to 23 kOe. We also studied the temperature dependences, in the vicinity of the Curie point, of the magnetization and the magnetocaloric effect in a wide range of magnetic fields. The paramagnetic susceptibility of both compounds was measured in the range from 250 to 500°K.

We found that at 4.2 and 77.4°K the magnetization permole of UH_3 exceeded the magnetization of UD_3 by 6% for all values of the magnetic field up to 23 kOe. The temperature dependence of the paramagnetic susceptibility χ of UH_3 and UD_3 cannot be described by the Curie-Weiss law, but is approximated by an expression of the type

$$\chi_{mol} = \frac{c_{mol}}{T - T_0} + \chi_0,$$

where $c_{mol} = 0.624$ deg mole^{-1} (for UH_3 and UD_3), and χ_0 is a temperature-independent term, equal to $+40 \cdot 10^{-5}$ g mole^{-1} for both substances; the paramagnetic Curie point T_0 for UH_3 is 176°K and for UD_3, 175°K. The ferromagnetic Curie points of UH_3 and UD_3 determined the maximum in the temperature dependence of the magnetocaloric effect are 182.0°K and 178.5°K, respectively.

At a field strength of 17 kOe the maximum value of the magnetocaloric effect in UH_3 is 0.53°C and in UD_3 0.4°C. Accordingly, the ratio of the maximum values of the magnetocaloric effect in UH_3 and in UD_3 is 1.5 ± 0.15.

The considerable difference between the magnetocaloric effects is mainly due to two factors: 1) near the Curie point the total heat capacity of UD_3 is 20% greater than that of UH_3 because of the difference between the contributions of deuterium and hydrogen to the heat capacity at these temperatures[6], and 2) according to our measurements, the derivative of magnetization with respect to temperature near the Curie point is 17% greater in UH_3 than in UD_3; the latter fact is related to the temperature behavior of the spontaneous magnetization of these compounds.

The results of our studies of the magnetocaloric effect are in satisfactory agreement with the data on the specific heat and magnetization of UH_3 and UD_3.

We wish to thank Academician I.K.Kikoin for his interest in the work and for useful discussions.

References

1. W.Trzebiatowski, A.Sliwa & B.Stalinski, Roczn.Chem., 26, 110 (1952); Ibid., 28, 12 (1954).
2. J.J.Katz & E.Rabinowitch, The Chemistry of Uranium, N.Y., 1951.
3. S.T.Lin & A.R.Kaufmann, Phys.Rev., 102, 640 (1956).
4. W.E.Henry, Phys.Rev., 109, 1976 (1958).
5. A.I.Karchevskii, Zhur.eksp.i teor.fiz., 36, 638 (1959). (Trans.Soviet Physics - JETP.)
6. B.M.Abraham, D.W.Osborne, H.E.Flotow & R.B.Marcus, J.Amer.Chem.Soc., 82, 1064 (1960).

* * * * * * *

MAGNETIC ANISOTROPY AND HYSTERESIS PROPERTIES OF RARE EARTH ORTHOFERRITES

- K.P.Belov, M.A.Zaitseva, A.M.Kadomtseva & V.A.Timofeeva

1. It will be recalled that rare earth orthoferrites (general formula: $MFeO_3$, where M is the rare earth ion), being antiferromagnets, exhibit weak ferromagnetism. These substances have a distorted perovskite structure: orthorhombic rather than cubic symmetry.

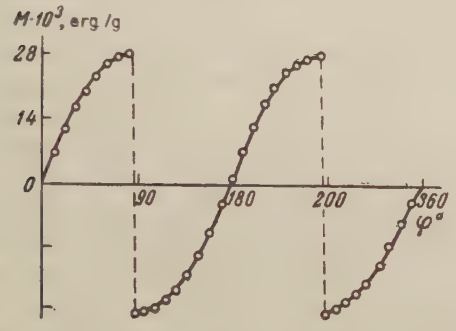

Fig.1. Torque diagram recorded for a $YbFeO_3$ single crystal at 20°C. φ - angle relative to the magnetic field; H = 19 kOe.

The nature of the weak ferromagnetism of antiferromagnets was explained in Refs.1 and 2. Neutron diffraction studies[3] have shown that the ordering of the magnetic spins of the rare earth ions occurs at temperatures below 20°K, while at higher temperatures antiparallel ordering of the spins obtains only for iron ions. According to theoretical ideas[1,2], the antiparallel ordering of the iron ion spins in orthoferrites is disturbed by the internal magnetic field of the crystal; this gives rise to a weak magnetic moment in the direction perpendicular to the antiferromagnetic array of the Fe^{3+} ion spins.

Turov & Naish[1] have demonstrated theoretically that weak ferromagnetism in orthoferrites should have a sharply anisotropic character. According to their evaluation, the fields needed to deflect the spontaneous magnetic moment from the direction of easy magnetization should be near the geometrical mean of the exchange field and the magnetic anisotropy field, i.e., about 10^5 Oe. There have been very few experimental studies devoted to the magnetic anisotropy of orthoferrite single crystals. In a search of the literature we found data only for a $GdFeO_3$ single crystal[4]; these data show that a 12 000 Oe magnetic field does not noticeably turn the magnetic moment from the direction of easy magnetization.

2. We grew single crystals of La, Pr, Nd, Sm, Eu, Gd and Yb orthoferrites by spontaneous crystallization from solutions in molten lead compounds (lead oxide and lead fluoride). A suspension anisometer was used to measure the torque of the crystals as a function of the angle of the specimen. Fig.1 shows the torque curve obtained at room temperature for $YbFeO_3$ orthoferrite; it will be seen that a magnetic field of about 20 kOe was not sufficient to deflect the spontaneous

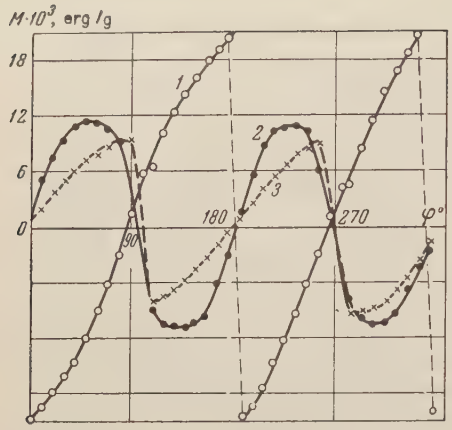

Fig.2. Torque diagrams for an $SmFeO_3$ single crystal, recorded in a 19 kOe field at different temperatures: 1) 20°, 2) 245°, 3) 400°.

magnetic moment from the direction of easy magnetization (c-axis) to the direction of the field (when the direction of the field was changed the specimen rotated sharply without reversal of the magnetization). Similar torque diagrams were obtained for other orthoferrite single crystals. The considerable stability of the magnetic moment with respect to its rotation by an external field is indicative of the extremely high magnetic anisotropy of these orthoferrites. The torque curves recorded for orthoferrites undergo little change with increase in temperature up to the Curie point; this indicates that there is little or no reduction of the anisotropy of weak ferromagnetism at these temperatures.

Bozorth[2] has reported that in $SmFeO_3$ single crystals at 210°C there occurs reorientation of the spontaneous magnetic moment from the a axis to the c axis. Fig.2 gives the torque curves for $SmFeO_3$, recorded below the temperature of reorientation of the axes (20°) and above this temperature (245°). As can be seen from Fig.2, at 20° the magnetization vector, aligned with the a axis, does not change its orientation under the influence of a magnetic field of about 20 kOe. At 245° the magnetic moment, having changed its orientation to the c axis, does not exhibit such stability, which is probably due to a diminution of the anisotropy constant. However, at higher temperatures the anisotropy constant again increases, as shown by the torque diagram recorded at 400°.

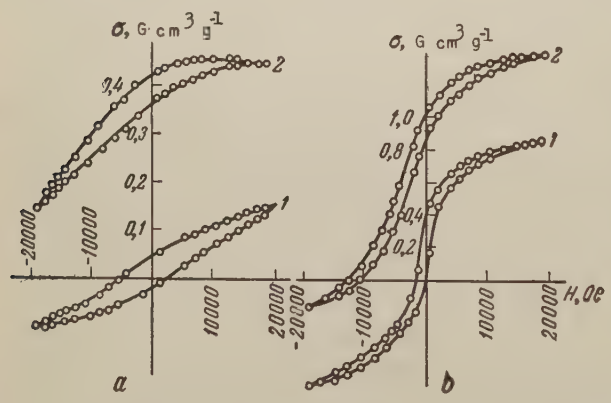

Fig.3. Magnetic hysteresis loops recorded at 20° for polycrystalline $LaFeO_3$ (a) and $YbFeO_3$ (b): 1) initial state, 2) after cooling in a magnetic field from the Curie point.

The large magnetic anisotropy is apparently due to the characteristic hysteresis and thermoresidual effects in rare earth orthoferrites. We observed these effects in polycrystalline specimens of La, Pr and Yb orthoferrites[5,6]. The magnetization curves and the magnetic hysteresis loops were recorded by a ponderomotive method in magnetic fields of up to 20 kOe. The hysteresis loops recorded for specimens cooled from the Curie point in a magnetic field were asymmetrical with respect to the coordinate axes (Fig.3) and were minor hysteresis loops. The thermoresidual magnetization was reduced to zero by a magnetic field of about 10 000 Oe, which points to the tremendous coercive forces in these orthoferrites.

We prepared polycrystalline La and Pr orthoferrites with the Fe^{3+} ions partially replaced by nonmagnetic Al^{3+} ions. The aim of these experiments was to reduce the "orthorhombic" distortion of the lattice by the introduction of Al^{3+} ions (at the Fe^{3+} sites), for Al^{3+} ions have a smaller ionic radius. In the substituted materials, $LaFe_{0.9}Al_{0.1}O_3$ and $PrFe_{0.9}Al_{0.1}O_3$, we observed a strong reduction of the coercive force and the

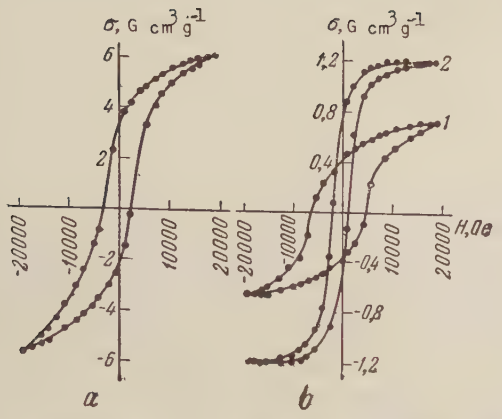

Fig.4. Magnetic hysteresis loops recorded at 20° after cooling in a magnetic field from the Curie point: a) $LaFe_{0.9}Al_{0.1}O_3$, b) $PrFeO_3$ (1) and $PrFe_{0.9}Al_{0.1}O_3$ (2).

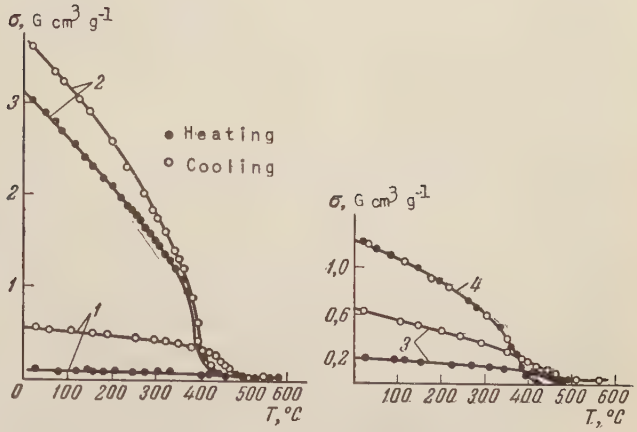

Fig.5. Temperature dependence of the specific magnetization of orthoferrites in a 4 kOe field: 1 - $LaFeO_3$. 2 - $LaFe_{0.9}Al_{0.1}O_3$, 3 - $PrFeO_3$, 4 - $PrFe_{0.9}Al_{0.1}O_3$.

thermoresidual effects (Fig.4); this may be due mainly to reduction in anisotropy. It is an interesting fact that these compositions showed a strong increase in magnetization; for the compound with La the increase was more than tenfold, and for the compound with Pr it was double (Figs.4 & 5). As we have already mentioned, the magnetic moment depends on the ratio of the exchange and crystal fields. When some of the Fe^{3+} ions are replaced by Al^{3+} ions, there apparently occurs a decrease of the exchange field, and at the same time there should be a reduction in the crystal field. The observed increase in magnetization may be due to predominance of the reduction of the exchange field, inasmuch as in this case there is an increase in the component of the magnetic moment in a direction perpendicular to the antiparallel array of the iron ion spins.

On the other hand, the increase in magnetization may also be due to the increased difference between the magnetizations of the two Fe^{3+} sublattices as some of the ions are replaced by nonmagnetic Al^{3+} ions. This may be due to the fact that in the range of low aluminum concentrations the Al^{3+} ions preferentially occupy certain sites in the perovskite lattice, thus giving rise to fluctuations in ionic concentration. Upon the introduction of appreciable numbers of Al^{3+} ions instead of Fe^{3+} ions, as in the case of $LaFe_{0.8}Al_{0.2}O_3$, there was observed a marked decrease in magnetization, presumably owing to the more uniform distribution of the Al^{3+} ions. In this case there was noted a certain increase of the coercive force, possibly due to hindrance of rotation, since in this case σH is too small to overcome the energy of magnetic anisotropy. In all cases replacement of Fe^{3+} ions by Al^{3+} ions leads to a lowering of the Curie point; this is apparently due to a reduction in the number of Fe^{3+}-O^{2-}-Fe^{3+} superexchange interactions.

We also studied compositions with some of the Fe^{3+} ions replaced by magnetic Cr^{3+} ions (ionic radius 0.64 Å). The introduction of Cr^{3+} ions into La and Pr orthoferrites causes a strong reduction of the coercive force, as compared with that in the stoichiometric compounds. In contrast to Al^{3+}, Cr^{3+} ions produce very little change in the magnetization; this is to be expected, since the exchange and the crystal fields should not undergo any appreciable changes in this case in view of the fact that the ionic radii and the magnetic moments of the Cr^{3+} and Fe^{3+} differ little from one another.

A.A.Katsnel'son and K.Yatskul'yan recorded Debye patterns for all the polycrystalline specimens; these patterns showed that the investigated compositions formed true solid solutions and did not contain any foreign phases.

We desire to thank E.A.Turov for valuable discussions of our experimental results.

Moscow State University

References

1. I.E.Dzyaloshinskii, Zhur.eksp.i teor.fiz., 32, 1547 (1957)(Trans.Soviet Physics - JETP); A.S.Borovik-Romanov, Ibid., 36, 75 (1959)(Trans.Ibid.); E.A. Turov & V.A.Naish, Fizika metallov i metallovedenie, 9, 10 (1960); 11, 161 (1960) (Trans.Physics of Metals and Metallography).

2. R.M.Bozorth, Phys.Rev.Letters, 1, 362 (1958).

3. W.C.Koehler, E.O.Wollan, C.K.Wilkinson & J.Cable, Acta Crystallogr., 10, 845 (1957).

4. M.A.Gilleo, J.Chem.Phys., 24, 1239 (1956).

5. K.P.Belov, M.A.Zaitseva & A.M.Kadomtseva, Zhur.eksp.i teor.fiz., 37, 1159 (1959). (Trans.Soviet Physics - JETP.)

6. H.Watanabe, J.Phys.Soc.Japan, 14, 511 (1959).

INVESTIGATION OF FERRIMAGNETS WITH THE STRUCTURE OF MAGNETOPLUMBITE AND GARNET IN STRONG PULSE MAGNETIC FIELDS

- G.A.Smolenskii & A.A.Andreev

The main purpose of the present work was to determine the saturation magnetization and spin configuration in the new group of rare earth hexoferrites synthesized in our laboratory. An additional purpose was to investigate the non-collinear arrangement of spins in rare earth garnets. Both purposes require the use of strong magnetic fields. Pulse magnetic fields (of up to 150 koe) were produced by discharge of a bank of capacitors. The pulse duration was up to $2 \cdot 10^{-3}$ sec; the inhomogeneity of the field in the 0.5 cm^3 working volume did not exceed a few percent.

For the measurements we used two series-opposing connected identical coils, into one of which we inserted the specimen of spherical or cylindrical shape with a volume of up to 50 mm^3. The output signals were observed on an oscillograph. The measurement error did not exceed 7%. The measurements were carried out both at room temperature and at liquid nitrogen temperature.

1. Bertaut[1] was the first to note the possibility of replacing the Ba ions by rare earth ions in barium hexoferrite, $BaFe_{12}O_{19}$, with the structure of magnetoplumbite. Bertaut introduced La^{3+}, Pr^{3+}, Nd^{3+}, Sm^{3+} and Eu^{3+} and obtained a limited region of solid solutions in all cases except that of La. Bertaut was not able to answer the question whether there occurs in these solid solutions change in the valence of part of the Fe ions or whether there form defects in one of the sublattices.

In our experiments we took into account the necessity of conservation of electric neutrality and, simultaneously with introduction of the trivalent rare earth ion (or Bi^{3+}) to replace Ba^{2+}, introduced a divalent ion - Ni^{2+}, Mg^{2+} or Co^{2+} - to replace an Fe^{3+} ion. Thus we were able to obtain a large group of solid solutions based on barium hexoferrite, including new compounds of the $M^{3+}Fe^{3+}_{11}M^{2+}O_{19}$ type with the magnetoplumbite structure.

We investigated solid solutions of the type

$$(1 - x)Ba^{2+}Fe^{3+}_{12}O_{19} - xM^{3+}Fe^{3+}_{11}M^{2+}O_{19},$$

where $M^{3+} = La^{3+}$, Pr^{3+} or Bi^{3+}, and $M^{2+} = Co^{2+}$ or Ni^{2+}.

The specimens were synthesized by reaction in the solid phase. By way of initial materials we used finely ground oxides and salts. The preliminary sintering of the mixtures containing the rare earth oxides was carried out at 1100°; the final sintering at 1250°. For the mixtures containing bismuth oxide, the preliminary sintering temperature was reduced to 800°, the final sintering temperature to 970-1100°; the roasting time in all cases was 2 hours.

X-ray diffraction studies, carried out at our request by A.G.Tutov, showed that in the

$$BaFe_{12}O_{19} - M^{3+}Fe^{3+}_{11}M^{2+}O_{19}$$

systems, where $M^{3+} = La^{3+}$ or Pr^{3+}, and $M^{2+} = Co^{2+}$ or Ni^{2+}, there form solid solutions of the magnetoplumbite type with concentrations of the second component up to 80 mole percent. The lattice parameters decrease only slightly with increase in the concentration of the second component. We were unable to obtain compounds of the $M^{3+}Fe^{3+}M^{2+}O_{19}$ type with the magnetoplumbite structure. A recent investigation[2] of the phase diagram of the La_2O_3—Fe_2O_3 system (actually the La_2O_3—Fe_2O_3—FeO system) showed that the analogous compound $LaFe^{3+}_{11}Fe^{2+}O_{19}$ does form,

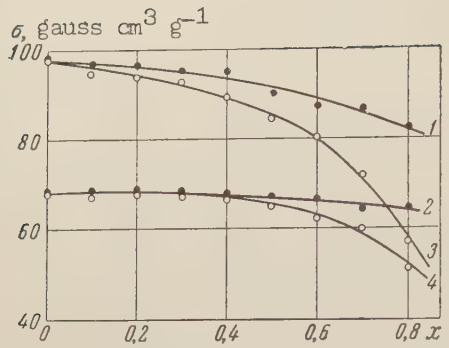

Fig.1. Variation of the saturation magnetization of $(1 - x)BaFe_{12}O_{19}$—$xM^{3+}Fe_{11}^{3+}M^{2+}O_{19}$ solid solutions with the concentration of the second component (x): 1 - $M^{3+} = La^{3+}$ & $M^{2+} = Co^{2+}$ (t = -196°); 2 - $M^{3+} = La^{3+}$ & $M^{2+} = Co^{2+}$ (t ≈ 20°); 3 - $M^{3+} = Pr^{3+}$ & $M^{2+} = Co^{2+}$ (t = -196°); 4 - $M^{3+} = Pr^{3+}$ & $M^{2+} = Co^{2+}$ (t ≈ 20°).

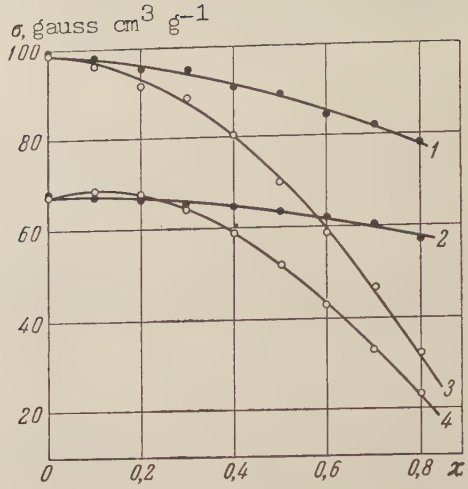

Fig.2. Variation of the saturation magnetization of $(1 - x)BaFe_{12}O_{19}$—$xM^{3+}Fe_{11}^{3+}M^{3+}O_{19}$ with the concentration of the second component (x): 1 - $M^{3+} = La^{3+}$ & $M^{2+} = Ni^{2+}$ (t = -196°), 2 - $M^{3+} = La^{3+}$ & $M^{2+} = Ni^{2+}$ (t ≈ 20°); 3 - $M^{3+} = Pr^{3+}$ & $M^{2+} = Ni^{2+}$ (t = -196°); 4 - $M^{3+} = Pr^{3+}$ & $M^{2+} = Ni^{2+}$ (t ≈ 20°).

but only in a very narrow temperature range. Solid solutions in the $BeFe_{12}O_{19}$—"$BiFe_{11}CoO_{19}$" system form in a more restricted range of second component concentrations (up to 40 mole percent). The same thing is observed for systems containing rare earth ions of small radius.

The results of our measurements of the saturation magnetization of some of the solid solutions (at H_{max} = 75 koe) are shown in Figs.1 & 2. It will be seen that in general the saturation magnetization of the solid solutions decreases with increase of the second component; for the system with Pr this effect is weaker.

The differential susceptibility in the high field region, as determined from the hysteresis loop, is small (within the limits of the experimental error), which indicates collinear arrangement of the magnetic moments. Introduction of the second component leads to increase of the coercive force several fold over the value for barium hexoferrite.

Similar data were obtained for $BaFe_{11}O_{19}$ — "$BiFe_{11}CoO_{19}$" solid solutions. The saturation magnetization decreases with increase of the second component (for 10 mole percent of the second component σ = 62.5%, while for 20 mole percent σ = = 59 gauss cm³ g⁻¹), while the coercive force at room temperature increases by a factor of 1.5 in going from the 10 to the 20 mole percent composition.

The experimental data on magnetization allow of drawing certain inferences regarding the spin configuration in the investigated ferrites. It is known that the unit cell of barium hexoferrite consists of spinel blocks separated by blocks with hexagonal dense packing of oxygen ions, one of which is replaced by a barium ion or in our case by a rare earth ion. Obviously, the cobalt or nickel ion, as in the corresponding invert spinels, replaces a trivalent Fe ion in the octahedral position in the spinel blocks. The unit cell contains two formula units: $BeFe_{12}O_{19}$. Of the 12 iron ions per formula unit two are in tetrahedral positions, nine in octahedral positions, and one is surrounded by five oxygen ions. The

magnetic moments of the ions in the tetrahedral positions are oriented antiparallel to the total magnetic moment of the other ions.

Knowing the composition of the solid solution, the distribution of cations between the sublattices and the signs of the exchange interactions, one can calculate the variation of the magnetization as a function of the second component concentration. We do not know, however, how the exchange interaction between the rare earth ion and the neighboring magnetic ions is realized or the sign of this interaction. Decrease of the saturation magnetization as a result of introduction of rare earth ions can be explained only on the assumption that the magnetic moments of these ions are oriented antiparallel to the total magnetic moment of the other ions. In this case one can readily calculate the magnetic moment per formula unit of the solid solution (in Bohr magnetons)

$$m = 4(1-x)\, m_{Fe^{3+}} + x\,(3m_{Fe^{3+}} + m_{M^{2+}} - m_{M^{3+}}),$$

where $m_{Fe^{3+}}$, $m_{M^{2+}}$ and $m_{M^{3+}}$ are the magnetic moments of Fe^{3+}, M^{2+} and M^{3+}, respectively. The results of such calculations are in fairly good agreement with experiment if one takes into account the orbital moments of the rare earth ions.

2. Recently, it was shown as a result of neutron diffraction studies[3] that the magnetic moments of the Ho^{3+} ions in HoFe garnet are oriented at an angle to [111], the direction of the moments of the iron atoms.

It is natural to assume that such an umbrella-shaped or conical magnetic structure will undergo appreciable deformation in a magnetic field. In connection with this, we investigated Y, Eu, Ho and Er iron garnets and $Ho_3Fe_2(Fe,Al)_3O_{12}$ and $Ho_3(Fe,Sc)_2Fe_3O_{12}$ solid solutions. The differential magnetic susceptibility in strong magnetic fields (~150 koe) was determined from the hysteresis loops. Holmium garnet, its solid solutions and erbium garnet are characterized by a high differential susceptibility ($\chi_g \approx (1\text{-}2)\cdot 10^{-4}$ cm^3/g). In contrast, the differential susceptibility of yttrium garnets is low. The noted high differential susceptibility of holmium and erbium garnets is observed both at room temperature and at liquid nitrogen temperature (77°K).

It is known that the compensation point in holmium garnet lies at 136°K. Above the compensation point there predominates the magnetic moment of the iron ion sublattices, while below the point the magnetic moment of the rare earth ion sublattices predominates. The differential susceptibility of holmium garnet both above and below the compensation point is of the same order of magnitude, and hence one can hardly attribute the high differential susceptibility to the paraprocess (reorientation of the magnetic moments) in the relatively weakly bound magnetic sublattice of the rare earth ions, particularly in view of the low value of the differential susceptibility in europium garnet. It would be of interest to determine the differential susceptibility of all rare earth garnets.

Taking into account the relatively weak exchange coupling in the rare earth sublattice in garnets, particularly in garnet solid solutions, one might expect flipping of the magnetic moments of this sublattice in fields of the order of a few kiloersted. However, we did not succeed in observing this effect in fields up to 150 koe for holmium garnet and its solid solutions either at room temperature or at liquid nitrogen temperature.

We desire to express our gratitude to E.S.Sher for preparing the specimens and A.G.Tutov for the x-ray diffraction studies.

Institute of Semiconductors,
Academy of Sciences of the USSR

References

1. A.Deschamps & E.Bertaut, Compt.rend., 244, 25, 3069 (1957).
2. V.L.Moruzzi & M.W.Shafer, J.Am.Ceram.Soc., 43, 7 (1960).
3. A.Herpin, W.C.Koehler & P.Meriel, Bull.Am.Phys.Soc., II, 5, 457 (1960).

* * * * * * *

INVESTIGATION OF THE MAGNETIC PROPERTIES OF SOME FERROMAGNETS WITH THE STRUCTURE OF PEROVSKITE AND GARNET

- G.A.Smolenskii, V.P.Polyakov & V.M.Yudin

1. Smolenskii et al[1] showed the possibility of preparing ferromagnets in the form of solid solutions with the perovskite structure through ordering of the ions in the octahedral sublattice. In the present work we checked the suggestion using $LaFeO_3$—$Sr(Ni_{0.5}W_{0.5})O_3$ solid solutions. The first compound is antiferromagnetic*, while the second is paramagnetic with ordered arrangement of the Ni^{2+} and W^{6+} ions in the octahedral positions[2].

The polycrystalline specimens were prepared from finely ground oxides of the appropriate metals ("chemically pure" or "reagent grade pure") by two stage sintering in air at temperatures of 1100° (2 hours at the maximum temperature) and 1350° (1 hour). The material was thoroughly ground after the first roasting.

X-ray diffraction studies, carried out by A.G.Tutov[2], showed that in the $LaFeO_3$—$Sr(Ni_{0.5}W_{0.5})O_3$ system there form solid solutions with the perovskite structure. Only a very small amount of second phase was present in most compositions. In addition, specimens containing 76 and 90% of the second component were studied petrographically. The first specimen was homogeneous and the second was heterogeneous; specimens containing more than 76% of the second component were therefore not investigated.

The magnetic moments of the specimens were determined by the Faraday method on a magnetic balance with a sensitivity of 10^{-5} g. Mohr's salt was used as the "standard". An inhomogeneous field with an adequate constant gradient was provided by Sucksmith pole pieces. The field intensity between the pole pieces attained 8000 Oe. The specimens were spheres ranging from 1 to 3 mm in diameter, depending on the magnetic moment in the material. The moments were measured in the temperature interval from -196 to +850°.

Fig.1 shows the temperature dependences of the saturation magnetization obtained for five solid solutions. The magnetization was determined by linear extrapolation of $m = f(H)$ to $H = 0$. It will be evident from Fig.1 that the phase transitions in the investigated solid solution are strongly smeared out; hence it is probably more appropriate to speak of a Curie region, rather than a Curie point. However, if we arbitrarily determine the Curie temperature θ, as shown in Fig.1, for the solid solution containing 60 mole percent $Sr(Ni_{0.5}W_{0.5})O_3$, we find that the concentration (x) dependence of θ is almost linear.

Fig.2 shows the variation of the magnetization of $(1 - x)LaFeO_3$—$xSr(Ni_{0.5}W_{0.5})O_3$ solid solutions with the concentration of the second component . Curve 1 corresponds to the calculated values at 0°K in the case of complete ordering of the ions, when only the spin moments are considered[1]. In this case the formula for the solid solutions can be written as follows

---

*Minor noncolinearity of the spin moments is neglected here.

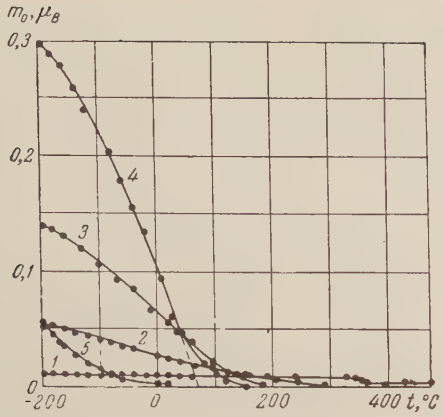

Fig.1. Temperature dependence of the saturation magnetization of solid solutions $(1-x)$-$LaFeO_3$—$xSr(Ni_{0.5}W_{0.5})O_3$ solid solutions with the perovskite structure: 1) $x = 0.2$, 2) 0.4, 3) 0.5, 4) 0.6, 5) 0.76.

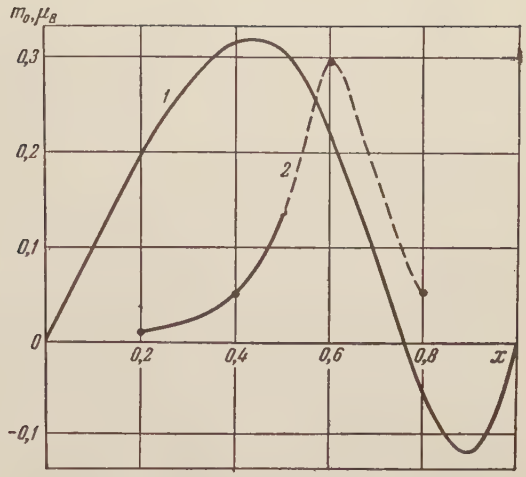

Fig.2. Calculated (1) and experimental (2) values of saturation magnetization of $(1-x)LaFeO_3$—$xSr(Ni_{0.5}W_{0.5})O_3$ solid solutions as a function of the second component concentration.

$$\underset{\text{I}}{La_{1-x}Sr_x(Fe_{\frac{1-x}{2}}Ni_{\frac{x}{2}})}\underset{\text{II}}{(Fe_{\frac{1-x}{2}}W_{\frac{x}{2}})}O_3.$$

Curve 2 is plotted on the basis of the values found experimentally at 77°K. For up to 55 mole percent of the second component the experimental curve lies lower than curve 1. This may be explained by incomplete ordering of the ions in this region of solid solutions. The displacement of curve 2 relative to curve 1 in the range above 55 mole percent of the second component may be due to the deviation from the statistical distribution of ions in the octahedral sublattices I and II or to the presence of a second phase in the actual solid solutions.

2. The second group of investigated ferromagnets consisted of two series of solid solutions with the garnet structure and having the following compositions:

$$1)\ (1-x)\{Y_3\}[Fe_2](Fe_3)O_{12} - x\{Ca_3^{2+}\}[Fe_2](Si_3^{4+})O_{12};$$

$$2)\ (1-x)\{Y_3\}[Fe_2](Fe_3)O_{12} - x\{Y_2Ca_2^{2+}\}[Fe_2](Fe_2V^{5+})O_{12}.$$

We felt that it would be of interest to use these solid solutions to check the validity of Gilleo's[3] calculations of the magnetic moments in mixed garnets. We recall the basic assumption underlying these calculations. A magnetic ion makes a contribution to the magnetization provided this ion has not less than two magnetic ions as nearest neighbors in the other sublattice. For garnets the magnetic moment (in Bohr magnetons) per formula unit for the first group of solid solutions is equal to

$$m = 5\{3(1-x) - 2[1-(6x^5 - 5x^6)]\}, \quad (1)$$

and for the second group

$$m = 5\left\{3\left(1-\frac{x}{3}\right)-2\left[1-\left(6\left(\frac{x}{3}\right)^5-5\left(\frac{x}{3}\right)^6\right)\right]\right\}. \qquad (2)$$

The above-mentioned solid solutions are convenient for checking these calculations, since we can ensure beforehand that practically all the small ions, Si^{4+} (r = 0.39 Å) and V^{5+} (r = 0.4 Å), will be located in the tetrahedral sublattice.

The specimens were prepared of "chemically pure" or "reagent grade pure" oxides of the corresponding metals. The first sintering was carried out at 1050-1100° (1 hour) for the first system and at 1000° (1 hour) for the second system. The final sintering temperatures were 1250-1400° (1 hour) for the first system and 1200-1300° (1 hour) for the second system. Formation of the solid solutions was checked by x-ray diffraction studies. The lattice parameters of the solid solutions decrease with increase of the second component. We did not succeed in obtaining a single phase solid solution in the case of $YtCa_2Fe_3VO_{12}$.

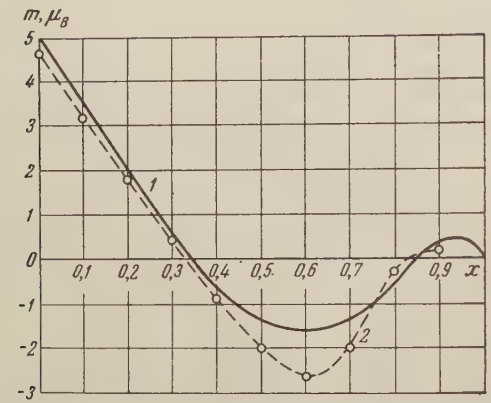

Fig.3. Calculated (1) and experimental (2) values of magnetization of $(1-x)Yt_3Fe_5O_{12}-xCa_3Fe_2Si_3O_{12}$ solid solution as a function of the second component concentration.

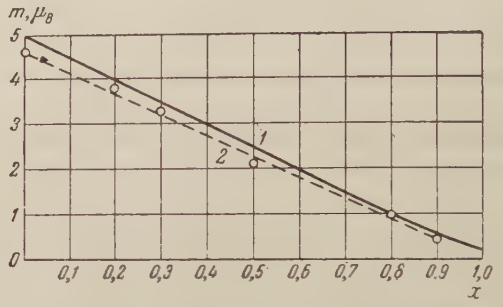

Fig.4. Calculated (1) and experimental (2) values of magnetization of $(1-x)Yt_3Fe_5O_{12}-xYtCa_2Fe_4VO_{12}$ solid solution as a function of the second component concentration.

Figs.3 and 4 show the relationships between the magnetization of the solid solutions and the concentration of the second components. At low concentrations the magnetization is described by the formula

$$\sigma_M = \sigma_\infty\left(1-\frac{a}{H^2_{\text{intnl}}}\right),$$

while at high concentrations it is given by

$$\sigma_M = \sigma_0 + \chi H_{\text{intnl}}.$$

The curves 1 correspond to the 0°K values calculated by means of Eqs.(1) and (2), taking into account only the spin moments and on the assumption that the small Si^{4+} and V^{5+} ions are situated at the tetrahedral positions. Curves 2 are plotted on the basis of values found experimentally at 77°K. It should be mentioned that the direction of the magnetization is not determined in the experiment. It will be evident that there is relatively good agreement between the calculated and experimental values. The greatest divergence is obtained for the first system in the region of the minimum.

We desire to thank E.S.Sher for preparing the specimens and A.G.Tutov for the x-ray diffraction studies.

References

1. G.A.Smolenskii, V.A.Isupov, N.N.Krainik & A.I.Agranovskaya, Present issue of the Bulletin, p.1345.
2. E.J.Fresia, Z.Katz & R.Ward, J.Amer.Chem.Soc., 81, 18, 4783 (1959).
3. M.A.Gilleo, J.Phys.Chem.Solids, 13, 33 (1960).

* * * * * * *

TEMPERATURE DEPENDENCE OF THE PARAMAGNETIC SUSCEPTIBILITY OF MIXED FERRITES

- V.I.Chechernikov

The magnetic susceptibility of most ferromagnetic metals and alloys at temperatures above the ferromagnetic Curie point (θ_f) varies with temperature according to the Curie-Weiss law. In the case of ferrites, however, this simple law does not hold.

The temperature dependence of the paramagnetic susceptibility of ferrites is described by a more complex law, first established by Néel[1], namely,

$$\frac{1}{\chi} = \frac{1}{\chi_0} + \frac{T}{C_H} - \frac{\sigma}{T - \theta}, \qquad (1)$$

where the constants θ, χ_0 and σ depend on the molecular field constants (n, α and β) characterizing the exchange interaction between the different sublattices (AB) and within the sublattices (AA and BB) and also on the number of magnetoactive iron ions (λ and μ), situated in these sublattices and their atomic constant C_H. This difference in the behavior of ferrites, as compared with metallic ferromagnets, is due to the substantial difference between their magnetic structures. The difference is evinced most clearly in their behavior in the paramagnetic region.

In the development of the theory of ferromagnetic alloys an important part was played by investigations into the dependence on the composition of the alloy of the parameters C and θ_p in the Curie-Weiss formula. We feel that it would now be of considerable interest to study the various systems of mixed ferrites with a view to elucidating the dependences of the constants C_H, θ, $1/\chi_0$ and σ on the composition of the ferrite, particularly since no such investigations have yet been carried out. For this purpose we studied several ferrite systems, deliberately choosing ferrites in which the magnetic properties vary strongly with the composition. Particular attention was paid to ferrites with mixed structure, where the ferrite gradually changes from inverted to normal. The following ferrite systems were investigated: $Fe_2O_3(1 - z)NiO \cdot zMO$, where M represents Zn, Cd, Mg or Mn and $Fe_2O_3(1 - z)CdO \cdot zPO$, where P stands for Cu or Li. The concentration z was varied from 0 to 1. The ferrite parameters were measured in the temperature range from the ferromagnetic Curie point to 1500°K.

Figure 1 shows the temperature dependence of the reciprocal of the molar susceptibility for some nickel-cadmium ferrites. It will be seen that the temperature dependences of $1/\chi$ are nonlinear: the curves are concave toward the temperature axis. It should be emphasized that with transition of the ferrite from the inverse to the normal form the curvature gradually decreases and for simple cadmium ferrite there obtains an almost linear relationship. In general, an analogous pattern is observed for the other systems with similar structure.

As regards ferrites with inverted structure, while they yield plots with the

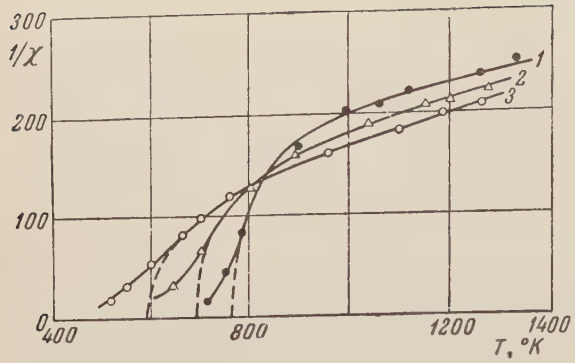

Fig.1. Reciprocal of the susceptibility versus temperature curves for the ferrites: 1 - $Fe_2O_3 \cdot 0.8NiO \cdot 0.2CdO$, 2 - $Fe_2O_3 \cdot 0.6NiO \cdot 0.4CdO$, 3 - $Fe_2O_3 \cdot 014NiO \cdot 0.6CdO$.

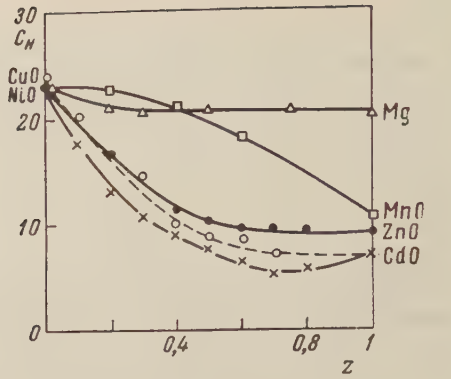

Fig.2. Variation of C_H with the composition of the ferrites.

greatest curvature, the character of the $1/\chi$ versus T curve does not change as much with composition.[2]

In order to compare the experimental results with theory it is essential to know the numerical values of the constants C_H, θ, $1/\chi_0$ and σ entering into Eq.(1). Unfortunately, it is difficult to evaluate these constants theoretically, not only for mixed ferrites but even for simple ferrites. Hence we determined these constants from experimental data obtained by the Néel method[1]. Using these values in Eq.(1) we obtained the theoretical dependences shown by the dashed curves in Fig.1. It can be seen that satisfactory agreement between the theoretical and the experimental data is obtained only at high temperatures. It must be emphasized that such agreement is observed for all the investigated ferrites, although the character of their $1/\chi$ versus T curves is extremely different. Divergence between the theoretical and experimental curves is evinced only near the ferromagnetic Curie point. Before dealing with the behavior of the mixed ferrites near θ_f, we shall consider the regularities obtained for the constants C_H, θ, $1/\chi_0$ and σ.

One of the important constants in Eq.(1) is C_H which, to some extent, should characterize the paramagnetic moment P_p of the ferrite. The variation of this constant with z is shown in Fig.2.

It can be seen that for all the ferrite systems based on nickel, C_H decreases with increase in the content of the second component, but not in direct proportion. From the results of an investigation of similar ferrites in the ferromagnetic region we know that the magnetic moment P_f, determined from the absolute saturation, at first increases with increase of z and then begins to decrease. The behavior of ferrites thus differs considerably from that of metallic ferromagnets, since it is well known that for metallic ferromagnets the variations of P_f and P_p are characterized by the same law. We must emphasize that the above argument is valid only provided C_H and P_p are related.

Figures 3,4 and 5 show the dependences of the constants θ, $1/\chi_0$ and σ. It will be evident that for almost all investigated ferrites these constants also decrease with increase in z.

From the described general variation of the Néel formula constants it can be inferred that their greatest change occurs in ferrites with mixed structure. In order to explain even qualitatively the observed regularities we must know the

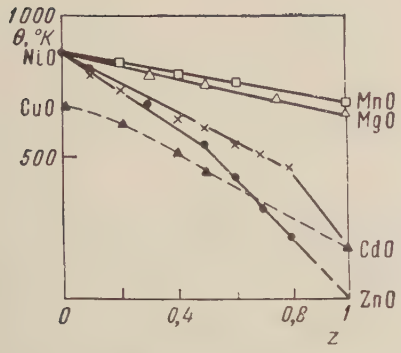

Fig.3. Variation of θ with composition

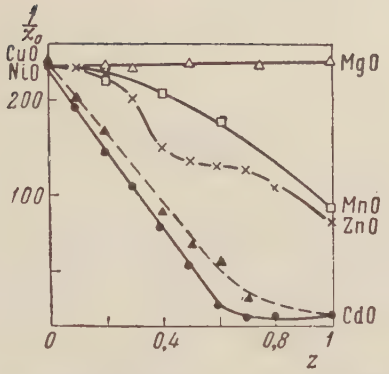

Fig.4. Variation of $1/\chi_0$ with composition.

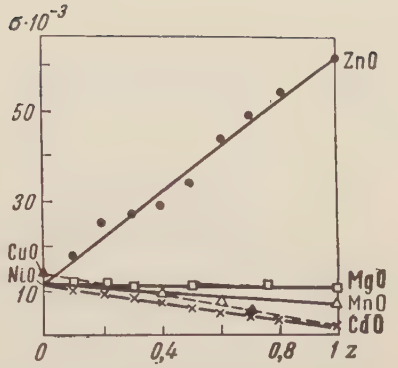

Fig.5. Variation of σ with composition.

relationship between the molecular field constants and the composition of the ferrites; this can only be obtained by investigating the ferrites in the ferromagnetic region.

We have already noted that near the Curie point the experimental results do not agree with the theoretical curves given by Eq.(1). The divergence may be due to two factors: the presence of a magnetic short-range order and/or inhomogeneity of the specimens as regards composition. In order to clarify this point we investigated some of the ferrites near the ferromagnetic Curie point. These studies showed that in all mixed ferrites, as in simple ferrites and metals, there exists a transition region where the magnetic susceptibility depends not only on the temperature but also on the magnetic field intensity. The extent of this transition region is appreciable: for some ferrites it attains a width of 200 to 250°.

It is an interesting fact that the wider the transition region, the greater the deviation of the experimental results from the theoretical curve. Our experiments have shown that the width of the transition region changes somewhat, depending on the heat treatment. Thus heating for 10 hours at 1200° followed by quenching in water reduces the width of the transition region for some ferrites by 50-60°.[3] In no case, however, did we observe complete suppression of the transition region. We note, incidentally, that for Yt-Fe, Eu-Fe and Gd-Fe garnets the width of the transition region is much narrower than for other ferrites (≤10°). For these ferrite-garnets there is agreement between theory and experiment over a wider temperature range than for ferrites with the spinel structure.

Conclusions

By systematically investigating a large group of mixed ferrites we were able to establish the composition dependences of the constants C_H, θ, $1/\chi_0$ and σ entering into the Néel formula for the paramagnetic susceptibility. It was demonstrated that there is good agreement between theory and experiment in the range of high temperatures.

Another important inference of the present work is that the magnetic structure of a material can be qualitatively determined from the character of the $1/\chi$ versus temperature curve in the paramagnetic region. When the temperature dependence is linear, i.e., the Curie-Weiss law holds, for $\theta_p > 0$ there obtains the magnetic structure of normal ferromagnets, while for $\theta_p < 0$ there is observed the structure of compensated antiferromagnets. As for ferrimagnets, they obey the

Néel law in the paramagnetic region.

Physics Faculty,
Moscow State University

References

1. L.Néel, Ann.Phys., 3, 137 (1948).
2. V.I.Chechernikov & V.G.Kol'chenko, Vestnik, Moscow State Univ., 1, 36 (1961).
3. V.I.Chechernikov & Yu.D.Volkov, Ibid., 2, 101 (1959).

* * * * * * *

FREQUENCY AND TEMPERATURE DEPENDENCES OF THE INITIAL PERMEABILITY OF FERRITES WITH THE GARNET STRUCTURE

- G.A.Smolenskii, Chang Tsung & E.S.Sher

In a recent brief paper[1] we reported on the effect of electron diffusion on the radiofrequency dispersion of the initial permeability μ' of ferrites with the garnet structure. In the present article, we give the results of investigation of the frequency and temperature dependences of μ' and μ'' of these ferrites subjected to different heat treatments.

The measurements were carried out on polycrystalline and single crystal specimens.[1] All the polycrystalline specimens were of high density (~94-96% of the theoretical).

Fig.1 shows the frequency dependence of μ' and μ'' of a polycrystalline yttrium ferrite specimen at different temperatures. This specimen was sintered at 1450°C (holding time 1 hour at maximum temperature) in air and had a resistivity

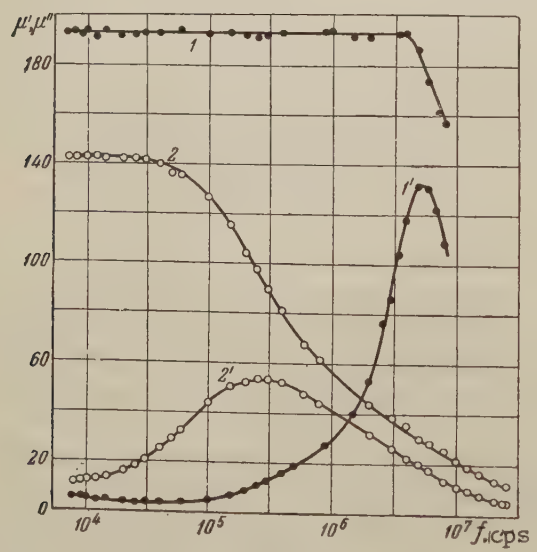

Fig.1. Frequency dependences of μ' (1,2) and μ'' (1',2') of a polycrystalline yttrium ferrite specimen at 100°C (1,1') and at 20°C (2,2').

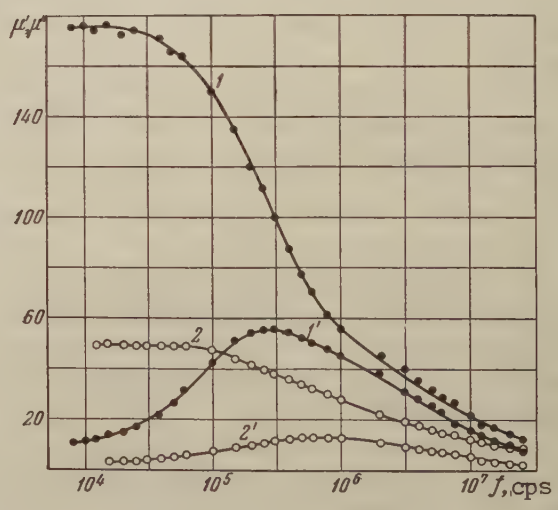

Fig.2. Frequency dependences of μ' and μ'' of a polycrystalline yttrium ferrite specimen in the zero-magnetization state (1,1') and in the remanence state (2,2').

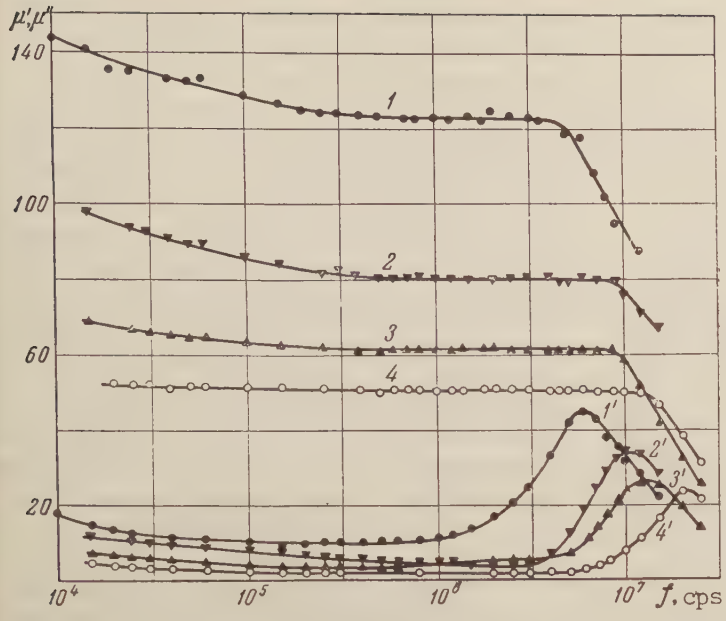

Fig.3. Frequency dependences of μ' (1-4) and μ'' (1'-4') of doped polycrystalline yttrium ferrite specimens: 1,1') 1% MnO, 100°; 2,2') 2% CuO, 100°; 3,3') 1% MnO, 20°; 4,4') 2% CuO, 20°.

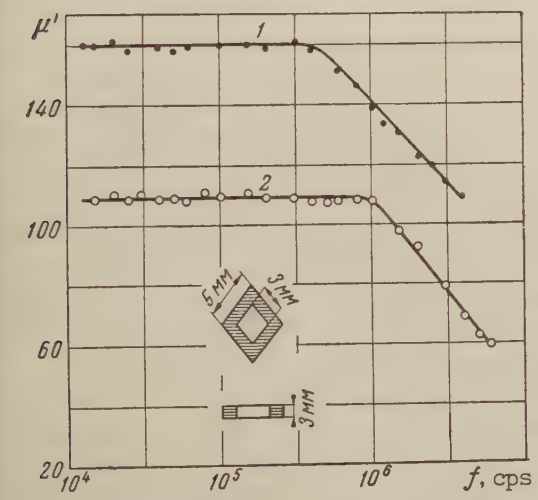

Fig.4. Frequency dependences of μ' of an yttrium ferrites specimen in the form of a frame cut from a single crystal at 100° (1) and at 20°C (2).

of ~10^6 ohm·cm at room temperature. The resistivity is indicative of the Fe^{2+} ion content. It will be evident from Fig.1 that at room temperature dispersion of the permeability may be attributed to a relaxation mechanism. With increase in temperature the μ' peak shifts to the side of higher frequencies. In the remanence state μ' decreases considerably as compared with the zero-magnetization state (see Fig.2).

The magnetic spectrum of polycrystalline ferrites with high resistivity differs considerably from that of ferrites with a low resistivity. The frequency dependences of μ' and μ'' of ferrites with a high resistivity ($\rho \approx 10^{10}$ ohm cm) at different temperatures are shown in Fig.3. The high resistivity of these ferrites is realized due to formation of donor-acceptor pairs (as a result of introduction of MnO) and by reduction in the sintering temperature of the specimens through addition of CuO. With increase in temperature the μ'' peak is displaced toward lower frequencies, i.e., there occurs resonance of the domain boundaries. A similar phenomenon was observed when studying a frame cut from a single crystal with high resistivity (Fig.4). The frame was cut in the (110) plane in such a way that the edges of the frame coincided with the direction of the volume diagonals of the unit cell.

However, the resonance frequency in the single crystal at room temperature is an order of magnitude lower than in a polycrystalline specimen. It is noteworthy that the initial permeability at low frequencies of high-resistivity ferrites of both polycrystalline and single crystals is lower than the initial low-frequency permeability of low-resistivity polycrystalline specimens.

The magnetic spectra of high-resistivity ferrites in the remanence state and in the zero-magnetization state hardly differ (Fig. 5, curves 3 and 4 pertain to a nonoriented single crystal).

It would obviously be interesting to study the magnetic spectra of the same specimen while varying its resistivity; this can be achieved by heat treatment in various gaseous media.

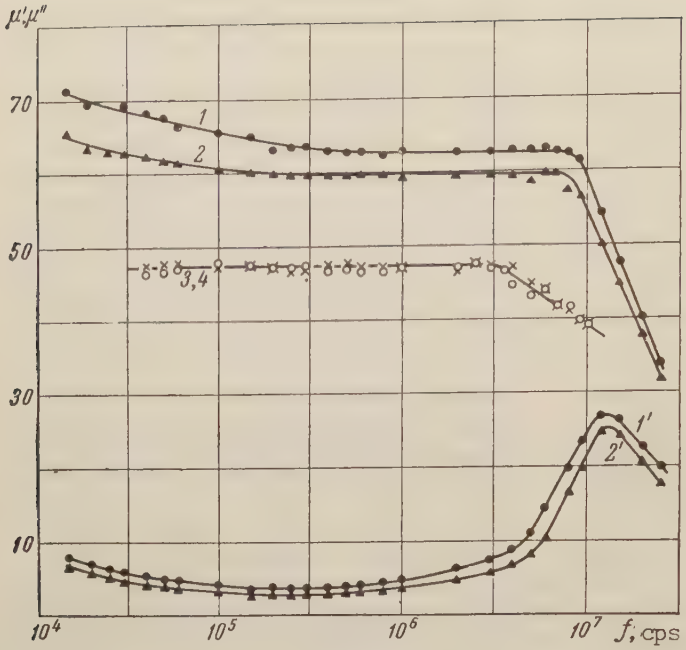

Fig.5. Frequency dependences of μ' and μ'' of yttrium ferrite in the remanence state (2,2',4) and in the zero-magnetization state (1,1',3); 1,1',2,2' - polycrystalline specimen doped with 1% MnO; 3,4 - single crystal.

Hence we carried out measurements before and after heat treatment on a specimen in the form of a toroid cut from a nonoriented single crystal. It was found in tests that reduction or oxidation of the whole specimen during heat treatment occurred only in the case of thin specimens. For heat treated thick specimens, after removal of the surface layer, the resistivity and initial permeability were the same as initially. Table 1 gives data on the resistivity ρ, dielectric constant ε' and initial permeability μ' of a single crystal toroid (d_1 = 3.7; d_2 = 2.8 and h = = 1.8 mm) before and after heat treatment.

The frequency dependences of μ' for this single crystal before and after heat treatments are shown in Fig.6.

On analyzing the results, we note a certain correlation between the resistivity and initial permeability in the low-frequency region: the lower the resistivity, the higher the initial permeability.

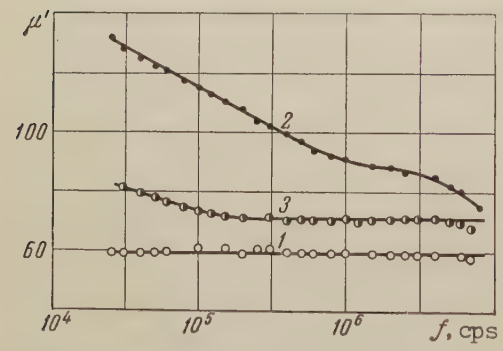

Fig.6. Frequency dependences of μ' of an yttrium single crystal: 1 - before treatment, 2 - after annealing in a stream of argon at 1400° (6 hr), 3 - after annealing in a stream of oxygen at 900° (80 hr).

Table 1

ρ, ε' and μ' of ferrite toroid cut from single crystal (values measured at ~20°C)

Heat treatment	ρ, ohm cm	ε' f = 20 kc	μ' f = 25 kc
Before treatment	10^{12}	17	58
Heating in stream of argon at 1400°C for 6 h	$7 \cdot 10^7$	17	130
Heating in a stream of oxygen at 900°C for 80 h	$5 \cdot 10^8$	17	82

The conductivity of ferrites depends on the concentration of Fe^{2+} ions and is determined by electron transfers (diffusion) between the Fe^{2+} and Fe^{3+} ions. We therefore hypothesized in Ref.1 that electron diffusion leads to increase of μ'. It was assumed that the increase in μ' is due to some new form of motion of

Table 2

Initial permeability of ferrite solid solutions

Composition, mole %		Final sintering		Initial permeability at 20°C low frequency
First component	Second component	Max. temp. °C	Time, h	
100% $Yb_3Fe_5O_{12}$	—	1350	3,0	63
80% $Yb_3Fe_5O_{12}$	20% $YbCa_2Zr_2Fe_3O_{12}$	1350	3,0	112
60% $Yb_3Fe_5O_{12}$	40% $YbCa_2Zr_2Fe_3O_{12}$	1350	2,0	250
80% $Yb_3Fe_5O_{12}$	20% $Yb_3Fe_2Al_3O_{12}$	1350	2,0	21
60% $Yb_3Fe_5O_{12}$	40% $Yb_3Fe_2Al_3O_{12}$	1320	2,5	2
100% $Nd_3Fe_5O_{12}$	—	1250	3,0	1,5
80% $Nd_3Fe_5O_{12}$	20% $NdCa_2Zr_2Fe_3O_{12}$	1350	2,0	18
60% $Nd_3Fe_5O_{12}$	40% $NdCa_2Zr_2Fe_3O_{12}$	1350	2,0	170
100% $Gd_3Fe_5O_{12}$	—	1350	1,0	1,5
80% $Gd_3Fe_5O_{12}$	20% $GdCa_2Zr_2Fe_3O_{12}$		4,0	36,6
60% $Gd_3Fe_5O_{12}$	40% $GdCa_2Zr_2Fe_3O_{12}$		4,0	94

the domain boundaries or to reduction of the magnetoelastic energy in the boundary layer, or possibly due to the development of "effective magnetic charges" at the boundary in the case of electron diffusion.

However, without rejecting these hypotheses, we cannot ignore the possibility of change of μ' during annealing as a result of change in the domain structure (decrease or increase in the size of the domains), owing to the appearance or disappearance of defects in the crystal.

It can also be seen from Table 1 that single crystals with both low and high resistivity have a small dielectric constant ϵ (this was first established by Ya. M.Ksendzov). Hitherto it has been assumed that ferrites with a low resistivity have a high ϵ. If these results are sufficiently general, then it is possible that the high dielectric constant of ferrites can be explained by macroheterogeneity of the specimens, as was assumed earlier.

In addition to yttrium ferrite, we studied solid solutions based on it. In Ref.2 we showed that in solid solutions wherein the Fe^{3+} ions in the octahedral positions are partially replaced by the diamagnetic ions (Sn^{4+}, Zr^{4+}, Ti^{4+}), there occurs an increase of the saturation magnetization, a lowering of the Curie point and, consequently, a reduction of the sublattice-sublattice exchange energy, and an increase of the initial permeability. We hypothesized in Ref.2 that with increase in the concentration of the diamagnetic ions the initial permeability increases due to a reduction of the exchange magnetostriction. Our basic premise was that with decrease of the exchange interaction energy, the dependence of the exchange integral on the separation between the ions weakens. However, the problem of the magnetostriction anisotropy still remains unclear. For the present we therefore feel that we can only speak of a certain correlation between the decrease in exchange energy and exchange magnetostriction and the increase in the initial permeability of ferrites.

Table 2 gives the values of the initial permeability for a number of ferrite solid solutions with the garnet structure. It will be seen that in the case of yttrium ferrite, as in the case of yttrium ferrite, as in the case of the rare earth ferrites, μ' increases only as a result of introduction of diamagnetic ions into the octahedral sublattice.

References

1. G.A.Smolenskii, Chang Tsung & L.K.Stankevich, Fizika tverdogo tela, 3, 663 (1961). (Trans.Soviet Physics - Solid State.)
2. G.A.Smolenskii, Chang Tsung & E.S.Sher, Ibid., 3, 1808 (1961). (Trans. Ibid.)

* * * * * * *

VISCOSITY AND HYSTERESIS PROPERTIES OF FERRITES, DUE TO ELECTRON DIFFUSION

- K.M.Bol'shova & T.A.Elkina

Manganese-iron ferrites with an excess of Mn exhibit a number of interesting properties at low temperatures. When studying these ferrites we found an extremely high magnetic viscosity and also observed the effect of this viscosity on the magnetostriction and the shape of the hysteresis loops. Doping with cobalt had a marked effect on all the above mentioned properties. Ferrites of the following compositions were studied:

Specimen No.	Formula
1	$Mn_{1,4}\ Fe_{1,6}O_4$
2	$Mn_{1,35}\ Co_{0,05}\ Fe_{1,6}O_4$
3	$Mn_{1,8}\ Fe_{1,2}O_4$
4	$Mn_{1,75}\ Co_{0,05}\ Fe_{1,2}O_4$

The magnetic viscosity was measured in static magnetic fields. The region in which viscosity was evinced was bounded by weak and medium fields (from 1 to 250 Oe).

Fig.1 shows the time-magnetization curves* for the No.4 specimen in a constant H = 18 Oe field at different temperatures. It will be seen that magnetic viscosity is clearly evinced only in a certain low temperature region. At -130° the magnetization continues to increase even after 2.5 days in the field.

The effect of magnetic viscosity on the process of magnetization reversal was particularly significant. In some cases when the direction of the field was reversed the ferrite specimen remained magnetized for several hours in the direction of the initial field. There are no references in the literature to the existence of such pronounced magnetic viscosity.

Fig.2 gives the reversing field dependences of the reversal or switching time** t_{rev} for specimens Nos.2 and 4. Fig.3 shows the variation of t_{rev} with temperature in a 19 Oe field for the same specimens.

It will be clear from the presented data that magnetic viscosity is evinced especially strongly in a certain region of low temperatures (somewhat different for the No.2 and No.3 specimens) and in weak and medium magnetic fields (the "strong viscosity" field region is also somewhat different for the No.2 and No.4 specimens). Consistently longer reversal times were obtained for specimen No.4

---

*The changes in the magnetization with time were recorded by the ballistic method. The procedure consisted in reading the galvanometer deflection upon flipping the specimen out of the ballistic coil; however, in the process the specimen remained within the uniform field of the magnetizing coil.

**t_{rev} is here defined as the time required for the magnetization to go to zero in the reversing field.

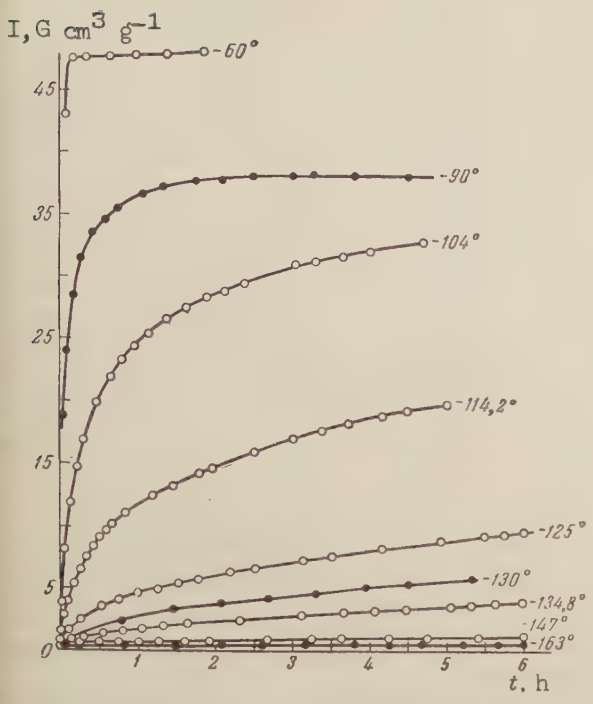

Fig.1. Magnetization of specimen No.4 as a function of the holding time in an 18 Oe field at different temperatures.

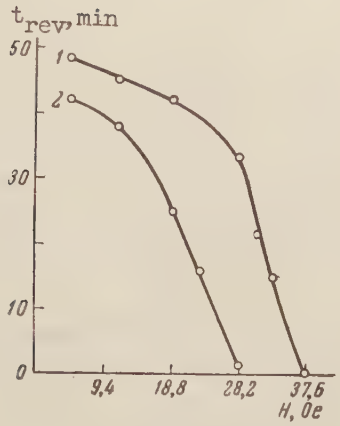

Fig.2. Field dependences of the reversal time t_{rev}. The specimens were held in the given field for 4 hours at -125° (1) and -150° (2).

which contained the greatest excess of manganese and a small amount of cobalt. In specimens Nos.1 and 3, which did not contain cobalt, the viscosity was evinced more weakly and in weaker fields.

We recorded the hysteresis loops for all the specimens in an alternating (50 cps) field in the field range wherein magnetic viscosity is clearly evinced. The oscillographic measurements showed that in weak fields, where the switching times are long, no true loops appear (the trace on the oscilloscope screen is an inclined line). As the field is increased, there first is observed a "perminvar" loop, then a normal loop and finally a rectangular loop. In the field range where the loops are rectangular, the switching times are so short that they could not be measured by our method; here, too, the effect of viscosity on the shape of the magnetization and reversal curves is much less significant. The above described changes in the shape of the loops with increase of the field pertain to the case when the specimen was demagnetized at the temperature of the measurement; with increase of the field, the inclined line trace seen in weak fields abruptly changes to a square loop ($I_r/I_s \approx 0.98$) at some field intensity.

Another feature of the hysteresis loops of the investigated ferrite specimens is worthy of mention. Between -100 and -150°, where the viscosity is especially high, with increase of the field there occurs a jump in induction, which is evinced by the appearance of a "step" in the loop. However, with increase of the holding time in the field the "step" gradually smoothes out and the loop assumes the regular shape.

Using the method of cemented-on strain gages, we measured the saturation magnetostriction λ_s of the same specimens in a magnetizing field of 2500 Oe. The results for specimens Nos.1 and 2 are given in Fig.4. The effect of viscosity on the magnetostriction was apparent in the No.2 specimen, which contained cobalt; in this case the magnetostriction was strongly dependent on the method of demagnetization. Curve 1 in Fig.4 pertains to the case when the specimen was demagnetized each time at room temperature, while curve 2 is for the case when the speci-

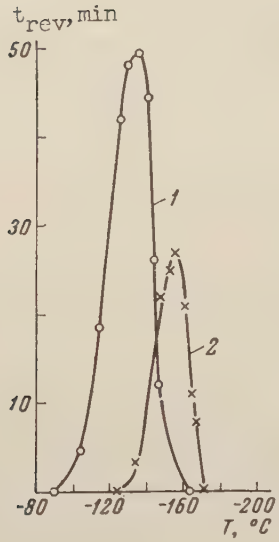

Fig.3

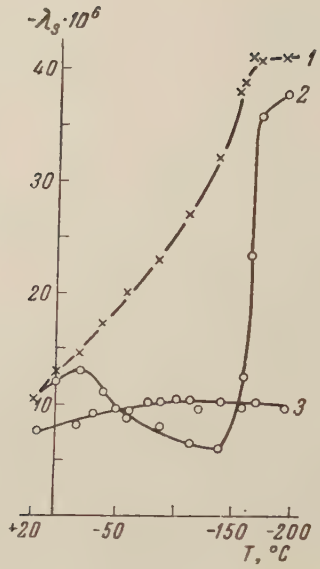

Fig.4

Fig.3. Temperature dependence of the reversal time t_{rev} for specimen No.4 (1) and No.2 (2). H = 19 Oe.

Fig.4. Dependence of the magnetostriction λ_s on the temperature and conditions of demagnetization for specimens Nos.2 (curves 1 & 2) and 1 (curve 3).

men was demagnetized at the temperature of the measurement. As will be evident from the figure, the difference between the values of λ_s found in the two cases is particularly appreciable in the temperature range where the reversal times are longest, i.e., where the magnetic viscosity is greatest. As compared with specimen No.2, the viscosity in specimen No.1 is much lower (No.1 contained no cobalt) and the value of λ_s for No.1 is independent of the method of demagnetization (curve 3 in Fig.4). The behavior of specimen No.4 was similar to that of No.2; the behavior of No.3 similar to that of No.1.

Our data point to a definite connection between the high magnetic viscosity of the investigated ferrites and their unusual hysteresis and magnetostrictive properties. The same mechanism is apparently responsible for this whole complex of properties. It will be recalled that "perminvar" loops are exhibited by materials in which the demagnetized state is especially stable. Stabilization of the demagnetized state can be realized by diffusion of atoms, ions or electrons if the diffusion process has the effect of superposing uniaxial anisotropy on whatever anisotropy is initially present; this uniaxial anisotropy depends on the direction of spontaneous magnetization in each domain. In this case "perminvar loops" appear in weak alternating fields and rectangular loops in stronger fields.

The formation of uniaxial anisotropy in our ferrites was presumably due to electron diffusion, since it is difficult to imagine that effective diffusion of ions could occur at the relatively low temperatures involved. It is very likely that exchange of electrons occurs between the manganese ions of different valence. The diffusion processes leading to the necessary regrouping of the valences in the crystal lattice (a consequence of which is anisotropic distribution of the ions, connected with the direction of spontaneous magnetization) proceed at a finite rate, which depends strongly on the temperature and magnetic field. This explains the limiting of the field and temperature ranges wherein there are observed "perminvar loops" and rectangular loops and high viscosity in the static

fields. It is not clear at present how cobalt acts to increase the viscosity of the investigated ferrites and to make them more sensitive to magnetic annealing.

The diffusion processes, which lead to stabilization of the demagnetized state and the appearance of the perminvar effect, at the same time give rise to a magnetic aftereffect of the Richter type, which is evinced in disaccomodation of the permeability and in the appearance of a maximum on the loss factor versus temperature curve. A relationship between the perminvar effect and the Richter type relaxation has been established experimentally for a number of ferrites.[1-3] Some question regarding the existence of this relationship stemmed from the fact that "perminvar" loops and effective magnetic annealing occurred in medium and strong fields, while the viscosity effects were observed mainly in fields of a few millioersted.

In our case we established a direct relationship between the viscosity properties of the investigated ferrites in static fields and the hysteresis characteristics in the same range of fields.

References

1. U.Enz, Physica, 28, 609 (1958).
2. A.Kienlin, Z.angew.Phys., 10, 167 (1958).
3. S.Krupicka & F.Vilim, Czechosl.J.Phys., 7, 723 (1957).

EFFECT OF GAMMA-IRRADIATION ON DISACCOMODATION IN Ni-Zn FERRITES

- E.I.Trinkler, V.A.Gol'din & V.B.Osipov

In earlier studies[1,2] we discovered the influence of γ-irradiation on the effect of disaccomodation of the initial permeability in nickel-zinc ferrites. It was established that γ-irradiation accelerates and intensifies disaccomodation, i.e., the process of decrease of the real part of the initial permeability with time.

This influence was observed at liquid nitrogen temperature; at room temperature the process of disaccomodation is not noticeably affected by irradiation. It was also found that heating to room temperature or complete demagnetization removes the effect of irradiation.

Prolonged holding of the specimen after irradiation at liquid nitrogen temperature does not lead to any increase of permeability with time; on the contrary, there is observed a further very slow decrease of μ. Comparison of the permeability versus time curves recorded for specimens subjected to different radiation doses showed that the decisive factor is the integral dosage.

The purpose of the present work was to determine the effect of γ-irradiation on disaccomodation in type F-1000, F-600 and F-250 nickel-zinc ferrites at different temperatures in the range from -200 to 0°C.

The specimens were irradiated in the universal K-60 000 irradiator equipment with a Co^{60} source having an activity of 45 000 r.e. in the "L.Ya.Karpov" Physical-Chemical Institute.[3] The specimens were placed in the cylindrical cavity of the irradiator (d = 180 mm, h = 320 mm, V = 8 liters). The dosage rate at the center of the cavity* was 510 r/sec. Some of the specimens, irradiated at -125°, were placed in a special cryostat contained in a Dewar. The design of the cryostat provides for remote control of the temperature and automatic liquid nitrogen feed during the course of the experiment. In the cryostat the dosage rate at the center of the irradiator was 367 r/sec (the reduction in rate is due to the absorption of the γ-radiation in the walls of the cryostat).

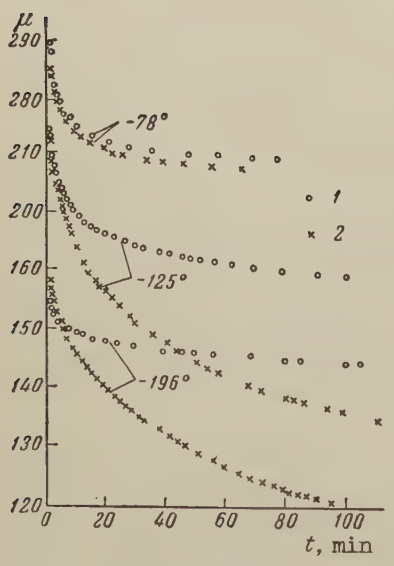

Fig.1. Disaccomodation in F-600 Ni-Zn ferrite prior to irradiation (1) and after irradiation (2) at -78°, -125° and -196°.

The initial permeability was measured at a frequency of 400 cps by means of a differential RH bridge coupled to the input of a narrow band amplifier tuned to the measurement frequency.

In contrast to the procedure employed in our earlier studies[1,2], in the present measurements we used a demagnetizing device of the type described by Enz[4].

Fig.1 shows the disaccomodation curves for a specimen of F-600 ferrite before irradiation and after irradiation at -78°, -125°, and -196°. There is clearly evident the temperature dependence characteristic of disaccomodation: the lower the temperature, the slower the process of decrease of permeability. It will be seen that the effect of irradiation is most strongly evinced at low temperatures (-196° and -125°).

To determine the temperature at which the influence of irradiation becomes nil, we carried out a special experiment involving slow warming of ir-

---

*The K-60 000 equipment has provision for varying the configuration of the irradiator in a wide range.

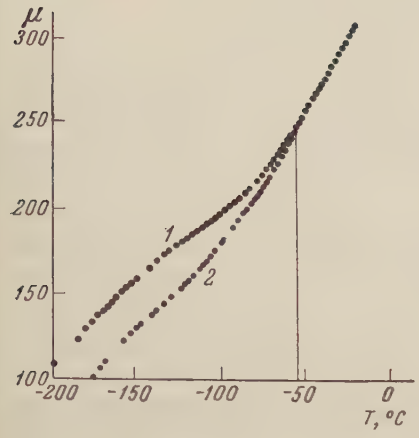

Fig.2. Increase in permeability with temperature for nonirradiated (1) and irradiated at -196° (2) specimens of F-600 ferrite.

radiated and nonirradiated specimens.

The resultant temperature dependences of the permeability are shown in Fig.2: curve 1 pertains to an F-600 ferrite specimen stored for 10 hours at -196° without irradiation; curve 2 pertains to the same specimen but irradiated for 10 hours. In both cases the specimens were warmed at a uniform rate for 3 hours. As will be evident the two curves merge at about -50°; above this temperature γ-irradiation has no noticeable effect on the process of disaccomodation.

We did not carry out analogous experiment with the F-1000 and F-250 ferrites, but it would appear from comparison of the permeability versus time curves recorded for specimens of these ferrites at -196° and -78° that the point of intersection of the disaccomodation curves for irradiated and nonirradiated specimens lies close to the value obtained for the F-600 ferrite.

In addition to recording the disaccomodation curves for irradiated and nonirradiated specimens, we also carried out measurements of the dielectric loss before and after irradiation. The measurements were carried out by means of KV-1 and IDI-1 Q-meters and UM-3 bridge at frequencies from 100 cps to 10 Mc at -196°. The specimens were in the form of silver-coated disks 0.8 mm thick prepared of the F-1000, F-600 and F-250 ferrites. No significant changes in capacitance as a result of irradiation were detected.

Although the amount of experimental material accumulated to date is not sufficient to give a clear picture of the interaction of γ-radiation with ferrites, it appears probable that we are dealing here with enhancement of electron diffusion, which is fundamental to the effect of disaccomodation. This increase in diffusion may occur for two reasons: electrons appearing as a result of the Compton effect ionize the ions constituting the ferrite and thereby lower the potential barrier for the diffusing electrons; moreover, in the process of being stopped in the lattice the secondary electrons transfer their energy to the electron shells, which, in turn, also leads to enhancement of the electron diffusion.

We are planning to continue our experiments, extending their scope for the purpose of more complete elucidation of the character of the interaction of the γ-rays with ferrite matter; in particular, we intend to determine the influence of irradiation on specimens with different contents of divalent iron.

References

1. E.I.Trinkler, Izv.AN Latv.SSR (Bulletin, Latvian SSR Ac.of Sci.), No.2, 95 (1961).

2. E.I.Trinkler, Materialy Vsesoyuznogo soveshchaniya (Transactions of the Second All-Union Conference), M., Dec.1960.

3. A.Kh.Breger, V.B.Osipov & V.A.Gol'din, Atomnaya energiya, No.5 (1960). (Trans.Soviet Physics - Journ.of Atomic Energy.)

4. U.Enz, Physica, 24, 609 (1958).

CONCERNING CORRELATION BETWEEN THE ELECTRIC AND MAGNETIC PROPERTIES OF Ni-Zn FERRITES

- L.I.Rabkin & Z.I.Novikova

In earlier contributions[1-4] we showed that the properties of ferrites are greatly affected by the presence in them of divalent iron ions. In the present paper we give the results of additional experiments undertaken for the purpose of determining the variation in the properties of ferrites as a function of the number of Fe^{2+} ions.

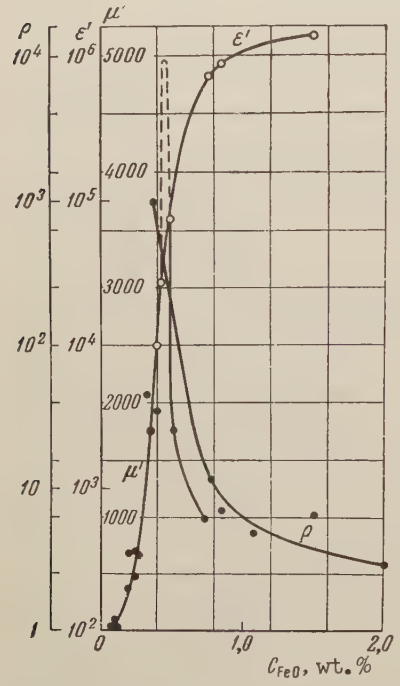

Fig.1. Variation of the resistivity ρ, dielectric constant ε' and permeability μ' as a function of the FeO content in Ni-Zn ferrites.

For example, the conductivity and low-frequency dielectric constant of Ni-Zn ferrites increase monotonically with increase in the number of Fe^{2+} ions in the solid solution. On the other hand, the permeability increases only up to a certain Fe^{2+} concentration and then begins to decrease (Fig.1).

We established a correlation between the activation energy for conduction and the resistivity of Ni-Zn ferrites: it was found that the activation energy increases with increase of the resistivity. Further measurements carried out on a large number of specimens of different composition substantiated this dependence (Fig.2 and table). For some of the specimens we determined the precise content of Fe^{2+} ions, which made it possible to establish the relation between their concentration and the value of the activation energy for conduction, given by the expression

$$E_\rho = \frac{A}{\log X},$$

where X is the FeO content in percent by weight (Fig.3).

Our investigations also showed that the value of the dielectric constant measured at low frequencies is closely determined by the value of the dc resistivity.[3]

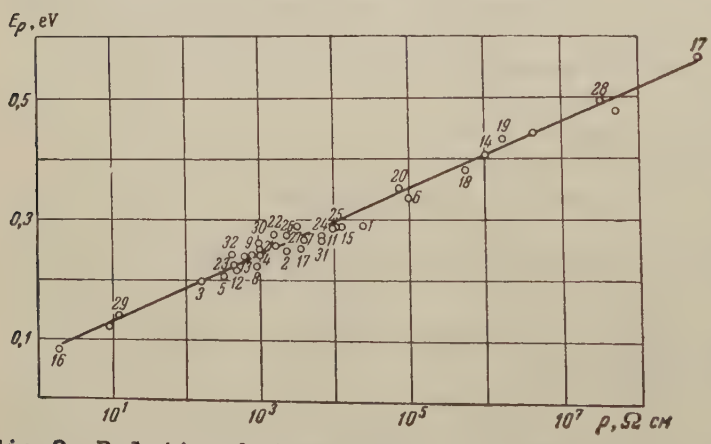

Fig.2. Relation between the dc resistivity of Ni-Zn ferrites and the activation energy for conduction.

In most cases the frequency dependence of the conductivity loss tangent, $\operatorname{tg}\delta_\rho$, calculated from the value of the dc resistivity, agrees with the experimental frequency dependence of the dielectric loss tangent, $\operatorname{tg}\delta_\varepsilon$.[3] The value of $\operatorname{tg}\delta_\varepsilon$ at the maximum increases with increase of the Fe^{2+} ion content and as a rule the dielectric loss tangent peak shifts to the side of higher frequencies, while the activation energy, evaluated from the temperature-frequency dependence of $\operatorname{tg}\delta_\varepsilon$, decreases (Fig.4).

Values of the resistivity and activation energy for conduction for Ni-Zn ferrites of different composition

Point No. in Fig. 2	Composition, mole %			Sintering temp. °C	Cooling	$\rho_{20°}$, Ω см	E_ρ, eV
	NiO	ZnO	Fe_2O_3				
1	2	3	4	5	6	7	8
1	50	—	50	1300	Slow	$2,74\times10^4$	0,29
2	25	25	50	1300	»	$2,42\times10^3$	0,25
3	—	50	50	1300	»	$1,48\times10^2$	0,19
4	15	35	50	1300	»	$1,09\times10^3$	0,24
5	—	50	50	1200	Fast	$3,51\times10^2$	0,20
6	50	—	50	1200	»	$9,67\times10^4$	0,33
7	50	—	50	1250	»	$4,03\times10^3$	0,265
8	50	—	50	1300	»	$9,425\times10^2$	0,22
9	10	40	50	1300	Slow	$7,61\times10^2$	0,24
10	15	35	50	1200	»	$1,68\times10^6$	0,43
11	15	35	50	1250	»	$9,3\times10^3$	0,23
12	15	35	50	1350	»	$4,72\times10^2$	0,21
13	35	15	50	1350	»	$6,73\times10^2$	0,24
14	14,3	33,3	52,4	1200	»	$1,02\times10^6$	0,405
15	15	35	50	1250	»	$1,32\times10^4$	0,29
16	—	41,6	58,4	1280	»	1,935	0,08
17	15	35	50	1100	»	$6,3\times10^8$	0,57
18	15	35	50	1100	Fast	$5,5\times10^5$	0,38
19	15	35	50	1200	Slow	$4,26\times10^6$	0,44
20	15	35	50	1200	Fast	$7,6\times10^4$	0,35
21	15	35	50	1300	»	$1,0\times10^3$	0,25
22	15	35	50	1250	Slow	$1,62\times10^8$	0,275
23	15	35	50	1350	»	$4,67\times10^2$	0,23
24	35	15	50	1300	»	$6,60\times10^3$	0,27
25	35	15	60	1300	»	$1,07\times10^4$	0,29
26	35	15	50	1300	Fast	$2,38\times10^3$	0,27
27	52,6	—	47,4	1300	»	$1,74\times10^8$	0,26
28	50	—	50	1200	Slow	$3,55\times10^7$	0,50
29	14,3	33,3	52,4	1300	»	$1,28\times10^1$	0,14
30	15	35	50	1300	»	$1,0\times10^3$	0,26
31	52,6	—	47,4	1300	»	$6,175\times10^3$	0,27
32	15	35	50	1350	»	$4,12\times10^2$	0,24

Note: The specimens were sintered in air for 4 hours; except specimen No.15 which was sintered for 6 hours.

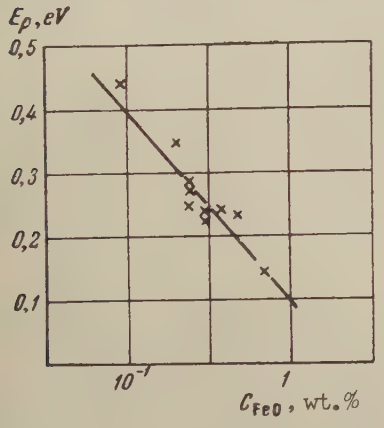

Fig.3. Variation of the activation energy for conduction with the FeO content in Ni-Zn ferrites.

The temperature - frequency dependences of the magnetic loss tangent $\operatorname{tg}\delta_\mu$, like the analogous dependences of $\operatorname{tg}\delta_\varepsilon$, of most of the investigated ferrites have in the frequency range from 1 to 100 kc one or two peaks, one of which is evinced in the vicinity of the Curie point, while the second appears in the range of low temperatures. We obtained analogous curves for Mn-Zn ferrites (Fig.5). The second, low temperature peak depends on both the frequency and temperature: with increase of frequency it shifts to the side of higher temperatures.

Investigation of the temperature-frequency dependences of $\operatorname{tg}\delta_\mu$ and $\operatorname{tg}\delta_\varepsilon$ carried out on the same ferrite specimens, showed that the $\operatorname{tg}\delta_\mu$ peak at a given frequency lies at lower temperatures than the $\operatorname{tg}\delta_\varepsilon$ peak. At the peak the value of $\operatorname{tg}\delta_\mu$ is 1-2 orders of magnitude smaller than the value of $\operatorname{tg}\delta_\varepsilon$.

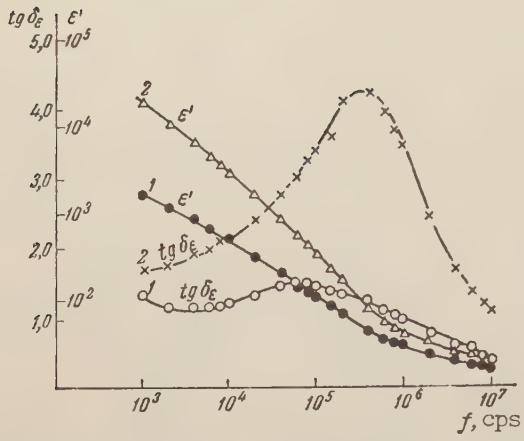

Fig.4. Frequency dependences of the dielectric constant and dielectric loss tangent for Ni-Zn ferrite specimens of stoichiometric composition (25% NiO + 25% ZnO + 50% Fe_2O_3) sintered at 1250° (1) and 1300° (2): 1 - 0.12 weight % FeO ($(tg\,\delta_\varepsilon)_{max}$ = = 1.5; E_ρ = 0.367 eV); 2 - 0.25 weight % FeO ($(tg\,\delta_\varepsilon)_{max}$ = 4.2; E_ρ = = 0.205 eV).

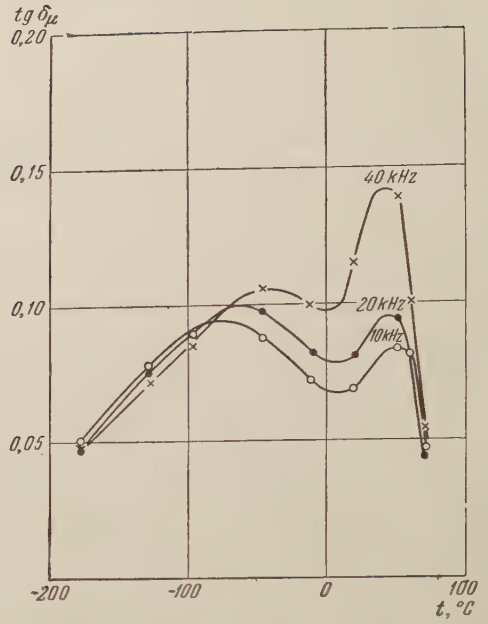

Fig.5. Temperature-frequency dependence of the magnetic loss tangent of Ni-Zn ferrites ($Ni_{0.3}Zn_{0.7}Fe_2O_4$) sintered for 4 hours at 1350° in oxygen.

The value of the activation energy for magnetic relaxation is, as a rule, close to the activation energy for dielectric relaxation.

Both relaxation processes are described by a formula of the same form, namely,

$$\tau = \tau_0 e^{E/kT},$$

where τ is the relaxation time, E is the activation energy for the relaxation process, and τ_0 is the time constant of the elementary process. Hence, in view of the near equality of the activation energies for magnetic and dielectric relaxation, τ_0 proves to be greater for the dielectric process.

The equivalences of the activation energies for the processes of conductivity and magnetic relaxation[5,8], conductivity and dielectric relaxation[6,7] and the processes of magnetic and dielectric relaxation give reason to assume that all these processes have a common origin and are due, as our studies have shown, to the electrons of the iron atoms participating in exchange of valences between Fe^{2+} and Fe^{3+}.

In an earlier paper by one of us[4] it was suggested that the high dielectric constant of ferrites is due to the strong polarization associated with the appreciable charges moving in ferrites under an applied field. The experimental data obtained in the present work required revision of this point of view in connection with taking into account the characteristics of electron transfers from Fe^{2+} to Fe^{3+} ions. The appearance of divalent iron ions in Ni-Zn ferrite is connected with the condition of conservation of macroscopic electric neutrality of the lattice as a result of formation in it of oxygen vacancies, which may be regarded as additional positive charges (so called F-centers).

Coulomb interaction between the positive charge of the F-center and the excess electrons, that produce the divalent iron ions, leads to the situation where the electrons in the absence of a field tend to arrange themselves in the vicinity of the anionic vacancies in the lattice. Upon application of a field, part of the electrons under the influence of this field go over to the next vacancy as a result of valence exchange between the Fe^{2+} and Fe^{3+} ions. The smaller the number of such vacancies and, consequently, the greater the separation between them, the greater will be the number of $Fe^{2+} \rightarrow Fe^{3+}$ electron transitions in the direction of the field and hence the greater will be the activation energy for conductivity. Thus, the electromagnetic properties of ferrites are determined by electron transitions of two types: 1) transitions between nearest neighbor Fe^{2+} and Fe^{3+} ions, and 2) transitions between Fe^{2+} ions close to one vacancy and Fe^{3+} ions located close to another vacancy.

Transitions of the second type are actually made up of a number or series of transitions of the first type. The activation energy in the case of transitions of the second type will be the greater, the greater the separation of the vacancies and, consequently, the smaller the number of oxygen vacancies in the ferrites. Only transitions of the first type can occur in iron ferrite (magnetite) free of lattice defects.

Preferential diffusion (drift) of electrons in the direction of the applied field leads to polarization of the specimen. When there are few divalent iron ions in the ferrite specimen, the polarization is low and, hence, the dielectric constant is small.

With increase in the number of Fe^{2+} ions the number of electron transitions between ions increases and, consequently, so does the polarization and the value of the dielectric constant. Upon application of an alternating field, beginning with a certain frequency, the electron transitions from one vacancy to another will not have time to follow the field, which leads to reduction of the dielectric constant. The smaller the separation between vacancies, the higher will be the frequency at which the dielectric constant begins to fall off.

The value of $\operatorname{tg} \delta_\varepsilon$ in the investigated frequency interval, as was shown in Ref.3, is determined mainly by the conduction losses. Owing to the strong frequency dependence of the dielectric constant, $\operatorname{tg} \delta_\rho$ may pass through a maximum. In this case the values of the activation energy calculated from the temperature-frequency dependence of $\operatorname{tg} \delta_\varepsilon$ and from the temperature dependence of the conductivity proved to be equal.

Actually, however, not all the electrons participate in the thru conduction. Part of the electrons (the low energy ones) are displaced under the influence of the field over distances smaller than the separation between vacancies. Such local displacements are the reason for the second $\operatorname{tg} \delta_\varepsilon$ peak in ferrites. The activation energy calculated on the basis of the temperature-frequency dependence of this peak will be lower than the activation energy evaluated for the process of true conduction.

The location of the $\operatorname{tg} \delta_\varepsilon$ peaks in certain frequency intervals[2] is, apparently, the consequence of electron transitions realized over short discrete distances from the F-centers, i.e., the drift process may actually consist of a different number of single-valence exchanges between the Fe^{2+} and Fe^{3+} ions. The value of $\operatorname{tg} \delta_\varepsilon$ at the peak is determined by the number of divalent iron ions in the ferrite solid solution. In the case of many specimens there obtains direct proportionality between these two quantities. Shift of the $\operatorname{tg} \delta_\varepsilon$ peak to the side of higher frequencies with increase in the number of Fe^{2+} ions present can, apparently, be explained by increase in the frequency of the electron transitions, connected with decrease of the separation between neighboring vacancies. The observed decrease of the activation energy with displacement of the loss tangent

peaks to the side of higher frequencies substantiates this inference.

In a magnetic field electron diffusion follows displacement of the interdomain boundaries (domain walls).[9,10] An electron in passing from one vacancy to another must overcome the same energy barrier as in the case of dielectric relaxation and conduction; consequently, there obtains equality of the activation energies for all three processes. In weak magnetic fields the magnitude of domain boundary displacements is small relative to the thickness of the domains. The electron oscillations, restricted by the walls, are realized only in a small part of the volume of the ferrite, which may be the reason for the smaller value of $\operatorname{tg}\delta_\mu$ as compared with $\operatorname{tg}\delta_\varepsilon$. In view of the above, the decrease of the activation energy for magnetic relaxation with increase in the number of Fe^{2+} ions can be explained in the same way as in the case of dielectric relaxation.

The difference between the time constants τ_0 in the magnetic and dielectric processes may be the consequence of different causes giving rise to electron diffusion. In the case of dielectric relaxation this cause may be the external electric field; in the case of magnetic relaxation it is displacement of the domain walls. The effect of dielectric relaxation is a manifestation of a collective event in which displacement of each electron is connected with displacement of its neighbors inasmuch as electrons cannot accumulate near a vacancy. Hence the mean time of transition of each electron from one vacancy to another is determined by the mean relaxation time for the whole process. The same thing applies to magnetic relaxation, but with the difference that in this case the intervacancy electron transition time is determined by displacement of the domain walls, and, inasmuch as wall motion under the influence of an applied field is essentially a low lag process and the number of migrating electrons is small, the time of magnetic relaxation will be shorter than the dielectric relaxation time. Displacement of electrons over distances less than the separation between vacancies may, therefore, in the case of magnetic losses as well, be the reason for the appearance of the second loss tangent peak associated with a lower activation energy.

References

1. L.I.Rabkin & Z.I.Novikova, Izv.AN SSSR, Ser.fiz., 23, 388 (1959). (Trans. Bulletin, 23, 373.)

2. Z.I.Novikova, Ibid., 23, 396 (1959). (Trans.Bulletin 23, 380.)

3. L.I.Rabkin & Z.I.Novikova, in "Ferrity" (Ferrites, Collected articles), Minsk, 1960.

4. L.I.Rabkin, Vysokochastotnye ferromagnetiki (High-frequency ferromagnets), M., 1960.

5. J.Smit & H.Wijn, Advances in Electronics and Electron Phys., 6, 69 (1954).

6. Kan-ichi Kamiyoshi, Phys.Rev., 84, 374 (1954).

7. V.A.Ioffe, G.I.Khvostenko & Z.I.Zonn, Zhur.tekh.fiz., 27, 1985 (1957). (Trans.Soviet Physics - Technical Physics.)

8. A.von Kienlin, Z.angew.Phys., 9, 245 (1957).

9. A.A.Shvarts, Nauchno-tekhnicheskii sbornik NII MRTP SSSR, No.5, L., 1955.

10. L.I.Rabkin, Izv.AN SSSR, Ser.fiz., 23, 318 (1959). (Trans.Bulletin, 23, 309.)

PHASE EQUILIBRIUM IN THE Fe_2O_3-BaO SYSTEM

- B.G.Livshits, S.A.Eliseev, B.A.Samarin & V.A.Somenkov

The present work was concerned with investigation of the phase diagram of the quasi-binary system Fe_2O_3-BaO; the characteristics of this system are of interest in connection with fabrication of barium hexaferrite permanent magnets.[1]

In the study we utilized the methods of structural analysis (x-ray diffraction and optical microscopy), measurement of structure-insensitive magnetic properties (saturation magnetization and Curie point) and microhardness gaging.

The specimens were prepared by sintering mixtures of Fe_2O_3 and $Ba(NO_3)_2$ at different temperatures. The compositions of the specimens are listed in the accompanying table.

Composition of the investigated specimens

Specimen No.	Molecular ratio	Mol % BaO	Specimen No.	Molecular ratio	Mol % BaO
1	Fe_2O_3	0	12	$\frac{11}{6}$ $BaO \cdot 6Fe_2O_3$	23,4
2	$\frac{1}{6}$ $BaO \cdot 6Fe_2O_3$	2,7	13	$\frac{12}{6}$ $BaO \cdot 6Fe_2O_3$	25,0
3	$\frac{1}{3}$ $BaO \cdot 6Fe_2O_3$	5,3	14	$\frac{13}{6}$ $BaO \cdot 6Fe_2O_3$	26,6
4	$\frac{1}{2}$ $BaO \cdot 6Fe_2O_3$	7,7	15	$\frac{14}{6}$ $BaO \cdot 6Fe_2O_3$	28,0
5	$\frac{2}{3}$ $BaO \cdot 6Fe_2O_3$	10,0	16	$\frac{15}{6}$ $BaO \cdot 6Fe_2O_3$	29,4
6	$\frac{5}{6}$ $BaO \cdot 6Fe_2O_3$	12,2	17	$\frac{16}{6}$ $BaO \cdot 6Fe_2O_3$	30,8
7	$BaO \cdot 6Fe_2O_3$	14,3	18	$\frac{17}{6}$ $BaO \cdot 6Fe_2O_3$	32,1
8	$\frac{7}{6}$ $BaO \cdot 6Fe_2O_3$	16,3	19	$\frac{18}{6}$ $BaO \cdot 6Fe_2O_3$	33,3
9	$\frac{4}{3}$ $BaO \cdot 6Fe_2O_3$	18,2	20	$\frac{19}{6}$ $BaO \cdot 6Fe_2O_3$	34,5
10	$\frac{3}{2}$ $BaO \cdot 6Fe_2O_3$	20,0	21		43,3
11	$\frac{5}{3}$ $BaO \cdot 6Fe_2O_3$	21,7	22		53,3

Microstructure and microhardness

We investigated the microstructure of specimens Nos.1 through 20, which were sintered at 1200° for 8, 24 and 32 hours; the specimens fired for 24 and 32 hours were ground and recompacted every 8 hours. We also investigated the microstructure of specimens obtained by sintering at 1300°: in the case of specimens Nos.1 through 9 for 4 hours, and in the case of specimens Nos.10, 11 & 12, for 1 hour. It was demonstrated for the specimens sintered both at 1200 and 1300° that composition No.7, the stoichiometric composition, is a single-phase solid solution, whereas after roasting compositions Nos.2-6 and Nos.8-20 are two-phase solutions.

In specimens Nos.2 through 6 the light phase is apparently hematite, while the dark phase is barium hexaferrite ($BaO \cdot 6Fe_2O_3$). The structure of ferrite specimen No.5 after sintering for 4 hours at 1300° is shown in Fig.1,a.

In ferrites Nos.8 through 20 the light phase is barium hexaferrite; the dark phase has not been identified, but we have reason to believe that it is $BaO \cdot Fe_2O_3$.

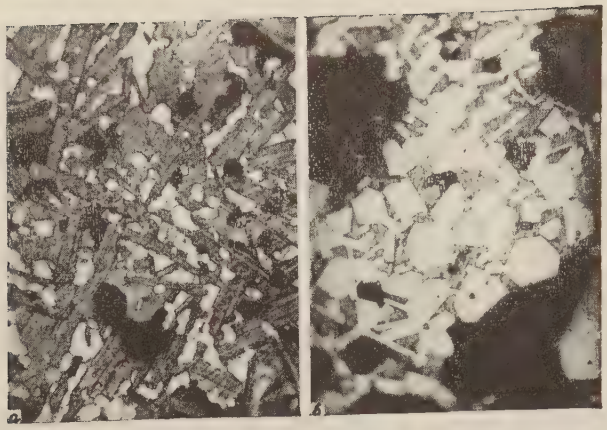

Fig.1. a - Ferrite specimen No.5 (sintering for 4 hours at 1300°); b - ferrite No.12 (sintering for 1 hour at 1300°). Magnification 1000 X.

A micrograph of the structure of ferrite No.12 after sintering for 1 hour at 1300° is shown in Fig.1,b. All three phases have a virtually constant characteristic hardness in almost all the specimens sintered at a given temperature and for a given time. The fact that the hardness of the phases remains constant despite variations in the barium oxide content indicates that the composition of these phases is the same in all the specimens.

With increase of the sintering time to 24 and 32 hours there is observed a small increase in the hardness of the barium hexaferrite in composition Nos.2,3 and 4, which may be taken as evidence of changes occurring in these phases as a result of prolonged heating.

Saturation magnetization and Curie point

We measured the saturation magnetization σ_s of the specimens of the quasibinary Fe_2O_3-BaO system prepared by sintering at 1200° for 8, 16, 24 and 32 hours with intermediate grinding and recompacting at 8 hour intervals.

As will be evident from Fig.2, the variation of σ_s with composition is linear in character with the maximum corresponding to the stoichiometric composition (No. 7) for all sintering times. Extrapolation of the linear plot to the right of the stoichiometric composition to its intersection with the horizontal axis (for 16 to 32 hours sintering) gives the composition with 50% BaO, in which, according to the data of Forestier[2], there exists the compound $BaO \cdot Fe_2O_3$. The reason for the anomalous slope of the straight line for 8 hours sintering is at present unclear; possibly it is connected with the kinetics of formation of the nonferromagnetic phase $BaO \cdot Fe_2O_3$ and the fact that the process of ferritization does not have time to go to completion in 8 hours. The linear decrease of σ_s with composition to both sides of $BaO \cdot 6Fe_2O_3$ indicates that in the 0 to 14.3% BaO and 14.3 to 50% BaO regions there exist two phases, namely, a magnetic phase ($BaO \cdot 6Fe_2O_3$) and a nonmagnetic phase. In the low BaO content region this is probably hematite (Fe_2O_3), while in the high BaO content region this is probably $BaO \cdot Fe_2O_3$.

The Curie point measurements were carried out on the same specimens, the Curie points being determined from the variation in residual induction B_r with change in temperature. The experimental results are shown in Fig.3. The fact that the Curie point remained constant in the BaO range from 14.3 to 50% is evidence of heterogeneity of the material in this region. The lowering of the Curie point in the neighborhood of compositions Nos.7-9 may be connected with the fact that there is a region of homogeneity (region of existence of $BaO \cdot 6Fe_2O_3$) in this section of the equilibrium diagram.

In the region of BaO content under 14.3%, for ferrites Nos.2, 3 & 4 sintered for 16 to 32 hours there is observed an anomalous reduction of the Curie point, which may be connected with change in composition or structure of the ferromagnetic phase (barium hexaferrite) in the process of prolonged heating (Fig.3).[3]

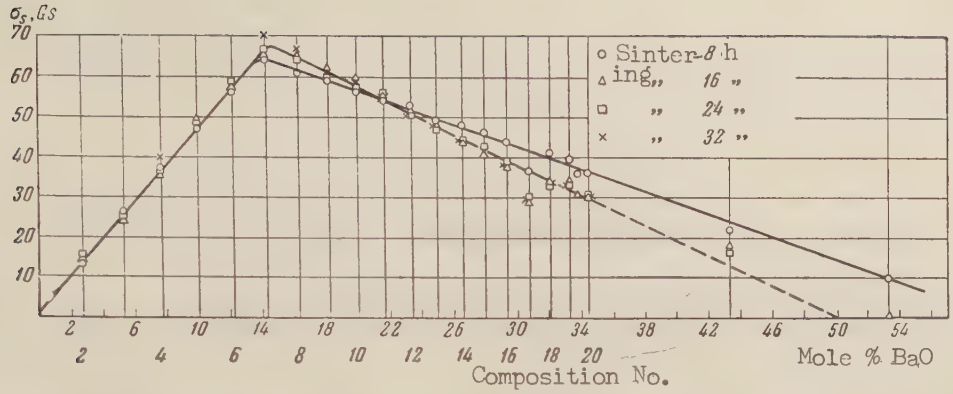

Fig.2. Variation of the saturation magnetization with composition in the Fe_2O_3-BaO system.

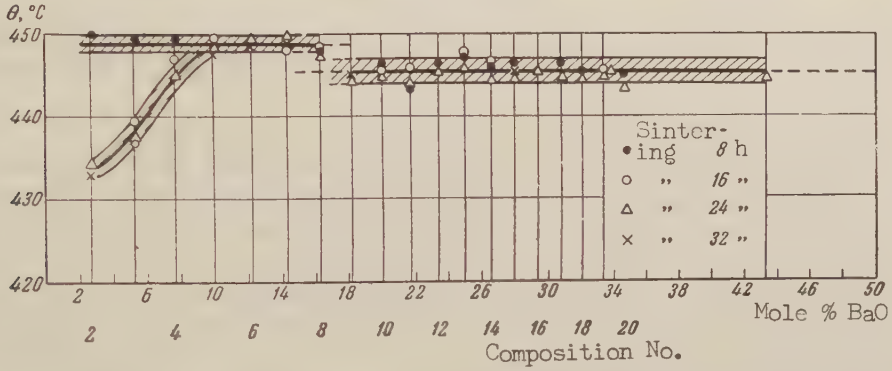

Fig.3. Variation of the Curie temperature with composition in the Fe_2O_3-BaO system.

X-ray phase analysis

Specimens Nos.2 through 6, sintered for 24 hours at 1200°, were subjected to phase analysis. These specimens consist of hematite and barium hexaferrite; with increase of the BaO content in the initial batch the intensity of the x-ray lines of hexaferrite increases, while the intensity of the hematite lines decreases.

In addition, we recorded x-ray diffraction patterns for specimens of the same composition but sintered for 32 hours at 1200°. These specimens were also found to be heterogeneous. For these specimens we also determined the lattice parameters from the lines with interplanar separations d = 1.387 (θ = 44°08', hkl - 20.14) and d = 1.088 (θ = 62°30').

Inasmuch as the line with interplanar separation d = 1.088 can be indexed either as (40.11) or (328), we calculated the lattice period on the basis of both the line pair (20.14)-(40.11) and the line pair (20.14)-(328) (curves 1 and 2, respectively in Fig.4). The results of these calculations are in qualitative agreement. It will be evident from Fig.4 that with increase of the BaO content in the initial batch the lattice period of the barium hexaferrite along the a axis in-

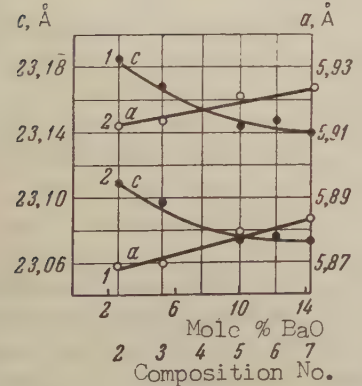

Fig.4. Variation of the lattice parameters a and c of barium hexaferrite as a function of the BaO content in the specimen.

creases, while the period along the c axis decreases somewhat. As a result of this the ratio c/a also decreases. The changes in the lattice parameters are very small, but are, nevertheless, greater than the experimental error. Such changes in lattice parameters should not occur in the heterogeneous region of a phase equilibrium diagram for a binary system.

References

1. N.N.Shol'ts and others, in "Ferrity" (Ferrites, Conf.reports), Minsk, 1960.
2. H.Forestier, Compt.rend., 192, 842 (1931).
3. Goto Yasumasa & Toshia Takada, J.Amer.Ceram.Soc., 43, 150 (1960).

* * * * * * *

SOME POSSIBILITIES OF IMPROVING THE QUALITY OF MICROWAVE FERRITES

- F.I.Kolomoitsev, F.F.Kodzhespirov, A.Ya.Yakunin & E.V.Sinyakov

The quality of ferrites used in microwave engineering is determined mainly by their activity (rotary power) and power absorption. For a given disc (plate) geometry and location one must insure a sufficient effective (non-mutual) phase shift (or rotation of the plane of polarization) and provide for a minimum power loss. It is not easy to meet both these requirements simultaneously, inasmuch as they are, to some extent, contradictory. Nevertheless, it is feasible, by varying the preparation technology and machining of the ferrite disc, to control the activity and the power loss separately.

1. We investigated Al-Mg ferrites having the composition $MgAl_{0.3}Fe_{1.7}O_4$.[1-3] These were prepared of the appropriate oxides by the usual procedure of two-step sintering at different temperatures of preliminary (T_{ps}) and final (T_{fs}) sintering. The ferrite plates were ground to the same dimensions and cemented to the narrow wall of a rectangular waveguide. The plate parameters were measured at a fixed frequency.

The data given below are mean values based on measurement of 10 specimens of each batch.

Fig.1 shows the variation of the effective (nonmutual) phase shift $\Delta\varphi$ as a function of the transverse magnetic field H for specimens sintered at T_{ps} from 1100 to 1300° and T_{fs} from 1000 to 1200° (the temperatures were varied in 100° steps). Increase of the preliminary sintering temperature, other conditions remaining equal, leads to increase of the activity (Fig.1,a). Increase of the final sintering temperature leads to analogous results (Fig.1,b). It must be noted, however, that the influence of the final sintering on the activity is of little significance when $T_{fs} \leqslant T_{ps}$, but when $T_{fs} > T_{ps}$ the effect of the conditions of final sintering becomes significant, inasmuch as under these conditions the spinel formation goes closer to completion and the polycrystalline ferrite consists mainly of coarse grains with dimensions of $\leqslant 2 \cdot 10^{-3}$ cm. At the same time there is observed increase in the density of the sintered plates (the x-ray density approaches 4.5 g/cm^3).

The rate of cooling after final sintering is particularly important. The decrease of temperature with time in the case of natural cooling with the furnace is usually exponential and can be characterized by a time constant τ that is different for different furnace designs. It will be evident from Table 1 in which

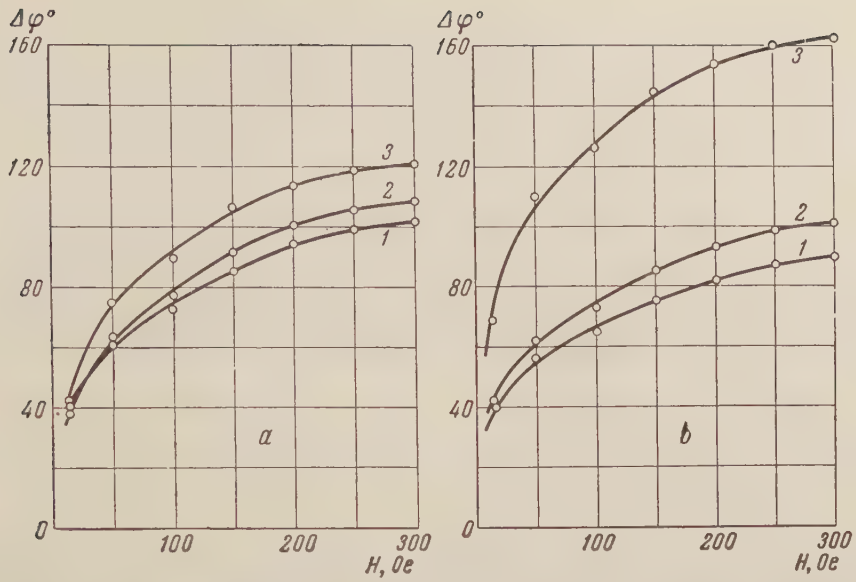

Fig.1. Variation of the effective phase shift $\Delta\varphi$ with the strength of the transverse magnetic field: a - T_{fs} = 1100°, T_{ps} = 1) 1100°, 2) 1200°, 3) 1300°; b - T_{ps} = 1100°, T_{fs} = 1) 1000°, 2) 1100°, 3) 1200°.

Table 1

Furnace No.	τ, hr	$\Delta\varphi$° at H = 300 Oe
1	14.7	81
2	18.7	72.3
3	22.2	69

we compare the values for $\Delta\varphi$ for plates sintered at T_{ps} = 1100° (4 hr) and T_{fs} = 1120° (4 hr) but cooled in furnaces with different τ, that in general slower cooling leads to reduction of the activity.

The limiting case of rapid cooling - quenching - leads to an even greater increase in activity and permeability. Ferrites sintered at T_{fs} = 1000° and slowly cooled with the furnace have an initial permeability μ_o = 2.5, while ferrites quenched by rapid cooling in air have μ_o = 4.3.

It may be assumed that μ_o and $\Delta\varphi$ are determined by the structure of the final sintered plate, i.e., by the distribution and arrangement of the di- and trivalent metal ions in the A and B sublattices of the quasi-inverted spinel.

Under conditions of the usual technology, taking into account the fact that the Al ions are located in the B sublattice[4], it may be assumed that there forms a structure of the form

$$Mg_xFe_{1-x}[Mg_{1-x}Al_{0,3}Fe_{0,7+x}]O_4.$$

Using the indicative data of Gorter[5] we can infer that $x = 0.25$. Then the saturation magnetization m per molecule (in μ_B) will be close to unity. Change of x by variation of the heat treatment conditions leads to corresponding variation of m, μ_o and $\Delta\varphi$. Rapid cooling - quenching - allows of partial freezing of the high temperature chaotic distribution of ions in the sublattices with $x \approx 1/3$.

Experiments showed that the magnetization per formula unit, as determined by the ponderomotive procedure[6], varies in the range from 0.78 to 1.30 with changes in the sintering technology. Increase of the sintering temperatures with subsequent slow cooling leads to lower values of m, i.e., a more ordered spinel, and

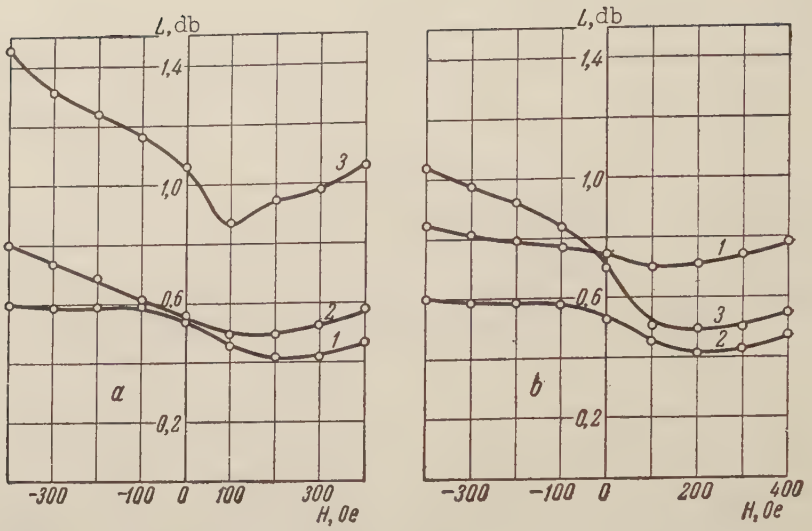

Fig.2. Variation of the attenuation in the waveguide as a function of the transverse magnetic field: a - T_{fs} = 1100°, T_{ps} = 1) 1100°, 2) 1200°, 3) 1300°; b - T_{ps} = 1100°, T_{fs} = 1) 1000°, 2) 1100°, 3) 1200°.

at the same time results in increase in the density ρ of the ferrite to the extent that the product $m\rho$ is increased and leads to increase in the activity of the plate. There is clear, definite correlation between the values of $m\rho$ and $\Delta\varphi$.

Quenching of the plates by a blast of cold air through the cooling furnace, cooling from high temperatures in open air and quenching in salt water all freeze the more chaotic distribution of metal ions and lead to higher values of m and, accordingly, $\Delta\varphi$.

The above inferences regarding freezing of the ionic disorder are substantiated by x-ray diffraction studies aimed at determining the lattice constant. The largest constant is obtained for ferrite quenched in water (a_0 = 8.3475 Å), the smallest for slowly cooled ferrite (a_0 = 8.3425 Å).

Table 2

T_{ps}°, C	T_{fs}°, C	Absorption, %		FeO wt.%
		H_{min}	$H = -400$ Oe	
1100	1000	15	18	0,56
1100	1100	9	13	0,04
1100	1200	11	21	0,36
1200	1100	11	17	0,62
1300	1100	18,5	28	0,94

2. The variation of the insertion attenuation as a function of the transverse field strength is shown in Fig.2. In agreement with the results of Mikaelyan[7], the attenuation varies with the field strength H and goes through a minimum ($H_{min} \approx$ +100 to +200 Oe). Increase of the sintering temperature leads to a stronger field dependence of the attenuation, measured in the range from +400 to -400 Oe (see Table 2).

It will be evident from Fig.2,a that increase of the preliminary sintering temperature leads to increase of the attenuation: the loss rises markedly in going through 1200°. This temperature appears to be critical as regards reduction of Fe_2O_3 and formation of divalent iron ions.[8,9]

The Fe content in the briquettes after preliminary sintering at 1100, 1200, and 1300° amounted to 0.04, 0.33 and 0.72 percent by weight, respectively. Approximately the same results were obtained after final sintering (Table 2). It is interesting to note that with increase in final sintering temperature the loss

in the ferrite plates passes through a minimum (Fig.2,b). Hence it appears feasible to realize a certain reduction of the loss by appropriate choice of the final sintering temperature. On the basis of the data shown in Figs.1 and 2 and the results of certain auxiliary studies, it may be inferred that to satisfy simultaneously the requirements of minimum attenuation and $\Delta\varphi = 90^\circ$ one should strive to realize the following heat treatment conditions for Al-Mg ferrites when employing a furnace with $\tau \simeq 15$ hours: T_{ps} = 1100-1120° (heating time 4-6 hr) and T_{fs} = 1200-1150° (heating time 4-6 hr).

3. Al-Mg ferrites, like ferrites of other types[8] can be improved as regards activity and power dissipation by additional heating in an appropriate atmosphere. Additional heating of the plates in a stream of oxygen at 600-700° usually reduces the power absorption. Heating in air, however, virtually does not reduce the loss, while heating in a stream of CO_2 leads to an appreciably increase in attenuation (Table 3).

Table 3

Annealing conditions			Power absorbed, %		Magnetic field strength for $\Delta\varphi = 90^\circ$	
Atmosphere	Temp. °C	Time, h	Prior to anneal	After anneal	Prior to anneal	After anneal
O_2	600—700	10	19,3	11,9	217	233
	640	7	15,4	13,3	217	150
	600	4	15,6	12,5	200	200
	540	5	15,1	13,6	275	225
	440	8	13,2	13,7	212	212
CO_2	640	6	15	22,3	300	225
Air	640	6	15,7	15,1	280	180

Comparing the results given in Tables 2 and 3, it may be inferred that annealing in an atmosphere of oxygen favors oxidation of the ferrous to ferric oxide, which leads to reduction of the absorption.

Annealing of the ferrite plates also results in change in their activity: usually the activity increases, although the reverse may also occur. The change in activity is apparently connected with the rate of cooling after annealing. Forced cooling by air blown through the furnace insures an increase in activity.

4. Our experiments have shown that there are definite possibilities for improving the quality of ferrites, i.e., that one can separately control the activity and the power absorption, increasing the former and reducing the latter. For Al-Mg ferrites it is not necessary to try to realize completion of spinel formation; one should strive to keep the sintering temperatures in the vicinity of 1200°.

From the standpoint of enhancing the activity rapid cooling after the final sintering is important, provided the sintering temperature and time have been correcly specified.

With a view to reducing attenuation one should employ sintering in an atmosphere enriched in oxygen or better, pure oxygen, and one should strive to avoid the formation of large crystallites in the polycrystalline system. Our experiments show, moreover, that it is feasible to improve the quality of poor ferrite plates by appropriate annealing.

References

1. G.A.Smolenskii & A.G.Gurevich, Poluprovodniki v nauke i tekhnike (Semiconductors in science and technology), Vol.II, M. 1958.
2. L.G.Vitert, I.P.Schafer & C.L.Hogan, J.Appl.Phys., 25, No.7 (1954).
3. L.G.Vitert, Ibid., 28, No.3 (1957).
4. N.A.Smol'kov & V.A.Eremkina, Vestnik, Moscow University, Math.-Phys.Series, No.2, (1959).
5. E.V.Gorter, Uspekhi fiz.nauk, 57, No.2, 3 (1955).
6. P.W.Selwood, Magnetochemistry.
7. A.L.Mikaelyan, Izv.AN SSSR, Ord.tekhn.nauk (Bulletin, USSR Ac.of Sci., Div.Tech.Sciences), No.3, 139 (1955).
8. L.I.Rabkin, Vsokochastotnye ferromagnetiki (High-frequency ferromagnets) M., 1960.
9. A.B.Blackman, J.Amer.Cer.Soc., III, 42, No.3 (1959).

* * * * * * *

SYNTHESIS OF MULTIPLE COMPONENT FERRITES WITH HIGH MAGNETOSTRICTIVE PARAMETERS

- P.L.Strelets, L.N.Syrkin & M.G.Tkachenko

In the present report we give the results of search for and investigation of ferrites with high dynamic magnetostrictive parameters. The search was based primarily on the work of Refs.1-6. The ferrite specimens were synthesized by the usual ceramic technology. The basic initial "system" was comprised of the oxides* $NiO-ZnO-CuO-CoO-Fe_2O_3$; for convenience this was subdivided into a number of "sybsystems".

The magnetostrictive parameters (electromechanical coupling coefficient K and magnetostrictive constant a) were measured by the resonance-antiresonance method[1] at low inductions ($B_m \approx 1$ G) and $H_0 = 10$ Oe. This choice of the measurement conditions was dictated by the necessity of checking the properties of a large number of specimens, which made it impossible to investigate the H_0 dependence of K and a for each one (the magnetostrictive parameters are virtually independent of B_m in the range under 100 G); on the other hand, near $H_0 = 10$ Oe the value of K for most of the investigated ferrites has a maximum, while the increase of a with $H_0 > 10$ Oe does not exceed 20-30% in most cases.

In Fig.1 we give curves characterizing the variation of the parameters K and a as a function of the $CoFe_2O_4$ content (x) in the $Ni_{1-x-y}Zn_yCo_xFe_2O_4$ system ("A system")** for different values of the $ZnFe_2O_4$ content (y). These specimens were sintered at $T_{sint} = 1400^o$.

In all cases the peaks of K and a appear in the vicinity of $x = 0.02$. The optimum $ZnFe_2O_4$ content $y_{opt} = 0.1$; for it $a = (1.8\text{-}1.9)\cdot 10^4$ dyn G^{-1} cm^{-2}, and $K = 0.26$ (composition No.1).

Analogous composition dependences are observed for the "B system" ($Ni_{1-x-y}Cu_y Co_xFe_2O_4$), however, in this case the a and K peaks are broader and correspond to values of x lying in the range from 0 to 0.01. The highest magnetostrictive parameters are obtained for composition No.2 ($y = 0.15$ and $x = 0.01$): $a = 1.5\cdot 10^4$ dyn G^{-1} cm^{-2} and $K = 0.21$.

---

*Except as noted, the oxides were chemically pure and reagent grade pure.

**The chemical formulas here and below are approximate.

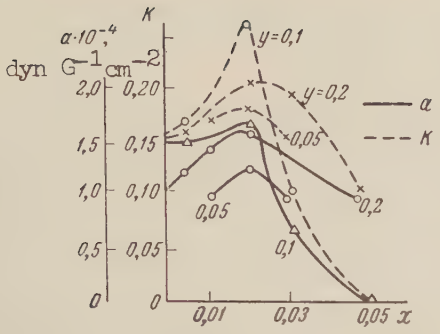

Fig.1

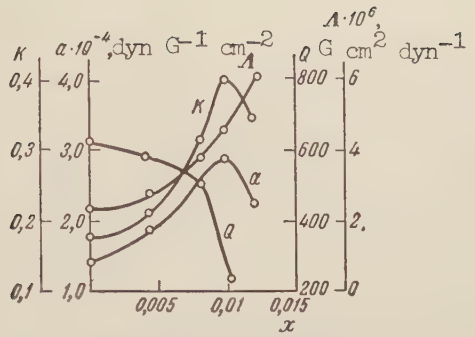

Fig.2

Fig.1. Composition dependence of the magnetostrictive constant a and electromechanical coupling coefficient K of $Ni_{1-x-y}Zn_yCo_xFe_2O_4$ ferrites.

Fig.2. Composition dependence of the parameters of ferrites of the $(Ni_{0,925}Cu_{0,075})_{1-x}Co_xFe_2O_4$ system; $T_{sint} = 1250^o$.

The maxima in the K versus $CoFe_2O_4$ content curves for the mixed ferrite are explained, as Van der Burgt[2,3] showed, by compensation of the magnetocrystalline anisotropy. Such compensation is possible owing to the difference between the signs of the anisotropy constants K_1 for $CoFe_2O_4$ and $NiFe_2O_4$ and also because K_1 for $CoFe_2O_4$ is greater in absolute magnitude than K_1 for other ferrites.

It will be evident from Figs.1 & 2 that similar less sharp peaks are evinced in the a versus x curves.

If one considers the familiar relation between the magnetostrictive parameters

$$a = K\sqrt{\frac{E}{4\pi\mu_r}} = \frac{\Lambda E}{4\pi\mu_r}$$

(E is Young's modulus, μ_r is the reversible permeability, Λ is the "sensitivity coefficient") taking into account the experimental dependences (Figs.1-3), it may be inferred that the values of μ_r and Λ are determined by different anisotropy energies, so that there obtains a resultant dependence of Λ/μ_r or K/μ_r on the anisotropy constant K_1.

For the purpose of systematic investigation of the influence of excess Fe_2O_3 in the ferrite on the dynamic magnetostrictive properties there was synthesized the "system" $Ni_{1-y}Co_yFe_2O_4$ $(Fe_2O_3)_x$, consisting of several "subsystems". The most interesting subsystem - "C system" - corresponds to the optimum $CoFe_2O_4$ content (y = 0.02), i.e., is the "subsystem" characterized by the formula

$$Ni_{0,98}Co_{0,02}Fe_2O_4(Fe_2O_3)_x$$

Curve 1 in Fig.3 shows the variation of a versus x for this "system" for specimens sintered at different T_{sint}. The maximum value of a ($(2.2\text{-}2.3)\cdot10^4$ dyn G^{-1} cm^{-2}) is obtained for composition No.3 (x = 0.025; T_{sint} = 1360°). The electromechanical coupling coefficient K attains a maximum value (0.3-0.32) at x_{opt} in the range between 0.025 and 0.035 (the value of x_{opt} depends on T_{sint}). The electromechanical coupling coefficient K_r in the remanence state attains 0.35, while the sensitivity constant Λ_r in this state equals $(6\text{-}7)\cdot10^6$ G cm^2 dyn^{-1}; these remanence values are three times greater than the corresponding values for $NiFe_2O_3$.

It is known that ferrites containing Co^{2+} and Fe^{2+} ions are highly sensitive to thermomagnetic treatment.[7] In particular, application of heat treatment in a

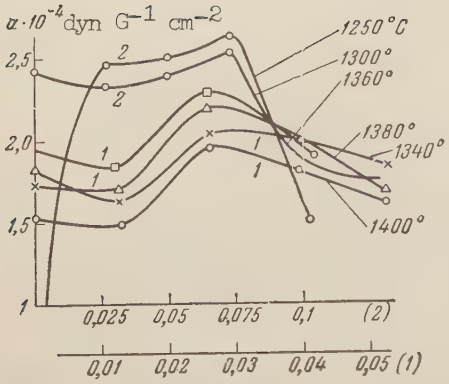

Fig.3. Composition dependence of the magnetostrictive constant at different sintering temperatures (T_{sint} indicated at the curves): 1 - $Ni_{0,98}Co_{0,02}Fe_2O_4(Fe_2O_3)_x$ "system", 2 - $Ni_{0,98-x}Co_{0,02}Cu_xFe_2O_4 \cdot (Fe_2O_3)_{0,025}$ "system".

magnetic field to this group of ferrites may provide the means for further increase of the electromechanical coupling coefficient and the mechanical quality.[8]

It must, however, be emphasized that the increase of the magnetostrictive parameters of ferrites by introduction of excess Fe^{2+} ions is accompanied by increase of the electromagnetic and mechanical losses.

An appreciable reduction of the electromagnetic (but not mechanical) losses with conservation or even some improvement of the parameters a and K can be attained by synthesis of multiple component ferrites containing $CuFe_2O_4$. Thus if in ferrites of the "A system" (Fig.1) part of the Ni ions are replaced by Cu ions*, the a versus $CoFe_2O_4$ content curve lies appreciably higher than the curve for the initial "system" even at lower sintering temperatures.

In the case of Ni-Co ferrites containing excess Fe_2O_3 replacement of part of the Ni ions by Cu ions also proved effective. In view of this, on the basis of composition No.3 ("C system") there was synthesized a group of specimens ("E system") having the approximate chemical formula $Ni_{0,98-x}Co_{0,02}Cu_xFe_2O_4 \cdot (Fe_2O_3)_{0,025}$. The measured values of the magnetostrictive constant in this "system" are shown in Fig.3 (curves 2, corresponding to different T_{sint}). The most interesting composition in this system is composition No.4 ($x = 0.075$) for which $a = 2.5 \cdot 10^4$ dyn G^{-1} cm^{-2}, $K = 0.38$ and $\Lambda = (6\text{-}7) \cdot 10^{-6}$ G cm^2 dyn^{-1} (at $H_0 = 10$ Oe).

Further improvement of the chemical composition of the Ni-Cu-Co ferrite led to the "F system": $(Ni_{0,925}Cu_{0,075})_{1-x}Co_x \cdot Fe_2O_4(CoFe_2O_4)_x$ (Fig.2). With increase of x the mechanical quality of the "F system" ferrite monotonically decreases, while the sensitivity coefficient Λ increases (apparently the maximum of Λ lies in the range of large x). The a and K curves exhibit maxima: $a_{max} \approx 2.9 \cdot 10^4$ dyn G^{-1} cm^{-2}; $K_{max} \approx 0.4$.

It will be evident from Fig.2 that the maximum values of a and K in this system are exhibited by the ferrite with $x = 0.01$ (composition No.5). The optimum temperatures for obtaining the maximum values of a and K differ somewhat: they are 1300 and 1250°, respectively.

Some difference between the optimum temperatures corresponding to the peak values of a and K is in general characteristic of the Ni—Zn—Cu—Co and Ni—Cu—Co systems, in contrast to the simpler (Ni—Cu and Ni—Zn—Co ferrite systems. This temperature dependence provides the means for controlling the properties to suit the particular technical requirements (Fig.4).

Use of technical grade raw materials instead of chemically pure oxides leads to reduction of the optimum values of T_{sint} (compare curves 3 and 4 in Fig.4); this is undoubtedly due to the presence of impurities, which play the role of mineralizers.

Our systematic investigation of the properties of ferrites in the NiO—ZnO—CuO—CoO—Fe_2O_3 "system" and of solid solutions containing excess Fe^{2+} ions has made it possible to identify compositions (in particular, compositions Nos.3,4 &

---

*We designate the $(Ni_{0,85}Cu_{0,15})_{1-x}Co_xFe_2O_4$ "system" as the "D system".

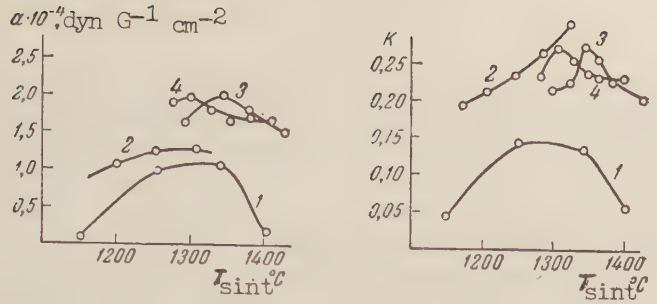

Fig.4. Variation of the magnetostrictive constant a and electromechanical coupling coefficient K of different ferrites as a function of the sintering temperature T_{sint}: 1 - $Ni_{0.85}Cu_{0.15}Fe_2O_4$, 2 - $Ni_{0.73}Zn_{0.1}Cu_{0.15}Co_{0.02}Fe_2O_4$, 3 - $Ni_{0.88}Zn_{0.1}Co_{0.02}Fe_2O_4$ (prepared of chemically pure oxides); 4 - $Ni_{0.88}Zn_{0.1}Co_{0.02}Fe_2O_4$ (prepared of technical grade raw materials.

5) characterized by higher values of K, a and Λ, as compared with earlier known compositions.

We feel, however, that the possibilities of improving the properties of ferrites - even of those belonging to the investigated "system" - have not been exhausted and that further research should bring to light other ferrites with superior parameters.

References

1. C.M.Van der Burgt, Philips Res.Repts, 8, 91 (1953).
2. C.M.Van der Burgt, Ibid., 12, 97 (1957).
3. C.M.Van der Burgt, Philips Techn.Rev., 18, No.10, 285 (1956/57).
4. J.Kikuchi et al, Part I, Ni-Zn Ferrite, RITUB, Vol.7, p.1, 1955; Part II, Ni-Cu Ferrite, RITUB, Vol.7, p.171, 1955.
5. I.P.Golyamina, Akust.zhur., 2, 255 (1956). (Trans.Soviet Physics - Acoustics.)
6. L.N.Syrkin, in "Ferrity" (Conference reports on ferrites), p.226, Minsk, 1960.
7. L.Weil, Compt.rendu, 234, 1351 (1952).
8. L.N.Syrkin, in "Sbornik nauchno-tekhnicheskoi informatsii po priborostroeniyu (Scientific-technical articles on instrument building), No.1 (13), 22, L., 1960.

FERRITES WITH HIGH SATURATION MAGNETIZATION AND A NARROW RESONANCE ABSORPTION LINE AT MICROWAVE FREQUENCIES

- V.A.Fabrikov, Z.M.Gushchina & V.D.Kudryavtsev

We have developed a number of new types of ferrites characterized by a high saturation magnetization and a narrow resonance absorption peak at microwave frequencies. Some of these - specifically those designated P-28, M-55 and M-258 - may prove of practical value for use in microwave rectifiers and similar equipment.

P-28 ferrite in an improved modification of type P-1 Mg-Mn-Zn ferrite[1]. It has the following composition: Fe_2O_3 - 53.55, MgO - 6.76, $MnCO_3$ - 30.35, and ZnO - 9.34 percent by weight. P-28 ferrite has the following characteristics: saturation magnetization M_s = 3200-3400 G, resonance line width at a wavelength of 3 cm ΔH = 50-70 Oe (for individual carefully polished specimens one can obtain $\Delta H < 40$ Oe), Curie temperature T_c = 170-180°C, dc resistivity $\rho = 10^7$ ohm-cm. Preliminary sintering in briquette form is carried out at 900° for 6 hours; the final sintering is effected in air at 1370° for 5 hours with subsequent cooling in vacuum with the furnace switched off.

M-55 ferrite, which is an improved modification of M-50 ferrite, has the following composition: Fe_2O_3 - 63.79, NiO - 20.95, $MnCO_3$ - 4.89, and ZnO - 10.37 percent by weight. This ferrite has the following characteristics: M_s = 4300-4500 G, ΔH = 230-250 Oe, T_c = 330-350°C, ρ = 10.7 ohm-cm. Preliminary sintering - 2 hours at 1100°; final sintering in air at 1300° for 4 hours.

M-258 ferrite was developed on the basis of the American Ni-Zn-Mg-Mn ferrite marketed under the trade name "Ferramic C" (Ref.2) by the addition to it of 20 mole percent copper oxide. It has the following characteristics: M_s = 4600-4800 G, ΔH = 120-140 Oe, T_c = 300°C, $\rho = 10^5$ ohm-cm. This ferrite is prepared of a mixture having the following composition: 66.38% Fe_2O_3, 8.11% ZnO, 9.93% NiO, 7.63% $MnCO_3$, 1.34% MgO and 6.61% CuO. The compacted briquettes are first fired at 600° for 2 hours; the final sintering is carried out in air at 1150°C for 20 hours.

All the developed ferrites were tested at liquid helium temperature. The test procedures and measurement results are given in Ref.3 (following article). At this temperature the ferromagnetic resonance line for polycrystalline specimens is appreciably broadened, attaining a width of 800 Oe (M-258 ferrite) or more (P-28 and M-55 ferrite).

The saturation magnetization at helium temperatures increases only slightly (it rises to about 5600 gauss for M-258 ferrite).

References

1. V.A.Fabrikov, Z.M.Gushchina & V.D.Kudryavtsev, Radiotekhnika i elektronika, 4, No.11, 1940 (1959). (Trans.Radio Engineering & Electronics.)

2. American Institute of Physics Handbook, p.5-217, N.Y., 1957.

3. G.S.Misezhnikov, Ya.I.Rozenberg & V.B.Shteinshleiger, Present issue of the Bulletin, p.1441.

MEASUREMENT OF THE PARAMETERS OF FERROMAGNETIC RESONANCE IN POLYCRYSTALLINE AT LIQUID HELIUM TEMPERATURE

- G.S.Misezhnikov, Ya.I.Rozenberg & V.B.Shteinshleiger

In the present report we give the results of observation of ferromagnetic resonance in polycrystalline ferrites with a high saturation magnetization at liquid helium temperature (4.2°K). Specifically, we measured the band width ΔH and the external field at resonance H_r for specimens in the form of spheres and thin disks. From the observed values of H_r we determined the saturation magnetization M_0.

For measuring these parameters of ferromagnetic resonance with a wide absorption band ($\gtrsim$1000 Oe) we used the following simple but accurate procedure. With sufficiently slow change of the magnetizing field H, its strength can be varied in the wide range necessary for observing broad resonance lines on the screen of an oscillograph with a long persistence. The microwave frequency detector is coupled, via a dc amplifier, to a low frequency oscillograph with a long persistence screen. The sweep of the oscillograph is synchronized with the variation of the magnetizing field by applying to the horizontal deflecting plates a voltage proportional to the current in the winding of the electromagnet. The block diagram of the set-up is shown in the accompanying figure.

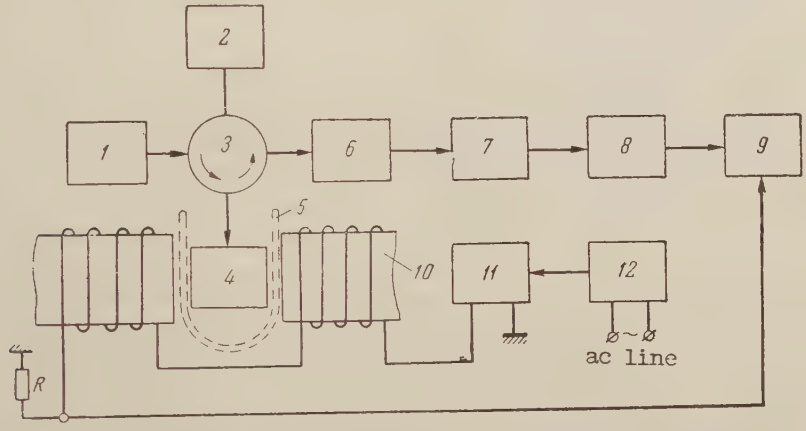

Block diagram of the experimental set-up: 1) klystron, 2) load, 3) ferrite circulator, 4) cavity with ferrite specimen, 5) cryostat with liquid helium, 6) attenuator, 7) detector, 8) dc amplifier, 9) oscillograph with long persistence screen, 10) electromagnet, 11) rectifier, 12) autotransformer.

In varying the strength of the magnetic field in the appropriate range by means of the autotransformer 12, there is observed on the oscillograph screen 9 a trace of the ferromagnetic resonance absorption, and the horizontal deflection of the beam gives the value of the field H. To minimize errors in measuring the line width, connected with the influence of dispersion[1], the cavity-waveguide coupling was chosen large enough so that the loaded Q was appreciably smaller than the Q of the cavity with the ferrite specimen at ferromagnetic resonance.

The resonance band width ΔH was measured at half power of the maximum absorption in a spherical specimen. For the same specimen we also determined the value of the component H_a of the anisotropy field in the direction of the external field H:

$$H_a = \frac{\omega}{\gamma} - H_{sp}$$

where ω is the angular frequency of the signal, γ is the gyromagnetic ratio, and H_{sp} is the external field at resonance for a sphere.

The saturation magnetization M_0 was determined for a thin disk magnetized tangentially to its plane, making use of Kittel's formula[2] which in this case can be written in the form

$$\omega = \gamma \{H_0 [H_0 + (4\pi - 3N_z) M_0]\}^{\frac{1}{2}}, \qquad (1)$$

where $H_0 = H_d + H_a$ (H_d is the value of the external field at resonance for the disk) and N_z is the demagnetizing factor in the direction of the external field.

The factor N_z was determined experimentally at 293°K, using formula (1), on the basis of the observed value of H_0 and the value of the saturation magnetization M_0 determined by the ballistic procedure.

The measurements were carried out at a wavelength of 3.2 cm in a cylindrical cavity (diameter 22 mm) excited in the H_{111} mode. The cavity with the specimen was immersed in a cryostat with liquid helium and the entire assembly was mounted between the pole pieces of the electromagnet.

For the measurements we had a number of different ferrites with high saturation magnetization, namely, Mg-Mn ferrite type P-28 and Ni-Zn ferrites types M-55 and M-258 (Ref.3 - preceding article).

The best results (i.e., the narrowest resonance line) were obtained for M-258 ferrite (composition: 66.38% Fe_2O_3, 8.11% ZnO, 9.93% NiO, 7.63% $MnCO_3$, 1.34% MgO, and 6.61% CuO). Somewhat poorer results were obtained for the M-55 ferrite. In the case of the P-28 ferrite specimens the resonance line at 4.2°K was so greatly smeared out and the resonance intensity was so low that no accurate measurements could be made.

Parameter	At 293°K	At 4.2°K	Remarks
H_{sp}, Oe	3015	2270	
H_d, Oe	1720	850	Field H parallel to plane of disk
ΔH, Oe	120	800	For sphere
H_a, Oe	315	1060	
M_0, G	380	420	

The values obtained for M-258 ferrite as a result of measurements on specimens in the form of a 0.5 mm sphere and a 0.16 mm thick disk 1.17 mm in diameter are given in the table.

Thus it will be evident that in the investigated polycrystalline ferrites the width of the ferromagnetic resonance band broadens appreciably at liquid helium temperature. The narrowest band width (800 Oe) was observed for the M-258 Ni-Zn ferrite.

We desire to thank V.A.Fabrikov and A.G.Gurevich for helpful discussions.

References

1. A.A.Manenkov & A.M.Prokhorov, Radiotekhnika i elektronika (Radio Engineering & Electronics), No.4, 469 (1956).

2. C.Kittel, Phys.Rev., 73, 155 (1948).

3. V.A.Fabrikov, Z.M.Gushchina & V.D.Kudryavtsev, Present issue of the Bulletin, p.1440.

Bulletin of the Academy of Sciences of the USSR - Physical Series
Vol. 25, No.11 - November 1961

Transactions of the (First) Conference on Ferromagnetism & Antiferromagnetism
(To be continued in Vol.25, No.12 & Vol.26, No.2)

TABLE OF CONTENTS

	Page Orig.	Trans.
Some aspects of the modern theory of ferro- and antiferromagnetism (Condensation of a review) - S.V.Vonsovskii	1314	1325
Non-collinear ferro- and antiferromagnetism - E.A.Turov	1315	1326
Influence of the magnetic sublattice structure of ferrites on their physical properties - K.P.Belov	1320	1332
Regarding the normal energy state of ferrite with three magnetic sublattices - A.A.Gusev & A.S.Pakhomov	1327	1338
Concerning the co-existence of the ferroelectric and ferrimagnetic states - G.A.Smolenskii, V.A.Isupov, N.N.Krainik & A.I.Agranovskaya	1333	1345
Energy spectrum of current carriers in ferro- and antiferromagnets - E.K.Kudinov & A.G.Samoilovich	1339	1351
Contribution to the theory of kinetic effects in NiO type semiconductors - M.I.Klinger	1342	1354
Contribution to the theory of nonresonance absorption of an alternating magnetic field by a ferromagnetic dielectric at low temperatures - M.I.Kaganov & V.M.Tsukernik	1346	1358
Concerning a mechanism of absorption of the longitudinal magnetic field by a ferromagnetic dielectric - M.I.Kaganov & V.M. Tsukernik	1352	1364
Temperature dependence of the width of ferromagnetic resonance peaks - Mêng Hsien-Cheng	1353	1366
Ferromagnetic resonance in ferrites in strong alternating magnetic fields - A.G.Gurevich & S.S.Starobinets	1357	1371
Effect of induced anisotropy on ferromagnetic resonance - A.G. Gurevich, A.P.Safant'evskii, V.I.Solov'ev & E.S.Sher	1361	1374
Experimental investigation of the effects in yttrium ferrite single crystals, associated with nutational oscillations of the magnetization of the material under conditions of ferromagnetic resonance - V.A.Fabrikov, V.P.Kozlov, V.T.Kadeev & V.D.Kudryavtsev	1367	1380
Magnetic and resonance properties of yttrium-iron garnets with the Yt^{3+} ions replaced by Tb^{3+}, Nd^{3+} and Lu^{3+} ions - K.P.Belov & L.A.Malevskaya	1371	1384
Effect of the boundary condition for the magnetic moment on spin-wave resonance in metals - M.I.Kaganov & Yü Liu	1375	1388
Temperature dependence of the conductivity and Hall effect in metallic gadolinium - N.V.Volkenshtein & G.V.Fedorov	1379	1391
Magnetoelastic properties of terbium and holmium (partial report) - K.P.Belov, R.Z.Levitin & S.A.Nikitin	1382	1394
Determination of the parameters characterizing the cation distribution in multiple component spinels - A.N.Men'	1385	1396
Magnetization and the magnetocaloric effect in uranium hydride and deuteride - A.I.Karchevskii & E.M.Buryak	1387	1400

Magnetic anisotropy and hysteresis properties of rare earth orthoferrites - K.P.Belov, M.A.Zaitseva, A.M.Kadomtseva & V.A.Timofeeva 1389 1401
Investigation of ferrimagnets with the structure of magnetoplumbite and garnet in strong pulse magnetic fields - G.A.Smolenskii & A.A.Andreev 1392 1405
Investigation of the magnetic properties of some ferromagnets with the structure of perovskite and garnet - G.A.Smolenskii, V.P. Polyakov & V.M.Yudin 1396 1408
Temperature dependence of the paramagnetic susceptibility of mixed ferrites - V.I.Chechernikov 1399 1411
Frequency and temperature dependences of the initial permeability of ferrites with the garnet structure - G.A.Smolenskii, Chang Tsung & E.S.Sher 1402 1414
Viscosity and hysteresis properties of ferrites, due to electron diffusion - K.M.Bol'shova & T.A.Elkina 1407 1418
Effect of gamma-irradiation on disaccomodation in Ni-Zn ferrites - E.I.Trinkler, V.A.Gol'din & V.B.Osipov 1411 1422
Concerning correlation between the electric and magnetic properties of Ni-Zn ferrites - L.I.Rabkin & Z.I.Novikova 1413 1424
Phase equilibrium in the Fe_2O_3-BaO system - B.G.Livshits, S.A. Eliseev, B.A.Samarin & V.A.Somenkov 1418 1429
Some possibilities of improving the quality of microwave ferrites - F.I.Kolomoitsev, F.F.Kodzhesnirov, A.Ya.Yakunin & E.V.Sinyakov 1422 1432
Synthesis of multiple component ferrites with high magnetostrictive parameters - P.L.Strelets, L.N.Syrkin & M.G.Tkachenko 1426 1436
Ferrites with high saturation magnetization and a narrow resonance absorption line at microwave frequencies - V.A.Fabrikov, Z.M. Gushchina & V.D.Kudryavtsev 1429 1440
Measurement of the parameters of ferromagnetic resonance in poly-crystalline ferrites at liquid helium temperature - G.S.Misezhnikov, Ya. I. Rozenberg & V.B.Shteinshleiger 1430 1441

Translated in 1962 by
Columbia Technical Translations
5 Vermont Ave., White Plains, N.Y.

Transactions

of the

(First) Conference on Ferromagnetism & Antiferromagnetism

(5-11 March 1961, Leningrad)

(Continued from Vol.25, No.11; to be continued in Vol.26, No.2)

CHANGE IN CONDUCTIVITY INCIDENT TO MAGNETIZATION AND MAGNETIC ANISOTROPY IN FERRITE SINGLE CRYSTALS OF THE $Mn_xFe_{3-x}O_4$ SYSTEM

- K.P.Belov & A.V.Zalesskii

Until recently it was assumed (for example, see Ref.1) that the magnetic anisotropy constant K_1 of ferrites with the spinel structure, with the exception of compositions containing Co ions, is constant. However, as was shown by Penoyer & Shafer[2] and subsequently by Funatogava et al[3], in solid solutions of magnetite with manganese ferrite (general formula $Mn_xFe_{3-x}O_4$) the anisotropy constant K_1 at room temperature goes through zero twice and is positive in the $0.6 < x < 0.8$ interval. This fact was surprising, for there was no reason to expect that in solid solutions of two close isomorphous substances characterized by a negative constant there will be observed violation of additivity in the variation of the magnetic anisotropy energy. One of the possible reasons for this anomaly may be connected with the variation of the ion distribution in going from inverse spinel (magnetite) to almost normal spinel (manganese ferrite)[3]. It may be inferred from the data in the literature, however, that in solid solutions of spinels of the same (inverse) type (magnetite + nickel ferrite) a number of intermediate compositions at room temperature have a smaller anisotropy constant than the end compositions (in $Ni_{1.0}Fe_{2.0}O_4$ $K_1 = -63\cdot10^3$ erg/cm^3 (Ref.4), in $Ni_{0.95}Fe_{2.05}O_4$ $K_1 = -68\cdot10^3$ erg/cm^3 (Ref.5), in $Ni_{0.75}Fe_{2.25}O_4$ $K_1 = -49\cdot10^3$ erg/cm^3 (Ref.5), in $Ni_{0.8}Fe_{2.2}O_4$ $K_1 = -39\cdot10^3$ erg/cm^3 (Ref.4) and in Fe_3O_4 $K_1 = -108\cdot10^3$ erg/cm^3 (Ref.6)).

The ferrites of the $Mn_xFe_{3-x}O_4$ system have a number of distinctive magnetostrictive and galvanometric properties. It is known, for instance, that magnetite is characterized by the magnetostriction constants $\lambda_{100} = -19\cdot10^{-6}$ and $\lambda_{111} = -81\cdot10^{-6}$ (Ref.4), while $Mn_{0.98}Fe_{1.86}O_4$ is characterized by $\lambda_{100} = -14\cdot10^{-6}$ and $\lambda_{111} = -1\cdot10^{-6}$ (Ref.4). In going from manganese ferrite to magnetite there occurs a change in the sign of the magnetostriction in the [111] direction. According to the indirect measurements of Braginskii[7], this change is observed in the $x = 1.00$ to 1.06 interval. The anisotropy of the change in resistivity under the influence of magnetization (an even effect analogous to magnetostriction) in magnetite is characterized, in the "two-constant approximation", by the constants $h_{100} = 13\cdot10^{-4}$ and $h_{111} = -6\cdot10^{-4}$ (Ref.8), while in Mn ferrite with $x = 1.12$ $h_{100} = 4.425\cdot10^{-3}$ and $h_{111} = 0.9\cdot10^{-3}$ (Ref.9). Consequently, the longitudinal galvanomagnetic effect in the [111] direction must change sign in a certain concentration interval.

In the present report we give the results of measurements of the temperature dependence of the magnetic anisotropy constant K_1 for the $Mn_xFe_{3-x}O_4$ system in the temperature range from 20° to 300° (measurements in the range of lower temperatures were carried out by Penoyer & Shafer[2]), and also of the composition dependence of the galvanomagnetic effect constants at room temperature. The anisotropy constant was measured by the torque procedure on spherical specimens. The single crystals were grown by the Verneuil technique and analyzed for composition by A.A. Popova in the Institute of Crystallography. The same specimens were used for measuring the variation in resistivity (for these measurements the spherical specimens were reduced to thick disks by grinding off the top and bottom of the spheres parallel to definite crystallographic planes). Detailed results of the anisotropy of resistivity measurements will be found in Refs.8 and 9.

Studies showed that for satisfactory description of the anisotropy of the variation in resistivity due to processes of technical magnetization in the $Mn_xFe_{3-x}O_4$ system it is sufficient to use the two constants h_{100} and h_{111} in the even effect law

$$\left(\frac{\Delta R}{R}\right)_s = \frac{3}{2}h_{100}\left(\sum_i \alpha_i^2\beta_i^2 - \frac{1}{3}\right) + 3h_{111}\sum_{i\neq j}\alpha_i\alpha_j\beta_i\beta_j.$$

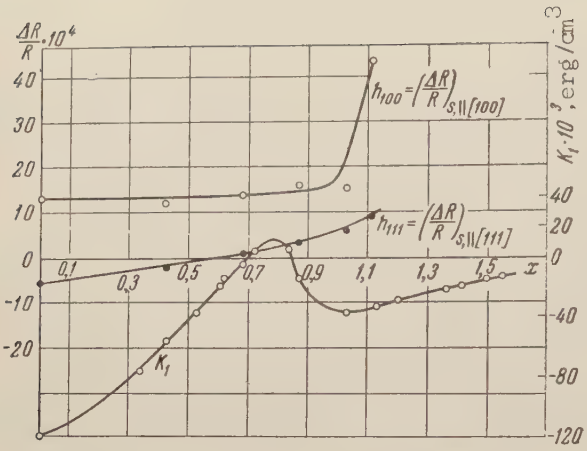

Fig.1

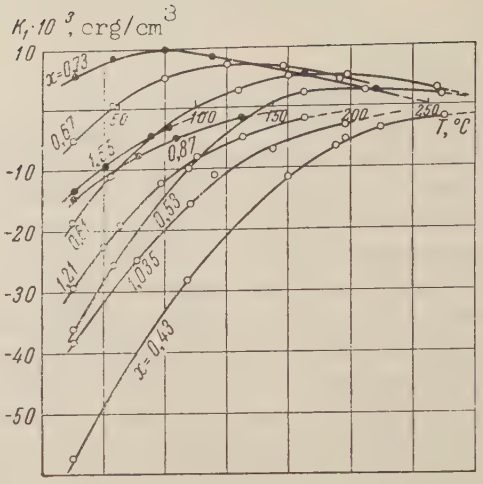

Fig.2

Fig.1. Variation of the galvanomagnetic effect constants h_{100} and h_{111} and the magnetic anisotropy constant K_1 as a function of the composition parameter x in the $Mn_xFe_{3-x}O_4$ system.

Fig.2. Temperature dependence of the magnetic anisotropy constant K_1 of different ferrites in the $Mn_xFe_{3-x}O_4$ system.

Only in the case of magnetite is better agreement with experiment obtained by using the five-constant formula.

Fig.1 shows the variation of the magnetic anisotropy constant and the constants h_{100} and h_{111}, characterizing the longitudinal galvanomagnetic effect in the [100] and [111] directions with variation of the composition parameter x at room temperature. The variation of the anisotropy constant is in general agreement with the results obtained by Penoyer & Shafer[2] and Funatogava et al[3]. The sole difference is that the region of positive values of K_1 is shifted somewhat to the side of higher values of x, which may be due to the fact that owing to local fluctuations the composition in the parts of the single crystal specimens taken for chemical analysis differed slightly from the composition of the specimens used for the measurements. The strong composition dependence of K_1 in the region of the "isotropic points" leads to strong dependence of the constant on inhomogeneities and other defects in the crystal. We observed the interesting fact that in some specimens with a composition close to the "isotropic point" the easy magnetization axes did not agree with any "simple" crystallographic directions. It was found, however, that reduction of the specimen diameter almost always led to elimination of this effect.

It will be evident from Fig.1 that the longitudinal galvanomagnetic effect in the [100] direction remains positive for all compositions, whereas the longitudinal effect in the [111] direction changes sign. The change in sign occurs approximately for compositions that are characterized by the dip in the magnetic anisotropy constant curve. Thus there is yet another anisotropic property that undergoes a marked change in going from manganese ferrite to magnetite. There is evinced a definite correlation between the magnetostriction and the change in resistivity under the influence of magnetization. As was noted above, the magnetostriction constant λ_{111} changes sign (although at other values of x and in the opposite sense compared to h_{111}), while the constant λ_{100} remains negative for all compositions.

The temperature dependences of the magnetic anisotropy constant K_1 for a number of different compositions in the $Mn_xFe_{3-x}O_4$ system are shown in Fig.2. The general regularities of these dependences are the following. In the 0.87 to 1.55 range of x the constant is negative at all temperatures. With increase of temperature the constant gradually decreases. In the x = 0.69 to 0.85 range at room temperature is positive. With increase in temperature the constant first increases somewhat and then falls off approximately linearly. In the x = 0.43 to 0.69 range K_1 is negative at room temperature. With increase of temperature K_1 changes sign (this does not occur for compositions located on the right-hand branch of the K_1 curve with $x > 0.84$ in Fig.1). With decrease of x from 0.69 to 0.43 the "isotropic point" shifts to the side of higher temperatures, and the "positive component" of the anisotropy constant decreases. According to our evaluations (on the basis of the torque curve in the (110) plane), the maximum possible contribution of the constant K_2 at the K_1 = 0 points does not exceed 10^3 erg/cm^3 in absolute value.

Measurements of the temperature dependence of the change in resistivity under magnetization showed that in the $0.6 < x < 0.7$ region the constants h_{100} and h_{111} decrease linearly with temperature and do not undergo any marked changes at the temperatures where K_1 changes sign.

We take this opportunity to express our gratitude to A.A.Popova for preparing and analyzing the ferrite single crystals.

Institute of Crystallography,
Academy of Sciences of the USSR

References

1. J.Smit & H.P.J.Wijn, Ferrites, Eindhoven, 1959.
2. R.F.Penoyer & M.W.Shafer, J.Appl.Phys., suppl., 30, No.4, 315 (1959).
3. Z.Funatogava, N.Miyata & S.Usami, J.Phys.Soc.Japan, 14, No.11, 1583 (1959).
4. R.M.Bozorth, E.F.Tilden & A.J.Williams, Phys.Rev., 99, 1788 (1955).
5. W.A.Yager, J.K.Galt & F.R.Merritt, Phys.Rev., 99, 1203 (1955).
6. L.R.Bickford, Phys.Rev., 78, 449 (1950).
7. A.Braginskii, Czechosl.fiz.zhur. (Czech.Phys.Journal), 9, No.6, 755 (1959).
8. A.V.Zalesskii, Kristallografiya, 6, No.2, 231 (1961). (Trans.Soviet Physics - Crystallography.)
9. A.V.Zalesskii, Ibid., 4, No.6, 867 (1959). (Trans.Ibid.)

TEMPERATURE DEPENDENCE OF THE LOW-FIELD MAGNETIZATION OF MANGANESE FERRITE

- E.F.Kovtun & A.S.Mil'ner

1. Phase transitions are observed in magnetite (Fe_3O_4) at about 110°K and in cobalt ferrite ($CoOFe_2O_3$) at about 90°K. Below these temperatures the arrangement of the doubly and triply ionized metal ions in the spinel type lattice is ordered, while above these temperatures disorder obtains.[1,2] Incident to the phase transition the magnetic symmetry of the ferrites changes. Thus in magnetite above 110°K there are four directions of easy magnetization of the [111] type, while below 110°K there is only one easy direction. When these ferrites are heated in a magnetic field (weaker than the saturation field), the magnetization in going through the phase transition point increases abruptly.[3-6] Cooling of these ferrites in a magnetic field stimulates such transfer of electrons between the divalent and trivalent ions that the only easy magnetization direction appearing incident to transition through the phase transformation temperature is more or less aligned with the applied field. Thus the specimen proves to be "magnetically textured" and the magnetization of such a specimen changes little in going through the phase transformation temperature. If such a specimen is heated in a field oriented perpendicular to the field applied during cooling, the jump in magnetization becomes particularly great.[3-6]

2. In manganese ferrite ($MnOFe_2O_3$) there was observed in weak fields (2-3 Oe) anomalous variation of the magnetization in the 320 to 120°K temperature interval.[7,8] In contrast to the anomaly in magnetite and Co ferrite, in which a sharp decrease in magnetization occurs in a narrow temperature interval (5-12°), in Mn ferrite the decrease in magnetization extends over a range of 200° (from 320 to 120°K). In magnetite and Co ferrite this magnetization anomaly is observed not only in weak fields but in fields up to 1000 Oe and higher. In Mn ferrite this effect is observed only in weak fields ($\leq$10 Oe). Belov & Nikitina[9] made a detailed investigation of the temperature variation of the galvanomagnetic and electric properties of Mn ferrite. The character of the observed anomalies also indicates that in Mn ferrite there also occurs rearrangement of the electron energy spectrum in the low temperature region and that this may in fact be more complicated than occurs, for example, in magnetite.

3. In order to compare the processes occurring in Mn ferrite with the transformations taking place in magnetite and Co ferrite, we measured the variation of I of manganese ferrite single crystals in the temperature range from liquid nitrogen to room temperature in three cases: 1) the ferrite was cooled beforehand in zero field, 2) the ferrite was cooled in a magnetic field, and 3) the ferrite was heated in a field oriented perpendicular to the field applied during cooling. The measurements were carried out by means of a pendulum magnetometer[5,10] in relative units. In the first case during heating the temperature dependence of the magnetization is analogous to that described by Okamura & Simoizaka[7] (curve a in the accompanying figure), i.e., the magnetization increases with increase of the temperature from 80 to 280°K. In the second case the magnetization at 80°K was found to be greater than in the first case and in heating gradually decreased (curve b). In the third case the temperature variation of the magnetization during heating is of the same character as in the second case.

In addition to the magnetometer measurements, we determined the induction of the Mn ferrite by the ballistic procedure in a field produced by Helmholtz coils at room temperature and at liquid nitrogen temperature after cooling in zero field and after cooling in a 5 Oe field. The data obtained by this procedure do not differ significantly from the results of the magnetometer measurements.

4. Thus the first two cases are reminiscent of the temperature variation of the magnetization in magnetite and Co ferrite in analogous cases with the signifi-

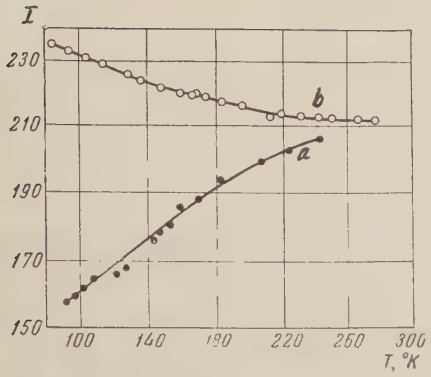

Temperature dependence of the magnetization of Mn ferrite.

cant difference, however, that the temperature range in which the magnetization changes is appreciably greater in the case of Mn ferrite. In the third case, however, when the heating was carried out in a field oriented perpendicular to the direction of the field applied during cooling, the behavior of the Mn ferrite differed significantly from that of magnetite and Co ferrite under like conditions. In magnetite and Co ferrite in this case the magnetization proved to be lower than in the case of cooling in the absence of a field; this may be explained by the fact that the magnetization was effected in the direction perpendicular to the easy direction. In contrast, in the case of Mn ferrite, in heating a magnetic field always increases the magnetization regardless of whether this field is parallel or perpendicular to the field applied during cooling. This observation shows that if there does occur rearrangement of the electron energy spectrum in Mn ferrite in the region of low temperatures[9], this rearrangement must be considerably more complex than in magnetite.

"A.M.Gor'kii" Khar'kov State University

References

1. E.Verwey & M.Heilmann, J.Chem.Phys., 15, 174 (1945).
2. E.Verwey, P.Haymann & F.Romaijn, Ibid., 15, 181 (1947).
3. C.A.Domenicali, Phys.Rev., 78, 459 (1950).
4. N.S.Korolevskaya & A.S.Mil'ner, Fizika metallov i metallovedenie (Physics of Metals and Metallography), 3, 186 (1956).
5. A.S.Mil'ner, E.F.Kovtun & I.N.Popov, Ibid., 7, 832 (1950).
6. E.F.Kovtun & A.S.Mil'ner, (Ferrites, Collection of reports presented at the Conference on Ferrites), Minsk, 1960.
7. T.Okamura & J.Simoizaka, Phys.Rev., 83, 664 (1951).
8. K.P.Belov, Magnitnye prevrashcheniya (Magnetic transformations), p.225, M., 1958.
9. K.P.Belov & S.A.Nikitina, Kristallografiya, 5, 726 (1960). (Trans.Soviet Physics - Crystallography.)
10. C.A.Domenicali, Rev.Sci.Instr., 21, 327 (1950).

BEHAVIOR OF DOMAIN STRUCTURE DURING MAGNETIZATION

- V.A. Ignatchenko, I.F. Degtyarev & Yu.V. Zakharov

Experimental studies have shown that in a thin iron single crystal plate, cut parallel to the (011) planes, there is, as a rule, established the simplest domain structure with antiparallel domains. Few if any closure domains form owing to the high anisotropy energy. In exceptional cases there are observed irregular reverse magnetization spikes at the edges of the crystal.

The present work was devoted to investigation of domain structure of this type. It must be noted that in transformer steel most of the crystallites are of the (011) type with the [001] direction in most of them oriented in the direction of rolling. Hence with good approximation one can regard "polycrystalline" specimens of transformer steel as single crystals of the (011) type and, therefore, apply to them the results of the present investigation.

1. Demagnetizing field energy

In calculating domain structure with free poles, the basic problem consists in taking into account the energy of the demagnetizing fields. The problem for the case of periodic distribution of the poles over an infinite plane xOy was solved by Kittel[1] and in somewhat more general form by Goodenough[2]. Below we recapitulate the latter's deductions with a view to eliminating some of the inaccuracies.

The space in the $-z_0 \leqslant z \leqslant 0$ layer is filled with the ferromagnetic substance, which is broken up into domains with their magnetization vectors parallel to the z axis. In the $z=0$ and $z=-z_0$ planes there form magnetic poles with a surface density $\omega(x, y)$ that is periodic along the x axis with a period $2\pi L_x$ and along the y axis with a period $2\pi L_y$. From symmetry considerations it will be evident that the energy density of the demagnetizing field per unit area of one of the surfaces will be given by

$$\Upsilon_{\text{M}} = -\frac{1}{4\pi^2}\int_0^{2\pi} d\xi \int_0^{2\pi} d\eta \int_{-\frac{z_0}{2}}^{0} H_z(\xi, \eta, z)\,\omega(\xi, \eta)\,dz, \tag{1.1}$$

where $\xi = x/L_x$ and $\eta = y/L_y$. In order to find the demagnetizing field H_z, we must solve the equation

$$\overline{\nabla}^2\varphi = 0. \tag{1.2}$$

We separate the potential into three parts: $\varphi^{(1)}$ - the potential in the space above the ferromagnet layer, $\varphi^{(2)}$ - the potential in the layer, and $\varphi^{(3)}$ - the potential below the layer.

Expanding each potential in a double Fourier series

$$\varphi(x, y, z) = \sum_{-\infty}^{+\infty}\sum_{-\infty}^{+\infty} \varphi_{mn}(z)\, e^{i(m\xi+n\eta)}, \tag{1.3}$$

where

$$\varphi_{mn}(z) = \frac{1}{4\pi^2}\int_0^{2\pi}\int_0^{2\pi} \varphi(\xi, \eta, z)\, e^{-i(m\xi+n\eta)} d\xi\, d\eta,$$

and inserting these into (1.2), we obtain our solution in the form

$$\varphi_{mn}^{(k)} = A_{mn}^{(k)} e^{P_{mn}z} + B_{mn}^{(k)} e^{-P_{mn}z} \qquad (k = 1, 2, 3),$$

where $P_{mn}^2 = (m/L_x)^2 + (n/L_y)^2$. We determined the constants $A_{mn}^{(k)}$ and $B_{mn}^{(k)}$ from two conditions at infinity, two conditions for conjunction and two conditions for discontinuity of the field at the layer boundaries. From the expressions for $\varphi^{(2)}$ we obtain

$$H_{zmn} = -\frac{\partial \varphi_{mn}}{\partial z} = -2\pi\omega_{mu}\,(e^{-P_{mu}(z+z_0)} + e^{P_{mu}z}). \tag{1.4}$$

H_{zmn} is the coefficient of the expansion of the magnetic field H_z in the double Fourier series

$$H_z(x, y, z) = \sum_{-\infty}^{+\infty}\sum_{-\infty}^{+\infty} H_{zmn} e^{i(m\xi+n\eta)}. \tag{1.5}$$

Inserting (1.5) in (1.2), noting that $\omega_{mn}^* = \omega_{-m-n}$ and integrating over z, we obtain

$$\gamma_m = 2\pi\omega_{00}^2 z_0 + 2\pi \sum_{-\infty}^{+\infty}{}' \sum_{-\infty}^{+\infty}{}' \omega_{mn}\omega_{-m-n} P_{mn}^{-1}\,(1 - e^{-P_{mn}z_0}), \tag{1.6}$$

where the primes indicate that the term with $m = n = 0$ is excluded from the summation.

For the case when the surface density of the poles is periodic only along the x axis and does not depend on y ("infinitely thick" crystal) we readily obtain

$$\gamma_m = 2\pi\omega_0^2 z_0 + 2\pi L_x \sum_{-\infty}^{+\infty}{}' \frac{\omega_m\omega_{-m}}{|m|}\,(1 - e^{-P_{mn}z_0}), \tag{1.7}$$

where

$$\omega_m = \frac{1}{2\pi}\int_0^{2\pi} \omega(\xi)\, e^{-im\xi} d\xi.$$

Of greatest practical interest is the case when the surface magnetic pole density is periodic along x and vanishes everywhere along y except for the interval $(-y_0/2, y_0/2)$. In this case the problem, which is analogous to that considered above, is solved by expansion of φ, H_z and ω in a Fourier series in x and a Fourier integral in y:

$$\omega(x, y) = \sum_{-\infty}^{+\infty} \int_{-\infty}^{+\infty} \bar{\omega}_m(v)\, e^{i(m\xi+vy)}\, dv,$$

$$\bar{\omega}_m(v) = \frac{1}{4\pi^2}\int_{-\infty}^{+\infty} dy \int_0^{2\pi} \omega(\xi, y)\, e^{-i(m\xi+vy)}\, d\xi$$

and so on. Finally, we obtain the formula

$$\gamma_m = \frac{4\pi^2}{y_0}\int_{-\infty}^{+\infty} \frac{\bar{\omega}_0(v)\,\bar{\omega}_0(-v)}{|v|}(1 - e^{-|v|z_0})\, dv + \frac{4\pi^2}{y_0}\sum_{-\infty}^{+\infty}{}' \int_{-\infty}^{+\infty} \frac{\bar{\omega}_m(v)\,\bar{\omega}_{-m}(-v)}{Q_m(v)}\,(1 - e^{-Q_m z_0}) dv, \tag{1.8}$$

where $Q_m^2(v) = v^2 + (m/L_x)^2$. The exponential in the last term can be dropped for $\frac{z_0}{L_x} \gg 1$. Lastly, for the case of a crystal with finite dimensions x_0, y_0, z_0, expanding $\omega(x, y)$ in a double Fourier integral, we obtain

$$\gamma_m = \frac{8\pi^2}{x_0 y_0}\int_{-\infty}^{+\infty}\int_{-\infty}^{+\infty} \frac{\bar{\omega}(u, v)\,\bar{\omega}(-n, -v)}{R(u, v)}\,(1 - e^{-R(u, v)z_0}) du dv, \tag{1.9}$$

where $R^2 = u^2 + v^2$ and $\bar{\omega}(u, v) = \frac{1}{4\pi^2} \int_{-\infty}^{+\infty} \int_{-\infty}^{+\infty} \omega(x, y)\, e^{-i(ux+vy)}\, dxdy.$

2. Domain structure and its behavior in a magnetic field - calculation

Consider a domain structure of the type shown in Fig.1. Such a structure is established in an iron crystal if the xOz plane of the crystal is parallel to the (011) planes, the [001] axis is aligned with the z axis and y_0 is small compared with x_0 and z_0.

Initially, however, we will neglect the last condition and make use of Eq. (1.7), which is valid only for very large y_0. This greatly simplifies the calculations and enables us to obtain some of the features of the behavior of the domain structure in explicit form; one should not, of course, expect to obtain quantitative agreement with experiment. Applying Eq.(1.7) to this structure and utilizing the approximation $z_0/L_x \gg 1$, we obtain

$$\gamma_m = 2\pi\omega^2(1-q)^2 z_0 + \frac{8\omega^2}{\pi^2} Df(q), \tag{2.1}$$

where

$$f(q) = \sum_{m=1}^{\infty} \frac{1 - \cos m\pi q}{m^3},$$

$$2D = d_1 + d_2, \quad q = d_2/D.$$

Functions of the form of $f(q)$ and their derivatives have been tabulated by Kitover[3].

For determining the free energy (per unit volume of the crystal), which consists of the energy of the demagnetizing field, the domain wall energy and the energy of the external magnetic field H (directed along the z axis), we have the expression

$$F(D,q) = 2\pi\omega^2(1-q)^2 + \frac{8\omega^2}{\pi^2 z_0} Df(q) + \frac{\gamma}{D} - \omega H(1-q), \tag{2.2}$$

where γ is the surface density of the wall energy. For an "ideal" domain devoid of reverse magnetization spikes (or other irregularities) both at the edges and at any inclusions, $\omega = I_s$. If this condition is not fulfilled, then by ω one should understand a certain mean or effective magnetization of one domain.[4]

From the conditions for minimum energy

$$\partial F(D, q)/\partial D = 0, \quad \partial F(D,q)/\partial q = 0$$

we obtain the following relations describing the equilibrium domain configuration for any value of the external field H:

$$D = \frac{\pi}{\omega}\left[\frac{z_0\gamma}{8f(q)}\right]^{1/2}, \tag{2.3}$$

$$-4\pi\omega(1-q) + f'(q)\left[\frac{8\gamma}{\pi^2 z_0 f(q)}\right]^{1/2} + H = 0. \tag{2.4}$$

For $\omega \approx 10^3$, $z_0 \approx 1$, and $\gamma = 1.8$, the initial value of D, i.e., D_0 - the width of the domains in the demagnetized state, will be $\sim 10^{-3}$; in this case the second term in (2.4) can be neglected and the magnetization curve will be a straight line, and the susceptibility χ_0 will equal $1/4\pi$ (the experimental values of D_0 and χ_0 for a specimen in the form of a disk with $z_0 = 1.5$, and $y_0 = 3 \cdot 10^{-2}$ are $\sim 4 \cdot 10^{-2}$ and 6, respectively).

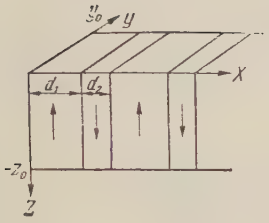

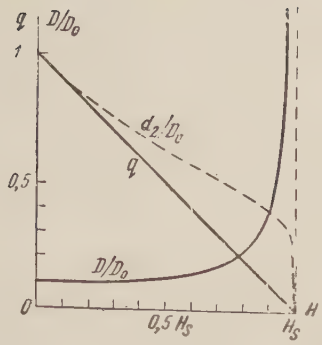

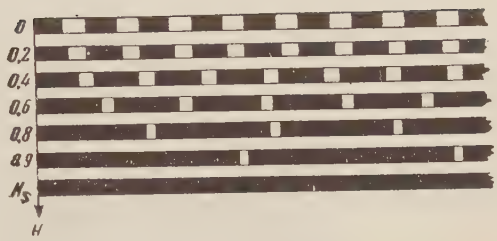

Fig.1 Fig.2 Fig.3

Fig.1. Analyzed domain structure.

Fig.2. Theoretical field dependences of the domain structure parameters D/D_0, q and d_2/D_0 (H_S is the saturation field).

Fig.3. Schematic representation of change in the domain structure with increase of the field.

The field dependences of D and q given by Eqs.(2.3) and (2.4) are shown in Fig.2. It is interesting to note that the domain width D increases with increase of the field. This means that magnetization must be realized not only by decrease in the width of the disadvantageously magnetized domains but also by "spreading out" of the other domains; these results are shown schematically in Fig.3.

Now let us attempt to take into account finiteness of the crystal along the y axis. Application of Eq.(1.8) to the structure shown in Fig.1 leads to the expression

$$\Upsilon_m = \frac{4\omega^2}{y_0}(1-q)^2 \int_{-\infty}^{+\infty} \frac{\sin^2 \frac{uy_0}{2}(1-e^{-|u|z_0})}{u^3}\,du + \frac{8\omega^2}{\pi^2 y_0} \sum_{-\infty}^{+\infty}{}' \frac{1-\cos m\pi q}{m^2} \int_{-\infty}^{+\infty} \frac{\sin^2 \frac{uy_0}{2}\,du}{u^2\sqrt{u^2+(\pi m/D)^2}}, \qquad (2.5)$$

where, unfortunately, strict integration in the second term is impossible.

The first term in (2.5) differs from the first term in (2.1) by the coefficient

$$K = \frac{4}{\pi y_0 z_0} \int_0^{\infty} \frac{\sin^2 \frac{uy_0}{2}(1-e^{-|u|z_0})}{u^3}\,du = \frac{2}{\pi}\left[\operatorname{arctg}\frac{y_0}{z_0} + \frac{y_0}{4z_0}\ln\left(\frac{z_0^2}{y_0^2}+1\right) - \frac{z_0}{4y_0}\ln\left(\frac{y_0^2}{z_0^2}+1\right)\right]. \qquad (2.6)$$

The integral under the summation sign

$$\int_{-\infty}^{+\infty} \frac{\sin^2 \frac{uy_0}{2}\,du}{u^2\sqrt{u^2+a^2}} = 2\int_0^{\infty} \frac{\sin^2 \frac{uy_0}{2}\,du}{u^2\sqrt{u^2+a^2}} = 2G$$

may be calculated as follows. The main part of the integrand is concentrated in the section $0 \leqslant u \leqslant 2\pi/y_0$, where $2\pi/y_0$ is the first zero of the function under the integral. The integration interval may be divided into three parts: in the section $[0, 2\pi/45y_0]$ the integral is obtainable if one expands $\sin^2\frac{uy_0}{2}$ into a series and retains only the first term; in the section $[2\pi/45y_0,\ 2\pi/y_0]$ the integral may be calculated by means of Simpson's formula (for $n = 4$); in the section $[2\pi/y_0, \infty]$ the mean value of $\sin^2\frac{uy_0}{2}$ is taken out from under the integral and the remaining ex-

pression is integrated. Then we obtain

$$G = \frac{y_0^2}{4} \operatorname{Ar\,sh} \frac{2D}{45 y_0 m} + \frac{11 \cdot 15 \cdot 45}{2\pi^2} y_0 D \left[\frac{4{,}872 \cdot 10^{-3}}{\sqrt{4 (D/y_0)^2 + 45^2 m^2}} + \right.$$
$$\left. + \frac{0{,}5522}{36 \sqrt{576 (D/y_0)^2 + 45^2 m^2}} + \frac{2 \cdot 0{,}9988}{23^2 \sqrt{46^2 (D/y_0)^2 + 45^2 m^2}} + \frac{0{,}4651}{17^2 \sqrt{68^2 (D/y_0)^2 + 45^2 m^2}} \right] +$$
$$+ \frac{D y_0}{4\pi^2 m^2} \sqrt{4 (D/y_0)^2 + m^2} - \frac{D^2}{2\pi^2 m^2} . \qquad (2.7)$$

Consequently, taking into account finite thickness of the crystal, Eq.(2.2) becomes

$$F(D, q) = K\left(\frac{y_0}{z_0}\right) 2\pi\omega^2 (1-q)^2 + \frac{8\omega^2}{\pi^2 z_0} D \Psi (D/y_0, q) + \frac{\gamma}{D} - \omega H (1-q), \qquad (2.8)$$

where

$$\Psi (D/y_0, q) = \frac{4}{D} \sum_{m=1}^{\infty} \frac{1 - \cos m\pi q}{m^2} G.$$

From the condition of minimum energy there were obtained complicated equations which were investigated graphically. It was established that for $y_0 \approx 10^{-2}$ the value of D differs little from the value of D for an infinitely thick crystal (Eq.(2.3)). For the susceptibility there was obtained the approximate expression

$$\chi_0 \approx \left[4\pi K\left(\frac{y_0}{z_0}\right)\right]^{-1}, \qquad (2.9)$$

which yields a value close to the experimental one (χ_0 = 2.5 for y_0/z_0 = 0.02). The character of the change in domain structure with increase of the field in this case as well is illustrated in Figs.2 and 3.

An attempt to allow for finiteness of the crystal dimensions along all three coordinate axes, i.e., an attempt to use Eq.(1.9), leads to expressions that are too complicated to manipulate without the aid of a computer.

3. Domain structure and its behavior in a magnetic field - experiment

The domain structure on silicon iron single crystals was observed by means of the meridional Kerr effect. The specimens were in the form of disks 15 mm in diameter and 0.3 mm thick with the surface parallel to the (011) planes. In the demagnetized state there were observed approximately 40 domains on the surface of the specimen; the magnetization vectors in the domains were directed along the easy axis lying in the plane of the specimen. The behavior of the domain structure on one of the specimens with increase of the magnetic field at the rate of 0.05 Oe/sec is shown in the photographs reproduced in Fig.4. The patterns were photographed by a motion picture camera at the rate of 30 frames per minute. It will be seen that in fields up to 136 Oe the dark bands (domains) increase in width, while in fields from 136 to 160 Oe individual light bands vanish abruptly. As a rule, prior to its disappearance the width of a light-band domain remains constant in a field interval of 10 to 12 Oe, even though its residual width amounts to only about 0.1 the initial width. Thus in Fig.4,c there appear four light domains, while in Fig.4,d only three are visible. The width of this domain did not change in the field range from 126.5 to 136.8 Oe, and then with further increase of the field to 136.83 Oe it vanished. Similar disappearances of light domains may be noted by comparing Figs.f & g and h & i. In some cases, however, we observed not abrupt but gradual disappearance of domains. The domain structure was completely effaced from the surface of the specimen at a field of ~160 Oe.

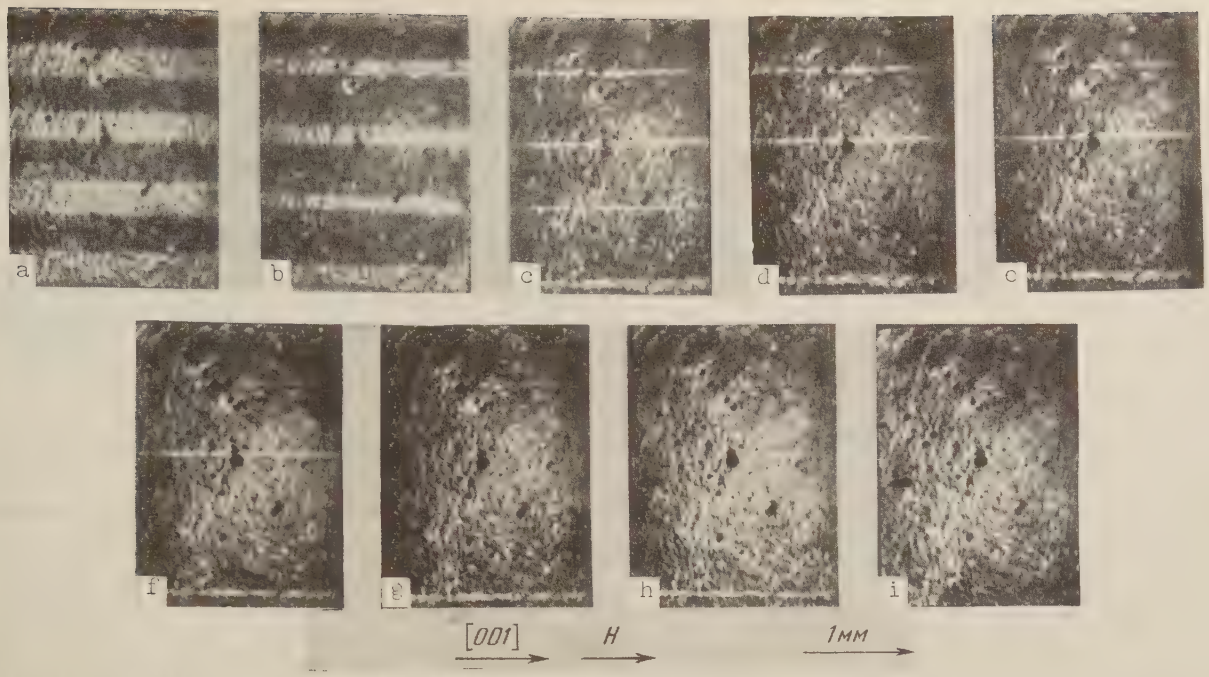

Fig.4. Domain structure at different values of the applied field H: a - H = 0, b - 60 Oe, c - 136.8 Oe, d - 136.83 Oe, e - 139.2 Oe, f - 149.4 Oe, g - 149.43 Oe, h - 157.8 Oe, i - 157.83 Oe.

Naturally, only qualitative comparison of the experimental data with the results of our calculations are feasible, inasmuch as the observed specimen had a shape differing from that assumed for the calculations. Moreover, in experiments there is inevitably observed a process in which there are deviations from the ideal macroscopic equilibrium state. However, the large number of domains observed in the initial state and fulfillment of the condition $z_0/L_x \gg 1$ up through fields close to H_s give reason to assert that in our experiments we observed the predicted effect of increase of the average width D with increase of H. Obviously, the mechanism of the process cannot be inferred from the above mentioned macroscopic thermodynamic relationships for an ideal crystal.

Institute of Physics,
Siberian Division of the
Academy of Sciences of the USSR

References

1. C.Kittel, Revs.Mod.Phys., 21, 541 (1949).
2. J.Goodenough, Phys.Rev., 102, 356 (1956).
3. K.A.Kitover, Priklad.matem.i mekhan., (Applied Mat. & Mechanics), 12, 233 (1948).
4. L.V.Kirenskii, V.A.Ignatchenko & A.M.Rodichev, Zhur.eksp.i teor.fiz., 39, 1263 (1960). (Trans.Soviet Physics - JETP.)

Note added in proof: In a recent study (Philips.Res.Repts., 15, 7, 1960) there was investigated the process of magnetization along the easy axis perpendicular to the surface of a thin $BeFe_{12}O_{19}$ film; there was theoretically deduced and experimentally observed the effect of "spreading out" of the domains similar to that shown in Figs.2 and 3.

VARIATION OF THE MAGNETIZATION SWITCHING PROCESS WITH REDUCTION IN PARTICLE SIZE

- E.V.Shtol'ts, A.A.Glazer & Ya.S.Shur

Investigation of magnetic powders has shown that decrease of particle size is accompanied by regular change in the value of the coercive force H_c.[1] As will be evident from Fig.1, where the variation of H_c with particle size d is shown schematically, except for the region of very small particles (section DE)*, H_c increases with decrease of particle size. It is natural to assume that the observed growth of H_c is due to hindrance of the magnetization reversal process with approach to the single domain state. At present little is known regarding the character of the processes of magnetization reversal in minute particles and, consequently, the reasons for the growth of H_c are obscure. The purpose of the present work, accordingly, was investigation of the processes of magnetization reversal in small particles of MnBi alloy.

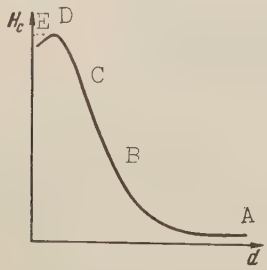

Fig.1. General character of variation of coercive force with particle size.

Specimen No.	Particle size, μ	Relative residual magnetization I_r/I_s	Coercive force H_c, Oe
1	100 x 20	0.21	200
2	70 x 20	0.54	600
3	16 x 3	0.73	2 900
4	4 x 4	0.96	12 500

MnBi was chosen for the investigation owing to its large anisotropy constant; because of the large value of the anisotropy constant the critical size for transition to single domain structure is large. Hence it was feasible in the case of MnBi alloy to observe visually the process of magnetization reversal even in single domain particles.[3] The domain structure was observed both by the colloidal suspension (powder particle) technique and with the aid of the magneto-optical Kerr effect. Inasmuch as MnBi is a magnetically uniaxial material it was feasible to prepare pseudosingle domain specimens by growing single crystal particles and by sintering the alloy in a magnetic field. The studies were carried out on specimens with a small concentration of ferromagnetic particles so that the effect of interaction between particles was largely eliminated. The values of the coercive force and relative residual magnetization along the texture axis of the pseudosingle crystal specimen with different particle dimensions are given in the accompanying table.

As will be evident from the table, with decrease of the particle size from 100 x 20 to 4 x 4 μ the relative residual magnetization increases from 0.21 to 0.96, and the coercive force from 200 to 12 500 Oe.

We now turn to the results of visual observation of the domain structure in particles of different size in the process of switching. In Fig.2 we reproduce photographs of powder patterns obtained on individual MnBi alloy particles of different size in the remanence state after magnetization in a field of 20 000 Oe along the easy axis.

---

*In such superfine powders decrease of H_c may be due to the effect of supermagnetism and approach to the dimensions at which ferromagnetism disappears.[2]

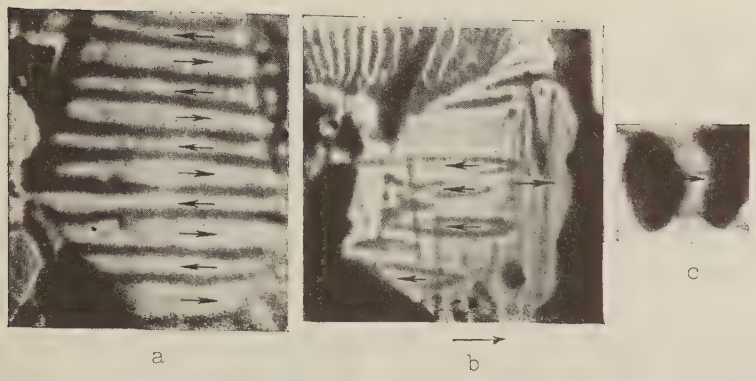

Fig.2. Domain structure of particles of different size in the remanence state. The arrow indicates the direction of the magnetizing field.

The domain structure of large MnBi particles has the same appearance as that of uniaxial bulk material. In the remanence state (Fig.2,a) such particles are subdivided into domains with antiparallel orientation of the magnetization, and the volume of the domains in which the magnetization vector I_s agrees with the direction of the field applied during magnetization is somewhat greater than the volume of the domains with opposite orientation of I_s. In consequence, the value of the relative residual magnetization is small (I_r/I_s = 0.20-0.30). The process of reversal in large particles occurs by wall motion.[3,4] The coercive force in this case amounts to 200-300 Oe (see data for specimen No.1 in table), which is, apparently, due to the appreciable inhomogeneity of the crystal structure of the particles.

In going to particles of smaller size the multiple domain structure persists, but in the remanence state (Fig.2,b) each particle consists of only one domain, the direction of magnetization in which agrees with the direction of the magnetic field applied during magnetization, and a number of closure domains with antiparallel orientation of I_s. As compared with larger particles, the value of the relative residual magnetization increases appreciably (I_r/I_s = 0.71-0.73). Switching of such particles is realized by growth of reverse-magnetization nuclei and wall motion; however, in view of hindrance of this process the coercive force rises to 2000 to 3000 Oe (table - specimen No.3). The reason for hindrance of the processes of growth of reverse-magnetization nuclei and wall motion is apparently increase of the wall energy density. Theoretical calculations[5] have shown that increase of the wall energy density with decrease of particle size may be due to increase of the magnetostatic wall energy.

Thus, it may be tentatively assumed that hindrance of the processes of growth of reverse-magnetization nuclei and wall displacement is the reason for the increase of H_c over the section AB of the curve in Fig.1.

With further decrease of the particle size, the particles in the remanence state remain single domain ones and the direction of the magnetization vector coincides with the direction of the magnetizing field (Fig.2,c). The value of the relative residual magnetization in this case is close to unity (table - specimen No.4).

Depending on their size, such particles may have either "transition type"[6] or single domain structure. If the domain structure is of the transition type, then under the influence of a certain magnetic field the particle may be transformed to the multiple domain state, which is the stable state for the given particle dimension. A single domain particle under the influence of any magnetic field retains its single domain structure, corresponding to minimum energy.

The photographs reproduced in Fig.3 (obtained by means of the magneto-optical Kerr effect) show the changes in domain structure of particles with the transition structure under the influence of different magnetic fields. In the demagnetized state the particle has a multidomain structure (Fig.3,a). If the demagnetized particle is then magnetized in a field H = 15 000 Oe, then after switching off the

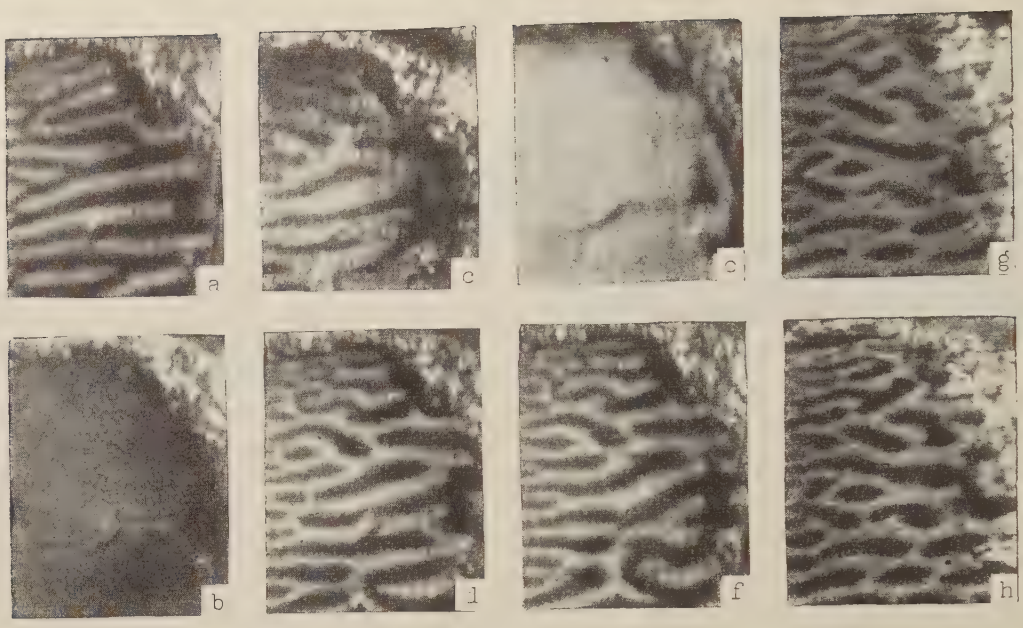

Fig.3. Variation of the domain structure of particles with the transition type structure in a magnetic field: a - demagnetized state; b - H = 0 after magnetization along the [1000] axis in a field H_{max} = 15 000 Oe. After H_{max} = 15 000 Oe: c - H = -2700 Oe, d - along the return curve H = 0. After H_{max} = 21 700 Oe: e - H = -4500 Oe, f - along the return curve H = 0. After H_{max} = 21 700 Oe: g - H = = 5300 Oe with field applied in the direction perpendicular to the [1000] axis; h - H = 0 after magnetization in the direction perpendicular to the [1000] axis.

field in the remanence state the particle retains the single domain structure (Fig.3,b). This single domain structure persists in negative fields to -2700 Oe (the entire particle in the Kerr-effect photograph remains dark). With further increase of the negative field the particle abruptly breaks up into domains (Fig. 3,c). If the intensity of the negative field is now reduced, there is observed increase of the domains with the initial direction of I_s (dark domains). The appearance of the domain structure obtained after reduction of the field to zero is shown in Fig.3,d. If the particle was first magnetized by a field of 21 700 Oe, then in a reverse magnetic field of -4500 Oe it is wholly reversed (from dark becomes light: Figs.3,b and 3,e). However, upon reduction in the intensity of the negative field the particle breaks up into domains (Fig.3,f). If the same particle, initially in the single domain state (Fig.3,b) is magnetized in a difficult direction, then in the process of magnetization the particle becomes a multiple domain one (Fig.3,g) and upon switching off of the field the appearance of the domain structure remains virtually unchanged (Fig.3,h).

This behavior of the domain structure can be understood if it is assumed that at large values of the magnetizing field there are destroyed all reverse-magnetization nuclei and that the formation of these nuclei upon reduction of the magnetic field is greatly hampered owing to appreciable increase of the wall energy density (for the reasons outlined above). As a result, reverse-magnetization nuclei appear only in strong negative fields. It must be emphasized that MnBi alloy has a very large anisotropy constant so that switching by irreversible rotation of the magnetization vector in the entire volume of the particle requires a very strong field

Let us consider the process of reverse-domain nucleation. In an actual crys-

tal there are always present inhomogeneities of the crystal structure, which give rise to the appearance of local internal magnetic fields that may significantly reduce the magnetic anisotropy in the given section of the crystal. Upon application of a negative magnetic field there begins first rotation of the spins in the sections with reduced magnetic anisotropy. In cases when the spins are arrayed completely parallel and in places with inhomogeneous crystal structure there persist residues of reverse zones, the process of formation of reverse magnetization nuclei occurs in weaker fields than in the case when the spins are initially fully parallel. Depending on the strength of the field in which reverse-magnetization nuclei begins to appear, the particle in the process of reversal may break up into domains (Fig.3,c) or switch fully (Fig.3,e). The last occurs when the appearance of reverse-magnetization nuclei takes place in fields close to the saturation field (for MnBi particles at room temperature this field is of the order of 5000 Oe). However, inasmuch as fields of this magnitude are inadequate for complete destruction of a reverse-magnetization nuclei, upon decrease of the negative field there is observed growth of the nuclei and their transformation into regular domains with reverse magnetization (Fig.3,f). Inasmuch as creation of reverse-magnetization nuclei is hindered, after attainment of certain dimensions further growth of the nuclei does not require increase of the field, which leads to abrupt rearrangement of the domain structure, i.e., reversal.

A field oriented perpendicular to the magnetization vector in a particle with transition structure that is in the single domain state of residual magnetization also produces rotation of the spins, which favors appearance of revers-magnetization nuclei and thus transition of the particle to the multiple domain state.

The increase in coercive force due to hindrance of formation of reverse-magnetization nuclei is shematically represented by section BC of the curve in Fig.1.

In particles of very small size with a stable single domain structure, reverse-magnetization nuclei do not appear under the influence of any magnetic field and the particle switches by the process of flip of the magnetization vector[3] in the entire volume of the particle. Theoretical calculations[7] have shown that in single domain particles rotation of the magnetization vectors may occur incoherently, which is evinced in the value of the coercive force of the particles. It must be noted that inhomogeneity of the crystal structure of single domain particles may be an additional cause of nonuniform rotation of the magnetization vector in the process of magnetization reversal.

The increase in coercive force in particles with single domain structure is represented by the section CD of the curve in Fig.1.

References

1. F.Bertaut, Compt.rendu, 229, 417 (1949); C.Guillaud, J.phys.et radium, 12, 492 (1951); Ya.S.Shur, T.D.Zotov & I.A.Chebotarev, Doklady AN SSSR, 81, 387 (1951); E.V.Shtol'ts & Ya.S.Shur, Ibid., 95, 781 (1954).

2. S.V.Vonsovskii, Sovremennoi uchenie o magnetizme (Modern magnetic theory), M., 1953.

3. Ya.S.Shur, E.V.Shtol'ts & V.I.Margolina, Zhur.eksp.i teor.fiz., 38, 46 (1960). (Trans.Soviet Physics - JETP.)

4. E.V.Shotl'ts & Ya.S.Shur, Fiz.metallov i metallovedenie (in press) (Trans. Physics of Metals & Metallography.)

5. L.Néel, J.phys.et radium,17, 250 (1956); H.Amar, J.Appl.Phys.,29,542 (1958).

6. Ya.S.Shur, E.V.Shotl'ts, G.S.Kandaurova & L.V.Bulatova, Fiz.metallov i metallovedenie, 5, 234 (1957) (Trans.Physics of Metals & Metallography); E.V. Shtol'ts, Ya.S.Shur & G.S.Kandaurova, Ibid., 5, 412 (1957). (Trans.Ibid.)

7. E.I.Kondorskii, Doklady AN SSSR, 82, 365 (1952).

INVESTIGATION OF DOMAIN WALLS IN TRANSFORMER STEEL

- M.K.Savchenko & V.I.Sinegubov

Neighboring ferromagnetic regions (domains), magnetized in different directions, are separated by a boundary layer, commonly called a domain wall. The first investigation of such boundary layers was carried out by Bloch[1]. The theory of domain walls was further developed by Landau & Lifshits[2] and for specimens in the form of very thin layers by Néel[3].

Domain walls have also been investigated experimentally[4-6]; however, the experimental procedures employed did not allow of direct measurement of the wall thickness. In our earlier work[7] we developed an improved procedure for investigating domain walls by means of the polar Kerr effect. The developed set-up made it possible to carry out measurements of wall thickness. In the present work the procedure has been applied to investigation of the polarity of domain walls and to the geometry of walls in silicon-iron crystals under the influence of a magnetic field and elastic stresses.

Experiment

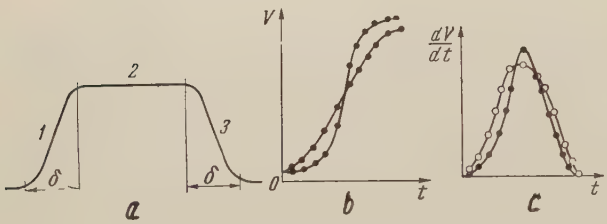

Fig.1. a - curve recorded by recording voltmeter incident to passage of a domain wall under the microscope slit; b - one of the sections of curve a (integral curve); c - differential curves corresponding to curves b (the wall thickness is determined by the abscissae at the base of the curve). t is the time of passage of the wall under the microscope slit.

The experimental set-up has been described in Ref.7. The polarizer and analyzer were slightly uncrossed so as to give incomplete extinction. The specimen is mounted on a mechanical stage and moved past the slit of the microscope. When a wall passes under the microscope slit the analyzer field lightens or darkens, depending on the polarity of the wall. Accordingly, the photomultiplier viewing the analyzer yields a varying signal, which, after appropriate amplification and detection, is recorded by a recording voltmeter. The appearance of the curve recorded on the voltmeter chart is shown in Fig.1,a. The rising section (1) corresponds to the instant of passage of the front edge of the wall under the slit; section 2 corresponds to passage of the wall under the slit, and section 3 corresponds to exit of the wall from under the slit. The height of the rise is proportional to the normal component of I_s. Thus knowing the rate of displacement of the specimen (i.e., of the wall) and the rate of advance of the recorded chart, one can readily determine the wall thickness from the width of sections 1 and 3.

Inasmuch as sections 1 and 3 of the curve are symmetrical, for determining the wall thickness one can use not the entire curve but only one of the rising sections. Two such sections are shown separately in Fig.1,b (integral curves). If one plots the curves for the derivatives of the functions describing the curve shown in Fig.1,b, one obtains differential curves of the type shown in Fig.1,c from which one can deduce the distribution of I_s across the wall.

In the present work we investigated the 180° walls in large iron crystals, containing 3% Si. The specimens were in the form of 0.4 x 6 x 30 mm strips, the surface of which was parallel to the (110) planes. Prior to measurements the

strips were carefully ground, electrolytically polished and annealed under high vacuum. The rate of displacement of the specimen under the microscope was 1 μ per 20 sec.

Initial state of the annealed specimens

We carried out measurements of the wall thickness in four specimens cut from different crystals. In each specimen we measured the thickness of 6 neighboring walls. These measurements show that the wall thickness varies both in different crystals and for the walls in the same crystal; the wall thickness fluctuates in the range from 0.46 to 0.60 μ. In fact we observed that the thickness of one and the same wall varied in approximately the same range.

Change in domain walls incident to magnetization

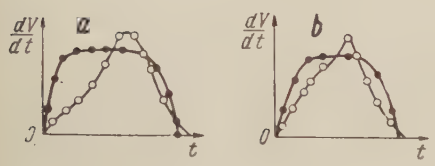

Fig.2. Variation in the distribution of magnetization in a wall incident to longitudinal magnetization (a) and magnetization normal to the surface of the specimen (b).

Fig.2 shows the variation in the distribution of the magnetization over a wall incident to magnetization of the specimens by longitudinal and normal magnetic fields. In the case of longitudinal magnetization the field was applied along the length of the specimen, which coincided with an easy magnetization axis. The measurements were carried out in zero fields and in fields close to the value corresponding to completion of the process of wall movement. In the case of normal magnetization a field of the order of 100 Oe was applied in the two opposite directions. The results of measurements of the domain wall thickness for specimen No.2 are summarized in Table 1.

Table 1

Domain wall thickness in specimen No.2 in zero field and in longitudinal and normal fields

Field direction	Wall thickness, μ					
	1	2	3	4	5	6
$H = 0$	0,55	0,50	0,51	0,52	0,46	0,53
Parallel to surface	0,52	0,48	0,40	0,49	0,46	0,50
Normal to surface	0,46	0,45	0,50	0,42	0,46	0,50
(in 2 opposite directions)	0,52	0,48	0,46	0,50	0,48	0,46

As will be evident from Table 1 and Fig.2, the wall thickness decreases slightly as a result of application of longitudinal or normal fields. There is no substantial difference between the cases of longitudinal and normal magnetization. Apparently, in the case of a normal field the principal changes in magnetization occur along the surface of the specimen. The greatest changes in the walls are connected with redistribution of the value of I_s across them. The sharp upper sections of the walls are smoothed out by magnetization, which can be explained by rotation (in the direction of the field) of the spins oriented closest to the normal to the surface of the specimen. The wall contours become more distinct as a result of magnetization.

Polarity of the walls

Analysis of the records obtained in measuring the wall thickness showed that the polarity of different walls differs, but in no consistent manner. On the average, however, the number of walls with positive and negative polarity is the same. It was noted that one and the same wall may change its polarity. Usually the change in polarity is observed at the points where the wall intersects some defect or inhomogeneity in the crystal.

Application of a magnetic field may reverse the wall polarity; this reversal usually occurs at the very beginning of the process of wall displacements. To what extent the process is ordered we have not yet been able to determine, but in many cases we noted that the domains which shrink in the process of wall movement have walls of the same polarity.

Influence of elastic stresses

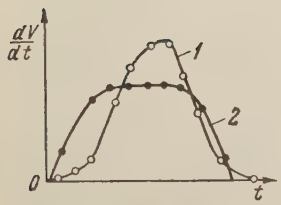

Fig.3. Effect of stresses on the structure of domain walls: 1 - no load, 2 - specimen elongated by a load of 26 kg/mm^2.

For the purpose of observing the influence of stresses on the domain walls the specimens were subjected to elongation along the easy axis. The results of our measurements are summarized in Table 2 and the curves obtained for one of the walls are shown in Fig.3. As compared with magnetic fields, the effect of stresses on the walls is more noticeable as regards both the change in thickness and redistribution of the magnetization. Smoothing out of the curves characterizing the distribution of I_s in the center of the wall indicates that the spins oriented most disadvantageously as regards the stress undergo rotation. The results of observation are in qualitative agreement with the theoretical deductions of Landau & Lifshits[2].

Conclusions

1. In transformer steel in the initial state the wall width on a (110) surface varies in the range from 0.4 to 0.6 microns.

2. The polarity of the walls differs, but there is no consistent pattern or sequence in the variation. The wall polarity may reverse under the influence of a magnetic field.

3. Domain walls change shape under the influence of an applied magnetic field and stresses. The extent of these changes is not great, which can be explained by

Table 2

Effect of stresses on domain wall thickness

Specimen No.	Stress, kg/mm^2	Wall thickness, μ					
		1	2	3	4	5	6
5	0	0,57	0,54	0,55	0,50	0,47	0,50
	26	0,50	0,47	0,48	0,45	0,44	0,46
6	0	0,60	0,60	0,49	0,52	0,45	0,47
	26	0,55	0,56	0,45	0,48	0,42	0,45

the small values of the energy of the magnetic field and stresses as compared with the appreciable values of the exchange energy and anisotropy that are involved in the formation of the domain walls. It may be assumed that in materials with low anisotropy the domain walls should be less "rigid".

Institute of Physics,
Siberian Division of the
Academy of Sciences of the USSR

References

1. F.Bloch, Z.Phys., 74, 295 (1932).
2. L.D.Landau & E.M.Lifshits, Sov.Phys., 8, 153 (1935).
3. L.Néel, Compt.rendu, 241, 533 (1955).
4. D.J.Craik, Proc.Phys.Soc., B 69, 6, No.438 (1956).
5. L.V.Kirenskii & V.V.Veter, Doklady AN SSSR, 125, 526 (1959). (Trans. Soviet Physics - Doklady.)
6. H.W.Fuller & M.E.Haale, J.Appl.Phys., 31, 238 (1960).
7. V.I.Sinegubov & M.K.Savchenko, Izv.AN SSSR, Ser.fiz., 25, 599 (1961). (Trans.Bulletin 25, 609.)

INFLUENCE OF THE DIRECTION OF DEMAGNETIZATION ON THE MAGNETIC STRUCTURE OF CRYSTALS IN SHEET SILICON STEEL

- V.R.Abel's

Introduction

The character of the anisotropy of the coercive force and initial permeability in ferromagnetic materials is determined by the concentrations of the magnetic phases.[1] Hence it is important to know how these concentrations depend on the method of producing the magnetic state in which the magnetization is zero, in particular on the direction of the magnetic field acting on the specimen during demagnetization or magnetization. Clarification of this matter was the primary purpose of the present study.

In addition, we tried to determine whether the decrease of permeability with time may be due to resorption of the magnetic structure, occurring as a result of the magnetization of the specimen.[2] This explanation for the decrease of permeability with time has been suggested by Al'tgauzen et al[3].

Specimens and measurement procedure

We investigated both hot-rolled and cold-rolled silicon steel (3-4% Si) in sheets ranging from 0.08 to 0.5 mm in thickness. The specimens - in the form of disks and wound toroids - were prepared of the same rolled ribbon and for relief of work hardening strains were annealed in vacuum or hydrogen at 1100°C. The magnetic structure of the disk specimen was observed by the powder pattern procedure. The magnetic properties were measured by the ballistic technique, using the wound specimens.

The specimens were demagnetized by a gradually reduced alternating magnetic field. The maximum amplitude of the demagnetizing field was 10 Oe; the minimum amplitude 0.001 Oe; the demagnetizing time was about 30 sec.

In other cases the specimens were magnetized to saturation by a constant fiel and then there was applied to them a reverse field equal either to the coercive force or of such value as to result in zero magnetization upon its removal.

The spiral wound specimens were demagnetized either along the magnetic circui by a current sent through a winding applied to the specimen or along the axis of the specimen by means of a solenoid.

Observation of powder patterns

We observed the powder patterns on a large number of crystals from different specimens. It was found that in most cases the character of the magnetic structur remained the same after demagnetization of the specimen by an alternating field in different directions. Even in cases where there were observed on the same crystal lite two systems of domains we were unable to change the type of structure on the given section by altering the direction of demagnetization.

It must be noted, however, that in the case of a few specimens, particularly thin ones, we succeeded in finding crystallites in which the character of the magnetic structure did depend on the direction of the demagnetizing field.

In cases when the state with zero magnetization according to the hysteresis loop was obtained, the character of the magnetic structure also usually depended little on the direction of the applied magnetic field: in this case the appearance of the powder patterns was very similar to that observed in the case of demagnetization of the specimen by a decreasing alternating field.

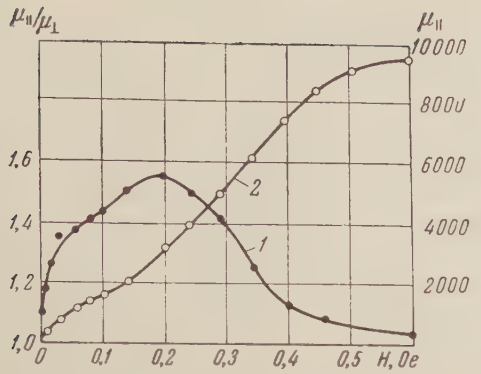

Fig.1

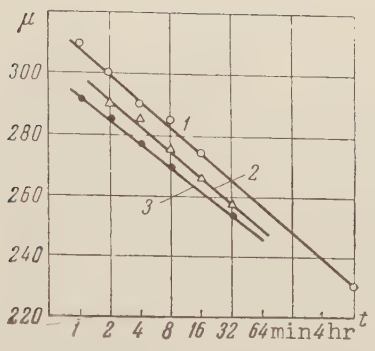

Fig.2

Fig.1. Influence of the direction of demagnetization on the permeability: 1) ratio of the permeabilities after longitudinal and transverse demagnetization, 2) permeability after longitudinal demagnetization.

Fig.2. Decrease of permeability with time: 1) after longitudinal demagnetization, 2) after transverse demagnetization, 3) after transverse magnetization by a constant field and application of the reverse field yielding I = 0 after it is cut off.

Thus for each section of a crystallite in the state with zero magnetization there exists only one stable distribution of the concentration of magnetic phases. After departure from the state of saturation the magnetic structure tends to this distribution, regardless of the direction of the demagnetizing field. The distribution of magnetic phase concentrations is determined by the shape of the specimen, the configuration of internal stresses and the interaction between crystallites, but usually does not depend on the direction of the applied magnetic field. From this it follows that demagnetization cannot lead to the formation of substantial magnetic structure.

Dependence of the permeability on the direction of demagnetization

Fig.1 shows the variation of the ratio of the permeabilities obtained after demagnetization by a longitudinal and a transverse magnetic field with the strength of the magnetic field. In the same figure we show the field dependence of the permeability after longitudinal demagnetization. Such curves with maxima were obtained for all the investigated specimens.

The values of the reversible permeability at I = 0 after demagnetization by longitudinal and transverse magnetic fields are given in the table. These values of the permeability do not differ by more than 10-20%, whereas the maximum differences of the permeability taken from the curve amounted to 50 to 200%.

Time variation of the permeability

The permeability was measured at different times after obtaining a given magnetic state. In these measurements the magnetic field was switched on only for the period necessary for measurement. In the region of weak magnetic fields regardless of the method of demagnetization (obtaining the initial magnetic state), the permeability decreased with time. The curves for three different cases are shown in Fig.2. It must be noted that although the permeability decreased in all cases, in the region of weak fields the decrease was not always exponential.

Values of reversible permeability after demagnetization

Material	Thickness, mm	Holding time, min	Permeability at H = 0.001 Oe			
			A	B	C	D
Cold-rolled 3% Si steel	0.35	10		840	880	830
	0.08	60		300	310	290
Hot-rolled 4% Si steel	0.5	60	310	290	300	260

Note: A = After longitudinal demagnetization.
B = After transverse demagnetization.
C = After application of a constant reverse field in the direction of measurement.
D = After application of a constant reverse field perpendicular to the direction of measurement.

It follows from the results of our experiments that the reason for the decrease of permeability with time cannot be resorption of the magnetic structure, inasmuch as such dissipation of the magnetic structure after transverse demagnetization should lead to increase of the permeability.

No decrease of permeability with time was observed in the region of fields wherein the ratio of the permeabilities after longitudinal demagnetization and after transverse demagnetization attained a maximum.

Conclusions

1. The magnetic structure of sheet silicon steel does not, as a rule, depend on the direction of demagnetization.

2. In the I = 0 state obtained by application of a field $H = -H_c$ the magnetic structure is close to the magnetic structure obtained after demagnetization of the specimen by an alternating field of decreasing amplitude, and differs from the latter only by a certain amount of additional irregularity.

3. The initial permeability depends little on the direction of demagnetization.

4. The decrease in permeability with time in the region of weak fields cannot be due to resorption of the magnetic structure.

References

1. S.V.Vonsovskii & Ya.S.Shur, Ferromagnetizm (Ferromagnetism), M., 1948.

2. R.I.Yanus & V.I.Drozhzhina, Zhur.tekh.fiz., 9, 1960 (1939). (Trans.Soviet Physics - Technical Physics.)

3. O.N.Al'tgauzen, N.A.Semenova & I.N.Stepanova, Elektrichestvo (Electricity) No.1 (1961).

4. Ya.S.Shur & V.R.Abel's, Fiz.metallov i metallovedenie (Physics of Metals & Metallography), 1, 11 (1955).

REGARDING THE STABILITY OF THE MAGNETIC STATE OF SOFT MATERIALS

- V.A.Zaikova & I.E.Startseva

1. The magnetic state of a ferromagnetic specimen, which may be characterized by its magnetization I, is determined by its domain structure. It follows from this that the stability of the magnetic state as regards different external factors or influences (magnetic fields, temperature fluctuations, mechanical stresses and the like[1-7]) is determined primarily by the stability of the domain structure. In actual ferromagnets with multiple domain structure a number of different domain structure configurations may correspond to the same magnetic state. Hence one may reasonably assume that different domain structures will undergo different alterations under the influence of the same external factor, i.e., that the stability of the domain structure with respect to a given external factor will differ, depending on the specific conditions under which the given magnetic state was formed. The stability of the magnetic state of ferromagnets is, of course, of great practical importance. Many scientific instruments and pieces of equipment contain components made of soft magnetic materials, and frequently it is essential that the state of these soft magnetic materials not change under the influence of external factors.

Hitherto the stability of the magnetic state of soft materials has not been adequately studied, so that it is difficult at present to recommend specific procedures for insuring a highly stable state of the domain structure. Accordingly, the aim of the present work was to study experimentally the influence of different ways of obtaining the magnetic state on its stability as regards alternating magnetic fields and tensile stresses.

2. The experiments were carried out on coarse-grained specimens of silicon steel. To eliminate the influence of demagnetizing fields on the magnetic state of the specimen the stability as regards alternating magnetic fields was investigated using ring-shaped specimens with an outside diameter of 40 mm, an inside diameter of 34 mm and a thickness of 0.2 to 0.5 mm. For studying the stability of the magnetic state as regards tensile stresses we used strip specimens measuring 450 x 3 x 0.3 mm; the ends of the specimen were magnetically shorted by a yoke of the same material. The stability was determined from the change in magnetic induction B of the specimen, and also from the extent of change of the domain structure observed on individual crystallites. The induction was measured by the ballistic procedure; for observing the domain structure we used the powder pattern technique.

We investigated the stability of the demagnetized state obtained by different methods as regards the influence of alternating fields and elastic stresses applied in the presence of a weak constant magnetic field, which was appreciably weaker than the coercive force of the specimen; conditionally we shall call this weak field the "earth's" magnetic field and shall designate it by H_e. In selecting the methods of demagnetization we tried to choose methods that would be distinctly different as regards the forms of influence employed in the process of obtaining the demagnetized state. Specifically, the stability was investigated after demagnetizing by the following four methods:

1) The specimen was demagnetized by an alternating field gradually reduced to zero amplitude in the absence of an external magnetic field.

2) The specimen was first magnetized in the H_e direction to the maximum value of the residual induction; then there was applied a field opposed to the "earth's" field, the intensity of which was chosen so that upon removal of this field and subsequent application of the field H_e the specimen was demagnetized.

3) The specimen, first demagnetized by procedure 1), was magnetized in a field

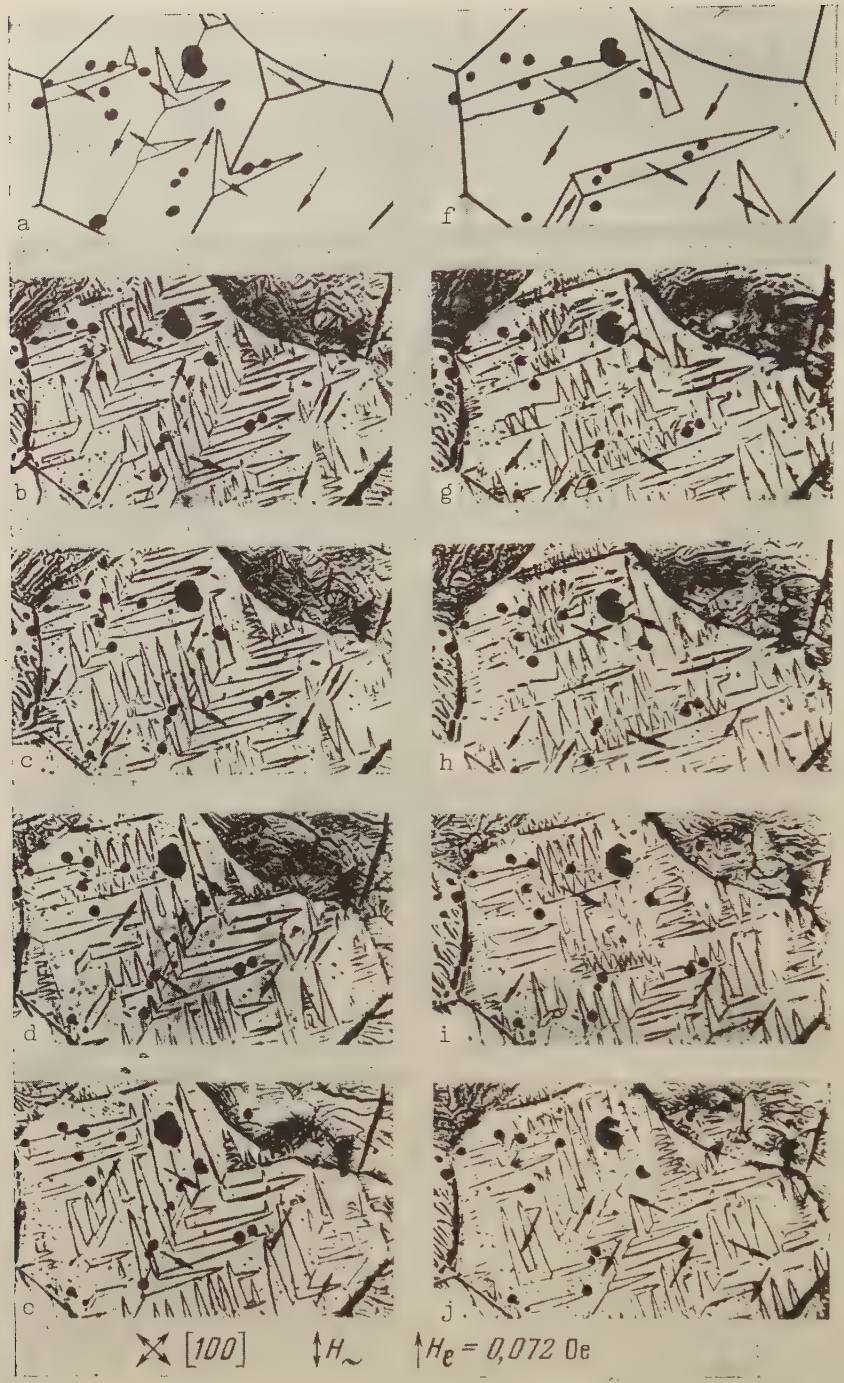

Fig.1. Change under the influence of an alternating field of the domain structure of a crystallite in a specimen demagnetized by methods 2) and 3). Method 2): a - initial state, b - $H_\sim$ = 0.103 Oe, B = 1300 G, c - $H_\sim$ = 1.55 Oe, B = 2100 G; d - $H_\sim$ = 0.195 Oe, B = 2600 G, e - $H_\sim$ = 0.270 Oe, B = 3110 G. Method 3): f - initial state; g - $H_\sim$ = 0.155 Oe, B = 0; h - $H_\sim$ = 0.206 Oe, B = 140 G; i - $H_\sim$ = 0.226 Oe, B = 750 G; j - $H_\sim$ = 0.277 Oe, B = 1580 G.

opposite in direction to the "earth's" field, with simultaneous application to it of an alternating field gradually reduced to zero amplitude. After removal of this reverse field the specimen acquired negative residual magnetization. Then there was applied the field H_e in the presence of which the specimen was demagnetized by a decreasing alternating field; the maximum amplitude of this alternating field $H_{\sim}$ was chosen so that after decrease of this field to zero the induction of the specimen would be zero.

4) As in the preceding case, after demagnetization by procedure 1), the specimen was placed in a field opposite in direction to the "earth's" field and in the presence of this field subjected to elastic stress. Then this field was cut off and there was applied the field H_e in the presence of which the load was removed. The magnitude of this load was chosen so that after its removal the induction of the specimen fell to zero.

3. Observations of the domain structure showed that the most stable structure as regards the effect of alternating fields is the structure obtained after demagnetization by method 3), and the least stable is that obtained by method 2). Fig. 1 shows how the domain structure of one of the crystallites of a ring specimen changed under the influence of alternating magnetic fields after demagnetization of the specimen by method 2) (Fig.1, a - e) and 3) (Fig.1, f - j). The examined surface was close to a (001) plane. In the first case the crystallite in the initial state (Fig.1,a) is broken up into three principal domains. The action of even a weak alternating field leads to displacement of one of the walls, a wall which in the initial state passed through a defect. This results in growth of the domain in which the vector I_s is advantageously oriented with regard to the constant field (Fig.1,b). With increase of the applied alternating field this domain gradually displaces one of the regions with opposite orientation of I_s (Fig.1,c & d); with still further increase of the alternating field there appears a new domain with advantageous orientation of I_s with respect to the field (Fig.1,e).

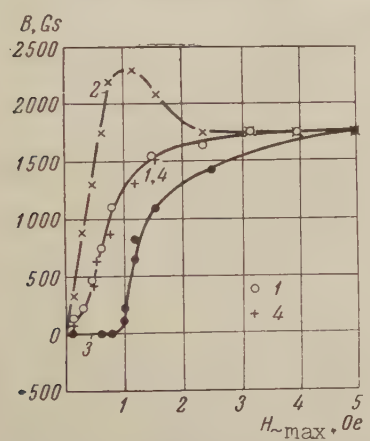

Fig.2. Variation of the magnetic induction of specimens demagnetized in different ways under the influence of an alternating field applied in the presence of a weak constant field. The figures at the curves denote the method of demagnetization.

In the second case (Fig.1,f) as a result of the operation of demagnetization the examined crystallite proved to be magnetized, although the net magnetization of the specimen itself was zero. This was presumably due to magnetic interaction of the given crystallite with its neighbors. On its surface there appear only closure domains, magnetized antiparallel and at an angle of 90° to the direction of magnetization of the grain (Fig.1,f). In this case the magnetic structure does not change up to fields of maximum amplitude approximately equaled to the field $H_{\sim}$ used in demagnetizing the specimen (g & h). In stronger fields there appears a domain with opposite orientation of I_s. There is also observed some change in the appearance of the closure domains (Fig.1,i). Further increase of the alternating field results in even more substantial rearrangement of the magnetic structure.

The curves of Fig.2 show the change in induction of a strip specimen demagnetized by different methods as a result of application of an alternating field in the presence of a constant magnetic field (H_e). The figures at the curves indicate the method of demagnetization. It will be seen that the most appreciable change in the magnetic state of the specimen

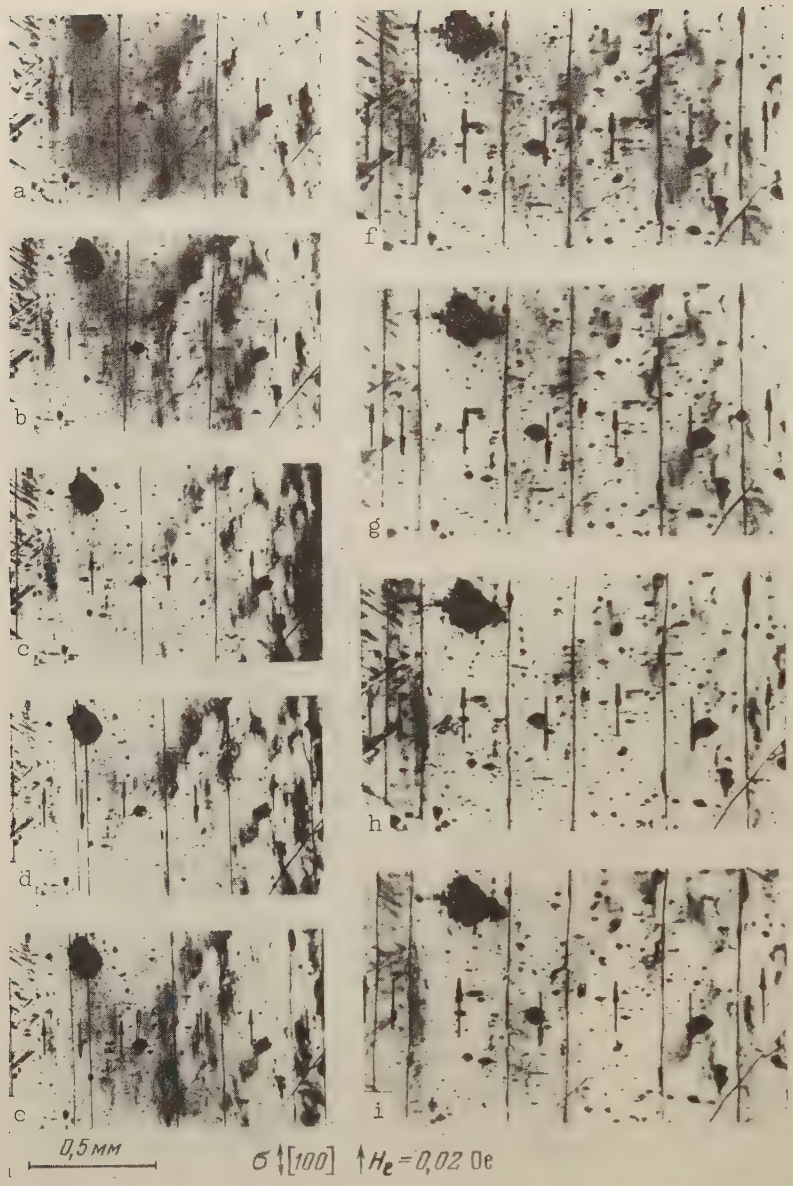

Fig.3. Variation under the influence of stresses of the domain structure of a crystallite in a specimen demagnetized by methods 2) and 4): a - initial state, $\sigma = 0$, $B = 0$; b - $\sigma = 0.9$ kg/mm^2, $B = 180$ G; c - $\sigma = 1.9$ kg/mm^2, $B = 900$ G; d - $\sigma = 3.8$ kg/mm^2, $B = 1400$ G; e - $\sigma = 8.0$ kg/mm^2, $B = 1950$ G; f - initial state; g - $\sigma = 0.9$ kg/mm^2, $B = 0$; h - $\sigma = 2.8$ kg/mm^2, $B = 30$ G; i - $\sigma = 8.0$ kg/mm^2, $B = 400$ G.

occurs after its demagnetization by method 2). In this case application of even a weak alternating field leads to substantial magnetization of the specimen in the direction of the field H_e. In the case of demagnetization by method 3) the application of alternating fields the maximum amplitude of which is less than $H'_{\sim}$ does not result in magnetization of the specimen; magnetization begins only in fields exceeding $H'_{\sim}$. The experimental points obtained after the demagnetizing specimens

by methods 1) and 4) virtually lie on the same curve (curve 1,4) which occupies an intermediate position between the curves obtained after demagnetization by methods 2) and 3).

It follows from the photographs reproduced in Fig.1 and the curves of Fig.2 that the most stable demagnetized state as regards the influence of alternating magnetic fields applied in the presence of a weak constant magnetic field (H_e) is the state obtained by method 3), when the final stage of the demagnetization process is the application of an alternating field gradually reduced to zero amplitude.

We now turn to the results obtained when the specimen is acted upon by tensile stresses in the presence of a constant magnetic field. Observations of the domain structure show that the most stable structure as regards the influence of stresses is that obtained by method 4), and the least stable is the structure obtained by method 2). By way of illustration, in Fig.3 we give series of powder pattern photographs representing the domain structure of a crystallite, the surface of which is parallel to the (011) plane under the influence of external loads in the case of a specimen demagnetized by method 2) (Fig.3,a - e) and by method 4) (Fig.3,f - l). It will be seen that in the case of demagnetization by method 2) even a small stress leads to an appreciable change in the initial magnetic structure. The domains in which I_s is parallel to the external field H_e increase in size (Fig.3,b & c). At a stress $\sigma = 3.8$ kg/mm^2 (Fig.3,d) there appears a new reverse magnetization domain, which with further increase of the load grows in size (Fig.3,e). In contrast, in the case of demagnetization by method 4) no significant changes in the domain structure occur up to the value of the stress applied during demagnetization (compare Fig.3,f,g & h); only at a higher stress (Fig.3,i) is there observed minor displacement of some of the domain walls resulting in growth of the domains with I_s parallel to H_e.

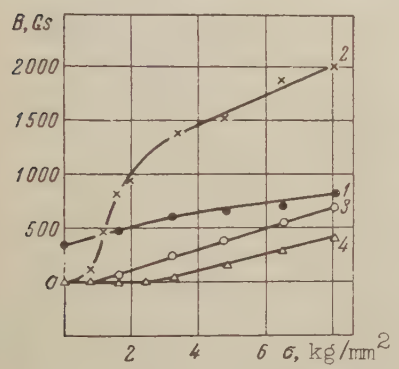

Fig.4. Variation of the magnetic induction of specimens demagnetized in different ways under the influence of stresses applied in the presence of a weak constant magnetic field. The figures at the curves indicate the method of demagnetization.

The B versus σ curves for specimens demagnetized in different ways are shown in Fig.4. It will be evident from this figure that the greatest change in induction as a result of loading occurs, as in the preceding case of application of an alternating field, after demagnetization of the specimen by method 2). After demagnetization by method 4) the specimen remains demagnetized until the applied stress begins to exceed the stress employed in the process of demagnetization. Further increase of the load leads to some magnetization of the specimen. Stressing of the specimen demagnetized by method 3) leads to a more substantial change in induction than after demagnetization by method 4).

It follows from the powder patterns of Fig.3 and the curves of Fig.4 that the most stable state as regards the effect of external loading in the presence of a weak constant field is the state obtained by method 4), in which the final stage of the demagnetization process is the application of a stress.

The state obtained by method 3) is more stable as regards stresses than the states obtained by methods 1) and 2), but less stable than the state obtained by method 4).

4. The results obtained show that the stability of the demagnetized state of a ferromagnet as regards the influence of external factors applied in the presence of a weak constant field depends substantially on the method employed in obtaining the demagnetized state.

The most stable state as regards a given external factor is the state to obtain which the given factor was applied in the last stage of the process of demagnetization. It is also evident that the allowable magnitude of the external influence in the process of operation should not exceed the magnitude of the same influence (alternating field or stress) employed in the last stage of demagnetization.

As the results of our powder pattern studies show, this behavior of a ferromagnet can be explained by the fact that the domain walls in the same magnetic state of the specimen (for example, the demagnetized state) are located in different sections of the crystal depending on the method of obtaining the given state (method of demagnetization) and, consequently, exhibit a different stability as regards different external factors. The stability of the domain structure as regards a given disturbing factors (alternating field or elastic stresses) will be highest if the same "factor" was employed in the final stage of producing the desired magnetic state of the ferromagnet and thus operated to help "fix" the domain walls at certain locations in the crystal. Thus, if an alternating field (stress) serves to form and fix a given structure, subsequent application of a weaker field (stress) should not significantly change the location of the domain walls.

References

1. H.Williams, R.Bozorth & W.Shockley, Phys.Rev., 75, 155 (1949).

2. Ya.S.Shur & V.R.Abel's, Fiz.metallov i metallovedenie, 6, 556 (1958). (Trans.Physics of Metals & Metallography.)

3. Ya.S.Shur & I.E.Startseva, Ibid., 6, 614 (1958). (Trans.Ibid.)

4. L.Dykstra & U.Martins, Revs.Mod.Phys., 25, 146 (1953).

5. Ya.S.Shur & V.A.Zaikova, Fiz.metallov i metallovedenie, 6, 545 (1958). (Trans.Physics of Metals & Metallography.)

6. Ya.S.Shur & I.E.Startseva, Zhur.eksp.i teor.fiz., 39, 566 (1960). (Trans. Soviet Physics - JETP.)

7. L.V.Kirenskii, V.D.Dylgerov & M.K.Savchenko, Izv.AN SSSR, Ser.fiz., 21, 1168 (1957). (Trans.Bulletin, 21, 1157.)

EFFECT OF ULTRASONIC VIBRATION AND ALTERNATING MAGNETIC FIELDS ON THE DOMAIN STRUCTURE OF SILICON STEEL

- D.A.Laptei & V.S.Cherkashin

It is known[1,2] that where a number of ferromagnetic materials are concerned different external factors (magnetic treatment, mechanical and thermal "shaking", etc.) can lead to suppression of magnetic hysteresis effects. A theoretical explanation of this effect has been given by Kondorskii[3] who showed that the condition for stability of the 180° walls as regards variation of external stresses is the absence of a field acting on the walls and that this condition is fulfilled in structures obtained by "ideal" magnetization. Kondorskii notes that in general this is valid for all stresses including those due to periodic elastic vibrations.

However, as far as we know there have been no direct observations of the changes in domain structure under the influence of the above mentioned factors, except for the work of Haacke & Jaumann[4] who used the powder pattern technique to investigate the movement of individual walls in an ultrasonic field.

The purpose of the present work was to investigate the influence of mechanical stresses of ultrasonic frequency and alternating magnetic fields on the domain structure of silicon steel in the process of magnetization.

Experimental part

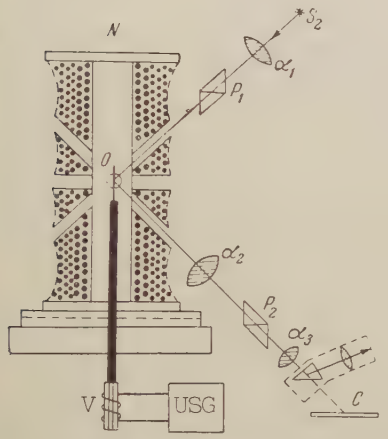

Fig.1. Experimental set-up: N - magnetizing coils, P_1 & P_2 - analyzer and polarizer, α_1, α_2 & α_3 - lenses, C - camera (dash-line contour - prism and lens employed for visual observation), O - specimen, USG - ultrasonic generator, V - vibrator.

Our experimental arrangement is diagramed in Fig.1. As will be evident from the figure, the domain structure was observed by means of the meridional Kerr effect[5,6]. The resultant magnetization of the specimens was measured on an astatic magnetometer simultaneously with observation of the domain structure. The specimens were "sonetized" by means of a magnetostrictive ultrasonic generator operating at a frequency of 20 kc. The applied magnetic fields were of commercial frequency (50 cps).

The experiments were carried out on single crystal specimens of 3% Si steel, cut in the form of 40 x x 8 x 0.28 mm strips and in the form of disks 20 mm in diameter. The surface of the specimens was parallel to the (110) planes. Prior to observation the specimens were subjected to mechanical and electrolytic polishing and vacuum (10 mm Hg) anneal at 1100°. The directions of the applied magnetizing field and propagation of the sound waves agreed with the principal crystallographic axes.

In investigating the magnetic structure we employed the following general procedure. Initially the specimen was demagnetized by means of an alternating field gradually reduced to zero amplitude. Then a constant magnetic field was applied and the domain structure observed in the process of increase of this field. Next, the specimen was again demagnetized and the process of magnetization and observation of the domain structure repeated with the difference that at certain fixed values of the magnetizing field the specimen was subjected to ultrasonic "shaking" or the influence of an alternating magnetic field gradually decreased to zero amplitude. Generally the domain structure was observed visually (by means of the attachment indicated by the dashed line contour in Fig.1). We also photographed the powder patterns on the surface

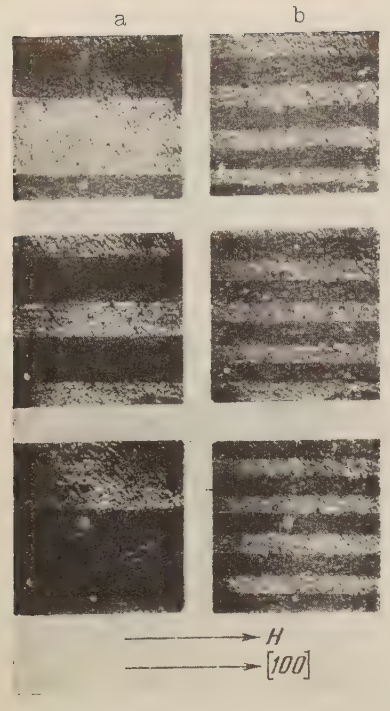

←Fig.2. Change in the domain structure under the influence of ultrasonic vibration for different initial magnetic states: 1 & 3 - states corresponding to the H = 6.4 Oe point on the ascending and descending branches of the hysteresis loop, 2 - H = 6.4 Oe point on the initial magnetization curve. a - initial state; b - after sonetization.

1

2 of the specimen after demagnetization and after subjecting it to ultrasonic and magnetic "shaking".

Results

Figs.2,a show the domain structure in three different states corresponding to points on the ascending and descending hysteresis loops and on the initial magnetization curve at a field of 6.4 Oe. In each of these states the specimen was subjected to ultrasonic vibration of the same intensity. The structure after sonetization is shown in the photographs of Fig.2,b. The change in structure consisted of increase in the number of domains as a result of fragmentation of the initial structure. Comparison of the photographs of Fig.2,b show that ultrasonic vibration in all cases leads to formation of structure of the same type regardless of its initial state. This is observed both in the absence of a field and with the magnetizing field applied in all three principal crystallographic directions.

3

The alterations in domain structure under the influence of ultrasonic vibration and an alternating magnetic field incident to magnetization along the principal crystallographic axes were the following.

Magnetization along [100]

After the initial demagnetization by an alternating field of decreasing magnitude there formed on the surface of the specimen the structure shown in Fig.3,a,1 Upon subsequent magnetization in the [100] direction, the structure altered in accord with the usual process of displacement of the 180° walls. If in any of the partially magnetized states the specimen is subjected to "shaking" by an alternating field, no substantial alteration of the initial structure is observed (Figs. 3,b); there occurs only partial displacement of the domains, but the total number of domains remains the same. This is due to the fact that the crystal is fairly uniform and $H_c < 0.1$ Oe & $I_r < 5$ G, and the initial magnetization curve virtually coincides with the ideal (anhysteretic) curve.

If, however, the specimen is subjected to ultrasonic vibration, the domain structure changes markedly. Sonetization results in fragmentation of the initial structure; the total number of domains approximately doubles. In fields stronger than 32 Oe structure disappears from the surface of the specimen, and in this case it does not reappear after sonetization.

Magnetization along [110]

The following changes occur in the domain structure of a specimen during

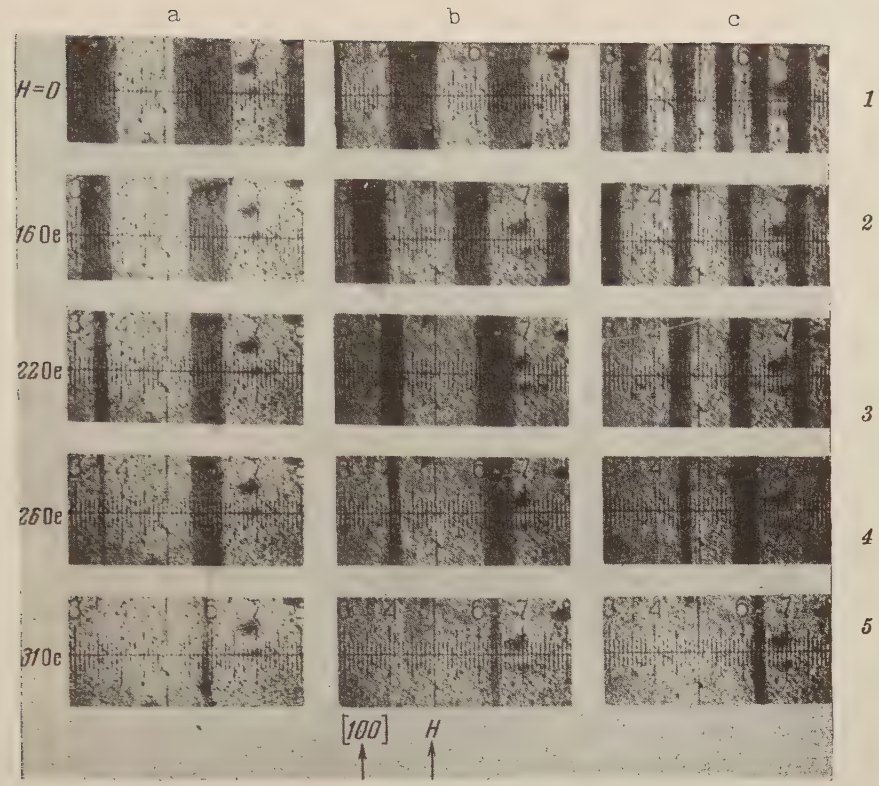

Fig.3. Change in the structure incident to magnetization along the [100] axis: a - initial structure, b - after application of an alternating field of decreasing amplitude, c - after ultrasonic vibration. 1 division on the scale = 0.07 mm.

magnetization along the intermediate magnetization axis: the usual displacement of the 180° walls with increase of the field is not observed (Fig.4,a). The initial structure breaks up into a number of distinct rectilinear bands forming an angle of 35° with the direction of the field. With increase of the field this alteration spreads from the edges to the center of the specimen.

As a result the entire surface of the specimen becomes covered with a sawtooth structure (Fig.4,a,3). In yet stronger fields this sawtooth structure breaks up (Fig.4,a,4) and gradually converts to a finer structure in the form of wavy lines oriented along the field.

If these structures are subjected to an alternating magnetic field, they change very little (Fig.4,b): mainly the secondary structure becomes sharper, the rectilinearity of the domain walls becomes more pronounced and the period of the sawtooth patterns of the newly formed structure increases.

Observations of the influence of ultrasonic vibration on the domain structure during magnetization in the [110] direction (Fig.4,c) showed that in the absence of a field the effect of sonetization amounts to fragmentation of the structure, much as in the case of magnetization in the [100] direction. With increase of the field there occurs some increase in the width of the domains in which the vector I_s is parallel or antiparallel to the [100] axis with the result that the number of such domains increases. The domain walls tend to warp or bend. The formation of the new structure terminates in weaker fields than in the absence of ultrasonic vibration (Fig.4,c,2), and this newly formed structure undergoes substantial

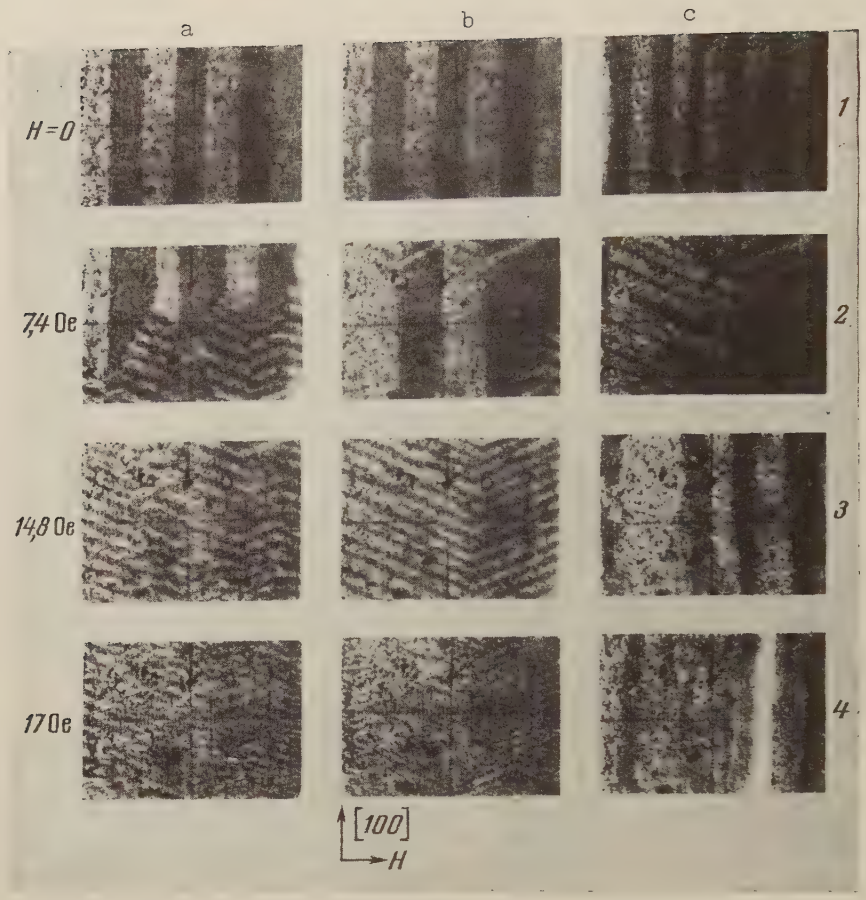

Fig.4. Change in the domain structure during magnetization along the [110] axis: a - initial structure, b - after application of an alternating field, c - after ultrasonic vibration. 1 scale division = 0.07 mm.

changes in the process of sonetization. In stronger fields this structure is gradually broken up by ultrasonic vibration and acquires the appearance shown in Fig. 4,c,3. It will be seen that the structure shown in Fig.3,c,2 disappears: the domain walls become less distinct. Finally, this process leads to formation of a fine structure in the form of wavy lines; this occurs much earlier than in specimens not subjected to ultrasonic vibration.

It must be noted that the structure formed as a result of ultrasonic "shaking" can be liquidated by the application of an alternating field. In this case there reappears the structure shown in Fig.4,b; this structure, again, can be destroyed by sonetization. This mutually cancelling influence of ultrasound and an alternating field of decreasing amplitude is characteristic for all crystallographic directions.

Magnetization along [111]

Two processes are veinced in the change in domain structure in the case of magnetization along the difficult axis (Fig.5,a): first there occurs the usual displacement of 180° walls, then there appears a new structure which comes to

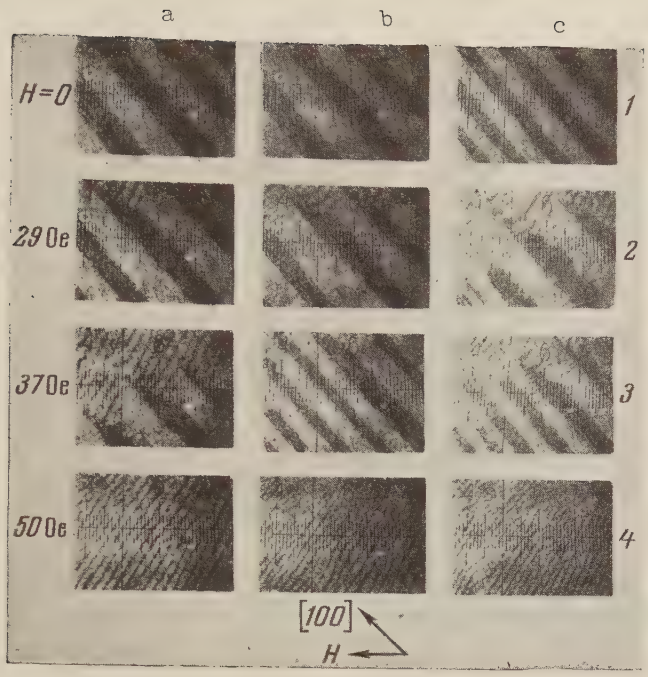

Fig.5. Change in the domain structure during magnetization along the [111] axis: a - initial structure, b - after application of an alternating field, c - after ultrasonic vibration. 1 scale division = 0.07 mm.

predominate in stronger fields. Wall displacements occur in both the newly formed structure and in the persisting initial structure. On the other hand, application of an alternating field in the process of magnetization produces virtually no changes in the structure. As in the case of magnetization along the [100] and [110] axes, the effect of ultrasonic vibration amounts mainly to fragmentation of both the basic and the secondary structures.

Conclusions

1. Ultrasonic vibration of a single crystal of silicon steel in the process of magnetization in the [100] direction leads to fragmentation of the domain structure and increase in the number of domains by a factor of about two. It may be assumed that this fragmentation is connected with decrease of the magnetic energy of the specimen. The structure formed does not depend on the initial magnetic state of the specimen but is determined mainly by the intensity of the magnetizing field. Ultrasonic vibration of the crystals being magnetized in the [110] and [111] directions results in more complex alteration of the domain structure.

2. The structure corresponding to the ideal (anhysteretic) magnetization curve, obtained by application of an alternating field gradually reduced to zero amplitude, is not stable as regards ultrasonic vibration. The structure produced by ultrasonic vibration can be eradicated by the application of a decreasing alternating field.

3. Visual observation carried out in the process of sonetization showed that with gradual increase in the intensity of the ultrasonic vibration initially there occurs displacement of some of the domain walls and at the same time movement of

the domains as a whole; individual domains being to fragment. With further increase of the ultrasonic vibration intensity these effects are enhanced and at the maximum sound intensity the pattern on the surface of the specimen becomes blurred. With decrease in the intensity of ultrasonic vibration there is gradually established the structure shown in Figs.3,c, 4,c and 5,c.

Institute of Physics,
Siberian Division of the
Academy of Sciences of the USSR

References

1. S.V.Vonsovskii & Ya.S.Shur, Ferromagnetizm (Ferromagnetism), M., 1948.
2. K.M.Polivanov, Ferromagnetiki (Ferromagnets), M., 1957.
3. E.I.Kondorskii, Zhur.eksp.i toer.fiz., 37, 1110 (1959). (Trans.Soviet Physics - JETP.)
4. G.Haacke & J.Jaumann, Z.angew.Phys., 12, 289 (1960).
5. L.V.Kirenskii & I.F.Degtyarev, Zhur.eksp.i teor.fiz., 35, 584 (1958). (Trans.Soviet Physics - JETP.)
6. V.D.Dylgerov & I.F.Degtyarev, Kristallografiya, 5, 809 (1960). (Trans. Soviet Physics - Crystallography.)

DEVELOPMENT OF MIRROR ELECTRON MICROSCOPY OF MAGNETIC MICROFIELDS

- G.V.Spivak, L.V.Kirenskii, R.D.Ivanov & N.N.Sedov

Introduction

In the present paper we reproduce electron micrographs of the domain structure of different ferromagnetic materials and compare the images obtained with the aid of an electron mirror with photographs of powder patterns. Also, on the basis of investigation of the contrast of the electron image, we obtain quantitative data on the distribution of the local stray magnetic fields over the surface of some specimens.

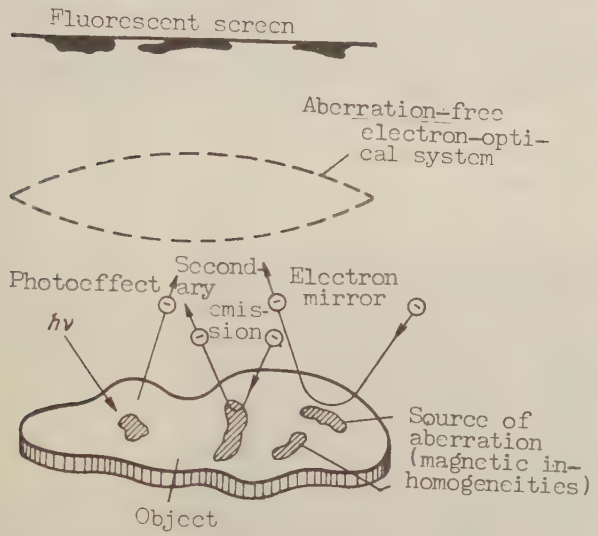

Fig.1. Principle of obtaining electron optical images in emission and quasi-emission systems.

Use of an electron mirror for imaging magnetic microfields was first proposed back in 1955 in the work of Ref.1. Subsequently, an instrument was developed and in further experimentation its use was extended to ferroelectrics and the patch fields of electron emitters.[2]

In a report[3] presented at the Third All-Union Conference on Electron Microscopy there was described the design of an all-metal electron mirror microscope with in vacuo photographing; the improvements made in this design provided for obtaining high quality images of magnetic microfields.

In addition to the electron mirror, we have in the past proposed two other methods for obtaining microfield images: secondary emission and the photoeffect (Fig.1). Both these approaches appear promising. However, at present the electron mirror has a number of advantages, namely, a) high sensitivity to relatively weak fields, b) high image contrast, and c) the possibility of observing the magnetic field configuration at different distances from the object.

The sensitivity of the electron mirror, which is essentially a "quasiemission" system, is due to the fact that the illuminating electron beam is stopped at the object and appreciable contrast is provided by virtue of forward and reverse motion of the electrons in the microfields. Since the electrons can be stopped and reversed by an appropriate electric field there is realized the possibility of probing the spatial structure of the field.

In addition to the high sensitivity of the electron mirror, which is provided by modulation of slow electrons, it is essential that the electrons entering the optical system of the instrument be accelerated to an appreciable velocity. The employed high accelerating potential (50 kV), narrowing the electron beam, greatly improves the resolution of the instrument.[4]

Observation of magnetic microfields and comparison with powder patterns

Electron mirror and powder pattern micrographs of the same section of a magnetoplumbite crystal are reproduced in Fig.2. In general there is good agreement between the two images. However, some of the details evident in the powder picture

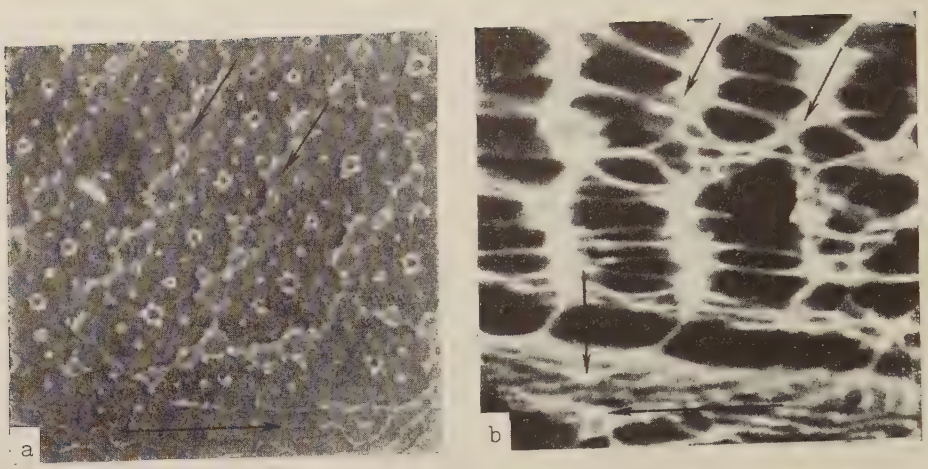

Fig.2. Domain structure of magnetoplumbite $PbO(Fe_2O_3)_6$; (0001) plane; magnification 400 X. a - powder pattern; b - electron image.

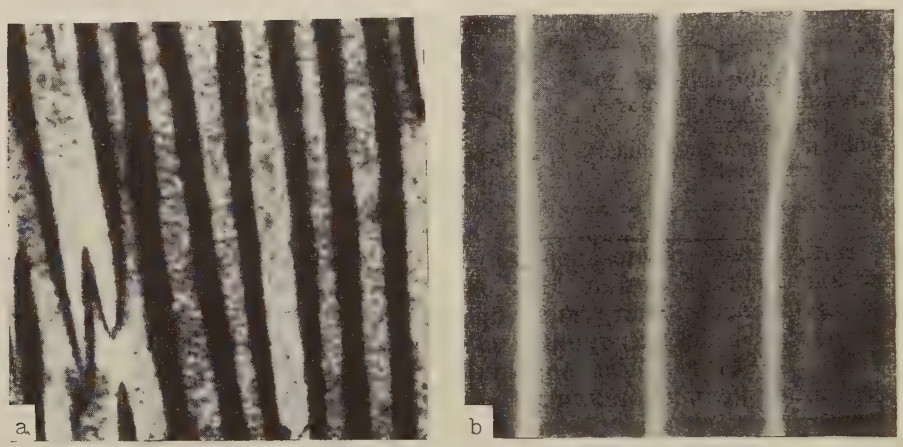

Fig.3. Domain structure of cobalt; surface almost parallel to the hexagonal axis. a - powder pattern (400 X); b - electron image (800 X).

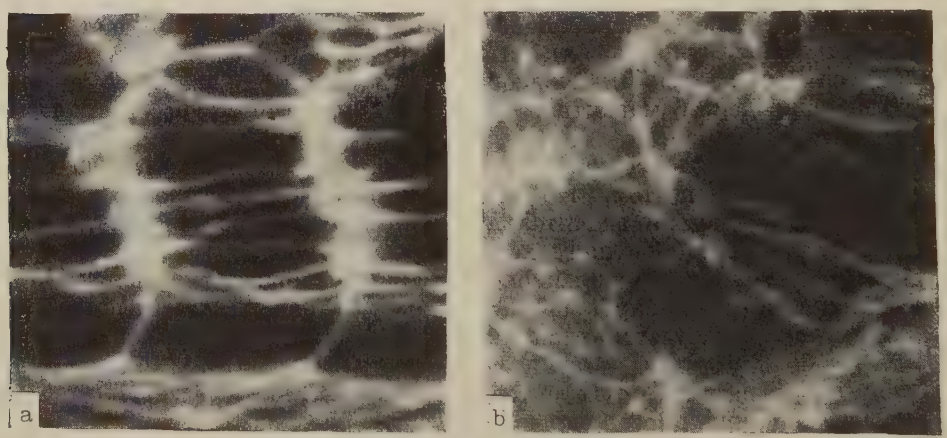

Fig.4. Domain structure of $PbO(Fe_2O_3)_6$; electron mirror images; (0001) plane. a - 800 X, b - 1500 X.

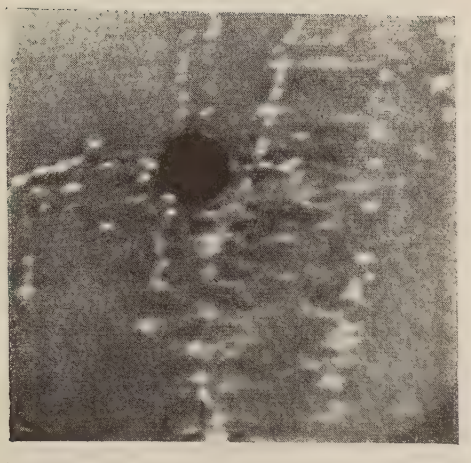

Fig.5. Domain structure of ~1000 Å thick cobalt film; electron image; 400 X.

are absent from the electron micrograph. This is explained by the fact that the electron image in the given case corresponds not to the surface field but to the field at a certain distance from the crystal and, consequently, represents the configuration of the field persisting at this distance. It will be noted that the contrast of the electron micrograph is high.

Electron and powder pattern micrographs of the domain structure of cobalt are juxtaposed in Fig.3. Here again there is good agreement (the magnification of the electron image is twice that of the powder picture); in fact one may say that the quality of the electron image is superior to that of the powder pattern photograph.

Fig.4 shows two electron mirror images of a section of the domain structure of magnetoplumbite obtained at magnifications of 800 X and 1500 X. The images are quite sharp, so that it is evident that such magnifications are still useful.

Lastly, in Fig.5 we show the electron mirror image of the domains in a ~1000 Å thick cobalt film. The film was prepared by cathode sputtering[5]. The domain structure is typical of such cobalt films and corresponds to the powder patterns.

Evaluation of local fields from the contrast of the mirror image

Measurement of the intensity of local stray magnetic fields is of substantial interest in investigating different objects: 1) domain structures, 2) magnetic inhomogeneities in alloys, 3) the coatings of magnetic tape, etc. The question of the relation between the contrast of the image yielded by an emission system and the intensity of local magnetic fields has been discussed earlier.[6]

In the present work the evaluative procedure has been extended to electron mirror images of domain structures. Our purpose was to determine the decrease with distance from the surface of the specimen of the domain wall field. Calculations show that the contrast of the image depends both on the strength of the field H acting on the electrons and the effective extent z of this field, i.e., on the product Hz.

For calibrating the electron mirror we used an artificial specimen consisting of an alteration of brass and iron strips (see insert in Fig.6,a). The surface of the specimen was polished and sputtered with silver to eliminate the effect of contact fields.[7] The magnetic field above such a specimen was measured by means of a bismuth wire microprobe and it was found that the fall-off of the field was approximately exponential (Fig.6,a). Fig.6,b shows the calibration curve obtained for the electron mirror, namely, the variation of blackening of the negative (i.e., the logarithm of the relative brightness on the screen) with the product Hz. By varying the negative potential on the specimen in the instrument, we change the height at which the electrons are stopped, and thus can measure the field at different elevations above the surface of the specimen.

The variations of the local field above the surface of magnetoplumbite and cobalt are shown in Fig.6,c & d. It will be seen that the falling off of the field with distance is approximately exponential. It follows from the measurements that the constant z_0 for magnetoplumbite is smaller than that for cobalt

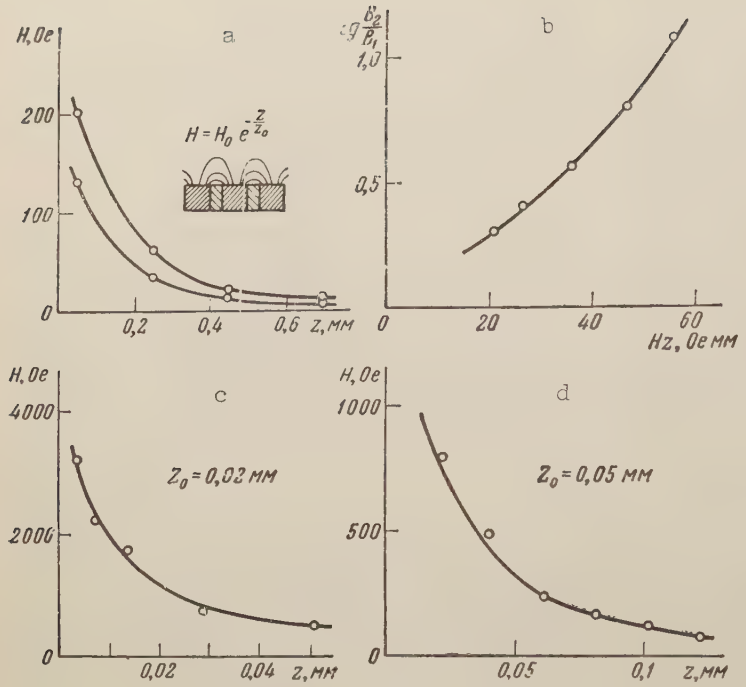

Fig.6. a - Field above an artificial specimen of brass and iron strips (insert) measured by a bismuth wire probe at different values of the magnetizing current; the decrease in field is approximated by $H = H_0 e^{-z/z_0}$; b - calibration curve for electron mirror; c - stray field above the hexagonal plane of a magnetoplumbite crystal, z_0 = = 0.02 mm; d - stray field above the surface of cobalt, almost parallel to the hexagonal axis, z_0 = 0.05 mm.

by a factor of 2.5. Thus the local domain boundary field of the given specimen of magnetoplumbite falls off appreciably more rapidly with distance than the corresponding field of cobalt.

Conclusions

The mirror electron microscope, which has been described earlier[2], is capable of recording high quality images of the configuration of the magnetic field of bulk and film specimens; it can also be utilized for observation of the behavior of microfields and for measuring the strength of such stray fields at different distances from the surface of the specimen. The greatest useful magnification (~2000 X) obtained so far is not the limiting value.

Physics Faculty,
Moscow State University &
Institute of Physics,
Siberian Division of the
Academy of Sciences of the
USSR

References

1. G.V.Spivak, I.N.Prilezhaeva & V.K.Azovtsev, Doklady AN SSSR, 105, 965 (1955).

2. G.V.Spivak, I.A.Pryamkova & E.Igras, Izv.AN SSSR, Ser.fiz., 23, 729 (1959) (Trans.Bulletin, 23, 723); G.V.Spivak & I.A.Pryamkova, IN "Magnitnyay struktura ferromagnetikov" (Magnetic structure of ferromagnets), p.185, Novosibirsk, 1960.

3. G.V.Spivak, I.A.Pryamkova, D.V.Fetisov, A.N.Kabanov, L.V.Lazareva & A.I. Shilina, Izv.AN SSSR, Ser.fiz., 25, 683 (1961) (Trans.Bulletin 25, 698). (Also see European Regional Conference on Electronmicroscopy, Delft, 1960.)

4. S.Leisegang, Elektronmikroskopie.

5. R.D.Ivanov, G.V.Spivak & I.G.Sirotenko, Izv.AN SSSR, Ser.fiz., 25, 581 (1961). (Trans.Bulletin, 25, 585.)

6. N.N.Sedov, G.V.Spivak & N.F.Isaeva, Ibid., 25, 725 (1961).(Trans.Bulletin, 25, 737.)

7. G.V.Spivak, I.A.Pryamkova & V.N.Lepeshinskaya, Doklady AN SSSR, 130, 751 (1960). (Trans.Soviet Physics - Doklady.)

CONCERNING THE RECTANGULARITY OF THE HYSTERESIS LOOPS OF Mg-Mn FERRITES

- I.E.Startseva & Ya.S.Shur

The shape of the hysteresis loops of Mg-Mn ferrites may vary greatly, depending on the composition of the material and the heat treatment to which it has been subjected. Under certain conditions these ferrites exhibit spontaneous rectangularity of the hysteresis loops[1], which is evinced in the minor hysteresis cycles in cases when the maximum magnetizing field exceeds the coercive force of the material. The maximum rectangularity coefficient or squareness ratio $P_r = (B_r/B_m)_{max}$ of some Mg-Mn ferrite specimens attains 0.95-0.98. Here B_r and B_m are the minor loop values of the residual and maximum induction.

So far no one has successfully explained the reasons for the distinctive hysteresis loops of these ferrites.

Our earlier observations[2] of the domain structure in individual crystallites of polycrystalline Mg-Mn specimens showed that a characteristic feature of the domain structure of ferrites with a spontaneously rectangular loop is curvature of the domain walls. It was hypothesized that this curvilinearity of the boundaries is due to inhomogeneities of the crystal structure. Obviously, such inhomogeneities, if they exist, must also affect all the other magnetic properties of such ferrites. Hence for clarifying the causes responsible for the different shape of the hysteresis loop of Mg-Mn ferrites we felt it would be of interest to investigate further their magnetic properties and crystal structure. In the present work we observed the behavior of the domain structure of Mg-Mn ferrites with large values of P_r with variation of the magnetic state along a minor hysteresis loop and investigated the effect of the method of demagnetization on the shape of the initial magnetization curve of ferrite specimens with large values of the squareness ratio.

We observed the domain structure on the surface of individual crystallites of a polycrystalline toroidal specimen of MM-7 type ferrite ($P_r = 0.97$) by the powder pattern technique[3]. The dimensions of the individual crystallites attained 1 mm. The influence of the method of demagnetization on the shape of the initial magnetization curves was investigated for two series of toroidal Mg-Mn ferrite specimens of different composition, namely, types MM-6 and PP-24.* In each series there were specimens with different values of P_r.

The magnetization curves were recorded by the ballistic method. Prior to measurement of each point the specimen was demagnetized either by a circular alternating field gradually reduced to zero amplitude or by heating to above the Curie point.

Observations of the domain structure showed that the maximum value of P_r is obtained for the particular loop for which there disappear most of the domains with disadvantageous orientation of the magnetization relative to the field in most of the crystallites in the state of maximum induction. In this state the individual crystallites proved to be magnetized mainly in the easy magnetization direction closest to the field. Moreover, in each crystallite and on its surface, possibly, at internal defects of the crystal lattice, there persist closure domains with an orientation of the magnetization differing from the orientation in the main volume of the crystal. The boundaries between these closure domains and the principal domains are usually curved.[2] No substantial increase in the size of the closure domains is observed upon reduction of the magnetizing field to zero. As a result of this, the value of B_r on such a minor hysteresis loop proves to be close to the value of B_m; P_r approaches unity.

---

*The ferrite specimens were made available by L.I.Rabkin.

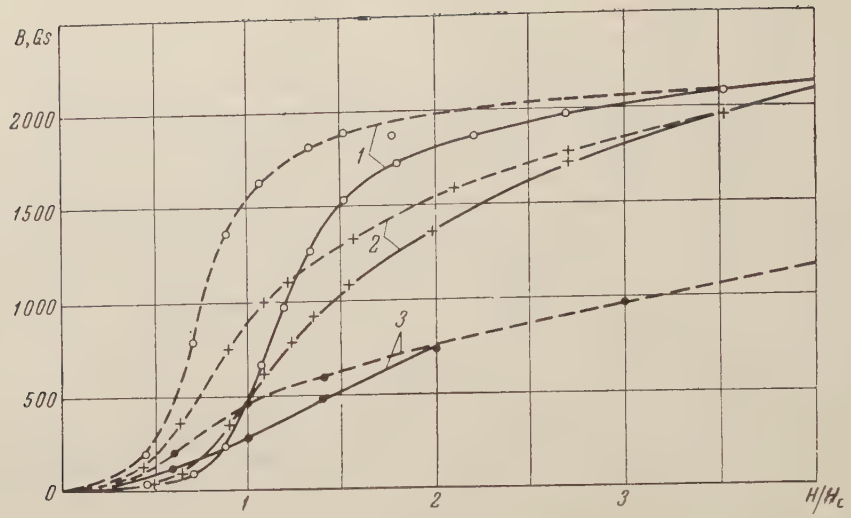

Initial magnetization curves for Mg-Mn ferrite specimens, recorded after demagnetization by heating to above the Curie point (dashed lines) and by an alternating field of decreasing amplitude (solid lines). Curves 1, 2 & 3 were obtained, respectively, for specimens with P_r = 0.95, 0.83 and 0.63.

The initial magnetization curves for three specimens of MM-6 ferrite having different squareness factors are shown in the accompanying figure. Here the horizontal scale is laid off in terms of the ratio of the magnetizing field H to the coercive force H_c of the specimen; the vertical scale is laid off in values of the induction B of the specimen in the field H. Curves 1, 2 & 3 pertain to specimens with P_r = 0.95, 0.83 and 0.63, respectively.

As will be evident from the figure, in all three cases the initial sections of the magnetization curves obtained after demagnetization by heating lie higher than the corresponding sections of the curves obtained after demagnetization by an alternating field. The differences between the curves are the greater, the higher the value of the squareness factor of the specimen. In each case the two curves merge in the region of high fields.

Similar results were obtained for specimens of PP-24 type ferrite.

Thus the experimental results show that, in contrast to metallic ferromagnets[4-6], the permeability of Mg-Mn ferrites in weak fields is substantially lower after demagnetization by an alternating field than after demagnetization by heating. Apparently this is due to the existence of a distinctive form of inhomogeneities or imperfections in the crystal structure of the ferrites.

In actual ferromagnets a number of different domain structure configurations may correspond to any given magnetic state of the specimen, in particular, the demagnetized state. Accordingly, depending on the method of demagnetization, the boundary between the domains may be located at different points and may have different stability as regards the action of a constant magnetic field.[5,7] In a demagnetized crystal the domain walls tend to arrange themselves in a pattern corresponding to minimum total wall energy, the value of which is proportional to the wall energy density and the area of the walls. The wall energy density is a function of the coordinates in materials with an imperfect crystal structure.

In the process of demagnetization of ferrites by an alternating magnetic

field, wherein wall displacements are involved, individual sections of the domain walls may be caught or retained at points corresponding to minimum wall energy density. As a result the wall is bent or curved. On such a curved wall there must appear magnetic poles, leading to increase of the magnetostatic energy of the crystal. The magnitude of this energy is proportional to I_s^2. In Mg-Mn ferrites the saturation magnetization is relatively low (in PP-24 type ferrite I_s = = 230 gauss, whereas in silicon iron with 3% Si I_s = 1600 gauss), consequently, curvature of the domain walls in them does not result in appreciable increase of the crystal energy. In metals, in contrast, curvature of the walls is apparently energetically disadvantageous, so that such retention of walls in metals plays only a secondary role.

In the case of demagnetization of ferrite specimens by heating, domains nucleate in the process of cooling at the instant of passage through the Curie point. Continued cooling to room temperature should lead to some displacement of these walls. In this case, however, the walls move a shorter distance, so that their retention and fixation at given points is less clearly evinced. Moreover, after demagnetization by heating the domain walls may be in metastable states because of the existence of temperature hysteresis of the domain structure.[8]

The increasing difference between the initial magnetization curves obtained after demagnetization by heating and by an alternating field with increase of the squareness factor of the specimens indicates that in the states with large P_r there probably exist inhomogeneities that strongly hinder wall displacement. These inhomogeneities also, apparently, hamper rearrangement of the domain structure with decrease of the field bringing the specimen to the B_m state on the minor hysteresis loop, i.e., are responsible for the large value of P_r in Mg-Mn ferrites.

Thus, the above described experimental data substantiate our earlier hypothesis that the spontaneous rectangularity of the hysteresis loop of Mg-Mn ferrites is due to the existence in them of a distinctive form of inhomogeneities or imperfections of the crystal structure. The nature of these inhomogeneities can only be ascertained by further detailed investigations of the structure of such ferrites.

References

1. L.I.Rabkin, Vysokochastotnye ferromagnetiki (High-frequency ferromagnets), M., 1960.

2. I.E.Startseva & Ya.S.Shur, Fiz.metallov i metallovedenie, 11, 158 (1961). (Trans.Physics of Metals and Metallography.)

3. H.J.Williams, R.M.Bozorth & W.Shirley, Phys.Rev., 75, 155 (1949).

4. S.V.Vonsovskii & Ya.S.Shur, Ferrmagnetizm (Ferromagnetism), p.348 (1948).

5. G.Sommerkogn, Techn.Mitt.Krupp, 13, No.4, 71 (1955).

6. A.Smolinski, Brit.J.Appl.Phys., 12, No.2, 81 (1961).

7. V.A.Zaikova & I.E.Startseva, Present issue of the Bulletin, p.1469.

8. I.E.Startseva, A.A.Glazer & Ya.S.Shur., Izv.AN SSSR, Ser.fiz., 26, No.2 (1962). (Trans.Bulletin, 26, No.2.)

TEMPERATURE DEPENDENCE OF THE FIRST ANISOTROPY CONSTANT AND THE MAGNETIC STRUCTURE OF Fe-Mn FERRITES

- L.V.Kirenskii, A.I.Drokin, V.D.Dylgerov, N.I.Sudakov & E.K.Zagirova

Introduction

In recent years there have been a number of studies of the crystal anisotropy of ferrites[1], the temperature dependence of the anisotropy[2,3] and the domain structure of ferrite crystals[4-9].

In 1950 Bickford[2] used the microwave resonance absorption technique to determine the temperature dependence of the first anisotropy constant for natural magnetite. He found that with increase of the temperature to -80° the anisotropy constant decreases and then, with further warming of the specimen, increases somewhat.

The temperature dependence of the first anisotropy constant of cobalt ferrites was investigated by Perekalina & Askochenskii[3]. These authors showed that this dependence obeys the experimental Bryukhatov-Kirenskii law

$$K = K_0 e^{-aT^2}, \tag{1}$$

where K is the value of the first anisotropy constant at T°K, K_0 is the value of the constant at 0°K, and a is a constant. Recently, Turov & Mitsek[10] published a theoretical investigation of the temperature dependence of the anisotropy constant of ferrites.

In the present work, using the torque measurement procedure, we investigated the temperature dependence of the first magnetic anisotropy constant of single crystal iron-manganese ferrite concurrently with observation of its domain structure. Ferrite of this composition is typical of most monoferrites with the spinel structure; in it - in contrast to cobalt ferrite - the easy magnetization directions are parallel to the <111> axes.

Experimental Procedure

For preparing the specimens we used single crystals of manganese ferrite ($Mn\,Fe_2O_4$) with an excess of manganese (25% hausmannite - Mn_3O_4). The single crystal boules were grown by the Verneuil technique by A.A.Popova in the Institute of Crystallography of the USSR Academy of Sciences. These single crystal boules were turned down to form spheres from 4 to 8 mm in diameter.

For determining the first anisotropy constant and its temperature dependence we used the method of measuring the torque acting on the specimen in a uniform magnetic field produced by a rotatable electromagnet. The uniformity of the field was checked by the ballistic method. The electromagnet angles were set with the aid of a special vernier dial to within 0.5'. The torques were measured by means of an Akulov type anisometer (torquemeter) with a somewhat modified strain gage. The sensitivity of the anisometer was $1.3 \cdot 10^2$ erg/cm^3 per 1 mm scale. According to our estimates, the error in measuring the torques did not exceed 2%; the uncertainty in measuring the temperatures did not exceed 2°.

The easy magnetization axes were determined by means of a specially designed Cardan suspension. The torques were measured in the (100) plane.

First we recorded the curves for torque versus angle between the field and the [100] direction in different fields at room temperature and at liquid oxygen temperature. Then we recorded the variation of the maximum torque in the (100) plane with variation of the temperature during heating from -183° to +300° and

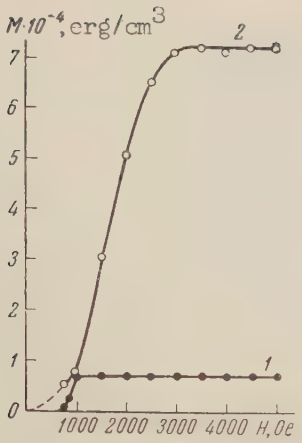

Fig.1. Variation of the maximum torque with the intensity of the external magnetic field: 1) at 22°, 2) at -183°.

subsequent cooling back to -183°. The field strength in these measurements was 5100 Oe, which insured technical saturation of the specimen.

The domain structure was observed in the (110) plane; to this end appropriate flats were ground and carefully polished, after which the specimens were etched by boiling in 30% sulfuric acid. For obtaining the powder patterns we employed the colloidal suspension technique developed by Elmore[11]. The powder patterns were observed and photographed by means of an MBI-6 microscope at linear magnifications of 117 and 234.

Experimental Results and Analysis

The torque curves recorded at both room and liquid oxygen temperature were regular sine curves with a period of $\pi/2$ (the main difference was that the low temperature curves had an appreciably greater amplitude). The fact that the torque curves recorded with clockwise and counterclockwise rotation of the field were displaced relative to each other indicated the presence of hysteresis losses in strong rotating fields.

The variation of the maximum torque in the (100) plane as a function of the magnetic field at 22° and -183° is shown in Fig.1. It will be seen that at 22° the torque is virtually nil in fields up to 750 Oe. This means, of course, that the Fe-Mn ferrite is virtually isotropic in fields to 750 Oe. In fields from 750 to 1000 Oe the torque increases, attaining a value of $0.71 \cdot 10^{-4}$ erg/cm^3 and then remains at this value with further increase of the field strength. Sharp increase of the torque at liquid oxygen temperature is observed in magnetic fields ranging up to 3000 Oe. It will also be evident from Fig.1 that with reduction of the temperature from 22° to -183° the torque increases by a factor of about 10.

Inasmuch as the torque measurements were carried out in the (100) plane, the value of the first anisotropy constant K_1 was calculated by means of the formula

$$M = \frac{K_1}{2} \sin 4\psi, \qquad (2)$$

where M is the torque (mechanical moment), ψ is the angle between the field H and the [100] direction. At $\psi = 22°30'$ the constant $K_1 = 2M$.

The temperature dependence of the first anisotropy constant is shown in Fig. 2. It will be seen that for our Fe-Mn ferrite K_1 is negative and decreases in absolute magnitude with increasing temperature in the range from -183° to +220°.

A plot of $\ln K_1$ versus T^2 is shown in Fig.3. The fact that the variation is linear indicates that the Bryukhatov-Kirenskii experimental law is valid for crystals of this type as well. Extrapolation of the straight line plot to absolute zero yields $K_0 = 17 \cdot 10^{-4}$ erg/cm^3.

Our observations of the domain structure indicate that the character of the structure depends on the direction of demagnetization of the specimen. In the case of demagnetization in the [110] direction the powder patterns on a (110) surface have the appearance of thick parallel lines oriented at right angles to one of the easy magnetization axes (Fig.4,a). Between the main heavy lines there is observed a secondary spike-type structure, which indicates that actually the specimen surface was inclined at a slight angle to the (110) planes.

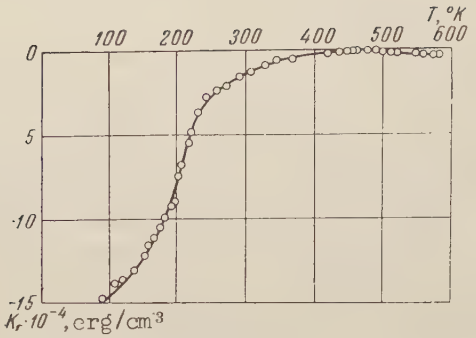

Fig.2. Variation of the first anisotropy constant with temperature.

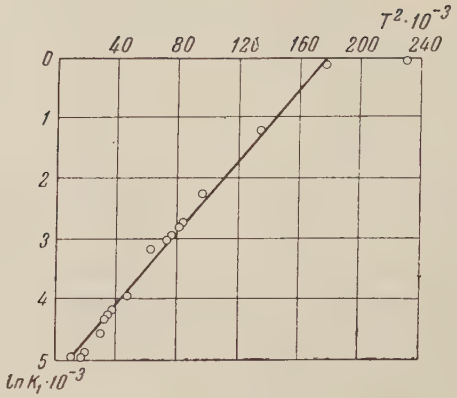

Fig.3. Variation of $\ln K_1$ with T^2.

No significant alteration of the domain structure is observed during magnetization in the [110] direction in fields up to 400 Oe (Fig.4,b). With further increase of the field to 600 Oe only the secondary structure changes (Fig.4,c). In the field range from 750 to 1000 Oe, however, there occurs a pronounced change in the domain structure (Fig.4,d & e). In this field interval there appear new walls, extending at right angles to the second direction of easy magnetization. A secondary spike-type structure is again observed between the new walls. In fields of about 1000 Oe (Fig.4,f) the process of formation of new walls terminates and the old walls disappear almost completely. The newly formed walls diffuse and disappear in a field of about 1300 Oe.

It must be noted that the new walls do not appear everywhere on the (110) surface. In areas where new walls do not appear, after demagnetization in the [110] direction there is established a domain structure analogous to the initial one. No change in the structure is observed with increase of the field to 723 Oe (except for some minor changes in the secondary spike-type structure). With further increase in the field strength the main lines (walls) diffuse at some points and then disappear completely at a field of about 1300 Oe. We did not observe any wall displacements.

Comparison of the variation in torque and the alteration of domain structure with increase of the field strength indicates that the greatest changes in domain structure are observed at field intensities corresponding to sharp increase of the crystal anisotropy.

It is impossible at present to propose any satisfactory model for either the domain structure or its variation with the field intensity.

We desire to express our deep gratitude to A.A.Popova for making available the single crystal ferrite specimens.

Institute of Physics,
Siberian Division of the
Academy of Science of the USSR,
"M.I.Kalinin" Institute of Nonferrous Metals &
Krasnoyarsk Pedagogical Institute

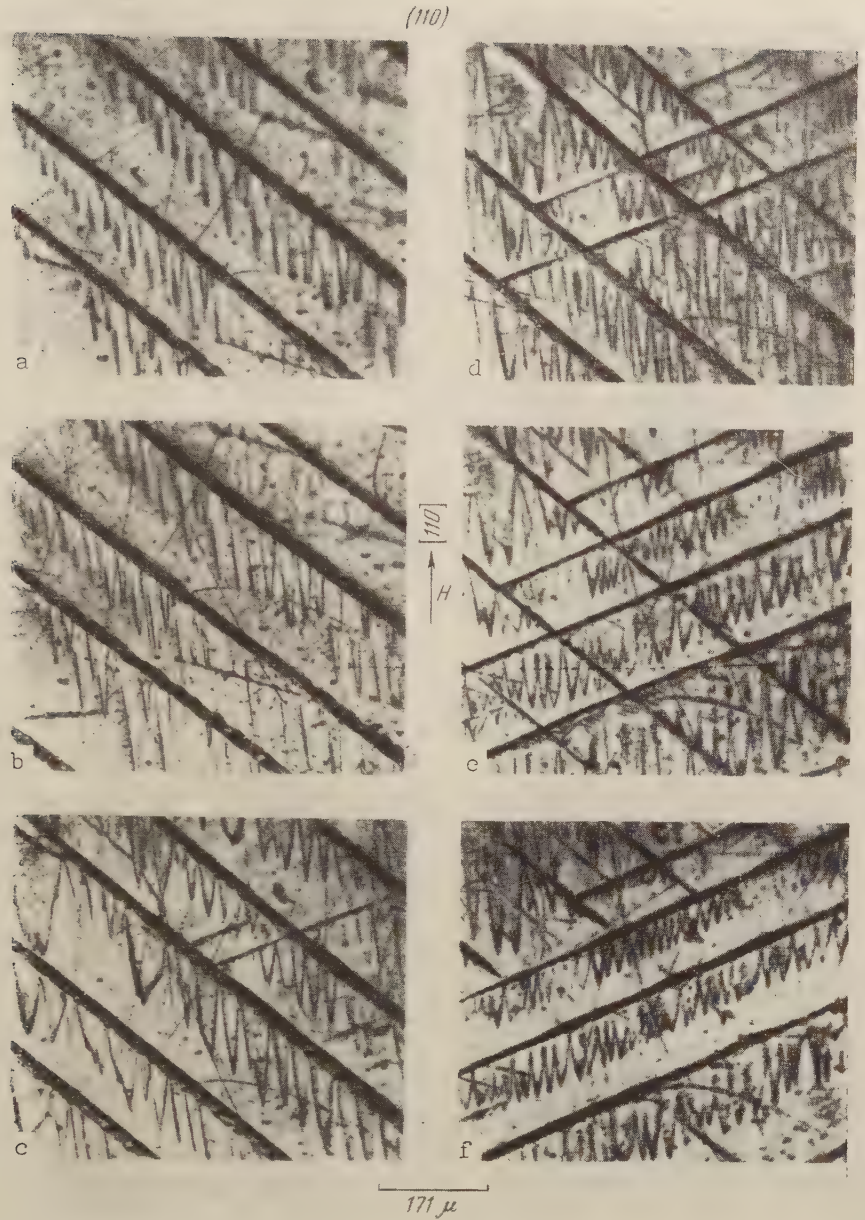

Fig.4. Domain structure on a (110) surface: a) H = 0, b) H = 400 Oe, c) H = 600 Oe, d) H = 760 Oe, e) H = 800 Oe, f) H = 1000 Oe.

References

1. R.M.Bozorth, E.F.Tilden & A.J.Williams, Phys.Rev., 99, 1788 (1955).
2. L.R.Bickford, Phys.Rev.,78, 449 (1950).
3. T.M.Perekalina & A.A.Askochenskii, in "Ferrity" (Ferrites, Conference reports on), Minsk, 1960.
4. L.F.Bates, D.J.Crail, P.M.Griffiths & E.D.Isaac, Proc.Royal Soc., A 253, 1 (1959).
5. A.W.Smith & G.W.Williams, Canad.J.Phys., 38, 9, 1187 (1960).

6. Ya.S.Shur & G.S.Kandaurova, in "Ferrity" (Ferrites, Conference reports on), Minsk, 1960.
7. V.D.Dylgerov & A.I.Drokin, Kristallografiya, 5, 6, 945 (1960). (Trans. Soviet Physics - Crystallography.)
8. I.E.Startseva & Ya.S.Shur, Fiz.metallov i metallovedenie, 2, 158 (1961). (Trans.Physics of metals & metallography.)
9. A.I.Drokin, V.D.Dylgerov & Yu.M.Zolotareva, Fizika tverdogo tela, 3, 2, 553 (1961). (Trans.Soviet Physics - Solid State.)
10. E.A.Turov & A.I.Mitsek, in "Ferrity" (Ferrites, Conference reports on), Minsk, 1960.
11. W.C.Elmore, Phys.Rev., 51, 10, 1092 (1938); 62, 486 (1942).

* * * * * * *

DETERMINATION OF THE CHARACTER OF THE MAGNETIC ANISOTROPY OF ALLOYS WITH SINGLE DOMAIN STRUCTURE FROM THEIR RESIDUAL MAGNETIZATION

- M.G.Luzhinskaya

1. Where high-coercivity ferromagnets with a single domain magnetic structure are concerned, a significant consideration is the character and nature of the magnetic anisotropy of the single domain formations, for it will be recalled that single domain magnetic structure leads to a large coercive force H_c only in the presence of a sufficiently large magnetic anisotropy. According to theory, there are three possible sources of magnetic anisotropy of single domain formations: the natural crystalline anisotropy K, anisotropy proportional to $\lambda\sigma$ (λ is the magnetostriction) and associated with the presence of anisotropy of internal stresses σ, and anisotropy of the shape of the single domain particles. In the case of most high-coercivity alloys it is generally impossible to establish which of these factors is responsible for the large value of H_c, inasmuch as the high coercivity state corresponds to a finely dispersed crystalline structure at the initial stage of structural transformations. It is impossible in practice to determine K and λ of the individual structural formations and the distribution of internal stresses. It is a risky and doubtful procedure to apply to individual structural formations the values of the constants obtained in measurements on bulk alloy specimens. The shape of the structural components can rarely be determined precisely if at all. In cases when the shape of the structural components is known, one must still determine whether it plays a dominant role.

One of the methods of determining the character of the anisotropy in materials with a single domain magnetic structure is comparison of the calculated and measured values of the relative residual magnetization $j_r = I_r/I_s$, where I_r is the absolute residual magnetization and I_s is the saturation magnetization.

According to the recent calculations of Wohlfarth & Tonge[1], in the case of uniform distribution in space of n directions of easy magnetization in each particle for a large number of chaotically oriented single domain particles j_r = 0.5, 0.74, 0.83 and 0.86 for n = 2, 4, 6 and 8, respectively.

In metallic ferromagnets there are known to be cases with n = 2 (uniaxial), n = 6 and n = 8 (cubic anisotropy). Uniaxial anisotropy may be due either to natural crystal anisotropy or to anisotropy of the stresses or shape of the ferromagnetic formations. Cubic anisotropy, apparently, cannot arise owing to stress

or shape anisotropy but is always associated with anisotropy of the cubic crystal lattice.

If a given alloy has a single domain magnetic structure and is isotropic, one can from the measured value of j_r judge of the number of directions of easy magnetization in the material. It must be borne in mind, however, that the above mentioned method of calculation of j_r does not take into account magnetic interaction between the individual single domain formations. If this interaction is appreciable, the results of calculation may be misleading.[2]

The purpose of the present work was to establish the character of the magnetic anisotropy in the high-coercivity alloys Alni and Vicalloy by comparing the measured and calculated values of j_r. It is known[3,4] that these alloys have a single domain magnetic structure. It has been shown for Alni alloy that its high coercive force is connected with uniaxial magnetic anisotropy.[5] As far as we know, there are no data in the literature regarding the magnetic anisotropy of Vicalloy.

2. In the case of Alni alloy (24.5% Ni, 13% Al, 3.5% Cu and 59% Fe) specimens the measurements were carried out on bars measuring 48 x 4 x 4 mm, cut from different sections of an ingot in two mutually perpendicular directions. The measurements were carried out in a solenoid and an electromagnet with and without armco iron bridging yokes designed to reduce the demagnetizing effect of the ends of the specimen. It was established that the magnetic properties of the initial casting are isotropic within the limits of the measurement error. The coercive force of the alloy was found to be 500 Oe. Measurements on ten different specimens yielded j_r = 0.5 (experimental uncertainty 5%). This value of j_r corresponds to the relative residual magnetization calculated for the case of single domain structure with uniaxial magnetic anisotropy.

The Vicalloy specimens were prepared of sheets 1 mm thick (composition: 12% V, 50% Co and 38% Fe) and sheets 0.6, 0.4 and 0.2 mm thick (composition: 11% V, 52% Co and 37% Fe). The specimens, measuring 140 mm in length and 4 mm in width, were cut at angles 0, 45 and 90° to the direction of rolling. The measurements were carried out in a solenoid with fields of up to 2700 Oe. The 2700 Oe field is sufficient for obtaining the maximum values of I_r for the given specimens. The value of I_s was found by extrapolation to an infinitely strong field.

Our measurements showed that Vicalloy sheets have a minor degree of texture. In all sheets the values of H_c and j_r in the direction of rolling are somewhat greater than in the direction perpendicular to that of rolling, but the difference does not exceed 10%. At an angle of 45° to the direction of rolling the values of H_c and j_r are intermediate between those for 0 and 90°. For the 1 mm thick sheet the value of H_c in the direction of rolling is 320 Oe; across the sheet 300 Oe. For the 0.2, 0.4 and 0.6 mm sheets H_c = 225-230 Oe in the direction of rolling and 205-220 Oe across the sheet. The value of j_r for all the specimens equalled 0.80-0.84 in the direction of rolling and 0.74-0.79 at right angles to the direction of rolling.

From the measured values of j_r it may be inferred that the magnetic anisotropy in Vicalloy cannot be purely uniaxial. In fact, it may be asserted that the dominant role in Vicalloy is played by cubic magnetic anisotropy associated with the natural crystalline anisotropy of the ferromagnetic α-phase, which has a body-centered cubic lattice.[6] According to the calculations of Tonge & Wohlfarth[7], in the presence of two forms of anisotropy - uniaxial and cubic - the influence of the former on the value of j_r should predominate. Our results, however, show that in Vicalloy uniaxial anisotropy does not predominate over cubic anisotropy.

In Alni alloy there also obtains cubic magnetic anisotropy associated with anisotropy of the crystal lattice, but here the predominant role is played by uni-

axial anisotropy of the single domain formations; this anisotropy is due to the shape of the structural components which are individual domains.[5]

As for the possible influence of magnetic interaction of the single domain formations on j_r, the agreement of our inferences regarding the magnetic anisotropy of Alni alloy with the results of other studies indicate that in the given alloy magnetic interaction between the formations does not play a significant role, at least where the value of j_r is concerned. In Vicalloy this interaction must be even weaker; we arrive at this conclusion in view of the following considerations. In Alni alloy in the high coercivity state both the phases present are ferromagnetic and differ little as regards their magnetic properties; in contrast, in Vicalloy one of the phases present is ferromagnetic, while the other is paramagnetic. The dimensions of the individual phase regions in both alloys are of the order of hundreds of angstroms[3,8]; the values of I_s for the two alloys are also close. Consequently, comparison of the measured value of j_r with the calculated value on the assumption that magnetic interaction between single domain formations is justified.

3. Thus by comparing the measured and calculated values of the relative residual magnetization in Vicalloy and Alni alloys we have substantiated the available data on the predominant role of uniaxial magnetic anisotropy in Alni alloy and have established that in Vicalloy the magnetic anisotropy is cubic in character and is associated with magneto-crystalline anisotropy of the ferromagnetic phase.

References

1. E.P.Wohlfarth & D.G.Tonge, Philos.Mag., 2, 1333 (1957).
2. E.P.Wohlfarth, J.phys.et radium, 20, 295 (1959).
3. E.P.Wohlfarth, Philos.Mag., Suppl., 8, 87 (1959).
4. Ya.S.Shur, M.G.Luzhinskaya & L.A.Shubina, Fiz.metallov i metallovedenie, 4, 54 (1957). (Trans.Physics of Metals & Metallography.)
5. E.A.Nesbitt, H.J.Williams & R.M.Bozorth, Appl.Phys., 25, 1014 (1954).
6. W.Köster & H.Schmid, Arch.Eisenhüttenwesen, 26, 345 (1955).
7. D.G.Tonge & E.P.Wohlfarth, Philos.Mag., 3, 536 (1958).
8. L.M.Magat, M.G.Luzhinskaya & Ya.S.Shur, Fiz.metallov i metallovedenie (In press). (Trans.Physics of Metals & Metallography.)

ON THE NATURE OF THE COERCIVE FORCE IN ALNICO ALLOYS

- A.S.Ermolenko & Ya.S.Shur

1. It is known[1,2] that alloys based on the Fe-Ni-Al system, which are extensively used for fabrication of permanent magnets, owe their properties to the presence in them, after appropriate heat treatment, of phases differing markedly as regards their magnetic attributes. These phases segregate as a result of decomposition of the supersaturated solid solution. In the state with maximum coercive force these phases are present in the form of finely dispersed segregations or formations that are anisotropic as regards shape. This leads to single domain magnetic structure of the alloy, which, in conjunction with the shape anisotropy, results in the high coercivity of the material.

In distinction to other disperse-hardening alloys used for permanent magnets, Fe-Ni-Al base alloys have the characteristic that the maximum coercive force in them is obtained not after rapid quenching from the temperature of the single phase state and subsequent annealing (hereinafter type I heat treatment), but after cooling from this single phase state temperature at a certain critical rate. Usually for obtaining the best characteristics additional annealing after cooling at the critical rate is required. We shall hereinafter refer to such heat treatment - cooling at a critical rate followed by annealing - as type II treatment.

It has been shown by Lifshits & L'vov[2,3] that in the case of type II heat treatment the decomposition of these alloys is a two step process. In the upper temperature interval there occurs a preparatory process, while actual final decomposition takes place in the lower temperature interval. As a result there is obtained a structure that cannot be obtained by type I heat treatment, which does not include the high temperature decomposition stage. Little as yet is known regarding the nature of the processes occurring during type I and II heat treatments and there is only scanty information on the difference between the structures formed. The available electron microscopic data[4,5] are scanty and contradictory.

In the present work we attempted to determine the reasons for the difference between type I and type II heat treatments by investigating the magnetic properties of single crystals of the alloy with the composition 24% Co, 14% Ni, 8% Al, 3% Cu and 51% Fe. The regularities characterizing the decomposition of this alloy are similar to those for alloys of the Fe-Ni-Al system, while the difference in properties after treatments I and II is particularly pronounced.

2. The single crystals were obtained by the method of collective recrystallization. The specimens were prepared in the form of disks 6 mm in diameter and 0.35 mm thick. The surface of the disks deviated by not more than 2° from the (100) planes. The orientation of the single crystals was determined by magnetic and x-ray diffraction studies. All the heat treatments were carried out in an atmosphere of argon.

The investigated magnetic characteristics and parameters (saturation magnetization and its temperature behavior, temperature dependence of the coercive force, torque curves and rotational hysteresis) were measured by means of a Williams type[6] magnetometer. The coercive force at room temperature was measured by the conventional ballistic procedure.

Specimen No.1 after heating to 1250° was quenched by contact with a cold metal surface and had a coercive force $H_c \leqslant 2$ Oe. Specimen No.2 was cooled from 1250° at a rate of ~1.5 degree/sec in the temperature interval from 950 to 700° and had $H_c = 220$ Oe. After this both specimens were annealed at 625°. Thus, in effect, specimen No.1 was subjected to type I heat treatment; specimen No.2 to type II heat treatment.

3. The curves in Fig.1 give the variation of the coercive force (upper curves) and the amplitude of the torque curves measured in a field of 16 600 Oe (lower curves) as a function of the heating time at 625°. It will be seen that the coercive force of specimen No.2 rapidly attains its limiting value of 430 Oe and then remains virtually constant. The coercive force of specimen No.1 after 60 hour annealing at 625° attains a value of 90 Oe.* The amplitudes of the torque curves of the two specimens become virtually equal after 54 hours heating at 625°, but with further heating the amplitude for specimen No.1 becomes even greater.

Fig.2 shows the variation of the amplitude of the torque curves with the intensity of the external magnetic field after different heat treatments. After quenching from 1250° (curve 1) the amplitudes are negative in the entire investigated field range and are only weakly dependent on the field strength. After cooling at the critical rate from 1250° (curve 2) the amplitude is positive in fields weaker than 800 Oe and negative in stronger fields. After 60 hours annealing at 625° (curves 3 & 4) the amplitudes are positive in the entire investigated field range.

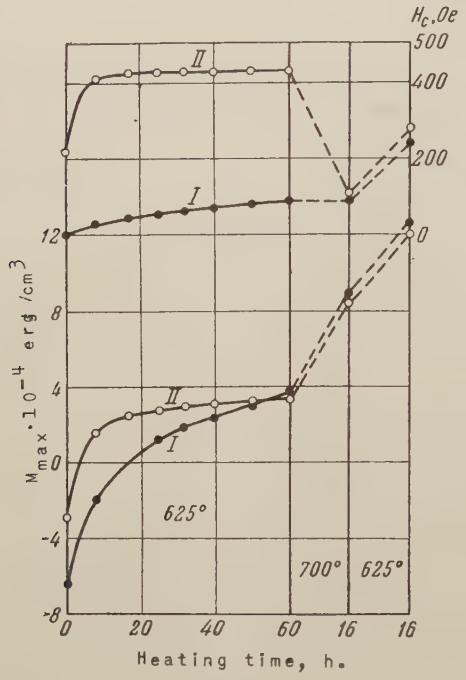

Fig.1

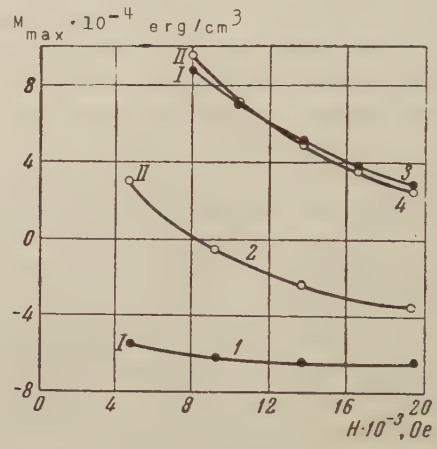

Fig.2

Fig.1. Variation of the coercive force H_c and amplitude M_{max} of the torque curves as a function of the time and temperature of annealing for type I and II heat treatments.

Fig.2. Variation of the torque curve amplitude with the intensity of the external field for single crystals subjected to different heat treatments: 1 - quenching from 1250°, 2 - cooling at critical rate from 1250°, 3 - same as 1 but followed by 60 hour annealing at 625°, 4 - same as 2 but followed by 60 hour annealing at 625°.

---

*It must be noted that this is not the maximum coercive force that can be obtained after type I heat treatment. Thus, additional heating at 700° with subsequent annealing at 625° leads to an appreciably higher coercive force (Fig.1). As was noted, however, the purpose of the present work was not to obtain the maximum coercive force, but to investigate the magnetic properties obtaining at a certain stage of annealing after slow and rapid cooling with a view to clarifying the characteristics of decomposition incident to different heat treatments.

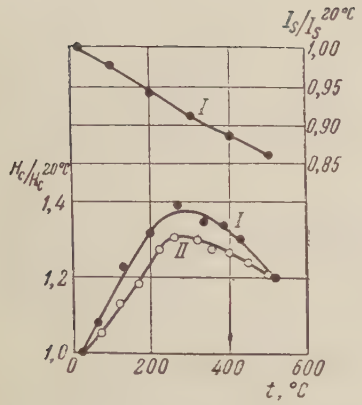

Fig.3

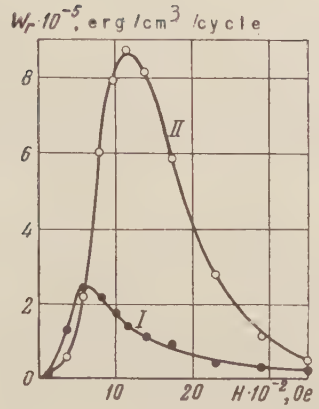

Fig.4

Fig.3. Temperature dependences of the relative saturation magnetization and coercive force after type I (specimen No.1) and type II (specimen No.2) heat treatment.

Fig.4. Variation of the rotational hysteresis loss as a function of the external magnetic field after type I (specimen No.1) and type II (specimen No.2) heat treatment.

The character of the torque curves obtained in our case is connected with the presence in the specimens of two forms of anisotropy: 1) magnetic crystallographic anisotropy, and 2) anisotropy associated with the shape of the phase segregations (stray field anisotropy). As was shown by Nesbitt et al[7] in recording torque curves the effect due to shape anisotropy is opposite in sign to the effect of crystallographic anisotropy and, moreover, with increase of the field at first increases and then decreases.

It will be evident from Fig.2 that in the process of decomposition of the alloy the role of stray field anisotropy increases: the curves shift from negative to positive values. After 60 hours heating at 625° the torque curves for the specimen subjected to treatments I and II (curves 3 & 4) have virtually equal amplitudes in a wide field range, whereas the coercive forces of the specimens differ by a factor of almost five.

Investigation after these two treatments of the temperature dependences of the saturation magnetization I_S and the coercive force H_C in the temperature range wherein these characteristics vary reversibly, showed that I_S and its temperature dependence are identical for both specimens, and the H_C versus T curves are similar but somewhat separated (Fig.3). As regards saturation magnetization the points of specimen No.2 coincided with the points of specimen No.1. The breaks in the I_S versus T plots and the peaks in the H_C versus T curves, which are associated with the Curie point of the weakly magnetic phase[8], occur at the same temperature (~300°) for both specimens. This indicates that the phases resulting from decomposition are identical or close in composition regardless of the type of heat treatment. The relative amounts of the phases also cannot differ greatly. It follows, therefore, that the magnetic crystallographic anisotropy of the alloy also cannot differ greatly in the course of heat treatments of type I and II. Consequently, the effective stray field anisotropy after type I treatment is not less than after type II treatment and the observed difference in coercive force cannot be explained by difference of the particle shape anisotropy.

Fig.4 shows the rotational hysteresis loss W_r versus external field strength recorded for specimens No.1 and 2 after 60 hour annealing at 625°. Rotational hysteresis has the same nature as ordinary hysteresis in an alternating magnetic field. Hence its magnitude in our case will depend on the individual coercive forces of the particles, and the shape of the W_r versus H curve will quantitatively characterize the volume distribution of particles as regards coercive force.

It will be evident from Fig.4 that the range of fields in which rotational hysteresis is observed is the same in the case of type I and type II heat treatments, which indicates that the coercive forces of the phase segregations lie in the same range. But the distribution of the segregations as regards values of the coercive force in this range is different. In the case of type II heat treatment the peak of the W_r versus H curve is shifted to the side of much stronger fields, which indicates the presence of a largervolume of segregations with a small coercive force in the case of type I heat treatment as compared with type II heat treatment.

4. Such distribution of the particles in H_c allows of explaining the great difference between the coercive forces of the specimens after treatments I and II despite the equal amplitudes of the torque curves. The effect of shape anisotropy is additive and may have the same value for different distributions of the segregations. The presence in the system of particles with a small coercive force reduces the coercive force of the specimen as a whole.

The principal reason for the different distribution of particles in H_c after different heat treatments may be due to difference of distribution of the particles in size. Other conditions being equal, the coercive force of particles is a function of their size, and the size dependence of H_c has a maximum.[1] Hence a certain optimum particle size is necessary for obtaining the maximum coercive force. Moreover, the magnitude of the shape anisotropy, which is directly connected with the magnitude of the coercive force, may also depend on the particle size if the shape of the particles changes in the process of growth.

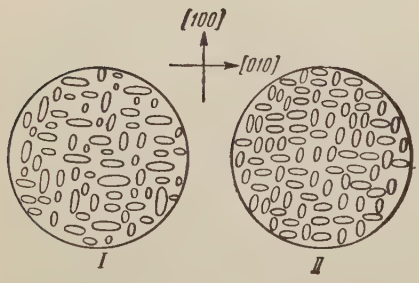

Fig.5. Schematic representation of the structure of single crystals after type I and II heat treatments.

We hypothesize that a distinctive feature of type II heat treatment is that it allows of obtaining a structure with segregations of approximately the same size and moreover with dimensions corresponding to a high coercive force (Fig.5). In contrast, as a result of type I heat treatment there is obtained a structure with a wide scatter of the particles as regards size with the result that the coercive force is much lower than in the case of type II heat treatment.

A possible structure formation mechanism is the following. It is known[9] that the maximum rate of formation of new phase nuclei in phase transformations in solids occurs in a temperature interval lying somewhat below the temperature of complete solubility. In the case of type II heat treatment cooling through this temperature interval occurs slowly enough to permit formation of a large number of new phase nuclei. But the time interval in which the nuclei form and grow is rather narrow so that the segregations are more or less uniform in size (narrow scatter of particles in size). On the other hand, in the case of quenching, cooling through the temperature interval of intensive new phase nucleation is rapid. Hence there is formed only a small number of new phase nuclei. At the temperature of subsequent annealing the rate of nucleation is low and the process is extended in time. Hence, on the one hand, the earlier formed nuclei have time to grow to large size and, on the other hand, there form new nuclei, i.e., there results wide scatter of the particles in size.

These characteristics of the decomposition of these alloys are explained by the fact that diffusion in them proceeds very slowly and redistribution of the particles in size at low temperatures is virtually impossible. Heating to a higher temperature (700°), obviously, makes such redistribution in size possible and

the difference between type I and type II heat treatments is obliterated, as will be evident from the high annealing temperature portion of the curves in Fig.1. In this case the W_r versus H curves (not shown) are virtually identical for both specimens.

Admittedly, the proposed explanation stands in need of experimental verification.

We desire to thank L.V.Smirnov for growing the single crystals and L.M.Magat for determining their crystallographic orientations.

Institute of the Physics of Metals,
Academy of Sciences of the USSR

References

1. E.P.Wohlfarth, Philos.Mag., Suppl., 8, 87 (1959).
2. B.G.Lifshits & V.S.L'vov, Vysokokoertsitivnye splavy (High-coercivity alloys), M., 1960.
3. B.G.Lifshits & V.S.L'vov (Abstract), Izv.AN SSSR, Ser.fiz., 21, 1232 (1957). (Trans.Bulletin, 21, 1223.)
4. N.N.Buinov & R.M.Lerinman, Doklady AN SSSR, 79, 69 (1951).
5. Yu.Skakov, Doklady AN SSSR, 79, 77 (1951).
6. H.J.Williams, Rev.Scient.Instrum., 8, 56 (1937).
7. E.A.Nesbitt, H.J.Williams & R.M.Bozorth, J.Appl.Phys., 25, 1014 (1954).
8. A.G.Clegg & M.McCaig, Proc.Phys.Soc.London, B, 70, 817 (1957).
9. J.S.Fisher, J.H.Hollomon & D.Turnbull, J.Appl.Phys., 19, 775 (1948).

CARBONYL IRON POWDERS

- V.L.Volkov, I.S.Tolmasskii & A.E.Fridenberg

The rapid growth of electronics has stimulated the need for development of new magnetic materials characterized by superior electromagnetic properties in a wide frequency range. Among such materials are magnetodielectrics (molded cores) made of various ferromagnetic powders[1], and of these the most important for high frequency applications are carbonyl iron powders.[2]

We recently established certain relations between the physical-chemical and electromagnetic properties of carbonyl iron and, on the basis of this, developed some new types of powder: low loss carbonyl iron (type KZh),[3] carbonyl iron-nickel powders with different nickel contents[4] and decarbonized carbonyl iron (type VKZh).

Table 1 lists the electromagnetic parameters of toroidal cores fabricated of these and other carbonyl powders. In Table 1 and below, we use the following notation: μ_0 - initial permeability, δ_{hR} - Rayleigh hysteresis loss factor, $\delta_{f\tau}$ - loss factor due to eddy currents and viscosity[5], δ_{0h} - initial hysteresis loss factor, and t.c.μ_0 - temperature coefficient of the initial permeability.

Table 1

Electromagnetic Parameters of Carbonyl Powders

Powder	Composition, %					μ_0	$\delta_{hR}\cdot10^3$	$\delta_{f\tau}\cdot10^3$	$\delta_{0h}\cdot10^3$	t.c.$\mu_0\cdot10^6$
	Fe	C	N	O	Ni					
(KZh) КЖ	97,29	0,95	0,86	0,90	—	11	0,3	2,5	0,20	175
(N-5) Н-5	94,99	0,01	—	—	5	22,3	4,3	5,2	0,60	120
(N-50) Н-50	49,99	0,01	—	—	50	24	0,95	3,3	0,82	100
(VKZh) ВКЖ	99,99	0,01	—	—	—	26	5,8	11	0,85	260

Table 2

Electromagnetic Parameters of Type KZh Carbonyl Iron Powders of Different Chemical Composition

Composition, %				μ_0	$\delta_{hR}\cdot10^3$	$\delta_{f\tau}\cdot10^3$	$\delta_{0h}\cdot10^3$	t.c.$\mu_0\cdot10^6$
Fe	C	N	O					
97,11	0,93	1,06	0,9	12,6	0,160	1,33	0,1	136
97,83	0,76	0,71	0,7	13,7	0,2	1,10	0,14	97
97,87	0,68	0,59	0,86	12,9	0,12	0,9	0,12	66
98,00	0,65	0,65	0,7	12,8	0,079	0,88	0,06	62
98,31	0,58	0,46	0,65	11,2	0,11	1,2	0,13	15

The electromagnetic parameters of type KZh powders with the same degree of dispersion (mean particle size $d_{av} = 2.27\text{-}2.37$ μ) but different compositions are listed in Table 2.

The particle size dependence of the electromagnetic parameters of type KZh carbonyl iron with the same chemical composition (~0.65% C, 0.65% N) is given in Table 3.

Curves illustrating the influence of the presence of nonspherical particles (irregular fragments and particles with bulbous structure) in type KZh powders[16] on the magnetic loss tangent of the molded specimens are shown in Fig.1.

The frequency dependences of the magnetic loss tangent of cores of two carbonyl iron powders are shown in Fig.2.

Table 3

Electromagnetic Parameters of Type KZh Carbonyl Iron Powders of Different Grain Size

d_{av}, μ	μ_0	$\delta_{hR} \cdot 10^3$	$\delta_{f\tau} \cdot 10^9$	$\delta_{0h} \cdot 10^3$	t.c. $\mu_0 \cdot 10^6$
1,86	10,1	0,05	0,60	0,12	—25
2,27	12,8	0,079	0,88	0,06	31
2,65	13,4	0,11	1,17	0,20	52

Properties of the Different Types of Carbonyl Powder

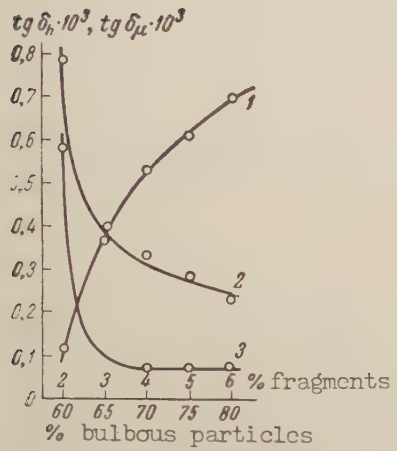

Fig.1. Dependence of magnetic loss tangent on percentage of irregular fragments and bulbous particles contained in powder: 1 - dependence of tan δ_μ on percentage of fragments; 2 - dependence of tan δ_μ on percentage of bulbous particles; 3 - analogous dependence for tan δ_h.

Measurements have shown (Table 1) that the initial permeability of type KZh powder is well below that of powders of types VKZh, N-5 and N-50. This difference is explained by the much larger contents of carbon and nitrogen (in the form of iron carbide and nitride) in the KZh powders, as well as the bulbous structure of the particles, which inhibits domain wall motion in the applied magnetic field.

Decarbonization of carbonyl iron produces a substantial increase of the magnetic losses. For example, the eddy current loss in type VKh powder is five times and the hysteresis loss twelve times the equivalent losses in type KZh powder. That this is a consequence of break up of the regular bulbous structure of carbonyl iron is clearly evinced by the curves of Fig.1, which show the dependence of tan δ_μ and tan δ_h on the number of particles with a bulbous structure.

It is also evident from Table 1 that the losses in carbonyl iron-nickel powders (type N-50 in particular), as compared to type VZKh, are appreciably lower, a fact which is explained by the reduction in conductivity as a result of alloying the iron with nickel.[7] The decarbonized powders, in contrast to the type KZh powder, are characterized by a high value of the t.c. μ_0 apparently as a result of enhanced domain wall motion owing to elimination of the impurities.

The electromagnetic parameters of type KZh powders are determined to a considerable extent by their chemical composition and particle size. Our investigations of a group of these powders with the same average particle size (~3 μ) and different chemical compositions (Table 2) show that as the percentage of carbon and nitrogen is reduced, the hysteresis loss falls off to a certain minimum value. Further reduction of the impurity content leads to increase of the hysteresis and eddy current losses as the result of reduction in number of particles with bulbous structure.

It is further apparent from Table 2 that a reduction of the impurity content of type KZh powder is accompanied by a decrease in the t.c. μ_0. This is a result of change in the conditions of preparation of the powder. Strongly carbonized powders are obtained at a higher dissociation temperature of iron pentacarbonyl,

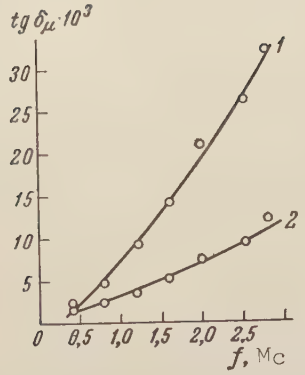

Fig.2. Frequency dependence of tan δ_μ for carbonyl iron magnetodielectrics with the following impurity contents: 1 - 0.93% C & 1.06% N; 2 - 0.58% C & 0.76% N.

which reduces the stresses that arise in the crystal lattice during formation of the powder grains. This ultimately leads to an increase of the

An increase in the particle size of type KZh powders with a given composition leads to an increase of the hysteresis and eddy current losses and an increase of the t.c. μ_0; this is plainly evident from Table 3. The greater hysteresis loss is explained[8] by an increase in the microeddy currents induced by domain wall motion in the corresponding volume of the ferromagnet. The higher value of the t.c. μ_0 may be attributed to reduction of the stresses in the crystal lattice with growth in particle size. The higher losses associated with increase in the number of irregular fragments (curve 1, Fig. 1) are a result of impairment of the insulation between particles in the process of compacting the core, i.e., formation of intergranular contacts as a result of friction.

It may be noted that the curves of Fig.2 substantiate the existence of impurity-induced magnetic viscosity in carbonyl iron.

References

1. L.K.Rabkin & N.N.Shol'ts, Magnetodielektriki i ferrokatushki (Magnetodielectrics and iron core coils), M., 1949.

2. A.Z.Mittasch, Z.angew.Chem., 41, 829 (1928).

3. V.L.Volkov, A.E.Fridenberg & I.S.Tolmasskii, Otchet organizatsii p/ya 4019, 1959.

4. V.L.Volkov, M.V.Ivashova & I.S.Tolmasskii, Otchet organizatsii p/ya 4019, 1958.

5. K.M.Polivanov, L.N.Kolli & L.P.Soboleva, Izv.AN SSSR Ser.fiz., 23, 311 (1959). (Trans.Bulletin 23, 302.)

6. A.A.Petrova, N.A.Tsvetkova, A.E.Fridenberg & I.S.Tolmasskii, Doklad na Vsesoyuznoi konferentsii po elektronnoi mikroskopii (Report presented at the All-Union Conference on Electron Microscopy), Leningrad, 1960.

7. R.M.Bozorth, Ferromagnetism, N.Y., 1951.

8. C.E.Richards, Post Office Eng.Res.Station, 1952.

INVESTIGATION OF ROTATIONAL HYSTERESIS IN COLD ROLLED AND RECRYSTALLIZED NICKEL

- N.L.Bryukhatov & N.A.Grinchar

There have been numerous investigations devoted to the energy dissipated in rotational hysteresis: investigators have measured the rotational hysteresis loss in polycrystalline materials[1-9] and in single crystals[10-16]. In these studies, however, there were not taken into account such factors as internal stresses and the orientation of the crystallographic axes relative to the rotating field, factors which, as our experiments show, have a strong influence on the magnitude of the loss.

Experimental results

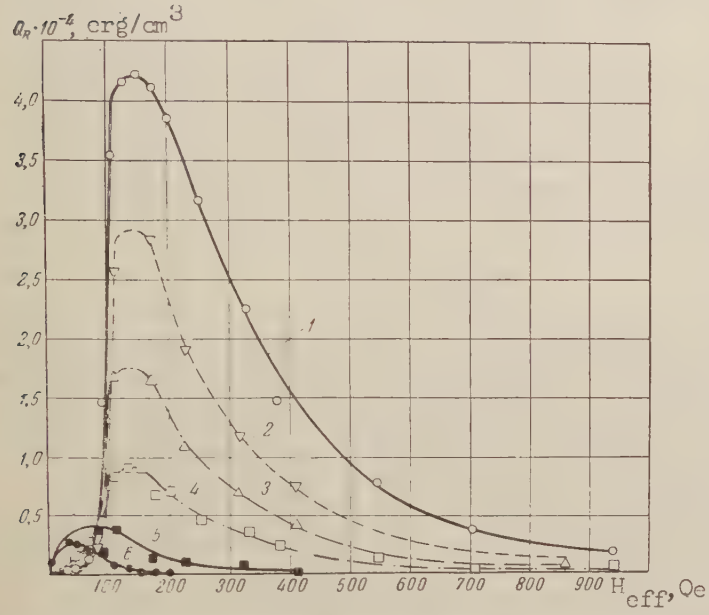

Fig.1. Experimental rotational hysteresis loss curves: 1) specimen No.73 prior to annealing, 2) specimen No.57 after annealing at 365°, 3) specimen No.62 after annealing at 370°, 4) specimen No.73 after annealing at 380°, 5) specimen No.17 with cube texture after annealing at 1100°, 6) specimen No.74 with cube texture after annealing at 1120°.

The measurements were carried out on specimens of high purity electrolytic nickel: total impurity content 0.03% including 0.012% cobalt. The nickel was rolled at low pressure, the total reduction being 90% as a result of 200 passes. As a result of such cold rolling there is realized in high purity nickel "cold roll texture" with uniform distribution of the crystallites among the (110) [112] and (112) [111] groups and there are induced internal stresses.[17,18] So-called "cube oriented texture" (hereinafter "cube texture") was formed as a result of collective recrystallization in specimen No.17 after 2 hour vacuum annealing at 1100° and in specimen No.74 after 2 hour annealing at 1120°. The specimens were in the form of disks 15 mm in diameter and 0.125 mm thick.

The torque curves were recorded on a string torquemeter.[19] The stationary magnetic field was produced in the plane of the disk by an electromagnet. By successive rotations, the disks were set at different angles of the rolling direction relative to the magnetic field. As usual, the values of the torque were determined from the torsion of the calibrated filament necessary to compensate the torque produced by the field.

The value of the rotational hysteresis loss was determined by planimetric measurement of the areas between the torque curves recorded for clockwise and counterclockwise rotation.

We investigated three specimens cut from the same sheet of cold rolled nickel. For each of these specimens prior to annealing we recorded torque curves at room temperature and on the basis of these plotted the rotational hysteresis loss as a function of the effective field H_{eff}. These curves were very similar in character (Fig.1). Further, each of the specimens was annealed in vacuum for half an hour at different temperatures. As a result of this annealing, which relieved

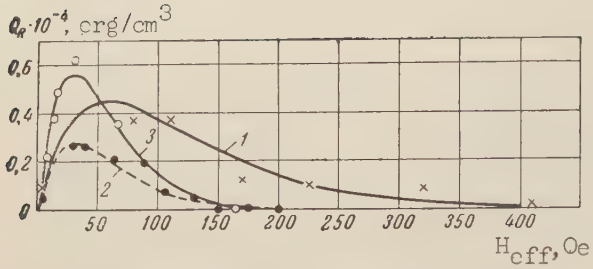

Fig.2. Experimental hysteresis loss curves plotted to an enlarged scale: 1) specimen No.17 with cube texture, 2) specimen No.74 with cube texture, 3) nickel single crystal. Losses in the (100) plane[11].

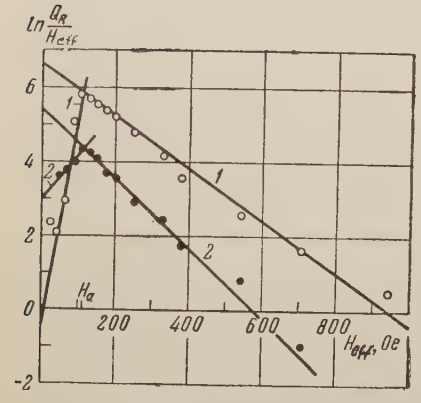

Fig.3. $\ln(Q_R/H_{eff})$ versus H_{eff}: 1) specimen No.73 prior to annealing, 2) specimen No.73 after annealing at 380°.

the internal stresses to different degrees[17,18], the rotational hysteresis losses, again measured at room temperature, were significantly reduced, the decrease being greater for higher annealing temperatures (see Fig.1). The lowest losses were obtained for the two disks with cube texture (curves 5 & 6). Noteworthy is the pronounced difference between curves 1-4 (cold rolled nickel) and curves 5-6 (cube texture obtained as a result of high temperature annealing). In Fig.2 we show the loss versus effective field curves for the cube texture specimens (curves 1 & 2) to an enlarged scale and for comparison the data for a nickel single crystal from Ref. 11 (curve 3 - nickel single crystal in the form of a sphere, for which the losses were determined in the plane parallel to a cube face).

Discussion

The phenomenon of rotational hysteresis is usually described in terms of lag of the magnetization vector I_s behind the external field in the rotating ferromagnetic specimen. Thus, Gans & Loyarte[4] represent the angle of lag of the induction vector behind the effective field as a function of the induction B. Akulov[20] showed that the greatest hysteresis loss should correspond to transition of the spin from coupling with the lattice to coupling with the magnetic field. Experimental data on investigation of Barkhausen jumps incident to magnetization reversal in rotating fields in single crystals[11,21-24] and in polycrystalline materials[25,26] show that these jumps correspond to transverse flip of whole complexes of spins. It follows from the work of Brion[26] that at first there occur individual large jumps and then with increase of the field the number of such jumps increases but the jumps become smaller. Degtyarev & Dylgerov[24] showed that rearrangement of the domain structure incident to magnetization reversal in rotating fields occurs by jumps.

These effects can be explained by splitting of the total spin of a region of spontaneous magnetization into spin complexes, coupled in different ways with the crystal lattice (see below). Analysis of the experimental data for specimens Nos. 73, 57 and 62 (curves 1,2,3 & 4 in Fig.1) leads to the following empirical relationship

$$Q_R = Ae^{-BH}H. \qquad (1)$$

This is illustrated by the plot for specimen No.73 in Fig.3. Similar plots were obtained for specimens Nos.57 and 62. In Fig.4 we show the curves plotted on the basis of relationship (1) for these specimens together with the experimental points.

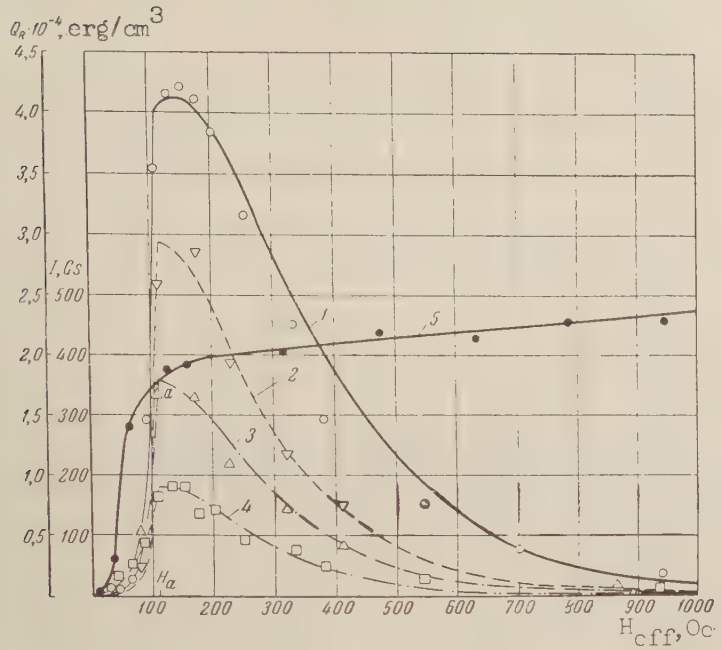

Fig.4. Rotational hysteresis loss curves plotted on the basis of relationship (1) and experimental points: 1) specimen No.73 prior to annealing, A = 799 G, B = 0.00714 G^{-1}, 2) specimen No.57 after annealing, A = 722 G, B = = 0.00907 G^{-1}, 3) specimen No.62 after annealing, A = 455 G, B = 0.00926 G^{-1}, 4) specimen No.73 after annealing, A = 226 G, B = 0.00923 G^{-1}; 5) magnetization curve for cold rolled nickel.

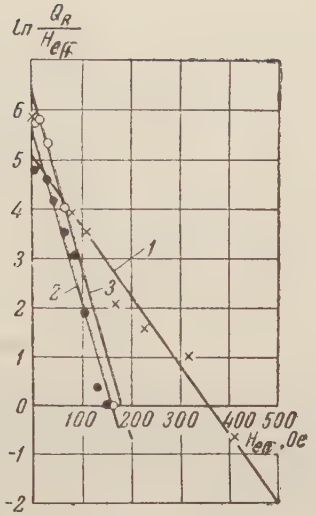

Fig.5. $\ln(Q_R/H_{eff})$ versus H_{eff}: 1) specimen No.17 with cube texture, 2) specimen No.74 with cube texture, 3) nickel single crystal.

In the same figure we give the magnetization curve for cold rolled nickel. It will be seen that relationship (1) satisfactorily describes the field dependence of the hysteresis loss beginning with the "anisotropy point" on the magnetization curve, corresponding to the region of greatest loss. For specimens with cube texture and for a spherical single crystal nickel specimen relationship (1) describes the field variation of the losses beginning with the weakest fields, as will be evident from Figs.5 and 2. The values of the coefficients A and B are given in the caption under Fig.4.

Statistical distribution of spin complexes as regards coupling with the crystal lattice

Because of splitting of the total spin of a region of spontaneous magnetization into spin complexes the effect of rotational hysteresis at any given value of the magnetic field must correspond to the state of dynamic equilibrium between the group of spins entrained by the crystal lattice and the spin complexes breaking away from the lattice and "latching on" to the magnetic field upon attainment of a certain limiting lag angle ψ. This is the mean angle of lag of the split spin vector behind the effective magnetic field. The number of spin complexes undergoing this switch or transition within a given time interval determines the magnitude of the irreversible jump and, consequently, the magnitude of the hysteresis loss. Assuming that the number of such complexes is characterized by the Boltzmann distribution law, we obtain

$$N_1 = Ne^{-\frac{I_s \cos\psi}{NkT}H}, \tag{2}$$

where N is the number of complexes per unit volume (1 cm^3) brought to the metastable state by the rotating magnetic field, N_1 is the number of complexes receiving an activation energy $-\frac{I_s}{N}\cos\psi H$ for breaking the coupling with the lattice in the given rotating field at the mean value of the lag angle ψ, and H is the effective field.

The total torque acting on the N_1 complexes is

$$M = \frac{I_s}{N}\sin\psi H N_1. \tag{3}$$

In the torque measurements it is balanced by torsion of the suspension filament. The work performed by this torque in rotating the disk through an angle $\alpha = 2\pi$, i.e., the rotational hysteresis loss per cycle, equals

$$Q_R = \int_0^{2\pi} M\, d\alpha, \tag{4}$$

whence

$$Q_R = 2\pi I_s \sin\psi e^{-\frac{I_s\cos\psi}{NkT}H} H. \tag{5}$$

Equation (5) corresponds to relationship (1). Thus, using the experimental data to evaluate the constants A and B one can determine the number N and the mean lag angle ψ. Thus, for example, for polycrystalline cold rolled nickel

	№ 73	№ 57	№ 62	№ 73 Annealed
ψ	14°14′	13°15′	8°20′	4°10′
N	$1.69\cdot10^{18}$	$1.34\cdot10^{18}$	$1.33\cdot10^{18}$	$1.35\cdot10^{18}$

For specimens with cube texture and a spherical nickel single crystal:

	№ 17	№ 74	Single crystal
ψ	4°	4°40′	10°
N	$7.2\cdot10^{17}$	$3.6\cdot10^{17}$	$3.5\cdot10^{17}$

The experimental results (Figs.1 & 2) show that splitting of the domain spins into complexes, transition of them into the metastable state and their activation begin earliest and proceed most easily in single crystals and single crystal mosaics with rotation of the magnetic field in the plane parallel to the cube face. In this case noticeable losses begin in very weak fields (~3 Oe) and are due to transverse flip of the spin complexes between the easy magnetization axes, i.e., the diagonals of the cube not lying in the plane of rotation of the magnetic field. In the case of nickel specimens with cold roll texture and in the presence of internal stresses spin splitting and transverse spin flips are hindered despite the fact that there are eight directions of easy magnetization in the plane of rotation of the magnetic field. As a result, the rotational hysteresis loss in weak fields is nil, and the loss begins to grow only when the internal stresses are relieved by annealing. Rapid growth of the hysteresis loss begins in fields corresponding to the "anisotropy point" on the magnetization curve. In this range of fields there begin the processes of domain splitting, transition of the spin complexes into the metastable state, and, accordingly, the hysteresis loss begins to grow.

The field dependence of the hysteresis loss for specimens with cold roll texture (Figs.3 & 4) can be described by the empirical relationship

$$Q_R = ae^{bH}H. \tag{6}$$

The parameters a and b determined from the experimental data, have the following values:

	№ 73	№ 57	№ 62	№ 73 Annealed
a, Gs	0.273	0.065	6.090	9.400
b, Gs^{-1}	0.066	0.074	0.029	0.020

Equation (6) can be expanded in a series in powers of H:

$$Q_R = aH + abH^2 + \frac{ab^2}{2}H^3 + \frac{ab^3}{3}H^4 + \ldots \tag{7}$$

In view of the fact that the parameter b is small for weak fields, one need retain only the first three terms, which is in agreement with the results obtained by Akulov & Elkina[6-8], who showed that in weak fields, for which Rayleigh's formulas are valid, in a magnetically uniaxial ferromagnetic crystal, in the absence of "transverse inversion", the loss in a rotating magnetic field occurs due to longitudinal magnetization reversal and increases in proportion to H^3.

Moscow Institute of Railway Transport Engineers

References

1. M.Beattie, Philos.Mag., 1, 642 (1901).
2. P.Weiss & V.Planner, J.de Phys., 7, 5 (1908).
3. A.Perrier, Arch.d.Sci.Phys.et nat., 28, 5; 119; 258 (1909); A.Perrier, J. de Phys., 9, 785 (1910).
4. R.Gans & R.Loyarte, Arch.Elektrotechnik, 3, 139 (1915).
5. F.Brailsford, J.Inst.Electr.Engrs., 83, 566 (1938); 84, 399 (1939).
6. N.Akulov & T.Elkina, Doklady AN SSSR, 59, 1085 (1948).
7. T.Elkina, Zhur.eksp.i teor.fiz., 20, 84 (1950).
8. T.Elkina, Vestnik, Moscow State Univ., Phys.-Math.Series, 8, 95 (1952).
9. V.Drozhzhina, R.Yanus & V.Vershinina, Izv.AN SSSR, Ser.fiz., 16, 695 (1952).
10. P.Weiss & J.Kunz, J.Phys., 4, 847 (1905).
11. A.Baskakov & N.Bryukhatov, Zhur.eksp.i teor.fiz., 9, 984 (1939).
12. P.Sarapkin, Izv.AN SSSR, Ser.fiz., 16, 688 (1952).
13. V.Vtyurin, Ibid., 16, 690 (1952).
14. N.Bryukhatov, Ibid., 21, 1268 (1957). (Trans.Bulletin, 21, 1257.)
15. L.Kirenskii, N.Sudakov & L.Slobodskoi, in "Magnitnaya struktura ferromagnetikov" (Magnetic structure of ferromagnets), M., 1060.
16. N.Narovskaya, Izv.AN SSSR, Ser.fiz., 22, 1200 (1958).(Trans.Bulletin, 22, 1194.)
17. N.Bryukhatov, N.Grinchar & I.Ekamasov, Ibid., 22, 1237 (1958). (Trans. Bulletin, 22, 1229.)
18. N.Bryukhatov & N.Grinchar, Doklady AN SSSR, 126, 990 (1959). (Trans. Soviet Physics - Doklady.)
19. N.Akulov & N.Bryukhatov, Zhur.eksp.i teor.fiz., 3, 59 (1933); N.Bryukhatov, Zavodskaya laboratoriya (Industrial lab.), 10, 42 (1933).
20. N.Akulov, Uch.zapiskii (Scientific notes), Moscow State University, No.2, 137 (1934); N.Akulov, Ferromagnetizm (Ferromagnetism), M., 1939.

21. F.Beck & L.McKeehan, Phys.Rev., 42, 715 (1932).
22. L.McKeehan & R.Clash, Phys.Rev., 45, 839 (1934).
23. R.Clash & F.Beck, Phys.Rev., 47, 158 (1935).
24. I.F.Degtyarev & V.D.Dylgerov, in Magnitnaya struktura ferromagnetikov (Magnetic structure of ferromagnets), M., 1960.
25. R.Bozorth & J.Dillinger, Phys.Rev., 41, 345 (1932).
26. H.Brion, Ann.Physik, 15, 167 (1932).

* * * * * * *

ROTATIONAL HYSTERESIS OF MAGNETOSTRICTION IN FERROMAGNETS

- L.V.Kirenskii & V.S.Afoshin

Magnetostriction λ of ferromagnets is a multiple valued function of the magnetic field H, the external elastic stress σ, the temperature T and the angle φ between the field vector and some arbitrarily chosen direction in the crystal:

$$\lambda = f(H, \sigma, T, \varphi).$$

The fact that λ is not a single valued function of the enumerated parameters is evinced by hysteresis of the magnetostriction. Different forms of hysteresis are observed, depending on the choice of fixed parameters. Thus if H, σ and T are constant, the magnetostriction will be a multiple valued function of φ. In this case by analogy with rotational hysteresis of magnetization one can speak of rotational hysteresis of magnetostriction (hereinafter RHM). In the present work we investigated RHM in a polycrystalline nickel specimen reduced by rolling from a thickness of 3.3 mm to 1 mm. The specimen was in the form of a disk 18 mm in diameter and was annealed in vacuum at 1100°. The RHM was determined from the change in magnetostriction with rotation of the field from the chosen initial setting 360° clockwise and counterclockwise, i.e., was taken as $\Delta\lambda = \lambda_2 - \lambda_1$, where λ_1 is the magnetostriction recorded with rotation of the field clockwise and λ_2 the magnetostriction for counterclockwise rotation. We measured the RHM as a function of H for different values of the angle φ and as a function of φ at fixed values of the field H.

Inasmuch as there has been only one earlier investigation of RHM,[1] we deem it desirable to start by defining the quantities by means of which one can characterize RHM; these quantities are the following:

1) $\Delta\lambda$, the difference between the initial and final values of magnetostriction over a complete cycle, and

2) the average (over the area of the curves) value of RHM given by the relation

$$(\Delta\lambda)_{av} = \frac{1}{2\pi}\int_0^{2\pi} |\Delta\lambda| \, d\varphi,$$

or its relative value $(\Delta\lambda)_{av}/\lambda_o$, where λ_o is the maximum value of the magnetostriction in the $\varphi = 0$ direction, agreeing with the direction of rolling.

The measurement results are presented in the accompanying figures.

Fig.1 shows the field dependence of $\Delta\lambda$ for different angles φ between the direction of measurement and the direction of the field. It will be evident from Fig.1 that with increase of the field the absolute value of $\Delta\lambda$ increases to a

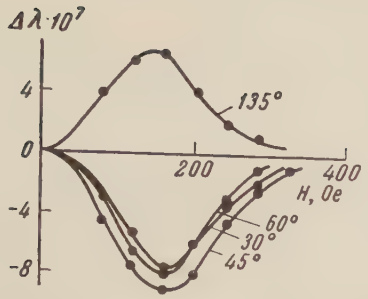

Fig.1. Field dependence of RHM at different angles φ between the direction of measurement and the direction of the field.

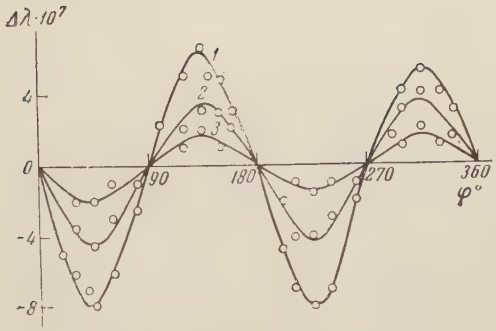

Fig.2. Variation of RHM with φ in different fields: 1 - 200 Oe, 2 - 240 Oe, 3 - 280 Oe.

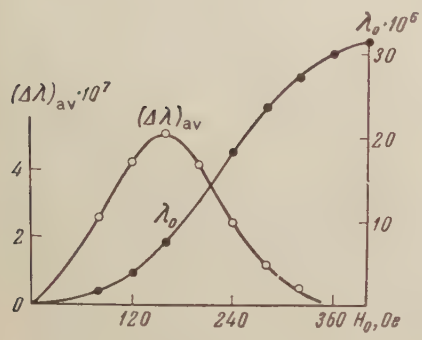

Fig.3

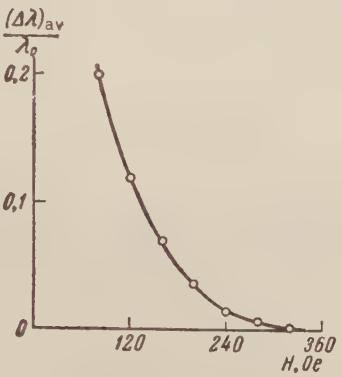

Fig.4

Fig.3. Field dependences of the mean rotational hysteresis of magnetostriction and longitudinal magnetostriction in the direction of rolling.

Fig.4. Field dependence of the relative RHM.

maximum at H = 160 Oe. With further increase of the field $\Delta\lambda$ falls off, dropping virtually to zero at H = 360 Oe. The maximum value of $\Delta\lambda$ at $\varphi = 45^\circ$ and H = 160 Oe is $9\cdot10^{-7}$, which amounts to less than 2.5% the saturation magnetostriction of nickel. For angles from 0 to 90° $\lambda_1 < \lambda_2$, i.e., $\Delta\lambda$ is negative, while for angles from 90° to 180° $\Delta\lambda$ is positive. For angles from 180° to 360° the alternation in sign repeats (even effect).

Fig.2 shows the variation of RHM with angle in different magnetic fields. The figure shows the curves only for H = 200, 240 and 280 Oe; analogous curves were recorded at other field values. It will be evident from Fig.2 that $\Delta\lambda$ is a periodic function of φ and that the period of this function is equal to the period of variation of the magnetostriction, i.e., 180°. The crest values of $\Delta\lambda$ depend on H. Thus, for example, at H = 200 Oe, $\Delta\lambda_{crest} = 8\cdot10^{-7}$; at H = 280 Oe, $\Delta\lambda_{crest} = 2\cdot10^{-7}$.

The variation of $(\Delta\lambda)_{av}$ with H is shown in Fig.3. The indicated values were obtained by averaging $\Delta\lambda$ for different angles φ at the given field value. With increase of the field $(\Delta\lambda)_{av}$ increases from 0 to maximum value of $5\cdot10^{-7}$ at H = = 160 Oe, and then falls off, going virtually to zero at H = 360 Oe. In Fig.3 we also give the field dependence of the longitudinal magnetostriction in the direction of rolling (φ = 0).

Fig.4 shows the field variation of $(\Delta\lambda)_{av}/\lambda_o$.

It is interesting to note that the shape of the $\Delta\lambda = f(H)$ and $(\Delta\lambda)_{av}/\lambda_o = f(H)$ curves is in quantitative agreement with the shape of the corresponding curves for temperature magnetic hysteresis.[2]

Rotational hysteresis of magnetostriction as a result of ambiguity of the domain structure

Hysteresis effects in ferromagnets are generally explained by irreversible changes of the domain structure. Comparing the character of the technical magnetization curve with the field variation of $\Delta\lambda$, we note the following. In fields where the magnetization occurs owing to reversible wall displacements the value of $\Delta\lambda$ or $(\Delta\lambda)_{av}$ (like the hysteresis of any other quantity) is very small. With increase of the field, the relative importance of irreversible boundary displacements increases; accordingly, the RHM also increases (Figs.1 & 3) to a certain maximum value, which is in agreement with present day concepts regarding the magnetization mechanism in ferromagnets.

In strong fields the role of displacement processes is diminished, which leads to decrease of the RHM. Finally, in the field region where rotation processes predominate RHM vanishes.

The observed regularities of rotational hysteresis of magnetostriction are consistent with modern theories of hysteresis effects.

Krasnoyarsk pedagogical Institute

References

1. L.V.Kirenskii, A.Ya.Vlasov, N.I.Vtyurin, A.I.Drokin, V.F.Ivlev & R.I. Tukalov, Izv.AN SSSR, Ser.fiz., 21, 1262 (1957). (Trans.Bulletin, 21, 1251.)

2. D.A.Laptei, Izv.vyssh.uchebn.zaved.,Fizika (Bulletin of Higher Schools, Physics), No.1, 136 (1959).

CRYSTAL AND MAGNETOELASTIC ANISOTROPY AND ITS TEMPERATURE DEPENDENCE IN IRON-NICKEL SINGLE CRYSTALS

- I.M.Puzei

In earlier studies[1,2] we found that the sign of the anisotropy constant in nickel and invar changes at high temperatures. This discovery stimulated the present investigation aimed at more detailed determination of the temperature variation of the anisotropy constant in iron-nickel single crystals in the high temperature region and at elucidating the physical reasons for the change in sign of the constant.

The first part of the study was carried out using spherical single crystal specimens grown from the melt by slow cooling. The experimental procedure has been described earlier and hence will not be detailed here. The specimens were cooled rapidly after high-temperature annealing.

Fig.1 shows the variation of the anisotropy constant of nickel in the temperature range from 160 to 375° (curve 1). It will be seen that at 215° the constant changes sign and that it falls to zero at the Curie point.

The analogous dependence for iron-nickel alloy with 87.8% Ni is shown in Fig.2. In this alloy the temperature at which the constant changes sign is already 444°. There is good reason to assume that with decrease of the nickel content down to 85-82% the anisotropy constant will change sign at ever higher temperatures.

The temperature dependence of the anisotropy constant of invar (36% Ni) is shown in Fig.3. In this alloy the constant changes sign at 100°.

Fig.4 shows the analogous curve for a single crystal specimen of alloy with 50% Ni. It will be seen that this alloy becomes isotropic at a temperature of 425°. The plot at the right gives a section of the same curve to a reduced scale. It may be assumed that with increase of the nickel content above 50% the temperature of isotropy will rise.

Thus, it may be said that in the region of the face-centered phase in the iron-nickel system there are actually two composition regions in which the anisotropy constant changes sign. The first region begins with pure nickel and extends to alloys containing up to 85% Ni; for these the temperature of isotropy increases with decrease of the nickel content. The second region comprises compositions with from 30 to 55-60% Ni. In the first region the constant changes from negative to positive; in the second region, from positive to negative.

In an attempt to elucidate the reasons for the change in sign of the anisotropy constant in the two regions we hypothesized that the change in sign is determined by the magnetoelastic component of the anisotropy energy. In order to check this we undertook an investigation of 1) the elasticity coefficients of iron-nickel alloy single crystals and the dependence of these on temperature and field, and 2) the magnetostriction parameters of iron-nickel single crystals and their dependence on temperature and field.

Specifically, we measured the parameters of single crystals having the following compositions:

Composition	No.1	No.2	No.3	No.4
Ni, %	100	76	80	36
Fe, %	0	24	50	64

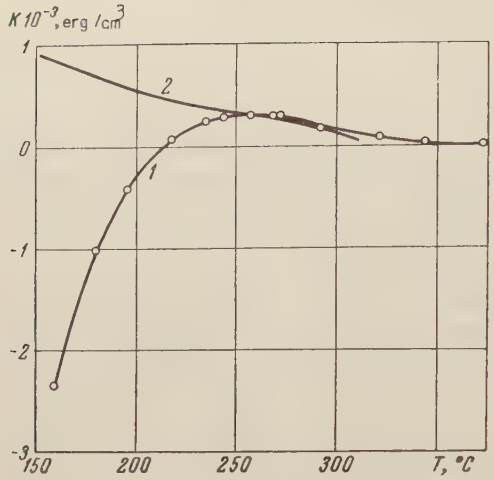

Fig.1. Temperature dependence of the anisotropy constant (1) and its magnetoelastic component (2) in pure nickel.

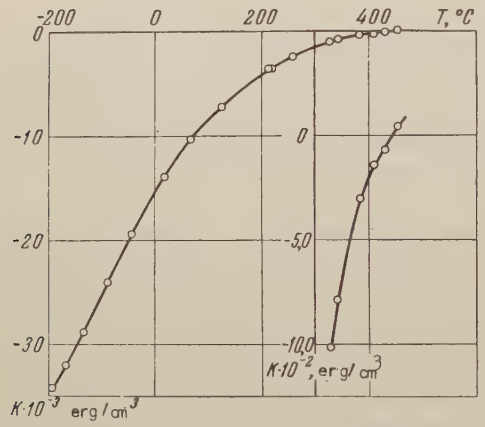

Fig.2. Temperature dependence of the anisotropy constant of iron-nickel alloy with 87.8% Ni. At right - section of the same curve plotted to a smaller scale.

Specimens Nos.3 and 4 after high temperature annealing were cooled rapidly from 650°; specimens Nos.1 and 2 were cooled very slowly. Hence it could be assumed that alloy No.2 was ordered.

The specimens used for measuring the elasticity coefficients were in the form of cylinders 3.5 mm in diameter and 18 to 25 mm in length. For each composition we took two specimens of different orientation: close to [100] and [110].

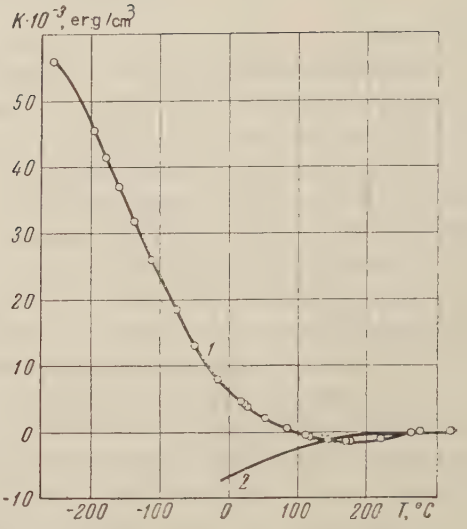

Fig.3. Temperature dependence of the anisotropy constant (1) and its magnetoelastic component (2) in iron-nickel alloy with 36% Ni.

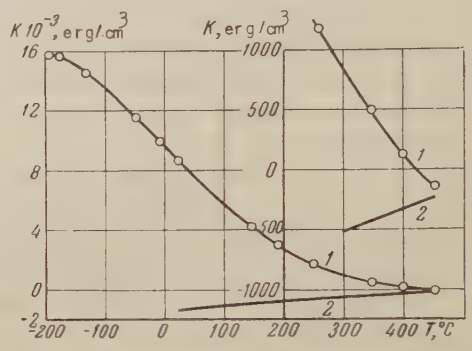

Fig.4. Temperature dependence of the anisotropy constant (1) and its magnetoelastic component (2) in single crystal of alloy with 50% Ni.

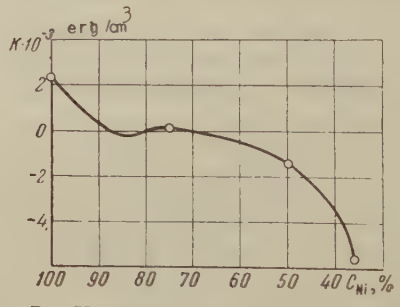

Fig.5. Variation of the magnetoelastic component of the anisotropy constants with the composition in the iron-nickel system.

We used the composite vibrator method for determining the elasticity coefficients. The specimens were cemented with heat-resistant cement to X and Y cut piezoelectric quartz bars. The assembled vibrators were inserted into a solenoid (field up to 5000 Oe) and there were determined the main resonance frequencies for the longitudinal and torsional modes at different values of the field and temperature. The principal intrinsic frequency of the single crystal specimen was then calculated by means of the formulas for a nonsymmetrical vibrator[3,4] and then there were found the shear modulus and elasticity modulus. On the basis of these there were determined for the two crystals with different orientation the values of the elasticity coefficients C_1, C_2 and C_3 free of the ΔE effect (measurements in saturation fields).

The temperature dependences of the coefficients C_2 and C_3 entering into the formula[5] for the magnetoelastic energy change with the composition. In nickel these coefficients decrease with increase of temperature with a noticeable break in the curve at the Curie point. Our values for C_2 and C_3 are some 5% lower than the data of Alers et al[6]; however, the elasticity constants for polycrystals calculated according to the method of Huber & Schmid[7] on the basis of the data of single crystals agree in both cases with good accuracy. The divergence between our values of C_2 and C_3 and those of Alers et al may be explained by errors in determining the orientation of the specimens.

Monotonic decrease of C_2 and C_3 with increasing temperature is also observed for the specimens with 76 and 50% Ni. In invar C_2 increases slightly with increasing temperature, C_3 decreases, while the coefficients C_{11} and C_{12} rise rapidly.

The specimens for measuring the magnetostriction were single crystal disks 10-11 mm in diameter and parallel to the (110) plane. Resistance strain gages were cemented to these disks by means of heat-resistant cement. The magnetostriction was calculated by the two-constant formula. In the region of high temperatures there obtains linear decrease of λ_{100} and λ_{111} up to the Curie point in nickel and invar and in the 76% and 50% Ni alloys.

On the basis of the measured values of the elasticity coefficients C_1, C_2 and C_3, the magnetostriction constants λ_{100} and λ_{111}, and their temperature dependences there was calculated the magnetoelastic component of the anisotropy energy. Fig. 5 shows the variation of this component with the composition at room temperature (points = experimental data). The fluctuation of the magnetoelastic energy in the concentration range from 70 to 90% Ni is due to change in the sign of the parameters at nickel concentrations of 80 and 83%, respectively.

In general it may be said that in the region of compositions with a high nickel content the magnetoelastic energy is positive; in the invar region it is negative, whereas the total anisotropy energy is negative in the nickel region and positive in the invar region.

The elasticity moduli vary relatively little with temperature, while the magnetostriction varies linearly. Inasmuch as the magnetoelastic energy is proportional to the square of the magnetostriction constants, the magnetoelastic energy will vary with temperature according to the same law, i.e., much more slowly than the crystal component of the anisotropy energy. As a result, at high temperatures the common anisotropy constant changes sign, inasmuch as the signs of the crystal and magnetoelastic components of the anisotropy energy are different.

It will be evident from Fig.1 that beginning with 250° the main contribution to the anisotropy in nickel is made by the magnetoelastic component (curve 2), and that at about this temperature the crystal component vanishes.

As was noted above, in the case of the alloy with 76% Ni the elasticity and magnetostriction constants were measured with the solid solution in the ordered

state; here the magnetoelastic component of the anisotropy energy is small compared with the total anisotropy energy. We did not carry out any measurements for the alloy in the disordered state.

The temperature dependence of the magnetoelastic component of the anisotropy in the alloy with 50% Ni is shown by curve 2 in Fig.4. After the change in sign of the common anisotropy constant the predominant role is played by the magnetoelastic energy.

An analogous situation is observed in invar (Fig.3). Here the magnetoelastic energy after the change in sign of the anisotropy constant at 100° decreases more rapidly than might be expected from the data on the temperature dependence of the common anisotropy constant and its crystal component. Possibly this is connected with inaccuracy in determining the elasticity coefficients of invar, owing to the appreciable experimental difficulties (instability of the solid solution, strong damping, etc.). There can be no doubt, however, that the sign of the magnetoelastic component is negative, and this explains the observed change in sign of the common anisotropy constant of invar at 100°.

I desire to thank V.I.Goman'kov, V.N.Gorbachev and A.I.Rad'kov for assistance in carrying out the measurements of the elastic and magnetostriction constants.

References

1. I.M.Puzei, Izv.AN SSSR, Ser.fiz., 21, 1088 (1957). (Trans.Bulletin, 21, 1077.)

2. I.M.Puzei, Fiz.metallov i metallovedenie, 11, 525 (1961). (Trans.Physics of metals & metallography.)

3. F.C.Rose, Phys.Rev., 45, 50 (1936).

4. V.A.Solov'ev & I.G.Mikhailov, Izv.AN SSSR, Ser.fiz., 20, 261 (1956). (Trans.Bulletin, 20, 243.)

5. S.V.Vonsovskii & Ya.S.Shur, Ferromagnetizm (Ferromagnetism), M., 1948.

6. G.A.Alers, J.R.Neighbour & J.Sato, J.Phys.Chem.Solids, 13, No.1-2, 40 (1960).

7. A.Huber & E.Schmid, Helv.phys.acta, 7, 620 (1934).

EFFECT OF THE FIELD STRENGTH IN MAGNETIC ANNEALING ON THE MAGNETIC PROPERTIES OF COLD-ROLLED ELECTRICAL STEEL

- D.D.Mishin, T.I.Bychkova & V.A.Smagin

Introduction

There have been numerous experimental and theoretical investigations[1-11] of the influence of thermomagnetic treatment or magnetic annealing (hereinafter MA) on the magnetic properties of ferromagnetic materials. Nevertheless, some of the theoretical and practical aspects of the effect of MA are still obscure. An important question, for example, is the influence of the field strength during MA on the magnetization curve and the hysteresis loops of magnetically soft materials. The purpose of this work was experimental investigation of the influence of the magnetic field strength during MA on the magnetization curve and the hysteresis loop of cold-rolled grain-oriented Type E310 electrical steel.

Experimental Procedure

A shortcoming of most previous studies of the effect of MA was that experimenters used specimens only in the forms of strips; it is difficult in employing such specimens to realize a uniform magnetic field both during heat treatment and measurement, particularly in the range of fields corresponding to maximum permeability. One can eliminate inhomogeneity of the magnetic field in the specimens during MA and at the same time achieve more accurate determination of the effect of MA by using "closed loop" specimens. In our work the "closed loop", i.e., ring shaped, specimens 7 cm in diameter were prepared of 23 x 3 x 0.05 cm strips annealed beforehand for 5 hours in hydrogen at 1100°. The annealed strips were bent to form rings in a special device which had provision for heating them to 100-150°, which prevented development of cracks. To insure good contact and full closure of the magnetic circuit the ends of the specimens were joined by spot welding.

In view of the pronounced crystallographic (110) [001] texture, specimens prepared of strips cut along, across and at an angle of 55° to the rolling direction can serve for investigation of the magnetic properties in the tetragonal, digonal and trigonal directions of pseudosingle crystals of iron with 3% Si. For brevity, we shall hereinafter refer to these specimens as "tetragonal", "digonal" and "trigonal".

The specimens were subjected to ordinary heat treatment and magnetic annealing in a special set-up which insured uniform heating during the holding period and uniform cooling of the specimens in a neutral medium (argon). For relief of the strains produced in bending the strips the specimens were first heated for 30 min at 900°, cooled at the rate of 70 degree/hour to 500° and then allowed to cool further with the furnace switched off. The MA conditions were the following: heating to 900°, holding time 30 min, cooling to 700° over a period of 1 hour, holding for 1 hour, cooling at the rate of 70° degree/hr to 500° and final cooling with the furnace switched off. The 50 cps magnetic field was applied prior to the holding at 700° and switched off at 200°. The magnetic field strengths in the different magnetic anneals were 0.07, 0.5, 7.0 and 70 Oe. The specimens were demagnetized by a 50 cps field of decreasing amplitude. The ballistic procedure was used for measuring the magnetization curves and hysteresis loops.

Measurement Results and Discussion

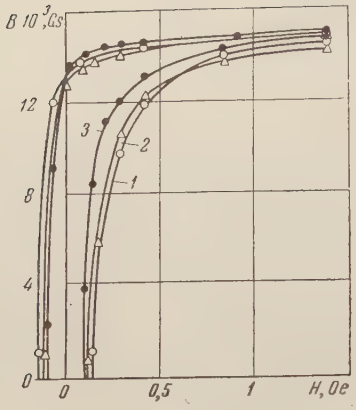

Fig.1. Magnetic hysteresis loops of tetragonal specimen: 1) before MA, 2) after MA in a 0.07 Oe field, 3) after MA in a 70 Oe field.

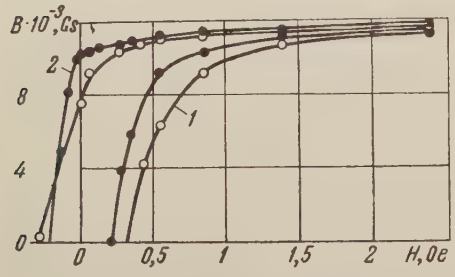

Fig.3. Magnetic hysteresis loops of trigonal specimen: 1) before MA, 2) after MA in a 70 Oe field.

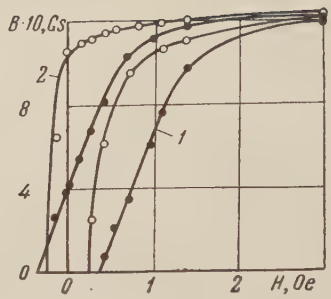

Fig.2. Magnetic hysteresis loops of digonal specimen: 1) before MA, 2) after MA in a 70 Oe field.

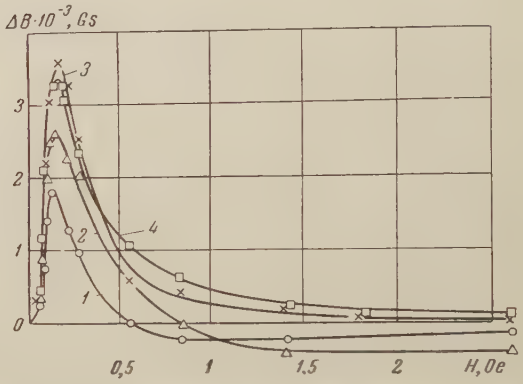

Fig.4. Increment in magnetic induction of tetragonal specimen after MA: 1) field during annealing 0.07 Oe, 2) 0.50 Oe, 3) 7 Oe, 4) 70 Oe.

The results of measurements of the hysteresis loops of the tetragonal, digonal and trigonal specimens are shown in Figs.1, 2 & 3, respectively, It will be evident from Fig.1 that after MA the hysteresis loops of tetragonal specimens become narrower with increase of the magnetic field acting during MA. The hysteresis loops of the trigonal and, particularly, the digonal specimens change markedly after MA in a field of 70 Oe; weaker fields during annealing do not produce any significant change in the hysteresis loops of these specimens.

The changes in magnetic induction after MA in different fields for the tetragonal, digonal and trigonal specimens are shown in Figs.4, 5 and 6. It will be seen that the $\Delta B = f(H)$ curves for all three types of specimens have a peak. The position of this peak with increase of the field applied during MA shifts somewhat to the side of stronger fields. This peak is observed for the tetragonal specimen at a field strength of about 0.2 Oe, and for the digonal and trigonal specimens at 0.5 Oe. The height of the peak, i.e., the maximum value of ΔB, is strongly dependent on the intensity of the field applied during MA. In fields stronger than 0.5-1 Oe there is observed sharp decrease of ΔB; in fact, in sufficiently strong fields ΔB becomes negative. This regularity was first discovered by Shur[2] in working with polycrystalline silicon iron specimens and was explained by Vonsovskii[3] on the basis of the theory of thermomagnetic treatment developed by him.

Effects of ordinary and magnetic annealing on the magnetic properties of cold-rolled E310 electrical steel

Specimen No.	μ_{max} after ordinary anneal, G/Oe	Field strength during MA H, Oe	μ'_{max} after MA, G/Oe	$\frac{\mu'_{max}-\mu_{max}}{\mu_{max}}$, %	Coercive force H_c after ordinary anneal, Oe	$\frac{H_c-H'_c}{H'_c}$, %	Residual induction B_r after ordinary anneal, G	Residual induction B'_r after MA, G	$\frac{B_r-B'_r}{B_r}$, %
Tetragonal specimens									
2	36 400	0,07	45 000	23	0,14	14	13 200	13 000	2
3	41 500	0,5	53 500	29	0,14	14	13 100	13 400	2
1	35 200	7,0	55 000	55	0,14	55	12 800	13 400	4
7	44 500	7,0	63 500	43	0,14	25	13 600	14 000	3
5	35 200	70,0	54 000	53	0,14	25	12 800	13 600	6
2	36 400	70,0	54 500	50	0,14	25	13 200	13 600	3
Trigonal specimens									
15	12 600	0,5	13 800	15	0,24	17	8 000	8 600	5
12	11 300	7,0	15 500	37	0,26	23	7 200	8 800	20
13	11 400	70,0	16 000	29	0,30	33	7 600	10 200	37
Digonal specimens									
16	7 000	7,0	11 150	56	0,34	40	4 400	7 600	73
18	6 900	70,0	20 600	190	0,36	41	4 000	10 400	180

The changes in maximum permeability, coercive force and residual induction produced by MA at different field strengths in the three different types of specimens are summarized in the accompanying table. It will be evident from the table and the figures that the magnetic parameter most sensitive to MA is the maximum permeability where all three types of specimens are concerned. The residual induction of the trigonal and, particularly, the digonal specimens increases sharply after MA, while for the tetragonal specimen the increase in residual induction is small. The coercive force of all three types of specimens is reduced significantly by MA.

Conclusions

1. The hysteresis loops of tetragonal specimens as a result of MA in fields of up to 7 Oe become narrower and more rectangular, the change being the greater the stronger the magnetic field applied during annealing. No further significant change is evinced in the hysteresis loops of these specimens with increase of the field during MA from 7 to 70 Oe. The hysteresis loops of the digonal and trigonal specimens after MA in a field of 70 Oe change greatly and become significantly more rectangular.

2. Increase of the magnetic induction ΔB occurs in weak and medium fields during MA. The $\Delta B = f(H)$ curves have a maximum in the field region corresponding to maximum permeability. The increment in residual induction for tetragonal specimens increases with increase in the strength of the magnetic field applied during MA from 0.07 to

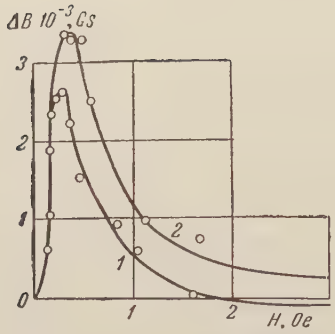

Fig.5. Increment in magnetic induction of digonal specimen after MA: 1) field during annealing 7 Oe, 2) 70 Oe.

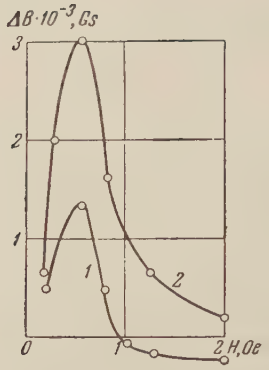

Fig.6. Increment in magnetic induction of trigonal specimen after MA: 1) field during annealing 0.5 Oe, 2) 7 and 70 Oe.

7 Oe, while with further increase of the field during MA from 7 to 70 Oe little additional effect is evinced. In the 1-1.5 Oe field region there is observed a decrease of the magnetic induction after MA, i.e., ΔB becomes negative.

3. The magnetic parameter most sensitive to MA is the maximum permeability, which for all three types of specimens increases significantly as a result of MA. The residual induction of digonal and trigonal specimens increases sharply after MA, whereas for tetragonal specimens the increase in residual induction is insignificant. The coercive force of all three types of specimens is noticeably reduced by MA.

4. Inasmuch as magnetic annealing of cold-rolled electrical steel results in an appreciable increase of the permeability in weak and medium fields, this type of heat treatment may be recommended for magnetic circuit components in which the effective permeability in weak and medium fields is a significant operating characteristic.

References

1. R.M.Bozorth, J.Appl.Phys., 8, 575 (1937).

2. Ya.S.Shur, Doklady AN SSSR, 23, 455 (1939); Zhur.eksp.i teor.fiz., 10, 441 (1940).

3. S.V.Vonsovskii, Zhur.eksp.i teor.fiz., 9, 702 (1939).

4. M.Gertz, J.Appl.Phys., 22, No.7, 984 (1951).

5. R.M.Bozorth, Ferromagnetism, N.Y., 1951.

6. L.Néel, J.phys.et radium, 15, No.4, 225 (1954).

7. D.D.Mishin & M.M.Belenkova, Fiz.metallov i metallovedenie, 2, No.2, 370 (1956).

8. Tez.doklad.Soveshch.po fizike magnitnykh yavlenii (Program of conference on the physics of magnetic phenomena), M., 1956.

9. A.A.Glazer & Ya.S.Shur, Izv.AN SSSR, Ser.fiz., 22, 1205 (1958) (Trans. Bulletin, 22, 1198); Fiz.metallov i metallovedenie, 3, 568 (1956); 5, 355 (1957); 6, 52 (1958). (Trans.Physics of Metals & Metallography.)

10. H.Fiedler & R.Pry, J.Appl.Phys., Suppl., 30, 109 (1959).

11. R.Heidenreich, E.Nesbitt & Berbank, J.Appl.Phys., 30, No.7, 955 (1959).

MAGNETIC TEXTURE OF FERROMAGNETS SUBJECTED TO EXTERNAL STRESSES

- F.N.Dunaev

Under the influence of deforming stresses within the elastic limit there forms in ferromagnets magnetic texture, i.e., preferential orientation of the spontaneous magnetization vectors I_s in certain directions. It is known[1-3] that the character of this magnetic texture is determined by the relative signs of the external stress σ and the saturation magnetostriction λ_s. If the signs of σ and λ_s are the same (elongation of ferromagnetic material with $\lambda_s > 0$ or compression of material with $\lambda_s < 0$), the spontaneous magnetization vectors I_s are oriented in directions close to the direction of the stress.

It is also known that the degree of this texture is determined by the relation between the crystallographic anisotropy energy

$$F_K = K(\alpha_1^2\alpha_2^2 + \alpha_2^2\alpha_3^2 + \alpha_1^2\alpha_3^2) \tag{1}$$

and the magnetoelastic energy

$$F_\sigma = -\frac{3}{2}\sigma[\lambda_{100}(\alpha_1^2\gamma_1^2 + \alpha_2^2\gamma_2^2 + \alpha_3^2\gamma_3^2) + 2\lambda_{111}(\alpha_1\alpha_2\gamma_1\gamma_2 + \alpha_2\alpha_3\gamma_2\gamma_3 + \alpha_1\alpha_3\gamma_1\gamma_3)], \tag{2}$$

where K is the magnetic anisotropy constant, λ_{100} and λ_{111} are the magnetostriction constants, the α_i are the direction cosines of I_s, and the γ_i are the direction cosines of σ. The most pronounced texture will form when

$$F_\sigma \gg F_K \tag{3}$$

or

$$\lambda_s\sigma \gg K. \tag{4}$$

Hence to obtain the most pronounced magnetic texture under stress (uniaxial magnetic texture in the limit) it is essential that the material have a small magnetic anisotropy or a high elastic limit.

Analysis of the behavior of the magnetoelastic energy and certain experimental facts give reason to infer that the above concepts regarding the character of magnetic texture and the factors determining the degree of this texture are in need of modification.

In the absence of a magnetic field and in the range of small internal stresses σ_i the orientation of the vector I_s in a crystal is determined by the minimum of $F_K + F_\sigma$. However, simple search for the minimum of $F_K + F_\sigma$ does not allow of clarifying the role of the individual terms entering into F_σ.

As we see, the expression for F_σ consists of two polynomial terms, one of which contains λ_{100}, and the other λ_{111}.

Let us write F_K and F_σ in the form

$$F_K = K \cdot A, \tag{5}$$

and

$$F_\sigma = F_{\sigma\lambda_{100}} + E_{\sigma\lambda_{111}} = \lambda_{100} \cdot \sigma \cdot B + \lambda_{111}\sigma \cdot C. \tag{6}$$

At sufficiently high stresses, when the anisotropy introduced by each of the terms in F_σ is greater than the anisotropy F_K, the position of the minimum will be determined mainly by these two terms. In order to evaluate the role played by each term individually, let us find their separate minima.

The role of these terms can be elucidated by calculating and comparing the functions A, B and C for different orientations of σ. This is equivalent to comparison of the values of F_K, $F_{\sigma\lambda_{100}}$ and $F_{\sigma\lambda_{111}}$ under the condition

$$K = |\sigma\lambda_{100}| = |\sigma\lambda_{111}| \text{ and } |\lambda_{100}| = |\lambda_{111}|. \quad (7)$$

First, from the form of function B it will be evident that the term $F_{\sigma\lambda_{100}}$ is symmetrical relative to the tetragonal axes of the crystal, just as is F_K. Consequently, at any values of the stress this term cannot produce a change in the position in the minimum of F_K, i.e., deflection of the easy magnetization axes from the tetragonal axes of the crystal. (In the present analysis we consider only ferromagnets with $K > 0$.) This term can only deepen some of the minima of F_K and, consequently, produce displacement of the 90° walls. The position of the minimum can be changed only by the term $F_{\sigma\lambda_{111}}$, containing λ_{111}.

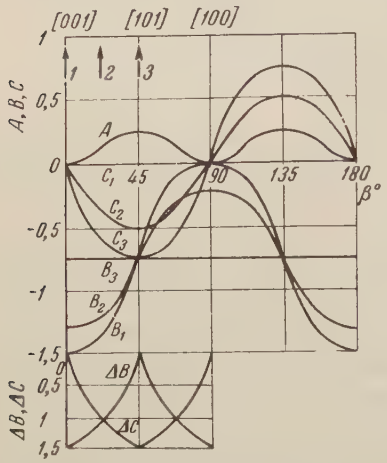

Fig.1. Dependence of the functions A, B and C and their amplitudes ΔB and ΔC on the orientation of σ in the (010) plane: 1 - $\sigma \| [001]$, 2 - σ oriented at an angle of 22° relative to the [001] axis, 3 - $\sigma \| [101]$

The behavior of the functions A, B and C for three orientations of σ in the (010) plane is shown in Fig.1. It will be seen that for any orientation of σ the minimum of B is located in the tetragonal direction closest to the direction of σ, while the minimum of C is located in the diagonal direction closest to the direction of σ. An analogous picture is obtained for any orientation of σ in the crystal. The values of $F_{\sigma\lambda_{100}}$ and $F_{\sigma\lambda_{111}}$ differ from B and C by the corresponding coefficients $\lambda_{100}\cdot\sigma$ and $\lambda_{111}\cdot\sigma$. If $\lambda_{100}\sigma > 0$ and $\lambda_{111}\sigma > 0$, i.e., if the signs of λ_{100} and σ and of λ_{111} and σ are the same, the positions of the minima of $F_{\sigma\lambda_{100}}$ and $F_{\sigma\lambda_{111}}$ agree with the positions of the minima of B and C, respectively. If the signs are opposite, $F_{\sigma\lambda_{100}}$ and $F_{\sigma\lambda_{111}}$ will be flipped over relative to the horizontal axis and their minima will be located in the tetragonal and diagonal directions furthest from the direction of σ. In addition, we note that the amplitudes ΔB and ΔC (by the amplitudes we mean the difference between the maximum and minimum values of B and C, respectively) depend on the orientation of σ. These dependences are also shown in Fig.1.

Inasmuch as "rotation" of the minima is produced only by the term $F_{\sigma\lambda_{111}}$, containing λ_{111}, only λ_{111} (but not λ_{100} or λ_s) can appear in Eq.(4) in the case of either a single crystal or a polycrystalline specimen.

The most important circumstance is that $F_{\sigma\lambda_{100}}$ not only does not produce rotation of the minimum but, in fact, hinders such rotation inasmuch as it deepens the minimum of F_K. The quantities F_K and $F_{\sigma\lambda_{100}}$ in effect "operate" in unison against $F_{\sigma\lambda_{111}}$. Hence the condition for establishment of the most pronounced magnetic texture cannot be (3) or more accurately the condition

$$\Delta F_\sigma \gg \Delta F_K \quad (8)$$

where $F_{\sigma\lambda_{100}}$ and $F_{\sigma\lambda_{111}}$ appear on the same side of the inequality.*

Fig.2 shows the influence of the functions B and C on the position of the minimum of A in the case when the stress σ is oriented in the (010) plane at an angle $\beta = 22°$ relative to the [001] axis. The minimum of A, located in the [001] direction, is not displaced but is only deepened under the influence of B (see

---

*See footnote on next page.

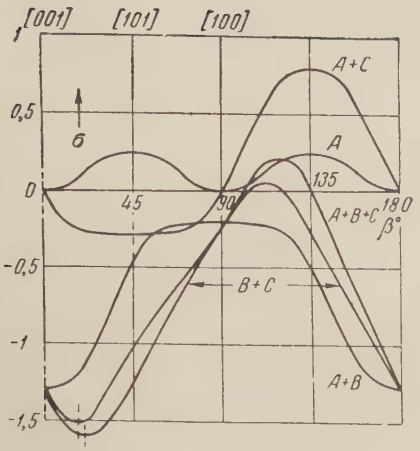

Fig.2. Influence of the functions B and C on the position of the minimum of A.

the $A+B$ curve). Under the influence of C this minimum is shifted in the [101] direction ($A+C$ curve), but under the simultaneous influence of B and C, owing to the fact that B hinders displacements of the position of the minimum, the minimum is displaced only by ~20° ($A+B+C$ curve).

Even under our condition (7) the magnetic anisotropy energy F_K has little effect on the position of the minimum, which is apparent from comparison of the positions of the minima of the $A+B+C$ and $B+C$ curves. At sufficiently large values of σ, when $|\lambda_{100}\cdot\sigma|>K$ and $|\lambda_{111}\cdot\sigma|>K$, the role played by F_K is even smaller and the position of the minimum is determined by the "competition" between the two terms entering into F_σ, of which one ($F_{\sigma\lambda_{100}}$) tends to hold the minimum in the tetragonal direction, while the other ($F_{\sigma\lambda_{111}}$) tends to shift it to the diagonal direction. Other conditions being equal, the extent of rotation of the minimum will be greater in ferromagnets in which the ratio $\left|\frac{\lambda_{111}}{\lambda_{100}}\right|$ is larger.

It follows, therefore, that the relationship determining the degree or intensity of the texture forming as a result of rotation of the directions of easy magnetization under the influence of an external stress should be the inequality

$$\Delta F_{\sigma\lambda_{111}} > \Delta F_K + \Delta F_{\sigma\lambda_{100}}, \tag{9}$$

or, what is the same thing,

$$|\Delta C\cdot\lambda_{111}\cdot\sigma| > \Delta A\cdot K + |\Delta B\cdot\lambda_{100}\cdot\sigma|, \tag{10}$$

where, it will be noted, $\Delta F_{\sigma\lambda_{100}}$ and $\Delta F_{\sigma\lambda_{111}}$ appear on different sides of the inequality sign. At sufficiently large σ, the term $\Delta A\cdot K$ may be neglected.

Analogously, relation (4) should be replaced by

$$|D\cdot\lambda_{111}\cdot\sigma| > K + |E\cdot\lambda_{100}\cdot\sigma|, \tag{11}$$

where D and E in the case of a single crystal are functions of the orientation of σ (inasmuch as ΔC and ΔB change with changes in the orientation of σ in the crystal) and in the case of a polycrystalline specimen are numerical coefficients.**

---

*(Footnote from previous page)

Inequality (3), which is used by some investigators, must be employed with caution, inasmuch as F_K and F_σ are actually different functions of the orientation of the spontaneous magnetization and for a given material and given values and direction of the stress F_K and F_σ may take on different values depending on the direction of I_s. In order to determine whether the magnetic anisotropy or the magnetoelastic anisotropy predominates one must compare the amplitudes of these functions, i.e., ΔF_K and ΔF_σ (the differences between the maximum and minimum values of F_K and F_σ).

**The form of the functions and the numerical values of D and E for an ideal polycrystal will be given in a future paper.

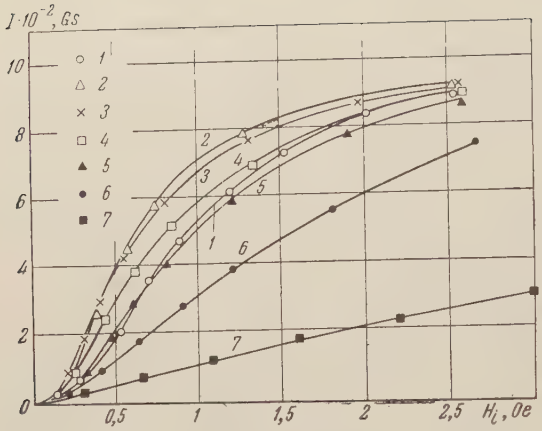

Fig.3

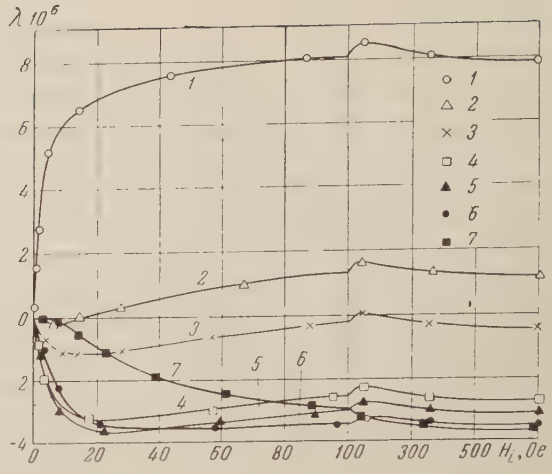

Fig. 4

Fig.3. Magnetization curves of silicon iron at different tensile stresses: 1) σ = = 0, 2) 0.7, 3) 1, 4) 2, 5) 3, 6) 6, 7) 27 kg/mm^2.

Fig.4. Magnetostriction curves for silicon iron at different tensile stresses (curve numbers and stresses same as in Fig.3).

It will be evident from expressions (9), (10) and (11) that for obtaining a completely uniaxial magnetic structure it is not sufficient to fulfill condition (8); one must also insure that the ratio $\left|\frac{\lambda_{111}}{\lambda_{100}}\right|$ is sufficiently large.* For example, for small $\left|\frac{\lambda_{111}}{\lambda_{100}}\right|$, even with $K = 0$, uniaxial magnetic structure will not be established at any stress, inasmuch as the main hindrance as regards rotation of the minimum will be $\Delta F_{\sigma\lambda_{100}}$ rather than ΔF_K.

In general, magnetic texture under the influence of stresses is established both due to displacement of the 90° walls and due to rotation of the spontaneous magnetization vectors. So far we have considered only the relationships determining the degree of texture due solely to the process of rotation. By way of relationship determining the degree of texture due to wall displacements one can use the following (but only to a rough approximation):

$$|\sigma| > |\sigma_i|. \qquad (12)$$

The character of the structure due to rotation processes, as was evident in considering A, B and C, is determined by the relation between the signs of σ and λ_{111}, while the character of the texture due to wall displacements is determined by the relationship of the signs of σ and λ_{100} regardless of whether we are dealing with a single crystal or a polycrystalline specimen (we suggest that it is incorrect to determine the character of the texture for polycrystalline specimens on the basis of the relation of the signs of σ and λ_s).

In order to help distinguish more clearly between the magnetic textures due, on the one hand, to wall displacement processes and, on the other hand, to rotation processes, it would appear desirable to introduce an appropriate terminology.

---

*Except for some special cases of orientation of σ in the crystal, when ΔB = = 0 and relationship (9) becomes equivalent to (8), as for example, in the case of orientation of σ along the diagonal axis of the crystal.

One might, for example, call the texture forming as a result of wall displacement processes "displacement texture" and the other "rotation texture".

The utility of introducing such a terminology is evident from the fact that, for example, in material with pronounced anisotropy of magnetostriction (λ_{100} and λ_{111} having different signs) under the influence of a stress having the same sign the displacement texture will be opposite in character to the rotation texture.

Figs.3 and 4 show the magnetization and magnetostriction curves for a polycrystalline silicon iron specimen (3.5% Si) at different tensile stresses. The saturation magnetostriction of this alloy is positive. Hence in the case of elongation one should expect a formation of a magnetic texture with orientation of the magnetization vectors along the line of elongation and, consequently, only raising of the magnetization curves and reduction of the magnetostriction with increase of σ. Actually, however, the observed deformation of the $I(H)$ and $\lambda(H)$ curves is more complicated: the $I(H)$ curves up to a certain stress rise, and then descend and become increasingly rectilinear. The magnetostriction decreases, changes sign, and grows in absolute magnitude. Beginning at a certain stress, however, the magnetostriction in weak fields decreases in absolute magnitude, although λ_s continues to grow slowly. Such deformation of the $I(H)$ and $\lambda(H)$ curves in the range of sufficiently high stresses is reminiscent of the deformation of the $I(H)$ and $\lambda(H)$ curves for nickel under elongation where, as is known, there forms a magnetic structure with orientation of the vectors $\mathbf{I}_s$ in the plane perpendicular to $\vec{\sigma}$.

Apparently, in this alloy at first - in the range of small σ, giving rise mainly to wall displacements - there forms a magnetic texture in which the $\mathbf{I}_s$ in the crystallites are oriented along the direction of easy magnetization closest to the line of elongation, inasmuch as σ and λ_{100} have the same sign (positive). Owing to the fact, however, that $\lambda_{111} < 0$ (Ref.4), these directions of easy magnetization themselves under the influence of the tensile stress ($\sigma > 0$) deviate from the tetragonal axes of the crystallites to the side of the plane perpendicular to the line of elongation, i.e., there begins to form a magnetic texture opposite in character to the initial one. At sufficiently high stresses this deflection of the magnetization vectors gives rise to the observed deformation of the magnetization and magnetostriction curves.

In view of the fact that the increase of $\sigma\,|\lambda_s|$ in the range of high stresses is small (curves 6 & 7 in Fig.3), it follows that the deviation of the directions of easy magnetization towards the plane perpendicular to $\vec{\sigma}$ must be small. This is in agreement with the inference that for obtaining a pronounced "rotation texture" one must have a large value of the ratio $\left|\frac{\lambda_{111}}{\lambda_{100}}\right|$. Actually, for the given silicon-iron alloy this ratio is small: $\left|\frac{\lambda_{111}}{\lambda_{100}}\right| \approx 0.1$ (Ref.4).

"A.M.Gor'kii" Ural State University

References

1. N.S.Akulov, Ferromagnetizm (Ferromagnetism), M., 1939.
2. S.V.Vonsovskii & Ya.S.Shur, Ferromagnetizm (Ferromagnetism), M., 1948.
3. R.M.Bozorth, Ferromagnetism, N.Y., 1951.
4. D.A.Shturkin, Izv.AN SSSR, Ser.fiz., 11, 718 (1947).

INVESTIGATION OF THE EFFECT OF CREEP OF NONSYMMETRICAL HYSTERESIS LOOPS

- O.V.Rosnitskii

The effect known as creep of nonsymmetrical hysteresis loops of polycrystalline ferromagnets may be described as follows: when the magnetization J is repeatedly reversed over a nonsymmetrical cycle by varying the external field from H_A to H_B, where $H_B \neq -H_A$, the hysteresis loops remain open and shift continuously along the J axis. Néel was the first to carry out a theoretical analysis of the creep effect.[1,2]

Investigation of the creep effect is of interest not only to physicists working in the field of magnetism but also to engineers engaged in developing various magnetic components and, in particular, matrix memories employing ferrite cores with square hysteresis loops, the $J(H)$ curves of which are nonlinear.[3] In this case the linear approximations adopted in the work of Néel are hardly warranted inasmuch as the curvature of the $J(H)$ characteristics can substantially affect the variation in magnetization during the creep process. It is expedient, therefore, to take into account at least the first derivative of the susceptibility and instead of Eq.(2) in Néel's paper[1] to write the Taylor series

$$J_n = J_A + S_A x_n h_r + \frac{S_A'}{2!}(x_n h_r)^2, \tag{1}$$

where J_n is the magnetization for the n-th application of the field H_A, J_A is the magnetization corresponding to the first application of the field H_A, S_A is the irreversible susceptibility at the point (H_A, J_A) on the given minor cycle, h_r is the rms value of the creep field, and x_n is the normalized value of the average maximum value of the creep field for n applications of the field H_A.

For an external field H_A approximately equal to the coercive force H_c, when $S_A' \approx 0$, Néel's formula is obtained from Eq.(1). In general, however, the x_n dependence of J_n is not linear: for $H_A > H_c$ the magnetization increases more slowly and for $H_A < H_c$ more rapidly than linearly.

According to Eq.(1) in Ref.1, the value of x_n is given by the integral

$$x_n = \int_{-\infty}^{\infty} x \frac{dP^n}{dx} dx, \tag{2}$$

where $P = \int_{-\infty}^{x} p(x)\,dx$ is the probability that the creep field strength in a given test is less than xh_r.

On the basis of Gauss' law for $p(x)$, Néel calculated the values of x_n for n up to 10^6 and obtained an analytic expression for determining x_n for $n \geqslant 10$. According to Néel, x_n increases infinitely in the limit as $n \to \infty$. If, however, we assume that the values of the creep field are contained in the finite interval $[-x_m h_r, x_m h_r]$, then from (2) we readily obtain

$$x_n = x_m - \int_{-x_m}^{x_m} P^n dx, \tag{3}$$

whence it follows that in the limit as $n \to \infty$, x_n has a limit equal to the chance maximum value x_m. It can easily be seen that Néel's result is connected with the assumption of a Gaussian distribution which permits the appearance of arbitrarily high creep field values, albeit with low probability.

If the probability density $p(x)$ for a given x in the interval $[-x_m, x_m]$ is constant and equal to $1/2x_m$, we obtain

$$x_n = x_m - \frac{2x_m}{n+1}. \tag{4}$$

This analytic expression is analogous to the empirical formula deduced by Bouty[4] for the variation of the residual magnetization incident to magnetization of steel needles.

Actually, evaluation of x_m can be based on the consideration that the magnetization J_n is in practice always smaller than the saturation magnetization J_s, i.e.,

$$x_m < \frac{J_s - J_A}{S_A h_r}. \tag{5}$$

In view of this, good agreement with experiment for $H_A > H_c$, as well as for large n, can be obtained by means of the function

$$J_n = J_A + (J_s - J_A)\{1 - \exp(-\frac{S_A}{J_s - J_A} x_n h_r)\}, \tag{6}$$

whence there is obtained in the linear approximation Néel's formula; from this it follows that this approximation is permissible for $x_n \ll x_m$.

It follows that the position of the nonsymmetrical hysteresis loops should become stabilized in the process of creep. This stabilization will set in sooner for values of H_A exceeding H_c and also for large values of S_A. Thus, linear dependence of the magnetization on x_n is the exception rather than the rule and can be observed up to large values of n only in materials with a nonrectangular hysteresis loop and in fields close to H_c. In materials with a rectangular loop linear dependences of J_n on x_n are difficult to observe, inasmuch as the slightest instability of the magnetizing current and of the ambient temperature leads to change in the character of the x_n dependence of J_n

Obviously, creep can affect the operation of components of magnetic automation equipment. In this connection it is essential to distinguish between the influence of the creep effect and the superficially similar influence of magnetic viscosity, when the current pulses in the winding have a duration inadequate for complete reversal of the core.[5] In high speed elements the influences of magnetic viscosity and creep obtain simultaneously up to a certain pulse duration, but creep is evinced no matter how long the duration of the current pulses.

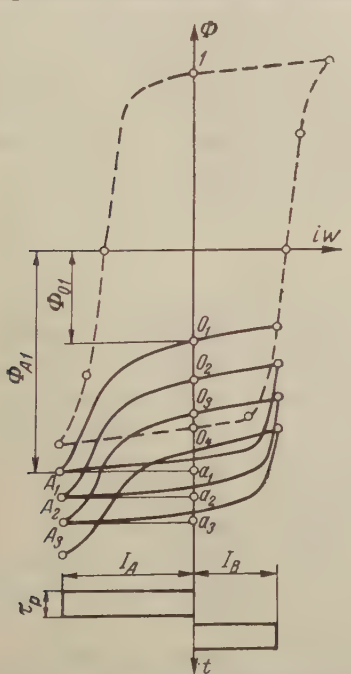

Fig.1. Working hysteresis cycles of an MM core.

The strongest influence of the creep effect may be observed in the cores of matrix memories (MM). In particular, Yu.N.Glukhov and the writer[3] in 1956 established experimentally that creep has a strong effect on the "0" readout signal from a plane matrix. Below we shall consider this question in greater detail.

In reading and regeneration of a "1" an MM core in the simplest case is subjected to symmetrical excitation by current pulses I_A and $I_B = -I_A$. The corresponding hysteresis cycle is shown by the dashed line in Fig.1. In reading and regeneration of a "0" the core is subjected to a nonsymmetrical excitation by current pulses I_A and I_B, where, as a rule, $I_B = -I_A/2$ (solid curve in Fig.1). Thus, if after an appreciable number of repeated "1" readings and regenerations the core is transferred to reading "0", owing to creep during the "1" readings, the "0" signal in the winding of the core will change from one cycle to another.[8]

The "0" reading signal $U_c(0)_n$ in a one-turn winding in a cycle of arbitrary number n is related to the change

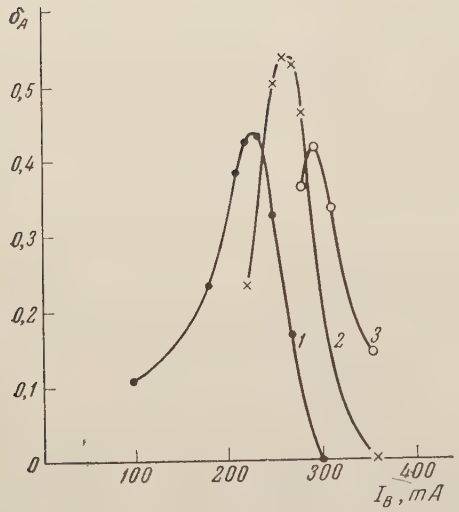

Fig.2

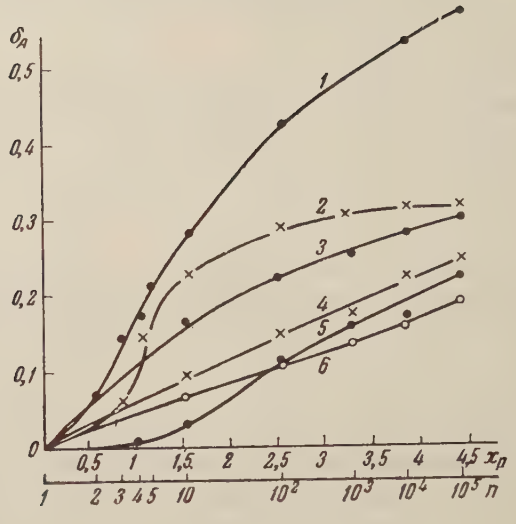

Fig.3

Fig.2. Creep in K-28 core for $n = 10^5$: 1 - I_A = 300 mA, 2 - 360 mA, 3 - 500 mA.
Fig.3. Creep curves for K-28 (1) and K-65 (2-6) cores: 1 - I_A = 360 mA, and I_B = 260 mA, 2 - 160 and 10 mA, 3 - 240 and 120 mA, 4 - 240 and 150 mA, 5 - 160 and 90 mA, 6 - 240 and 155 mA.

in magnetic flux in the core by the simple expression

$$\Phi_{An} - \Phi_{0n} = \int_0^{\tau_i} U_c(0)_n dt, \qquad (7)$$

where Φ_{An} is the absolute magnitude of the maximum magnetic flux in the core, attained at the end of the n-th I_A current pulse, Φ_{0n} is the absolute magnitude of the residual flux before the beginning effect of the n-th I_A current pulse, and τ_i is the duration of the reading pulses in the MM magnetizing conductors.

In investigating the creep effect, it is essential to minimize the influence of magnetic viscosity, hence the duration of the current pulses should be made greater than the duration of the reading signal. The relative change in the area under the "0" reading signal in the process of creep may be written in the form

$$\delta_f = \alpha x_n + \beta x_n^2, \qquad (8)$$

where α and β are coefficients analogous in meaning to $S_A h_r$ and $S'_A h_r^2/2$ in Eq.(1).

Photographs of the oscillograms of pulses recorded in the process of creep showed that their shape does not change and that the relative changes in the amplitudes of the signals (δ_A) and fluxes (δ_f) are equal. Therefore the regularities in the change in amplitude of the "0" signals during the creep process must agree with the regularities governing the creep of magnetization.

The greatest creep should be observed in fields close to the coercive force. Inasmuch as precise determination of the coercive force in miniature cores is difficult, we can make use of the fact that the maximum switching time over a symmetrical cycle obtains in fields of the same strength (p.21, Ref.3). Fig.2 shows the variation of δ_A with I_B at different I_A for a toroidal core of K-28 ferrite (d_o = 1.4 mm, d_i = 1 mm, h = 0.5 mm) for $n = 10^5$. The greatest creep occurs at I_A = 360 mA (in the one-turn winding), when the longest switching time is evinced for the given core.

The curves of δ_A vs x_n, according to the outlined theory, may differ appreciably in character. The experimental curves are shown in Fig.3; it will be seen that in the investigated range of x_n a linear dependence is obtained in one particular case (curve 4). The K-65 ferrite core had the following dimensions: d_o = 2.1 mm, d_i = 1.2 mm, and h = 1 mm.

Knowledge of the regularities involved in the creep effect from the standpoint of its influence on the operation of magnetic memory and similar components is important inasmuch as conventional oscillographic observation of signals and noise under steady conditions cannot give complete information on the behavior of the magnetic component in a process of actual operation, when the cores are subjected to the action of different and varying sequences of current pulses.

I desire to express my deep gratitude to K.M.Polivanov for his guidance in the work.

References

1. L.Néel, Compt.rend., 244, No.19-20, 2441 (1957).

2. L.Néel, Compt.rend., 244, No.21-22, 2668 (1957).

3. O.V.Rosnitskii, Matrichnye zapominayushchie ustroistva na magnitnykh serdechnikakh (Magnetic core matrix storage devices), M., 1960.

4. E.Bouty, Compt.rend., 78, 842 (1874).

5. N.Ya.Matyukhin & O.V.Rosnitskii, In "Vychislitel'naya tekhnika" (Computer technology), p.123, M., 1958.

6. O.V.Rosnitskii, in "Trudy I mezhdunarodnogo kongressa Mezhdunarodnoi federatsii po avtomaticheskomu upravleniyu" (Transactions of the 1st International Congress of the International Federation on Automatic Control), Vol.IV, M., 1961.

STABILITY OF THE MAGNETIZATION OF FERROMAGNETS AS A FUNCTION OF THE MAGNETIZING PROCESS

- L. Ya. Frimerman

One of the ways of obtaining stable (with respect to external mechanical factors such as shock or vibration) magnetization of ferromagnets is appropriate choice of the magnetizing procedure.

Considering ideal magnetization of a ferromagnetic single crystal by a constant field H_0 and a decaying alternating field with initial amplitude h_0 directed along an axis of easy magnetization, Kondorskii[1] showed the following:

a) If h_0 is sufficiently large, namely,

$$h_0 \geqslant H_{c\,max} + H_0 + \nu I_s, \tag{1}$$

the result of the magnetizing process will be a magnetization

$$I_0 = \frac{H_0}{\nu}, \tag{2}$$

where $H_{c\,max}$ is the maximum coercive force of the domains (regions of spontaneous magnetization), I_s is the saturation magnetization, and ν is the internal demagnetizing factor.

The initial value of the resultant internal field in the H_0 direction will be

$$H_{init} = h_0 + H_0 - \nu I_s,$$

or, taking (1) into account

$$H_{init} = H_{c\,max} + 2H_0. \tag{3}$$

b) Growth of I_0 during the magnetizing process continues until the resultant internal field in the H_0 direction becomes equal in absolute magnitude to the opposed field and no further wall displacements occur under the influence of the positive half-waves of the alternating field.

c) The well known effect of substantial changes in the magnetization under the influence of external shock or vibration stresses is due to periodic changes (decreases) of the coercive force of the domains as these stresses are communicated to the ferromagnet. Obviously, the change in magnetization occurs, in the first place, owing to displacement of the boundaries of the domains with the lowest values of coercive force.

Let us consider the magnetization of a ferromagnetic single crystal in the same constant field H_0 but in the case of reduced initial amplitude of the alternating field*, i.e., a field of amplitude

$$h_k < H_{c\,max} + H_0 - \nu I_s. \tag{4}$$

We shall show that the resulting magnetization I_k in this case will always be smaller than I_0.

The number of domains determining the value of the magnetization is proportional to the difference between the initial and final fields causing preferential wall displacements in the H_0 direction, i.e., to the range ΔH_c of the co-

---

*Hereinafter for brevity we shall refer to magnetization by a field with initial amplitude h_k simply as "intermediate magnetization".

ercive forces of the domains responsible for the magnetization. In the case of ideal magnetization the initial field is

$$H_{init} = h_0 + H_0 - \nu I_s, \tag{5}$$

and the final field is

$$H_{fin} = h_0 - n_0 \Delta h_0 + H_0 - \nu I_s, \tag{6}$$

inasmuch as it is obvious that decrease of the saturation magnetization I_s in the H_0 direction begins only on termination of the process of formation of I_0. Here n_0 is the number of periods of the alternating field applied in the process of magnetization, and Δh_0 is the difference between successive amplitudes of the alternating field. Assuming that the field is reduced slowly, i.e., that $\Delta h_0 \ll \ll 2H_0$, we can set $\Delta h_0 = \text{const}$.

The difference between fields (5) and (6) is

$$\Delta H_{c0} = n_0 \Delta h_0. \tag{7}$$

In the case of intermediate magnetization the initial field equals

$$H_{init} = h_k + H_0 - \nu I_1, \tag{8}$$

and the final field

$$H_{fin} = h_k - n_k \Delta h_k + H_0 - \nu I_1, \tag{9}$$

where I_1 is the magnetization induced by H_{init}.

The difference between fields (8) and (9) is

$$\Delta H_{ck} = n_k \Delta h_k. \tag{10}$$

The difference between the absolute final values of the positive and negative resultant internal fields is zero. In the case of ideal magnetization the expressions for these fields are

$$\begin{aligned} H_{fin\ (+)} &= h_0 - n_0 \Delta h_0 + H_0 - \nu I_s, \\ |H_{fin\ (-)}| &= h_0 - n_0 \Delta h_0 - H_0 - \nu (I_s - n_0 2I_0'), \end{aligned} \tag{11}$$

where $2I_0'$ is the change in magnetization owing to decrease of the field by Δh_0. Assuming the difference between expressions (11) to be zero, we obtain

$$n_0 = \frac{H_0}{\nu I_0'}. \tag{12}$$

In the case of intermediate magnetization

$$\begin{aligned} H_{fin\ (+)} &= h_k + H_0 - n_k \Delta h_k - \nu I_1, \\ |H_{fin\ (-)}| &= h_k - (H_0 - 2\nu I_k'') - n_k \Delta h_k - \nu (I_1 - n_k 2I_k'), \end{aligned} \tag{13}$$

where $2I_k'$ is the change in magnetization owing to decrease of the field by Δh_k, and $2I_k''$ is the change in magnetization during the first period of the alternating field; this does not depend on n_k and occurs due to the difference $2H_0$ between the first negative value of the field and its first positive value. Assuming the

difference between expressions (13) to equal zero, we can write

$$n_k = \frac{H_0 - \nu I_k''}{\nu I_k'}. \tag{14}$$

Inserting (12) and (14) into (7) and (10), we obtain

$$\Delta H_{c0} = H_0 \frac{\Delta h_0}{\nu I_0'},$$
$$\Delta H_{ck} = (H_0 - \nu I_k'') \frac{\Delta h_k}{\nu I_k'}. \tag{15}$$

Invoking the fact that $\frac{\Delta h_k}{\nu I_k'} = \frac{\Delta h_0}{\nu I_0'}$, we have

$$\Delta H_{ck} < \Delta H_{c0}, \tag{16}$$

i.e., in the case of intermediate magnetization the range of the coercive forces of the domains responsible for the magnetization and, consequently, the number of these domains as well are less than in the case of ideal magnetization; hence so is the resultant magnetization. I_k'' can equal zero only when the first negative value of the field differs from the first positive value by the amount Δh. Obviously, this is possible if the first positive value of the field exceeds $H_{c\,max}$ by $2H_0$, which, according to (3), is the condition for ideal magnetization. This inference is also valid in the case when the initial amplitude of the resultant internal field $H_{init} > H_{c\,max}$, provided $H_{init} < H_{c\,max} + 2H_0$.

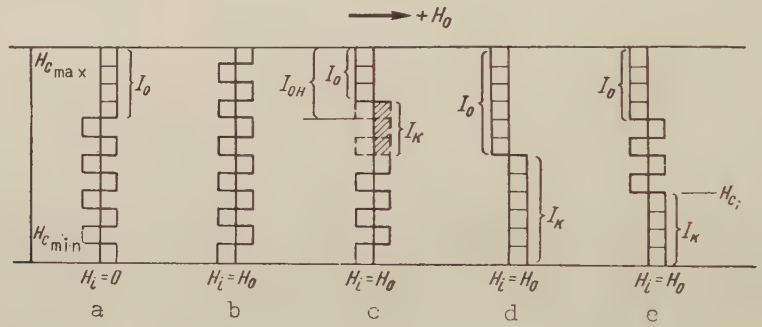

For $H_{init} < H_{c\,max}$, with decrease of h_k there will obviously arrive an instant after which I_k will have a lower bound, i.e., the magnetizing process will take in domains with $H_{c\,min}$ before equality of the positive and negative amplitudes of the resultant internal field is attained. Inasmuch as the upper bound of H_c of the domains participating in the formation of I_k will be reduced owing to decrease of h_k, the final result will be decrease of I_k.

On the basis of the foregoing we can now examine the stability of magnetization in a positive field H_0 after different methods of magnetizing. A finite magnetization that is stable in the field H_0 can obviously be produced by ideal magnetization in a field of this strength. In this case the internal field of the ferromagnet will be equal to zero, and shock stresses will not alter the magnetization (see diagram a).

Zero magnetization can be produced in two ways:

1. Ideal magnetization in an external field H_0 as a result of which domains with different H_c will have their boundaries uniformly shifted in the directions $\pm H_0$ (see diagram b). In this case the internal field H_i will equal H_0. The walls

of the domains with minimal H_c, initially shifted in the $-H_0$ direction, will be displaced in the $+H_0$ direction under the influence of external stresses (shock or vibration).

2. Ideal magnetization in a negative external field and subsequent intermediate magnetization in a field H_0, so that the resultant magnetization will equal zero:

$$\nu I = \nu I_0 - \nu I_k = 0. \tag{17}$$

In the case of ideal magnetization, owing to displacement of the walls of domains with high coercive force (diagram c) there will appear a magnetization I_{0H}. As was shown above, I_k cannot equal I_{0H}, and fulfillment of condition (17) requires us to choose a value of h_k such as will insure decrease of I_{0H} to $I_0 = I_k$, i.e., a value that will provide for participation in the intermediate magnetization process of part of the domains responsible for I_{0H} (the part of the domains with the lowest value of coercive force). The stability of the magnetization can be enhanced by increasing I_{0H} and I_k through increase of the external field in ideal magnetization. Indeed, the permanent internal field produced by intermediate magnetization is determined by the sum $H_0 + \nu I_0$, which makes it possible to increase I_k by increasing I_{0H}. Thus there can be obtained the more stable state represented by diagram d. A similar state can also be obtained without increasing the external ideal-magnetization field, if the intermediate magnetization is carried out in a field $m \times H_0$. At a sufficiently high value of the factor m there can be obtained the state represented by diagram e. This state will be stable with respect to external mechanical factors whose influence is equivalent to the influence of internal magnetic fields not exceeding H_{c_1}.

Reference

1. E.I.Kondorskii, Zhur.eksp.i teor.fiz., 37, 1110 (1960). (Trans.Soviet Physics - JETP.)

MAGNETIZATION AND MAGNETOSTRICTION JUMPS IN NICKEL

- A.Ya.Vlasov & Yu.D.Tropin

Magnetostriction jumps were first observed experimentally by Heaps[1,2]. In the present work, for detailed study of magnetization and magnetostriction jumps[3], there was assembled the set-up diagramed in Fig.1. The specimen 1 is held between the micrometric screw 2 and the piezoelectric crystal 3 (a bimorph cell of X-45° cut Rochelle salt); the entire assembly in the supporting frame 4 is mounted inside the solenoid 5. The solenoid itself is placed in a soundproof container. For recording magnetization jumps, we used the conventional search coil procedure (see Ref.4). The signals from the piezocrystal 3 and the search coil 6 are fed to the inputs of channels I and II, respectively. After appropriate amplification for visual observation and photography, the signals are transmitted to oscillographs (E0-7 and I0-4), and then to the shaping network SN which converts them to standard-shape pulses, and to photorecorders (FR-5). The pulse height discriminators PHD and scaling circuits SC (PS-10 000 scalers) are provided for determining the statistical distribution in magnitude of both types of jumps.

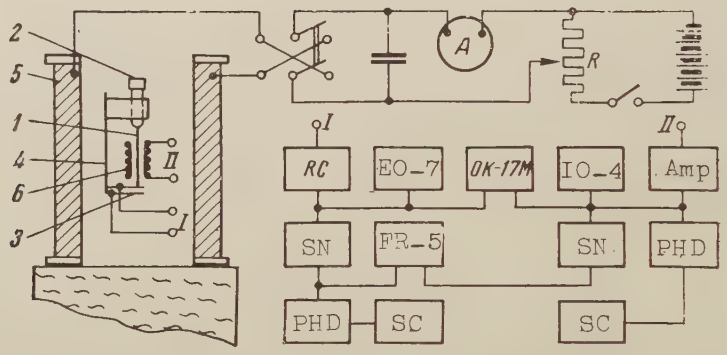

Fig.1. Set-up for simultaneous observation of magnetostriction and magnetization jumps: 1) specimen, 2) micrometric screw, 3) piezocrystal (bimorph cell), 4) supporting frame, 5) solenoid, 6) search coil. E0-7 & I0-4 - oscilloscopes, SN -shaping network, FR-5 - photorecorders, SC - scaler, PHD - pulse height discriminator.

The set-up is graduated for magnetization jumps[5] in $A = \left(\frac{dm}{dt}\right)_{max}$ units. The calibration for magnetostriction jumps is based on the following considerations. Incident to abrupt reversal of an elementary volume of the specimen, there occurs deformation of this volume and, consequently, an elastic stress pulse propagates along the specimen. The relative elongation of the specimen is given by[6]

$$\Delta\lambda = \frac{\Delta l}{l} = \frac{2}{El}\int_0^t \sigma dt. \qquad (1)$$

The stress pulse $\sigma(t)$ on reaching the piezocrystal, will bring it out of equilibrium and cause it to vibrate at its natural frequency. These damped vibrations are described by

$$\frac{d^2x}{dt^2} + 2h\frac{dx}{dt} + k^2x = f(t), \qquad (2)$$

where the second term characterizes the resistance of the medium and the internal friction, the third term - the elastic force tending to return the system to equi-

librium, and $f(t)$ is a free term characterizing the external perturbing force.

Solving this equation for the condition $\tau < T$, where τ is the effective time of the pulse and T is the vibration period of the system, we find the magnitude of the first maximum deflection of the crystal:

$$x = \frac{1}{p}\int_0^T \sigma(t)\, S\, dt, \tag{3}$$

From Eqs.(3) and (1), we obtain

$$\Delta\lambda = \frac{2xp}{EV}. \tag{4}$$

The vibration frequency p of the crystal and the volume V of the specimen are determined experimentally; Young's modulus E is taken from appropriate tables. Having established the deviation dependence of the signal $\mathscr{E}$ from the piezocrystal, we can readily calculate the magnetostriction of the specimen by means of Eq. (4). The smallest change in length detectable by the set-up is $6\cdot10^{-9}$ cm; accordingly, the minimum observable magnetization jump is $11\cdot10^{-3}$ G cm^3 sec^{-1}.

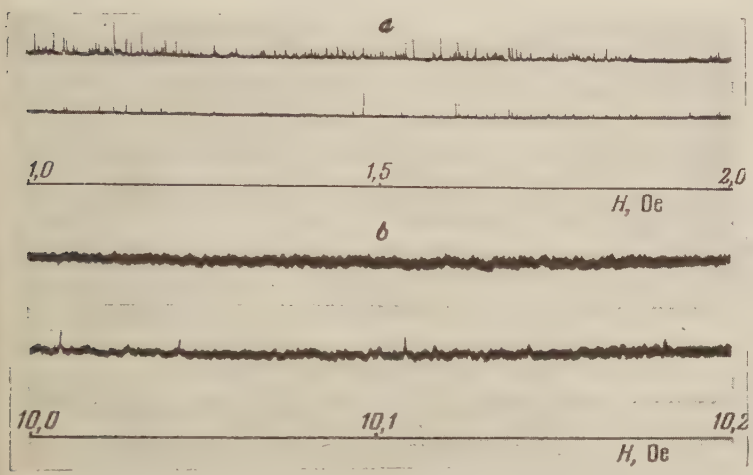

Fig.2. Oscillograms of magnetization (upper) and magnetostriction (lower) jumps in fields of 1-2 Oe (a) and 10-10.2 Oe (b).

The present measurements were carried out on an annealed nickel specimen 0.01 cm in diameter and 2.0 cm in length with the magnetization being varied over the H_c = 1.5 Oe hysteresis loop at the rate of 0.01 Oe/sec. The specimen was annealed in vacuum (10^{-4} mm Hg) at 1000°C for three hours, followed by slow cooling in a magnetic shield.

It will be evident from the oscillograms reproduced in Fig.2 that in weak fields intense and numerous jumps of both types are observed. With increase of the field both the number and magnitude of the jumps decreased and in fields of the order of 10 Oe the magnetization jumps fall below the noise level. At the same time, magnetostriction jumps can still be detected. No proportionality is observed between the magnitude of individual magnetization jumps and the magnitude of the corresponding magnetostriction jumps.

This result can be explained by the fact that the values of $\left(\frac{dm}{dt}\right)_{max}$ are not, in general, proportional to Δm. Probably the main reason, however, is that in polycrystalline specimens the angles between the magnetization vectors in neighboring domains can vary in a wide range (from 0 to 180°). The values of Δm and $\Delta\lambda$, however, depend differently on the angle through which the magnetization vectors in the domains change their direction incident to wall displacements.

Thus, from the relation between Δm and $\Delta\lambda$ for each abrupt wall displacement, we can judge of the type of displacements, while from the ratio of the total numbers of jumps of both types we can judge of the relation between the magnetic phases in the specimen and of its degree of texture (grain orientation).

The statistical distributions of both types of jumps (Fig.3) are qualitatively

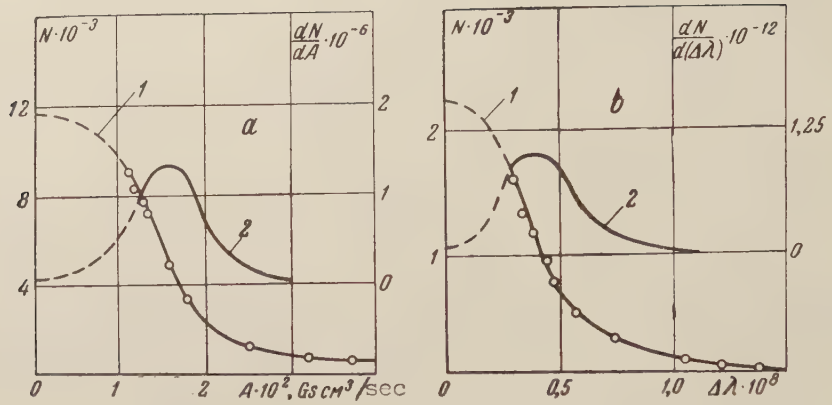

Fig.3. Integral (1) and differential (2) curve of the statistical distribution in magnitude of magnetization (a) and magnetostriction (b) jumps.

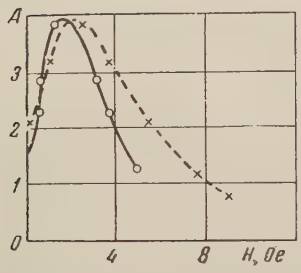

Fig.4. Field dependences of the magnitudes of the maximum magnetization (solid curve) and magnetostriction (dashed curve) jumps.

similar. The magnitude of the most probable magnetostriction jump $\Delta\lambda_H = 0.40 \cdot 10^{-8}$; the mean magnitude of a magnetostriction jump $\Delta\lambda_{av} = 0.46 \cdot 10^{-8}$. The value of the magnetostrictive change in specimen length, determined as the total magnitude of all the magnetostriction jumps, $\lambda = N\Delta\lambda_{av}$ (where N is obtained by extrapolation of the integral jump distribution curve) equals $10.6 \cdot 10^{-6}$.

Thus, irreversible wall displacement processes play a substantial role in magnetostriction. The distribution in field of the magnetostriction jumps differs somewhat from that of the magnetization jumps (see Fig.4). Wall displacement processes occurring in fields somewhat greater than the coercive force make a more substantial contribution to the magnetostriction. As the magnetization of the specimen approaches technical saturation, the magnitude of both types of jumps decreases, but the amount of decrease for magnetostriction jumps is appreciably less than for magnetization jumps.

Physical Institute,
Siberian Division of the
Academy of Sciences of the USSR

References

1. C.W.Heaps & A.B.Bryan, Phys.Rev., 36, 1930.
2. C.W.Heaps, Phys.Rev., 59, 585 (1941).
3. A.Ya.Vlasov & Yu.D.Tropin, Tezisy dokladov na Soveshchanii po ferromagnetizmu i antiferromagnetismu (Program of the (present) Conference on Ferromagnetism and Antiferromagnetism), 1961.
4. V.F.Ivlev & V.M.Rudyak, In "Magnitnaya struktura ferromagnetikov" (Magnetic structure of ferromagnets), p.101, M., 1960.
5. A.M.Rodichev, V.A.Ignatchenko & N.M.Salanskii, Ibid., p.113.
6. G.S.Gorelik, Kolebaniya i volny (Vibrations and waves), M., 1959.

EFFECT OF MECHANICAL FACTORS ON THE MAGNETIC STRUCTURE AND PROPERTIES OF ALLOYS

- L.N.Fedotov, V.P.Popova & B.V.Molotilov

I. Alloys with a reduced sensitivity of the permeability to mechanical factors

The development of alloys having high and stable magnetic properties is one of the pressing problems of alloy metallurgy. In discussing the stability of magnetic properties, we must bear in mind two groups of factors. The first group consists of purely magnetic factors associated with the choice of magnetizing procedure and the structure and mobility of the domain walls. The second group includes factors connected with the structural characteristics of the alloy: number of defects, ductility, etc. Below we present some data on the influence of mechanical stresses on the properties of alloys and analyze the conditions for stabilization of these properties.

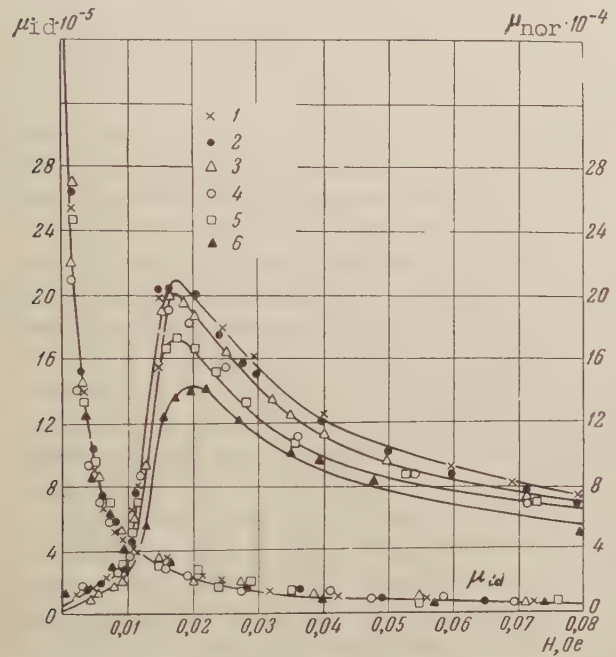

Fig.1. Influence of elastic stress σ on the permeability of 76NKhD alloy: 1) σ = 0, 2) σ = 1.48 g/mm^2, 3) σ = 2.76 g/mm^2, 4) σ = 4.45 g/mm^2, 5) σ = 8.15 g/mm^2, 6) σ = 20.2 g/mm^2. μ_{nor} - permeability evaluated from the normal magnetization curve; μ_{id} - permeability evaluated from the ideal magnetization curve.

Kondorskii[1] showed that the magnetization procedure employed can affect the degree of magnetic stability as regards elastic stresses. The state most stable as regards loads within the elastic limit is achieved by ideal magnetization (application of a constant field plus a decaying alternating field of sufficient initial amplitude). In this way one can obtain a stable state which, however, differs for different alloys.

Thus, for example, Figs.1 and 2 show the influence of compressive stresses, directed perpendicular to the magnetic flux, on the permeability in different fields, obtained in magnetizing along the normal curve and along the ideal curve for alloys 79NMA (79НМА) and 76NKhD (76НХД), which have approximately the same magnetostriction ($\lambda_s \approx 0.2 \cdot 10^{-6}$). It will be evident that change from the normal to the ideal magnetization curve enhances the stability of the magnetic state as regards compressive stresses. It will be noted, however, that the stabilization is different for the 76NKhD and 79NMA alloys: the improvement is more significant for the 76NKhD alloy.

Thus, although ideal magnetization leads to enhancement of the stability for all alloys, in view of the variation observed, it is evidently worth searching for materials exhibiting better stability when magnetized under the indicated conditions.

Actually the effect of external elastic stresses reduces to displacement of different types of domain boundaries. Fig.3 shows the domain structure in the (100) plane of 3.4% Si-iron alloy and the changes in the domain configuration incident to application of an elastic stress. Under a load of the order of 1 kg/mm^2 the most significant alterations are exhibited by the 90° walls; the 180° boundaries shift very little. Other experiments showed that the principal domain walls

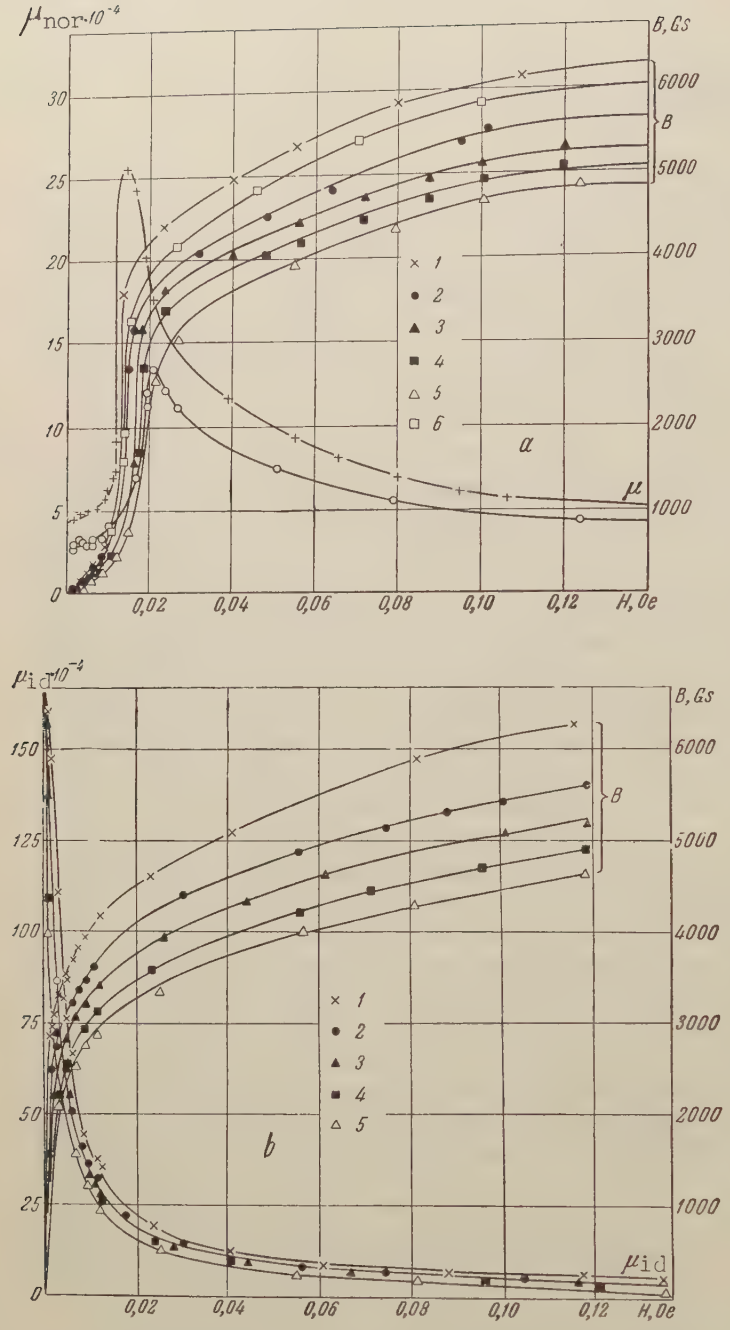

Fig.2. Influence of elastic stress σ on the magnetization curve and permeability of 79NMA alloy: 1) σ = 0, 2) σ = 0.8 g/mm^2, 3) σ = 2.3 g/mm^2, 4) σ = 4.4 g/mm^2, 5) σ = 8.1 g/mm^2, 6) σ = 0 (after removal of load); a - normal magnetization curves and permeabilities; b - ideal curves and permeabilities.

are generally less mobile in stress fields than the boundaries of subdomains and closure domains. Thus, it would appear the treatment of alloys leading to simplification of the magnetic structure, i.e., to a domain structure consisting only of 180° domains, should result in enhanced stability of the magnetic properties. At the same time, however, one cannot avoid some sacrifice in properties inasmuch as the 90° walls make a greater contribution to the susceptibility of ferromagnets in the field region of wall displacements than do the 180° walls. Nevertheless, in a number of cases it may be worth while to enhance the stabilization even at some sacrifice in properties.

A number of ways of simplifying the magnetic structure are known. One of the most direct expedients for eliminating auxiliary (closure) domains is that of reducing the thickness of the material. It is known[2] that beginning with a certain thickness (for transformer steel strips the critical thickness is 50 microns) there are no auxiliary domains in the domain structure. Auxiliary domains and 90° walls can be eliminated by texturing the material by appropriate thermomagnetic or thermomechanical treatment or by use of material in a prestressed state.

As will be evident from Fig. 3, the 180° walls are also displaced upon application of an elastic stress, although the displacement is appreciably smaller than for the 90° walls. The reason for displacement of the 180° walls was established by Kondorskii[1], who also developed the principles of stabilization of walls of this type. The principal condition for stability of the 180° walls is that the true

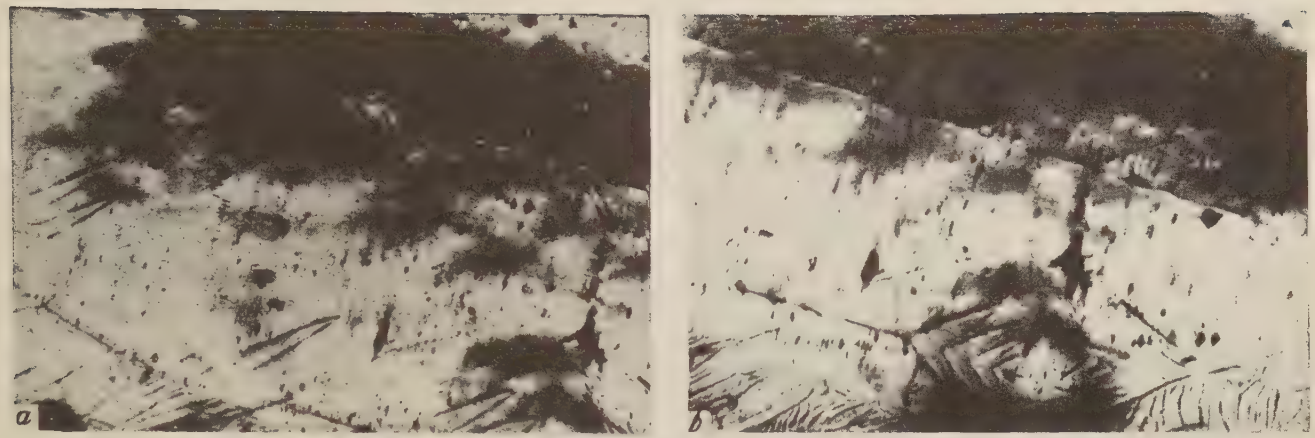

Fig.3. Displacement of domain walls in a specimen of 3.4% Si iron under the influence of elastic stresses - (100) surface. Load applied in the plane of the specimen: a) $\sigma = 0$, b) $\sigma = 1$ kg/mm^2.

internal field acting on them be equal to zero. This field is associated with the internal demagnetizing factor of the alloy. Most stable as regards stress are states for which the mean magnetization is determined as the quotient of the magnitude of the external field divided by the mean demagnetizing factor. The mean demagnetizing factor, in turn, is connected with the imperfection of the material (the concentration, type and distribution of defects). Thus in searching for stable materials one should give special attention to materials with defects, for it appears that an optimum number of defects may prove to be useful.

Theory[3] predicts enhanced stability of all types of domain walls for the case of a zero magnetostriction constant. This condition, however, is applicable only to homogeneous materials which have the same magnetostriction (zero) at all points of the crystal lattice. Actual alloys, of course, always contain different defects, fluctuations in concentration and so on, i.e., regions in which the magnetostriction differs from zero. Obviously, such a "quasiheterogeneous" ferromagnet can no longer be described by the simple condition $\lambda_s = 0$. Moreover, one must bear in mind the different capabilities of alloys to undergo microplastic deformation (strain occurring below the microscopic yield point). For purposes of illustration, let us consider two alloys with λ_s close to zero, namely, silicon-iron alloy with 6.2% Si ($\lambda_s = 0.3 \cdot 10^{-6}$) and 79NMA alloy ($\lambda_s = 0.2 \cdot 10^{-6}$). The magnetic-property stability of both alloys should be high if we go by the criterion $\lambda_s = 0$ and the 79NMA alloy should be somewhat more stable. As a matter of fact, however, it is found that under the influence of tensile stresses of the order of 1 kg/mm^2 the permeability of 79NMA alloy decreases by a factor of two, while the permeability of the 6.2% Si iron alloy falls off by only a few per cent. Moreover, after removal of the load the initial magnetic state of the 79NMA alloy is not re-established.

Fig.4 shows the magnetic structure of a specimen of silicon-iron alloy with 6.2% Si after brittle fracture. It will be seen that the magnetic structure even close to the boundary of the crack is little distorted. Fig.5 shows the powder pattern on a microsection of 79NMA alloy after the same deformation (0.5%). It will be seen that the magnetic suspension has settled along bands that are shear lines. In the unstressed state there does not occur any precipitation of the magnetic suspension on the surface of 79NMA alloy, owing to the fact that the

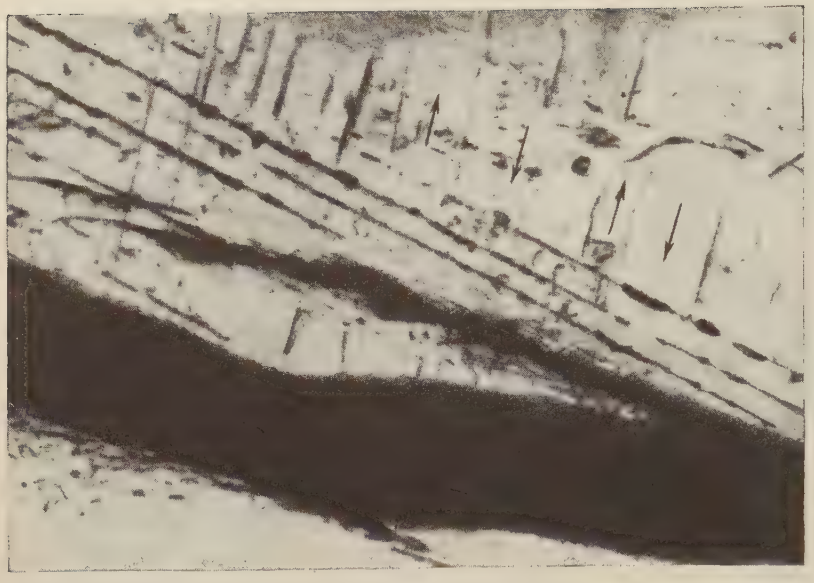

Fig.4. Magnetic structure of 6.2% Si-iron alloy near a brittle-destruction fracture (deformation 0.5%).

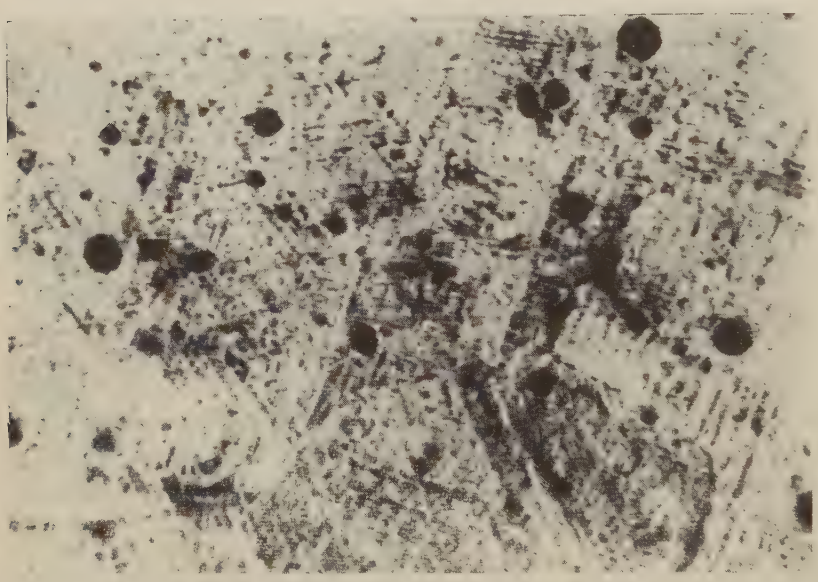

Fig.5. Powder patterns on the surface of a microsection of 79NMA alloy after 0.5% plastic deformation.

only in the case of brittle alloys.

magnetostriction and magnetic anisotropy constants of the material are close to zero. As a result of microplastic deformation, however, there appear sections of the crystal lattice where the constants are no longer zero. Thus, it is essential to take into account the microplastic deformability of alloys in designing stable materials. The most stable proved to be alloys capable of brittle fracture. These included, in addition to the above mentioned high silicon alloy, iron alloys with aluminum (16%) and iron alloys with silicon and nickel (for example, N12S8 alloy).

Above we spoke of fixation of the 180° walls by defects, particularly by inclusions. However, inclusions can also play a negative role in the matter of stability, when they act as stress concentrators. In this case, even at low or medium stresses there may build up near inclusions sufficiently high stresses as to produce displacement of the domain walls. In plastic alloys overstresses may lead to local plastic deformation, which will naturally result in irreversible changes in the properties of the material. It is preferable, therefore, to resort to fixation of the 180° walls by inclusions

II. Alloys with enhanced sensitivity of the impedance to mechanical factors.

We also investigated the variation in ac impedance of 68N and 79NMA alloys and an alloy consisting of 79% Ni, 3% Re and 18% Fe under the influence of elastic stresses. The impedance measurements were carried out by the bridge method at frequencies from 20 to 200 kc; the specimens were in the form of wires 0.2 mm in diameter and 150 to 170 mm in length. To avoid the possibility of chance de-

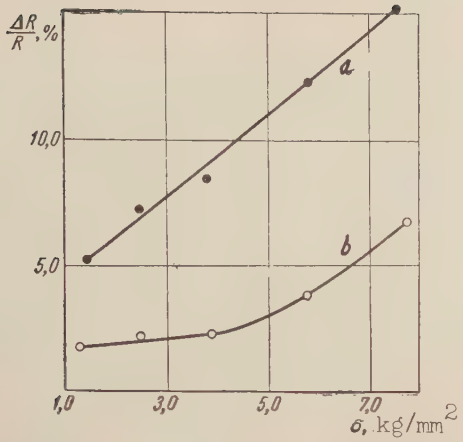

Fig.6. Variation of resistances as a function of stress: a - 79% Ni + 3% Re + 18% Fe alloy, annealed (125 kc), b - 79NMA alloy, optimum heat treatment (150 kc).

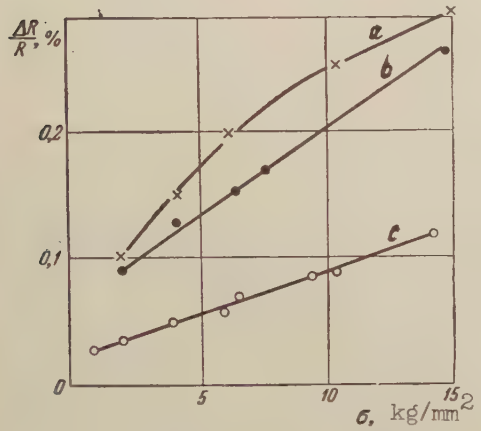

Fig.8. Galvanoelastic effect: a - 79% Ni + 3% Re + 18% Fe alloy, quenched; b - same alloy, annealed; c - 79NMA alloy, optimum heat treatment.

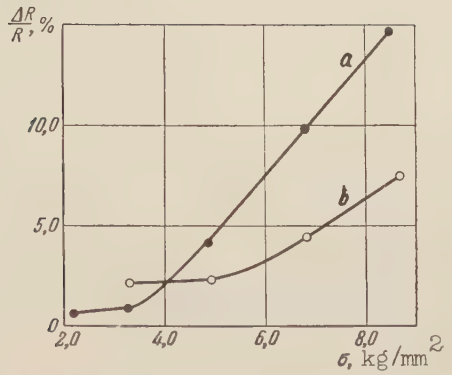

Fig.7. Variation of resistances as a function of stress: a - 68N alloy, optimum heat treatment (50 kc); b - 79NMA alloy, optimum heat treatment (150 kc).

formation the specimens were placed in quartz tubes, and were annealed and measured in these tubes.

The 68N and 79NMA alloy specimens were subjected to the optimum heat treatment recommended by the Institute of Precision Alloys. The specimens of the 79% Ni + 3% Re + 18% Fe alloy were subjected to the following heat treatments: quenching from 1000° or annealing at 1100° for three hours followed by cooling at the rate of 100 degree/hour to 400° and then in the vacuum container in air.

The variation of the change in resistance ($\Delta R/R$) at the frequency at which there was observed the greatest change in impedance under stress is shown in Figs. 6 & 7. The greatest change in resistance under the influence of stress is observed for the Ni-Re-Fe alloy and alloy 68N. For both these alloys $\Delta R/R$ equals about 15% at $\sigma = 7$ kg/mm^2. However, the alloy with Re exhibits some superior characteristics: 1) its resistivity is higher than that of the 68N alloy ($\rho = 0.22$ ohm mm^2 m^{-1} for the 68N alloy and $\rho = 0.44$ ohm mm^2 m^{-1} for the Ni-Re-Fe alloy), and 2) the Ni-Re-Fe alloy exhibits linear stress dependence of its resistance in the stress in the range from 1 to 8 kg/mm^2.

Fig.6 presents data on the galvanoelastic effect in annealed and quenched Ni-Re-Fe alloy and in Mo-containing alloy 79NMA. It will be seen that the effect is stronger in the former alloy.

The noted superiority of the Ni-Re-Fe alloy over the more stress-sensitive 68N alloy suggests that it may be suitable for use in resistance strain gages. The present indications are that strain gages of this alloy should have a sensitivity some two orders of magnitude higher than the usual gages employing alloys

of the constantan type.

Institute of Precision Alloys,
Central Scientific Research Institute of Ferrous Metals

References

1. E.I.Kondorskii, Zhur.eksp.i teor.fiz., 37, 1110 (1959). (Trans.Soviet Physics - JETP.)
2. V.R.Abel's & Ya.S.Shur, Fizika metallov i metallovedenie (Physics of metals and metallurgy), 3, 433 (1956).
3. S.V.Vonsovskii, Zhur.eksp.i teor.fiz., 17, 1094 (1947).

PROPERTIES OF FERROMAGNETIC FILMS PREPARED BY CATHODE SPUTTERING

- R.D.Ivanov, G.V.Spivak & G.K.Kislova

Earlier[1] we proposed a cathode sputtering procedure for preparing high quality single and multiple component ferromagnetic films.

In the present report we describe an improvement of this procedure, which makes it possible to record the magnetization curves and hysteresis loops of the sputtered films under vacuum (10^{-6} mm Hg).

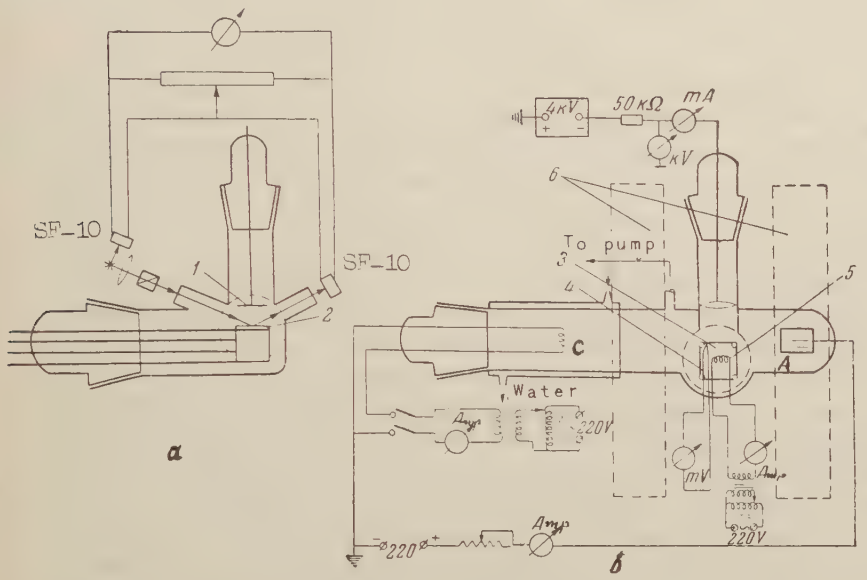

Fig.1. Diagram of the apparatus. a - circuit for measuring the hysteresis loop and magnetization curve: 1) sputtered film, 2) glass substrate; b - electric circuit for sputtering films: 3) casette with glass substrates, 4) thermocouple, 5) substrate heater, 6) Helmholtz coil for producing the forming field (field determining the easy magnetization axis) and reversing field. C - cathode, A - anode, SF-10 - selenium photocell.

For the purpose of determining the principal loop parameters of the films in the process of deposition we chose the magnetooptical method utilizing the equatorial Kerr effect in the form proposed by Krinchik[2].

A diagram of the equipment is shown in Fig.1. The main difference from the original apparatus[1] is the addition to the discharge tube of two branches with plane windows (Fig.1,a). Polarized light is directed through one window onto the surface of the film, and the reflected light is viewed by the photocell through the other window. By means of a bridge circuit comprising two SF-10 selenium photocells and an M21/2 galvanometer one can record the hysteresis loops under static conditions directly in the set-up without exposing the ferromagnetic film to the atmosphere. This provides for continuous monitoring of the quality of the films during sputtering. By means of this set-up we have obtained different ferromagnetic films (Mo-permalloy, iron, supermalloy, and others) and recorded their hysteresis loops and magnetization curves (Fig.2).

The films were deposted in a magnetic field; the measuring (reversing) field was applied in the direction of easy magnetization. The films were deposited on heated substrates. The sputtering conditions for all the films were approximately the same: discharge current 0.5-1 amp, specimen potential 1.8-2.2 kv relative to the cathode, inert gas (krypton) pressure in tube $(4-2)\cdot10^{-3}$ mm Hg, current density on specimen 1-3 ma/cm^2, forming field 44.2 oersted, sputtering time 2-3 min.

We felt it would be of interest to observe the variation in the coercive force from the time of preparation of the film in the apparatus and during its subsequent oxidation as a result of exposure to air. The variation of the co-

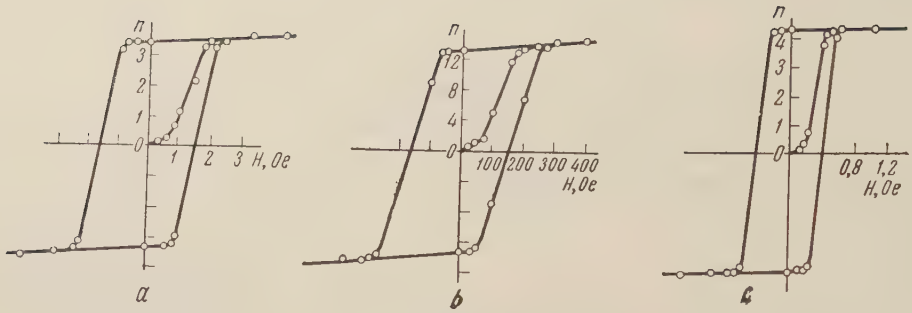

Fig.2. Magnetization curves and hysteresis loops recorded for 1000 Å thick films (n is the number of divisions on the scale of our instrument and is proportional to the magnetization): a - Mo-permalloy, b - pure iron, c - supermalloy.

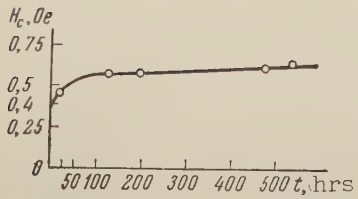

Fig.3. Variation of the coercive force of a 1000 A thick supermalloy film in the process of oxidation in air.

ercive force of a 1000 Å thick supermalloy film is shown in Fig.3. The point on the vertical axis was measured in the set-up (vacuum 10^{-6} mm Hg) immediately after deposition. The other points show how H_c varies with time when the film is exposed to the atmosphere. It will be seen that H_c of the film prior to oxidation is rather low. It increases noticeably during the first hours of exposure to air; then the growth of H_c levels off. Similar results were obtained for the other ferromagnetic films. This behavior of H_c indicates that the oxide coating forming on the film protects it against further changes of its magnetic properties.

Hence in the future it may be expedient to take measures to protect the films produced by sputtering so that they can be exposed to air without altering their magnetic properties; it may also be desirable to modify parts of the light detecting arrangement to permit oscillographic recording of the entire process of magnetization reversal.

Physics Faculty,
Moscow State University

References

1. G.V.Spivak, I.G.Sirotenko & R.D.Ivanov, Izv.AN SSSR, Ser.fiz., 25, 581 (1961). (Trans.Bulletin, 25, No.5.)

2. G.S.Krinchik, Fizika tverdogo tela, 2, No.8 (1960). (Trans.Soviet Physics - Solid State.)

Bulletin of the Academy of Sciences of the USSR - Physical Series
Vol.25, No.12 - December 1961

Transactions of the (First) Conference on Ferromagnetism & Antiferromagnetism
(Continued from Vol.25, No.11; to be continued in Vol.26, No.2)

Table of Contents

	Page Orig.	Trans.
Change in conductivity incident to magnetization and magnetic anisotropy in ferrite single crystals of the $Mn_xFe_{3-x}O_4$ system - K.P.Belov & A.V.Zalesskii	1434	1447
Temperature dependence of the low-field magnetization of manganese ferrite - E.F.Kovtun & A.S.Mil'ner	1437	1450
Behavior of domain structure during magnetization - V.A.Ignatchenko, I.F.Degtyarev & Yu.V.Zakharov	1439	1452
Variation of the magnetization switching process with reduction in particle size - E.V.Shtol'ts, A.A.Glazer & Ya.S.Shur	1445	1458
Investigation of domain walls in transformer steel - M.K.Savchenko & V.I.Sinegubov	1449	1462
Influence of the direction of demagnetization on the magnetic structure of crystals in sheet silicon steel - V.R.Abel's	1452	1466
Regarding the stability of the magnetic state of soft materials - V.A.Zaikova & I.E.Startseva	1455	1469
Effect of ultrasonic vibration and alternating magnetic fields on the domain structure of silicon steel - D.A.Laptei & V.S.Cherkashin	1461	1475
Development of mirror electron microscopy of magnetic microfields - G.V.Spivak, L.V.Kirenskii, R.D.Ivanov & N.N.Sedov	1465	1481
Concerning the rectangularity of the hysteresis loops of Mg-Mn ferrites - I.E.Startseva & Ya.S.Shur	1469	1485
Temperature dependence of the first anisotropy constant and the magnetic structure of Fe-Mn ferrites - L.V.Kirenskii, A.I. Drokin, V.D.Dylgerov, N.I.Sudakov & E.K.Zagirova	1472	1488
Determination of the character of the magnetic anisotropy of alloys with single domain structure from their residual magnetization - M.G.Luzhinskaya	1476	1492
On the nature of the coercive force in Alnico alloys - A.S. Ermolenko & Ya.S.Shur	1479	1495
Carbonyl iron powders - V.L.Volkov, I.S.Tolmasskii & A.E.Fridenberg	1483	1500
Investigation of rotational hysteresis in cold rolled and re-crystallized nickel - N.L.Bryukhatov & N.A.Grinchar	1486	1503
Rotational hysteresis of magnetostriction in ferromagnets - L.V.Kirenskii & V.S.Afoshin	1492	1508
Crystal and magnetoelastic anisotropy and its temperature dependence in iron-nickel single crystals - I.M.Puzei	1494	1511
Effect of the field strength in magnetic annealing on the magnetic properties of cold-rolled electrical steel - D.D.Mishin, T.I. Bychkova & V.A.Smagin	1498	1515
Magnetic texture of ferromagnets subjected to external stresses - F.N.Dunaev	1502	1519
Investigation of the effect of creep of nonsymmetrical hysteresis loops - O.V.Rosnitskii	1507	1524
Stability of the magnetization of ferromagnets as a function of the magnetizing process - L.Ya.Frimerman	1511	1528

Magnetization and magnetostriction jumps in nickel - A.Ya.Vlasov & Yu.D.Tropin 1514 1532
Effect of mechanical factors on the magnetic structure and properties of alloys - L.N.Fedotov, V.P.Popova & B.V.Molotilov 1518 1535
Properties of ferromagnetic films prepared by cathode sputtering - R.D.Ivanov, G.V.Spivak & G.K.Kislova 1524 1541

Translated in 1962 by
Columbia Technical Translations
5 Vermont Ave., White Plains, N.Y.

For Notes

For Notes

SUMMARY OF THE CONTENTS

of

VOLUME XXV

of the

BULLETIN OF THE ACADEMY OF SCIENCES OF THE USSR

- Physical Series -

SUBJECT SUMMARY - VOLUME 25

Transactions of the Tenth All-Union Conference on Nuclear Spectroscopy
(Concluded from Vol.24, Nos.3,7,9 & 12)

Number 1

	Page (Trans.)
Analysis of second forbidden β-spectra - M.Vindushka & L.N. Zyryanova	53
Systematics of reduced lifetimes for β-transitions of different degrees of forbiddenness - L.N.Zyryanova & V.M.Mikhailov	57
Internal conversion with pair production in the decay of Ta^{182} - S.S.Vasilenko, M.G.Kaganskii, D.L.Kaminskii & S.F.Koksharova	62
Determination of the K-shell conversion coefficient of the 143 Kev transition in Pr^{141} by means of a 4π scintillation spectrometer - L.Nemet	68
Coulomb excitation of nuclear levels in P^{31}, S^{33}, Mn^{55} and Pr^{141} by Ne^{20} ions - D.S.Andreev, A.P.Grinberg, K.I.Erokhina & I.Kh.Lemberg	70
Probabilities for gamma-transitions in odd-odd deformed nuclei - D.A.Varshalovich	76
Electromagnetic transitions in deformed nuclei - Yu.N.Gnedin	82
Investigation of the decay schemes of Gd^{146}, Gd^{147} and Gd^{149} by means of a β-γ coincidence spectrometer - E.E.Berlovich, O.V.Larionov, E.N.Tunimanova & D.M.Khai	88
The Photoritron (A gamma-spectrometer for the low-energy region) - B.S.Dzhelepov & Yu.V.Khol'nov	95
Determination of the relative probabilities for electron capture from the L and K shells in the decay of Cr^{51}, Zn^{65} and Ge^{71} - A.A. Konstantinov & V.V.Perepelkin	103
Decay of Dy^{159} - E.I.Biryukov, O.I.Grigor'ev, B.S.Kuznetsov & N.S. Shimanskaya	106
Nuclear moments of odd gadolinium isotopes - N.I.Kaliteevskii, M.P. Chaika, I.Kh.Pacheva & E.E.Fradkin	107
The (d,t) reaction on O^{16}, O^{18}, Mg^{24}, Mg^{25} and Mg^{26} - N.A.Vlasov, S.P. Kalinin, A.A.Ogloblin & V.I.Chuev	111
The (n,α) reaction in Pu^{239} induced by thermal neutrons - V.N.Andreev	116
Masses of heavy atoms and nuclear binding energies in the 174 to 239 A region - R.A.Demirkhanov, T.I.Gutkin & V.V.Dorokhov	119
Comparison and systematics of the binding energies of heavy nuclei from hafnium to francium - V.A.Kravtsov	125
Scattering of fast neutrons by nonaxial nuclei - V.I.Belyak	133
Determination of the mean lifetime of the excited states of U^{235} fission fragments - B.M.Shiryaev	137
Collective excitations in superfluid nuclear matter - B.B.Dotsenko	139
Method of discriminating pulses due to fast neutrons from pulses due to γ-rays by means of photomultiplier space charge - G.G.Doroshenko & E.L.Stolyarova	146
Longitudinal polarization of particles in weak four-fermion interaction - B.K.Kerimov	150
Electron-positron correlation in pair production by a polarized photon - B.K.Kerimov & I.M.Nadzhafov	156
Polarization electron-positron correlation in pair production taking into account finite nuclear size - B.K.Kerimov & F.S.Sadykhov	158

Transactions of the Ninth Conference on Luminescence (Crystal Phosphors)

Opening address - V.L.Levshin 3
Luminescence of semiconductor crystals with excitation in the discrete structure region of the absorption spectrum - I.S.Gorban', S.N.Rud'ko & A.A.Shishlovskii 7
Role of impurities in the luminescence of molecular crystals at low temperatures - M.T.Shpak 13
Piezospectroscopic effect in anisotropic centers in cubic crystals - A.A.Kaplyanskii 20
Mechanism of energy storage by crystal phosphors - Ch.B.Lushchik, G.G. Liid'ya & I.V.Yaek 23
Effect of isostructure on the spectra of activated mixed crystals - F.D.Klement & L.A.Teiss 28
Investigation of luminescence processes in alkali halide phosphors - L.M.Shamovskii & P.A.Pipinis 30
Concerning the mechanism of optical flash decay - I.A.Parfianovich & E.I.Shuraleva 37
Exciton excitation of luminescence in activated alkali iodides at low temperature - M.L.Kats, K.E.Gyunsburg & L.I.Golubentseva 43
Atomic centers in NaCl:Ag and KBr:Ag crystal phosphors - V.K.Nikol'skii 45
Luminescence of nonactivated alkali iodides - N.N.Vasil'eva & Z.L. Morgenshtern 47

Number 3

Concerning excitation of crystal phosphors by ions - B.M.Nosenko & N.A. Strukov 303
Thermostimulated luminescence with different forms of excitation - B.M. Nosenko, L.S.Revzin, V.Ya.Yaskolko & A.R.Krasnaya 307
Single crystal cathodoluminescent screens - M.A.Vasil'eva, V.V.Kuprevich, P.P.Feofilov & I.V.Stepanov 311
Investigation of activatorless ZnS sublimate phosphors - E.Ya.Arapova 313
Some characteristics of zinc sulfide-selenide sublimate screens - V.V. Golubets 315
Luminescence properties of cerium activated aluminum oxide and helenite under cathode-ray excitation - T.V.Oranovskaya 317
Cathodoluminophors with very short persistence and emission in the blue, yellow and red regions - Z.I.Klabukova & A.V.Morozova 320
Cathodoluminescence of europium activated strontium phosphates - V.P. Nazarova 322
Comprehensive investigation of the optical and thermooptical properties of polyactivated alkali-halide crystal phosphots - A.Kh.Khalilov, E.Yu. Salaev, A.P.Mamedov, T.D.Alieva & F.K.Isaev 325
Origin of the long wavelength luminescence bands of alkali-halide phosphors - N.I.Ivanova, L.I.Tarasova & A.P.Zhukovskii 331
Sensitized luminescence of KCl-Pb:Mn phosphor - K.K.Shvarts & G.K.Vale 333
Concentration and temperature quenching of luminescence in some silver activated alkali-halide phosphors - L.A.Rebane 335
Luminescence of ammonium halide phosphors - A.Ya.Pae & L.Ya.Uibo 337
Detection of lattice defects in alkali-halide crystals by means of electrolytic coloring - V.M.Bezruchko & A.A.Shatalov 339

Structural defects in crystal phosphors - L.M.Shamovskii & A.S.Shibanov 341
Decoration of dislocations and activator distribution in unstable alkali-halide phosphors - R.I.Gindina 344
Electron diffraction study of the influence of gases on the structure of sublimated layers of alkali-halide salts - A.A.Khaav 346
Kinetics of the luminescence of phosphors with several types of traps - V.V.Anvonov-Romanovskii 348
Effect of the size of natural and crushed crystals on the luminescence of zinc sulfide phosphors - V.L.Levshin & B.D.Syzhikov 353
Kinetics of the luminescence of ZnS:Cu with excitation by alpha-particles and short light pulses - T.P.Belikova & M.D.Galanin 355
Effect of hydrostatic compression on the spectral characteristics of alkali-halide phosphors - Ya.Ya.Kirs & A.I.Laisaar 357
Investigation of photoelectric polarization of zinc sulfide phosphors - I.K.Vitol & I.A.Tale 359
Dielectric changes in ZnS:Cu:Fe phosphors during thermostimulation - P.E.Ramazanov 361
Temperature dependence of the roentgenoluminescence and dark conductivity of Yakutsk diamonds - K.N.Pogodaev & E.S.Vilutis 364
Luminescence of thallium chloride single crystals - N.A.Tolstoi & V.A. Sokolov 366
Concerning the mechanism of excitation and de-excitation of recombination luminescence of alkali-halide phosphors - Ya.A.Valbis, I.K.Vitol & V.E.Zirap 368
Investigation of the efficiency of recombination luminescence of alkali-halide phosphors - I.V.Yaek 370
Photo- and thermostimulated electron emission from alkali-halide phosphors excited by ultraviolet radiation - A.I.Belkind & Kh.F.Kyaembre 371
Investigation of optical dissociation of F centers in alkali-halide crystals - I.A.Parfianovich & E.I.Shuraleva 373
Optical properties of alkali-halide crystals doped with O, S, Se and Te - O.A.Shmits & Yu.R.Zakis 375
Interaction of activators in alkali-halide phosphors - A.T.Khlevnyuk 377
Effect of different gases on the formation of luminescence centers in silver halides - S.I.Golub & N.A.Orlovskaya 379
Luminescence of alkali-halide phosphors activated by antimony trichloride - A.S.Andrianov & M.L.Kats 381
Investigation of the effect of double activation of silver and samarium on trapping levels in and the luminescence of zinc sulfide phosphors - V.L.Levshin, Yu.V.Voronov, V.B.Gutan, S.A.Fridman & V.V.Shaenko 383
Flare-up of ZnS phosphors and competition of the luminescence bands - N.A.Tolstoi, A.M.Tkachuk, V.A.Sokolov, A.V.Burlakov, A.I.Ryskin, Z.S.Mansurova & M.V.Epifanov 389
Characteristics of cathodoluminescence at high excitation densities - Yu.M.Popov 395
Effect of the chemical nature of the flux on the luminescence properties of zinc sulfide and zinc-cadmium sulfide phosphors - A.A.Bundel', A.A. Glagoleva, Z.I.Guretskaya, O.A.Danilevskaya, Dou Kai-khua & L.N.Sokolova 398
Concerning the influence of flux on the optical properties of zinc sulfide phosphors - A.M.Gurevich 400
Influence of fluxes on the properties of electroluminophors - M.A.Berchenko 404
Effect of high pressures on the formation of crystal phosphors and their properties - S.I.Kunenkov 408

Spectroscopic analysis of some luminescence-pure materials and luminophors - L.A.Dvorzhetskaya, L.Ya.Khlebnikova & M.K.Shvaneva 410
On the question of radical-recombination luminescence of crystal phosphors - V.A.Sokolov & A.N.Gorban' 412
Recombination luminescence of Sn^{4+} in aqueous solutions of LiCl and HCl at low temperature - M.U.Belyi, B.A.Okhrimenko & B.F.Rud'ko 414
Correlation between the thermal activation energy for conductivity and the absorption and phosphorescence spectra of some organic substances - A.T.Vartanyan & L.D.Rozenshtein 416
Excitation wavelength dependence of the blue luminescence yield of cadmium sulfide crystals at 20°K - V.L.Broude & V.S.Medvedev 419
Luminescence of Se activated cadmium iodide - I.P.Shapiro 422
Improvement of phosphors for light sources - R.A.Nilender & D.P.Troshenskii 424

Number 4

Different types of phosphor crystallochemical systems and their luminescence properties - M.A.Konstantinova-Shlezinger 435
Thermodynamics of the mechanism of activation of sulfide and sulfide-selenide phosphors - A.A.Bundel', Z.I.Guretskaya & L.B.Taushkanova 438
Influence of oxygen on the luminescence properties of activatorless zinc selenide - L.Ya.Markovskii & R.I.Smirnova 442
Concerning the valence of Sn and Mn activators in crystal phosphors - N.A.Gorbacheva & V.V.Osiko 446
Phosphate luminophors for fluorescent lamps with improved color characteristics - N.A.Gorbacheva, B.M.Gugel', M.A.Konstantinova-Shlezinger, E.S. Lapir & T.G.Rutshtein 447
Effect of replacement of the base materials of phosphors on their luminescence properties - M.-L.Yu.Allsalu 450
Luminescence of lanthanides in thorium oxide - A.K.Trofimov 453
Influence of the synthesis conditions on the luminescence of zinc oxide - Ya.M.Zelikin 455
Quenching and stimulation of the luminescence of zinc oxide under the influence of adsorbed and capillary-condensed vapors and gases - K.V. Tagantsev 457
Investigation of the thermal activation energy for optical quenching of some crystal phosphors - V.L.Levshin & B.M.Orlov 460
Concerning the parameters of sticking centers which determine the kinetics of photo-thermostimulated effects - V.E.Khartsiev 463
Investigation of trapping levels in CaS phosphors by the methods of exo-electronic emission and thermostimulated luminescence - V.L.Levshin & P.A.Pipinis 465
On the possibility of thermal activation of current carrier trapping in crystal phosphors - Yu.L.Lukantsever & F.N.Zaitov 467
Rate of phosphorescence decay as a function of filling of electron traps and temperature - N.V.Zhukova, G.K.Evdokimova & V.L.Levshin 471
Variation of the steady-state luminescence of ZnS phosphors with the excitation intensity - K.-S.K.Rebane 473
Investigation of rare earth activated SrS phosphors by the method of electron paramagnetic resonance - V.V.Antonov-Romanovskii & V.G.Dubinin 475
Investigation of electroluminescence pulses emitted by ZnS:Cu:Al phosphors with a high Cu concentration - A.M.Bonch-Bruevich & V.A.Molchanov 477

Investigation of the electroluminescence of ZnS:Cu and ZnS:Cu:Mn phosphor layers with excitation by dc and pulse voltages - V.N.Favorin, G.S. Kozina & I.D.Anisimova 482
Experimental investigation of the possibility of realizing multiple component electroluminescent devices employing ferroelectric materials - I.Ya.Lyamichev, I.N.Orlov, G.G.Pershin & N.I.Taborko 487
On enhancing the efficiency of a scintillation type slow neutron detector - B.S.Grebenskii, T.V.Timofeeva, S.P.Khormushko & O.S.Tsvetkov 494
Dispersed fast neutron detector - G.V.Gorshkov, B.S.Grebenskii, S.P. Khormushko & O.S.Tsvetkov 498
Selection of phosphor coatings for x-ray screens - A.M.Gurvich & R.V. Katomina 500
Use of strontium sulfide phosphors for making luminous signs - T.A.Krasnova 503
Photoelectric photometer for determination of uranium in sodium fluoride beads - Z.M.Sverdlov 505
Instrument for determining the parameters of fluorescent screens (PRS) - B.I.Pochtarev, K.K.Raspletin & D.V.Fetisov 508
Attachment for the PRS instrument for investigating phosphors from the bombarded side - B.I.Pochtarev 509
Investigation of the electroluminescence of zinc sulfide single crystals - V.E.Oranovskii 512
Electroluminescence and surface properties of crystal phosphors - I.K. Vereshchagin 514
Regarding the possibilities of stimulating the electroluminescence properties of crystals - I.S.Andreev, G.B.Arzumanyan & L.V.Zyrina 516
Effect of ultraviolet irradiation on the luminescence characteristics of an electroluminophor - I.P.Shapiro & N.I.Kuznetsov 519
Investigation of the electroluminescence of some phosphors with excitation by unipolar pulses - V.L.Rabotkin & V.A.Sokolov 520
Some results of an investigation of the deterioration of phosphors during electroluminescence - N.N.Grigor'ev & Yu.A.Kulyupin 522
Use of electroluminescence for character indicators - F.V.Sorkin, A.P. Belyaeva & N.S.Borodin 523
Measurement of losses in an electroluminescent capacitor - E.E.Bukke 526
Investigation of the luminescence of CdS single crystals at low temperatures - E.F.Gross & M.A.Yakobson 527
Investigation of the absorption and luminescence of ZnS and ZnSe single crystals - E.F.Gross & L.G.Suslina 529
Concerning interaction of the activator with not fully symmetrical local vibrations - N.N.Kristofel' 530
Contribution to the theory of electronic-vibrational transitions in crystals and molecules - K.K.Rebane & O.I.Sil'd 532
Contribution to the theory of luminescence of activated phosphors - A.M. Ratner & G.E.Zil'berman 533
Luminescence of copper-activated glasses - G.O.Karapetyan 535
Investigation of photoluminescence and scintillation of silicate glasses - S.M.Brekhovskikh & I.F.Shapovalova 537
Luminescence of crystals surface-activated with uranyl ions - G.I.Kobyshev 539
Luminescence of LiF crystals activated by uranyl nitrate - E.P.Alekseeva 541
Influence of infrared light on the luminescence of silver chloride - V.M.Belous & N.G.D'yachenko 543
Luminescence of uranium activated sodium and lithium fluoride single crystals - L.M.Belyaev, G.F.Dobrzhanskii & P.P.Feofilov 545

Investigation of the relaxation time of the photodielectric effect in ZnS:Cu:Co phosphor - G.M.Malkin 553
Concurrent investigation of the photodielectric effect and light sum stored in ZnS:Cu:Co phosphor - G.M.Malkin 556
Closing address - V.L.Levshin 559

Transactions of the Eleventh Annual Conference on Nuclear Spectroscopy

Number 2

Structure of light nuclei - V.V.Balashov, V.G.Neudachin & Yu.F.Smirnov 165
Shape of the β-spectrum of A^{41} - G.R.Kartashov, N.A.Burgov & A.V.Davydov 184
Conversion electron spectrum of the holmium fraction formed in proton bombardment of Ta - A.S.Basina, K.Ya.Gromov, B.S.Dzhelepov & V.A.Morozov 188
Relative intensities of some gamma-lines in the spectrum of Ta^{182} - V.D.Vitman, N.A.Voinova, B.S.Dzhelepov & A.A.Karan 192
Relative intensities of gamma-rays from RaC in the 1300 to 2520 keV region - V.D.Vitman, B.S.Dzhelepov & A.A.Karan 194
Gamma-radiation from Eu^{146} - E.E.Berlovich, V.N.Klement'ev, L.V.Krasnov & M.K.Nikitin 200
Levels of Eu^{147}, Eu^{149} and Au^{151} - E.E.Berlovich, V.N.Klement'ev, L.V.Krasnov & M.K.Nikitin 204
Measurements of the lifetimes of the first excited states of Tb^{159} and Yb^{173} by means of a multichannel time analyzer - E.E.Berlovich, M.P.Bonitz & V.V.Nikitin 210
Determination of the K fluorescence coefficients of V^{51}, Mn^{55}, Cu^{65} and Ga^{71} - A.A.Konstantinov, I.A.Sokolova & T.E.Sazonova 219
Gamma-radiation from Ta^{182} - N.A.Voinova, B.S.Dzhelepov & Yu.V.Khol'nov 223
A high-resolution ionization alpha-spectrometer - G.E.Kocharov & G.A.Korolev 227
A mercury gamma-calorimeter - E.A.Khol'nova 246
Two-crystal spectrometer and its use for investigating the (p,γ) reaction - Yu.P.Antuf'ev, V.Yu.Gonchar, E.G.Kopanets, A.N.L'vov & S.P.Tsytko 249
Radiative proton capture by S^{34} - Yu.P.Antuf'ev, A.K.Val'ter, V.Yu.Gonchar, E.G.Kopanets, A.N.L'vov & S.P.Tsytko 252
Measurement of the number of gamma-rays per decay of Mo^{99} - A.N.Silant'ev 256
Measurement of the number of gamma-rays per decay of Ba^{140} and Pr^{144} - B.S.Kuznetsov & A.N.Silant'ev 258
Conversion transitions accompanying β-decay of Th^{229} and the level diagram for Ra^{225} - E.F.Tret'yakov, N.I.Pirogova & L.L.Gol'din 260
Concerning electromagnetic transitions of multipole order $L = |J_i + J_f| + 1$ - M.E.Voikhanskii 271
Distinctive features of deformed odd-odd nuclei with K = 0 - D.A. Varshalovich & L.K.Peker 274
Concerning selection rules for β- and γ-transitions in odd-odd nuclei - M.E.Voikhanskii & L.K.Peker 284
Yield of gamma-radiation in inelastic scattering of neutrons from antimony nuclei - D.L.Broder, A.I.Lashuk & I.P.Sadokhin 296

Number 7

New results in the theory of nonaxial nuclei - A.S.Davydov 793
Calculation of the probability of the Auger effect - M.A.Listengarten 803
Investigation of the decay scheme of Gd^{147} - A.A.Sorokin & K.P.Mitrofanov 810
Investigation of the decay scheme of Gd^{149} - A.A.Sorokin & K.P.Mitrofanov 819

Investigation of neutron-deficient Tb isotopes - A.T.Strigachev, L.S. Novikov, A.A.Sorokin, V.A.Khalkin, N.V.Tsvetkova & V.S.Shpinel' 824
Positron spectra of neutron deficient terbium and neodymium isotopes - N.A.Bonch-Osmolovskaya, B.S.Dzhelepov, O.E.Kraft & Chou Yüeh-wa 837
Investigation of Coulomb excitation of nuclear levels by means of multiply charged ions - D.S.Andreev, V.D.Vasil'ev, G.M.Gusinskii, K.I.Erokhina & I.Kh.Lemberg 842
Beta- and gamma-spectra of radioactive Sb^{113} and Sb^{115} and a new Sn^{113} isomer - I.P.Selinov, V.L.Chikhladze, D.E.Khulelidze & N.A.Vartanov 857
Investigation of the levels of P^{31} by means of the $Si^{30}(p,\gamma)P^{31}$ reaction - A.K.Val'ter, S.P.Tsytko, Yu.P.Antuf'ev, E.G.Kopanets & A.N.L'vov 862
Total ionization produced by alpha-particles in gas mixtures - G.E.Kocharov 873
Concerning the operation of proportional counters - G.A.Korolev & G.E. Kocharov 877
Atomic masses of tin and antimony isotopes - R.A.Demirkhanov, T.I.Gutkin, O.A.Samadashvili & I.K.Karpenko 882
Alpha-decay to electron capture ratios for Po^{200}, Po^{201} and Po^{203} - B.N.Belyaev, A.V.Kalyamin & A.N.Murin 886
Reduced derivative width δ_L^2 for polonium isotopes - B.N.Belyaev, A.V. Kalyamin & A.N.Murin 890
Calculation of yield cross sections for spallation reactions - V.I. Baranovskii & A.N.Murin 893
Emission, absorption and reabsorption of gamma-rays by impurity nuclei in solid solutions - I.P.Dzyub & A.F.Lubchenko 903
Resonance scattering of gamma-rays by nuclei in a solid - I.P.Dzyub & A.F.Lubchenko 911

Number 9

Magnetic spectrometer for detecting internal conversion electrons from the (n,γ) reaction - V.I.Pelekhov & A.F.Malov 1077
Investigation of the positron and conversion electron spectra of Tb^{152} - K.Ya.Gromov, B.S.Dzhelepov, Zh.T.Zhelev & A.V.Kudryavtseva 1092
Internal conversion coefficients of some transitions in Yb^{171} - N.M. Anton'eva & B.S.Dzhelepov 1096
Conversion electron spectrum of Tm^{165} - Kang Meng-Hua, Ya.Gromov, B.S. Dzhelepov, V.Zvol'ska & I.Zvol'skii 1099
Conversion electrons from the erbium fraction formed in spallation of tantalum - A.A.Abdurazakov, K.Ya.Gromov, B.S.Dzhelepov & V.A.Khalkin 1103
Decay scheme of Eu^{147} - I.Vizi, K.Gromov, B.Dzhelepov, Zh.Zhelev & Yu. Yazvitskii 1108
Investigation of the conversion electron spectra of neutron-deficient isotopes of erbium and holmium - K.Ya.Gromov & I.S.Dneprovskii 1112
Investigation of the radiation of Mn^{56} - S.S.Vasil'ev, No Sen Ch'ang & L.Ya.Shavtvalov 1122
Properties of low-lying states of Li^5 and Be^8 evinced in disintegration reactions involving light nuclei - S.S.Vasil'ev, V.V.Komarov & A.M. Popova 1124
Electron-neutrino angular correlation in free neutron decay - V.V. Vladimirskii, V.K.Grigor'ev, V.A.Ergakov, D.P.Zharkov, & Yu.V. Trebukhovskii 1128
Remarks on the excited states of the odd-odd nuclei Ho^{166} and Cs^{134} - L.F.Kalinkin, A.S.Melioranskii & I.V.Estulin 1130

Levels in Cu^{64}, excited in the $Ni^{64}(p,n\gamma)Cu^{64}$ reaction - A.K.Val'ter, I.I.Zalyubovskii, A.P.Klyucharev & V.A.Lutsik 1133
Polarization of the γ-rays from the $Si^{30}(p,\gamma)P^{31}$ reaction - P.M. Tutakin 1137
Levels excited in the $F^{19}(\alpha,p)Ne^{22}$ reaction - A.M.Romanov, E.V.Myakinin & M.P.Konstantinova 1140
Spin and parity assignments for some states of Cd^{112}, Sn^{118} and Sn^{120} - O.F.Nemets & V.V.Tokarevskii 1143
Angular distribution of photoelectrons ejected from Ag and Bi targets by Cs^{137} γ-rays - K.K.Aglintsev, V.V.Mitrofanov, A.A.Rimskii-Korsakov & V.V.Smirnov 1146
Excited states of Li^7 with energies up to 9 MeV - V.G.Shevchenko & B.A. Yur'ev 1151
On the influence of collective excitations of the superfluid phase in nuclei on the nuclear moments of inertia - B.B.Dotsenko 1154
Pair correlations and single-nucleon reduced level widths in nuclei - V.B.Belyaev & B.N.Zakhar'ev 1157
Probabilities for E2 and E1 transitions from some excited levels in Tb^{159}, Ho^{165} and Tm^{169} - V.I.Popov 1160
On the possibility of determining reduced widths from polarization effects in direct nuclear reactions - G.L.Vysotskii 1166
Rotational states of nonspherical even-even nuclei - V.I.Belyak & D.A.Zaikin 1168
On collection excitations in nonspherical nuclei - Yu.T.Grin' & D.F. Zaretskii 1174
Investigation of the decay scheme of Eu^{145} - Yu.A.Aleksandrov & M.K. Nikitin 1181
Quadrupole moments and isotope shifts of barium isotopes - N.I.Kaliteevskii, E.E.Fradkin & M.P.Chaika 1183
Generator of short light pulses - G.S.Vil'dgrube, Yu.A.Kolosov & Zh.M. Ronkin 1185
Light-pulse characteristics of louvre type photomultipliers - G.S.Vil'dgrube, N.K.Dalinenko, N.V.Dunaevskaya & Zh.M.Ronkin 1188
Numbers of photons per decay of Ce^{144} and Eu^{155} - A.N.Silant'ev & B.S.Kuznetsov 1191
Use of an ionization α-spectrometer with a time analyzer for determining decay periods - Yu.M.Volkov, A.P.Komar, G.A.Korolev & G.E.Kocharov 1193

Number 10

Investigation of the properties of strongly deformed nuclei on the basis of a nuclear model taking into account pair correlations - V.G.Solov'ev 1207
$Yb^{166} \rightarrow Tm^{166} \rightarrow Er^{166}$ decay chain - E.P.Grigor'ev, K.Ya.Gromov, B.S. Dzhelepov, Zh.T.Zhelev, V.Zvol'ska & I.Zvolskii 1227
Coincidences between conversion electrons emitted in the decay of Ho^{160} and Dy^{160} - B.S.Dzhelepov, I.Zvol'skii & V.Z.Sergienko 1238
Coincidences between conversion electrons of the dysprosium fraction from proton bombarded tantalum - B.S.Dzhelepov, I.Zvol'skii, M.K.Nikitin & V.A.Sergienko 1257
Supplementary data on neutron-deficient osmium isotopes - T.V.Malysheva & B.A.Khotin 1267
Investigation of the conversion electron spectrum of neutron-deficient platinum isotopes - L.N.Kryukova, V.V.Murav'eva, L.Duda, T.V.Malysheva & B.A.Khotin 1269

Investigation of the radiation from neutron-deficient hafnium isotopes - B.Brabec, B.Kracik, T.Kracikova, Z.Miligi, M.Weis, A.Mashtalka, M.Vobecky & V.Gnatovicz 1277
Photodisintegration of Li^7 by bremsstrahlung of up to 9.5 MeV - V.G.Shevchenko & B.A.Yur'ev 1280
Probabilities for single-particle transitions in Yb^{173} - E.E.Berlovich, M.P.Bonitz, Yu.K.Gusev & M.K.Nikitin 1286
Gamma-rays produced in inelastic scattering of 2.95 MeV neutrons by I^{127}, La^{139} and Bi^{209} - L.Ya.Graudynya, K.A.Petrzhak & A.V.Sorokina 1291
Semiconductor spectrometers for charged particles - L.A.Zubritskii, A.I.Popov, P.V.Sorokin & V.F.Samoilov 1296
Eleven-counter instrument for measuring γ-γ angular correlation - A.I.Belyaevskii & Yu.A.Gur'yan 1300
Beta-spectrometer with two fold $\pi\sqrt{2}$ focusing - S.A.Shestopalova 1312
Use of an ionization chamber for particle selection by measuring E(dE/dx) - Yu.V.Gofman, V.N.Dobrikov, N.I.Zaika & O.F.Nemets 1315
Spin and parity assignments for some states of Si^{30}, Zr^{91}, Zr^{92} and Cd^{114} - N.I.Zaika & O.F.Nemets 1317

Transactions of the Symposium on Thin Ferromagnetic Films

Number 5

Thin magnetic films in present-day physics and engineering - K.M.Polivanov & A.L.Frumkin 569
Influence of the technique of preparation and thickness of thin ferromagnetic films of Fe-Ni-Mo alloy and their domain structure - L.V.Kirenskii & V.A.Buravikhin 572
Domain walls in thin ferromagnetic films - L.V.Kirenskii & V.A. Buravikhin 578
Domain structure and coercivity of thin ferromagnetic films - L.V.Kirenskii, V.A.Buravikhin & A.G.Zvegintsev 581
Domain structure of ferromagnetic films prepared by cathode sputtering - G.V.Spivak, I.G.Sirotenko & R.D.Ivanov 585
Investigation of the magnetic structure of thin ferromagnetic films by means of the Kerr magneto-optical effect - L.V.Kirenskii, S.V.Kan & I.F.Degtyarev 589
Behavior of the domain structure of thin ferromagnetic films in the process of slow magnetization reversal - L.V.Kirenskii & S.V.Kan 598
Variation of the domain structure of thin ferromagnetic films in a magnetic field - L.V.Kirenskii, V.A.Buravikhin & M.K.Savchenko 604
New procedure for measuring the thickness of domain walls by means of the Kerr effect - V.I.Sinegubov & M.V.Savchenko 609
Barkhausen effect in thin Mo-Permalloy films - M.M.Salanskii, A.M.Rodichev & M.K.Savchenko 612
Nucleation and the Barkhausen effect in ferromagnetic films - V.F.Ivlev & V.S.Prokopenko 616
Investigation of the duration of Barkhausen jumps in an iron film - G.M.Rodichev & P.D.Kim 620
Contribution to the theory of high field magnetization reversal in thin films - A.M.Rodichev 624
Apparatus for investigating pulse switching of thin ferromagnetic films - T.N.Nikitina & R.V.Telesnin 630

Nanosecond current pulse generator for investigating the behavior of ferromagnetic films - O.S.Kolotov & T.N.Nikitina 633
Amplification of nanosecond pulses - O.S.Kolotov & T.N.Nikitina 635
Domain structure of uniaxial ferromagnetic films - V.V.Kobelev & A.A.Korsunskii 639
Investigation of the switching time of ferromagnetic film elements - I.A.Efimov 647
Ferromagnetic resonance in thin films - L.V.Kirenskii, V.A.Ignatchenko & O.G.Baklanov 652
Measurement of the hysteresis loss in thin films in a rotating magnetic field - N.I.Sudakov, M.K.Savchenko, E.K.Zagirova & I.I.Starostin 655
Use of thin films for measurement of magnetostrictive and other strains - V.A.Yugov & G.P.D'yakov 659
Preparation of single crystal films - N.G.Nifontov 663
Some electric properties of very thin metal films - N.G.Nifontov 665
Magnetic properties of nickel deposits obtained by chemical plating - N.V.Kotel'nikov & V.I.Gachegov 668

Transactions of the Third All-Union Conference on Electron Microscopy

Number 6

Calculation of electron lens fields - A.G.Vlasov & D.M.Krupp 677
Concerning aberration of electron-optical systems - P.P.Kas'yankov & K.P.Dutova 680
Electron optics of probe systems - G.G.Dutov 683
Achromatization of lenses in multiple-lens magnetic electron microscopes - P.A.Stoyanov 687
Design of magnets for the lenses of magnetostatic electron microscopes - G.V.Der-Shvarts & V.P.Rachkov 691
Optics of the ÉM-5 and ÉM-7 electron microscopes - V.N.Vertsner, Yu.M. Vorona, Yu.V.Vorov'ev, G.A.Bogdanovskii & Yu.V.Chentsov 695
Mirror electron microscope for studying the structure of surfaces - G.V. Spivak, I.A.Pryamkova, D.V.Fetisov, A.N.Kabanov, L.V.Lazareva & A.I. Shilina 698
Some questions arising in the development of an x-ray microanalyzer - A.M.Solov'ev & V.N.Vertsner 706
Scanning electron microscope and x-ray microanalyzer - Yu.M.Kushnir, D.V.Fetisov, K.K.Raspletin, B.I.Pochtarev, F.U.Spektor, A.N.Kabanov & V.F.Anisimov 709
Use of gas microcells in electron microscopy - I.G.Stoyanova 715
The UIT-3 unit for etching metals, semiconductors and dielectrics by ion bombardment - G.V.Spivak, F.F.Kushnir & V.E.Yurasova 722
Magnetic objective lens for an emission electron microscope - A.M. Rozenfel'd & P.V.Zaitsev 726
Investigation of the magnetic circuits of electron microscope lenses - P.A.Stoyanov & L.Yu.Vol'fson 730
Modernization of the UEM-100 electron microscope - G.V.Der-Shvarts, Yu.M. Kushnir, L.B.Rozenfel'd, P.V.Zaitsev & S.V.Bezlepkin 733
Electron-optical measurements of electric and magnetic microfields on surfaces - N.N.Sedov, G.V.Spivak & N.F.Isaeva 737
Procedure for determining the work function of microsections on the surface of thermionic cathodes - A.V.Druzhinin 742

Electron microscopic investigation of semiconductor whiskers - I.G.Sirotenko, G.V.Spivak, I.G.Stoyanova & Z.M.Osad'ko 748
Structure and emf of photovoltaic PbS layers prepared by vacuum sublimation - R.Ya.Berlaga & M.I.Rudenok 751
Electron microscopic observation of magnetic microfields by means of replicas - L.V.Lazareva & G.V.Spivak 753
Objective method of recording electron energy spectra with an electrostatic analyzer - A.N.Kabanov, Yu.M.Kushnir & D.V.Fetisov 759
Use of an analyzer for investigating the energy distribution of electrons reflected from metals - Yu.M.Kushnir & A.N.Kabanov 762
Ion-optical technique for preparing small diameter apertures - L.B. Rozenfel'd & A.I.Makarov 764
Investigation of some types of photographic plates suitable for use in electron microscopy - I.S.Renskii & P.A.Stoyanov 766
Some characteristics of carbon and silica replicas made from polished surfaces - L.V.Lazareva & T.F.Filippova 769
Evaluation of the performance of the UMT-2 ultramicrotome - Ya.Yu. Komissarchik & V.F.Mashanskii 772
Armored high-voltage lead-in - D.V.Fetisov & A.N.Kabanov 775
High-voltage source with a high degree of regulation - A.V.Iz'yurov 777
Power supply for a microscope with a resolution of 5 A - V.V.Polivanov, R.V.Pogudina & V.V.Il'in 780
Vacuum system selector valve with one control knob - D.V.Fetisov, B.I. Pochtarev & A.N.Kabanov 785

Transactions of the Fifth Conference on X-ray Spectroscopy

Number 8

Use of x-ray bremsstrahlung for investigation of absorption spectra in the ultrasoft region - A.P.Lukirskii 923
Spectrometer for ultrasoft x-radiation with combined detection by means of secondary-electron multipliers and a Geiger counter - A.P.Lukirskii 926
Microfocus x-ray spectrograph - I.B.Borovskii, S.A.Ditsman & V.G.Bogdanov 932
Investigation of the region of a microfocus source in an x-ray microanalyzer - S.A.Ditsman 935
On the possibility of quantitative analysis by means of x-ray spectra without the use of standards - N.P.Il'in 940
Vacuum x-ray spectrometer with ionization recording - V.A.Batyrev & V.G. Bogdanov 944
Constant vacuum x-ray tube for a long-wavelength x-ray spectrometer - K.I.Narbutt, E.M.Fridman & G.M.Nikolaenko 947
Reflection of hard x-radiation by bent crystals - S.A.Ditsman 949
Regarding the resolution of Johann mounting single-crystal spectrographs - N.D.Borisov & V.V.Nemoshkalenko 954
Experimental investigation and calculation of the L absorption spectra of noble gases - R.L.Barinskii 958
Regarding the asymmetry of the $K\alpha_1$ and $K\alpha_2$ lines of atoms of the iron group - L.K.Izraileva 965
Theory of the fine structure of x-ray absorption spectra - A.I.Kozlenkov 968
Contribution to the theory of the temperature dependence of the fine structure of x-ray absorption spectra - V.V.Shmidt 988

Influence of tungsten impurities on the temperature dependence of the K absorption spectrum of iron - I.B.Borovskii & V.V.Shmidt 994
Influence of the chemical bond on the energy and intensity of the x-ray lines of atoms in compounds - A.T.Shuvaev 996
Investigation of the K absorption spectra of calcium in some compounds - A.T.Shuvaev & V.F.Demekhin 1001
Investigation of the binding forces in Ni-Mo solid solutions by observing the fine structure of the absorption spectra - V.A.Trapeznikov 1003
X-Ray spectroscopic investigation of intermetallic compounds in the Cu-Zn system - V.A.Batyrev 1006
Influence of thermal vibrations of atoms on the process of "melting" of the fine structure of the x-ray absorption spectra. I. Investigation of a Cu-Pt solid solution - I.B.Borovskii & G.N.Ronami 1008
Concerning the electron configuration in metals of the iron group - N.D.Borisov & V.V.Nemoshkalenko 1011
The $K\beta_x$ emission band and K absorption edge of aluminum in some alloys with transition metals - S.A.Nemnonov & L.D.Finkel'shtein 1015
Computer for correcting the shape of emission spectra - M.I.Korsunskii & Ya.E.Genkin 1020
Comparison of two methods of correcting experimental curves (column and matrix methods) - Ya.E.Genkin & I.A.Rumyantsev 1023
Corrected $L\beta_2$ emission band in the spectra of pure niobium and its compounds - M.I.Korsunskii & Ya.E.Genkin 1033
On determining the Fermi level from x-ray emission bands - M.I.Korsunskii & Ya.E.Genkin 1036
On finding the true shape of spectra using the Shannon approximation - V.P.Sachenko 1043
Concerning the shape of the $K\beta_5$ emission band of iron. Part I - I.Ya.Nikiforov 1048
On the "derivative method" for correcting the shape of spectra - V.P.Sachenko 1052
Comparison of different methods of correcting the shape of spectra - I.Ya.Nikiforov, V.P.Sachenko & M.A.Blokhin 1057
Concerning the use of secondary-emission multipliers for investigating soft x-ray spectra - M.A.Rumsh, A.P.Lukirskii & V.N.Shchemelev 1063
Quantum sensitivity of photographic materials to x-radiation with wavelengths from 1.54 to 113 A - M.A.Rumsh, V.N.Shchemelev & A.P.Lukirskii 1069

Transactions of the Conference on Ferromagnetism & Antiferromagnetism

Number 11

Some aspects of the modern theory of ferro- and antiferromagnetism (Condensation of a review) - S.V.Vonsovskii 1325
Non-collinear ferro- and antiferromagnetism - E.A.Turov 1326
Influence of the magnetic sublattice structure of ferrites on their physical properties - K.P.Belov 1332
Regarding the normal energy state of ferrite with three magnetic sublattices - A.A.Gusev & A.S.Pakhomov 1338
Concerning the coexistence of the ferroelectric and ferrimagnetic states - G.A.Smolenskii, V.A.Isupov, N.N.Krainik & A.I.Agranovskaya 1345
Energy spectrum of current carriers in ferro- and antiferromagnets - E.K.Kudinov & A.G.Samoilovich 1351

Contribution to the theory of kinetic effects in NiO type semiconductors - M.I.Klinger 1354
Contribution to the theory of nonresonance absorption of an alternating magnetic field by a ferromagnetic dielectric at low temperatures - M.I.Kaganov & V.M.Tsukernik 1358
Concerning a mechanism of absorption of the longitudinal magnetic field by a ferromagnetic dielectric - M.I.Kaganov & V.M.Tsukernik 1364
Temperature dependence of the width of ferromagnetic resonance peaks - Mêng Hsien-Cheng 1366
Ferromagnetic resonance in ferrites in strong alternating magnetic fields - A.G.Gurevich & S.S.Starobinets 1371
Effect of induced anisotropy on ferromagnetic resonance - A.G.Gurevich, A.P.Safant'evskii, V.I.Solov'ev & E.S.Sher 1374
Experimental investigation of the effects in yttrium ferrite single crystals, associated with nutational oscillations of the magnetization of the material under conditions of ferromagnetic resonance - V.A. Fabrikov, V.P.Kozlov, V.T.Kadeev & V.D.Kudryavtsev 1380
Magnetic and resonance properties of yttrium-iron garnets with the Yt^{3+} ions replaced by Tb^{3+}, Nd^{3+} and Lu^{3+} ions - K.P.Belov & L.A.Malevskaya 1384
Effect of the boundary condition for the magnetic moment on spin-wave resonance in metals - M.I.Kaganov & Yü Liu 1388
Temperature dependence of the conductivity and Hall effect in metallic gadolinium - N.V.Volkenshtein & G.V.Fedorov 1391
Magnetoelastic properties of terbium and holmium (Partial report) - K.P.Belov, R.Z.Levitin, & S.A.Nikitin 1394
Determination of the parameters characterizing the cation distribution in multiple component spinels - A.N.Men' 1396
Magnetization and the magnetocaloric effect in uranium hydride and deuteride - A.I.Karchevskii & E.M.Buryak 1400
Magnetic anisotropy and hysteresis properties of rare earth orthoferrites - K.Belov, M.A.Zaitseva, A.M.Kadomtseva & V.A.Timofeeva 1401
Investigation of ferrimagnets with the structure of magnetoplumbite and garnet in strong pulse magnetic fields - G.A.Smolenskii & A.A.Andreev 1405
Investigation of the magnetic properties of some ferromagnets with the structure of perovskite and garnet - G.A.Smolenskii, V.P.Polyakov & V.M.Yudin 1408
Temperature dependence of the paramagnetic susceptibility of mixed ferrites - V.I.Chechernikov 1411
Frequency and temperature dependences of the initial permeability of ferrites with the garnet structure - G.A.Smolenskii, Chang Tsung & E.S.Sher 1414
Viscosity and hysteresis properties of ferrites, due to electron diffusion - K.M.Bol'shova & T.A.Elkina 1418
Effect of gamma-irradiation on disaccomodation in Ni-Zn ferrites - E.I.Trinkler, V.A.Gol'din & V.B.Osipov 1422
Concerning correlation between the electric and magnetic properties of Ni-Zn ferrites - L.I.Rabkin & Z.I.Novikova 1424
Phase equilibrium in the Fe_2O_3-BaO system - B.G.Livshits, S.A.Eliseev, B.A.Samarin & V.A.Somenkov 1429
Some possibilities of improving the quality of microwave ferrites - F.I.Kolomoitsev, F.F.Kodzhesnirov, A.Ya.Yakunin & E.V.Sinyakov 1432
Synthesis of multiple component ferrites with high magnetostrictive parameters - P.L.Strelets, L.N.Syrkin & M.G.Tkachenko 1436

Ferrites at high saturation magnetization and a narrow resonance absorption line at microwave frequencies - V.A.Fabrikov, Z.M.Gushchina & V.D. Kudryavtsev 1440
Measurement of the parameters of ferromagnetic resonance in polycrystalline ferrites at liquid helium temperature - G.S.Misezhnikov, Ya.I.Rozenberg & V.B.Shteinshleiger 1441

Number 12

Change in conductivity incident to magnetization and magnetic anisotropy in ferrite single crystals of the $Mn_xFe_{3-x}O_4$ system - K.P.Belov & A.V. Zalesskii 1447
Temperature dependence of the low-field magnetization of manganese ferrite - E.F.Kovtun & A.S.Mil'ner 1450
Behavior of domain structure during magnetization - V.A.Ignatchenko, I.F. Degtyarev & Yu.V.Zakharov 1452
Variation of the magnetization switching process with reduction in particle size - E.V.Shtol'ts, A.A.Glazer & Ya.S.Shur 1458
Investigation of domain walls in transformer steel - M.K.Savchenko & V.I.Sinegubov 1462
Influence of the direction of demagnetization on the magnetic structure of crystals in sheet silicon steel - V.R.Abel's 1466
Regarding the stability of the magnetic state of soft materials - V.A. Zaikova & I.E.Startseva 1469
Effect of ultrasonic vibration and alternating magnetic fields on the domain structure of silicon steel - D.A.Laptei & V.S.Cherkashin 1475
Development of mirror electron microscopy of magnetic microfields - G.V. Spivak, L.V.Kirenskii, R.D.Ivanov & N.N.Sedov 1481
Concerning the rectangularity of the hysteresis loops of Mg-Mn ferrites - I.E.Startseva & Ya.S.Shur 1485
Temperature dependence of the first anisotropy constant and the magnetic structure of Fe-Mn ferrites - L.V.Kirenskii, A.I.Drokin, V.D.Dylgerov, N.I.Sudakov & E.K.Zagirova 1488
Determination of the character of the magnetic anisotropy of alloys with single domain structure from their residual magnetization - M.G.Luzhinskaya 1492
On the nature of the coercive force in Alnico alloys - A.S.Ermolenko & Ya.S.Shur 1495
Carbonyl iron powders - V.L.Volkov, I.S.Tolmasskii & A.E.Fridenberg 1500
Investigation of rotational hysteresis in cold rolled and recrystallized nickel - N.L.Bryukhatov & N.A.Grinchar 1503
Rotational hysteresis of magnetostriction in ferromagnets - L.V.Kirenskii & V.S.Afoshin 1508
Crystal and magnetoelastic anisotropy and its temperature dependence in iron-nickel single crystals - I.M.Puzei 1511
Effect of the field strength in magnetic annealing on the magnetic properties of cold-rolled electrical steel - D.D.Nishin, T.I.Bychkova & V.A.Smagin 1515
Magnetic texture of ferromagnets subjected to external stresses - F.N.Dunaev 1519
Investigation of the effect of creep of nonsymmetrical hysteresis loops - O.V.Rosnitskii 1524
Stability of the magnetization of ferromagnets as a function of the magnetizing process - L.Ya.Frimerman 1528

Magnetization and magnetostriction jumps in nickel - A.Ya.Vlasov & Yu.D.Tropin 1532
Effect of mechanical factors on the magnetic structure and properties of alloys - L.N.Fedotov, V.P.Popova & B.V.Molotilov 1535
Properties of ferromagnetic films prepared by cathode sputtering - R.D.Ivanov, G.V.Spivak & G.K.Kislova 1541

RESUME OF THE CONFERENCE TRANSACTIONS PUBLISHED IN VOLUME 25

of the

BULLETIN OF THE USSR ACADEMY OF SCIENCES

- Physical Series -

	Issue No.
Nuclear spectroscopy (Tenth Conference - concluded from Vol. 24)	1
Crystal phosphors (Ninth Conference on Luminescence - Crystal Phosphors)	1, 3 & 4
Nuclear spectroscopy (Eleventh Conference on Nuclear Spectroscopy)	2,7,9 & 10
Thin ferromagnetic films (Symposium on Thin Ferromagnetic Films)	5
Electron microscopy (Third Conference on Electron Microscopy)	6
X-Ray spectroscopy (Fifth Conference on X-Ray Spectroscopy)	8
Ferromagnetism & antiferromagnetism (Conference on Ferromagnetism & Antiferromagnetism)	11 & 12

Columbia Technical Translations
5 Vermont Ave., White Plains, N.Y.